Related titles

Polymer Composites in the Aerospace Industry
(ISBN 978-0-85709-523-7)

Fatigue and Fracture of Adhesively-bonded Composite Joints
(ISBN 978-0-85709-806-1)

Fatigue of Textile Composites
(ISBN 978-1-78242-281-5)

Woodhead Publishing Series in Composites Science and Engineering: Number 57

Structural Integrity and Durability of Advanced Composites

Innovative Modelling Methods and Intelligent Design

Edited by

P.W.R. Beaumont, C. Soutis and A. Hodzic

AMSTERDAM • BOSTON • CAMBRIDGE • HEIDELBERG
LONDON • NEW YORK • OXFORD • PARIS • SAN DIEGO
SAN FRANCISCO • SINGAPORE • SYDNEY • TOKYO
Woodhead Publishing is an imprint of Elsevier

Woodhead Publishing is an imprint of Elsevier
80 High Street, Sawston, Cambridge, CB22 3HJ, UK
225 Wyman Street, Waltham, MA 02451, USA
Langford Lane, Kidlington, OX5 1GB, UK

British Library Cataloguing-in-Publication Data
A catalogue record for this book is available from the British Library

Library of Congress Control Number: 2015931793

ISBN 978-0-08-100137-0 (print)
ISBN 978-0-08-100138-7 (online)

List of contributors

R.D. Adams University of Bristol, Bristol, UK; University of Oxford, Oxford, UK

H. Arora Imperial College London, London, UK

K.H.G. Ashbee Shrewsbury, UK

I.A. Ashcroft University of Nottingham, Nottingham, UK

E. Barbieri Queen Mary University of London, London, UK

P.W.R. Beaumont Cambridge University Engineering Department, Cambridge, UK

N. Bellinger National Research Council of Canada, Ottawa, ON, Canada

T. Breitzman Air Force Research Laboratory, Dayton, OH, USA

R. Brighenti University of Parma, Parma, Italy

A.R. Bunsell Mines ParisTech, Paris, France

P.A. Carraro University of Padova, Vicenza, Italy

N. Carrère LBMS, ENSTA Bretagne, Univ. Brest, Brest, France

J.P. Casas-Rodriguez Universidad de los Andes, Bogota, Colombia

A. Collins University of Bristol, Bristol, UK

D. Cooper University of Bristol, Bristol, UK

J.L. Curiel-Sosa University of Sheffield, Sheffield, UK

J.P. Dear Imperial College London, London, UK

M.W. Digby University of Bristol, Bristol, UK

R.G. Dillingham Brighton Technologies Group, Inc., Cincinnati, OH, USA

A.W. Farmer University of Bristol, Bristol, UK

S. Fischer Institute of Aircraft Design, University Stuttgart, Stuttgart, Germany

C. Gonzalez IMDEA Materials Institute, Getafe, Madrid, Spain; Polytechnic University of Madrid, Madrid, Spain

R.M. Groves Delft University of Technology, Delft, The Netherlands

I.A. Guz University of Aberdeen, Aberdeen, UK

E.V. Iarve University of Dayton Research Institute, Dayton, OH, USA

A. Johnson Stuttgart, Germany (formerly of German Aerospace Center (DLR), Stuttgart, Germany)

M. Kashtalyan University of Aberdeen, Aberdeen, Scotland, UK

M. Kelly Imperial College London, London, UK

S. Kilchert Fraunhofer Ernst Mach Institute, Germany (formerly of German Aerospace Center (DLR), Stuttgart, Germany)

Y.W. Kwon Naval Postgraduate School, Monterey, CA, USA

A. Laurence University of Bristol, Bristol, UK

D. Leguillon IJLRA, CNRS UMR 7190, Univ. P. et M. Curie, Paris, France

J. LLorca IMDEA Materials Institute, Getafe, Madrid, Spain; Polytechnic University of Madrid, Madrid, Spain

C.S. Lopes IMDEA Materials Institute, Getafe, Madrid, Spain

S. Lurie Institute of Applied Mechanics of Russian Academy of Sciences, Moscow, Russia

E. Martin LCTS, CNRS UMR 5801, Univ. Bordeaux, Pessac, France

F. Martínez-Hergueta IMDEA Materials Institute, Getafe, Madrid, Spain

M. Martinez Delft University of Technology, Delft, The Netherlands

G. Meneghetti University of Padova, Padova, Italy

M. Menshykova University of Aberdeen, Aberdeen, UK

M. Minhat UniKL Malaysian Institute of Aviation Technology, Dengkil, Malaysia

Y. Miyano Kanazawa Institute of Technology, Hakusan, Japan

M. Nakada Kanazawa Institute of Technology, Hakusan, Japan

G.C. Papanicolaou University of Patras, Patras, Greece

K. Patel University of Bristol, Bristol, UK

D.V. Portan University of Patras, Patras, Greece

A. Poursartip The University of British Columbia, Vancouver, BC, Canada

M. Quaresimin University of Padova, Vicenza, Italy

B. Rasuo University of Belgrade, Belgrade, Serbia

M. Ricotta University of Padova, Padova, Italy

E.R. Ripberger Air Force Research Laboratory, Dayton, OH, USA

B. Rocha National Research Council of Canada, Ottawa, ON, Canada

S. Roy University of Alabama, Tuscaloosa, AL, USA

M.B. Ruggles-Wrenn Air Force Institute of Technology, Wright-Patterson Air Force Base, OH, USA

S. Sádaba IMDEA Materials Institute, Getafe, Madrid, Spain

R.M. Sencu University of Manchester, Manchester, UK

M.C. Serna Moreno Mecánica de los Medios Continuos y Teoría de Estructuras, E.T.S.I. Industriales, Ciudad Real, Spain

V.V. Silberschmidt Loughborough University, Loughborough, UK

C.V. Singh University of Toronto, Toronto, ON, Canada

C. Soutis University of Manchester, Manchester, UK

M. Stevens University of Bristol, Bristol, UK

R. Talreja Texas A&M University, College Station, TX, USA; Luleå University of Technology, Luleå, Sweden

A. Thionnet Mines ParisTech, Paris, France; Université de Bourgogne, Dijon, France

N. Toso-Pentecôte German Aerospace Center (DLR), Stuttgart, Germany

J. Varna Lulea University of Technology, Lulea, Sweden

Y.C. Wang University of Manchester, Manchester, UK

R. Watkins University of Bristol, Bristol, UK

Z.J. Yang University of Manchester, Manchester, UK; Zhejiang University, Hangzhou, China

M. Yanishevsky National Research Council of Canada, Ottawa, ON, Canada

R.J. Young University of Manchester, Manchester, UK

N. Zobeiry The University of British Columbia, Vancouver, BC, Canada

Woodhead Publishing Series in Composites Science and Engineering

1 **Thermoplastic aromatic polymer composites**
F. N. Cogswell
2 **Design and manufacture of composite structures**
G. C. Eckold
3 **Handbook of polymer composites for engineers**
Edited by L. C. Hollaway
4 **Optimisation of composite structures design**
A. Miravete
5 **Short-fibre polymer composites**
Edited by S. K. De and J. R. White
6 **Flow-induced alignment in composite materials**
Edited by T. D. Papthanasiou and D. C. Guell
7 **Thermoset resins for composites**
Compiled by Technolex
8 **Microstructural characterisation of fibre-reinforced composites**
Edited by J. Summerscales
9 **Composite materials**
F. L. Matthews and R. D. Rawlings
10 **3-D textile reinforcements in composite materials**
Edited by A. Miravete
11 **Pultrusion for engineers**
Edited by T. Starr
12 **Impact behaviour of fibre-reinforced composite materials and structures**
Edited by S. R. Reid and G. Zhou
13 **Finite element modelling of composite materials and structures**
F. L. Matthews, G. A. O. Davies, D. Hitchings and C. Soutis
14 **Mechanical testing of advanced fibre composites**
Edited by G. M. Hodgkinson
15 **Integrated design and manufacture using fibre-reinforced polymeric composites**
Edited by M. J. Owen and I. A. Jones
16 **Fatigue in composites**
Edited by B. Harris
17 **Green composites**
Edited by C. Baillie
18 **Multi-scale modelling of composite material systems**
Edited by C. Soutis and P. W. R. Beaumont

19 **Lightweight ballistic composites**
Edited by A. Bhatnagar
20 **Polymer nanocomposites**
Y-W. Mai and Z-Z. Yu
21 **Properties and performance of natural-fibre composite**
Edited by K. Pickering
22 **Ageing of composites**
Edited by R. Martin
23 **Tribology of natural fiber polymer composites**
N. Chand and M. Fahim
24 **Wood-polymer composites**
Edited by K. O. Niska and M. Sain
25 **Delamination behaviour of composites**
Edited by S. Sridharan
26 **Science and engineering of short fibre reinforced polymer composites**
S-Y. Fu, B. Lauke and Y-M. Mai
27 **Failure analysis and fractography of polymer composites**
E. S. Greenhalgh
28 **Management, recycling and reuse of waste composites**
Edited by V. Goodship
29 **Materials, design and manufacturing for lightweight vehicles**
Edited by P. K. Mallick
30 **Fatigue life prediction of composites and composite structures**
Edited by A. P. Vassilopoulos
31 **Physical properties and applications of polymer nanocomposites**
Edited by S. C. Tjong and Y-W. Mai
32 **Creep and fatigue in polymer matrix composites**
Edited by R. M. Guedes
33 **Interface engineering of natural fibre composites for maximum performance**
Edited by N. E. Zafeiropoulos
34 **Polymer-carbon nanotube composites**
Edited by T. McNally and P. Pötschke
35 **Non-crimp fabric composites: Manufacturing, properties and applications**
Edited by S. V. Lomov
36 **Composite reinforcements for optimum performance**
Edited by P. Boisse
37 **Polymer matrix composites and technology**
R. Wang, S. Zeng and Y. Zeng
38 **Composite joints and connections**
Edited by P. Camanho and L. Tong
39 **Machining technology for composite materials**
Edited by H. Hocheng
40 **Failure mechanisms in polymer matrix composites**
Edited by P. Robinson, E. S. Greenhalgh and S. Pinho
41 **Advances in polymer nanocomposites: Types and applications**
Edited by F. Gao
42 **Manufacturing techniques for polymer matrix composites (PMCs)**
Edited by S. Advani and K-T. Hsiao

43 **Non-destructive evaluation (NDE) of polymer matrix composites: Techniques and applications**
Edited by V. M. Karbhari
44 **Environmentally friendly polymer nanocomposites: Types, processing and properties**
S. S. Ray
45 **Advances in ceramic matrix composites**
Edited by I. M. Low
46 **Ceramic nanocomposites**
Edited by R. Banerjee and I. Manna
47 **Natural fibre composites: Materials, processes and properties**
Edited by A. Hodzic and R. Shanks
48 **Residual stresses in composite materials**
Edited by M. Shokrieh
49 **Health and environmental safety of nanomaterials: Polymer nanocomposites and other materials containing nanoparticles**
Edited by J. Njuguna, K. Pielichowski and H. Zhu
50 **Polymer composites in the aerospace industry**
Edited by P. E. Irving and C. Soutis
51 **Biofiber reinforcement in composite materials**
Edited by O. Faruk and M. Sain
52 **Fatigue and fracture of adhesively-bonded composite joints: Behaviour, simulation and modelling**
Edited by A. P. Vassilopoulos
53 **Fatigue of textile composites**
Edited by V. Carvelli and S. V. Lomov
54 **Wood composites – from nanocellulose to superstructures**
Edited by M. Ansell
55 **Toughening mechanisms in composite materials**
Edited by Q. Qin and J. Ye
56 **Advances in composites manufacturing and process design**
Edited by P. Boisse
57 **Structural integrity and durability of advanced composites: Innovative modelling methods and intelligent design**
Edited by P. W. R. Beaumont, C. Soutis and A. Hodzic
58 **Recent advances in smart self-healing polymers and composites**
Edited by G. Li and H. Meng
59 **Manufacturing of nanocomposites with engineering plastics**
Edited by V. Mittal
60 **Fillers and reinforcements for advanced nanocomposites**
Edited by Y. Dong, R. Umer and A. Kin-Tak Lau
61 **Biocomposites: Design and mechanical performance**
Edited by M. Misra, J. K. Pandey and A. K. Mohanty
62 **Numerical modeling of failure in advanced composite materials**
Edited by P. Camanho and S. Hallett

This book is dedicated to the memory of, **Professor TONY KELLY** (1929–2014) of Cambridge University who played a major role in establishing the principles of fibre reinforcement of materials and thereby helped clear the ground for the emergence of contemporary composite materials in the new technology of engineering composite structures.

Tony Kelly and the editors assembled at a luncheon in 2014 when the progress in writing this book was assessed and the major themes of a Royal Society Research Meeting in 2016 based upon the book's chapters were considered.

Editors' Foreword

It is an unusual privilege for us to assist in the writing of this book on such an occasion and on a topic in materials science and the various connecting branches of engineering. The subject matter is self-evident when the purpose of producing this book was to mark the 85th birthday of Anthony Kelly, known to those in the field of composite materials as Tony. It is with sadness that Tony died in the year of its preparation and never saw its completion.

Tony Kelly served on many bodies charting the development of materials of high-knowledge content, often referred to as *advanced materials.* His innovative contributions to materials in general and composite materials in particular were enormous, recognized and justly awarded with the highest accolades in science and engineering. He was a world-renowned researcher, scientist, Founding Fellow of Churchill College and Emeritus Professor of the Department of Materials Science at Cambridge University. Tony's brilliance, enthusiasm, unquenched intellectual curiosity and vision are inspirational as we shall see throughout the pages of this book.

It was to the speakers of a recent 3-day meeting at Queens' College, Cambridge to celebrate Tony's 85th that we turned for our chapter writers. We saw this occasion as an opportunity to bring together the viewpoints of top researchers and those tailoring material properties to today's needs. We hope this book will act as a spur to their alignment of objectives, from the exciting but rather academic goals in the attainment of specific properties and behaviour, to the pragmatic but still exciting objectives in the manufacture and performance of the final structure.

As editors, we were gratified by the extent to which the speakers accepted this brief and enriched their presentation in the writing of these chapters. This book is the better for the acceptance of a principal theme namely *Structural Integrity* and we hope that it will be the longer lasting because of it. While the *words of wisdom* of the speakers may not come across in the pages of this book, this assembly of chapters of significance does come through their excellence now presented.

We take this opportunity to thank the writers for their support in producing this book in honour of Tony Kelly.

Peter W.R. Beaumont
University of Cambridge

Constantinos Soutis
University of Manchester

Alma Hodzic
University of Sheffield

Foreword by Tony Kelly

The theme at the Queens' Meeting in Cambridge that emerged was the characterising of the new advanced materials and processes which are successful in the market place – leaner, cheaper, faster, lighter, sustainable machines and structures. The theme characterising the speakers and listeners especially in the discussion times was transmission of information and communication between researchers and end users, freely informed and sometimes humorous. And the conclusion, that forms the basis of the book which is to follow, is the need to reinforce the interactions between practitioner and researcher across disciplines.

I have enjoyed for many years the good fortune that has enabled me to mix in all cadres of society and helped me to clearly see my own activities in the context of those of my colleagues at the time. We must all look outwards and share information to mutual benefit, while recognising clearly and acknowledging the contribution each individual makes.

I am of course grateful to all who participated in this venture, to those who presented at Cambridge, to those who assisted by their presence, to those who will go on to write the chapters, and to those unable to come to the meeting and who wished me well in my 85th year.

Churchill College, Cambridge

Preface

Since the discovery and public announcement of carbon fibre 50 years ago only to be followed within 5 years by the dramatic failure of the carbon fibre compressor blades of the Rolls-Royce RB211 engine during impact by 'bird strike' under maximum load, there has been a plethora of papers published in a growing number of journals and books on a variety of aspects of composite materials behaviour and design methods of composite structures. But remarkably few (in percentage terms) have provided in-depth understanding of why composite materials fail and structures collapse over a spectrum of industrial applications and public sectors. In scientific terms, there has not been a thorough quantitative formulation of the relationships that connect processing and design of composite on the one hand, and durability and reliability of composite structure on the other. As a result, there lacks an appreciation of what structural integrity of a composite actually means. Structural integrity is the optimisation of microstructure by intelligent processing of material in order to maximise safe mechanical performance of structure, thereby overcoming calamity and misfortune.

Consider airframes made from a composite. The overall stress field of fuselage components during flight is two-dimensional; engine thrust works against drag, and lift works against payload. Hence, for aircraft with engines mounted on wings below the fuselage, during normal flight the fuselage is subjected to bidimensional compression force and to shear aft of the wings. Even when subjected to bidimensional compression, pre-existing cracks can be expected to propagate if and when the principal stresses become strongly unequal as happens to airframes during both air turbulence and 'heavy' landing.

An example is the Airbus A350 containing more than 50% by weight of composite. At the moment, we arrive at the probability of a successful outcome of a safe design by using intuition and our experience of circumstances that we have encountered before. Our comprehension of structural changes in composite materials, however, which take place continuously and cumulatively, is lacking in detail. More often than not, these simultaneously acting microscopic (or atomistic) processes are simply not known. Consequently, recent design codes both for material and structure have had to resort to flexible numerical modelling tools to simulate the conditions of creep, fatigue and environmental failure. Thus, failure criteria (stress or fracture based) are not universally acceptable in practice so leaving further unresolved issues. This is of particular importance for modern manufacturing challenges in the aerospace industry where the

aircraft production speed dominates the global demand, and machining of composites plays a major role in defining quality of the finished structures and consequently aircraft performance.

To predict a result, say lifetime or a stress response by a numerical method, there must be a self-evident truth that the mechanism regime in which the component is operating must be known. In other words, the important design issues must all be embedded in the same model of material and component behaviour that must also include the dominant mechanism(s) of structural change over orders of magnitude of size. And there still remains the difficulty in connecting results at the different scale levels and how damage transfers from a lower scale to a higher scale. To imagine the future differently, then composite material and engineering disaster as an act of God or of bad luck has to go. Total safety is the 'only show in town'.

If we begin design at the micron level of size (or below), basic research seeks a detailed understanding of the problem of structural failure through elegant modelling or experimentation with conspicuous absence of immediate need for solution or time constraints. At the other end of the size scale, solutions to applied structural problems need not necessarily be complete and in fact, a full understanding of the situation is rarely required. These solutions require synthesis, optimisation, approximation and '*feel*', and they generally have a time constraint.

Undoubtedly, progress has been made in the past decade in bringing together the basic concepts of physical modelling, mathematical and continuum models and in reconciling them with each other. But the rate of progress has been slow and the burden of cost so enormous that industry can reasonably be expected to ask for a condensation of all this work to a set of effective design codes that can be applied by those who understand and recognise the likely dangers and limitations of the large-scale structure.

It is time to apply existing knowledge and 'know-how' to the development and exploitation of design methods for safe life prediction of large structures; to reappraise current design practice and future design strategies; and to develop and validate risk-based assessment methodologies. This requires an integration of scientific disciplines, skills and understanding across a broad spectrum of size-scale. And this comes from the condensation of a wealth of knowledge of experimental information and applied analytical procedures, and from the application of modelling of various kinds including computer-based high-fidelity simulation.

We need to reconcile the irregularities of microstructure with the assumed continua of computational methods of modelling through an integrated multiscale approach to design. The benefits include shortening of the design-cycle time (reducing costs), optimisation of safe performance of structure and raising confidence levels in life prediction of highly stressed structures.

There is another set of issues that cannot be ignored and runs through this book like a leitmotif: what is a scientific discipline; how do disciplines emerge and differentiate; can a discipline also be interdisciplinary or multidisciplinary? Perhaps it is the last of these questions which gave the editors the impetus to embark on a book having such a wide range of themes and *disciplines*. The illustration below might help us see the

connections. When targeting the problem to find a solution, size it seems does matter as does the method of attack as chapters will show.

Peter W.R. Beaumont
Constantinos Soutis
Alma Hodzic

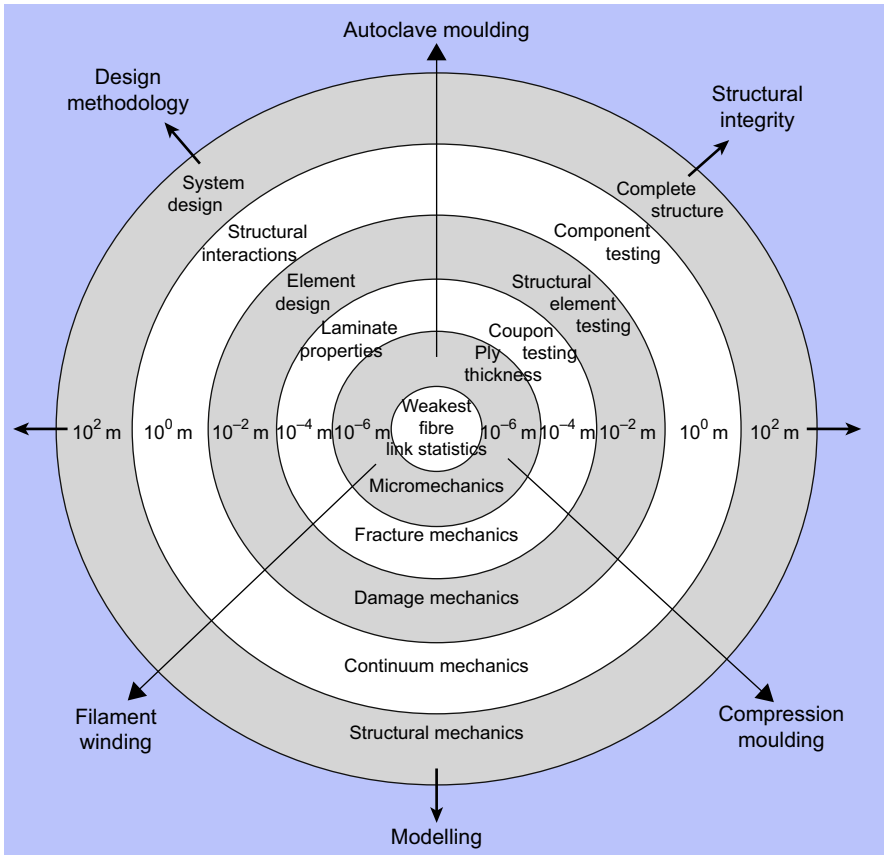

Composite micromechanics: from carbon fibres to graphene

1

R.J. Young
University of Manchester, Manchester, UK

1.1 Introduction

In the quest to understand fibre reinforcement, this chapter traces the development of the subject of composite micromechanics from its earliest roots to the most recent analysis of the deformation of graphene-reinforced nanocomposites. It is shown first how, employing concepts introduced by Kelly, it is possible through the use of shear-lag theory to predict the distribution of stress and strain in a single discontinuous fibre in a low-modulus matrix. For a number of years the shear-lag approach could only be used theoretically as there were no techniques available to monitor the stresses within a fibre in a resin. It will be shown that Raman spectroscopy and the discovery of stress-induced Raman bands shifts in reinforcing fibres have enabled us to map out the stresses in individual fibres in a transparent resin matrix, and thereby both test and develop Kelly's pioneering analytical approach.

In view of the growing interest in the study of polymer-based nanocomposites, it is shown how the shear-lag methodology can be modified to predict the distribution of stress and strain in nanoplatelets reinforcing a polymer matrix and an analogous set of relationships is obtained for nanoplatelet reinforcement to those obtained for fibre reinforcement. Because of the very strong resonance Raman scattering, it is shown that well-defined Raman spectra can be obtained from graphene monolayers. Large stress-induced band shifts can be obtained from these sheets when embedded in a polymer matrix, which has enabled the prediction of the shear-lag model to be validated. It is shown further how the shear-lag model can be used to model reinforcement by bilayer graphene.

1.2 Fibre reinforcement – theory

1.2.1 Composite micromechanics

Interest in the mechanics of fibre reinforcement can be traced back to the first uses of high-modulus fibres to reinforce a low-modulus matrix. A useful relationship developed to describe this reinforcement is the so-called 'rule of mixtures' in which, for stress parallel to the fibre direction, the Young's modulus of a composite E_c consisting of infinitely long aligned fibres is given by an equation of the form (Young & Lovell, 2011).

Structural Integrity and Durability of Advanced Composites. http://dx.doi.org/10.1016/B978-0-08-100137-0.00001-8

$$E_c = E_f V_f + E_m V_m \tag{1.1}$$

where E_f and E_m are the Young's modulus of the fibre and matrix and V_f and V_m are the volume fraction of the fibre and matrix, respectively. This equation captures the essence of fibre reinforcement and is found to work well in the specific conditions outlined above when high-modulus fibres are incorporated into low-modulus matrix materials. Since the strain in the fibre and matrix are the same, the stress in the fibres is much higher than that in the matrix, hence the fibres take most of the load and so reinforce the polymer matrix.

In reality, however, composites do not consist of infinitely long aligned fibres and are not always stressed parallel to the fibre direction. The full analysis of the situation in reality is the subject of many composites textbooks. The deformation of composites containing fibres of finite length deformed axially has been considered by a number of authors including Krenchel (1964). In addition, he also analysed the situation with fibres aligned randomly in plane and also randomly in three dimensions (Krenchel, 1964).

The problem of transfer of stress from the matrix to a fibre and the subsequent variation of stress along a fibre of finite length in a matrix was first tackled properly by Kelly (1966) in his classical text, *Strong Solids*. This ground-breaking work involved both the revival of the shear-lag concept of Cox (1952) and considerable intuition on his part. Indeed, in the introductory text to Chapter 5 of *Strong Solids* (Kelly, 1966) he makes the following statement: 'In this chapter we will discuss firstly how stress can be transferred between the matrix and fibre. This will be done in a semi-intuitive fashion since it is a difficult problem to solve exactly'.

Kelly's analysis became the foundation of a new research field known as 'composite micromechanics'. It will be shown how this field gave us the framework for the study of fibre reinforcement at both a theoretical and practical level, also enabling us to use the approach to tailor the properties of fibre−matrix interfaces in composites.

1.2.2 Discontinuous fibres

In the case of discontinuous fibres reinforcing a composite matrix, stress transfer from the matrix to the fibre takes place through a shear stress at the fibre−matrix interface as shown in Figure 1.1. It is envisaged that parallel lines perpendicular to the fibre can be drawn from the matrix through the fibre before deformation. When the system is subjected to an axial stress σ_1 parallel to the fibre axis, the lines become distorted since the Young's modulus of the matrix is much lower than that of the fibre. This induces a shear stress at the fibre/matrix interface, and the axial stress in the fibre builds up from zero at the fibre ends to a maximum value in the middle of the fibre. The assumption of uniform strain means that in the middle of the fibre the strain in the fibre equals that in the matrix, if the fibre is long enough. Since the fibres generally have a much higher Young's modulus than the matrix, the fibres then carry most of the stress (and hence load) in the composite − this is essentially how composites work.

It is now necessary to introduce the concept of interfacial shear stress (Kelly, 1966). The relationship between the interfacial shear stress τ_i near the fibre ends and the fibre stress σ_f can be determined by using a balance of the shear forces at the interface and

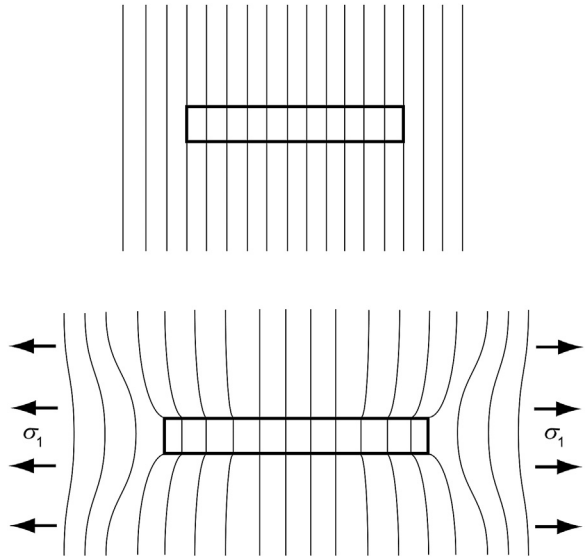

Figure 1.1 Deformation patterns for a discontinuous high-modulus fibre in a low-modulus polymer matrix. The top diagram shows the situation before deformation, and the bottom diagram shows the effect of the application of a tensile stress, σ_1, parallel to the fibre.

the tensile forces in a fibre element, as shown in Figure 1.2. The main assumption is that the force due to the shear stress τ_i at the interface is balanced by the force due to the variation of axial stress $\mathrm{d}\sigma_f$ in the fibre such that

$$2\pi r\tau_i \mathrm{d}x = -\pi r^2 \mathrm{d}\sigma_f \tag{1.2}$$

$$\text{and so} \quad \frac{\mathrm{d}\sigma_f}{\mathrm{d}x} = -\frac{2\tau_i}{r} \tag{1.3}$$

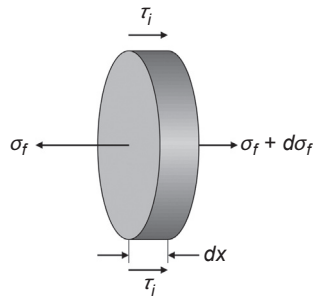

Figure 1.2 Balance of stresses acting on an element of the fibre of thickness dx in the composite.

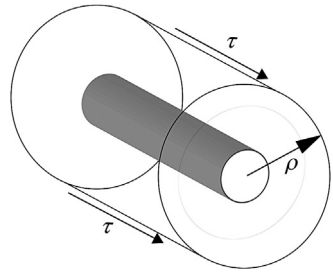

Figure 1.3 Model of a fibre undergoing deformation within a resin used in shear-lag theory. The shear stress τ acts at a radius ρ from the fibre centre.

1.2.2 Elastic stress transfer

The behaviour of a discontinuous fibre in a matrix can be modelled using shear-lag theory, developed initially by Cox (1952) to model the mechanical properties of paper. It is assumed in the theory that the fibre is surrounded by a cylinder of resin extending to a radius ρ from the fibre centre, as shown in Figure 1.3. In this model it is assumed that both the fibre and matrix deform elastically and that the fibre−matrix interface remains intact. If u is the displacement of the matrix in the fibre axial direction at a radius ρ, then the shear strain γ at that position is given by

$$\gamma = \frac{\mathrm{d}u}{\mathrm{d}\rho} \tag{1.4}$$

The shear modulus of the matrix is defined as $G_m = \tau/\gamma$, hence it follows that

$$\frac{\mathrm{d}u}{\mathrm{d}\rho} = \frac{\tau}{G_m} \tag{1.5}$$

The shear force per unit length carried by the matrix cylinder surface is $2\pi\rho\tau$ and is transmitted to the fibre surface though the layers of resin, and so the shear stress at radius ρ is given by

$$2\pi\rho\tau = 2\pi r\tau_i \tag{1.6}$$

$$\text{and so } \tau = \left(\frac{r}{\rho}\right)\tau_i \tag{1.7}$$

It follows that using Eqn (1.5),

$$\frac{\mathrm{d}u}{\mathrm{d}\rho} = \left(\frac{r}{\rho}\right)\frac{\tau_i}{G_m} \tag{1.8}$$

It is possible to integrate this equation using the limits of the displacement at the fibre surface ($\rho = r$) of $u = u_f$ and the displacement at $\rho = R$ of $u = u_R$

$$\int_{u_f}^{u_R} \mathrm{d}u = \left(\frac{r\tau_i}{G_m}\right) \int_{r}^{R} \frac{\mathrm{d}\rho}{\rho} \tag{1.9}$$

$$\text{hence } u_R - u_f = \left(\frac{r\tau_i}{G_m}\right) \ln\left(\frac{R}{r}\right) \tag{1.10}$$

These displacements can be converted into strain since the fibre strain e_f and matrix strain e_m can be approximated as $e_f \approx \mathrm{d}u_f/\mathrm{d}x$ and $e_m \approx \mathrm{d}u_R/\mathrm{d}x$. It should be noted that this shear-lag analysis is not rigorous, as shown by Nairn (1997), but it serves as a simple illustration of the process of stress transfer from the matrix to a fibre in a short-fibre composite. In addition, τ_i is given by Eqn (1.3), and so differentiating Eqn (1.10) with respect to x leads to

$$e_f - e_m = -\frac{r^2}{2G_m} \left(\frac{\mathrm{d}^2\sigma_f}{\mathrm{d}x^2}\right) \ln\left(\frac{R}{r}\right) \tag{1.11}$$

Furthermore, multiplying through by E_f gives

$$\frac{\mathrm{d}^2\sigma_f}{\mathrm{d}x^2} = -\frac{n^2}{r^2}(\sigma_f - e_m E_f) \tag{1.12}$$

where $n = \sqrt{\frac{2G_m}{E_f \ln(R/r)}}$

This differential equation has the general solution

$$\sigma_f = E_f e_m + C \sinh\left(\frac{nx}{r}\right) + D \cosh\left(\frac{nx}{r}\right)$$

where C and D are constants of integration. Now, Eqn (1.12) can be simplified and solved by double differentiation of the general solution, if it is assumed that the boundary conditions are that there is no stress transmitted across the fibre ends, that is, if $x = 0$ in the middle of the fibre where $\sigma_f = E_f e_m$ then $\sigma_f = 0$ at $x = \pm l/2$ where l is the length of the fibre. This leads to $C = 0$ and comparing terms gives

$$D = -\frac{E_f e_m}{\cosh(nl/2r)}$$

Finally, the equation for the distribution of fibre stress as a function of distance, x along the fibre, is

$$\sigma_f = E_f e_m \left[1 - \frac{\cosh(nx/r)}{\cosh(nl/2r)}\right] \tag{1.13}$$

1.2.3 Interfacial shear stress

It is possible, now, to determine the distribution of interfacial shear stress along the fibre using Eqn (1.3), which by differentiation of Eqn (1.13) leads to

$$\tau_i = \frac{n}{2} E_f e_m \frac{\sinh(nx/r)}{\cosh(nl/2r)} \tag{1.14}$$

It is convenient to introduce the concept of fibre aspect ratio s ($=l/2r$), which is dimensionless, so that the two above equations can be rewritten as

$$\sigma_f = E_f e_m \left[1 - \frac{\cosh(ns\frac{2x}{l})}{\cosh(ns)}\right] \tag{1.15}$$

for the axial fibre stress and as

$$\tau_i = \frac{n}{2} E_f e_m \frac{\sinh(ns\frac{2x}{l})}{\cosh(ns)} \tag{1.16}$$

for the interfacial shear stress. The effect of the different parameters upon the variation of stress in a fibre is demonstrated in Figure 1.4 for different values of the product ns. It can be seen from this figure that the fibre is most highly stressed, that is, the most efficient fibre reinforcement is obtained when the product ns is high. This implies that a high aspect ratio s is desirable along with a high value of n for the best reinforcement.

1.3 Fibre reinforcement – experiment

Following this original theoretical determination of stresses in discontinuous fibres, researchers had to rely upon it for the analysis of the micromechanics of composites, since there were initially no experimental methods available to measure local fibre stress or strain. Experimental measurement of the fibre stress and strain in discontinuous fibres in a composite under stress has now become available through the use of Raman spectroscopy (Huang & Young, 1994). Many high-performance fibres have well-defined Raman spectra (Young, 1995) as shown in Figure 1.5 for PAN- and pitch-based carbon fibres. In all cases the spectra exhibit the same appearance, that is, four well-resolved bands, namely D ($\sim$1330 cm^{-1}), G ($\sim$1580 cm^{-1}), D′ ($\sim$1620 cm^{-1}) and 2D ($\sim$2660 cm^{-1}) along with additional weaker features. Figure 1.5 shows spectra for the fibres both untreated and treated with oxygen plasma to improve fibre–matrix adhesion (Montes-Morán & Young, 2002a). No differences

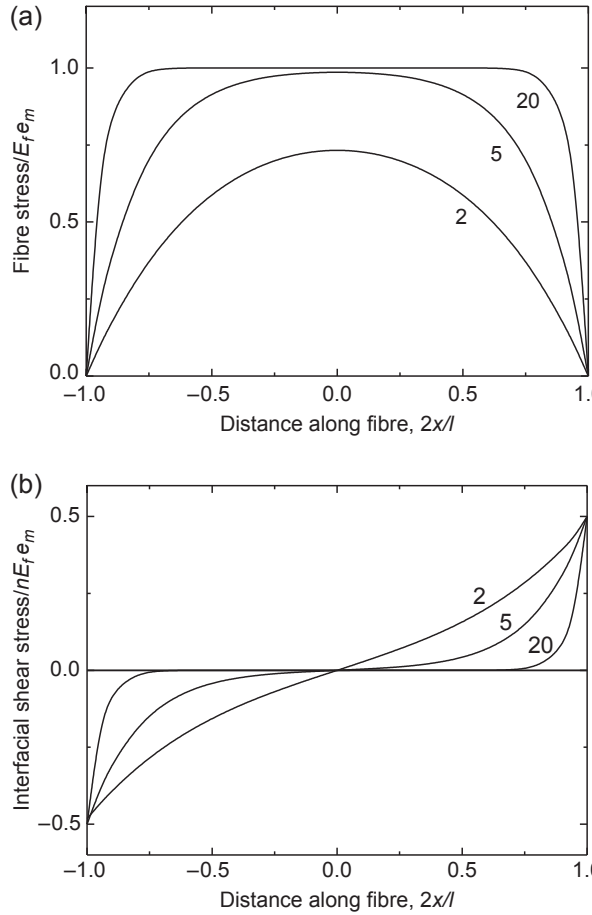

Figure 1.4 (a) Predicted variation of fibre stress with distance along the fibre for a short fibre in matrix. (b) Predicted variation of interfacial shear stress with distance along the fibre for a short fibre. (The values of the product *ns* are indicated in each case.)

were observed in Raman band positions and widths after the plasma treatment of the fibres, but the intensity ratio of the two first-order bands D and G is always higher after the plasma treatment, showing that this treatment introduces defects and functionality into the fibre surface, from which we will see results in better fibre−matrix adhesion.

The positions of all the Raman bands are found to shift when the carbon fibres are subjected to tensile deformation as shown in Figure 1.6 for the 2D band of the T50 and P100 fibres. In both cases there is an approximately linear shift of the band position with tensile strain. Since the fibres deform in an approximately linearly elastic manner, there is also a linear shift with stress. It will be shown that Figure 1.6 can be used as a calibration to determine the distribution of stress along a fibre using a Raman laser beam focused onto individual fibres inside the matrix resin. It is also important to point

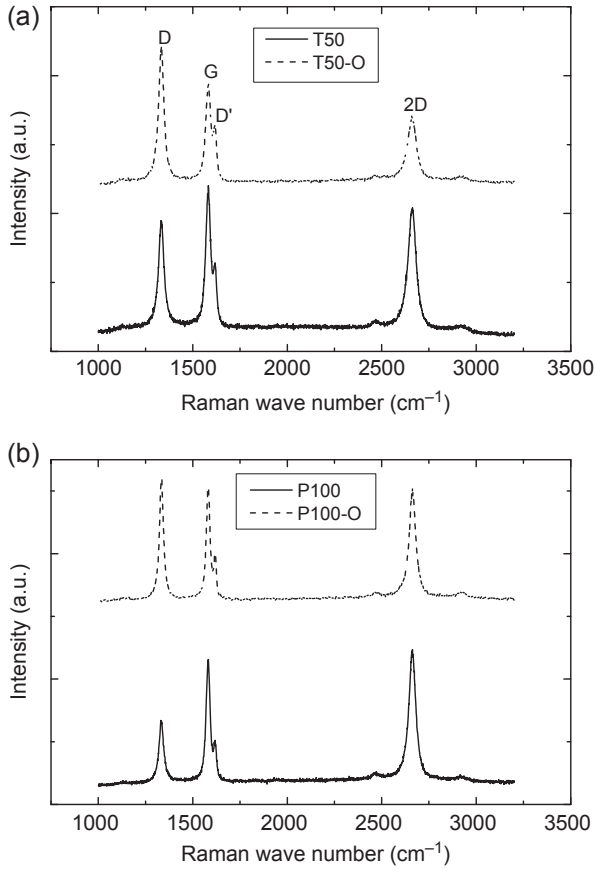

Figure 1.5 Raman spectra of (a) T50 PAN-based carbon fibres and (b) P100 pitch-based carbon fibres (untreated (top) and plasma treated (bottom)).

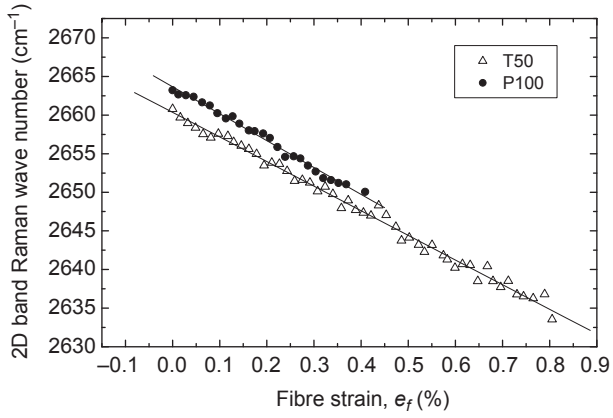

Figure 1.6 Variation of the 2D Raman band peak position with strain in as-received T50 and P100 carbon fibres.

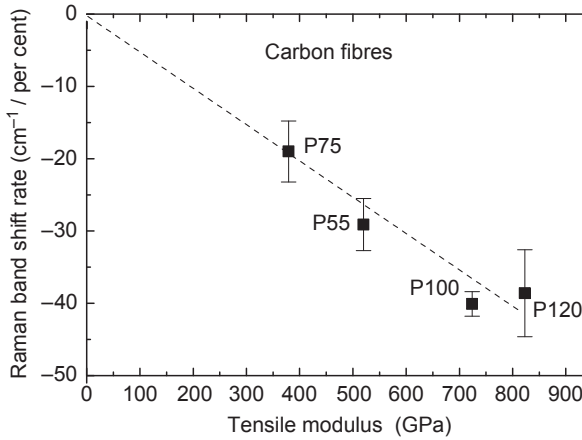

Figure 1.7 Shift rate of the 2D Raman band per unit strain as a function of the tensile Young's modulus for a number of different pitch-based carbon fibres.

out that the slope of the lines in Figure 1.6 is found to depend upon the Young's modulus of the carbon fibres (Cooper, Young, & Halsall, 2001). This is shown in Figure 1.7 for a number of pitch-based carbon fibres. It can be seen that there is an approximately linear dependence of the band shift rate upon the fibres' Young's modulus, and the slope of the dashed line is of the order of -50 to $-60\,\mathrm{cm}^{-1}$/TPa. It is found that this is a universal relationship for the 2D band applicable to all different forms of graphite carbon materials (Cooper et al., 2001) such as carbon fibres, carbon nanotubes and, as we will see, graphene.

The fibre stress or strain can be determined from the stress-induced shift of the Raman bands obtained from the fibre using a laser beam focused onto an individual fibre inside the matrix resin as shown in Figure 1.8. The laser beam diameter in a typical modern microscope-based Raman spectrometer is typically $\sim 1\,\mu\mathrm{m}$. This is significantly smaller than the usual fibre diameter ($5-10\,\mu\mathrm{m}$), which means that fibre stress and strain mapping can now be undertaken at high precision along individual fibres (Montes-Morán & Young, 2002b).

Figure 1.9(a) shows the variation of fibre strain $e_f\,(=\sigma_f/E_f)$ along a T50-O plasma-treated carbon fibre in an epoxy resin subjected to different levels of matrix strain, e_m.

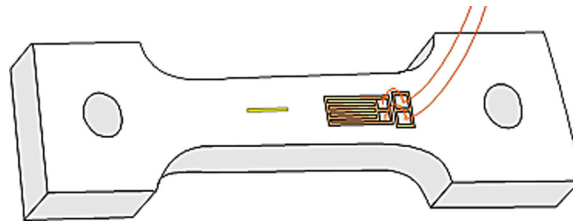

Figure 1.8 Model composite specimen containing a single fibre embedded within a transparent polymer resin. The matrix strain is determined by the resistance strain gauge and fibre strain by obtaining Raman spectra along the length of the fibre.

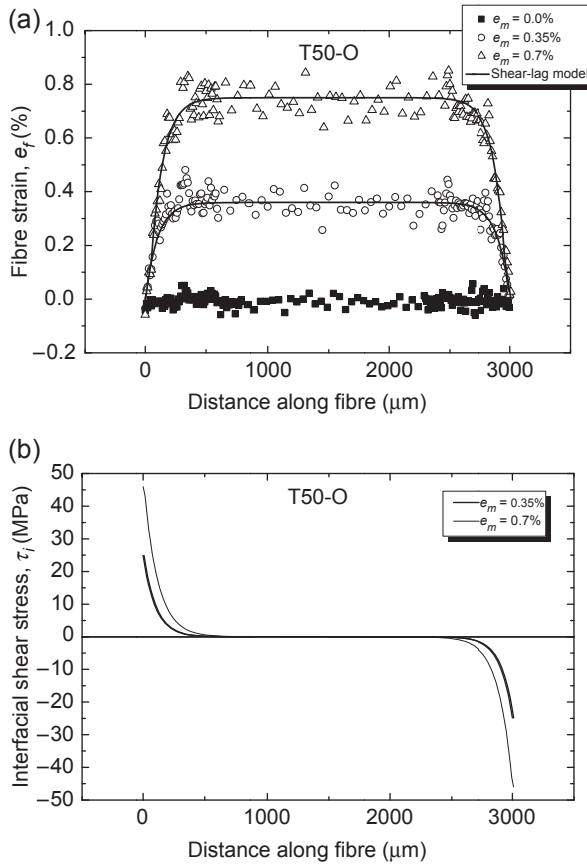

Figure 1.9 (a) Fibre strain distributions determined from strain-induced Raman band shifts at different levels of matrix strain in an epoxy resin for a plasma-treated T50-O fibre up to 0.7% strain. (b) Derived distribution of interfacial shear stress along the fibre.

The data have been fitted to Eqn (1.15) using the aspect ratio of the fibre, s, and by choosing appropriate values of n, and it can be seen that there is a close correlation between the theoretical curves and experimental data points. Moreover, it can be seen that the strain in the fibre is that same as the matrix strain in the middle of the fibres as was assumed in the theoretical analysis earlier. It should be noted, however, that Eqn (1.15) cannot be used to determine n since the value of $\ln(R/r)$ is essentially indeterminate. It is more appropriate to think of n as a fitting parameter that characterises the efficiency of stress transfer between the matrix and fibre (Young & Lovell, 2011). It is possible, however, to determine the distribution of interfacial shear stress τ_i along the fibre as shown in Figure 1.9(b). It can be seen that the interfacial shear stress is highest at the fibre ends (where there is a gradient of fibre strain or stress). For a matrix strain of 0.7% the value increases to around 50 MPa, which is approaching the shear yield stress of the resin.

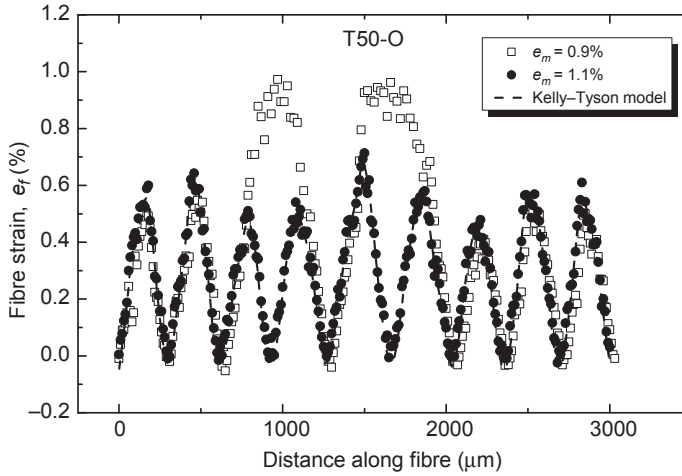

Figure 1.10 Fibre strain distributions determined from strain-induced Raman band shifts at different levels of matrix strain (up to 1.1%) in an epoxy resin for a plasma-treated T50-O fibre showing the effect of fibre fragmentation.

The effect of increasing the matrix strain to 0.9% is shown in Figure 1.10. At this matrix strain level the T50-O fibre undergoes fragmentation (the strain falls to zero at the fibre breaks), which saturates at a matrix strain of 1.1%. In this case the interfacial adhesion has been lost, and stress transfer at the interface is essentially frictional so that there is an approximately triangular variation along the length of each fragment (Kelly & Tyson, 1965). Moreover, it can be seen that the peak fragment strain is well below the matrix strain, indicating that once the fibres have undergone fragmentation reinforcement is diminished.

The behaviour of a T50 fibre that had not been modified by plasma treatment is shown in Figure 1.11. The distribution of strain in the fibre at 0.35% matrix strain follows the shear-lag model defined by Eqn (1.15). When the matrix strain is increased to 0.7%, however, the distribution of strain is somewhat different with approximately linear behaviour at the two ends. This is an indication that the fibre has undergone debonding that starts at the fibre ends and progresses along the fibre as the level of matrix strain is increased (Montes-Morán & Young, 2002b). This can be compared with the behaviour shown in Figure 1.9(a) for the T50-O fibre at 0.7% strain.

1.4 Nanoplatelet reinforcement – theory

It is of interest to see if the reinforcement of composites with nanoplatelets can also be analysed using continuum mechanics. In the case of nanoplatelets such as a discontinuous graphene flake reinforcing a composite matrix, stress transfer from the matrix to the flake will also be assumed to take place through a shear stress at the flake/matrix interface (Gong et al., 2010). This can also be represented diagrammatically by

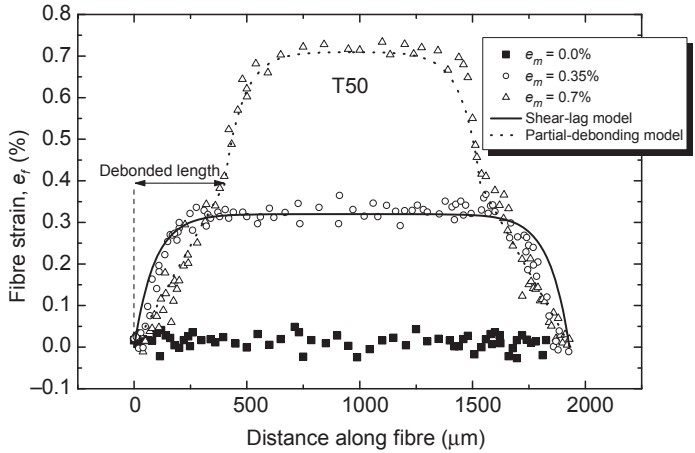

Figure 1.11 Fibre strain distributions determined from strain-induced Raman band shifts at different levels of matrix strain in an epoxy resin for an untreated T50 fibre, showing the effect of debonding at the fibre−matrix interface at the higher strain level.

Figure 1.1 where the rectangle in this case represents the two-dimensional section through a nanoplatelet in a matrix rather than along the middle of a fibre. Before deformation, parallel lines perpendicular to the flake can again be drawn from the matrix through the flake. When the system is subjected to axial stress, σ_1, parallel to the flake axis, the lines become distorted since the Young's modulus of the matrix is much less than that of the flake. This induces a shear stress at the flake/matrix interface. The axial stress in the flake will build up from zero at the flake ends to a maximum value in the middle of the flake. The uniform strain assumption means that, if the flake is long enough, in the middle of the flake the strain in the flake equals that in the matrix. Since the nanoplatelets have a much higher Young's modulus, it means that the nanoplatelets carry most of the stress, and therefore load, in the composite.

The relationship between the interfacial shear stress, τ_i, near the flake ends and the flake stress, σ_f, can be determined by using a force balance of the shear forces at the interface and the tensile forces in a flake element as shown in Figure 1.12. The main assumption is that the forces due to the shear stress at the interface, τ_i, are balanced by the force due to the variation of axial stress in the flake, $d\sigma_f$, such that if the element shown in Figure 1.12 is of unit width

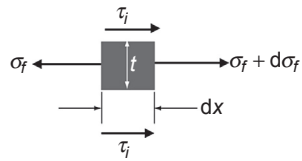

Figure 1.12 Balance of stresses acting on an element of length, dx, of the flake of thickness, t, in the composite.

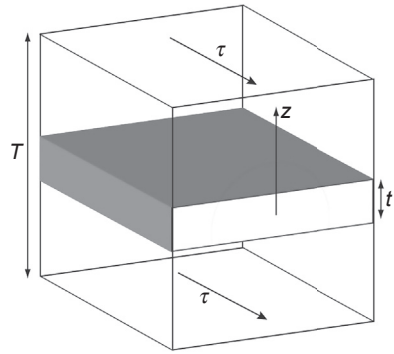

Figure 1.13 Model of a flake within a resin used in shear-lag theory. The shear stress τ acts at a distance z from the flake centre.

$$\tau_i \mathrm{d}x = -t\mathrm{d}\sigma_f \tag{1.17}$$

$$\text{and so } \frac{\mathrm{d}\sigma_f}{\mathrm{d}x} = -\frac{\tau_i}{t} \tag{1.18}$$

The behaviour of a discontinuous flake in a matrix can be modelled using shear-lag theory in which it is assumed that the flake is surrounded by a layer of resin at a distance, z, from the flake centre as shown in Figure 1.13. The resin has an overall thickness of T. It is assumed that both the flake and matrix deform elastically and the flake−matrix interface remains intact. If u is the displacement of the matrix in the flake axial direction at a distance, z, then the shear strain, γ, at that position is given by

$$\gamma = \frac{\mathrm{d}u}{\mathrm{d}z} \tag{1.19}$$

The shear modulus of the matrix is defined as $G_m = \tau/\gamma$, hence

$$\frac{\mathrm{d}u}{\mathrm{d}z} = \frac{\tau}{G_m} \tag{1.20}$$

The shear force per unit length carried by the matrix is transmitted to the flake surface through the layers of resin, and so the shear strain at any distance z is given by

$$\frac{\mathrm{d}u}{\mathrm{d}z} = \frac{\tau_i}{G_m} \tag{1.21}$$

This equation can be integrated using the limits of the displacement at the flake surface ($z = t/2$) of $u = u_f$ and the displacement at $z = T/2$ of $u = u_T$

$$\int_{u_f}^{u_T} \mathrm{d}u = \left(\frac{\tau_i}{G_m}\right) \int_{t/2}^{T/2} \mathrm{d}z \tag{1.22}$$

$$\text{hence } u_T - u_f = \left(\frac{\tau_i}{2G_m}\right)(T - t) \tag{1.23}$$

It is possible to convert these displacements into strain since the flake strain, e_f, and matrix strain, e_m, can be approximated as $e_f \approx \mathrm{d}u_f/\mathrm{d}x$ and $e_m \approx \mathrm{d}u_T/\mathrm{d}x$. It should be noted again that this shear-lag analysis is not rigorous but it serves as a simple illustration of the process of stress transfer from the matrix to a flake in a graphene-flake composite. In addition, τ_i is given by Eqn (1.18), and so differentiating Eqn (1.23) with respect to x leads to

$$e_f - e_m = \frac{tT}{2G_m}\left(\frac{\mathrm{d}^2\sigma_f}{\mathrm{d}x^2}\right) \tag{1.24}$$

since $T \gg t$. Multiplying through by E_f gives

$$\begin{aligned} &\frac{\mathrm{d}^2\sigma_f}{\mathrm{d}x^2} = \frac{n^2}{t^2}(\sigma_f - e_m E_f) \\ &\text{where } n = \sqrt{\frac{2G_m}{E_f}\left(\frac{t}{T}\right)} \end{aligned} \tag{1.25}$$

This differential equation has the general solution

$$\sigma_f = E_f e_m + C \sinh\left(\frac{nx}{t}\right) + D \cosh\left(\frac{nx}{t}\right)$$

where C and D are constants of integration. This equation can be simplified and solved if it is assumed that the boundary conditions are that there is no stress transmitted across the flake ends, that is, if $x = 0$ in the middle of the flake where $\sigma_f = E_f e_m$ then $\sigma_f = 0$ at $x = \pm l/2$. This leads to $C = 0$ and

$$D = -\frac{E_f e_m}{\cosh(nl/2t)}$$

The final equation for the distribution of flake stress as a function of distance, x along the flake, is then

$$\sigma_f = E_f e_m \left[1 - \frac{\cosh(nx/t)}{\cosh(nl/2t)}\right] \tag{1.26}$$

Finally, it is possible to determine the distribution of interfacial shear stress along the flake using Eqn (1.18), which leads to

$$\tau_i = nE_f e_m \frac{\sinh(nx/t)}{\cosh(nl/2t)} \tag{1.27}$$

It is convenient at this stage to reintroduce the concept of flake aspect ratio, defined in this case as $s = l/t$, so that the two equations above can be rewritten as

$$\sigma_f = E_f e_m \left[1 - \frac{\cosh(ns\frac{x}{l})}{\cosh(ns/2)}\right] \tag{1.28}$$

for the axial flake stress and as

$$\tau_i = nE_f e_m \frac{\sinh(ns\frac{x}{l})}{\cosh(ns/2)} \tag{1.29}$$

for the interfacial shear stress.

It can be seen that the nanoplatelet is most highly stressed, that is, the most efficient flake reinforcement is obtained when the product ns is high. This implies that a high aspect ratio, s, is desirable along with a high value of n. The similarity of this analysis for the nanoplatelet to the shear-lag analysis for a fibre and of the equations derived is remarkable. The reason for this is that the shear-lag analysis considers only axial stresses and the shear-lag model represented by Figure 1.1 is applicable to both situations.

1.5 Nanoplatelet reinforcement – experiment

As in the case of carbon fibres, Raman spectroscopy can be employed to follow the micromechanics of reinforcement by graphene nanoplatelets in nanocomposites (Gong et al., 2010). Figure 1.14 shows a schematic diagram of a model composite specimen consisting of a single graphene monolayer sandwiched between two polymer layers. The SU-8 epoxy was spin coated onto a poly(methyl methacrylate) (PMMA) beam and allowed to cure. The graphene monolayer was produced by repeated cleavage of a graphite crystal with adhesive tape and pressed onto the

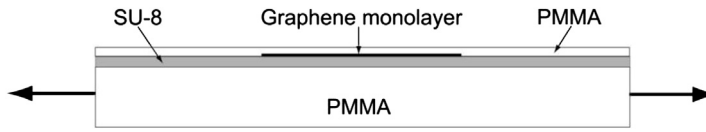

Figure 1.14 Schematic diagram (not to scale) of a section through a single monolayer graphene composite.

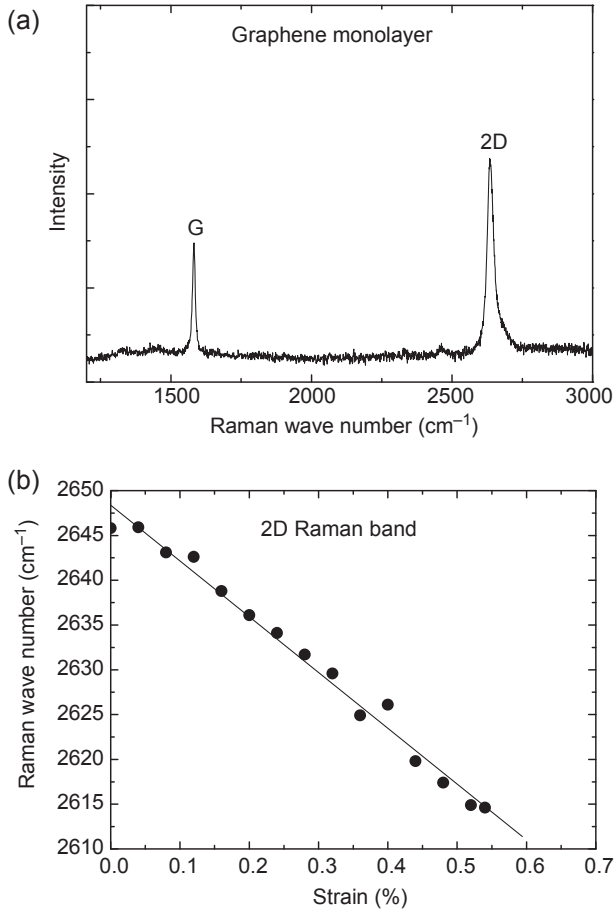

Figure 1.15 (a) Raman spectrum for a graphene monolayer. (b) Shift of the Raman 2D band with strain for the graphene monolayer.

beam. The PMMA top coat was spin coated to seal the monolayer on the beam. Deformation was applied by bending the PMMA beam and monitoring the matrix strain using a resistance strain gauge (Gong et al., 2010).

Graphene undergoes very strong resonance Raman scattering (Malard, Pimenta, Dresselhaus, & Dresselhaus, 2009), which means that it is possible to obtain a spectrum from a single-atom-thick monolayer embedded in several microns of PMMA (Gong et al., 2010). Figure 1.15(a) shows the Raman spectrum obtained from a single graphene monolayer. It can be seen that it consists of two sharp bands with the 2D band being characteristically stronger than the G band for the monolayer (Ferrari et al., 2006). The absence of a D band also shows that the graphene is relatively defect free. Both bands are found to shift to lower wave number with deformation as shown in Figure 1.15(b) for the 2D band. It can be seen that there is a large, approximately linear shift of the band, with a shift rate of the order of $-60\ \text{cm}^{-1}$/percent strain. Assuming

that the relationship for carbon fibres between band shift rate and Young's modulus shown in Figure 1.7 is also applicable to monolayer graphene, this would imply that the graphene has a Young's modulus in excess of 1000 GPa, similar to the value determined by direct measurement (Lee, Wei, Kysar, & Hone, 2008). As with carbon fibres, the relationship shown in Figure 1.15(b) can also be used to determine stress or strain distributions in graphene nanoplatelets in nanocomposites (Young, Kinloch, Gong, & Novoselov, 2012).

The experimental data on the variation of graphene strain across the middle of a monolayer flake are shown in Figure 1.16(a). The data were fitted to Eqn (1.28) of the shear-lag analysis derived above. It can be seen that the fits of the theoretical shear-lag curves to the strain distribution are sensitive to the value of *ns* chosen. The derived interfacial shear stress distributions are shown in Figure 1.16(b), and the value of interfacial shear stress at the flake ends is also very sensitive to the values of *ns* chosen. The best fit to the experimental data is for an *ns* value of 20, giving a maximum interfacial shear stress of around 2 MPa, well below the value of 50 MPa found for the carbon fibres in Figure 1.9(b). The graphene has an inert, atomically smooth surface such that any interactions with the polymers will be through van der Waals bonding. The T50-O carbon fibres on the other hand had been plasma oxidised and had rough surfaces, leading to much stronger bonding with the polymer matrix.

The deformation micromechanics of few-layer graphene in composites has also been investigated using Raman spectroscopy as shown in Figure 1.17 (Gong et al., 2012). The distribution of strain across a graphene flake containing both monolayer and bilayer regions is shown in Figure 1.17(a). This shows two important findings. Firstly, the data can again be fitted well to the shear-lag model (Eqn (1.28)). Secondly, it can be seen that the strain in the bilayer regions is identical to that in adjacent monolayer regions. Figure 1.17(b) shows the strain distribution across a bilayer flake that has fragmented due probably to cracking in the polymer coating (Gong et al., 2012). In this case triangular strain distributions are obtained, indicating damage to the interface and stress transfer by frictional sliding, analogous to the behaviour shown for carbon fibres in Figure 1.10.

A clear conclusion of this study is that the micromechanics of deformation of graphene nanoplatelets can be analysed in terms of the shear-lag theory developed originally for fibre reinforcement. It also means that the use of continuum mechanics is applicable for the analysis of deformation on the nanoscale.

1.6 Future trends and challenges

1.6.1 Fibre reinforcement

The work presented here has been concentrated upon the fundamentals of fibre reinforcement from both a theoretical and experimental viewpoint. The issue of reinforcement by a single discontinuous fibre is now well understood, but there are still challenges to be addressed in terms of the fundamental mechanics such as developing better analytical methods that do not suffer from some of the issues that arise using the shear-lag approach. There continue to be developments in numerical methods such as

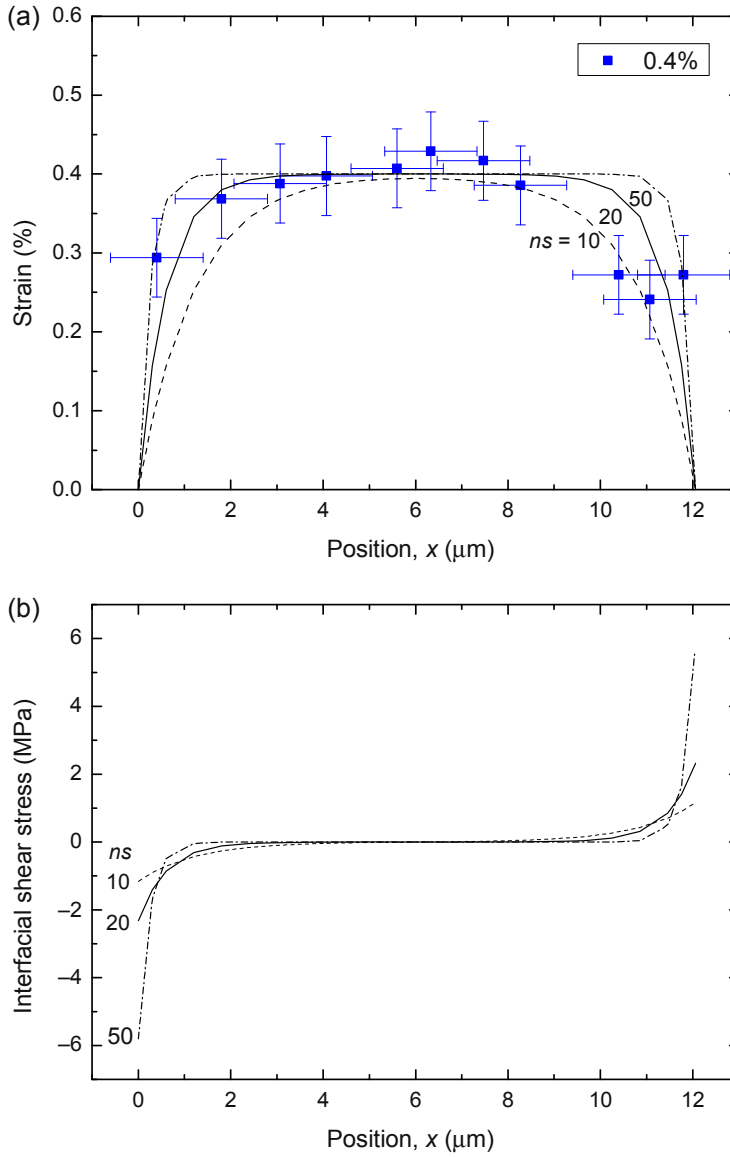

Figure 1.16 (a) Distribution of strain at 0.4% matrix strain in direction of the tensile axis across a graphene monolayer. The curves are fits of Eqn (1.15). (b) Variation of interfacial shear stress with position determined from Eqn (1.16).

finite element analysis, and the increasing power of computer systems offers scope for solving even more complex problems.

There are unsolved problems in the field of composite micromechanics that include:

- Fibre compression – the extent to which failure occurs through geometrical instabilities or internal compressive failure processes is still not resolved.

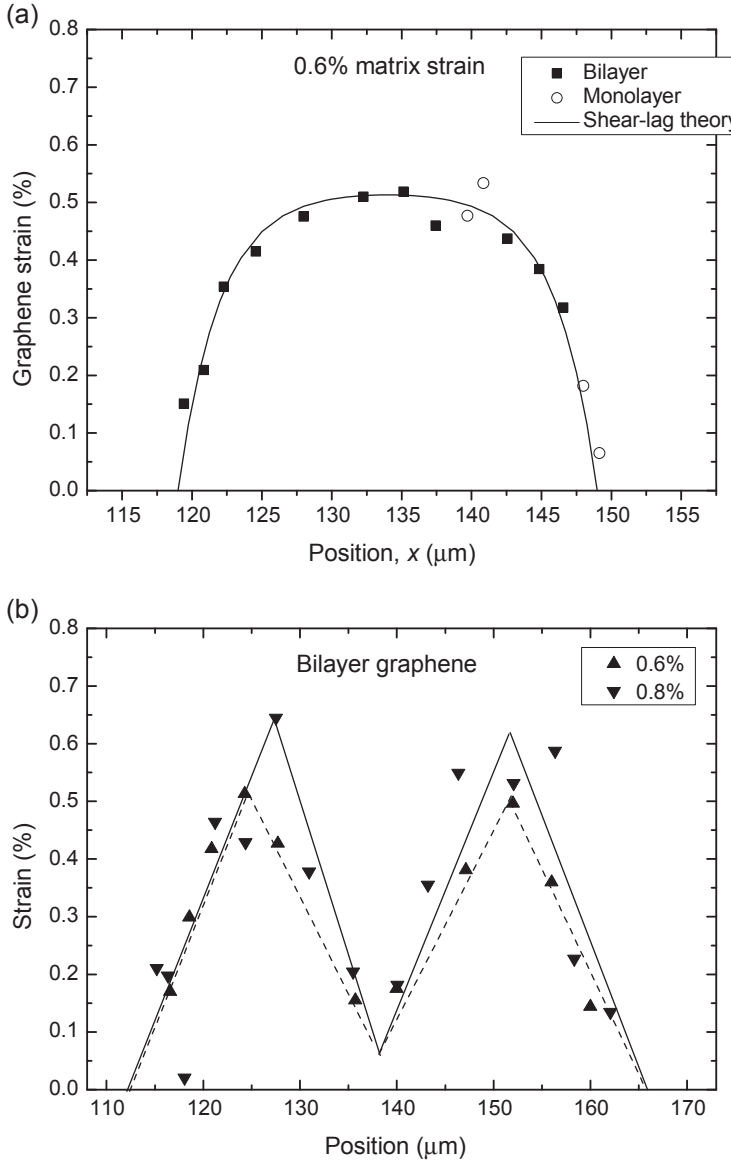

Figure 1.17 Distributions of strain at different matrix strain levels in the direction of the tensile axis across a graphene nanoplatelet. (a) Region with both monolayer and bilayer graphene at 0.6% matrix strain. (b) Bilayer region showing the effect fragmentation at 0.6% and 0.8% strains.

- Effect of fibre orientation and waviness – it is still not fully understood how fibre waviness affects properties, especially when a composite is subjected to axial compression.
- Reinforcement with nanofibres and nanotubes – there is no clear indication as yet as to the extent to which the deformation of nanofibres and nanotubes within a composite can be modelled using continuum mechanics. The experience with graphene now indicates that it may also be applicable in this case.

1.6.2 Nanoplatelet reinforcement

Although the analysis of fibre reinforcement has been taking place for over 50 years, it is still not yet fully understood. The study of nanoplatelet reinforcement in nanocomposites has been undertaken over a much shorter period and so is far less well developed. It has been shown that it appears that continuum mechanics is still applicable at the nanoscale, and so much of the analysis undertaken for macroscopic composites can be employed and adapted. Nevertheless, it remains to be seen how far it is possible, at the nanoscale, to use this analytical methodology and when it is necessary to employ numerical techniques such as the finite element method.

There are various challenges that exist in developing micromechanics at the nanoscale, including:

- Axial compression – it is not clear how nanoplatelets respond to in-plane compression and what deformation modes lead to ultimate failure.
- Nanoplatelet/nanoplatelet interactions, including restacking – the effect of nanoplatelet separation and restacking upon mechanical properties is yet to be analysed.
- Nanoplatelet/crack interactions – this is an area that has not yet been explored.
- Effect of nanoplatelet orientation, waviness and wrinkling – it is thought that waviness and wrinkling may lead to inferior mechanical properties for nanoplatelet-reinforced nanocomposites, but this is yet to be put on a firm theoretical foundation.
- Effect of nanoplatelet surface treatment and modification – it is highly likely that the chemical modification of nanoplatelet surfaces will affect stress transfer in nanocomposites, but no systematic studies have yet been undertaken.

Many of these problems and issues are similar at both the macroscopic and nanoscales. Some of them are different, but the finding outlined in this chapter that continuum mechanics is still applicable for the understanding of nanomechanics gives us confidence that further rapid progress will be made in the years to come.

1.7 Sources of further information

1.7.1 Encyclopaedia

O'Brien, P. (Ed.), (2013). Nanoscience. In *Nanostructures through chemistry: Vol. 1*. Cambridge: Royal Society of Chemistry.

Vajtai, R. (Ed.), (2013). *Springer handbook of nanomaterials*. Berlin: Springer-Verlag.

Wiley Encyclopedia of composites (2012), 2nd Edition, Wiley Online Library, Wiley-VCH Verlag.

1.7.2 Textbooks

Gibson, R. F. (2012). *Principles of composite material mechanics* (3rd ed.). Boca Raton: CRC Press.

Hull, D., & Clyne, T. W. (1996). *An introduction to composite materials*. Cambridge: Cambridge University Press.

Kelly, A., & Macmillan, N. H. (1986). *Strong solids* (3rd ed.). Oxford: Clarendon Press.

Young, R. J., & Lovell, P. A. (2011). *Introduction to polymers*. Boca Raton: CRC Press.

References

Cooper, C. A., Young, R. J., & Halsall, M. (2001). Investigation into the deformation of carbon nanotubes and their composites through the use of Raman spectroscopy. *Composites A: Applied Science and Manufacturing, 32*, 401−411.

Cox, H. L. (1952). The elasticity and strength of paper and other fibrous materials. *British Journal of Applied Physics, 3*, 72−79.

Ferrari, A. C., Meyer, J. C., Scardaci, V., Casiraghi, C., Lazzeri, M., Mauri, F., et al. (2006). Raman spectrum of graphene and graphene layers. *Physical Review Letters, 97*, 187401.

Gong, L., Kinloch, I. A., Young, R. J., Riaz, I., Jalil, R., & Novoselov, K. S. (2010). Interfacial stress transfer in a graphene monolayer nanocomposite. *Advanced Materials, 22*, 2694−2697.

Gong, L., Young, R. J., Kinloch, I. A., Riaz, I., Jalil, R., & Novoselov, K. S. (2012). Optimizing the reinforcement of polymer-based nanocomposites by graphene. *ACS Nano, 6*, 2086−2095.

Huang, Y., & Young, R. J. (1994). Analysis of the fragmentation test for carbon fibre/epoxy model composites using Raman spectroscopy. *Composites Science and Technology, 52*, 505−517.

Kelly, A. (1966). *Strong solids*. Oxford: Clarendon Press.

Kelly, A., & Tyson, W. R. (1965). Tensile properties of fibre-reinforced metals - copper/tungsten and copper/molybdenum. *Journal of the Mechanics and Physics of Solids, 13*, 329−350.

Krenchel, H. (1964). *Fibre reinforcement*. Copenhagen: Akademisk Forlag.

Lee, C., Wei, X. D., Kysar, J. W., & Hone, J. (2008). Measurement of the elastic properties and intrinsic strength of monolayer graphene. *Science, 321*, 385−388.

Malard, L. M., Pimenta, M. A., Dresselhaus, G., & Dresselhaus, M. S. (2009). Raman spectroscopy in graphene. *Physics Reports, 473*, 51−87.

Montes-Morán, M. A., & Young, R. J. (2002a). Raman spectroscopy study of HM carbon fibres: effect of plasma treatment on the interfacial properties of single fibre/epoxy composites, Part I: fibre characterisation. *Carbon, 40*, 845−855.

Montes-Morán, M. A., & Young, R. J. (2002b). Raman spectroscopy study of HM carbon fibres: effect of plasma treatment on the interfacial properties of single fibre/epoxy composites, Part II: characterisation of the fibre/matrix interface. *Carbon, 40*, 857−875.

Nairn, J. A. (1997). On the use of shear-lag methods for analysis of stress transfer unidirectional composites. *Mechanics of Materials, 26*, 63−80.

Young, R. J. (1995). Monitoring deformation processes in high-performance fibres using Raman spectroscopy. *Journal of the Textile Institute, 86*, 360−381.

Young, R. J., Kinloch, I. A., Gong, L., & Novoselov, K. S. (2012). The mechanics of graphene nanocomposites: a review. *Composites Science and Technology, 72*, 1459−1476.

Young, R. J., & Lovell, P. A. (2011). *Chapter 24, introduction to polymers*. Boca Raton: CRC Press.

A mechanisms-based framework for describing failure in composite materials

2

R. Talreja[1,2]
[1]Texas A&M University, College Station, TX, USA; [2]Luleå University of Technology, Luleå, Sweden

2.1 Introduction

Lack of dependable design procedures for composite structures for their safe and reliable performance during service life is a major roadblock in enhancing their usage in practical applications. Their lightweight and varied architecture offer potential for transformative and innovative designs in many fields such as aerospace, automotive, and wind energy generation. However, today's design procedures are either overly conservative or uncertain, or both. A main reason is the current use of composite failure criteria, which lack connection with physical mechanisms of failure and have their beginnings in behavior of metals. A large number of corrective measures to the fundamentally flawed theories have only produced confusing situations where a designer cannot know the degree of inaccuracy in predictions and the errors could render the predictions conservative or otherwise.

This discussion is aimed at clarifying the nature of the macroscopic failure theories that are commonly described in introductory texts on composite materials, generating the impression among practicing engineers that these are established theories. Experience over many years has, however, produced evidence of uncertain predictions by such theories. Four commonly known and used failure theories will be focused on for examination of the causes of their inability to capture the composite failure behavior. For more extensive scrutiny of the failure theories, the reader is referred to the Worldwide Failure Exercise (WWFE) (Hinton, Kaddour, & Soden, 2004) where the participating theories are examined for their ability to describe test data. Our purpose here is to have an in-depth look at the fundamental assumptions underlying their methodology. For this, we do not conduct an exhaustive survey of all theories but instead take a few that are believed to be representative of the nature of those assumptions. The reader is referred to other articles written recently by the author for more elaborate and complementary discussions on this topic (Talreja, 2014a,b).

This chapter is organized as follows. First, selected failure theories are reviewed, followed by discussion of the limitations of the theories. To improve the failure analysis of composite materials, an alternative path is proposed. The elements of this approach are described and illustrated by recent work. Finally, a comprehensive scheme for addressing the failure assessment of composite structures is outlined as a proposed future direction in this field.

Structural Integrity and Durability of Advanced Composites. http://dx.doi.org/10.1016/B978-0-08-100137-0.00002-X

2.2 Phenomenological failure theories

This class of theories for composite materials has its origin in the paper by Azzi and Tsai (1965), commonly referred to as the Tsai−Hill failure criterion in most introductory texts on composite materials, for example, Jones (1999). This theory takes its starting point in the generalization of the von Mises yield theory for isotropic metals to orthotropic metals proposed by Hill (1948). As is well known, the von Mises criterion is based on the hypothesis that metal yielding is governed by the second invariant of the deviatoric stress tensor. In arbitrary rectangular coordinate axes x−y−z, the von Mises criterion takes the form

$$\left(\sigma_y - \sigma_z\right)^2 + \left(\sigma_z - \sigma_x\right)^2 + \left(\sigma_x - \sigma_y\right)^2 + 6\left(\tau_{yz}^2 + \tau_{xz}^2 + \tau_{xy}^2\right) = 2Y_0^2 \tag{2.1}$$

where Y_0 is the yield stress obtained in a uniaxial test in any direction, and σ and τ denote normal and shear stresses, respectively.

Hill's generalization of this equation to orthotropic solids is totally of mathematical nature, where the multiplying constant $\frac{1}{2Y_0^2}$ on each term on the l.h.s. of Eqn (2.1) is replaced by an independent material constant. Thus, the generalized equation takes the form

$$F\left(\sigma_y - \sigma_z\right)^2 + G\left(\sigma_z - \sigma_x\right)^2 + H\left(\sigma_x - \sigma_y\right)^2 + 2L\tau_{yz}^2 + 2M\tau_{xz}^2 + 2N\tau_{xy}^2 = 1 \tag{2.2}$$

where F, G, H, L, M, and N are the new material constants. As shown by Hill (1948), these constants can be related to the six independent yield stress values X, Y, and Z resulting from uniaxial normal stresses in x, y, and z directions, respectively, and R, S, and T resulting from shear stresses in y−z, x−z, and x−y planes, respectively. Azzi and Tsai (1965) restricted themselves to the two-dimensional case of a UD composite layer and assumed that the yield stresses X and Y can be taken to represent strengths in x and y directions, respectively, and the in-plane shear yield value T can similarly be viewed as the shear strength of the thin composite layer. Furthermore, they assumed isotropy in the cross-sectional plane of the fiber-reinforced composite, yielding $Y = Z$. With these replacements the Hill criterion reduces to the following:

$$\left(\frac{\sigma_1}{X}\right)^2 - \left(\frac{\sigma_1\sigma_2}{X}\right)^2 + \left(\frac{\sigma_2}{Y}\right)^2 \left(\frac{\tau_{12}}{T}\right)^2 = 1 \tag{2.3}$$

where indices x and y are replaced by 1 and 2, respectively, indicating the renaming of the axes of symmetry by x_1 and x_2 aligned respectively with the fiber direction and normal to it in the plane of the composite layer. Azzi and Tsai (1965) showed that this equation was able to describe the tensile strength variation with the off-axis angle, that is, the angle between the loading and fiber directions. More general cases of test results under in-plane loading of a UD composite could not, however, be described by this equation with the same accuracy.

It is not possible to determine why some test data are successfully described while others are not with the Tsai−Hill equation, Eqn (2.3), since the source of error cannot be found. All that can be said is that this equation describes a particular form of quadratic interaction between the individual effects of failure under a single stress component when the three stress components are applied simultaneously.

It is also important to understand that there is no energy consideration underlying the Tsai−Hill criterion, Eqn (2.3). To appreciate this, let us note that the von Mises yield criterion, Eqn (2.1), can also be obtained by casting the yield hypothesis in terms of the distortional strain energy density, as was shown by Hencky (1924). However, the mathematical generalization by Hill (1948) of the von Mises criterion to yielding in orthotropic solids cannot be achieved by resorting to the energy of distortion. Hill (1948) instead gave his criterion a foundation in energy by postulating a plasticity potential from which the criterion could be derived. This is justified by the fact that in an orthotropic metal a single mechanism (dislocation motion) of plastic deformation exists that leads to six different yield stresses (threshold values). It can be shown that the Hill criterion reduces to the von Mises criterion when all three normal yield stresses are equal and the three shear yield stresses are the same and equal to half the normal yield stresses, that is, $X = Y = Z = 2R = 2S = 2T = Y_0$. In a UD composite, the failure mechanisms underlying the three limit states in Eqn (2.3), given by $\sigma_1 = X$, $\sigma_2 = Y$, and $\tau_{12} = T$, are widely different (Talreja, 2014a). Therefore, it is expected that the criticalities of energy associated with each of the three failure mechanisms would be different. In other words, while in orthotropic metal plasticity a plastic potential governs yielding caused by any combination of stresses, in a UD composite the energies involved in the three failure mechanisms cannot be added to the same critical energy for failure in all combinations of the applied stresses.

The inability of the Tsai−Hill criterion to describe all test data prompted the need for a more versatile quadratic expression. Tsai and Wu (1971) found a source of such an expression in a paper by Goldenblat and Kopnov (1965) who proposed a very general interaction equation for "strength" in anisotropic solids in the following form:

$$\left(F_{ij}\sigma_{ij}\right)^{\alpha} + \left(F_{ijkl}\sigma_{ij}\sigma_{kl}\right)^{\beta} + \left(F_{ijklmn}\sigma_{ij}\sigma_{kl}\sigma_{mn}\right)^{\gamma} + \cdots = 1 \tag{2.4}$$

where F_{ij}, etc. stand for tensor-valued strength constants and α, β, γ are arbitrary constants. Setting $\alpha = \beta = 1$ and neglecting higher order terms in Eqn (2.4), Tsai and Wu (1971) specialized the general tensor polynomial equation to the following simple form for UD composites:

$$F_p\sigma_p + F_{pq}\sigma_p\sigma_q = 1 \tag{2.5}$$

where $p, q = 1, 2$, and 6, and the stress components are written in the Voigt notation given by, $\sigma_1 = \sigma_{11}$, $\sigma_2 = \sigma_{22}$, and $\sigma_6 = \sigma_{12} = \sigma_{21}$. This equation describes a quadric surface in the σ_1 $-\sigma_2-$ σ_6 space. It can be shown that of 17 possible surfaces described by Eqn (2.5) only ellipsoids are acceptable for representing strengths of real materials.

Fitting an ellipsoidal surface to the strength of a UD composite requires determining the three constants F_p that locate the origin of the ellipsoid and the six independent constants F_{pq} ($F_{pq} = F_{qp}$ due to symmetry of stress components). Because of the strength in shear being independent of the sign, $F_6 = F_{16} = F_{26} = 0$. Thus, of the remaining six constants, F_1, F_2, F_{11}, and F_{22} are found by test data on normal strengths, and F_{66} is given by the in-plane shear strength. The last remaining constant F_{12} can only be fixed by making additional assumptions, which renders its value non-unique. For instance, if the constant is determined by a biaxial test, then the value of the constant depends on the ratio of the two stresses used in testing, and obviously also on the loading path. Its value is, however, bounded by its ratio to $\sqrt{F_{11}F_{22}}$, which must be within the range $(-1,1)$ given by the geometric condition that the ellipsoid has a closed surface. There is no physical condition concerning the nature of material strength, or its value, that determines F_{12} uniquely. In fact, one particular choice of F_{12}, namely $F_{12} = -0.5\sqrt{F_{11}F_{22}}$, allows the resulting ellipsoid to describe the Hill criterion for orthotropic solids stressed in a single plane.

It is clear that the Tsai–Wu criterion is not a composite material failure criterion in any sense. It is simply a versatile curve-fitting scheme for fitting ellipsoids to strength test data of orthotropic solids. As noted above, it can also describe yield data of orthotropic metals as a special case. In contrast to metals, fiber-reinforced composite materials fail in different failure modes. In fact, there is no fundamental physical reason or observation that suggests that the mutual interactions of the failure modes be generally described by a single quadratic equation.

Noting the non-unique nature of the constant F_{12}, Hashin (1980) suggested to use piecewise smooth surfaces (or curves in the two-dimensional case) to describe failure interaction under combined stresses instead of a single ellipsoid (or ellipse in 2-D). This will also avoid forcing all failure interactions to follow the same single quadratic equation. Hashin (1980) argued that a linear form of failure interaction may not suffice and proposed to use quadratic forms in all cases, that is, the individual pieces of a piecewise smooth surface should be quadric surfaces. This essentially means retaining only the first two terms of Eqn (2.4) with $\alpha = \beta = 1$, as done by Tsai and Wu (1971), except different F-constants should be determined for each part of the failure surface.

Hashin (1980) proceeded to construct his quadratic failure criteria by assuming a UD composite to be transversely isotropic with the cross-sectional plane x_2–x_3 as the plane of isotropy. He used the stress invariants for this symmetry given by

$$\begin{aligned} I_1 &= \sigma_{11} \\ I_2 &= \sigma_{22} + \sigma_{33} \\ I_3 &= \sigma_{23}^2 - \sigma_{22}\sigma_{33} \\ I_4 &= \sigma_{12}^2 + \sigma_{13}^2 \\ I_5 &= 2\sigma_{12}\sigma_{23}\sigma_{13} - \sigma_{22}\sigma_{13}^2 - \sigma_{33}\sigma_{12}^2 \end{aligned} \tag{2.6}$$

A general quadratic polynomial in stress components constructed from these invariants takes the following form (Hashin, 1980):

$$A_1 I_1 + B_1 I_1^2 + A_2 I_2 + B_2 I_2^2 + C_{12} I_1 I_2 + A_3 I_3 + A_4 I_4 = 1 \tag{2.7}$$

Considering only in-plane stresses in a UD composite, and using the Voigt notation, Eqn (2.7) can be reduced to the following form:

$$A_1 \sigma_1 + B_1 \sigma_1^2 + (A_2 - A_3)\sigma_2 + B_2 \sigma_2^2 + C_{12} \sigma_1 \sigma_2 + A_4 \sigma_6^2 = 1 \tag{2.8}$$

Remarkably, this equation is identical to the Tsai–Wu failure criterion, Eqn (2.5), when the constants in the two equations are equated as follows:

$$F_1 = A_1, F_2 = A_2 - A_3, F_{11} = B_1, F_2 = B_2, 2F_{12} = C_{12}, F_{66} = A_4 \tag{2.9}$$

Thus, using a tensor polynomial, as done by Tsai and Wu (1971), or a polynomial with stress invariants, as done by Hashin (1980), lead to the same result for the case of UD composites under in-plane stresses.

Hashin (1980) specified the basic failure criterion for UD composites, Eqn (2.8), for different assumed "failure modes," such as fiber failure modes in tension and compression, and matrix failure modes in tension, compression, and shear.

For the fiber failure mode, Hashin (1980) separated failure in tension from that in compression. For the tension failure mode he assumed influence of the in-plane shear stress on this failure mode by a quadratic curve given by

$$F_{11} \sigma_1^2 + F_{66} \sigma_6^2 = 1 \tag{2.10}$$

where the Tsai–Wu strength coefficients are used. It is noted that Hashin (1980) neglects the linear term in σ_1 present in Eqn (2.5). In terms of the composite strength values, the criterion for fiber failure mode in tension, Eqn (2.10), can be written as

$$\left(\frac{\sigma_1}{X}\right)^2 + \left(\frac{\sigma_6}{T}\right)^2 = 1 \tag{2.11}$$

Although this equation provides a curve-fitting basis for describing the combined effect of axial normal stress and in-plane shear stress on the fiber failure mode, Hashin (1980) admitted that there was no physical reason for the interaction to be described this way. In fact, he recommended that the second term in Eqn (2.11) be neglected, both for tension and compression. In other words, his preference was not to account for the effect of shear rather than risk accounting for it incorrectly.

For failure modes in a UD composite where the fibers remain intact, there could be different possibilities of failure in the matrix and at the fiber/matrix interface. Since the failure criteria by choice are to be formulated on a homogeneous composite, one cannot separate matrix failure from that of the interface. Also, the local stress states

in the matrix and at the interface cannot be known for a homogenized composite. Hashin (1980) therefore took a pragmatic approach of assuming that failure will initiate between fibers on a plane whose inclination will be determined by the stress state in the homogeneous composite. Since this failure plane must not cut through fibers (otherwise they will not be intact), its inclination is restricted to planes parallel to fibers (i.e., the normals to the planes are also normal to the fiber axis). Assuming the angle θ to describe this inclination, the failure function can be expressed as

$$f(\sigma_2, \sigma_6, \theta) = 1 \tag{2.12}$$

Hashin (1980) suggested that the value of θ that maximizes the function f would give the inclination of the failure plane. However, he did not offer a procedure for determining that value. Instead, he proposed the matrix failure criteria based on considerations of the nature of failure interactions due to normal and shear stresses.

For tensile matrix failure, Hashin (1980) suggested a quadratic interaction between σ_2 and σ_6, as for the tensile fiber failure mode, giving

$$\left(\frac{\sigma_2}{Y}\right)^2 + \left(\frac{\sigma_6}{T}\right)^2 = 1 \tag{2.13}$$

After elaborate arguments concerning the effect of shear stress on the matrix failure mode in compression, Hashin (1980) formulated the following criterion that requires distinguishing between shear strength in the axial and transverse directions:

$$\left(\frac{\sigma_2}{2T'}\right)^2 + \left[\left(\frac{Y'}{2T'}\right)^2 - 1\right]\frac{\sigma_2}{Y'} + \left(\frac{\sigma_6}{T}\right)^2 = 1 \tag{2.14}$$

where the prime on Y denotes the strength in compression and that on T indicates the transverse shear strength.

It is noted that no practical method exists to experimentally determine the "transverse" shear strength. In fact any attempt to induce failure in a UD composite under in-plane shear stress results in failure along fibers, which is interpreted as failure in "axial shear," given by $\sigma_6 = T$. For instance, applying torsion on a thin tube with fibers running in the circumferential direction produces failure along fibers.

The contributions made by Hashin (1980) can be summarized as follows. First, Hashin demonstrated that a single ellipsoidal description of UD composite failure, as in Tsai and Wu (1971), leads to physically unacceptable results, and consequently he proposed piecewise smooth surfaces as descriptors of failure interactions under different combinations of stress components. Hashin in that paper also separated fiber failure modes from matrix failure modes. For matrix failure modes, he postulated failure to occur on surfaces parallel to fibers but inclined otherwise at an angle for which he proposed an unspecified minimization principle.

Although the general failure criterion for UD composites under in-plane stresses, Eqn (2.8), is the same in Hashin (1980) as in Tsai and Wu (1971), Hashin's further

development of this criterion removed the inconsistency resulting from a single failure surface in the Tsai−Wu criterion and showed a way to improve description of failure for UD composites regarded as homogeneous orthotropic solids. This path was taken to further develop failure criteria in what has become known as Puck's failure theory (Puck, 1992; Puck & Schürmann, 1998).

The inclined failure plane postulated by Hashin (1980) and employed in Puck's theory is illustrated in Figure 2.1 (Puck, Kopp, & Knops, 2002), which shows the three traction components σ_n, τ_{nl}, and τ_{nt} acting on the failure plane. These traction components along with the plane's inclination angle θ_{fp} are the variables in the Puck theory. As described in Puck et al. (2002), a function $f_E(\theta)$, called the stress exposure factor or "risk of fracture", is defined based on suggestions in Hashin (1980), and fracture is assumed on the plane where this function takes its maximum with respect to the angle θ.

The seven parameters (or material constants) in the Puck theory for matrix failure modes are three strength constants and four so-called "inclination parameters." The latter are characteristic angles in the "master curves," which are graphical depictions of the assumed quadratic interactions between normal and shear tractions on the failure plane (see Figure 2.2). The interaction between tensile traction σ_n and either of the two shear tractions on the failure plane is assumed to be elliptical, as in most other theories, and this interaction for the case of compressive traction σ_n is taken to be parabolic. The argument for the parabolic assumption is that the presence of compressive normal traction impedes failure induced by shear on the failure plane. The inclination parameters (denoted by p with subscripts referring to tension, compression, or shear) are the angles with respect to the σ_n-axis made by tangents to the master curves at points of junction between the elliptical and parabolic parts of the master curves, as illustrated in

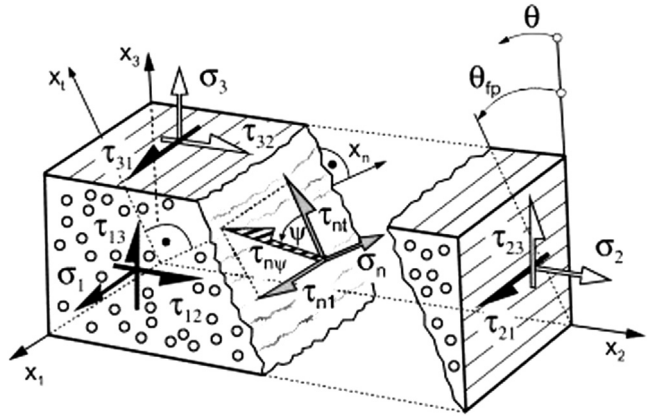

Figure 2.1 Illustration of the failure plane of inclination angle θ_{fp} with respect to the x_1−x_3 plane and the resolved normal stress σ_n and shear stresses τ_{nl} and τ_{nt} acting on the failure plane. Puck, A., Kopp, J., & Knops, M. (2002). Guidelines for the determination of the parameters in Puck's action plane strength criterion. *Composites Science and Technology*, *62*, 371−378.

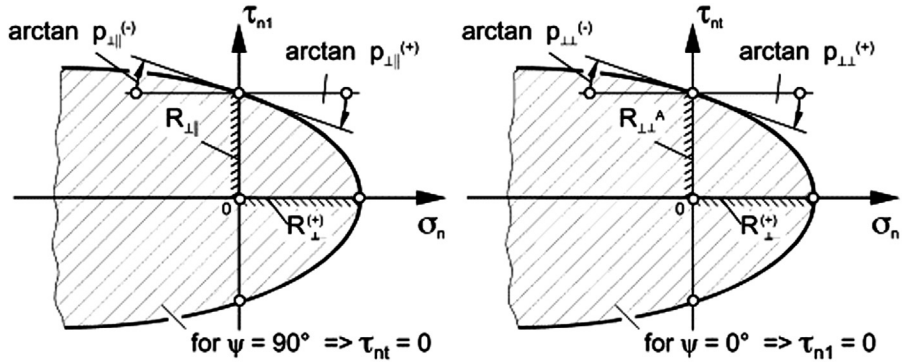

Figure 2.2 Sections of the master failure surface for $\psi = 90°$ (left) and $\psi = 0°$ (right). The angle ψ, as shown in Figure 2.1, is the angle between the transverse component τ_{nt} of the shear traction on the failure plane.
Puck, A., Kopp, J., & Knops, M. (2002). Guidelines for the determination of the parameters in Puck's action plane strength criterion. *Composites Science and Technology*, *62*, 371−378.

Figure 2.2. The procedures to determine the seven parameters are quite elaborate and are treated in Puck et al. (2002).

Over the years, several more failure theories have been advanced for UD composites treated as homogeneous orthotropic (or transversely isotropic) solids. For review of these theories, see Hinton et al. (2004). The discussion of the four theories above suffices to illustrate the nature of such theories. Based on the critical examination of the assumptions underlying the theories, it can be stated that there are severe limitations to describing the failure conditions for composite materials by the approach represented by these theories. The theory advanced in Azzi and Tsai (1965), that is the Tsai−Hill criterion, is based on a wrong underlying mechanism (metal yielding), while the Tsai−Wu criterion (Tsai & Wu, 1971) is simply a curve-fitting procedure in which a single quadratic failure interaction is assumed. The Hashin failure theory (Hashin, 1980) introduces multiple failure modes and assumed quadratic interaction between normal and shear stresses in each failure mode. It also introduces the concept of failure plane, which requires additional analysis and physical information. Puck's failure theory (Puck, 1992; Puck & Schürmann, 1998) continues on Hashin's proposed path and results in an elaborate process of data analysis.

It is this author's contention that the inherent limitations in the so-called phenomenological failure theories, illustrated by the four theories discussed above, make failure analysis by this approach of limited value. The early developments exemplified by the Tsai−Hill and Tsai−Wu criteria were justified at that time because of inadequate understanding of the failure mechanisms. Hashin's corrective measures improved the purely curve-fitting nature of these theories but have been shown to be limited by what can be done in the context of homogeneous solids. In view of the advances made in the past three decades, it is time now to take a mechanisms-based approach to composite failure. In the following section, the framework for such an approach will be described.

2.3 Mechanisms-based failure analysis

The first thing to recognize in a mechanisms-based approach is that failure is a local phenomenon, that is, governed by the stress/strain fields at the scale of the failure events. In fiber-reinforced composites, failure initiates at the so-called microscopic scale, which for polymer matrix composites of interest in most applications is in the range of one to a few multiples of fiber diameter. Depending on the remotely applied stress to a UD composite, the failure events consist of fiber breakage (in tension), fiber microbuckling and kinking (in compression), matrix cracking (brittle or ductile), and fiber/matrix debonding. While the fiber failure events can be analyzed in terms of the (uniaxial) fiber stress, influenced by any shear stress present, the matrix and interface failure events are governed by the inherently local triaxial stress state. The matrix failure events can be viewed as crack initiation followed by crack propagation, leading to eventual instability. The crack initiation process in a polymer matrix can involve phenomena at molecular scales, such as molecular chain stretching, rotation, and breakage, which can effectively be carried to the homogenized polymer description in terms of strain energy of the deformed polymer. Once a crack has formed, its propagation in brittle or ductile manner can be analyzed by fracture mechanics methods using stress intensity factors, energy release rates, fracture toughness, etc. Alternatively, cohesive zone-based methodologies can be used.

Practical composite materials are inherently nonuniform in a variety of ways. Depending on how they have been processed and manufactured, their interior contains irregularities and defects, for example, nonuniform fiber diameters, misaligned and wavy fibers, broken fibers, and nonuniformly distributed fibers in the UD composite cross-section, partially cured regions and voids in matrix, and unbonded fiber/matrix and lamina/lamina interfaces. These irregularities and defects affect the local stress fields that govern the failure events. Thus, analyzing failure events requires properly accounting for these effects. The approach to achieving this is discussed next.

2.3.1 Representative volume element for failure analysis

The field of micromechanics treats representative volume element (RVE) as a basic concept for estimating average or overall properties of heterogeneous solids (see, e.g., Nemat-Nasser & Hori, 1993). For regular microstructures, a unit cell or a repeating region is used for the averaging procedures involved. The success of micromechanics has prompted multiscale modeling as an extension and generalization of this field. In particular, the availability of increasing computer power has popularized the multiscale modeling methodology to the extent that the US National Research Council (2008) proposed this as the basis for the Integrated Computational Materials Engineering (ICME) approach to materials development. Before proceeding with this approach to address failure in composite materials, a word of caution is warranted: the multiple scale hierarchy necessary for analyzing deformation of heterogeneous solids does not necessarily apply when failure is considered. The failure events in a composite structure do not always progress in concert with the geometrical hierarchy of the

internal structure. The interactions and connectivity of the failure entities can result in a different hierarchy of scales, as discussed in Talreja (2010).

A systematic way to develop a methodology for mechanisms-based failure analysis is to first delineate failure mechanisms operating in elementary loading modes followed by examining interactions under combined loading conditions. In the following discussion this procedure will be outlined for UD composites. Laminates will be treated subsequently.

2.3.2 Tensile loading parallel to fibers

Under an imposed tensile load parallel to fibers, sporadic fiber breakage occurs at load levels much below the failure load. These fiber breakages occur at weak points along fibers, that is where fiber surface defects are sufficiently severe to reach the fiber failure stress. As loading increases, more fibers fail at smaller defects and in the vicinity of already broken fibers. The connectivity of the fiber breaks through matrix cracking eventually generates a plane in which a cluster (core) of fiber failures produces a crack-like entity that grows unstably, causing total failure (Figure 2.3). The progression of failure events is inherently stochastic, governed by the conditions (fiber defects and distribution) in a local failure region. Although it is common in failure theories to assign a tensile strength $\sigma_{xx} = X$, where σ_{xx} is the remotely applied average stress, to the fiber failure mode, the failure process can only be reasonably described in statistical terms. A large body of work in this field exists; for a review, see Phoenix and Beyerlein (2000).

2.3.3 Compressive loading parallel to fibers

The failure events in UD composites subjected to axial compression are largely different from those under tension described above. The fibers can undergo

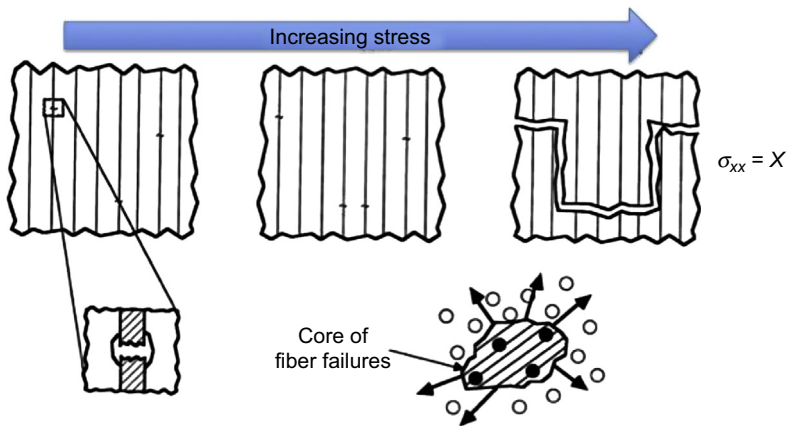

Figure 2.3 Schematic illustration of the sequence of failure events leading to failure under imposed axial tensile loading.

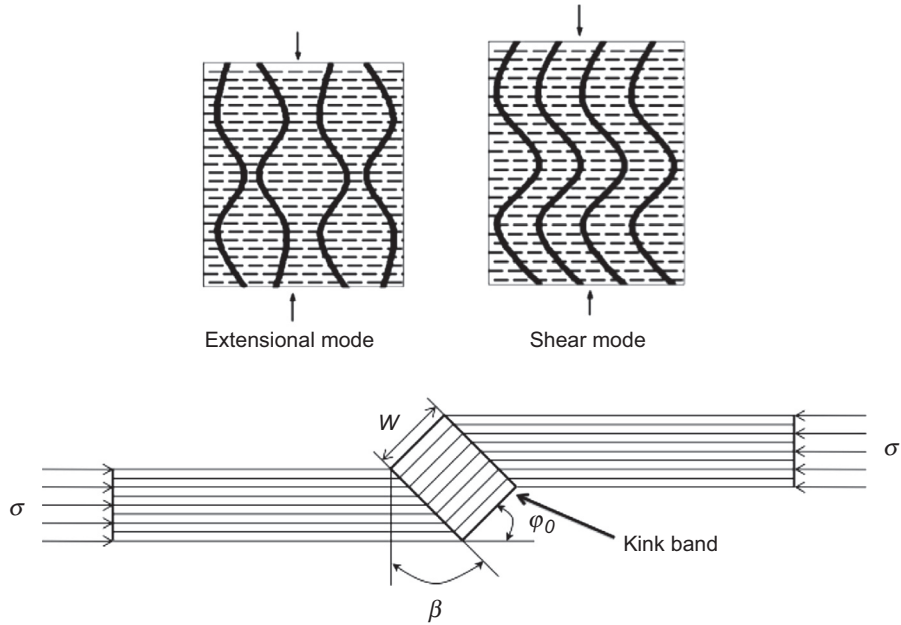

Figure 2.4 Schematic illustration of failure modes in UD composites under compression.

compression buckling at a microscopic scale, that is, over a short length equal to a few fiber diameters. This so-called microbuckling can ideally occur either in an extensional mode or in a shear mode (Figure 2.4), as first proposed by Rosen (1965). Triggered by the local shear stress, for example, caused by matrix defects, kink bands (Figure 2.4) are found to form from the microbuckled fibers. For a review of the kink band formation and propagation to failure, see a review by Budiansky and Fleck (1994), and for an overview of all possible failure events in compression, see Jelf and Fleck (1992). Vogler, Hsu, and Kyriakides (2000) have studied failure of UD composites under combined compression and shear. Their work shows that the interaction of compression and shear stresses in initiating compression failure is quite different from that of tension and shear stresses in tensile failure.

2.3.4 Tensile loading normal to fibers

Observations of failure under this imposed loading show that the initiation of cracks occurs at the fiber/matrix interface followed by their coalescence to a large crack described as a transverse matrix crack (Figure 2.5). Asp, Berglund, and Talreja (1996a) studied the crack initiation phenomenon under stress states resembling those that come about under transverse loading of UD composites with glassy polymers as matrix. They found that yielding of the matrix in such stress states is suppressed while dilatation-induced cavitation is more likely. By systematically examining the local stress states in transversely loaded UD composites of different fiber packing arrangements and fiber volume fractions, Asp, Berglund, and Talreja (1996b) then found that

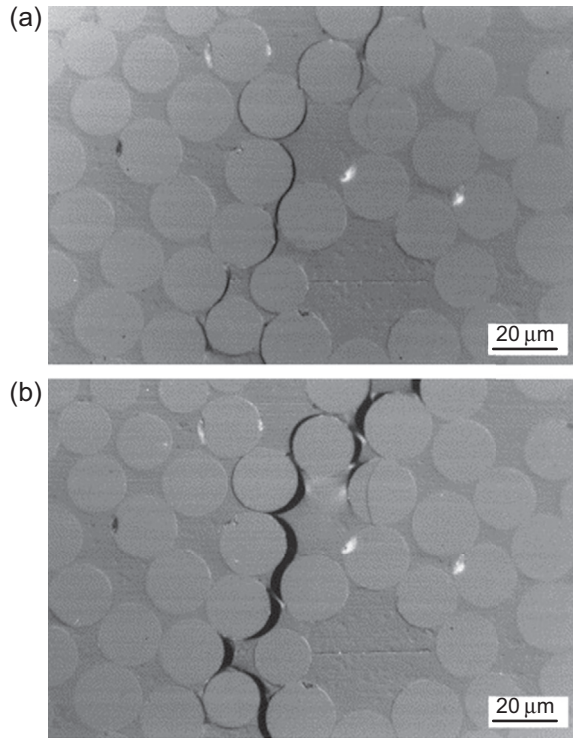

Figure 2.5 (a) Fiber-matrix debonds and (b) matrix crack formed by coalescence of debonds. Gamstedt, E. K., & Sjogren, B. A. (1999). Micromechanisms in tension-compression fatigue composite laminates containing transverse plies. *Composites Science and Technology*, *59*, 167−178.

the critical energy density for dilatation (associated with failure from triaxial tension) was generally lower than the critical energy density for distortion (associated with yielding) in the matrix within the composite. Also, the locations in the matrix within the composite where the largest values of the two energies occurred were different. More importantly, the sites where the dilatation energy density attained high values were found to be close to the fiber surface in the matrix. Asp et al. (1996b) therefore concluded that what appeared to be fiber/matrix debonding was indeed cavitation-induced brittle failure of the matrix, leading to fiber/matrix interface failure.

In real composites, the distribution of fibers in the cross-section is generally nonuniform and depends on the manufacturing process. Bulsara, Talreja, and Qu (1999) treated the problem of characterizing arbitrary fiber distributions by statistical methods that use the cross-sectional images of actual composites for estimating the statistical parameters. A basic issue in this approach is how large the field of observed images needs to be in order to be representative of the microstructure. Bulsara et al. (1999) studied the RVE size of a ceramic matrix composite and applied appropriate failure criteria for two failure modes, viz fiber/matrix debonding and radial cracking. They evaluated the level of the applied thermal or mechanical loading associated with initiation of a given failure mode and suggested selecting the RVE size that minimizes the coefficient of variation of the estimated applied failure stress.

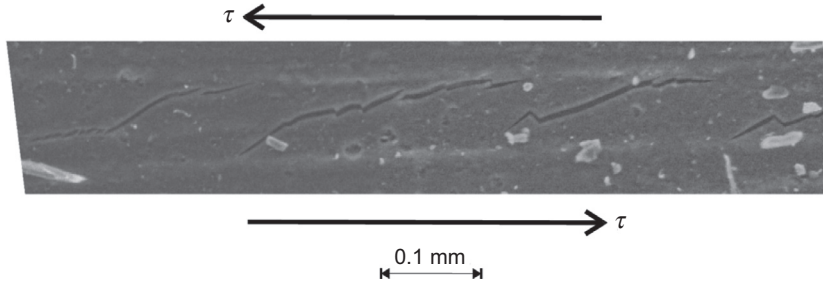

Figure 2.6 Cracks generated under axial shear stress along planes inclined to fibers. Redon, O. (2000). Fatigue damage development and failure in unidirectional and angle-ply glass fibre/carbon fibre hybrid laminates. Risø-R-1168, Risø National Laboratory: Roskilde, Denmark.

2.3.5 In-plane shear stresses

When the loading mode on a UD composite is such that the major stress produced is the in-plane shear stress in the material coordinate system, for example under torsion of a tube having fibers in the circumferential direction, it is commonly assumed that the failure mechanism is a "shear failure." In fact, evidence suggests that the failure is not initiated by the shear stress itself but by the maximum tensile stress on planes inclined to the fiber direction. Such evidence was reported by Redon (2000) and is shown in Figure 2.6. Carraro and Quaresimin (2014) more recently reported similar evidence in tubes subjected to combined cyclic torsion and tension normal to fibers. These observations suggest that in a polymer matrix reinforced by stiff fibers of high volume fraction the matrix material is under high triaxiality of stress state when the remote loading is in-plane shear stress such that the energy of distortion is low, leading to conditions suited for brittle failure. The governing condition for this brittle failure is not the same as that for brittle failure resulting from cavitation, which is driven by the dilatation energy density. For brittle cracking on an inclined plane (as seen in Figure 2.6), the driving force is the tensile stress acting normal to the plane. Carraro and Quaresimin (2014) found this to be the case by investigating the crack initiation process at different ratios of the imposed shear and transverse stresses characterized by the ratio $\lambda_{12} = \sigma_6/\sigma_2$. At high values of this ratio they found the local maximum principal stress to correlate with the fatigue life, while in purely transverse loading cases the dilatation energy density criterion (Asp et al., 1996a,b) described the failure initiation well.

2.3.6 Compressive loading normal to fibers

Failure initiation in this loading mode is not as well understood as in the other loading modes because of the difficulties involved in experimental testing and observations. Vogler and Kyriakides (1999) conducted tests on a UD carbon/PEEK composite under pure transverse compression, pure in-plane shear, and in combinations of compression and shear. They studied the deformation response, which displayed nonlinearity, partly due to time-dependent behavior, in both compression and shear. Their failure-related

observations were primarily based on the fracture surface images. The initiation of failure events and their progression was not clarified. Gonzales and Llorca (2007) studied failure of a UD carbon/epoxy composite under transverse compression and found inelastic deformation of the matrix and interface debonding to play roles in the failure process. They performed a computational simulation of the deformation and failure of the composite by using assumed models for matrix inelasticity and interface failure. Totry, González, and LLorca (2008) extended this approach to include longitudinal shear combined with transverse compression on a carbon/PEEK composite.

2.3.7 Laminate failure

When a UD composite is in the form of a ply (or a set of aligned plies) within a laminate, it experiences in-plane stresses resulting from loads on the laminate. The initiation of failure in a given ply of a laminate can then be analyzed by the multiscale failure analysis by imposing these stresses on the RVE boundary. However, such analysis will only provide failure initiation conditions, as discussed above. The subsequent failure progression will be different from what occurs in a UD composite in the free condition, that is not bonded to differently oriented plies in a laminate. The ply failure in a laminate is a constrained failure process whose analysis will be discussed next.

The constrained ply failure process in laminates has been studied experimentally and analyzed by a variety of models since the beginning of the 1970s. An excellent summary of this process is captured in Figure 2.7 (Jamison, Schulte, Reifsnider, & Stinchcomb, 1984), which qualitatively depicts the stages in the progression of the process. Although it was developed based on observations of failure mechanisms in tension−tension fatigue of carbon/epoxy laminates, it is illustrative of the failure process in quasi-static loading as well. Overall, the early part of the process involves multiplication of cracks within the plies of a laminate, leading to saturation of the crack density in individual plies. On continued loading, the ply cracks tend to divert into the ply interfaces, thereby connecting with neighboring cracks. Further interface cracking leads to separation of plies (delamination), and subsequent fiber breakage in plies resulting in final failure.

For a ply within a laminate under a general loading, the stress state imposed on the ply can be determined analytically, for example by the classical laminate theory for simple geometry and loading cases, or numerically for more complex situations. The local stress fields at the scale of fiber size can then be determined within an appropriately constructed RVE (see discussion above). The initiation of the first crack formation in a ply is governed by the local stress state and can be analyzed by the multiscale approach discussed above for the case of failure initiation in a free (unconstrained) ply. If the failure initiation process in a UD composite is fiber/matrix debonding, then its subsequent development to unstable crack growth is almost immediate. However, when the same UD composite is in a constrained environment within a laminate, the failure initiation process will still be the same, but the constraint will reduce the crack surface separation when a crack has formed. Furthermore, the crack growth in most cases will be arrested at the interfaces, leading further crack growth to proceed in the direction of fibers in the ply. This crack growth has in a part of the literature been

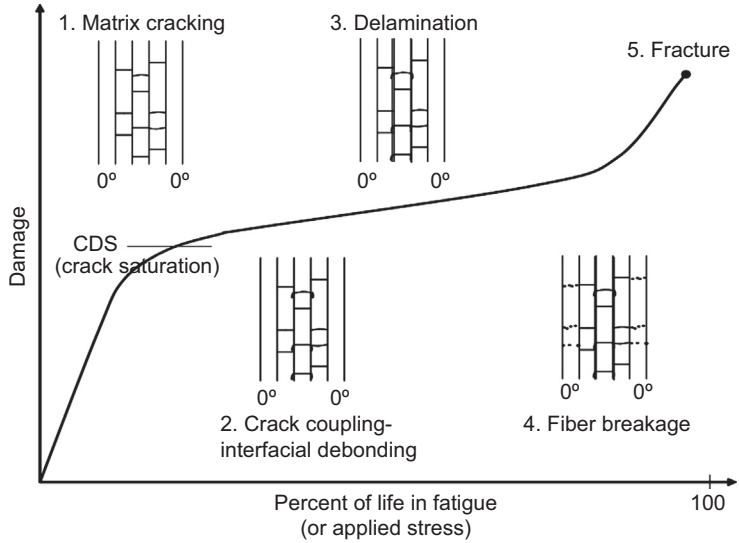

Figure 2.7 A schematic depiction of the evolution of damage (failure events) in a composite laminate.
Jamison, R. D., Schulte, K., Reifsnider, K. L., & Stinchcomb, W. W. (1984). Characterization and analysis of damage mechanisms in tension-tension fatigue of graphite/epoxy laminates. Effects of defects in composite materials. *ASTM STP*, *836*, 21−55; Reprinted, with permission, from ASTM STP 836 effects of defects in composite materials, copyright ASTM International, 100 Barr Harbor Drive, West Conshohocken, PA 19428.

described as "tunneling." These tunneling cracks form initially at random locations in a ply, without interaction with one another, but once their mutual spacing reduces, interactions occur. The interactive cracking process generates more cracks with reducing average crack spacing, tending to a limiting value. The vast literature related to the multiple ply cracking has been comprehensively reviewed in Talreja and Singh (2012).

Continued loading on a laminate beyond the point of ply cracking saturation results in cracks diverting into the ply/ply interfaces, eventually connecting in the interface planes and causing delamination (Figure 2.7). Final failure in the form of separation of parts is often too complex to analyze and perhaps of little value since in many cases the structure loses its functionality before that point.

2.4 A comprehensive failure analysis strategy

Figure 2.8 depicts the proposed procedure for conducting failure analysis for laminated structures. It reflects the remedies for removing the limitations inherent in the phenomenological approaches. In fact, the strategy governing the proposed procedure is an alternative approach that addresses failure assessment not by a set of assumptions concerning the material failure but instead by analyzing the failure at the local scale where

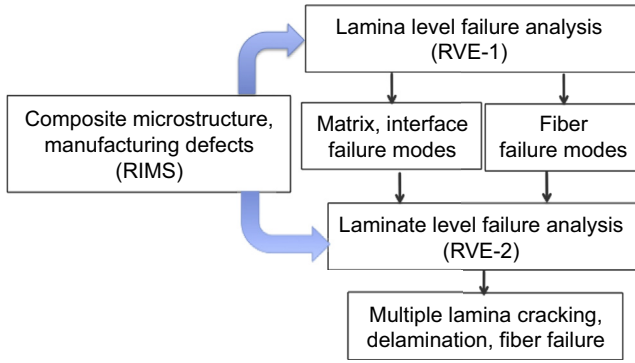

Figure 2.8 A multiscale failure analysis procedure for laminates.

the failure mechanisms operate. Also, the procedure accounts for real material constitution by incorporating microstructure (including defects) using the notion of RVE. Furthermore, the multiscale analysis in the proposed procedure is conducted in concert with the observed hierarchy of failure mechanisms, also with the RVEs of appropriate sizes.

Referring to Figure 2.8, the failure analysis starts by identifying the real initial material state (RIMS) as produced by the manufacturing process of the composite part at hand. The information acquired about the morphology of the internal composite structure, including defects, is then fed into the lamina-level RVE in which failure analysis is conducted based on the stress fields resulting from the specified imposed loading. The outputs of the failure analysis, organized as failure events and their progression (failure modes), are fed into the higher (laminate) level RVE, which is constructed from information concerning the RIMS and the lamina failure modes. The stress and failure analyses of this RVE provide the constrained lamina cracking, the ply interface failure (delamination), and fiber failure that all determine the loss of functionality of the laminate.

2.5 Conclusions

Failure in composite materials occurs by a variety of mechanisms depending on the imposed loading, but in each case the failure events and their progression are governed by the local conditions. From the lowest scale where the first failure events occur to the structural scale of final failure there is a hierarchy of scales that is not always aligned with that of the microstructure. A multiscale framework to conduct failure analysis of composite laminates has been proposed here that uses the concept of material state at different length scales through representative volume elements, which incorporate nonuniformities of microstructure and defects induced by manufacturing. This approach to failure analysis is justified as an alternative to the currently used phenomenological failure theories. A few of such theories that are representative of this class of

theories have been examined here to clarify their inability to describe failure in composite materials on fundamental grounds.

References

Asp, L., Berglund, L. A., & Talreja, R. (1996a). Prediction of matrix initiated transverse failure in polymer composites. *Composites Science and Technology, 56*, 1089−1097.

Asp, L., Berglund, L. A., & Talreja, R. (1996b). A criterion for crack initiation in glassy polymers subjected to a composite-like stress state. *Composites Science and Technology, 56*, 1291−1301.

Azzi, V. D., & Tsai, S. (1965). Anisotropic strength of composites. *Experimental Mechanics, 5*, 283−288.

Budiansky, B., & Fleck, N. A. (1994). Compressive kinking of fiber composites: a topical review. *Applied Mechanics Reviews, 47*, S246−S250.

Bulsara, V. N., Talreja, R., & Qu, J. (1999). Damage initiation under transverse loading of unidirectional composites with arbitrarily distributed fibers. *Composites Science and Technology, 59*, 673−682.

Carraro, P. A., & Quaresimin, M. (2014). A damage based model for crack initiation in unidirectional composites under multiaxial cyclic loading. *Composites Science and Technology, 99*, 154−163.

Gamstedt, E. K., & Sjogren, B. A. (1999). Micromechanisms in tension-compression fatigue composite laminates containing transverse plies. *Composites Science and Technology, 59*, 167−178.

Goldenblat, I. I., & Kopnov, V. A. (1965). Strength criteria for anisotropic materials. Mecchanica IMZGA, Izvestia Academy. *Nauk USSR, 6*, 77−83.

González, C., & LLorca, J. (2007). Mechanical behavior of unidirectional fiber-reinforced polymers under transverse compression: microscopic mechanisms and modeling. *Composites Science and Technology, 67*, 2795−2806.

Hashin, Z. (1980). Failure criteria for unidirectional fiber composites. *Journal of Applied Mechanics, 47*, 329−334.

Hencky, H. (1924). Zur Theorie plastischer Deformationen und der hierdurch im Material hervorgerufenen Nachspannungen. *ZAMM Journal of Applied Mathematics and Mechanics/Zeitschrift für Angewandte Mathematik und Mechanik, 4*, 323−334.

Hill, R. (1948). A theory of the yielding and plastic flow of anisotropic materials. *Proceedings of Royal Society London, A193*, 281−297.

Hinton, M. J., Kaddour, A. S., & Soden, P. D. (Eds.), (2004). *Failure criteria in fibre reinforced polymer composites: The world-wide failure exercise*. Amsterdam: Elsevier.

Jamison, R. D., Schulte, K., Reifsnider, K. L., & Stinchcomb, W. W. (1984). Characterization and analysis of damage mechanisms in tension-tension fatigue of graphite/epoxy laminates. Effects of defects in composite materials. *ASTM STP, 836*, 21−55.

Jelf, P. M., & Fleck, N. A. (1992). Compression failure mechanisms in unidirectional composites. *Journal of Composite Materials, 26*, 2706−2726.

Jones, R. M. (1999). *Mechanics of composite materials*. Philadelphia: Taylor & Francis.

National Research Council (US) Committee on Integrated Computational Materials Engineering. (2008). *Integrated computational materials engineering: A transformational discipline for improved competitiveness and national security*. National Academies Press.

Nemat-Nasser, S., & Hori, M. (1993). *Micromechanics: Overall properties of heterogeneous materials*. Amsterdam: Elsevier.

Phoenix, S. L., & Beyerlein, I. J. (2000). Statistical strength theory for fibrous composite materials. *Comprehensive Composite Materials, 1*, 559−639.

Puck, A. (1992). A failure criterion shows the direction. Kunststoffe. *German Plastics, 82*, 29−32 (German text pp. 607−610).

Puck, A., Kopp, J., & Knops, M. (2002). Guidelines for the determination of the parameters in Puck's action plane strength criterion. *Composites Science and Technology, 62*, 371−378.

Puck, A., & Schürmann, H. (1998). Failure analysis of FRP laminates by means of physically based phenomenological models. *Composites Science and Technology, 58*, 1045−1067.

Redon, O. (2000). *Fatigue damage development and failure in unidirectional and angle-ply glass fibre/carbon fibre hybrid laminates*. Roskilde, Denmark: Risø-R-1168, Risø National Laboratory.

Rosen, B. W. (1965). *Mechanics of composite strengthening. Fiber composite materials* (2nd ed.) (pp. 37−75). Philadelphia: American Society of Metals.

Talreja, R. (2010). On multi-scale approaches to composites and heterogeneous solids with damage. *Philosophical Magazine, 90*, 4333−4348.

Talreja, R. (2014a). An assessment of the fundamentals of failure theories for composite materials. *Composites Science and Technology, 105*, 190−201.

Talreja, R. (2014b). Analysis of failure in composite structures. In H. Altenbach, & T. Sadowski (Eds.), *Failure and damage analysis of advanced materials* (pp. 255−278). Springer.

Talreja, R., & Singh, C. V. (2012). *Damage and failure of composite materials*. Cambridge University Press.

Totry, E., González, C., & LLorca, J. (2008). Prediction of the failure locus of C/PEEK composites under transverse compression and longitudinal shear through computational micromechanics. *Composites Science and Technology, 68*, 3128−3136.

Tsai, S. W., & Wu, E. M. (1971). A general theory of strength for anisotropic materials. *Journal of Composite Materials, 5*, 58−80.

Vogler, T. J., & Kyriakides, S. (1999). Inelastic behavior of an AS4/PEEK composite under combined transverse compression and shear. Part I: experiments. *International Journal of Plasticity, 15*(8), 783−806.

Vogler, T. J., Hsu, S. Y., & Kyriakides, S. (2000). Composite failure under combined compression and shear. *International Journal of Solids and Structures, 37*, 1765−1791.

The origins of residual stress and its evaluation in composite materials

3

N. Zobeiry, A. Poursartip
The University of British Columbia, Vancouver, BC, Canada

3.1 Introduction

It is now well accepted that the development of residual stresses during the manufacturing of structural components made of high-performance composites leads to dimensional changes in the final cured component. Based on tolerance requirements for the final part, these dimensional changes have to be remedied, either before manufacturing using methods such as tool/mold compensation (nowadays often by process simulation) (Fernlund et al., 2003; Johnston, Vaziri, & Poursartip, 2001) or after manufacturing through more costly methods such as shimming (Fernlund et al., 2001). Consequently, process simulation is increasingly the method of choice to predict residual stress development and resulting dimensional changes (Fernlund, Abdel-Rahman, et al., 2002; Fernlund et al., 2001, 2003; Johnston, 1997; Johnston, Hubert, Fernlund, Vaziri, & Poursartip, 1996; Johnston et al., 2001).

However, while designers are increasingly aware of the effects of residual stress on dimensional changes of composites (often presented in terms of spring-in or warpage), and the tools to predict them (Fernlund, Abdel-Rahman, et al., 2002; Fernlund et al., 2003; Johnston et al., 1996, 2001), the effects of residual stresses on the mechanical performance of composites strength are poorly understood and are mostly benignly neglected by at best assuming a constant value.

There are many factors contributing to the formation of residual stress in composite materials (Johnston, 1997; Parlevliet, Bersee, & Beukers, 2006). These factors can be divided into four categories: micro-level, macro-level, coupon-level, and component-level factors. The root cause of residual stress at the micro level is the development of free strains due to thermal changes (i.e., coefficients of thermal expansion (CTE) effect) and phase changes (i.e., cross-linking or crystallization). As a result, the mismatch of free strains in fiber and matrix leads to residual stress development (Johnston, 1997). At the laminate level, stress discontinuities between plies, coupled with the gradients in temperature and degree of cure, further contributes to the level of residual stress (Johnston, 1997). At the coupon and component levels, other factors such as tool growth coupled with tool/part interaction, ply drop-off, and inserts might play a role to further increase the residual stress (Fernlund, Abdel-Rahman, et al., 2002; Twigg, Poursartip, & Fernlund, 2004a, 2004b).

Structural Integrity and Durability of Advanced Composites. http://dx.doi.org/10.1016/B978-0-08-100137-0.00003-1

At the end of manufacturing process, due to all of the above contributing factors, stress is locked within the material and consequently reduces its load bearing capacity. Although the level of residual stress might be negligible compared to the fiber strength, it becomes comparable to the design allowables at the matrix level. By understanding the effect of the various processing parameters on residual stress development, one might be able to reduce the amount of residual stress and consequently increase the mechanical performance and design allowables of the matrix.

3.2 Origins of residual stress

3.2.1 Formation of free strains

Free strains are the root cause of residual stresses in laminated composites. During and/or after the manufacturing process, development of free strains and the mismatch of these strains between different components lead to the formation of residual stresses. In general, the free strains are divided into three categories:

- Strains due to thermal changes (i.e., thermal expansion/shrinkage)
- Strains due to phase changes of the matrix (i.e., cross-linking or crystallization)
- Strains due to moisture absorption

In a homogeneous and unbounded body, the development of free strains does not create any stresses, hence the name (i.e., free strains). However, as a result of anisotropy of the material behavior (i.e., mismatch of free strains) and/or due to the external constraints (e.g., boundary conditions), residual stresses are developed in a composite material.

Consider a homogeneous body subjected to a uniform change of temperature, ΔT, as depicted in Figure 3.1. In this case, the dimensional changes due to the temperature change are without developing any stresses. The total strain in the body can be calculated using the following equation:

$$\{\varepsilon\}_{\text{free}} = \{\alpha\}\Delta T \tag{3.1}$$

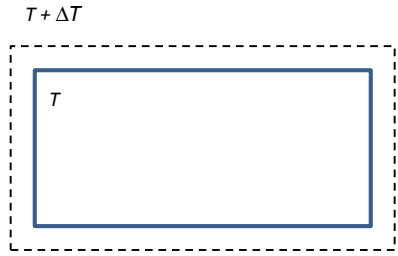

Figure 3.1 Dimensional changes in an unbounded homogeneous body subjected to change in the temperature from T to $T + \Delta T$.

in which α is the matrix of the CTEs. In such a system, subjected to external loads or constraints, the stress−strain relationship is modified as follows to calculate the total strain:

$$\{\varepsilon\}_{\text{total}} = [C]\{\sigma\} + \{\alpha\}\Delta T \tag{3.2}$$

in which C is the material compliance matrix and σ is the stress matrix. Combining Eqns (3.1) and (3.2), we can calculate the stresses as follows:

$$\{\sigma\} = [S](\{\varepsilon\}_{\text{total}} - \{\varepsilon\}_{\text{free}}) = [S](\{\varepsilon\}_{\text{mechanical}}) \tag{3.3}$$

in which S is the material stiffness matrix. This equation implies that free strains do not contribute to the overall stresses in the body, and only the mechanical portion of the total strains results in the stress formation.

As mentioned earlier, the free strains in the body can be divided into three categories:

$$\{\varepsilon\}_{\text{free}} = \{\varepsilon\}_{\text{thermal}} + \{\varepsilon\}_{\text{moisture}} + \{\varepsilon\}_{\text{phase changes}} \tag{3.4}$$

The phase change strains are related to cross-linking/crystallization process during which material shrinks (i.e., curing/crystallization shrinkage). Moisture absorption results in the development (or typically reduction) of in-service free strains.

3.2.2 Development of residual stresses

As mentioned in the previous section, absent any constraints or mismatch of strains, the development of free strains does not lead to development of residual stresses. However, in laminated composites, considering the anisotropy of material behavior in different directions, including the mismatch of thermal and phase-change properties between fiber and matrix, residual stresses are formed, which in turn results in reducing the mechanical performance and the dimensional changes of the material. Coupled with the mismatch of free strains between fiber and matrix are other factors such as the mismatch of thermal properties between the tool and the composite part and the imposed constraints on the part through the tool/part interaction.

Different factors contribute to the development of residual stresses at different size scales. These scales can be divided into four categories of micro, laminate, coupon, and component levels as shown in Figure 3.2. These factors are briefly explained in the next sections.

3.2.2.1 Micro level

At the micro level, due to the mismatch of free strains in fiber and matrix, residual stresses are developed. As a simple example, consider the mismatch of free strains in a unidirectional lamina subjected to no external load as shown in Figure 3.3.

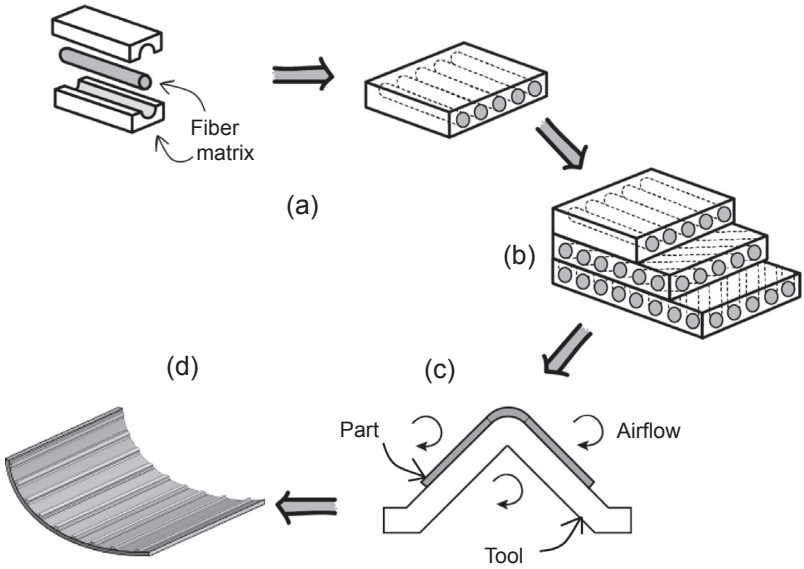

Figure 3.2 Different size scale levels for laminated composites, (a) micro level, (b) laminate level, (c) coupon level, and (d) component level.

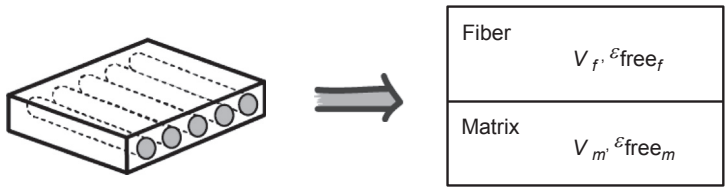

Figure 3.3 Representative volume element for a lamina with known volume fractions.

In this case, the total stress on a representative volume element (RVE) is equal to zero. Therefore, the equilibrium equation can be written as follows:

$$V_m \cdot \sigma_{\text{residual}_{\text{matrix}}} + V_f \cdot \sigma_{\text{residual}_{\text{fiber}}} = 0 \tag{3.5}$$

in which V_f and V_m are the volume fractions of fiber and matrix, respectively. Substituting from Eqn (3.3), we can rewrite Eqn (3.5) as

$$V_m \cdot E_m\left(\varepsilon - \varepsilon_{\text{free}_m}\right) + V_f \cdot E_f\left(\varepsilon - \varepsilon_{\text{free}_f}\right) = 0 \tag{3.6}$$

in which ε is the total strain of the RVE. This strain can now be calculated as

$$\varepsilon = \frac{V_m E_m \varepsilon_{\text{free}_m} + V_f E_f \varepsilon_{\text{free}_f}}{E} \tag{3.7}$$

in which E is the total modulus of the RVE. Finally, the residual stress in the matrix can be calculated as

Table 3.1 Parameters that will affect the mismatch of free strains and development of residual stresses at the micro level

Object	Parameter	
Material	Fiber	Elastic and viscoelastic properties
		Volume fraction
		Architecture
		Thermal properties (i.e., coefficients of thermal expansion (CTE))
	Matrix	Elastic and viscoelastic properties
		Cross-linking/crystallization kinetics
		Cross-linking/crystallization shrinkage
		Thermal properties (e.g., CTE, conductivity)
		Volume fraction
	Interface (i.e., sizing)	Bonding properties
	Void	Volume fraction
Process	Temperature cycle (i.e., heating and cooling cycle)	

$$\sigma_{\text{residual}_{\text{matrix}}} = \frac{V_f \cdot E_f E_m \left(\varepsilon_{\text{free}_m} - \varepsilon_{\text{free}_f}\right)}{E} \tag{3.8}$$

This equation shows that the residual stress in matrix is a function of mismatch of free strains, elastic properties, and volume fractions. Aside from these properties, at the micro level there are various other parameters that can affect the development of free strains in fiber and matrix and consequently affect the development of residual stresses. Equation (3.8) was derived with the assumption that fiber and matrix behave elastically. In reality, the viscoelastic properties of the material significantly affect the development of residual stresses. Coupled with the viscoelastic properties are other factors including cross-linking/crystallization shrinkage during the manufacturing process and also the effect of the process temperature cycle. All the parameters that can affect the development of residual stresses at the micro level are listed in Table 3.1.

3.2.2.2 Laminate level

At the laminate level, the constraints and stresses imposed by the layers oriented along different directions further contribute to the development of residual stresses. For a laminated composite, the extension, coupling, and bending stiffness (A, B, and D, respectively) are defined as follows:

$$[A] = \sum_{k=1}^{n} \left[\overline{S_k}\right] \cdot t_k \tag{3.9}$$

$$[B] = \sum_{k=1}^{n} \left[\overline{S_k}\right] \cdot t_k \cdot \overline{z_k} \tag{3.10}$$

$$[D] = \sum_{k=1}^{n} \left[\overline{S_k}\right] \cdot \left(t_k \cdot \overline{z_k}^2 + \frac{t_k^3}{12} \right) \tag{3.11}$$

in which S_k is the stiffness matrix of the kth layer, t_k is the thickness of the kth layer, and z_k is the distance of the center of the layer to the center of the laminate. The force strain is modified to include the effect of free strains as follows:

$$\begin{Bmatrix} N \\ M \end{Bmatrix} = \begin{bmatrix} A & B \\ B & D \end{bmatrix} \begin{Bmatrix} \varepsilon_0 \\ \kappa_0 \end{Bmatrix} - \begin{Bmatrix} N_{\text{free}} \\ M_{\text{free}} \end{Bmatrix} \tag{3.12}$$

in which N and M are the applied load and moment, ε_0 and κ_0 are the strain and curvature of the mid-plane of the laminate. N_{free} and M_{free} are force and moment related to the free strains and can be calculated as follows:

$$[N_{\text{free}}] = \sum_{k=1}^{n} \left[\overline{S_k}\right] \cdot t_k \cdot \left\{\varepsilon_{\text{free}_k}\right\} \tag{3.13}$$

$$[M_{\text{free}}] = \sum_{k=1}^{n} \left[\overline{S_k}\right] \cdot t_k \cdot \overline{z_k} \cdot \left\{\varepsilon_{\text{free}_k}\right\} \tag{3.14}$$

Equation (3.12) resembles Eqn (3.3) in the sense that free strains do not contribute to the development of forces. It is in fact the mismatch of free strains between layers with different orientations that leads to the development of residual stresses. These equations also show that the lay-up sequence and also thicknesses of the layers affect the residual stress development. Additional parameters at the laminate level that might contribute to the development of residual stresses are listed in Table 3.2.

3.2.2.3 Coupon level

At the coupon level, a simple system of part(s), tool(s), and processing environment as shown in Figure 3.2(c) is considered. In such a system, along with the material properties mentioned in the micro and laminate levels, the interactions of tool and part and also the tool properties play a role in the development of residual stresses. During the manufacturing process, the thermal expansions of the tool and part are coupled via tool/part interaction to create residual stresses in the part. For the part, the phase change related strains must be added to the thermal expansion.

Table 3.2 Additional parameters that will affect the formation of residual stresses at the laminate level

Object	Parameter
Part	Lay-up
	Thickness
Process	Through thickness temperature gradient

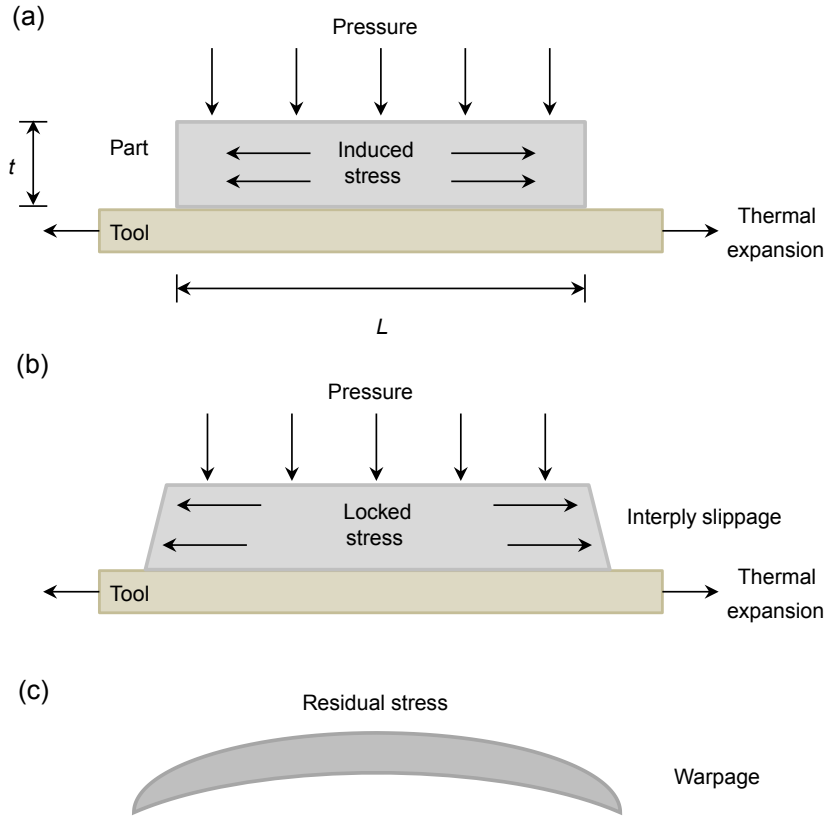

Figure 3.4 Tool–part interaction and residual stress development: (a) tool expands on heating and friction/bonding at the interface induces tensile stresses in the part; (b) some of the stresses are relieved through interply slippage, and a stress gradient is locked in the part as curing progresses, and (c) demolding results in the formation of compressive residual stresses and warpage.

Table 3.3 Additional parameters that will affect the formation of residual stresses at the coupon level

Object	Parameter	
Part	Geometry	
Tool	Soft tooling	Thermal properties
		Thickness
	Hard tooling	Thermal properties
		Thickness
		Surface roughness
		Surface preparation (i.e., release agents)
Process	Pressure cycle	
Facility	Heat transfer coefficients	

As a simple example, the manufacturing process of a thermoset-based flat composite part on a flat tool is depicted in Figure 3.4(a). During the manufacturing process while heating up the part, the tool expands. The expansion of the tool imposes stresses on the part through friction/bonding. Since the matrix is not cured yet, some of the stress is relieved though interply slippage (Fernlund & Floyd, 2007; Ridgard, 1993; Twigg et al., 2004a, 2004b). The final stress gradient is locked in the material as cure progresses (Figure 3.4(b)). At the end of the manufacturing process and demolding of the part, the balance of forces results in the relief of some of the residual stresses in the part and a final warped balanced geometry (Figure 3.4(c)). It has been shown that in such a case, aside from the interface bonding/friction properties and the temperature cycle, the most important parameters are part dimensions (i.e., length and thickness) (Fernlund & Floyd, 2007; Twigg et al., 2004a, 2004b). Table 3.3 summarizes the additional parameters that affect the development of residual stress at this level.

3.2.2.4 Component level

At the component level, the important parameters can be divided into two groups:

- Process parameters
- Post-process parameters

The post-process refers to activities such as demolding, trimming, cutting, drilling, and post-curing. Aside from post-curing, any of these activities can potentially relieve some of the locked stresses in the part and consequently additional dimensional changes of the part.

During the manufacturing process, variation of airflow in the facility (i.e., oven/autoclave) may result in the variation of temperature histories at different locations

Table 3.4 Additional parameters that will affect the development of residual stresses at the component level

Object	Parameter
Part	Inserts (e.g., sandwich cores)
	Ply drop-off
	Geometrical features (e.g., holes, sharp corners, noodle regions, etc.)
Tool	Substructure
Facility	Variation of the temperature histories (i.e., lead and lag locations)
Post-process	Demolding
	Trimming and chamfering
	Cutting
	Drilling
	Post-curing/co-bonding

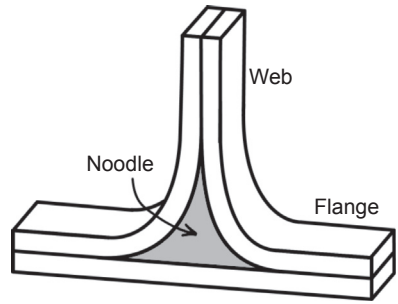

Figure 3.5 Noodle region between a flange and web.

in the part. Coupled with the variation of the base airflow, the tool substructure may also additionally influence the airflow under the tool. The variations of airflow may result in the variation of heat transfer coefficients in different zones of the part and consequently large variations in the temperature histories in the part (i.e., significantly different lead and lag locations). This potentially changes the curing process at different locations of the part and results in further mismatch of free strains in the part, which in turn further increases the residual stresses.

Other geometrical features such as ply drop-offs, sharp corners, or noodle regions (Figure 3.5) may create stress discontinuities to further increase the residual stresses, consequently resulting in the development of microcracks even during processing. Table 3.4 summarizes the additional parameters that affect the development/relief of residual stresses to create the final balanced geometry.

3.3 Measurements and predictions

3.3.1 Experimental measurements

In recent years, many experimental techniques have been proposed and used to measure residual stresses in laminated composites (e.g., see Parlevliet, Bersee, & Beukers, 2007). In general, these techniques can be divided into two main categories: (1) measuring residual stresses during processing of laminated composites and (2) measuring residual stresses after the manufacturing process. Most notable techniques in the literature are listed in Table 3.5.

There is a variety of measurement techniques based on embedding sensors in composites. Most notable ones are embedding strain gauges (e.g., Crasto et al., 2002; Jeronimidis & Parkyn, 1988; Kim & Daniel, 2002; Unger & Hansen, 1993; Wisnom et al., 2006) and fiber optic sensors (FOS) (e.g., Chehura et al., 2005; Leng & Asundi, 2002; Okabe et al., 2002; Sorensen, Gmür, & Botsis; Zhou & Sim, 2002) in a part to monitor the residual stress level during the manufacturing process. Although there are some limitations associated with these approaches, including the sensitivity of strain gauges to high temperatures and bonding of FOS to the uncured prepreg, these approaches have gained much attention and popularity in recent years.

The bi-material beam test method (Thorpe, 2013) is another promising approach that indirectly measures the development of residual stresses through the measurement of deformation. In this approach, a bi-material beam of uncured prepreg and steel shim is constructed (Figure 3.6). The beam is then placed in a dynamic mechanical analyzer (DMA) and monitored during the curing. Curing results in the warpage of the beam due to the mismatch of thermal strains. By monitoring the warpage of the beam during processing, free strains and residual stresses in the prepreg can be back-calculated.

In recent years, several destructive techniques including first ply failure (e.g., Cowley & Beaumont, 1997; Jeronimidis & Parkyn, 1988; Kim & Hahn, 1979; Li et al., 2014), layer removal (e.g., Chapman et al., 1990; Crasto & Kim, 1993; Deshpande & Seferis, 1996; Gascoigne, 1994; Joh et al., 1993), blind hole drilling (e.g., Cowley & Beaumont, 1997; Ersoy & Vardar, 2000; Jeronimidis & Parkyn, 1988; Parlevliet et al., 2007; Wu & Lu, 2000), and successive grooving (e.g., Ersoy & Vardar, 2000; Parlevliet et al., 2007; Sunderland et al., 2001) techniques have been developed to measure the residual stresses in composites. Among these methods, the first ply failure method is considered a more accurate and direct approach (Parlevliet et al., 2007). In this approach, a cross-ply laminate is tested under tensile loading conditions. As the loading increases, the cracks start to form in the 90° layers. The first ply failure stress can provide insights into the level of the residual stress in the laminate. In one approach (Li et al., 2014), the crack density in 90° layers were monitored for cross-ply laminates manufactured using different cure cycles to examine the effect of cure cycle on the final level of residual stress.

In recent years, there has been an increasing amount of attention on nondestructive techniques. Aside from the well-established techniques to measure the warpage of laminated composites and back calculate the residual stresses (e.g., Barnes & Byerly, 1994; Cowley & Beaumont, 1997; Nairn & Zoller; Parlevliet et al., 2007), several

Table 3.5 Notable experimental methods to measure residual stresses in laminated composites

Category		Method
During processing		Embedded strain gauges (e.g., Crasto, Kim, & Russell, 2002; Kim & Daniel, 2002; Jeronimidis & Parkyn, 1988; Unger & Hansen, 1993; Wisnom, Gigliotti, Ersoy, Campbell, & Potter, 2006)
		Embedded fiber optic sensors (e.g., Chehura et al., 2005; Leng & Asundi, 2002; Okabe, Yashiro, Tsuji, Mizutani, & Takeda, 2002; Sorensen, Gmür, & Botsis; Zhou & Sim, 2002)
		Interrupted warpage test (Wisnom, Gigliotti, Ersoy, Campbell, & Potter, 2006)
		Bi-material beam (BMB) test (Li, Zobeiry, Chatterjee, & Poursartip, 2014)
After processing	Destructive	First ply failure (e.g., Cowley & Beaumont, 1997; Jeronimidis & Parkyn, 1988; Kim & Hahn, 1979; Li et al., 2014)
		Layer removal (e.g., Chapman, Gillespie, Pipes, Manson, & Seferis, 1990; Crasto & Kim, 1993; Deshpande & Seferis, 1996; Gascoigne, 1994; Joh, Byun, & Ha, 1993)
		Blind hole drilling (e.g., Cowley & Beaumont, 1997; Jeronimidis & Parkyn, 1988; Ersoy & Vardar, 2000; Parlevliet et al., 2007; Wu & Lu, 2000)
		Successive grooving (e.g., Ersoy & Vardar, 2000; Parlevliet et al., 2007; Sunderland, Yu, & Manson, 2001)
	Nondestructive	Warpage/Curvature measurement (e.g., Barnes & Byerly, 1994; Cowley & Beaumont, 1997; Nairn & Zoller; Parlevliet et al., 2007)
		Interferometry (e.g., Lee, Molimard, Vautrin, & Surrel, 2004; Parlevliet et al., 2007; Pechersky, 2001)
		Photoelasticity (e.g., Nairn & Zoller, 1985)
		Raman spectroscopy (e.g., (Filiou, Galiotis, & Batchelder, 1992)
		Electrical conductance (e.g., Chung, 2001; Mei & Chung, 2000)

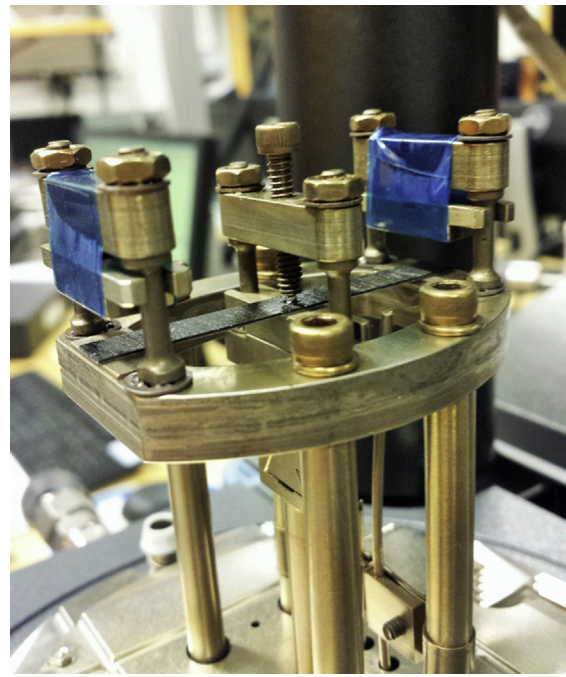

Figure 3.6 Bi-material beam sample mounted in a dynamic mechanical analyzer (DMA) using three-point bending clamps.

other techniques including interferometry (e.g., Lee et al., 2004; Pechersky, 2001; Parlevliet et al., 2007), photoelasticity (e.g., Nairn & Zoller, 1985), Raman spectroscopy (e.g., Filiou et al., 1992), and electrical conductance (e.g., Chung, 2001; Mei & Chung, 2000) methods have been utilized. There are, however, limitations associated with these techniques as listed below (Parlevliet et al., 2007):

- Interferometry: provides only surface strains and surface information
- Photoelasticity: transparent matrix is required
- Raman spectroscopy: transparent matrix is required
- Electrical conductance: electrically conducted fibers are required

In general, there are limitations and potential drawbacks associated with other techniques as well. These limitations are summarized in Table 3.6. Although there is no perfect method to measure residual stresses, however, depending on the situation and application, one or more of these techniques might be appropriate and accurate enough to measure the residual stresses.

3.3.2 Analytical and numerical approaches

Conceptually, the development of residual stresses can be simply attributed to the mismatch of free strains, but the task of predicting residual stresses in laminated composites, by either analytical or numerical methods, is far from trivial. There are

Table 3.6 Limitations of experimental methods to measure residual stresses

Method	Potential limitations
Embedded strain gauges	Sensitivity to the temperature
Embedded fiber optic sensors	Bonding issues before vitrification, resin rich areas
Interrupted warpage test	Limited accuracy
Bi-material beam (BMB) test	Only applicable to cross-ply laminates
First ply failure	Only applicable to cross-ply laminates
Layer removal	Limited accuracy
Blind hole drilling	Low accuracy
Successive grooving	Low accuracy
Warpage/Curvature measurement	Limited accuracy
Interferometry	Only surface strains and surface information
Raman spectroscopy	Transparent matrix is required
Photoelasticity	Transparent matrix is required
Electrical conductance	Electrically conducted fibers are required

various issues associated with predicting the residual stresses that make this a significant task:

- Prediction of residual stresses in laminated composites is linked to the manufacturing process simulation, which has to address a complex systems problem describing the combined part, tool, and curing environment. This complexity is also coupled with the complexity of the viscoelastic behavior of the material to make the prediction task quite challenging.
- Aside from the mismatch of free strains at the micro level, as discussed in Section 3.2, the many other parameters that affect the development of residual stresses at the laminate level, coupon level, and component level must be considered as appropriate. A successful prediction approach should at least consider a majority of these parameters.
- Uncertainty associated with many of the aforementioned parameters is another issue that challenges the prediction of the residual stresses. Examples are variability in airflow inside an autoclave or the tool surface condition to quantify the tool/part interaction.
- Thermochemical and mechanical properties of the fiber and matrix play an essential role in the development of free strains and residual stresses. Consequently, it is important to properly characterize the relevant material properties as input to any analytical/numerical approach.

Considering the importance of residual stresses and dimensional variations, it is not surprising that process modeling has been the topic of much research. Perhaps the earliest work was by Hahn and Pagano (1975). In their approach, a linear elastic constitutive model was used with some simplified assumptions. Many studies after this initial study were conducted to include more of the existing complexities in the system

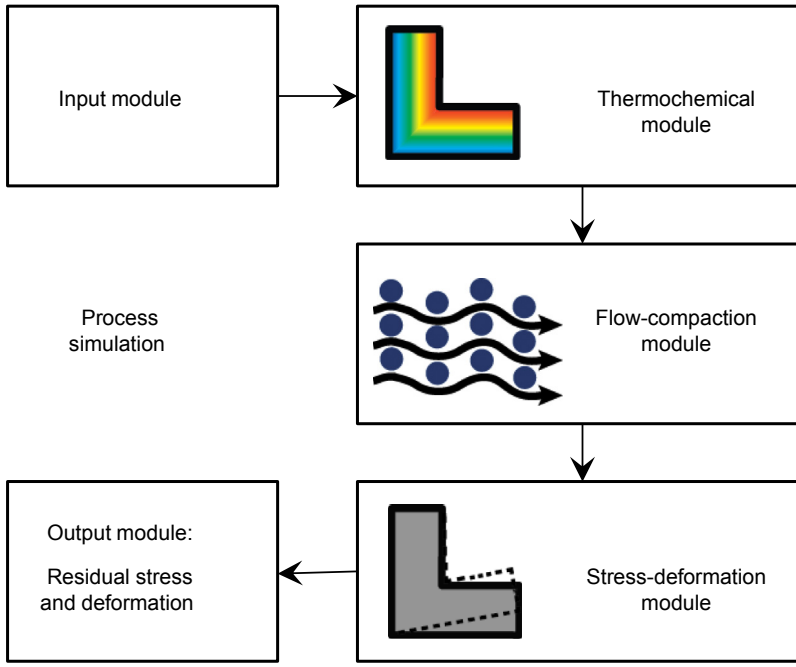

Figure 3.7 Integrated submodule approach in a commercial process modeling code, COMPRO.

(e.g., Antonucci, Cusano, Giordana, Nasser, & Nicolais, 2006; Bogetti & Gillespie, 1991, 1992; Clifford, Jansson, Yu, Michaud, & Manson, 2006; Johnston et al., 2001; Kiasat, 2000; Kim, Bernet, Sunderland, & Manson, 2002; Loos & Springer, 1983; White & Hahn, 1992a, 1992b). Currently, one of the main trends in process simulation is to use an intergraded submodel approach to break down the complexity of the system into several simpler submodels (e.g., Johnston et al., 2001). Usually in such an approach each submodel represents one aspect of the material behavior. As an example, the submodel approach used in the commercial code COMPRO (Convergent Manufacturing, 2014) is depicted schematically in Figure 3.7. In this code, the process simulation is broken down into three steps of thermochemical simulation, flow-compaction simulation, and stress-deformation simulation.

There are two important issues to be considered in any simulation approach: material constitutive model (e.g., elastic vs viscoelastic modeling) and the method to solve the equations over the domain of interest. In terms of material models, as mentioned before, it is important to capture the complexity of the behavior of the material in order to accurately predict the development of residual stresses. For composites, the following material constitutive models have been used by researchers:

- Elastic model: Early process models used elastic models to describe the behavior of the material (e.g., Harper & Weitsman, 1981; Loos & Springer, 1983; Nelson & Cairns, 1989; Stango & Wang, 1984). In these models, the stress calculation is based on the final relaxed modulus of the material:

$$\sigma(t) = E \cdot \varepsilon \tag{3.15}$$

Although this type of model might provide some insights into the behavior of the material and development of residual stresses, it cannot capture the complexity of the problem or give quantitatively good results.

- Pseudo-viscoelastic model: the cure hardening instantaneously linear elastic models (CHILE) have been used by some researchers for process simulation (e.g., Bogetti & Gillespie, 1992; Fernlund, Abdel-Rahman, et al., 2002; Fernlund, Griffith, Courdji, & Poursartip, 2002; Fernlund et al., 2003; Johnston et al., 2001; Lange, Toll, & Manson, 1995). In these models, the modulus changes as a function of degree of cure and temperature:

$$\sigma(t) = \int_0^t E'(T,\alpha)\frac{\mathrm{d}\varepsilon}{\mathrm{d}\tau}\cdot \mathrm{d}\tau \tag{3.16}$$

in which E' is the instantaneous modulus of elasticity (storage modulus), T is the temperature, α is the degree of cure, and τ is the time integration variable. Although these models do not capture the full complexity of viscoelastic materials, in general, it has been shown that the CHILE approach provides good predictions for curing of thermoset resins (Fernlund, Griffith, et al., 2002; Fernlund et al., 2003; Zobeiry, 2006).

- Viscoelastic model (VE): It is well known that polymers generally exhibit viscoelastic behavior. As a result, for predicting the residual stresses in composites, some researchers have employed full viscoelastic equations (e.g., Zobeiry, 2006; Zobeiry, Vaziri, & Poursartip, 2010). In such models, the modulus varies with time, temperature, and degree of cure. Based on the time-temperature-cure superposition assumption (e.g., Zobeiry, 2006), the constitutive equation can be written as follows:

$$\sigma(t) = \int_0^t E(t-\tau,T,\alpha)\frac{\mathrm{d}\varepsilon}{\mathrm{d}\tau}\cdot \mathrm{d}\tau \tag{3.17}$$

In general, VE models are the most accurate model to capture the complex behavior of the material. However, due to the complexity of these models and also the difficulties associated with characterizing the viscoelastic material properties, pseudo-viscoelastic models are the alternative faster models but with less accuracy.

These three material models are schematically depicted and compared in Figure 3.8.

As mentioned earlier, another important issue to consider is the method to solve the governing equations to predict the residual stresses. Over the past decades, three methods have been used to solve the relevant equations: laminate plate theory (LPT; e.g., Hahn & Pagano, 1975; Loos & Springer, 1983), finite difference method (FDM; e.g., Bogetti & Gillespie, 1992), and finite element method (FEM; e.g., Zobeiry

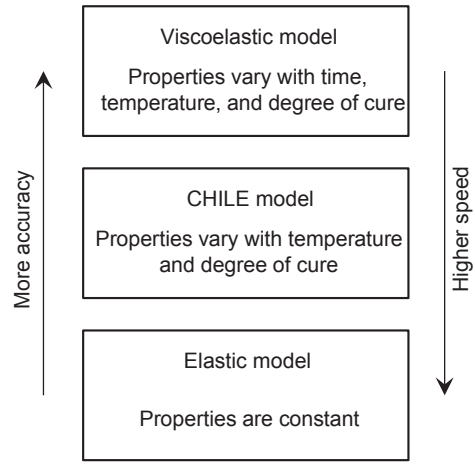

Figure 3.8 Different material constitutive models to predict residual stresses in composites (Zobeiry, 2006).

et al., 2010). However, FEM has been the method of choice for most studies, and commercial simulation packages have been developed based on this method (Convergent Manufacturing, 2014).

3.4 Effects and mitigations

3.4.1 Effects of residual stresses

In general, the effects of residual stresses can be divided into two categories:

- Geometry-related effects (e.g., Figure 3.9)
- Performance-related effects

By definition, any deviation from design that is not within the acceptable tolerance is assumed to be a defect. Based on this definition, notable outcomes of interests related to residual stresses in composites are as follows:

- Geometric deviations: warpage, spring-in (e.g., Albert & Fernlund, 2002; Fernlund, 2005; Radford & Diefendorf, 1993)
- Reduced performance: low mechanical properties, microcracks (e.g., Li et al., 2014)

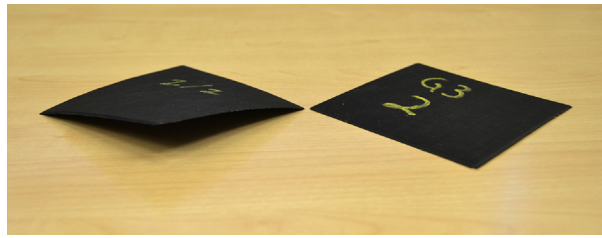

Figure 3.9 Effect of residual stress on the geometry of an unbalanced laminate.

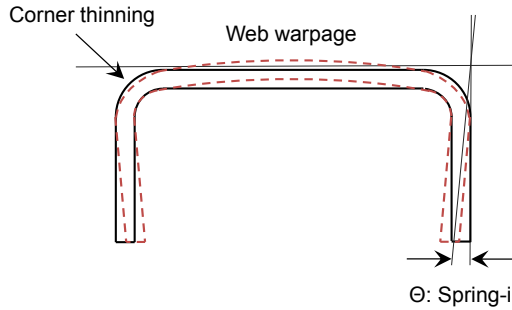

Figure 3.10 Geometric deviations (spring-in and warpage) due to the formation of residual stresses in a U-shaped composite part.

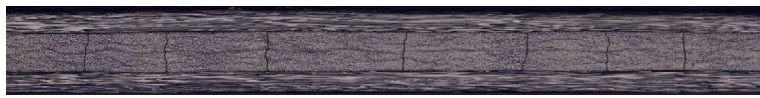

Figure 3.11 Transverse crack formation in the off-axis plies of a cross-ply laminate (Li et al., 2014).

Most notable geometric deviations due to residual stresses are spring-in and warpage as depicted in Figure 3.10 for a U-shaped composite part. When parts are out of dimensional tolerance, the following problems may arise:

- Poor fit-up or forced fit-up, which in turn increases the residual stresses and reduces the mechanical performance
- Unintended changes in the structural response (i.e., deflection shape, aerodynamics)
- Compromised structural integrity

Aside from geometric deviations, reduction of mechanical properties is the other effect of residual stresses, and this is usually neglected by assuming it is a constant effect. The reduction of mechanical properties is most pronounced when considering matrix-dominated properties and design allowables derived from these properties. In a study by Li et al. (2014), it is shown that by modifying the cure cycle, the strain to failure of an epoxy matrix material was increased by about 0.1%. Given a baseline tensile strain to failure of about 0.8% for the epoxy resin in the study, and designs that will typically allow in-service strains of 0.25−0.4%, an additional margin of 0.1% would be a significant improvement for the performance of the matrix material. More typically, the accumulation of residual stresses in resin-rich areas or areas with stress discontinues (e.g., a noodle region as shown in Figure 3.5) might result in the formation of microcracks even during cure or de-tooling, which is highly undesirable (Figure 3.11).

3.4.2 Mitigation strategies and tools

In general, there are three different strategies to mitigate the effects of residual stresses on geometric deviations:

- Design compensation
- Assembly compensation
- Mold geometry compensation

In design and assembly compensation approaches (Figure 3.12(a) and (b)), the presence of geometric deviations is accepted and mitigated by using techniques such as shimming. Putting aside the undesired incremental cost of such approaches, utilizing these mitigation strategies results in increasing residual stresses and consequently further reducing mechanical properties.

The preferable method is obviously the mold compensation approach (Figure 3.12(c)). In this approach, the deformed geometry of the part is predicted using process simulation tools (e.g., Convergent Manufacturing, 2014). The negative geometry of the prediction is then used to compensate the mold geometry. Using this compensated geometry, parts with geometric deviations within the design tolerances can be manufactured.

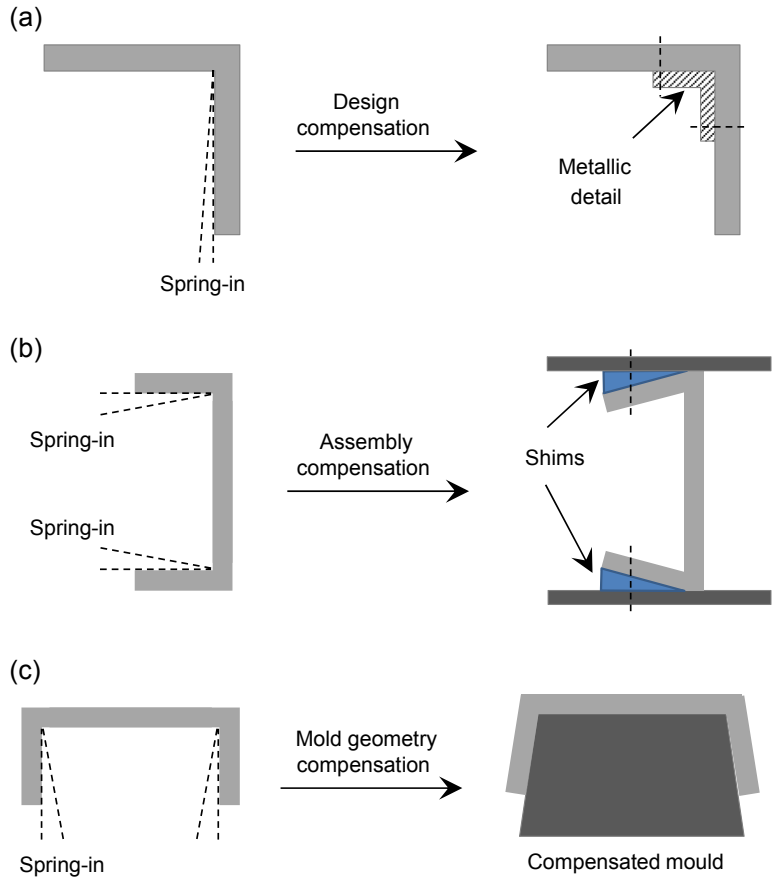

Figure 3.12 Mitigation strategies for geometric deviations: (a) design compensation, (b) assembly compensation, and (c) mold geometry compensation.

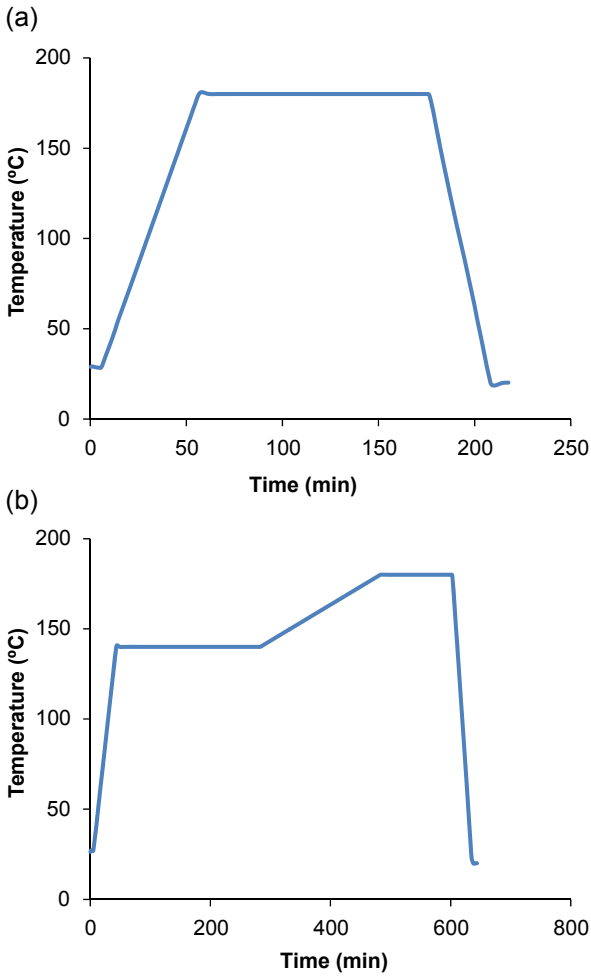

Figure 3.13 Modifying the cure cycle from (a) a one-hold cycle to (b) a two-hold cycle to minimize the effect of residual stresses on mechanical performance (Li et al., 2014).

Typically, the current approach to managing the effect of residual stress on design allowables in aerospace applications is to ensure that the coupons used to generate design allowables have seen exactly the same process cycle as the structure to be certified. In this manner, it is expected that residual stresses are the same in both coupons and structure, and thus the effect is accounted for, even if not quantified directly. This is likely a conservative approach, even though there appear to be no documented studies to verify this. Nonconservative conditions may apply to geometrical features such as stringer noodles and the like.

If there is an opportunity to control the process to manipulate and minimize residual stress, the following workflow may be used to achieve the lowest possible residual stress:

1. Systematically evaluate relevant parameters, listed under Section 3.2 at the micro level, laminate level, coupon level, and component level, and modify within the allowable ranges. Some of these parameters may be fixed (e.g., geometry of the part). Some other parameters such as temperature cycle may be modified easily (e.g., lower heating rates) and should be considered first.
2. Numerical tools (e.g., Convergent Manufacturing, 2014) or experimental approaches may be used to quantify the effect of modifying parameters.
3. Repeat above steps until satisfactory or optimum results are achieved.

In a case study demonstrating this workflow, Li et al. (2014) modified the cure cycle of an AS4/8552 cross-ply laminate from a one-hold cycle to a two-hold cycle (Figure 3.13), reducing the residual stress and consequently increasing the strain to failure by about 15% above the baseline.

3.5 Residual stresses in carbon-epoxy composites and typical material properties

In this section, the development of free strains and residual stresses in a typical carbon-epoxy laminate are considered. Material properties are provided for HEXCEL AS4/8552 prepreg from various sources in the literature (Albert & Fernlund, 2002; Ersoy et al., 2010; Garstka, Ersoy, Potter, & Wisnom, 2007; Li et al., 2014; Prasatya, McKenna, & Simon, 2001; Van Ee & Poursartip, 2009; Yu, Mhaisalkar, & Wong, 2005). At the micro level, as discussed previously, mismatch of free strains (i.e., thermal and phase-change strains) is the main cause of the formation of residual stresses. As curing progresses during manufacturing, material properties such as modulus evolve. CTE of the material changes as the resin goes from the rubbery state to a glassy state. Due to the cross-linking development, CTE at a rubbery state is higher than the CTE at a glassy state. In Figure 3.14, this behavior is depicted for a typical prepreg. For a UD AS4/8552 lamina, Ersoy et al. (2010) reported a value of $35 \times 10^{-6}/°C$ for the glassy CTE at 100 °C. For the rubbery CTE at 200 °C, a value of about $120 \times 10^{-6}/°C$ has been reported (Ersoy et al., 2010).

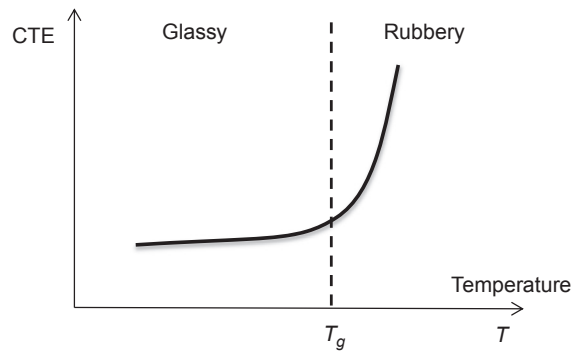

Figure 3.14 Thermal effect on CTE as a laminate goes from the glassy state to a rubbery state (Ersoy et al., 2010).

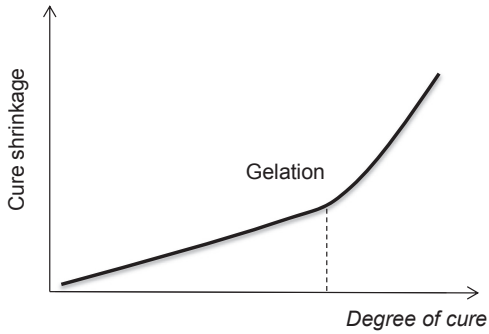

Figure 3.15 Typical cure shrinkage versus degree of cure curve for an epoxy resin (Yu et al., 2005).

As curing progresses, cure shrinkage increases. The relation of cure shrinkage and degree of cure can be approximately assumed to be linear with perhaps a small change of slope around the gelation point as shown in Figure 3.15. For AS4/8552, volumetric cure shrinkage of 4.94% has been reported in the literature (Garstka et al., 2007). For 8551-7 epoxy resin, a value of 8% has been reported (Prasatya et al., 2001).

Modulus development during cure cycle can be measured using a DMA (e.g., Li et al., 2014). Figure 3.16 shows transverse modulus development for a UD AS4/8552 laminate subjected to the recommended one-hold cure cycle (Van Ee & Poursartip, 2009). In this cycle, the temperature is increased from the room temperature to 180 °C with a heating rate of 3 °C/min. The temperature is then held at 180 °C for 2 h followed by cooling down to the room temperature with the rate of 5 °C/min. During the hold, modulus starts to build up as the instantaneous glass transition of the resin increases due to cure, approaches, and exceeds the hold temperature, and thus the resin vitrifies. Modulus development slows down as vitrification halts cure advancement, but there is a final increase during cooldown due to thermoelastic effects. For this cure cycle, the degree of cure and glass transition temperature increase can be predicted using openly available NCAMP cure kinetics and related models within the RAVEN process simulation software (Convergent Manufacturing Technologies,

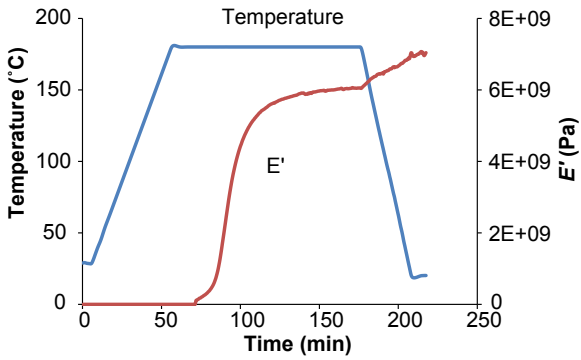

Figure 3.16 Transverse modulus development (E_{22}) in a UD AS4/8552 prepreg during the cure cycle (Li et al., 2014).

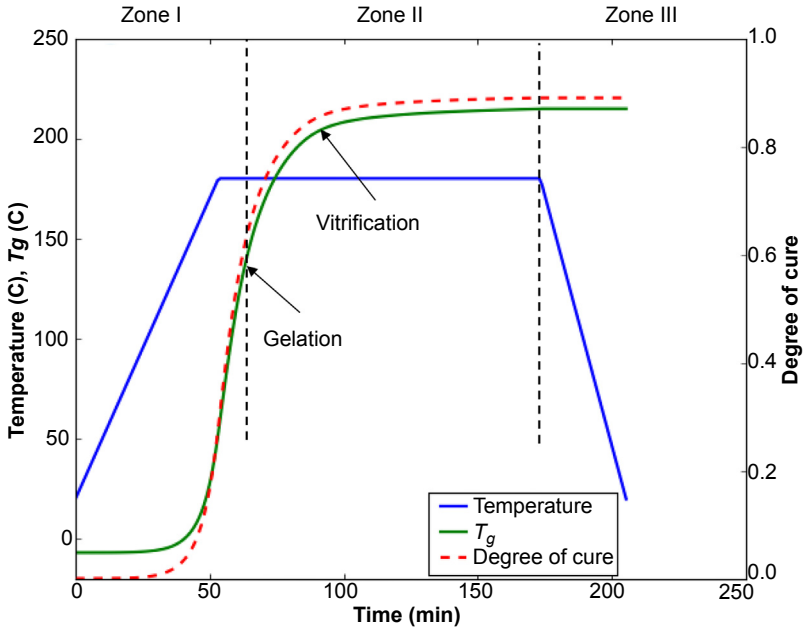

Figure 3.17 One-hold cure cycle of an AS4/8552 laminate (Albert & Fernlund, 2002).

2013), as shown in Figure 3.17. Gelation of the material occurs at about a DOC of 0.55 (Van Ee & Poursartip, 2009), and vitrification is complete once $T_g > T + 28\ ^\circ\text{C}$ (50 °F) (CMH-17, 2012). Figure 3.17 shows that both gelation and vitrification occur during the 180 °C hold. Residual stress development in the material for this cure cycle can be divided into three zones:

- Zone I, before onset of vitrification: By increasing the temperature, resin viscosity drops and resin starts to flow. Onset of cure increases viscosity and reduces resin flow. Once gelation occurs (in this case DOC $\sim$ 0.55) a three-dimensional network has been created, and the material has a measurable, rubbery storage modulus. Cure shrinkage and thermal expansion of fiber and resin do not contribute to the development of residual stresses in this zone since the resin has negligible modulus before gelation, and a low rubbery modulus even past gelation.
- Zone II, after onset of vitrification but before cooling down ($T_g \geq T$): Resin cure shrinkage is coupled with significant modulus development in the resin, resulting in the development of significant residual stress.
- Zone III, during cool down: By the end of the hold, the material has fully vitrified, cure advance has stopped, and accordingly the modulus has stabilized. During cooldown, there is negligible further cure and associated shrinkage in the resin. However, there is a thermoelastic effect on the modulus. In this cooldown phase, the significant mismatch in thermal free strains between fiber and resin (mismatch in CTE) leads to a very significant increase in the residual stress level.

The residual stress formation for this cure cycle has been predicted using a combination of the bi-material beam technique and a pseudo-viscoelastic model, CHILE, (Li et al., 2014) and is depicted in Figure 3.18.

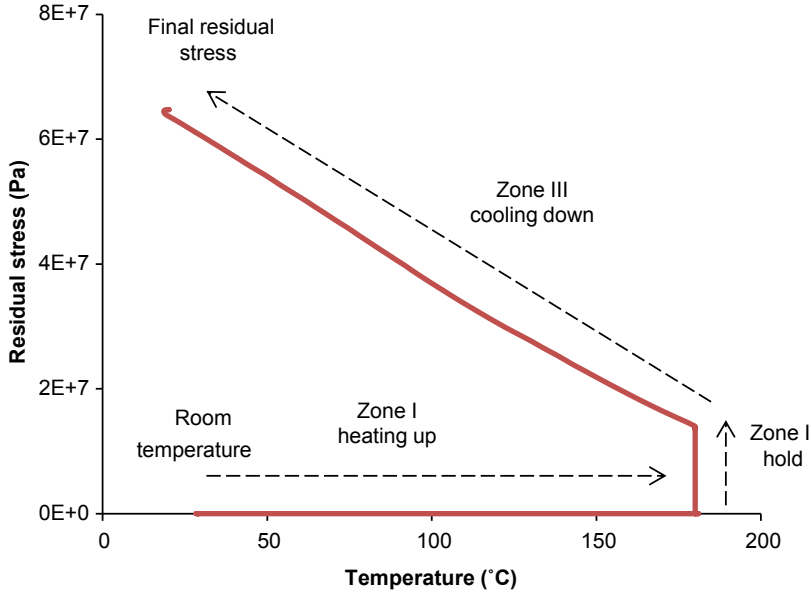

Figure 3.18 Development of residual stress in a cross-ply AS4/8552 laminate during a one-hold cure cycle as shown in Figure 3.17 (Albert & Fernlund, 2002).

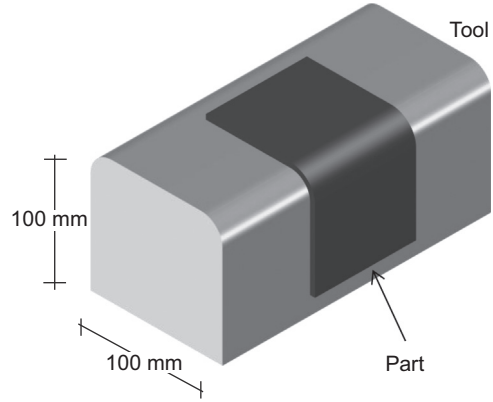

Figure 3.19 Manufacturing of L-shaped parts on steel and aluminum tools to study the effect of residual stresses on spin-in angle (Albert & Fernlund, 2002).

It is of great interest to compare the relative contributions of thermal-induced free strains (CTE effect) and phase-change-induced free strains (e.g., cure shrinkage) on the overall residual stress level and geometry variations (i.e., spring-in and warpage). This comparison is also valuable in building up an understanding of how to minimize the effect of residual stresses (e.g., Li et al., 2014). Although it might seem that the cure shrinkage effect should be much larger than the CTE effect due to the high volumetric cure

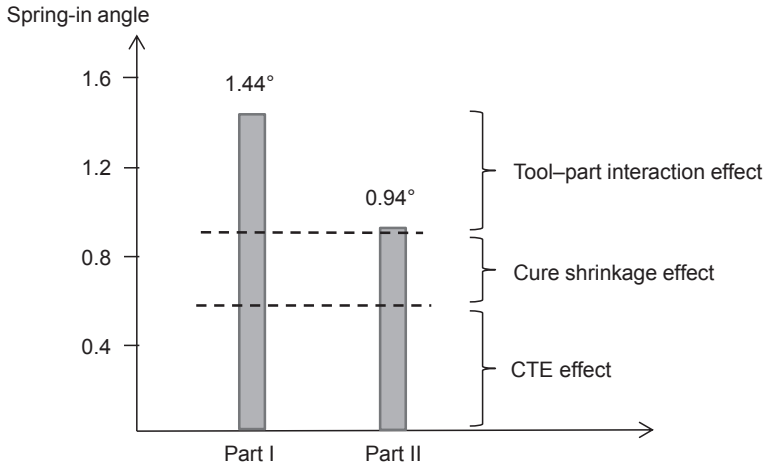

Figure 3.20 Effects of coefficients of thermal expansion (CTE), cure shrinkage, and tool−part interaction on the spring-in angle of L-shaped parts (Albert & Fernlund, 2002).

shrinkage, this in fact is not correct. The majority of cure shrinkage occurs while the resin has negligible modulus, and consequently the CTE effect is more important.

In a study by Albert and Fernlund (Albert & Fernlund, 2002), the effects of these two free strains were compared on the final spring-in angle of L-shaped parts (Figure 3.19). In their study, a spring-in angle of about 1.5° was measured in L-shaped parts. Upon minimizing the tool−part interaction by using FEP sheets between the tool and part, this value decreased to about 1° (Figure 3.20). It was also observed that for the case with minimized tool−part interaction, the contribution ratios for the effects of CTE and cure shrinkage on spring-in angle were approximately 2/3 and 1/3, respectively.

3.6 Discussion

As explained in detail in Section 3.2, conceptually the mismatch of free strains results in the development of residual stresses in laminated composites. These free strains might form due to thermal changes, phase changes, or moisture absorption. However, considering all the levels of complexities of a composite part at the micro level, laminate level, coupon level, and component level, there are many contributing/relieving factors that affect the final level of the residual stresses. A summary of these factors is listed in Table 3.8.

In Section 3.3, various experimental and numerical approaches were presented to measure/predict the residual stresses in a laminated composite part. Although prediction approaches vary in terms of level of complexity, generally speaking, viscoelastic and pseudo-viscoelastic-based approaches are sufficiently accurate. Currently, only pseudo-viscoelastic approaches are mature enough for general use, but viscoelastic

Table 3.7 The matrix of outcomes of interests related to residual stresses

Geometry related		Performance related	
Spring-in	Warpage	Low mechanical properties for resin-dominated properties	Microcracks

Table 3.8 Parameters that affect the formation of residual stresses in laminated composites

Object	Parameter	
Material	Fiber	Elastic and viscoelastic properties
		Architecture
		Density and thermal properties
		Volume fraction
	Matrix	Elastic and viscoelastic properties
		Cross-linking/crystallization kinetics
		Cross-linking/crystallization shrinkage
		Density and thermal properties
		Volume fraction
	Interface	Bonding properties
	Void	Morphology
		Volume fraction
Part	Geometry	
	Lay-up	
	Inserts	
	Ply drop-offs	
	Geometrical features (e.g., holes, sharp corners, noodle regions, etc.)	
Tool	Soft tooling	Density and thermal properties
		Thicknesses
	Hard tooling	Density and thermal properties
		Thicknesses
		Surface roughness
		Surface preparation
		Substructure

Continued

Table 3.8 Continued

Object	Parameter
Process	Pressure cycle
	Temperature cycle
Facility	Variation of the temperature histories
	Heat transfer coefficients
Post-process	Demolding
	Trimming and chamfering
	Cutting
	Drilling
	Post-curing/co-bonding
	Moisture absorption

approaches are increasingly considered for the more complex out-of-autoclave cycles that often have off-tool post-cures.

As discussed in Section 3.4, when considering residual stresses, the outcomes of interests can be divided into two main categories of geometric-related and performance-related outcomes. The notable outcomes of interests are presented in Table 3.7.

When it comes to mitigation strategies, geometry-related deviations can be mitigated using approaches such as tool geometry compensation, which relies on numerical techniques to predict the deformed geometry. For performance-related outcomes, a systematic workflow might be followed to minimize the effects of residual stresses by modifying the parameters listed in Table 3.8.

References

Albert, C., & Fernlund, G. (2002). Spring-in and warpage of angled composites laminates. *Composites Science and Technology, 62*, 1895−1912.

Antonucci, V., Cusano, A., Giordano, M., Nasser, J., & Nicolais, L. (2006). Cure-induced residual strain build-up in a thermoset resin. *Composites Part A: Applied Science and Manufacturing, 37*(4), 592−601.

Barnes, J. A., & Byerly, G. E. (1994). The formation of residual-stresses in laminated thermoplastic composites. *Composites Science and Technology, 51*(4), 479−494.

Bogetti, T. A., & Gillespie, J. W. (1991). Two-dimensional cure simulation of thick thermosetting composites. *Journal of Composite Materials, 25*(3), 239−273.

Bogetti, T. A., & Gillespie, J. W. (1992). Process-induced stress and deformation in thick-section thermoset composite laminates. *Journal of Composite Materials, 26*(5), 626−660.

Chapman, T. J., Gillespie, J. W., Pipes, R. B., Manson, J. A. E., & Seferis, J. C. (1990). Prediction of process-induced residual-stresses in thermoplastic composites. *Journal of Composite Materials, 24*(6), 616–643.

Chehura, E., Skordos, A. A., Ye, C. C., James, S. W., Partridge, I. K., & Tatam, R. P. (2005). Strain development in curing epoxy resin and glass fibre/epoxy composites monitored by fibre Bragg grating sensors in birefringent optical fibre. *Smart Materials and Structures, 14*(2), 354–362.

Chung, D. D. L. (2001). Continuous carbon fiber polymer–matrix composites and their joints, studied by electrical measurements. *Polymer Composites, 22*(2), 250–270.

Clifford, S., Jansson, N., Yu, W., Michaud, V., & Manson, J.-A. (2006). Thermoviscoelastic anisotropic analysis of process induced residual stresses and dimensional stability in real polymer matrix composite components. *Composites Part A: Applied Science and Manufacturing, 37*(4), 538–545.

CMH-17 Volume 1 *Polymer matrix composites guidelines for characterization of structural materials*. CMH-17-1G. (2012). Warrendale, PA: SAE International. CD-ROM.

Convergent Manufacturing Technologies. (2013). *RAVEN simulation software (Version 3.4.7)*. Available from http://www.convergent.ca/products/raven-simulation-software.

Convergent Manufacturing Technologies. (2014). *COMPRO simulation software*. Available from http://www.convergent.ca/products/compro-simulation-software.

Cowley, K. D., & Beaumont, P. W. R. (1997). The measurement and prediction of residual stresses in carbon–fibre/polymer composites. *Composites Science and Technology, 57*(11), 1445–1455.

Crasto, A. S., & Kim, R. Y. (1993). On the determination of residual-stresses in fiber-reinforced thermoset composites. *Journal of Reinforced Plastics and Composites, 12*(5), 545–558.

Crasto, A. S., Kim, R. Y., & Russell, J. D. (2002). In situ monitoring of residual strain development during composite cure. *Polymer Composites, 23*(3), 454–463.

Deshpande, A. P., & Seferis, J. C. (1996). Processing characteristics in different semi-crystalline thermoplastic composites using process simulated laminate (PSL) methodology. *Journal of Thermoplastic Composite Materials, 9*(2), 183–198.

Ersoy, N., Garstka, T., Potter, K., Wisnom, M. R., Porter, D., Clegg, M., et al. (2010). Development of the properties of a carbon fibre reinforced thermosetting composite through cure. *Composites Part A, 41*, 401–409.

Ersoy, N., & Vardar, O. (2000). Measurement of residual stresses in layered composites by compliance method. *Journal of Composite Materials, 34*(7), 575–598.

Fernlund, G. (2005). Spring-in of angled sandwich panels. *Composites Sciences and Technology, 65*, 317–323.

Fernlund, G., Abdel-Rahman, N., Courdji, R., Poursartip, A., Willden, K., & Nelson, K. (2002). Experimental and numerical study of the effect of cure cycle, tool surface, geometry, and lay-up on the dimensional fidelity of autoclave-processed composite parts. *Composites Part A: Applied Science and Manufacturing, 33*(3), 341–351.

Fernlund, G., Courdji, R., Poursartip, A., Hendrickson, L., Nelson, K., & George, P. (November 2001). Process induced deformations of the Boeing 777 Trailing Edge Aft Strut Fairing. In *International SAMPE Technical Conference Series* (Vol. 33, pp. 347–355).

Fernlund, G., & Floyd, A. (2007). Process analysis and tool compensation for a complex composite panel. In *Proceedings of the 22nd ASC Annual Technical Conference, Seattle*.

Fernlund, G., Griffith, J., Courdji, R., & Poursartip, A. (2002). Experimental and numerical study of the effect of caul-sheets on corner thinning of composite laminates. *Composites Part A: Applied Science and Manufacturing, 33*(3), 411–426.

Fernlund, G., Osooly, A., Poursartip, A., Vaziri, R., Courdji, R., Nelson, K., et al. (2003). Finite element based prediction of processes-induced deformation of autoclaved composite structures using 2D process analysis and 3D structural analysis. *Composite Structures, 62*(2), 223−234.

Filiou, C., Galiotis, C., & Batchelder, D. N. (1992). Residual-stress distribution in carbon−fiber thermoplastic matrix preimpregnated composite tapes. *Composites, 23*(1), 28−38.

Garstka, T., Ersoy, N., Potter, K. D., & Wisnom, M. R. (2007). In situ measurements of through-the-thickness strains during processing of AS4/8552 composite. *Composites Part A: Applied Science and Manufacturing, 38*(12), 2517−2526.

Gascoigne, H. E. (1994). Residual surface stresses in laminated crossply fiber−epoxy composite-materials. *Experimental Mechanics, 34*(1), 27−36.

Hahn, H. T., & Pagano, N. J. (1975). Curing stresses in composite laminates. *Journal of Composite Materials, 9*, 91−106.

Harper, B. D., & Weitsman, Y. (1981). Residual thermal stresses in an unsymmetrical cross-ply graphite/epoxy laminate. In *22nd Structures, Structural Dynamics and Materials Conference* (pp. 325−332).

Jeronimidis, G., & Parkyn, A. T. (1988). Residual stresses in carbon fiber-thermoplastic matrix laminates. *Journal of Composite Materials, 22*(5), 401−415.

Joh, D., Byun, K. Y., & Ha, J. (1993). Thermal residual-stresses in thick graphite−epoxy composite laminates—uniaxial approach. *Experimental Mechanics, 33*(1), 70−76.

Johnston, A. (1997). *An integrated model of the development of process-induced deformation in autoclave processing of composites structures* (Ph.D. thesis). Vancouver: The University of British Columbia.

Johnston, A., Hubert, P., Fernlund, G., Vaziri, R., & Poursartip, A. (1996). Process modelling of composite structures employing a virtual autoclave concept. *Science and Engineering of Composite Materials, 5*(3−4), 235−252.

Johnston, A., Vaziri, R., & Poursartip, A. (2001). A plane strain model for process-induced deformation of laminated composite structures. *Journal of Composite Materials, 35*(16), 1435−1469.

Kiasat, M. S. (2000). *Curing shrinkage and residual stresses in viscoelastic thermosetting resins and composites*. Delft University of Technology.

Kim, B. S., Bernet, N., Sunderland, P., & Manson, J.-A. (2002). Numerical analysis of the dimensional stability of thermoplastic composites using a thermoviscoelastic approach. *Journal of Composite Materials, 36*(20), 2389−2403.

Kim, Y. K., & Daniel, I. M. (2002). Cure cycle effect on composite structures manufactured by resin transfer molding. *Journal of Composite Materials, 36*(14), 1725−1743.

Kim, R. Y., & Hahn, H. T. (1979). Effect of curing stresses on the first ply-failure in composite laminates. *Journal of Composite Materials*. *13*(JAN), 2−16.

Lange, J., Toll, S., & Manson, J.-A. (1995). Residual stress build-up in thermoset films cured above their ultimate glass transition temperature. *Polymer, 36*(16), 3135−3141.

Lee, J. R., Molimard, J., Vautrin, A., & Surrel, Y. (2004). Application of grating shearography and speckle shearography to mechanical analysis of composite material. *Composites Part A: Applied Science and Manufacturing, 35*(7−8), 965−976.

Leng, J. S., & Asundi, A. (2002). Real-time cure monitoring of smart composite materials using extrinsic Fabry−Perot interferometer and fiber Bragg grating sensors. *Smart Materials and Structures, 11*(2), 249−255.

Li, C., Zobeiry, N., Chatterjee, S., & Poursartip, A. (2014). Advances in the characterization of residual stress in composite structures. In *SAMPE Conference, Society for the Advancement of Material and Process Engineering, Seattle*.

Loos, A. C., & Springer, G. S. (1983). Curing of epoxy matrix composites. *Journal of Composite Materials, 17*(2), 135−169.

Mei, Z., & Chung, D. D. L. (2000). Thermal stress-induced thermoplastic composite debonding, studied by contact electrical resistance measurement. *International Journal of Adhesion and Adhesives, 20*(2), 135−139.

Nairn, J. A., & Zoller, P. (1985). Matrix solidification and the resulting residual thermal-stresses in composites. *Journal of Materials Science, 20*(1), 355−367.

Nairn, J. A., Zoller, P. The development of residual thermal stresses in amorphous and semi-crystalline thermoplastic matrix composites. In *Proceedings of toughened composites conference, Houston, TX, USA, March 13−15, 1985* (pp. 328−341).

Nelson, R. H., & Cairns, D. S. (1989). Prediction of dimensional changes in composite laminates during cure. In *34th International SAMPE Symposium, May 8−11* (pp. 2379−2410).

Okabe, Y., Yashiro, S., Tsuji, R., Mizutani, T., & Takeda, N. (2002). Effect of thermal residual stress on the reflection spectrum from fiber Bragg grating sensors embedded in CFRP laminates. *Composites Part A: Applied Science and Manufacturing, 33*(7), 991−999.

Parlevliet, P., Bersee, H., & Beukers, A. (2006). Residual stresses in thermoplastic composites—a study of the literature—part I: formation of residual stresses. *Composites Part A: Applied Science and Manufacturing, 37*(11), 1847−1857.

Parlevliet, P., Bersee, H., & Beukers, A. (2007). Residual stresses in thermoplastic composites—a study of the literature—part II: experimental techniques. *Composites Part A: Applied Science and Manufacturing, 38*(3), 651−665.

Pechersky, M. J. (2001). *Determination of residual stresses by thermal relaxation and speckle correlation interferometry*. Aiken, SC: Westinghouse Savannah River Company. p. 15.

Prasatya, P., McKenna, G. B., & Simon, S. L. (2001). A viscoelastic model for predicting isotropic residual stresses in thermosetting materials: effects of processing parameters. *Journal of Composite Materials, 35*(10), 826−848.

Radford, D. W., & Diefendorf, R. J. (1993). Shape instabilities in composites resulting from laminate anisotropy. *Journal of Reinforced Plastics and Composites, 12*, 58−75.

Ridgard, C. (1993). Accuracy and distortion of composite parts and tools: causes and solutions. In *SME Tech Paper, Tooling Compos* (Vol. 93, pp. 93−113).

Sorensen, L., Gmür, T., Botsis, J. Residual strain development in laminated thermoplastic composites measured using fibre Bragg grating sensors. In *Proceedings of CompTest 2004 conference. Bristol, UK, September 21−23, 2004* (pp. 145−146).

Stango, R. J., & Wang, S. S. (1984). Process-induced residual thermal stresses in advanced fiber-reinforced composite laminates. *Journal of Engineering for Industry, 106*, 48−54.

Sunderland, P., Yu, W. J., & Manson, J. A. (2001). A thermoviscoelastic analysis of process-induced internal stresses in thermoplastic matrix composites. *Polymer Composites, 22*(5), 579−592.

Thorpe, R. (2013). *Experimental characterization of the viscoelastic behavior of a curing epoxy matrix composite from pre-gelation to full cure* (M.A.Sc. thesis). Vancouver: The University of British Columbia.

Twigg, G., Poursartip, A., & Fernlund, G. (2004). Tool-part interaction in composites processing. Part I: experimental investigation and analytical model. *Composites Part A: Applied Science and Manufacturing, 35*(1), 121−133.

Twigg, G., Poursartip, A., & Fernlund, G. (2004). Tool-part interaction in composites processing. Part II: numerical modelling. *Composites Part A: Applied Science and Manufacturing, 35*(1), 135−141.

Unger, W. J., & Hansen, J. S. (1993). The effect of thermal-processing on residual strain development in unidirectional graphite fiber reinforced PIIK. *Journal of Composite Materials, 27*(1), 59−82.

Van Ee, D., & Poursartip, A. (2009). *HexPly 8552 material properties database for use with COMPRO CCA and Raven, created for NCAMP*. Available from http://www.niar.wichita.edu/coe/ncamp_documents/Hexcel%208552/Hexcel8552MaterialCharacterizationBinderV0-9.pdf.

White, S. R., & Hahn, H. T. (1992). Process modeling of composite materials: residual stress development during cure. Part II. Experimental validation. *Journal of Composite Materials, 27*(16), 2423−2453.

White, S. R., & Hahn, H. T. (1992). Process modeling of composite materials: residual stress development during cure. Part I. Model formulation. *Journal of Composite Materials, 26*(16), 2402−2422.

Wisnom, M. R., Gigliotti, M., Ersoy, N., Campbell, M., & Potter, K. D. (2006). Mechanisms generating residual stresses and distortion during manufacture of polymer-matrix composites structures. *Composites Part A: Applied Science and Manufacturing, 37*(4), 522−529.

Wu, Z., & Lu, J. (2000). Study of surface residual stress by three-dimensional displacement data at a single point in hole drilling method. *Journal of Engineering Materials and Technology, 122*(2), 215−220.

Yu, H., Mhaisalkar, S. G., & Wong, E. H. (2005). Observations of gelation and vitrification of a thermosetting resin during the evolution of polymerization shrinkage. *Macromolecular Rapid Communication, 26*(18), 1483−1487.

Zhou, G., & Sim, L. M. (2002). Damage detection and assessment in fibre reinforced composite structures with embedded fibre optic sensors—review. *Smart Materials and Structures, 11*(6), 925−939.

Zobeiry, N. (2006). *Viscoelastic constitutive models for evaluation of residual stresses in thermoset composites during cure* (Ph.D. thesis). Vancouver: The University of British Columbia.

Zobeiry, N., Vaziri, R., & Poursartip, A. (2010). Computationally efficient pseudo-viscoelastic models for evaluation of residual stresses in thermoset polymer composites during cure. *Composites Part A: Applied Science and Manufacturing, 41*(2), 247−256.

A multiscale synergistic damage mechanics approach for modeling progressive failure in composite laminates

4

C.V. Singh
University of Toronto, Toronto, ON, Canada

4.1 Introduction

Failure in polymer composites is different than in metallic and ceramic materials. In composites, the failure occurs progressively through a variety of damage mechanisms that cause loss of load-bearing capabilities of the composite structures. Therefore, composites may develop significant amounts of damage without causing catastrophic failure. In most cases, when composite laminates consisting of a designed layup is loaded in tension, this progressive damage begins through the initiation of microcracks in the matrix resin, which quickly give rise to cracks in the ply transverse to the loading direction. These "ply cracks," being unstable in nature, grow through the lamina thickness and width directions, and thus can be considered as *fully developed*. On increased external loading, more such cracks form in the transverse plies, without causing ultimate structural failure. If a mix of ply orientations is used to define composite layup, ply cracks may initiate in multiple directions. Since ply cracking does not cause final failure, this is considered *subcritical damage*. This can, however, lead to critical forms of damage such as delamination, and it is therefore necessary to accurately predict material behavior under practical conditions. Additionally, ply cracking causes a reduction in the stiffness moduli of the composite laminate, thereby reducing its load-carrying capability. The field of damage mechanics deals with understanding the growth of such damage and its effect on the stiffness properties of damaged laminates. In this chapter, we describe a newly developed multiscale synergistic damage mechanics (SDM) approach for predicting the stiffness degradation of multidirectional composite laminates with ply cracking in multiple orientations. The methodology is an extension of the continuum damage mechanics (CDM), and thus we begin by providing a brief overview of the CDM concepts. The issues with CDM will then be identified, leading to SDM formulation. Later sections will describe the SDM procedure and showcase its application for a selected set of multidirectional laminates. We will end the chapter by highlighting concurrent issues, future trends, resources for further information, and concluding remarks.

Structural Integrity and Durability of Advanced Composites. http://dx.doi.org/10.1016/B978-0-08-100137-0.00004-3

4.2 Continuum damage mechanics

For undamaged laminate, the constitutive relationship can be written as

$$\sigma_{ij} = C_{ijkl}\varepsilon_{kl} \tag{4.1}$$

where σ_{ij}, ε_{kl}, and C_{ijkl} denote the tensors of stress, strain, and stiffness, respectively, at a point in the continuum body. For a prescribed layup, C_{ijkl} can be obtained using classical laminate theory (CLT). When this laminate is subjected to quasi-static loading, it would develop ply cracking, typically beginning from the transverse plies. Since continuous loading would cause further crack development, the nature of these entities constituting damage is evolving. The damage processes create free surfaces in the material continuum, and thus lead to perturbations in the stress and strain fields, finally leading to a reduction in the load carrying capacity, or magnitude of stiffness properties. CDM deals with analyzing the response of the laminate subsequent to damage development (Talreja & Singh, 2012). Initial developments of internal variable-based damage mechanics were related to metals, ceramics, rocks, and concrete materials (Chaboche, 1984, 1988a, 1988b; Kachanov, 1999; Lemaitre, 1985; Murakami & Ohno, 1981; Robotnov, 1969). In the 1980s, Talreja and Allen independently laid the foundations of CDM approaches for composite materials (Allen, Harris, & Groves, 1987; Talreja, 1985a, 1985b, 1990, 1994). Their work was initially focused on cross-ply laminates. Since then, significant improvements have been made on the initial models for their application for ceramic matrix composites (Talreja, 1991), and with regard to cracking in off-axis plies (Varna, Akshantala, & Talreja, 1999, Varna, Joffe, & Talreja 2001a, 2001b). More recent efforts have focused on the development of SDM for multimode cracking in multidirectional laminates (Singh & Talreja, 2007, 2008, 2009, 2013; Singh, 2013) and the multiscale aspects of damage (Singh, 2008; Talreja & Singh, 2008). Aspects related to the damage evolution have also been included into the SDM (Singh & Talreja, 2010); in addition, work is ongoing on predicting stiffness changes under multiaxial loading (Montesano & Singh, 2015a, 2015b). The concepts underlying the CDM approach will be described in this section with more recent developments covered in subsequent sections.

Figure 4.1 shows the basic concepts underlying the CDM approach developed by Talreja (1985a, 1985b, 1990, 1994). The actual material continuum consists of heterogeneities. Some of the microstructural entities such as distribution of fibers and other reinforcing constituents are "stationary" in nature, that is, they do not evolve during deformation. On the other hand, the damage entities would increase in density upon increased loading. In the first step, the stationary microstructure is homogenized over the continuum body, resulting in an "effective" medium with thermomechanical properties equivalent to that of original continuum in undamaged state. In the second step, the evolving microstructure (i.e., damage entities) is homogenized to yield a fully homogenized continuum with properties equivalent to damaged composite. The first step could be easily achieved through CLT or any other micromechanical

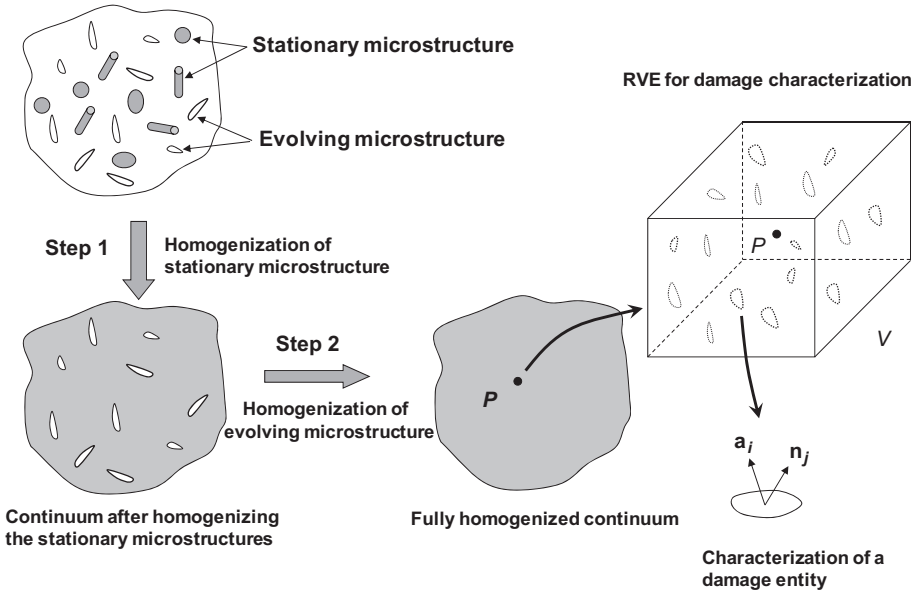

Figure 4.1 Basic concept behind CDM approach for characterizing continuum body with damage. In the first step, the stationary microstructure is homogenized. The second step involves description of evolving damage and homogenization over a representative volume element (RVE). A tensorial characterization of a damage entity inside RVE near point P is depicted in the bottom right.
Reprinted with kind permission from Singh, C. V., & Talreja, R. (2013). A synergistic damage mechanics approach to mechanical response of composite laminates with ply cracks. *Journal of Composite Materials*, *47*, 2475−2501, Copyright © 2013 by Sage Publications.

models. CDM mainly concerns the second step. Suppose P is an arbitrary point in the continuum body, then the region around this point can be described by defining a representative volume element (RVE). There are N damage entities in the RVE, at a given loading condition, each characterized through its normal vector $\mathbf{n}$ (for direction) and an influence vector $\mathbf{a}$. Following Vakulenko and Kachanov (1971), the variable describing damage can be formed by a dyadic product of the two vectors, that is,

$$d_{ij} = \int_S \mathbf{a}_i \mathbf{n}_j \mathrm{d}S \tag{4.2}$$

where $\mathbf{a}_i$ and $\mathbf{n}_j$ represent the components of influence and normal vectors, respectively, and S denotes the damage entity surface. Once all damage entities inside the RVE are so characterized, they could be grouped into categories representing different damage modes depending on their nature. For instance, if ply cracks are present in two orientations, they can be grouped in Mode 1 and Mode 2. Consequently,

homogenization over this RVE can be performed, resulting in the following damage mode tensors:

$$D_{ij}^{(\alpha)} = \frac{1}{V}\sum_{k_\alpha}\left(d_{ij}\right)_{k_\alpha} \tag{4.3}$$

where k_α is the number of damage entities in the αth mode, and V denotes the RVE volume.

For the case of ply cracking in a given off-axis layer, the RVE can be simplified as consisting of periodic cells of ply cracks as shown in Figure 4.2. For the sake of clarity, cracks are shown in only one damage mode, although they can appear in multiple off-axis plies depending upon laminate layup and loading scenario. The damage mode tensor for this situation can be derived as (see Talreja & Singh, 2012 for more details)

$$D_{ij}^{(\alpha)} = \frac{\kappa t_c^2}{st\sin\theta}\mathbf{n}_i\mathbf{n}_j \tag{4.4}$$

where κ, known as the constraint parameter, is an unspecified constant of (assumed) proportionality between $\boldsymbol{a}$ and the crack size t_c (also cracked-ply thickness), t is the total laminate thickness and $\mathbf{n}_i = (\sin\theta,\cos\theta,0)$ represents normal vector for crack surface.

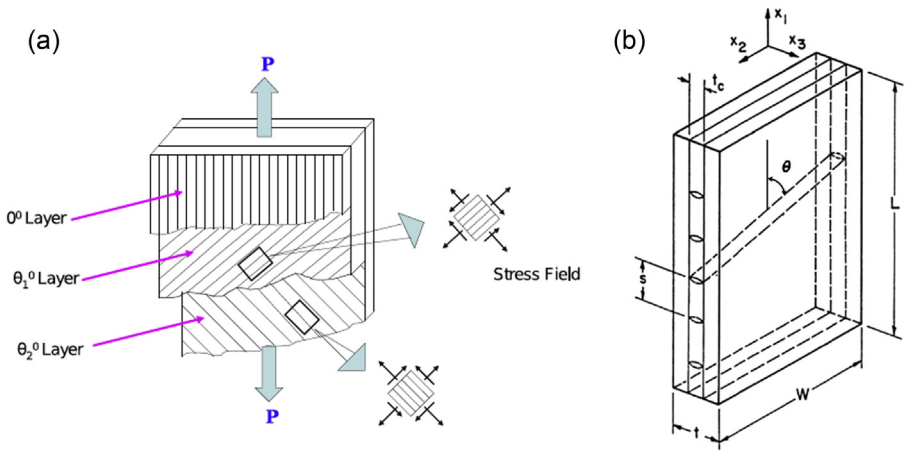

Figure 4.2 (a) A multidirectional composite laminate with off-axis laminate sequence undergoing damage in multiple off-axis plies. (b) A representative volume element describing intralaminar multiple cracking in a general off-axis ply.
Reprinted with kind permission from Singh, C. V., & Talreja R. (2009). A synergistic damage mechanics approach for composite laminates with matrix cracks in multiple orientations. *Mechanics of Materials*, *41*, 954−968, Copyright Elsevier (2009).

In order to obtain the mechanical response of damaged laminate, consider the Helmholtz free energy for the body, which is a function of strain tensor as well as damage mode tensor, that is,

$$\psi = \psi_P\left(\varepsilon_{ij}, D_{ij}^{(\alpha)}\right) \tag{4.5}$$

where ψ_P stands for the polynomial functional form for the free energy that considers integrity basis to enforce inherent material symmetries. For simplicity, let us first consider the case of single damage mode, for example, 90° ply cracking in a cross-ply laminate. In order to maintain material symmetry for constitutive law, the polynomial is expressed in terms of the invariants representing orthotropic symmetry described by Spencer (1971) and Adkins (1960). We will further restrict the polynomial terms to consider thin laminates with plane stress conditions. Henceforth, the most general polynomial form for Helmholtz free energy, restricted to second-order terms in the strain components and first-order terms in damage tensor components, can be written as

$$\begin{aligned}\rho\psi = {} & P_0 + \left\{c_1\varepsilon_1^2 + c_2\varepsilon_2^2 + c_3\varepsilon_6^2 + c_4\varepsilon_1\varepsilon_2\right\} \\ & + \left\{c_5\varepsilon_1^2 D_1 + c_6\varepsilon_1^2 D_2\right\} + \left\{c_7\varepsilon_2^2 D_1 + c_8\varepsilon_2^2 D_2\right\} + \left\{c_9\varepsilon_6^2 D_1 + c_{10}\varepsilon_6^2 D_2\right\} \\ & + \left\{c_{11}\varepsilon_1\varepsilon_2 D_1 + c_{12}\varepsilon_1\varepsilon_2 D_2\right\} + \left\{c_{13}\varepsilon_1\varepsilon_6 D_6 + c_{14}\varepsilon_2\varepsilon_6 D_6\right\} \\ & + P_1\left(\varepsilon_p, D_q\right) + P_2\left(D_q\right)\end{aligned} \tag{4.6}$$

where P_0 and c_i, $i = 1,2,\ldots,14$ are material constants, P_1 is a linear function of strain and damage tensor components, and P_2 is a linear function of damage tensor components. The strain and damage tensor components are denoted through Voigt notation as $\varepsilon_1 \equiv \varepsilon_{11}$, $\varepsilon_2 \equiv \varepsilon_{22}$, $\varepsilon_6 \equiv \varepsilon_{12}$, $D_1 \equiv D_{11}$, $D_2 \equiv D_{22}$, $D_6 \equiv D_{12}$. Since the free energy will be zero for unstrained and undamaged material, we obtain $P_0 = 0$. Additionally, if we assume that the unstrained material of any damaged state is stress-free, we get $P_1 = 0$. This assumption is considered valid since stress field around a crack changes from predamaged state only when the crack surfaces are displaced. The stress tensor components (Voigt notation) can be derived from the free energy function as

$$\sigma_p = \rho\frac{\partial\psi}{\partial\varepsilon_p} \tag{4.7}$$

where $p = 1,2,6$. Using Eqns (4.1), (4.6), and (4.7), the stiffness tensor for damaged laminate is obtained, given by

$$C_{pq} = C_{pq}^0 + C_{pq}^{(1)} \tag{4.8}$$

where

$$C^0_{pq} = \begin{bmatrix} 2c_1 & c_4 & 0 \\ & 2c_2 & 0 \\ \text{Symm} & & 2c_3 \end{bmatrix} = \begin{bmatrix} \dfrac{E^0_x}{1-\nu^0_{xy}\nu^0_{yx}} & \dfrac{\nu^0_{xy}E^0_y}{1-\nu^0_{xy}\nu^0_{yx}} & 0 \\ & \dfrac{E^0_y}{1-\nu^0_{xy}\nu^0_{yx}} & 0 \\ \text{Symm} & & G^0_{xy} \end{bmatrix} \tag{4.9}$$

denotes the orthotropic stiffness matrix for undamaged composite material, where $E^0_x, E^0_y, \nu^0_{xy}, G^0_{xy}$ represent effective elastic moduli for the virgin laminate (can be easily obtained through CLT), and

$$C^{(1)}_{pq} = \begin{bmatrix} 2c_5D_1 + 2c_6D_2 & c_{11}D_1 + c_{12}D_2 & c_{13}D_6 \\ & 2c_7D_1 + 2c_8D_2 & c_{14}D_6 \\ \text{Symm} & & 2c_9D_1 + 2c_{10}D_2 \end{bmatrix} \tag{4.10}$$

represents the change in stiffness tensor brought about by the damage in mode 1. For the special case of cross-ply laminates, $\theta = 90^o$, Eqn (4.8) simplifies to

$$C_{pq} = \begin{bmatrix} \dfrac{E^0_x}{1-\nu^0_{xy}\nu^0_{yx}} & \dfrac{\nu^0_{xy}E^0_y}{1-\nu^0_{xy}\nu^0_{yx}} & 0 \\ & \dfrac{E^0_y}{1-\nu^0_{xy}\nu^0_{yx}} & 0 \\ \text{Symm} & & G^0_{xy} \end{bmatrix} + \frac{\kappa t_c^2}{st} \begin{bmatrix} 2a_1 & a_4 & 0 \\ & 2a_2 & 0 \\ \text{Symm} & & 2a_3 \end{bmatrix} \tag{4.11}$$

where new material constants are defined as $a_1 = c_5$, $a_2 = c_7$, $a_3 = c_9$, and $a_4 = c_{11}$. As expected, the orthotropic symmetry is retained for intralaminar cracking in cross-ply laminates. In order to derive engineering moduli for the damaged laminate, the following relationships can be utilized:

$$\begin{aligned} E_x &= \frac{C_{11}C_{22} - C_{12}^2}{C_{22}} \quad & E_y &= \frac{C_{11}C_{22} - C_{12}^2}{C_{11}} \\ \nu_{xy} &= \frac{C_{11}}{C_{22}} & G_{xy} &= C_{66} \end{aligned} \tag{4.12}$$

Thus, they are given as:

$$
\begin{aligned}
E_x &= \frac{E_x^0}{1-\nu_{xy}^0\nu_{yx}^0} + 2\frac{\kappa t_c^2}{st}a_1 - \frac{\left[\dfrac{\nu_{xy}^0 E_y^0}{1-\nu_{xy}^0\nu_{yx}^0} + \dfrac{\kappa t_c^2}{st}a_4\right]^2}{\dfrac{E_y^0}{1-\nu_{xy}^0\nu_{yx}^0} + 2\dfrac{\kappa t_c^2 \sin\theta}{st}a_2} \\
E_y &= \frac{E_y^0}{1-\nu_{xy}^0\nu_{yx}^0} + 2\frac{\kappa t_c^2}{st}a_2 - \frac{\left[\dfrac{\nu_{xy}^0 E_y^0}{1-\nu_{xy}^0\nu_{yx}^0} + \dfrac{\kappa t_c^2}{st}a_4\right]^2}{\dfrac{E_x^0}{1-\nu_{xy}^0\nu_{yx}^0} + 2\dfrac{\kappa t_c^2}{st}a_1} \\
\nu_{xy} &= \frac{\dfrac{\nu_{xy}^0 E_y^0}{1-\nu_{xy}^0\nu_{yx}^0} + \dfrac{\kappa t_c^2}{st}a_4}{\dfrac{E_y^0}{1-\nu_{xy}^0\nu_{yx}^0} + 2\dfrac{\kappa t_c^2}{st}a_2} \\
G_{xy} &= G_{xy}^0 + 2\frac{\kappa t_c^2}{st}a_3
\end{aligned}
\tag{4.13}
$$

From Eqns (4.11) and (4.13), it can be seen that we require four phenomenological constants, a_i, $i = 1,2,3,4$ for a complete prediction of stiffness moduli as a function of crack density. They depend on the material and laminate configuration and can be determined for a selected laminate from experimental or numerical data for stiffness properties at some known crack density. Suppose we know the stiffness moduli for a damaged cross-ply laminate at 90° crack spacing of $s = s_1$, then using Eqn (4.11), we get

$$
\begin{aligned}
a_1 &= \frac{s_1 t}{2\kappa t_c^2}\left[\frac{E_x}{1-\nu_{xy}\nu_{yx}} - \frac{E_x^0}{1-\nu_{xy}^0\nu_{yx}^0}\right] \\
a_2 &= \frac{s_1 t}{2\kappa t_c^2}\left[\frac{E_y}{1-\nu_{xy}\nu_{yx}} - \frac{E_y^0}{1-\nu_{xy}^0\nu_{yx}^0}\right] \\
a_3 &= \frac{s_1 t}{2\kappa t_c^2}\left[G_{xy} - G_{xy}^0\right] \\
a_4 &= \frac{s_1 t}{\kappa t_c^2}\left[\frac{\nu_{xy}E_y}{1-\nu_{xy}\nu_{yx}} - \frac{\nu_{xy}^0 E_y^0}{1-\nu_{xy}^0\nu_{yx}^0}\right]
\end{aligned}
\tag{4.14}
$$

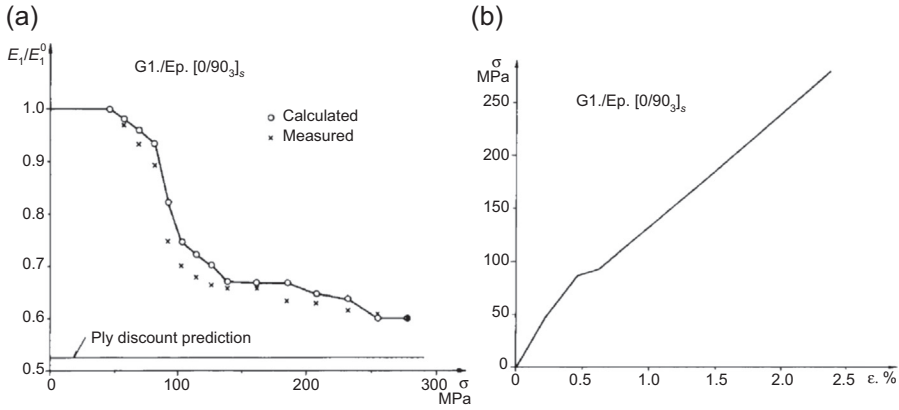

Figure 4.3 Stiffness degradation and stress−strain response for glass/epoxy $[0/90_3]_s$ laminate: (a) variation of longitudinal Young's modulus, normalized with the magnitude for undamaged laminate, with applied stress; (b) longitudinal stress−strain plot.
Reprinted with kind permission from Talreja, R. (1985). Transverse Cracking and Stiffness Reduction in Composite Laminates. *Journal of Composite Materials*, *19*, 355−375, Copyright © 1985 by Sage Publications.

The overall CDM procedure for prediction of stiffness changes subsequent to transverse ply cracking thus follows: First we compute (or measure) the constraint parameter, Eqn (4.4), for a given composite laminate. Thereafter, four phenomenological constants are determined using Eqn (4.14). For this step, stiffness properties of damaged composite at a specific crack density are needed. In the final step, elastic moduli are predicted over the range of crack density of interest using Eqn (4.13). This approach has been successfully used to predict degradation in the longitudinal and transverse moduli and the Poisson's ratio for a variety of laminate layups, for example, $[0/90_3]_s$, $[90_3/0]_s$, $[0/\pm45]_s$, as reported in studies by Talreja (1985a; 1985b; 1990; 1994). As an example, Figure 4.3 (a) illustrates comparison of CDM predictions for the longitudinal Young's modulus with experimental data in a $[0/90_3]_s$ glass/epoxy laminate with the applied tensile stress reported in Talreja (1985b). Figure 4.3 (b) displays the corresponding stress−strain response along longitudinal direction. Clearly, the predictions agree with the observed values fairly well in the entire range of cracking. In Figure 4.3 (a), predictions using ply discount method are also shown and they are found to overestimate the total modulus reduction. This indicates the importance of accurately predicting the progressive degradation of stiffness properties.

4.3 Synergistic damage mechanics

The chief issue with the CDM approach described in the previous section is that it needs evaluation of phenomenological constants, a_i, each time the laminate sequence

is changed. Furthermore, experimental data for off-axis ply cracking are very scarce and difficult to obtain, thereby limiting our ability to predict effects of damage in multidirectional laminates. In order to overcome these limitations, CDM was combined with computational micromechanics in a synergistic manner. The new methodology, known as SDM, is based on the observation that the constraint parameter, κ, can be considered as a carrier of the local effects of damage entities within an RVE, while the a_i-constants are material constants. The damage constants can thus be evaluated for a preselected "reference" laminate sequence and thus be assumed constant for a class of similar laminates. In this way, stiffness predictions can be made for off-axis cracking in multidirectional laminates. Since transverse ply cracking in cross-ply laminates has been extensively studied, both experimentally and analytically, an easy choice for reference laminate is of $[0/90]_s$ layup. The stiffness data for this laminate at a specific crack density can be obtained by (1) utilizing independent experimentally measured data for stiffness degradation, as reported in Varna, Joffe, Akshantala, & Talreja (1999), (2) using analytical predictions of an accurate damage model such as a variational analysis, or (3) conducting computations through finite element method (FEM), see, for example, Singh and Talreja (2009).

For describing damage in off-axis plies of a multidirectional laminate using SDM methodology, the relative change in the constraint parameter, as the laminate sequence and hence the damage orientation changes, is the most important factor. In general, the constraint parameter denotes the crack surface displacements in different scenarios. Hence, the relative change in crack opening displacement (COD) with respect to COD for the reference laminate is taken as the relative change in the constraint parameter. Changes in the crack sliding displacement (CSD) are also important, especially in multiaxial loading cases; however, for simplicity, we would not consider it in the following analysis. In this section, we describe the overall SDM approach and showcase its application for the case of one, two, and three damage modes.

4.3.1 90° ply cracking in cross-ply laminates

Let us first consider the case of one damage mode: transverse cracks in cross-ply laminates, $[0_m/90_n]_s$. In this case, the damage constants can be computed by fitting the previously described CDM model (see Eqn (4.14)) for reference cross-ply laminate, that is, given values of 0° and 90° ply thicknesses, m and n.

The influence of crack opening is calculated by the normalized average COD, which can be computed numerically (using FEM); or experimentally. The constraint parameter for this case is defined as

$$\kappa = \frac{\overline{\Delta u_y}}{t_c} \tag{4.15}$$

where t_c is the cracked ply thickness (representing the crack size of fully developed ply cracks) and $\overline{\Delta u_y}$ represents the average COD, which is defined as

$$\overline{\Delta u_y} = \frac{1}{t_c} \int_{-t_c/2}^{t_c/2} \Delta u_y(z) \mathrm{d}z \tag{4.16}$$

In the above expression, $\Delta u_y(z)$ denotes the COD, computed as the difference of nodal y-direction displacements, as a function of thickness (z-) direction. The relative magnitude of stiffness changes due to ply cracking in two different $[0_m/90_n]_s$ cross-ply laminates (with same ply material) that can be obtained by using Eqn (4.11), with damage constants evaluated for a reference laminate from Eqn (4.14), and relative value of the constraint parameter obtained from computational micromechanics through Eqns (4.15) and (4.16).

The same model is easily extendable to 90° ply cracking in $[\pm\theta_m/90_n]_s$ laminates. For small values of angle ply orientation (θ), the cracks would appear in 90° plies only. Thus, only a single damage mode would be active. The difference in damage influence for a specific θ can be determined by comparing the amount of opening of cracked surfaces with the opening for the case of the reference cross-ply laminate taken as $[0_2/90_4]_s$:

$$\kappa_{\mathrm{rel}}(\theta) = \frac{\left(\overline{\Delta u_y}\right)_{[\pm\theta_m/90_n]_s}}{\left(\overline{\Delta u_y}\right)_{[0_2/90_4]_s}} \tag{4.17}$$

However, if the cracking also occurs in the angle plies, multiple off-axis ply cracking modes will be active, and must be described as below.

4.3.2 Off-axis ply cracking

The stress state in damaged multidirectional laminate is quite complex and cannot be solved using other analytical approaches, except numerical procedures such as FEM. Nevertheless, the SDM approach is quite amenable to the case of cracking in plies oriented at an angle to the longitudinal directions. Based on experimental observations, ply cracks in off-axis plies originate only if the ply orientation is $\theta > 40°$ or so. Even then, there is only marginal damage; the significant damage occurs only for $\theta > 60°$. Laminates with multiple off-axis plies would undergo ply cracking in multiple orientations, grouped here into different damage modes. Here, we consider two such cases: a case with two damage modes, and another with three ply cracking modes.

4.3.2.1 Two cracking damage modes

When two ply cracking modes are active, the Helmholtz free energy function of the damaged laminate is written in terms of integrity basis, and using Voigt notation, as

$$\begin{aligned}\rho\psi \;=\; & P_0 + \left\{c_1\varepsilon_1^2 + c_2\varepsilon_2^2 + c_3\varepsilon_6^2 + c_4\varepsilon_1\varepsilon_2\right\} \\ & + \varepsilon_1^2\left\{c_5 D_1^{(1)} + c_6 D_2^{(1)} + c_7 D_1^{(2)} + c_8 D_2^{(2)}\right\} \\ & + \varepsilon_2^2\left\{c_9 D_1^{(1)} + c_{10} D_2^{(1)} + c_{11} D_1^{(2)} + c_{12} D_2^{(2)}\right\} \\ & + \varepsilon_6^2\left\{c_{13} D_1^{(1)} + c_{14} D_2^{(1)} + c_{15} D_1^{(2)} + c_{16} D_2^{(2)}\right\} \\ & + \varepsilon_1\varepsilon_2\left\{c_{17} D_1^{(1)} + c_{18} D_2^{(1)} + c_{19} D_1^{(2)} + c_{20} D_2^{(2)}\right\} \\ & + \varepsilon_1\varepsilon_6\left\{c_{21} D_6^{(1)} + c_{22} D_6^{(2)}\right\} + \varepsilon_2\varepsilon_6\left\{c_{23} D_6^{(1)} + c_{24} D_6^{(2)}\right\} \\ & + P_1\left(\varepsilon_p, D_q^{(1)}\right) + P_2\left(\varepsilon_p, D_q^{(2)}\right) + P_3\left(D_q^{(1)}\right) + P_4\left(D_q^{(2)}\right)\end{aligned} \tag{4.18}$$

where P_0 and c_i, $i = 1,2,\ldots,24$ are material constants, P_1 and P_2 represent linear functions of strain and damage tensor components, and P_3 and P_4 are linear functions of the damage tensor components. As explained before for cross-ply laminates, assuming the unstrained material of any damaged state to be stress-free, we obtain $P_0 = P_1 = P_2 = 0$. Considering the undamaged composite material to be orthotropic and proceeding in a similar manner as described in Section 4.2, the stiffness matrix for damaged multidirectional laminate can be derived as

$$C_{pq} \;=\; C_{pq}^0 + C_{pq}^{(1)} + C_{pq}^{(2)} \tag{4.19}$$

where $p,\ q = 1,2,6$; C_{pq}^0 represents the stiffness coefficient matrix of the virgin laminate, see Eqn (4.9); and the stiffness changes due to damage are represented by $C_{pq}^{(1)}$ and $C_{pq}^{(2)}$, for the two damage modes, respectively, and are given by

$$C_{pq}^{(1)} \;=\; \begin{bmatrix} 2c_5 D_1^{(1)} + 2c_6 D_2^{(1)} & c_{17} D_1^{(1)} + c_{18} D_2^{(1)} & c_{21} D_6^{(1)} \\ & 2c_9 D_1^{(1)} + 2c_{10} D_2^{(1)} & c_{23} D_6^{(1)} \\ \text{Symm} & & 2c_{13} D_1^{(1)} + 2c_{14} D_2^{(1)} \end{bmatrix}$$

$$C_{pq}^{(2)} \;=\; \begin{bmatrix} 2c_7 D_1^{(2)} + 2c_8 D_2^{(2)} & c_{19} D_1^{(2)} + c_{20} D_2^{(2)} & c_{22} D_6^{(2)} \\ & 2c_{11} D_1^{(2)} + 2c_{12} D_2^{(2)} & c_{24} D_6^{(2)} \\ \text{Symm} & & 2c_{15} D_1^{(2)} + 2c_{16} D_2^{(2)} \end{bmatrix} \tag{4.20}$$

The stiffness−damage relations for N damage modes, Eqn (4.19), are generally given as

$$C_{pq} = C^0_{pq} + \sum_{\alpha=1}^{N} C^{(\alpha)}_{pq} \tag{4.21}$$

With reference to Figure 4.4 where the orientations of the two damage modes are shown, the damage mode elements are given by

$$\alpha = 1 : n_i^{(1)} = (\sin\theta, \cos\theta, 0)$$

$$D_1^{(1)} = \frac{\kappa^{\theta^+} t_c^2}{s_n^{\theta^+} t} \sin^2\theta; \quad D_2^{(1)} = \frac{\kappa^{\theta^+} t_c^2}{s_n^{\theta^+} t} \cos^2\theta; \quad D_6^{(1)} = \frac{\kappa^{\theta^+} t_c^2}{s_n^{\theta^+} t} \sin\theta\cos\theta$$

$$\alpha = 2 : n_i^{(2)} = (\sin\theta, -\cos\theta, 0)$$

$$D_1^{(2)} = \frac{\kappa^{\theta^-} t_c^2}{s_n^{\theta^-} t} \sin^2\theta; \quad D_2^{(2)} = \frac{\kappa^{\theta^-} t_c^2}{s_n^{\theta^-} t} \cos^2\theta; \quad D_6^{(2)} = -\frac{\kappa^{\theta^-} t_c^2}{s_n^{\theta^-} t} \sin\theta\cos\theta \tag{4.22}$$

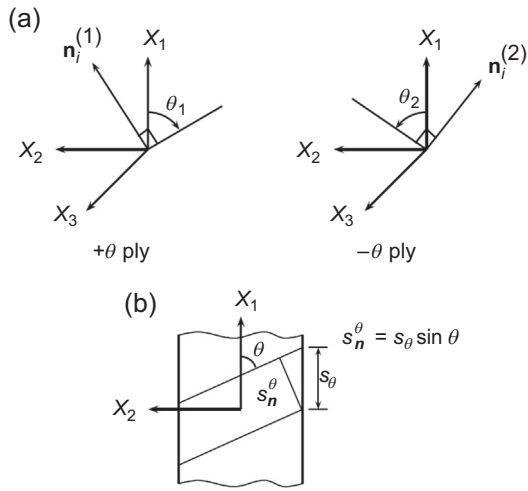

Figure 4.4 Characterization of ply cracking damage for two off-axis damage modes. (a) Normal crack spacing s_n^θ, and axial crack spacing s_θ in a cracked θ-ply, and (b) directions of normal vectors for cracks in $+\theta$ and $-\theta$ plies.
Reprinted with kind permission from Singh, C.V., & Talreja, R. (2009). A synergistic damage mechanics approach for composite laminates with matrix cracks in multiple orientations. *Mechanics of Materials*, *41*, 954−968, Copyright Elsevier (2009).

where the superscripts θ^+ and θ^- indicate variables for $+\theta$ and $-\theta$ plies, respectively. Assuming that the intensity and distribution of damage is same in θ^+ and θ^- plies, we have

$$\kappa^{\theta^+} = \kappa^{\theta^-} = \kappa^{\theta}; \; s_n^{\theta^+} = s_n^{\theta^-} = s_n^{\theta} \tag{4.23}$$

After substituting Eqns (4.22) and (4.23) into Eqn (4.21), and using some simplifications, we obtain

$$C_{pq} = \begin{bmatrix} \dfrac{E_x^0}{1-\nu_{xy}^0\nu_{yx}^0} & \dfrac{\nu_{xy}^0 E_y^0}{1-\nu_{xy}^0\nu_{yx}^0} & 0 \\ & \dfrac{E_y^0}{1-\nu_{xy}^0\nu_{yx}^0} & 0 \\ \text{Symm} & & G_{xy}^0 \end{bmatrix} + D_\theta \begin{bmatrix} 2a_1 & a_4 & 0 \\ & 2a_2 & 0 \\ \text{Symm} & & 2a_3 \end{bmatrix} \tag{4.24}$$

where $D_\theta = \dfrac{\kappa_\theta t_c^2}{s_n^\theta t}$ represents the effective damage parameter for this case. Please note that this relation is very similar to the expression for 90° cracking in a cross-ply laminate (Eqn (4.11)).

$$\kappa_{\text{rel}}(\theta) = \frac{\kappa_\theta}{\kappa_{90}} = \frac{\left(\overline{\Delta u_y}\right)_{\pm\theta_4}}{\left(\overline{\Delta u_y}\right)_{90_8}} \tag{4.25}$$

4.3.2.2 Three cracking damage modes

Consider the case of $[0_m/\pm\theta_n/90_r]_s$ laminate, with cracking in $+\theta$, $-\theta$, and 90° plies concurrently. It is apparent from Eqns (4.19), (4.21), and (4.24) that one needs to add stiffness degradation due to the 90° damage to stiffness expressions derived above for the case of two damage modes, Eqn (4.24). With some simplifications, as reported previously by Singh and Talreja (2009), $\Delta C_{pq} = C_{pq} - C_{pq}^0 = \sum_{\alpha=1}^{3} C_{pq}^{(\alpha)}$ for this scenario can be derived as

$$\Delta C_{pq} = D \begin{bmatrix} 2a_1' & a_4' & 0 \\ & 2a_2' & 0 \\ \text{Symm} & & 2a_3' \end{bmatrix} \tag{4.26}$$

where

$$D = \frac{2t_0^2}{t}\left[\frac{1}{s_n^\theta}\frac{\kappa_\theta}{\kappa_\theta|_{\theta=90}}\left\{2(2n+r)^2_{\kappa_{90_{4n+2r}}} - r^2\kappa_{90}\right\} + r^2\frac{\kappa_{90}}{s^{90}}\right] \tag{4.27}$$

where the relevant constraint parameters are derived as

$$\kappa_\theta = \frac{\left(\overline{\Delta u_y}\right)_{\pm\theta_{2n}}}{2nt_0}; \quad \kappa_{90_{4n+2r}} = \frac{\left(\overline{\Delta u_y}\right)_{90_{4n+2r}}}{(4n+2r)t_0}; \quad \kappa_{90} = \frac{\left(\overline{\Delta u_y}\right)_{90_{2r}}}{2rt_0} \tag{4.28}$$

Similar relations can be derived for the case where θ plies are centrally located in the laminate, that is, a $[0_m/90_r/\pm\theta_n]_s$ laminate. For full expressions of the relevant constraint parameters, the reader is referred to the original paper cited above.

4.3.2.3 Multiscale SDM procedure

The overall multiscale SDM flowchart to conduct structural analysis of damaged multidirectional composite laminates is illustrated in Figure 4.5. Here we consider the particular case of $[0_m/\pm\theta_n/0_{m/2}]_s$ laminate containing ply cracks in $+\theta$ and $-\theta$ layers. For a complete evaluation of the structural response, this procedure combines computational micromechanics with CDM. In order to compute constraint parameters

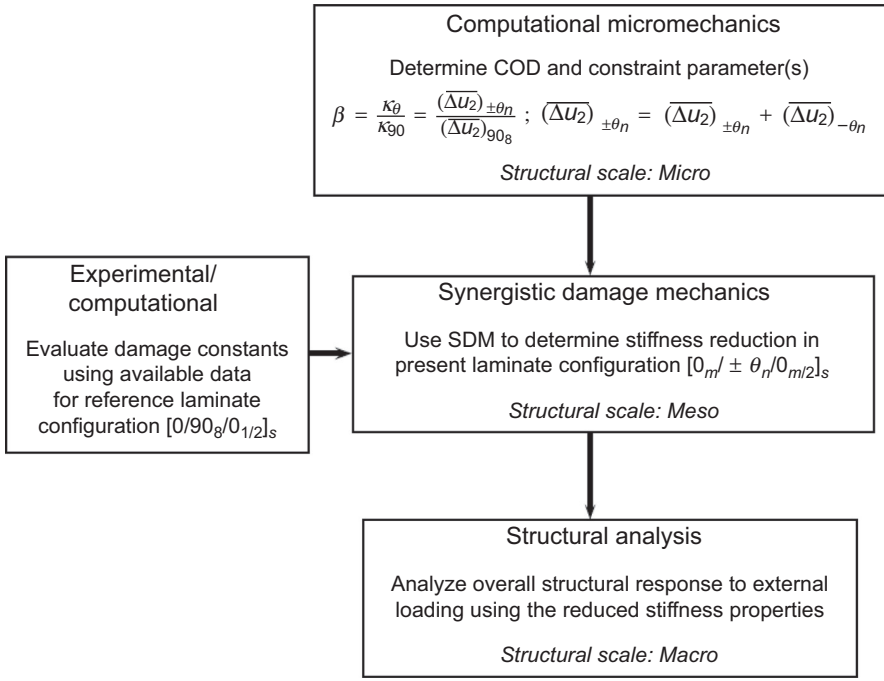

Figure 4.5 Flowchart illustrating the multiscale synergistic damage mechanics approach for analyzing damage behavior in $[0_m/\pm\theta_n/0_{m/2}]_s$ laminates with ply cracks in $+\theta$ and $-\theta$ layers. Reprinted with kind permission from Singh, C. V., & Talreja, R. (2008). Analysis of multiple off-axis ply crack in composite laminates. *International Journal of Solids and Structures, 45*, 4574–4589, Copyright Elsevier (2008).

for damage characterization, micromechanics through three-dimensional (3D) FE analysis over a periodic cell (RVE) of cracked laminate is performed for varying ply orientations as needed. Crack surface displacements are calculated from nodal displacement results under prescribed external loading conditions, and then averaged and normalized with respect to cracked ply thickness and the magnitude of the imposed strain. The so-determined constraint parameters are then carried over in the SDM formulation through stiffness−damage relationships, Eqn (4.24). Independent from this, the phenomenological damage constants a_i appearing in Eqn (4.24) are evaluated by fitting the SDM model to the stiffness data at prescribed crack density for a reference laminate using Eqn (4.14). Using the computed values of the damage constants and constraint parameters, the variation of elastic moduli with respect to crack density is predicted using the stiffness−damage relations described in Eqn (4.24). Subsequent structural analysis is conducted based on revised stiffness properties for the cracked laminate.

The simple method to measure COD is by utilizing a miniature materials tester (MINIMAT) developed by Varna, Akshantala, et al. (1999) and Varna, Joffe, et al. (1999). In this testing methodology, an open ply crack is observed under an optical microscope equipped with a video camera. The video signal is transmitted to a TV monitor display providing a 2000× magnification. This provides images of crack surface displacements from which COD can be measured as a function of cracked ply thickness. More recently, Katerelos, McCartney, and Galiotis (2005) developed an experimental approach based on Raman spectroscopy for COD measurement. The basic premise is that the Raman vibrational wave numbers of certain chemical groups of commercial reinforcing fibers, such as aramid or carbon, are dependent on the stress and strain levels. The methodology has been shown to work well for measuring evolution of ply cracking damage and resulting stiffness property changes, as reported in Katerelos, Lundmark, Varna, and Galiotis (2007), Katerelos, Kashtalyan, Soutis, and Galiotis (2008), and Katerelos, Varna, and Galiotis (2008).

4.3.2.4 Predictions for $[0_m/\pm\theta_n/0_{m/2}]_s$ laminate

The multiscale SDM approach described above has been used for multiple cases of ply cracking in multidirectional laminates in Singh and Talreja (2008, 2009, 2013) and Singh (2013). For the case of $[0_m/\pm\theta_n/0_{m/2}]_s$ glass/epoxy laminate, the FE model to conduct COD evaluation is shown in Figure 4.6, and the variations of average CODs with respect to cracked ply orientation are plotted in Figure 4.7. The comparison of calculated CODs with experimental data from Varna, Joffe, et al. (1999) shows a good agreement in numerical predictions and experimental measurements. In FE analyses, the loading was assumed in the longitudinal direction only, but it can be extended to multiaxial cases when needed. For further details of the FE models for multiple off-axis cracks in multidirectional laminates, please refer to our earlier reports in Singh and Talreja (2007, 2008, 2009, 2013), Singh (2013), and Li, Singh, and Talreja (2009). In particular, the definition of the RVE for a laminate with ply cracks in multiple orientations and its implication on the development of corresponding FE model has been covered by Li et al. (2009). As noted before, the main parameters

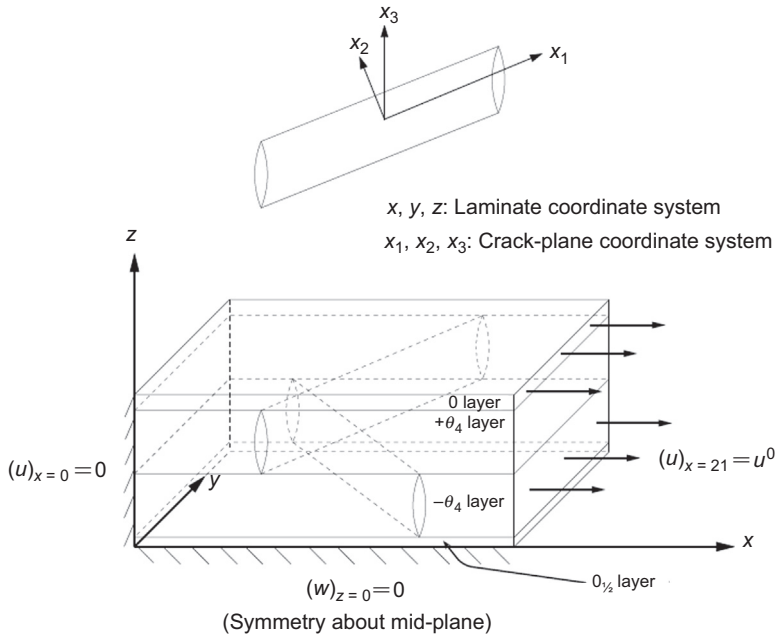

Figure 4.6 Representative 3D-FE unit cell for computation of COD for cracked $[0_m/\pm\theta_n/0_{m/2}]_s$ laminate.
Reprinted with kind permission from Singh, C. V., & Talreja, R. (2008). Analysis of multiple off-axis ply crack in composite laminates. *International Journal of Solids and Structures, 45*, 4574–4589, Copyright Elsevier (2008).

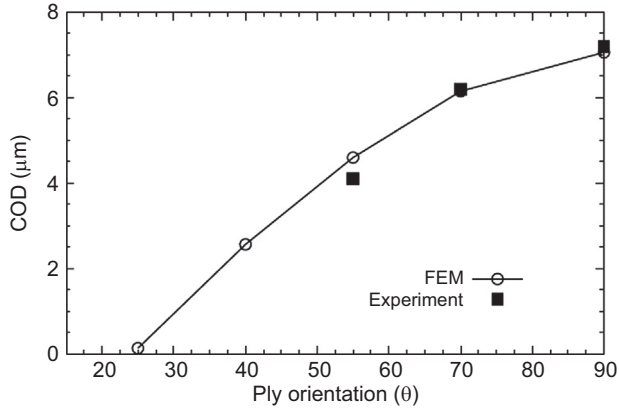

Figure 4.7 Variation in average COD as a function of cracked ply orientation for $[0_m/\pm\theta_n/0_{m/2}]_s$ glass/epoxy laminate. Experimentally, cracks were observed to form in this laminate only when $\theta \geq 55°$. Experimental values are taken from Varna, Joffe, et al. (1999).
Reprinted with kind permission, from Singh, C. V., & Talreja, R. (2008). Analysis of multiple off-axis ply crack in composite laminates. *International Journal of Solids and Structures, 45*, 4574–4589, Copyright Elsevier (2008).

that are evaluated using these FE analyses are the average CODs for ply cracks in each damage mode.

Figure 4.8 displays the SDM predictions for stiffness degradation with crack density for $[0/\pm\theta_4/0_{1/2}]_s$ laminates. In the figure, both Young's modulus and Poisson's ratio are normalized with the corresponding values for undamaged laminate. The model is found to be reasonable for $\theta = 70^\circ$, but for $\theta = 55^\circ$, predictions do not agree well with experimental data. This is because, in case of $[0/\pm 55_4/0_{1/2}]_s$ laminates, shear damage was also observed in experiments, which has not been accounted for in the model described here. When stiffness changes brought about by shear damage are taken into consideration, the SDM predictions are found to improve; however, agreement with the measured data is still limited. This points to the limitations of the SDM model described above: (1) it does not account for the effect of CSDs and (2) it does not account for nonlinearity in stiffness degradation at high crack densities. The second limitation has been resolved by developing a higher-order SDM model, as described in the next section. Further work is necessary to include the effect of sliding displacements. Furthermore, it is noted that the measured COD may be affected by the presence of other damage modes, like axial splitting and delaminations.

4.3.3 Higher-order SDM model

A key limitation of both CDM and SDM models is that their predictions for stiffness properties show a linear variation with respect to an increase in the ply crack density. This may work well in the early stages of damage development as the experimental results show significant (and almost linear) degradation in stiffness properties. However, experimental observations over a large variety of composite materials and laminate layups have shown that at high crack densities, the rate of change in the stiffness properties reduces, leading to an almost negligible degradation rate at large crack density levels (>1.0 crack per unit thickness of the cracked ply). This observation is clearly depicted in the damage evolution schematics shown in Figure 4.1. The nonlinearity in stiffness changes occurs because at high damage levels cracks are very close to each other and thus their stress fields start interacting in ways to reduce the propensity of the material to generate more cracks on further loading. This phenomenon is known as the crack shielding effect. A second limitation of the linear models is that they may show more severe degradation than practically possible based on a limiting minimum stiffness due to contributions from uncracked plies. This overprediction in stiffness degradation can be accounted by including second-order damage terms in the SDM model. In this section, a higher-order SDM model is described to accomplish this task. It enables prediction of stiffness properties of damaged laminates at high ply crack densities. The Helmholtz free energy function (Eqn (4.5)) is expanded to include nonlinear damage terms; and the corresponding stiffness−damage relations are derived for multiple multidirectional laminates undergoing ply cracking in multiple directions.

Let us first consider the case of thin ply laminates undergoing ply cracking via a single damage. The stress and damage state in the laminate, in the Voigt notation, is defined by: $\in_{11} = e_1$, $\in_{22} = e_2$, $\in_{12} = e_6$; $D_{11} = D_1$, $D_{22} = D_2$, and $D_{12} = D_6$.

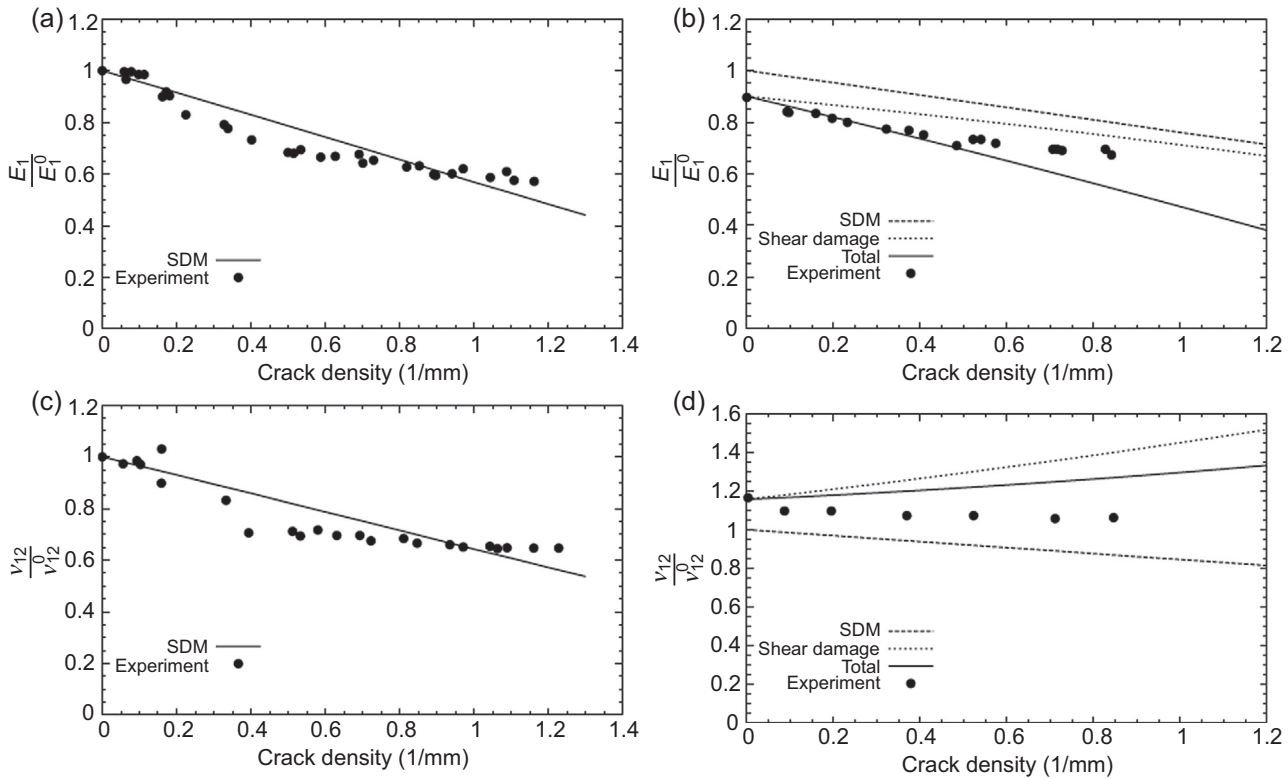

Figure 4.8 Variation of the longitudinal Young's modulus and Poisson's ratio for $[0/\pm\theta_4/0_{1/2}]_s$ laminates with respect to density of cracks in off-axis plies. (a), (b) are for $\theta = 70°$, whereas (c), (d) correspond to $\theta = 55°$.

Reprinted with kind permission from Singh, C. V., & Talreja, R. (2008). Analysis of multiple off-axis ply crack in composite laminates. *International Journal of Solids and Structures, 45*, 4574−4589, Copyright Elsevier (2008).

For the sake of simplicity, the superscript for damage mode α is dropped in case of single damage mode. The most general polynomial form for Helmholtz free energy (ψ), restricted to second-order terms in the strain and damage tensor components, is given by

$$\begin{aligned}\rho\psi \;=\; & P_0 + P_1\left(e_p, D_q\right) + P_2\left(D_q\right) + P_3\left(D_q^2\right) \\ & + \left\{c_1 e_1^2 + c_2 e_2^2 + c_3 e_6^2 + c_4 e_1 e_2\right\} + \left\{c_5 D_1 + c_6 D_2\right\} e_1^2 + \left\{c_7 D_1 + c_8 D_2\right\} e_2^2 \\ & + \left\{c_9 D_1 + c_{10} D_2\right\} e_6^2 + \left\{c_{11} D_1 + c_{12} D_2\right\} e_1 e_2 + c_{13} D_6 e_1 e_6 + c_{14} D_6 e_2 e_6 \\ & + \left\{c_{15} D_1^2 + c_{16} D_2^2\right\} e_1^2 + \left\{c_{17} D_1^2 + c_{18} D_2^2\right\} e_2^2 + \left\{c_{19} D_1^2 + c_{20} D_2^2\right\} e_6^2 \\ & + \left\{c_{21} D_1^2 + c_{22} D_2^2\right\} e_1 e_2 + c_{23} D_6^2 e_1 e_6 + c_{24} D_6^2 e_2 e_6 \end{aligned} \tag{4.29}$$

Using Eqn (4.7), we will obtain the following stiffness tensor for the damaged laminate:

$$C_{pq} \;=\; C_{pq}^0 + \sum_{\alpha} C_{pq}^{(\alpha)} \tag{4.30}$$

where $\sum\limits_{\alpha} C_{pq}^{(\alpha)} \;=\; C_{pq} - C_{pq}^0 \;=\; \Delta C_{pq}$ and the stiffness−damage tensor components for first and second order in damage terms are given by

$$\begin{aligned} C_{pq}^{(1)} \;&=\; \begin{bmatrix} 2c_5 D_1 + 2c_6 D_2 & c_{11} D_1 + c_{12} D_2 & c_{13} D_6 \\ & 2c_7 D_1 + 2c_8 D_2 & c_{14} D_6 \\ \text{Symm} & & 2c_9 D_1 + 2c_{10} D_2 \end{bmatrix} \\ C_{pq}^{(2)} \;&=\; \begin{bmatrix} 2c_{15} D_1^2 + 2c_{16} D_2^2 & c_{21} D_1^2 + c_{22} D_2^2 & c_{23} D_6^2 \\ & 2c_{17} D_1^2 + 2c_{18} D_2^2 & c_{24} D_6^2 \\ \text{Symm} & & 2c_{19} D_1^2 + 2c_{20} D_2^2 \end{bmatrix} \end{aligned} \tag{4.31}$$

As noted before, the off-axis ply cracks preferentially occur in plies with orientations, $\theta \geq 60^\circ$ to the axial loading direction. Therefore, shear deformation effects can be neglected and $D_1 \gg; D_2, D_6$. Based on these simplifications, and following the procedure detailed by Singh (2013), the following stiffness−damage relationships are obtained:

$$C_{pq} \;=\; C_{pq}^0 + D[a_i] + D^2[b_i] \tag{4.32}$$

where the matrices of damage constants are defined as

$$[a_i] = \begin{bmatrix} 2a_1 & a_4 & 0 \\ & 2a_2 & 0 \\ \text{Symm} & & 2a_3 \end{bmatrix}; \quad [b_i] = \begin{bmatrix} 2b_1 & b_4 & 0 \\ & 2b_2 & 0 \\ \text{Symm} & & 2b_3 \end{bmatrix} \tag{4.33}$$

In order to determine the eight damage constants, the stiffness data for a cracked reference laminate can be utilized. The choice of reference laminate has been described before. If we know the stiffness moduli of the damaged reference laminate at two crack densities, ρ_1 and ρ_2, then we can express the stiffness changes as

$$\begin{aligned} \Delta C_{pq} &= D[a_i] + D^2[b_i] \\ s = s_1 \text{ or } \rho = \rho_1 : \Delta C_{pq}(\rho_1) &= D_1[a_i] + D_1^2[b_i] \\ s = s_2 \text{ or } \rho = \rho_2 : \Delta C_{pq}(\rho_2) &= D_2[a_i] + D_2^2[b_i] \end{aligned} \tag{4.34}$$

Solving the two equations in Eqn (4.34), we obtain

$$\begin{aligned} [a_i] &= \frac{1}{D_2 - D_1}\left[\frac{D_1}{D_2}\Delta C_{pq}(\rho_1) - \frac{D_2}{D_1}\Delta C_{pq}(\rho_2)\right] \\ [b_i] &= \frac{1}{D_2 - D_1}\left[\frac{1}{D_1}\Delta C_{pq}(\rho_2) - \frac{1}{D_2}\Delta C_{pq}(\rho_1)\right] \end{aligned} \tag{4.35}$$

where $D_1 = D(\rho_1)$; $D_2 = D(\rho_2)$.

The nonlinear SDM model developed above has been utilized to predict stiffness changes in a variety of multidirectional laminates: $[\pm\theta_m/90_n]_s$, $[0/\pm\theta_4/0_{1/2}]_s$, and $[0/90/\pm45]_s$, layups as reported in Singh (2013). The effective damage variables and corresponding constraint parameters are defined in Eqns (4.15)–(4.17), (4.25), (4.27), and (4.28). The constraint parameters were evaluated using computation of CODs from 3D FE analysis as described in Singh and Talreja (2008, 2009) and Li et al. (2009). Figures 4.9 and 4.10 show the comparison of normalized stiffness predictions for longitudinal Young's modulus and Poisson's ratio of two multidirectional laminates undergoing multimode cracking, using the nonlinear SDM model described above and the linear SDM model described before. The experimental data are shown in discrete points. The scenario with two off-axis damage modes is presented in Figure 4.9, whereas Figure 4.10 reports nonlinear SDM predictions for a three damage mode case. It is seen that the linear SDM model usually underpredicts the stiffness changes in the beginning of damage evolution, while it overpredicts the degradation in the damage effects at large crack densities. The nonlinear SDM model predictions, on the other hand, agree very well with the experimental data at the whole range of crack densities investigated here.

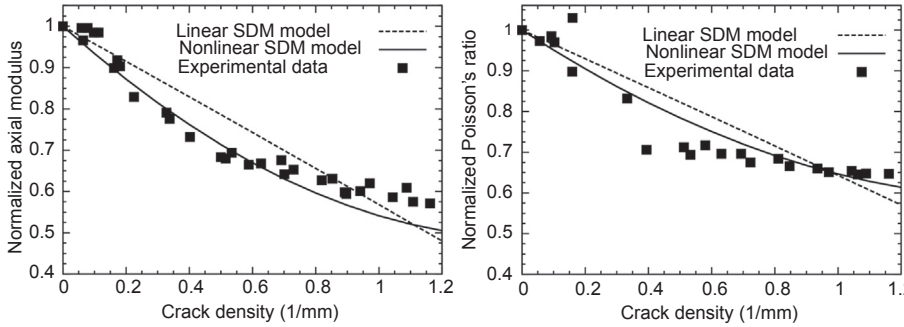

Figure 4.9 Comparison of nonlinear SDM model predictions and experimental data for stiffness degradation in $[0/\pm 70_4/0_{1/2}]_s$ laminate in comparison with experimental data. The data are taken from Varna, Joffe, et al. (1999), while the linear SDM model for two mode damage scenario is reported in Singh and Talreja (2008).
Adapted from C. V. Singh (2013). A higher-order synergistic damage model for prediction of stiffness changes due to ply cracking in composite laminates. *CMC: Computers Materials & Continua, 34*, 227−249.

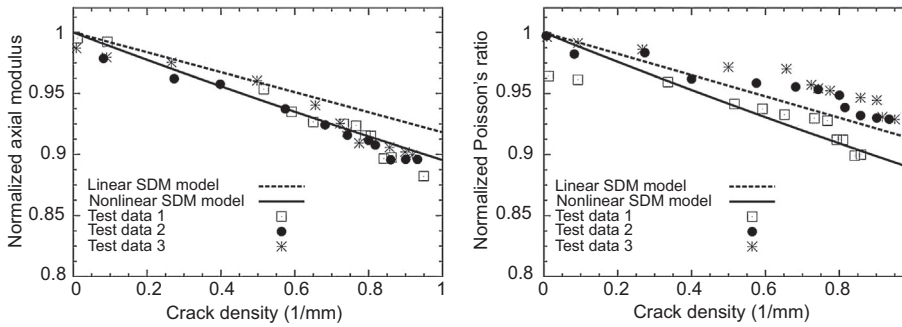

Figure 4.10 Nonlinear SDM model predictions for stiffness changes in quasi-isotropic $[0/90/\pm 45]_s$ laminate compared with experimental data reported in Tong, Guild, Ogin, and Smith (1997). The linear SDM model is from Singh and Talreja (2009).
Adapted from C.V. Singh (2013). A higher-order synergistic damage model for prediction of stiffness changes due to ply cracking in composite laminates, *CMC: Computers Materials & Continua, 34*, 227−249.

4.3.3.1 Results from Worldwide Failure Exercise III

Three worldwide failure exercises conducted over the past two decades have attempted to compare different models to predict failure in composite materials against independent experimental data. While the first two exercises were concerned with predicting ultimate failure (Hinton & Soden, 1998; Hinton, Kaddour, & Soden, 2002, 2004), the recently held WWFE III exercise provided an opportunity to examine initiation and evolution of subcritical damage and its effect on the overall mechanical response (Kaddour, Hinton, Smith, & Li, 2013). The SDM model was one of the participant

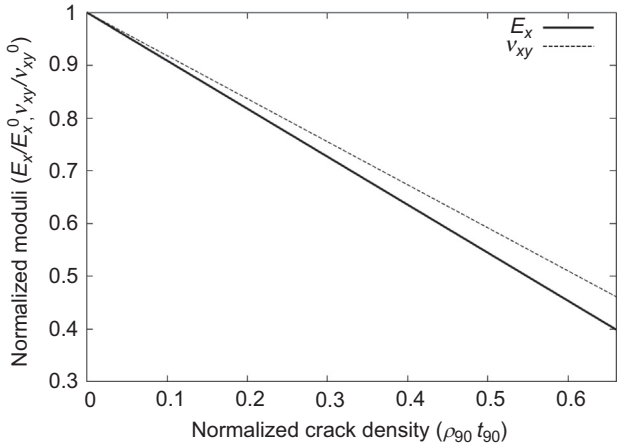

Figure 4.11 Degradation in normalized Young's modulus and Poisson's ratio for $[0/90_8/0]_T$ Glass/epoxy1 laminate, corresponding to Test Case 4 of WWFE III.
Reprinted with kind permission from Singh, C. V., & Talreja, R. (2013). A synergistic damage mechanics approach to mechanical response of composite laminates with ply cracks. *Journal of Composite Material, 47*, 2475−2501, Copyright © 2013 by Sage Publications.

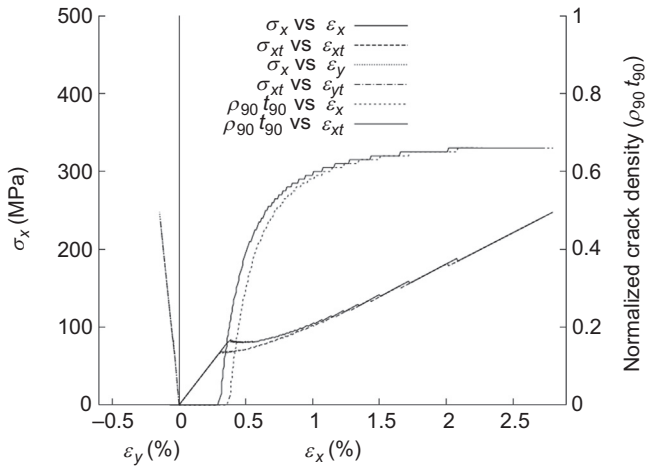

Figure 4.12 Stress−strain response and evolution of crack density for $[0/90_8/0]_T$ Glass/epoxy1 laminate, corresponding to Test Case 4 of WWFE III. Dashed lines (denoted in legend by second subscript t) include the effect of strains generated due to thermal mismatch between 0° and 90° plies during curing on damage initiation and progression.
Reprinted with kind permission from Singh, C. V., & Talreja, R. (2013). A synergistic damage mechanics approach to mechanical response of composite laminates with ply cracks. *Journal of Composite Material, 47*, 2475−2501, Copyright © 2013 by Sage Publications.

models focusing on selected test cases pertaining to ply cracking (see Singh & Talreja, 2013 for full report). Some results using the linear SDM model are shown here. Figure 4.11 displays the degradation in stiffness properties of $[0/90_8/0]_T$ Glass/epoxy1 laminate loaded in uniaxial tension along the longitudinal direction. Due to the fact that the transverse ply is very thick in this case, ply cracks cause significant damage to the load-bearing capabilities of the composite laminate. As depicted in Figure 4.12, the corresponding stress−strain response is highly nonlinear subsequent to damage initiation. Ply cracks are predicted to initiate approximately at 0.4% axial strain, and on increase in loading, cracks are found to multiply quickly to a large crack density with a magnitude of 0.6 when normalized to cracked ply thickness (i.e., the crack size). Thermal residual stresses incurred due to temperature mismatch between operating and manufacturing conditions change the initiation strain but not the overall trends in crack density evolution. The energy-based model to predict initiation and progress of ply cracks in multidirectional laminate was developed in Singh and Talreja (2010).

Figures 4.13−4.15 report the SDM predictions for the case of off-axis ply cracks in multiple directions, for quasi-isotropic laminate sequences. The variation of longitudinal Young's modulus and Poisson's ratio as a function of crack density in 90° ply is plotted in Figure 4.13 (a), and the moduli changes against applied strain values are presented in Figure 4.13(b). The initiation of off-axis cracks in 45° orientations are also identified by arrows. An important finding here is that 45° cracking not only causes additional stiffness changes but also increases stiffness degradation due to 90° cracking. This is because it increases the magnitude of 90° CODs. Stress−strain plots for both longitudinal and transverse directions are depicted in Figure 4.14. Crack density evolution plots suggest 90° cracking initiates first, which is as expected. The 45° cracking occurs at much higher strain levels and also does not grow as quickly as 90° cracking. The effect of ply thicknesses for this laminate sequence is reported in Figure 4.15.

4.4 Finite element (FE) implementation of synergistic damage mechanics (SDM) approach for structural analysis

In order to utilize the current SDM model for performing structural analysis of practical composite structures containing damage, the analytical constitutive equations must be implemented into a commercial FE software package. The corresponding iterative procedure is shown in Figure 4.16, which illustrates the general steps required to perform structural stress analysis. First, the geometry and FE mesh of the structure is created, and the laminate configuration and the undamaged material properties are specified. The in-service loading conditions are then imposed on the structure incrementally as shown. An initial stress analysis is performed, and based on the stress distribution, the regions that are potential sites for damage under the current loading conditions are identified. These regions can be stress concentrators, which may include a cutout or hole in a structure. Next, the damage state in these regions is quantified

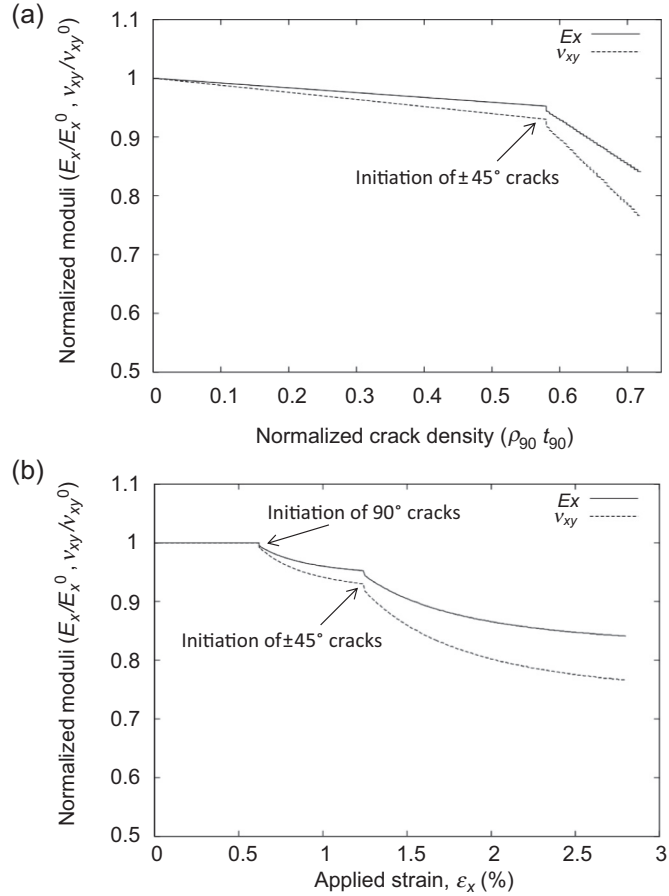

Figure 4.13 Variation of longitudinal Young's modulus and Poisson's ratio: (a) versus normalized crack density in 90° ply and (b) versus applied strain $[0/90/-45/+45]_s$ Glass/epoxy laminate, corresponding to Test Case 6 of WWFE III. Cracks in all off-axis modes are accounted for depending on their respective initiation strains and variation of crack densities with applied strain.

Reprinted with kind permission from Singh, C. V., & Talreja, R. (2013). A synergistic damage mechanics approach to mechanical response of composite laminates with ply cracks. *Journal of Composite Material, 47*, 2475−2501, Copyright © 2013 by Sage Publications.

using the multiscale modeling approach previously discussed. The local stiffness properties of the damaged regions are evaluated using the analytical constitutive equations (SDM model), and the subsequent stress analysis under the incremental loading condition is performed using these updated properties. The load is incrementally increased, and this process is repeated until failure of the structure is predicted based on specific design criteria.

To recap the SDM-based multiscale prediction model, the main components are illustrated in Figure 4.17. The microscale component is required to perform the

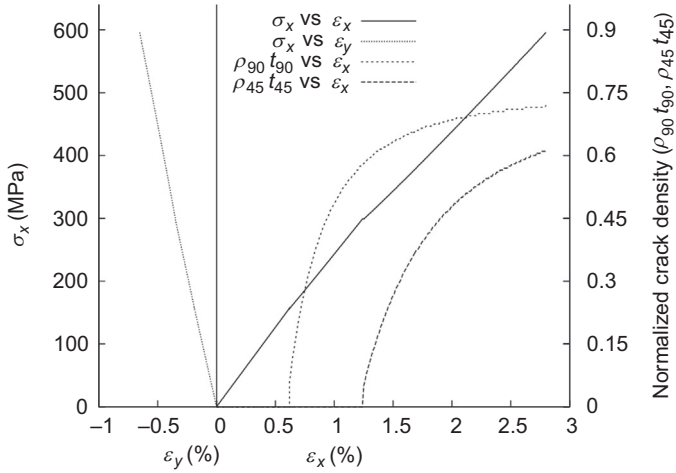

Figure 4.14 Stress−strain response and evolution of ply crack density for $[0/90/-45/+45]_s$ Glass/epoxy1 laminate with cracks in all off-axis modes, corresponding to Test Case 6 of WWFE III. The crack initiation and the crack density evolution in both 45° plies are assumed to be identical.

Reprinted with kind permission from Singh, C. V., & Talreja, R. (2013). A synergistic damage mechanics approach to mechanical response of composite laminates with ply cracks. *Journal of Composite Material, 47*, 2475−2501, Copyright © 2013 by Sage Publications.

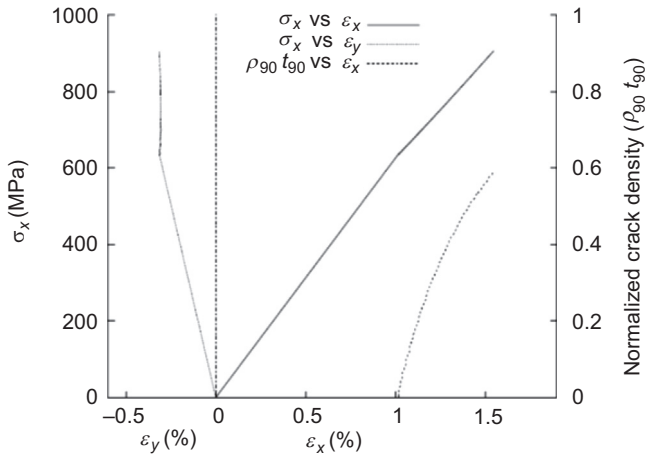

Figure 4.15 Stress−strain response and evolution of ply crack density for $[45_m/90_m/-45_m/0_m]_s$ IM7/8552 laminate, $m = 3$, with cracks in 90° plies only, corresponding to Test Case 13 of WWFE III. No thermal effects were taken into account.

Reprinted with kind permission from Singh, C. V., & Talreja, R. (2013). A synergistic damage mechanics approach to mechanical response of composite laminates with ply cracks. *Journal of Composite Material, 47*, 2475−2501, Copyright © 2013 by Sage Publications.

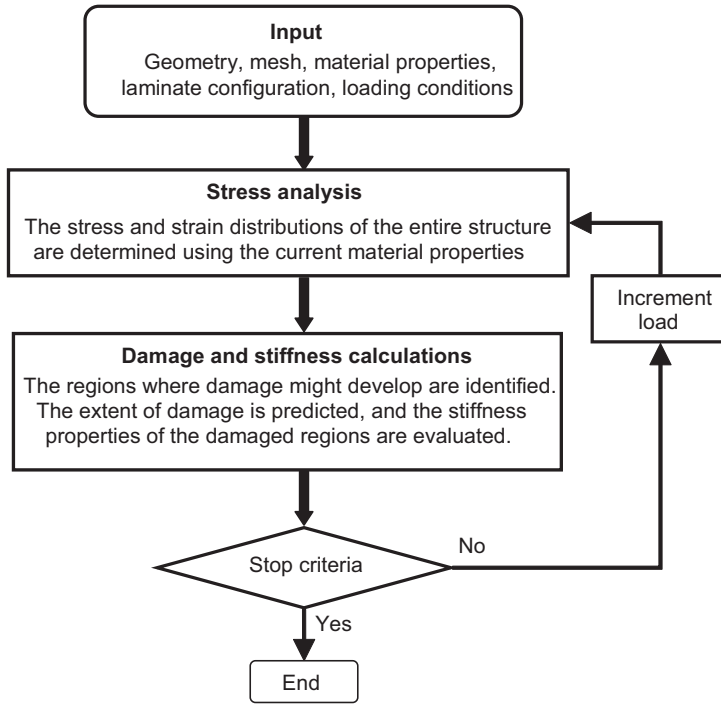

Figure 4.16 Flowchart illustrating structural analysis using SDM approach. The iterative procedure requires determination of stiffness properties for the laminated structure in the damaged regions, and reevaluation of its overall stress−strain response.

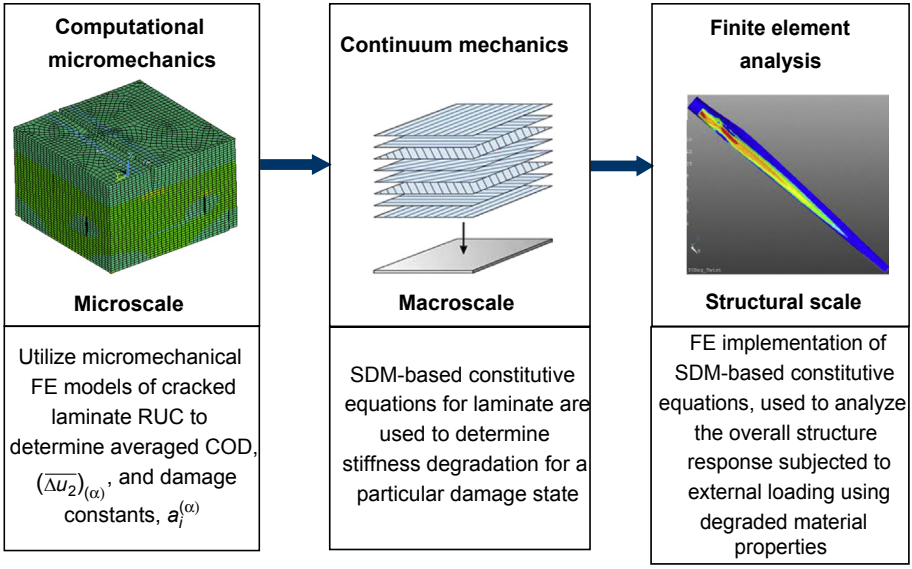

Figure 4.17 Multiscale SDM approach for predicting stiffness properties of a multidirectional laminated composite structure subsequent to damage in multiple off-axis orientations.

computational micromechanical analyses, which utilize 3D FE models of the cracked multidirectional laminate material. For a particular laminate, these models are utilized to define the corresponding crack surface displacements, which are then used to define the material constants for subsequent damage analysis. The macroscale component is used to define the analytical constitutive equations for the laminate, which are used to evaluate its stiffness properties based on the current damage state. Finally, the structural scale component is used to perform stress analysis of the composite structure by implementing the analytical SDM-based constitutive equations into a commercial FE software package.

4.5 Current issues and future trends

Reliably prediction of long-term performance of composite structures has been a key bottleneck in a variety of applications such as automotive and aerospace. In this chapter, we reviewed recent developments pertaining to the problem of multiple matrix cracking in multidirectional composite laminates. This ply cracking damage is subcritical in nature, and although it does not cause ultimate structural failure, it leads to loss in load-bearing capacity of the laminated structure and causes nucleation of more severe damage mechanisms. The ply cracking damage was described using an internal variable-based damage mechanics. First, the CDM was formulated. It was highlighted that CDM needs evaluation of damage constants for every new laminate, and hence cannot be applied for practical design problems. Furthermore, it needs experimental data. In order to overcome limitations, a newly developed SDM model was summarized. This methodology combines the strengths of computational microdamage mechanics with the CDM approach in a synergistic manner so as to yield predictions for stiffness changes in multidirectional composite laminates undergoing multimode ply cracking. The application of the SDM model to the case of single off-axis ply cracking, cracking in two orientations, and cracking in three orientations was presented along with verification with available experimental data and 3D-FE computations. Recent application of the SDM model for test cases of the recently conducted Worldwide Failure Exercise III was briefly highlighted. Finally, new improvements of the SDM model with respect to higher-order damage description and multiaxial loading were reported.

There are multiple challenges that are currently being addressed before the current SDM model can be fully implemented into a commercial FE software package. One of the main challenges is that practical structures undergoing realistic loading conditions will undoubtedly be subjected to very complex localized multiaxial stress states, which must be accounted for by the multiscale prediction model. Multiaxial stresses will directly influence the evolving damage states and therefore alter the degradation of the material stiffness properties. Currently, there are no rigorous and comprehensive prediction tools to assess the response of composite structures undergoing progressive damage while subjected to multiaxial stresses. This task is made even more complex since corresponding experimental data of damage evolution are currently lacking in the literature, which makes validation of prediction models difficult. Soutis and coworkers (Zhang, Fan, & Soutis, 1992a, 1992b; Kashtalyan & Soutis, 2000, 2007) have

analyzed the multiaxial effects on stiffness degradation. The SDM model has also been recently improved to account for the influence of multiaxial strains (Montesano and Singh, 2015a, 2015b). The second challenge is to define appropriate failure criteria for the structure being analyzed, which will allow for accurate prediction of the integrity and durability of these structures. Critical damage modes such as delamination and fiber fracture, which ultimately lead to the loss of the structure's load-bearing capacity, must be accounted for by the prediction model. Finally, the third challenge is to consider compressive stresses and the corresponding damage modes within the multiscale prediction model. Loaded practical structures will undoubtedly have regions where stresses are compressive, which may lead to alternate damage modes such as fiber kinking or microbuckling and matrix shearing. In addition, compressive stresses may also result in nonlinear material behavior that is dictated by the matrix properties. The effect of multiaxial stresses on compressive damage modes would also have to be considered.

It is important to note here that simpler models based on shear lag theory exist that account for multiaxial effects as well as interaction of multiple damage mechanisms. For instance, the delaminations induced by matrix cracks have been analyzed by Soutis and coworkers in multiple studies (Kashtalyan & Soutis, 2002, 2005; Zhang, Soutis, & Fan, 1994). A good comparison of different models for progressive damage in composite laminates has been provided in the recent Worldwide Failure Exercise (see the *Journal of Composite Materials*, 2012, issues 20−21).

4.6 Sources of further information and advice

Polymer composites continue to show huge potential for applications in aerospace, automotive, industry, and elsewhere. However, as noted by the US National Academy Press report (2005), "enormous uncertainty exists, however, in predicting long-term changes in properties of PMCs under extreme environmental conditions, which has limited their use." Over the past four decades, significant advances have been made in the understanding of damage and failure issues for these materials. The field of damage mechanics has grown from dealing with cross-ply laminates to multidirectional laminates, but significant challenges remain before failure models can be applied to industrial design of products. Future research in this area should focus on (1) multimode cracking in multidirectional laminates, (2) multiaxial loading scenario, (3) fatigue loading, and (4) implementation of accurate damage models into commercial finite element packages for practical applications. The SDM approach provides one such methodology, and improvements are being made to overcome these challenges.

For further information on recent relevant research, readers are advised to consult top journals in the area such as the *Composites A and B, Composites Science and Technology, Journal of Composite Materials, International Journal of Damage Mechanics, Mechanics of Materials, Journal of Materials Science, International Journal of Solids and Structures, Journal of Materials Science*, and *CMC: Computers, Materials & Continua*. For a good review of damage mechanics, see the recently published book *Damage and failure of composite materials* by Talreja and Singh (2012). Edited books include:

Comprehensive composite *materials*. Vol. 1. Amsterdam: Elsevier, 2000; *Multiscale modeling and simulation of composite materials and structures*, edited by Y. W. Kwon, D. H. Allen, R. Talreja, Springer, 2008. The following review papers also provide valuable information regarding the topic: (Berthelot & Le Corre, 2000; Talreja, 2006a, 2006b). Finally, see the results of all Worldwide Failure Exercises for useful information.

Acknowledgments

The author would like to acknowledge financial support from the Natural Sciences and Engineering Research Council (NSERC) of Canada and the University of Toronto; special thanks to Prof. Ramesh Talreja from Texas A&M University, and Dr John Montesano, a postdoctoral associate at the University of Toronto for valuable discussions and help regarding this research.

References

Adkins, J. (1960). Symmetry relations for orthotropic and transversely isotropic materials. *Archive for Rational Mechanics and Analysis, 4*(1), 193−213.

Allen, D. H., Harris, C. E., & Groves, S. E. (1987). A thermomechanical constitutive theory for elastic composites with distributed damage—I. Theoretical development. *International Journal of Solids and Structures, 23.9*, 1301−1318.

Berthelot, J. M., & Le Corre, J. F. (2000). Statistical analysis of the progression of transverse cracking and delamination in cross-ply laminates. *Composites Science and Technology, 60*(14), 2659−2669.

Chaboche, J. L. (1984). Anisotropic creep damage in the framework of continuum damage mechanics. *Nuclear Engineering and Design, 79*, 309−319.

Chaboche, J. L. (1988a). Continuum damage mechanics: Part I - general concepts. *Journal of Applied Mechanics Transactions-ASME, 55*(1), 59−64.

Chaboche, J. L. (1988b). Part II: damage growth, crack initiation, and crack growth. *Journal of Applied Mechanics, Transactions-ASME, 55*(1), 65−72.

Hinton, M. J., Kaddour, A. S., & Soden, P. D. (2002). Evaluation of failure prediction in composite laminates: background to 'part b' of the exercise. *Composites Science and Technology, 62*(12−13), 1481−1488.

Hinton, M. J., Kaddour, A. S., & Soden, P. D. (2004). Evaluation of failure prediction in composite laminates: background to 'part c' of the exercise. *Composites Science and Technology, 64*(3−4), 321−327.

Hinton, M. J., & Soden, P. D. (1998). Predicting failure in composite laminates: the background to the exercise. *Composites Science and Technology, 58*(7), 1001−1010.

Kachanov, L. M. (1999). Rupture time under creep conditions. *International Journal of Fracture, 97:1*, 11−18.

Kaddour, A. S., Hinton, M. J., Smith, P. A., & Li, S. (2013). The background to the third World-Wide Failure Exercise. *Journal of Composite Materials, 47*(20−21), 2417−2426.

Kashtalyan, M., & Soutis, C. (2000). Stiffness degradation in cross-ply laminates damaged by transverse cracking and splitting. *Composites Part A, 31*(4), 335−351.

Kashtalyan, M., & Soutis, C. (2002). Analysis of local delaminations induced by angle ply matrix cracks. *International Journal of Solids and Structures, 39*(6), 1515−1537.

Kashtalyan, M., & Soutis, C. (2005). Analysis of composite laminates with intra- and inter-laminar damage. *Progress in Aerospace Sciences, 41*(2), 152−173.

Kashtalyan, M., & Soutis, C. (2007). Stiffness and fracture analysis of laminated composites with off-axis ply matrix cracking. *Composites A, 38*(4), 1262−1269.

Katerelos, D. T. G., Kashtalyan, M., Soutis, C., & Galiotis, C. (2008). Matrix cracking in polymeric composites laminates: modelling and experiments. *Composites Science and Technology, 68*(12), 2310−2317.

Katerelos, D. T. G., Lundmark, P., Varna, J., & Galiotis, C. (2007). Analysis of matrix cracking in GFRP laminates using Raman spectroscopy. *Composites Science and Technology, 67*(9), 1946−1954.

Katerelos, D. G., McCartney, L. N., & Galiotis, C. (2005). Local strain re-distribution and stiffness degradation in cross-ply polymer composites under tension. *Acta materialia, 53*(12), 3335−3343.

Katerelos, D. T. G., Varna, J., & Galiotis, C. (2008). Energy criterion for modelling damage evolution in cross-ply composite laminates. *Composites Science and Technology, 68*(12), 2318−2324.

Lemaitre, J. (1985). A continuous damage mechanics model of ductile fracture. *Journal of Engineering Materials and Technology, Transactions of the ASME, 107*(42), 83−89.

Li, S., Singh, C. V., & Talreja, R. (2009). A representative volume element based on translational symmetries for FE analysis of cracked laminates with two arrays of cracks. *International Journal of Solids and Structures, 46*, 1793−1804.

Montesano, J. & Singh, C.V. A Synergistic damage mechanics based multiscale model for composite laminates subjected to multiaxial strains, *Mechanics of Materials*, *83*, 72−89.

Montesano, J., & Singh, C. V. (2015b). *Predicting evolution of ply cracks in composite laminates subjected to biaxial loading*. Composites B (in press). http://dx.doi.org/10.1016/j.compositesb.2015.01.039.

Murakami, S., & Ohno, N. (1981). A continuum theory of creep and creep damage. In A. R. S. Ponter & D. R. Hayhurst (Eds.), *Creep in structures, 3rd IUTAM Symposium* (pp. 422−444). Berlin, Germany: Springer-Verlag.

Robotnov, Y. N. (1969). *Creep problems in structural members*. Amsterdam: North-Holland.

Singh, C.V. (2008). *Multiscale modeling of damage in multidirectional composite laminates* (Ph.D. thesis in aerospace engineering). Texas A&M University: College Station, Texas.

Singh, C. V. (2013). A higher order synergistic damage model for prediction of stiffness changes due to ply cracking in composite laminates. *CMC: Computers Materials and Continua, 34*(3), 227−249.

Singh, C. V., & Talreja, R. (2007). Damage mechanics of composite laminates with transverse matrix cracks in multiple orientations. In *48th AIAA SDM Conf. Honolulu, Hawaii, USA*.

Singh, C. V., & Talreja, R. (2008). Analysis of multiple off-axis ply cracks in composite laminates. *International Journal of Solids and Structures, 45*(16), 4574−4589.

Singh, C. V., & Talreja, R. (2009). A synergistic damage mechanics approach for composite laminates with matrix cracks in multiple orientations. *Mechanics of Materials, 41*(8), 954−968.

Singh, C. V., & Talreja, R. (2010). Evolution of ply cracks in multidirectional composite laminates. *International Journal of Solids and Structures, 47*(10), 1338−1349.

Singh, C. V., & Talreja, R. (2013). A synergistic damage mechanics approach to mechanical response of composite laminates with ply cracks. *Journal of Composite Materials, 47*(20−21), 2475−2501.

Spencer, A. J. M. (1971). Theory of invariants. In C. A. Eringen (Ed.), *Continuum Physics* (pp. 239−353). New York: Academic Press.

Talreja, R. (1985a). A continuum-mechanics characterization of damage in composite-materials. *Proceedings of the Royal Society of London, Series A, 399*(1817), 195−216.

Talreja, R. (1985b). Transverse cracking and stiffness reduction in composite laminates. *Journal of Composite Materials, 19*(4), 355−375.

Talreja, R. (1990). Internal variable damage mechanics of composite materials. In J. P. Boehler (Ed.), *Yielding, damage, and failure of anisotropic solids* (pp. 509−533). London: Mechanical Engineering Publications.

Talreja, R. (1991). Continuum modeling of damage in ceramic matrix composites. *Mechanics of Materials, 12*(2), 165−180.

Talreja, R. (1994). Damage characterization by internal variables. In R. Talreja (Ed.), *Damage mechanics of composite materials* (pp. 53−78). Amsterdam: Elsevier.

Talreja, R. (2006a). Damage analysis for structural integrity and durability of composite materials. *Fatigue and Fracture of Engineering Materials and Structures, 29*(7), 481−506.

Talreja, R. (2006b). Multiscale modeling in damage mechanics of composite materials. *Journal of Materials Science, 41*(20), 6800−6812.

Talreja, R., & Singh, C. V. (2008). Multiscale modeling for damage analysis. In *Multiscale modeling and simulation of composite materials and structures* (pp. 529−578). US: Springer.

Talreja, R., & Singh, C. V. (2012). *Damage and failure of composite materials*. London: Cambridge University Press, ISBN 9780521819428.

Tong, J., Guild, F. J., Ogin, S. L., & Smith, P. A. (1997). On matrix crack growth in quasi-isotropic laminates - I. Experimental investigation. *Composites Science and Technology, 57*(11), 1527−1535.

US National Academy Press report. (2005). *Going to Extremes: Meeting the Emerging Demand for Durable polymer matrix composites* (A report by the Committee on Durability and Life Prediction of Polymer Matrix Composites in Extreme Environments).

Vakulenko, A. A., & Kachanov, M. (1971). Continual theory of a medium with cracks. Izv AN SSSR. *Mekhanika Tverdogo Tela (Mech Solids), 6*(4), 159.

Varna, J., Akshantala, N. V., & Talreja, R. (1999). Crack opening displacement and the associated response of laminates with varying constraints. *International Journal of Damage Mechanics, 8*, 174−193.

Varna, J., Joffe, R., Akshantala, N. V., & Talreja, R. (1999). Damage in composite laminates with off-axis plies. *Composites Science and Technology, 59*(14), 2139−2147.

Varna, J., Joffe, R., & Talreja, R. (2001a). A synergistic damage-mechanics analysis of transverse cracking in [+/-theta/90(4)](s) laminates. *Composites Science and Technology, 61*(5), 657−665.

Varna, J., Joffe, R., & Talreja, R. (2001b). Mixed micromechanics and continuum damage mechanics approach to transverse cracking in [S,90(n)](s) laminates. *Mechanics of Composite Materials, 37*(2), 115−126.

Zhang, J., Fan, J., & Soutis, C. (1992a). Analysis of multiple matrix cracking in [±θm/90n]s composite laminates. Part I: in-plane stiffness properties. *Composites, 23*(5), 291−298.

Zhang, J., Fan, J., & Soutis, C. (1992b). Analysis of multiple matrix cracking in [±θm/90n]s composite laminates. Part II: development of transverse ply cracks. *Composites, 23*(5), 299−304.

Zhang, J., Soutis, C., & Fan, J. (1994). Effects of matrix cracking and hygrothermal stresses on the strain energy release rate for edge delamination in composite laminates. *Composites, 25*(1), 27−35.

From micro to macro: simulating crack propagation in carbon fibre composites

5

R.M. Sencu[1], *Z.J. Yang*[1,2], *Y.C. Wang*[1]
[1]University of Manchester, Manchester, UK; [2]Zhejiang University, Hangzhou, China

5.1 Introduction

For many heterogeneous materials, simulating realistic crack growth at the structural level should take the mechanical effects of fine scales into account. This is because such materials contain inherent defects at multiple scales that affect the crack initiation and propagation processes. Finding an accurate way of transferring realistic crack paths across multiple scales is not a trivial task because of the existence of multiple material phases and their interactions. For example, most quasi-brittle materials, including fibre-reinforced plastics (FRP), have very narrow strain range of the individual phases. This alters the predictability of accurate crack sites at larger scales, especially when heterogeneity details at fine scales are disregarded in modelling. Secondly, such materials contain stochastic heterogeneity, which means that traditional repetitive approaches do not necessarily reflect the genuine behaviour.

There is now a strong interest in understanding and developing models of high geometrical fidelity of most important scales so as to accurately delimit the length scale domains with which cracks could interact. For example, the US Air Force Office of Scientific Research (AFOSR) is currently running a Multi-Scale Structural Mechanics and Prognosis program that uses such models to enhance the aerospace design process, to improve lifecycle estimation, to predict material structural resilience for unexpected events, and to plan maintenance schedules for various existing structural parts (Stargel, 2012). Many of these areas are fracture driven and therefore modelling of crack growth demands special attention. For example, the FRP materials used in aerospace are built by semi-organized fibre-reinforced plies that possess distinctive material properties for the interface bonding layer, the fibres, and the matrices. The plies are then stacked in multiple layers, forming laminates, which can be manufactured in various shapes, sizes, and thicknesses. In these manufacturing steps, artefacts such as matrix voids, debonding of fibres, partial wetting, fibre clusters, etc. often take place, and they influence crack initiation and propagation across all scales. This has important consequences at the structural level and makes accurate multi-scale modelling and validation difficult.

Traditionally, model validation of FRP parts for fracture resistance was done either by testing full-size components or by using a series of small probes (Kabele, 2007; Molent, Callinan, & Jones, 1989). An inverse modelling approach was then undertaken to extract

Structural Integrity and Durability of Advanced Composites. http://dx.doi.org/10.1016/B978-0-08-100137-0.00005-5

relevant material properties. This is a costly approach. More importantly, many essential mechanical data cannot be obtained due to a lack of intrusive measurements. A relatively new testing and validation direction for FRP materials is using X-ray computed tomography (XCT) technology (Coindreau, Vignoles, & Cloetens, 2003; Coindreau, Mulat, Germain, Lachaud, & Vignoles, 2011; Moffat et al., 2010; Rouse, 2012; Scott, Mavrogordato, Wright, Sinclair, & Spearing, 2011; Wright, Moffat, Renault, Sinclair, & Spearing, 2009). From such tests, image-based models can be built and used to simulate the realistic testing conditions, and then be validated against the actual physical phenomena. Although one may think the key of this practice is geometrical in nature, material nonlinearity and other material properties (creep, residual stresses, etc.) are also influential in the numerical validation process. Accurate multi-scale strategies are also needed to ensure that the uniqueness of the limited number of XCT experiments is applicable for other engineering scales and customized structural conditions.

Therefore, the contribution of this chapter is twofold. First, it reviews the most popular methods for multi-scale modelling of damage and fracture. Second, it outlines a new image-based model that is currently being developed by the authors.

The overview of the existing multi-scale modelling methods in Section 5.2 is based on constitutive finite element formulations. The discussion seeks to discover the advantages and shortcomings of these methods when modelling crack growth in heterogeneous materials like FRPs. An important objective is to investigate the scale coupling premises that allow a rational transfer from micro to macro scales. As definition, a 'good' multi-scale algorithm for crack propagation should include material damage entities (defects, random distribution of fibres, etc.), obey the conservation principles for fracture energy and preserve the crack orientation paths at both scales. In addition, such an algorithm should account for morphological continuity and use an accurate mapping projection of the material properties, especially when solutions to inverse problems are sought. Section 5.3 then gives a classification of the existing numerical crack models.

For illustration purpose, Section 5.4 presents results of crack growth from four stochastic transverse models for an hexagonal fibre arrangement. These simulations used image-based discretizations that were taken from a carbon fibre-reinforced polymer (CFRP) specimen (see Section 5.4). However, a detailed presentation of these models is beyond the scope of this chapter. Finally, Section 5.5 discusses the most important aspects of the chapter and highlights some important conclusions.

5.2 Overview of existing multi-scale modelling methods

Most commonly, the existing multi-scale modelling methods integrate fine-scale features (lower scale) within coarse-scale models. These methods can be classified into the following two main categories according to the sequence of operations and information exchange type:

- uncoupled models (also called one-way models): the information is transferred in one direction, either bottom-up or top-down.
- coupled models: information is exchanged in both directions.

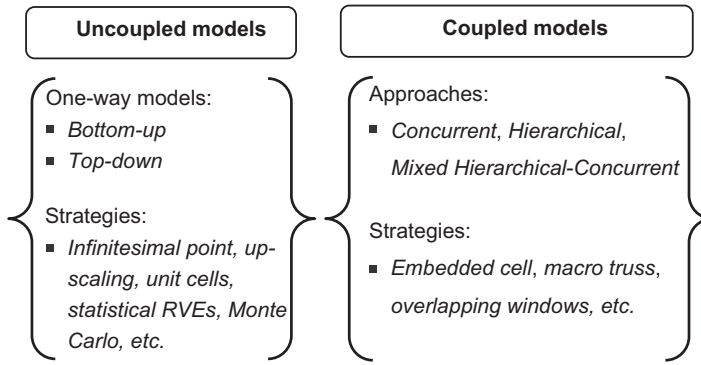

Figure 5.1 A summary of existing multi-scale models.

Figure 5.1 indicates the different modelling methods under these two categories. Sections 5.2.1 and 5.2.2 present further details of these models.

5.2.1 Uncoupled models

In an uncoupled model, the information from fine scales is used to drive processes on the coarse larger scales (bottom-up) or vice versa (top-down). Reviews of uncoupled bottom-up and top-down models can be found in Nguyen, Stroeven, and Sluys (2011) and Panchal, Kalidindi, and McDowell (2012). Examples of such models include the upscaling methods for atomic and molecular processes up to continuum matter, repetitive unit cells, infinitesimal point assumptions, reduced material phase assumptions, statistical representative volume elements (SRVE) and statistical Monte Carlo approaches (de Frías, Aquino, Pierson, Heinstein, & Spencer, 2014; Greco, Leonetti, & Lonetti, 2013; Ruggles, Rampton, Rose, & Fullwood, 2013; Singh & Talreja 2013; Su, Yang, & Liu, 2009; Xu, Chen, Li, & Wang, 2013; Yang & Xu, 2008; Yang, Su, Chen, & Liu, 2009).

Most of the one-way approaches neglect the microstructural continuity and sometimes do not consider the random distribution of fibres across the continuum. Some improvements have been made by employing an unstructured macro-scale truss whereby each linear element is associated with a detailed microscopic window simulation (Unger, 2013). The detailed windows of each oriented truss member assume constant geometries. The fracture process is not modelled in a discrete crack propagation sense, but only via some localized numerical degradation of linear lattice integration points. This makes this type of model similar to damage mechanics models by using admissible stresses or strengths. However, these models become computationally expensive, mainly because of the iterative inverse fitting of deformation rates from coarser scales to finer scales (top-down). For example, given an initial displacement of the macroscopic truss, the deformation rates at micro scale are iterated to fit the macro-scale behaviour.

A similar coupling enhancement was proposed in Verhoosel, Remmers, Gutiérrez, and de Borst (2010), where periodic windows were decomposed on a displacement basis

and solved to determine localization properties. This model excludes continuity of the morphology that results in side effects at macro scale, such as unreliable prediction of global elastic constants and ultimate loads. This is so because the global elastic constants are related to exact strain rates of the microstructure that were not linked to macro scale in this model. In addition, the fracture energy may be misinterpreted. The dissipated energy is a crack path-dependent parameter, which is paramount for accurate modelling of crack growth at macro scales.

Typical shortcomings of the uncoupled models are summarized below:

- deformation fields and rates often do not match at both scales;
- they are rarely accepted for fracture modelling at macro scale because of the weak form formulations;
- they are partly empirical and/or mathematical; for example the Hill-Mandel macro-homogeneity relation (Li, 2011) is incompatible with nonlinear materials;
- uncertainties exist on both scales.

5.2.2 Coupled models

The coupled models use information from both scales and combine them over the same temporal and/or spatial domains based on conservation principles. This means that dynamic constraints or structural links may be preformulated and reiterated to ensure deformation compatibility. Moreover, such models consider the expected macroscopic behaviour by boundary strategies, or by directly matching high-fidelity deformation fields. In practice, these models may use digital image correlation (DIC) techniques (Amini & Kumar, 2014; Shen & Paulino, 2011) or secondary hidden parallel simulations (Sencu, Yang, & Wang, 2014). The latter is an example of a boundary strategy using an inverse engineering approach to remotely approximate boundary conditions from the investigated detailed substructures. This model is further discussed in Section 5.2.2.2.

It is generally not possible to obtain fully accurate deformation fields, from either measuring or modelling the fine-scale substructures, so as to match the larger-scale simulations, especially when large-scale jumps are sought. This is so because the direct measuring techniques, such as the DIC method, that can be applied to XCT reconstructed volumes have limited fields of view. In addition, theoretical development of inverse procedures for remote boundary loads on composites lags behind experimental techniques because of the difficulties in understanding wave propagation, given some complicated time function disturbance of the composite material (Liu, Ma, & Han, 2002). Therefore the estimation of inverse stress fields remains unclear. In such a case, alternative statistical and/or local deformation compatibility methods may be used. The following section presents some coupling premises to minimize or partially eliminate the crack path bias effects at boundary locations.

The coupling techniques can be found in the literature under three main categories: Concurrent Approach (CA), Hierarchical Approach (HA), and Mixed Hierarchical-Concurrent Approach (MHCA).

Two-way coupling strategies were most commonly associated with CA models (Ghosh, Bai, & Raghavan, 2007; González & Llorca, 2006), but they can be mixed

with HA models as well (Trias, Costa, Fiedler, Hobbiebrunken, & Hurtado, 2006). Typically, the CA models use a single global analysis, which requires a hybrid mesh. This mesh contains various levels of discretization, which can go up to fully detailed microstructures of some limited region of interest (Ghosh, 2008; Ghosh et al., 2007). This idea is mainly used to capture damage localization based on some predefined computational areas that incorporate sufficiently fine details for the investigated phenomena. It also means that coarser regions require a computational homogenization scheme and the study of size dependence a priori. Once the complete modelling scheme is decided, the global simulation can be carried out deterministically. The approach is discussed in Section 5.2.2.1.

Generally, the HAs construct the final global analysis based on information of fully detailed fine-scale simulations. This means that computational homogenization may not be necessary. However, continuity should be ensured at fine scales in order to accurately capture crack initiation and propagation across multiple computational domains. Statistical expansion methods may be used to include some uncovered areas and to characterize the whole structural part (Clément, Soize, & Yvonnet, 2013; Guilleminot, Soize, & Kondo, 2009). It may also be obvious that when solving large degree-of-freedom (DOF) models, multiple meso-scale windows can be separated and computed in parallel. Using such strategies, effective computation of the entire domain can be enabled. This was recently developed by the authors in a multi-scale stochastic fracture mechanics method (MsSFrM) using an overlapping windows strategy (Sencu et al., 2014). The main advantage of the MsSFrM method is not only the reduction in total CPU time using either parallel or fully detailed simulations, but rather that it enables a powerful multi-scale tool to analyse very large DOF models (see Section 5.2.2.2).

The MHCA approach aims at minimizing the boundary effects on fine-scale analyses before scale transfer. An example of an MHCA model is the embedded cell approach (ECA). The ECA minimizes the boundary effects by using an ideally homogeneous buffer around the statistical computed window (Li & Zhou, 2013; Li, McDowell, & Zhou 2013; Trias et al., 2006). In this way, the boundary effects may be decided before the scale transfer. This approach is discussed in detail in Section 5.2.2.3.

Typical challenges of coupled models include high computational cost, large data memory, storage and transfer, complex mathematical formulations, difficult programming and difficulty in automation. The following sections focus on the most important premises of different researchers to solve the scale transfer problem under the above three distinct approaches.

5.2.2.1 *Concurrent approach*

The concurrent approach decomposes the computational domain into nonoverlapping sub-domains, which are discretized with different mesh densities (Ghosh & Paquet, 2013; González & Llorca, 2006; Llorca, González, Molina-Aldareguía, & Lópes, 2013). This means that some parts assume reduced-order definition, while other parts include more complicated definitions, such as detailed microstructural

evolution and damage. Periodic cells are usually employed in the sub-domains or where damage is rarely expected. The other sub-domains with damage potential are coupled with discretizations at finer levels and more complicated constitutive formulations. A popular concurrent model based on Voronoi cell discretization was reported in Ghosh (2008), Ghosh et al. (2007) and Ghosh and Paquet (2013). The homogenization for the upper scales uses the elastic constitutive behaviour, while the top-down scale transfer was ensured through localization and damage relationships. The Voronoi sub-domains recur at the structural level. From a macroscopic point of view the partition is repetitive; nevertheless, when appropriate partitioning is performed it may cover the most critical failure regions. However, so far this method has not been able to capture complete crack paths due to either restrictions posed on the boundaries of the Voronoi cells or reduced individual phases of the material. It was shown that fully detailed simulations could only consider fibre decohesion but not matrix cracking and other, more complicated crack mechanisms (Ghosh et al., 2007). The main advantage of this method is that it can make use of the well-known Voronoi fibre distribution statistics in Matsuda, Ohno, Tanaka, and Shimizu (2003) and Pyrz (1994), which may be linked directly to localized mechanisms when stochastic meso-scale windows with minimum boundary condition effects are simulated (Sencu et al., 2014).

5.2.2.2 Hierarchical approach

The HA methods are the most commonly used in literature. In general they work by linking different macro-scale sites with exact properties obtained from detailed analyses (Luscher, McDowell, & Bronkhorst, 2010; Unger, 2013; Verhoosel et al., 2010). In many cases, these methods are also statistical and may not necessarily consider continuity of the morphology. For example, in Doškář & Novák (2013) and Kaczmarczyk, Pearce, and Bićanić (2008) some randomly generated microstructure windows were sampled at arbitrary positions based on targeted volume fractions. Although nonlinear modelling was not conducted, this may still be a mathematical vicious circle of solving some simple statistical generated microstructures, which should be avoided through direct control of the macroscopic properties by similar statistics.

To avoid these problems, the previously mentioned MsSFrM framework proposed by the authors in Sencu et al. (2014) uses a new overlapping concept. The big picture of the framework is presented in Figure 5.2. The key steps of the framework are as follows: image acquisition, image-based model reconstruction and simulation using overlapped windows, adaptive mesh discretization at macro scale, point-wise mapping of properties and the simulation of the global model.

Continuity of the morphology is ensured by using the window overlapping concept (Sencu et al., 2014). The scale transfer can be systematically simulated with different overlapping distances against various meso-scale element (MeE) sizes and boundary effects. The macro-scale elements (MaE) are constructed using the crack paths obtained from detailed MeE simulations.

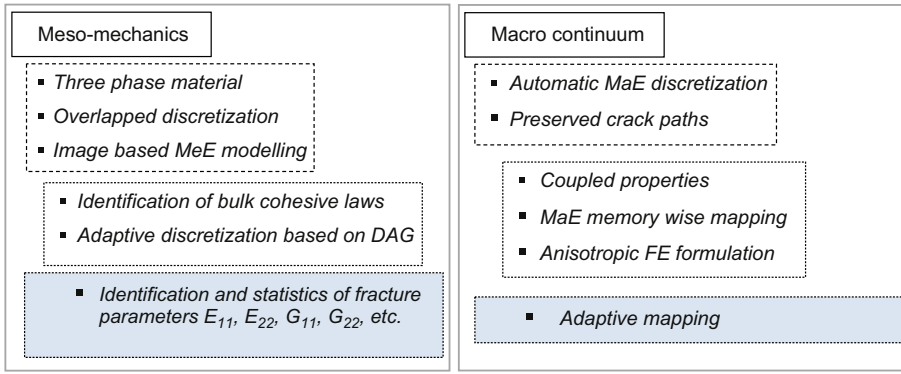

Figure 5.2 The big picture of the MsSFrM framework (Sencu et al., 2014).

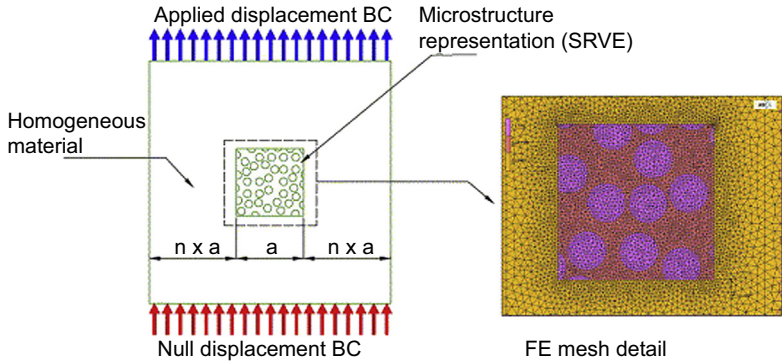

Figure 5.3 The embedded cell approach (ECA) (Trias et al., 2006).
Image courtesy of *Elsevier*.

5.2.2.3 Mixed hierarchical-concurrent approach

The MHCA coupling scheme in Trias et al. (2006) assumes random failure properties for MaE. At the fibre scale, the simulations use the statistically representative volume concept to represent the microstructure window embedded in a homogeneous cell (see Figure 5.3). Because the distribution of stresses and strains at macro-scale boundaries has arbitrary values, statistical expressions are necessary to compensate for the constitutive behaviour. This step is done before the scale transfer.

The statistical transformations are based on Weibull distributions of the strain energy density for fracture, which is also boundary dependent. First, the transformations are remotely applied to multiple meso-scale embedded windows. The macro scale is then related to these computational windows via a one-to-one relationship of the stress-invariant tensors. The first-order invariant stress tensor reads

$$I_1^x = \langle I_1^y \rangle = \langle \sigma_{11}^y \rangle + \langle \sigma_{22}^y \rangle + \langle \sigma_{22}^y \rangle \tag{5.1}$$

where $\langle \bullet \rangle$ is the average operator, such as in the effective medium theory (Trias et al., 2006). Here superscripts x and y stand for macro and micro scale, respectively. The dilatational energy density is given by

$$\left\langle \mathrm{U}_v^y \right\rangle = \frac{1-2\nu}{\mathrm{E}} \left\langle I_1^y \right\rangle^2 \tag{5.2}$$

Then, the Weibull probability density function becomes

$$f\left(\mathrm{U}_v^0; \lambda, k\right) = \begin{cases} \dfrac{k}{\lambda}\left(\dfrac{\mathrm{U}_v^0}{\lambda}\right)^{k-1} e^{-\left(\mathrm{U}_v^0/\lambda\right)^k} & \forall x \geq 0, \\ 0 & \forall x < 0 \end{cases} \tag{5.3}$$

where λ and k are the scale and shape parameters found from testing through trial and error. Equivalent expressions of the probability density function can be found for the corresponding macro-scale points, that is the $f(\mathrm{U}_v^x; \lambda, k)$ functions. The limitation in this case is that preserving the sampling continuity may be computationally costly (checking the construction steps of Weibull statistical spaces) and therefore the probability space at macro scale would not necessarily represent the genuine crack localization. In contrast, when using random fields to cover deformation fluctuations, the mapping continuity becomes a real challenge. This means that both the elastic constants and fracture energies are difficult to be preserved by exact integration of the domain and accurate deformation rates from fine scales.

The embedded cell idea was also used in Li and Zhou (2013a,b) and Li et al. (2013). In these studies, a three-dimensional (3D) multi-scale homogenization computational framework was developed to solve fracture problems with crystal plasticity. The method was based on the cohesive finite element model (CFEM) and used the Mori-Tanaka method for scale transfer. The bulk and shear moduli were estimated based on stress intensity factors computed using the J-integral concept (Li & Zhou, 2013)

$$\begin{cases} \overline{K} = K_0 + \dfrac{f(K_1 - K_0)(3K_0 + 4\mu_0)}{3K_0 + 4\mu_0 + 3(1-f)(K_1 - K_0)} \\ \overline{\mu} = \mu_0 + \dfrac{5f\mu_0(\mu_1 - \mu_0)(3K_0 + 4\mu_0)}{5\mu_0(3K_0 + 4\mu_0) + 6(1-f)(\mu_1 - \mu_0)(K_0 + 2\mu_0)} \end{cases} \tag{5.4}$$

where f is the volume fraction of reinforcement and K_i factors are the bulk and shear moduli for the two material phases bridged by a crack. The effective elasticity modulus and Poisson's ratio for the homogenized region are

$$\begin{cases} \overline{E} = \dfrac{9\overline{K}\overline{\mu}}{3\overline{K} + \overline{\mu}} \\ \overline{\nu} = \dfrac{3\overline{K} - 2\overline{\mu}}{6\overline{K} + 2\overline{\mu}} \end{cases} \tag{5.5}$$

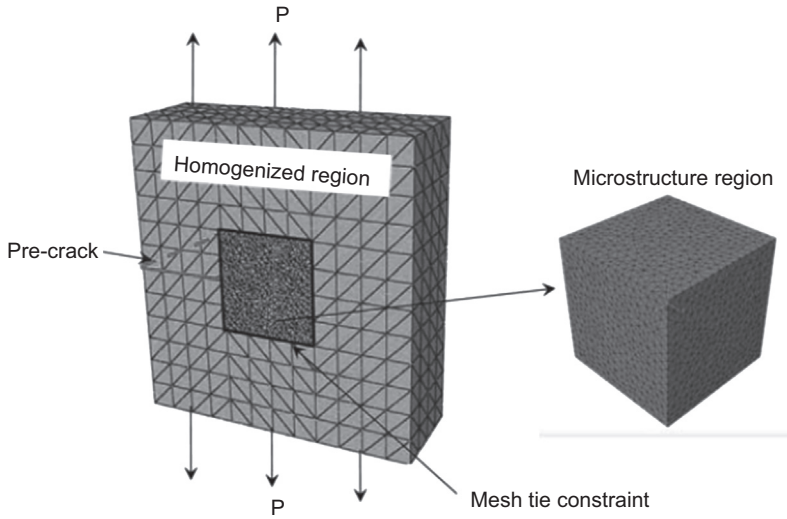

Figure 5.4 A model assembly for computational multi-scale homogenization after Li et al. (2013).
Image courtesy of *ICF13*.

The initial anisotropy due to the crystallographic orientations of the grains was not considered. Instead, in Li & Zhou (2013) the material phases were assumed to follow the isotropic linear elastic constitutive relations. It is also unclear how the global anisotropy is considered at the macro scale.

At the micro scale a hybrid mesh was used (Li et al., 2013). Figure 5.4 shows how the mesh embeds a polycrystalline sample. A kinematical tie constraint was used between the two regions so that mesh conformity was not needed. An initial pre-crack was inserted in the homogeneous mesh. The fracture toughness was then evaluated using a hidden structured mesh, which was also tied up to the realistic microstructure. In addition, there was no attempt to solve deformation continuity by means of compatible deformation rates between stochastic neighbouring samples. This is an essential step for further multi-scale modelling.

5.3 Numerical crack models

Numerical methods capable of modeling crack growth can be broadly categorized (Su, Yang, & Liu, 2010) as discrete crack models explicitly separating the crack surfaces, smeared crack models based on continuum mechanics, and more indirect models (lattice, truss, fractals, etc.). Discrete crack models were mainly developed for 2D problems and only recently, complicated 3D fracture behaviour has been simulated mainly in concrete materials (Gasser & Holzapfel, 2005; Rahman & Chakraborty, 2011; Su et al., 2010). The simplified 3D damage simulations for unidirectional fibre composites presented in Mishnaevsky (2012) and Mishnaevsky and

Brøndsted (2009) do not include discrete crack propagation. The broad assumptions of the different crack models are

1. Discrete crack models based on re-meshing techniques (Ooi & Yang, 2009; Réthoré, Gravouil, & Combescure, 2004; Yang & Chen, 2004): a representative semi-analytical method based on a re-meshing routine is the scaled boundary finite element method (Ooi & Yang, 2009). The method is designed for modelling problems with discontinuities and singularities (Ooi & Yang, 2011).
2. Smeared crack models in Pham, Al-Mahaidi, and Saouma (2006) involve an infinite number of parallel cracks of infinitesimal thickness that are distributed over the finite elements (Kwak & Filippou, 1990). The crack propagation is then introduced by reduction of the stiffness and strength of the material. A comprehensive literature review including limitations is given in Gálvez, Červenka, Cendón, and Saouma (2002).
3. Nodal enrichment models such as the extended finite element method (X-FEM) (Markus, 2007; Meschke & Dumstorff, 2007) endorse the concept of local nodal enrichment of the finite elements by partition, allowing discontinuous displacement fields to take place.
4. Cohesive crack models are based on pre-embedding cohesive interface elements without re-meshing (Su, Yang, & Liu, 2010; Su et al., 2009; Xie & Waas, 2006; Yang & Xu, 2008; Yang et al., 2009). They assume the existence of a fracture process zone, originally introduced by Barenblatt (1959) and Dugdale (1960) for elasto-plastic fracture of ductile materials and later elaborated by Hillerborg, Modéer, and Petersson (1976) to include quasi-brittle materials in their 'fictitious crack model' and adopted by many others including Bažant and Oh (1983), de Borst (2003), Carpinteri (1989), Seagraves and Radovitzky (2010), Tvergaard and Hutchinson (1992) and Yang and Xu (2008).

5.4 Modelling of transverse crack growth in a carbon fibre-reinforced polymer ply

This section uses the cohesive crack model in Yang et al. (2009) to simulate crack growth in a CFRP transverse ply. This model is based on pre-embedding of cohesive interface elements. The extension to multi-phase materials was developed by the authors in the MsSFrM framework (Sencu et al., 2014) (see also Figure 5.2). Four targeted image-based MeEs were extracted from optical micrographs taken from a CFRP ply (Figure 5.5).

The MeE windows contain different volume fractions and stochastic fibre distributions. Results are then compared with an ideal hexagonal fibre arrangement of 50% fibre volume fraction shown in Figure 5.6. As a rule of thumb, in uncoupled simulations the MeE window size has to be at least one order of magnitude larger than the length scale of the largest fibre diameter (Sencu et al., 2014). In this study, the carbon fibre diameter is approximately 5 μm and the considered MeE window size is 70×70 μm, as shown in Figure 5.5. The material properties for fracture modelling are given in Table 5.1.

The type of boundary condition considered in this work is a tensile mixed-mode loading configuration, as shown in Figure 5.7. This loading configuration allows core rotations and minimizes the global boundary effects on the computational area

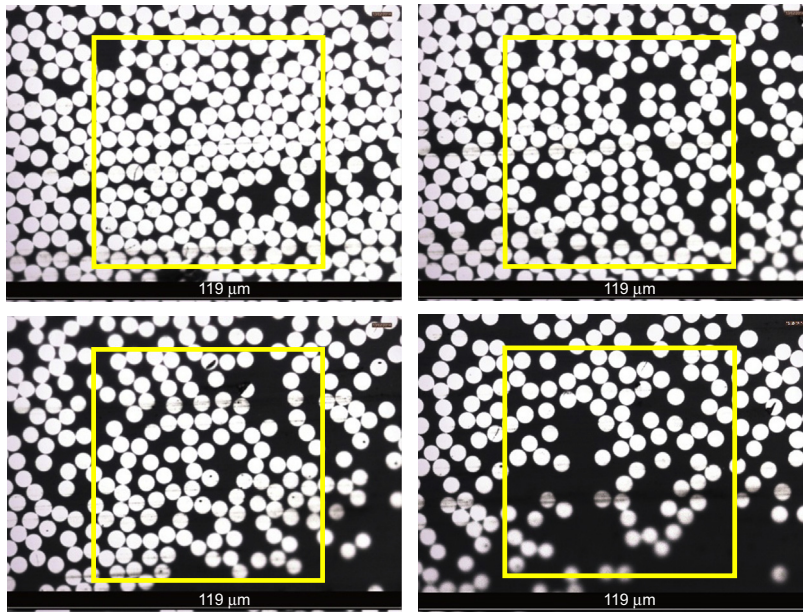

Figure 5.5 MeE windows at four positions from micrographs of a CFRP specimen.

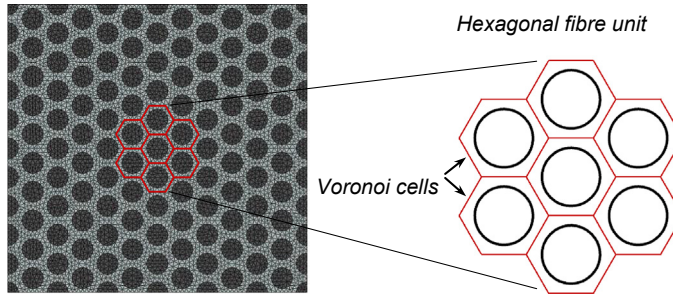

Figure 5.6 Ideal hexagonal fibre arrangement of 50% fibre volume fraction.

by allowing vertical sliding on the right edge. ABAQUS (Simulia/Abaqus) was the simulation platform and triangular first-order finite elements CPS3 with four-noded cohesive interface COH2D4 were used in these simulations. The approximate mesh size was 1.0 µm and the total number of finite elements of the largest model was 67,323, as seen in Table 5.2. This model has 69,126 degrees of freedom. Figure 5.7 shows the cohesive finite element sets that define the matrix and the interfaces between the matrix and individual fibres. It should be noted that the cracks were not allowed to propagate within fibres.

Crack initiation was determined by the maximum stress damage criterion (MAXS) available in ABAQUS (Simulia/Abaqus). The stress field mainly depends on the fibre

Table 5.1 Input material parameters for fracture modelling

Parameters	Units	Carbon fibre	Epoxy resin	Interface
Elastic modulus E	(GPa)	85	3.35	3.35
Traction strength $t_n = t_s$	(MPa)	600	82	45
Poisson's ratio ν		0.22	0.37	0.37
Fracture energy $G_{11} = G_{22}$	(N/mm)	20E−03	60E−03	35E−03
Density	(Kg/mc)		1500	

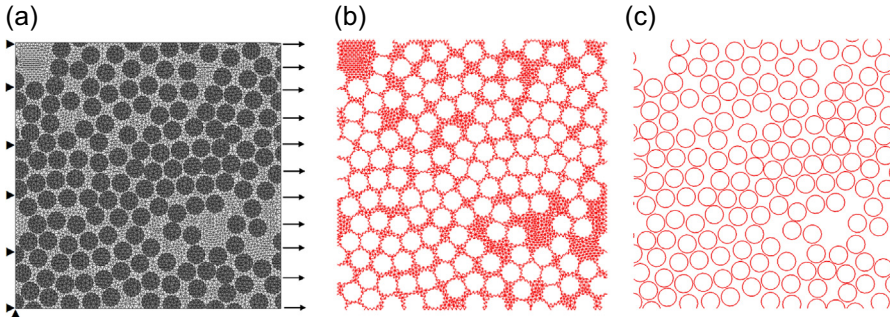

Figure 5.7 (a) Boundary conditions and cohesive element sets for (b) matrix interfaces and (c) matrix-to-fibre interfaces.

distribution and loading configuration. Before the onset of any crack, the stress field is influenced by the distribution of fibres and any considerably large fibre-free areas. After the first crack opening, further cracks tend to follow the shortest paths in the matrix and along the fibre/matrix interfaces. Interface cracking or decohesion occurred in Figure 5.8 because a relatively weak fibre−matrix interface is assumed.

Due to random distribution of fibres, the crack paths on different MeEs are different from each other. This means that due to stochastic arrangement of the microstructure of the material, both crack initiation and propagation are influenced by the location of the simulation window. Figure 5.8 shows how the stress contours develop in the four MeE models at three loading steps with the associated crack growth.

Figure 5.9 compares the stress−displacement and stress−strain relationships between the five models. The crack paths in Figure 5.8 are directly related to the softening curves in Figure 5.9. In general, a weak interface (e.g. MeE 2 in Figure 5.8) gives a more tortuous crack path, which ultimately results in a higher dissipated energy and permits de-cohesion. For the analytically created hexagonal fibre arrangements and MeE windows with relatively large matrix volume fractions, the fracture happens

Table 5.2 Mesh information of stochastic MeE models

Model	Fibre CPS3	Fibre COH2D4	Matrix CPS3	Matrix COH2D4	Interface COH2D4	Elements total	Insertion time (s)
MeE 1	6199	8020	5394	7034	2404	29,051	225.23
MeE 2	5320	6875	6490	8640	2065	29,390	240.05
MeE 3	4635	6010	7273	9956	1790	29,664	245.85
MeE 4	3075	3976	19,119	39,951	1202	67,323	306.48

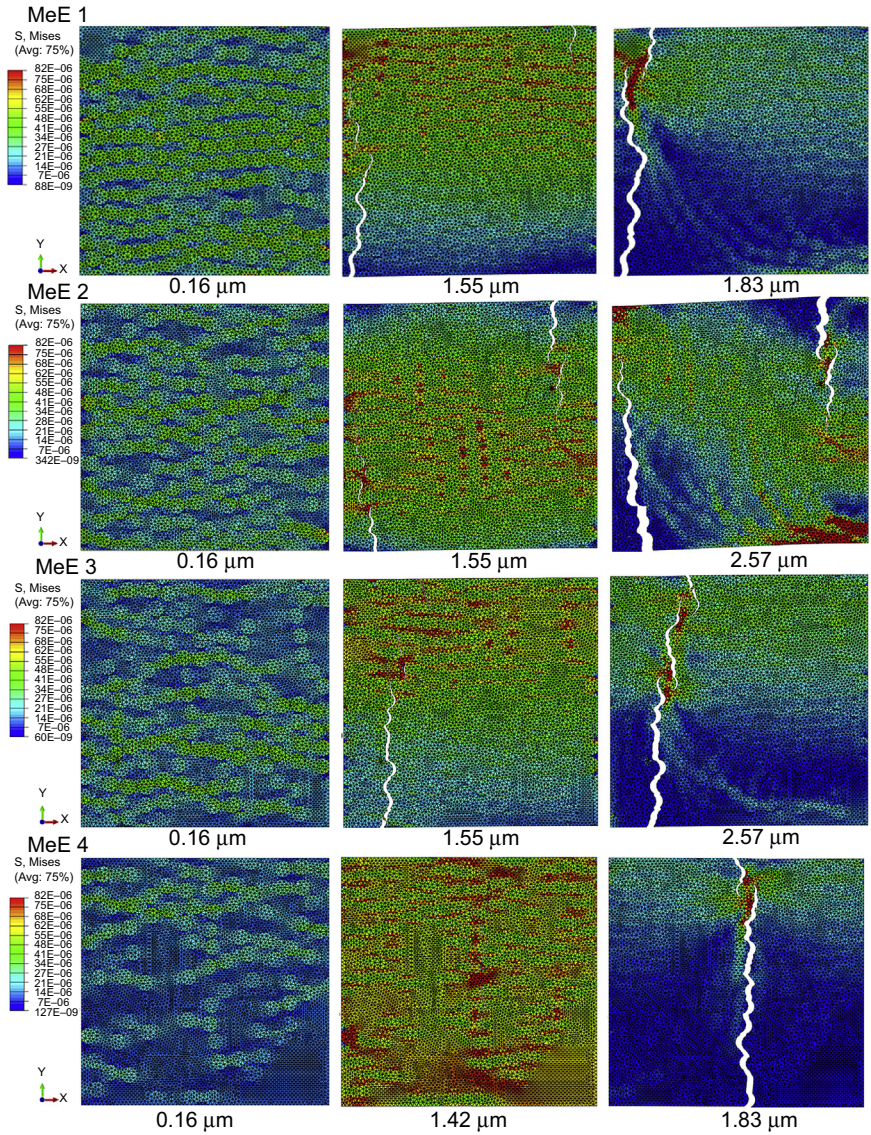

Figure 5.8 Stress contour plots at three different loading stages.

more suddenly, although higher transverse ultimate strengths are obtained (see Figure 5.10). This behaviour is associated with lower dissipated fracture energy.

Figure 5.10 compares the important results for the four image-based MeE models with the ideal hexagonal model.

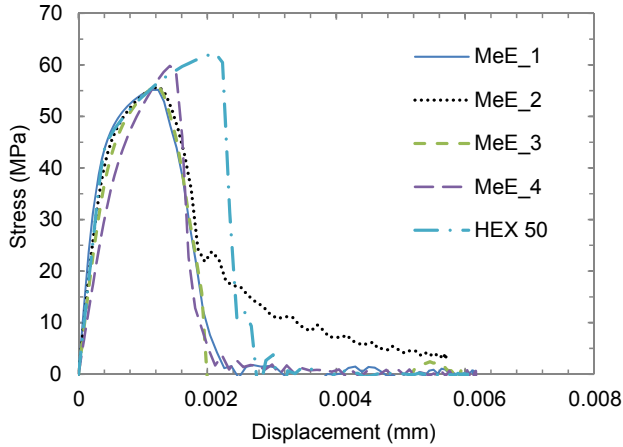

Figure 5.9 Stress−displacement curves.

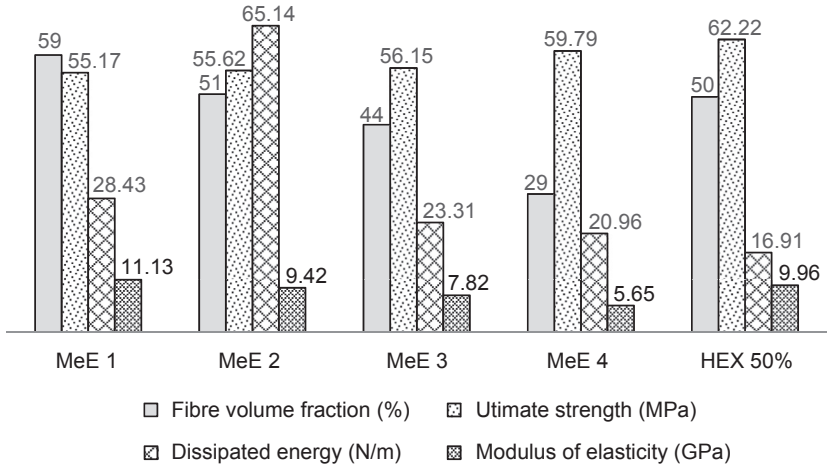

Figure 5.10 Comparison of volume fractions, ultimate strengths and dissipated energies.

5.5 Conclusions and final remarks

There exist two main multi-scale modelling methods, namely, the uncoupled and coupled.

- The uncoupled models (one-way models) start with either a macroscopic model (top-down) or a microscopic model (bottom-up). In the top-down model, the boundaries are commonly known a priori, as well as all the macroscopic details (e.g. the load−displacement curve, time to failure, etc.), while details that are necessary to capture the desired microstructural

response are decided based on enforced kinematical windows. However, even though a bottom-up starting point is assumed, difficulties still arise when finding the remote spatial-dependent properties without consideration of the microstructure morphology.

- The coupled models need some artificial boundary conditions to ensure compatibility for the two scales. The boundaries at the fine scale may be completely inexistent for certain phenomena. Two different routes exist: one using an object-oriented framework (such as the image-based route) to calibrate the material based on realistic XCT tests, and another using a mathematical framework for generation of prescribed microstructures. The second case is generally useful to generate new materials by being told how to arrange at various length scales. Such methods are usually based on the acquired or learned knowledge from workable numerical simulations.

So far, the coupling strategies reported in the literature pose various limitations, particularly related to their inability to incorporate random microstructures. This may have been necessary as a compromise to limit the computational cost. The concurrent approach is most commonly used where there is no need to assume the morphological continuity. Examples include problems related to some limited regions for accurate crack path investigations, such as sharp corner geometries, and stress concentration areas, such as for fibre clusters. Nevertheless, the use of reduced-order hierarchical models has the potential to overcome these challenges. For example, Section 5.4 of this chapter has demonstrated that a well-calibrated HA model, such as the MsSFrM model proposed by the authors in Sencu et al. (2014), may offer sufficiently accurate constitutive relations for certain multi-scale applications, including crack growth in FRP materials. Generally, the HA models work well for solving very large size phenomena if the scale transfer is built on energetic platforms. This platform may or may not be strictly crack path dependent.

Finally, it should be understood that hierarchical and concurrent models do not mean fine and coarse representations, respectively, but rather they are two main multi-scale coupling tools depending on certain criteria previously discussed throughout this chapter.

Acknowledgements

This study is funded by a US Air Force EOARD grant (No. FA8655-12-1-2100) and an EPSRC grant (No. EP/J019763/1).

References

Amini, S., & Kumar, R. S. (2014). A high-fidelity strain-mapping framework using digital image correlation. *Materials Science and Engineering: A*, *594*(0), 394−403.

Barenblatt, G. I. (1959). The formation of equilibrium cracks during brittle fracture: general ideas and hypothesis, axially symmetric cracks. *Applied Mathematics and Mechanics*, *23*, 622−636.

Bažant, Z., & Oh, B. (1983). Crack band theory for fracture of concrete. *Materials and Structures*, *16*(3), 155−177.

Carpinteri, A. (1989). Softening and snap-back instability in cohesive solids. *International Journal for Numerical Methods in Engineering*, *28*(7), 1521−1537.

Clément, A., Soize, C., & Yvonnet, J. (2013). Uncertainty quantification in computational stochastic multiscale analysis of nonlinear elastic materials. *Computer Methods in Applied Mechanics and Engineering*, *254*(0), 61−82.

Coindreau, O., Mulat, C., Germain, C., Lachaud, J., & Vignoles, G. L. (2011). Benefits of X-ray CMT for the modeling of C/C composites. *Advanced Engineering Materials*, *13*(3), 178−185.

Coindreau, O., Vignoles, G., & Cloetens, P. (2003). Direct 3D microscale imaging of carbon−carbon composites with computed holotomography. *Nuclear Instruments and Methods in Physics Research Section B: Beam Interactions with Materials and Atoms*, *200*(0), 308−314.

de Borst, R. (2003). Numerical aspects of cohesive-zone models. *Engineering Fracture Mechanics*, *70*(14), 1743−1757.

de Frías, G. J., Aquino, W., Pierson, K. H., Heinstein, M. W., & Spencer, B. W. (2014). A multiscale mass scaling approach for explicit time integration using proper orthogonal decomposition. *International Journal for Numerical Methods in Engineering*, *97*(11), 799−818.

Doškář, M., & Novák, J. (2013). Compression of heterogeneous material systems based on wang tilings. *Key Engineering Materials*, *592−593*, 149−152.

Dugdale, D. S. (1960). Yielding of steel sheets containing slits. *Journal of the Mechanics and Physics of Solids*, *8*(2), 100−104.

Gálvez, J. C., Červenka, J., Cendón, D. A., & Saouma, V. (2002). A discrete crack approach to normal/shear cracking of concrete. *Cement and Concrete Research*, *32*(10), 1567−1585.

Gasser, T. C., & Holzapfel, G. A. (2005). Modeling 3D crack propagation in unreinforced concrete using PUFEM. *Computer Methods in Applied Mechanics and Engineering*, *194*(25−26), 2859−2896.

Ghosh, S. (2008). *Adaptive concurrent multi-level model for multiscale analysis of composite materials including damage*. US: Springer, 83−163.

Ghosh, S., Bai, J., & Raghavan, P. (2007). Concurrent multi-level model for damage evolution in microstructurally debonding composites. *Mechanics of Materials*, *39*(3), 241−266.

Ghosh, S., & Paquet, D. (2013). Adaptive concurrent multi-level model for multi-scale analysis of ductile fracture in heterogeneous aluminum alloys. *Mechanics of Materials*, *65*(0), 12−34.

González, C., & Llorca, J. (2006). Multiscale modeling of fracture in fiber-reinforced composites. *Acta Materialia*, *54*(16), 4171−4181.

Greco, F., Leonetti, L., & Lonetti, P. (2013). A two-scale failure analysis of composite materials in presence of fiber/matrix crack initiation and propagation. *Composite Structures*, *95*(0), 582−597.

Guilleminot, J., Soize, C., & Kondo, D. (2009). Mesoscale probabilistic models for the elasticity tensor of fiber reinforced composites: experimental identification and numerical aspects. *Mechanics of Materials*, *41*(12), 1309−1322.

Hillerborg, A., Modéer, M., & Petersson, P. E. (1976). Analysis of crack formation and crack growth in concrete by means of fracture mechanics and finite elements. *Cement and Concrete Research*, *6*(6), 773−781.

Kabele, P. (2007). Multiscale framework for modeling of fracture in high performance fiber reinforced cementitious composites. *Engineering Fracture Mechanics*, *74*(1−2), 194−209.

Kaczmarczyk, Ł., Pearce, C. J., & Bićanić, N. (2008). Scale transition and enforcement of RVE boundary conditions in second-order computational homogenization. *International Journal for Numerical Methods in Engineering*, *74*(3), 506−522.

Kwak, H. G., & Filippou, F. C. (1990). *Finite element analysis of reinforced concrete structures under monotonic loads*. A Report on Research Conducted under Grant RTA-59M848 from the California Department of Transportation.

Li, J. (2011). Establishment of strain gradient constitutive relations by homogenization. *Comptes Rendus Mécanique*, *339*(4), 235−244.

Li, Y., McDowell, D. L., & Zhou, M. (2013). Computational prediction of fracture toughness of polycrystalline metals. In *13th international conference on fracture, Beijing, China (June 16−21, 2013)*.

Liu, G. R., Ma, W. B., & Han, X. (2002). An inverse procedure for identification of loads on composite laminates. *Composites Part B: Engineering*, *33*(6), 425−432.

Li, Y., & Zhou, M. (2013). Prediction of fracture toughness of ceramic composites as function of microstructure: I. Numerical simulations. *Journal of the Mechanics and Physics of Solids*, *61*(2), 472−488.

Li, Y., & Zhou, M. (2013). Prediction of fracturess toughness of ceramic composites as function of microstructure: II. Analytical model. *Journal of the Mechanics and Physics of Solids*, *61*(2), 489−503.

Llorca, J., González, C., Molina-Aldareguía, J. M., & Lópes, C. S. (2013). Multiscale modeling of composites: toward virtual testing … and beyond. *JOM*, *65*(2), 215−225.

Luscher, D. J., McDowell, D. L., & Bronkhorst, C. A. (2010). A second gradient theoretical framework for hierarchical multiscale modeling of materials. *International Journal of Plasticity*, *26*(8), 1248−1275.

Markus. P. (2007). *Modellierung von Rissausbreitung unter Verwendung der p-Version der XFEM mit einer adaptiven Integrauibsmethode* (Ph.D. thesis). Germany: Ruhr University.

Matsuda, T., Ohno, N., Tanaka, H., & Shimizu, T. (2003). Effects of fiber distribution on elastic−viscoplastic behavior of long fiber-reinforced laminates. *International Journal of Mechanical Sciences*, *45*(10), 1583−1598.

Meschke, G., & Dumstorff, P. (2007). Energy-based modeling of cohesive and cohesionless cracks via X-FEM. *Computer Methods in Applied Mechanics and Engineering*, *196*(21−24), 2338−2357.

Mishnaevsky, L., Jr. (2012). Composite materials for wind energy applications: micromechanical modeling and future directions. *Computational Mechanics*, *50*(2), 195−207.

Mishnaevsky, L., Jr., & Brøndsted, P. (2009). Micromechanisms of damage in unidirectional fiber reinforced composites: 3D computational analysis. *Composites Science and Technology*, *69*(7−8), 1036−1044.

Moffat, A. J., Wright, P., Helfen, L., Baumbach, T., Johnson, G., Spearing, S. M., et al. (2010). In situ synchrotron computed laminography of damage in carbon fibre−epoxy [90/0]s laminates. *Scripta Materialia*, *62*(2), 97−100.

Molent, L., Callinan, R. J., & Jones, R. (1989). Design of an all boron/epoxy doubler reinforcement for the F-111C wing pivot fitting: structural aspects. *Composite Structures*, *11*(1), 57−83.

Nguyen, V. P., Stroeven, M., & Sluys, L. J. (2011). Multiscale continuous and discontinuous modeling of heterogeneous materials: a review on recent developments. *Journal of Multiscale Modelling*, *03*(04), 229−270.

Ooi, E. T., & Yang, Z. J. (2009). Modelling multiple cohesive crack propagation using a finite element−scaled boundary finite element coupled method. *Engineering Analysis with Boundary Elements*, *33*(7), 915−929.

Ooi, E. T., & Yang, Z. J. (2011). Modelling crack propagation in reinforced concrete using a hybrid finite element−scaled boundary finite element method. *Engineering Fracture Mechanics*, *78*(2), 252−273.

Panchal, J. H., Kalidindi, S. R., & McDowell, D. L. (2012). Key computational modeling issues in integrated computational materials engineering. *Computer-Aided Design*, *45*(1), 4−25.

Pham, H. B., Al-Mahaidi, R., & Saouma, V. (2006). Modelling of CFRP−concrete bond using smeared and discrete cracks. *Composite Structures*, *75*(1−4), 145−150.

Pyrz, R. (1994). Quantitative description of the microstructure of composites. Part I: morphology of unidirectional composite systems. *Composites Science and Technology*, *50*(2), 197−208.

Rahman, S., & Chakraborty, A. (2011). Stochastic multiscale fracture analysis of three-dimensional functionally graded composites. *Engineering Fracture Mechanics*, *78*(1), 27−46.

Réthoré, J., Gravouil, A., & Combescure, A. (2004). A stable numerical scheme for the finite element simulation of dynamic crack propagation with remeshing. *Computer Methods in Applied Mechanics and Engineering*, *193*(42−44), 4493−4510.

Rouse, J.E. (2012). *"Characterisation of impact damage in carbon fibre reinforced plastics by 3D X-ray tomography."* A Doctor of Engineering (EngD) thesis, University of Manchester.

Ruggles, T. J., Rampton, T. M., Rose, S. A., & Fullwood, D. T. (2013). Reducing the micro-structure design space of 2nd order homogenization techniques using discrete fourier transforms. *Mechanics of Materials*, *59*(0), 14−23.

Scott, A. E., Mavrogordato, M., Wright, P., Sinclair, I., & Spearing, S. M. (2011). In situ fibre fracture measurement in carbon−epoxy laminates using high resolution computed tomography. *Composites Science and Technology*, *71*(12), 1471−1477.

Seagraves, A., & Radovitzky, R. (2010). *Advances in cohesive zone modeling of dynamic fracture*. US: Springer, 349−405.

Sencu, R. M., Yang, Z., & Wang, Y. C. (2014). A multiscale stochastic fracture modelling calibration using monte carlo simulations. In *Proceedings of the 22nd UK conference of the association for computational mechanics in engineering, university of Exeter, Exeter, british library cataloguing-in-publication data*.

Shen, B., & Paulino, G. H. (2011). Identification of cohesive zone model and elastic parameters of fiber-reinforced cementitious composites using digital image correlation and a hybrid inverse technique. *Cement and Concrete Composites*, *33*(5), 572−585.

Simulia/Abaqus - Abaqus theory manual. Online version 6.12.

Singh, C. V., & Talreja, R. (2013). A synergistic damage mechanics approach to mechanical response of composite laminates with ply cracks. *Journal of Composite Materials*, *47*(20−21), 2475−2501.

Stargel, D. (2012). *Multi-scale structural mechanics and prognosis* Accessed from https://community.apan.org/afosr/w/researchareas/7693.multi-scale-structural-mechanics-and-prognosis.aspx on 18.05.2014. Arlington, VA 22203., AFOSR.

Su, X., Yang, Z., & Liu, G. (2009). Monte carlo simulation of complex 2D cohesive fracture in random heterogeneous quasi-brittle materials. In Y. Yuan, J. Cui, & H. Mang (Eds.), *Computational structural engineering* (pp. 1081−1087). Netherlands: Springer.

Su, X., Yang, Z., & Liu, G. (2010). Finite element modelling of complex 3D static and dynamic crack propagation by embedding cohesive elements in abaqus. *Acta Mechanica Solida Sinica*, *23*(3), 271−282.

Su, X. T., Yang, Z. J., & Liu, G. H. (2010). Monte carlo simulation of complex cohesive fracture in random heterogeneous quasi-brittle materials: a 3D study. *International Journal of Solids and Structures*, *47*(17), 2336−2345.

Trias, D., Costa, J., Fiedler, B., Hobbiebrunken, T., & Hurtado, J. E. (2006). A two-scale method for matrix cracking probability in fibre-reinforced composites based on a statistical representative volume element. *Composites Science and Technology*, *66*(11−12), 1766−1777.

Trias, D., Costa, J., Mayugo, J. A., & Hurtado, J. E. (2006b). Random models versus periodic models for fibre reinforced composites. *Computational Materials Science*, *38*(2), 316−324.

Tvergaard, V., & Hutchinson, J. W. (1992). The relation between crack growth resistance and fracture process parameters in elastic-plastic solids. *Journal of the Mechanics and Physics of Solids*, *40*(6), 1377−1397.

Unger, J. F. (2013). An FE2-X1 approach for multiscale localization phenomena. *Journal of the Mechanics and Physics of Solids*, *61*(4), 928−948.

Verhoosel, C. V., Remmers, J. J. C., Gutiérrez, M. A., & de Borst, R. (2010). Computational homogenization for adhesive and cohesive failure in quasi-brittle solids. *International Journal for Numerical Methods in Engineering*, *83*(8−9), 1155−1179.

Wright, P., Moffat, A. J., Renault, A., Sinclair, I., & Spearing, S. M. (2009). High resolution computed tomography for modelling laminate damage. In *ICCM17 proceedings*.

Xie, D., & Waas, A. M. (2006). Discrete cohesive zone model for mixed-mode fracture using finite element analysis. *Engineering Fracture Mechanics*, *73*(13), 1783−1796.

Xu, Q., Chen, J., Li, J., & Wang, M. (2013). Multi-scale numerical model for simulating concrete material based on fractal theory. *Acta Mechanica Solida Sinica*, *26*(4), 344−352.

Yang, Z. J., & Chen, J. (2004). Fully automatic modelling of cohesive discrete crack propagation in concrete beams using local arc-length methods. *International Journal of Solids and Structures*, *41*(3−4), 801−826.

Yang, Z. J., Su, X. T., Chen, J. F., & Liu, G. H. (2009). Monte carlo simulation of complex cohesive fracture in random heterogeneous quasi-brittle materials. *International Journal of Solids and Structures*, *46*(17), 3222−3234.

Yang, Z. J., & Xu, F. X. (2008). A heterogeneous cohesive model for quasi-brittle materials considering spatially varying random fracture properties. *Computer Methods in Applied Mechanics and Engineering*, *197*(45−48), 4027−4039.

Multi-scale modeling of high-temperature polymer matrix composites for aerospace applications

6

S. Roy
University of Alabama, Tuscaloosa, AL, USA

6.1 Introduction

It is now well established that in the presence of a large fracture process zone near the crack tip, the basic assumptions of linear elastic fracture mechanics are no longer valid (Kanninen & Popelar, 1985; Roy, Dexter, & Fossum, 1993; Williams, 1984). Specifically, in some polymers such as toughened epoxies, the occurrence of void nucleation and growth ahead of the crack tip results in a damage (process) zone that is not traction free. Further, for a crack in a fiber-reinforced polymer matrix composite, fiber bridging may also be present within the damage zone (Sorensen & Jacobsen, 2003). Therefore, in such cases, a cohesive layer modeling approach would be more accurate in accounting for the nonlinear processes that occur within the "damage zone."

The cohesive zone model was first introduced by Barenblatt (1962) and Dugdale (1960) in the 1960s. In the 1970s, Hillerborg, Modéer, and Petersson (1976) employed the cohesive model to predict the strength of concrete structures. In the 1980s, applications of cohesive zone models to determine strength of composites and adhesive joints were introduced by Backlund (1981) and Stigh (1988). Needleman (1987) and Stigh (1987) demonstrated how the cohesive zone model fits within the scope of conventional stress analysis using finite element analysis (FEA).Daphalapurkar, Lu, Coker, and Komanduri (2007) simulated dynamic crack propagation capable of capturing the Burridge-Andrew mechanism using the material point method. Cohesive zone models have seen an almost explosive increase in use and applications during recent years. There are many researchers, such as Remmers, de Borst, and Needleman (2008), Zhang and Paulino (2005), and Yang and Deeks (2007), who have proposed new cohesive models to predict the crack propagation path. With cohesive modeling, no additional properties are necessary to simulate crack growth. Only the cohesive law is needed to analyze both initiation and growth of a crack. Typically, cohesive elements in FEA codes follow a predefined traction−separation law that simulates the crack initiation and propagation. Another advantage of cohesive zone models is that these models can simulate different types of failure mechanisms, such as fiber-matrix debond and interlaminar delamination. This is also a drawback in modeling

Structural Integrity and Durability of Advanced Composites. http://dx.doi.org/10.1016/B978-0-08-100137-0.00006-7

flexibility; namely, if the fracture toughness changes with crack growth, a conventional cohesive law cannot capture this phenomenon by itself. Remedies have been suggested in recent work done by Yang and Cox (2005), Dávila, Rose, and Camanho (2009), and Yang, Cox, Nalla, and Ritchie (2006). Work done by Yang and Cox (2005) presented a three-dimensional cohesive element where it is demonstrated how the process zone size depends on the failure mode for delamination and splitting cracks in composite laminates.

In order to develop a cohesive zone model that does not require a prescribed traction−separation law, Allen and Searcy (2001) proposed a viscoelastic cohesive zone model and demonstrated the use of this model by numerically solving example problems with different displacement boundary conditions and strain rates. They also proposed a damage evolution law that was phenomenologically derived due to the absence of near-tip experimental data. In this context, the process zone ahead of the crack tip is usually very small compared with the specimen size in most materials. Therefore, experimentally it is quite challenging to precisely determine the traction−separation law in the cohesive zone. This chapter employs a modified version of the viscoelastic cohesive layer model proposed by Allen and Searcy (2001), but the damage evolution law is fully characterized based on actual data from experiments. Sorensen and Jacobsen (2003) presented a review of existing experimental procedures to estimate the cohesive law and underlined two major approaches. The first approach is to use a direct tension test, with the assumption that a uniform damage state evolves across the ligament. In reality, it is very difficult to achieve a uniform damage state in a ligament during a direct tension test, and therefore this approach is impractical. The second approach is the J-integral approach, where macro-level J-integral data are used to extract the micro-level constitutive (traction−separation) behavior in the process zone. This approach was first used by Li and Ward (1989). Sorensen and Jacobsen (2003) adapted the same approach to conduct their ongoing research. Recently, Fuchs and Major (2011) used the J-integral approach to determine the cohesive zone models for glass fiber-reinforced composites and studied the effect of loading direction on the constitutive cohesive law.

In this chapter, the J-integral approach is employed to determine the damage evolution law for delamination behavior of IM-7/bismaleimide (BMI) unidirectional laminates, before and after isothermal aging at 260 °C for 1000 h. For this purpose, double cantilever beam (DCB) experiments were conducted to acquire the macro-level J-integral data, and the displacement and strain fields in the process zone were obtained using digital image correlation (DIC). From experimental data, cohesive law and damage evolution parameters were determined and used in the viscoelastic cohesive layer model to simulate delamination growth.

A rate-dependent viscoelastic cohesive layer model was implemented in an in-house test-bed finite element analysis code (NOVA-3D) to simulate the delamination initiation and propagation in unidirectional polymer composites before and after isothermal aging in air. To determine the damage mechanics-based model parameters, DCB experiments were conducted on both pristine and isothermally aged IM-7/BMI composite specimens. The J-integral approach was adapted to extract cohesive stresses near the crack tip. A principal stretch-dependent internal damage state variable defines

the damage in the cohesive layer. Within the cohesive layer, pristine and cohesive stresses were compared to estimate the material damage parameters. The J-integral approach presented in this chapter relates macro-scale loading to micro-scale crack growth and cohesive stresses, thereby enabling the prediction of both macro-scale and micro-scale behavior accurately, as described later in this chapter.

Once the material damage parameters had been characterized, the test-bed FEA code employed a micromechanics-based viscoelastic cohesive layer model to simulate interlaminar delamination. This unified model is fully rate dependent and does not require a preassigned traction−separation law. The final shape of traction−separation law depends on (1) the strain rate via the viscoelastic constitutive relationship, (2) the degree of thermo-oxidative aging via the changes in the experimentally measured creep compliance due to oxidation, and via changes in the critical principal stretch measure, and (3) the evolution of the internal state variable defining the state of damage. From a numerical stability standpoint, the "viscous regularization" effect of the viscoelastic constitutive equations in the cohesive layer help mitigate numerical instabilities caused by sudden elastic energy released due to crack growth, thereby enabling the FEA model to simulate the load−deflection response of the composite structure well beyond peak load. The present cohesive layer-based FEA model was able to accurately predict not only the macro-level load−displacement curve beyond peak load, but also the micro-level crack growth history in IM-7/BMI laminate before and after thermal aging, as discussed in the "Results" section.

The next section presents an overview of the materials processing and DCB experiments that were used to obtain J-integral data.

6.2 DCB experiment

6.2.1 Specimen preparation and double cantilever beam specimen geometry

A total of 16 plies of IM-7/BMI prepreg sheets were stacked to form a unidirectional $[0]_{16}$ composite laminate. The fiber volume fraction was 0.6. The specimens were cut from the composite panel using a diamond saw blade. The test configuration is shown in Figure 6.1. The specimens are 140 mm long, 14 mm wide, and 2.46 mm thick and have a 70 mm long pre-crack. A pre-crack in the fiber direction was prepared in the specimen for interlaminar delamination growth. To verify that no intralaminar damage was induced, a scanning electron microscopy image was acquired on the open crack surface.

A pair of piano hinges was glued to the specimen for gripping the DCB specimen during testing. The side edge of the DCB specimen was polished and sprayed with black paint as dots on white background that produced a speckle of good contrast for determining the crack position. The typical spacing between dots is usually a few microns.

To study the effect of thermal oxidation, isothermal aging of IM-7/BMI composite panels was conducted inside a convection oven for approximately 1000 h at 260 °C in

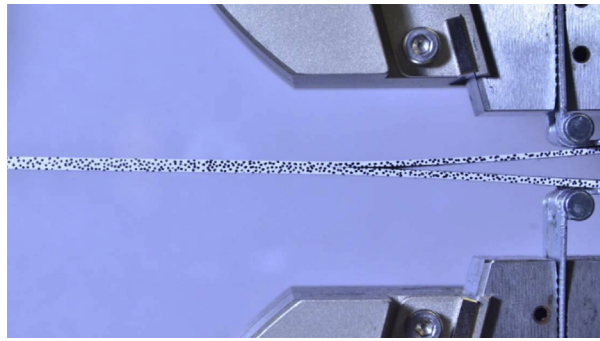

Figure 6.1 An image of the test configuration for delamination-type DCB specimen having pre-crack under initial loading.

air environment. After 1000 h of aging at 260 °C, the coupons were removed from the oven and cooled down slowly to room temperature to conduct DCB experiments under ambient condition at a temperature of 23 ± 1 °C and a relative humidity of 35% ± 3%.

6.2.2 Experimental method

Mode I fracture toughness experiments (ASTM D5528-01) were conducted on pristine (unaged) unidirectional IM-7/BMI specimens, and also on IM-7/BMI specimens after thermo-oxidative aging of 1000 h. For each case at least four specimens were tested to verify the repeatability of test data. The tests were performed using an Instron 5969 dual-column tabletop universal testing machine with a 50 kN load cell. The tests were conducted in displacement control and the upper cross-head movement rate was 1 mm/min. A crack was allowed to grow until 25 mm of cross-head displacement was reached. The load displacement data were recorded and digital images were taken by a Nikon D7000 DSLR camera with 200 mm macro lens. The DIC code developed by Lu and Cary (2000) was used to analyze the images taken during the experiment. To accurately determine the crack length, the digital image was converted to a grayscale and a negative was created to highlight the contrast due to the crack within the accuracy of the single pixel (representing about 25 m) using an image processing software. The next section discusses the micromechanics-based viscoelastic cohesive layer model employed to simulate delamination in IM-7/BMI unidirectional composite.

6.3 Viscoelastic cohesive layer model

6.3.1 Preliminary discussion

Micrographs taken during the DCB experiments on IM-7/BMI indicate the existence of fibrillar crack bridging, especially after thermal aging, analogous to the idealized schematic in Figure 6.2. In this context, in the micromechanics-based material model,

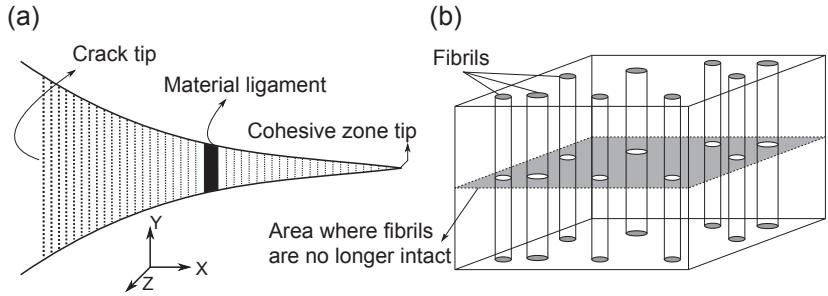

Figure 6.2 (a) Opening debond containing cohesive ligament. (b) Reduction of idealized RVE to cohesive zone by area averaging the fibril tractions.

the area averaged stresses within a cross-sectional area of the cohesive layer representative volume element (RVE) in a bridged delamination or debond ligament, as shown in Figure 6.2, is given by (Allen & Searcy, 2001)

$$\overline{\sigma}_{ij} = (1-\alpha)\sigma_{ij}^{\text{fibril}} \tag{6.1}$$

where $\sigma_{ij}^{\text{fibril}}$ is the viscoelastic stress in each polymer fibril within the RVE and $\alpha(t)$ is a scalar-valued internal damage parameter representing the time-varying area fraction of the growing voids with respect to the cross-sectional area of the RVE,

$$\alpha(t) = \frac{A - \sum_{k=1}^{N} A_k(t)}{A} \tag{6.2}$$

Here, $A_k(t)$ is the cross-sectional area of kth fibril and A is the cross-sectional area of the RVE. In Roy and Reddy (1987), the multiaxial viscoelastic stress−strain law for an individual polymer fibril may be expressed in matrix notation as

$$\{\sigma(t)\}^{\text{fibril}} = [M(t)](\{\varepsilon(t)\} - \{H(t)\}) \tag{6.3}$$

where $[M(t)]$ is a 6×6 matrix of time-dependent viscoelastic stiffness coefficients, $\{\varepsilon(t)\}$ is the vector containing the components of mechanical strains at time t, and $\{H(t)\}$ contains the hereditary (load history-dependent) strain components. Details regarding the derivation of the $[M]$ matrix and $\{H\}$ vector from the viscoelastic convolution integral can be found in Roy and Reddy (1988). Combining Eqns (6.1) and (6.3) gives the homogenized constitutive relationship between rate-dependent area-averaged viscoelastic stresses and strains within a cohesive RVE ligament at an interlaminar interface including evolving damage, strain rate, and moisture and temperature effects through the time−temperature−moisture superposition principle,

$$\left\{\overline{\sigma(t)}\right\} = (1-\alpha(t))[M(t)](\{\varepsilon(t)\} - \{H(t)\}) \tag{6.4}$$

6.3.2 Damage evolution law for micromechanical representative volume element

Within the cohesive layer RVE, damage initiation (i.e., initiation of voids and/or polymer fibrils) is assumed to occur if the applied principal stretch along the fibril exceeds the critical value of the principal stretch, that is, $\lambda > \lambda_{cr}$. Because the change of fibril diameter as a function of time is proportional to the applied principal stretch along the polymer fibril, a phenomenological power law-based damage evolution law is adapted (Upadhyaya, Singh, & Roy, 2011), given by

$$\frac{d\alpha}{dt} = \begin{cases} \alpha_0 \overline{\lambda}^m(t), & \text{if } \dot{\lambda} \geq 0 \text{ and } \alpha < 1 \\ 0, & \text{if } \dot{\lambda} < 0 \text{ and } \alpha < 1 \end{cases} \tag{6.5}$$

where $\overline{\lambda} = \lambda - \lambda_{cr}$ is a principal stretch measure within the RVE (Upadhyaya et al., 2011), and α_0 and m are material constants that are assumed to be dependent on environmental conditions but independent of the applied strain rate. These material constants are actually evaluated in this chapter by performing fracture experiments using DCB specimens in conjunction with DIC, as described in Section 6.5.

6.4 Extraction of cohesive law from experimental data through J-integral

For a monotonically increasing deformation within the process zone, the cohesive traction−separation law relates the stress state across the failure zone to the local separation distance. It is assumed that the cohesive stress depends on the local separation and its rate, and that a critical opening separation exists, beyond which the cohesive stress vanishes. The cohesive law approach is particularly attractive for modeling large-scale bridging (LSB) process zones (Sorensen & Jacobsen, 2003) where process zone size in one direction is very large compared with other directions. To determine the cohesive stresses, the J-integral as a function of crack opening displacement (COD) was determined experimentally. From the experimental data, J-integral for a DCB specimen was calculated by using the following relationship (Anthony & Paris, 1988):

$$J = \frac{2P\theta}{b} \tag{6.6}$$

where P is the reaction force at the loading pin location measured during the DCB experiment, θ is rotation at the loading pin acquired through DIC calculation, and b is the width of the specimen. As described by Fuchs and Major (2011), for Mode I-type failure, cohesive stresses can be evaluated by taking the first derivative of J-integral with respect to COD (δ). The COD can be determined precisely by measuring the difference of y displacements between two points (one above and one below) at the location of the crack tip in the unloaded state. To be consistent with the mathematical

framework of the J-integral derivation, it is imperative to select these two points to be right at the initial crack tip, even though it may be difficult to determine the exact location of the pre-crack. After calculating the J-integral from the DCB experimental data as a function of COD, a "smoothing" spline fit is obtained for J-integral versus COD data. The spline is then used to take the first derivative of J-integral with respect to COD (δ) at each data point, that is,

$$\sigma^{cohesive} = \frac{\partial J}{\partial \delta} \tag{6.7}$$

In Figure 6.3(a) and (b), J-integral versus COD (δ) experimental data as well as the smoothing spline fit are plotted for the pristine (unaged) specimens and for specimens aged for 1000 h at 260 °C, respectively. J-integral curves typically have a sigmoidal shape as a function of COD, and reach a steady-state plateau that indicates that the cohesive zone is fully developed. Data smoothing was performed to avoid the influence of measurement noise on cohesive stress estimation. For this purpose, smoothing spline fits were applied on the J-integral-COD data, using the spap2 function available in MATLAB (Matlab R2009b, TheMathWorks Inc., Natick, MA). It is important to note that the crack starts to propagate when the cohesive stress reaches its peak value (see Figure 6.4). From the DIC analysis of recorded images, the time when the crack starts to propagate for each specimen was determined carefully. The cohesive laws for pristine specimens and aged specimens determined using Eqn (6.7) are shown in Figure 6.4(a) and (b), respectively. The inter-ply region in a unidirectional laminate is polymer matrix dominated and therefore the strength of polymer corresponds to the maximum value of the cohesive stress, that is, 29.2 MPa for pristine and 5.6 MPa for specimens isothermally aged for 1000 h at 260 °C. The cohesive stress attains its peak value at 303 s for the pristine case, and at 215 s for specimens aged for 1000 h, respectively. Therefore, a significant degradation of 80% in the peak cohesive stress was observed after 1000 h of thermo-oxidative aging, and is corroborated by the earlier crack initiation in the aged specimen. The methodology adapted to estimate the viscoelastic damage evolution parameters is presented in the next section.

6.5 Evaluation of damage evolution law

In the current work, a principal stretch-based failure criterion is used for damage initiation in the cohesive layer. As alluded to in Section 6.3.1, damage initiates in the cohesive layer as the local principal stretch value exceeds the critical value of principal stretch λ_{cr}, which corresponds to the peak stress in the cohesive traction−separation law (see Figure 6.4). The complete definition of this model requires three scalar-valued material parameters: critical principal stretch value λ_{cr}, α_0, and m. The principal stretch values were calculated from the displacement gradients recorded in the damage zone from DIC image analysis. The right Cauchy-Green strain tensor was calculated from the strain gradients, and the square root of eigen values for right

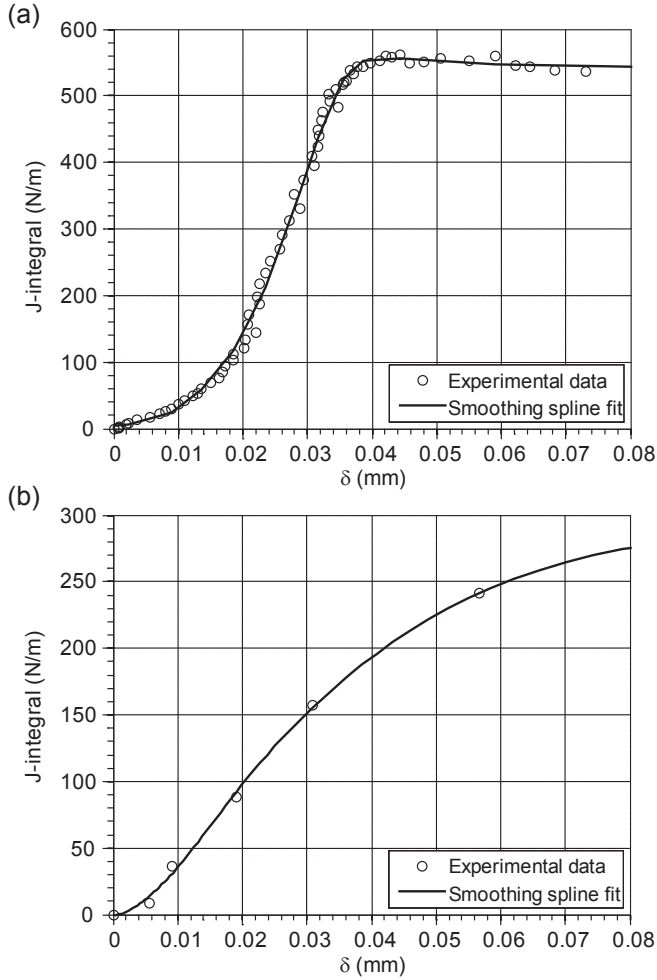

Figure 6.3 J-integral versus COD (δ) for (a) pristine specimen and (b) specimen isothermally aged for 1000 h at 260 °C.

Cauchy-Green strain tensor gives the principal stretches. The principal stretch value that corresponded to the crack initiation time and maximum cohesive stress for each case (pristine and aged) was taken as the critical principal stretch value for each case. The critical principal stretch values thus obtained for pristine and aged specimens are reported in Table 6.1.

By definition, the cohesive stress history (see Figure 6.4) obtained through the J-integral includes damage state after peak stress has been reached. To evaluate the damage parameter $\alpha(t)$, a comparison between the cohesive stresses for undamaged and damaged (cohesive) material was performed. Strain data acquired from DIC calculations near the crack tip were used to obtain these undamaged material stresses.

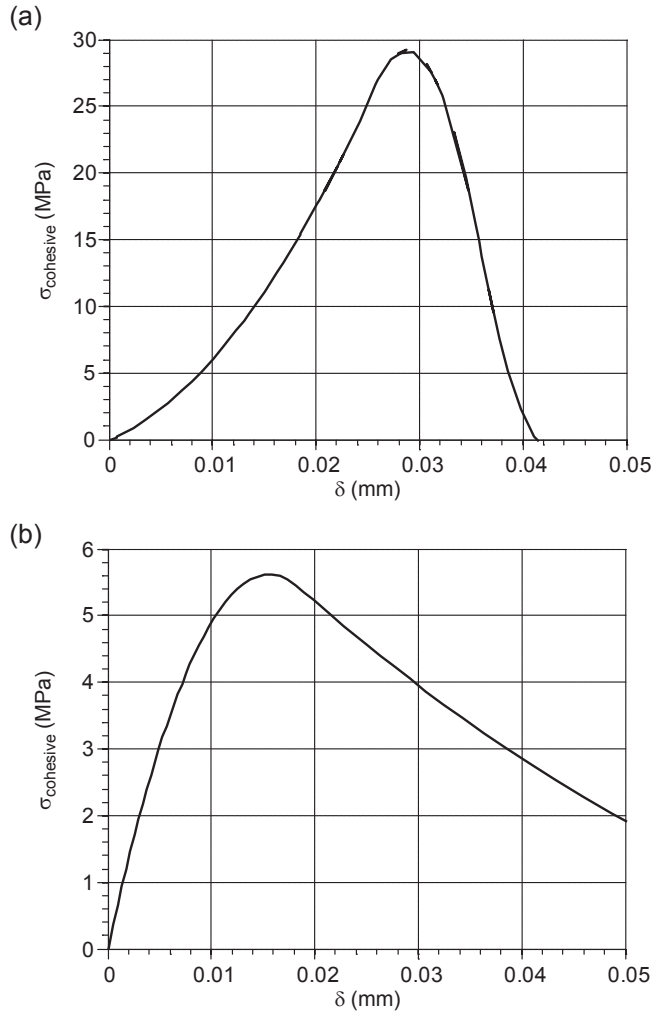

Figure 6.4 Cohesive stress versus COD (δ) (a) pristine and (b) 1000 h aged specimens at 260 °C.

Table 6.1 Damage evolution parameters used in FEA model for IM-7/BMI

	λ_{cr}	α_0	m
Pristine	1.0264	0.0507	0.45
Aged[a]	1.0148	0.0415	0.83

[a]Specimens were aged for 1000 h at 260 °C.

For undamaged material, volume-averaged stresses are obtained through the following viscoelastic stress−strain relationship:

$$\left\{\overline{\sigma(t)}\right\}^{ud} = [M(t)](\varepsilon(t) - \{H(t)\}) \tag{6.8}$$

where $\{\overline{\sigma(t)}\}^{ud}$ is the volume-averaged stresses within the RVE in a viscoelastic cohesive layer without any damage. The delamination zone is assumed to be resin rich, and therefore material properties of BMI are used for the calculation of undamaged stresses within the cohesive layer. To calculate the viscoelastic stiffness coefficients, viscoelastic properties of aged as well as pristine BMI were used from the creep experiments performed by Luo, Roy, and Lu (2012).

Although the material under consideration is viscoelastic, stress−strain behavior is fairly linear because the time duration for the DCB experiment is very small and material did not exhibit significant stress relaxation within the time scale of the experiment. Incorporating the induced damage through the internal damage parameter $\alpha(t)$, the governing equation for viscoelastic cohesive layer is given as (Upadhyaya et al., 2011)

$$\left\{\overline{\sigma(t)}\right\}^{cohesive} = (1 - \alpha(t))[M(t)](\varepsilon(t) - \{H(t)\}) \tag{6.9}$$

Therefore, combining Eqns (6.8) and (6.9) in the cohesive layer, we can rewrite the governing viscoelastic damage law equation in terms of undamaged and damaged material stresses and solve for $\alpha(t)$ to obtain

$$\alpha(t) = 1 - \frac{\sigma^{cohesive}}{\overline{\sigma}^{ud}} \tag{6.10}$$

It is important to note that the damage parameter $\alpha(t)$ is meaningful only after damage initiation has taken place. In the current DCB experiments, maximum cohesive stress (29.2 MPa) is reached at 303 s from the start of loading for pristine specimens. Similarly, for aged cases, maximum cohesive stress (5.6 MPa) is reached at 215 s. Therefore, damage parameter evaluation is performed only after the damage initiation time for both cases. In Figure 6.5(a) and (b), a complete data set for scalar damage parameter $\alpha(t)$ is plotted for pristine and isothermally aged cases, respectively. As can be seen from these plots, the damage parameter increases with time and then plateaus at a value close to 1 (complete crack-face separation), which corroborates the definition of $\alpha(t)$. Since the damage growth rate, $\dot{\alpha}$, follows a power law behavior, damage law parameters α_0 and m can be determined by taking logarithm on both sides of the Eqn (6.5), giving

$$\log \dot{\alpha} = \log \alpha_0 + m \log \overline{\lambda} \tag{6.11}$$

After determining principal stretch measure $\overline{\lambda}$, a smoothing spline fit was used to differentiate $\alpha(t)$ with respect to time to obtain $\dot{\alpha}$. A line was fitted to $\log \dot{\alpha}$ versus

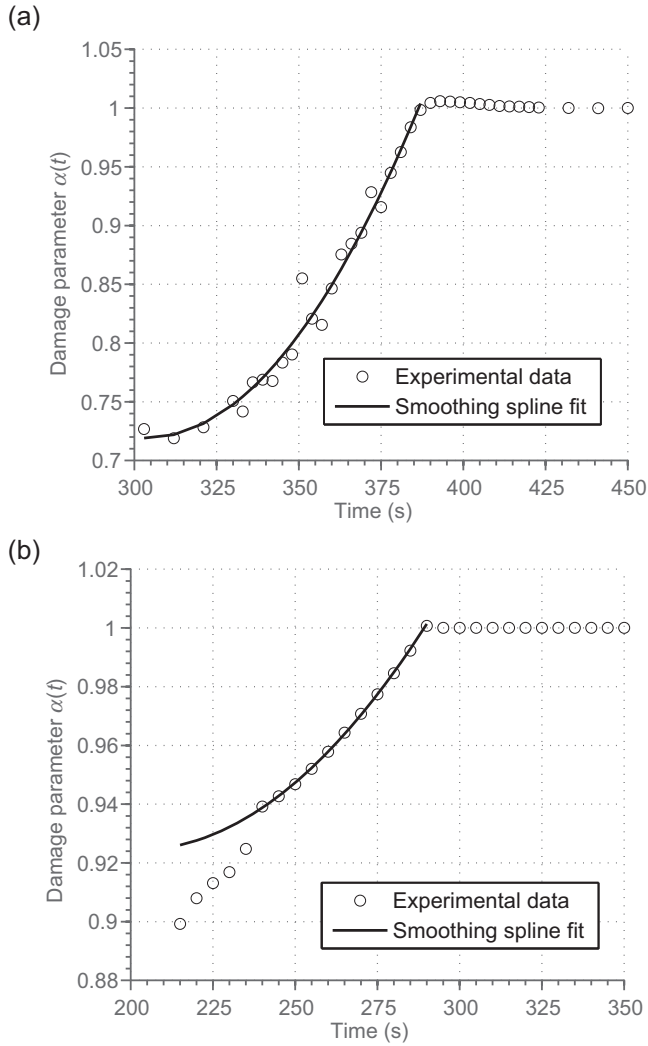

Figure 6.5 Alpha versus time from experiment and smoothing spline fit for (a) pristine specimen and (b) specimen isothermally aged for 1000 h at 260 °C.

log $\overline{\lambda}$ data (after critical stress has been reached) and α_0 and m were calculated from the intercept and the slope of this linear fit. In Figure 6.6(a) and (b), experimental log $\dot{\alpha}$ versus log $\overline{\lambda}$ as well as the linear fit is plotted for a pristine and isothermally aged specimen, respectively. The calculated damage evolution parameters are tabulated in Table 6.1. These material parameters were subsequently used in our FEA model to simulate the delamination growth for pristine as well as isothermally aged specimens. Details of these numerical simulations are presented in the next section.

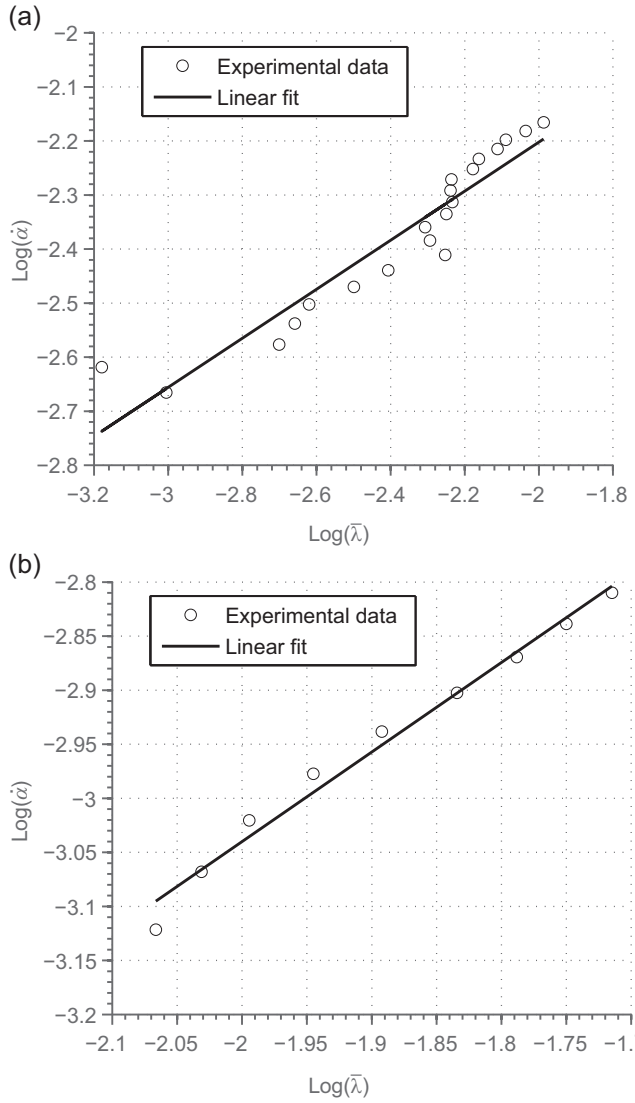

Figure 6.6 log $\dot{\alpha}$ versus log $\bar{\lambda}$ for (a) pristine specimen and (b) DCB specimen isothermally aged for 1000 h at 260 °C.

6.6 Numerical results and discussion

A two-dimensional (2-D) plane strain FEA model using the in-house test-bed code (NOVA-3D) was used to simulate DCB experiments. A 2-D FEA mesh was generated as shown in Figure 6.7. The mesh consists of a total of 2694 eight-noded

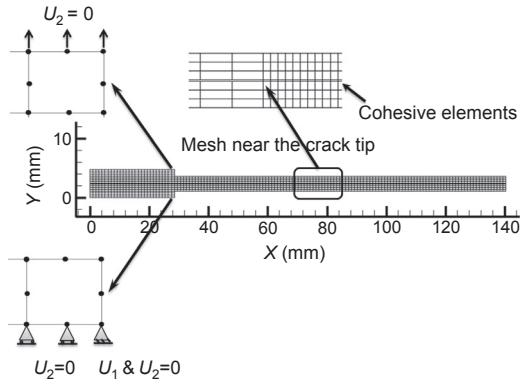

Figure 6.7 Meshed DCB specimen of IM-7/BMI with applied boundary conditions.

quadratic elements, out of which 300 elements are viscoelastic cohesive layer elements placed along the midplane of the DCB specimen. This layer of viscoelastic cohesive elements ahead of the crack tip and along the length of the specimen was employed to simulate delamination in IM-7/BMI laminate. The thickness of cohesive layer elements was carefully chosen to match the thickness of the strain localization zone in the DCB specimens by looking at the high-resolution images taken during the experiments. Using this approach, the cohesive layer thickness used in these simulations was 0.06 mm, which is very small compared with the overall specimen thickness (2.34 mm). Micromechanical damage evolution parameters used in FEA modeling for IM-7/BMI are given in Table 6.1 for pristine and isothermally aged specimens. Elastic properties of IM-7/BMI unidirectional lamina for 0.6 fiber volume fraction were taken from work published by Andrews and Garnich (2008). Significant (~40%) degradation was observed in the elastic material properties of IM-7/BMI after 1000 h of thermo-oxidative aging at 260 °C in air. This degradation was estimated by comparing the initial slope of load displacement curves for pristine and isothermally aged cases. Elastic properties for pristine and aged unidirectional IM-7/BMI composites are given in Table 6.2. The piano hinge attached to the specimen is made of aluminum, and was modeled as such in the FEA simulation. The elastic modulus for aluminum was taken to be 70 GPa and Poisson's ratio was 0.33.

Table 6.2 Elastic properties of transversely isotropic IM-7/BMI lamina

	E_1 (GPa)	$E_2 = E_3$ (GPa)	G_{12} (GPa)	υ_{12}	υ_{23}
Pristine	174	12.1	9.1	0.36	0.45
Aged[a]	104	11.4	7.14	0.36	0.45

[a]Specimens were aged for 1000 h at 260 °C.

The cohesive layer is modeled as a viscoelastic matrix material with evolving damage. The viscoelastic properties for pristine and aged BMI were taken from work done by Luo et al. (2012). Figure 6.7 shows the FEA mesh and boundary conditions used in numerical simulation of the DCB specimen, with a zoomed-in view of the mesh near the crack tip with viscoelastic cohesive elements. From the damage

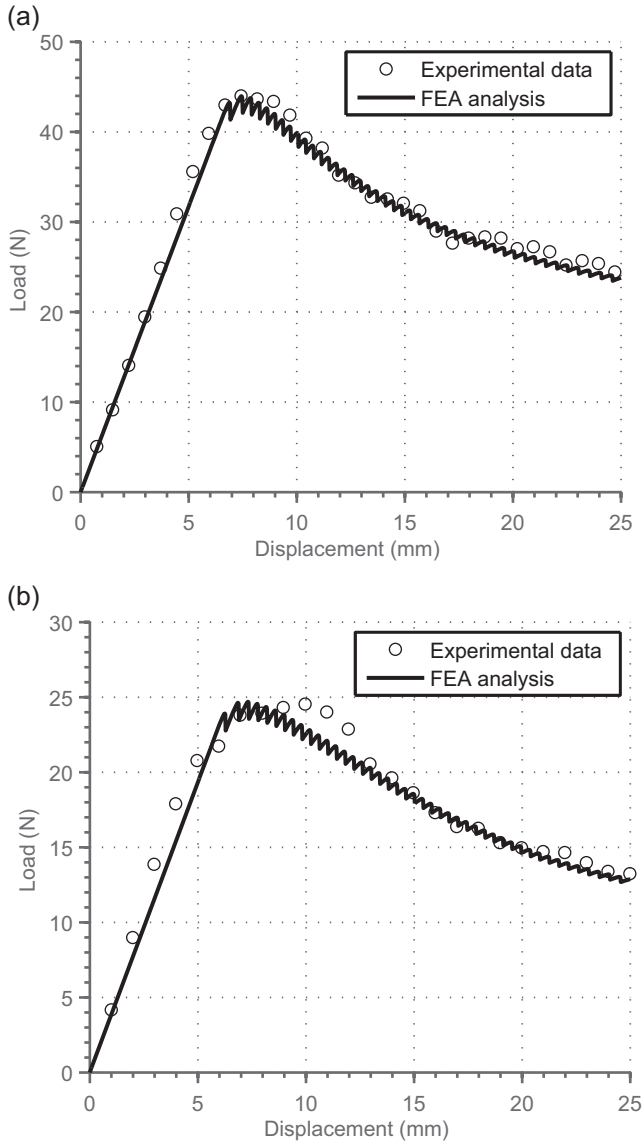

Figure 6.8 Comparison of load versus displacement for DCB experiment: (a) pristine specimen; (b) specimen isothermally aged for 1000 h at 260 °C.

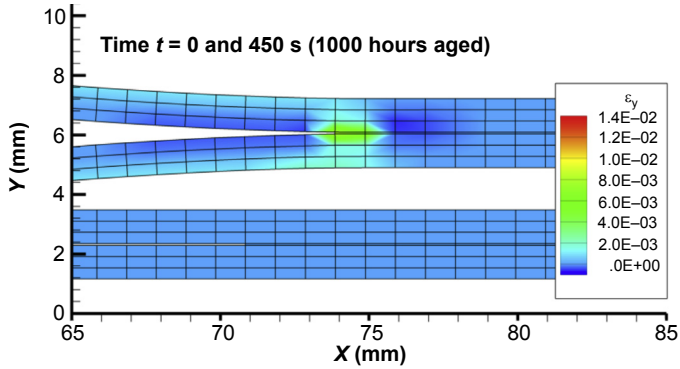

Figure 6.9 Contour plots showing ε_y for specimens isothermally aged for 1000 h at 260 °C, and clearly showing crack propagation from 70 to 74 mm at 450 s.

propagation standpoint, the scalar damage parameter $\alpha(t)$ at each Gaussian integration point in each cohesive element was checked at every time step. The element was deleted if the scalar damage parameter $\alpha(t)$ reached the value of 1 at any gauss point in that element. Ideally, such deleted elements should not have any stiffness at all, but instead of assigning these elements zero stiffness a very small stiffness was prescribed to avoid numerical instabilities. The FEA model was able to accurately simulate the actual DCB experiment at the macro- and micro-scales, as discussed in the next paragraph.

To compare the macro-level load displacement results for the DCB, Figure 6.8(a) and (b) show a comparison of the experimental and simulated load versus displacement curves for pristine specimens and specimens aged for 1000 h at 260 °C, respectively. As can be observed, the FEA simulation results show very good agreement with experimental data, even beyond peak load. The saw-tooth pattern observed in the simulated load displacement curve is due to successive failure of cohesive elements. The applied load drops after a cohesive element fails, and then again increases until the next element failure occurs. Figure 6.9 depicts the ε_y contour plot for an aged case showing strain concentration near the crack tip. A deformed mesh plot depicting crack propagation due to interlaminar delamination at 450 s is also shown in this figure (see deleted elements), and is compared with the undeformed plot (lower plot) showing the original crack location. Comparison of experimentally measured crack propagation length versus time and results from FEA analysis for pristine and isothermally aged specimens are plotted in Figure 6.10(a) and (b), respectively. As is evident from Figure 6.10, the viscoelastic cohesive layer-based FEA analysis accurately captures the crack propagation history. Therefore, unlike most existing models, the multi-scale FEA model presented in this chapter is capable of accurately modeling the macro-level load displacement behavior in conjunction with the micro-level crack growth history, using only three material damage constants, λ_{cr}, α_0, and m.

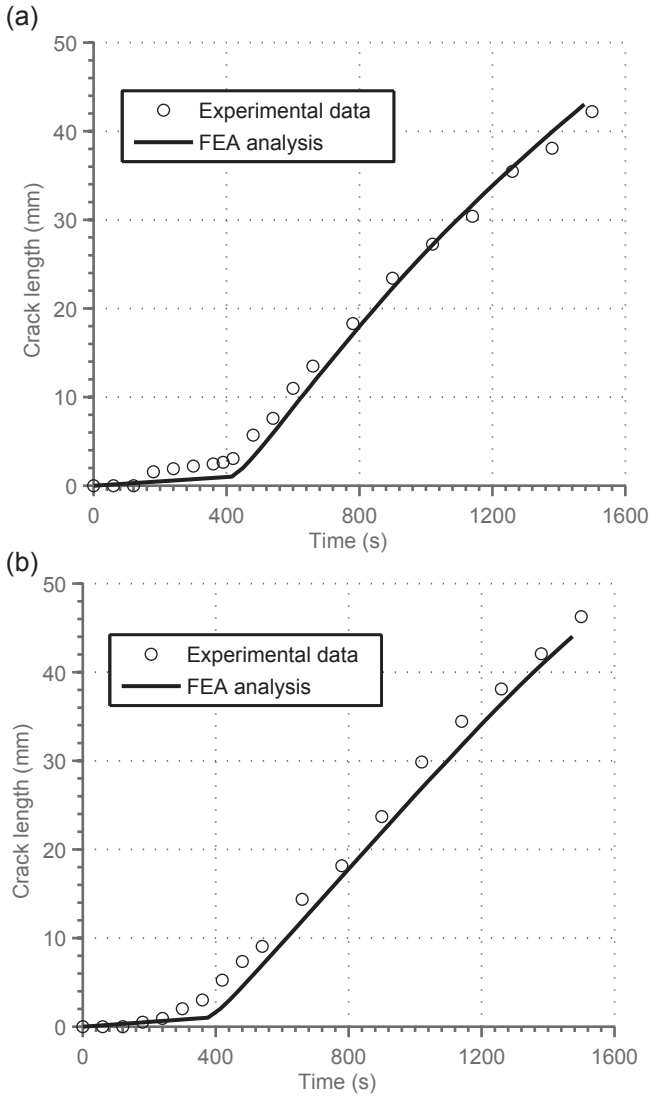

Figure 6.10 Comparison of crack length versus time for DCB experiment: (a) pristine specimen; (b) specimen isothermally aged for 1000 h at 260 °C.

6.7 Conclusions

In this chapter, DCB testing in conjunction with DIC technique is used to experimentally determine the coupled viscoelasticity−damage cohesive law for IM-7/BMI unidirectional composite for both aged and unaged cases. A novel numerical−experimental approach is proposed to determine the micro-scale cohesive layer properties for unidirectional composite from macro-scale observations (J-integral). Assuming the process

zone to be small compared with the specimen size, the J-integral is differentiated with respect to COD to estimate the cohesive stresses in the damage zone ahead of the crack tip. A digital camera in combination with DIC algorithm is used to precisely measure the COD. The damage model used in this work is a principal stretch-based failure model and the critical principal stretch for pristine BMI is found to be 1.0264 from the DIC experiment. The critical stretch value for the isothermally aged BMI is 1.0148, indicating a loss of ductility due to aging. The scalar damage parameters involved in the damage evolution law are estimated by comparing damaged material stresses to the undamaged material stresses. A viscoelastic cohesive zone model is implemented in an in-house test-bed FEA code (NOVA-3D) to numerically simulate the DCB experiment. At the macro scale, the load displacement curve obtained numerically matches very well with the experimental data. At the micro-scale, crack propagation length also shows good agreement with experimentally measured values. Work is currently underway to extend this approach to delaminations under mixed-mode loading.

References

Allen, D., & Searcy, C. (2001). A micromechanical model for a viscoelastic cohesive zone. *International Journal of Fracture, 107*(2), 159−176. http://dx.doi.org/10.1023/A:1007693116116.

Andrews, E. W., & Garnich, M. R. (2008). Stresses around fiber ends at free and embedded ply edges. *Composites Science and Technology, 68*(15−16), 3352−3357. http://dx.doi.org/10.1016/j.compscitech.2008.09.001.

Anthony, J., & Paris, P. (1988). Instantaneous evaluation of J and C*. *International Journal of Fracture, 38*(1), 19−21. http://dx.doi.org/10.1007/BF00034281.

Backlund, J. (1981). Fracture analysis of notched composites. *Computers and Structures, 13*(1−3), 145−154. http://dx.doi.org/10.1016/0045-7949(81)90119-X.

Barenblatt, G. I. (1962). The mathematical theory of equilibrium cracks in brittle fracture. In H. L. Dryden, T. von Kármán, G. Kuerti, F. H. van den Dungen, & L. Howarth (Eds.), *Advances in applied mechanics* (Vol. 7, pp. 55−129). Elsevier.

Daphalapurkar, N. P., Lu, H., Coker, D., & Komanduri, R. (2007). Simulation of dynamic crack growth using the generalized interpolation material point (GIMP) method. *International Journal of Fracture, 143*(1), 79−102. http://dx.doi.org/10.1007/s10704-007-9051-z.

Dávila, C. G., Rose, C. A., & Camanho, P. P. (2009). A procedure for superposing linear cohesive laws to represent multiple damage mechanisms in the fracture of composites. *International Journal of Fracture, 158*, 211−223. http://dx.doi.org/10.1007/s10704-009-9366-z.

Dugdale, D. S. (1960). Yielding of steel sheets containing slits. *Journal of the Mechanics and Physics of Solids, 8*(2), 100−104. http://dx.doi.org/10.1016/0022-5096(60)90013-2.

Fuchs, P. F., & Major, Z. (2011). Experimental determination of cohesive zone models for epoxy composites. *Experimental Mechanics, 51*(5), 779−786. http://dx.doi.org/10.1007/s11340-010-9370-2.

Hillerborg, A., Modéer, M., & Petersson, P. E. (1976). Analysis of crack formation and crack growth in concrete by means of fracture mechanics and finite elements. *Cement Concrete Research, 6*, 773−782. http://dx.doi.org/10.1016/0008-8846(76)90007-7.

Kanninen, M. F., & Popelar, C. H. (1985). *Advanced fracture mechanics*. New York: Oxford University Press.

Li, V. C., & Ward, R. J. (1989). A novel testing technique for post-peak tensile behavior of cementitious materials. In Mihashi, et al. (Eds.), *Fracture toughness and fracture Energy* (pp. 183−195). Rotterdam: Balkema.

Lu, H., & Cary, P. D. (2000). Deformation measurements by digital image correlation: implementation of a second-order displacement gradient. *Experimental Mechanics, 40*(4), 393−400. http://dx.doi.org/10.1007/BF02326485.

Luo, H., Roy, S., & Lu, H. (2012). Dynamic compressive behavior of unidirectional IM7/5250-4 laminate after thermal oxidation. *Composites Science and Technology, 72*(2), 159−166. http://dx.doi.org/10.1016/j.compscitech.2011.10.012.

Needleman, A. (1987). A continuum model for void nucleation by inclusion debonding. *Journal of Applied Mechanics, 54*(3), 525−531. http://dx.doi.org/10.1115/1.3173064.

Remmers, J. J. C., de Borst, R., & Needleman, A. (2008). The simulation of dynamic crack propagation using the cohesive segments method. *Journal of the Mechanics and Physics of Solids, 56*(1), 70−92. http://dx.doi.org/10.1016/j.jmps.2007.08.003.

Roy, S., Dexter, R. J., & Fossum, A. F. (1993). A computational procedure for the simulation ductile fracture with large plastic deformation. *Engineering Fracture Mechanics, 45*(2), 277−293.

Roy, S., & Reddy, J. N. (1987). A finite element analysis of adhesively bonded composite joints including geometric nonlinearity, nonlinear viscoelasticity, moisture diffusion and delayed failure. Accession Number ADA190025, Final Report to ONR.

Roy, S., & Reddy, J. N. (1988). Finite-element models of viscoelasticity and diffusion in adhesively bonded joints. *International Journal for Numerical Methods in Engineering, 26*(11), 2531−2546. http://dx.doi.org/10.1002/nme.1620261111.

Sorensen, B. F., & Jacobsen, T. K. (2003). Determination of cohesive laws by the J integral approach. *Engineering Fracture Mechanics, 70*(14), 1841−1858. http://dx.doi.org/10.1016/S0013-7944(03)00127-9.

Stigh, U. (1987). Initiation and growth of an interface crack. In G. Verchery, & A. H. Cardon (Eds.), *Mechanical behaviour of adhesive joints: Proceedings of the european mechanics colloquium 227* (pp. 237−248). Paris, France.

Stigh, U. (1988). Damage and crack growth analysis of the double cantilever beam specimen. *International Journal of Fracture, 37*(1), R13−R18. http://dx.doi.org/10.1007/BF00017826.

Upadhyaya, P., Singh, S., & Roy, S. (2011). A mechanism-based multi-scale model for predicting thermo-oxidative degradation in high temperature polymer matrix composites. *Composites Science and Technology, 71*(10), 1309−1315. http://dx.doi.org/10.1016/j.compscitech.2011.04.018.

Williams, J. G. (1984). *Fracture mechanics of polymers.* Ellis Horwood Series in Engineering Science, Chichester.

Yang, Q., & Cox, B. (2005). Cohesive models for damage evolution in laminated composites. *International Journal of Fracture, 133*, 107−137. http://dx.doi.org/10.1007/s10704-005-4729-6.

Yang, Q. D., Cox, B. N., Nalla, R. K., & Ritchie, R. O. (2006). Re-evaluating the toughness of human cortical bone. *Bone, 38*, 878−887. http://dx.doi.org/10.1016/j.bone.2005.10.014.

Yang, Z. J., & Deeks, A. J. (2007). Fully-automatic modelling of cohesive crack growth using a finite element-scaled boundary finite element coupled method. *Engineering Fracture Mechanics, 74*(16), 2547−2573. http://dx.doi.org/10.1016/j.engfracmech.2006.12.001.

Zhang, Z., & Paulino, G. H. (2005). Cohesive zone modeling of dynamic failure in homogeneous and functionally graded materials. *International Journal of Plasticity, 21*(6), 1195−1254. http://dx.doi.org/10.1016/j.ijplas.2004.06.009.

Modeling of damage evaluation and failure of laminated composite materials across length scales

7

S. Lurie[1], *M. Minhat*[2]
[1]Institute of Applied Mechanics of Russian Academy of Sciences, Moscow, Russia;
[2]UniKL Malaysian Institute of Aviation Technology, Dengkil, Malaysia

7.1 Introduction

The evolution of damage in fiber-reinforced composite materials is a complex process due to the heterogeneity and anisotropy of these materials. Unlike the case for metallic materials, when fiber-reinforced composites are subjected to static or cyclic loading conditions at relatively high amplitudes, they accumulate damage in scattered rather than localized fashion. This *damage-accumulation* process, which is related to the initiation and growth of damage, often reduces the elastic properties of composite materials, a well-known phenomenon commonly referred to as *stiffness degradation* (Bazant, Daniel, & Li, 1996; Davila, Camanho, & Rose, 2005; Harris, 2003; Hinton & Soden, 1998; Jain & Ghosh, 2009; Rosen, 1964; Rosen & Dow, 1972; Tsai & Wu, 1971; Vasiliev & Morozov, 2013; Vasiliev & Tarnopolskii, 1990). In fact, the change in stiffness due to degradation is generally greater than the change in residual strength of a fiber composite material, during its fatigue life (Vassilopolous & Keller, 2011). Furthermore, failure in a composite does not always result solely from a single macrocrack propagating in the structure, since the formation of microdefects always precedes that of macrocracks (Gamstedt & Andersen, 2001; Obchiskii, 1988; Tamuja & Pratacova, 1986; Vasiliev & Morozov, 2013; Vasiliev & Tarnopolskii, 1990; Vassilopolous & Keller, 2011). Depending on the level of inhomogeneity and anisotropy, as well as the loading conditions applied, various microdamage mechanisms are initiated; these can appear and grow independently or in combination, and lead to various scenarios of property degradation and composite material failure (Camponeschi & Stinchcomb, 1982; Gamstedt & Andersen, 2001; Johnson & Chang, 2001a,b; Obchiskii, 1988; Tamuja & Pratacova, 1986; Vasiliev & Morozov, 2013; Vasiliev & Tarnopolskii, 1990; Vassilopolous & Keller, 2011; Yang, Jones, Yang, & Meskini, 1990). Moreover, mechanisms of property degradation and composite failure depend on the scaling parameters of the composite structure (Beaumont & Sekine, 2005; Dudchenko, Lurie, & Halim, 2006; Johnson & Chang, 2001a,b;

Structural Integrity and Durability of Advanced Composites. http://dx.doi.org/10.1016/B978-0-08-100137-0.00007-9

Kwon, Allen, & Tarelja, 2008; Lurie, 1994; Singh & Talreja, 2010; Soutis & Beaumont, 2005). As such, multiscale approaches for modeling the damage-accumulation process in relation to property degradation are necessary. Suffice it to say, once again, that these microdamage mechanisms and scale parameters, as observed experimentally, play decisive roles in the property degradation, failure, and destruction of fiber-reinforced composite materials. Nevertheless, the processes of composite material damage and failure related to the appearance and growth of macrocracks, as well as the total destruction of the composite structure, are not the central themes of our research problem. Instead, we are focused on modeling the damage accumulation and property degradation associated with the birth and growth of microdefects in a fiber-reinforced composite system. As we shall see, multiscale models of damage accumulation and property degradation are formulated using a mechanism-based approach. Since physical modeling forms the foundation of our approach, in the next section we address the typical underlying microstructural mechanisms of damaged fiber composites.

7.2 Microdamage mechanisms in fiber-reinforced composites

In this section, we briefly describe some typical microdamage mechanisms initiated and accumulated in fiber-reinforced composite laminates. The idea is to emphasize typical and primary damage mechanisms that cause property degradation in composite materials, rather than providing a comprehension exposition on the damage-accumulation process that leads to failure of microdamage mechanisms at the ply and constituent scales for fiber composite materials under differential loading conditions.

7.2.1 Typical microdamage mechanisms

Some microdamage mechanisms are readily apparent during the manufacturing process (built-in defects), such as volumetric voids in matrix, broken fibers, fiber misalignment, and disbonds (interface areas that have become unbonded as a result of the debonding process) at fiber−matrix interfaces. Although these mechanisms are very small and therefore unlikely to induce the final failure of the composite, they can degrade its effective properties as they accumulate. Likewise, voids can adversely affect the mechanical properties of composite materials (Beaumont & Sekine, 2005; Dudchenko et al., 2006). These voids, broken fibers, and disbonds can also act as stress risers, accumulating and/or initiating other microdamage mechanisms when loads are initially applied to composites. As such, these damage processes, depending on their sizes, shapes, and distributions, may seriously affect the deformation behavior and failure of fiber composite materials.

Damage evolution or development in fiber-reinforced composite materials starts early in the loading process due to the inherent inhomogeneity of composites

(Uhl, Lucht, Jeong, & Hsu, 1988); that is, the mismatched properties of fiber, matrix, and interfaces, as well as anisotropy—that is, a fiber's orientation in laminate, and the directional properties of fibers and matrices such as isotropic and transversely isotropic. Due to these characteristic of composites, severe inhomogeneous stress and strain fields develop when external loads are applied (Ghiorse, 1993). Stress inhomogeneity in composites is further enhanced by geometric-scale structural parameters such as fiber volume fraction, ply thickness, number of layups, and localized fiber spacing and packing. Moreover, built-in defects can further increase the stress inhomogeneity of composites. As a result, some microvolumes in the composite have higher localized stress than others, leading to the initiation of the same or new types of microdamage in constituents and interfaces, and expansion of prior microdamage if higher localized stresses exceed their particular strength limits in the early loading process. As load is increased in quasistatic loading, or the number of loading cycles is increased in fatigue loading, additional microdamage is initiated and subsequently grows; this damage-accumulation process leads to further severe stress inhomogeneity and stress redistribution in the composite, due to the increased presence and larger size of microdefects. As a result, a change or reduction in the effective properties of a fiber composite material occurs as the magnitude of load or number of loading cycles is increased. Toward the middle and final stages of the loading process, some microdamage may reach saturation points or coalesce, forming additional microdamage mechanisms and causing macrocracks to appear, which may then lead to the final failure of the fiber composite material. Here, we are mostly interested in microdamage mechanisms initiated and grown during early and middle stages of composite material loading processes (see Figure 7.1).

As mentioned earlier, apart from a composite's inhomogeneity and anisotropy, microdamage mechanisms are initiated based on the loading conditions applied to

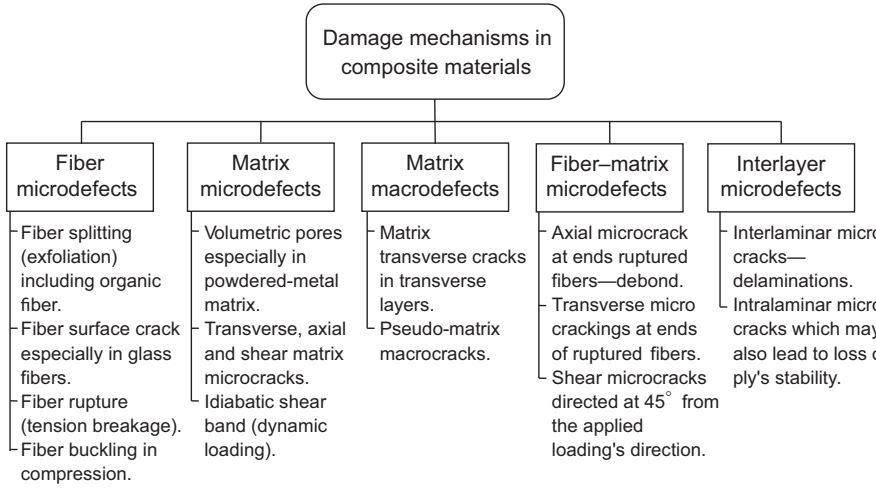

Figure 7.1 Classification of microdefects and a few important macrodefects found in composite materials.

the composite material. For a unidirectional fiber composite under quasistatic or cyclic tensile loading along the fibers, virtually all of the load is carried by the fibers, so individual fibers will fail at their weakest points. Flaws within the fiber architecture, or built-in defects in and adjacent to the fibers, may define these weak points. In any case, fiber breakage is the primary damage mechanism in the early loading process, and controls local microdamage development and accumulation leading to final failure of the composite. This is because when fiber breakage occurs, local stress in the vicinity of the broken fiber is perturbed, thus causing stress redistribution between the fibers and the matrix. Zero stress occurs at the fiber breakage location, with stress gradually restored some length from the break—this length is known as an ineffective length (see Figure 7.1). Furthermore, the stress is redistributed to adjacent fibers through the fiber−matrix interface and matrix, resulting in an area of higher stress concentrated in the vicinity of broken fibers and creating additional fiber breakage if the fiber's strength limit is exceeded. This high-concentration local area is also likely to initiate additional microdamage mechanisms in the matrix and at the interface, such as transverse microcracks (cracks perpendicular to the fiber) and longitudinal microcracks (cracks parallel to the fiber). A transverse microcrack in the matrix can grow from the ends of broken fibers to reach neighboring fibers. At this point, if the crack continues to propagate around adjacent fibers, a fiber-bridge crack is said to occur. On the other hand, the crack may be arrested at the interfaces of adjacent unbroken fibers, thus initiating longitudinal microcracks at adjacent fibers. In a longitudinal microcrack initiated by a broken fiber, the crack propagates at the fiber−matrix interface, which is known as debonding, or alternatively in the matrix. Scenarios of damage progression depend on interfacial adhesion strength, thus emphasizing the significant role of the interface in the microdamage mechanisms of composite materials (Bolotin, 1984; Drzal & Madhucar, 1993; Dzenis & Qian, 2001; Pagano, 1993; Paipetis & Galiotis, 2001; Reifsnider, 1994; Tsai & Hahn, 1980). If the interface is strong, transverse matrix microcracks will appear and grow; if it is relatively weak, axial or longitudinal interface microcracks will develop and accumulate.

For multidirectional laminates subjected to quasistatic and fatigue tensile-loading conditions, the axial or longitudinal plies are still the critical structural elements that sustain applied loading and retain the functionality of the composite structure. However, microdefects that develop and accumulate in transverse and symmetric off-axis plies of the laminate, as well as the stacking sequences of these plies, can significantly influence the performance of the longitudinal plies in the composite; that is, the rate of initiation and accumulation of microdamage mechanisms in transverse and off-axis plies can adversely affect the inhomogeneous stress distributions in longitudinal plies, hence influencing the birth and growth rates of the microdamage mechanisms described earlier. Let us consider the typical damage evolution in cross-ply laminates under quasistatic tensile or fatigue loading conditions. During initial loading, disbonds and matrix microcracks may appear in transverse plies. Of the two damage indicators, debonding microdamage is likely to dominate in transverse plies, as in most cases both the fiber and the matrix are stronger than the interface. As loading continues, unbroken fibers located near disbonds act as stress risers,

and matrix microcracks begin to appear. These cracks then coalesce with disbonds to eventually form cracks that span the thickness of the transverse ply. A series of multiple transverse-ply cracks can occur in the respective plies. In turn, the appearance of transverse-ply cracks creates high-concentration areas at the interfaces between transverse and axial plies, which can lead to ply-separation microdamage that is better known as delamination or interlaminar cracking. Delamination, depending on its size and distribution, can severely impair the functionality and integrity of fiber composites under tensile and tension−compression fatigue loading, and also under compressive loading conditions (Drzal & Madhucar, 1993; Pagano, 1993). Delamination is also likely to occur at the edges of composite structures. When off-axis plies are present in the laminate, such as the case with quasi-isotropic laminates, similar damage evolution can be seen, although microcracks in off-axis plies are initiated at higher applied axial strains than they are in transverse plies; curved or oblique microcracks form in off-axis plies as well. Ply orientation, group thickness, stacking sequence, and loading direction may significantly affect the initiation and accumulation of the microcracks described earlier, thus affecting the property degradation and failure of composite materials.

In compressive quasistatic and fatigue loading of unidirectional laminate, it is generally accepted that fiber microbuckling/kink-band formation is the main contributor to the failure of longitudinal plies (Budiansky & Fleck, 1993; Fleck, 1997; Guz, 1990; Kachanov, 1988; Soutis, Fleck, & Smith, 1991; Tsampas, Greenhalgh, Ankerson, & Curtis, 2012). When a composite is increasingly loaded, the fiber fractures at two points, an event often initiated by initial built-in defects such as fiber misalignment. The kinking process then occurs abruptly and may lead to catastrophic failure of the fiber composite material. Due to redistribution of stress around the damaged fiber, other types of defects are induced, and upon increased loading, microcracks in the matrix, disbonds at fiber−matrix interfaces, and delamination between plies may develop. Accordingly, interactions among these damage mechanisms are important to the damage growth and catastrophic failure of fiber composite materials under compressive loading conditions. However, due to the very short duration of the kinking process, the actual mechanism that leads to kink-band formation is still being debated; that is, it has been argued that ply splitting is the mechanism that causes kink-band formation, rather than fiber microbuckling (Tsampas et al., 2012). The formation, growth, and interaction of microdamage mechanisms that lead to catastrophic failure are still vague, at least from a microscopic point of view, especially at the constituent scale. This is true for both multidirectional laminates subjected to quasistatic and fatigue compressive loads, and unidirectional and multidirectional laminates subjected to tension−compression and multiaxial fatigue loading conditions. Nevertheless, these loading conditions are more damaging to composite materials, and the development and accumulation of their underlying microdamage mechanisms, especially at the constituent scale, have not been entirely defined.

Based on data from the literature, here we propose several important classifications of microdefects, as well as a few important macrodefects, observed in composite materials under various loading conditions (see Figure 7.1).

7.2.2 Micromechanical model of damage-accumulation process and stiffness degradation in composite materials

As discussed earlier, modeling the damage-accumulation process and stiffness degradation is an enormous challenge when we consider the numerous parameters that may influence various governing damage mechanisms that are initiated and grow in fiber composite materials. Due to this difficulty and complexity, most industry research and practices have taken the empirical path. This approach, although it provides simplicity for practical purposes, with an empirical mathematical model fitted to experimental data, can be very cost-ineffective, as the scope of experimental programs could be massive. Furthermore, predictive ability beyond the boundaries of experimental constraints may well be limited. On the other hand, a more viable approach—mechanism-based—has more predictive power if one understands the underlying physical mechanisms of the composite damage-accumulation process. As mentioned earlier, however, addressing all physical mechanisms, especially with the large number of composite material parameters such as constituent properties, stacking sequences, ply orientations, and other complex architectures and geometries, is challenging. As an alternative, one could focus on the essential damage mechanisms that largely control damage processes under specific loading conditions applied to composite structures, and establish their relationships with continuum micromechanical models, using empirical data for model refinement (Beaumont & Sekine, 2005).

7.3 Modeling microdefect evolution in a lamina and stiffness degradation of unidirectional composites

In this section, we shall evaluate damage evolution in composite material at a lamina level. In describing damage behavior of fiber-reinforced composite structures, we are interested in defining this behavior based on some local measure of damage in real time as it accumulates. Moreover, it is desirable to include both the birth and the growth processes of microdefects simultaneously in order to accurately describe the damage-accumulation process in composite structures, which in turn influences the effective characteristics of the composite material. We propose that the microdamage-accumulation process is basically a consequence of actions governed by physical thermodynamic laws—an entropy-based approach. The entropy-based approach seems promising when estimating damage increment, which is associated with kinetic and diffusion processes, chemical reactions, and thermal effects, as well as an inelastic material system (Kanaun & Chudnovskii, 1970; Kiyalbaev & Chudnovskii, 1970; Lurie, 1994; Soborejo, 1967). A micromechanical approach is utilized to associate the damage state of a material with its properties, and empirical parameters are used with the proposed micromechanical model to precisely describe property degradation effects (Dudchenko et al., 2006; Luat, Lurie, & Dudchenko, 2010; Movchan, 1990). Since the damage-accumulation process is modeled at the lamina scale, we may assume that the scale that is characteristic of microstructures in damaged lamina; that is, fiber diameters, distances between fibers, sizes of various

microcracks, etc., can be considered. Hereafter, we shall refer to this entropy-based damage-accumulation model as the *kinetic model*. Later in this section, a micromechanical degradation model associated with the kinetic model is presented to describe property degradation in a unidirectional composite.

7.3.1 Features of kinetic model of the evolution of microdefects

Here, we will introduce some basic requirements for the kinetic model. Firstly, damage parameters involved in the kinetic model, which will be associated with the stress and strain distribution in composite lamina, will be defined using micromechanical parameters at the microstructural scale; that is, the length or size of microcracks. The use of appropriate techniques allows us to develop some procedures or schemes that can measure the level of damage in composite lamina that is subjected to appropriate loading conditions. In such an approach, we assume that damage can be portrayed by some state variables, and together with stress and strain variables, they obey the laws of thermodynamics (the entropy-based approach) (Lurie, 1994; Soborejo, 1967). As a result, it is possible to write some formal relationships among the stress, strain, and damage parameters. Secondly, as mentioned earlier, it is necessary for the kinetic model to consider simultaneously the two processes that cause damage increments in composite material: the birth of new microdefects, and the growth of existing and new microdefects. Next, some features and characteristics of microdefects will be given.

7.3.1.1 Characteristics of microdefects

First, we need to explain certain characteristics of microdefects, which can be designated as microparameter s. In general, this parameter can be understood as the length or area of the microcrack in the matrix material, the length of matrix delamination (debonding) from fiber, the length or squared length of a crack between layers, and the volume of micropores. This microparameter can be further characterized by the ratio of stress intensity at the crack tip to the actual stress value in a lamina.

For the different types of microdefects, various measures of microparameter s_i are introduced; these may be scalars, vector functions, or tensors. For example, a flat microdefect is characterized by a vector; that is, its length is equal to the magnitude of a vector running from tip to tip of a microcrack, and its direction coincides with a normal vector defined in the specific coordinate system of the composite structure. In most cases, a scalar measure of microdefects is used. Another characteristic of these microparameters is that they must be invariant to transformation of a coordinate system that represents elements in linear space. In other words, these parameters can be determined with usual mathematical operations such as summation, subtraction, and multiplication, and give the same values regardless of the coordinate system used.

Last, to fully describe the damage-accumulation process, we introduce a monotonically increasing parameter t, which depends on the nature of loading conditions applied to composite material. For static or quasistatic loading conditions, this parameter can be represented by the stress or strain level, length of loading or deformation

arc, etc. For cyclic loading conditions, this parameter is usually related to the number of loading cycles n.

7.3.1.2 Kinetic damage-accumulation model

Here, we shall first introduce a general damage characteristic S, defined as the sum of all microdefects s_i available at a given point of the damage process in the representative volume element being considered. Furthermore, we shall consider that property degradation also depends on this damage value. For specific types of microdefects, the value s varies during the loading process; that is, it depends on the process parameter t and the parameter value t_0, which is the time at which the microdefect is born or initiated. Thus, we have

$$s = s(t, t_0) \tag{7.1}$$

The birth (initiation) process of microdefects in the present representative volume of a material is given by the value that defines the birth rate of microdefects $v(t,S)$. Let N be the number of microdefects in a lamina. In order to calculate the number of microdefects initiated over the small time interval dt_0, we use the following formula:

$$dN = v(t_0, S)dt_0 \tag{7.2}$$

By using Eqns (7.1) and (7.2), the total damage defined by the amount of microdefect initiated in the interval dt_0 to time t can be found as

$$dS(t, t_0) = s(t, t_0)v(t, S)dt_0$$

Thus, by integrating the last equation shown above, the measure of damage caused by the emergence of microdefects at different intervals can be represented as

$$S = \int_0^t s(t, t_0)v(t_0, S)dt_0 \tag{7.3}$$

Here we note that the parameter S shown in Eqn (7.3), which characterizes the overall state of damage, satisfies the Volterra integral evolution equation.

Next, we shall define the development or growth process of microdefects using the following differential function:

$$ds/dt = f(t, s, S) \tag{7.4}$$

Combining Eqns (7.3) and (7.4), we have

$$dS/dt = s(t, t)v(t, S) + \int_0^t f(t, s(t, t_0)v(S, t_0)dt_0 \tag{7.5}$$

We can expand the function $f(t,s,S)$ in Eqn (7.4) by using small-parameter Taylor expansion s and limiting ourselves to the first two terms. Finally, based on Eqns (7.2), (7.4), and (7.5), we obtain the following system of kinetic equations describing the whole damage-accumulation process:

$$\mathrm{d}N/\mathrm{d}t = v(t,S), \quad \mathrm{d}s/\mathrm{d}t \approx a(t,S) + b(t,S)s$$

$$\mathrm{d}S/\mathrm{d}t \approx s_0 v(t,S) + b(t,S)S + a(t,S)N \tag{7.6}$$

Here, $a(t,S)$ and $b(t,S)$ are scalar microparameters related to the growth of microdefects. Finally, the system of kinetic equations shown in Eqn (7.6) should satisfy these initial conditions:

$$S|_{t=0} = S_0, \quad s|_{t=0} = s_0, \quad v|_{t=0} = v_0 \tag{7.7}$$

The resulting system of kinetic equations could be generalized to the case where local microdefects and total damage are characterized by tensor parameters.

7.3.2 Damage-accumulation process in lamina—birth and growth of microdefects

In this section, we shall consider several variants of the damage-accumulation process using the two kinetic Eqns (7.6) and (7.7) given in the previous section. Some examples showing the birth and growth process for typical microdefects will be illustrated.

7.3.2.1 Models of the birth and growth of microdefects—matrix microcracking and fiber–matrix debonding

Here, we model the damage-accumulation process using several damage scenarios that typically occur in fiber composite materials subjected to either quasistatic or fatigue loading conditions.

Case 1. Let us consider the birth process of microdefects in which the birth rate is constant ($v = v_0 =$ constant). As such, we have

$$\mathrm{d}N/\mathrm{d}t = 0$$

We then assume that the growth rate of such microdefects does not depend on the size of microdefects

$$\mathrm{d}s/\mathrm{d}t = a(t), \quad b(t) = 0$$

Thus, all of these microdefects, regardless of whether they are small (i.e., just being initiated) or large (i.e., microdefects that appeared in earlier stages of the loading process and have grown over time), will grow at the same rate. This growth

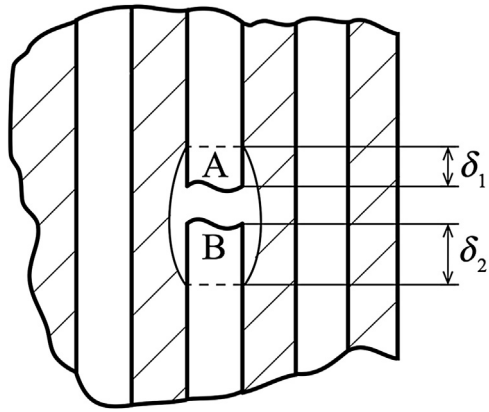

Figure 7.2 Debonding of fiber−matrix at broken fiber ends.

rate is notable because it depends only on loading process parameters. Such growth processes are typically found in disbonds—microcracks at the fiber−matrix interface near broken fiber ends (see Figure 7.2). Such microdefects occur under static and cyclic loading if joint strength (i.e., adhesion) between the matrix and reinforcing element is weaker than matrix shear strength. In this case, the damage state s represents the length of the disbond (the area that has been debonded), $s = \delta_1 + \delta_2$.

For static loading ($t \equiv \sigma$), the coefficient $a(t)$ does not depend on delamination length but on the applied stress σ. Nevertheless, in the first approximation, coefficient $a(t)$ could be considered independent of the actual stress. Considering this simple model of debonding occurring at broken fiber ends, where we assume that the following relationships are valid for kinetic equations (7.6) and (7.7)—$dN/dt = 0$, $v = v_0 = \text{constant}$ and $s_0 = \text{constant}$—with a zero initial condition for the total damage characteristic, the solution to kinetic Eqn (7.6) can be obtained as

$$S = s_0 vt + (1/2)avt^2 \tag{7.8}$$

When the initial disbond length is much greater than its incremental length during the growth process—that is, $s_0 \gg at$—total damage S becomes a linear function of the process parameter. On the other hand, if incremental growth in the disbond length is greater than its initial value—that is, $s_0 \ll at$—the damage process is accelerated.

Under cyclic loading conditions (stress or strain), it is possible to propose that delamination growth in each half cycle does not depend on the number of loading cycles. We can then estimate the growth rate of disbond length per cycle as follows:

$$ds/dt = 2c_1\sigma_a \quad \text{if } \sigma_{\min} > 0, \quad \sigma_a = (\sigma_{\max} - \sigma_{\min})/2,$$

and

$$ds/dt = c_1\sigma_{max} - c_2\sigma_{min} \text{ if } \sigma_{min} < 0,$$

where c_1, c_2 represent the delamination growth rate under tension and compression, respectively.

Case 2. For most microdefects, the growth rates of microdefects in composite lamina depend on their current lengths, for which the following equalities are used:

$$a(t) = 0, \quad ds/dt = b(t)s$$

In this case, when the damage growth process occurs in a constant condition, we have exponential growth of microdefects; that is,

$$s = s_0 \exp b(t - t_0) \text{ when } t \geq t_0$$

For example, the growth rate of fatigue microcracks in metals is proportional to the current length of such microcracks, if the current length exceeds the grain size of a material. Such a model of microdefect growth is typical for longitudinal matrix microcracks in composite lamina, and also for longitudinal debonding microcracks oriented along the direction of the reinforcements, which usually occur in the transverse ply. Here, the damage kinetic Eqn (7.6) has the simpler form

$$dS/dt = s_0 v + bS$$

Solving the above equation using the initial conditions, we obtain

$$S = s_0 v(\exp(bt) - 1)/b \tag{7.9}$$

If there are barriers to microdefect growth, the microdefect growth rate will decrease as microdefects reach barriers. In this case, we must use the following relationship:

$$ds/dt = b(t)\cdot(d - s)$$

where d is the geometric parameter; that is, the grain size or the distance between layers or fibers in the composite, s is the length of microcrack, and $b(t)$ is an initiation model parameter that depends on specific loading parameters. The above equation might not be suitable for describing *longitudinal* microcracks in the matrix or the interfaces of transverse plies—total damage from longitudinal microcracks is more appropriately described by Eqn (7.9)—but is appropriate for *transverse* microcracks such as those shown in Figure 7.3. Parameter δ defines an ineffective length.

Such a model is notable because it can describe the damage development of penny-shaped microcracks of mode 1 (transverse microcracks of normal opening mode) at the ends of fiber breaks. In this case, s is the radius of the disklike crack $d = R - r$, R is the

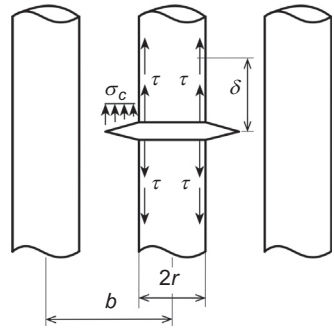

Figure 7.3 Matrix microcracks in the normal opening mode in fiber composites.

distance between the center of adjacent fibers, and r is the filament radius. In this case, parameter $b(t)$ does not depend on s, but is a function of applied stress only. For such a damage process, the kinetic equations can be integrated to give us

$$S = v\mathrm{d}t - (v/b)(d - s_0)[1 - \exp(-bt)] \tag{7.10}$$

Next, we examine the damage-accumulation process for the three cases described by Eqns (7.8)–(7.10): (1) microcracks associated with fiber–matrix debonding at broken ends of fibers in longitudinal plies, (2) transverse microcracks occurring at broken ends of fibers, and (3) longitudinal microcracks that develop in the direction of reinforcement elements in transverse plies. The results are illustrated in Figure 7.4. It should be remembered that all three processes are assumed to occur with a constant birth rate of microdefects. Furthermore, the asymptotic

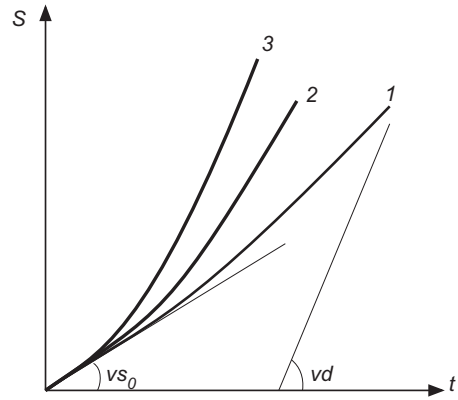

Figure 7.4 Schematic curves of damage accumulation in fiber composite material, defined by the following microdefects: curve 1 represents matrix microcracks of normal opening mode at the broken ends of the fiber, curve 2 signifies fiber–matrix debonding at broken ends of the fiber, and curve 3 represents longitudinal microcracks developed along reinforcement fibers in a transverse ply.

behavior for small values of process parameter t is equal; that is, they have a common tangent at zero defined by the equation $S = vs_0t$. Here, the slowest damage growth is for transverse microcracks with normal opening mode (curve 1), and the next slowest growth is for fiber–matrix debonding at the broken ends of fibers (curve 2). Interestingly, damage from longitudinal or axial microcracks, having the asymptote $(vd)t$, occurs more rapidly than it does from other types (curve 3). This indicates that longitudinal or axial microdamage can lead to severe property degradation in the composite structure. Nevertheless, this microdefect, which occurs in transverse plies of the laminate and leads to ply cracking, is not determinative; that is, axial microcracks are generated only at the initial state, and the formation of new microdefects stops upon reaching a saturation point (Reifsnider, 1988; Reifsnider & Highsmith, 1981).

For concrete examples, let us consider two typical loading processes that contribute to the microdamage described earlier. The purpose of this example is to show the relationship between the proposed kinetic and empirical models, in order to precisely describe the damage-accumulation process in a unidirectional composite subjected to differential loading conditions.

1. Damage-accumulation process for microdefects that are associated with fiber–matrix debonding at broken fiber ends under quasistatic loading. The system of kinetic equations is as follows:

$$\mathrm{d}s/\mathrm{d}t = b, \quad \mathrm{d}N/\mathrm{d}t = v, \quad \mathrm{d}S/\mathrm{d}t = s_o v + bN$$

The above system has damage-accumulation conditions that differ from those described in Case 1, although both equations represent the same type of microdefect. We shall assume that for quasistatic loading condition $t = \sigma/\sigma_b$, we have $N = A(\sigma/\sigma_b)^m$ and $v = Am(\sigma/\sigma_b)^{m+1}$, and that σ_b is the tensile strength of the composite. Integrating the kinetic equation and satisfying the initial conditions, we have the following relationship:

$$S = A\left[s_o(\sigma/\sigma_b)^m + b(\sigma/\sigma_b)^{m+1}/(m+1)\right]$$

Based on known experimental data, it can be argued that the parameter m is normally large enough for static loading conditions, and thus the damage-accumulation process is accelerated.

2. Damage-accumulation process for microdefects that are associated with the same mode of damage described above, but with the composite subjected to cyclic loading conditions. Under cyclic loading condition $t = n$, with a positive cycle asymmetry where $r = \sigma_{\max}/\sigma_{\min} > 0$, the kinetic model gives the following relationship:

$$S = \frac{A}{k}\left[\left(\sigma_{\max}/\sigma_{b_1}\right)^m - \left(|\sigma_{\min}|/\sigma_{b_2}\right)^m\right]\left(s_0 n^k + 2c_1\sigma_a\frac{n^{k+1}}{(k+1)}\right)$$

For negative cycle asymmetry $\sigma_{\min} < 0$, by considering that damage does not increase with decreasing $|\sigma|$, we have

$$\Delta N = \left[A_1\left(\sigma_{\max}/\sigma_{b_1}\right)^{m_1} + A_1\left(|\sigma_{\min}|/\sigma_{b_2}\right)^{m_2}\right] n^{k-1}$$

Integrating the kinetic equation and satisfying the initial conditions, we obtain

$$S = \frac{1}{k}\left[A_1\left(\sigma_{\max}/\sigma_{b_1}\right)^{m_1} + A_1\left(|\sigma_{\min}|/\sigma_{b_2}\right)^{m_2}\right] s_0 n^k + (c_1\sigma_{\max} - c_2\sigma_{\min}) n^{k+1}/(k+1)$$

Here, σ_{b_i} represents limiting stresses under tension and compression, and based on the experimental data, we normally have a parameter k value of nearly 1: $0 < k < 1$ and $1 \sim< k + 1$.

Case 3. Finally, we construct a kinetic model for a unidirectional composite lamina subjected to off-axis fatigue loading with angle α. The microcrack typically appears in the matrix and grows in a plane perpendicular to the direction of loading until it reaches the adjacent fibers. The microcrack resembles the typical shear-mode delamination (mode II and/or III) of quasibrittle material systems (Bradley, Corleta, & Goetz, 1987; Clarke & Bader, 1986). Furthermore, crack growth appears to stop short of the nearest adjacent fiber. However, the adjacent fiber is not the only barrier, as there are certainly fibers just at the top or beneath the plane that are responsible for arresting the process of crack growth. Nevertheless, the crack growth process does not stop there, but instead changes direction and begins to grow along the fibers (see Figure 7.5).

For structures with a high volume fraction of fiber, the duration of the change in direction during the crack growth process is negligible. Therefore, this process can be considered a single act of originating a complex microdefect (oblique microcrack). The relationship that determines the initial length of the microdefect is given as $s_0 = (d - 2r)\,tg\alpha$. The damage-accumulation process of microdefects in the absence of barriers has been considered previously, and is well-described by the relationship $ds/dt = b\,s$, $(t = n)$. On the other hand, let us consider Paris' law for small crack

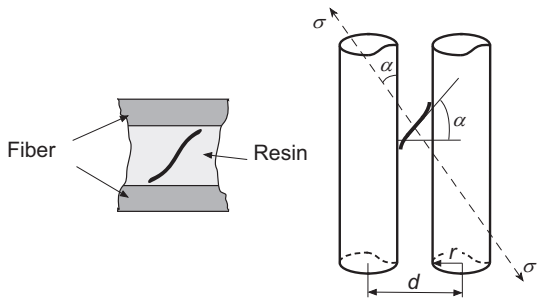

Figure 7.5 Shear type microcrack in the matrix and its idealization.

growth in normal opening mode $ds/dn = AK_I^m$, where $K_I = \sigma\sqrt{\pi s}$, and K_I is the stress intensity factor of normal opening, thus giving us $ds/dn = A\sigma\,\pi^{m/2}s^{m/2}$. When comparing the last ratio with microdefect growth law $ds/dt = b\,s$, we see that these formulas are equivalent if $m = 2$. Therefore, we can rewrite the growth law for the oblique microdefect in the form $ds/dn = AK_I^2$, which is generally valid only for crack opening mode. However, it is well known that in crack opening mode, the energy release rate γ is proportional to K_I^2, and thus we have $ds/dn = A\gamma$. We can then propose that this relationship is formally applicable for any arbitrary type of crack. Let us further generalize the growth law for microdefects under both crack opening and shearing mode. We then have γ proportional to $K_I^2 + K_{II}^2$, in which K_{II} represents stress intensity factor in shearing mode. As a result, we have the following relationship:

$$ds/dn = \overline{A}\left(K_I^2 + K_{II}^2\right) \tag{7.11}$$

where $\overline{A}$ is the micromechanical parameter. Substituting the relations $K_I = \sigma_1 F_\sigma\sqrt{\pi l}$ and $K_{II} = \tau_1 F_\tau\sqrt{\pi l}$ in Eqn (7.11), we have

$$ds/dn = \pi l\overline{A}\left(F_\sigma^2\sigma_1^2 + F_\tau^2\tau_1^2\right)$$

where F_σ, F_τ are shape functions and σ_1, τ_1 are normal and shear stresses in the coordinate system associated with microcrack direction. Expressing these stresses in terms of the corresponding applied stress, where $\sigma_1 = \sigma\sin^2\alpha$ and $\tau_1 = \sigma\sin\alpha\cos\alpha$, the final form of Eqn (7.11) can be written as

$$ds/dn = \overline{A}\pi l\sigma^2\left(F_\sigma^2\sin^4\alpha + F_\tau^2\sin^2\alpha\cos^2\alpha\right) \tag{7.12}$$

7.3.2.2 *Birth model of microdefects—fiber rupture damage (fiber breakage)*

In this section, we consider several examples of the damage-accumulation model of fiber breakage in lamina that is subjected to tensile loading in the direction of its reinforcement.

Case 1. It is well known that under cyclic and monotonic loading conditions, the birth rate of this type of microdefect is well approximated by power laws $v = At^k$ and $N = At^{k+1}/(k+1)$. For fatigue loading, the rate of birth decreases from cycle to cycle, giving us $-1 < k < 0$, while for monotonic loading $k \geq 0$. Based on initial conditions $s_{t=0} = s_0$, $S_{t=0} = 0$, the total damage measure is found to be

$$S = As_0t^{k+1}\left[1 - at/s(k+2)]/(k+1)\right]$$

As before, the cycling loading process parameter t equals the number of cycles (or half cycles) n, such that $t \equiv n$. It is easy to see that for small values of n, the damage-accumulation process decelerates, while for large values of n, we have the inequality

$d^2S/dt^2 > 0$, and thus damage accumulation accelerates. As a result, the function $S(n)S$ has a somewhat S-shaped curve (Tamuja & Pratacova, 1986). Figure 7.6 illustrates experimental data for the percentage of fractured fibers in unidirectional carbon fiber–reinforced plastic composite subjected to quasistatic loading conditions, where the solid line shows the numerical result of our proposed model, and the dots represent experimental data. As we can see, the dependence of fiber breakage on loading level is well approximated by the power function $N = A(\sigma/\sigma_{\max})^k$. Here, the parameters A and n are found by the method of least squares, from which we derive $A = 0.379$ and $k = 4.779$.

Case 2. For a power approximation of the birth rate of microdefects, the dependence of the number of such microdefects is linear in double-logarithmic coordinates $\ln N \sim \ln t$. Under cyclic loading conditions, however, the dependence of the number of microdefects is often shown as a linear function in semilogarithmic coordinates $N = \ln t$ and $v = b/t$, with $t \geq 0$. As such, we have the following initial value conditions for the number of microdefects: $dN/dt = b/t$, $N|_{t=1} = A$, $t \equiv n$, where A is the number of microdefects generated in the first cycle. The solution to this problem has the form $N = c + b\ln t$, where constants c and b can be found using the method of least squares when approximating the experimental data (linear regression in the semilogarithmic coordinates). As an example, we provide experimental data measuring fiber fragmentation damage for boron–aluminum composites at low cycle fatigue (Tamuja & Pratacova, 1986). Damage behavior is well approximated by a semilogarithmic dependence $N = c + b\ln t$ (see Figure 7.7), from which we derive $b = 1.577$ for a unidirectional composite, and $c = 18.76$ and $b = 1.887$ for fabric composites.

In semilogarithmic approximation, the damage kinetic Eqn (7.6) can be solved with the initial condition $S|_{t=1} = s_0A$. In this case, the solution to the kinetic equation has the following form:

$$S = s_0(A + b\ln t) + c(t - 1(A - b) + cbt\ln t$$

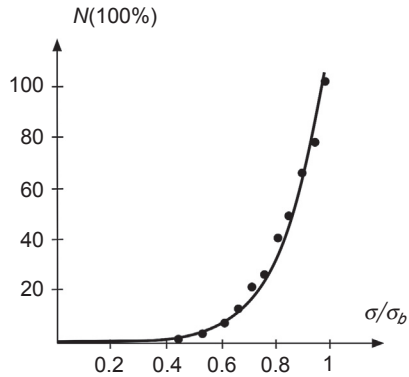

Figure 7.6 Dependence of the fracture number on loading level for carbon-reinforced composite material.

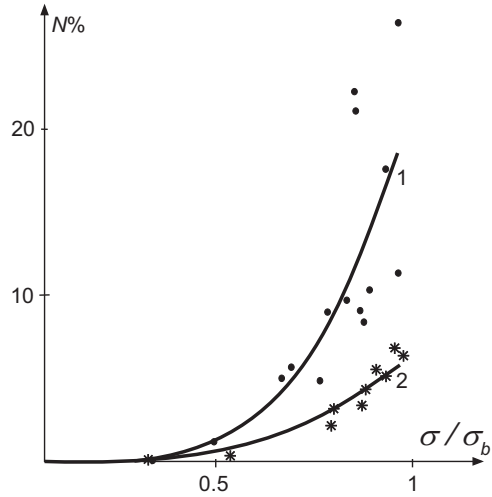

Figure 7.7 The dependence of fiber breakage of boron−aluminum fiber composites on stress loading levels: (1) fabric composites; and (2) unidirectional composite.

It is easy to see that in the general case of damage accumulation, the curve is *S*-shaped with an inflection point $t = s_0/c$. When the ratio s_0/c decreases, the length of the retarded area decreases, while the length of the accelerated area increases. Interestingly, when $s_0 = 0$, the damage-accumulation curve is concave; for $c = 0$, meanwhile, we have a convex point.

7.3.3 Property degradation modeling of unidirectional composites

In this section, we will estimate the property degradation of a unidirectional composite lamina. Several examples, describing various damage mechanisms and damage-accumulation processes that lead to reduction of properties of a unidirectional composite lamina, will be given.

7.3.3.1 Stiffness degradation—fiber rupture damage and debonding initiated by broken fibers

In fiber-reinforced composites, the stiffness of the matrix is typically much less than that of the fibers, and the matrix virtually does not take the load applied in the direction of fiber. However, the influence of the matrix can be quite significant. For example, bonding fibers with the matrix, even with relatively low matrix stiffness, can change the mechanism of fiber interaction. In fact, fiber bundles in which the fibers are embedded together in the matrix demonstrate significantly higher strength than that of dry fiber bundles (Vasiliev & Morozov, 2013). To clarify the role of a matrix in composite materials, consider the simple model of a unidirectional ply. We will assume that the central fiber has a crack. Far away from the crack, the fibers are

uniformly loaded with stress σ. In the vicinity of the crack, the load carried by the cracked fiber is transmitted to adjacent fibers by shear through the matrix. At some distance from the end of the broken fiber, which is greater than some value δ (ineffective length), the stress in the broken fiber is restored and behaves as if the crack does not exist. A portion of this fiber, corresponding to $x < \delta$, is not fully capable of resisting the applied load. Since a fiber's defects are randomly distributed along its length, their influence on ply strength is minimal unless there are other defects in the central fiber and its adjacent fibers within distance δ of the crack. In the work of Vasiliev and Morozov (2013), the formula of ineffective length is obtained as follows:

$$\delta = 2.3d\sqrt{\frac{(1-\chi)}{\chi}\frac{E_f}{G_m}}$$

where d is fiber diameter, χ is volume fraction of fiber, E_f is the fiber's Young's modulus, and G_m is matrix shear modulus. From this, it is obvious that when matrix stiffness G_m is reduced, the fiber's ineffective length increases and becomes infinitely large as stiffness goes to zero. Using this reasoning, it seems desirable that the level of matrix stiffness should be as high as possible. However, an upper limit for matrix stiffness exists. If the value of G_m is higher, the shear stress concentration of the matrix in the vicinity of crack will also be higher; if the maximum shear stress τ_m acting in the matrix reaches its limiting value, debonding will occur at the fiber−matrix interface. As such, the ability of the matrix to transfer the load from the broken fiber to adjacent fibers diminishes. Also, fiber stiffness can influence maximum shear stress in the matrix; that is, a lower fiber modulus value will increase the maximum shear stress value.

Let us consider the modeling of degradation of elastic moduli in unidirectional fiber lamina loaded in the direction of reinforcement, where the composite system contains damage in the form of fiber breakage and matrix delamination at broken fibers. To achieve our objectives, we will use the kinetic micromechanical model of damage accumulation, accounting for scale structural parameters when estimating the extent of microdamage. Many experimental tests have demonstrated that stiffness reduction in a unidirectional composite correlates with the total length of debonding. To describe this phenomenon of property degradation, and for first approximation analysis, we can use the well-known rule-of-mixtures formula to describe the axial Young's modulus of a perfect composite material

$$E = \chi E_f + (1-\chi)E_m$$

Here, E_f and E_m are the axial Young's moduli of the fiber and matrix, respectively. For this case, we only consider the loaded parts of fibers when defining the fiber volume fraction χ. Typically, when a fiber ruptures, the stress in the fiber falls on two segments (see Figure 7.2), where length is equal to the ineffective length of fiber δ. As a result, the volume of loaded fibers is reduced by the amount $\Delta V = \pi r^2(l + \kappa\delta)$, where r is the fiber radius and κ is a factor accounting for the loading of broken fibers when debonding is absent. If N is the number of fiber ruptures accompanied by debonding

lengths l_i $(i = 1,2\ldots n)$ in the representative volume element of composite material, the total volume reduction of loaded fibers will be $\Delta V = \pi r^2(\kappa N\delta + \sum l_i)$. We assume that the value of the representative volume element of composite lamina equals 1. Thus, the decrease in volume fraction of loaded fibers will be expressed by the same formula, $\Delta\chi = \pi r^2(\kappa N\delta + \sum l_i)$. By changing χ to $\chi - \Delta\chi$ in the rule-of-mixtures formula shown earlier, the axial Young's modulus of elasticity for damaged composite materials becomes

$$E = E_b\left(\chi - \pi r^2(\kappa N\delta + S)\right) + E_m(1 - \chi) \tag{7.13}$$

In Eqn (7.13), we introduce the notation S as $S = \sum l_i$. Hence, the relationship of longitudinal modulus for damaged and undamaged material can be found as

$$\frac{E}{E_0} = 1 - \pi r^2 \frac{E_b}{E_b\chi + E_m(1 - \chi)}(\kappa N\delta + S) \tag{7.14}$$

The value S is a variable representing an additive macroparameter, where the changes in its value can be defined using the micromechanical procedure shown earlier. Several process parameters can be chosen and defined—that is, loading cycles n, the microdamage mechanism, and the mechanism's characteristics. In this case, the microdamage mechanism is a microdefect in the form of fiber breakage, where debonding occurs at broken ends of fiber. As such, the length of debonding l can be viewed as a scale characteristic for this type of microdefect.

In formulating the damage growth process for the debonding model, we use a hypothesis that the growth rate of debonding length l does not depend on the current delamination. This hypothesis is justified because stresses at the tips of broken fibers are absent, and therefore a fiber's current length does not affect the disbond's further growth. Hence, the equation for the growth process has the following form: $\mathrm{d}l/\mathrm{d}n = b$, where value b depends on cycle parameters, temperature T, etc., but not on l. The last equation is a special case of the general relationship (7.6). For cyclic loading conditions, the system of kinetic Eqn (7.6) takes the following form:

$$\frac{\mathrm{d}S}{\mathrm{d}n} = v(n)l^0 + b(n)N, \quad \frac{\mathrm{d}N}{\mathrm{d}n} = v(n) \tag{7.15}$$

where l^0 is the initial size of the disbond formed at the ends of broken fibers. Let us use the following relations for the growth rate of the disbond and the formation rate of fiber breakage under positive cycle asymmetry tensile-loading conditions:

$$v = A\frac{\sigma_{\max}^m - \sigma_{\min}^m}{\sigma_b^m}n^{k-1}, \quad \frac{\mathrm{d}l}{\mathrm{d}n} = \gamma\frac{\sigma_{\max} - \sigma_{\min}}{\sigma_b}$$

For the pulsating cycle, we can write $v = A(\sigma_{\max}/\sigma_b)^m n^{k-1}$, $\mathrm{d}l/\mathrm{d}n = \gamma(\sigma_{\max}/\sigma_b)$. Here, $\sigma_{\max}$ and $\sigma_{\min}$ are the maximum and minimum amplitudes of cyclic stress,

σ_b is ultimate strength, and A, m, k, and γ are material constants. The resulting system using Eqn (7.15) then has the following form:

$$\begin{aligned}\frac{\mathrm{d}S}{\mathrm{d}n} &= Al_0\left[\left(\frac{\sigma_{\max}}{\sigma_b}\right)^m - \left(\frac{\sigma_{\min}}{\sigma_b}\right)^m\right]n^{k-1} + 2\gamma\frac{\sigma_{\max}-\sigma_{\min}}{\sigma_b}N \\ \frac{\mathrm{d}N}{\mathrm{d}n} &= A\left[\left(\frac{\sigma_{\max}}{\sigma_b}\right)^m - \left(\frac{\sigma_{\min}}{\sigma_b}\right)^m\right]n^{k-1}\end{aligned} \tag{7.16}$$

Equation (7.16) can be integrated for any arbitrary irregular loading, and the value $\sigma_{\max}$ must be set as a function of the number of loading cycles, such as $\sigma_{\max} = \sigma_{\max}(n)$. It is convenient to introduce the following notations: $\omega = \kappa N\delta + S$, $\eta = N/A$. Thus, the system of the kinetic equation can be rewritten as follows:

$$\mathrm{d}\omega/\mathrm{d}n = \alpha(\sigma_{\max}/\sigma_b)^m n^{k-1} + \beta(\sigma_{\max}/\sigma_b)\eta, \quad \mathrm{d}\eta/\mathrm{d}n = (\sigma_{\max}/\sigma_b)^m n^{k-1}$$

where $\alpha = A(l^0 + \kappa\delta)$, $\beta = A\gamma$, m, k are the four material parameters that can be found from the experimental data. The last system of equations must be integrated using the initial conditions $\omega|_{n=0} = 0$, $\eta|_{n=0} = 0$ for perfect composites. In particular, for regular cyclic loading with pulsating cycle $\sigma_{\max} = \text{const}$, we obtain

$$\omega = \kappa N\delta + S = \frac{\alpha n^k}{k}\left(\frac{\sigma_{\max}}{\sigma_b}\right)^m\left(1 + \frac{\beta}{\alpha}\frac{\sigma_{\max}}{\sigma_b}\frac{n}{k+1}\right)$$

Substituting this into Eqn (7.14), we find the following equation for property degradation:

$$\frac{E}{E_0} = 1 - \frac{\pi r^2}{\mu}\frac{1}{1 - \frac{E_m}{E_b}\frac{1-\chi}{\chi}}\frac{\alpha n^k}{k}\left(\frac{\sigma_{\max}}{\sigma_b}\right)^m\left(1 + \frac{\beta}{\alpha}\frac{\sigma_{\max}}{\sigma_b}\frac{n}{k+1}\right) \tag{7.17}$$

In this case, only two of the parameters of Eqn (7.17) are unknowns: α and $\eta = \beta/\alpha = \gamma/(l^0 + \kappa\delta)$. Parameter α can be found using the fatigue curve for specific composite material. The equation for the fatigue curve may be written as $N_f = F\left(\frac{\sigma_{\max}}{\sigma_b}\right)$, where N_f is the number of cycles to failure. Assuming that θ defines the limit value of modulus E^* for that particular damage process, we use $\theta = E^*/E_0$, and can rewrite Eqn (7.17) as follows:

$$\frac{E}{E_0} = 1 - \left[(1-\theta)n^k\left(1 + \eta\frac{\sigma_{\max}}{\sigma_b}\frac{n}{k+1}\right)\right] \Bigg/ \left[F^k\left(\frac{\sigma_{\max}}{\sigma_b}\right)\left(1 + \eta\frac{\sigma_{\max}}{\sigma_b}\frac{F\left(\frac{\sigma_{\max}}{\sigma_b}\right)}{k+1}\right)\right]$$

In the case where we have power law for the fatigue equation $N_f = B(\sigma_{\max}/\sigma_b)^{-p}$, we find the final form of the Eqn (7.17) as

$$\frac{E}{E_0} = 1 - \left[(1-\theta)n^k\left(1+\eta\frac{\sigma_{\max}}{\sigma_b}\frac{n}{k+1}\right)\right] \Bigg/ \left[\left(\frac{\sigma_{\max}}{\sigma_b}\right)^{-kp}\left(1+\eta\frac{\sigma_{\max}}{\sigma_b}\frac{B\left(\frac{\sigma_{\max}}{\sigma_b}\right)^{-p}}{k+1}\right)\right]$$

The last equation now has only one parameter, $\eta = \gamma/(l^0 + \kappa\delta)$, which must be deduced from the experimental data with E/E_0 dependent on the number of cycles n for some value $\sigma_{\max}/\sigma_b$. The numerical result for stiffness reduction of carbon-fiber composite subjected to cyclic loading is illustrated in Figure 7.8. One can see that our predicted values are consistent with the experimental results of Yang et al. (1990).

In a subsequent section, Eqns (7.15)–(7.17) serve as the basis for forecasting the stiffness properties of multidirectional carbon fiber composite with the microdamage mechanism of transverse-ply cracking. Nevertheless, in order to use these equations we must have experimental data that reflect the initiation and growth of such micro-defects, so that the identification of material empirical parameters is possible.

7.3.3.2 *Stiffness degradation—development of longitudinal microcracks in the matrix of a lamina*

Consider a unidirectional composite lamina loaded in perpendicular to the direction of its reinforcements, in which microcracks develop along the fibers, thus creating damage that leads to reduction in transverse stiffness. The strain energy for such a layer

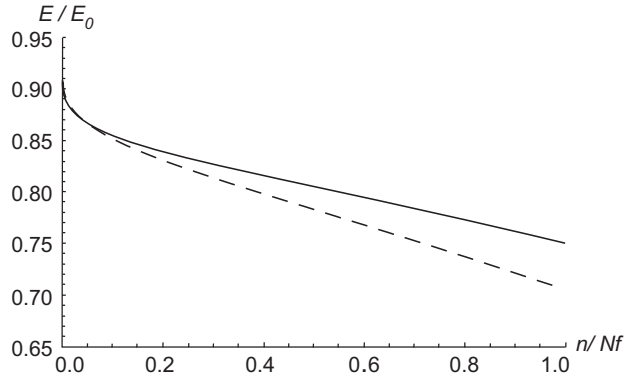

Figure 7.8 Dependence of stiffness degradation of carbon fiber–reinforced composite on the number of cycles under low-cycle loading (solid line: $\sigma_{\max}/\sigma_b = 0.5$; dotted line: $\sigma_{\max}/\sigma_b = 0.75$).

under rigid loading conditions has the form $U = \int_V \int_0^{\varepsilon} \sigma \varepsilon \mathrm{d}\varepsilon = Pu/2$, and u is the given edge displacement of the layer. It can be shown that a crack with length l will reduce the elastic energy of the layer, and thus we have $U_1 = U - \pi l^2 = P_1 u/2$. Considering the last two equalities, we obtain $E_1/E = P_1/P = 1 - \pi l^2/U$. Consequently, the stiffness reduction of a transverse layer associated with the formation of cracks is proportional to l^2. When there are several formations of n parallel microcracks, the following is the assessment of the change in the transverse Young's modulus:

$$E_1/E = 1 - \lambda \sum_{i=1}^{n} l_1^2 \tag{7.18}$$

Unlike in the earlier cases, Eqn (7.17) shows that the macrodamage characteristic does not depend on the sum of the measures of microdamage mechanisms, but on the sum of the *squares* of these measures.

$$S_2 = \int_0^t l^2(t, t_0) v(t_0) \mathrm{d}t_0$$

$$\mathrm{d}S_2/\mathrm{d}t = l^2(t, t_0) v(t_0) + 2 \int_0^t l(t, t_0) [\mathrm{d}l(t, t_0)/\mathrm{d}t] v(t_0) \mathrm{d}t_0$$

The equation for the growth of microdefects has the form $\mathrm{d}l/\mathrm{d}t = \mathrm{f}(l,t)$. Assuming the rate of microdefect development is a linear function of current microdevelopment size, we obtain the following kinetic equations for the damage macroparameter as

$$\mathrm{d}S_2/\mathrm{d}t = l^2(t, t_0) v(t) + 2a(t) \int_0^t l(t, t_0) v(t_0) \mathrm{d}t_0 + 2b(t) \int_0^t l^2(t, t_0) v(t_0) \mathrm{d}t_0$$

Let us introduce the conventional linear macroparameter of damage as $S_1 = \int_0^t l(t, t_0) v(t_0) \mathrm{d}t_0$. Thus, we can write the system of kinetic equations in the following form:

$$\mathrm{d}S_2/\mathrm{d}t = l^2(t, t_0) v(t) + 2a(t) S_1 + 2b(t) \int_0^t l^2(t, t_0) v(t_0) \mathrm{d}t_0$$

$$\mathrm{d}S_1/\mathrm{d}t = l(t, t_0) v(t) + 2a(t) N + 2b(t) S_1, \; \mathrm{d}N/\mathrm{d}t = v$$

In the particular case where $a(t) = 0$, $dl/dt = b(t)l$, and $dS_2/dt = l^2(t,t_0)v(t) + 2b(t)S_2$; that is, the system of equations splits up, so there is no need for us to introduce linear parameters of macrodamage.

Under cyclic loading conditions, we have $t = n$ and $b(t) = \pi c\sigma_{\max}^2$. The last equality is equivalent to the Paris' law formula with the index equal to 2, $dl/dn = cK_I^2$. Here, in accordance with the experimental data, we consider that the microcrack increment per cycle depends only on the corresponding microcrack stresses and not on the number of cycles. As a result, we obtain

$$dS_2/dt = A\sigma_{\max}^m + 2\pi c\sigma_{\max}^2 S_2$$

where m, A, c are microparameters that can be defined from experiments. Integrating the last macrodamage equation, we find

$$S_2 = A\left(\sigma_{\max}^{m-2}/2\pi c\right)\left[\exp\left(2\pi c\sigma_{\max}^2 n\right) - 1\right],$$

and thus in accordance with Eqn (7.6), the following equation is found:

$$E_1/E = 1 - \alpha\left(\sigma_{\max}^{m-2}/2\pi c\right)\left(\exp\left(2\pi c\sigma_{\max}^2 n\right) - 1\right)$$

As usual, the parameters α, m, c (the constants λ and A are combined into one new constant $\alpha = A\lambda$) can be found by the method of least squares applied to the results of experimental data that describe changes in the transverse Young's modulus of a unidirectional composite subjected to cyclic loading conditions perpendicular to the direction of ply reinforcement.

7.3.3.3 *Stiffness degradation—unidirectional composites loaded by the pulsating stresses at an angle to the direction of reinforcement*

Referring to Eqn (7.12), we have

$$ds/dn = \overline{A}\pi l\sigma^2\left(F_\sigma^2 \sin^4\alpha + F_\tau^2 \sin^2\alpha \cos^2\alpha\right)$$

We assume that the microcracks are very small, and thus it is possible to use $F_\sigma = F_\tau = 1$. As such, the growth rate for such microdefects can be written as

$$ds/dn = \overline{A}\pi l\sigma_{\max}^2 \sin^2\alpha$$

As a result, the equation for the summation of squared length of microcracks in the representative volume element takes the following form (see previous section):

$$dS_2/dt = A\sigma_{\max}^m + 2\pi c\sigma_{\max}^2 S_2 \sin^2\alpha$$

By integrating the above equation for specific cyclic loading conditions ($t = n$), it is possible to find the damage characteristics S_2. Next, by using appropriate degradation model, we can find the reduction in transverse Young's modulus E_2 as well as in shear modulus G. Furthermore, the algorithm shown in the previous section defines the change in axial Young's modulus E_1 (direction of reinforcement). For the change in modulus of elasticity in the direction of applied loading, the following formula can be used (Fukuda, Yakushiji, & Wada, 1997):

$$E^* = \left[\frac{\cos^4\alpha}{E_1} + \frac{\sin^4\alpha}{E_2} + \left(\frac{1}{G_{12}} - \frac{2\mu_{12}}{E_1}\right)\cos^2\alpha\sin^2\alpha\right]^{-1}$$

7.3.4 Concluding remarks

Here, we provide a summary of some possible kinetic microdamage models characterized for fiber composite materials where scale characteristics are taken into account. The scalar damage characteristic S in quasistatic and cyclic loading conditions, which accounts for the birth [$dN/dt = v(t)$] and growth ($ds/dt = f(t) \approx a + bs$) of microdefects, is defined by integrating the kinetic Eqn (7.6). As usual, the initial conditions (7.7) must be satisfied once the integration is performed.

Case 1. For damage controlled by microcracks related to fiber–matrix debonding occurring at the ends of broken fibers ($a = a_0$ and $b = 0$), where the birth rate of new microdefects v is constant ($v = c$), scalar damage characteristics are given as

$$S = \frac{1}{2}a_0c(t - t_0)^2 + \left(s^0c + a_0P_0\right)(t - t_0) + S_0$$

For the zero initial condition ($t = t_0$), we have

$$\frac{S}{s_0v_0} = \frac{1}{2}mt^2 + t, \frac{a_0}{s_0} = m$$

where t_0 is the threshold value of time when microdamage appears and starts to develop. Nevertheless, for quasistatic conditions, this value depends on the stress level σ_0—that is, $t_0 = \sigma_0 / \sigma_b$.

Case 2. For damage controlled by microcracks related to the same fiber–matrix debonding occurring at the ends of broken fibers ($a = a_0$ and $b = 0$), but where the breakage rate of fibers depends on the stress level by power law $v = ct^k$, the scalar damage characteristic for quasistatic loading conditions is given as

$$S = \frac{a_0c}{(k+1)(k+2)}t^{k+2} - \frac{a_0c}{k+1}t_0^{k+1}t + \frac{a_0c}{k+2}t_0^{k+2} + \frac{s^0c}{k+1}\left(t^{k+1} - t_0^{k+1}\right) + a_0P_0(t - t_0) + S_0$$

Again, for the zero initial condition ($t = t_0$), we have

$$\frac{S}{s_0 v_0} = \frac{m}{(k+1)(k+2)} t^{k+2} + \frac{1}{k+1} t^{k+1}$$

Case 3. For damage controlled by the same microcracks in Case 2, ($a = a_0$ and $b = 0$), but with the composite experiencing cyclic loading conditions ($t = n$, $v = c/n$ and $N = c \cdot \ln \frac{n}{n_0} + N_0$), the scalar damage characteristics can be represented as

$$S = c(s_0 + a_0 n) \cdot \ln \frac{n}{n_0} + a_0 (N_0 - c)(n - n_0) + S_0$$

As before, by considering the initial condition where $n = n_0$, we have

$$\frac{S}{s_0 v_0} = (1 + mn) \cdot \ln \frac{n}{n_0} - m(n - n_0)$$

Case 4. For damage controlled by normal microcrack opening mode (transverse microcrack) related to fiber breakage ($a = a_0$ and $b = b_0$), with the fiber breakage rate increasing by exponential law $N = N_* - (N_* - N_0) \cdot e^{-c(t-t_0)}$ and $v = c(P_* - P_0) \cdot e^{-c(t-t_0)}$, the scalar damage characteristic is defined as

$$S = \left(s_0 - \frac{a_0}{c}\right)(P_* - P_0) \cdot \left[1 - e^{-c(t-t_0)}\right] + a_0 P_* (t - t_0) + S_0$$

By considering the initial condition $t = t_0$, we have

$$\frac{S}{s_0 N_*} = \left(1 - \frac{m}{c}\right) \cdot \left(1 - e^{-ct}\right) + mt$$

In the particular case of cyclic loading when $a \ll s_0$, we obtain the scalar damage characteristic as

$$S \approx N_* \cdot \left(1 - e^{-ct}\right)$$

Case 5. For damage controlled by axial or longitudinal microcracks related to fiber breakage ($a = 0$ and $b = b_0$), where the birth rate of microdefects is constant ($v = \text{Const}$) under cyclic loading conditions, the scalar damage characteristic can written as

$$S = \left(S_0 + \frac{s_0 v}{b_0}\right) \cdot e^{b_0 (n - n_0)} - \frac{s_0 v_0}{b_0}$$

Accounting for the initial condition where $n = n_0$, we have

$$\frac{S}{s_0 v_0} = e^{b_0 t} - 1$$

Case 6. For damage simultaneously controlled by both transverse and axial microcracks related to fiber breakage ($a = a_0$ and $b = b_0$), and where the birth rate of microdefects is constant ($v = \text{Const}$), the scalar damage characteristic gives

$$S = S_0 e^{b_0(n-n_0)} + \left(\frac{s_0 v + a_0 P_0}{b_0} + \frac{a_0 v}{b_0^2}\right)\left(e^{b_0(n-n_0)} - 1\right) - \frac{a_0 v}{b_0}(n - n_0)$$

Based on the initial condition when $n = n_0$, we obtain

$$S = s_0 v\left[(1+g)\cdot e^{b_0 n} - b_0 n - (1+g)\right], \quad g = \frac{a_0}{s_0 b_0}$$

As we can see, the kinetic damage-accumulation model allows us to account for the scale parameters of microstructures, and serves as a basis for assessing the property degradation of each individual layer of a loaded composite laminate. The model is also useful for assessing damage growth of a lamina when the laminate is subjected to multistage loading conditions; that is, multistage cyclic loads where each loading stage is associated with a different damage mechanism. In such cases, the linear summation rule cannot be used, as it will lead to overestimation and underestimation of property degradation.

7.4 Modeling of stiffness degradation of laminated composite materials across length scales

We earlier formulated kinetic damage-accumulation models that can account for scale characteristics of fiber composite materials at differing microstructural scales; that is, corresponding to the microstructural level of constituents (fiber and matrix), as well as the size characteristics of a ply or group of plies. Next, we include these models when modeling the damage-accumulation process at the structural level for the whole composite laminate.

The algorithm for damage assessment for composite laminates uses the following assumptions:

1. The composite laminate is in the plane stress condition.
2. A change in quasistatic or cyclic loading conditions will result in a proportional change in the stress component of the composite laminate (i.e., in one cycle, the stress components change proportionally).
3. The fibers in each ply are not susceptible to damage.

4. The damage-accumulation process is related to the following damage mechanisms and damage growth scenarios:
   a. Damage accumulation in the laminate occurs due to growth in damage to composite laminate plies.
   b. Damage to the matrix system is in the form of fiber−matrix microcracking, which is the main mechanism of damage growth in the composite laminate.

In 4(a), we propose that ply damage defines the damage state of fiber composite materials. We further assume that the contacts between plies remain intact; that is, interface boundaries are not damaged. In 4(b), we assert that the damage mechanism not only influences property degradation of the transverse layer where ply cracking takes place, but also leads to stress redistribution in plies that further influences damage growth in the individual plies of the composite laminate. Furthermore, the damage mechanism for transverse cracking (ply crack) precedes the damage mechanism for ply delamination, where significant reduction of composite laminate properties can be observed.

As a result, we need to solve two problems. In the first, we will examine property degradation related to the birth and growth of microdamage in the unidirectional plies of composite laminate, and an algorithm to assess this property degradation will be constructed. In the second, we will analyze property degradation associated with matrix microcracking, as well as the interface damage mechanism for individual transverse plies of the composite laminate, and develop the corresponding assessment algorithm.

7.4.1 Modeling property degradation of fiber composite laminate due to damage in plies

The main objective of this section is to develop the algorithm that will allow us to predict the degradation effects in the effective mechanical properties of an arbitrary laminate structure, based on parameters derived from a large quantity of experimental data obtained for some specific composite laminate configurations.

The prime objective of describing the process of damage accumulation in composite materials is to assess the changes in mechanical characteristics of the materials while they are in service. In general, when composite structures are subjected to quasistatic and cyclic loading conditions over time, their elastic properties are reduced, a long-observed phenomenon known as property degradation. This phenomenon is attributed to damage accumulation in composites, or more accurately to the level of damage accumulation. Again, as a rule we will use simple property degradation models that account for the relative values of stiffness reduction (e.g., changes in strength and wear). In modeling property degradation, the relative value of the reduction in mechanical properties of the composite can be thought of as a measure of damage. As such, we can write the following expressions to describe damage in terms of changes in the modulus of elasticity, bending stiffness, and strength, respectively:

$$S^* = 1 - \frac{E}{E_0},\ S^* = 1 - \frac{EI}{E_0 I_0},\ S^* = 1 - \frac{\sigma_b}{\sigma_{b_0}} \tag{7.19}$$

Here, S^* is the damage value that depends on the process parameter t. These values vary from zero to their limiting values, which correspond to the end of the damage-accumulation process or the start of the macrofracturing process. Furthermore, if damage limiting values are normalized, it follows that S^* can be written in the form $S^* = k \cdot S(t)$. The coefficient k is found from the limiting conditions. For example, we have $\frac{EI}{E_0 I_0} \approx 0.75, \ldots, 0.85$. Practically, the value is considered to be $k \approx 0.2$. Next, the following expression can be used for changes in modulus of elasticity for fiber composite materials: $E = E_0(1 - k_1 S)$. Operating properties for the elements of composite structures are in fact defined by the mechanical properties of the materials. Suppose that a property of the material—for example, elastic stiffness tensor—depends on the real-time t : $\Delta E_{\text{ijkm}} = E^0_{\text{ijkm}} - E^{\text{damage}}_{\text{ijkm}}$, where E^0_{ijkm} is the elastic stiffness tensor of undamaged or parent material, and the value $\Delta E_{\text{ijkm}}(t)$ corresponds to the reduction in mechanical properties over time t, which is related to the degradation phenomenon due to damage accumulation. Let the tensor $(\Delta E_{\text{ijkm}}(t))_{\text{cr}}$ in (7.19) be the critical allowable tensor degradation value portion of mechanical properties, a value for which the structure does not lose its operating properties. Then, it is possible to formulate the following criteria for structural efficiency that retains its performance or operational characteristics:

$$\min_{\text{ijkm}} \left(\int_0^{t^*} \Delta E_{\text{ijkm}}(t) \right)_{\text{cr}} \mathrm{d}t \;=\; \Delta E_{\text{cr}} \tag{7.20}$$

At specific condition t^*, the formula represents the critical *lifetime*—it determines the actual durability of the structure—which is the period for which operational characteristics are preserved. In general, the values $(\Delta E_{\text{ijkm}}(t))_{\text{cr}}$ are derived from the limitation values of strength, stiffness, or other conditions; for example, the condition where natural frequencies stay within a predetermined range. In reality, the maximum relative decrease of characteristics does not exceed 15%; in some cases, we can estimate the value t^* explicitly, if explicit time dependence for degradation characteristics of material can be used.

In Figure 7.9, we can see that the damage evolution of fiber composite laminate is divided into three areas. The damage-accumulation process in the first stage (area I) is mainly controlled by fiber−matrix microcracks and matrix microcracks, which typically make up the first 10% to 20% of the whole damage evolution process that ends with the complete failure of the composite structure. In the second stage (area II), the microcracks grow and coalesce into ply cracks (transverse cracking). In reality, a series of ply cracks can exist in transverse plies. At the same time, interlayer cracks (delamination) are initiated at the ends of ply cracks. This type of damage could be the main source of changes in the elastic moduli of composites (Kashtalyan & Soutis, 2001, 2002a,b, 2005). It is said that the delamination length strongly influences the laminate's effective properties, which can be degraded more than 30% from the initial effective values of an undamaged composite laminate. In

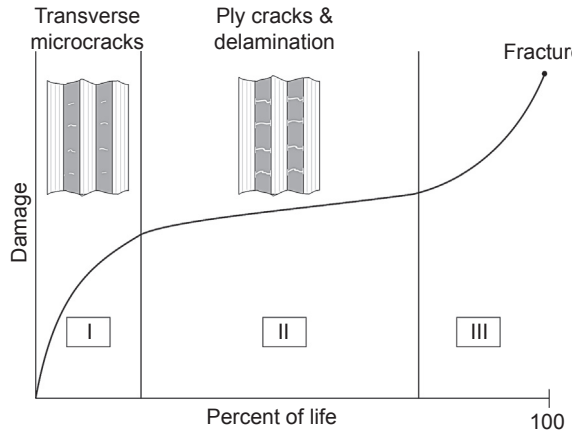

Figure 7.9 Typical damage evolution in transverse plies of composite laminate.

the final stage (area III), the damage-accumulation process is determined mainly by interlayer cracks (delamination). Excessive growth of the delamination length, as well as new formations in the last stage of composite damage evolution (area III) will lead to total failure of the composite structure. Here, we will focus in detail on the damage evolution of fiber composite materials in area I, and particularly area II.

To model the first two mechanisms of damage (areas I and II), a two-stage damage growth model is considered. In the first stage, the appearance and development of transverse microcracks will be modeled, and in the second stage, the development of the ply cracks will be analyzed. The development and growth of interlayer cracks will be also investigated.

First, we will examine the damage-accumulation process related to the birth and growth of transverse microcracking in the transverse ply. To describe this defect, the following assumptions are set forth:

1. The elastic modulus in the direction of reinforcing fibers (axial Young's modulus) of a ply does not degrade.
2. We consider that the property degradation of composite laminate, in general, is defined by the damage-accumulation process occurring in the matrix only, due to transverse microcracking in the individual transverse layer, and consequently we can say that property degradation is completely due to the appearance of ply cracking. These cracks can appear and grow only when the corresponding stresses exceed the limiting transverse strengths of the matrix system.
3. Before the appearance of ply cracks, the values for transverse Young's modulus and shear modulus are given by the following equations derived from the simplified rules of degradation in Eqn (7.20):

$$E_2^i = E_{2o}[1 - S_E(t, \sigma, \tau)], G_{12}^i = G_{12o}\left[1 - S_G(t, \sigma, \tau)\right] \tag{7.21}$$

where E_{2o}, G_{12o} represent the elastic moduli of undamaged material (perfect material). When selecting an appropriate model, one must always be guided by physical reasoning that justifies the use of the selected model, and simplification is desirable and necessary. We now propose that the rate of change in the length of transverse microcracks is proportional to the length, and at the same time remains constant. As such, we can consider the growth of transverse microcracks to occur at a constant rate and sufficiently far from the ply boundaries that their growth is not retarded. In this case, based on Eqn (7.21), the damage model in transverse layers can be written in the form

$$S_{E,G}(t,\sigma,\tau) = K^i_{E,G}\left(1 - e^{-b_{E,G}n}\right) \tag{7.22}$$

The parameters K^i_E and K^i_G determine the rate of change for transverse Young's modulus and shear modulus, which depend on corresponding stresses in a lamina. Furthermore, it is assumed that microcracks resulting from compression will not grow. In the general case, microparameters of the damage-accumulation model, b_E and b_G, and parameters of the stiffness degradation model, K_{Eo} and K_{Go}, must be defined from microscopic and macroscopic experiments performed for individual lamina. However, it is possible to use purely phenomenon-based methods to identify model parameters, when the parameters are determined from the macroscopic experiments conducted for a finite set of tests on composite structures.

4. The main part of damage is related to across-thickness transverse microcracks or ply cracks. An algorithm that accounts for this type of damage is given in the next section.

In general, the effective characteristics of composite materials with specific layups in a laminate (the number and thickness of plies with various orientations) are already known. We also consider that for specific laminate structures, constructed from several laminae with known properties, the dependence of effective properties on loading process parameters is also known. Special interest is given when we account for damage growth and its influence on the stress−strain distribution in the stress concentration area. If any element in the vicinity of the high stress concentration area has a corresponding stress value close to the limiting strength value, damage development can often lead to the violation of strength conditions. As such, degradation of the effective properties of the composite laminate occurs.

The following steps define the algorithm of the model:

1. After the stresses in each layer of laminate are defined, we use the relations that account for the lamina damage model given in Eqns (7.21) and (7.22). Next, we find the formula describing the degradation of effective characteristics of the laminate as follows:

$$E_{x,y} = E_{x,y}(S(\sigma,\tau)),\ G_{12} = G_{xy}(S(\sigma,\tau))$$

2. The model parameters are found by comparing the results of experimental data with theoretical values. For a laminate subjected to quasistatic loading conditions, stress levels of structural elements define the process parameter t,$t = \sigma/[\sigma_b]$, but for each ply of the laminate and every damage development related to the degradation of transverse Young's and shear moduli, the time-related process parameter t_i represents the stress level of each layer.

When using the above scheme, once the effective characteristics of the laminate are determined, one must calculate the stress and strain states using strain compatibility equations. Using Hooke's law, stresses in the individual ply can be obtained and checked against the strength conditions. Finally, the proposed algorithm must be repeated in order to calculate the effective characteristics of a laminate, should the fractured transverse layer affect the laminate's other plies.

7.4.2 Influence of matrix cracking in transverse layer on the distribution of stresses in a laminate structure

The objective of this section is to determine the stress state in the vicinity of damage or the fractured zone, and also changes in the local and effective moduli of elasticity. We now examine the damage development process until the appearance of a ply crack, for a symmetrical orthotropic laminate under tension (Figure 7.10):

Let us consider a laminate subjected to tension p, and constructed of two outer plies having the same thickness h_1, with internal transverse ply of thickness 2 h_2. Furthermore, it is assumed that the internal ply experiences ply cracking. The proposed technique is generalized enough to use for ply cracking in any layer of the composite laminate (see Vasiliev & Morozov, 2013). The algorithm given here is written in a coordinate system with its origin at the defect transverse layer. All remaining plies will be defined by material characteristics with matrix B_{ij}, and the thickness is divided by $^1/_2$ and designated as h_1. The resulting equation of equilibrium for laminate is

$$\text{Along axis Ox} : 2(\sigma_{x_1} h_1 + \sigma_{x_2} h_2) = p \tag{7.23}$$

$$\text{Along axis Oz} : 2(\sigma_{z_1} h_1 + \sigma_{z_2} h_2) = 0$$

To determine the stresses in local plies in Eqn (7.23), we use the following well-known formula:

$$\begin{aligned} \sigma_x^i &= \sigma_1^i \cos^2(\varphi_i) + \sigma_2^i \sin^2(\varphi_i) - \tau_{12}^i \sin(2\varphi_i) \\ \sigma_z^i &= \sigma_1^i \sin^2(\varphi_i) + \sigma_2^i \cos^2(\varphi_i) + \tau_{12}^i \sin(2\varphi_i) \end{aligned} \tag{7.24}$$

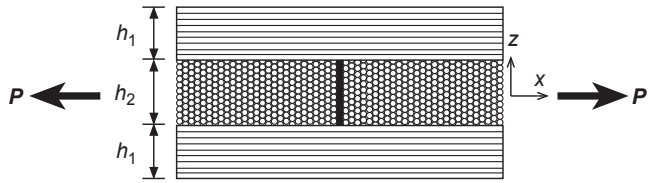

Figure 7.10 A ply crack in the transverse layer.

These relations define the stresses in individual layers for strength assessment

$$\sigma_1^i = \overline{E}_1\left(\varepsilon_1^i + \mu_{12}\varepsilon_2\right), \quad \sigma_2^i = \overline{E}_2\left(\varepsilon_2^i + \mu_{21}\varepsilon_1\right), \quad \tau_{12}^i = G_{12}\gamma_{12} \tag{7.25}$$

Meanwhile, the strains of individual layers are defined by the following formula:

$$\begin{aligned}
\varepsilon_1^i &= \varepsilon_x \cos^2(\varphi_i) + \varepsilon_z \sin_2(\varphi_i) + \gamma_{xz}\sin(\varphi_i)\cos(\varphi_i) \\
\varepsilon_2^i &= \varepsilon_x \sin^2(\varphi_i) + \varepsilon_z \cos^2(\varphi_i) - \gamma_{xz}\sin(\varphi_i)\cos(\varphi_i) \\
\gamma_{12}^i &= (\varepsilon_z - \varepsilon_x)\sin(2\varphi_i) + \gamma_{xz}\cos(2\varphi_i)
\end{aligned} \tag{7.26}$$

Using Eqns (7.24) and (7.26), we find

$$\begin{aligned}
\sigma_x^i &= b_{11}^i\varepsilon_x + b_{12}^i\varepsilon_z + b_{13}^i\gamma_{xz} \\
\sigma_z^i &= b_{21}^i\varepsilon_x + b_{22}^i\varepsilon_z + b_{23}^i\gamma_{xz}
\end{aligned} \tag{7.27}$$

Substituting (7.27) into (7.23), we obtain

$$\begin{aligned}
\left(b_{11}^1\varepsilon_x + b_{12}^1\varepsilon_z\right)h_1 + \left(b_{11}^2\varepsilon_x + b_{12}^2\varepsilon_z\right)h_2 &= p/2 \\
\left(b_{21}^1\varepsilon_x + b_{22}^1\varepsilon_z\right)h_1 + \left(b_{21}^2\varepsilon_x + b_{22}^2\varepsilon_z\right)h_2 &= 0
\end{aligned}$$

or

$$\begin{aligned}
\left(b_{11}^1h_1 + b_{11}^2h_2\right)\varepsilon_x + \left(b_{12}^1h_1 + b_{12}^2h_2\right)\varepsilon_z &= p/2 \\
\left(b_{21}^1h_1 + b_{21}^2h_2\right)\varepsilon_x + \left(b_{22}^1h_1 + b_{22}^2h_2\right)\varepsilon_z &= 0
\end{aligned} \tag{7.28}$$

where we have

$$\begin{aligned}
\varepsilon_x &= \frac{0,5p\left(b_{22}^1h_1 + b_{22}^2h_2\right)}{\left(b_{11}^1h_1 + b_{11}^2h_2\right)\left(b_{22}^1h_1 + b_{22}^2h_2\right) - \left(b_{12}^1h_1 + b_{12}^2h_2\right)^2} = \frac{0,5p}{h_1 + h_2}\frac{B_{22}}{B_{11}B_{22} - B_{12}^2} \\
\varepsilon_y &= \frac{-0,5p\left(b_{12}^1h_1 + b_{12}^2h_2\right)}{\left(b_{11}^1h_1 + b_{11}^2h_2\right)\left(b_{22}^1h_1 + b_{22}^2h_2\right) - \left(b_{12}^1h_1 + b_{12}^2h_2\right)^2} = -\frac{0,5p}{h_1 + h_2}\frac{B_{12}}{B_{11}B_{22} - B_{12}^2}
\end{aligned} \tag{7.29}$$

and

$$
\begin{aligned}
b_{11}^{i} &= \overline{E}_1\cos^4(\varphi_i) + \overline{E}_1\mu_{12}\sin^2(\varphi_i)\cos^2(\varphi_i) + \overline{E}_2\sin^4(\varphi_i) + G_{12}\sin^2(2\varphi_i) \\
b_{12}^{i} &= b_{21}^{i} = \left(\overline{E}_1 + \overline{E}_2 - 4G_{12}\right)\sin^2(\varphi_i)\cos^2(\varphi_i) + \overline{E}_1\mu_{12}\left(\sin^4(\varphi_i)\right. \\
&\quad \left. +\cos^4(\varphi_i)\right) \\
b_{22}^{i} &= \overline{E}_1\sin^4(\varphi_i) + \overline{E}_1\mu_{12}\sin^2(\varphi_i)\cos^2(\varphi_i) + \overline{E}_2\cos^4(\varphi_i) + G_{12}\sin^2(2\varphi_i) \\
B_{11} &= \left(b_{11}^{1}h_1 + b_{11}^{2}h_2\right)/h; \quad B_{12} = \left(b_{12}^{1}h_1 + b_{11}^{2}h_2\right)/h \\
B_{22} &= \left(b_{22}^{1}h_1 + b_{22}^{2}h_2\right)/h \\
h &= (h_1 + h_2)
\end{aligned}
$$

If we were to consider further that $\mu_{12} = 0$, $\varepsilon_z = 0$, then from (7.28) and (7.29), we can obtain the following stresses for undamaged perfect material along axis Ox subjected to tension loading condition:

$$
\sigma_{x1} = \frac{0,5p}{h_1 + h_2}\frac{b_{11}^{1}}{B_{11}}, \quad \sigma_{x2} = \frac{0,5p}{h_1 + h_2}\frac{b_{11}^{2}}{B_{11}} \tag{7.30}
$$

We propose that under tensile load, a damage mechanism causes a defect in the form of a ply crack to form between the fibers in the internal transverse layers. As a result, a perturbation to the stress state at both sides of the crack in the direction of axial axis Ox will occur. Next, we assume that the stresses are constant regardless of the thickness of the layer, since it is very thin in nature. Then, the perturbation state of stresses in the laminate, where we assumed that the transverse internal layer has ply cracks, and the axial external layers that are loaded along axis Ox, can be written as follows:

$$
\sigma_{x1} = \sigma_{x3} = \sigma_{10} + \tilde{\sigma}_{x1}(x), \quad \sigma_{x2} = \sigma_{20} - \tilde{\sigma}_{x2}(x) \tag{7.31}
$$

where σ_{10} and σ_{20} represent the unperturbed stress values and are constant with Eqn (7.29). The stress variables $\tilde{\sigma}_{x1}$ and $\tilde{\sigma}_{x2}$ (see Eqn (7.31)) in the perturbed zone are self-equilibrated in thickness and satisfy the following relation:

$$
\tilde{\sigma}_{x1}h_1 = \tilde{\sigma}_{x2}h_2 \tag{7.32}
$$

Again, we consider the stress state to be constant along the thickness of the individual layer, satisfying the equation of equilibrium in every ply of the laminate:

$$
\frac{\partial\tilde{\sigma}_{xi}}{\partial x} + \frac{\partial\tau_i}{\partial z} = 0, \quad \frac{\partial\tau_i}{\partial x} + \frac{\partial\sigma_{zi}}{\partial z} = 0 \quad (i = 1,2,3) \tag{7.33}
$$

Here, the x-coordinate is along the plate's length and the z-coordinate is along the height of the laminate's plate. Resolving Eqn (7.33) relative to stresses τ_i and σ_{zi}, and accounting for surface contact conditions, we have the following form:

$$
\text{when}: \; z = \pm(h_1 + h_2): \quad \sigma_{z1} = \sigma_{z3} = \tau_1 = \tau_3 = 0
$$

$$
\text{when}: \; z = \pm h_2: \sigma_{z1} = \sigma_{z3}, \sigma_{z3} = \sigma_{z2}, \tau_1 = \tau_3, \tau_2 = \tau_3
$$

and thus by considering the conditions in Eqns (7.31) and (7.32), we have

$$\sigma_{x1} = \sigma_{x3} = \sigma_{10} + \tilde{\sigma}_{x2}\frac{h_2}{h_1},\ \sigma_{x2} = \sigma_{20} - \tilde{\sigma}_{x2}(x)$$

$$\tau_2 = \tilde{\sigma}'_{x2}y, \sigma_{z2} = -\frac{1}{2}\tilde{\sigma}''_{x2}\left[y^2 - h_2(h_1+h_2)\right]$$

$$\tau_i = -\frac{h_2}{h_1}\tilde{\sigma}_{x2}[y \mp (h_1+h_2)], \sigma_{zi} = \frac{h_2}{2h_1}\tilde{\sigma}''_{x2}[y \mp (h_1+h_2)]^2, (i = 1;3) \quad (7.34)$$

The upper stroke in Eqn (7.34) signifies derivation in x-coordinate. All unknowns of the perturbed stress state now depend on one parameter, $\tilde{\sigma}_{x2}$, which is a statically indeterminate problem. For simplicity, we rewrite the symbol for the stress variable $\tilde{\sigma}_{x2}$, and we use the symbol $\tilde{\sigma}_{x2} = \sigma$ instead. Next, the stored energy system can be written as

$$U = \int_0^1 \sum_{i=1}^{3} \int_{h_i} \left[\frac{\sigma_{xi}^2}{2E_{xi}} + \frac{\sigma_{zi}^2}{2E_{zi}} - \frac{1}{2}\left(\frac{\mu_{xzi}}{E_{xi}} + \frac{\mu_{zxi}}{E_{zi}}\right)\sigma_{xi}\,\sigma_{zi} + \frac{\tau_i^2}{2G_i}\right] \mathrm{d}x\ \mathrm{d}z$$

and by varying the above equation by the unknown function $\tilde{\sigma}_{x2}$, we obtain the strain compatibility equation in the form of

$$\sigma^{\mathrm{IV}} - 2a^2\sigma^{\mathrm{II}} + b^4\sigma = 0,$$

where $a^2 = A/C$ and $b^4 = B/C$, and

$$A = \frac{h_2^3}{3G_2} + \frac{1}{3G_1}\left(h_2^2h_1 + 3h_2^3 + 3h_2^4/h_1\right) + \frac{1}{2}\left(\frac{\mu_{xy2}}{E_{x2}} + \frac{\mu_{yx2}}{E_{y2}}\right)\left(\frac{2}{3}h_2^3 + h_2^2h_1\right)$$

$$+ \frac{1}{6}\left(\frac{\mu_{xy1}}{E_{x1}} + \frac{\mu_{yx1}}{E_{y1}}\right)\left(h_2^2h_1 + 3h_2^3 + 3h_2^4/h_1\right)$$

$$B = 2h_2^2\left(\frac{1}{h_1E_1} + \frac{1}{h_2E_2}\right)$$

$$C = \frac{1}{2E_{y2}}\left[\frac{1}{5}h_2^5 - \frac{2}{3}h_2^4(h_1+h_2) + h_2^3(h_1+h_2)^2 + \frac{1}{5}h_1^3h_2^2\right]$$

$$+ \frac{1}{10E_{y1}}\left[h_1^3h_2^2 + 5h_2^6/h_1 + 5h_1^2h_2^3 + 10h_1h_2^4 + 10h_2^5\right] \quad (7.35)$$

It is common that for such a composite structure, the coefficients a and b have the relationship $b^2 > a^2$, and thus the solution to the characteristic Eqn (7.35) can be written as

$$\sigma = e^{-k_1 x}(C_1 \sin k_2 x + C_2 \cos k_2 x) + e^{k_1 x}(C_3 \sin k_2 x + C_4 \cos k_2 x) \tag{7.36}$$

where k_1 and k_2 are roots to the characteristic equation. Here, the perturbed stress state at both sides of the ply crack is distributed symmetrically, and therefore coefficients C_3 and C_4 in Eqn (7.36) can be taken to equal zero, while coefficients C_1 and C_2 are defined from the condition $\sigma_{x2} = \tau_2 = 0$ at $x = 0$. Thus, the solution can be represented as

$$\sigma_{x2} = \sigma_{20}\left[1 - e^{-k_1 x}\left(\frac{k_1}{k_2}\sin k_2 x + \cos k_2 x\right)\right] \tag{7.37}$$

$$\tau_2 = \sigma_{20}\frac{k_1^2 + k_2^2}{k_2}\, e^{-k_1 x}(\sin k_2 x)z. \quad \text{where}: \quad k_{1,2} = \sqrt{\frac{b^2 \pm a^2}{2}}$$

As an example, let us consider a laminate such as that of Figure 7.3, with the orientations of plies in the laminate given as $\varphi_1 = -\varphi_3 = 45°$, $\varphi_2 = \pi/2$, and the corresponding thicknesses given as $h_2 = 2h_1 h_2 = 0.5\, h_1$ and $h_3 = h_1 = 0.001$ m. The assumed ply properties are as follows: axial Young's modulus $E_1 = 120{,}000$ MPa, transverse Young's modulus $E_2 = 9000$ MPa, and shear modulus $G_{12} = 6000$ MPa. For this type of laminate, the stress distributions in transverse ply $\sigma_{x2} \equiv \sigma_{x2}^{(2)}$, $\sigma_{20} \equiv \sigma_{20}^{(2)}$ (second ply) along the length of laminate for each laminate's ply are illustrated in Figures 7.11 and 7.12.

After formation of the first ply crack, the second system of transverse microcracks starts to form, and the distance between them is considered to be $2X_f$. For example, if we consider loading condition σ_2 as defined by formula (7.38), such that it exceeds the limiting stress value $[\sigma_2] = \sigma_{b2}$, a system of microcracks will exist where the distance

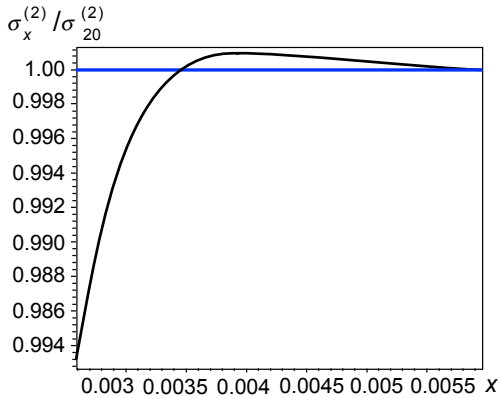

Figure 7.11 The change of stresses $\sigma_x^{(2)}/\sigma_{20}^{(2)}$ along the length.

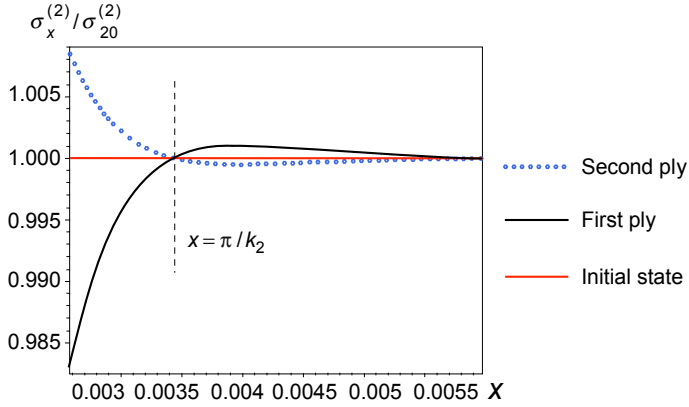

Figure 7.12 The change of stresses $\sigma_x^{(2)}/\sigma_{20}^{(2)}$ in plies along the length.

between them equals $2X_f', X_f' = X_f/2$. When $x = l_1 = \pi/k_2$, the stress value σ_{x2} becomes maximal, and its value may be greater than the limiting strength of that ply; that is, $(\sigma_{x2})_{\max} > \sigma_{b2}$. In that particular moment, shear stress also equals zero ($\tau_2 = 0$). As mentioned earlier, a system of cracks is formed in the middle transverse layer with some distance between them, and that distance also equals π/k_2 (see

Figure 7.13 Transverse stress values between cracks formed in the transverse layer.

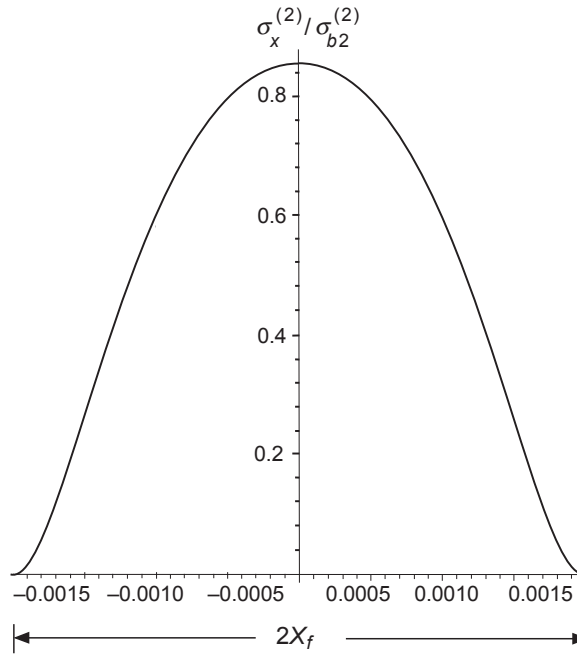

Figure 7.13). In that case, the area between the cracks will have a transverse stress value as given here:

$$\sigma_{x2} = \frac{\sigma_{20}}{sh(\pi k_1/2k_2)}\left(sh\frac{\pi k_1}{2k_2} - \frac{k_1}{k_2}ch(k_1x)\cos(k_2x) - sh(k_1x)\sin(k_2x)\right) \quad (7.38)$$

7.4.3 Defining the ply's transverse Young's modulus after the appearance of ply cracks

In the following discussion, we will assume that after the formation of systems of transverse microcracks in the transverse ply, only the transverse Young's modulus E_2 value is changed. To determine the effective local transverse Young's modulus E_2 in the fractured crack zone, we use the following simplified relationship:

$$\left\langle E_{2(k)}\right\rangle = \left\langle \sigma_{2(k)}\right\rangle / \left\langle \varepsilon_{2(k)}\right\rangle, \left\langle \sigma_{2(k)}\right\rangle = \frac{1}{2X_f}\int_{-X_f}^{X_f} \sigma_2 \mathrm{d}x \quad (7.39)$$

where

$$\langle \varepsilon_2\rangle_{(k)} = 2W/\langle \sigma_2\rangle, \langle \sigma_2\rangle = 0,5P/(h_1 + h_2)$$

Next, the average strain energy density W is calculated from the following formula:

$$W = \frac{1}{2X_f}\int_{-X_f}^{X_f}\sum_{i=1}^{3}\int_{h_i}\left[\frac{\sigma_{xi}^2}{2E_{xi}} + \frac{\sigma_{zi}^2}{2E_{zi}} - \frac{1}{2}\left(\frac{\mu_{xzi}}{E_{xi}} + \frac{\mu_{zxi}}{E_{zi}}\right)\sigma_{xi}\sigma_{zi} + \frac{\tau_i^2}{2G_i}\right]\mathrm{d}x\,\mathrm{d}z \quad (7.40)$$

The stresses inside the integrals of Eqn (7.39) are calculated using the formula given in Eqns (7.34) and (7.37). A simplification is possible when one considers $\tau_i = 0$. To determine the effective stiffness of a composite laminate in the loading direction (transverse to the system of transverse matrix microcracking), the following steps shall be followed:

1. Calculate the average strain energy density given in Eqn (7.40).
2. Determine the average strain value after the appearance of ply cracks using the formula: $\langle \varepsilon_2\rangle = \frac{2W}{\langle \sigma_2\rangle}$.
3. Finally, the effective axial Young's modulus can be found by using the formula $\langle E_2\rangle = \langle \sigma_2\rangle_{(k)}/\langle \varepsilon_2\rangle_{(k)}$.

As before, the procedure of calculating W should be repeated when another ply crack exists in the same layer.

Let us consider a symmetrical laminate constructed from three plies of unidirectional composite lamina with an orientation of 0° for the outer layers and 90° for an

internal layer. The thickness of axial and transverse plies is given as h_1 and h_2, respectively, and h_1 should remain constant. The following material parameters will be assumed: axial Young's modulus of lamina is $E_1 = 120$ GPa, transverse Young's modulus is $E_2 = 9$ GPa, shear modulus is $G_{12} = 6$ GPa, Poisson ratio is $\mu_{21} = 0.28$, and the limiting strength in the fiber's direction is $\sigma_{b1} = 1200$ MPa, and in the transverse direction is $\sigma_{b2} = 40$ MPa. For base calculation, we have $h_1 = h_b = 1$ mm, and we shall consider three different thickness parameters to show the effects of the microscale characteristics of a lamina: $h_2 = h_1 = h_b$, $h_2 = 0.5\ h_1 = 0.5\ h_b$, and $h_2 = 0.25\ h_1$. Next, we use the algorithm provided in Section 7.4.1 (see Eqns (7.39) and (7.40)).

Figure 7.14 illustrates the strains of transverse defect ply under the action of external tensile loading applied to all layers including the axial plies; the sequence of damage can be clearly seen.

From Figure 7.14, it is obvious that after the appearance of a second ply crack in the transverse layer, the layer itself loses the capacity to reinforce the composite laminate. In that case, the following relationship must be adopted: $\langle E_2 \rangle_{(k)} = 0$.

By examining the same laminate structure, but using the algorithm described in this section, we can construct a figure that shows force versus strain for a composite laminate, as shown in Figure 7.15 below. Similarly, the vertical axis designates the force in Newton while the horizontal axis indicates the strains of the laminate, and as before, three different thickness parameters of the transverse layer are examined: ($h_2 = h_1$, $h_2 = 0.5\ h_1$, and $h_2 = 0.25\ h_1$). The sequence of defects is shown in the figure as well, and in all cases it shows two consecutive ply cracks in the transverse layer. As mentioned earlier, after the appearance of a second ply crack, the transverse layer has zero transverse effective value. As such, only axial plies are responsible for work under the action of tensile loading, until complete failure of the laminate.

One may note that when the transverse layer is completely fractured ($\langle E_2 \rangle_{(k)} = 0$), the stiffness of the structure is defined only by the stiffness of the fibers, as shown in

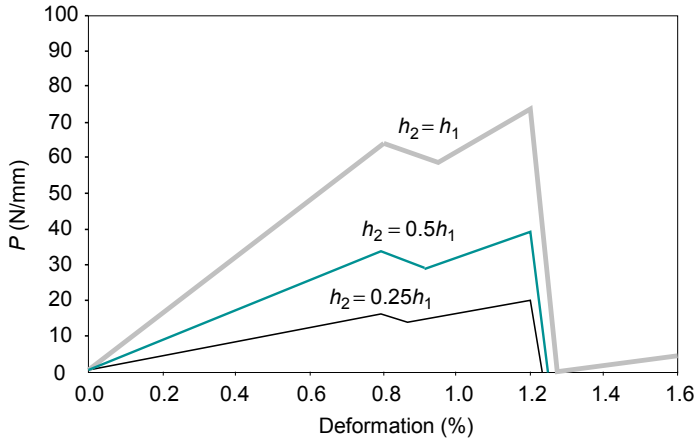

Figure 7.14 Force per unit length versus strain in transverse layer after the appearance of ply cracks.

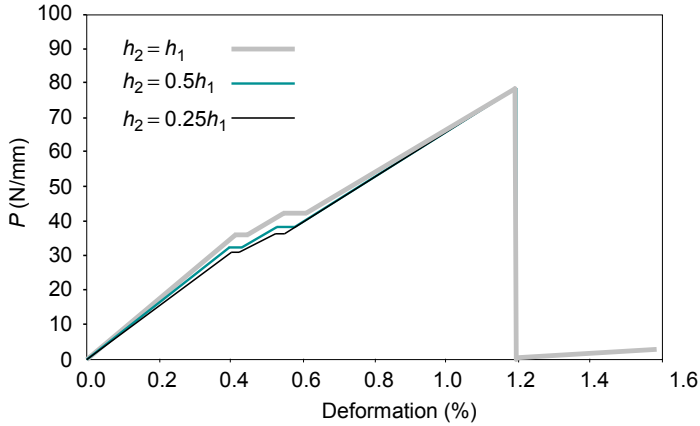

Figure 7.15 Deformation of composite laminate due to ply crack.

Figure 7.15. This scenario of the damage development process can be represented as follows: Let loading $P = P_1$ be the loading in which the first system of microcracks appears, so that we have $[\sigma_2^{(2)}]_{\max} = [\sigma_2^{(90)}]_{\max} = [\sigma_{b2}]$. Let $P = P_2$ be a loading that corresponds to the maximum value shown in Figure 7.15 (the formation of the second system of transverse microcracking). When load P changes from P_1 to P_2, the transverse Young's modulus $E_2^{(90)}$ does not equal zero, but changes as the crack grows (see Eqn (7.39)). If $P > P_2$, only then $E_2^{(90)} = 0$, and in that condition, if the local shear strength condition is violated such that $\tau_{12}^{(i)} > [\tau] \quad \Rightarrow \quad G_{12}^{(i)} = 0$, then only fiber properties are functioning in the damaged ply.

Finally, even when transverse stresses in the transverse layer exceed the limiting strength, the ply should still be able to sustain transverse loading. As a result of damage growth related to the ply cracking, however, part of the matrix has to be excluded, or complete removal of the matrix from the operating mechanism of the laminate must be performed in relation to transverse deformation. If we were to examine the local shear strength criteria at that layer, it would be possible to obtain more information on the matrix operating mechanisms with regard to the shear loading characteristic.

7.4.4 Modeling property degradation for composite laminates

In this section of our work, we will examine a few characteristic examples of modeling the mechanical property degradation process of composite laminate, considering the characteristic parameters on the scales of both the individual ply and the composite laminate as a whole.

In modeling the property degradation of individual plies, we propose to use the kinetic model of damage accumulation, which accounts for micromechanical parameters of damage, in order to capture the birth processes of various potential microdefects, and their growth during loading processes. This was covered in Section 7.2.

The general property degradation process of composite laminate is conditionally divided into two stages. In the first stage, we propose that the property degradation of effective properties of composite laminate is defined by the processes of individual layers that depend on ply stress levels in the composite laminate. In the second stage, we consider ply cracks, which are widely characterized as a damage mechanism in composite laminate. This damage can occur in one or a few layers of the composite laminate, leading to the formation of a system of ply cracks in a ply. This mechanism was described in Section 7.3.4. In this stage, the process parameter is defined as the point at which ply cracks start to occur in one or a few transverse layers of composite laminate. This parameter is controlled by the stress level in each ply that is subjected to a loading process condition. Furthermore, whenever any layer in a composite has ply cracks, the transverse Young's modulus value for that layer is adjusted or refined. The degradation process of composite laminate is again adjusted and refined, by repeating the proposed degradation algorithm with new transverse characteristics in layers where ply cracks have taken place.

As an example, we will consider and examine a scenario of the damage-accumulation process where transverse matrix cracks emerge and grow in layers of the composite laminate. For this case, the damage process can be characterized by transverse matrix microcracks in the transverse plies, where the microcracks are initiated by the broken fibers or microdefects of another nature (such as micropores). We will assume here that microcracks are oriented perpendicular to the direction of reinforcements. As discussed earlier, in such a model, the characteristic growth rate of damage may be linear or exponential for fiber composites under quasistatic and cyclic loading conditions during the initial growth of the defect, and slows upon reaching a stabilization stage.

7.4.4.1 Degradation model of ply cracks in local layers of composite laminate

In describing property degradation of composite laminates, we use the microdefect growth model, where we assume that $a = 0$, $b \neq 0$. Furthermore, the following assumptions are used:

1. Damage accumulation in fibers is absent. Thus, the modulus of elasticity of fibers in the layer is not reduced or degraded.
2. We consider that property degradation of composites is in general defined by damage accumulation in the matrix (microcracking).
3. For transverse modulus of elasticity and shear modulus, the following are simplification rules of degradation in relation to formula (7.5):

$$E_2^i = E_{2o}\left[1 - K_E^i S_E(t,\sigma,\tau)\right], G_{12}^i = G_{12o}\left[1 - K_G^i S_G(t,\sigma,\tau)\right],$$

where E_{2o} and G_{12o} represent the modulus of elasticity of perfect material.

4. We propose that the rate of change in the length of the short transverse microcrack is proportional to its length, while at the same time remaining constant. As such, we can consider that microcrack growth occurs at a constant rate and sufficiently far from the ply boundaries to ensure that it is not retarded. In this case, based on Eqn (7.22), the damage model in the transverse layers of laminate can be written in the form

$$S_{E,G}(t,\sigma,\tau) = \left(1 - e^{-b_{E,G}n}\right)$$

Then, we will obtain the following degradation model of the transverse modulus:

$$E_2^i = E_{2o}\left[1 - K_E^i\left(1 - e^{-b_E n}\right)\right], G_{12}^i = G_{12o}\left[1 - K_G^i\left(1 - e^{-b_G n}\right)\right] \tag{7.41}$$

Here, K_E^i and K_G^i are parameters of the degradation model that depend on the level of stress, and $b_{E,G}$ are microparameters defined from the experiments.

5. Parameters K_E^i depend on the rate of change of the modulus in the plies that are experiencing transverse stresses. At least for compression, microcracks are assumed not to grow. Therefore, we have

$$K_E^i = K_{Eo} f_{KE}\left(\sigma_2^i\right) = K_{Eo}\left\{\frac{\sigma_2^i + \left|\sigma_2^i\right|}{2\sigma_b}\right\}^{m_0}, \tag{7.42}$$

where m_0 is the microparameter defined from the experiment, K_{Eo} is the parameter defined from the typical experiment to determine the mechanical properties of materials; for example, the modulus of elasticity.

6. The parameter K_G^i depends on the rate of change in shear modulus in the plies that are experiencing transverse and shear stresses:

$$K_G^i = K_{Go} f_{KG}\left(\sigma_2^i, \tau_{12}^i\right) = K_{Go}\left\{\alpha\left(\frac{\tau_{12}^i}{\tau_b}\right)^{m_\tau} + \left(\frac{\sigma_2^i + \left|\sigma_2^i\right|}{2\sigma_b}\right)^{m_\sigma}\right\}, \tag{7.43}$$

where m_τ, m_σ, and α are microparameters defined from the experiment that pertain to degradation effects for specific plies due to the damage-accumulation process, and K_{Go} is defined from the experiment mentioned above. As a result of these assumptions, the proposed algorithm will allow us to predict the mechanical properties of various laminated structures, using the specific mechanical properties of the ply that are obtained from the degradation process under specific loading process parameters.

Next, some examples of modeling the degradation process of laminate structures will be introduced, using a phenomenological method to identify the parameters used in the damage-accumulation and degradation models. We will now show the steps for identifying the parameters according to the experimental data. In this case, the effective characteristics of a composite with a specific configuration, such as the number of layers, and the thickness of layers with various orientations, are initially known. We will also assume that for a specific composite laminate

structure constructed from laminae with known properties, the dependences of effective properties on process parameters are also known. As an example, we examine cyclic loading conditions with pulsating cycles. As such, it is safe to assume that the degradation process is defined only by the maximum stress reached for that particular loading condition. The case of general cyclic loading conditions is not considered here. This restriction is not a fundamental issue when assessing the property degradation of composite laminates, although it requires careful half-cycle cyclic stress analysis in order to accurately describe the dependence of parameters K_E^i and K_G^i on cyclic stress parameters such as average stress, maximum stress, coefficient of asymmetric cycle, etc.

The main content of the proposed methodology is the model parameters of damage and degradation, which are defined from specific experimental testing. Only then is it possible to analyze the character of degradation in the individual layers of composite systems, examine the sequence of critical damage in the individual layers, and predict the behaviors of other structures built from those layers.

As a reminder, if the transverse Young's or shear modulus in any lamina decreases and drops below a given critical value due to the damage-accumulation process, the material characteristics for that lamina are assumed to equal zero. Furthermore, the final transverse Young's modulus will equal zero only when it reaches critical values for positive transverse stresses; that is, when the transverse layer is subjected to tensile loading. In compressive loading, the lamina retains its original properties. For lamina in which one or both of these characteristics are reset to zero upon reaching their critical values, loading is sustained in the direction of reinforcing fibers, meaning that fiber properties are not degraded.

When changes in lamina properties take place, the corresponding characteristics are then reset to the changed values (only in the corresponding ply), and the parameters of structures are again recalculated. In this way, the process of property degradation can still be described, while the model parameters do not change. At the same time, with the new effective values, the stresses or strains in a lamina are checked to see if they have reached critical stress or strain levels (fracture stresses or strains). In a situation involving a transverse ply, for example, the transverse modulus at that point will decrease abruptly when the first ply crack appears. The approximate level of jump in the transverse shear modulus can be computed by the following formula:

$$\Delta E_2 = E_2^0 - E_2^{\text{damage}}$$

where E_2^0 is the transverse modulus of elasticity at the point of interest without microcracks, while E_2^{damage} is the transverse modulus of elasticity at the point of interest after the ply crack takes place. The value E_2^{damage} can be calculated using the procedure described in Section 7.3.4. We can also estimate E_2^{damage} using the following simplified equation:

$$E_2^{\text{damage}} = E_2^0 / \left[1 + (1/2l_f) \int_{-l}^{l} \sigma_2(x) \mathrm{d}x / \sigma_{20} \right]$$

where σ_{20} is the amplitude value in the expression for $\sigma_2(x)$ (see Eqn (7.38)). In general, after obtaining the overall picture of degradation in individual plies, the stress levels in all elements of the composite structure are calculated and redefined; based on these new stress distributions, the property degradation of the laminate is recalculated using the algorithm described earlier. Similarly, it is possible to predict the behavior of various composite structures under loads that differ from test loading conditions.

7.4.4.2 Numerical examples of modeling property degradation

We will examine the first composite structure, $(0,\pm45)_s$, under tension loading conditions applied along axis Ox only. In this case, the limiting value (i.e., the loading maximum cyclic load) is chosen to correspond with 70% of the limiting strength state ($\sigma_2 \approx \leq 0.7\sigma_{b2}$). We assume that the mechanical properties of the plies in the composite are the following: $E_1 = 137{,}000$ MPa, $E_2 = 6400$ MPa, $G_{12} = 4410$ MPa, $\mu_{21} = 0.28$, $\sigma_{b2} = 10$ MPa, and $\tau_b = 40$ MPa (Reifsnider, 1988; Reifsnider & Highsmith, 1981). Using the algorithm described above, we established the following degradation model parameters for the lamina: $\alpha = 12.7$, $K_{E0} = 2.04$, $K^i_{G0} = 1$, $m_0 = 0.88$, $m_\tau = 0.3$, and $m_\sigma = 1$. The results are shown in Figure 7.16, with the solid curve reflecting the obtained theoretical line of a given experiment. As a result, it is possible to find the characteristic of degradation with transverse matrix cracking excluded.

In the next stage, we receive the refined results that account for transverse matrix cracking in the individual lamina (see Figure 7.17). Curves marked with asterisks show the refined results associated with transverse matrix cracking. As shown in the graphs, the refinement associated with the stress distributions in the layers can be very substantial (curves marked with asterisks show the new graphics associated with the refined results). We see that for this particular structure, the shear and transverse moduli of elasticity in the transverse ply (+45°) are reduced significantly. It can be seen that despite this degradation in properties, the transverse ply is not yet fractured. Let us examine the strength condition, which is dictated by transverse strength. It can be seen that despite the property degradation, fracture in the composite structure

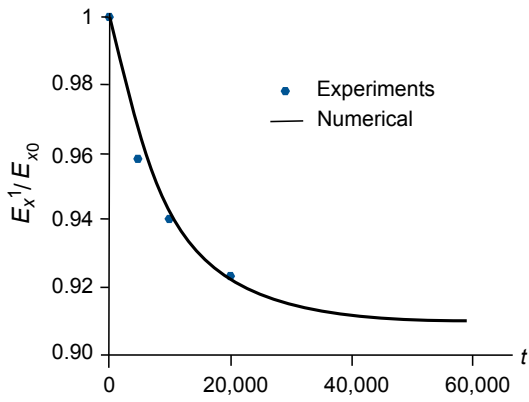

Figure 7.16 Variation of effective Young's modulus for structure $(0,\pm45)_s$

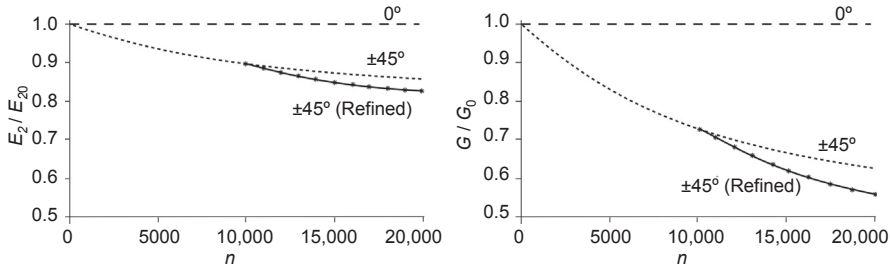

Figure 7.17 Refined transverse Young's and shear moduli of plies in composite laminate $(0,\pm45)_s$

does not occur; that is, the strength condition is satisfied. The curves marked by asterisks are obtained by considering the redistribution of stress in the composite structure and accounting for degradation effects, both of which are considered to be refinements of the original results. These refinements show the stabilization effect of property degradation for individual layers as well as the whole structure. In relation to the significant reduction of properties in transverse plies, however, one must always be aware of the possibility of fracture due to changes in the direction of loading applied to the composite structure, and also the fracture strength in *complex* loading conditions; that is, the existence of simultaneous tensile and shear load conditions. In such cases, detailed examination of the strength levels that result from such loads must always be performed.

The results shown in Figure 7.18 demonstrate that the proposed algorithm allows us to predict the degradation process for the effective properties of composite laminates after the formation of cut-through transverse matrix cracking.

Next, we examine the second type of structure, $(0.90,\pm45)_s$. The theoretical and experimental results are shown for the damage initial state; that is, damage from transverse microcracking (see Figure 7.19). The solid line corresponds to theoretical values constructed from the obtained model parameters. Basically, the line is described by the

Figure 7.18 Refined effective Young's and shear moduli for composite laminate $(0,\pm45)_s$

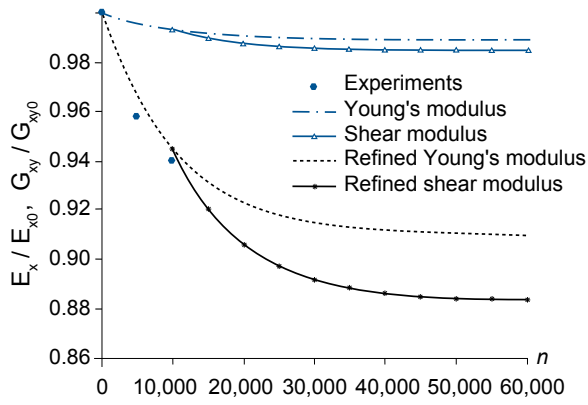

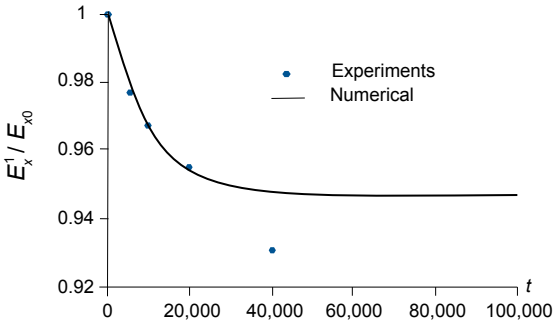

Figure 7.19 Variation of effective Young's modulus for composite laminate $(0.90,\pm45)_s$

same parameters $m_0 = 1$, $m_\tau = 0.3$, and $m_\sigma = 1$ used in the first composite laminate described earlier. By considering various structures in the experimental testing, these parameters could be adjusted to account for the specific degrees of stress in those structures. Therefore, it is desirable to have not just one testing structure, but a few.

As shown in Figure 7.20, computation of degradation of the lamina using the obtained model parameters reveals that transverse characteristics and shear modulus in the individual layers are greatly degraded. The significant property degradation of individual plies may cause fractures to take place in the structure when complex loading conditions exist, or when a change in loading direction occurs.

Nevertheless, these degradations do not lead to significant degradations in the effective properties of the composite structure (see Figure 7.21).

Based on the numerical examples shown here, a few concluding remarks are derived:

1. The proposed model is sufficient to adequately reflect the damage behaviors for a variety of composite structures.
2. It is expected that such a model will allow us to predict damage behavior for composites that have the same specific configuration as the composite structure, but different loading conditions. This is particularly important because it is well known that when prediction of damage and degradation is a concern, the superposition method by different types of loading conditions cannot be applied.

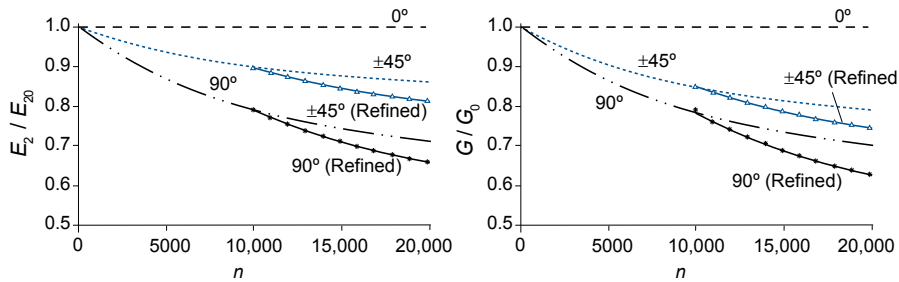

Figure 7.20 Refined Young's and shear moduli of plies in composite laminate $(0.90,\pm45)_s$

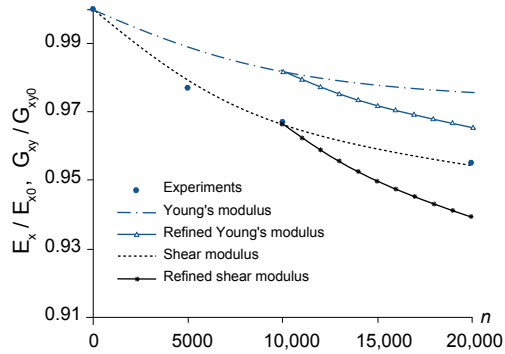

Figure 7.21 Refined effective Young's and shear modulus for composite laminate $(0.90,\pm45)_s$

7.4.5 The dependence of interlayer delamination cracks on ply cracks

In composite laminates, the birth of a system of interlayer cracks (delamination cracks) is due to high stress concentrations caused by ply cracks. Because of this, interlayer cracks typically appear in the vicinity of ply cracks. As discussed earlier, ply cracks can significantly influence the effective properties of composite laminates, especially shear characteristics, and this phenomenon has been investigated extensively. However, as far as we know, the influence of this type of defect on the appearance and growth of interlayer microcracks has not been widely studied, although such a damage development process is typical and crucial in fiber-reinforced composites.

In this section, we will examine the property degradation model for fiber-reinforced composite materials as it applies to damage caused by ply delamination that occurs following the formation of ply cracks. The main idea in the proposed method is that it is sufficient to describe the degradation model of the effective properties of composite laminates based on property degradation of the composite's lamina or ply. Furthermore, reduction in effective properties will be determined directly from the typical relationships of the effective mechanical properties of composite materials.

Let E_{i0} and G_{i0} be the characteristics of a lamina ($i = 1,2$). We will consider the layers to be sufficiently thin, such that the stresses are distributed uniformly over the thickness of the layer (see Figure 7.22). The part of the layer corresponding to the interlayer cracking of length $2l$ is excluded from the calculation. Furthermore, by accounting for the strain compatibility condition, we can assume that the following

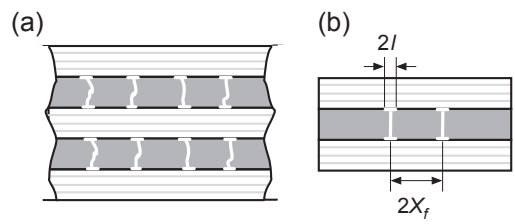

Figure 7.22 (a) Delamination and ply cracks; and (b) schematic of property degradation due to delamination and ply cracks.

equalities hold: $E_1F = E_{10}(F - \Delta F)$, where $F = 2X_f h$ and $\Delta F = k^E 2lh$. Here, the value ΔF is part of the cross-sectional area in the vicinity of the interlayer crack that is not included for calculation in the current analysis. We shall then have the relation $E_1 = E_{10}(1 - k^E\Delta)$, where $\Delta = l/X_f$, $2l$ is the length of delamination crack, and $2X_f = \pi/k_2$ is the distance between two ply cracks. Analogously, a similar equality is obtained for shear modulus. As a result, we have the following equations: $E_1^{(1)} = E_{10}$, $E_2^{(1)} = E_{20}$, $G_{12}^{(1)} = G_{120}, E_1^{(2)} = E_{10}(1 - k^E\Delta)$, and $G_{12}^{(2)} = G_{120}(1 - k^G\Delta)$. Again, with similar reasoning, the transverse elastic modulus for the second layer is given as

$$E_2^{(2)} = \left(\sigma_{20}^{(2)}\right)^2 X_f h_2 \Bigg/ \left(\int_{-(X_f-1)}^{(X_f-1)} \int_{-h_2/2}^{h_2/2} \frac{\left(\sigma_{20}^{(2)}\right)^2}{2E_{20}} \mathrm{d}x\mathrm{d}y \right) \tag{7.44}$$

The parameters k^E and k^G can be found later by comparing with the experimental data, or from comparison with more precise results from experimental investigations. Nevertheless, one should generally use the following property degradation model:

$$\begin{aligned} E_1^{(1)} &= E_{10}, E_2^{(1)} = E_{20}, G_{12}^{(1)} = G_{120}, \\ E_1^{(2)} &= K_E E_{10}\left(1 - k^E\Delta\right), G_{12}^{(2)} = K_G G_{120}\left(1 - k^G\Delta\right), \end{aligned} \tag{7.45}$$

where the values $K_E E_{10}$ and $K_G G_{120}$ correspond to the *real* (damage of ply cracks) values of effective elastic moduli at the point when the growth of delamination-caused defects began.

Next, we propose the algorithm for the recalculation of the effective properties of composite laminates that account for the interlayer delamination crack. In plies where ply cracks have occurred, the effective characteristics are determined from Eqns (7.44) and (7.45). As a result, we find the characteristics of rigidity b_{ij} and B_{ij} as functions of parameter Δ. Thereafter, the effective properties of composite laminate can be calculated. For example, for orthotropic composite laminate, we have

$$\begin{aligned} E_x &= E_x(\Delta) = B_{11}(\Delta) - \frac{B_{12}^2(\Delta)}{B_{22}^2(\Delta)} \\ E_y &= E_y(\Delta) = B_{22}(\Delta) - \frac{B_{12}^2(\Delta)}{B_{22}^2(\Delta)} \\ G_{xy} &= G_{xy}(\Delta) = B_{33}(\Delta) \end{aligned} \tag{7.46}$$

Next, we will show that applied property degradation models (7.44) and (7.45) allow us to accurately predict changes in the effective properties of composite laminates. For this purpose, we shall use the results of investigations (Kashtalyan & Soutis, 2001, 2002a,b, 2005) that were devoted to studying the influence of delamination on

the properties of the composite laminate. We shall see that for a specific composite structure, by selecting appropriate parameters introduced in the degradation model of effective properties for lamina, one can successfully model the property degradation caused by delamination damage occurring as a result of ply cracks. We now consider a T300/5208 composite having the configuration $[0_2/90_4]$. The material characteristics of a lamina are as follows: $E_{10} = 134$ GPa, $E_{10} = 10.5$ GPa, $E_{10} = 5.5$ GPa, and $\mu_{12} = 0.28$. The ply thickness is assumed to be 0.14 mm. Using Eqns (7.25)−(7.27), we find

$$G_{xy} = B_{33} = \frac{G_{120}\left[h_1 + K_{Go}\left(1 - k^G\Delta\right)h_2\right]}{(h_1 + h_2)} = \frac{G_{120}\left[1 + 2K_{Go}\left(1 - k^G\Delta\right)\right]}{3},$$

$$E_x = \frac{\overline{E}_1 + 2E_2^{(2)}}{3} - \left(\mu_{12}\frac{\overline{E}_1 + 2K_E\overline{E}_1\left(1 - k^E\Delta\right)}{3}\right)^2 \Bigg/ \left(\frac{\overline{E}_2 + 2K_E\overline{E}_1\left(1 - k^E\Delta\right)}{3}\right) \tag{7.47}$$

Using these relations, and comparing them with results obtained for the same composite laminate in Kashtalyan and Soutis (2001, 2002a,b, 2005), we obtain $K_E = 0.9582$, $k^E = 0.855$, $K_G = 0.8875$, $k^G = 2.197$.

Figure 7.23 indicates that using these parameter values, changes in the effective properties of such a composite laminate are in agreement with numerical results of precise and exact models found in prior work (Kashtalyan & Soutis, 2001, 2002a,b, 2005). This allows us to state that the more simplified degradation model given by Eqns (7.44)−(7.47) can ensure factually accurate prediction of property degradation caused by delamination resulting from ply cracks. Again, the parameters k^E, k^G, $(1 - k^G\Delta)$, and $(1 - k^E\Delta)$ correspond to the area of the matrix in which the damaged lamina are excluded from the analysis, and the values give the *real* (damage of ply

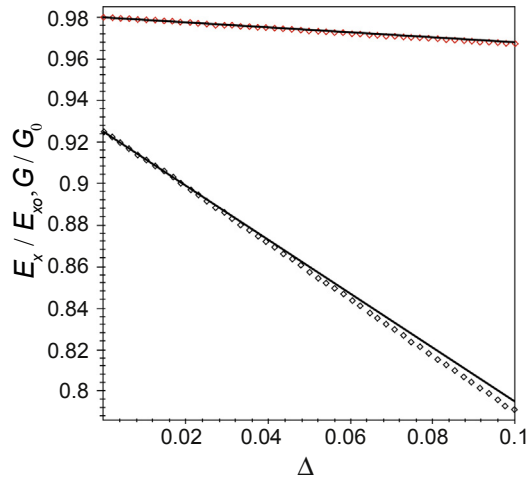

Figure 7.23 Stiffness reduction of $[0_2/90_4]$ for interlayer crack length. (Solid line—(Kashtalyan & Soutis, 2001, 2002a,b, 2005)) and dotted line—proposed model).

cracks) values of effective elastic moduli when the growth of delamination-caused defects starts.

7.4.6 On the identification of micromechanical parameters of damage accumulation of the degradation model

The micromechanical approach proposed in the damage-accumulation and degradation models requires that we account for processes that occur in the composite laminate at the micro level. Based on the analysis of damage evolution equations given in this work, this approach uniquely accounts for scale effects, because the birth and growth processes of microdefects occur at varying scales. The most important step in implementing this micromechanical approach for describing damage accumulation and stiffness degradation is to identify model parameters, and this requires us to use the experimental empirical data to ensure that the model will provide sufficiently reliable descriptions of the processes, corresponding to physical reality and the results of specific experimental testings.

We will now focus briefly on the three damage-accumulation mechanisms discussed earlier as they apply to the three types of microdefects: debonding (matrix delamination) at the ends of broken fibers, microcracks along the longitudinal reinforcements, and microcracks in the matrix, which are transverse to the direction of reinforcement and initiated by broken fibers. We mention here that model parameters derived from microbased experiments yield the most accurate and reliable results, and the selected parameters themselves do not represent damage accumulation, but rather two individual elements representing the birth and growth of microdefects. Thus, for the first and second types of defects, it is necessary to determine the number of fibers broken in a particular number of cycles. For example, we consider the burned-resin test, for which we burned carbon-reinforced plastic composite for 15 h at 40 °C, and from that we can determine the fiber breakage number. The process of removing resin in order to reveal the number of broken fibers is very complex, and is difficult because of the risk of further damage to fibers. Furthermore, testing with several samples must be carried out in order to account for various stress ranges and loading cycles. However, for the quasistatic loading procedure we can use acoustic emission signals to detect the number of fibers broken in testing. Nevertheless, going back to the identification problem, for boron−aluminum and carbon-reinforced plastic composites (Tamuja & Pratacova, 1986), it is possible to use the dependence of fiber breakage on stress level, calculated as $N = \gamma(\sigma)^k$ (where N is the number of broken fibers and σ is the applied stress level), for which the parameters are found using the method of least squares. The direct experimental identification of model parameters is always associated with great technical difficulties; as a result, it is sometimes necessary to add an additional hypothesis to the problem. For example, under cyclic loading conditions, we can use a linear logarithmic function when modeling the birth process of microdefects: $N = A + B\ln n$. It is possible for us to further assume that (1) the parameter β does not depend on the applied stress loading σ: $N = A(\Delta\sigma) + B\ln n$, and (2) dependence of the fiber breakage number on the number of cycles can be represented by $N = A(\Delta\sigma)(1 + B\ln n)$. In both cases, the parameter again does not depend

on loading cycles, and from the first hypothesis, the expression means that the number of fiber fractures depends only on ln n. The second hypothesis basically follows from the general and more realistic assumption of similarities between the dependence curve of broken fibers, and applied loading $\Delta\sigma$ and loading cycles ln n, such as $N(\Delta\sigma,n) = f_1(\Delta\sigma)f_2(n)$. In both cases, the damage evolution in Eqn (7.6) contains one parameter describing the damage initiation process—the initial size of microdefects s_0. This value must be defined in the microexperiments. In cyclic loading, it is sufficient to determine the average size of the microdefect after the first cycle. Thus, when there is a sufficiently strong bond between the fiber and matrix, it is possible to assume that the broken fibers lead to fiber−matrix debonding, and growth of the disbond will take place after the next cycle. In that case, we can use $s_0 = 0$. In the case of low shear strength bonding of fiber−matrix, it is possible to use $s_0 = k\chi$, where k is a constant and χ is an effective length. If the microdefect is determined to consist of microcracks in the matrix that are perpendicular to broken fibers, then we can naturally take the initial defect length equal to the diameter of fiber.

With regard to the origin of microdefect (7.2), experimental data in the literature suggest that at a fixed range of stresses, the birth rate of microdefects does not depend on the number of loading cycles; that is, $v = v(\Delta\sigma)$ and $v = \partial N/\partial t$. Generally, it is possible to have the form $v = v_0(\Delta\sigma)^m$, where v_0 and m are model parameters defined by the method of least squares on the lines plotted by acoustic emission. For the growth model under quasistatic loading conditions, it is possible to use the linear growth model of debonding microdefects, $l = l_0 + \alpha(\sigma/\sigma_b)$, where σ_b is the ultimate stress. As an example, the identification of model parameters based on Rosen et al.'s data (Rosen & Dow, 1972) gives us the values $l_0(mm) = -0.221$ and $\alpha(mm) = 0.4944$. For microdefects—debonding at the ends of broken fibers under quasistatic loading—we use the hypothesis that disbond birth rate and current length are independent; that is, $\mathrm{d}l/\mathrm{d}\sigma = \alpha = \text{const}$. In cyclic loading, it is natural to assume that the growth of disbonds in every half cycle does not depend on the number of loading cycles or increases resulting from growth in stress levels, just as with static loading. Under those assumptions, we have $\Delta l = \int_{\sigma_{\min}}^{\sigma_{\max}} (\mathrm{d}l/\mathrm{d}\sigma)\mathrm{d}\sigma = \alpha(\sigma_{\max} - \sigma_{\min}) = 2\alpha\sigma_a$. In particular for glass-reinforced plastic composite testing (Tamuja & Pratacova, 1986), the growth rate of debonding is $v = 1.044\ (\sigma_a/\sigma_b)$.

In identifying degradation model parameters, we use the microexperimental data and the results of macroscopic testing, since the degradation model consists of the damage-accumulation process plus additional parameters. As mentioned earlier, however, due to the complexity and difficulty of defining model parameters based on microscopic testing, we use other equivalent methods to combine the micromechanical and phenomenological methods of identification, using the model parameters in the damage-accumulation and degradation models obtained from macroexperiments. For example, for the models discussed earlier, the parameters $b_{E,G}$ and $m_0,m_{\sigma,\tau}$ can be defined from microexperiments, while degradation parameters K_{E_0,G_0} come from macroexperiments. For the equivalent method, all parameters are obtained from the system of macroexperiments performed with composite-structure testing. Such an

approach is useful, for example, when these parameters are derived from macroexperiments for the reduction of effective properties E_x, E_y, and G_{xy} in one or several testing structures; using these parameters to predict property degradation for other types of structures will yield sufficiently reliable and satisfying results. In other words, the obtained parameters used for modeling and prediction of stiffness degradation of an individual layer can also be used to predict the degradation of other composite laminate structures constructed from the same type of ply.

7.5 Conclusions

In this chapter, damage-accumulation and degradation models based on a micromechanical−empirical approach have been proposed. Although many such models have been proposed by various authors to describe damage evolution in composite materials, they mostly focus on growth and degradation of microdefects during the middle and late stages of damage evolution in fiber-reinforced composite materials. The proposed model is framed by the early and middle stages of the damage evolution process that are also the central focus of this chapter. As such, the damage-accumulation and stiffness-degradation models contain both damage initiation and growth processes of microdefects in composite materials. Furthermore, the proposed models are robust enough to cover the spectrum of microdefects that are commonly cited as the main damage mechanisms in the reduction of the effective properties of fiber composite materials under various loading conditions.

As mentioned earlier, damage evolution in fiber-reinforced composite materials is a very complex process due to its heterogeneity and anisotropy. Nevertheless, the modeling and prediction of the damage-accumulation process and its influence on the effective characteristics of composites can be made simpler if the damage mechanisms most likely to be responsible for stiffness degradation can be identified. Furthermore, the property degradation that may set the fatigue limit of any composite material structure—for example, ply orientation, stacking sequence, and degree values such as 0°, 45°, or 90°—can be easily assessed using microdamage-accumulation and degradation models (for a ply or plies) that are likely to cause stiffness degradation in the laminate structure of fiber composite materials. However, to ensure the reliability and accuracy of results in accordance with the available experimental data, an empirical model is also taken into account. By doing this, the proposed models can also be used to predict the stiffness degradation of fiber composite materials with different architectures, thus giving these proposed models the capability to predict the behavior of fiber-reinforced composite materials that are outside the constraints of experimental conditions.

Acknowledgment

The authors are indebted to Prof. Valery Vasiliev for all the fruitful discussions and guidance in this advanced area of composite materials that you have pioneered.

References

Bazant, Z. P., Daniel, I. M., & Li, Z. (1996). Size effect and fracture characteristics of composite laminates. *Journal of Engineering Materials and Technology—Transactions of the ASME, 118*, 317−324.

Beaumont, P. W. R., & Sekine, H. (2005). Cracking models. In C. Soutis, & P. W. R. Beaumont (Eds.), *Multi-scale modeling of composite material system − The art of predictive damage modeling* (pp. 124−195). Cambridge: Woodhead Publishing Ltd.

Bolotin, V. V. (1984). Delamination type of defect in composite materials and constructions. *Mechanics of Composite Materials, 2*, 239−255 (In Russian).

Bradley, W. L., Corleta, C. R., & Goetz, D. P. (1987). *Fracture physics of delamination of composite materials*. AF0SR-TR-88−0020.

Budiansky, B., & Fleck, N. A. (1993). Compressive failure of fiber composites. *Journal of the Mechanics and Physics of Solids, 41*, 183−211.

Camponeschi, E. T., & Stinchcomb, W. W. (1982). Stiffness reduction as an indicator of damage in graphite-epoxy laminates. In *Composite materials: testing & design (6th conference) ABTM STP 787* (pp. 225−246).

Clarke, D. A., & Bader, M. Q. (1986). Direct observation of fibre fracture in a model composite. *Journal of Materials Science Letters, 5*(9), 903−904.

Davila, C. G., Camanho, P. R., & Rose, C. A. (2005). Failure criteria for FRP laminates. *Journal of Composite Materials, 39*(4), 323−345.

Drzal, L. T., & Madhucar, M. (1993). Fiber-matrix adhesion and its relationship to composite mechanical properties. *Journal of Material Science, 28*, 569−610.

Dudchenko, A. A., Lurie, S. A., & Halim, K. (2006). Multiscale modeling on damage mechanics of laminated composite materials. In *Proceedings of conference on damage in composite materials: Simulation and non-destructive testing, Stuttgart*.

Dzenis, Y. A., & Qian, J. (2001). Analysis of micro damage evolution histories in composites. *International Journal of Solids and Structures, 38*(10), 1831−1854.

Fleck, N. A. (1997). Compressive failure of fiber composites. *Advances in Applied Mechanics, 33*, 44−117.

Fukuda, H., Yakushiji, M., & Wada, A. (1997). Loop test for the strength of monofilaments. In M. L. Scott (Ed.), *Textile composites and characterization: Vol. 5. Proceedings of 11th International Conference on Composite Materials (ICCM-11)* (pp. 886−892). Australia: Woodhead Publishing Ltd.

Gamstedt, E. K., & Andersen, S. I. (2001). *Fatigue degradation and failure of rotating composite structures − Materials characterization and underlying mechanisms*. Denmark: Riso National Laboratory.

Ghiorse, S. (1993). Effect of void content on the mechanical properties of carbon/epoxy laminate. *SAMPE Quarterly, 24*(2), 54−59.

Guz, A. N. (1990). *Fracture mechanics of composite materials in compression*. Kiev: Naukova Dumka (In Russian).

Harris, B. (2003). In B. Harris (Ed.), *A historical review of the fatigue behavior of fibre-reinforced plastics/Fatigue in composites* (pp. 1−35). Woodhead Publishing Ltd and CRC Press.

Hinton, M. J., & Soden, P. D. (1998). Predicting failure in composite laminates: the background to the exercise. *Composites Science and Technology, 58*(7), 1001−1010.

Jain, J. R., & Ghosh, S. (2009). Damage evolutions in composites with a homogenization-based continuum damage mechanics model. *International Journal of Damage Mechanics, 18*(6), 533−568.

Johnson, P., & Chang, F. K. (2001a). Characterization of matrix crack-induced laminate failure − Part I: Experiments. *Journal of Composite Materials, 35*(22), 2009−2035.

Johnson, P., & Chang, F. K. (2001b). Characterization of matrix crack-induced laminate failure − Part II: Analysis and verifications. *Journal of Composite Materials, 35*(22), 2037−2074.

Kachanov, L. (1988). *Delamination buckling of composite materials*. Netherland: Kluwer Academic Publishers.

Kanaun, C. K., & Chudnovskii, A. I. (1970). Quasi-brittle fracture. *Mechanics of Solid Body, 3*, 185−186 (In Russian).

Kashtalyan, M., & Soutis, C. (2001). Mechanisms of internal damage and their effect on the behavior and properties of cross-ply composite laminates. *International Journal of Fracture, 112*, L3−L8.

Kashtalyan, M., & Soutis, C. (2002a). Analysis of local delaminations in composite laminates with angle-ply matrix cracks. *International Journal of Solids and Structures, 39*, 1515−1537.

Kashtalyan, M., & Soutis, C. (2002b). Mechanisms of internal damage and their effect on the behavior and properties of cross-ply composite laminates. *International Applied Mechanics, 38*(6), 641−657.

Kashtalyan, M., & Soutis, C. (2005). Analysis of composite laminates with intra- and inter-laminar damage. *Progress in Aerospace Sciences, 41*, 152−173.

Kiyalbaev, D. A., & Chudnovskii, A. I. (1970). On fracture of deformable body. *PMGF, 3*.

Kwon, Y. W., Allen, D. H., & Tarelja, R. (Eds.). (2008). *Multiscale modeling and simulation of composite materials and structures*. Springer.

Luat, D. C., Lurie, S. A., & Dudchenko, A. A. (2010). Modeling of degradation of the composite properties on cracking and delamination when subjected to static and cyclic loading. *Composites: Mechanics, Computations, Applications: An International Journal, 1*(1), 1−19.

Lurie, S. A. (1994). On the entropy damage accumulation model of composite materials. In *Proceedings of workshop on computer synthesis structure and properties of advanced composites − Russia−US* (pp. 6−18). Institute of Applied Mechanics.

Movchan, A. A. (1990). Micromechanical approach in the problem of describing anisotropic scattered damage accumulation. *Solid Mechanics, 3*, 115−123 (In Russian).

Obchiskii, A. C. (1988). *Failure and destruction processes in composite materials*. Moscow: Science (In Russian).

Pagano, J. N. (Ed.). (1993). *Interface effect in composite materials*. Moscow: World (In Russian).

Paipetis, A., & Galiotis, C. (2001). Modelling the stress transfer efficiency of carbon-epoxy interfaces. *Proceedings of the Royal Society − A Mathematical, Physical and Engineering Science, London, 457*, 1533−1785.

Reifsnider, K. L. (1988). Service induced damage in composite structures/Handbook of composites. In C. T. Herakovich, & Yu. T. Tarnopolskii (Eds.), *Structures and design* (Vol. 2, pp. 231−262).

Reifsnider, K. L. (1994). Modeling of the interphase in polymer-matrix composite material systems. *Composites, 25*(7), 461−469.

Reifsnider, K. L., & Highsmith, A. L. (1981). *Characteristic damage states: A new approach to representing fatigue damage in composite laminates/Materials: Experimentation and design in fatigue*. Surrey: Westbury House, 246−260.

Rosen, B. W. (1964). Tensile failure of fibrous composites. *AIAA Journal, 2*, 1985−1991.

Rosen, B. W., & Dow, N. F. (1972). Mechanics of failure of fibrous composites. In H. Liebovitz (Ed.), *Fracture* (Vol. 7, pp. 300−366). Academic Press.

Singh, C. V., & Talreja, R. (2010). Evolution of ply cracks in multidirectional composite laminates. *International Journal of Solids and Structures, 47*(10), 1338−1349.

Soborejo, A. B. O. (1967). Use of entropy principles in estimating reliability functions for creep rupture characteristics of engineering materials a1 high temperatures. In *Proceedings of international conference on the strength of metals and alloys, Tokyo* (pp. 252−256).

Soutis, C., & Beaumont, P. W. R. (Eds.). (2005). *Multi-scale modeling of composite material system − The art of predictive damage modeling*. Cambridge: Woodhead Publishing Ltd.

Soutis, C., Fleck, N. A., & Smith, P. A. (1991). Failure prediction technique for compression loaded carbon fiber-epoxy laminates with open holes. *Journal of Composite Materials, 25*, 1476−1498.

Tamuja, V. A., & Pratacova, V. D. (Eds.). (1986). *Fractures of structures made from composite materials*. Riga: Zinatie (In Russian).

Tsai, S. W., & Hahn, H. T. (1980). *Introduction to composite materials*. Technomic, Conn.

Tsai, S. W., & Wu, E. M. A. (1971). General theory of strength for anisotropic materials. *Journal of Composite Materials, 5*, 58−80.

Tsampas, S. A., Greenhalgh, E. S., Ankerson, J., & Curtis, P. T. (2012). On compressive failure of multi-directional fibre-reinforced composites. *Composites: Part A, 43*, 454−468.

Uhl, K. M., Lucht, B., Jeong, H., & Hsu, D. K. (1988). Mechanical strength degradation of graphite fiber reinforced thermoset composites due to porosity. *Review of Progress in Quantitative Nondestructive Evaluation*, 1075−1082.

Vasiliev, V. V., & Morozov, E. V. (2013). *Advanced mechanics of composite materials and structural elements* (3rd ed.). Elsevier.

Vasiliev, V. V., & Tarnopolskii, Y. M. (Eds.). (1990). *Composite materials: Handbook*. Moscow: Mashinastronie (In Russian).

Vassilopolous, A. P., & Keller, T. (2011). *Fatigue of fiber reinforced composites*. Springer.

Yang, J. N., Jones, D. L., Yang, S. H., & Meskini, A. A. (1990). Stiffness degradation model for graphite-epoxy laminates. *Journal of Composite Materials, 24*, 753−769.

Computational techniques for simulation of damage and failure in composite materials

8

J.L. Curiel-Sosa[1], *R. Brighenti*[2], *M.C. Serna Moreno*[3], *E. Barbieri*[4]
[1]University of Sheffield, Sheffield, UK; [2]University of Parma, Parma, Italy; [3]Mecánica de los Medios Continuos y Teoría de Estructuras, E.T.S.I. Industriales, Ciudad Real, Spain; [4]Queen Mary University of London, London, UK

8.1 Introduction

The mechanical behaviour of composite materials is the result of several concurrent phenomena due to the complex nature of such a class of materials. Several kinds of composite materials are available: laminates, materials with particle reinforcement, long and short fibre-reinforced materials, flake reinforcement and filler reinforcement. Due to their wide variety it is clear that the bearing mechanisms are very different from one class to another, and so are the damage and failure phenomena. In order to get reliable composite materials, their safety factor during the service life must be assessed with proper accuracy; for such a purpose several phenomenological or approximation techniques (Berea, Bercea, & Nemesb, 2012; Puck & Schurmann, 1998; Willoughby, Parnell, Hazel, & Abrahams, 2012) and computational approaches (Berger et al., 2003; Maligno, Warrior, & Long, 2008; Radtke, Simone, & Sluys, 2010) have been developed and applied. For several decades, there has been a steady commitment to the simulation of failure in composites based on stress criteria or strain criteria. There is no doubt that they have been successful in many situations, and indeed the industry has embraced them for the solution of practical problems. Nowadays, there is a need to cope with challenging problems that need to be resolved, for example, three-dimensional gradual stiffness degradation due to distinct mixed damage modes at different strain rates. Furthermore, integration of criteria on numerical platforms or integration within finite element software packages has failed to provide the desired convergence on challenging applications: for instance, in the case of element erosion due to the satisfaction of certain criteria, or the abortion of the numerical execution due to instabilities generated by the not-so-robust nonlinear criteria. Later on, progressive damage models (PDMs) emerged. PDMs conduct a realistic approach in the sense that they perform the gradual degradation of stiffness and, eventually, characterise failure. However, PDMs are not exempt from problems. Their embedment into the finite element method (FEM) has highlighted further problems. Firstly, there is the need of calculation of a tangent modulus if it is to be included into an implicit FEM, which could be straightforward for isotropic material but not for composites. One must also mention the need to characterise the distinct mixed damage modes associated with general composite structures.

Structural Integrity and Durability of Advanced Composites. http://dx.doi.org/10.1016/B978-0-08-100137-0.00008-0

Indeed, there is no such problem if the PDM is embedded into an explicit FEM. However, explicit FEM is conditionally stable and, hence, not always keen on challenging problems. Secondly, in the aforementioned challenging problems, PDM are responsible for the abortion of the execution when computing the softening regime once the initiation criteria are satisfied. Finally, PDMs are local in essence and, hence, mesh-dependent, which necessitates that they be corrected by regularisation techniques or nonlocal modelling strategies. Developments including interface – also named cohesive or de-cohesive – elements for characterisation of delamination or cracks have been proposed. Techniques including the blend of interface elements and initiation criteria, and/or PDMs, have proved successful in numerous applications, overall on those applications in which a good estimation of the damaged zone is known a priori. The main disadvantage is that the only zones prone to crack/fracture are those with cohesive and, hence, the use of cohesive elements cannot be generalised to industrial-scale applications for predicting damage. In the industrial environment, steady progress is envisaged on the embracement of new numerical strategies. There are rather advanced and robust proposals providing the desired convergence in difficult problems. There have been extraordinary recent developments in numerical methodologies for the assessment of the structural integrity of composite structures. Thus, just to mention a few relatively novel techniques that could be a great asset to modelling damage, fracture or failure in composite structures and that are worth exploring in more detail:

- Extended finite element method (XFEM), in which the propagation of cracks and, therefore, delamination and transversal cracks are characterised by means of adequate enrichment interpolation functions added on the displacement field. XFEM has no need of re-meshing unless really intricate curved cracks are present or expected to develop. Even in such cases, the remeshing needed is minimal.
- Isogeometric analysis (IGA) and its variant, extended isogeometric analysis (XIGA), have been proposed very recently. However, they are not tested yet on composite structures at the expected rate. IGA permits the integration of analysis methods within CAD tools and vice versa. As the time from design to analysis is significantly reduced, IGA leads to reduction of the computational cost. This method should indeed be an asset for the simulation of failure on large-scale complex composite structures.
- Peridynamics is a type of particle method and, hence, mesh-free with all the advantages that it carries; for example, fracture is modelled in terms of the distance generated among particles.
- For completeness, a few more: phantom node method (PNM), reproducing kernel particle methods (RKPM), smooth particle hydrodynamics (SPH), blending between FEM and meshless methods, etc.
- Some excellent works have already been published by researchers on composite failure using some of these methods applied to composite structures. Of course, the set of techniques mentioned above do not pretend to be exhaustive or representative of any kind of application in particular. Rather, the purpose is to drive attention to new developments on strategies that may be utilised in the characterisation of failure in composites and that have the potential to outcompete traditional ones – for the specified reasons and thanks to enhanced computational power – in the near future. The present chapter will be mainly focussed on the most recent computational techniques that have been developed to tackle such complex mechanical problems. In particular, the numerical approaches that have been proposed for fibre-reinforced composites (FRC) will be considered; nevertheless, the presented approaches are often applicable to a wider range of composite materials as well as other anisotropic

materials. The chapter does not provide a comprehensive review of all the available computational approaches, as this would require an entire book. However, representative and relevant ones in terms of computational method used and recency will be considered for their application to composite damage and failure modelling.

8.2 Semi-numerical techniques

Based on the observation of the mechanical behaviour of composite materials at the mesoscale, FRC modelling can be developed by taking into account the main phenomena occurring in such a class of materials under mechanical actions. In such a context, the development of computational approaches based on the quantitative description of the mesomechanics-bearing mechanisms can be classified as so-called semi-numerical approaches. In the present section, some recent computational mesomechanical-based models developed by the authors are briefly presented and discussed, focussing on their principal aspects in the FRC mechanical description.

8.2.1 Progressive damage models within finite element methods

PDMs have been steadily appearing for the modelling of damage in composites since the late 1990s. Herein, PDM refers to the characterisation of degradation of the material by progression of some damage internal variables to be dependent upon distinct damage modes. Note that some collateral use of progressive damage modelling can be found in laminates, meaning that a sequential failure of plies or layers is taking place, for example, the ply discount method. Every failed ply satisfies a stress failure criterion. That has nothing to do with a PDM based in a thermodynamics framework, as described below. Some PDMs have successfully been implemented in computational finite software, for example, Matzenmiller's (Matzenmiller, Lubliner, & Taylor, 1995). A strain-based PDM for an anisotropic material that, in general, may be considered with metallic constituents is derived from a thermodynamics potential, such as the free energy potential:

$$\Phi := \frac{1}{2}\boldsymbol{\varepsilon} : \boldsymbol{C} : \boldsymbol{\varepsilon} - \boldsymbol{\sigma}_p : \boldsymbol{\varepsilon} + \Omega(\alpha) \tag{8.1}$$

where C is a fourth-order damaged stiffness tensor. The word 'damaged' is emphasised in the name to account for the degradation of stiffness components due to damage internal variables. p is the plastic stress tensor, ε is the strain tensor and $\Omega(\alpha)$ is the dissipation associated to hardening, which depends upon the hardening internal variables tensor α. Note that the plastic and hardening terms can be discarded in case of nonmetallic composites. The stress−strain relationship is then obtained as follows:

$$\sigma = \frac{\partial \Phi}{\partial \varepsilon} = C : \varepsilon - \sigma_p \tag{8.2}$$

Bearing in mind that dissipation due to damage must be positive, it leads to

$$\Psi_d := -\varepsilon : \dot{C} : \varepsilon \geq 0 \tag{8.3}$$

and, also, the plastic dissipation must be positive:

$$\Psi_p := \sigma_p : \varepsilon + \nabla\Omega(\alpha) \bullet \dot{\alpha} \tag{8.4}$$

The stiffness matrix can be computed as

$$C = 2\frac{\partial \Phi}{\partial \varepsilon \otimes \varepsilon} \tag{8.5}$$

The evolution of damage can be characterised by means of the irreversibility concept and an undamaged domain formed by the intersection of damage surfaces in the strain space. This undamaged domain may evolve with the damage internal variables by contracting itself to replicate the softening regime or brittle behaviour. Distinct damage modes can be associated to different strain damage surfaces, as proposed by Curiel-Sosa et al. (Curiel Sosa, Phaneendra, & Munoz, 2013). For instance, damage surfaces characterising matrix cracking, fibre rupture, delamination, and fibre kinking but not restricted thereto. Thus the model will depend not only on the constitutive law of the material but also on the distinct damage modes that potentially may develop. So this undamaged elastic domain in the strain space is defined as

$$g\left(\varepsilon \otimes \varepsilon, c_j\right) := G(\varepsilon \otimes \varepsilon) - c_j \tag{8.6}$$

where c_j is the threshold for the strain damage surface j. The dissipative evolution or degradation is modelled by means of

$$\dot{C} = -\nu \frac{\partial g\left(\varepsilon \otimes \varepsilon, c_j\right)}{\partial \varepsilon \otimes \varepsilon} \tag{8.7}$$

$$\dot{\nu} \geq 0 \quad g\left(\varepsilon \otimes \varepsilon, c_j\right) \leq 0 \quad \dot{\nu}\, g\left(\varepsilon \otimes \varepsilon, c_j\right) = 0 \tag{8.8}$$

which are the Kühn−Tucker conditions. An example of PDM can be visualised in Box 8.1; see also Figure 8.1 for an example of application of the PDM proposed in Curiel Sosa et al. (2013). Among others, the following PDMs can be highlighted:

- Lee (2001) presented a progressive degradation model characterising the damage variables by means of the Weibull function. He embedded the constitutive model within DYNA3D and applied it to the simulation of damage on an impact biaxial loading test and four-point bending test. Fibre debonding was modelled as damage mechanism adjusting the Weibull parameter. The algorithm was presented showing clear details of the computation of damage using the Weibull function. Further correlation, either to experiments or against results from the literature, could add to the relevance of such an approach.

Box 8.1 Example of PDM for composites

1. The stress is measured using the definition of effective stress $\widehat{\sigma}_n$ by Chaboche (1981), Eqn (8.9). η is the internal damage vector. Subscript n denotes the time step in a marching numerical scheme.

$$\widehat{\sigma}_n = D(\eta_n) \bullet \sigma_n \tag{8.9}$$

2. The stress−strain relationship integrates the damage tensor D:

$$\sigma_n = D^{-1}(\eta_n) \bullet C_0 \bullet \varepsilon_n = C_n \bullet \varepsilon_n \tag{8.10}$$

3. The stress damage surfaces (one per each damage mode ξ):

$$f(\sigma_n, \eta_n) := \sigma_n^T \bullet F^{\xi}(\eta_n) \bullet \sigma_n - 1 \quad \xi = 1, 2, \ldots, m \tag{8.11}$$

4. After mapping to the strain space, the damage surfaces become

$$g^{\xi}(\varepsilon_n, \eta_n) := \varepsilon_n^T \bullet G^{\xi}(\eta_n) \bullet \varepsilon_n - 1 \quad \xi = 1, 2, \ldots, m \tag{8.12}$$

where

$$G^{\xi}(\eta_n) = C_n^T \bullet F^{\xi}(\eta_n) \bullet C_n \quad \xi = 1, 2, \ldots, m \tag{8.13}$$

5. Criteria for damage mode ξ initiation

$$\nabla_{\varepsilon} g_n^{\xi} \bullet \dot{\varepsilon}_n > 0 \quad g_n^{\xi}(\varepsilon_n, \eta_n) \geq 0 \quad \xi = 1, 2, \ldots, m \tag{8.14}$$

6. The characterisation of damage mode directions $\mathbf{d}^{\xi}$ is given by

$$d_n^{\xi} := \varepsilon_n^T \bullet \left(G_n^{\xi T} + G_n^{\xi}\right) / \left\| \nabla_{\varepsilon} g_n^{\xi} \right\| \quad \xi = 1, 2, \ldots, m \tag{8.15}$$

7. The potential growth of distinct damage modes is modelled as follows:

$$\psi_n^{\xi} := \left(\nabla_{\varepsilon} g_n^{\xi} \ \dot{\varepsilon}_n\right)^{1/p} \quad \xi = 1, 2, \ldots, m \tag{8.16}$$

8. Finally, the computation of damage internal variables rate as superposition of distinct damage modes:

$$\dot{\eta}_n = \sum_{\xi=1}^{m} \psi_n^{\xi} d_n^{\xi} \tag{8.17}$$

For further details refer to Curiel Sosa et al. (2013).

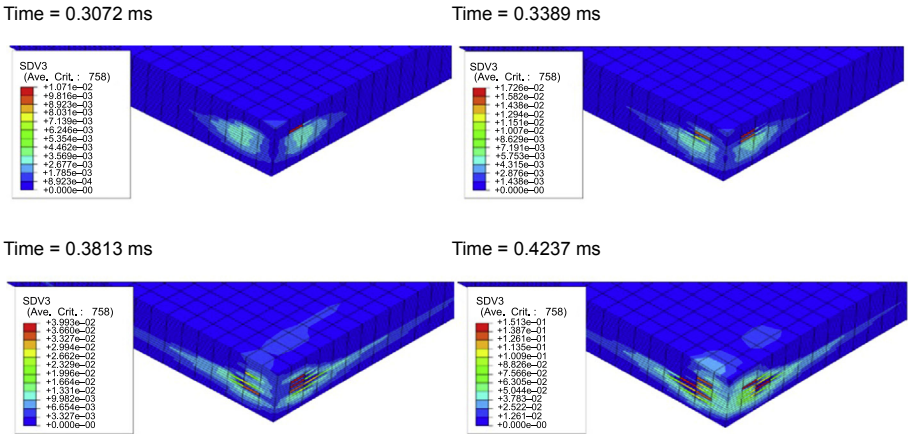

Figure 8.1 Example of simulation of progression of damage (delamination) on a cross-ply laminate subjected to low-velocity impact by a rigid projectile.
Data from Curiel Sosa et al. (2013).

- Angioni, Visrolia, and Meo (2012) proposed a combination of XFEM and multilevel mesh superposition (MMS). The interlaminar stresses are not accurately calculated by the classical laminate theory as the state of plane stress is assumed in every laminate. MMS performs the calculation of the global displacements by superposition of local displacements in two or more plate models associated to each ply. MMS was first introduced by Fish (1992).

Angioni et al. results showed that the technique is convenient for the estimation of intralaminar stresses in composite laminates.

- Shi, Swait, and Soutis (2012) proposed a progressive model applied to cross-ply laminates subjected to low-velocity impact. It is based on stress criteria in which delamination is simulated by means of interface elements. Their results are compared to assess impact damage by means of X-ray Non Destructive Technique technique. In addition, the fracture criterion was also integrated in the model.

A drawback of using PDMs is their mesh dependency. To overcome this, regularisation approaches have already been proposed:

- Raimondo, Iannucci, Robinson, and Curtis (2012) addressed the problem of damage localisation by regularisation techniques. These include a characteristic length, for example, a side length of one element, within the constitutive relationship characterising the damage process.
- Patel and Gupta (2014) proposed a nonlocal PDM for laminates based on nonlocal strain and damage variables. The computation of nonlocal variables is derived from the local ones by means of layer-wise elements with quadratic variations. Although the approach is novel, additional results in terms of stresses in this direction could provide further insight on the convenience of these approaches.

8.2.2 *Interface/cohesive elements for the progressive degradation of laminates*

There have been numerous cohesive elements proposed for composite analysis between 2000 and 2010 (Balzani & Wagner, 2008; Haj-Ali, 2009; Tay, Liu, Tan,

Sun, & Pham, 2008). These special finite elements (FE) can split or divide when subjected to a criterion or set of criteria. They are named in the literature in different ways: cohesive, decohesive or interface elements. They could be classified as smeared cohesive elements, in which the cohesive zone model is included on the constitutive relationship. The elements are located between interfaces that can debond. To do this the element must be very thin. This causes high-aspect-ratio elements and weird deformations. The mesh generation is also an issue as the elements must be pre-allocated in the interfaces.

Below are presented some of the most interesting methods for simulating fracture on composites. Shi, Swait, and Soutis (2012), Shi, Zhang, Wang, and Wang (2012) incorporated solid-shell interface elements between laminae subjected to progressive degradation. The key point is that the interface element is not subjected to failure criteria for the splitting. Interestingly, they used a scalar parameter evolving in a time-marching scheme that they integrated within ANSYS, which is one of the few works in this direction.

8.3 Meshless methods

Mesh-free methods for the solution of partial differential equations (PDEs) in elasticity have come a long way since the very first papers of Libersky and co-workers on SPH: in Larry, Libersky, & Petschek (1991) a meshless method is applied for the first time in solid mechanics. The original versions of SPH lacked the property of consistency (or reproducibility, i.e. the ability of the approximation to reproduce polynomial fields), especially at the boundaries. The landmark papers by Belytschko and co-workers (Belytschko, Lu, & Gu, 1994; Belytschko, Gu, & Lu, 1994; Belytschko, Lu, & Gu, 1995) on element-free Galerkin (EFG), contemporary with the papers by Liu and co-workers (Chen, Pan, Wu, & Liu, 1996; Liu, Jun, & Zhang, 1995; Liu, Jun, Li, Adee, & Belytschko, 1995) on the RKPM, opened the way to the widespread diffusion of mesh-free methods for linear and nonlinear elasticity. Conversely from SPH, both methods satisfy reproducibility conditions, guaranteeing the mathematical prerequisites for convergence when used in a Galerkin formulation (Hughes, 1987). Both methods are substantially equivalent, though originated from different points of view: EFG from computer graphics, where moving least squares (MLS) basis functions are used for surface reconstructions from a cloud of scattered points, and RKPM from wavelet theory. Still around that time, many other mesh-free methods were developed; a probably not comprehensive list includes the material point method (MPM) (Sulsky, Chen, & Schreyer, 1994), the hp-clouds (Armando Duarte & Tinsley Oden, 1996), finite point method (Onate, Idelsohn, Zienkiewicz, & Taylor, 1996), the free-mesh method (Yagawa & Yamada, 1996), the meshless local Petrov-Galerkin (Atluri & Zhu, 1998), local boundary integral equation (Zhu, Zhang, & Atluri, 1998), natural element method (Sukumar, 1998), meshless finite element method (Sergio, Idelsohn, Onate, Calvo, & Pin, 2003), the cracking particles method (Rabczuk & Belytschko, 2004) and, lastly, peridynamics (Silling & Askari, 2005). There is a reasonably large literature of applications of (various) mesh-free methods to composite plates or, more generally, orthotropic materials: probably the very first work on

material discontinuity (i.e. gradients of displacements are discontinuous) is (Cordes & Moran, 1996) where inhomogeneities are treated by truncating the kernels at the material interface. We will, however, focus on modelling damage, and more generally, failure of composites with mesh-free schemes. Mesh-free methods can be broadly categorised (with some exceptions) into two categories: particle methods or Galerkin methods. Some authors (Fries & Matthies, 2003) classify collocation methods (i.e. finite differences as a mesh-free method) as well, although these schemes are not well suited for PDEs containing discontinuities (where derivatives are not defined in the classic sense) in their primary unknown, such as the displacements. In the particle methods, the history of state variables is tracked at discrete points (particles), without needing any mesh: these methods can be thought of as physical particles interacting with each other, with their interaction regulated by some constitutive model. Examples of this class are the MPM and peridynamics. In the Galerkin methods, the PDE is converted into a weak formulation, generating usually an algebraic system of equations. The methods are more akin to FE, and can actually be thought of as their element-free version, where particles are more mathematical particles rather than physical particles (i.e. the vertices of the elements). SPH are, in this sense, a hybrid, since the unknown in the original PDEs (usually balance laws) is approximated by its convolution with a kernel function, allowing derivatives of the approximation to be mathematically defined. The result is a particle-like method, where the constitutive interaction law derives directly from these convolution integrals. Chen (Chen & Kulasegaram, 2009), for example, used SPH to simulate fracture in particulate composites, such as cement. Guida (Guida, Marulo, Meo, Grimaldi, & Olivares, 2011; Guida, Marulo, Polito, Meo, & Riccio, 2009) employed SPH to model bird-strike on a composite leading-edge wing.

8.3.1 Peridynamics

An example of the particle method is peridynamics, which can be thought of as the continuum version of molecular dynamics: in fact, forces are exchanged only with the surrounding particles at a finite distance, and localisation and subsequent fracture are a consequence of the increase of the relative distance due to these forces. Using peridynamics, Xu, Askari, Weckner, and Silling (2008) simulated delamination and matrix damage process in composite laminates due to low-velocity impact, whilst Kilic, Agwai, and Madenci (2009) described the process of fibre failure and damage initiation from the matrix for different fibre orientation. Recently, Hu, Doh Ha, and Bobaru, (2012) showed dynamic brittle fracture for unidirectional FRC, observing matrix−fibre splitting fracture, matrix cracking and crack migration in the matrix, including crack branching in the matrix, using an homogenised model of the ensemble fibre−matrix.

8.3.2 Element-free galerkin

Galerkin methods include EFG or RKPM, where test and trial functions are sets of MLS (substantially equivalent to RKPM). Two manners exist in the literature for

introducing discontinuities: extrinsic and intrinsic. In extrinsic methods, similarly to XFEM (Barbieri & Meo, 2009, 2011; Barbieri, 2010), extrinsic enrichments are used to simulate benchmark cases (double cantilevered beam, end notched flexure and end loaded split) of delamination in layered composites for Modes I and II. Guiamatsia, Falzon, Davies, and Iannucci (2009) simulated mixed-mode delamination growth in composite beams, using virtual crack closure technique and an interaction power law to predict damage growth. Li, Aliabadi, and Wen (2012) used radial basis function and moving Kriging interpolation in a Galerkin formulation to model the failure of two different unit cell models for woven composites: a straight-edge and smooth fabric unit cell model. Daniel, Simkins, Collier, and Alford (2013) used the visibility condition to build discontinuous mesh-free shape function to explicitly model cracks and holes propagating inside a laminated composite.

8.4 Partition of unity methods

8.4.1 The extended finite element method

XFEM is becoming very popular in the composites community for structural integrity analyses. This is because of the capability of XFEM to replicate virtual fracture without − or with minimum − re-meshing. This has two clear advantages:

- A reduction of the computational cost with respect to classical FEM. This is critical when dealing with the simulation of complex engineering components subjected to failure.
- Introduction of the discontinuity associated to cracks, delamination, etc. straightforward by means of additional degrees of freedom in the so-called enriched nodes. This provides a more realistic approach with respect to the computation of jump in stress, strain and internal variables if it is to be compared with FEMs, including material constitutive relationships based on continuum damage mechanics alone.

XFEM falls within the partition of unity methods (PUM) category. PUM permits the introduction of enrichment functions that may be replicated by the numerical strategy used. If the enrichment functions chosen are discontinuous, then this allows the simulation of discontinuities such as cracks. The enrichment is carried out in a part of the mesh. This part of the mesh will be able to replicate such discontinuities depending upon the enrichment type chosen. In particular, XFEM integrates a PUM within a FE context. Therefore, XFEM can be implemented straightforward within an FEM code.

8.4.1.1 How are cracks modelled within the extended finite element method?

One great feature of XFEM is that the crack is allowed to split FEs, that is, it is not restricted to propagation between the FEs boundary. In addition, no re-meshing or very little re-meshing is necessary. The modelling involves selection of certain parts of the mesh for enrichment, which can potentially allow the crack simulation if the

constitutive behaviour requires it. In general, two types of enrichment functions are possible:

- Enrichment functions at crack tips to reproduce the asymptotic field
- Enrichment at the sides of the current crack

Some re-meshing is necessary in the case of extremely curved cracks.

Note that the assignation of those enrichments will vary in a dynamic crack propagation. XFEM enriches the displacement approximation of the corresponding mesh nodes as follows:

$$u(x) = \sum_{i\subset\Omega} N_i(x)\, u_i + \sum_{j\subset\Omega^1} \breve{N}_j\big(H(x) - H(x_j)\big)\, a_j + \sum_{k\subset\Omega^2} \breve{N}_k \sum_{\gamma} \big(B_\gamma(x) - B_\gamma(x_k)\big)\, b_{\gamma k} \tag{8.18}$$

where $N_i, \breve{N}_j$ denote FE shape functions, u_i the nodal displacements, and a_j and $b_{\gamma k}$ additional degrees of freedom for the displacement approximation. $H(x)$ is a Heaviside function, taking the value $+1$ at one side of the crack and -1 at the opposite side of the crack. $B_\gamma(x)$ are support functions to replicate the asymptotic field ahead of the crack tip. For an example of simulation using XFEM, see Figure (8.2).

8.4.2 Phantom node method

PNM is a variation of XFEM that allows the initiation of the cracks in any part of the mesh. However, a minimum distance between cracks has to be fixed when there is only one layer of FEs. Seminal works on PNM applied to composites are proposed by Ling, Yang, and Cox (2009) and Van der Meer and Sluys (2009). In Van der Meer and Sluys (2010) a combination of PNM and cohesive elements is proposed for tackling matrix cracking and delamination, respectively. In addition, Van der Meer and Sluys (2010) propose a continuum-based model for fibre failure. Their results in open-hole laminates justify such combination and tackle the size effect

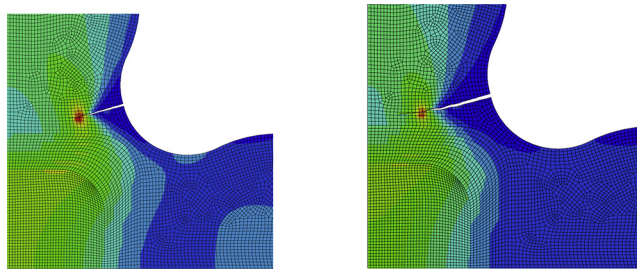

Figure 8.2 Illustrative detail of crack propagation using XFEM on a cruciform specimen designed for biaxial loading tests. The sample, made of a glass-reinforced polyester composite, is subjected to double load in the vertical arm with respect to that in the horizontal arm.

problem. However, doubts arise about the PNM performance in composites failure prediction without such combination involving more than one technique, which could be cumbersome for the software developer. Furthermore, the asymptotic field enrichment is not possible with PNM, which leaves the special stress field ahead of the crack tip not properly simulated. PNM is a promising technique for replication of composite failure, but improvement will be needed to solve the aforementioned issues.

8.5 Multiscale and homogenisation

Phenomena taking place at the macroscopic level are strictly related to the physics and mechanics of the background microstructure; the resulting overall behaviour of micro-nonhomogeneous materials is strongly affected by the spatial distribution, size, shape and mechanical properties of the constituents and of their joining interfaces at the microscopic level. The proper knowledge of the effective relation between micro-scale phenomena and the macroscopic behaviour on the one hand allows the overall description of multiphase materials, and on the other hand provides a microstructure design tool for the development of material having the required mechanical characteristics. A further potentiality of multiscale modelling is its capability to simply deal with the development of functional and smart materials obtained from complex forming processes.

In real problems it must be also considered that the microstructure may change and evolve under macroscopic mechanical actions, which lead to a degradation of the resulting composite material mechanical properties.

Under the undamaged material hypothesis, the simplest way to get the homogenised moduli of a heterogeneous material is based on the so-called rule of mixtures, operating through a weighted average (by using their volume fractions) over the properties of the constituents; this implies that only one microstructural characteristic, the volume ratio of the heterogeneities, is taken into consideration in the average process. Starting from the 1970s, the fast development of micromechanics allowed for a more effective and practical study of composite materials and structures; most of the early studies on this subject have been mainly devoted to theoretical modelling in the elastic behaviour regime.

The homogenisation approach for heterogeneous materials provides a rigorous method to determine the macroscopic response of composite materials by accurately taking into account microstructural characteristics and their evolution. The effective elastic medium approximation − as proposed by Eshelby (1957) and other authors (Hashin, 1962; Mori & Tanaka, 1973) − is a more realistic model for heterogeneous materials: the properties of the macroscopically equivalent material are obtained from the analytical solution of a boundary value problem (BVP) for an inclusion having a simple shape (such as an ellipsoid) embedded in an infinite matrix made of a different material. These approaches are suitable and give reasonable results when applied to heterogeneous materials having geometrical regularity, but they are not suitable, for example, for materials having clustered characteristics. The use of a micro−macro strategy does not require the definition of constitutive equations at the macroscopic

level that, in the case of complex microstructures, generally would be an awkward task. On the other hand, the description of the constitutive behaviour at some macroscopic integration points (such those used in FE numerical quadrature formula), through homogenisation techniques, operates by averaging the response of the deforming microstructure, enabling a straightforward application of the method to geometrically and physically nonlinear problems.

In order to deal with materials showing nonlinear properties, an extension of the above-mentioned self-consistent approach has been proposed by introducing its incremental formulation (Hill, 1965).

The asymptotic homogenisation theory, based on the asymptotic expansion of displacement and stress fields on a material scale parameter (typically the heterogeneities' characteristic size and a macrostructure length ratio), has also been developed, providing the effective overall material properties as well as the local stress and strain values (Bensoussan, Lionis, & Papanicolaou, 1978; Ghosh, Lee, & Moorthy, 1996; Kalamkarov, Andrianov, & Danishevs'kyy, 2009; Nemat-Nasser & Hori, 1993). The possibility to homogenise a composite material with a regular structure, that is, the study of an equivalent homogeneous solid instead of the original inhomogeneous one, and the use of its effective properties, determined through the solution of so-called local problems formulated on the unit cell of the composite material, is one of the main capabilities of this approach.

Suquet (1987), Suquet et al. (1985) introduced the use of the homogenisation theory into plastic mechanics in the 1980s: according to such an approach the macroscopic behaviour of composite materials could be determined thanks to the concept of a representative volume element (RVE); the composite properties are determined by fitting the averaged microscopic stress−strain fields, obtained from the analysis of a microstructural representative cells under given mechanical actions.

The RVE can be defined as a statistically representative portion of the material, including a sampling of all possible microstructural configurations present in the composite; alternatively, it can be considered as the smallest microstructural volume that properly represents the overall macroscopic properties.

Computational homogenisation has also been developed by applying numerical analyses on an RVE with proper boundary conditions in order to obtain the relation between the macroscopic input and output quantities (Michel, Moulinec, & Suquet, 1999). Such an approach for the mechanical characterisation of multiphase materials has several advantages, such as the possibility to avoid the explicit knowledge of the macroscopic local constitutive equations (these are obtained by the solution of the corresponding microscale BVP), the possibility to include large strains as well as the nonlinear mechanical behaviour and the consideration of evolving microstructural information (Brighenti & Scorza, 2012b; Greco & Luciano, 2011; Kalamkarov & Liu, 1998; Kalamkarov & Georgiades, 2002; Romanowicz, 2013; Willoughby et al., 2012).

The computational homogenisation technique has been recognised to be a useful and suitable tool to obtain the nonlinear micro−macro structure−property relations, especially in the cases involving a high complexity of the mechanical and geometrical microstructural properties, by also allowing their eventual evolving character; other homogenisation methods cannot be competitive for such complex situations.

8.5.1 Energy-based homogenisation approach for short fibre-reinforced materials

Homogenisation-based approaches can be conveniently formulated through an energy balance between the REV effective microstructure and its macroscopic counterpart (Brighenti & Scorza, 2012b; Kalamkarov & Liu, 1998; Willoughby et al., 2012); in other words, the assumption that the material at the micro scale is energetically equivalent to that at the macro scale is the main physical assumption of the method.

As a representative case, in the present section a FRC material will be considered for applying the above-mentioned energy approach.

An FRC composite material is microscopically heterogeneous while it can be assumed to be macroscopically homogeneous if the fibres are uniformly dispersed in the matrix material; moreover, if the fibres are randomly oriented in all the possible 3-D directions, the composite is also macroscopically isotropic, whereas the composite is macroscopically homogeneous and anisotropic (more precisely, transversally isotropic) if the fibres are oriented by following a preferential direction.

The composite material is herein assumed to be characterised by macroscopical mechanical characteristics equal to those of a small reference elementary volume (RVE); moreover, for the sake of simplicity, the fibres are assumed to be not interacting; that is to say that the so-called dilute composite hypothesis is made. Under such a hypotheses (often valid for fibre content not greater than about $\sim 20\%$), the averaged properties of the composite can be easily determined.

Dealing with problems involving mechanical nonlinearities, the main degradation phenomena occurring in FRC materials must be considered. Schematically the main mechanically damaging phenomena can be recalled to be matrix damage (such as plastic deformation), matrix cracking, fibre debonding, fibre breaking, fibre buckling (micro-buckling occurring in partially debonded fibres in periodic composites can be responsible for size effect and loss of the periodic structure characteristic) (Willoughby et al., 2012), etc. Among the above-listed damage occurrences, fibre debonding is one of the most important (Brighenti, Carpinteri, & Scorza, 2013; Brighenti & Scorza, 2012b), and several technological researches have been performed in order to reduce such detrimental effects (Lu, & Mai, 1995). From the mechanical point of view the debonding phenomenon can be synthetically quantified through a scalar parameter s aimed at measuring the fibre−matrix strain mismatch or fibre−matrix sliding, $[[\varepsilon_{f-m}]]$ (Brighenti & Scorza, 2012b):

$$[[\varepsilon_{f-m}]] = \varepsilon_f^m - \varepsilon_f = \underbrace{[(k \otimes k) : \varepsilon]}_{\varepsilon_f^m} \cdot \left(1 - s\left(\varepsilon_f^m\right)\right) = \varepsilon_f^m \cdot \left(1 - s\left(\varepsilon_f^m\right)\right) = \varepsilon_f^m \cdot d \quad \text{or} \tag{8.19a}$$

$$\varepsilon_f = \varepsilon_f^m \cdot s\left(\varepsilon_f^m\right) \tag{8.19b}$$

where k (the unit vector identifying the fibre direction) has been introduced, ε_f is the fibre strain and ε_f^m is the matrix strain evaluated in the fibre direction. Values of $s(\varepsilon_f^m)$ tending to 1 indicate a perfect fibre−matrix bonding (i.e. no strain jump), while values of $s(\varepsilon_f^m)$ tending to 0 denote a complete fibre−matrix detachment, that is, $[[\varepsilon_{f-m}]] = \varepsilon_f^m$; for sake of simplicity in Eqn (8.19) the value $s(\varepsilon_f^m)$ can be considered as its averaged value evaluated along the fibre. The damage parameter in Eqn (8.19a), defined as $d = (1 - s)$, can be considered as a measure of the composite damage associated with the fibre−matrix detachment.

Taking into account such a degrading effect by writing the energy equivalence over a suitable REV between the microscopically heterogeneous and the corresponding macroscopically homogeneous one, the equivalent tangent stiffness tensor of the macroscopically homogenous fibre-reinforced material can be written (Brighenti & Scorza, 2012a):

$$C_h' = \mu_m \cdot C_m' + \mu_f \cdot \left[E_f' \cdot \left(s\left(\varepsilon_f^m\right) + \varepsilon_f^m \cdot \frac{ds(\varepsilon_f^m)}{d\varepsilon_f^m} \right) \cdot \int_{\Xi} p_\varphi(\varphi) \cdot p_\theta(\theta) \cdot \Lambda \otimes \Lambda d\,\Xi \right] \tag{8.20}$$

where the second-order tensor Λ is defined as $\Lambda = k \otimes k$, E_f' is the tangent elastic modulus of the fibres (evaluated with respect to the matrix strain in the fibre direction, i.e. $E_f' = d\sigma_f / d\varepsilon_f^m$), $\mu_m = V_m/V$ and $\mu_f = V_f/V$ are the matrix and fibre volume fractions, respectively, while the last integral is intended to be evaluated over the solid angle Ξ.

Finally, it can be observed that the effective spatial orientation of the fibres inside the bulk material has been considered through the probability density functions p_φ and p_θ (Brighenti & Scorza, 2012a), expressed in terms of the orientation angles φ and θ. Thanks to such probability density functions, the nonisotropic damage effects of fibre debonding on the tangent stiffness tensor of the composite material can be taken into account.

The fibre−matrix strain sliding value can be obtained from the knowledge of the strain distribution along a partially detached fibre; this result can be conveniently obtained by solving the corresponding fracture mechanics problem, related to the crack-like assumption of the fibre−matrix detached area (Brighenti & Scorza, 2012a), in order to get the current adhesion length; the fibre and matrix stress and strain can be finally estimated through the classical shear lag model (Cox, 1952).

By considering one single fibre as not influenced by the surrounding ones for sake of simplicity (for common FRC materials containing low fraction values of the reinforcing phase this usually applies), the remotely applied stress field can be decomposed along the axial and transversal fibre directions and the related mixed-mode stress-intensity factors (SIFs) can be obtained. The critical condition for incipient fibre debonding growth can be written as

$$K_{ic} = A \cdot \tau_{f,u} \cdot f\left(K_{i,\mathrm{eq}}\right) \quad \text{or} \quad G_{ic} = \frac{A^2 \cdot \tau_{f,u}^2 \cdot f^2\left(K_{i,\mathrm{eq}}\right)}{E_i} \tag{8.21}$$

where A is a constant, depending on the fibre geometric and mechanical properties, and $f(K_{i,\mathrm{eq}})$ is a function of the equivalent interface SIF, while K_{ic}, G_{ic}, $\tau_{f,u}$ are the characteristic values of the fibre matrix interface mechanical properties, that is, the interface fracture toughness, interface critical fracture energy and fibre−matrix limit shear stress, respectively. The above equations provide a relationship linking the fracture and shear lag approach to fibre debonding.

As an example, in Figure 8.3 the remote axial stress versus the dimensionless detached fibre length obtained through the above-described fracture mechanics approach is represented and compared with experimental results (Wang, 1997).

It is worth mention that the use of a fracture mechanics approach to quantitatively describe fibre debonding enables the straightforward treatment of damage phenomena related to repeated loading, such as fatigue in the high-cycle regime; proper crack growth rate laws allow the estimation of progressive and stable fibre detachment once the fatigue properties of the interface are known. On the other hand, the fatigue damage occurring in the matrix can also be considered through classical damage accumulation evaluated through, for instance, the well-known empirical Wöhler or the Basquin models (Basquin, 1910).

The mechanical degrading effects on the bulk material can be accounted for by the energy-based homogenisation approach through the actual matrix tangent stiffness tensor C'_m (Eqn (8.20)), which can be evaluated on the basis of the current damage level corresponding to the load history applied to the composite. Damage produced by plastic deformation (such as for load level exceeding the elastic limit of the material or in cases of low-cycle fatigue), for metal or polymeric matrix materials, as well as damage corresponding to diffused or concentrated cracks, can be considered. As

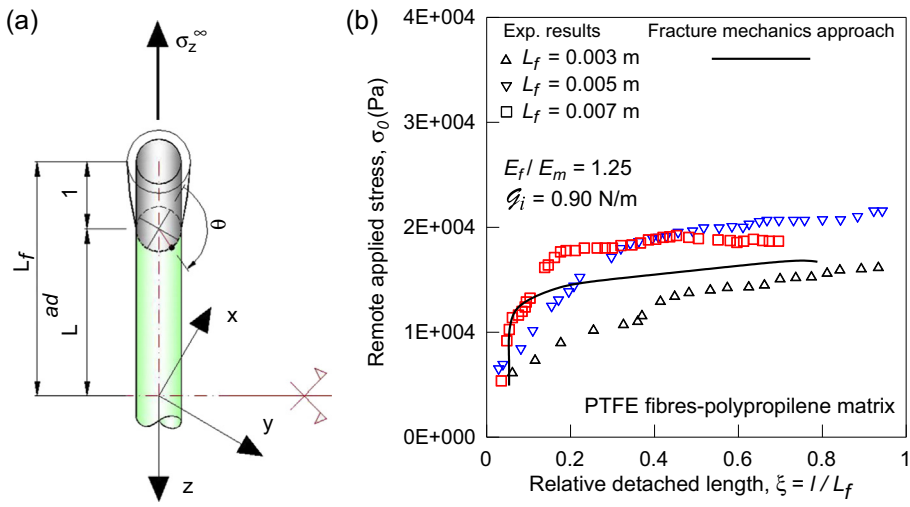

Figure 8.3 Partially debonded fibre, corresponding to a 3D fracture mechanics problem, under remote axial (σ_z^{∞}) stress (a). Remote matrix stress versus the relative fiber debonding: experimental (data from (Basquin, 1910)) and fracture mechanics results (b).

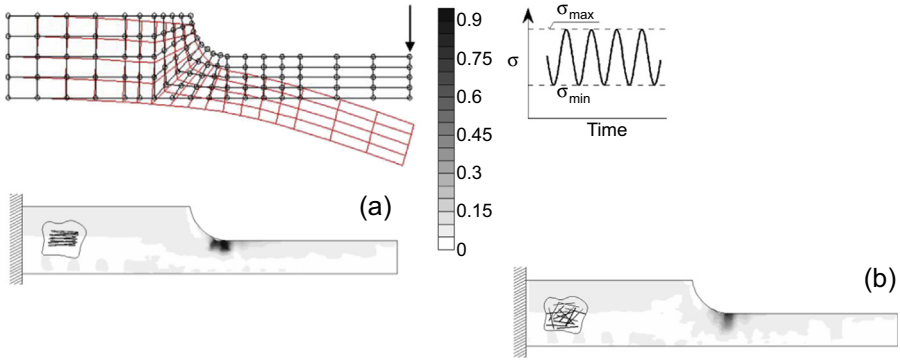

Figure 8.4 Maps of the dimensionless debonded length $\xi = l/L_f$ (see Figure 8.2) for horizontal (a) and random fibres distribution (b) in a notched beam under fatigue loading ($\mu_f = 3\%$, $\Delta\sigma = \sigma_{\max} - \sigma_{\min} = 10$ MPa) after 90,000 cycles.

mentioned in the previous sections, the latter case requires proper regularisation techniques, such as nonlocal modelling or fracture consistence energy-based approaches, to avoid mesh dependence (Greco & Luciano, 2011) and get reliable results.

A representative example of the fatigue-based damage approach to fibre debonding is given in Figure 8.4, where a notched cantilever beam under fatigue bending (constant amplitude loading) is reported; cases of both aligned horizontal and random fibres are plotted.

The above-presented homogenisation approach − capable to consider also the mechanical damaging effects− can be easily implemented in FE code, where such energy-based equivalence can be written at the Gauss point level (if the mesh size is properly sized with respect to the effective fibre length), enabling a straightforward calculation of the damage dependence of the stiffness matrix.

References

Angioni, S. L., Visrolia, A., & Meo, M. (2012). Combining X-FEM and a multilevel mesh superposition method for the analysis of thick composite structures. *Composites Part B: Engineering, 43*(2), 559−568.

Armando Duarte, C., & Tinsley Oden, J. (1996). Hp clouds-an hp meshless method. *Numerical Methods for Partial Differential Equations, 12*(6), 673−706.

Atluri, S. N., & Zhu, T. (1998). A new meshless local petrov-galerkin (mlpg) approach in computational mechanics. *Computational Mechanics, 22*(2), 117−127.

Balzani, C., & Wagner, W. (2008). An interface element for the simulation of delamination in unidirec-tional fiber-reinforced composite laminates. *Engineering Fracture Mechanics, 75*(9), 2597−2615. Cited by (since 1996) 43.

Barbieri. E. (2010). *Meshfree methods for the analysis of composite materials* (Ph.D. thesis). University of Bath.

Barbieri, E., & Meo, M. (2009). A meshfree penalty-based approach to delamination in composites. *Composites Science and Technology, 69*(13), 2169−2177.

Barbieri, E., & Meo, M. (2011). A meshless cohesive segments method for crack initiation and propagation in composites. *Applied Composite Materials, 18*(1), 45−63.

Basquin, O. (1910). The exponential law of endurance tests. *Proceedings ASTM, 10*, 625−630.

Belytschko, T., Gu, L., & Lu, Y. Y. (1994). Fracture and crack growth by element-free Galerkin methods. *Modelling Simulation Material Science Engineering, 2*, 519−534.

Belytschko, T., Lu, Y. Y., & Gu, L. (1994). Element-free Galerkin methods. *International Journal for Numerical Methods in Engineering, 37*(2), 229−256.

Belytschko, T., Lu, Y. Y., & Gu, L. (1995). Crack propagation by element-free Galerkin methods. *Engineering Fracture Mechanics, 51*(2), 295−315.

Bensoussan, A., Lionis, J. L., & Papanicolaou, G. (1978). *Asymptotic analysis for periodic structures*. Amsterdam: North-Holland.

Berea, P., Bercea, P., & Nemesb, O. (2012). Phenomenological fracture model for biaxial fibre reinforced composites. *Composites Part B: Engineering, 43*, 2237−2243.

Berger, H., Gabbert, U., Koppe, H., Rodriguez-Ramos, R., Bravo-Castillero, J., Guinovart-Diaz, R., et al. (2003). Finite element and asymptotic homogenization methods applied to smart composite materials. *Computer Mechanics, 33*, 61−67.

Brighenti, R., Carpinteri, A., & Scorza, D. (2013). Fracture mechanics approach for a partially debonded cylindrical fiber. *Composites Part B: Engineering, 53*, 169−178.

Brighenti, R., & Scorza, D. (2012). A micro-mechanical model for statistically unidirectional and randomly distributed fibre-reinforced solids. *Mathematical Mechanics Solutions, 17*(8), 876−893.

Brighenti, R., & Scorza, D. (2012). Numerical modelling of the fracture behaviour of brittle materials reinforced with unidirectional or randomly distributed fibres. *Mechanics of Materials, 52*, 12−27.

Chaboche, J. L. (1981). Continuous damage mechanics−a tool to describe phenomena before crack initiation. *Nuclear Engineering and Design, 64*, 233−247.

Chen, Y., & Kulasegaram, S. (2009). Numerical modelling of fracture of particulate composites using sph method. *Computational Materials Science, 47*(1), 60−70.

Chen, J. S., Pan, C., Wu, C. T., & Liu, W. K. (1996). Reproducing kernel particle methods for large deformation analysis of non-linear structures. *Computer Methods in Applied Mechanics and Engineering, 139*(1), 195−227.

Cordes, L. W., & Moran, B. (1996). Treatment of material discontinuity in the element-free galerkin method. *Computer Methods in Applied Mechanics and Engineering, 139*(1), 75−89.

Cox, H. L. (1952). The elasticity and strength of paper and other fibrous materials. *Britain Journal of Applied physics, 3*, 72−79.

Curiel Sosa, J. L., Phaneendra, S., & Munoz, J. J. (2013). Modelling of mixed damage on fibre reinforced composite laminates subjected to low velocity impact. *International Journal of Damage Mechanics, 22*(3), 356−374.

Eshelby, J. D. (1957). The determination of the field of an ellipsoidal inclusion and related problems. *Proceedings of the Royal Society London A, 241*, 376−396.

Fries, T. P., & Matthies, H. G. (2003). *Classification and overview of meshfree methods*. Brunswick: Institute of Scientific Computing, Technical University Braunschweig, Germany. Informatik-bericht Nr, 3.

Ghosh, S., Lee, K., & Moorthy, S. (1996). Two scale analysis of heterogeneous elastic−plastic materials with asymptotic homogenisation and Voronoi cell finite element model. *Computer Methods in Applied Mechanics and Engineering, 132*, 63−116.

Greco, F., & Luciano, R. (2011). A theoretical and numerical stability analysis for composite microstructures by using homogenization theory. *Composites Part B, 42*(3), 382−401.

Guiamatsia, I., Falzon, B. G., Davies, G. A. O., & Iannucci, L. (2009). Element-free galerkin modelling of composite damage. *Composites Science and Technology, 69*(15), 2640−2648.

Guida, M., Marulo, F., Meo, Michele, Grimaldi, A., & Olivares, G. (2011). Sph−lagrangian study of bird impact on leading edge wing. *Composite Structures, 93*(3), 1060−1071.

Guida, Michele, Marulo, Francesco, Polito, Tiziano, Meo, Michele, & Riccio, Massimo (2009). Design and testing of a fiber-metal-laminate bird-strike-resistant leading edge. *Journal of Aircraft, 46*(6), 2121−2129.

Haj-Ali, R. (2009). Cohesive micromechanics: a new approach for progressive damage modeling in laminated composites. *International Journal of Damage Mechanics, 18*(8), 691−719.

Hashin, Z. (1962). The elastic moduli of heterogeneous materials. *Journal of Applied Mechanics, 29*, 143−150.

Hill, R. (1965). A self-consistent mechanics of composite materials. *Journal of the Mechanics and Physics of Solids, 13*, 213−222.

Hu, Wenke, Doh Ha, Youn, & Bobaru, Florin (2012). Peridynamic model for dynamic fracture in unidirectional fiber-reinforced composites. *Computer Methods in Applied Mechanics and Engineering, 217*, 247−261.

Hughes, T. J. R. (1987). *The finite element method*. Dover.

Kalamkarov, A. L., Andrianov, I. V., & Danishevs'kyy, V. V. (2009). Asymptotic homogenization of composite materials and structures. *Applied Mechanics Reviews, 62*(3), 030802.

Kalamkarov, A. L., & Georgiades, A. V. (2002). Micromechanical modeling of smart composite structures. *Smart Materials and Structures, 11*, 423−434.

Kalamkarov, A. L., & Liu, H. Q. (1998). A new model for a multiphase fibre-matrix composite materials. *Composites Part B, 29*, 643−653.

Kilic, B., Agwai, A., & Madenci, E. (2009). Peridynamic theory for progressive damage prediction in center-cracked composite laminates. *Composite Structures, 90*(2), 141−151.

Libersky, Larry D., & Petschek, A. G. (1991). Smooth particle hydrodynamics with strength of materials. In *Advances in the free-lagrange method including contributions on adaptive gridding and the smooth particle hydrodynamics method* (pp. 248−257). Springer.

Lee, H. K. (2001). A computational approach to the investigation of impact damage evolution in discontinuously fiber reinforced composites. *Computational Mechanics, 27*(6), 504−512.

Li, L. Y., Aliabadi, M. H., & Wen, Pi Hua (2012). Meshfree continuum damage mechanics modelling for 3d orthogonal woven composites. *Key Engineering Materials, 488*, 759−762.

Ling, D., Yang, Q. D., & Cox, B. N. (2009). An augmented finite element method for modeling arbitrary discontinuities in composite materials. *International Journal of Fracture, 156*(1), 53−73.

Liu, W. K., Jun, Sukky, Li, Shaofan, Adee, Jonathan, & Belytschko, Ted (1995). Reproducing kernel particle methods for structural dynamics. *International Journal for Numerical Methods in Engineering, 38*(10), 1655−1679.

Liu, W. K., Jun, S., & Zhang, Y. I. (1995). Reproducing kernel particle methods. *International Journal for Numerical Methods in Fluids, 20*(8−9), 1081−1106.

Lu, G. Y., & Mai, Y. W. (1995). Effect of plastic coating on fibre-matrix interface debonding. *Journal of Materials Science, 30*, 5872−5878.

Maligno, A. R., Warrior, N. A., & Long, A. C. (2008). Finite element investigations on the microstructure of fibre-reinforced composites. *Express Polymer Letters, 2*, 665−676.

Matzenmiller, A., Lubliner, J., & Taylor, R. L. (1995). A constitutive model for anisotropic damage in fiber-composites. *Mechanics of Materials, 20*, 125−152.

Michel, J. C., Moulinec, H., & Suquet, P. (1999). Effective properties of composite materials with periodic microstructure: a computational approach. *Computer Methods in Applied Mechanics and Engineering, 172*, 109−143.

Mori, T., & Tanaka, K. (1973). Average stress in the matrix and average elastic energy of materials with misfitting inclusions. *Acta Metallurgica, 21*, 571−574.

Nemat-Nasser, S., & Hori, M. (1993). *Micromechanics: Overall properties of heterogeneous materials*. Amsterdam: Elsevier.

Onate, E., Idelsohn, S., Zienkiewicz, O. C., & Taylor, R. L. (1996). A finite point method in computational mechanics: applications to convective transport and fluid flow. *International Journal for Numerical Methods in Engineering, 39*(22), 3839−3866.

Patel, B. P., & Gupta, A. K. (2014). An investigation on nonlocal continuum damage models for composite laminated panels. *Composites: Part B, 60*, 485−494.

Puck, A., & Schurmann, H. (1998). Failure analysis of FRP laminates by means of physically based phenomenological models. *Composites Science and Technology, 58*, 1045−1067.

Rabczuk, T., & Belytschko, T. (2004). Cracking particles: a simplified meshfree method for arbitrary evolving cracks. *International Journal for Numerical Methods in Engineering, 61*(13), 2316−2343.

Radtke, F. K. F., Simone, A., & Sluys, L. J. (2010). A partition of unity finite element method for obtaining elastic properties of continua with embedded thin fibres. *International Journal for Numerical Methods in Engineering, 84*(6), 708−732.

Raimondo, L., Iannucci, L., Robinson, P., & Curtis, P. T. (2012). A progressive failure model for mesh-size-independent fe analysis of composite laminates subject to low-velocity impact damage. *Composites Science and Technology, 72*(5), 624−632.

Romanowicz, M. (2013). Numerical homogenization of fiber-reinforced composites with complex microstructural features. *Journal of Theoretical and Applied Mechanics, 51*(4), 883−890.

Idelsohn, Sergio R., Onate, Eugenio, Calvo, Nestor, & Pin, Facundo Del (2003). The meshless finite element method. *International Journal for Numerical Methods in Engineering, 58*(6), 893−912.

Shi, Y., Swait, T., & Soutis, C. (2012). Modelling damage evolution in composite laminates subjected to low velocity impact. *Composite Structures, 94*(9), 2902−2913.

Shi, G., Zhang, H., Wang, J., & Wang, Z. (2012). Progressive delamination simulation of laminated plates based on a solid-shell interface element with damage-node model. *Procedia Engineering, 31*, 324−330.

Silling, Stewart Andrew, & Askari, Ebrahim (2005). A meshfree method based on the peridynamic model of solid mechanics. *Computers & Structures, 83*(17), 1526−1535.

Simkins, Daniel C., Jr., Collier, Nathan, & Alford, Joseph B. (2013). Meshfree modeling in laminated composites. In *Meshfree methods for partial differential equations VI* (pp. 221−233). Springer.

Sukumar. N. (1998). *The natural element method in solid mechanics* (Ph.D. thesis). Northwestern University.

Sulsky, D., Chen, Zhen, & Schreyer, Howard L. (1994). A particle method for history-dependent materials. *Computer Methods in Applied Mechanics and Engineering, 118*(1), 179−196.

Suquet, P. M. (1985). Local and global aspects in the mathematical theory of plasticity. In A. Sawczuk, & G. Bianchi (Eds.), *Plasticity today: Modelling, methods and applications* (pp. 279−310). London: Elsevier Applied Science Publishers.

Suquet, P. M. (1987). *Homogenization techniques for composite media. Lecture notes in physics* (Vol. 272). Springer.

Tay, T. E., Liu, G., Tan, V. B. C., Sun, X. S., & Pham, D. C. (2008). Progressive failure analysis of composites. *Journal of Composite Materials, 42*(18), 1921−1966.

Van der Meer, F. P., & Sluys, L. J. (2009). A phantom node formulation with mixed mode cohesive law for splitting in laminates. *International Journal of Fracture, 158*(2), 107−124.

Van der Meer, F. P., & Sluys, L. J. (2010). Mesh-independent modeling of both distributed and discrete matrix cracking in interaction with delamination. *Engineering Fracture Mechanics, 77*(4), 719−735.

Wang, C. (1997). Fracture mechanics of single-fiber pull-out test. *Journal of Materials Science, 32*, 483−490.

Willoughby, N., Parnell, W. J., Hazel, A. L., & Abrahams, I. D. (2012). Homogenization methods to approximate the effective response of random fibre-reinforced composites. *International Journal of Solids and Structures, 49*, 1421−1433.

Xu, Jifeng, Askari, Abe, Weckner, Olaf, & Silling, Stewart (2008). Peridynamic analysis of impact damage in composite laminates. *Journal of Aerospace Engineering, 21*(3), 187−194.

Yagawa, G., & Yamada, T. (1996). Free mesh method: a new meshless finite element method. *Computational Mechanics, 18*(5), 383−386.

Zhu, Tulong, Zhang, J. D., & Atluri, S. N. (1998). A local boundary integral equation (LBIE) method in computational mechanics, and a meshless discretization approach. *Computational Mechanics, 21*(3), 223−235.

Appendix: nomenclature

a_j, $b_{\gamma k}$	FE additional degrees of freedom for the displacement approximation
B_γ	support functions
C	fourth-order damaged stiffness tensor
C'_h, C'_m	composite homogenised and matrix tangent stiffness tensor, respectively
c_j	threshold for the strain damage surface j
C_0	'*Virgin*' stiffness matrix
E_i	Young modulus of the fibre−matrix interface
G_{ic}	fracture energy of the fibre−matrix interface
D	damage tensor
K_{ic}	fibre−matrix interface fracture toughness
$H(x)$	Heaviside function
$N_i, \widetilde{N}_j$	FE shape functions
$f(\sigma_n, \eta_n)$, F^ξ	stress damage surface and corresponding tensor
G^ξ	strain damage tensor
$g(\varepsilon \otimes \varepsilon, c_j) = G(\varepsilon \otimes \varepsilon) - c_j$	undamaged elastic domain in the strain space
$p_\varphi(\varphi)$, $p_\theta(\theta)$	probability distribution functions of the fibre orientation angles
$s(\varepsilon_f^m)$	function quantifying the fibre−matrix strain jump due to debonding

$\boldsymbol{x}$	position vector
$\boldsymbol{u}(\boldsymbol{x})$	displacement field
$\boldsymbol{u_i}$	nodal displacements
$\boldsymbol{\alpha}$	hardening internal variable tensor
$\boldsymbol{\varepsilon}$	strain tensor
$\boldsymbol{\Phi}$	thermodynamic potential such as the free energy one
$\boldsymbol{\mu_{\mathrm{m}} = V_m/V,\ \mu_f = V_f/V}$	matrix and fibre volume content, respectively
$\boldsymbol{\nu}$	damage directional vectors
$\boldsymbol{\Psi_d}$	damage dissipation
$\boldsymbol{\Psi_p}$	plastic dissipation
$\boldsymbol{\sigma_p}$	plastic stress tensor
$\boldsymbol{\tau_{f,u}}$	ultimate fibre−matrix shear stress
$\boldsymbol{\Omega(\alpha)}$	dissipation associated to hardening

Damage evolution modelling in laminates

9

J. Varna
Lulea University of Technology, Lulea, Sweden

9.1 Introduction

Final failure of composite laminate, subjected to complex combinations of thermo-mechanical and environmental loads, is preceded by initiation and evolution of several micro-damage modes in layers. Macroscopically, in in-plane loading cases considered in this chapter, the laminate is in iso-strain condition. The transverse tensile strain to failure of the unidirectional (UD) composite layer is lower than other failure strain components. Hence, cracking of layers with off-axis orientation with respect to the main load direction is usually the first mode of damage (Jamison, Schulte, Reifsnider, & Stinchcomb, 1984; Parvizi & Bailey, 1978). Cracking is caused by a combined action of transverse tensile stress and shear stress considered in the local coordinate system of the layer. The crack (see Figure 9.1(a) and (b)) is usually well defined; it runs parallel to fibres in the layer and the crack plane is transverse to the laminate middle plane. Often the crack covers the whole thickness of the layer and propagates over the whole width of the tensile test specimen. An exception may be laminates with very thin layers and/or low-stress cyclic loading cases. These cracks, which in this chapter we call intralaminar cracks, are often called matrix cracks, tunnelling cracks or transverse cracks. Intralaminar cracks do not usually cause final failure of a laminate. They may significantly impair the effective properties of the laminate (Ogin, Smith, & Beaumont, 1985) and serve as a source for initiation of other damage modes, such as delamination (Kashtalyan & Soutis, 2005; Takeda, Ogihara, & Kobayashi, 1995) (Figure 9.1(c)), and fibre breaks (Figure 9.1(c)) in adjacent plies.

With increasing applied load or with the number of cycles in fatigue loading, the number of cracks increases. Initiation, evolution and effect of these cracks on laminate stiffness has been discussed in many papers; see for example review papers (Nairn & Hu, 1994; Berthelot, 2003). The extent of cracking in a layer is quantified with an average measure called crack density: number of cracks in a layer over a certain distance, measured transverse to the fibre direction in the layer. We denote the crack density in k-th layer as ρ_k (cracks/mm). A number inverse to the crack density, which characterizes the average distance between cracks, is called average crack spacing $2l_k = 1/\rho_k$. Elastic stress distribution between cracks at certain applied macroscopic strain depends neither on the crack spacing nor on the ply thickness as long as the geometrical ratios (ply thickness ratio and spacing/ply thickness ratio) are kept the same. Hence instead of measuring the distance between cracks in, for example, millimetres it is useful to express it in a form normalized with respect to cracked ply

Structural Integrity and Durability of Advanced Composites. http://dx.doi.org/10.1016/B978-0-08-100137-0.00009-2

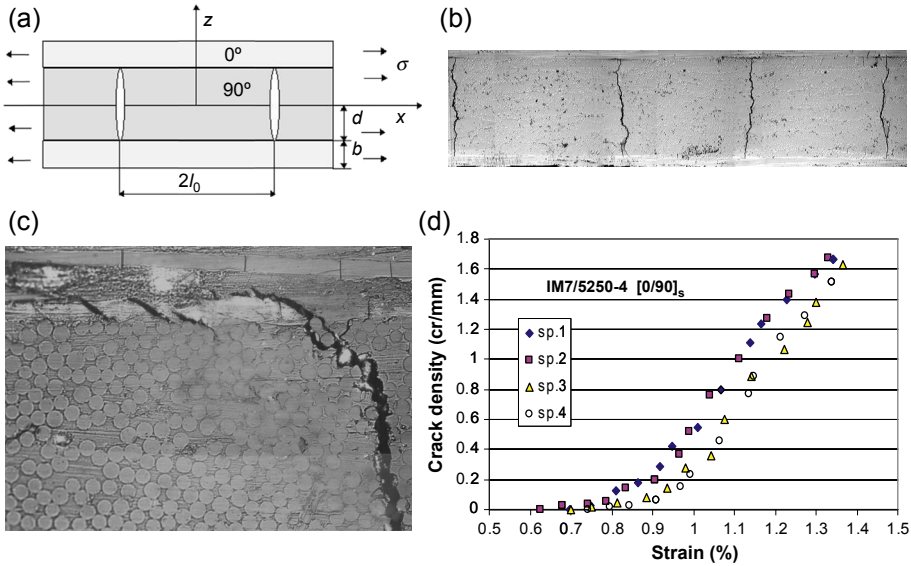

Figure 9.1 Intralaminar cracks in cross-ply laminate: (a) schematic representation of laminate with cracks in middle 90-layer; (b) multiple cracks with rather uniform distribution; (c) crack tip region at the 0/90 interface with local interlayer delamination and fibre breaks in the 0-layer; and (d) crack density increase with increasing applied strain (different symbols correspond to different specimens of the same plate).

thickness t_k. It is similar as for short fibre composites: the real parameter is the aspect ratio of the fibre. So, a proper measure is so-called normalized crack spacing and normalized crack density

$$2l_{kn} = 2l_k/t_k \quad \rho_{kn} = \rho_k t_k \tag{9.1}$$

Each cracking event in a layer creates two new traction-free surfaces. This means that the in-plane transverse and shear stresses on the crack surface are equal to zero and new cracks close to the existing crack cannot be expected. With increasing distance from the crack the transverse and in-plane shear stresses start to recover, and when the distance is large they may asymptotically approach the value as it was in the layer before cracking (far-field stress). The stress transfer mechanism from the undamaged layer to the damaged is through high intralaminar shear stresses at the layer interface in the vicinity of the crack. The efficiency of the stress transfer (the distance needed to recover most of the far-field stress state) depends on elastic and geometrical parameters and on the interface quality. The distance can be very large in the case of delaminations progressing from the intralaminar crack. The described stress transfer mechanism resulting in stress recovery in the damaged layer allows for multiple cracking in the same layer. If the spacing between cracks is larger than $5t_k$ cracks

are usually considered as noninteractive (as a consequence of St Venant's principle the stress perturbations caused by them do not overlap). A very high normalized crack density, close to the maximum observed in tests (often called saturation region or the region with strong crack interaction), is when $\rho_{kn} \approx 1$.

So, the distance from the crack to recover the far-field stresses in a laminate with ply thickness 0.125 mm is less than 1 mm. A relevant question following the above description is: why in a specimen with gauge length 100 mm do we not see at least 50 cracks appearing simultaneously with the first crack? Experiments show (see Figure 9.1(d)) that each new crack requires an increase of the applied strain. The reason is that the transverse and shear failure properties are not the same along the transverse direction of the layer: there are some weaker positions where the first cracks occur and more strong positions requiring larger applied strain. As will be shown in following sections, the transverse failure properties have statistical distribution, for example, it can be Weibull distribution for strength (Huang, Varna, & Talreja, 2011; Peters, 1984; Varna, 2006). As a result, only a few cracks are created at relatively low load because there are just a few weak locations. Then the cracking rate increases with increasing load because we are reaching loads where the material has the highest probability density of failure and many positions have similar failure properties. After that the multiple cracking slows down because there are only a few positions with a high value of failure properties (the probability density curve approaches zero).

There is another mechanism slowing down the rate of cracking in the high-crack-density region. The stress distribution between two cracks depends on the distance between them (normalized spacing). When the normalized crack density is very high, there is not enough distance for stress recovery and even the maximum values of the in-plane stresses between two cracks become significantly lower than the far-field value. The creation of a new crack there requires significantly higher macroscopic load applied to the laminate. This, in addition to the fact that the remaining positions for cracking are very strong, slows down and eventually stops the intralaminar cracking reaching so-called 'characteristic damage state'. Certainly, the damage development does not stop: instead of rather well-defined intralaminar cracks, new damage modes like delta cracks and curved cracks emerge.

As will be described in following sections, two major stages can be recognized in development of each intralaminar crack: initiation and propagation. Whereas the initiation is often considered as independent of geometrical parameters allowing use of approaches with 'in-situ' strength, the propagation (growth of the tunnel along fibres) is analysed using linear elastic fracture mechanics (LEFM), using the concept of released potential energy during the growth of the tunnel. In both cases the stress state between two cracks has to be determined first.

The commonly used approach for stress state determination, called micromechanics modelling (see review e.g. in Nairn and Hu, 1994), is based on perturbation stress analysis. Most of the analytical models are focussed on approximate description of the local stress distribution in the repeating element between two cracks. The simplest calculation schemes used are based on shear lag assumption or variational principles

(Hashin, 1984; Nairn & Hu, 1994; Smith & Wood, 1990; Varna & Berglund, 1991; Varna & Berglund, 1994). Most of the analytical solutions are applicable to cross-ply type of laminates with cracks in 90 layers only. The most accurate numerical routines based on Reissner's variational principle are presented in McCartney et al. (2000) with even higher efficiency than commercial finite element method's (FEM) codes. It is worth highlighting the 'equivalent constraint model' introduced in Zhang, Fan, and Soutis (1992) to determine the effective properties of the damaged layer. In Zhang, Fan, and Soutis (1992) this approach was used together with the shear lag model. With the improved stress model it has the potential of accounting for interaction of cracks belonging to different layers of laminates.

In the following sections we will show that the energy release rate due to crack growth is proportional to the average values of the crack face opening (COD) and crack sliding displacements (CSD). Certainly, the rate depends also on crack density in the layer as well as elastic and geometrical constants. Derivations presented in Loukil, Hussain, Kirti, Pupurs, and Varna (2013) show that a unique simple link exists between average stress change in the damaged layer and average COD and CSD of these cracks.

So, dependent on the convenience of the model used, the energy release rate can be calculated in terms of average stress change or in terms of average COD and CSD, both leading to the same result if solutions are accurate. The former method is suitable when analytical stress distributions are available, whereas the latter is preferable when crack face displacements have been calculated (e.g. using FEM) with results summarized in simple fitting expressions. Using analytical solutions, one could find the average value of the stress change in the cracked layer and, from there, the average COD and CSD.

To explain the relationship between the average stress change between cracks and the average value of COD and CSD, we imagine that somehow the corresponding points on both crack faces are kept together (it would require application of tractions on crack surfaces), not allowing the crack to open or the faces to slide (COD = CSD = 0). Then the stress between cracks would be the same as in undamaged laminate. However, we know that under in-plane tension cracks open, under shear their surfaces slide and under compression they are closed. In the tensile case, as soon as we allow for separation of points on crack faces (opening or sliding), the stress between cracks is reduced. The larger the COD and CSD, the larger is the average stress reduction. The most extreme case is a fully delaminated unit between two cracks. Then there is no stress transfer between layers and in-plane stresses in the cracked layer are zero. This corresponds to the maximum possible COD and CSD, which can be easily estimated knowing that the 90-layer material is not deformed and the whole load is carried by the rest of the layers.

Most of the existing micromechanical models use the assumption that cracks are uniformly distributed in the layer with equal spacing between them. Repeating unit is used to simplify analysis. However, the crack distribution in the layer may be highly nonuniform. This is more typical in the beginning of the cracking process when the average crack density is relatively low. The reason is the mentioned random

distribution of transverse and shear failure properties along the transverse direction of the layer. At low crack density the stress distribution between two existing cracks has a large plateau region with constant high stress, and any position there is a site of possible failure. At high crack density there is a distinct maximum in the stress distribution between cracks, and a new crack has a higher probability of being created in the middle between existing cracks.

The possible inaccuracy introduced in COD and CSD calculations by using the assumption of uniform spacing between cracks in a layer has been addressed in Loukil, Varna, and Ayadi (2012) and McCartney and Schoeppner (2000). To calculate the COD of a crack in a nonuniform case in Loukil et al. (2012) the so-called 'double-periodic' approach was suggested, obtaining COD as the average from two solutions for periodic crack systems representing the two different distances to neighbouring cracks. Very good agreement of this approach was found with direct FEM solution. It was shown that at fixed crack density the crack opening COD is highest if the cracks are uniformly distributed, and in this sense periodic crack distribution models give an upper bound to released energy.

Due to progressing micro-cracking, the macroscopic thermo-mechanical properties of the laminate are degraded. It can be shown using the divergence theorem (Allen & Yoon, 1998) that the average stress applied to the laminate has a rule of mixtures (RoM) relationship to average stresses in layers. In 90-layer the average transverse stress between two cracks is always lower than the far-field stress $\sigma_{x0}^{90^\circ}$. Hence, from RoM and the force equilibrium follows that the average stress in the undamaged 0-layer of cross-ply laminate is higher than $\sigma_{x0}^{0^\circ}$, leading to larger axial strain than in the undamaged case, that is lower laminate modulus. Obviously, realization that the average values of in-plane stresses are proper parameters and that details of the stress distribution are not important simplifies the quantification of properties reduction. Since the average stress reduction can be expressed through COD and CSD, the damaged laminate stiffness can be expressed in terms of density of cracks and two parameters: average COD and CSD, as done in the GLOB-LOC model (Varna, 2013).

Deviations from ideal straight crack geometry (branched cracks, delta cracks) affect the opening (COD) and the sliding (CSD) of crack surfaces and, thus, the amount of released energy and stiffness reduction. Therefore experimental measurements of COD and CSD were performed to compare with calculated values from idealized models. The first measurements of the CODs were reported in Varna, Berglund, Talreja, and Jakovics (1993). The distance between crack faces as a function of layer thickness coordinate was measured from micrographs and also using image analysis. In spite of measurement errors due to uncertainties in focussing the microscope to the exact crack surface position and due to filtering when image analysis was used, it was found that the average value of COD depends on the stiffness ratio of the cracked and the supporting layer and on their thickness ratio. These findings were later confirmed with FEM calculations. Recently, more accurate and reliable COD and CSD measurements were performed using electronic speckle pattern interferometry and assumption of ideal crack geometry was validated (Loukil, Ayadi, & Varna, 2014; Loukil, Varna, & Ayadi, 2013b).

9.2 Damage initiation and growth

9.2.1 Initiation stress and propagation stress

We will distinguish two phases in development of each individual intralaminar crack: initiation and propagation (growth). We will focus on cases when the local transverse stress, which consists of thermal and mechanical parts, is tensile or at least non-negative and contributes to intralaminar crack initiation and propagation in the layer under consideration. Existence of large in-plane shear stresses in the layer facilitates the process. Experiments show that tensile transverse stress has a major role for crack initiation and also for the crack growth: the crack opening mode (Mode I) is the dominant mode. In modelling sometimes the in-plane shear stresses' contribution to the cracking process is even neglected. This simplification of the analysis reflects the fact that the resistance to crack growth in shear is usually much higher. This simplification is not critical for the simulation methodology described in this section and generalizing mixed-mode criteria can be easy implemented if available.

We start with a rather 'diffuse' definition of the initiation and propagation. Initiation is a process on fibre/resin scale (micro-scale) that leads to development of a meso-scale damage entity (defect, flaw, etc.) whose further development is considered as propagation and analysed on meso-scale, ignoring the fibre/matrix microstructure and considering the layer in the laminate as an homogeneous material.

Detailed analysis of initiation is very complex and it is outside the scope of this chapter. Generally speaking, the sequence of micro-events is known: dependent on interface properties, it is a combination of failure of interface leading to prolonged debonds and/or resin failure followed by coalescence of these small damage entities into a large damage entity, which, after reaching certain size, starts to grow unstable in the layer thickness direction. This unstable growth in thickness direction is arrested when the crack approaches the interface with the neighbouring layer. This process has been analysed using LEFM in homogenized layer analytically (Varna & Berglund, 1993), as well as numerically with FEM (Paris, Blazquez, McCartney, & Mantic, 2010). From a stress state point of view, the expected region for initiation is at the specimen edges, where the transverse stress is slightly higher than in the interior of the specimen. Another important parameter for locus of the initiation is microstructural; it is the local variation of fibre volume fraction: in several locations fibres are very close to each other or even touching. These locations are randomly distributed in the specimen; there: (1) the stress concentrations are higher than in a unit cell with average fibre content; and (2) due to limited space between fibres impregnation with resin is more difficult than in average, leading to reduced interface and resin failure properties.

Since suitable and reliable micromechanics analysis for evaluating the necessary applied strain or stress level for crack initiation does not exist, we will employ here a pragmatic approach stating that there is a material system-dependent stress level σ_{in} required to initiate a defect large enough to grow unstably in the thickness direction, which at that stress may or may not propagate along fibres to become an intralaminar crack. The notation σ_{in} can be considered as a symbolic notation for

simultaneously acting transverse and shear stress in the layer, most probably expressed through stress invariants. It is convenient to assume that the initiation stress level does not depend on the thickness of the layer. Certainly, a weak reduction with increasing volume (layer thickness) is still possible, even because of increasing probability to find locations with very unfortunate combinations of geometrical and failure parameters. However, the volume effect in the Weibull strength distribution (Peters, 1984) is weak. For very thin layers with thickness of about 5−7 fibre diameters we can expect increasing initiation stress because the layer boundaries with almost iso-strain condition are too close to the fibre/matrix unit cell and periodic conditions are not valid anymore. Even without the above effects, the initiation stress σ_{in} in transverse loading is expected to be higher than the transverse tensile strength of the same UD composite, σ_T^+. The reason is that for the layer inside the laminate comparing with free-standing UD composite, the severity of large surface defects is reduced due to the bond with the neighbouring layer. Simple analysis in Berglund, Varna, and Yuan (1991) shows that by suppressing surface defects the initiation stress can be 50% higher than the transverse tensile strength

$$\sigma_{\text{in}} = 1.12\sqrt{2}\sigma_T^+ \tag{9.2}$$

LEFM can be applied for propagation of the initiated crack: the available potential energy has to be equal to or larger than the work required in creating a new crack surface. The above expressed in terms of LEFM for Mode I growth states: the Mode I potential energy release rate has to be equal to or larger than its critical value G_c, which is material property (energy needed to create a unit of new crack surface). In the presence of in-plane shear stresses mixed-mode propagation takes place and a criterion, which involves Mode I and Mode II energy release rate as well the corresponding critical values, has to be formulated.

The energy release rate in Mode I is proportional to the square of the in-plane transverse stress in the layer in the location of cracking. It is a linear function of the intralaminar crack size in thickness direction, which is equal to the cracked layer thickness. From here and the propagation criterion, the stress level σ_{prop} for crack growth can be calculated. From the form of the energy release rate described above we can conclude that σ_{prop} depends on the cracked layer thickness t_k. Using a critical strain energy release rate-based failure criterion, the stress for crack propagation σ_{prop} has $1/\sqrt{t_k}$ dependence on ply thickness t_k and therefore stress level for crack propagation in thin layers is higher than in thick layers. The phenomenon that the laminate strain for first ply failure in thin layers becomes ply thickness dependent was experimentally observed in Flaggs and Kural (1982), Joffe, Krasnikovs, and Varna (2001), Lundmark and Varna (2011) and called 'in situ strength'.

Two different scenarios can describe what follows after initiation:

1. The stress level that was necessary to initiate the crack is high and the layer thickness is large

$$\sigma_{\text{in}} > \sigma_{\text{prop}} \tag{9.3}$$

In this case the crack after initiation will propagate in an unstable manner. In terms of released energy it means that at the initiation stress level the available strain energy release rate is much higher than the critical value. In this case the initiation stress governs the multiple cracking and fracture mechanics is not an applicable tool for multiple cracking simulation.

2. The stress for the initiation, σ_{in}, is rather low and/or the ply is very thin, resulting in

$$\sigma_{in} < \sigma_{prop} \tag{9.4}$$

The crack after initiation will not propagate. In other words, at the initiation stress level the available strain energy release rate for crack propagation is lower than the critical value. In this case nothing will happen until higher stress is applied. The stress level for propagation can be calculated using fracture mechanics. In this case cracking is propagation governed.

So, in thin layers a crack may be initiated at roughly the same stress as in thick layers but its propagation is delayed. Unfortunately, the thickness of the layer at which transition takes place from the initiation stress σ_{in} controlled cracking behaviour to ply thickness-dependent propagation stress σ_{prop} controlled behaviour (fracture mechanics) is different for different composite systems and has to be determined in tests. Comparison of crack density curves for several ply thicknesses is the proper way to find the transition thickness.

9.2.2 Statistical nature of initiation stress distribution

We will explain the statistical treatment considering a simplified case when transverse tensile stresses only are responsible for cracking, as it is, for example, in cross-ply laminates subjected to uniaxial loading. The ideas and methodology are applicable for general in-plane loading and expressions are easy to generalize. For example, instead of considering transverse stress only, one can use forms containing stress invariants or expressions similar to those used when failure indexes are calculated in multiaxial failure criteria.

We assume statistical distribution of transverse cracking initiation stress σ_{in} along the transverse direction of the layer. Each layer where cracks may be expected is considered as consisting of many small elements in its transverse direction. Each element has its individual intralaminar cracking initiation stress. Weibull strength distribution is assumed to describe the variation in σ_{in} between elements, whereas the geometrical position of an element with a given σ_{in} is random. The Weibull crack initiation stress σ_{in} distribution is in the form

$$P_{in} = 1 - \exp\left[-\frac{V}{V_0}\left(\frac{\sigma_T}{\sigma_{in0}}\right)^{m_\sigma}\right] \tag{9.5}$$

In Eqn (9.5) P_{in} is the probability that crack is initiated when the transverse tensile stress in the element is σ_T; m_σ and σ_{in0} are the shape and the scale parameters obtained

in tests with reference specimens of element volume V_0; V is the volume of the considered element.

In the simple approach presented below, the length of the element in the transverse direction is related to the maximum possible crack density and is selected so that each element may crack not more than once. As a rough estimate based on experimental observations and stress analysis, one can assume that in internal layers at highest crack density the average distance between cracks is approximately equal to the thickness of this layer:

$$\rho_{k,\max} = 1/t_k \tag{9.6}$$

So, the element size has to be taken to be equal to or smaller than the ply thickness. In the surface layer the spacing at highest crack density (saturation) is approximately two times larger:

$$\rho_{k,\max} = 1/2t_k \tag{9.7}$$

According to Eqns (9.6) and (9.7) the number of elements in a layer with index k is

$$M = \frac{L}{t_k} = L \cdot \rho_{k,\max} \tag{9.8}$$

The analysis presented in this section is not a Monte Carlo type of simulation where failure of each individual element is considered explicitly based on local stress distribution and its individual failure properties. In Monte Carlo simulations each element has to be significantly smaller. Here we express the probability of cracking through crack density without specifying which particular element has failed and ignoring the effect of a crack on stress distribution in neighbouring elements. The effect of cracks is accounted for by using the average stress in Weibull distribution. The presented analysis is more accurate for low crack densities.

Crack density versus transverse stress in the cracked layer for 90 layers in cross-ply laminates can be used to determine parameters in Eqn (9.5). We cannot count initiated cracks because their opening before propagating through the specimen is small. It is much easier to detect fully propagated cracks. To ensure that directly after initiation all cracks propagate, the 90-layer thickness should be in the region where cracking is initiation stress governed (0.5 mm and more). The crack will be well defined and the number of cracks can be counted on any specimen edge. The number of fully developed cracks is equal to the number of initiated cracks.

The number of cracks at arbitrary far-field stress in the layer, $\sigma_{T0}^{(k)}$, is related to average spacing, $2l_k$, between them (index '0' is used for stresses according to CLT):

$$M_{\mathrm{cr}} = \frac{L}{2l_k} = L \cdot \rho_k\left(\sigma_{T0}^{(k)}\right) \tag{9.9}$$

The probability of crack initiation at certain stress $P_{\text{in}}(\sigma_T)$ can be defined as the number of elements with initiated cracks M_{cr} versus the total number of elements M in the layer:

$$P_{\text{in}} = \frac{M_{\text{cr}}}{M} \tag{9.10}$$

Substituting Eqns (9.8) and (9.9) in Eqn (9.10), we obtain a relationship linking the probability of crack initiation P_{in} with the crack density at certain stress level $\sigma_{T0}^{(k)}$ in a layer with index k:

$$P_{\text{in}}^{(k)} = \frac{\rho_k\left(\sigma_{T0}^{(k)}\right)}{\rho_{k,\max}} \tag{9.11}$$

Three to five specimens usually give enough data for statistical analysis. Using in Eqn (9.11) experimental crack density data for the 90-layer thickness in cross-ply laminate, we obtain P_{in}^{90} dependence on transverse stress σ_{T0}^{90}. The stress is calculated using CLT from the applied strain and from the temperature difference ΔT between manufacturing and testing temperature:

$$\sigma_{T0}^{90} = \sigma_{T0}^{90\text{mech}} + \sigma_{T0}^{90\text{thermal}} \tag{9.12}$$

Then, expecting that Eqn (9.5) is applicable, standard procedure is applied to the obtained experimental relationship: we present the data as double logarithm of P_{in}^{90} against $\ln(\sigma_{T0}^{90})$. If the data really follow Weibull distribution, the obtained relationship will be linear. Using linear fit to these data (e.g. trend line in EXCEL) we obtain parameters m_σ and σ_{in0} from fitting function.

More accurate values of Weibull parameters can be found comparing Monte Carlo simulations with experiment (Joffe & Varna, 1999) or using the probabilistic approach developed in Huang, Varna, and Talreja (2014). Both approaches require analytical models for stress distribution between two cracks being applicable for high crack density.

9.2.3 Simulation of multiple cracking initiation and growth

The Weibull distribution for crack initiation stress (Eqn (9.5)) with known parameters m_σ and σ_{in0} and propagation stress σ_{prop} (to be discussed in Section 9.3) can be used to predict the density of initiated cracks, ρ_k^{in}, and also the density of fully developed cracks, ρ_k, in an arbitrary kth layer of a multidirectional laminate subjected to increasing thermo-mechanical loading. The proposed approach is very simple and has no ambition for high accuracy. The application routine differs depending on the level of the transverse stress, σ_{prop}, for crack propagation with respect to the initiation stress region given by Eqn (9.5).

In thin layers the propagation stress may be very high and most of the potential cracks in the layer may be initiated before the transverse stress becomes equal to σ_{prop}.

Then simulations of growing density of initiated cracks can be performed by combining Eqns (9.5) and (9.11) (this time for initiated cracks that are not propagating):

$$\rho_k^{\text{in}} = \rho_{k,\max}\left\{1-\exp\left[-\frac{V}{V_0}\left(\frac{\sigma_{T0}^{(k)}}{\sigma_{\text{in}0}}\right)^{m_\sigma}\right]\right\} \quad \sigma_T = \sigma_{T0}^{(k)} < \sigma_{\text{prop}} \qquad (9.13)$$

$$\rho_k = 0$$

As before, we assume that only one crack can initiate in each element and therefore in Eqn (9.13) $\rho_{k,\max}$ is the highest possible crack density in the kth layer, corresponding to all broken elements in the model. All initiated cracks are relatively short in the fibre direction and in different elements they can be in different positions along fibres. Because of that, interaction between initiated cracks may be neglected and the CLT transverse stress in the layer, $\sigma_{T0}^{(k)}$, can be used in Eqn (9.13). Since we assume that crack initiation is only weakly dependent on ply thickness, this expression can be used for all layers independent of their thickness.

Another extreme case is when the propagation stress is low and each initiated crack immediately propagates, leading to 'fully developed' cracks. The transverse stress $\sigma_T^{(k)}$ in any point between two cracks is lower than the stress in the undamaged layer at the same applied load:

$$\sigma_T^{(k)} \leq \sigma_{T0}^{(k)} \qquad (9.14)$$

The average value of the stress is also lower:

$$\sigma_{T(\text{av})}^{(k)} = k_\sigma(\rho_k)\sigma_{T0}^{(k)} \quad k_\sigma < 1 \qquad (9.15)$$

Coefficient k_σ depends on the density of fully developed cracks. It can be calculated using relationship with the average crack opening (Loukil, Hussain, et al., 2013). Equations (9.5) and (9.11) are still applicable, but it is unclear what we should use for $\sigma_T^{(k)}$. One obvious option is to use the maximum value of the stress between two cracks, stating that this is the location of the next crack, but one could argue that even if the stress reaches maximum in that point the transverse failure stress is randomly distributed. It could be very high in that particular point and the next crack may come where stress is lower but the strength is even lower. Another alternative used in this chapter is to employ the average stress between cracks, Eqn (9.15), when estimating the probability of occurrence of a new crack. Average stress may be even more representative and it is easier to use it in simulations. The expression for crack density in this case is

$$\rho_k^{\text{in}} = \rho_k = \rho_{k,\max}\left\{1-\exp\left[-\frac{V}{V_0}\left(\frac{\sigma_{T0}^{(k)}k_\sigma}{\sigma_{\text{in}0}}\right)^{m_\sigma}\right]\right\} \qquad (9.16)$$

The most complex is the case when the propagation stress σ_{prop} is somewhere in the middle of the initiation stress region. In this case, as long as $\sigma_{T0}^{(k)} < \sigma_{\text{prop}}$, initiation follows:

$$\rho_k^{\text{in}} = \rho_{k,\max}\left\{1 - \exp\left[-\frac{V}{V_0}\left(\frac{\sigma_{T0}^{(k)}}{\sigma_{\text{in}0}}\right)^{m_\sigma}\right]\right\}, \quad \sigma_{T0}^{(k)} < \sigma_{\text{prop}} \tag{9.17}$$

$$\rho_k = 0$$

Just before $\sigma_{T0}^{(k)} = \sigma_{\text{prop}}$ we have initiated crack density ρ_{k0}^{in}. As soon as we reach equality all initiated cracks propagate and instantly become fully developed with crack density $\rho_k = \rho_{k0}^{\text{in}}$. Since scatter in fracture toughness for crack propagation is inevitable, in reality the crack density jump will not be instant but will be over a certain stress region. Maybe this 'scatter' can also be described by a Weibull type of distribution. After that, with increasing load new cracks initiate but they will immediately grow in fully developed cracks according to the rule:

$$\rho_k^{\text{in}} = \rho_k = \rho_{k,\max}\left\{1 - \exp\left[-\frac{V}{V_0}\left(\frac{\sigma_{T0}^{(k)} k_\sigma}{\sigma_{\text{in}0}}\right)^{m_\sigma}\right]\right\}, \quad \sigma_{T0}^{(k)} k_\sigma > \sigma_{\text{prop}} \tag{9.18}$$

To illustrate the described ideas we will consider the crack density data in Figure 9.1(d). Thermo-elastic constants of the IMT/5240-4 composite are: $E_L = 174$ GPa, $E_T = 11$ GPa, $G_{LT} = 5.5$ GPa, $\nu_{LT} = 0.36$, $\alpha_L = 1.0 \times 10^{-6}$ 1/°C, $\alpha_T = 21.9 \times 10^{-6}$ 1/°C, ply thickness is 0.125 mm. The temperature difference after cooling down to room temperature was −165 °C. The thermal transverse stress in the 90-layer calculated using CLT is 34.13 MPa. Since the test was performed in uniaxial tensile loading, the axial strain in Figure 9.1(d) can be recalculated using CLT to transverse mechanical stress in the 90-layer. The total far-field stress in the layer is the sum of both; see Eqn (9.12).

The crack density was recalculated to probability of failure using Eqn (9.11) where $\rho_{k,\max}$ was 4 cr/mm (according to Eqn (9.6)). The crack density in Figure 9.1(d) is much lower than $\rho_{k,\max}$ and the interaction between cracks is relatively weak.

Calculation results are presented in Figure 9.2. According to Figure 9.2(a) first cracks appear at 110 MPa, which is even higher than the upper estimate (Eqn (9.2)). This was expected because the 90-layer thickness is only 0.25 mm and the propagation stress should be enhanced. Rather unexpected is that the experimental relationship in log−log axes in Figure 9.2(b) is rather far from linear, which means that it is not a Weibull distribution.

The trend line in Figure 9.2(b) does not give a good fit. However, one can notice that the experimental relationship is more like bi-linear and different trend lines can be drawn in two different stress regions as shown in Figure 9.3(a). Equations of trend lines are given in Figure 9.3.

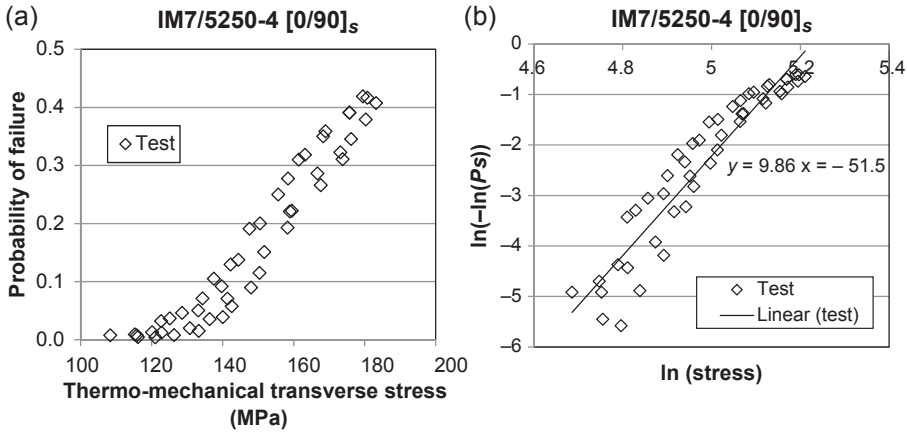

Figure 9.2 Probability of intralaminar cracking in 90-layer as a function of far-field transverse stress in the layer: (a) probability of failure and (b) the same in log−log axis.

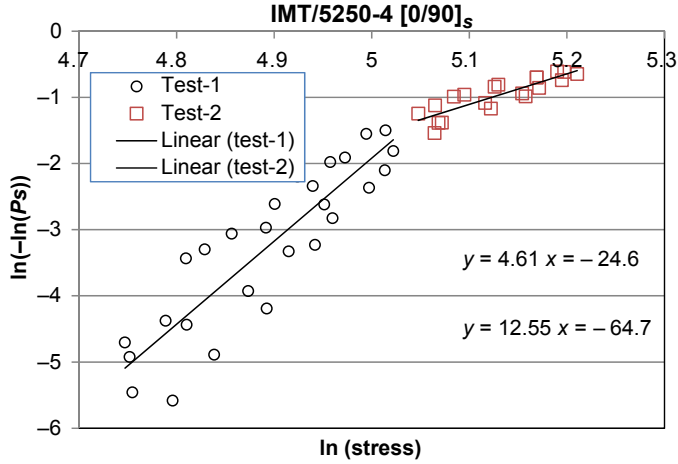

Figure 9.3 Two stress regions in probability of failure where the relationship in log−log axes is linear.

Weibull parameters in the lower stress region (Region 1) are: $m_{\sigma 1} = 12.55$, $\sigma_{\text{in}01} = 172.9$ MPa. In the higher stress region (Region 2) they are: $m_{\sigma 2} = 4.61$, $\sigma_{\text{in}02} = 208.6$ MPa.

We can see in Figure 9.4, where also experimental data are presented, that each distribution fits perfectly the data in the corresponding region but totally fails in the other region: distribution Pf-2 obtained from Region 2 predicts cracks at much lower stresses than is observed experimentally, whereas distribution Pf-1 from Region 1 gives unrealistic crack density at high stresses.

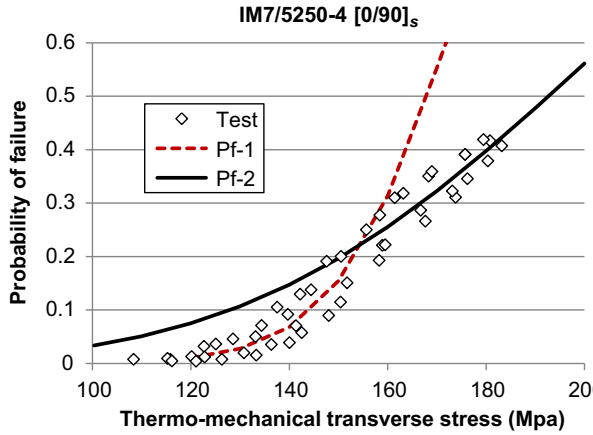

Figure 9.4 Experimental data and predicted probability of failure according to Weibull parameters in two regions: Region 1 (dashed curve) and Region 2 (solid curve).

These observations and discrepancies can be explained using the theoretical discussion in the beginning of this section. Since the 90-layer is thin we have the case described by Eqns (9.17) and (9.18): at lower stresses the initiated cracks cannot propagate because the propagation stress is higher. If so, the first part of the experimental crack density curve describes the 'scatter' in the propagation stress with $m_{\sigma 1} = 12.55$. Uniform fracture toughness would mean constant propagation stress and $m_{\sigma 1} = \infty$. When the stress is higher (in Region 2) each new initiated crack is able to propagate and the initiated crack density is equal to the fully developed crack density; see Eqn (9.18). In this region the probability of failure data (corresponding to crack density data in Figure 9.1(d)) reflect the statistical nature of crack initiation.

Summarizing: the crack density (probability of failure) data would follow the solid line (Pf-2) in Figure 9.4 if the ply would be thicker and, hence, the propagation stress always lower than the initiation stress. In our case the crack initiation still follows the Pf-2 line but the crack propagation in Region 1 is delayed by statistically distributed fracture toughness (propagation stress).

9.3 Energy release rate-based analysis of intralaminar crack propagation

9.3.1 Steady-state solution for noninteractive cracks

Propagation of intralaminar crack along the fibre direction in a layer of laminate is illustrated in Figure 9.5 (L is the fibre direction). Except for the growth in the specimen edge region where the stress state is three-dimensional and except for relatively very short cracks in other locations, the intralaminar crack growth is in a self-similar manner

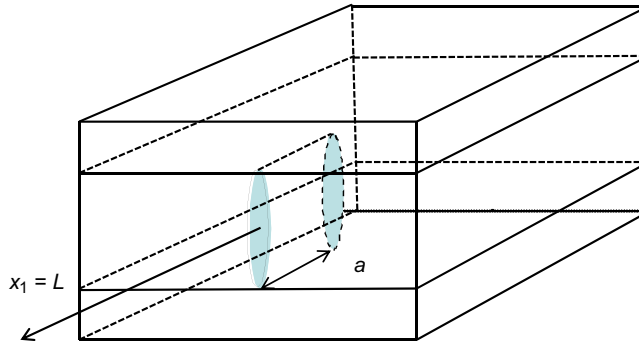

Figure 9.5 Schematic representation of intralaminar crack with length a propagating parallel to fibres.

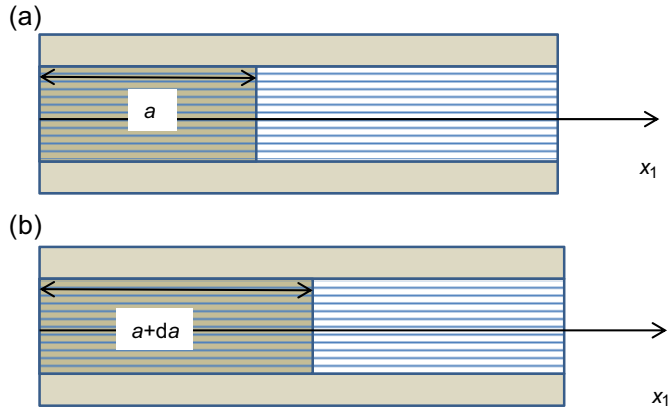

Figure 9.6 Intralaminar crack propagation along x_1: (a) crack length a; (b) crack length $a + \mathrm{d}a$.

(so-called steady-state growth). The condition for that is that the tunnelling crack front is far away from both specimen edges.

The meaning of a self-similar propagation is explained in Figure 9.6, where a section of the laminate parallel to the crack plane in the position of the crack is shown. In Figure 9.6(a) the crack length is a. The shape of the crack front and the stress state there are very complex and not known. Nevertheless, the stress state at the front of the crack of length $a + \mathrm{d}a$ in Figure 9.6(b) is assumed to be the same as in Figure 9.6(a). The stress distribution is just shifted in x_1 direction by $\mathrm{d}a$. The stress state at specimen edges is also complex, but it is not changing due to crack propagation by $\mathrm{d}a$. Using the made assumption that the crack front is far away from specimen edges, we conclude that between the specimen edges and the crack front we have two rather large regions where the stress distribution does not depend on x_1 (plateau regions). When the crack propagates by $\mathrm{d}a$ the plateau region (with crack) to the left of the crack front increases by $\mathrm{d}a$, whereas the plateau region to the right (without crack) decreases by the same amount. Thus the only change is that region of length $\mathrm{d}a$ without crack is

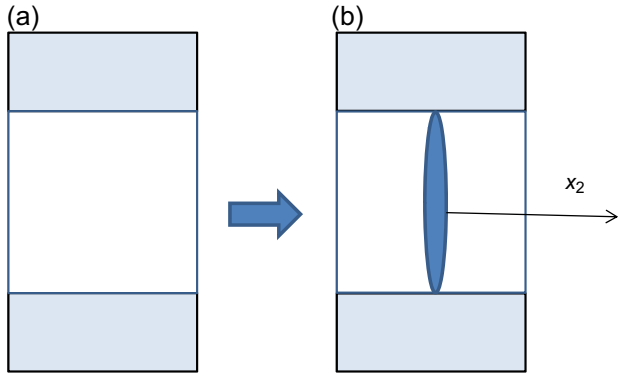

Figure 9.7 Schematic representation of the undamaged region (a) replaced with region containing crack (b).

replaced by region of the same length with crack and the corresponding change of potential energy can be easy calculated.

The region without crack and the newly created region of length da in x_1 direction on the left of the crack front are shown in Figure 9.7. The potential energy change in the system is equal to the energy change when a region without crack in Figure 9.7(a) is replaced with a cracked region in Figure 9.7(b). The change could be determined by first calculating the stress state and strain energy (e.g. using CLT for the region in Figure 9.7(a) and FEM for the region in Figure 9.7(b)) and then finding the additional work on outer boundaries due to cracking. However, there is a simpler way: the potential energy change is equal to the work that has to be performed on crack surfaces to close it. This procedure brings the region back to the undamaged state. We will demonstrate the procedure in detail for a crack opening case and first for a crack that does not interact with other cracks in the same layer (low crack density).

We consider surface element with area dzda on the opened crack face in Figure 9.8(a) and apply to it increasing force dF_2 in the x_2 direction until it is closed. To close it, we have to apply displacement $u_2^{(k)}(z)$, which is equal to 1/2 of the displacement gap between crack faces at given z-coordinate. The transverse stress when the crack is closed is $\sigma_{T0}^{(k)}$, the same as before cracking (CLT). In the definition used in this chapter COD is equal to $u_2^{(k)}(z)$.

The force in the closing instant is $\mathrm{d}F_2 = \sigma_{T0}^{(k)}\mathrm{d}z\mathrm{d}a$ and the performed work by closing (see Figure 9.8(b)):

$$\mathrm{d}W_2 = \frac{1}{2}u_2^{(k)}(z)\mathrm{d}F_2 = \frac{1}{2}\sigma_{T0}^{(k)}u_2^{(k)}(z)\mathrm{d}z\mathrm{d}a \tag{9.19}$$

The work to close both crack surfaces is

$$W_2 = 2\cdot\frac{\mathrm{d}a}{2}\,\sigma_{T0}^{(k)}\int_{-\frac{t_k}{2}}^{+\frac{t_k}{2}} u_2^{(k)}(z)\mathrm{d}z \tag{9.20}$$

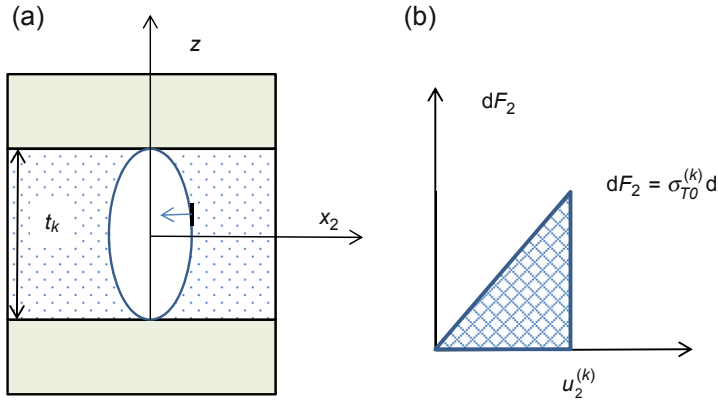

Figure 9.8 Schematic representation of (a) force applied to the element on crack surface and (b) the work to move this element to position when the crack is closed.

Average value of any function $\phi(z)$ in segment $\left[-\frac{t_k}{2}, +\frac{t_k}{2}\right]$ is defined as

$$\phi_a = \frac{1}{t_k} \int_{-\frac{t_k}{2}}^{+\frac{t_k}{2}} \phi(z) \mathrm{d}z \tag{9.21}$$

Hence

$$W_2 = \sigma_{T0}^{(k)} u_{2a}^{(k)} t_k \mathrm{d}a \tag{9.22}$$

where $u_{2an}^{(k)}$ is the average value of the COD in kth layer defined according to Eqn (9.21). In linear elastic solution the average COD, $u_{2a}^{(k)}$, is proportional to the far-field transverse stress in the layer, $\sigma_{T0}^{(k)}$, and to the dimensions of the model represented by the transverse size of the crack, which is equal to the ply thickness t_k. It motivates introduction of normalized average COD, defined as follows:

$$u_{2an}^{(k)} = \frac{u_{2a}^{(k)}}{\sigma_{T0}^{(k)} t_k} E_T \tag{9.23}$$

In Eqn (9.23) factor E_T is introduced to have $u_{2na}^{(k)}$ as a dimensionless parameter. Using Eqn (9.23) we can rewrite W_2 in terms of average normalized COD:

$$W_2 = \left[\sigma_{T0}^{(k)}\right]^2 \frac{t_k^2}{E_T} \cdot u_{2an}^{(k)} \mathrm{d}a \tag{9.24}$$

The strain energy release rate in Mode I, G_I, is defined as the work to create the crack surface with area $da \cdot t_k$ and therefore

$$G_I = \sigma_{T0}^{(k)} u_{2a}^{(k)} \tag{9.25}$$

In terms of normalized average COD, Eqn (9.25) can be written as

$$G_I = \left[\sigma_{T0}^{(k)}\right]^2 \frac{t_k}{E_T} \cdot u_{2an}^{(k)} \tag{9.26}$$

Due to its importance in released energy calculation and also in stiffness reduction predictions, the normalized average COD, $u_{2an}^{(k)}$, and its dependence on elastic and geometrical parameters of layers and the laminate lay-up have been studied extensively using numerical methods (Joffe et al., 2001; Lundmark & Varna, 2005, 2006, 2011; Loukil, Varna, & Ayadi, 2013a). It was found that $u_{2an}^{(k)}$ is a robust parameter slightly dependent on cracked layer and neighbouring layer elastic modulus ratio in a direction transverse to the crack and on the thickness ratio of these layers. Simple fitting expressions for $u_{2an}^{(k)}$ obtained in FEM parametric analysis were presented. The normalized average COD, $u_{2an}^{(k)}$, is a function of crack density. Expressions are given in the Appendix.

Similar analysis can be performed for crack face sliding (CSD) and the strain energy release rate in Mode II cracking. The crack face sliding displacement, $u_1^{(k)}(z)$, is introduced as half of the gap in fibre direction between corresponding points on both crack surfaces. The normalized average CSD is introduced as

$$u_{1an}^{(k)} = \frac{u_{1a}^{(k)}}{\sigma_{LT0}^{(k)} t_k} G_{LT} = \frac{G_{LT}}{\sigma_{LT0}^{(k)} t_k^2} \int_{-\frac{t_k}{2}}^{+\frac{t_k}{2}} u_1^{(k)}(z)\mathrm{d}z \tag{9.27}$$

and the energy release rate in Mode II is

$$G_{II} = \left[\sigma_{LT0}^{(k)}\right]^2 \frac{t_k}{G_{LT}} \cdot u_{1an}^{(k)} \tag{9.28}$$

9.3.2 Energy release rate at high crack density

Equations (9.26) and (9.28) for energy release rates are applicable only for so-called 'noninteractive' cracks when the stress in the crack position after the crack closing is equal to the far-field value $\sigma_{T0}^{(k)}$. At higher crack density it is not correct. The stress at the closed crack is lower because of neighbouring cracks.

To analyse a case with interactive cracks we assume having two cracks with distance between them $2l_k$, as shown in Figure 9.9(a). For simplicity we assume that the considered element between the two vertical lines is a repeating element. Focussing on Mode I, at first, we will calculate the strain energy release rate when the new crack is created in the middle between these two existing ('old') cracks, as in Figure 9.9(b).

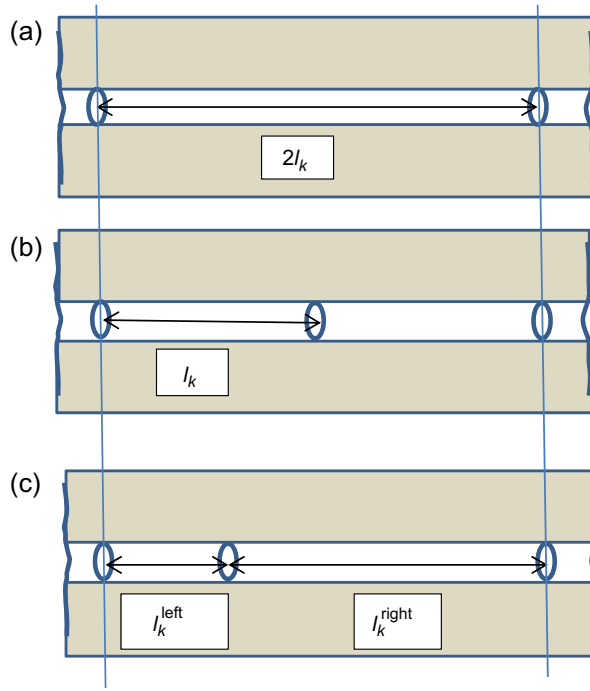

Figure 9.9 A 'new' crack propagating between two 'old' cracks: (a) damage state with two 'old' cracks; (b) 'new' crack in the middle between two 'old' cracks; and (c) 'new' crack in an arbitrary position between two 'old' cracks.

We can employ the approach used above and calculate the work to close the 'new' crack but the obtained expression would contain the stress $\sigma_T^{(k)}$ in the middle between two 'old' cracks which is an unknown and depends on the 'old' crack density (spacing $2l_k$). Instead we will find the work to close the 'new' crack, realizing that we can close ALL cracks in two different ways: (1) closing them all simultaneously; or (2) first closing the 'new' ones and then the 'old' ones. The work to close all cracks in the repeating element simultaneously is denoted $W_{\text{all}\to 0}$, the work to close the 'old' cracks when the 'new' cracks are already closed is $W_{\text{old}\to 0}$, and the searched work to close the 'new' cracks in the presence of 'old' cracks is $W_{\text{all}\to\text{old}}$.

The total work is independent on the used sequence

$$W_{\text{all}\to 0} = W_{\text{all}\to\text{old}} + W_{\text{old}\to 0} \tag{9.29}$$

From Eqn (9.29):

$$W_{\text{all}\to\text{old}} = W_{\text{all}\to 0} - W_{\text{old}\to 0} \tag{9.30}$$

The work to close all cracks at once can be calculated as in section 9.3.1. After closing, the stress in the layer is the far-field stress $\sigma_{T0}^{(k)}$. In Figure 9.9(b) in the unit between

vertical lines we have one 'new' crack in the middle and two halves of the 'old' cracks to close. The crack spacing is l_k. The expression is

$$W_{\text{all}\to 0} = 2\left[\sigma_{T0}^{(k)}\right]^2 \frac{t_k^2}{E_T}\cdot u_{2an}^{(k)}(l_k)\cdot \mathrm{d}a \tag{9.31}$$

Notation $u_{2an}^{(k)}(l_k)$ is used to emphasize that the normalized average COD is calculated for crack spacing l_k corresponding to crack density $\rho_k = 1/l_k$.

The work to close the 'old' cracks (two halves of them belong to the analysed region) when the 'new' is already closed is

$$W_{\text{old}\to 0} = \left[\sigma_{T0}^{(k)}\right]^2 \frac{t_k^2}{E_T}\cdot u_{2an}^{(k)}(2l_k)\cdot \mathrm{d}a \tag{9.32}$$

In Eqn (9.32) $u_{2n(av)}^{(k)}(2l_k)$ is the normalized average COD for crack spacing $2l_k$. Expressions (9.31) and (9.32) are substituted in Eqn (9.30) to obtain the work to close the 'new' crack:

$$W_{\text{all}\to \text{old}} = \left[\sigma_{T0}^{(k)}\right]^2 \frac{t_k}{E_T}\cdot \left[2u_{2an}^{(k)}(l_k) - u_{2an}^{(k)}(2l_k)\right] t_k \mathrm{d}a \tag{9.33}$$

Dividing by the new created surface $t_k da$, we obtain

$$G_I = \left[\sigma_{T0}^{(k)}\right]^2 \frac{t_k}{E_T}\cdot \left[2u_{2an}^{(k)}(l_k) - u_{2an}^{(k)}(2l_k)\right] \tag{9.34}$$

Similar expression for Mode II crack propagation reads:

$$G_{II} = \left[\sigma_{LT0}^{(k)}\right]^2 \frac{t_k}{G_{LT}}\cdot \left[2u_{1an}^{(k)}(l_k) - u_{1an}^{(k)}(2l_k)\right] \tag{9.35}$$

The obtained expressions are valid for a periodic array of cracks. This may not correspond to reality and the distance to the next crack to the left and right is different: l_k^{left} and l_k^{right}, respectively. The COD of the left face of the crack is different than that of the right face. It is smaller on the left because $l_k^{\text{left}} < l_k^{\text{right}}$ and the interaction with the 'old' crack on the left is stronger. This means that the work to close the left face of the 'new' crack is different than the one for the right 'face'. Numerical results presented in Loukil et al. (2012) show that the COD of a given crack face depends only on the distance to the next crack on the same side. The position of the neighbouring crack on the other side of the crack and the positions of other, more far apart cracks are not important. Based on this finding the so-called 'double-periodic approach' was suggested. In this approach the average normalized COD of the left crack face is calculated considering periodic crack distribution with spacing l_k^{left}, whereas the COD of the right crack face is calculated considering periodic cracks with spacing l_k^{right}. For work calculation

we can use the same approach as before, which is based on Eqn (9.30). The work to close all cracks is

$$W_{\text{all}-0} = \left[\sigma_{T0}^{(k)}\right]^2 \frac{t_k^2}{E_T} \cdot \left[u_{2an}^{(k)}\left(l_k^{\text{left}}\right) + u_{2an}^{(k)}\left(l_k^{\text{right}}\right)\right] \mathrm{d}a \tag{9.36}$$

Work to close 'old' cracks is given by Eqn (9.32). From Eqns (9.30) and (9.36), (9.32) the energy release rate due to crack which is not in the middle is

$$G_{I\text{nonun}} = \left[\sigma_{T0}^{(k)}\right]^2 \frac{t_k}{E_T} \cdot \left[u_{2an}^{(k)}\left(l_k^{\text{right}}\right) + u_{2an}^{(k)}\left(l_k^{\text{left}}\right) - u_{2an}^{(k)}(2l_k)\right] \tag{9.37}$$

Crack propagation criteria have to be formulated to use the derived expressions for strain energy release rates. In the simplest case they are $G_I = G_{Ic}$ and $G_{II} = G_{IIc}$. A large variety of mixed-mode criteria are available, but at present there is rather limited knowledge about interaction between different fracture modes in composites. Substituting the derived expressions for energy release rate in the selected criterion, we obtain the expected σ_{prop} dependence on the cracked ply thickness, crack density and other parameters:

$$\left[\sigma_{T0}^{(k)}\right]^2 \frac{t_k}{E_T} \cdot f(\text{stiffness ratio}, \text{thickness ratio}, \text{crack density}) = \text{const} \tag{9.38}$$

9.4 Summary

A lot of research is still required in deepening our understanding of micro-cracking initiation and propagation in layers of laminates and the available simulation tools are far from perfect. The methodology presented in this chapter describes in a simplified way how the experimental data can be used to obtain statistical parameters for crack initiation simulation. For cracking initiation a strength-based approach is suggested. The crack propagation is expected to follow rules of fracture mechanics with the corresponding methodology described in the chapter. Expressions for energy release rate due to steady-state crack propagation are presented. The obtained expressions contain normalized crack opening and sliding displacements, which have been analysed using FEM and are described by simple fitting functions.

References

Allen, D. H., & Yoon, C. (1998). Homogenization techniques for thermo-viscoelastic solids containing cracks. *International Journal of Solids and Structures, 35*, 4035−4053.

Berglund, L. A., Varna, J., & Yuan, J. (1991). Effect of intralaminar toughness on the transverse cracking strain in cross-ply laminates. *Advanced Composite Materials, the Official Journal of the Japan Society for Composite Materials, 1*(3), 225−234.

Berthelot, J.-M. (2003). Transverse cracking and delamination in cross-ply glass-fiber and carbon-fiber reinforced plastic laminates: static and fatigue loading. *Applied Mechanics Reviews, 56*(1), 111−147.

Flaggs, D. L., & Kural, M. H. (1982). Experimental determination of the in situ transverse lamina strength in graphite/epoxy laminates. *Journal of Composite Materials, 16*, 103−115.

Hashin, Z. (1984). Analysis of cracked laminates: a variational approach. *Mechanics of Materials*. North-Holland, 4, 121−136.

Huang, Y., Varna, J., & Talreja, R. (2011). The effect of manufacturing quality on transverse cracking in cross ply laminates. In D. Bhattacharyya, R. Lin, & T. Srivatsan (Eds.), *Processing and fabrication of advanced materials* (Vol. XlX, pp. 552−559). Auckland: Centre for Advanced Composite Materials, University of Auckland, 8 s.

Huang, Y., Varna, J., & Talreja, R. (2014). Statistical methodology for assessing manufacturing quality related to transverse cracking in cross ply laminates. *Composites Science and Technology, 95*, 100−106.

Jamison, R. D., Schulte, K., Reifsnider, K. L., & Stinchcomb, W. W. (1984). Characterization and analysis of damage mechanisms in tension-tension fatigue of graphite/epoxy laminates. *ASTM STP, 836*, 21−55.

Joffe, R., Krasnikovs, A., & Varna, J. (2001). COD-based simulation of transverse cracking and stiffness reduction in [S/90n]s laminates. *Composites Science and Technology, 61*, 637−656.

Joffe, R., & Varna, J. (1999). Damage evolution in multi-directional laminates and the resulting inelastic response. In *Proceedings of ICCM-12, CD, Paris* (p. 10).

Kashtalyan, M., & Soutis, C. (2005). Analysis of composite laminates with intra- and inter-laminar damage. *Progress in Aerospace Sciences, 41*, 152−173.

Loukil, M., Ayadi, Z., & Varna, J. (2014). ESPI analysis of crack face displacements in damaged laminates. *Journal of Composites Science and Technology, 94*(9), 80−88.

Loukil, M. S., Hussain, W., Kirti, A., Pupurs, A., & Varna, J. (2013). Thermoelastic constants of symmetric laminates with cracks in 90-layer: application of simple models. *Plastics, Rubber and Composites, 42*(4), 157−166.

Loukil, M. S., Varna, J., & Ayadi, Z. (2012). Applicability of solutions for periodic intralaminar crack distributions to non-uniformly damaged laminates. *Journal of Composite Materials, 47*(3), 287−301.

Loukil, M. S., Varna, J., & Ayadi, Z. (2013a). Engineering expressions for thermo-elastic constants of laminates with high density of transverse cracks. *Composites A, 48*, 37−46.

Loukil, M. S., Varna, J., & Ayadi, Z. (2013b). Damage characterization in glass fiber/epoxy laminates using electronic speckle pattern Interferometry. *Experimental Techniques*. http://dx.doi.org/10.1111/ext.12013.

Lundmark, P., & Varna, J. (2005). Constitutive relationships for laminates with ply cracks in in-plane loading. *International Journal of Damage Mechanics, 14*(3), 235−261.

Lundmark, P., & Varna, J. (2006). Crack face sliding effect on stiffness of laminates with ply cracks. *Composites Science and Technology, 66*, 1444−1454.

Lundmark, P., & Varna, J. (2011). Stiffness reduction in laminates at high intralaminar crack density: effect of crack interaction. *International Journal of Damage Mechanics, 20*, 279−297.

McCartney, L. N., & Schoeppner, G. A. (2000). Predicting the effect of non-uniform ply cracking on the thermo-elastic properties of cross-ply laminates. *Composites Science and Technology, 62*, 1841−1856.

McCartney, L. N., Schoeppner, G. A., & Becker, W. (2000). Comparison of models for transverse ply cracks in composite laminates. *Composites Science and Technology, 60*, 2347−2359.

Nairn, J., & Hu, S. (1994). Matrix microcracking. In R. B. Pipes, & R. Talreja (Eds.), *Dam. mech. comp. mater: Vol. 9. Comp. mater. series* (pp. 187−243). Amsterdam: Elsevier.

Ogin, S. L., Smith, P. A., & Beaumont, P. W. R. (1985). Matrix cracking and stiffness reduction during the fatigue of a [0/90]s GFRP laminate. *Composites Science and Technology, 22*, 23−31.

Paris, F., Blazquez, A., McCartney, L. N., & Mantic, V. (2010). Characterization and evolution of matrix and interface related damage in [0/90]s laminates under tension. Part I: numerical predictions. *Composites Science and Technology, 70*(7), 1168−1175.

Parvizi, A., & Bailey, J. E. (1978). On multiple transverse cracking in glass fibre epoxy cross-ply laminates. *Journal of Materials Science, 13*, 2131−2136.

Peters, P. W. M. (1984). The strength distribution of 90-plies in 0/90/0 graphite-epoxy laminates. *Journal of Composite Materials, 18*, 545−556.

Smith, P. A., & Wood, J. R. (1990). Poisson's ratio as a damage parameter in the static tensile loading of simple cross-ply laminates. *Composites Science and Technology, 38*, 85−93.

Takeda, N., Ogihara, S., & Kobayashi, A. (1995). Microscopic fatigue damage progress in CFRP cross-ply laminates. *Composites, 26*, 859−867.

Varna, J. (2006). Quantification of damage and evolution modeling in multidirectional laminates. In *Proc. of the 27th RISÖ international symposium on material science, Roskilde, Denmark* (pp. 349−356).

Varna, J. (2013). Modeling mechanical performance of damaged laminates. *Journal of Composite Materials, 47*(20−21), 2443−2475.

Varna, J., & Berglund, L. A. (1991). Multiple transverse cracking and stiffness reduction in cross-ply laminates. *Journal of Composites Technology and Research, JCTRER, 13*(2), 97−106.

Varna, J., & Berglund, L. A. (1993). Two-dimensional transverse cracking in [0m/90n]S cross-ply laminates. *European Journal of Mechanics A/Solids, 12*(5), 699−723.

Varna, J., & Berglund, L. A. (1994). Thermo-elastic properties of composite laminates with transverse cracks. *Journal of Composites Technology and Research, 16*(1), 77−87.

Varna, J., Berglund, L. A., Talreja, R., & Jakovics, A. (1993). A study of the crack opening displacement of transverse cracks in cross ply laminates. *International Journal of Damage Mechanics, 2*, 272−289.

Zhang, J., Fan, J., & Soutis, C. (1992). Analysis of multiple matrix cracking in $[\pm\theta_m/90_n]$s composite laminates. Part 1. In-plane stiffness properties. *Composites, 23*(5), 291−304.

Appendix: expressions for crack force opening displacements (COD) and crack sliding displacements (CSD)

The COD, u^0_{2an}, of **noninteractive crack** we consider in a coordinate system where the cracked layer has 90-orientation with respect to the *x*-axis. In other words *x*-direction is direction 2 for the layer with crack. Index *k*, denoting the layer, is omitted in the expressions below. A distinction has to be made between cracks in surface layers and cracks in inside layers. The normalized average COD of surface cracks is larger because the cracked layer is supported only from one side. The fitting expressions are presented for a symmetric case when the upper support layer S1 has properties, orientation and geometry equal to lower support layer S2; see Figure 9.10. The expression for u^0_{2an} is

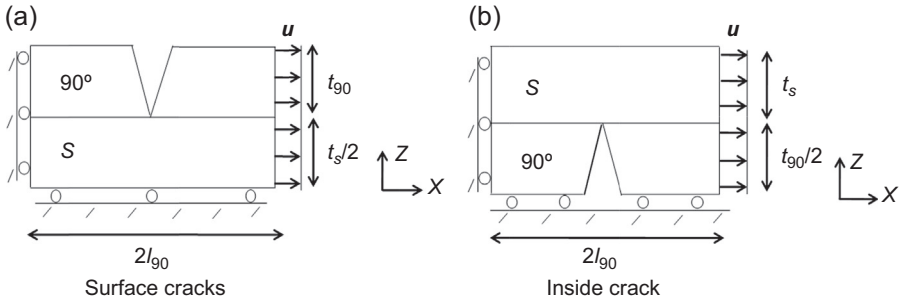

Figure 9.10 FEM models used to calculate COD of interactive cracks: (a) in surface layers and (b) in inside layers.

$$u^0_{2an} = A + B\left(\frac{E_2}{E^S_x}\right)^n \tag{A1}$$

In Eqn (A1) E^S_x is the Young's modulus of the support layer measured in the x-direction. For a crack in an internal layer:

$$A = 0.52 \quad B = 0.3075 + 0.1652\left(\frac{t_{90}}{2t_s} - 1\right)$$

$$n = 0.030667\left(\frac{t_{90}}{2t_s}\right)^2 - 0.0626\frac{t_{90}}{2t_s} + 0.7037 \tag{A2}$$

In Eqn (A2) t_s is thickness of the adjacent support layer and t_{90} is thickness of the cracked layer.

For a crack in surface layer:

$$A = 1.2 \quad B = 0.5942 + 0.1901\left(2\frac{t_{90}}{t_s} - 1\right)$$

$$n = -0.52292\left(\frac{t_{90}}{t_s}\right)^2 + 0.8874\frac{t_{90}}{t_s} + 0.2576 \tag{A3}$$

Suggestions for calculations in more realistic cases when the support layers S1 and S2 are different are given in Varna (2013).

Crack face sliding displacements (CSD), u^0_{1an} (see Lundmark & Varna, 2006 for details), also follows a power law:

$$u^0_{1an} = A + B\left(\frac{G_{12}}{G^S_{xy}}\right)^n \tag{A4}$$

In Eqn (A4) G_{xy}^{S} is the in-plane shear modulus of the support layer.
For cracks in the internal layer:

$$A = 0.3 \quad B = 0.066 + 0.054\frac{t_{90}}{2t_s} \quad n = 0.82 \tag{A5}$$

For cracks in the surface layer:

$$A = 0.6 \quad B = 0.134 + 0.105\frac{t_{90}}{t_s/2} \quad n = 0.82 \tag{A6}$$

Expressions show that the normalized average COD and CSD are larger for less stiff surrounding layers and approach a certain asymptotic value with increasing support layer and cracked layer stiffness ratio. For thicker support layers the COD and CSD is smaller. This effect of neighbouring layers on the crack face displacements is called the 'constraint effect'.

The u_{2an}^{k} has been related to COD of noninteractive cracks, u_{2an}^{0k}, by relationship (Lundmark & Varna, 2011):

$$u_{2an}^{k} = \lambda_k(\rho_{kn})u_{2an}^{0k} \tag{A7}$$

The crack interaction function λ depends on crack density in the layer and on material and geometrical parameters of the cracked layer and surrounding layers. For noninteractive cracks $\lambda = 1$. Detailed analysis of the effect of different parameters on interaction function was performed in Loukil, Varna, et al. (2013) using FEM. Empirical relationship was obtained by fitting.

$$\lambda_k = \tanh\left(\frac{\alpha}{\rho_{kn}}\right) \tag{A8}$$

For internal cracks (Figure 9.10(b)) the constant α is defined by

$$\alpha^2 = C \times \left(\frac{t_s G_{23} + t_{90}/2\, G_{12}}{(t_s + t_{90}/2)G_{23}}\right)\left(1 + \frac{t_{90}/2\, E_2}{t_s E_s}\right) \quad C = 0.52 \tag{A9}$$

For surface cracks in cross-ply laminates (see Figure 9.10(a)):

$$\alpha^2 = C \times \left(\frac{t_s/2\, G_{23} + t_{90}\, G_{12}}{(t_s/2 + t_{90})G_{23}}\right)\left(1 + \frac{t_{90}E_2}{t_s/2\, E_s}\right) \quad C = 0.085 \tag{A10}$$

The effect of nonuniform crack distribution on COD was analysed in Loukil et al. (2012).

Virtual testing of impact in fiber reinforced laminates

10

S. Sádaba[1], F. Martínez-Hergueta[1], C.S. Lopes[1], C. Gonzalez[1,2], J. LLorca[1,2]
[1]IMDEA Materials Institute, Getafe, Madrid, Spain; [2]Polytechnic University of Madrid, Madrid, Spain

10.1 Introduction

Carbon fibre–reinforced polymers are nowadays extensively used in applications where outstanding mechanical properties are necessary in combination with weight saving. Good examples are the Airbus A350 XWB and the Boeing 787 Dreamliner, where fibre composites are used for up to $\approx 50\%$ of wings, fuselage sections and tail surfaces. Although the demanding in-plane loads are perfectly covered by the high strength and stiffness of the carbon laminates, it is well known that such laminates are very sensitive to out-of-plane loads coming from impacts during maintenance (i.e. tools drops) and service operations (e.g. runway debris or bird and lightning impacts) (Abrate, 1998). The traditional strategy to guarantee structural integrity is based on extensive and costly experimental campaigns in which the burden of testing is immense (up to $\approx 10^4$ tests are required for certification of an airframe structure (Cox & Yang, 2006; MIL-HDBK-17-1F, 2002)). Experimental tests include those ranging from simple coupons (tension, compression, shear) to small components (damage tolerance) up to the final composite structure (fuselage barrel or wing). Recent developments in material modelling, together with increased computational power and improvements in computing tools, are rapidly changing the aforementioned scenario of costly and time-consuming testing. Nowadays it is becoming possible to accurately predict the behaviour until failure of composite materials and small components by computer-assisted virtual testing (LLorca et al., 2011; LLorca, González, Molina Aldareguía, & Lopes, 2013).

Structural composites are manufactured by stacking different composite layers (unidirectional or woven) into a laminate with a given stacking sequence. Different damage mechanisms co-exist during composite deformation and can lead to laminate failure. Fracture due to tensile stresses parallel to the fibres is controlled by the tensile fracture of fibres, while compressive stresses along the fibres lead to kinking. Stresses perpendicular to the fibre induce failure by matrix cracking in tension or shear and interface decohesion. In addition, interply delamination is a typical failure mechanism in laminates due to the thermoelastic mismatch between adjacent plies. Accurate models to predict the failure of composite

Structural Integrity and Durability of Advanced Composites. http://dx.doi.org/10.1016/B978-0-08-100137-0.00010-9

laminates should include all these failure modes as well as the complex interactions among them.

Modelling of impact damage presents additional difficulties because it is important to take into account the dynamic structural behaviour and the local effects at the impact point. As a result, the use of analytical models often results in an oversimplification of the problem and thus inaccurate predictions. On the contrary, numerical simulations based on the finite element model can account for the complex constitutive behaviour of the composite material at the local (element) level together with the simulation of complex structural behaviour under complex external loads and boundary conditions.

The present chapter presents a virtual testing methodology to simulate the mechanical performance of composite laminates under impact by means of computational mesomechanics. This strategy is based on fully coupled modelization of intralaminar and interlaminar failure mechanisms in composite laminates, and is described in detail in Section 10.2. Intralaminar failure is addressed within the framework of continuum damage mechanics (CDM). Interply damage by delamination is taken into account by a cohesive crack approach that uses either cohesive elements or cohesive surfaces between adjacent plies. Two applications of this modelling strategy devoted to low- and high-velocity impact are presented in Sections 10.3 and 10.4 respectively. Future trends and expected developments in the field are briefly outlined in the last section of this chapter.

10.2 Mesomechanical modelling strategy of composite laminates

Individual plies are the basic building blocks in the computational mesomechanics of laminates. A virtual laminate is thus built with plies made up of different unidirectional or woven fibres (carbon, glass, aramid, etc.) embedded in a matrix (normally an epoxy resin) according to a predefined stacking sequence, as shown in Figure 10.1. The ply interfaces are also explicitly included in the model. The finite element discretization of the laminate is carried out using solid or continuum shell elements for the plies, while interface elements (or cohesive surface interactions) are used to take into account the interply delamination. This modelling strategy can account for full three-dimensional stress states, as opposed to simulations based on standard composite shell elements. Moreover, this strategy allows for analysis of the interaction between intraply and interply damage mechanisms. Obviously, computational cost limits its applicability to composite coupons or structural details and it cannot be used to model a full aeroplane.

The constitutive equation and the failure mechanisms of each ply (unidirectional or woven) are naturally constrained by the anisotropy induced by the fibre architecture

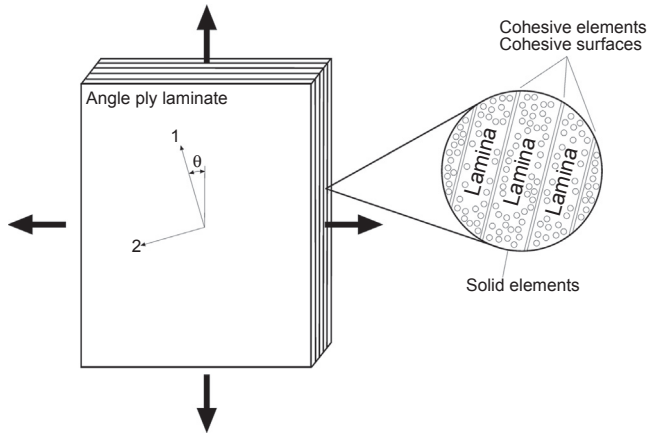

Figure 10.1 Schematic of computational mesomechanics approach.

and the orientation of the plies. The elastic behaviour of single plies is included by means of a linear elastic orthotropic constitutive equation, while the onset of damage can be predicted using the different failure criteria available in the literature. (For instance, see Puck & Schurmann (2002); Dávila, Camanho, & Rose (2005); Pinho, Dávila, Camanho, Iannucci, & Robinson (2005); Pinho, Iannucci, & Robinson (2006a), and the relevant work of Kaddour, Hinton, & Soden (2004) in relation to the World-Wide Failure Exercise, in which different failure criteria were compared with experimental results under different loading conditions.) These failure criteria provide the critical multiaxial stress state that triggers damage in each ply for each particular failure mode (matrix splitting, fibre kinking, etc.). However, the occurrence of damage in an individual ply is not associated with the final failure of the laminate. The damage progresses in each ply, and damage interaction between plies is handled by a combination of CDM and cohesive interply decohesion, each of which is detailed below.

10.2.1 Intraply damage: continuum damage mechanics

CDM treats damage by assuming a homogeneous dispersion of cracks within a continuum (Kachanov, 1986; Lemaitre, 1996). Assuming a linear elastic material containing a random and homogeneous dispersion of cracks, damage is represented by damage variable d expressed as

$$d = \frac{A - \overline{A}}{A} \tag{10.1}$$

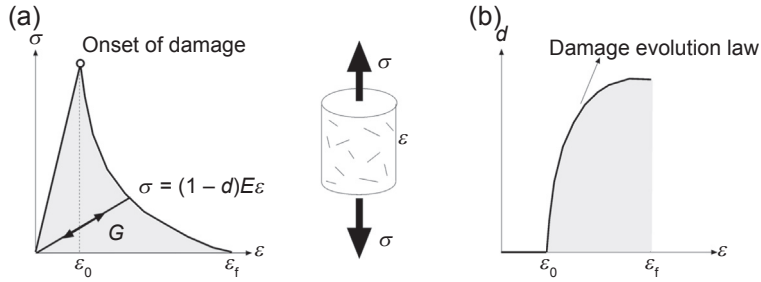

Figure 10.2 (a) Stress−strain curve of a material under uniaxial loading according to continuum damage mechanics, where g is the volumetric fracture energy (energy per unit volume) associated with the area under the $\sigma-\varepsilon$ curve. (b) Evolution of the damage variable d with strain.

where $\overline{A}$ is the net effective area (net area contributing to the load-carrying capacity of the material not including the crack area) while A stands for the nominal area of the specimen (Figure 10.2). Therefore, the damage variable ranges from $0 \leq d < 1$, with $d = 0$ in the undamaged or virgin state when no cracks are present in the material and $d = 1$ in the fully damaged condition when the net effective area is $\overline{A} = 0$. If the undamaged material is a linear and elastic solid with elastic modulus E, the nominal stress in the damaged material σ can be expressed as a function of the damage variable d in the form

$$\sigma = (1-d)E\varepsilon = (1-d)\tilde{\sigma} \tag{10.2}$$

where $\tilde{\sigma} = E\varepsilon$ represents the effective stress in the material in the undamaged state.

The response of the material is initially elastic up to an initial strain $\varepsilon_0(d = 0)$ (damage onset); from that point, damage grows until complete fracture occurs at $\varepsilon_f(d = 1)$. The damage variable controls the evolution of damage and may depend on any internal variable (stress, strain, elastic energy, etc.). The area under the stress−strain curve corresponds with the volumetric fracture energy g (energy dissipated during failure per unit of volume of material) and can be computed by integration of the stress−strain relationship along the loading path according to

$$g = \int_0^{\varepsilon_f} \sigma(\varepsilon)\, \mathrm{d}\varepsilon \tag{10.3}$$

The extrapolation of the elastic and isotropic behaviour described in Eqn (10.2) to anisotropic materials is straightforward (Matzenmiller, Lubliner, & Taylor, 1995). It will be assumed that the unidirectional fibre−reinforced composite behaves as a

linear elastic orthotropic solid, and the corresponding compliance matrix – the relation between stress and strain tensor – is expressed (in Nye notation) as

$$\begin{bmatrix} \varepsilon_1 \\ \varepsilon_2 \\ \varepsilon_3 \\ \gamma_{13} \\ \gamma_{23} \\ \gamma_{12} \end{bmatrix} = \begin{bmatrix} \frac{1}{(1-d_1)E_1} & -\frac{\nu_{12}}{E_1} & -\frac{\nu_{13}}{E_1} & 0 & 0 & 0 \\ -\frac{\nu_{12}}{E_1} & \frac{1}{(1-d_2)E_2} & -\frac{\nu_{23}}{E_2} & 0 & 0 & 0 \\ -\frac{\nu_{13}}{E_1} & -\frac{\nu_{23}}{E_2} & \frac{1}{(1-d_3)E_3} & 0 & 0 & 0 \\ 0 & 0 & 0 & \frac{1}{(1-d_4)G_{13}} & 0 & 0 \\ 0 & 0 & 0 & 0 & \frac{1}{(1-d_5)G_{23}} & 0 \\ 0 & 0 & 0 & 0 & 0 & \frac{1}{(1-d_6)G_{12}} \end{bmatrix} \begin{bmatrix} \sigma_1 \\ \sigma_2 \\ \sigma_3 \\ \tau_{13} \\ \tau_{23} \\ \tau_{12} \end{bmatrix} \tag{10.4}$$

where E_1, E_2, E_3, ν_{12}, ν_{13}, ν_{23}, G_{12}, G_{13}, G_{23} are the nine elastic constants that determine the elastic behaviour of the undamaged orthotropic material in the local axis material orientation, and d_1, d_2, d_3, d_4, d_5, d_6 stand for the six damage variables that control the evolution of damage during loading. Of the latter group, d_6 accounts for damage during in-plane shear deformation while d_1 and d_2 stand for the mechanisms associated with failure parallel and perpendicular to the fibres in unidirectional laminae (or weft and warp directions in woven structures). Additionally, the variables d_4, d_5 and d_3 control the respective out-of-plane shear and normal stresses τ_{13}, τ_{23} and σ_3 that could potentially contribute to damage during impact loading conditions due to contact stresses with the impactors. Nevertheless, the dominant damage mechanisms are found in the laminate plane in most composite structures and therefore $d_3 = d_4 = d_5 = 0$.

The onset of damage is dictated by the failure locus of the ply given by, for instance, the LaRC04 failure criterion (Dávila, Camanho, & Rose, 2005) that has been validated

extensively for predicting the failure of uniaxially reinforced plies. The damage model used in this work is based on extending the LaRC04 plane-stress formulation proposed by Maimí, Camanho, Mayugo, and Dávila (2007a,b) to three-dimensional loading scenarios. Four failure functions, ϕ_{1+}, ϕ_{1-}, ϕ_{2+}, ϕ_{2-}, are defined in LaRC04 to account for the four in-plane damage mechanisms, and define ply failure locus as a function of the ply elastic constants and the strength for a given effective-stress state (stress obtained assuming undamaged state), as shown in Figure 10.3. The failure functions depend on the strength of the lamina in the different in-plane directions: X_T, longitudinal tensile strength; X_C, longitudinal compressive strength; Y_T, transverse tensile strength; Y_C, transverse compressive strength; and S_L, in-plane shear strength (Figure 10.3).

Out-of-plane shear and normal strengths in tension and compression (S_T, Z_T and Z_C) should be considered when out-of-plane failure mechanisms are taken into account with additional failure functions. The onset and propagation of damage is controlled by damage-activation function F_N, which is associated with failure mechanisms in the longitudinal ($N = 1+, 1-$) and transverse ($N = 2+, 2-$) directions. It is expressed as

$$\text{Tensile fibre failure} \qquad F_{1+} = \phi_{1+} - r_{1+} \leq 0 \tag{10.5}$$

$$\text{Compressive fibre kinking} \qquad F_{1-} = \phi_{1-} - r_{1-} \leq 0 \tag{10.6}$$

$$\text{Tensile matrix failure} \qquad F_{2+} = \phi_{2+} - r_{2+} \leq 0 \tag{10.7}$$

$$\text{Compressive matrix failure} \qquad F_{2-} = \phi_{2-} - r_{2-} \leq 0 \tag{10.8}$$

where r_{1+}, r_{1-}, r_{2+}, r_{2-} are the damage thresholds – internal variables of the model that are initially equal to 1 and increase monotonically during the loading history. When damage-activation functions satisfy $F_N < 0$, material response is elastic. If $F_N = 0$ and $\dot{\phi}_N \leq 0$, the state is that of elastic unloading or neutral loading. Finally, if $F_N = 0$ and $\dot{\phi}_N > 0$, there is a damage evolution controlled by the Kuhn–Tucker consistency condition

$$\dot{F}_N = \dot{\phi}_N - \dot{r}_N = 0 \tag{10.9}$$

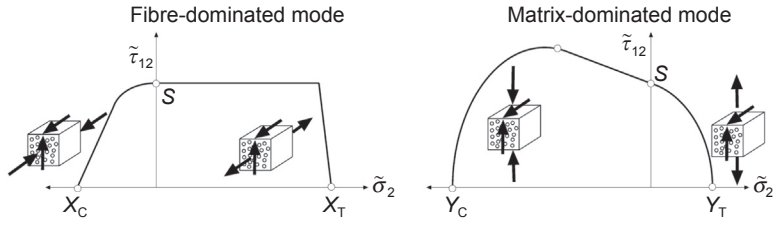

Figure 10.3 LaRC04 failure surfaces of the virgin material represented in $\tilde{\sigma}_1 - \tilde{\tau}_{12}$ (fibre-dominated modes ϕ_{1+} and ϕ_{1-}) and $\tilde{\sigma}_2 - \tilde{\tau}_{12}$ (matrix-dominated modes ϕ_{2+} and ϕ_{2-}).

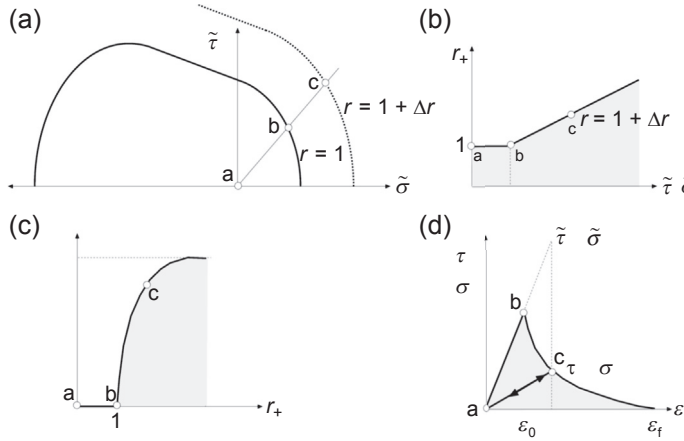

Figure 10.4 Damage-evolution process: (a) loading in the effective-stress state, (b) increment of the internal variables of the model, (c) damage variable update and (d) softening effect in the stress−strain curve.

The procedure is shown in Figure 10.4. Initially, the load is introduced in the composite until the onset of damage occurs, represented by point b in Figure 10.4(a). At this point, the stress state is over the failure locus of the ply, and additional strain increments produce an outward movement of the damage-activation function F_N, leading to a corresponding increment of the damage threshold variable to fulfil the Kuhn−Tucker condition, as indicated by point c in Figure 10.4(a) and (b).

The evolution of the damage variable with respect to damage thresholds is usually taken into account through exponential expressions of the type

$$d_N = 1 - \frac{1}{r_N}\exp[A_N(1 - r_N)] \quad \text{where} \quad N = 1+,\ 1-,\ 2+,\ 2- \tag{10.10}$$

which are valid for tension and compression modes in directions parallel and perpendicular to the fibres in unidirectional composites, as shown in Figure 10.4(c). The evolution of the damage variable affecting the shear response of the composite is expressed as

$$d_6 = 1 - \left(\frac{1}{r_{2+}}\exp[A_6(1 - r_{2+})]\right)(1 - d_{1+}) \tag{10.11}$$

indicating that matrix and fibre cracks modify the shear response of the material. Crack-closure effects under load reversal cycles are also taken into account.

The coefficients $A_{1+}, A_{1-}, A_{2+}, A_{2-}, A_6$ are softening parameters that can be used to ensure mesh objectivity of the model − the model should independently dissipate the same amount of energy during failure, irrespective of the size of finite elements in the discretization. This method, known as Bazant's crack band model (Bažant & Oh, 1983), allows for regularization of the finite element problem with regard to the

size of finite element discretization. Otherwise, the model results would depend on the size of the finite element used in the mesh. The coefficients are computed from the volumetric fracture energy for a given fracture mode, g_N, and the corresponding material toughness of the composite material, G_N, measured through specific fracture tests according to

$$g_N = \frac{G_N}{l_{\text{ch}}} \tag{10.12}$$

where l_{ch} is the characteristic length of the finite element used in the simulations.

The elastic properties of unidirectional plies (E_1, $E_2 = E_3$, $\nu_{12} = \nu_{13}$, ν_{23}, $G_{12} = G_{13}$, G_{23}) and ply strengths (X_T, X_C, Y_T, Y_C, S_L) can be measured using standard tests or estimated by means of computational micromechanics (LLorca et al., 2011, 2013; Canal, González, Segurado, & LLorca, 2012; González & LLorca, 2007). The four components of fracture toughness, associated with longitudinal failure in tension and compression (G_{1+} and G_{1-} respectively) and transverse failure in tension and shear (G_{2+} and G_6 respectively) can also be measured from independent tests. For instance, G_{2+} can be obtained using a standard test procedure devised by the ASTM, while G_{1+} and G_{1-} are determined from compact tension and compact compression tests developed by Pinho, Robinson, & Iannucci (2006b). Transverse failure in shear G_6 can be measured using the four-point bending end-notched flexure test proposed by Martin, Elms, & Bowron (1998). Finally, the fracture toughness G_{2-} can be calculated from G_6 and the ply fracture angle for pure transverse compression (Maimí et al., 2007a,b).

10.2.2 Interply delamination: cohesive crack model

Interply delamination is a typical failure mode in composite laminates because of the stress concentration induced by the elastic mismatch of adjacent plies with different fibre orientations. The crack path is defined a priori, and progressive interply delamination under mixed-mode loading can be analysed by means of a cohesive crack model coupled with interface elements between the ply surfaces (Camanho & Dávila, 2002; Turón, Camanho, Costa, & Dávila, 2006) or cohesive interactions between surfaces (Abaqus, 2014).

The mechanical behaviour of the interface can be expressed in terms of a traction–separation law relating the displacement jumps between adjacent plies of the interface with the traction vectors acting on it. For instance, Figure 10.5 shows a sketch of an

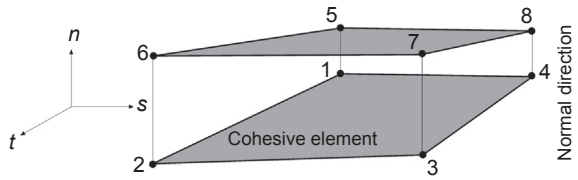

Figure 10.5 Interface element notation.

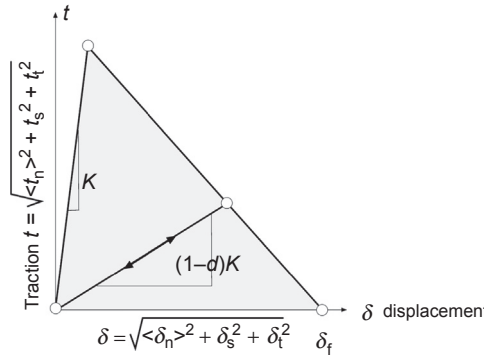

Figure 10.6 Constitutive equation for the cohesive crack under mixed-mode loading.

eight-node standard cohesive element. In the absence of damage, the interface elements are linear elastic with an initial stiffness given by K, where K can be treated as a numerical parameter that should be large enough to ensure the displacement continuity at the interface, avoiding distortions of the stress fields in the absence of damage (Figure 10.6). The traction vector is given by $\overrightarrow{t} = t_n \overrightarrow{e}_n + t_s \overrightarrow{e}_s + t_t \overrightarrow{e}_t$ being the traction components $t_n = K\delta_n$, $t_s = K\delta_s$ and $t_t = K\delta_t$, and $\overrightarrow{\delta} = \delta_n \overrightarrow{e}_n + \delta_s \overrightarrow{e}_s + \delta_t \overrightarrow{e}_t$ as the respective conjugate displacement jump at the interface. The onset of damage occurs when the traction vector acting on the interface reaches the interface strength dictated, for instance, by a quadratic interaction stress criterion that could read as

$$\left(\frac{\langle t_n \rangle}{N}\right)^2 + \left(\frac{t_s}{S_S}\right)^2 + \left(\frac{t_t}{S_T}\right)^2 = 1 \tag{10.13}$$

where N, S_S and S_T stand for the interface strength in tension and shear in the s and t directions, respectively, and $<>$ stands for the Macaulay brackets. As the interply is a matrix-rich region, the matrix strength in tension and shear are appropriate lower bounds for these parameters, although corresponding ply normal and shear strengths can be used in the absence of more specific data. Therefore, $N \approx Y_T$ and $S_S = S_T \approx S_L$.

After the onset of damage, the stress transmitted by the cohesive crack is reduced according to the damage parameter D, which evolves from 0 in the absence of damage to 1 when the physical interaction across the crack disappears. The actual reduction of the stress transferred through the cohesive crack is defined by the slope of the softening region in the $t-\delta$ constitutive equation, which depends on the interply strength and fracture toughness G_c (the area under the $t-\delta$ curve), as shown in Figure 10.6.

The interply toughness depends on mode mixity and can be determined according to the Benzeggagh–Kenane criterion (Benzeggagh & Kenane, 1996) as

$$G_c = G_{Ic} + (G_{IIc} - G_{Ic})\left\{\frac{G_s + G_t}{G_n + G_s + G_t}\right\}^{\eta} \tag{10.14}$$

where G_n, G_s and G_t are the work done by the tractions and their conjugate relative displacements in the normal, first and second shear directions, respectively. Interply fracture toughness is represented by G_{Ic} and G_{IIc} in modes I and II respectively (it was assumed again that $G_{IIc} = G_{IIIc}$), and η determines the increase in toughness with the amount of mode mixity. Standard mixed-mode fracture tests are used to obtain G_{Ic}, G_{IIc} and η. Except for the parameter η, the material properties required in order to define the cohesive model are common to those required in defining the intraply damage model. In order to define the parameter η, the mixed-mode bending test proposed by Crews and Reeder (1998) should be carried out − a standard value of $\eta = 1.75$ is commonly used.

The choice of the cohesive element thickness e_{coh} and stiffness K is also a common source of problems during explicit integration in finite element codes. Typically, the stable time increment Δt used in central differences explicit integration schemes is based on a conservative estimation using the Courant number. The stable time increment is element dependent, and the local estimator to be used for cohesive elements is

$$\Delta t = l_{ch}\sqrt{\frac{\overline{\rho}}{K}} \tag{10.15}$$

where l_{ch} is the in-plane characteristic length of the cohesive element and $\overline{\rho}$ the surface density. Therefore, the thinner the cohesive elements, the lower the stable time increment required for the integration of the motion equations, thereby increasing computational efforts. As a rule of thumb, choosing the cohesive element thickness as a small fraction of the ply thickness (for instance, $e_{coh} \approx 0.05 e_{ply}$) and estimating the penalty stiffness as $K \approx E_{resin}/e_{coh}$ leads to reasonable results in terms of accuracy and computing time. Mass scaling of the cohesive elements can also improve the computational efficiency, while accuracy is not affected by simply adding a small artificial mass to the cohesive element. Cohesive models also present a characteristic length proportional to the length of the fracture process zone, usually given by

$$l_{ch} = \gamma \frac{E_M G_M}{X_M^2} \tag{10.16}$$

where E_M, X_M and G_M are the material modulus, strength and fracture toughness, respectively, while γ a dimensionless parameter of the order of unity. In order to adequately capture the stress distribution within the fracture process zone, the cohesive element length should be adapted to this characteristic length. Cohesive surface modelling (Abaqus, 2014) offers capabilities similar to those of standard cohesive elements. In this case, the constitutive behaviour of the cohesive layer is lumped into a surface-to-surface interaction following the classical formulation of contact problems. This simulation strategy allows for definition of nonconformal meshes between adjacent plies, alleviating the discretization problem that arises when complex geometries and stacking sequence layups are used.

10.3 Use case 1: low-velocity impact due to drop weight

Finite element models were developed in Abaqus/Explicit to simulate several physical processes that occur during low-velocity impact on composite laminates. The emphasis was placed on the correct geometric representation of the impact problem, including loads, boundary conditions, material behaviour and contact conditions between the bodies. Impacts on specimens with the same ply layup, $[\pm 45/90/0/45/0_4/-45/0_2]_s$, were simulated with different impact energies, and the predictions were in good agreement with experimental results reported in Lopes, Seresta, Gürdal, Camanho, & Thuis (2009). The 4.368-mm-thick specimens included 24 AS4/8552 plies with a nominal individual thickness of 0.182 mm. Since some plies were clustered at 0°, the effective number of plies was only 15. VUMAT user subroutines were used to implement the CDM model that accounts for intraply damage, while cohesive interactions were used to address interply delamination.

10.3.1 Model definition

The geometry and boundary conditions described in the 'standard test method for measuring the damage resistance of a fibre-reinforced polymer matrix composite to a drop-weight impact event' of ASTM D7136 are shown in Figure 10.7. Composite panels of 150 × 100 mm^2 were fixed between a steel support and four rubber clamps. The support has a free area of 125 × 75 mm^2 in the centre, and the panel was placed on the support fixed by the four rubber clamps. In the simulations, the support was considered a rigid solid in contact with the panel. The rubber clamps were also rigid and in contact with the specimen, and each one transmitted a vertical force of 1 kN to the specimen. The impactor was modelled as a rigid body with a lumped mass equal to

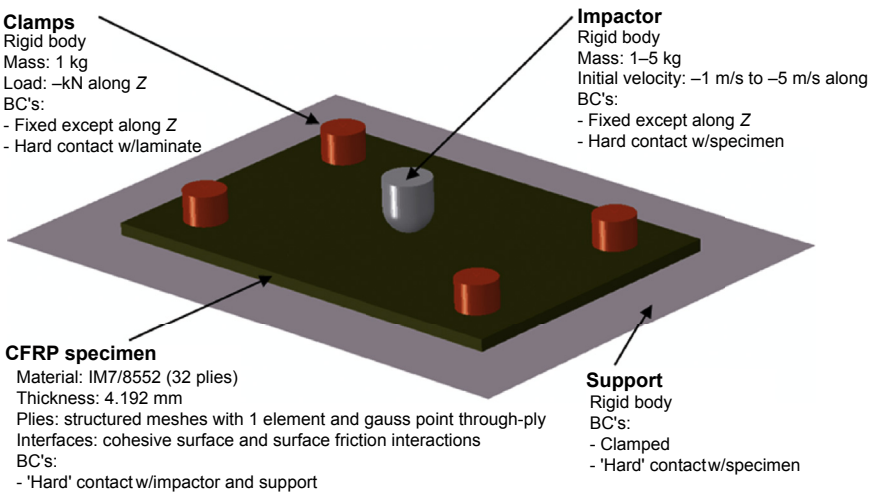

Figure 10.7 Virtual low-velocity impact test setup.

the experimental one. It has a sphere-shaped impact surface with a diameter of 16 mm. An initial velocity in the vertical direction is prescribed to the impactor, simulating the impact velocity measured during the tests.

The finite element model has four distinct parts: specimen, impactor, bottom support and rubber clamps. The impactor was modelled as a rigid analytical surface associated with the pointwise mass. The bottom support was a rigid body discretized with rigid elements. The composite specimen was discretized in two different zones kinematically tied together. Far away from the impact point, only the elastic behaviour is taken into account, by means of a single layer of continuum shell elements that represent the whole laminate. In the region around the impact point, each ply was independently modelled with one layer of solid 'C3D8R' elements. An enhanced-strain method was used to prevent hourglassing of the elements with reduced integration. The interfaces between each ply were modelled with a penalty contact algorithm coupled with cohesive surfaces to simulate delamination by means of the traction−displacement laws described above, and to prevent interpenetration of the delaminated surfaces (Abaqus, 2014).

The simulation of cracking and fracture by means of CDM models is mesh-dependent. There are two main sources of mesh dependency, mesh alignment and element size. Cracks tend to follow mesh lines and therefore random meshing may cause the incorrect prediction of crack propagation. In the case of matrix cracking, this may influence delamination patterns as well, since there is a strong interaction between these two failure modes, especially in low-velocity impact situations. In the present work, each ply was meshed independently, with mesh lines aligned with fibre orientations to facilitate propagation of matrix cracking following the fibre direction. This creates nonconformal ply meshes through the thickness of the laminate, an issue that is easily dealt with by means of the ply-to-ply contact algorithm coupled with cohesive surfaces.

The mesh regularization to minimize effects due to element size was carried out using the element characteristic length l_{ch} as a variable (Maimí et al., 2007a,b) (see Figure 10.8). In nonaligned meshes, l_{ch} is the typical distance across the element surface that favours the use of square surface elements. In material-aligned meshes, two independent characteristic lengths, $l_{ch}(1+, 1-)$ and $l_{ch}(2+, 2-, 6)$, can be devised

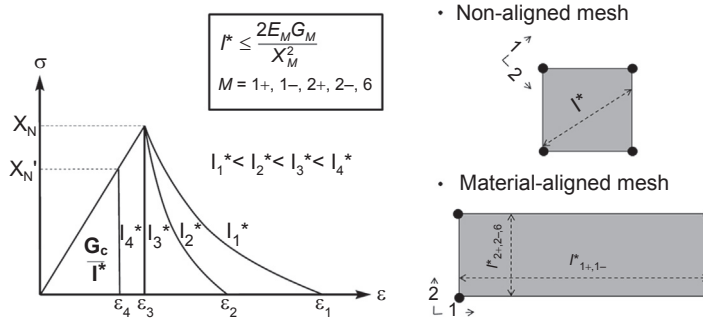

Figure 10.8 Mesh-regularization strategy.

and used with fibre- and matrix-dominated damage modes, respectively. In this work, $l_{ch}(1+, 1-) = 0.6$ mm and $l_{ch}(2+, 2-, 6) = 0.3$ mm.

Element erosion is important in impact analysis in order to prevent high element distortions that reduce the stable time increment during explicit integration, and allow for a good description of the kinematics of the impact process, from crack opening and fibre entanglement to specimen perforation. In the current analyses, finite elements were eroded when the fibre damage variable d_{1+} reached a value of 0.999, or the transverse tensile damage variable d_{2+} reached a value of 0.99.

Contact between the impactor and laminate was modelled by the 'general contact algorithm' in Abaqus/Explicit, which uses a penalty enforcement contact method. This contact formulation is also applied between the different composite layers when the cohesive surfaces become fully damaged. Friction is introduced between all the contacting surfaces with a friction coefficient μ. The friction coefficient between surfaces depends on the materials in contact and on surface quality. Several authors have studied the friction between metals and composite laminates, as well as between delaminated surfaces (Sung & Suh, 1979; Schön, 2000). In the last case, the friction coefficient was a function of the angle between fibres in adjacent plies, which can be as low as 0.2 for 0°/0° interplies and as high as 0.8 for 90°/90° interplies. In this work, an average friction coefficient of 0.5 was applied between ply surfaces, independent of the interply angle. A value of $\mu = 0.3$ was used for metal−laminate contact (impactor−laminate and laminate−supports).

The number of elements in the finite element meshes was over one million. On average, each run takes 48 h to complete using a cluster of 40 Intel Ivy Bridge 2.6 GHz CPUs. Such a long calculation time is a direct result of the small stable time increment required by Abaqus/Explicit to handle elements of 0.6 mm by 0.3 mm in size. Mass scaling was applied to the model while keeping the total mass increase under 2%.

10.3.2 Simulation results

Figure 10.9 shows the specimen at maximum impactor penetration for four impact energies. It can be clearly seen that damage increases rapidly with the impact energy of 19.7−50.8 J. The only damage found at 19.7 J was fibre splitting in the centre of the specimen at the rear surface. This phenomenon is due to the transverse tension of the 45° ply. Fibre splitting was extended towards the edges of the specimens at 29.7 and 39.4 J. At these energies, damage becomes visible at the inner plies in the form of matrix cracks and fibre breakage. The impactor partially perforated the specimen at 50.8 J, as indicated by the large penetration of the indentor into the specimen as well as the damage pattern.

The experimental and simulated force versus displacement curves are plotted in Figure 10.10 for tests carried out with 19.7, 29.7, 39.4 and 50.8 J. The oscillations in the experimental load versus displacement curves were due to dynamic coupling between the specimen and the metallic supports that was not replicated by the explicit finite element simulations, inevitably including unrealistic viscous-dissipation mechanisms that damped the dynamic response. However, the agreement between

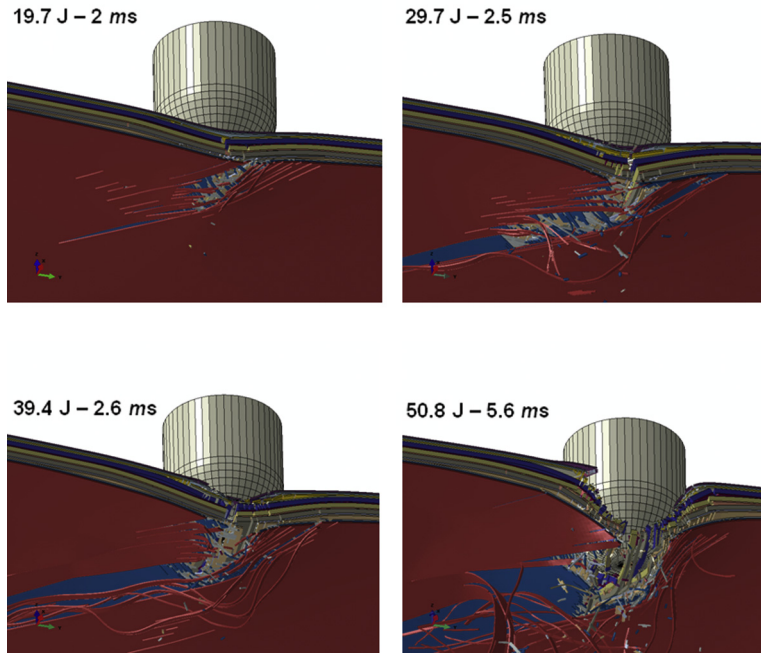

Figure 10.9 Deformation and damage mechanisms at maximum impactor penetration for four impact energies.

experiments and simulations is very good. The maximum impact force was well predicted, with the exception of the tests with the largest impact energies, in which numerical simulations overestimated the maximum load.

Regardless of the dynamic oscillations, the initial stiffness of the specimens is generally well predicted by the numerical model. The maximum impactor displacements were also in good agreement with the experimental results except for the impact at 50.8 J. The specimen was close to perforation with this impact energy. A precise result is more difficult to obtain under these circumstances, and the predicted unloading curves differed from the experimental ones. There was a permanent indentation in the specimen after impact due to intraply frictional resistance, fibre entanglement and matrix plastic behaviour under shear deformation. However, permanent indentation was not captured by the accelerometer at the impactor tup because there was a loss of impactor−specimen contact, and the force measured by the load cell was reduced to zero before the composite specimen sprang back. The impact simulations took into account intraply frictional resistance and fibre entanglement. Furthermore, they were highly damped, and there was less loss of contact between impactor and specimen before total spring-back. Therefore, the unloading curves tend to better simulate the permanent indentation values, as shown in Figure 10.10. The experimental and numerical simulations of permanent indentation in the composite specimen impacted with 29.7 J are shown in Figure 10.11.

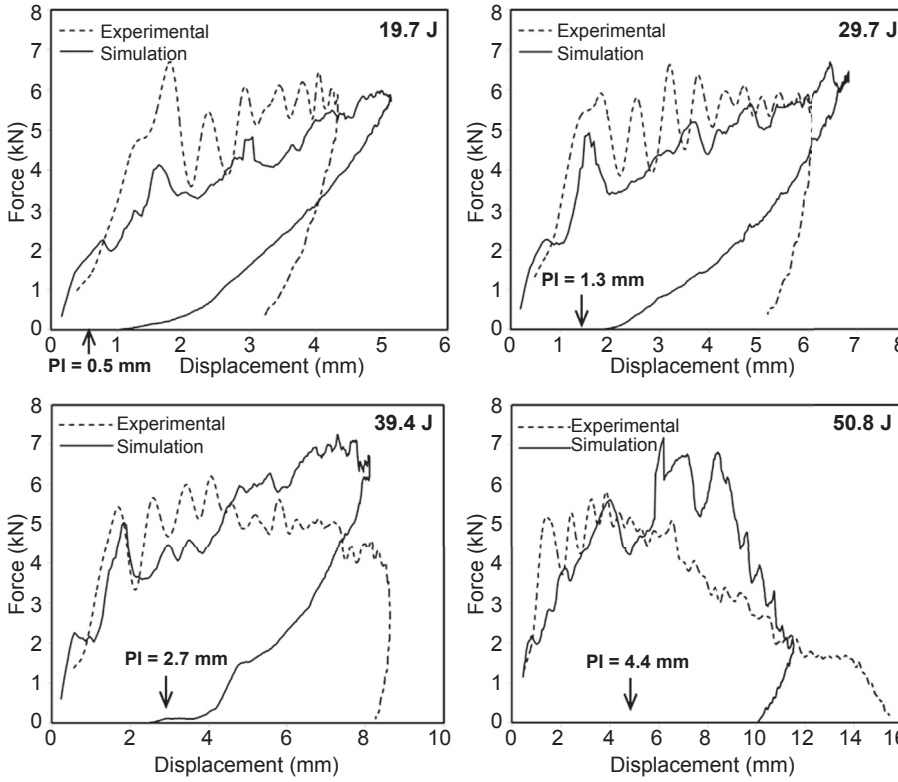

Figure 10.10 Load versus displacement curves of low-velocity impact tests at different impact energies (PI = permanent indentation − experimental).

The predicted damage footprint is roughly the superimposition of delaminations at all interfaces, since the other damage modes are concentrated in narrow regions around the impact point. The predictions for the damage footprint are compared in Figure 10.12 with the actual damage footprint measured by C-scan (Lopes et al., 2009). Considering the limitations of the ultrasonic C-scan technique, the simulated projected damage area in each configuration agreed reasonably well with the experimental results for all impact energies, especially for the 19.7 J case. The models were relatively accurate in the identification of delamination of the rear ply (45°) triggered by face-ply matrix cracking and fibre splitting.

Both the experimental and numerical results show that the damage footprint did not increase much for impact energies above 30 J. This was because fibre breakage replaced delamination as the main damage mode, and the impactor began to penetrate the specimen, as shown in Figure 10.9, without further delamination.

Matrix cracking and fibre breakage appeared to be the first damage phenomena to occur in composite laminates undergoing impact loads, especially around the impact point. Above an impact energy threshold, which for the present configuration was

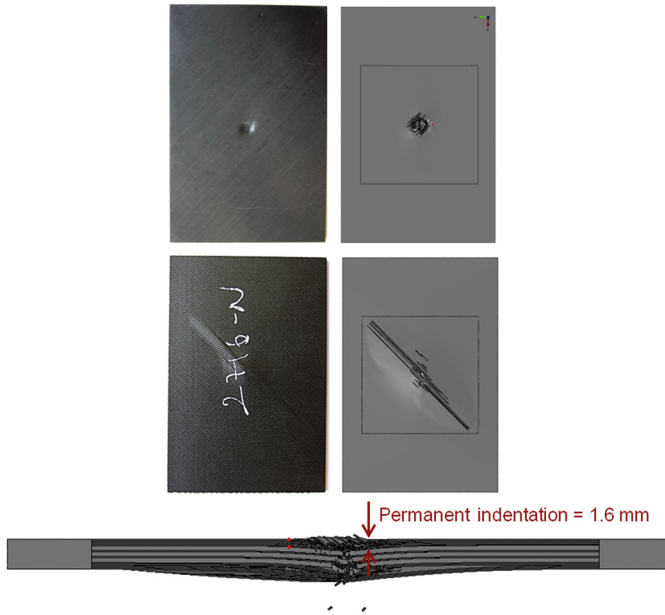

Figure 10.11 Experimental and simulated permanent indentation on the 29.7 J impact specimen due to intraply friction and fibre entanglement.

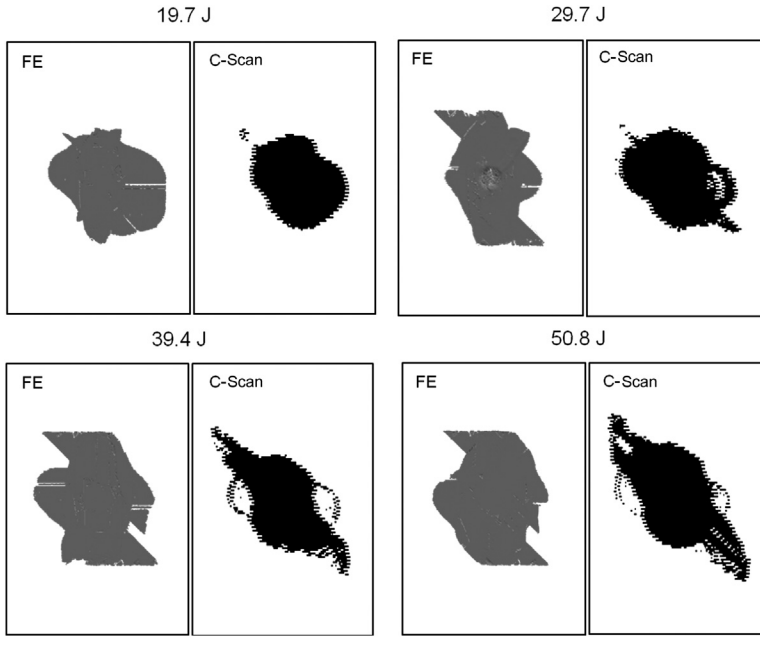

Figure 10.12 Simulated impact damage contours compared with C-scan results.

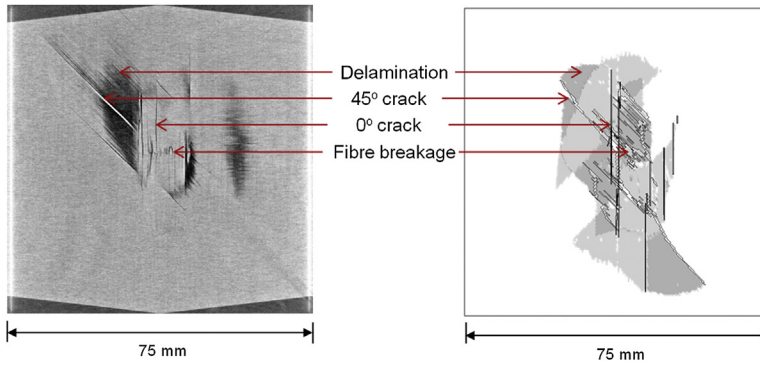

Figure 10.13 X-ray tomography section of the composite specimen impacted at 19.7 J compared with simulation results. The X-ray tomography section shows a planar section of the impacted specimen at 3.6 mm from the impact face. Parts of plies 19 (0°) and 20 (45°) are visible, as is part of their interface. The simulation shows the corresponding plies and their interface.

determined to be in the range of 5−10 J, matrix cracks propagated along with delaminations. Fibre breakage also played a role in the damage process above an even higher energy level. These three damage modes are depicted in Figure 10.13, which shows a section of the composite specimen impacted with 19.7 J obtained by means X-ray tomography. The section of the impacted specimen was obtained at 3.6 mm from the impact face. Due to the specimen indentation, parts of plies 19 (0°) and 20 (45°) are visible in this section as well as a part of their interface. The simulation results corresponding to these two plies are also shown in this figure, and they are in good correlation with the experimental results.

Both Figures 10.9 and 10.10 show that matrix cracks parallel to the fibre directions were accurately predicted by the model, in agreement with experimental data. This was achieved because the mesh in each ply was aligned in the fibre direction. The interaction between matrix cracks and delamination is also visible in these figures: delaminations in many plies were driven or bounded by matrix cracks. In some plies, matrix cracks induced the 'jump' of the delaminations from one interface to another (e.g. 9/10 to 10/11, and 14/15 to 15/16).

10.4 Use case 2: high-velocity impact

Finite element models were also generated in Abaqus/Explicit to simulate the high-velocity impact of a steel sphere on an angle-ply composite laminate. The impact was normal to the laminate plane. The stacking sequence of the laminate in this case was $[0, \pm 45, 0, 90]_{4s}$ and was manufactured using T800S/M21 prepreg sheets. The total laminate thickness was 5.2 mm, and the cured ply thickness was 130 μm. VUMAT user subroutines were used to implement CDM models to simulate intraply damage, while cohesive elements with conformal meshes were used to address interply

delamination. An additional damage-activation function for out-of-plane loads based on out-of-plane shearing was introduced in the VUMAT user subroutine.

10.4.1 Experimental results and model definition

Coupons of 100 × 100 mm^2 were impacted with steel spheres of 5.5 mm diameter using a SABRE gas gun. The impact-velocity range was set to 350−550 m/s to adequately capture the ballistic limit (≈400 m/s). A Phantom V12 high-speed video camera was used to obtain the initial and residual velocities of the projectile and to determine the energy-absorption capacity of the laminate. The results of the impacts are summarized in Figure 10.14, where the residual velocity is shown against the initial impact velocity. In the simulations, the steel sphere is assumed to behave as a rigid solid, as no evidence of plastic deformation was observed after the impact tests. An initial velocity in the through-the-thickness direction of the composite plate is applied to the steel sphere within the experimental range. In addition, the edges of the laminate were simply supported, although the influence of the boundary conditions was negligible due to the high velocity of the impacts in relation to the time-of-flight of the elastic waves in reaching the boundaries.

The failure mechanisms of the impacted specimens were also studied by X-ray tomography. Figure 10.15 shows the tomogram reconstructions of one of the specimens impacted at 522 m/s, where the two main damage mechanisms, intraply and interply, are clearly identified. The high stresses arising at the impact point produced significant out-of-plane crushing and shear deformations, while evidence of fibre splitting at

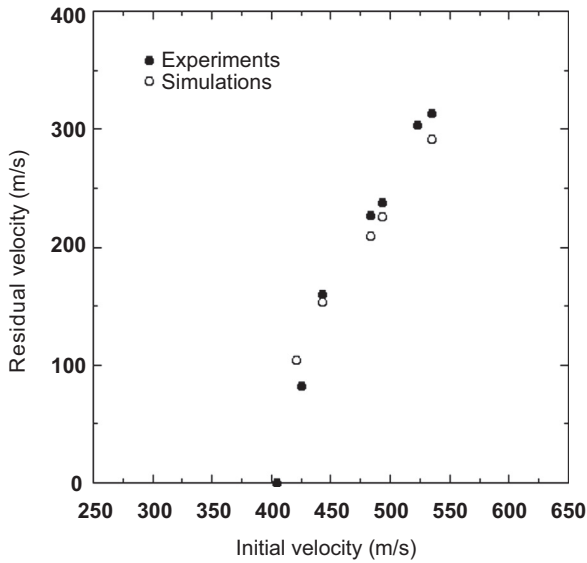

Figure 10.14 Ballistic curve and numerical predictions for a 5.5-mm-diameter steel sphere impacting T800S/M21 composite laminate.

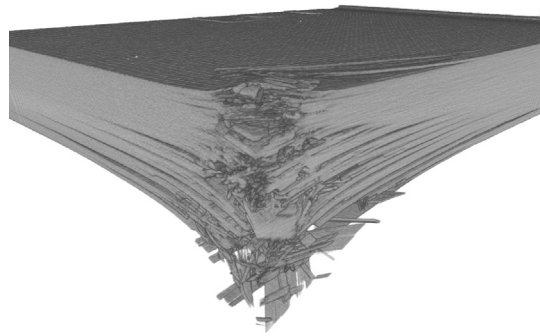

Figure 10.15 X-ray tomography reconstruction of the specimen impacted at 522 m/s.

the rear surface due to local bending was also observed. Interply delaminations (Figure 10.17(a) were also generated by local shearing stresses at the impacted area. They were longer in the lower part of the specimen due to local bending of the remaining undamaged section, as seen in Figure 10.15. Very interestingly, the shape of the projected delaminated area was elliptical due to the laminate stacking sequence, which favoured the extension of the cracks in the 0° direction. This effect was found in all specimens that were impacted with different velocities.

The specimen was discretized with a conformal structured mesh made up of eight-node C3D8R hexahedral elements, with reduced integration using the enhanced-strain method to minimize the effect of hourglassing. The mesh was aligned with the edges of the laminate irrespective of ply orientation. COH3D8 cohesive elements were inserted at the interface between adjacent plies using a conformal mesh. Damage was localized around the impact zone, and the influence of mesh orientation on the propagation of damage was of less importance than in the low-velocity impact case. The thickness of the cohesive layer (representative of the matrix-rich region between adjacent plies) was set to 8.75 μm, a small fraction of the total ply thickness (130 μm). This was a compromise between the accuracy of the stress prediction and the excessive penalty introduced in the stable time increment during the explicit integration. Mesh regularization was carried out using a common element characteristic length, independent of the failure mechanisms, of $l_{ch}(1+, 1-, 2+, 2-, 6) = 1.0$ mm around the impact area. The element size increased towards the boundaries of the plate where the material behaviour was elastic.

Contact between the steel sphere and laminate specimen was modelled with the general contact algorithm in Abaqus/Explicit as in the previous case. Cohesive elements were removed after the corresponding damage variable reached $D = 0.99$. A Coulomb interaction between plies was introduced afterwards with a friction coefficient of $\mu = 0.3$ to model ply sliding after delamination. This element-removal mechanism also allowed for simulation of steel sphere penetration into the laminate. The use of cohesive elements with finite thickness between adjacent plies (in opposition to cohesive surfaces) introduced additional dynamic wave effects when they came into contact after cohesive elements were removed. These effects were proven to be negligible for the general penetration dynamics problem, given the small thickness of the

cohesive elements used. A total of ≈2,000,000 elements were used for the complete discretization of the specimens. Each simulation spent ≈2 days in a cluster of 40 Intel Ivy Bridge 2.6 GHz CPUs.

10.4.2 Simulation results

One-fourth of the deformed laminate perpendicular to the composite coupon is plotted in Figure 10.16 at 15 and 75 μs after impact, in combination with the fibre and matrix damage variables d_1 and d_2, respectively, for the case with initial velocity of 421 m/s. The impact velocity was above the ballistic limit, and therefore the laminate was fully perforated. The simulations showed that the two main damage mechanisms appeared shortly after the impact, namely out-of-plane shearing and crushing dictated by the high stresses arising at contact with the impactor sphere, and fibre tensile splitting located at the lower part of the specimen due to localized plate bending, as shown in Figure 10.16(b). Both damage mechanisms, matrix cracking and fibre breakage, were concentrated at the impact area, and only delamination extended out of bounds of the projected area of the steel sphere. The aforementioned bending effects were favoured by ply delamination that increased the local compliance of the plate around this area once the plies were fully debonded. The extension of the interply delaminations (as indicated by the interply damage parameter D) is shown in Figure 10.17(c), in which the contours of all delamination surfaces were superposed and compared with the X-ray tomography inspections of Figure 10.17(a). The average delamination area projection was adequately captured by the model not only in extension but also in the elliptical shape, which was slightly elongated in the 0°direction favoured by the $[0, \pm 45, 0, 90]_{4s}$ stacking sequence.

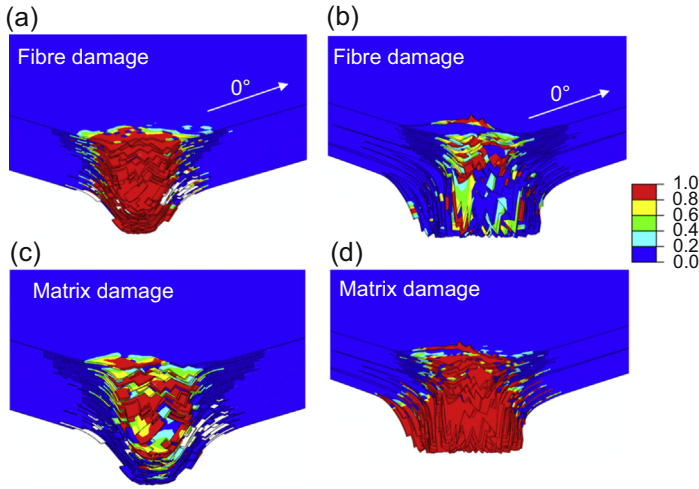

Figure 10.16 Simulated impact at 421 m/s. Fibre damage d_1 at (a) $t = 15$ μs and (b) $t = 75$ μs. Matrix damage d_2 at (c) $t = 15$ μs and (d) $t = 75$ μs.

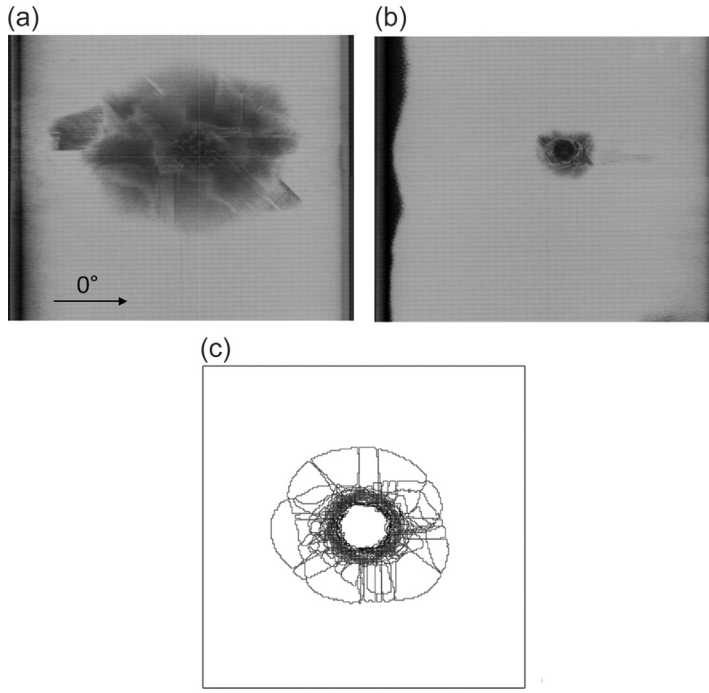

Figure 10.17 X-ray tomography—projected delaminated areas: (a) lower half of the laminate and (b) upper half of the laminate. Simulation-projected delaminated area (c). Impact velocity 522 m/s.

The model was also able to predict the increasing number of ply delaminations in the lower half of the laminate shown in Figure 10.17(a) and (b), and Figure 10.15. Local bending effects favour these phenomena once the contact loads transmitted by the impactor are redistributed over a wider volume in the material (cone-like shape). At the beginning of the impact, delaminations were controlled by shear stresses, and propagation occurred essentially under mode II. However, once the delaminations exceeded the area directly affected by the contact stresses, propagation was mainly mode I driven and controlled by the membrane stresses in the fully debonded plies of the lower part of the laminate. The ballistic curve was computed with the model and compared with the experimental results, and was able to capture the ballistic limit of the material as well as the residual energy after in the high-velocity regime (Figure 10.14).

10.5 Conclusions and future trends

Computational mesomechanics is an attractive and powerful tool for determining the mechanical behaviour of angle-ply composite laminates by means of models that contain information about physical deformation and damage mechanisms. This physical enrichment allowed for establishment of the relationships among the laminate

structural unit, laminate ply, and final composite laminate. Nevertheless, computational mesomechanics requires continuous improvement in order to enhance the accuracy level, computing time and robustness of the method. The development of multiscale-based computational mechanics, where material input properties (elastic, strength and toughness) are obtained by means of the simulation and homogenization is carried out at a lower level (for instance, by means of computational micromechanics, LLorca et al., 2011) is envisaged for the near future in order to attain the specific goal of the reduction of experimental testing campaigns by means of virtual simulations. However, there are still specific areas for significant improvement in CDM, especially those related to mesh-dependency problems (mesh size, bias and direction) that limit the application field of this discipline. In the same direction as the development of multiscale models, X-FEM models have emerged that represent mesh-independent embedded cracks with minimal mesh modifications, allowing for capture of the effect of the microstructure on the intraply transverse-to-fibre failure of a unidirectional fibre−reinforced composite material. By using combined CDM models for fibre-dominated failure modes with X-FEM for matrix cracking damage, interactions among failure mechanisms can be modelled so that these models provide results consistent with experimental findings (Iarve, 2003; van der Meer & Sluys, 2009).

Acknowledgements

This investigation was supported by the Ministerio de Economía y Competitividad of Spain through the grant MAT2012-37552, Spanish Ministry of Education grant FPU12/02087 and Airbus Spain and Centro para el Desarrollo Tecnologico Industrial CDTI through TARGET CENIT Programme 2010. In addition, the authors want to acknowledge the support of Dr Francisco Gálvez and Dr Federico Sket for some of the experimental results shown in this investigation.

References

Abaqus, Inc. (2014). *Abaqus version 6.13 user's manual*. RI, USA: Pawtucket.

Abrate, S. (1998). *Impact on composite structures*. Cambridge, England: Cambridge University Press.

Bažant, Z. P., & Oh, B. H. (1983). Crack band theory for fracture of concrete. *Materials and Structures, 16*, 155−157. RILEM Paris.

Benzeggagh, M. L., & Kenane, M. (1996). Measurement of mixed-mode delamination fracture toughness of unidirectional glass/epoxy composites with mixed-mode bending apparatus. *Composite Science and Technology, 56*, 439.

Camanho, P. P., & Dávila, C. G. (2002). Mixed-mode decohesion finite elements for the simulation of delamination in composite materials. *NASA/TM, 2002*(211737), 1−37.

Canal, L. P., González, C., Segurado, J., & LLorca, J. (2012). Intraply fracture of fibre-reinforced composites: microscopic mechanisms and modeling. *Composite Science and Technology, 72*, 1223−1232.

Cox, B., & Yang, Q. (2006). In quest of virtual tests for structural composites. *Science, 314*, 1102.

Crews, J. H., & Reeder, J. R. (1998). *A mixed-mode bending apparatus for delamination testing*. Tech. rep. Hampton, VA: NASA, Langley Research Center. NASA/TM-100662

Dávila, C. G., Camanho, P. P., & Rose, C. A. (2005). Failure criteria for FRP laminates. *Journal of Composite Materials, 39*, 323.

González, C., & LLorca, J. (2007). Mechanical behavior of unidirectional fiber-reinforced polymers under transverse compression: microscopic mechanisms and modelling. *Composite Science and Technology, 67*, 2795−2806.

Iarve, E. V. (2003). Mesh independent modelling of cracks by using higher order shape functions. *International Journal for Numerical Methods in Engineering, 56*, 869−882.

Kachanov, L. (1986). *Introduction to continuum damage mechanics*. Springer.

Kaddour, A. S., Hinton, M. J., & Soden, P. D. (2004). A comparison of the predictive capabilities of current failure theories for composite laminates: additional contributions. *Composite Science and Technology, 64*, 449.

Lemaitre, J. (1996). *A course on damage mechanics*. Springer.

LLorca, J., González, C., Molina Aldareguía, J. M., & Lopes, C. S. (2013). Multiscale modeling of composites: toward virtual testing … and beyond. *JOM, 65*, 215−225.

LLorca, J., González, C., Molina-Aldareguía, J. M., Segurado, J., Seltzer, R., Sket, F., et al. (2011). Multiscale modeling of composite materials: a roadmap towards virtual testing. *Advanced Materials, 23*, 5130−5147.

Lopes, C. S., Seresta, O., Gürdal, Z., Camanho, P. P., & Thuis, B. (2009). Impact behaviour of dispersed stacking sequence laminates. Part I: experiments. *Composites Science and Technology, 69*, 926−936.

Maimí, P., Camanho, P. P., Mayugo, J. A., & Dávila, C. G. (2007a). A continuum damage model for composite laminates - Part I: constitutive model. *Mechanics of Materials, 39*, 897−908.

Maimí, P., Camanho, P. P., Mayugo, J. A., & Dávila, C. G. (2007b). A continuum damage model for composite laminates - Part II: computational implementation and validation. *Mechanics of Materials, 39*, 909−919.

Martin, R., Elms, T., & Bowron, S. (1998). Characterization of mode II delamination using the 4ENF. In *Proceedings of the 4th european conference on composites: Testing and standardization, Lisbon, Portugal*.

Matzenmiller, A., Lubliner, J., & Taylor, R. L. (1995). A constitutive model for anisotropic damage in fibre-composites. *Mechanics of Materials, 20*, 125.

MIL-HDBK-17-1F. (2002). Department of defense handbook, composite materials handbook. In *Polymer matrix composites, guidelines for characterization of structural materials* (Vol. 1).

Pinho, S. T., Dávila, C. G., Camanho, P. P., Iannucci, L., & Robinson, P. (2005). *Failure models and criteria for FRP under in-plane or three-dimensional stress states including shear non-linearity*. Tech. rep. Hampton, VA: NASA, Langley Research Center. NASA/TM-2005−213530.

Pinho, S. T., Iannucci, L., & Robinson, P. (2006). Physically-based failure models and criteria for laminated fibre-reinforced composites with emphasis on fibre kinking: Part I: development. *Composites Part A - Applied Science and Manufacturing, 37*, 63−73.

Pinho, S. T., Robinson, P., & Iannucci, L. (2006). Fracture toughness of the tensile and compressive fibre failure modes in laminated composites. *Composites Science and Technology, 66*, 2069−2079.

Puck, A., & Schurmann, H. (2002). Failure analysis of FRP laminates by means of physically based phenomenological models. *Composites Science and Technology, 62*, 1633−1662.

Schön, J. (2000). Coefficient of friction of composite delamination surfaces. *Wear, 237*, 77−89.

Sung, N., & Suh, N. (1979). Effect of fiber orientation on friction and wear of fiber reinforced polymeric composites. *Wear, 53*, 129−141.

Turón, A., Camanho, P. P., Costa, J., & Dávila, C. G. (2006). A damage model for the simulation of delamination in advanced composites under variable-mode loading. *Mechanics of Materials, 38*, 1072−1089.

van der Meer, F. P., & Sluys, L. J. (2009). A phantom node formulation with mixed mode cohesive law for splitting in laminates. *International Journal of Fracture, 158*, 107−124.

Mixed-mode fatigue of bonded joints in composites: experiments and modelling

11

M. Quaresimin[1], *P.A. Carraro*[1], *G. Meneghetti*[2], *M. Ricotta*[2]
[1]University of Padova, Vicenza, Italy; [2]University of Padova, Padova, Italy

11.1 Introduction

Structural components made of composite materials often require joining different parts by means of bonded connections. As a consequence, given the increasing use of composite structures in many fields, reliable criteria describing the static and fatigue behaviour of bonded joints are highly desirable in the industrial environment to make the design process safer and cheaper.

Of particular interest is the fatigue behaviour, which has been found to be divided in a nucleation and a propagation phase, both for joints in composites and in metallic materials (Johnson & Mall, 1986; Potter, Guild, Harvey, Wisnom, & Adams, 2001; Quaresimin & Ricotta, 2006a,b). One or more macrocracks typically nucleate from critical points such as edges and corners, and then they propagate until they reach a critical length for the unstable growth. A model was proposed by the authors to estimate the fatigue life of bonded joints, by treating separately the initiation and the propagation phases, on the basis of the nucleation of a small technical crack of 0.3 mm (Meneghetti, Quaresimin, & Ricotta, 2010; Quaresimin & Ricotta, 2006b). The life spent for crack propagation was described by means of a Paris-like power law relating the strain energy release rate (SERR or G) to the crack growth rate (CGR). It was also pointed out that, for the single lap geometry studied in those papers, the propagation occurred in mixed-mode I + II conditions and that the ratio between the mode I and the mode II components was not constant, because it is a function of the crack length. Mode mixity changes during crack propagation are likely to occur also in real structures; therefore, because fatigue resistance to the crack propagation in bonded joints strongly depends on the loading mode, this phenomenon has to be taken into account in the design process.

Some examples of the fracture toughness dependence on the loading mode, relevant to the static case, can be found in Ducept, Davies, and Gamby (2000), de Moura, Oliveira, Morais, and Dourado (2011) and Wang (1997). Concerning the fatigue behaviour, in Azari, Papini, Schroeder, and Spelt (2010), Cheuk, Tong, Wang, Baker, & Chalkley (2002) and Xu, Crocombe, and Smith (1995) it is shown that different Paris-like curves relating the SERR to the CGR describe the fatigue crack propagation under different mixed-mode conditions.

Structural Integrity and Durability of Advanced Composites. http://dx.doi.org/10.1016/B978-0-08-100137-0.00011-0

For common bonded joint geometries, some attempts at describing the crack propagation phenomenon by means of different forms of the Paris-like law can be found in the literature, leading sometimes to contradictory results.

Curley, Hadavinia, Kinloch, and Taylor (2000) tried to predict the life spent for crack propagation in bonded single lap aluminium joints by using the total SERR as the driving force in the Paris-like equation, whose coefficients were evaluated considering a pure mode I double cantilever beam (DCB) test. This approach neglects the influence of the mode mixity on the fatigue behaviour, resulting in a conservative prediction of the fatigue life.

Abdel Wahab, Ashcroft, Crocombe, and Smith (2002) reanalysed the data from Curley et al. (2000) using only the mode I SERR as the propagation driving force in the Paris equation (rather than both mode I and mode II contributions) and were able to obtain much better life predictions. Eventually, they proposed to account also for mode II, by considering the CGR under mixed-mode conditions as the sum of the contributions evaluated separately, that is, calculated by means of the Paris-like equations obtained from pure mode I and II tests. However, this criterion was not validated because of the lack of information about the coefficients of the Paris-like law for pure mode II.

Kinloch and Osiyemi (1993) studied the propagation life of composite single lap joints by using the analytically derived mode I component of the SERR and a Paris-like law obtained from a pure mode I DCB test. Similar to Abdel Wahab et al. (2002), they found a good correlation with experimental data, even if this approach does not account for the mode mixity, which varies during the crack propagation.

Cheuk et al. (2002) studied double lap composite/metal joints under a mode I/mode II ratio of 0.15, which means near the pure mode II condition. They first tried to make predictions of the CGR by using the total SERR as input driving force in a Paris-like law calibrated on pure mode II tests. This approach resulted in a much lower CGR than measured in the experiments. Then they defined an equivalent SERR, G_{eq}, in which the mode II contribution was weighted by means of the ratio between the static critical values of G_I and G_{II}, obtaining a better agreement. Another attempt to define an equivalent SERR accounting for the mode mixity condition was made by Quaresimin and Ricotta (2006c). In this case, the mode II component was multiplied by the ratio between G_{II} and the total SERR. This definition accounts for the mode mixity, but does not consider the dependence of the crack propagation resistance on the loading mode.

Moroni and Pirondi (2011) developed a procedure for simulating crack growth in bonded joints by means of a cohesive model implemented in a finite element code. The code required as input the cohesive law for the interface elements, the Paris-like equation, and its dependence on the mode mixity. The latter was modelled by means of three criteria: the equivalent SERR proposed by Quaresimin−Ricotta (2006c), the superposition of the mode I and II equations proposed by Abdel Wahab et al. (2002), and an approach proposed by Kenane and Benzeggagh (1997) for mixed-mode delamination in composite laminates. The latter approach describes the crack propagation by means of a Paris-like law expressed in terms of the total SERR, in which the coefficients depend on the mode mixity according to phenomenological laws. Satisfactory results were obtained adopting all three mentioned criteria.

After this brief review, it can be concluded that a well-established criterion for fatigue crack propagation in composite bonded joints is not available in the literature yet. In addition, an extensive experimental investigation to characterize crack growth in a wide range of mode mixities from mode I to mode II is also missing. As a consequence, at present, a considerable and expensive experimental effort is needed to obtain reliable design data for fatigue life estimation. A crack propagation criterion of general validity, which takes into account the influence of the mode mixity on the basis of the actual damage and propagation mechanisms, would be very useful in the scientific and industrial community.

In this direction, an important contribution to the definition of a damage-based criterion for the description of the static strength of scarf-bonded joints under mixed-mode loading was provided by Wang (1997). Wang underlined the existence of two different propagation modes, occurring near the pure mode I and mode II condition, respectively. According to the observation of the damage mechanisms, Wang proposed to use the mode I stress intensity factor only as the driving force near a pure mode I condition, and the principal strain evaluated at a generic point at the interface for mode II-dominated loading conditions. For the principal strain criterion, Wang obtained a simple analytical expression based on the interface fracture mechanics, including also a material constant describing the adhesive sensitivity to the hydrostatic pressure, which can be used indeed as a fitting parameter. However, according to the experimental evidence reported later in this chapter, a point-related criterion does not seem to address mode II propagation properly, because damage accumulates in a well-defined process zone in front of the crack tip. The concept of the process zone associated to bonded joints is not new in the literature. In fact, some researchers proposed to use stress criteria for predicting static failure in bonded joints based on the idea that a finite volume or a finite length of adhesive controls the crack initiation phenomenon (Clark & McGregor, 1993; Nguyen, Kweon, & Choi, 2009; Sheppard, Kelly, & Tong, 1998).

This chapter presents first the results of static and fatigue tests on composite bonded joints under pure mode I, pure mode II, and several mixed-mode conditions. The static experimental results are reported in terms of the total critical SERR (G_c) against the mode mixity. The fatigue crack growth data are interpolated with Paris-like curves relating the total SERR to the CGR. The propagation modes during fatigue tests have been analysed by means of an optical microscope, and they have been found to depend on the mixed-mode condition. The observed mechanisms were the basis to conceive a process zone- and damage-based mixed-mode propagation criterion for bondline cracks in bonded joints. Experimental results and the theoretical model are presented in Carraro, Meneghetti, Quaresimin, and Ricotta (2013a,b), respectively.

11.2 Materials and test equipment

Laminates with a stacking sequence $[0]_{12}$ were produced by hand lay-up of carbon/epoxy fabric tape CC206, T300 twill 2 × 2 carbon fabric/ET442 toughened epoxy matrix, from seal Texi-preg®, and cured in an autoclave, with a permanence for one

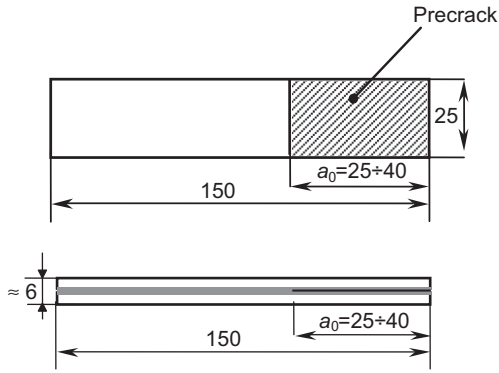

Figure 11.1 Specimen's geometry (units in millimetres).

hour at a temperature of 125 °C and a pressure of 7 bar. Then, two laminates were bonded with a 0.15 mm layer of the two-part epoxy adhesive 9323 B/A by 3M and cured in an oven at 65 °C for two hours. To keep a uniform adhesive thickness, glass spheres with a 0.15 mm diameter were used.

A 50 μm thick kapton film was inserted between the two adherends to obtain a precrack of length a_0. Specimens were eventually cut according to the typical geometry shown in Figure 11.1. The elastic properties of the materials are listed in Table 11.1, in which the subscripts L and T refer to the longitudinal and transverse directions, respectively.

Static and fatigue tests were carried out varying the mode mixity from pure mode I (DCB test) to pure mode II (end notch flexure (ENF) test), through mixed I + II mode (mixed-mode bending (MMB) tests). Equipment and reference procedures for these tests can be found in the recommendations ASTM-D 5528-01 (2001), ASTM-D 3115-97 (1997), prEN 6034 and ASTM-D 6671-01 (2001).

The mixed-mode condition was expressed by means of the following mode mixity parameter:

$$MM = \frac{G_{II}}{G_I + G_{II}} \tag{11.1}$$

Accordingly, the pure mode I (DCB) test is characterized by $MM = 0$, and the pure mode II (ENF) test is characterized by $MM = 1$. Four intermediate MM values

Table 11.1 Elastic properties of adhesive and adherends

Adherends	E_L (MPa)	E_T (MPa)	G_{LT} (MPa)	ν_{LT}
	58,080	58,080	3300	0.06
Adhesive	E (MPa)	ν		
	2879	0.37		

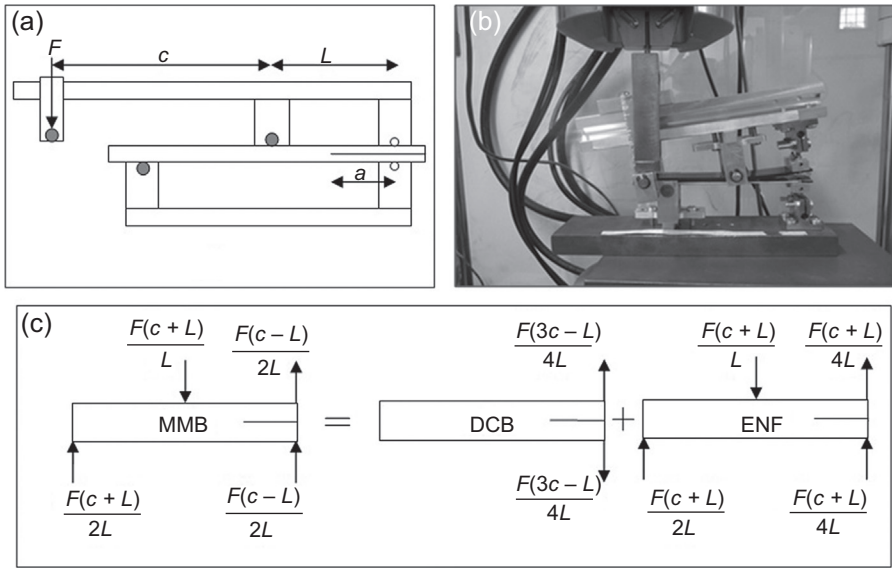

Figure 11.2 (a) Schematic representation, (b) picture of the MMB test equipment and (c) load condition for an MMB test.

($MM = 0.15, 0.36, 0.52, 0.75$) were investigated with MMB tests, by varying the lever arm length c (see Figure 11.2) and keeping L equal to 58.5 mm.

Tests were carried out on an MTS 858 servo-hydraulic machine equipped with a 1.5/15 kN load cell. The crack length was measured by means of a travelling optical microscope with a magnification of 40×. Fatigue tests were characterized by a nominal load ratio, defined as $R = F_{min}/F_{max}$, equal to 0.1, and an initial frequency of 8 Hz. Typically the frequency was decreased to 2 Hz in the final part of the tests because of the large displacements in the presence of long cracks.

11.3 Calculation of the strain energy release rate

As highlighted in the introduction, the results of static and fatigue tests are traditionally presented in terms of SERR. Because the mode mixity is an additional fundamental parameter to account for, the different contribution of mode I and II components in the total SERR ($G_{tot} = G_I + G_{II}$) need to be evaluated. An analytical formulation is proposed for the calculation of the mode I and II SERR components by ASTM-D 6671-01 (2001), which is valid for symmetrically cracked specimens, as in the case of interlaminar toughness characterization of composite laminates. This is not the case of bonded joints, in which the crack tip is usually at the adhesive−adherend interface and not in the mid-thickness of the adhesive layer, as shown later in the chapter. In fact, in the present case, the use of the formulation proposed in ASTM-D 6671-01 (2001) would lead to wrong estimations of both the total SERR and even worse

evaluations of the mode mixity, characterized by errors up to 80%. A formulation explicitly derived for bonded joints was proposed by Liu, Gibson, and Newaz (2002), suitable to account for the presence of the adhesive layer. The mode I and II components were obtained by differentiating the global compliance with respect to the crack length. Because this formulation was developed for joints with interface cracks, it is capable of estimating correctly the total SERR. However, the adopted global approach based on the compliance derivation is not very accurate in the evaluation of the mode mixity. Therefore, in this work, the SERR components were calculated by means of linear elastic FE analyses performed with ANSYS® code combined with the Virtual Crack Closure Technique (VCCT), which has been widely adopted in the literature (Ashcroft, Casas-Rodriguez, & Silberschmidt, 2008, 2010; Liu et al., 1995; Quaresimin & Ricotta, 2006c; Xu et al., 1995). This technique involves local nodal forces and displacements at the crack tip and represents a reliable procedure for the accurate estimation of the mode I and II SERR components, it being based on local quantities.

The VCCT requires that the elements close to the crack tip are of the same size Δa (see Figure 11.3). On the basis of a previous sensitivity analysis (Quaresimin & Ricotta, 2006c), the element size was fixed equal to 0.03 mm to balance the need for a sufficient number of elements through the adhesive thickness and a reasonable independence of the calculated SERR components on the mesh size. In fact, unreliable values of the mode I and II components will be obtained if the element size is too low. This is a consequence of the unrealistic oscillatory behaviour of stress and displacement fields in a region very close to the tip of an interface crack, as highlighted also by Sun and Jih (1987).

In this work, according to previous results (Quaresimin & Ricotta, 2006c) and to the experimental evidences shown later on, the crack was modelled at the

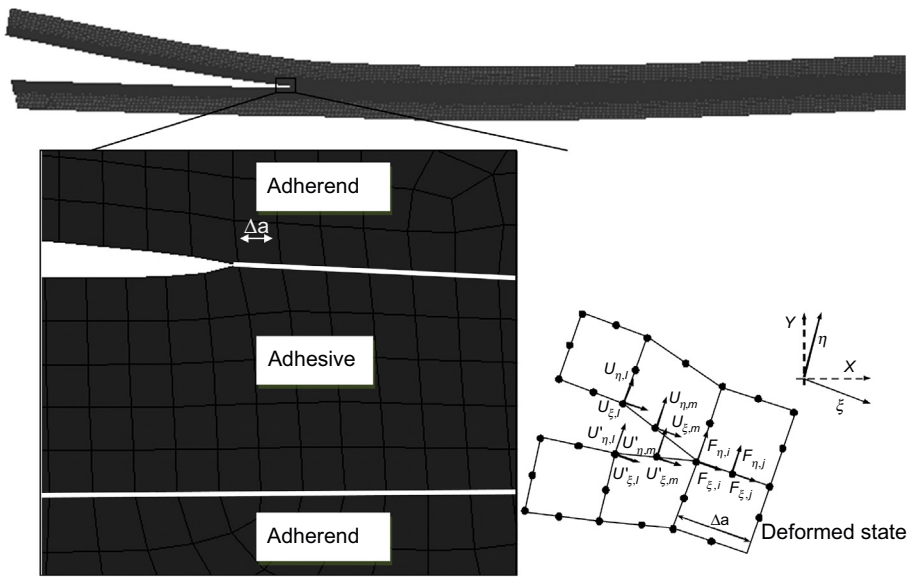

Figure 11.3 Deformed mesh around the crack tip for an MMB specimen.

adhesive−adherend interface. Eight-node isoparametric elements were used in the numerical models with a plane strain behaviour. According to the VCCT, Eqns (11.2a) and (11.2b) have been adopted to calculate G_{I} and G_{II}, in which the symbols are defined in Figure 11.3.

$$G_{\mathrm{I}} = -\frac{1}{2\Delta a}\left[F_{\eta,i}\left(U_{\eta,l} - U'_{\eta,l}\right) + F_{\eta,j}\left(U_{\eta,m} - U'_{\eta,m}\right)\right] \tag{11.2a}$$

$$G_{\mathrm{II}} = -\frac{1}{2\Delta a}\left[F_{\xi,i}\left(U_{\xi,l} - U'_{\xi,l}\right) + F_{\xi,j}\left(U_{\xi,m} - U'_{\xi,m}\right)\right] \tag{11.2b}$$

In the FE models of the MMB specimens, the loads were applied according to the schematic shown in Figure 11.2(c). The influence of the lever weight was also taken into account as proposed by ASTM-D 6671-01 (2001). Because the mode mixity slightly changed during propagation, the average value of the *MM* parameter was chosen as representative for each test. However, *MM* variations with the crack length were within the range ±5%, which can be considered negligible.

11.4 Static test results

Load and displacement were recorded during the static tests. For the calculation of the critical values of the SERR for crack initiation, the procedure recommended in ASTM-D 5528-01 (2001) has been adopted. Accordingly, the critical load was identified as the maximum load before the propagation or, alternatively, the load corresponding to the 5% increase of the compliance, if the latter occurred first. All static tests results are plotted in Figure 11.4, in terms of total SERR $G_{\mathrm{c}} = (G_{\mathrm{I}} + G_{\mathrm{II}})_{\mathrm{c}}$ versus the mode mixity, showing that pure mode II condition is far less critical than mode I, as usually found in literature (Ducept et al., 2000; Liu et al., 1995; Liu et al., 2002; de Moura et al., 2011; Wang, 1997). According to the present results, G_{IIc} is about three times higher than G_{Ic}.

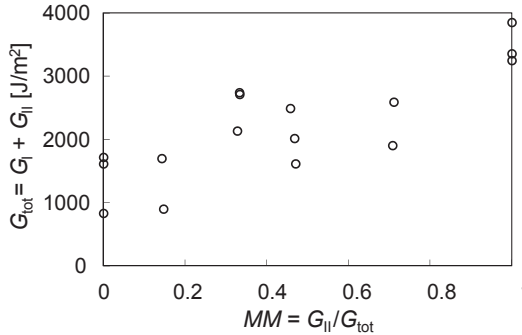

Figure 11.4 Total critical SERR versus mode mixity.

11.5 Damage evolution under cyclic loading

Fatigue tests were carried out by imposing the six *MM* values previously adopted for static tests. Different propagation and damage mechanisms were identified by varying the *MM*, and they are schematically summarized in Figure 11.5.

DCB specimens were characterized by a continuous crack propagation in the adhesive or at the adhesive−adherend interface, as illustrated in Figure 11.6.

For $MM = 0.15$ and 0.36, the damage evolution was more complex, and crack propagation was not continuous. Typically, at the beginning of the fatigue test, a crack propagated at the adhesive−adherend interface. After a certain number of cycles, independent and separated delaminations occurred beyond the main crack tip in the upper adherend, as shown in Figure 11.7. In such a condition, it was observed that the main crack did not propagate for thousands of cycles. Conversely, the delaminations propagated in the adherend and then often joined, thus creating a longer delamination, as shown in Figure 11.8. The further evolution of the damage in the same specimen is shown in Figure 11.9. It can be seen that the delamination propagated in the adherend, while the main crack, which indeed is still much shorter, propagated at the interface below the delamination itself.

Specimens tested at $MM = 0.52$ were not characterized by the nucleation of separated delaminations as in the previous cases, and the propagation occurred at the interface with some deviations in the upper adherend. However, it is worth noting

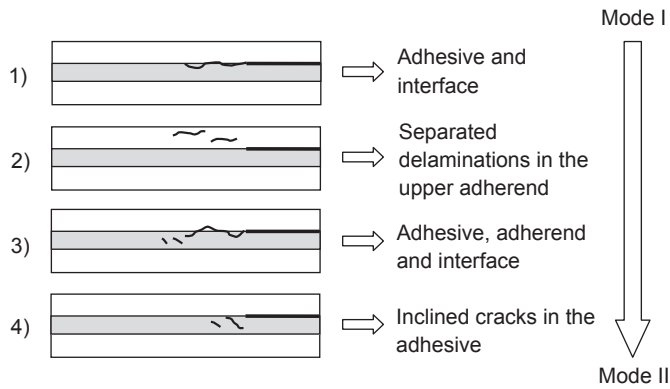

Figure 11.5 Crack location and propagation modes.

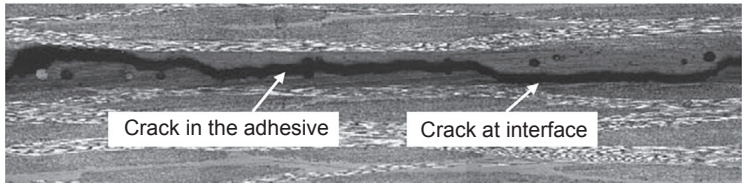

Figure 11.6 Typical crack propagation for a DCB specimen.

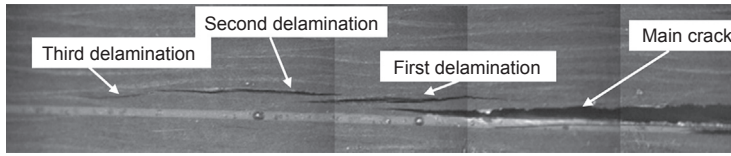

Figure 11.7 Delaminations, mode mixity = 0.15.

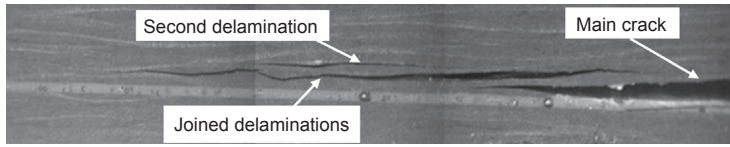

Figure 11.8 Joined delaminations, mode mixity = 0.15.

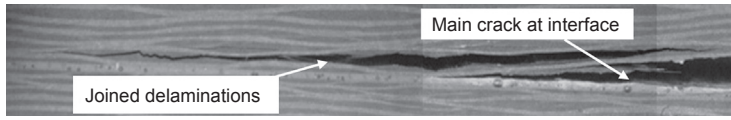

Figure 11.9 Joined delaminations and main crack interface propagation, mode mixity = 0.15.

that for $MM = 0.52$, some inclined microcracks started to nucleate in the adhesive layer in front of the main crack tip, as shown in Figure 11.10. This mechanism played an important role for mode mixity equal to or higher than 0.52. In fact, in the case of loading conditions near to the pure mode II ($MM = 0.75$), the initial damage mechanism consisted of the initiation of separated inclined microcracks in the adhesive layer, which were stopped after reaching the adhesive−adherend interface, as shown in Figure 11.11. After thousands of cycles, these cracks coalesced, thus creating a continuous crack in the adhesive, which sometimes deviated its path in the upper adherend, as shown in Figure 11.12.

In the case of pure mode II loading, the damage evolution always consisted of multiple initiations of inclined microcracks followed by their coalescence into a macrocrack and propagation through the adhesive layer. This behaviour of mode II-loaded bonded joints is consistent with the published literature (Blackman, Kinloch, & Paraschi, 2005; Leffler, Alfredsson, & Stigh, 2007; Liu et al., 2002).

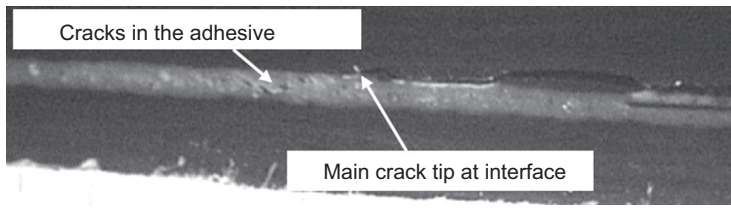

Figure 11.10 Typical crack propagation for mode mixity = 0.52.

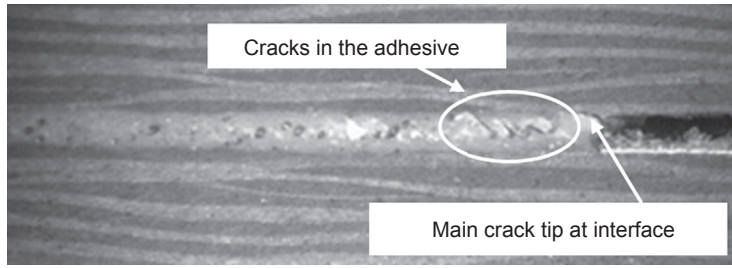

Figure 11.11 Inclined cracks in the adhesive for mode mixity = 0.75.

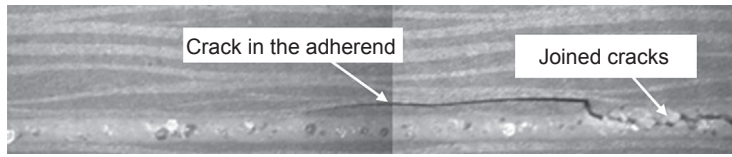

Figure 11.12 Joined inclined cracks and propagation in the adherend for mode mixity = 0.75.

During fatigue tests, the crack length a was measured and plotted against the number of cycles. In case of a noncontinuous crack propagation, as for instance for $MM = 0.15$ and 0.36, the crack length was considered to be the distance between the load application point and the tip of the farthest crack or delamination, as shown in Figure 11.13.

However, when the measured CGRs were relevant to delaminations growth (like in the case shown in Figure 11.13) and not to a bondline crack, the data were not considered in subsequent analyses (see comments on next Figure 11.16), because they are not characteristic of the adhesive−adherend interface (which the chapter is focused on), but rather of the fatigue behaviour of the adherend. Examples of crack propagation (a−N) curves are shown in Figure 11.14 for six specimens representative of mode I, mode II, and mixed=mode loadings. For easiness of representation, the number of cycles and the crack length are normalized with respect to the final number of cycles N_f and to the initial precrack length a_0, respectively. For the DCB test, the final number of cycles corresponds to the complete separation of the arms of the specimen. For $MM > 0$, N_f corresponds to the end of tests, occurring when the crack tip reached the position of the upper roller of the testing device (see Figure 11.2(a)), in correspondence of mid-span between the support rollers.

From Figure 11.14, it is clear that most of the propagation phase takes place in the final part of the tests, that is, from a number of cycles around 75% of the total life, this

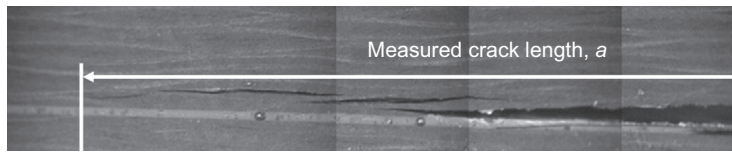

Figure 11.13 Criterion for crack length measurement in the case of separated delaminations.

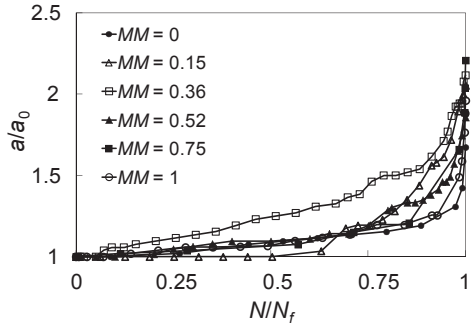

Figure 11.14 Normalized crack length versus normalized number of cycles.

being a typical behaviour for load-controlled fatigue tests. Concerning the curves for $MM = 0.15$ and 0.36, some independent delaminations started to appear at about 85% and 75% of the fatigue life, respectively. Then they propagated with a higher rate with respect to the main crack at the interface, leading to the typical configuration shown previously in Figure 11.9. The curve obtained at $MM = 0.52$ shows a crack acceleration around $N/N_f = 0.75$. This is due to the fact that the main crack deviated from the interface to the upper adherend because the tip met a resin-rich region of the laminate, which promoted the propagation in a more favourable direction. This kind of propagation, although occurring in the laminate, has been considered consistent with the present analysis because it is not characterized by the nucleation of delaminations separated from the main crack, as has been observed sometimes for $MM = 0.15$ and 0.36. However, after the crack had propagated about 2 mm inside the adherend, the crack tip turned back at the interface.

Starting from the $a-N$ curves, the CGR was calculated and plotted versus the value of ΔG_{tot} ($G_{tot,max} - G_{tot,min}$), calculated by means of FE analyses, obtaining the Paris-like curves shown in Figure 11.15. It can be clearly seen that the curves expressed in terms of the total SERR gradually shift from left to right as the *MM*

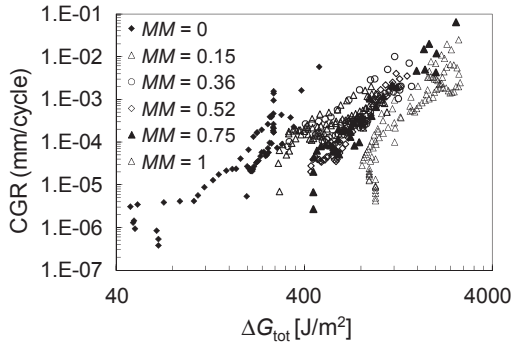

Figure 11.15 Paris curves in terms of total SERR.

increases. Even concerning the fatigue behaviour, the pure mode II condition is far less critical than the pure mode I loading. This means that, for a fixed value of ΔG_{tot}, a lower CGR is reached as the mode II contribution increases.

The Paris-like curves can be described by means of a power law expressed in the form:

$$\frac{da}{dN} = D \times (\Delta G_{tot})^m \tag{11.3}$$

The coefficients of the Paris-like curves for every mixed-mode condition are listed in Table 11.2.

An alternative form to present fatigue data is by means of constant-CGR curves in the $MM-\Delta G_{tot}$ plane, as in Figure 11.16. This picture is consistent with that adopted for the static behaviour in Figure 11.4. The data points in Figure 11.16 are calculated by means of the Paris-like law expressed in Eqn (11.3) for each tested specimen.

Table 11.2 Coefficients of the Paris laws for the different mode mixities investigated (valid for CGR expressed in mm/cycle and SERR in J/m^2)

MM	D	n
0	3.04E−12	3.16
0.15	5.66E−08	2.03
0.36	4.20E−08	2.40
0.52	2.02E−08	4.59
0.75	2.02E−08	4.35
1	1.34E−08	4.10

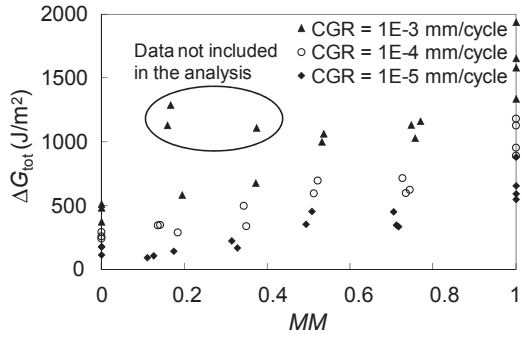

Figure 11.16 Constant-CGR curves in the $MM-\Delta G_{tot}$ plane.

As can be seen from Figure 11.16, some points are characterized by unreasonably high values of the total SERR, which are clearly out of the general trend. These points are related to the damage mode consisting in the initiation and propagation of independent delaminations occurring for $MM = 0.15$ and 0.36. For this reason, because this propagation mode is not related to the bondline but to the damage in the laminate, these points are not considered in subsequent analyses.

11.6 Analysis of damage mechanisms

To develop a reliable criterion for fatigue crack propagation, the observed damage mechanisms have to be taken into account. In particular, two propagation modes have been observed: a continuous crack propagation occurring mainly at the interface near the pure mode I loading and inclined microcracks in the adhesive near the pure mode II, which is reasonably due to the maximum principal stress field in the vicinity of the crack tip.

As already mentioned, the damage mode consisting of independent delaminations (number 2 in Figure 11.5) is not considered here.

It is first important to understand the reason of the change in the propagation mode, which seems to occur around a mode mixity MM of 0.5.

As described by Richard, Fulland, and Sander (2005), if a crack is subjected to a mixed-mode I + II loading, it tends to propagate in a direction that is different from that of the crack itself. In the case of a composite-bonded joint loaded in mixed mode, if a crack is at the adhesive−adherend interface, its deviation is prevented by the presence of the fibres of the adherends. In fact, crack propagation into the laminates would require a high amount of energy to break the 0° fibres or to bow between them (Evans, 1972). As a consequence, if the loading condition is mode I dominated, the crack will keep propagating at the interface in a self-similar manner. This mechanism is driven only by the mode I SERR component G_{I}, the contribution of the mode II to make a crack propagating in a self-similar way being negligible.

On the other hand, if the loading condition is mode II dominated, an unreasonably high load would be required to reach the critical condition for the self-similar interface crack propagation. In this condition, the adhesive will start damaging in a zone ahead of the main crack tip, promoting the initiation and further coalescence of multiple inclined microcracks, which resemble the typical brittle failure normal to the maximum principal stress direction. The maximum principal stress in a finite zone ahead of the crack tip can therefore be assumed as the driving force for this kind of mechanism.

These mechanisms are summarized in Figure 11.17.

In Figure 11.18, the sound agreement between the principal directions calculated by means of an FE analysis and the inclined microcracks for a specimen tested under $MM = 0.75$ seems to support the idea that such microcracks nucleate and grow in a direction that is normal to the maximum principal stress.

As aforementioned, the observed fatigue crack propagation mechanisms in the adhesive does not claim for a point-related approach, because damage takes place in

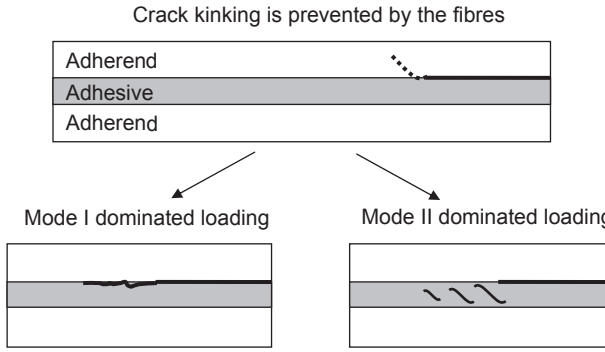

Figure 11.17 Schematic of the main observed fatigue propagation modes.

a small finite region, that is, the so-called process zone. A clear evidence is shown in Figure 11.19, which refers to a specimen tested at $MM = 0.75$.

In Figure 11.19(a), the initial crack tip is at the interface between the adhesive and the upper laminate, and it is followed by a region in which the adhesive whitening indicates where the fatigue damage evolution is in progress. In Figure 11.19(b), it can be seen that the abovementioned process zone, after 10,000 cycles, is characterized by

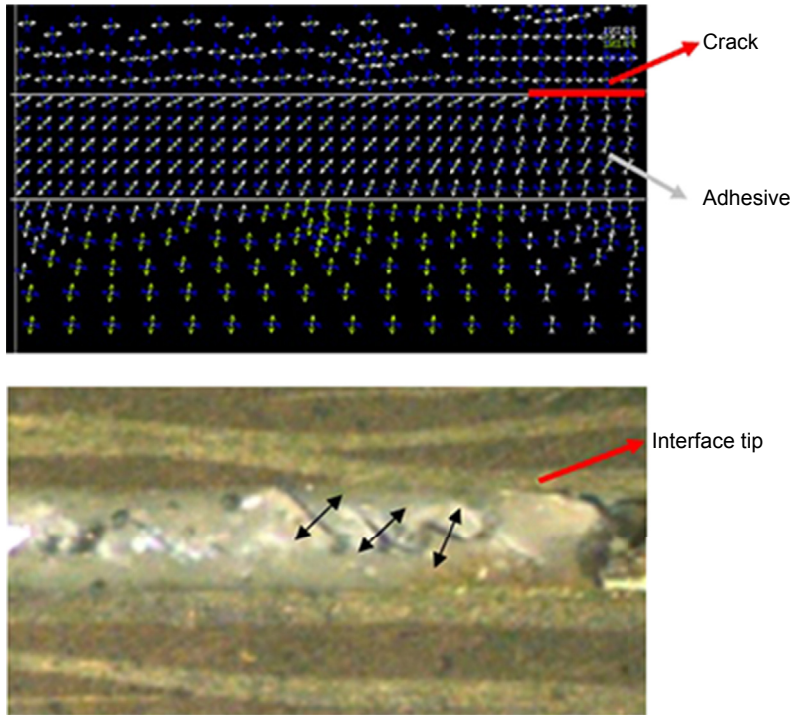

Figure 11.18 Comparison between FE principal directions and microcracks in the adhesive, $MM = 0.75$.

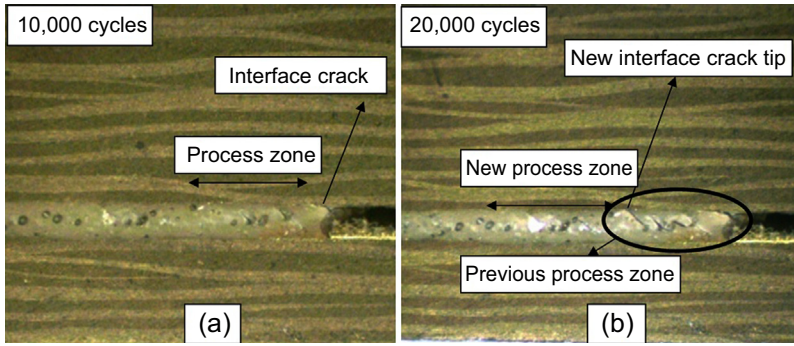

Figure 11.19 Damage evolution and process zone for a specimens tested with $MM = 0.75$ after (a) 10,000 and (b) 20,000 cycles.

the presence of inclined microcracks that start joining in a single macrocrack. The new interface crack tip was conventionally considered to be the last tip at the interface (the farther from the loading point), in front of which a new process zone is formed in the crack propagation direction. As a conclusion, two mechanisms have been identified as the leading ones under mode mixity lower or higher than 0.5, each of them being controlled by a different driving force.

In the literature there is sufficient experimental evidence that the self-similar crack propagation at the interface typical of mixed-mode loading conditions characterized by predominance of mode I is controlled by the mode I component of the SERR, G_I. On the other hand, an established model for the crack propagation in near mode II conditions is still not available. Therefore, in the following paragraph, a new criterion, based on the existence of a process zone, will be defined to model the damage mode consisting of inclined microcracks in the adhesive occurring during fatigue tests for sufficiently high mode mixities (here higher than 0.5).

11.7 A new criterion for crack propagation in bonded joints

As it has been shown above, if the *MM* is high enough, the maximum principal stress field ahead of the crack tip seems to play an important role for the damage progression and crack propagation. In addition, it is clear that the damage involves a process zone ahead of the crack tip that is longer than the adhesive thickness t. On these bases, we assume that the damage process is controlled by the maximum principal stress averaged over a control volume V_c representative of the process zone. The control volume was assumed to be rectangular in shape, involving the whole adhesive thickness and with a length equal to $3t$, as shown in Figure 11.20. The length $3t$ was chosen as an average value of experimental observations. It is the authors' opinion that the size of the control volume is characteristic of the joints tested and presented in this chapter. Therefore care should be taken when analysing bonded joints involving geometries and materials different from those adopted here.

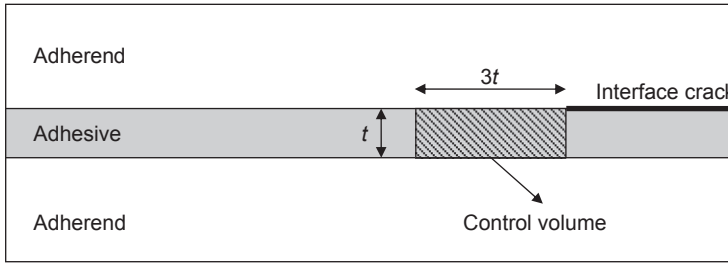

Figure 11.20 Schematic representation of the control volume.

Therefore when the propagation mode consists of the initiation and coalescence of inclined microcracks, the following stress parameter, S, is proposed as representative of the driving force:

$$S = \frac{1}{V_c} \int_{V_c} \sigma_1 \mathrm{d}V \tag{11.4}$$

in which σ_1 is the maximum principal stress.

The parameter S was calculated by means of FE models, and a convergence analysis was carried out to check its sensitivity to the adopted element size. Two mesh strategies were adopted: (1) the typical mesh for the SERR calculation by using the VCCT previously described in paragraph three of this chapter, by varying the element size Δa from 0.01 to 0.075 mm; and (2) a typical mesh for crack modelling, with an element size of 10^{-5} mm at the crack tip. It was found that the S parameter is mesh insensitive, its variation being lower than 1% in the analysed range of element size. This can be explained by considering that the volume size equal to $3t$ is much longer than the singularity dominated zone, which extends up to a distance lower than the adhesive thickness, as demonstrated by the stress analyses reported in Carraro et al. (2013b).

It is interesting to note that a square root dependence exists between the total SERR, G_{tot}, and the stress parameter S, as in Eqn (11.5):

$$S = k(MM) \times \sqrt{G_{\mathrm{tot}}} \tag{11.5}$$

The coefficient $k(MM)$ is a function of the mode mixity, and it was calculated by means of FE analyses in Carraro et al. (2013b). Its values for the cases investigated in the present experimental program are listed in Table 11.3.

After introducing the stress parameter S and keeping in mind the damage mechanisms observed during the fatigue tests, the following criteria are proposed:

- For $MM \leq MM^*$, the mode I SERR contribution only, G_{I}, drives the interface crack propagation;
- For $MM \geq MM^*$, the parameter S controls crack propagation in the form of initiation and coalescence of inclined microcracks in the adhesive.

Table 11.3 Values of $k(MM)$ for the considered MM calculated via FE simulations

MM	*k*
0	2
0.15	2.63
0.36	2.73
0.52	2.68
0.75	2.55
1	2

Carraro et al. (2013b).

*MM** is the value of the mode mixity corresponding to the transition between the two damage modes and therefore between the two driving force parameters to be used. According to the experimental evidences reported in paragraph 5, *MM** is approximately equal to 0.5 for the joints tested in the present work.

11.8 Reanalysis of fatigue test results

The abovementioned criterion is now applied to fatigue experimental results previously presented, which are here reanalysed in terms of G_I and S.

The constant-CGR data shown in Figure 11.16 are presented in Figures 11.21 and 11.22 in terms of S and G_I, respectively.

Figure 11.21 shows that the ΔS parameter is able to rationalize the crack growth data for *MM* greater than 0.5, while it assumes lower values otherwise. Conversely, Figure 11.22 shows that the ΔG_I parameter correctly summarizes the experimental data for $MM < 0.5$, then assuming decreasing values as *MM* increases outside this range.

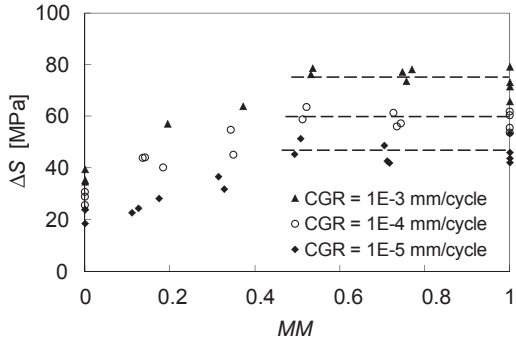

Figure 11.21 Fatigue results in terms of ΔS versus mode mixity, for different values of the CGR.

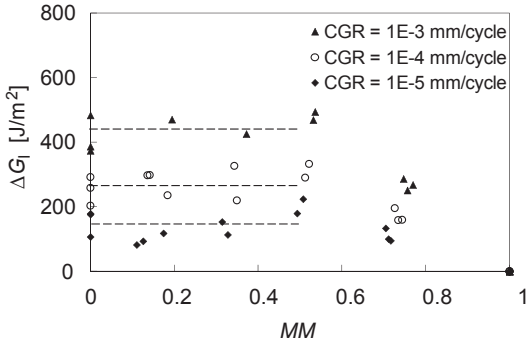

Figure 11.22 Fatigue results in terms of ΔG_I versus mode mixity, for different values of the CGR.

As shown in paragraph 5, different Paris-like curves in terms of the total SERR are associated to different values of the mode mixity. However, if they are presented in terms of ΔG_I and ΔS, for mode-mixity values lower and higher than 0.52, respectively, two master curves are able to rationalize the propagation data under the full mode-mixity range. Figures 11.23 and 11.24 report such Paris-like curves along with the 10−90% relevant scatter bands. The results shown in Figures 11.23 and 11.24 demonstrate that only pure mode I and pure mode II fatigue tests are really necessary to characterize the joints' behaviour for any mode mixity. As a further validation of the proposed model, a comparison with the fatigue crack growth data obtained by Quaresimin and Ricotta (2006b) for single lap joints is shown in Figure 11.25. The materials involved are the same adopted in the present activity, and the values of G_I and G_{II} were calculated from FE analyses in Quaresimin & Ricotta (2006c). The resulting values of the mode mixity were always lower than 0.5, apart from a few points, and therefore the criterion to use for CGR predictions should be the pure mode I-driven propagation. In fact, if the crack growth data from Quaresimin & Ricotta (2006b) are plotted in terms of ΔG_I, they fall well inside the scatter band obtained from the present data and shown in Figure 11.23.

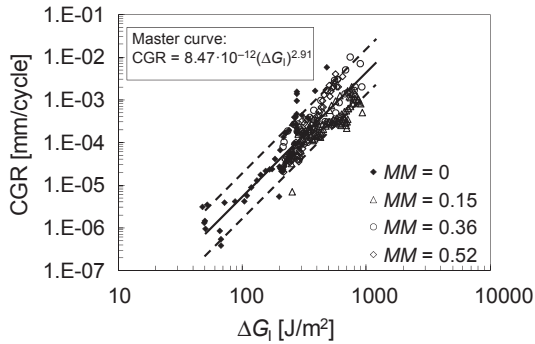

Figure 11.23 Paris-like curves in terms of ΔG_I for $MM \leq 0.52$.

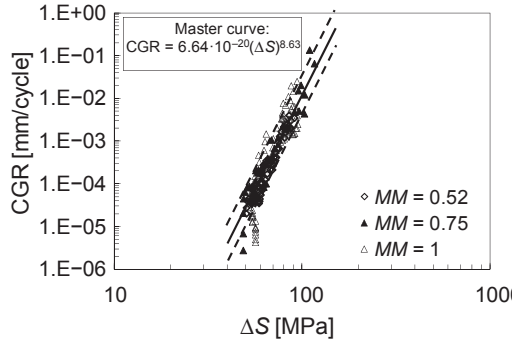

Figure 11.24 Paris-like curves in terms of ΔS for $MM \geq 0.52$.

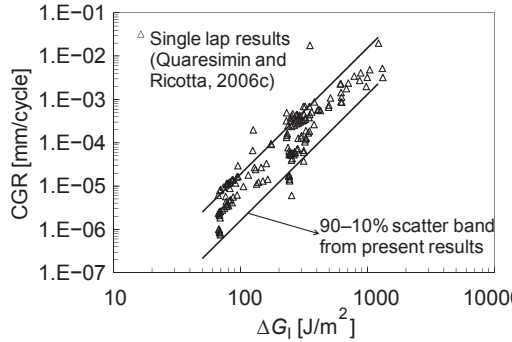

Figure 11.25 Comparison between the present scatter band and the results from Quaresimin & Ricotta (2006c) in terms of ΔG_I.

Results shown in Figure 11.25 are in agreement with the good correlation between the crack growth data collected from the single lap joints and the Paris curve calibrated on pure mode I tests found by Abdel Wahab et al. (2002) and Kinloch and Osiyemi (1993).

11.9 Conclusions

The static and fatigue crack propagation in composite bonded joints have been analysed under mixed-mode I + II loadings.

The main findings are summarized in the following points:

- Under static loading, the critical total SERR under pure mode II is about three times that under pure mode I;
- Concerning fatigue loading, the Paris-like curves relating the CGR to the total SERR are dependent on the mode mixity: in particular, a higher value of the total SERR is required to obtain a given CGR as the pure mode II condition is approached;

- Damage and propagation mechanisms strongly depend on the mixed-mode condition: a mostly self-similar interface crack propagation is typical of mode I-dominated conditions, whereas multiple microcrack initiation in the adhesive and subsequent coalescence occur under predominant mode II loading.

On the basis of these observations, the driving forces for the two mechanisms have been identified as the mode I SERR and a newly defined stress parameter S, respectively, corresponding to the maximum principal stress averaged over a control volume in the adhesive.

It has been proved that two scatter bands, expressed in terms of G_I and S, are suitable to describe the mixed-mode propagation under the full range of mode mixities. Therefore, only two tests are necessary for the material characterization, for example a pure mode I (DCB) test and a pure mode II (ENF) test.

Although the validation of the new damage model provided good agreement with fatigue experimental data, it is the authors opinion that additional work is still needed to conceive an efficient model based on the process zone (or control volume) concept.

References

Abdel Wahab, M. M., Ashcroft, I. A., Crocombe, A. D., & Smith, P. A. (2002). Numerical prediction of fatigue crack propagation lifetime in adhesively bonded structures. *International Journal of Fatigue, 24*(6), 705−709. http://dx.doi.org/10.1016/S0142-1123(01)00173-6.

Ashcroft, I. A., Casas-Rodriguez, J. P., & Silberschmidt, V. V. (2008). Mixed-mode crack growth in bonded composite joints under standard and impact-fatigue loading. *Journal of Materials Science, 43*(20), 6704−6713. http://dx.doi.org/10.1007/s10853-008-2646-6.

Ashcroft, I. A., Casas-Rodriguez, J. P., & Silberschmidt, V. V. (2010). A model to predict the anomalous fatigue crack growth behaviour seen in mixed mechanism fracture. *Journal of Adhesion, 86*(5−6), 522−538. http://dx.doi.org/10.1080/00218464.2010.484306.

ASTM-D 3115−97. (1997). Mode I fatigue delamination growth onset of unidirectional fiber-reinforced polymer matrix composites. *ASTM International*.

ASTM-D 5528−01. (2001). Standard test method for mode I interlaminar fracture toughness of unidirectional fiber-reinforced polymer matrix composites. *ASTM International*.

ASTM-D 6671−01. (2001). Standard test method for mixed mode I-II interlaminar fracture toughness of unidirectional fiber-reinforced polymer matrix composites. *ASTM International*.

Azari, S., Papini, M., Schroeder, J. A., & Spelt, J. K. (2010). The effect of mode ratio and bond interface on the fatigue behavior of a highly-toughened epoxy. *Engineering Fracture Mechanics, 77*(3), 395−414. http://dx.doi.org/10.1016/j.engfracmech.2009.09.011.

Blackman, B. R. K., Kinloch, A. J., & Paraschi, M. (2005). The determination of the mode II adhesive fracture resistance, G_{IIC}, of structural adhesive joints: an effective crack length approach. *Engineering Fracture Mechanics, 72*(6), 877−897. http://dx.doi.org/10.1016/j.engfracmech.2004.08.007.

Carraro, P. A., Meneghetti, G., Quaresimin, M., & Ricotta, M. (2013). Crack propagation analysis in composite bonded joint under mixed-mode (I + II) fatigue loadings: experimental investigation and phenomenological modeling. *Journal of Adhesion Science and Technology, 27*(11), 1179−1196. http://dx.doi.org/10.1080/01694243.2012.735902.

Carraro, P. A., Meneghetti, G., Quaresimin, M., & Ricotta, M. (2013). Crack propagation analysis in composite bonded joint under mixed-mode (I + II) fatigue loadings: a damage-based model. *Journal of Adhesion Science and Technology, 27*(13), 1393−1406. http://dx.doi.org/10.1080/01694243.2012.735901.

Cheuk, P. T., Tong, L., Wang, C. H., Baker, A., & Chalkley, P. (2002). Fatigue crack growth in adhesively bonded composite-metal double-lap joints. *Composite Structures, 57*(1−4), 109−115. http://dx.doi.org/10.1016/S0263-8223(02)00074-0.

Clark, J. D., & McGregor, I. J. (1993). Ultimate tensile stress over a zone: a new failure criterion for adhesive joints. *Journal of Adhesion, 42*, 227−245. http://dx.doi.org/10.1080/00218469308026578.

Curley, A. J., Hadavinia, H., Kinloch, A. J., & Taylor, A. C. (2000). Predicting the service-life of adhesively-bonded joints. *International Journal of Fracture, 103*(1), 41−69. http://dx.doi.org/10.1023/A:1007669219149.

Ducept, F., Davies, P., & Gamby, D. (2000). Mixed mode failure criteria for a glass/epoxy composite and an adhesively bonded composite/composite joint. *International Journal of Adhesion and Adhesives, 20*(3), 233−244. http://dx.doi.org/10.1016/S0143-7496(99)00048-2.

Evans, A. G. (1972). Strength of brittle materials containing second-phase dispersions. *Philosophical Magazine, 26*(6), 1327−1344. http://dx.doi.org/10.1080/14786437208220346.

Johnson, W. S., & Mall, S. (1986). Influence of interface ply orientation on fatigue damage of adhesively bonded composite joints. *Journal of Composites Technology and Research, 8*(1), 3−7. http://dx.doi.org/10.1520/CTR10314J.

Kenane, M., & Benzeggagh, M. L. (1997). Mixed-mode delamination fracture toughness of unidirectional glass/epoxy composites under fatigue loading. *Composites Science and Technology, 57*(5), 597−605. http://dx.doi.org/10.1016/S0266-3538(97)00021-3.

Kinloch, A. I., & Osiyemi, S. O. (1993). Predicting the fatigue life of adhesively-bonded joints. *Journal of Adhesion, 43*(1−2), 79−90. http://dx.doi.org/10.1080/00218469308026589.

Leffler, K., Alfredsson, K. S., & Stigh, U. (2007). Shear behaviour of adhesive layers. *International Journal of Solids and Structures, 44*(2), 530−545. http://dx.doi.org/10.1016/j.ijsolstr.2006.04.036.

Liu, Z., Gibson, R. F., & Newaz, G. M. (2002). Improved analytical models for mixed-mode bending tests of adhesively bonded joints. *Journal of Adhesion, 78*(3), 245−268. http://dx.doi.org/10.1080/00218460210410.

Liu, S., Mei, Y., & Wu, T. Y. (1995). Biomaterial interfacial crack growth as a function of mode-mixity. *IEEE Transactions on Components, Packaging and Manufacturing Technology−Part A, 18*, 618−626. http://dx.doi.org/10.1109/95.465161.

Meneghetti, G., Quaresimin, M., & Ricotta, M. (2010). Influence of the interface ply orientation on the fatigue behaviour of bonded joints in composite materials. *International Journal of Fatigue, 32*(1), 82−93. http://dx.doi.org/10.1016/j.ijfatigue.2009.02.008.

Moroni, F., & Pirondi, A. (2011). A procedure for the simulation of fatigue crack growth in adhesively bonded joints based on the cohesive zone model and different mixed-mode propagation criteria. *Engineering Fracture Mechanics, 78*(8), 1808−1816. http://dx.doi.org/10.1016/j.engfracmech.2011.02.004.

de Moura, M. F. S. F., Oliveira, J. M. Q., Morais, J. J. L., & Dourado, N. (2011). Mixed-mode (I + II) fracture characterization of wood bonded joints. *Construction and Building Materials, 25*(4), 1956−1962. http://dx.doi.org/10.1016/j.conbuildmat.2010.11.060.

Nguyen, K. H., Kweon, J. H., & Choi, J. H. (2009). Failure load prediction by damage zone method for single-lap bonded joints of carbon composite and aluminum. *Journal of Composite Materials, 43*(25), 3031−3056. http://dx.doi.org/10.1177/0021998309345295.

Potter, K. D., Guild, F. J., Harvey, H. J., Wisnom, M. M., & Adams, R. D. (2001). Understanding and control of adhesive crack propagation in bonded joints between carbon fibre composite adherends I. Experimental. *International Journal of Adhesion and Adhesives, 21*(6), 435−443. http://dx.doi.org/10.1016/S0143-7496(01)00020-3.

prEN 6034. Determination of interlaminar fracture toughness energy mode II-G_{IIc}.

Quaresimin, M., & Ricotta, M. (2006a). Fatigue behaviour and damage evolution of single lap bonded joints in composite material. *Composites Science and Technology, 66*(2), 176−187. http://dx.doi.org/10.1016/j.compscitech.2005.04.026.

Quaresimin, M., & Ricotta, M. (2006b). Life prediction of bonded joints in composite materials. *International Journal of Fatigue, 28*(10), 1166−1176. http://dx.doi.org/10.1016/j.ijfatigue.2006.02.005.

Quaresimin, M., & Ricotta, M. (2006c). Stress intensity factors and strain energy release rates in single lap bonded joints in composite materials. *Composites Science and Technology, 66*(5), 647−656. http://dx.doi.org/10.1016/j.compscitech.2005.07.036.

Richard, H. A., Fulland, M., & Sander, M. (2005). Theoretical crack path prediction. *Fatigue & Fracture of Engineering Materials & Structures, 28*(1−2), 3−12. http://dx.doi.org/10.1111/j.1460-2695.2004.00855.x.

Sheppard, A., Kelly, D., & Tong, L. (1998). A damage zone model for the failure analysis of adhesively bonded joints. *International Journal of Adhesion and Adhesives, 18*(6), 385−400. http://dx.doi.org/10.1016/S0143-7496(98)00024-4.

Sun, C. T., & Jih, C. J. (1987). On strain energy release rates for interfacial cracks in bi-material media. *Engineering Fracture Mechanics, 28*(1), 13−20. http://dx.doi.org/10.1016/0013-7944(87)90115-9.

Wang, C. H. (1997). Fracture of interface cracks under combined loading. *Engineering Fracture Mechanics, 56*(1), 77−86. http://dx.doi.org/10.1016/S0013-7944(96)00111-7.

Xu, X. X., Crocombe, A. D., & Smith, P. A. (1995). Mixed-mode fatigue and fracture behaviour of joints bonded with either filled or filled and toughened adhesive. *International Journal of Fatigue, 17*(4), 279−286. http://dx.doi.org/10.1016/0142-1123(95)93540-I.

A general and rigorous accelerated testing methodology for long-term life prediction of polymeric materials

12

M. Nakada, Y. Miyano
Kanazawa Institute of Technology, Hakusan, Japan

12.1 Introduction

Carbon fiber reinforced plastics (CFRP) are now being used in primary structures of airplanes, ships, and other vehicles and for applications that demand sustained high reliability during long-term operations. Therefore, an accelerated testing methodology (ATM-1) must be established for long-term life prediction of CFRP structures exposed to actual environments with exposure to extreme temperatures, water, and other potentially destructive phenomena.

A strategy for accelerated testing is shown as the following steps: (1) data collection by accelerated testing; (2) durability design; and (3) development of highly reliable structures. First, an ATM-1 should be established for polymer composites. Our developed methodology will be generic and will be applicable to centrifuges, generators, flywheels, aircraft, wind turbines, marine, automobiles, and so on.

Previously, we developed a conventional ATM-1 to predict the long-term fatigue life of CFRP laminates based on the time−temperature superposition principle (TTSP) applied to the viscoelastic behavior of matrix resin. ATM-1 enables us to describe the long-term life using master curves covering wide ranges of loading and environmental conditions, including load duration, temperature, frequency of load cycles, load amplitudes, and so on (Miyano, Nakada, Kudoh, & Muki, 1999; Miyano, Nakada, McMurray, & Muki, 1997; Miyano, Nakada, & Muki, 1999; Miyano, Nakada, & Sekine, 2005; Nakada & Miyano, 2009). Furthermore, we have proposed a method of formulating master curves based on the simple equation as functions of time to failure, temperature, loading frequency, and number of cycles to failure (Miyano, Nakada, & Cai, 2008). However, this equation has not directly taken into account the viscoelastic coefficients of matrix resin. Therefore, the equation cannot be applied to the life prediction of CFRP laminates exposed to an actual load and temperature histories.

In this paper, we propose an advanced accelerated testing methodology (ATM-2) that is applicable to the life prediction of CFRP laminates exposed to an actual load and environment history by taking into account the viscoelastic coefficients of matrix resin. The most important point about ATM-2 is the fact that the same

Structural Integrity and Durability of Advanced Composites. http://dx.doi.org/10.1016/B978-0-08-100137-0.00012-2

TTSP that holds for the viscoelastic behavior of matrix resin holds for the static, creep, and fatigue strengths of CFRP laminates. Furthermore, three conditions are added with the scientific bases in ATM-2. The long-term fatigue strength of CFRP laminates under actual loading is formulated based on these conditions. The viscoelastic coefficients of matrix resin, which perform an important role for the time and temperature dependence of long-term life of CFRP laminates, are also formulated based on TTSP. The applicability of ATM-2 is demonstrated by predicting the long-term fatigue strengths in four typical loading directions for unidirectional CFRP laminates.

12.2 Time–temperature superposition principle

Thermosetting resins used as the matrix for CFRP laminates are amorphous and show linear viscoelastic behavior that is time- and temperature-dependent mechanical behavior, not only in the region above the glass transition temperature T_g, but also in the region below T_g. For instance, the viscoelastic materials show strain response for the input of step stress shown in Figure 12.1. The strain increases concomitantly with increasing time and increases with temperature. When the TTSP holds for viscoelastic behavior, the time–temperature shift factor $a_{T_0}(T_i)$ is definable by the following equation:

$$a_{T_0}(T_i) = \frac{t_i}{t_0} \tag{12.1}$$

in which, t_0 is time for a strain ε_0 at temperature T_0 and t_i is time for the same strain ε_0 at temperature T_i.

Figure 12.2 shows the time and temperature dependence of static, creep, and fatigue strengths of CFRP laminates for three loading patterns of a constant strain rate (static), a constant stress, and a cyclic stress. When the same TTSP for viscoelastic behavior of

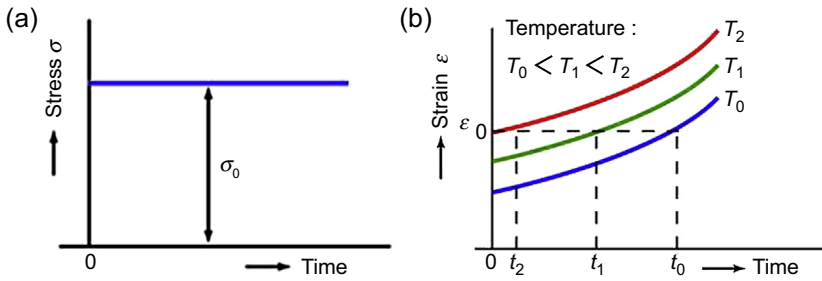

Figure 12.1 Viscoelastic behavior of amorphous resin, (a) stress input, (b) strain response. Advanced accelerated testing methodology for long-term life prediction of CFRP laminates, *Journal of Composite Materials*, http://dx.doi.org/10.1177/0021998313515019, Sage.

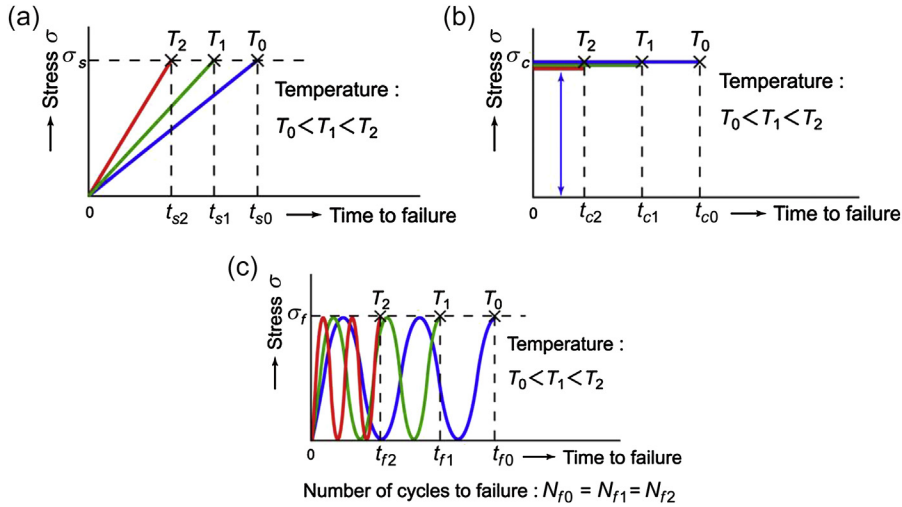

Figure 12.2 Time- and temperature-dependent strength, (a) static load, (b) creep load, (c) cyclic load. Advanced accelerated testing methodology for long-term life prediction of CFRP laminates, *Journal of Composite Materials*, http://dx.doi.org/10.1177/0021998313515019, Sage.

matrix resin holds for the static, creep, and fatigue strengths of CFRP laminates, $a_{T_0}(T_i)$ for these strengths can be expressed as

$$a_{T_0}(T_i) = \frac{t_i}{t_0} = \frac{t_{si}}{t_{s0}} = \frac{t_{ci}}{t_{c0}} = \frac{t_{fi}}{t_{f0}} \tag{12.2}$$

in which t_{s0}, t_{c0}, and t_{f0} are the times to failure of CFRP laminates by three loading patterns at temperature T_0, and t_{si}, t_{ci}, and t_{fi} are the times to failure at temperature T_i. The subscripts s, c, and f respectively denote the static, creep, and fatigue. We have demonstrated experimentally and theoretically in our previous works (Miyano et al., 2008) that the strength of PAN (polyacrylonitrile)-based CFRP laminates meets the same TTSP for the viscoelastic behavior of matrix resin irrespective of the structural configuration and loading style.

12.3 Advanced accelerated testing methodology

ATM-2 is established with the following three conditions: (A) the failure probability of CFRP laminates is independent of time, temperature, and load history; (B) the time and temperature dependence of strength of CFRP laminates is controlled by the viscoelasticity of matrix resin, therefore, the same TTSP for the viscoelasticity of matrix resin holds for the strength of CFRP laminates; (C) the slope of the S−N curve is determined by maximum stress and stress ratio. It is independent of time, temperature, and frequency.

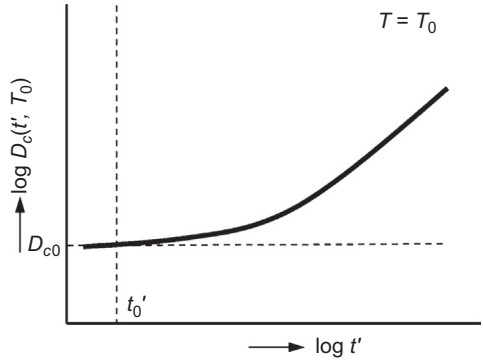

Figure 12.3 Master curve of creep compliance against the reduced time at a reference temperature of matrix resin.
Advanced accelerated testing methodology for long-term life prediction of CFRP laminates, *Journal of Composite Materials*, http://dx.doi.org/10.1177/0021998313515019, Sage.

Based on the three conditions (A), (B), and (C), the long-term strength σ_f of CFRP laminates is proposed by the following equation as a simple approach:

$$\sigma_f = \sigma_0 f_A f_B f_C \text{ or } \log \sigma_f = \log \sigma_0 + \log f_A + \log f_B + \log f_C \tag{12.3}$$

In those equations, σ_0 and f_A are the static strength and its scatter determined by the failure probability P_f at room temperature determined by the types of fiber and weave, volume fraction of fiber, load direction, and other factors; f_B is the strength variation attributable to the viscoelasticity of matrix resin D^*; and f_C is the strength degradation determined by the stress range $\Delta\sigma$ and number of cycles to failure N_f.

The master curves of static and fatigue strengths of CFRP laminates and the creep compliance are obtainable against the reduced time t' at a reference temperature T_0 based on TTSP. Figure 12.3 shows the master curve of creep compliance D_c against the reduced load time t' at reference temperature T_0 constructed by shifting D_c at various temperatures T_i. Figure 12.4 shows the master curves of static and fatigue strengths against the reduced failure time t' at a reference temperature T_0 of CFRP laminates. The three parameters f_A, f_B, and f_C are explained in the following three sections.

12.3.1 Failure probability independent of time, temperature, and load history

Strength σ_f can be shown generally by the following equation with a Weibull distribution:

$$\sigma_f(P_f) = \sigma_0[-\ln(1 - P_f)]^{\frac{1}{\alpha}} \tag{12.4}$$

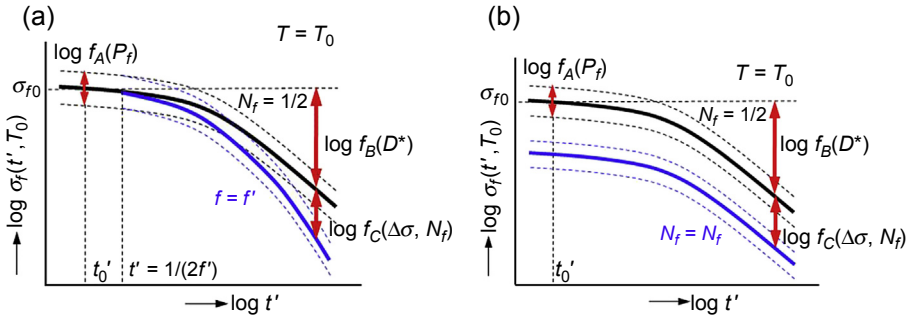

Figure 12.4 Master curves of static and fatigue strengths against reduced failure time at a reference temperature of carbon fiber reinforced plastics laminates, (a) case of constant frequency, (b) case of constant number of cycles to failure.
Advanced accelerated testing methodology for long-term life prediction of CFRP laminates, *Journal of Composite Materials*, http://dx.doi.org/10.1177/0021998313515019, Sage.

in which σ_0 is a scale parameter, α is a shape parameter, and P_f is the failure probability.

Christensen and Miyano (2006) found theoretically and experimentally that α is independent of time and temperature, as shown in Figure 12.4. From Eqn (12.4), the static strength σ_0 and the scatter of static strength f_A are expressed as follows:

$$\sigma_0 = \sigma_f\left(t_0', T_0\right) \tag{12.5}$$

$$\log f_A = \log\left[\frac{\sigma_f\left(P_f, t_0', T_0\right)}{\sigma_f\left(t_0', T_0\right)}\right] = \frac{1}{\alpha}\log\left[-\ln(1-P_f)\right] \tag{12.6}$$

In those equations, $\sigma_f(P_f, t_0', T_0)$ and $\sigma_f(t_0', T_0)$ at reference reduced time to failure t_0' and reference temperature T_0 are the scattered static strength to be the function of failure probability P_f and the scale parameter of static strength. The reference reduced time to failure and reference temperature can usually be chosen at $t_0' = 1$ min and $T_0 = 25\ ^\circ\mathrm{C}$.

12.3.2 Time and temperature dependence of strength controlled by the viscoelasticity of matrix resin

We proposed the formulation to predict the long-term strength of CFRP laminates as an ATM-1 (Miyano et al., 2008). The viscoelastic behavior of matrix resin was just fitted by two tangential lines, and then fitting parameters were simply applied to the strength deviation of CFRP laminates by time and temperature.

In our previous paper (Nakada & Miyano, 2013), we found that the time and temperature dependence of static strengths in the longitudinal tension, bending, and transverse bending for unidirectional CFRP against the inverse of viscoelastic coefficient of matrix resin $1/D^*$ are determined uniquely. These slopes are each

constant. Based on these facts that the strength of CFRP laminates σ_f is indicated by the power function of viscoelastic coefficient of matrix resin D^* as expressed by:

$$\log f_B = \log\left[\frac{\sigma_f(P_f, t', T_0)}{\sigma_f(P_f, t'_0, T_0)}\right] = -n_r \log\left[\frac{D^*(t', T_0)}{D_c(t'_0, T_0)}\right] \tag{12.7}$$

in which n_r is the parameter determined by the failure mode, which is independent of time and temperature, and D_c is the creep compliance of the matrix resin. The viscoelastic coefficient D^* and the reduced time t' are expressed respectively by the following equations based on the theory of linear viscoelasticity:

$$D^*(t', T_0) = \frac{\varepsilon(t', T_0)}{\sigma(t', T_0)} = \frac{\int_0^{t'} D_c(t' - \tau', T_0)\frac{\mathrm{d}\sigma(\tau')}{\mathrm{d}\tau'}\mathrm{d}\tau'}{\sigma(t', T_0)} \tag{12.8}$$

In that equation, t' is defined as shown below:

$$t' = \int_0^t \frac{\mathrm{d}\tau}{a_{T_0}(T(\tau))}$$

Therefore, the viscoelastic coefficient D^* is the function of stress history $\sigma(\tau)$ and temperature history $T(\tau)$ (Miyano, Shimbo, & Kunio, 1982).

12.3.3 Strength degradation caused by cyclic loading

We propose here the strength degradation of CFRP laminates based on the linear cumulative damage rule well-known as the Miner's rule. It is presumed that the slope of S−N curve is determined by the stress ratio and that it is independent of time, temperature, and frequency.

Based on this simple assumption, the S−N curve of CFRP laminates is formulated as the equation presented below:

$$\log \sigma_f(N_f) = \log \sigma_f(N_0) - \frac{(1-R)}{2} n_f \log\left(\frac{N_f}{N_0}\right) \tag{12.9}$$

In this equation, N_0 is simply 1/2, and $\sigma_f(N_0)$ denotes the strength under monotonic loading. N_f and R respectively denote the number of cycles to failure and the stress ratio. n_f is a material parameter.

The strength degradation of CFRP caused by cyclic loading is described in Figure 12.5(a) and is formulated as

$$\log f_C = \log\left[\frac{\sigma_f(N_f)}{\sigma_f(N_0)}\right] = -\frac{(1-R)}{2} n_f \log\left(\frac{N_f}{N_0}\right) + n_f^* \log(1 - k_D) \tag{12.10}$$

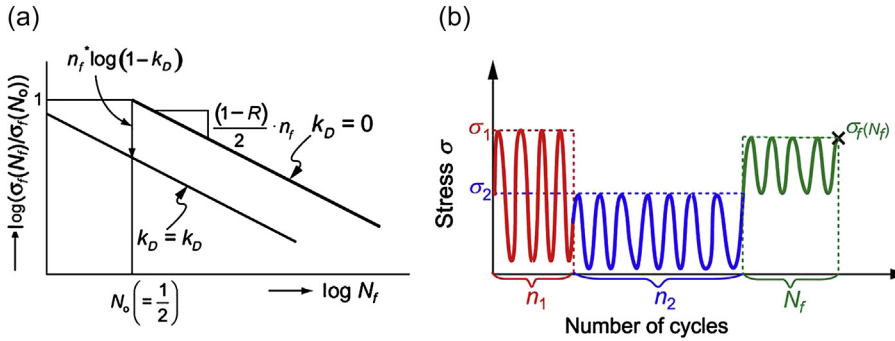

Figure 12.5 Strength degradation of carbon fiber reinforced plastics laminates by cyclic loading, (a) S−N curve, (b) typical cyclic load pattern.
Advanced accelerated testing methodology for long-term life prediction of CFRP laminates, *Journal of Composite Materials*, http://dx.doi.org/10.1177/0021998313515019, Sage.

in which k_D and n_f^* respectively represent the accumulation index of damage and the material parameter.

The accumulation index of damage k_D is defined by the following equation based on the Miner's rule:

$$k_D = \sum_{i=1}^{n} \frac{n_i}{N_{fi}} < 1 \tag{12.11}$$

In that equation, n_i and N_{fi} respectively stand for the number of cycles and the number of cycles to failure at the loading of step i shown in Figure 12.5(b). For virgin materials, $k_D = 0$ and $n_f^* = 0$. k_D increases with increase of number of load cycle, and then the residual strength decreases.

12.3.4 Formulation based on ATM-2

The long-term strength under an actual loading history of stress $\sigma(\tau)$ and temperature $T(\tau)$ for CFRP laminates can be expressed by the following equation based on the previous three sections:

$$\log \sigma_f = \log \sigma_0\left(t_0', T_0\right) + \frac{1}{\alpha}\log[-\ln(1-P_f)] - n_r \log\left[\frac{D^*(t', T_0)}{D_c\left(t_0', T_0\right)}\right] - \frac{(1-R)}{2} n_f \log(2N_f) + n_f^* \log(1-k_D) \tag{12.12}$$

The determination of material parameters in the formulation for ATM-2 should be done by determining the parameters of a_{T_0} and D_c of matrix resin as the first step and determining the parameters of σ_0, α, n_r, and n_f of CFRP laminates as the

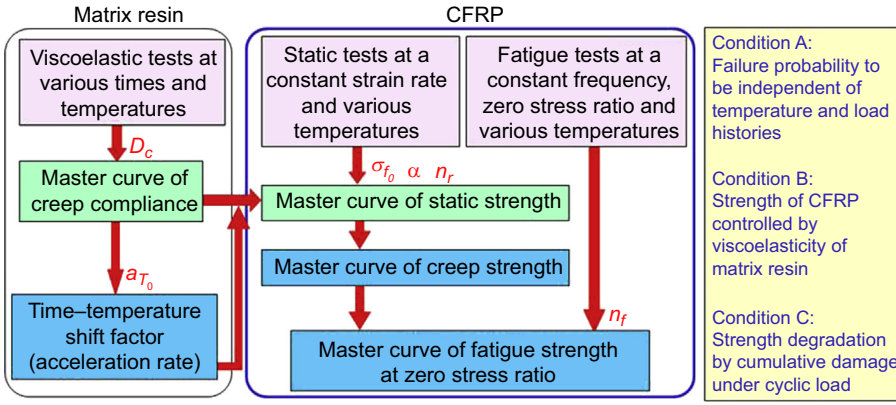

Figure 12.6 Formulation procedure based on advanced accelerated testing methodology. Advanced accelerated testing methodology for long-term life prediction of CFRP laminates, *Journal of Composite Materials*, http://dx.doi.org/10.1177/0021998313515019, Sage.

second step shown in Figure 12.6. First, the viscoelastic test for matrix resin is conducted at various temperatures. The master curve of creep compliance D_c is constructed using measured data based on TTSP, and the time−temperature shift factor a_{T_0} is determined. Second, the master curve of static strength is constructed using the static strengths measured at various temperatures for CFRP laminates and the time−temperature shift factor a_{T_0} of matrix resin. The master curve of creep strength is determined from the master curve of static strength using Eqn (12.12). The master curve of fatigue strength is constructed using the fatigue strengths measured at various temperatures for CFRP laminates and the time−temperature shift factor a_{T_0} of matrix resin. The parameters of σ_0, α, n_r, and n_f of CFRP laminates are determined from these master curves.

12.3.5 Formulation for master curve of creep compliance and shift factors for matrix resin

The most important procedure for ATM-2 is the reliable formulation for the master curve of creep compliance and shift factors for matrix resin. Figure 12.7 shows the formulation procedure. First, the smooth master curve of creep compliance of matrix resin shown on the right side of Figure 12.7(a) is obtainable by shifting the creep compliances measured at various temperatures vertically and horizontally. The slightly vertical shift should be done to obtain the reliable horizontal shift factor to be the rate of acceleration, which is the most important parameter for long-term life prediction (Nakada, Miyano, Cai, & Kasamori, 2011).

The master curve of creep compliance D_c can be formulated as

$$\log D_c = \log D_{c,0}\left(t'_0, T_0\right) + \log\left[\left(\frac{t'}{t'_0}\right)^{m_g} + \left(\frac{t'}{t'_g}\right)^{m_r}\right] \tag{12.13}$$

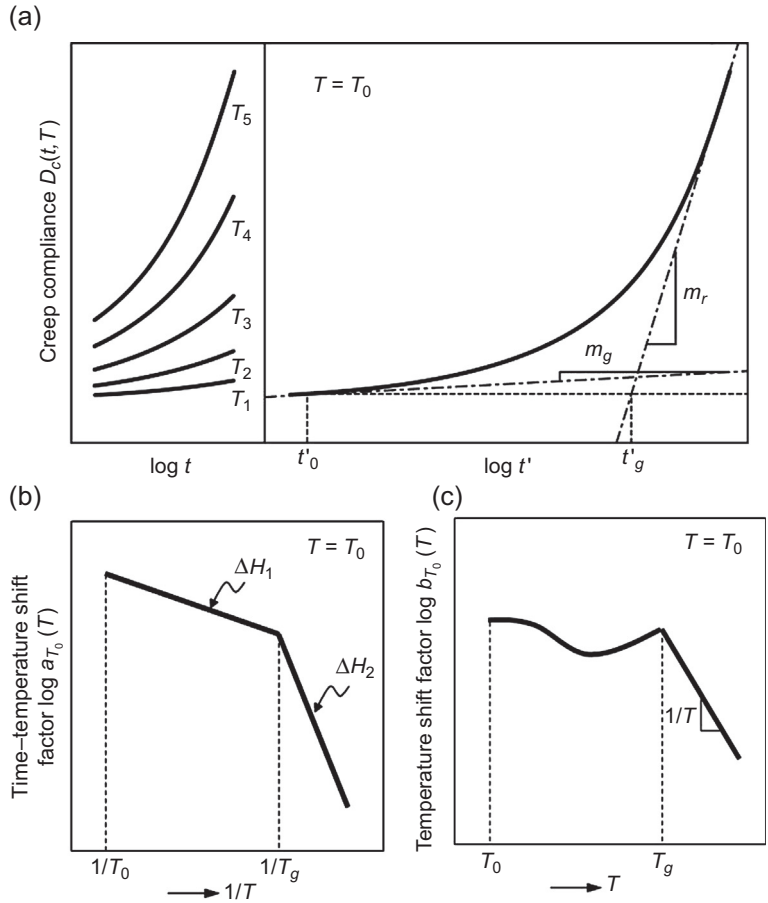

Figure 12.7 Formulation for master curve of creep compliance and shift factors for matrix resin, (a) master curve of creep compliance of the matrix resin, (b) time−temperature shift factor, (c) temperature shift factor.
Advanced accelerated testing methodology for long-term life prediction of CFRP laminates, *Journal of Composite Materials*, http://dx.doi.org/10.1177/0021998313515019, Sage.

in which $D_{c,0}$ stands for the creep compliance at reference time t'_0 and reference temperature T_0, t'_g signifies the glassy reduced time on T_0, and m_g and m_r respectively denote the gradients in glassy and rubbery regions of D_c master curve.

The time−temperature shift factor $a_{T_0}(T)$, which is the horizontal shift amount shown by (b) in Figure 12.7, can be formulated as the following equation (Cai, Nakada, & Miyano, 2013):

$$\log a_{T_0}(T) = \frac{\Delta H_1}{2.303G}\left(\frac{1}{T}-\frac{1}{T_0}\right)H(T_g - T) + \frac{\Delta H_1}{2.303G}\left(\frac{1}{T_g}-\frac{1}{T_0}\right) + \frac{\Delta H_2}{2.303G}\left(\frac{1}{T}-\frac{1}{T_g}\right)\left(1 - H(T_g - T)\right) \tag{12.14}$$

In this equation, G is the gas constant, 8.314×10^{-3} (kJ/(K·mol)), ΔH_1 and ΔH_2 respectively represent the activation energies below and above the glass transition temperature T_g, and H is the Heaviside step function. The temperature shift factors, $b_{T_0}(T)$, which are the amount of vertical shift below and above T_g, are represented by straight lines for general purpose epoxy resin (Cai et al., 2013). However, we found that the $b_{T_0}(T)$ below T_g for heat resistant epoxy resin cannot be expressed by straight line as shown in Figure 12.7(c). Therefore, we used the fourth-order polynomial function as

$$\log b_{T_0}(T) = \left[\sum_{j=0}^{4} b_n (T - T_0)^j\right] H(T_g - T) + \left[\sum_{j=0}^{4} b_n (T_g - T_0)^j + \log\frac{T_g}{T}\right] \times \left(1 - H(T_g - T)\right) \tag{12.15}$$

in which b_j is the fitting parameters.

12.4 Experiments

12.4.1 Specimens and test methods

The test specimens were fabricated from unidirectional CFRP laminates of MR60H/1053, which consist of MR60H carbon fiber and epoxy resin 1053. All laminates were produced using the autoclave technique. The curing procedure includes heating at 180 °C for 2 h and then postcuring at 160 °C for 70 h. The volume fraction of fiber is approximately 0.55. The laminates were cut to the specific size for the tests using a diamond-grit wheel.

The dynamic viscoelastic tests were performed for various frequencies and temperatures for the transverse direction of unidirectional CFRP laminates. The master curve of creep compliance and the time−temperature shift factor for matrix resin can be obtained indirectly from data obtained from these dynamic viscoelastic tests.

Static and fatigue tests under various temperatures were conducted in four typical loading directions for unidirectional CFRP laminates. Four typical loading directions are the tension and compression directions in the fiber direction and transverse to the fiber direction. From these tests, we evaluated the static and fatigue strengths in longitudinal tensile (X), longitudinal compression (X'), transverse tension (Y), and transverse compression (Y'). The details for test methods and tests results shown here were published in our previous paper (Miyano et al., 2008). Therefore, the explanation presented here addresses the formulations of ATM-2 using the measured data.

12.4.2 Creep compliance of matrix resin

The master curve of creep compliance and the time−temperature shift factor of matrix resin can be determined practically by the storage modulus for the transverse direction of unidirectional CFRP laminates measured at various frequencies and temperatures using the dynamic viscoelastic testing machine. The left side of Figure 12.8(a) shows the storage modulus E' for the transverse direction of unidirectional CFRP laminates versus time t, in which time t is the inverse of frequency. The right side shows the master curve of E', which is constructed by shifting E' at various constant temperatures along the logarithmic scale of t and logarithmic scale of E' until they overlapped each other, for the reduced time t' at the reference

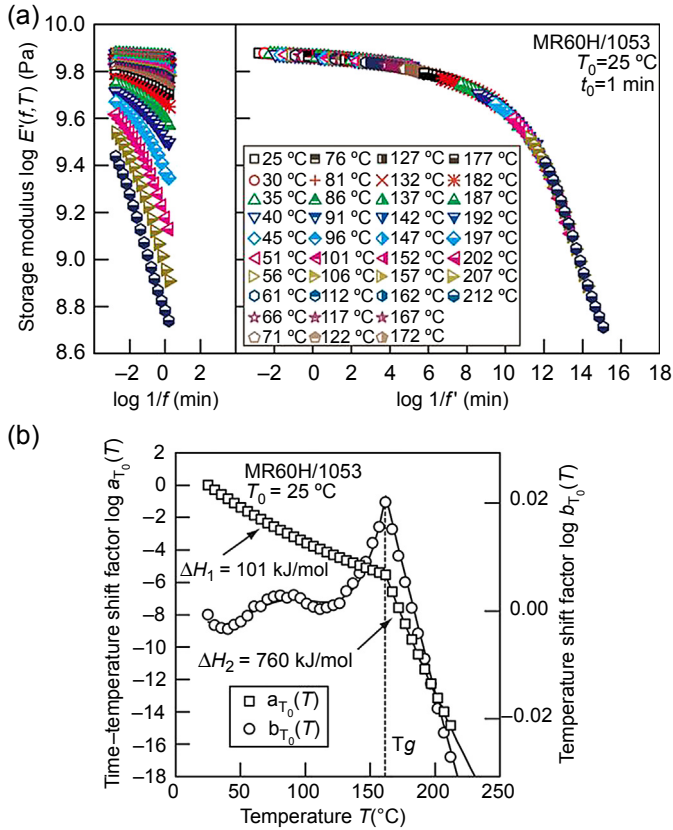

Figure 12.8 Master curve and shift factors for storage modulus in the transverse direction of unidirectional carbon fiber reinforced plastics laminates, (a) master curve of storage modulus, (b) time−temperature shift factor and temperature shift factor.
Advanced accelerated testing methodology for long-term life prediction of CFRP laminates, *Journal of Composite Materials*, http://dx.doi.org/10.1177/0021998313515019, Sage.

temperature $T_0 = 25\ ^\circ\mathrm{C}$. E' at various constant temperatures can be superimposed so that a smooth curve is constructed. Therefore, TTSP is applicable for the storage modulus for the transverse direction of unidirectional CFRP laminates.

The time–temperature shift factor $a_{T_0}(T)$, which is the horizontal shift amount shown by rectangular symbols in Figure 12.8(b), can be formulated by Eqn (12.14). The temperature shift factor $b_{T_0}(T)$, which is the amount of vertical shift, shown by circular symbols in Figure 12.8(b), can be fit with Eqn (12.15).

The creep compliance D_c of matrix resin was back-calculated from the storage modulus E' for the transverse direction of unidirectional CFRP laminates using (Christensen, 1982)

$$D_c(t) \sim 1/E(t), \quad E(t) \cong E'(\omega)|_{\omega \to 2/(\pi t)} \tag{12.16}$$

and a modified rule of mixture by Tsai (1992) as

$$\frac{1}{E_m} = \frac{1}{V_y^*}\left[\frac{1+V_y^*}{E_T} - \frac{1}{E_{fT}}\right], V_y^* = 0.516\frac{V_m}{V_f} \tag{12.17}$$

in which E_m and E_{fT} respectively denote Young's modulus of matrix resin and transverse modulus of fiber. V_m and V_f respectively stand for the volume fraction of matrix and fibers. The master curve of back-calculated D_c of matrix resin is shown in Figure 12.9. The master curve of D_c can be formulated as Eqn (12.13). Parameters obtained from the formulations for $a_{T_0}(T)$, $b_{T_0}(T)$, D_c, and parameters E_{ft}, V_m, and V_f for back-calculation of D_c are listed in Table 12.1.

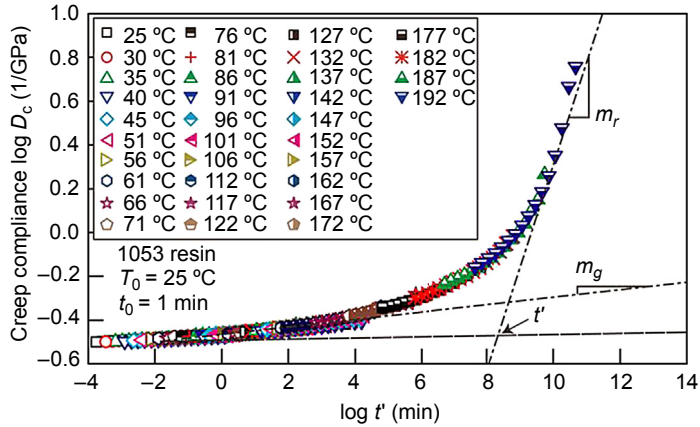

Figure 12.9 Master curve of creep compliance for matrix resin calculated from the storage modulus for the transverse direction of unidirectional carbon fiber reinforced plastics laminates.

Advanced accelerated testing methodology for long-term life prediction of CFRP laminates, *Journal of Composite Materials*, http://dx.doi.org/10.1177/0021998313515019, Sage.

Table 12.1 Parameters for master curve of creep compliance for matrix resin

T_0 (°C)	25
D_{c0} (1/GPa)	0.330
T'_0 (min)	1
m_g	0.00950
m_r	0.260
t'_g (min)	1.12E08
ΔH_1 (kJ/mol)	101
ΔH_2 (kJ/mol)	760
T_g (°C)	162
B_0	1.13E-02
B_1	−9.85E-04
B_2	2.43E-05
B_3	−2.23E-07
B_4	6.98E-10
E_{fl} (GPa)	29.3
V_m	0.45
V_f	0.55

Advanced accelerated testing methodology for long-term life prediction of CFRP laminates, *Journal of Composite Materials*, http://dx.doi.org/10.1177/0021998313515019, Sage.

12.4.3 Master curves of static and fatigue strengths for unidirectional CFRP

For strength $\sigma_f(t',T_0)$ under static loading, Eqn (12.12) can be simplified to

$$\log \sigma_f(P_f, t', T_0) = \log \sigma_0\left(t'_0, T_0\right) + \frac{1}{\alpha}\log[-\ln(1-P_f)] - n_r \log\left[\frac{D^*(t', T_0)}{D_c\left(t'_0, T_0\right)}\right] \tag{12.18}$$

in which D^* is the viscoelastic coefficient to the input of constant strain rate and is obtained using the following equation (Nakada & Miyano, 2013):

$$D^*(t', T_0) \approx D_c\left(\frac{t'}{2}, T_0\right) \tag{12.19}$$

For strength $\sigma_f(t', T_0)$ under cyclic loading in which stress ratio R is zero and the accumulation index of damage k_D is zero, Eqn (12.12) can be simplified to

$$\log \sigma_f(P_f, t', T_0, N_f, R) = \log \sigma_0\left(t_0', T_0\right) + \frac{1}{\alpha}\log[-\ln(1-P_f)] - n_r \log\left[\frac{D^*(t', T_0)}{D_c\left(t_0', T_0\right)}\right] - \frac{1}{2} n_f \log(2N_f) \tag{12.20}$$

in which D^* is expressed by the following equation for sinusoidal cyclic load pattern:

$$D^*(t', T_0) \approx \frac{1}{2} D_c(t', T_0) + \frac{1}{2} D_c\left(\frac{1}{4f'}, T_0\right), \quad f' = \frac{N_f}{t'} \tag{12.21}$$

In this equation, f' is the reduced frequency at reference temperature T_0.

Figure 12.10(a) shows the Weibull distribution of static strength of CFRP laminates at $T = 25\ ^\circ\mathrm{C}$ for four directions of X, X', Y, and Y'. From these results, the scale and shape parameters σ_{0s} and α_s for the static strength at $T = 25\ ^\circ\mathrm{C}$ can be determined as listed in Table 12.2. Figure 12.11 shows the temperature dependence of static strength of CFRP laminates for four directions of X, X', Y, and Y'. These strengths clearly depend on temperature. Figure 12.12 shows the relation between the static strength of CFRP laminates and the viscoelastic compliance of matrix resin corresponding at same time and temperature. The time and temperature dependence of static strengths for CFRP laminates against the viscoelastic compliance of matrix resin are determined uniquely. These slopes are each constant. The material parameter n_r can be determined as the slop of this relation. Figure 12.10(b) shows the Weibull distribution of static strength of CFRP laminates for all temperatures tested. From these results, the scale and shape parameters σ_{0r} and α_r for the static strength for all temperatures tested can be determined as listed in Table 12.2. The σ_{0r} and α_r are almost same to σ_{0s} and α_s for each direction. Therefore, the failure probability of static strength of CFRP laminates in each direction is independent of temperature.

Figure 12.13 shows the fatigue strength of CFRP laminates versus number of cycles to failure for all temperatures tested. The fatigue strength in each direction clearly depends on temperature. Figure 12.14(a) shows the strength degradation of CFRP laminates versus number of cycles to failure. The strength degradation of CFRP laminates that is f_C can be determined by subtracting the strength variation by viscoelastic compliance of matrix resin from the fatigue strength in Figure 12.13. Figure 12.10(c) shows the Weibull distribution of strength degradation of CFRP laminates for all temperatures tested. From these results, the scale and shape parameters σ_{0f} and α_f can be determined as listed in Table 12.2. The α_f for each direction is much smaller than α_r of static strength for all temperatures tested. It is considered that the fatigue failure mechanism for each direction at high temperature (150 °C)

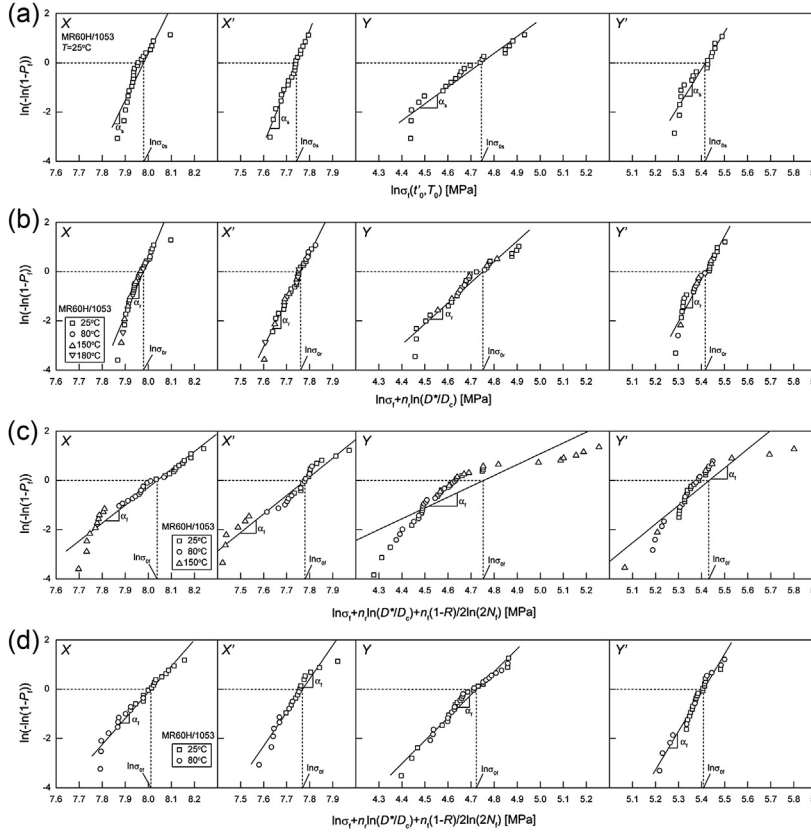

Figure 12.10 Weibull distributions for the strength of carbon fiber reinforced plastics laminates, (a) Static strength of CFRP laminates at $T = 25$ °C, (b) Static strength of CFRP laminates for all temperatures tested, (c) Fatigue strength of CFRP laminates for all temperatures tested, (d) Fatigue strength of CFRP laminates at $T = 25$ °C and 80 °C.
Advanced accelerated testing methodology for long-term life prediction of CFRP laminates, *Journal of Composite Materials*, http://dx.doi.org/10.1177/0021998313515019, Sage.

is different with those at 25 and 80 °C. Therefore, we determined the strength degradation of CFRP laminates except the data measured at 150 °C. Figures 12.14(b) and 12.10(d) respectively show the strength degradation of CFRP laminates versus number of cycles to failure and the Weibull distribution of strength degradation at 25 and 80 °C. From these results, the scale and shape parameters σ_{0f} and α_f can be determined as listed in Table 12.2. The α_f for each direction is almost similar to that of static strength α_r except the results for X direction. It can be presumed that the tensile fatigue strengths for X direction are affected by stress concentration in the grip of specimen; therefore, the scatter of fatigue strength is large.

Figures 12.15 and 12.16 respectively show the master curves of static and fatigue strengths of CFRP laminates for each direction. The solid, dashed, and dotted lines show the scale parameter and failure probability levels for 90% and 10%,

Table 12.2 Parameters for master curve of fatigue strength for unidirectional carbon fiber reinforced plastics laminates

	X	*X′*	*Y*	*Y′*
n_r	0.165	0.605	1.54	2.11
n_f	0.0903	0.0455	0.0785	0.0335
n_f[a]	0.0728	0.0343	0.122	0.0417
σ_{0s} (MPa)	2923	2305	115	225
σ_{0r} (MPa)	2919	2349	116	225
σ_{0f} (MPa)	3098	2394	116	229
σ_{0f} (MPa)[a]	3016	2367	113	223
α_s	19.1	23.1	6.81	15.0
α_r	22.3	18.9	8.39	17.3
α_f	7.26	7.55	4.39	7.61
α_f[a]	10.6	13.6	9.31	15.7

[a]Except the data measured at 150 °C.
Advanced accelerated testing methodology for long-term life prediction of CFRP laminates, *Journal of Composite Materials*, http://dx.doi.org/10.1177/0021998313515019, Sage.

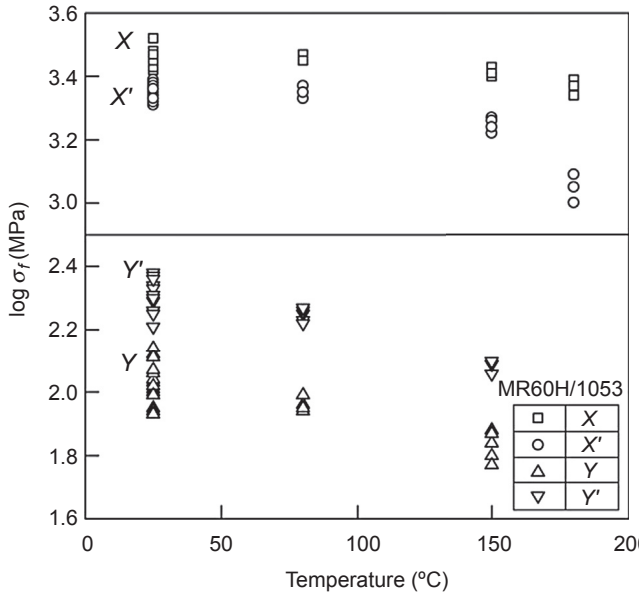

Figure 12.11 Temperature dependence for the static strength of carbon fiber reinforced plastics laminates.
Advanced accelerated testing methodology for long-term life prediction of CFRP laminates, *Journal of Composite Materials*, http://dx.doi.org/10.1177/0021998313515019, Sage.

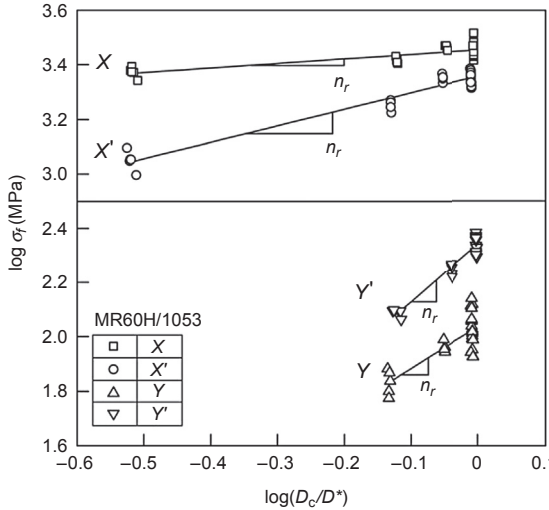

Figure 12.12 Static strength of carbon fiber reinforced plastics laminates versus viscoelastic compliance of matrix resin.
Advanced accelerated testing methodology for long-term life prediction of CFRP laminates, *Journal of Composite Materials*, http://dx.doi.org/10.1177/0021998313515019, Sage.

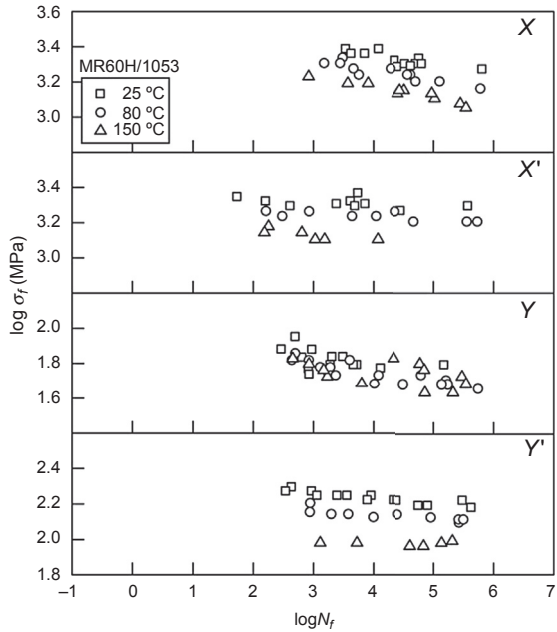

Figure 12.13 Fatigue strength of carbon fiber reinforced plastics laminates versus number of cycles to failure at various temperatures.
Advanced accelerated testing methodology for long-term life prediction of CFRP laminates, *Journal of Composite Materials,* http://dx.doi.org/10.1177/0021998313515019, Sage.

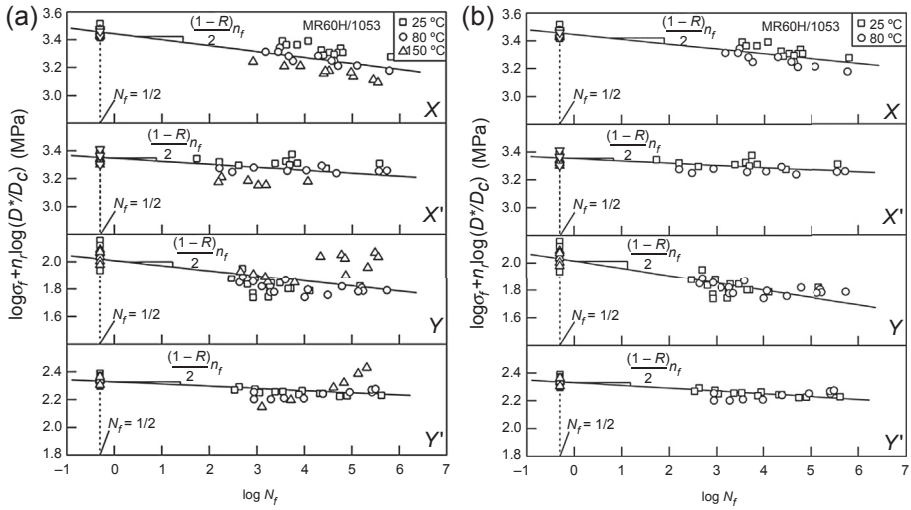

Figure 12.14 Strength degradation of carbon fiber reinforced plastics laminates by the number of cycles to failure at various temperatures, (a) include the data measured at all temperatures tested, (b) except the data measured at 150 °C.
Advanced accelerated testing methodology for long-term life prediction of CFRP laminates, *Journal of Composite Materials*, http://dx.doi.org/10.1177/0021998313515019, Sage.

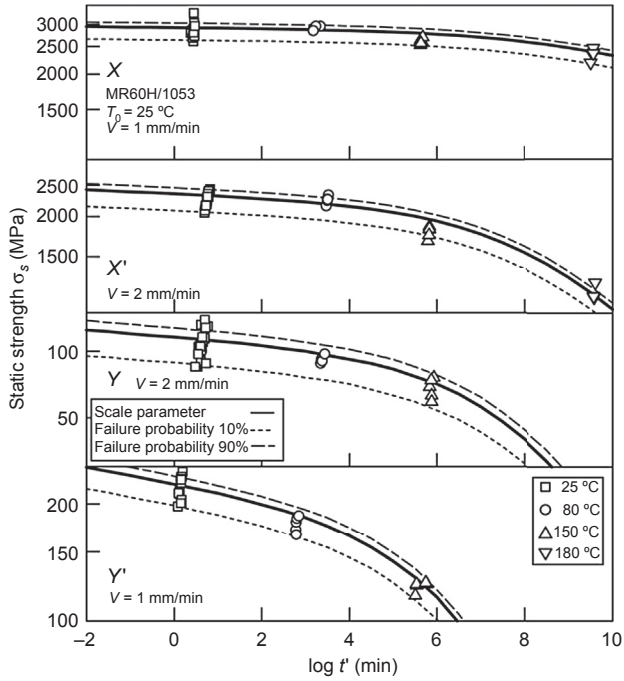

Figure 12.15 Master curves for static strength of carbon fiber reinforced plastics laminates.
Advanced accelerated testing methodology for long-term life prediction of CFRP laminates, *Journal of Composite Materials*, http://dx.doi.org/10.1177/0021998313515019, Sage.

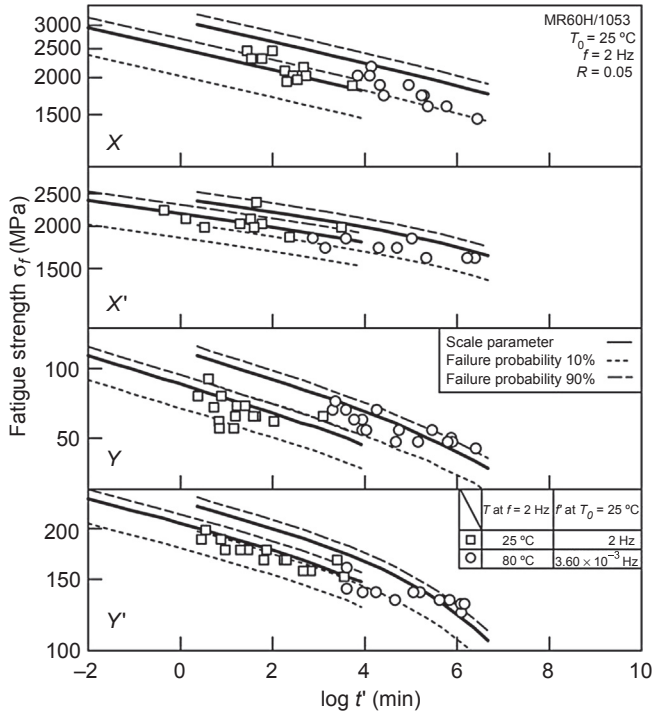

Figure 12.16 Master curves for fatigue strength of carbon fiber reinforced plastics laminates. Advanced accelerated testing methodology for long-term life prediction of CFRP laminates, *Journal of Composite Materials*, http://dx.doi.org/10.1177/0021998313515019, Sage.

respectively. The master curves of static strength for each direction agree well with experimental data for all temperatures tested. The master curves of fatigue strength for each direction agree well with experimental data, except those measured at 150 °C. The failure mechanism of CFRP laminates for cyclic loading at high temperature near the glass transition temperature should be discussed in another paper.

12.5 Conclusions

We proposed an ATM-2 for long-term life prediction of CFRP laminates exposed to actual loading with a general stress and temperature history based on the conventional ATM-1 established for the long-term life prediction of CFRP laminates exposed to stress and temperature. The most important condition for ATM-1 is that the TTSP held for the viscoelastic behavior of matrix resin holds also for the static, creep, and fatigue strengths of CFRP laminates. We introduced three conditions as the scientific bases of ATM-2: (A) the failure probability of CFRP laminates is independent of time, temperature, and load history; (B) the time and

temperature dependence of strength of CFRP laminates is controlled by the viscoelasticity of matrix resin, therefore, the same TTSP for the viscoelasticity of matrix resin holds for the strength of CFRP laminates; and (C) the slope of S−N curve is determined by maximum stress and stress ratio. It is independent of time, temperature, and frequency.

The long-term fatigue strength of CFRP laminates under an actual loading was formulated based on the three conditions. The viscoelastic coefficients of matrix resin, which perform an important role for the time and temperature dependence of long-term life of CFRP laminates, were also formulated based on TTSP. The applicability of ATM-2 was confirmed by predicting the long-term fatigue strengths in four typical loading directions for unidirectional CFRP laminates.

The predicted results from coupon data can be useful as the failure criteria in the tension and compression directions in the fiber direction and transverse to the fiber direction. The long-term performance of lager plates/structures will be estimate from these data by using some finite element analyses.

Acknowledgments

The authors thank the Office of Naval Research (ONR) for supporting this work through an ONR award with Dr. Yapa Rajapakse as the ONR program officer. Our award, numbered as N000140611139, is "Verification of Accelerated Testing Methodology for Long-Term Durability of CFRP laminates for Marine Use." The authors thank Professor Richard Christensen, Stanford University, as a consultant for this project.

References

Cai, H., Nakada, M., & Miyano, Y. (2013). Simplified determination of long-term viscoelastic behavior of amorphous resin. *Mechanics of Time-Dependent Materials, 17*, 137−146. http://dx.doi.org/10.1007/s11043-012-9174-0.

Christensen, R. M. (1982). *Theory of viscoelasticity* (2nd ed.). Mineola, NY: Dover Publications, Inc.

Christensen, R. M., & Miyano, Y. (2006). Stress intensity controlled kinetic crack growth and stress history dependent life prediction with statistical variability. *International Journal of Fracture, 137*, 77−87. http://dx.doi.org/10.1007/s10704-005-9062-6.

Miyano, Y., Nakada, M., & Cai, H. (2008). Formulation of long-term creep and fatigue strengths of polymer composites based on accelerated testing methodology. *Journal of Composite Materials, 42*, 1897−1919. http://dx.doi.org/10.1177/0021998308093913.

Miyano, Y., Nakada, M., Kudoh, H., & Muki, R. (1999). Prediction of tensile fatigue life under temperature environment for unidirectional CFRP. *Advanced Composite Materials, 8*, 235−246.

Miyano, Y., Nakada, M., McMurray, M. K., & Muki, R. (1997). Prediction of flexural fatigue strength of CFRP composites under arbitrary frequency, stress ratio and

temperature. *Journal of Composite Materials, 31*, 619−638. http://dx.doi.org/10.1177/002199839703100605.

Miyano, Y., Nakada, M., & Muki, R. (1999). Applicability of fatigue life prediction method to polymer composites. *Mechanics of Time-Dependent Materials, 3*, 141−157.

Miyano, Y., Nakada, M., & Sekine, N. (2005). Accelerated testing for long-term durability of FRP laminates for marine use. *Journal of Composite Materials, 39*, 5−20. http://dx.doi.org/10.1177/0021998305046430.

Miyano, Y., Shimbo, M., & Kunio, T. (1982). Viscoelastic analysis of residual stress in quenched thermosetting resin beams. *Experimental Mechanics, 22*, 310−316.

Nakada, M., & Miyano, Y. (2009). Accelerated testing for long-term fatigue strength of various FRP laminates for marine use. *Composites Science and Technology, 69*, 805−813. http://dx.doi.org/10.1016/j.compscitech.2008.02.030.

Nakada, M., & Miyano, Y. (2013). Formulation of time- and temperature-dependent strength of unidirectional carbon fiber reinforced plastics. *Journal of Composite Materials, 47*, 1897−1906. http://dx.doi.org/10.1177/0021998312452025.

Nakada, M., Miyano, Y., Cai, H., & Kasamori, M. (2011). Prediction of long-term viscoelastic behavior of amorphous resin based on the time-temperature superposition principle. *Mechanics of Time-Dependent Materials, 15*, 309−316. http://dx.doi.org/10.1007/s11043-011-9139-8.

Tsai, S. W. (1992). *Theory of composites design*. Dayton, OH: Think Composites.

Effects of environment on creep behavior of three oxide–oxide ceramic matrix composites at 1200 °C

13

M.B. Ruggles-Wrenn
Air Force Institute of Technology, Wright-Patterson Air Force Base, OH, USA

13.1 Introduction

Advances in power generation systems for aircraft engines, land-based turbines, rockets, and, most recently, hypersonic missiles and flight vehicles have raised the demand for structural materials that have superior long-term mechanical properties and retained properties under high temperature, high pressure, and varying environmental factors, such as moisture (Schmidt et al., 2004; Zawada, Staehler, & Steel, 2003; Zok, 2006). Typical components include combustors, nozzles, and thermal insulation. Ceramic matrix composites (CMCs), capable of maintaining excellent strength and fracture toughness at high temperatures are prime candidate materials for such applications. Because these applications require exposure to oxidizing environments, the thermodynamic stability and oxidation resistance of CMCs are vital issues. The need for environmentally stable composites motivated the development of CMCs based on environmentally stable oxide constituents (Lange, Tu, & Evans, 1995; Moore, Mah, & Keller, 1994; Mouchon & Colomban, 1995; Sim & Kerans, 1992; Szweda, Millard, & Harrison, 1997; Tu, Lange, & Evans, 1996).

The main advantage of CMCs over monolithic ceramics is their superior toughness, tolerance to the presence of cracks and defects, and noncatastrophic mode of failure. It is widely accepted that to avoid brittle fracture behavior in CMCs and improve the damage tolerance, a weak fiber/matrix interface is needed, which serves to deflect matrix cracks and to allow subsequent fiber pullout (Evans & Zok, 1994; Kerans, Hay, Parthasarathy, & Cinibulk, 2002; Kerans & Parthasarathy, 1999). It has been demonstrated that similar crack-deflecting behavior can also be achieved by means of a finely distributed porosity in the matrix instead of a separate interface between matrix and fibers (Levi, Yang, Dalgleish, Zok, & Evans, 1998). This microstructural design philosophy implicitly accepts the strong fiber/matrix interface. The concept has been successfully demonstrated for oxide–oxide composites (Hegedus, 1991; Kanka & Schneider, 2000; Lange et al., 1995; Lu, 1996; Szweda et al., 1997; Tu et al., 1996). Resulting oxide/oxide CMCs exhibit damage tolerance combined with inherent oxidation resistance. An extensive review of the mechanisms and mechanical properties of porous-matrix CMCs is given in Zok (2006 and Zok and Levi (2001).

Structural Integrity and Durability of Advanced Composites. http://dx.doi.org/10.1016/B978-0-08-100137-0.00013-4

Porous-matrix oxide/oxide CMCs exhibit several behavior trends that are distinctly different from those exhibited by traditional CMCs with a fiber−matrix interface. Most silcon carbide fiber-containing CMCs with dense matrix exhibit longer life under static loading and shorter life under cyclic loading (Lee, Zawada, Staehler, & Folsom, 1998). For these materials, fatigue is significantly more damaging than creep. Zawada, Hay, Lee, and Staehler (2003) examined the high-temperature mechanical behavior of a porous matrix Nextel™610/aluminosilicate composite. Results revealed excellent fatigue performance at 1000 °C, the material exhibited high fatigue limit, long fatigue life, and near 100% strength retention. Conversely, creep lives were short, indicating low creep resistance and limiting the use of that CMC to temperatures below 1000 °C.

Recently, several research groups investigated high-temperature mechanical properties and behavior of oxide−oxide CMCs based on different constituents and processing techniques (Buchanan, John, & Zawada, 2008; Hackemann, Flucht, & Braue, 2010; Jackson, Ruggles-Wrenn, Baek, & Keller, 2007; Jefferson, Keller, Hay, & Kerans, 2008; Ruggles-Wrenn, Musil, Mall, & Keller, 2006; Ruggles-Wrenn, Yeleser, Fair, & Davis, 2009; Schmucker & Mechnich, 2008; Zawada, Hay, et al., 2003). Oxide−oxide CMCs have been shown to exhibit good stability in ambient air at elevated temperatures (Antti, Lara-Curzio, & Warren, 2004; Carelli, Fujita, Yang, & Zok, 2002; Davis, Marshall, & Morgan, 1999; Holmquist & Lange, 2003). A number of studies evaluated effects of exposure to simulated service environments on microstructural stability and tensile properties of oxide−oxide CMCs (Mattoni, Yang, Levi, & Zok, 2005; More, Lara-Curzio, Tortorelli, Brummet, & Szweda, 2005; Parthasarathy et al., 2005; Staehler & Zawada, 2000; Wannaparhun & Seal, 2003; Zawada, Staehler, et al., 2003). Nextel™720/aluminosilicate composite exhibited excellent strength retention and showed no evidence of environmental attack following ground testing on a General Electric F110 turbofan engine (Staehler & Zawada, 2000). Exposure to moisture or to salt fog had no effect on the high-temperature fatigue performance or on the retained strength values of the N610/aluminosilicate and N720/alumina composites (Zawada, Staehler, et al., 2003). Long-term (3000 h) exposure to high temperatures and pressures like those in advanced gas turbine combustor environment had minimal effect on the microstructure and strength of N720/alumina composite (More et al., 2005). Likewise, exposure in a combustor rig only slightly reduced tensile strength of the oxide−oxide CMCs (Mattoni et al., 2005; Parthasarathy et al., 2005). In these studies, the test specimens were exposed to degrading environments (long-term exposure) prior to testing, and the test results differed little from the results obtained for as-received (unexposed) specimens. However, if the specimen is subjected to mechanical loading in degrading environment, the load may change the microstructure, thereby accelerating environmental degradation.

The objective of this chapter is to review recent efforts to assess the effects of environment on high-temperature creep performance of three oxide−oxide CMCs, consisting of a porous oxide matrix reinforced with woven mullite/alumina (Nextel™720) fibers: Nextel™720/alumina, Nextel™720/aluminosilicate, and Nextel™720/alumina−mullite. Because creep is shown to be considerably more damaging to porous-matrix oxide/oxide CMCs (Lee et al., 1998; Zawada, Hay, et al., 2003), creep testing is well suited for assessing the long-term durability and

high-temperature performance of the oxide–oxide ceramic composites with porous matrix. Resulting creep performance imposes limitations on the use of these materials in high-temperature applications. High-temperature water vapor is one of several combustion products, and thus a significant component of combustion environment. Therefore, to evaluate the performance of oxide–oxide CMCs in combustion environment, it is important to understand the effects of steam on their mechanical performance and durability. Results discussed in this chapter were obtained in experiments that combined environmental exposure (i.e., air, steam, or argon and elevated temperature) with mechanical loading. The details of the experimental setup are given elsewhere (Ruggles-Wrenn & Braun, 2008; Ruggles-Wrenn & Genelin, 2009; Ruggles-Wrenn, Koutsoukos, & Baek, 2008; Ruggles-Wrenn & Kutsal, 2010; Ruggles-Wrenn et al., 2009).

13.2 Experimental arrangements

The three representative materials discussed here are Nextel™720/alumina (N720/A), Nextel™720/aluminosilicate (N720/AS), and Nextel™720/alumina–mullite (N720/AM) oxide–oxide CMCs consisting of a porous oxide matrix reinforced with 0/90 woven Nextel™720 fibers. The N720/AM composite contained approximately 12.5% (by volume) of mullite in the matrix composition. The composites were manufactured using the same processing techniques. The fiber fabric was infiltrated with the matrix in a sol–gel process. The laminate was dried with a "vacuum bag" technique under low pressure and low temperature, then pressureless sintered (Jurf & Butner, 1999). No coating was applied to the fibers. The damage tolerance of the N720/A, N720/AS, and N720/AM composites is enabled by a porous matrix. Representative micrograph of the untested N720/A material is presented in Figure 13.1(a), which shows 0° and 90° fiber tows and numerous matrix cracks. In the case of the as-processed material, most are shrinkage cracks formed during processing

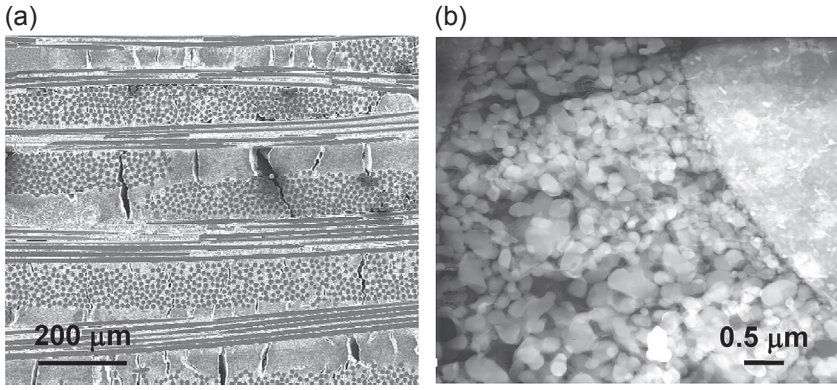

Figure 13.1 Typical microstructure of the N720/A ceramic composite: (a) overview; (b) porous nature of the matrix is evident.

rather than matrix cracks generated during loading. The porous nature of the matrix is seen in Figure 13.1(b). The untested N720/AS and N720/AM composites exhibit similar microstructural features. Basic properties of the three composites are summarized in Table 13.1.

A servocontrolled MTS (Mechanical Testing Systems) mechanical testing machine equipped with hydraulic water-cooled wedge grips, a compact two-zone resistance-heated furnace, and two temperature controllers was used in all tests. An MTS TestStar II digital controller was used for input signal generation and data acquisition. Strain measurement was accomplished with an MTS high-temperature air-cooled uniaxial extensometer of 12.5-mm gage length. Tests in the steam environment used an alumina susceptor (tube with end caps), which fits inside the furnace. The specimen gage section is located inside the susceptor, with the ends of the specimen passing through slots in the susceptor. Steam is introduced into the susceptor (through a feeding tube) in a continuous stream with a slightly positive pressure, expelling the dry air, and creating a near 100% steam environment inside the susceptor. Tests in argon environment also used an alumina susceptor. In this case ultrahigh purity argon gas (99.999% pure) was supplied to the susceptor from a high-pressure cylinder, creating an inert gas environment around the test section of the specimen. For elevated temperature testing, thermocouples were bonded to the specimen using alumina cement (Zircar) to calibrate the furnace on a periodic basis. The furnace controllers (using noncontacting thermocouples exposed to the ambient environment near the test specimen) were adjusted to determine the settings needed to achieve the desired temperature of the test specimen. The determined settings were then used in actual tests. The power settings for testing in steam (argon) were determined by placing the specimen instrumented with thermocouples in steam (argon) environment and repeating the furnace calibration procedure. Fracture surfaces of failed specimens were examined using a scanning electron microscope (SEM; FEI Quanta 200 HV) and an optical microscope (Zeiss Discovery V12). The SEM specimens were carbon coated.

All tests were performed at 1200 °C. Dog bone-shaped specimens of 152 mm total length with a 10-mm-wide gage section were used in all tests. In all tests, a specimen was heated to test temperature in 25 min and held at temperature for additional 30 min prior to testing. In air, tensile tests were performed in stroke control with a constant displacement rate of 0.05 mm/s. Creep-rupture tests were conducted in load control

Table 13.1 Average physical properties of the Nextel™720/alumina (N720/A), Nextel™720/aluminosilicate (N720/AS), and Nextel™720/alumina−mullite (N720/AM) composites

Property	N720/A	N720/AS	N720/AM
Fiber volume (%)	44	48	40
Porosity (%)	23	22	28
Density (g/cm^3)	2.79	2.68	2.57

in accordance with the procedure in ASTM standard C 1337 in laboratory air, steam, and argon. In all creep tests, the specimens were loaded to the creep stress level at the stress rate of 15 MPa/s. Creep run-out was defined as 100 h at a given creep stress. In each test, stress–strain data were recorded during the loading to the creep stress level and the actual creep period. Thus, both total strain and creep strain could be calculated and examined. To determine the retained tensile strength and modulus, specimens that achieved run-out were subjected to tensile test to failure at 1200 °C.

13.3 Mechanical behavior – effects of environment

13.3.1 Tensile stress–strain behavior

Tensile properties of the N720/A, N720/AS, and N720/AM composites at 1200 °C (Ruggles-Wrenn et al., 2008; Ruggles-Wrenn & Braun, 2008; Ruggles-Wrenn & Genelin, 2009; Ruggles-Wrenn & Kutsal, 2010) are summarized in Table 13.2. The stress–strain curves shown in Figure 13.2 typify the tensile response of the three composites at 1200 °C. The tensile properties and stress–strain behaviors of the three composites are similar. Tensile stress–strain behavior is nearly linear to failure. The three CMCs exhibit typical fiber-dominated composite behavior.

13.3.2 Creep-rupture

The tensile creep behavior of N720/A, N720/AS, and N720/AM composites with 0/90 fiber orientation was investigated at 1200 °C in laboratory air, steam, and argon (Ruggles-Wrenn & Braun, 2008; Ruggles-Wrenn & Genelin, 2009; Ruggles-Wrenn & Kutsal, 2010; Ruggles-Wrenn, Koutsoukos, et al., 2008). Results of the creep-rupture tests are summarized in Table 13.3. In tests performed at 1200 °C in air, the three composites exhibit primary and secondary creep, but no tertiary creep regime (Figures 13.3–13.5). Transition from primary to secondary creep occurs early in creep

Table 13.2 Average tensile properties of the Nextel™720/alumina (N720/A), Nextel™720/aluminosilicate (N720/AS), and Nextel™720/alumina–mullite (N720/AM) composites at 1200 °C in laboratory air

Property	N720/A	N720/AS	N720/AM
Elastic modulus (GPa)	74.7	59.6	74.0
Ultimate tensile strength (UTS) (MPa)	192	207	170
Failure strain (%)	0.38	0.47	0.35

All data are adjusted for V_f =0.44. After Ruggles-Wrenn & Braun, 2008; Ruggles-Wrenn & Genelin, 2009; Ruggles-Wrenn, Koutsoukos, et al., 2008; Ruggles-Wrenn & Kutsal, 2010.

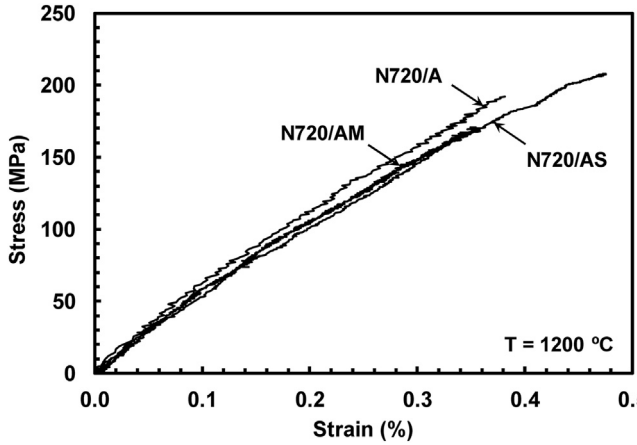

Figure 13.2 Tensile stress−strain curves for N720/A, N720/AS, and N720/AM ceramic composites obtained in tests conducted at 0.05 mm/s at 1200 °C in laboratory air. All data are adjusted for $V_f = 0.44$.

life; primary creep persists during the first ~10 h of the creep test. Secondary creep continues to failure. At a given stress, the N720/A composite accumulates larger creep strain than N720/AS or N720/AM. For N720/A and N720/AM CMCs, all creep strains accumulated in air significantly exceed the failure strain obtained in tension tests at 1200 °C. In the case of N720/AS composite, only the creep strains accumulated at stresses higher than 100 MPa exceed the failure strain produced in the tension test.

The test environment has little influence on the appearance of the creep curves obtained for all three composites at stresses ≥100 MPa, when only primary and secondary creep regimes are observed. Conversely, creep curves obtained at 80 MPa in argon and in steam show primary, secondary, and tertiary creep. In the case of N720/A and N720/AS composites, the creep strains accumulated in argon are comparable to those accumulated in air. In contrast, argon environment has a significant effect on creep strains accumulated by N720/AM composite at stresses ≤100 MPa. The presence of argon increases creep strain of N720/AM nearly tenfold at 80 MPa and by a factor of 5 at 100 MPa. Notably, the presence of steam has a considerable effect on creep strains of all three CMCs. Creep strain produced at 80 MPa in steam was five times that produced in air for N720/A, three times that obtained in air for N720/AS, and four times that in air for N720/AM.

Minimum creep rates of N720/A, N720/AS, and N720/AM composites are profoundly influenced by environment (Figure 13.6). As expected, the creep strain rates increase with increasing applied stress. At 1200 °C in air, the secondary creep rate of N720/A can be as high as 100 times that of N720/AS and 10 times that of N720/AM CMC. The creep rates of all three composites increase dramatically in steam. For a given creep stress, the N720/A creep rate in steam is approximately an order of magnitude higher than that in air. In the case of N720/AS and N720/AM composites, the creep rates in steam are nearly two orders of magnitude higher than the

Table 13.3 Summary of creep-rupture results for the Nextel™720/alumina (N720/A), Nextel™720/aluminosilicate (N720/AS), and Nextel™720/alumina–mullite (N720/AM) composites at 1200 °C in laboratory air, argon, and steam environments

Test environment	Creep stress (MPa)	Creep strain (%)	Time to rupture (h)
N720/Alumina			
Air	80	0.59	100[a]
Air	100	1.52	41.0
Air	125	1.28	18.1
Air	150	0.58	0.27
Argon	80	0.66	100[a]
Argon	100	0.96	100[a]
Argon	125	1.89	36.3
Argon	150	0.33	0.88
Steam	80	2.96	46.0
Steam	100	1.41	2.49
Steam	125	0.90	0.24
Steam	150	0.40	0.03
N720/Aluminosilicate			
Air	80	0.26	100[a]
Air	100	0.40	100[a]
Air	125	0.59	30.7
Air	150	0.53	10.0
Argon	80	0.36	100[a]
Argon	100	0.49	100[a]
Argon	125	0.39	1.77
Argon	150	0.61	1.45
Steam	80	0.79	10.9
Steam	100	0.36	0.27
Steam	125	0.58	0.20

Continued

Table 13.3 Continued

Test environment	Creep stress (MPa)	Creep strain (%)	Time to rupture (h)
N720/Alumina−Mullite			
Air	80	0.60	100[a]
Air	100	0.59	100[a]
Air	125	0.47	22.3
Air	150	0.28	0.59
Argon	80	5.86	92.8
Argon	100	2.99	18.8
Argon	125	0.66	0.45
Argon	150	0.62	0.07
Steam	80	2.49	37.0
Steam	100	1.57	4.18
Steam	125	0.48	0.38
Steam	150	0.11	0.01

[a]Run-out.
All data are adjusted for V_f =0.44. After Ruggles-Wrenn & Braun, 2008; Ruggles-Wrenn & Genelin, 2009; Ruggles-Wrenn, Koutsoukos, et al., 2008; Ruggles-Wrenn & Kutsal, 2010.

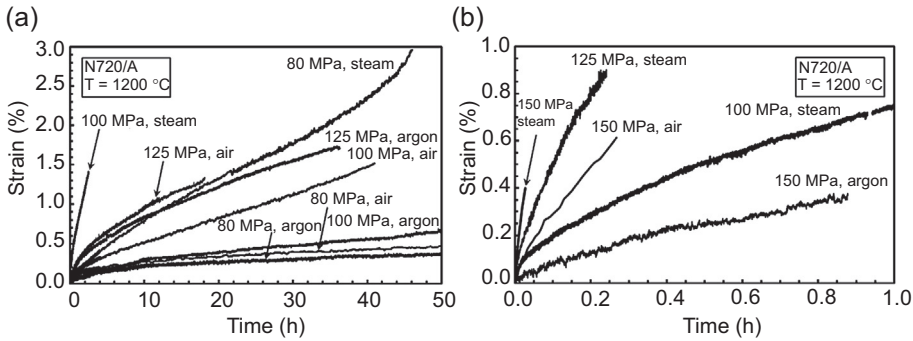

Figure 13.3 Creep strain versus time curves for N720/alumina composite at 1200 °C in air, steam, and argon: (a) at 80, 100, and 125 MPa; (b) at 125 and 150 MPa. All data are adjusted for $V_f = 0.44$.
After Ruggles-Wrenn & Braun, 2008; Ruggles-Wrenn, Koutsoukos, et al., 2008.

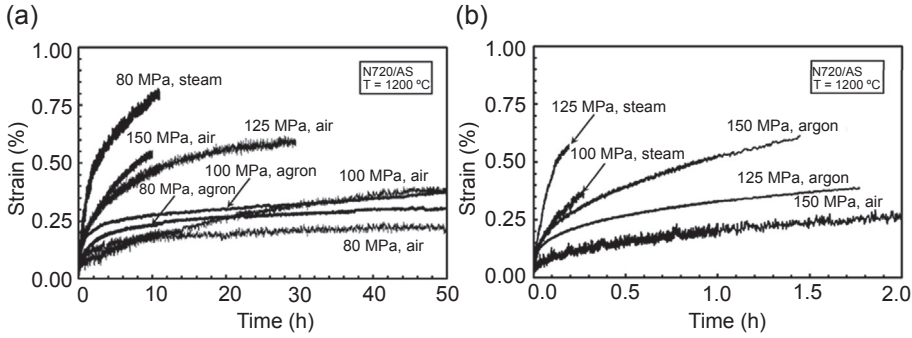

Figure 13.4 Creep strain versus time curves for N720/aluminosilicate composite at 1200 °C in air, steam, and argon: (a) at 80, 100, and 125 MPa; (b) at 125 and 150 MPa. All data are adjusted for $V_f = 0.44$.
After Ruggles-Wrenn, Koutsoukos, et al. (2008).

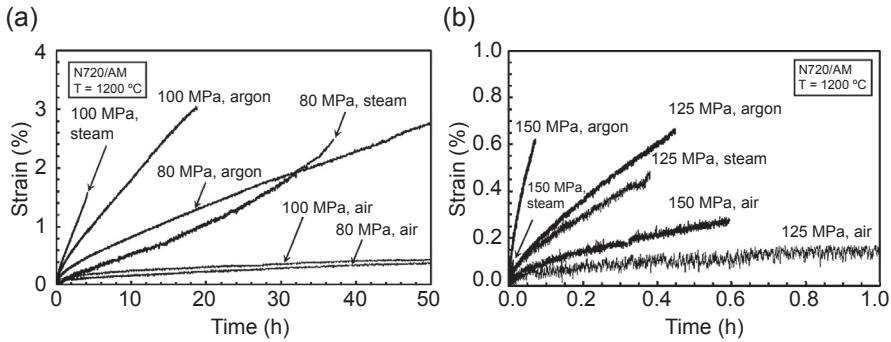

Figure 13.5 Creep strain versus time curves for N720/alumina−mullite composite at 1200 °C in air, steam, and argon: (a) at 80 and 100 MPa; (b) at 125 and 150 MPa. All data are adjusted for $V_f = 0.44$.
After Ruggles-Wrenn & Genelin, 2009; Ruggles-Wrenn & Kutsal, 2010.

creep rates obtained in air. In steam, the N720/AS creep rates are approximately an order of magnitude lower than the N720/A rates, while the N720/AM creep rates are only slightly lower than those observed for N720/A. It is noteworthy that the presence of argon also accelerates the creep rates of N720/AS and N720/AM composites. The N720/AS creep rates in argon are approximately one order of magnitude higher than those in air. The N720/AM creep rates obtained in argon are two orders of magnitude higher than the rates obtained in air and close to the rates produced in steam for a given applied stress. Contrastingly, the presence of argon did not increase the N720/A creep rates. The N720/A creep rates produced in argon are somewhat lower than those obtained in air.

The stress-rupture behavior of N720/A, N720/AS, and N720/AM composites is summarized in Figure 13.7. At 1200 °C in air, creep run-out stress was 80 MPa

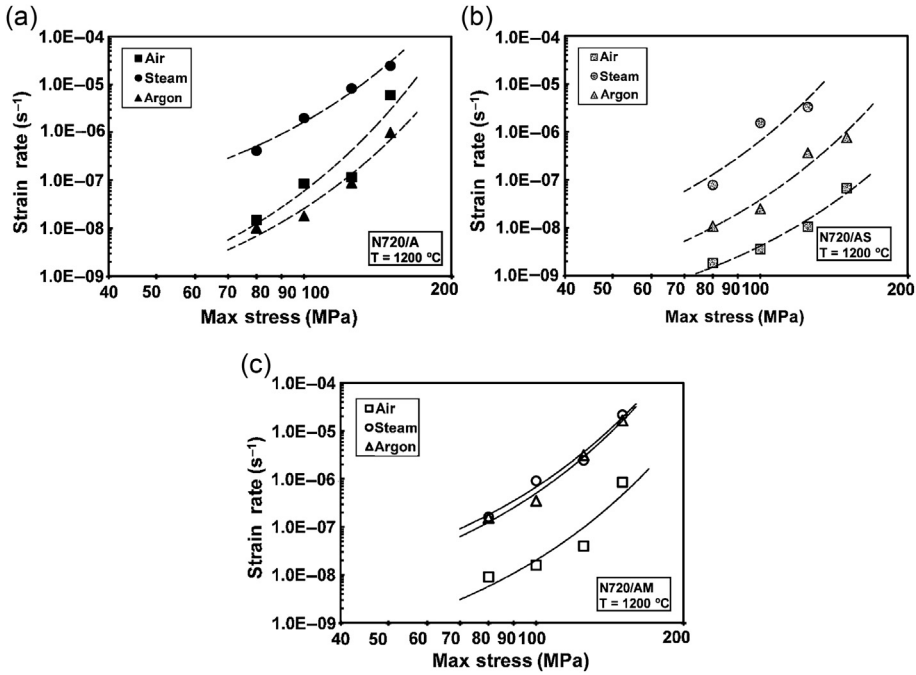

Figure 13.6 Minimum creep rate as a function of applied stress at 1200 °C in air, argon, and steam for (a) N720/A; (b) N720/AS; and (c) N720/AM ceramic composites. All data are adjusted for $V_f = 0.44$.
After Ruggles-Wrenn & Braun, 2008; Ruggles-Wrenn & Genelin, 2009; Ruggles-Wrenn, Koutsoukos, et al., 2008; Ruggles-Wrenn & Kutsal, 2010.

(∼40%UTS) for N720/A, 100 MPa (∼48%UTS) for N720/AS, and 100 MPa (∼60%UTS) for N720/AM. The presence of steam drastically reduced the creep lifetimes of N720/A, N720/AS, and N720/AM composites. For stresses ≥100 MPa, creep lifetimes of all three composites were reduced by at least 90% due to steam. None of the composites achieved creep run-out at 1200 °C in steam. The presence of argon had a beneficial effect on creep performance of N720/A, increasing the creep lifetimes at least twofold. Contrastingly, argon environment had a detrimental effect on creep lifetimes of the N720/AS and N720/AM composites. While both N720/A and N720/AS composites achieved creep run-out at 100 MPa in argon, at stresses higher than 100 MPa, creep lifetimes of N720/AS were reduced by approximately 90% due to argon. The N720/AM specimen tested at 80 MPa in argon survived 92.8 h, almost achieving creep run-out of 100 h. However, at stresses higher than 80 MPa, the presence of argon degraded creep lifetimes of N720/AM by at least 80%.

Retained tensile strength of each specimen that achieved creep run-out was evaluated in a tensile test performed at 1200 °C (Table 13.4). Prior creep at 1200 °C in either air or argon did not degrade the tensile strength of N720/AM composite. Conversely, prior creep at 1200 °C in air or in argon had a degrading effect on tensile strength of

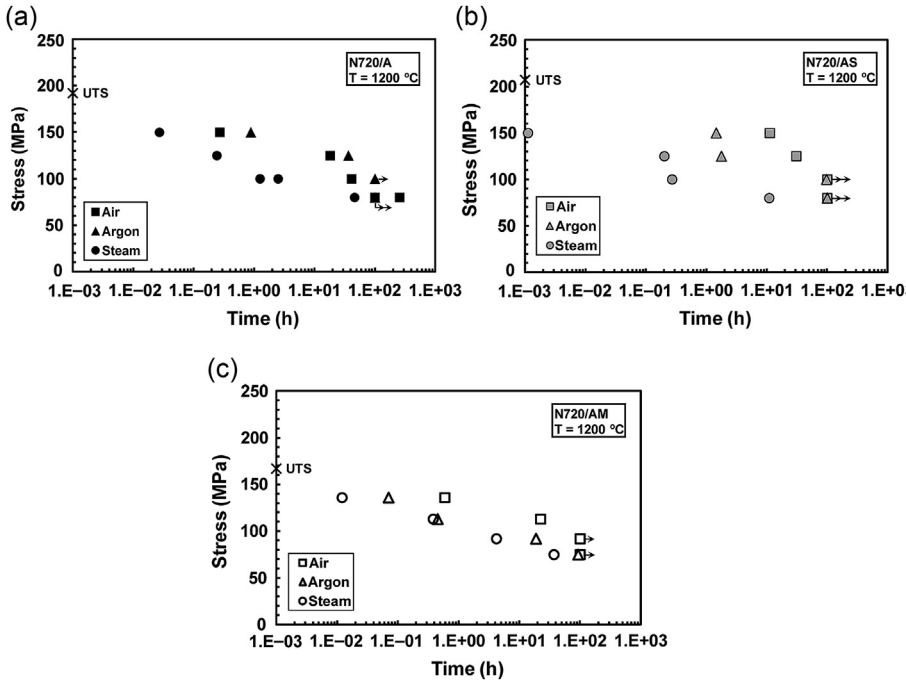

Figure 13.7 Creep stress versus time to rupture at 1200 °C in air, argon, and steam for (a) N720/A; (b) N720/AS; and (c) N720/AM ceramic composites. All data are adjusted for $V_f = 0.44$.
After Ruggles-Wrenn & Braun, 2008; Ruggles-Wrenn & Genelin, 2009; Ruggles-Wrenn, Koutsoukos, et al., 2008; Ruggles-Wrenn & Kutsal, 2010.

N720/A and N720/AS composites. The N720/A composite subjected to 100 h of creep in air retained more than 90% of its tensile strength, while the specimens pre-crept in argon retained 84−94% of their tensile strength. The N720/AS specimens subjected to 100 h of creep in air retained 43−51% of their tensile strength, whereas the specimens pre-crept in argon retained only 38−46% of their tensile strength.

Because the creep performance of the composite with 0°/90° fiber orientation is dominated by the fibers, fiber degradation is a likely source of the composite degradation. It is recognized that stress corrosion of the N720 fibers may be the mechanism behind reduced creep resistance of N720/A, N720/AS, and N720/AM composites at 1200 °C in steam. Earlier studies (Charles & Hillig, 1962, 1965; Wiederhorn, 1967, 1972; Wiederhorn, Freiman, Fuller, & Simmons, 1982) suggested that static fatigue (i.e., delayed fracture under a sustained constant load) of silica-based glasses was a chemical process, in which subcritical (slow) crack growth resulted from and was controlled by a stress-enhanced chemical reaction between glass and water in the environment. Michalske et al. (Michalske & Freiman, 1983; Michalske & Bunker, 1984, 1993) examined the role of mechanical strain in accelerating chemical reactions between the silicon monoxide (Si−O) bonds at the crack tip and environmental

Table 13.4 Retained tensile strength of the N720/A, N720/AS, and N720/AM specimens subjected to prior creep in laboratory air and in argon at 1200 °C. Retained strength measured at 1200 °C in laboratory air

Environment	Creep stress (MPa)	Retained strength (MPa)	Strength retention (%)
N720/Alumina			
Air	80	175	91
Argon	80	180	94
Argon	100	161	84
N720/Aluminosilicate			
Air	80	106	51
Air	100	89.0	43
Argon	80	96.2	46
Argon	100	79.7	38
N720/Alumina−Mullite			
Air	80	186	109
Air	100	184	108

All data are adjusted for V_f=0.44. After Ruggles-Wrenn & Braun, 2008; Ruggles-Wrenn & Genelin, 2009; Ruggles-Wrenn, Koutsoukos, et al., 2008; Ruggles-Wrenn & Kutsal, 2010.

molecules and found that the highly strained Si−O bonds reacted with water at least eight orders of magnitude faster than the unstrained bonds. Michalske and Bunker (Michalske & Bunker, 1993) proposed a quantitative chemical-kinetics-based model to predict the rate of crack growth in silica glass in humid condition as a function of the applied stress. This model describes a fracture rate law in which the crack growth rate increases exponentially with the applied stress intensity.

For glass and ceramic materials that have slow crack growth due to stress corrosion as a unique, time-dependent failure mechanism, it is possible to predict the cyclic fatigue lifetime from the static fatigue (creep) data by using a linear elastic crack growth model (Evans & Fuller, 1974). Ruggles-Wrenn, Hetrik, and Baek (2008) applied the fracture mechanics approach proposed by Evans and Fuller (Evans & Fuller, 1974) to the cyclic and static fatigue data obtained for N720/A at 1200 °C in steam. Excellent agreement between predicted cyclic lifetimes and experimental results at 0.1 Hz in steam showed that slow crack growth due to stress corrosion was the governing failure mechanism. However, for the frequencies of 1.0 and 10 Hz and applied stress levels <170 MPa, cyclic lifetimes were underestimated. Improved fatigue durability was attributed to the beneficial effect of progressive matrix cracking, suggesting that matrix plays a considerable role in the overall composite performance.

The results of the present study emphasize the importance of the matrix contribution to the overall composite performance and durability. It is seen that the three composites comprising the same N720 fibers but three different matrix materials exhibit significantly different behaviors at 1200 °C in steam. Recall that the N720/A, N720/AS, and N720/AM composites derive their damage tolerance from porous matrices. Therefore the stability of the matrix porosity against densification is critical to the composite's long-term durability. The loss of matrix porosity would inhibit crack deflection, reduce damage tolerance, and accelerate failure. Reports on the thermal degradation of porous matrix, oxide–oxide ceramic composite are scarce and somewhat conflicting. Jurf and Butner (1999) observed a ~30% decrease in tensile strength of N720/AS composite after 1000 h at 1100 °C in air, while Antti et al. (2004) reported that after 100 h at 1100 °C the strength of N720/AS fell to less than one-third of the as-processed strength. Both studies attributed the loss of tensile strength to matrix densification and increased fiber–matrix bonding. Jurf and Butner (1999) reported that N720/A composite showed full strength retention after 1000 h at 1200 °C in air. However, Fujita et al. (Fujita, Jefferson, McMeeking, & Zok, 2004; Fujita, Levi, Zok, & Jefferson, 2005) reported that for a composite consisting of Nextel™720 fibers in a porous alumina matrix, a porosity reduction of ~6% was observed after a 10-min exposure at 1200 °C, which was caused by additional sintering of the matrix. It is likely that the N720/A, N720/AS, and N720/AM specimens subjected to creep at 1200 °C in steam undergo matrix changes leading to the loss of matrix porosity. Under sustained loading, the loss of matrix porosity and the stress corrosion of the fibers work together to accelerate failure and to reduce lifetime of the composite. Microstructural examination presented below confirms that differences in the response of the matrix materials to thermal and environmental exposure under sustained loading are behind the dramatically different creep behaviors of the N720/A, N720/AS, and N720/AM composites in steam.

13.4 Composite microstructure

Optical micrographs of fracture surfaces of the as-processed N720/A, N720/AS, and N720/AM specimens tested in tension to failure are presented in Figure 13.8. All three composites exhibit damage-tolerant behavior as indicated by fibrous fracture. The fracture surfaces obtained in 125 MPa creep tests on N720/A, N720/AS, and N720/AM composites are shown in Figures 13.9, 13.10, and 13.11, respectively. The test environment appears to have little effect on the fracture surface topography of N720/A (Figure 13.9) and N720/AM (Figure 13.11) composites. The fracture surfaces obtained in steam or argon are similar to those obtained in air. The N720/A and N720/AM fracture surfaces produced in all creep tests exhibit fibrous fracture. In contrast, fracture surfaces of N720/AS composite (Figure 13.10) produced in creep tests reflect the influence of test environment. The N720/AS fracture surface produced in air exhibits substantial amount of fibrous fracture. In contrast, the N720/AS fracture surfaces obtained in argon and in steam are dominated by near-planar fracture. The N720/AS fracture surface obtained in argon shows little uncoordinated fiber failure, and that obtained in steam exhibits no fibrous fracture at all.

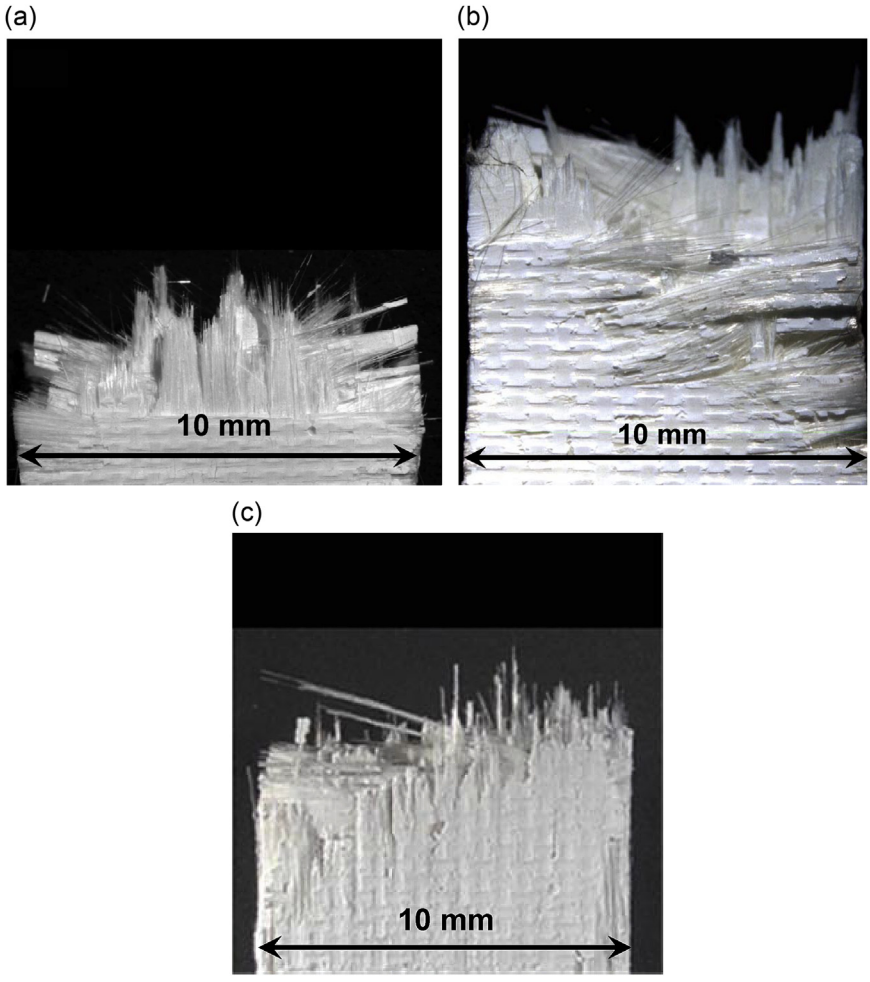

Figure 13.8 Fracture surfaces obtained in tension tests at 1200 °C for (a) N720/A; (b) N720/AS; and (c) N720/AM ceramic composites.

Further understanding of the influence of environment on the fracture surface topography and the microstructure of N720/A, N720/AS, and N720/AM specimens tested in creep at 1200 °C can be gained by examining SEM micrographs in Figures 13.12−13.14. The fracture surface of the N720/A composite obtained in argon (Figure 13.12(a)) exhibits both regions of nearly planar failure and regions of uncorrelated fiber fracture, where individual fibers are clearly discernable. While the N720/A fracture surface produced in air (Figure 13.12(b)) still exhibits some areas of fibrous fracture, areas of planar fracture become more prevalent. Finally, the N720/A fracture surface produced in steam (Figure 13.12(c)) is dominated by planar regions of coordinated fiber failure. Notably, as the extent of correlated fiber failure increases, the creep lifetime decreases. It is recognized that the increase in

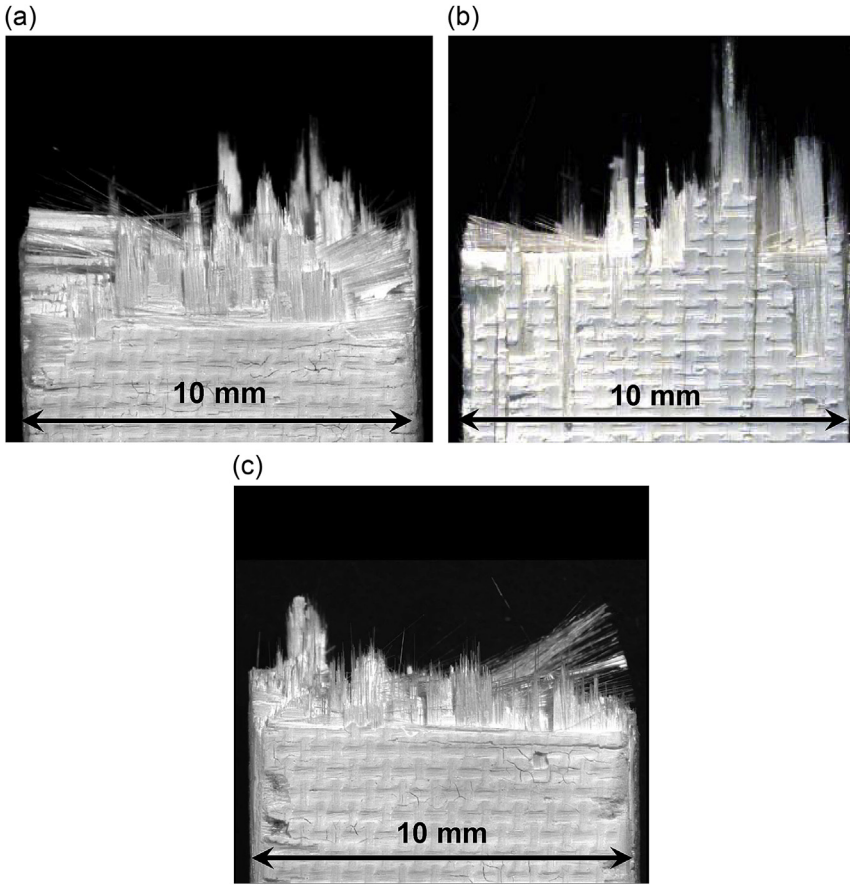

Figure 13.9 Fracture surfaces of N720/A ceramic composite obtained in creep tests at 125 MPa at 1200 °C in (a) air, $t_f = 18.1$ h; (b) argon, $t_f = 36.3$ h; and (c) steam, $t_f = 0.24$ h.

the spatial correlation in the fiber failure locations is among the main manifestations of the matrix densification (Fujita et al., 2004, 2005). The near-planar fracture surface obtained in steam indicates the loss of matrix porosity and subsequent matrix densification due to additional sintering. As a result, the N7820/A composite exhibits decreased damage tolerance and a reduced lifetime.

The fracture surfaces of the N720/AS composite obtained in air (Figure 13.13(a)) and in argon (Figure 13.13(b)) are dominated by areas of planar fracture. The fiber pullout is negligible. The 0° fibers fail in a coordinated fashion, only very short pullout of sintered bundles can be found. Yet individual 90° fibers are still observed. A dramatically different fracture surface topography is produced in steam (Figure 13.13(c)). The fracture surface is characteristic of brittle failure; the fibers and the matrix break essentially in a coplanar fashion. The material exhibits no fiber pullout, an increased fiber−matrix bonding is apparent. Furthermore, large voids can be seen throughout the fracture surface. A magnified view of a typical void is

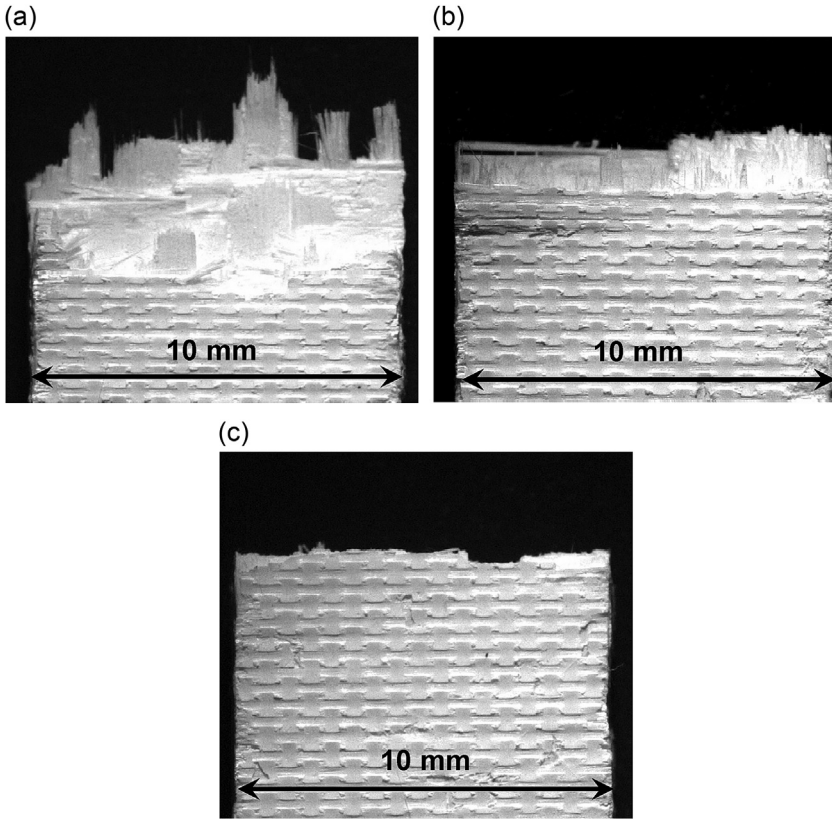

Figure 13.10 Fracture surfaces of N720/AS ceramic composite obtained in creep tests at 125 MPa at 1200 °C in: (a) air, $t_f = 30.7$ h; (b) argon, $t_f = 1.77$ h; and (c) steam, $t_f = 0.2$ h.

shown in Figure 13.13(d). The matrix of the N720/AS composite consists of Al_2O_3 particles bonded together by a continuous SiO_2 film. Matrix porosity comes from incomplete filling of the interparticle voids. The SiO_2 in the matrix is three-dimensionally constrained by the tightly packed Al_2O_3 grains and the surrounding fibers. Under this nearly hydrostatic constraint, thermal exposure leads to coarsening of the pore-size distribution, rather than to the densification of the matrix (Sherer, 1998). Pore-coarsening occurs as the regions of high capillary pressure (i.e., small pores) contract and cause larger pores to expand (Bordia & Jagota, 1993). While the total volume of the composite is constrained dimensionally by the fiber skeleton and cannot change, the smaller matrix pores shrink forcing the larger ones to grow. As a result, some matrix regions densify, while other dilate, forming voids as that seen in Figure 13.13(d). The coarsening of the porosity of the aluminosilicate matrix and the increased fiber-matrix bonding inhibit crack deflection, resulting in reduced damage tolerance and poor creep performance of the N720/AS composite in steam.

In the case of the N720/A composite tested at 1200 °C in air, argon, and steam, the fracture surface appearance could be correlated with the failure time, with a

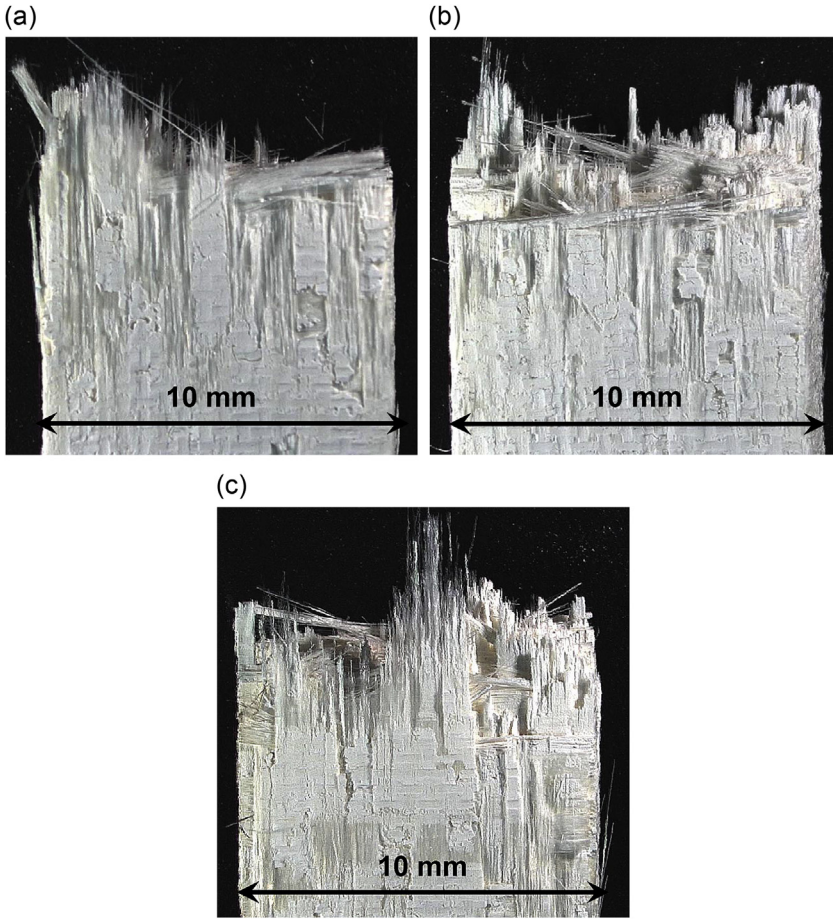

Figure 13.11 Fracture surfaces of N720/AM ceramic composite obtained in creep tests at 125 MPa at 1200 °C in (a) air, $t_f = 22.3$ h; (b) argon, $t_f = 0.45$ h; and (c) steam, $t_f = 0.38$ h.

predominantly planar fracture surface corresponding to a short life and fibrous fracture indicating longer life. The near-planar fracture surfaces were attributed to matrix densification and subsequent loss of matrix porosity, which resulted in decreased damage tolerance. In contrast, the SEM micrographs of the N720/AM fracture surfaces obtained in creep tests at 1200 °C in air, argon, and steam (Figure 13.14) indicate that for N720/AM, the fracture surface appearance cannot be directly correlated with the creep lifetime. All fracture surfaces in Figure 13.14 are dominated by planar regions of coordinated fiber failure. Even the specimens that produced the longest creep lifetimes had fracture surfaces with only minimal amounts of fibrous fracture (Figure 13.14(a) and (c)).

Figures 13.15 and 13.16 show the fracture surfaces obtained in tensile tests of the N720/A, N720/AS, and N720/AM specimens tested in creep at 80 MPa in air and in argon, respectively. Whereas all three composites achieved 100-h creep run-out at

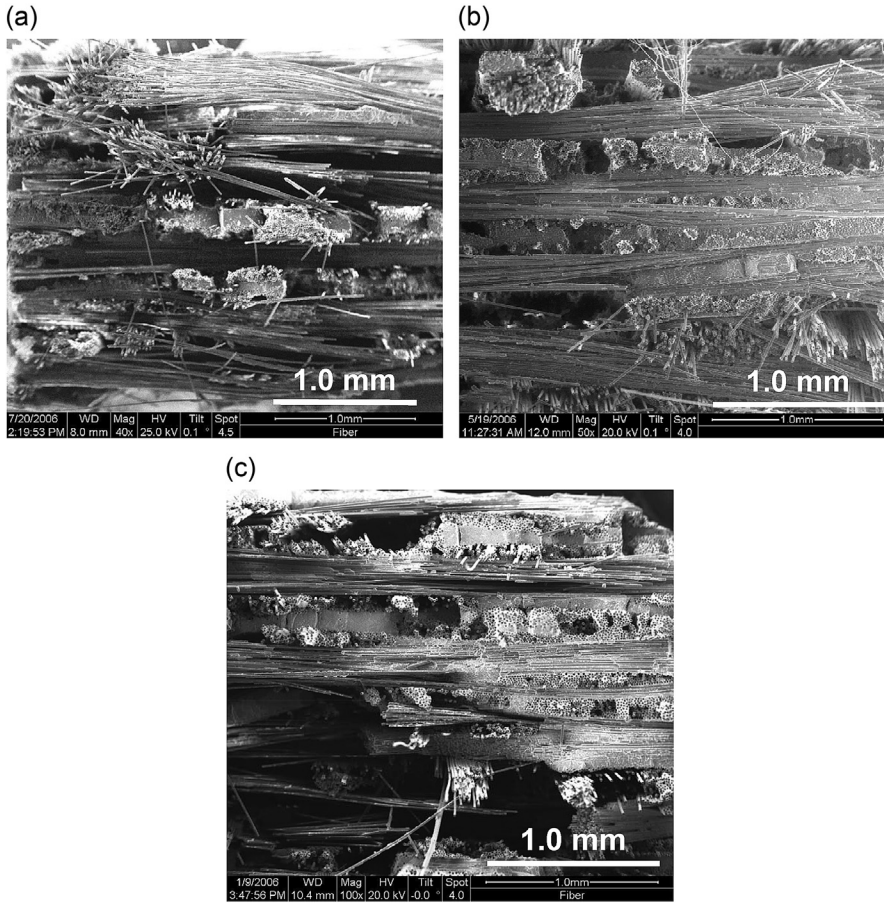

Figure 13.12 Fracture surfaces of N720/A ceramic composite obtained in creep tests at 125 MPa at 1200 °C in (a) argon, $t_f = 36.3$ h; (b) air, $t_f = 18.1$ h; and (c) steam, $t_f = 0.24$ h.

80 MPa in air, the retained properties of the three CMCs were very different. The fracture surface of the N720/A run-out specimen tested in air (Figure 13.15(a) and (b)) shows extensive fibrous fracture, as does the N720/A fracture surface produced in the 125 MPa creep test in air. The fracture surface of the N720/AM specimen tested in air (Figure 13.15(e) and (f)) also shows the largest amount of fibrous fracture among the N720/AM fracture surfaces produced in creep. Recall that the N720/A and N720/AM specimens subjected to 100-h of prior creep at 80 MPa in air retained ~94% and 100% of their tensile strength, respectively. Conversely, the fracture surface of the N720/AS run-out specimen tested in air (Figure 13.15(c) and (d)) has the same appearance as the fracture surface of the N720/AS specimen subjected to creep in steam. The near-planar fracture surface in Figure 13.15(c) is dominated by areas of coordinated fiber failure and shows increased fiber−matrix bonding. In addition, multiple large voids, as the one shown in Figure 13.15(d), are also seen.

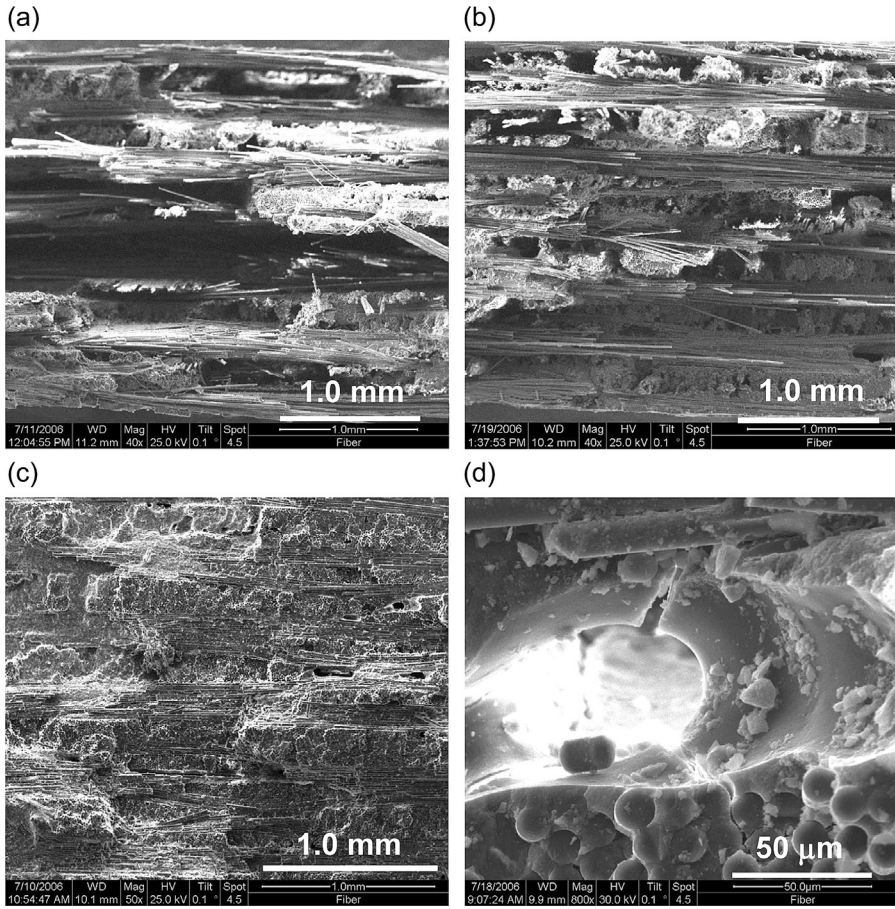

Figure 13.13 Fracture surfaces of N720/AS ceramic composite obtained in creep tests at 125 MPa at 1200 °C in (a) air, $t_f = 30.7$ h; (b) argon, $t_f = 1.77$ h; (c) steam, $t_f = 0.2$ h; and (d) steam, showing a matrix void.

It appears that coarsening of the matrix porosity occurred during the 100 h creep test at 80 MPa in air, which led to loss of nearly 50% of tensile strength.

The fracture surfaces in Figure 13.16 suggest that the same conclusions can be drawn with respect to the N720/A and N720/AS specimens subjected to 100 h of creep at 80 MPa in argon. The fracture surface of the N720/A composite (Figure 13.16(a) and (b)) shows fairly extensive regions of uncorrelated fiber fracture. This suggests that matrix changes and, consequently, degradation of retained properties were limited. Indeed, the N720/A specimen subjected to 100-h of prior creep at 80 MPa in argon retained ~94% of its tensile strength. In contrast, the N720/AS fracture surface in Figure 13.15(c) and (d) shows planar failure and increased fiber–matrix bonding as well as numerous voids. Apparently 100-h exposure under load at 1200 °C in argon also causes changes in the aluminosilicate matrix that lead to considerable loss of tensile strength.

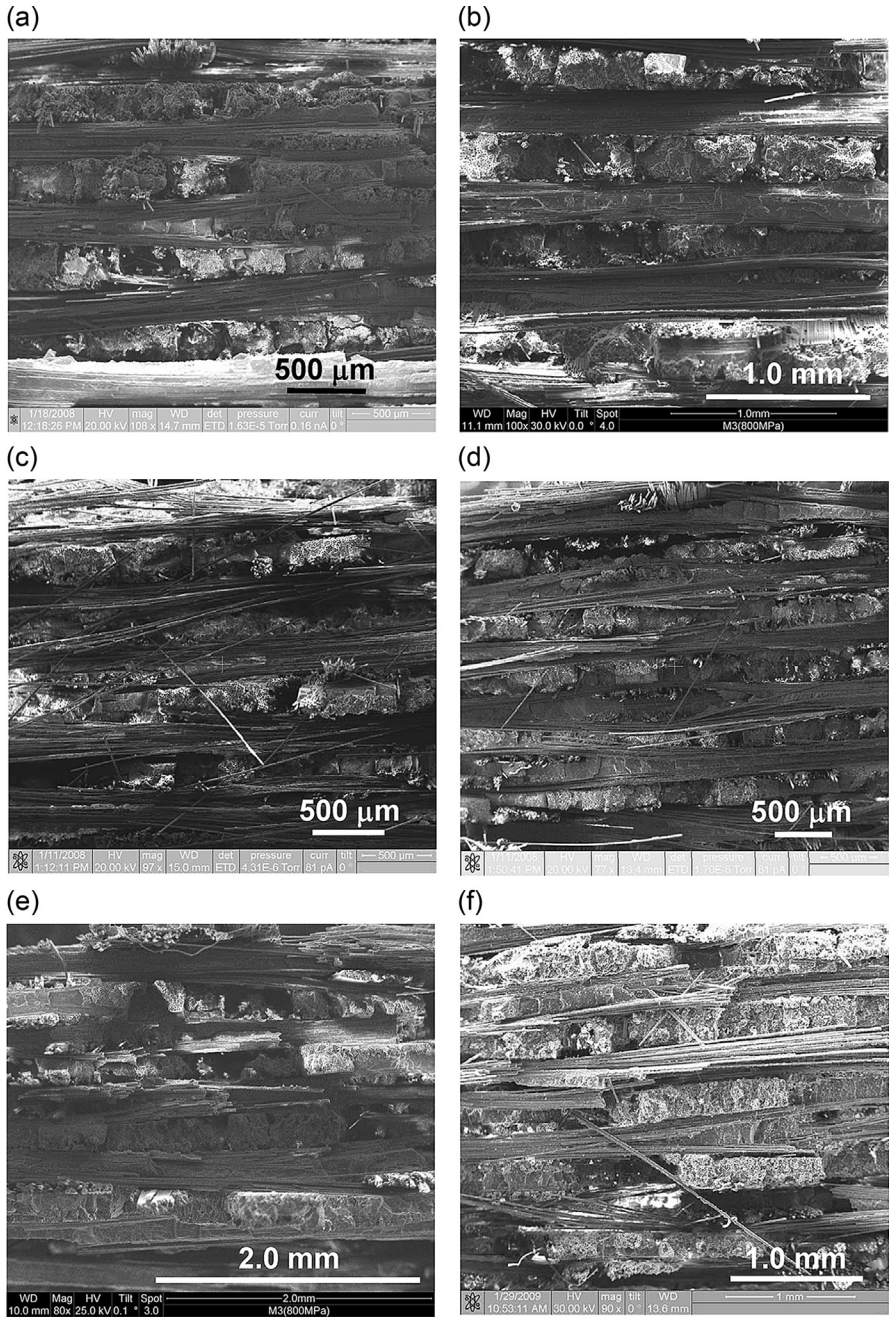

Figure 13.14 Fracture surfaces of N720/AM ceramic composite obtained in creep tests at 1200 °C (a) at 80 MPa in air, $t_f > 100$ h; (b) at 150 MPa in air, $t_f = 0.59$ h; (c) at 80 MPa in argon, $t_f = 92.8$ h; (d) at 150 MPa in argon, $t_f = 0.07$ h; (e) at 80 MPa in steam, $t_f = 37$ h; and (f) at 150 MPa in steam, $t_f = 0.01$ h.

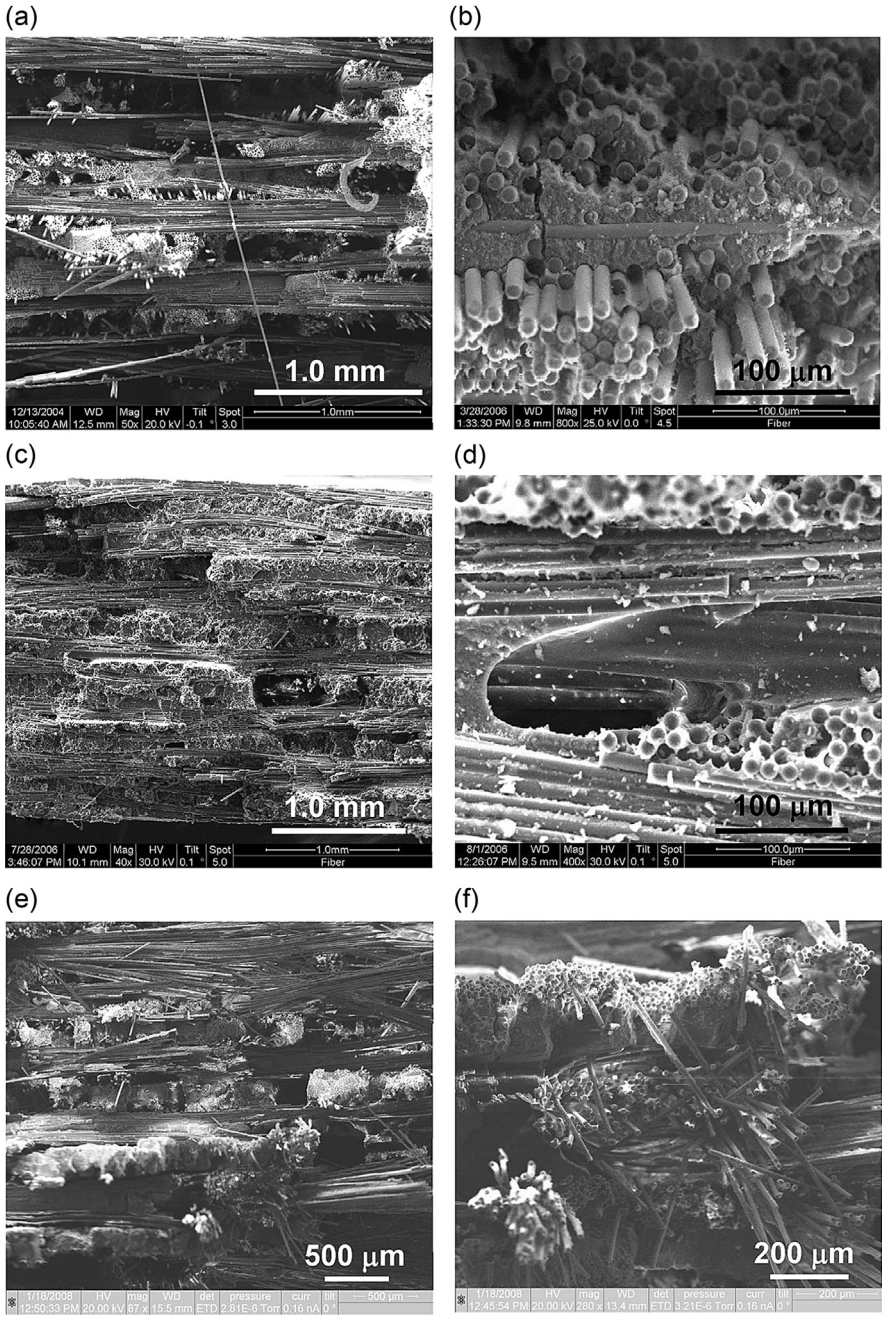

Figure 13.15 SEM micrographs of the fracture surfaces obtained in tensile tests conducted on specimens subjected to 100 h of prior creep at 80 MPa at 1200 °C in air. (a)−(b) N720/A; (c)−(d) N720/AS; (e)−(f) N720/AM.

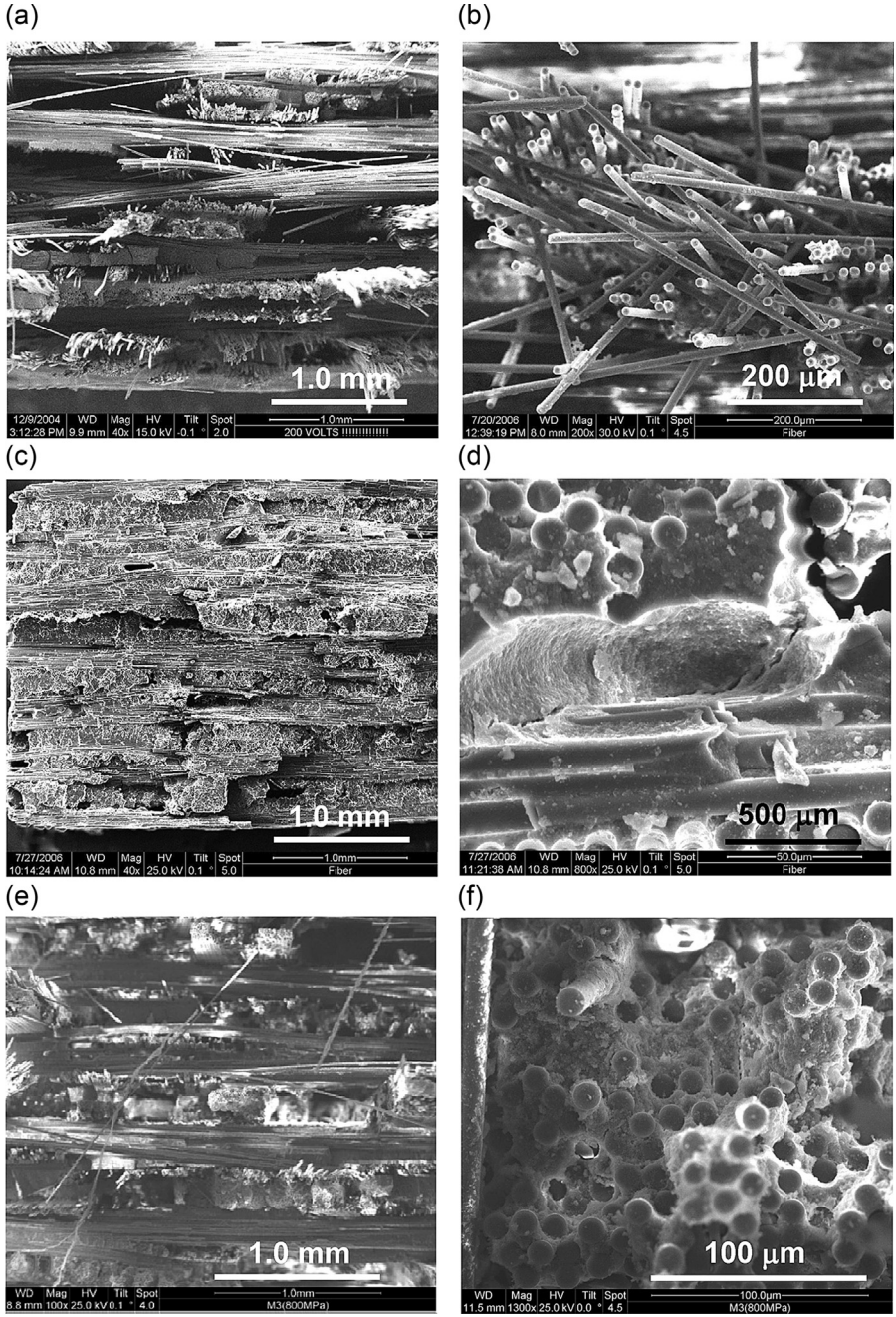

Figure 13.16 SEM micrographs of the fracture surfaces obtained in tensile tests conducted on specimens subjected to 100 h of prior creep at 80 MPa at 1200 °C in argon. (a)−(b) N720/A, $t_f > 100$ h; (c)−(d) N720/AS, $t_f > 100$ h; (e)−(f) N720/AM, $t_f = 92.8$ h.

The fracture surfaces of the N720/AM specimens tested at 80 MPa in air (Figure 13.15(e)) and in argon (Figure 13.16(e)) appear to have the same general features. However, larger magnification views of these fracture surfaces (Figures 13.15(f) and 13.16(f)) reveal notable differences. The specimen tested in air exhibits extensive fibrous fracture (Figure 13.15(f)), indicating that loss of matrix porosity was limited. Note that this specimen achieved a 100-h creep run-out and retained 100% of its tensile strength. In contrast, the specimen tested in argon shows mainly correlated fiber failure (Figure 13.16(f)), suggesting that the matrix porosity is diminished. As a result the creep lifetime was reduced, the specimen failed after 92.8 h at 80 MPa in argon.

13.5 Concluding remarks

The creep-rupture behaviors of the N720/A, N720/AS, and N720/AM composites were characterized at 12,000 °C in air, steam, and argon environments. In air, the three oxide−oxide composites exhibit primary and secondary creep regimes. Primary, secondary, and tertiary creep regimes are observed in argon and in steam. The creep strains accumulated by N720/A and N720/AS composites in argon were comparable to those produced in air. In contrast, N720/AM accumulated much larger creep strains in argon than in air. Creep strains accumulated by all three composites at 80 MPa in steam are significantly larger than those produced in air.

Minimum creep rate was reached in all tests. In air, the secondary creep rate of N720/A can be two orders of magnitude higher than that of the N720/AS and one order of magnitude higher than that of N720/AM. The presence of argon has little effect on the creep rates of N720/A, but accelerates the creep rates of N720/AS and N720/AM. Creep rates of all three composites increase dramatically due to steam. In air, all three composites achieved creep run-out of 100 h at stresses $\leq$100 MPa. The N720/A and N720/AM composites retained more than 90% of their strength. In contrast, the N720/AS lost nearly half of its tensile strength. In argon, both N720/A and N720/AS achieved creep run-out at 100 MPa. While the presence of argon had a beneficial effect on creep lifetimes of N720/A, it degraded the creep lifetimes of N720/AS and N720/AM at stresses higher than 100 MPa. Presence of steam dramatically reduced creep lifetimes of all three composites. None of the three composite achieved creep run-out in steam.

Analysis of the fracture surfaces revealed that considerable matrix densification occurred in all three composites during creep tests at 1200 °C. The densification of the matrix due to additional sintering was accelerated in the presence of steam. Matrix densification and subsequent loss of matrix porosity are the key mechanisms responsible for degradation of creep performance of N720/A, N720/AS, and N720/AM composites at 1200 °C in steam. However, the levels of matrix porosity in the oxide−oxide CMCs examined in this work are such that the fibers are also exposed to environmental attack. Therefore fiber degradation is a possible source of composite degradation. The effect of steam on the high-temperature performance of oxide fibers is the subject of an ongoing study.

References

Antti, M.-L., Lara-Curzio, E., & Warren, R. (2004). Thermal degradation of an oxide fibre (Nextel 720)/aluminosilicate composite. *Journal of the European Ceramic Society, 24*, 565−578.

Bordia, R. K., & Jagota, A. (1993). Crack growth and damage in constrained sintering films. *Journal of the American Ceramic Society, 76*(10), 2475−2485.

Buchanan, D. J., John, R., & Zawada, L. P. (2008). Off-axis creep behavior of oxide/oxide Nextel™720/AS-0. *Composites Science and Technology, 68*, 1313−1320.

Carelli, E. A. V., Fujita, H., Yang, J. Y., & Zok, F. W. (2002). Effects of thermal aging on the mechanical properties of a porous-matrix ceramic composite. *Journal of the American Ceramic Society, 85*(3), 595−602.

Charles, R. J., & Hillig, W. B. (1962). The kinetics of glass failure by stress corrosion. In *Symposium on mechanical strength of glass and ways of improving it. Florence, Italy, September 25−29, 1961* (pp. 511−527). Charleroi, Belgium: Union Scientifique Continentale du Verre.

Charles, R. J., & Hillig, W. B. (1965). Surfaces, stress-dependent surface reactions, and strength. In V. F. Zackey (Ed.), *High-strength materials* (pp. 682−705). New York: John Wiley & Sons, Inc.

Davis, J. B., Marshall, D. B., & Morgan, P. E. D. (1999). Oxide composites of Al_2O_3 and $LaPO_4$. *Journal of the European Ceramic Society, 19*(13−14), 2421−2426.

Evans, A. G., & Fuller, E. R. (1974). Crack propagation in ceramic materials under cyclic loading conditions. *Metallurgical and Materials Transactions, 5A*(1), 27−33.

Evans, A. G., & Zok, F. W. (1994). Review: the physics and mechanics of fiber-reinforced brittle matrix composites. *Journal of Materials Science, 29*, 3857−3896.

Fujita, H., G Levi, C., Zok, F. W., & Jefferson, G. (2005). Controlling mechanical properties of porous mullite/alumina mixtures via precursor-derived alumina. *Journal of the American Ceramic Society, 88*(2), 367−375.

Fujita, H., Jefferson, G., McMeeking, R. M., & Zok, F. W. (2004). Mullite/alumina mixtures for use as porous matrices in oxide fiber composites. *Journal of the American Ceramic Society, 87*(2), 261−267.

Hackemann, S., Flucht, F., & Braue, W. (2010). Creep investigations of alumina-based all-oxide ceramic matrix composites. *Composites A, 41*, 1768−1776.

Hegedus, A. G. (1991). *Ceramic bodies of controlled porosity and process for making same*, U.S. Pat. 5, 0177, 522.

Holmquist, M. G., & Lange, F. F. (2003). Processing and properties of a porous matrix composite reinforced with continuous oxide fibers. *Journal of the American Ceramic Society, 86*(10), 1733−1740.

Jackson, P. R., Ruggles-Wrenn, M. B., Baek, S. S., & Keller, K. A. (2007). Compressive creep behavior of an oxide−oxide ceramic composite with monazite fiber coating at elevated temperatures. *Materials Science and Engineering: A, 454−455*, 590−601.

Jefferson, G., Keller, K. A., Hay, R. S., & Kerans, R. J. (2008). Oxide/oxide composites with fiber coatings. In W. Krenkel (Ed.), *Ceramic matrix composites. Fiber reinforced ceramics and their applications* (pp. 187−204). Weinheim: Wiley-VCH Verlag.

Jurf, R. A., & Butner, S. C. (1999). Advances in oxide−oxide CMC. *Transactions of the ASME: Journal of Engineering for Gas Turbines and Power, 122*(2), 202−205.

Kanka, B., & Schneider, H. (2000). Aluminosilicate fiber/mullite matrix composites with favorable high-temperature properties. *Journal of the European Ceramic Society, 20*(5), 619−623.

Kerans, R. J., Hay, R. S., Parthasarathy, T. A., & Cinibulk, M. K. (2002). Interface design for oxidation-resistant ceramic composites. *Journal of the American Ceramic Society, 85*(11), 2599−2632.

Kerans, R. J., & Parthasarathy, T. A. (1999). Crack deflection in ceramic composites and fiber coating design criteria. *Composites A, 30*, 521−524.

Lange, F., Tu, W., & Evans, A. (1995). Processing of damage-tolerant, oxidation-resistant ceramic matrix composites by a precursor infiltration and pyrolysis method. *Materials Science and Engineering: A, 195*, 145−150.

Lee, S. S., Zawada, L. P., Staehler, J., & Folsom, C. A. (1998). Mechanical behavior and high-temperature performance of a woven Nicalon™/Si-N-C ceramic-matrix composite. *Journal of the American Ceramic Society, 81*(7), 1797−1811.

Levi, C. G., Yang, J. Y., Dalgleish, B. J., Zok, F. W., & Evans, A. G. (1998). Processing and performance of an all-oxide ceramic composite. *Journal of the American Ceramic Society, 81*, 2077−2086.

Lu, T. (1996). Crack branching in all-oxide ceramic composites. *Journal of the American Ceramic Society, 79*(1), 266−274.

Mattoni, M. A., Yang, J. Y., Levi, C. G., & Zok, F. W. (2005). Effects of combustor rig exposure on a porous-matrix oxide composite. *International Journal of Applied Ceramic Technology, 2*(2), 133−140.

Michalske, T. A., & Bunker, B. C. (1984). Slow fracture model based on strained silicate structures. *Journal of Applied Physics, 56*(10), 2686−2693.

Michalske, T. A., & Bunker, B. C. (1993). A chemical kinetics model for glass fracture. *Journal of the American Ceramic Society, 76*(10), 2613−2618.

Michalske, T. A., & Freiman, S. W. A. (1983). Molecular mechanism for stress corrosion in vitreous silica. *Journal of the American Ceramic Society, 66*(4), 284−288.

Moore, E. H., Mah, T., & Keller, K. A. (1994). 3D composite fabrication through matrix slurry pressure infiltration. *Ceramic Engineering and Science Proceedings, 15*(4), 113−120.

More, K. L., Lara-Curzio, E., Tortorelli, P. F., Brummet, T. M., & Szweda, A. (2005). The high-temperature stability of an oxide−oxide composite at high water-vapor pressure. In *Paper No. GT2005-69065 in proceedings of ASME Turbo Expo 2005*.

Mouchon, E., & Colomban, P. (1995). Oxide ceramic matrix/oxide fiber woven fabric composites exhibiting dissipative fracture behavior. *Composites, 26*, 175−182.

Parthasarathy, T. A., Zawada, L. P., John, R., Cinibulk, M. K., Kerans, R. J., & Zelina, J. (2005). Evaluation of oxide−oxide composites in a novel combustor wall application. *International Journal of Applied Ceramic Technology, 2*(2), 122−131.

Ruggles-Wrenn, M. B., & Braun, J. C. (2008). Effects of steam environment on creep behavior of Nextel™720 alumina ceramic composite at elevated temperature. *Materials Science and Engineering: A, 49*, 101−110.

Ruggles-Wrenn, M. B., & Genelin, C. L. (2009). Creep of Nextel™720/alumina-mullite ceramic composite at 1200°C in air, argon and steam. *Composites Science and Technology, 69*, 663−669.

Ruggles-Wrenn, M. B., Hetrick, G., & Baek, S. S. (2008). Effects of frequency and environment on fatigue behavior of an oxide−oxide ceramic composite at 1200°C. *International Journal of Fatigue, 30*, 502−516.

Ruggles-Wrenn, M. B., Koutsoukos, P., & Baek, S. S. (2008). Effects of environment on creep behavior of two oxide/oxide ceramic-matrix composites at 1200°C. *Journal of Materials Science, 43*, 6734−6746.

Ruggles-Wrenn, M. B., & Kutsal, T. (2010). Effects of steam environment on creep behavior of Nextel™720/alumina-mullite ceramic composite at elevated temperature. *Composites A, 41*, 1807−1816.

Ruggles-Wrenn, M. B., Musil, S. S., Mall, S., & Keller, K. A. (2006). Creep behavior of Nextel™610/monazite/alumina composite at elevated temperatures. *Composites Science and Technology, 66*, 2089−2099.

Ruggles-Wrenn, M. B., Yeleser, T., Fair, G. E., & Davis, J. B. (2009). Effects of steam environment on creep behavior of nextel 610/monazite/alumina composite at 1100°C. *Applied Composite Materials, 16*, 379−392.

Schmidt, S., Beyer, S., Knabe, H., Immich, H., Meistring, R., & Gessler, A. (2004). Advanced ceramic matrix composite materials for current and future propulsion technology applications. *Acta Astronautica, 55*, 409−420.

Schmucker, M., & Mechnich, P. (2008). All-oxide ceramic matrix composites with porous matrices. In W. Krenkel (Ed.), *Ceramic matrix composites. Fiber reinforced ceramics and their applications* (pp. 205−229). Weinheim: Wiley-VCH Verlag.

Sherer, G. W. (1998). Coarsening in a viscous matrix. *Journal of the American Ceramic Society, 81*(1), 49−54.

Sim, S. M., & Kerans, R. J. (1992). Slurry infiltration and 3-D woven composites. *Ceramic Engineering and Science Proceedings, 13*(9−10), 632−641.

Staehler, J., & Zawada, L. P. (2000). Performance of four ceramic-matrix composite divergent flap inserts following ground testing on an F110 turbofan engine. *Journal of the American Ceramic Society, 83*(7), 1727−1738.

Szweda, A., Millard, M. L., & Harrison, M. G. (1997). *Fiber-reinforced ceramic-matrix composite member and method for making* U.S. Pat. 5, 601, 674.

Tu, W. C., Lange, F. F., & Evans, A. G. (1996). Concept for a damage-tolerant ceramic composite with strong interfaces. *Journal of the American Ceramic Society, 79*(2), 417−424.

Wannaparhun, S., & Seal, S. (2003). A combined spectroscopic and thermodynamic investigation of Nextel-720/Alumina ceramic matrix composite in air and water vapor at 1100°C. *Journal of the American Ceramic Society, 86*(9), 1628−1630.

Wiederhorn, S. M. (1967). Influence of water vapor on crack propagation in soda-lime glass. *Journal of the American Ceramic Society, 50*(8), 407−414.

Wiederhorn, S. (1972). A chemical interpretation of static fatigue. *Journal of the American Ceramic Society, 55*(2), 81−85.

Wiederhorn, S. M., Freiman, S. W., Fuller, E. R., & Simmons, C. J. (1982). Effects of water and other dielectrics on crack growth. *Journal of Materials Science, 17*, 3460−3478.

Zawada, L. P., Hay, R. S., Lee, S. S., & Staehler, J. (2003). Characterization and high-temperature mechanical behavior of an oxide/oxide composite. *Journal of the American Ceramic Society, 86*(6), 981−990.

Zawada, L. P., Staehler, J., & Steel, S. (2003). Consequence of intermittent exposure to moisture and salt fog on the high-temperature fatigue durability of several ceramic-matrix composites. *Journal of the American Ceramic Society, 86*(8), 1282−1291.

Zok, F. W. (2006). Developments in oxide fiber composites. *Journal of the American Ceramic Society, 89*(11), 3309−3324.

Zok, F. W., & Levi, C. G. (2001). Mechanical properties of porous-matrix ceramic composites. *Advanced Engineering Materials, 3*(1−2), 15−23.

Anisotropic three-dimensional arrays of fibres

14

K.H.G. Ashbee
Shrewsbury, UK

14.1 Introduction

14.1.1 Laminates and delamination

Laminates are widely used in the manufacture of components of, for example, airframes. The overall stress field of fuselage components during flight is two-dimensional; engine thrust works against drag, and lift works against payload. Hence, for aircraft with engines mounted on wings below the fuselage, during normal flight the fuselage is subjected to bidimensional compression fore and to shear aft of the wings. However, laminates are prone to delamination and, just as is the case for other elastic solids such as ceramics and glass, laminates contain Griffith flaws of all orientations. However, unlike monolithic solids, laminates usually fail by way of crack propagation parallel to the plane of lamination. Griffith (1921, 1924) published two seminal papers on fracture. The earlier paper describes an energy criterion for fracture of elastic solids; the second describes a stress criterion. The two are differentially related, as was elegantly demonstrated by the trick first used by Frank and Lawn (1967), that is, the strain energy released can be calculated from the imaginary forces needed to close the crack. Because these are forces applied normal to the crack faces, by definition of a free surface, they are zero at the start. The required energy is therefore one-half the work done, that is:

$$\mathrm{d}U = \frac{1}{2}\sigma \cdot \mathrm{d}A \tag{14.1}$$

$$\text{i.e.} \quad \sigma = 2\,\mathrm{d}U/\mathrm{d}A \tag{14.2}$$

This is the formula for changing from the language of stress to the language of strain energy release.

Griffith's second paper says that, if it has any shear acting on it, a crack changes its direction. This is illustrated in Figure 14.1 for the case of laminate delamination. Note that, as is the case for most cracks, the delaminations shown here propagate from points on the surface of the pre-existing crack, on planes that are perpendicular to that surface. Griffith's second paper also reveals that even when subjected to bidimensional compression, pre-existing cracks can be expected to propagate if and when the principal stresses become strongly unequal, as happens to airframes during both air turbulence and 'heavy' landing. Orowan (1948–1949) has graphically illustrated this important feature of Griffith fracture; see also Ashbee (2006).

Structural Integrity and Durability of Advanced Composites. http://dx.doi.org/10.1016/B978-0-08-100137-0.00014-6

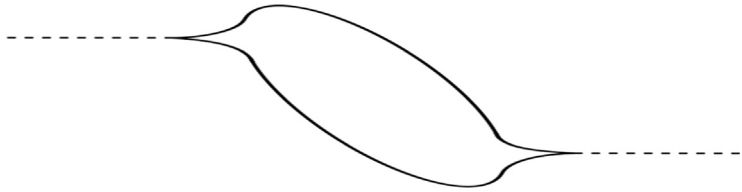

Figure 14.1 Illustrating the propagation of delamination cracks from a pre-existing flaw that is inclined to the (horizontal) laminate plane.

Thus, we need a fracture criterion with the supposition that a crack can change its plane. This is not catered by the classical fracture mechanics divisions mode I, II and III. It is a different mode of elastic strain energy release which does not open up the crack. In a perfect crystal, modes II and III correspond to the introduction of dislocations; in non-crystalline solids, bonds are stretched a little so that some atoms now have different neighbours (frustrated atoms) compared with the situation in mode I where some atoms have neighbours only on one side of the crack. Thus the specific fracture surface energy (γ) is different from that for mode I. Call it γ'. $\gamma' << \gamma$. In a crystal γ' corresponds to the introduction of a grain boundary. γ' is likely to be similar in magnitude for modes II and III. Hence the required value of γ for a crack to propagate with a continuous decrease of elastic strain energy is expected to be less than it is for mode I. In the case of delamination in fibre reinforce laminates, the magnitudes for the specific fracture surface energies for cracks propagating between fibre-reinforced layers are significantly less than that for cracks which intersect fibres. It is for this reason that, for use in three-dimensional stress fields, there is a need for three-dimensional fibre reinforcement. There are two possible solutions to this problem. For inflexible fibres, the solution is to find the minimum three-dimensional arrangement of individual fibres. For fibres that are sufficiently flexible to be woven, three-dimensional weaving offers a more convenient solution.

14.2 Fibre reinforcements designed to resist shear of all orientations

14.2.1 Preforms of mechanically rigid fibres

In Sir Charles and Lady Maita Frank's cottage at Coombe Dingle on the outskirts of Bristol, Charles had a large deformable plastic globe that he used to explain the curvature of island arcs, or rather, of the ocean trenches which lie outside them, as places where the Earth's crust, spreading from mid-oceanic ridges, bends downward into the Earth's mantle (Frank, 1968). By pushing his forefinger into the globe near the eastern coast of the Soviet Union, he would explain the origin of, for example, the Kuril 'island arc' south of the Kamchatka Peninsula and why earthquakes are located on a line dipping at 45° (expressed in angular measure on a sphere) to the Earth's surface.

Four earthquakes, which occurred off the coast of Kamchatka Peninsula in 1737, 1923, 1952 and 2006, were megathrust earthquakes and caused tsunamis. They

occurred where the Pacific plate subducts under the Okhotsk plate at the Kuril-Kamchatka Trench. The depth of the trench at the point of the earthquakes is 7000−7500 m. Northern Kamchatka lies at the western end of the Bering fault, between the Pacific plate and North American plate, or the Bering plate.

Early warnings of imminent tsunamis would demand that facilities be put in place for monitoring earth movements deep beneath the water, which, because large numbers of submersed sonic receivers would be needed even if only small distances of fault were to be monitored, calls for the development of inexpensive deep sea submersibles. To this end, the possibility of designing fibre-reinforced plastic containers within which to house monitoring devices, specifically 'listening devices', is examined here.

In the book 'An Eightieth Birthday Tribute to Sir Charles Frank' (Ashbee, 1991, Figure 8), the author wrote a chapter on bidimensional compression. Figure 14.2 illustrates how, by simultaneously advancing four inter-fitting G-shaped anvils, such a two-dimensional stress field can be created.

Figure 8(a) and (b) on page 360 of that book shows how five-member and six-member arrays of bidimensional compression anvils might be arranged and advanced so as to closely pack together fibres in hexagonal and pentagonal panels, with which a near spherical enclosure could be fabricated (Figure 14.3). Figure 14.4 is an optical micrograph of the cross-section of bidimensionally compressed glass fibre prepeg; refer to Ashbee (1986) for microgaphs of cross-sections of bidimensionslly compressed touching arrays manufactured from various prepregs.

If a 'soccer ball' enclosure of the design shown in Figure 14.3 were subjected to hydrostatic pressure, because the fibres are radially oriented and in 'touching' contact with one another, there is no space to accommodate fibre buckling. The inner surfaces of the bidimensionally compressed rig platens would have to be tapered to permit intimate contact between adjacent hexagonal/pentagonal panels when the enclosure is assembled. Radially fibre-reinforced 3D shells manufactured from matrix and fibre materials that allow transmission of elastic (sound) waves could provide inexpensive

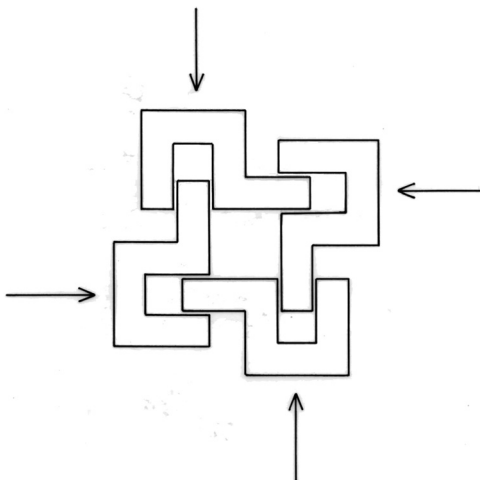

Figure 14.2 Illustating bidimensional compression by the advancement of four inter-fitting G-shaped anvils.

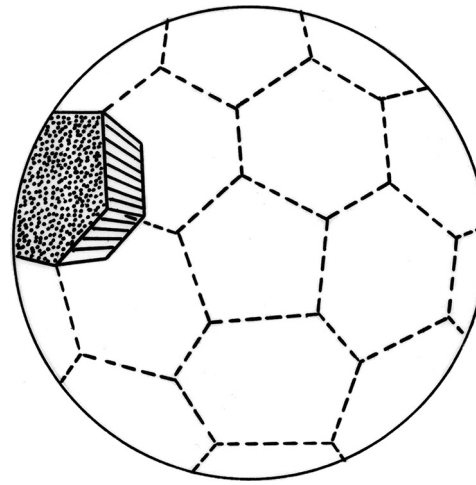

Figure 14.3 Radially fibre-reinforced spherical shell 'soccer ball' design for deep sea submersibles.

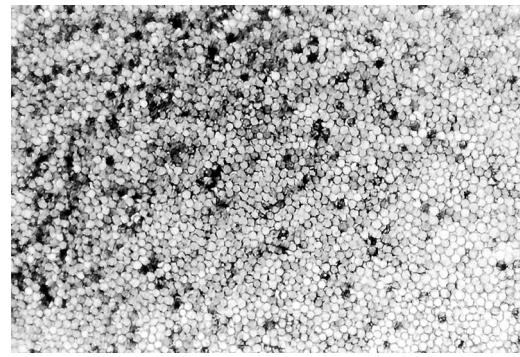

Figure 14.4 Closely packed bidimensionally compressed 10-μm diameter glass fibres.

enclosures within which to house underwater monitoring equipment and hence facilitate early detection of tectonic plate movements.

14.2.2 Sixfold arrays of rigid fibres

There are three, and only three, regular polyhedra that completely fill space, namely identical cubes, identical equilateral truncated octahedra and identical rhombic dodecahedra. The last of these is of particular interest here, because it is the body diagonals between its face centres that lie parallel to the six face diagonals of a cube, and elastically strong fibres relatively positioned in these six directions would remove all finite-valued shear moduli.

A 3D sketch to show how rhombic dodecahedra, each of which contains a single fibre between one pair of its parallel faces, may be packed together so as to completely fill space and at the same time reinforce the lay-up against shear in all three dimensions, has been published by the author (Ashbee, 2006). For carbon fibres that have

a negative axial coefficient of thermal expansion, and hence undergo zero thermal expansion in the directions parallel to conical generators with semi-apex angle $\phi = \tan^{-1} \sqrt{-}$alpha axial/alpha radial (Ashbee, 1993), such a lay-up may well exhibit near-zero overall thermal expansion.

The fibre crossovers are at point contacts for fibres with circular cross-section. For fibres with non-circular cross-sections, at least some fibre crossovers are line contacts. Single crystal sapphire fibre has a hexagonal cross-section and a model of hexagonal prisms spanning opposite faces of space-filling identical rhombic dodecahedra. Figure 6 in reference Ashbee (2006) reveals how they might be stacked together so as to reduce the number of line contacts by one half; it shows three pairs of two hexagonal fibres with their flat face areas of contact. The melting point of sapphire is 2326 K, which makes it a candidate material for (very high temperature) ceramic fibre/ceramic matrix aero engine components.

Figure 14.5 shows a 'mother' cube divided into octant cubes. Straight lines have been drawn from the centre of each face of the mother cube face toward the eight nearest edge centres to form the edges of a rhombic dodecahedron. The dodecahedron edges lie parallel to the four body diagonals that connect corners of the mother cube.

The body centres of the eight octant cubes define a cube of the same size and orientation as an octant cube, that is, a cube with volume equal to that of an octant cube. Adding to this, the volumes of the six pyramids with bases each defined by a face of an octant cube and with height one-half the octant cube edge length, that is, adding $6 \times l^2 \times {}^1/_2\ l$, in which l is the edge length of the octant cubes, shows that the volume of the rhombic dodecahedron is $4\ l^3$.

Turning now to the volume of fibre that spans opposite faces of the dodecahedron, Figure 14.6, the fibre length is one-half the face diagonal of the mother cube, and its diameter is the perpendicular distance between opposite edges of a dodecahedron face. Bearing in mind that the latter are parallel to the cube body diagonals, the acute angle

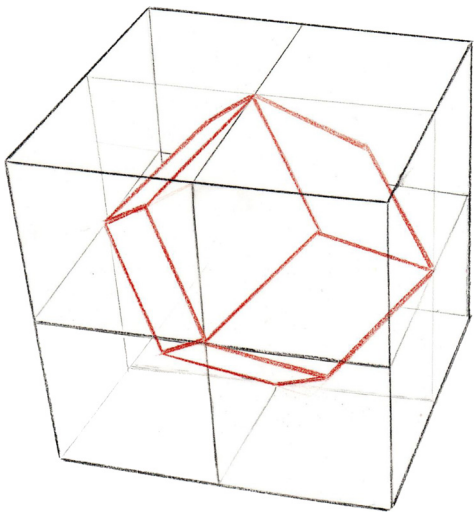

Figure 14.5 Construction for drawing a rhombic dodecahedron.

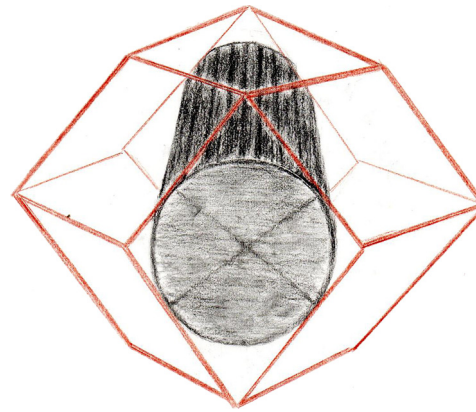

Figure 14.6 Rhombic dodecahedron illustrating a fibre spanning one of its six pairs of parallel faces.

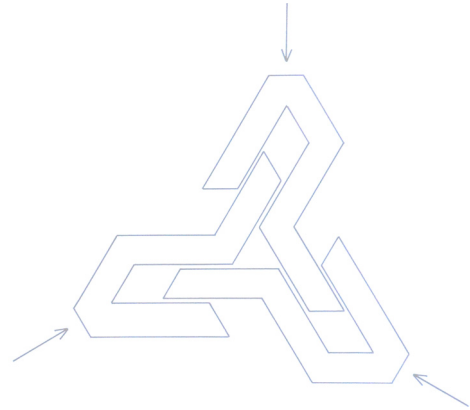

Figure 14.7 Three-member bidimensional method for fabricating isosceles triangular base prisms of closely packed fibre bundles.

between adjacent edges of a dodecahedron face is 70°32′, so the fibre volume is $\sim(3/4)l^3$, making the fibre packing fraction $\eta = 3/16$.

Rather than using a single fibre or a cylindrical bundle of touching fibres, it would be possible to completely fill the prism-shaped space between opposite faces of a rhombic dodecahedron with touching fibres. The volume of the prism-shaped space is equal to the volume of one octant cube, so this would increase η to $^1/_4$. The bidimensionally compressed fibre bundle could be conveniently manufactured as a pair of isosceles triangular base prisms of touching fibres; see Figure 14.7.

Note that, by virtue of the fact that the packing fraction for a bundle of touching identical parallel cylinders is $\eta = (\pi/2\sqrt{3})$ and not $\eta = 1$, the above packing fractions are marginally less than $\eta = 3/16$ and $\eta = {}^1/_4$.

14.2.3 Three-dimensional weaves of flexible fibres

When it comes to how best to weave a 3D array of flexible fibres, we turn to the filling of space by identical equilateral truncated octahedra, Figure 14.8. In Figure 14.8, just four families of flexible fibres overlap, at the points indicated by numerals, so as to

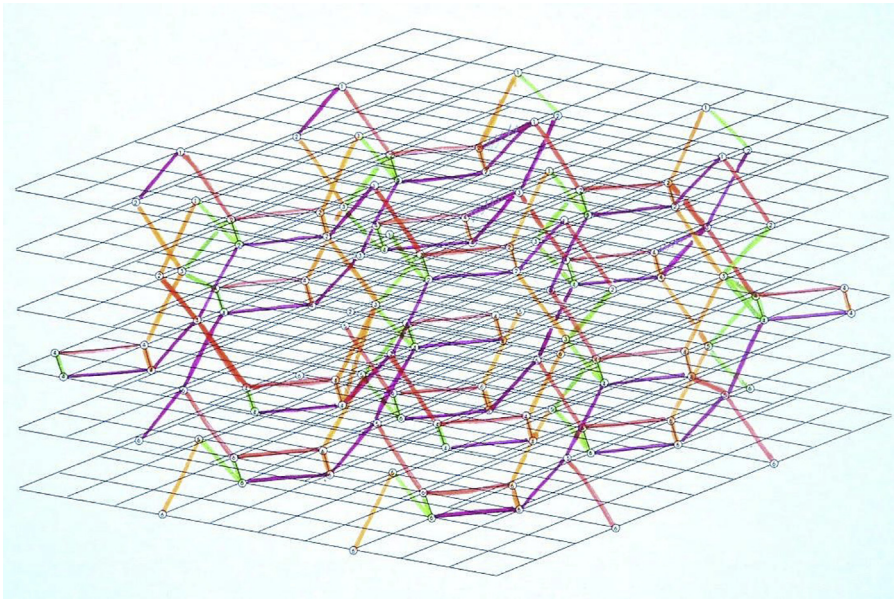

Figure 14.8 Four families of flexible fibres that overlap at the points indicated by numerals so as to create helical geometries with axes parallel to the body diagonals of a cube, but with segments of fibre length oriented parallel to the face diagonals of the same cube.

create helical geometries of overlapping fibres, each helical fibre having its axis parallel to a body diagonal of an imaginary cube, but with individual fibre segments oriented parallel to the face diagonals of the same imaginary cube.

The filling of space by equilateral truncated octahedra forms the 3D framework of tectosilicates such as ultramarine, Figure 14.9, and it was with this in mind that the author further pursued the structures of silicates when researching possible designs for strongly anisotropic 3D weaves.

For applications designed to withstand intermittent very high levels of torque, weaves with significantly higher packing fraction in two of the three dimensions than in the third may be preferable. It was therefore decided to explore a weave that mimics the crystal structure of high quartz (crystal symmetry class 62), the crystal structure of which is based on a hexagonal lattice of corner-sharing SiO_2^{4-} tetrahedra.

Figure 14.10(a) and (b) are drawings of a model of the crystal structure of high quartz viewed along one of the three diad axes in (a) and along the hexad axis in (b). There are two kinds of channel parallel to both the diad axes and the hexad axis, one of which is a single helix and the other a double helix of corner-sharing SiO_2^{4-} tetrahedra. As can be seen in Figure 14.10(a) and (b), both double helices are wound on hexagonal axes, but the single helix in Figure 14.10(a) has a twofold axis and the single helix in Figure 14.10(b) has a threefold axis (Ashbee, 1973).

For the purposes of designing a 3D weave that mimics the anisotropic symmetry of quartz, it is the silicon atomic sites that are of interest. The silicon atomic site coordinates (Frondel, 1962) are

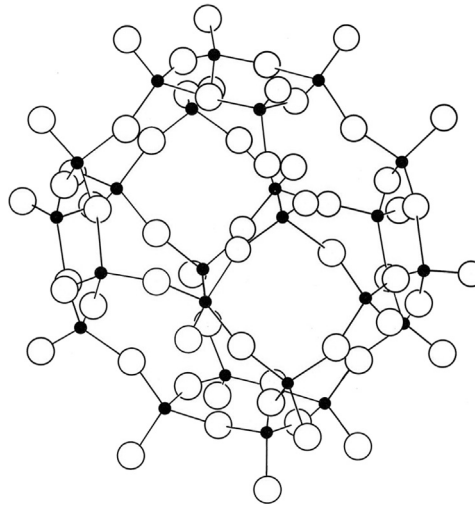

Figure 14.9 Equilateral truncated octahedron nature of the 3D framework of corner-sharing SiO_2^{4-} tetrahedra of tectosilicates. The ● denote silicon atoms; the ◯ denote oxygen atoms.

$$\overline{u}, \overline{u}, \frac{1}{3};\quad u\ \ 0\ \ 0;\quad 0, u, \frac{2}{3}$$

and are conveniently visualized as lying on the edges of almost square-base prisms defined by the body centres of the SiO_2^{4-} tetrahedra belonging to the rectangular channels of SiO_2^{4-} tetrahedra; the almost square-base prisms defined by the body centres of the SiO_2^{4-} tetrahedra are rotated about the diad axis by 45° relative to that of the rectangular-base prisms of 'open space' seen in Figure 14.10(a). There are three diad axes in all; the other two are defined by the body centres of the SiO_2^{4-} tetrahedra, which, in the view shown in Figure 14.10(a), make up the hexagonal channels.

The three square-base rectangular prisms have their long axes mutually inclined at 60° to each other. They make point contact where they cross one another at the silicon atomic sites. It is proposed that it is at these points of contact that fibre crossovers of flexible fibres wound on the prisms would be located to hold the weave in place so as to create a strongly anisotropic 3D composite. Individual sections of fibre length would be inclined to the prism edges by 30° and therefore contribute $\sqrt{3}$ more to the tensile modulus parallel to the diad axes than to the tensile modulus parallel to the triad axis.

The manufacture of 3D weaves demands a means by which all but one of the families of threads can be held in place while the remaining family of threads is 'looped' around the stationary families of threads. By omitting part of a layer of tetrahedra, space could be created for embedding adhesively bonded flanges manufactured from other engineering materials such as a metal, without having to sever any fibres. Figure 14.11, for example, shows a layer of missing tetrahedra, indicated with broken lines, that could accommodate a flange.

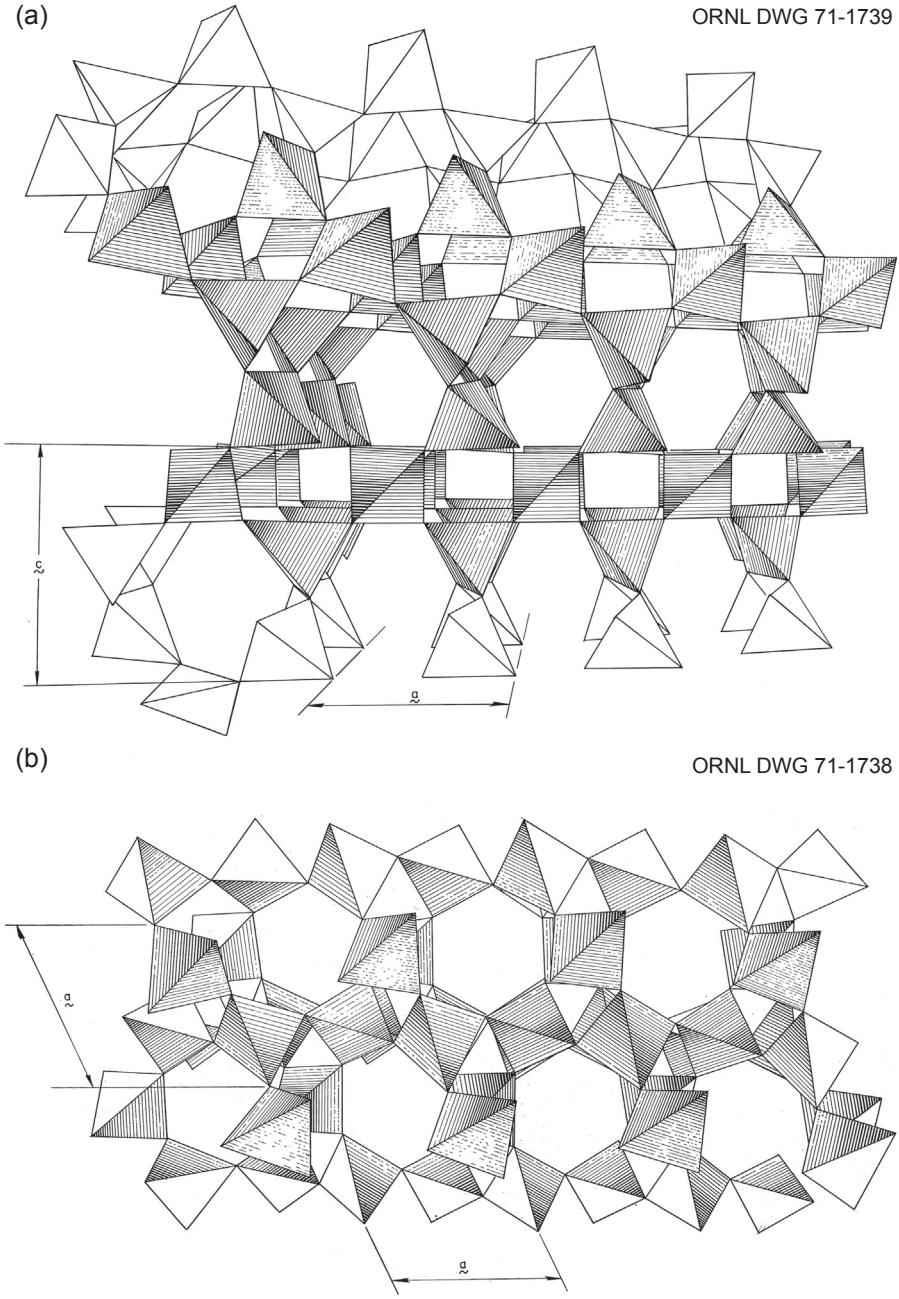

Figure 14.10 Corner-sharing SiO_2^{4-} tetrahedra model of crystalline high quartz. (a) Viewed along one of the diad axes. (b) Viewed along the hexad axis. The arrangement of single helix chains wound on rectangular prisms parallel to the three diad axes accounts, numerically, for all of the tetrahedra.

From Ashbee, K. H. G. (1973). The Peierls force in crystalline quartz. *American Mineralogist*, *58*, 947–948.

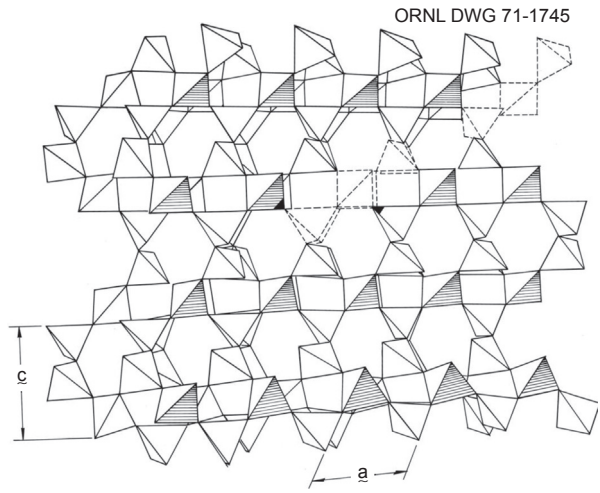

Figure 14.11 The layer of SiO_2^{4-} tetrahedra shown with broken lines illustrates how a woven fibre composite component might be joined to, for example, a flange of more conventional engineering material, for example, a metal, without having to sever the weave.

Acknowledgements

Figure 14.1 was computer generated by T.L. Ashbee. Figure 14.8 was computer generated by the patents section at the Wright Patterson AFB, Dayton, Ohio, during a visiting scientist assignment.

Figures 14.10(a, b) and 14.11 were drawn by the graphic arts department at the Oak Ridge National Laboratory, Tennessee, during a leave of absence from the University of Bristol.

References

Ashbee, K. H. G. (1973). The Peierls force in crystalline quartz. *American Mineralogist, 58*, 947−948.

Ashbee, K. H. G. (1986). Bi-dimensional compression moulding of super-high fibre volume fraction composites. *Journal of Composite Materials, 20*, 114−124.

Ashbee, K. H. G. (1991). *Sir Charles Frank, OBE, FRS an eightieth birthday tribute*. In R. G. Chambers, J. E. Enderby, A. Keller, A. R. Lang, & J. W. Steeds (Eds.) (p. 360). Bristol, Adam Hilger: IOP Publishing Ltd.

Ashbee, K. H. G. (1993). *Fundamental principles of fiber reinforced composites* (2nd ed.). (pp. 194−196). Lancaster: Technomic Publishing Co.

Ashbee, K. H. G. (2006). Moving away from anisotropic lay-ups; modeling of 3D preforms & weaves. *Journal of Material Science, 41*, 6520−6525.

Frank, F. C. (1968). Curvature of island arcs. *Nature, 220*, 363.

Frank, F. C., & Lawn, B. R. (1967). On the theory of Hertzian fracture. *Proceedings of Royal Society A, 299*, 291−306.

Frondel, C. (1962). The system of mineralogy of JD and ES Dana. In *Silica minerals* (7th ed.) (Vol. III, p. 18). New York and London: John Wiley & Sons.

Griffith, A. A. (1921). The phenomenon of rupture and flow in solids. *Philosophical Transactions of the Royal Society A, 221*, 163−198.

Griffith, A. A. (1924). The theory of rupture. In *First International Congress for Applied Mechanics,* (pp. 55−63).

Orowan, E. (1948-1949). Fracture and strength of solids. *Reports on Progress in Physics, XII*, 185−232.

Structural integrity and the implementation of engineering composite materials

15

P.W.R. Beaumont
Cambridge University Engineering Department, Cambridge, UK

15.1 Introduction

The driving force for developing advanced materials comes from society's need for large composite structures having structural integrity (SI); new engineering composite materials that operate reliably and safely at the frontiers of cutting-edge technologies – aerospace, ground and ocean transportation systems; defence and security applications; information and communications technology; climate change; energy sustainability; and material systems in support of the ailing human frame.

The demands made on structural materials in modern engineering design are increasingly stringent. Greater performance, lower costs, increased reliability and safety all require that the design engineer knows more and more of the materials available. Bringing together new knowledge contained in constitutive models of continuum design and empirical information from a girth of experience and experimentation is proving to be difficult because of the increasing number of service and process variables required for sophisticated optimal design. Understanding SI provides the key to successful design, certification and safety of large composite structures. This is because SI analysis simultaneously treats the materials used and design of microstructure, figures out how best components and parts are to be made and joined, and takes the total engineering design process, service and duty into account.

Structural integrity is a term that embraces contributions from materials science and the various branches of engineering; fabrication and processing technology, and manufacture; nondestructive inspection (NDI), through-service health monitoring and safety management; fracture mechanics, probabilistic assessment of failure, and 'human factors' across a broad spectrum of size scale (Figure 15.1). SI combines a number of interacting factors: the criticality of the application; the accessibility for and ability to inspect vital parts and components; the intended use of the material including load spectrum and time; the consequences of impact, fatigue, environment and temperature; the manufacturing technique and inherent flaws and their detection; and properties of the material system utilized. Quite simply, SI is the physical assessment of material and quality assurance of structure from 'cradle to grave' with safety first the only *show in town*.

This chapter is an overview of the implementation of engineering composite materials and structures in the twenty-first century; it is a perspective on designing

Structural Integrity and Durability of Advanced Composites. http://dx.doi.org/10.1016/B978-0-08-100137-0.00015-8

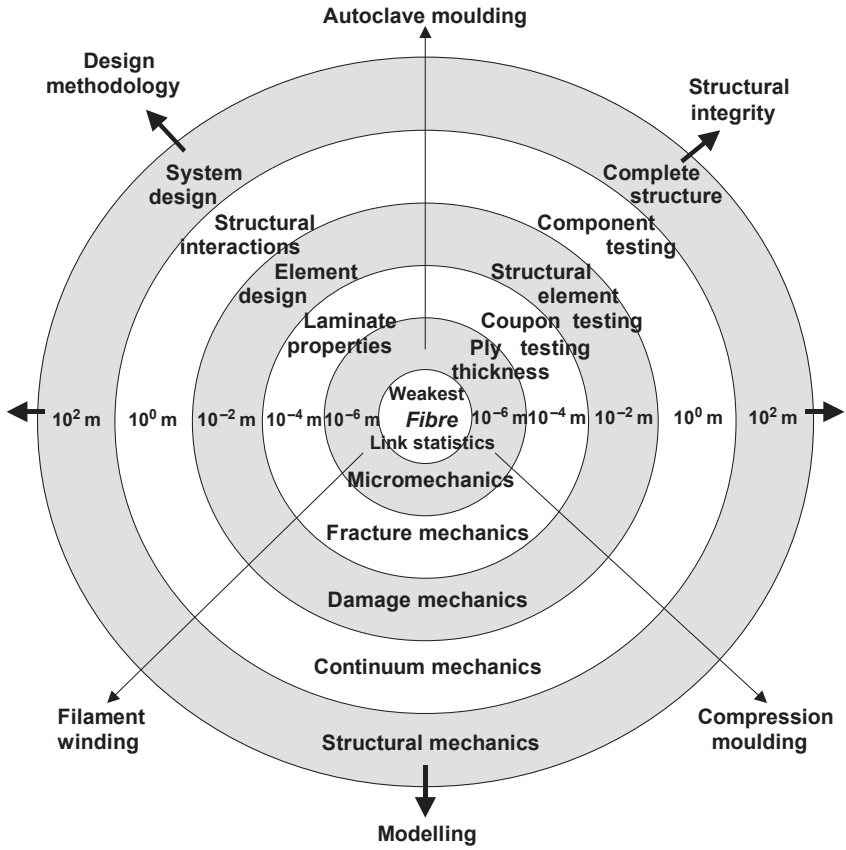

Figure 15.1 Hierarchy of structural scales ranges and discrete methods of analysis in design ranging from micromechanics to the higher structural levels of modelling, continuum mechanics, etc. Structural integrity embraces contributions from materials science and engineering, fabrication and processing technology, nondestructive inspection (NDI), fracture mechanics and probabilistic assessment of failure, across a broad spectrum of size scale (Beaumont, 2006).

composite structures having SI. Historians inform us that, to look forward, it is often helpful first to look backward − a perspective takes the long view.

15.2 Taking the long view

Historians tell us that before looking forward it is useful to take an historical look. Some 1.7 million years ago, Yuanmou Man in China moulded pots from clay mixed with crushed calcite rock, perhaps the earliest example of a particulate composite. The presence of rock particles rendered any small crack formed during firing of the clay innocuous by blunting them out at the filler−matrix interface. A solid rocket fuel

Figure 15.2 The traditional method of making sailboats from trees grown on the Islands of Micronesia is by gluing and stitching planks with natural fibre.

consists of brittle particles (the fuel) in a viscoelastic matrix, which controls the rate of burn. One of the earliest uses of a laminated structure is seen in the Shield of Achilles, a composite of laminated construction consisting of two outer layers of bronze, two inner laminae of tin and a single central lamina of pure gold. The material is similar in design to GLARE in modern aircraft design. (GLARE is glass laminated-reinforced epoxy, a laminate structure made by adhesively bonding layers of S-glass fibre-epoxy between layers of aluminium alloy (ca. 1985).) The upper part of the fuselage of the Airbus A380 aircraft consists of panels made of GLARE . In GLARE there is favourable resistance to fatigue crack growth around large wing joints. This is because any crack formed grows in a single layer only, the remaining intact layers effectively bridging the crack. The same effect is observed in wood where a split exhibits fibre bridging and carries traction, leading to crack arrest.

On the Islands of Micronesia, we observe the traditional method of making sailboats by gluing and stitching together hewn wooden planks with natural fibre to inhibit splitting and cracking (Figure 15.2). Modern protective clothing in the British Army consists of alternate layers of Kevlar/ceramic material. During Wimbledon's international tennis tournament in June 2009, on BBC television a commentator characterized the ideal *composite player* as combining the best attributes selected from the most outstanding tennis players in the history of the game. Indeed, *composite man* already exists thanks to advances in implant surgery in support of the ailing human frame.

However, the first use of the term *composites in engineering* refers to the composite construction of the nineteenth-century clipper ships, which was conventional wooden planking on novel iron frames. Most of the 170,000 airplanes built during World War I were constructed of wooden frames using adhesively bonded joints of spruce, birch plywood, or balsa wood across which was stretched a fabric covering impregnated with a resin for improved lightness. Today, in the wings of the Airbus A380 we have familiar aluminium skins on composite ribs and frames. The Airbus A350 XWB wing, however, is the largest single civil aviation part made from carbon fibre composite material, some 32 m long by 6 m wide. To improve efficiency at higher speeds, the A350 XWB can deflect its wing flaps both symmetrically and

Figure 15.3 Full-scale break test of the Boeing's 787 Dreamliner Wing. The structural flaw in was found ca. May 2009. Stresses at the ends of the long rods that stiffen the upper wing skin panels caused the fibrous layers of the composite to delaminate. Inside the fuselage, on the other side of where each wing joins the body of the aircraft, is the centre wing box constructed much like the outer wing, with composite skin panels stiffened by composite stringers. The upper and lower surfaces and wing spars are made from the same composite material as the fuselage, while the wing ribs are machined from single pieces of aluminium.

asymmetrically, optimizing the wing profile and providing better load control. For Boeing's 787 Dreamliner, the upper and lower surface panels and spars of the wing are made of carbon fibre composite on ribs of aluminium machined from a single plate. However, during tests under load (ca. May 2009), damage by delamination of composite sheets initiated in the wing, extending into the wing box (Figure 15.3).

The first major application of carbon fibre in aerospace did not begin with a success story. In 1971, the jet engine manufacturer Rolls-Royce (R-R) came 'unstuck' with their brand-new RB211 engine. The novel carbon fibre−epoxy composite known as Hyfil^{R} used in the fabrication of compressor fan blades shattered into pieces when a frozen chicken was fired into them at full speed to simulate foreign object impact. Those composite blades, which exhibited an extremely strong bond between fibre and matrix (a result of surface treating the fibre in a solution of sodium hypochlorite), exhibited notch brittleness in the absence of any crack tip blunting mechanism. The R-R Company went bankrupt, leaving the US airplane manufacturer Lockheed Aircraft at that time without an engine for its brand-new TriStar Jumbo jet, the L1011. However, unlike R-R, the company was 'bailed out' by 'Uncle Sam' (the US government). If only the process of stitching as practiced by the South Sea islanders (we know it today as z-pinning and tufting) had been adopted by the aerospace engineers at the Derby plant some 50 years ago. In private conversation with Leslie Phillips, coinventor of the RAE carbon fibre, Phillips informed me that he spied a stitched RB 211 blade in the corner of an R-R factory warehouse, on the same day the company closed its doors for the last time before becoming nationalized (for several years).

Likewise, the all-carbon fibre composite Lear Fan 2100 airplane exhibited notch brittleness and cracked at the wing root joint on flexing in a full-scale test (just like the Dreamliner) and like Roll-Royce also went bust. There is a more recent example.

Figure 15.4 An American Airlines Airbus A300-600 had its vertical carbon fibre fin blown away during the take-off stage, with disastrous consequences.

In the wake of a JAL Boeing 747 aircraft flying out of New York's JFK International Airport, the American Airlines Airbus A300-600 had its vertical carbon fibre fin blown away with disastrous consequences (Figure 15.4).

A few years ago, a carbon fibre composite pressure vessel filled with natural gas (200 bars (20 MPa)) exploded on the roof of a bus, totally destroying the bus and surrounding cars nearby. In the filament winding of a pressure vessel, the fibres are positioned on geodesic paths to provide maximum strength. Now carbon fibre exhibits a distribution in tensile strength. In this example, the dominant failure mechanism is fibre rupture over time. Damage is related to the accumulation of broken fibres, and with a progressively increasing damage rate, there is positive feedback. At the point where the vessel's residual strength equals the applied stress, crack instability occurs and the vessel explodes. Where the storage of hydrogen is concerned (700 bars (70 MPa)) absolute safety is vital. Periodic verification of SI is essential.

Other examples of catastrophe, which resulted in loss of function, include the Phillips ocean-going catamaran, losing part of its hull on hitting a violent wave (Figure 15.5) and massive delamination of a Formula One car tyre at high speed. In the summer of 2009 in

Figure 15.5 Team Phillips catamaran 2003 hits a freak wave with dire consequences, suffering a serious loss of function.

Afghanistan, the British Army suffered loss of personnel from surface mine blast impact damage of armoured (composite) fighting vehicles (AFVs). In these few examples, we see structure suffering a critical loss of function and in some cases loss of life.

15.3 Fitness considerations for long-life implementation

We are experiencing an evolution in certification methods (or changes in fitness considerations) for composite material systems and structures, an integration of predictive design methods and engineering performance, which target the connectivity between intelligent material selection, fabrication route and performance limit. Selecting the right material system at the very beginning of the design process requires material properties profiling. Dimensions must be consistent with the overall function including minimum weight, and there are databases for materials properties to which designers can refer (e.g. the Cambridge Materials Selector). When it comes to material property profiling, frequently Young's modulus E and density ρ are the *performance drivers*, in which case the materials engineer consults a chart having the axes E-ρ with superimposed lines of constant *design* or *merit indices*: (1) E/ρ for a strut; (2) $E^{1/2}/\rho$ for a beam; and (3) $E^{1/3}/\rho$ for a plate, where the index is maximized for optimum design.

Additional input in selecting the correct combination of fibre and matrix might include *thermal conductivity* (λ) and *thermal expansion coefficient* (α) (Figure 15.6). This chart displays a vast amount of thermal expansion coefficient data and thermal conductivity data for the widest possible range of engineering materials.

Each envelope encloses data for a given class of material, and the contours show the thermal distortion parameter α/λ. For thermal properties profiling, an expansion coefficient mismatch between ceramic constituents leads to *thermal fatigue cracking* or ratcheting in metal−matrix composites (MMC). This requirement constrains selection of fibre reinforcement and protective coatings for high-temperature application; Ti requires Al_2O_3 fibres, not SiC fibres. Ceramic−ceramic composites (CMC) preference is for SiC/SiC or mullite (aluminosilicate ceramic)/Al_2O_3 over SiC/Al_2O_3.

Where toughness is a critical requirement of a material, experience indicates a practical minimum level of fracture toughness (K_C) of 10−15 MPa $m^{1/2}$. Toughness, however, is not a unique property of composites, which complicates things. For example, 'blunting' mechanisms stabilize damage; examples include multiple matrix cracking, fibre bridging of delamination cracks, fibre buckling zones around notches or holes in compression, etc. Furthermore, the stress concentration factor around holes diminishes under increasing (and repeated) load because inelastic (damage) zones develop with an elevation in the local tensile strength. Multiple fibre fracture and matrix-dominated cracking below ultimate strength allows other inelastic mechanisms to activate in the matrix and stabilize the effect of damage, and the failure probability distribution is dramatically modified. Since notch strength scales with fracture toughness, notch sensitivity is a more robust, useful measure of material performance.

In service, composites can undergo combined attack from stress and environment. The result is the activation of a complexity of atomistic defects and microscopic flaws, and their accumulation over time will be felt at the component level of size. Corrosion

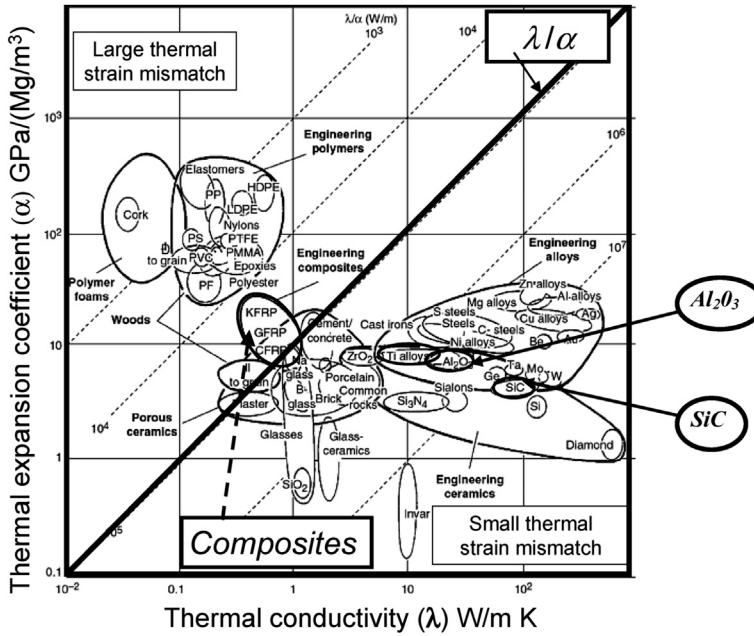

Figure 15.6 A material selection chart showing the properties of thermal expansion coefficient and thermal conductivity (The Cambridge Selector). This chart displays a vast amount of thermal expansion coefficient data and thermal conductivity data for the widest possible range of engineering materials. Each envelope encloses data for a given class of material. The contours show the thermal distortion parameter (Ashby, 2005).

fatigue degradation of glass fibres in epoxy, for example, occurs by two rate-limiting phenomena. Hostile species penetrate the composite through matrix cracks. Reaction with the fibres follows, which reduces their strength, and they fail at the matrix crack front. This is a reaction-controlled stress corrosion cracking process.

On the other hand, for a narrow matrix crack opening, concentration gradients develop along the crack and the stress corrosion cracking process becomes diffusion controlled (Figure 15.7). The chemically activated kinetics of the processes is thermally sensitive, so models based on statistical mechanics lead to a rate that depends upon temperature. The difficulty in solving this particular problem is that pure atomistic models on their own break down because certain structural variables (diffusion rates, jump frequencies, chemical activation energies, etc.) are not known; neither can they easily be measured.

15.4 The traditional approach to design

Whilst many ancient temples and cathedrals have stood the test of time, many others collapsed prematurely without warning leaving the builder not knowing why. History is littered with structural disasters where the crucial failure event eluded the

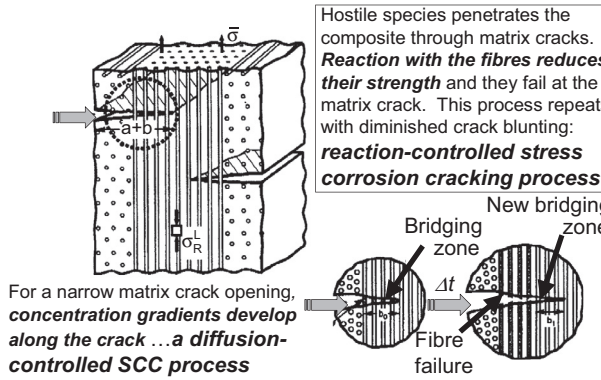

Figure 15.7 Corrosion fatigue degradation occurs by two rate-limiting phenomena in CMCs, MMCs and PMCs with crack acceleration and attendant embrittlement (after Prof Anthony Evans).

experimentalist. A few of the more recent ones with respect to composite materials were illustrated earlier. Yet despite an acquisition of vast collections of experimental data, information and compelling evidence, and an engineer's intuition based on 'feel' – experience coupled with intelligent observation, a phenomenology – our ability to fully understand that long-standing problem of structural failure remains unresolved. For half a century or longer, those factors that influence the endurance boundary of the composite material on the one hand and performance limit of the composite structure on the other have been the subject of a great number of analytical investigations, validated by precise measurement of critical property data. But predicting precisely where and at what instant in time a crack will develop in a material under stress, and exactly the length of period when catastrophic failure of the structure will occur, remains an unsolved mystery. Our comprehension of the sustainable damage of a composite material and the mechanical stability of a composite structure over a wide range of operating conditions remains restricted.

Traditionally, practical design methods followed time-consuming, expensive test programmes to establish damage tolerance certification of a large structure (Figure 15.8). The consequences of changing laminate design (fibre orientation, stacking sequence or ply thickness) or material system along the way would prove disastrous. A heavy price is paid for making mistakes using this approach. Quite simply, the entire test matrix for material qualification has to be repeated. Furthermore, there are complications as the result of laminates being heterogeneous elastic bodies containing sites of stress singularity; and secondly, the mechanisms controlling damage initiation and propagation are nonlinear. Nonetheless, the likelihood is those mechanisms would not be known let alone understood.

Traditional empirical design formulations have not done well dealing with these challenges. Quite simply, empirical 'laws' do not have the power of prediction. Successful prediction of mechanical behaviour of material and design life of a structure requires detailed information of all possible failure mechanisms across the widest

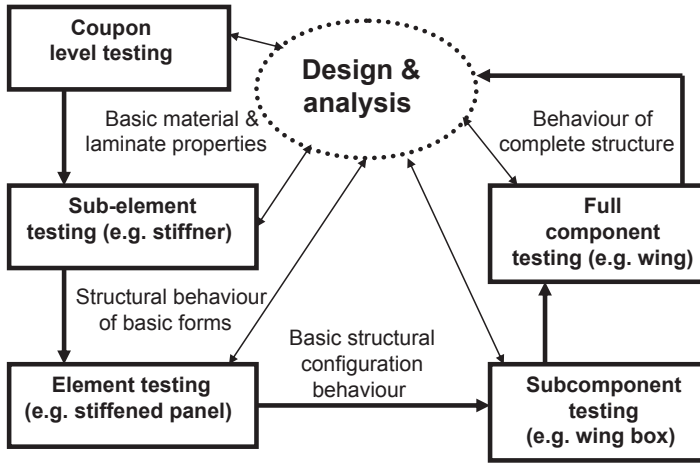

Figure 15.8 The 'building block' or traditional approach (Kedward & Beaumont, 1992).

spectrum of size scale under all sorts of operational conditions. To set up an experimental programme that covers all eventualities, the scope of the test programme would be immense and unaffordable. Not only would the findings be complicated to sort out because of the many different mechanisms of fracture and fatigue involved but the question of their interaction would have to be resolved. Moreover, material characterization over one range of temperature could not safely be extrapolated into another range – a new characterization would be needed for every set of composite layup, fibre and matrix system, operating conditions, and environment.

Eventually, the method of extended empiricism would just break down under such an unmanageable load of variables. Not surprisingly, the design and development of large structures based on full-scale testing is slow and expensive. Furthermore, the burden of testing to prove absolute safety of structure would be impossible to manage in practice.

Experimentally, Figure 15.9 illustrates the experimental challenge. There are two extreme forms of testing: either test thousands of coupon specimens to establish basic laminate properties, or have the knowledge to perform confidently just one or two tests on the complete aircraft or major components to ultimate load or fatigue life.

The reality is that there are still many tests in between (Figure 15.9) – from elements to components to substructures where internal stress fields are too intricate to evaluate by analysis. To follow the traditional route of engineering design is to attempt to ensure that a highly stressed critical component could not possibly fail within its design lifetime. This exercise involves deriving, over the entire life of the structure, the spectrum of loads experienced in service and to compare with materials test data; strength, fatigue and creep data; stress corrosion cracking rate; etc. – the phenomenology mentioned above. The next step would be to determine the component's dimensions to maintain the design loads and to guarantee the design life within a margin of safety, allowing for some acceptable risk of disaster. In this way, we build

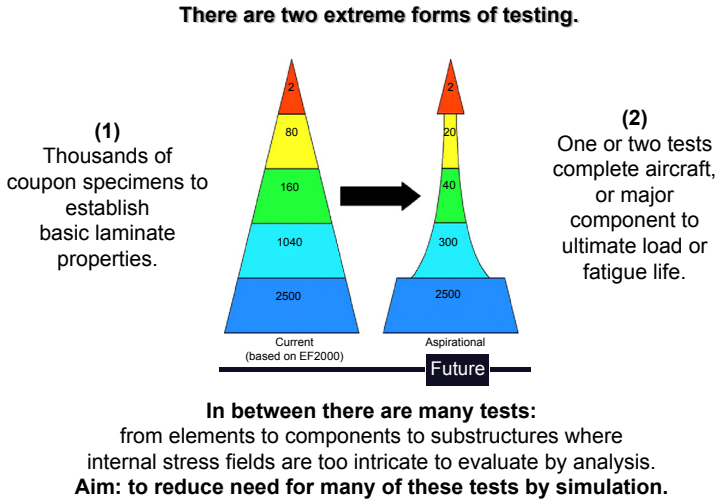

Figure 15.9 The experimental challenge (Courtesy of Prof Glyn Davies).

up to testing larger and larger items until the complete structure undergoes that single 'multimillion dollar' test to destruction. Determining the strength of a structure experimentally helps verify the analytical methods used to calculate the loads the structure will have to carry in service.

So why do we still encounter materials that crack and structures that fail? It is because our knowledge is based (almost) entirely on our store of information being empirical in nature. For decades, an 'invisible' college of continuum mechanics studied mechanical behaviour based on an idealization of what behaviour is, without any reference to microstructure. Test programmes must reveal all failure mechanisms that are likely to operate in service. And for composite materials, the components of damage are complex. How can we possibly deal with the complexity of crack nucleation and damage growth, and the multiplicity of interacting, competing cracks?

15.5 Evolution of mechanical design

In the twentieth century, modern mechanical design evolved with the development of the continuum theories of mechanics (mathematical and continuum models of elasticity and plasticity), diffusion and reaction rates. With the advent of computer power, this resulted in finite element (FE) modelling, numerical analyses and high-fidelity simulation. This leads to an optimization in design that minimizes cost or maximizes performance or safety.

Thus, the modern designer shows dexterity in the use of two boxes of tools: mathematics and continuum modelling, from which continuum theories and constitutive modelling have evolved (a sort of 'distilled empiricism'), and micromechanics modelling (or physical modelling). Using these tools to determine constitutive equations,

however, relies on knowledge of the rules of materials behaviour, which we learn at the undergraduate level of university.

Tools from Box 1 (continuum mechanics) describe structural interactions at the component level of size. Tools from Box 2 (micromechanics) use the constituent properties of the material on the microscopic scale where structure and spatial arrangement are the main variables of mathematical and physical models. The idea is that the response at one size level is described by one (or more) parameters and passed to the next level up (or down). Combining information from both paths leads to the development of 'damage mechanics:' constitutive equations based on physical models of deformation and fracture. Still, there is no getting away from the problem that constitutive equations of continuum design remain firmly based on experiment. Now micromechanics helps by identifying those mechanisms responsible for cracking and an understanding derived from the theory of reaction rates (e.g.) to model them. But micromechanical models have something else to offer − they point to rules that the constitutive equations must obey. Although micromechanical models cannot by themselves lead to precise constitutive laws, the result is a constitutive equation that contains the predictive power of physical modelling combined with the precision of ordinary curve fitting methods (called model-informed empiricism). Examples below help to understand this approach.

15.6 Structural integrity and length scale

Various design methodologies exist, all dealing with critical issues of structure and all common to the overall design process of production, maintenance and repair. Overlapping are two items: assessment by NDI and safety. Is safety compromised where the fatal flaw(s) in the structure is (are) smaller than the NDI detection limit? What initial flaw (damage) content is acceptable in the final structure as a result of the manufacturing process? Structures require though-life health monitoring of damage growth. But what is an appropriate inspection period? There are conflicting aims of designing a structure simultaneously for high efficiency and safety assurance throughout an economically viable lifetime and it comes down to the price of safety with an acceptable level of risk as decided by society's experts (Figure 15.10).

Put quite simply, how far from potential disaster are we prepared to go? An important feature of SI analysis is that it provides quantitative input to the formulation of an appropriately balanced response to that question. In short, it is the *design life* that determines the answer because it relates to that *loss of function* of the component. Absolute safety, then, is determined by SI, which defines design life. In short, design life is that point in time when a structure suffers loss of function for which it was intended.

A key role in failure prediction, from those empirical methods to state-of-the-art high-fidelity simulations of damage evolution, is played by certain physical length scales in the damaging processes, which provide a rationale for making modelling decisions. A length scale arises because of the complexity of the nature of cracks, for specific damaging mechanisms; examples include delamination and splitting (shear)

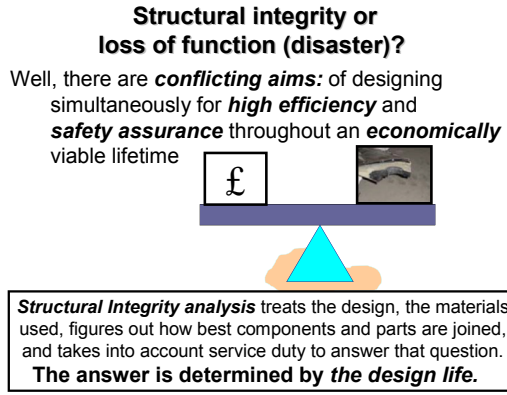

Figure 15.10 Structural integrity or loss of function? (After Prof J F Knott).

cracks (and associated interfacial friction), fibre rupture, fibre microbuckling or kink formation, and diffuse microcracking or shear damage. Corresponding sound physical models and mathematical theories need to describe these mechanisms on a microscale and cracking in the large engineering structure.

Boundaries on the length scale are likely to be delineated by a breakdown in the model and assumptions implicit to a particular size. Thus, we must define points on that scale by phenomena that are treated discretely from phenomena treated collectively. The two exceptions are the end points of the length scale. (Everything at the electronic level is treated discretely whereas everything at the macro size is treated collectively.) Our confusion over how damage is interpreted along this length scale is causing difficulty as progress is made from one design stage to the next, from the size of architectural feature of the laminate to that of structural element, and from component and to the fully assembled large-scale structure.

Nevertheless, it goes without saying that understanding damage by experimentation and modelling across orders of magnitude of structural dimension, and linking analyses systematically to provide a total predictive design strategy, remains lacking with respect to absolute reliability and guaranteed safety. This is particularly critical regarding two design issues: (1) a structure capable of sustaining a potential damaging event (*damage resistance*); and (2) a structure's ability to perform satisfactorily and safely with damage present (*damage tolerance*).

Even with the exponential growth of computational power, which has resulted in an abundance of numerical analytical models, there still exist fundamental barriers to overcome as progress is made by connecting one damage analysis to the next, from the time the smallest undetectable defect forms in the solid to the point where a visible crack is found in a full-scale engineering structure 'down the road'. Lack of mastery in combining architectural design of the material at the micron (or smaller) size with the design of elements of the engineering structure metres in length has led to the opening of a gap in our knowledge of composite failure. This weakness can be traced to the changing nature of cracking and fracture as

structural size increases. If we consider coming to terms with all sorts of material behavioural complexities at the submicroscopic end of the scale, we might say that we have characterized the properties of the composite by reference to the fibre only. In which case, there has been no real consideration of the make-up of the material or macroscopic geometry of the laminate or shape of part or component. Any notch, hole or cut-out is but a geometrical aberration. Conversely, at the size level of component design, the tendency has been to look at the overall geometric shape and to think of the material properties as being set (in a geometric sense) at global level.

Coming to terms with these differences of scale appears to be a key source of design difficulty because it is precisely at that size where the material problem becomes a structural one where this gap in understanding of composite failure has opened up. This gap has been partially filled using fracture (and damage) mechanics, where quantitative relationships between microscopic and macroscopic parameters exist. Once again, as before, damage tolerance certification of a material and structure requires time-consuming, expensive testing. Now with the development of computer power and appropriate software, this has led to a reduction in number of tests by substituting with high-fidelity damage simulations that serve as virtual tests of SI.

15.7 Structural integrity and multiscale modelling

Materials have to be processed, components shaped and structures assembled. Lack of attention to detail leads to premature failure after shorter-than-expected service duty because of the introduction at some stage of fatal flaws (voids, delaminations, fibre waviness, contamination at joints, etc.), and they all impact on structural performance. Predicting damage initiation followed by damage evolution and specifying accurately the safe operating limits is a major challenge. The problem is especially difficult if the damage is severe. Difficulties in prediction arise because composites modelled as heterogeneous elastic bodies contain sites of stress singularity, and also because the mechanisms controlling damage initiation and growth are nonlinear.

Multiscale problems of structural failure that occurs at the micro, meso and macro size of scale must be targeted by appropriate multiscale modelling methods. Testing and analysis across a size spectrum reflect responses at all structural levels, which we call *multiscale modelling* (Figure 15.11).

Successful implementation of long-life design requires precise modelling of composite behaviour under impact (blast, shock, ballistic, tyre debris impact, bird strike), fatigue and stress corrosion cracking, etc. at size levels needed to devise a robust life prediction methodology, preferably mechanism based.

15.7.1 Top-down versus bottom-up methods

The macroscopic response of a composite material system on the one hand and component on the other reflects responses at all levels. The idea is that the response at one

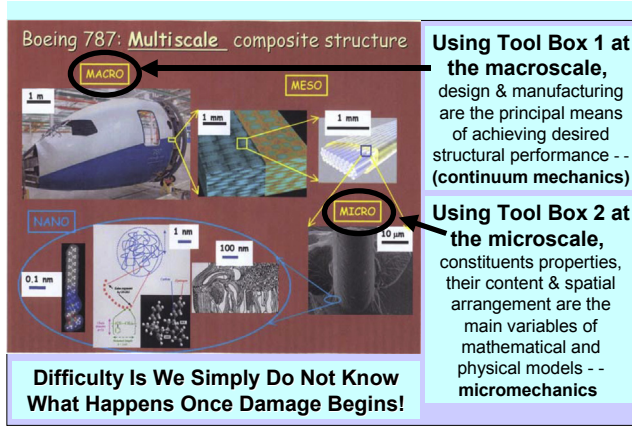

Figure 15.11 Structural integrity is affected from the *micro* to *meso* to *macro* size levels (Courtesy of Prof Josef Jančář, 2008). Testing and analysis across a size spectrum reflect responses at all structural levels, which we call multiscale modelling. This is illustrated with Boeing's 787 multiscale composite structure. Macroscopic response of material and component reflects responses at all levels beneath. Of particular interest is how damage transfers from a lower scale to a higher scale. This requires the entire range of length scale be probed in order to understand issues to do with connecting failure of the material and fracture of the engineering structure.

level is passed to the next level up (or down). Hierarchical and multiscale modelling links both top-down (TD) and bottom-up (BU) approaches. Almost always, behaviour at one level can be passed to the next level up (or down) as a simple mathematical function. Regrettably, distinct communities have pursued either TD or BU methods of design only occasionally transferring information from one to the other. The TD method begins with a macroscopic engineering model, a procedure that depends only on knowledge of straightforward, *macroscopically* measurable properties, like hardness or yield stress or ultimate tensile strength. This an engineer can handle. BU methods on the other hand, seek to model (or simulate) failure by building upon events that initially take place at the atomistic (or microscopic) level, which in engineering terms are difficult to determine, let alone quantify.

In the bottom-to-top strategy, component testing can be carried out through structural analysis using micromechanical models for the homogenized laminate behaviour (3-D-continuum shell and cohesive elements). These virtual experiments open revolutionary opportunities to reduce the number of costly tests to certify safety, to develop new materials configurations and to improve the accuracy of failure criteria.

However, the problem still remains that it is difficult to model first damage (matrix cracking) and then progression into a delamination crack. Whilst physical modelling as described by one (or more) parameters in a constitutive model, for example, can help rationalize those microscopic processes responsible for yield stress, toughness (notch sensitivity), fatigue, stress corrosion cracking, etc. generally, these models are too imprecise for an exact engineering solution. In fatigue,

for example, life prediction based on a physical model only might give a prediction within a factor of 10. That is because the material parameters of the physical model are not known with any certainty and they are too difficult to determine or measure with any confidence. They can be estimated only by empirical means. Knowledge of matrix crack density, for instance, would characterize the state of damage in a composite under fatigue, but there is no straightforward way of quantifying it in a large structure.

Such interplay of materials science and engineering is of crucial importance where composite material properties vary continuously with some internal parameter that relates to composite architecture in some way. Optimum material microstructure (and nanostructure) can then be forecast and designed rather than found by trial and error (with the possibility of calamity), whilst maximizing structural high performance and sustainable safe life. Then, when a set of properties is specified, it should be possible to select a particular layup or weave of an appropriate composite material system, and set of processing conditions, to meet that specification and provide SI.

We require mathematical formulations that link TD and BU approaches in single design codes that represent fine-scale phenomena embedded in calculations representing larger-scale phenomena, tracing damage mechanisms through all size scales. Beware of premature claims of success: those top-downers who fit engineering data with a large number of material and experimental parameters and infer their model is unique; and those bottom-uppers who project their mechanism as the dominant one amongst all others in order to control engineering behaviour (Dr Brian Cox, private communication). In reality, is there a mechanism that has not been observed; is there a significantly large crack that has gone undetected?

15.8 At the heart of structural integrity

Component failure is normally due to instability of one kind or another, and it is irrevocable. When a crack extends in a solid, energy is irreversibly lost. Load on the structural part is not indefinitely sustainable, and it eventually fails. Basically, we require in the design of a damage-tolerant composite material the presence of a *microscopically weak* structure built into a *macroscopically strong* solid that ensures any crack present becomes innocuous. This was most cogently argued in discourses by Alan Cottrell and Charles Frank to The Royal Society (London) 50 years ago (Cottrell, 1963). Cottrell presented a novel treatment of a long-standing problem, namely the crack with a force between its faces. His direct approach to finding a solution was to obtain general expressions for the force and displacement between the crack surfaces. In the case of the fibrous composite under tensile loading, carbon fibres in epoxy, for example, all the fibres in the fracture plane of the matrix crack do not snap at once; they do so in a sequential manner because of the variability in flaw size and flaw distribution along the fibre length. By careful manipulation of fibre−matrix bonding, the fibre−matrix interface is 'allowed' to fail by de-cohesion and, in so doing, blunts the tip of any small propagating crack present, whilst fibres bridging that crack remain intact and carry traction (Figure 15.12).

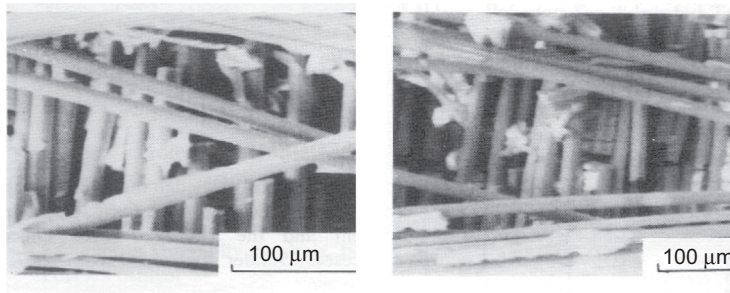

Figure 15.12 Crack propagation in an alumina fibre–alumina matrix ceramic composite showing a bridged crack and delamination and splitting modes of failure (Vekinis, Ashby, & Beaumont 1990, 1993; Vekinis, Shercliff, & Beaumont, 1991).

At the heart of the matter, then, is the matrix or interface crack between layers bridged by fibre that requires de-bonding to occur in preference to fibre fracture. In the absence of de-bonding or when the sliding (shear) resistance along the de-bonded interface is high, crack tip stresses are concentrated in the fibre and they decay rapidly with distance from the matrix crack plane. Consequently, fibres are more likely to snap at or near to the crack plane rather than pulling out, thus diminishing their vital role in bridging matrix cracks and delamination cracks. Under these circumstances, the composite would exhibit notch sensitivity (brittleness). Recall the fate of the original carbon fibre compressor blades of the RB211 jet engine with fibre too strongly bonded to the epoxy resin.

Thus, the critical issue concerning SI of the composite centres on the extent of this de-bonding mechanism and its dependence on interface properties, and its effect on crack opening and fibre fracture. These contributions on the dissipation of energy in a stable manner can be derived in terms of the constituent properties of the fibre and matrix, and the shear resistance or shear toughness of the interface. The question of SI, then, concerns the definition of optimum surface treatment of fibre and optimum properties of any coating or interphase between the fibre and matrix. Vitally important is the nature of the bond and integrity of the interface, and possible thermal stresses and shrinkage effects of the matrix during processing and expansion or contraction during ageing in wet and dry environments, and temperature fluctuations to the extreme. Thus, questions surrounding the mechanisms of mixed modes of splitting and delamination cracking require resolution. Another consideration is how to include in a physical model the probabilistic nature of the failure behaviour of the composite material.

Therefore, while our understanding of the deformation and fracture behaviour of materials based on defect theory and crack mechanics has advanced considerably, failure prediction of composite structures on a macroscale becomes problematic. At the heart of the problem lies those failure mechanism(s) best identified by direct observation (Figures 15.12–15.14). But that is not straightforward to undertake by any means. In addition, it is dangerous to assume an operative mechanism without direct evidence or that it is dominant. The next best thing is by indirect observation or measurement,

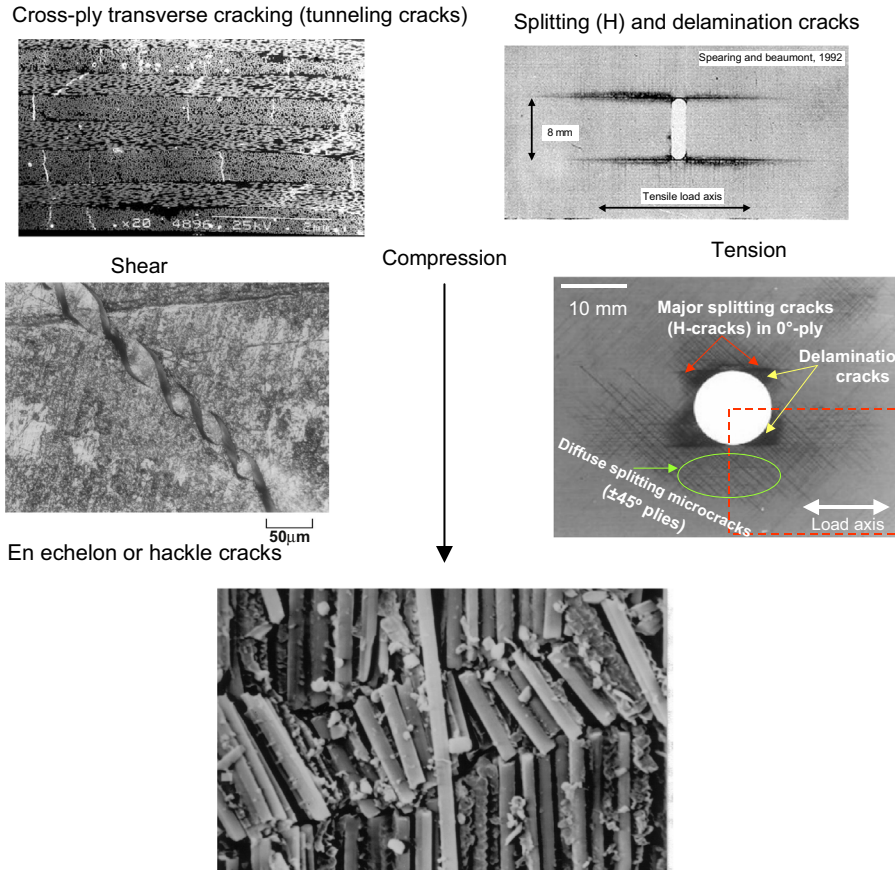

Figure 15.13 Failure mechanisms of interest (Courtesy of Dr Brian Cox, Prof Costas Soutis, Prof Mark Kortschot; also Jumahat, Soutis, & Hodzic, 2010; Soutis, 2009).

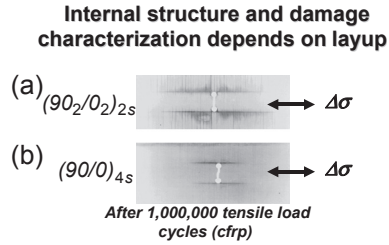

Figure 15.14 While (a) has sustained greater damage emanating from the notch tip in the form delamination, splitting and matrix cracking, the local tensile stress gradient is much reduced compared to (b) with a corresponding increase in residual tensile notch strength (Spearing & Beaumont, 1992, 1998; Spearing, Beaumont, & Ashby, 1992).

from which a mechanism(s) can be inferred by modulus or Poisson's ratio changes or by C-scan or by acoustic emission.

Perhaps the value of Poisson's ratio is a more sensitive indicator of the presence of cracks than is a direct measure of other elastic constants. On the contrary, some have argued, the principal Poisson's ratio of an aligned carbon fibre composite is very small, hence any change in its value is difficult to detect. One answer to this objection is that a composite has a number of Poisson's ratios, and so while a very small one may occur between one particular pair of directions, it will be accompanied by a much larger value shown when another pair of directions is taken for the measurements. Obviously, the latter pair should be chosen. An angle ply laminate has a very large value of the principal Poisson's ratio.

15.9 A guide to thinking and planning a physical model

Consider a physical model, which is a gross simplification of reality but captures the essentials of the situation. All successful models capture features that really matter by illuminating the principles that underlie key observations of material behaviour. An example is a skier's guide of a mountain in winter. While the map is unable to show us precisely the easiest way down the mountain in bad weather and so avoid crevasses, nevertheless, colour-coded pistes do indicate the direction for us novices to head for, more or less. Keep the model simple but not too simple (Albert Einstein).

First, identify the problem. Understand the nature of the problem (the mechanism(s)) such as matrix cracking, delamination, etc. Next, model each mechanism separately (coupling is the real challenge); then compare with data. Remember what the model is for: to gain physical insight; to capture material response in an equation or code; to predict material response under conditions not easily reproduced; and to allow extrapolation in time or temperature. What do you want from the model? (M F Ashby: private communications).

Identify the desired inputs and outputs of the model. A physical model is a transfer function. It transforms those inputs into outputs. When models couple, the outputs of one become the inputs to the next. What are the macroscopic variables and boundary conditions: *temperature, time, loads*, etc.? And at the heart of the model lie the physical mechanisms of structural change.

To construct the model, use standard techniques using the modelling tools of engineering and materials science: equations of fracture mechanics, kinetics, dynamics, etc. that we learnt at college. Exploit previously validated models of the problem using those tools. If parts of the process cannot be modelled, introduce an empirical fit to the data (e.g. a power law) that can be replaced later by a better model when it becomes available.

The point is this: physical models suggest forms for constitutive equations (laws), and for the significant groupings of the variables that enter them. Empirical methods can then be used to establish the precise functional relations between these groups. Finally, we finish up with a constitutive equation that contains the predictive power of micromechanical modelling with the precision of ordinary curve fitting of experimental data (Ashby: further private communications). In other words, input variables

like maximum stress, stress range or stress amplitude, frequency, etc., and temperature, concentration of chemical species and damage state are all embedded in the physical model. Examples below may help to illustrate this.

15.10 Modelling structure that evolves with time

A structure under stress suffers damage with time – cracks form, which in turn increase the rate of damage formation. There is positive feedback. Ageing weakens the material; its structure changes and constitutive models (equations) describe this sort of behaviour, best derived using the internal state variable method (Poursartip, Ashby, & Beaumont, 1982, 1986). (Recall that a constitutive model is a set of mathematical equations that describe the behaviour of a material element subjected to external influence: stress, temperature, etc. Constitutive equations take on many forms: algebraic, differential or integral equations, which may be embedded in a computation, e.g. FE analysis.)

15.10.1 Constitutive models: internal material state variable method

Briefly, the key ideas are based on the fact that constitutive models have two aspects: response equations and structural evolution equations. The response equation describes the relationship of (say) current modulus, E_c, of the laminate (a measure of the effect of damage), to the applied stress, σ, or stress range, $\Delta\sigma$, load cycles, N, and to the current value of the internal state variable, D. We call the internal state variable *damage* because it describes a change in the state of a material, brought about by an applied stress or by load cycling. It (meaning D) uniquely defines the current level of damage in the material, for a given set of test variables.

In this example, we observe changes in the composite modulus (stiffness) with the accumulation of fatigue damage. The response equation describes this change of (damaged) modulus, E_c, to the stress magnitude, temperature, time (number of load cycles), and to the current value of the internal state variable D:

$$E_c = f(\sigma, \Delta\sigma, \lambda, T, \Delta T, t, v_\sigma, v_T, D, \text{material properties}, \text{enviroment}) \qquad (15.1)$$

Damage due to delamination, for example, can be defined as total (meaning actual or measured) delamination crack area A normalized with respect to the total area A_o available for delamination, that is, $D = A/A_o$. But problems arise from a lack of detail of these microscopic parameters, including number (or density) of fibre breaks and matrix cracking, which can only be determined microscopically and this is not practical in real structures. Instead of characterizing a material property as a function of the independent variables, which experimentally is very (time-consuming and expensive), fit data to a coupled set of differential equations, one for the modulus E', for instance, and two (or more) depending on damaging mechanisms D_1', D_2'.

Since the internal state variable, D, evolves over time with the progressive nature of the damaging processes, its rate of change can be described by

$$D' = g(\sigma, \Delta\sigma, \lambda, T, \Delta T, t, v_\sigma, v_T, D, \text{material properties}, \text{environment}) \tag{15.2}$$

Where several mechanisms contribute simultaneously to the response, (e.g. where modulus degradation is the result of the coupling of delamination and matrix cracking), this time there are two internal state variables, one for each mechanism. Consequently, the model suggests a constitutive equation having a completely different form than before.

Instead of trying to characterize the modulus, E_c, as a function of the complete set of independent variables (although we could), we now seek to fit data to a coupled set of differential equations, one for the modulus E_c', and two (or more), depending on the number of damaging mechanisms, for damage propagation, namely D_1' and D_2':

$$E_c' = f(\sigma, \lambda, T, D_1, D_2, \text{etc. material properties}, \text{environment}) \tag{15.3a}$$

$$D_1' = g_1(\sigma, \lambda, T, D_1, D_2, \text{etc. material properties}, \text{environment}) \tag{15.3b}$$

$$D_2' = g_2(\sigma, \lambda, T, D_1, D_2, \text{etc. material properties}, \text{environment}) \tag{15.3c}$$

D_1 describes the damage due to one mechanism, and D_2 describes a different damaging mechanism that, when combined with the first, eventually lead to composite failure. E', D_1' and D_2' are their *rates of change* with time (or numbers of load cycles); f, g_1, g_2 are simple functions yet to be determined.

There are now three independent variables, (σ, T and stress state, λ), whereas before there were eight. These equations can be integrated to track out the change of modulus with the accumulation of damage, and ultimately used to predict fracture of a component or the design life in fatigue as shown in Figure 15.15 (Poursartip et al., 1982, 1986). Thus, the modulus-time (cycles) response is found by integrating the equations as a coupled set, starting with $E = E_o$ (the undamaged modulus) and $D = 0$ (no damage). Step through time (cycles), calculating the increments, and the current values, of E_c and D, and using these to calculate their change in the next step. Equation (15.3a) can now be adopted as the constitutive equation for fatigue, and empirical methods can be used to determine the functions f, g_1, g_2.

The state variable approach leads to the idea of a mechanism map or damage diagram, a versatile method of presenting both results of the model and experimental data. The conceptual map displays the response (loss of stiffness or strength), identifies the mechanisms and shows the extent of the damage for a given loading history.

However, the model points to something else, and it is of the greatest value; it suggests the proper form that the constitutive equation should take. This physical model–informed empiricism has led to the development of a new branch of mechanics called *damage mechanics*.

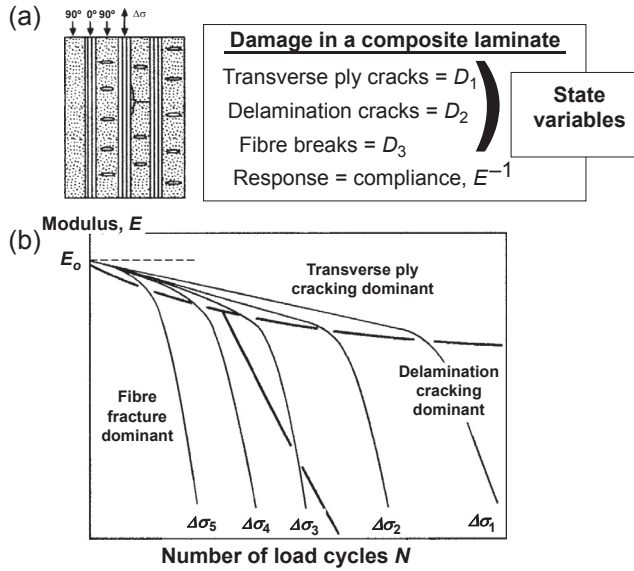

Figure 15.15 The state variable approach leads to the ideas of a mechanism map or damage diagram, a versatile method of presenting both results of the model and experimental data (Poursartip et al., 1982, 1986). The map displays the response (loss of stiffness), identifies the mechanisms and shows the extent of the damage for a given loading history. Various failure modes spread, reducing the section until the fracture load exceeds the residual strength, culminating in a cascade of breaking fibres.

There can be added complexity – spatial variation appears when stress and temperature or other field variables are nonuniform. While simple geometries can be treated analytically, using, for example, the modelling tools of fracture (damage) mechanics, more complex geometries require discrete methods. The FE method of modelling is an example. Here the material is divided into cells, which respond to temperature, body forces and stress via constitutive equations, with the constraints of equilibrium, compatibility and continuity imposed at their boundaries. Internal material state variable formulations for constitutive laws are embedded in the FE computations to give an accurate description of spatially varying behaviour.

15.10.2 Reliability-based design based on residual strength modelling

As a beginning, consider the example of a component in constant stress amplitude cyclic loading; the density of matrix cracks increases with time and the crack spacing becomes smaller. Acting simultaneously, any delamination cracks present will extend in length. In essence, the material 'work softens' and becomes more compliant, that is, the modulus falls. The result is that the strain to failure increases with the accumulation of fatigue damage.

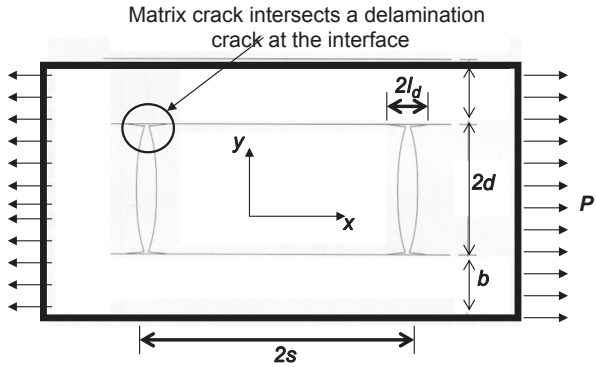

Figure 15.16 A physical model of a matrix crack, $2d$ intersecting a delamination crack $2l_d$ and matrix crack spacing $2s$ (Dimant, Shercliff, & Beaumont, 2002).

A physical model to illustrate combined matrix cracking and delamination cracking is shown in Figure 15.16 (after Dimant, Shercliff, & Beaumont, 2002). The damage parameters are illustrated in the sketch: the distance between two neighbouring delamination cracks, $2\ell_d$, and the matrix crack spacing $2s$.

To begin with, the damage parameter D is usually defined as $D = 1/s$, where s is matrix crack spacing. In this case, the internal state variable, the damage parameter D of Eqn (15.1) is given by $1/2s$. Alternatively, it might be useful to normalize matrix crack spacing, s, with delamination crack length l_d, (s/l_d), because of coupling effects between these two mechanisms.

For the reduced (damage) modulus E_c of the laminate (Dimant et al., 2002):

$$\left[\frac{E_c}{E_o}\right]_{\text{lam}} = \frac{\left[\frac{E_c}{E_o}\right]_a \left[\frac{E_c}{E_o}\right]_b (s)}{\left[\left[\frac{E_c}{E_o}\right]_a (s - \ell_d) + \left[\frac{E_c}{E_o}\right]_a (\ell_d)\right]} \tag{15.4}$$

where E_o is the undamaged (original) modulus of the laminate. This equation considers the transverse ply matrix crack and the delamination between off-axis plies; it ignores the possibility of fibre fracture in the principal stress direction.

In a tensile test (for small elastic displacement), the relation between ultimate tensile strength, σ_f, and ultimate failure strain, ε_f, is given simply by

$$\varepsilon_f = \frac{\sigma_f}{E_c} \tag{15.5}$$

(E_c is the damaged Young's modulus).

If, for the time being, we ignore any possible effect of broken fibres on the modulus, then by estimating the reduced (damage) modulus due to matrix and delamination cracking using Eqn (15.4), and substituting into Eqn (15.5), we can predict

Table 15.1 Ultimate laminate failure strain determined by inserting Eqn (15.5) into Eqn (15.4)

Static or cyclic loading	Laminate configuration	Glass fibre-epoxy ($\%\varepsilon_f$)	Carbon fibre-epoxy ($\%\varepsilon_f$)
Static	(0/90/0)	2.95	1.38
Static	$(0/90)_s$	2.72	1.36
Static	$(0/90_2)_s$	2.27	1.45
Static	$(0/90_4)_s$	1.88	1.46
Cyclic	(0/90/0)	2.55	1.48
Cyclic	$(0/90)_s$	2.65	1.51
Cyclic	$(0/90_2)_s$	2.52	1.53
Cyclic	$(0/90_4)_s$	2.33	1.48

the ultimate laminate failure strain (Table 15.1). Inputs to the model are the experimental measurements of crack spacing and delamination crack length. For the carbon fibre–epoxy laminate we took $s = 2d$ for static loading and $s = d$ for cyclic loading.

From Table 15.1 it is reasonable to conclude that increasing the thickness (number) of transverse plies reduces the tensile failure strain, ε_f, of the glass fibre–epoxy laminate. In contrast, however, the failure strain of carbon fibre–epoxy laminates seems to be independent of transverse ply thickness ($\varepsilon_f \sim 1.4$–1.5%). After cyclic loading, the strain to failure, ε_f, of glass fibre–epoxy laminates containing only one or two transverse plies decreases, whilst ε_f for the composite containing four and eight transverse plies increases. We know that the fatigued material is more compliant (its crack density is greater), and, therefore, according to Eqn (15.5) ε_f would be expected to increase. This logic seems to be valid only for the laminate containing the thicker (four or more) transverse plies. One possible explanation that is physically sound is to propose that fibre fracture has occurred in the laminate with the thinner (less than four) transverse plies.

The consequence of this would be to simultaneously reduce the fracture stress and failure strain of the laminate. For this suggestion to be consistent with an explanation of the fracture behaviour of the carbon fibre–epoxy laminate, we would have to argue in favour of little or no significant (meaning not detrimental) fibre breakage during fatigue prior to ultimate failure. In which case, our observation of a slight increase in strain to failure with cyclic loading would be due to some additional matrix cracking. In situ SEM studies of $(0°/90°/0°)$ and $(0°/90°)_s$ laminates clearly show a concentration of glass fibre and carbon fibre breaks within $(0°)$ longitudinal plies in front of matrix crack tips.

Ultimately, the aim would be to develop a design tool that incorporates an initial material variability and operating environment to provide a 'knockdown' factor f that corresponds to a specified probability of failure P_f.

Critical aspects include

1. Understanding of the expected load and environment for a particular structure based on a statistical description via a Monte Carlo simulation.
2. Development of a database of initial strength based on a Weibull distribution and residual (fatigue) strength evolution curves (the input) based on a stress analysis and structure evolution to support the 'informed empiricism' of a residual strength model.

15.11 Designing against stress corrosion cracking

Consider environmentally assisted crack growth in a glass fibre−epoxy composite under stress (Sekine & Beaumont, 1998). A micron-sized crack initiates at a surface flaw of the glass fibre. It propagates stably to begin with and extends rapidly through the remainder of the fibre (Figure 15.17).

In fracture mechanics terminology, the relation between crack propagation rate, da/dt, and crack tip stress intensity factor, K_I, in bulk glass is

$$\frac{\mathrm{d}a}{\mathrm{d}t} = AK_I^m \tag{15.6}$$

A and m are constants that depend on the material and environment. For an elastic solid, the average tensile stress σ_y over distance D immediately ahead of a macroscopic crack is

$$\sigma_y = \frac{1}{\mathscr{D}} \int_o^{\mathscr{D}} \frac{K_I^*}{\sqrt{2\pi x}} \mathrm{d}x$$

$$\sigma_y = K_I^* \sqrt{\frac{2}{\pi D}} \tag{15.7}$$

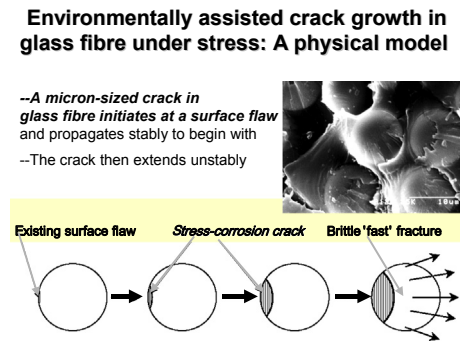

Figure 15.17 A micron-sized crack in glass fibre initiates at a surface flaw and propagates stably to begin with. The crack then extends unstably (Sekine & Beaumont, 1998).

D is the distance between two adjacent rows of glass fibre in a doubly periodic square array given approximately by

$$D = \sqrt{\frac{\pi}{V_f}} r_f \tag{15.8}$$

r_f is fibre radius and V_f is fibre volume fraction.

If we think of the average tensile stress as being supported essentially by the fibres-only σ_f, then

$$\sigma_y \approx \sigma_f V_f \tag{15.9}$$

Hence

$$\sigma_y \approx \sigma_f V_f \approx K_I^* \sqrt{\frac{2}{\pi D}} \tag{15.10}$$

Alternatively

$$\sigma_f = \beta K_I^* \tag{15.11}$$

where β is a geometrical factor.

$$\beta = \frac{1}{V_f} \sqrt{\frac{2}{\pi D}} \tag{15.12}$$

Recall the Arrhenius equation:

$$\frac{\mathrm{d}a}{\mathrm{d}t} = v \exp - \left(\frac{Q - \alpha K_I}{\mathrm{RT}} \right) \tag{15.13}$$

K_I: stress intensity factor; Q: activation energy of chemically activated process (sometimes predicted from molecular models); R: gas constant; T: absolute temperature; ν, α: empirical constants (often elude modelling methods).

Now insert for the crack tip stress intensity factor for the glass fibre:

$$K_I = \sigma_f \sqrt{2\pi r_f} \tag{15.14}$$

By inserting a substitution of the constant k:

$$k = \exp\left(-\frac{Q}{\mathrm{RT}} \right) \tag{15.15}$$

We arrive at

$$\mathrm{d}t = \frac{2r_f}{vk}\exp\left(-\frac{\alpha\beta\sqrt{2\pi r_f}}{\mathrm{RT}}K_I^*\right)\mathrm{d}a \tag{15.16}$$

Now integrate in order to obtain the time to fracture t_F of a single fibre:

$$t_F = \frac{2r_f}{vk}\int_{a_0}^{a_F} a\exp\left(-\frac{\alpha\beta(\sqrt{2\pi r_f})}{RT}K_I^*\right)\mathrm{d}a \tag{15.17}$$

a_0 initial (inherent) flaw size; a_F is the critical value at unstable fracture of the glass fibre (when $K_I = K_{IC}$).

Then make the approximation that the average crack growth rate $\mathrm{d}a/\mathrm{d}t$ between adjacent fibres

$$\frac{\mathrm{d}a}{\mathrm{d}t} \approx \frac{D}{t_F} \tag{15.18}$$

$\mathrm{d}a/\mathrm{d}t$ is given by Eqn (15.13); D is the distance between neighbouring rows of fibres in a doubly periodic square array of fibre given by Eqn (15.8); and t_f is given by Eqn (15.17).

Finally, making substitutions to simplify the final expression, we arrive at the crack velocity, $\mathrm{d}a^*/\mathrm{d}t$, as a function of K^*_I, a simple power law with the power of 2:

$$\frac{\mathrm{d}a^*}{\mathrm{d}t} = 0.625\zeta\mu^2 K_{Ia}^{*2} \tag{15.19}$$

where the following constants are summarized:

$$\xi = \frac{\sqrt{\pi}}{2}\left(\frac{vk}{\sqrt{V_f}}\right)$$

$$\mu = \frac{\alpha\beta\sqrt{2\pi r_f}}{RT}$$

β is given by Eqn (15.12) and k is given by Eqn (15.15). Verification of the model with experimental data is shown in Figure 15.18. The effect of inherent flaw size and the matrix bridging effect on the time to failure is shown in Figure 15.19. Over long periods of time, inherent flaw size becomes irrelevant and is only significant for time periods of less than 1 year.

15.12 Multiscale modelling and computer simulation

Modelling and simulation are becoming increasingly ambitious. On the one hand, there are calculations that aim at increasingly precise and detailed description.

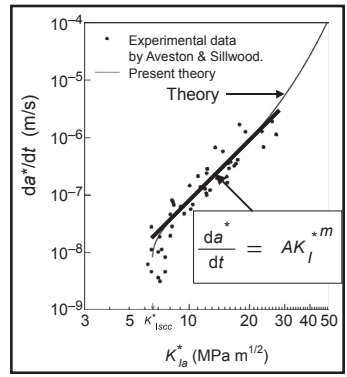

Figure 15.18 Verification of the model with experimental data (Sekine & Beaumont, 1998).

The number of assumptions is minimized, and empirical elements are replaced wherever possible. Improvements in detail yield improvements in accuracy and provide the potential tool to resolve previously intractable problems. On the other hand, increasingly large systems are being investigated. These have different challenges. The methods, which are best for studies at the atomistic level, are unlikely to be inefficient for larger structures. This is because atomistic models for service performance are too firmly rooted in the underlying atomistic processes, although understood, can be characterized only by microscopic measurements, which are impractical for an engineer. Furthermore, interpretation itself will be difficult without other aids. There is, therefore, a need to link experience at levels between the macroscopic size with understanding from an atomistic scale.

One way forward is to identify the broad rules governing material behaviour, and the rules governing the magnitudes of material properties, which are contained in the

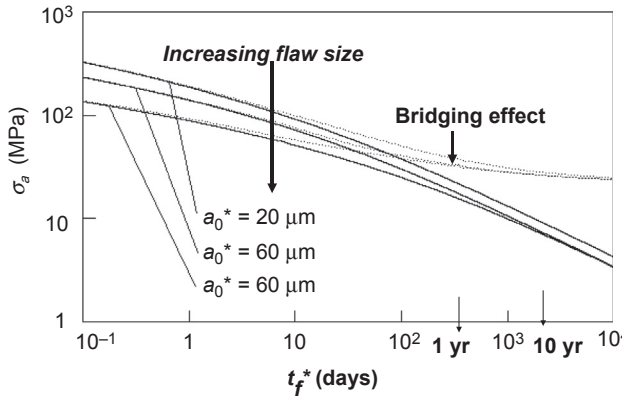

Figure 15.19 The effect of inherent flaw size and the matrix bridging effect on the time to failure. Over long periods of time, inherent flaw size becomes irrelevant and is only significant for time periods of less than 1 year (Sekine & Beaumont, 1998).

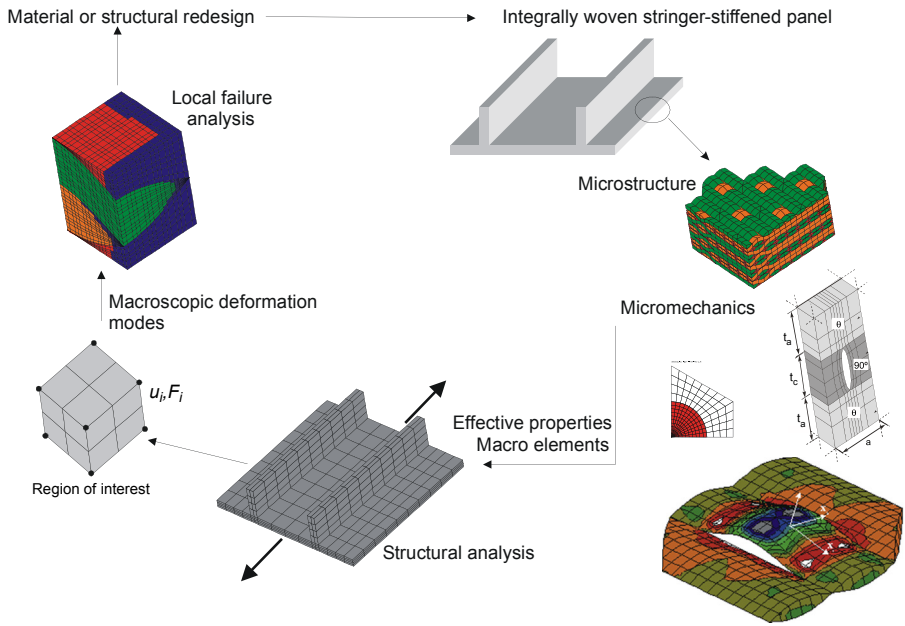

Figure 15.20 A typical multiscale challenge: a stringer-stiffened panel fabricated from a textile composite (Courtesy of Prof John Whitcomb).

atomistic models, and use them as the basis of a 'model-informed' empiricism. Figure 15.20 is a typical multiscale challenge based on a hierarchical strategy. It is a stringer-stiffened panel fabricated from a textile composite. The details of the microstructure at either the fibre—matrix or tow architectural scales are too complex to analyse.

Instead, micromechanical models are used to obtain the effective properties at the micron scale to obtain effective fibre tow properties. Then, a model or representative of a volume element is used to obtain the effective properties of the textile architecture at this size scale. Inserting these values into a structural model identifies the 'hot spots.' These hot spots are interrogated by reversing the process in order to determine whether the structure has to be redesigned or an alternative material system selected. Examples of challenges include dealing with large macroscopic gradients, nonperiodic loads, including transient loads, nonperiodic microstructure, mesh generation and data management.

In Figure 15.21, all of the pictures are synthesized from the same basic textile microstructure. The difference is the degree of repetition of the basic unit and, also, how closely the material has to be modelled (e.g. in the presence of large macroscopic strain gradients, a higher magnification is required). For coarse and fine microstructures, the analyses involve discrete and homogenized modelling, respectively. What is not so clear is how to handle the 'transitional microstructure,' for which there is too much detail for discrete modelling, but too little repetition of representative

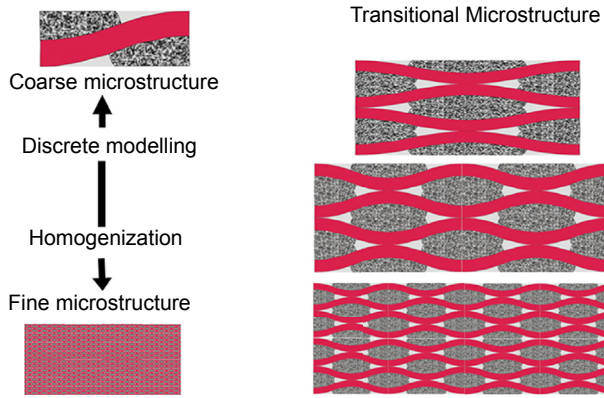

Figure 15.21 All of the pictures are synthesized from the same basic microstructure. The difference is the degree of repetition of the basic unit and also how closely the material must be modelled (Courtesy of Prof John Whitcomb).

behaviour to use homogenization. One way is to use homogenization, selective homogenization, macro elements (FE that allow complex variation of properties within an element), and global to local interfacing techniques, including one technique based on modal analysis.

An aspect of multiscale analysis often overlooked is the integration of different models. A common characteristic of many analytical studies is the need to construct and manipulate related models, related in the sense that they share some characteristics. In other words, there is a clear hierarchy in which many properties are 'passed on' via inheritance. The hierarchical analysis environment can be used in parametric studies of structures or situations in which the constitutive behaviour is defined in a hierarchical sense (John Whitcomb: private communication).

Recent developments in multiscale modelling strategies have led to the virtual mechanical testing of composite structures right up to the point of failure. In the virtual testing of realistic aerospace composite structures, the validation of FE predictions has been mostly proven for simple coupon and benchmark test specimens. The difficulty is simulating the correct failure mechanisms of realistic aerospace structures; for example, post-buckled compression panels, impact-damaged shells, major joints or any component with geometrical discontinuities. Commercial FE codes are powerful enough to capture the correct physics of the failure process. Some codes model the initiation of material failure followed by propagation to full structural failure.

Having an FE code is just the beginning; the modeller has to create an FE model that is capable of capturing the internal stress fields with the required accuracy. Assessing damage in sandwich structures under hard and soft impacts, for example, requires validated FE design tools together with structural impact test data in order to validate FE codes and airworthiness certification.

Simulation is a study of the dynamic response of a modelled system by subjecting the model to inputs, which simulate real events, ways in which complex structures

evolve without the need to perform expensive time-consuming experiments. This route leads to a quantitative prediction that represents the actual performance of the material or component or full-size structure across a broad spectrum of size (or multiscale) without the cost, time, accident risk, effort and repeatability, problems normally associated with real testing. But how much detail of failure mechanisms do we need to know in order that a successful physical model can be incorporated into a simulated virtual test that reproduces the outcome of a real structural situation? Creating physically sound damage simulations, however, is difficult because damage initiation must first be predicted for parts containing no cracks (Cox & Yang, 2006).

Advances in computer power have made it possible to simulate materials by describing the motion of each atom, rather than making the approximation that matter is continuous. Most simulations of cracks ignore the quantum-mechanical nature of the bonds between the atoms. This limitation is overcome by using a new technique called 'learn on the fly' (LOTF). This method uses a quantum-mechanical description of bonding near the tip of the crack, where essentially it is coupled almost seamlessly to a large (on the atomic scale) region described with an interatomic potential.

A crack simulation in a brittle material like silicon indicates rearrangements of atoms at the crack tip. Usually, this is associated with ductile materials, but unlike metals these plastic deformations remain trapped at the crack tip. Rather than crack tip shielding from high stress and resulting ductility, there is instability of the crack path. The rearrangements, called *crack tip reconstructions*, are asymmetric with respect to the orientation of the crack. This opens up the possibility of observing them in macroscopic experiments. There is a mesoscale model, which links the atomic scale phenomena to macroscopic length scales, and shows how the crack tip reconstruction could lead to ridges on the crack surface with well-defined shape. A key concept is *dynamic steering* of the atomic motions. When the crack propagates faster than a critical velocity, breaking of atomic bonds sequentially follows in quick succession and the system is steered away from the reconstructed state. This is why the surface behind a fast crack should be smooth.

Developments in nonlinear elements in computational mechanics have led to damage simulations of sufficient fidelity in engineering design (Dr Brian Cox). A key feature is the incorporation, into a FE formulation, of elements that can explicitly represent displacement discontinuities associated with cracks – so-called 'cohesive elements.' These elements relate the displacement discontinuity across a crack to tractions that act across that crack. Examples include fibrils in polymer craze zones, bridging fibres or ductile particles, fibre–matrix slippage following de-bonding (friction) and so on. Cohesive elements can be formulated that admit cracks crossing any surface within the FE, so that the developing crack path in a damage simulation need not be specified a priori; it can simply follow any locus that the mechanics of the evolving failure process has determined.

However, a number of minor difficulties still exist before damage simulations of sufficient fidelity can replace qualification tests: (1) the implications of length scales associated with nonlinear cohesive processes for correct mesh refinement; (2) the calibration of cohesive traction-displacement laws in order to confirm a physically sound model of the particular crack wake mechanism; and (3) the problem of instability in numerical iteration of nonlinear damage problems, which may have physical (not algorithmic) origins. Those damage growth mechanisms that have been observed in

laminates include delamination and splitting (shear) cracks, which grow in various orientations and change in shape with time; fibre rupture; fibre microbuckling or kink formation; global buckling of delaminated plies; and diffuse microcracking or shear damage within individual plies. These mechanisms (with the exception of global buckling) can be represented by cohesive elements, by collapsing the nonlinear processes onto surfaces, with the physics embedded in traction−displacement constitutive behaviour (rather than stress−strain behaviour).

Solving the problem of suitable mesh refinement might be achievable in terms of length scales associated with cohesive laws. Calibration of traction−displacement laws requires a successful physical model and appropriate set of experiments. This is not straightforward because different cohesive mechanisms often act simultaneously in a single crack, with their relative magnitudes depending on interaction effects with other cracks. Defining experiments is also challenged because traction laws must be deduced from experiments via inverse problem methods, which are vulnerable to numerical noise. Instability can be dealt with in one of two ways: (1) run the complete simulation as a dynamic model or (2) invent algorithms that stabilize the model by controlling local displacements.

15.12.1 Simulation of a delamination crack using a cohesive interface model

A composite can be modelled by layered elements (homogeneous and orthotropic) whose properties (e.g. stiffness) degrade by microcracking according to a continuum damage model (Dr Brian Cox). The coexistence (coupling) of discrete delamination cracking and continuum damage (matrix cracking) can be captured via a cohesive interface model (Figure 15.22). Microcracking is modelled by a nonlinear constitutive

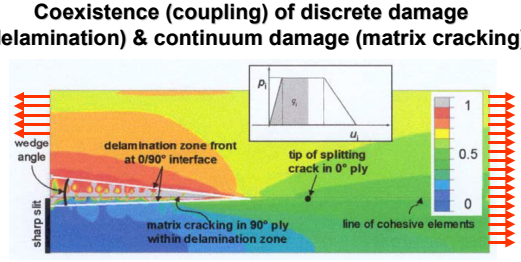

Figure 15.22 A realistic simulation of a delamination crack modelled by a cohesive zone idealization based on the finite element method, which computes stress distributions for generic geometry and loads. The need for finite elements smaller than the process zone at a crack tip means less than 1 mm for typical resins. A mesh this fine is unrealistic for a realistic structure (Courtesy of Dr Brian Cox).

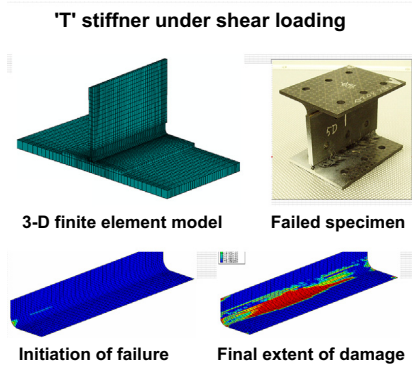

Figure 15.23 The need for finite elements smaller than the process zone at a crack tip means less than 1 mm for typical resins. A mesh this fine is unrealistic for a realistic structure. Most codes contain a local/global strategy whereby an existing coarse (global) finite element model has embedded a refined (local) region (Courtesy of Prof Glyn Davies) (Davies & Ankersen, 2008).

law to the individual ply that causes material degradation ('softening') according to the continuum damage model. The ply degradation parameters in the model are the internal state variables governed by damage evolution equations.

A cohesive zone idealization based on the FE method computes the stress distributions for generic geometry and applied load. A realistic model or simulation then predicts the effect of load, fibre orientation, and stress concentrator upon damage and strength. Strain energy concentrations suggest correctly that ply junctions are sites that initiate delamination cracks. Crack propagation needs an accurate representation of the stress field ahead of the crack front known as the 'process zone,' which may be small. The need for FE smaller than the process zone at a crack tip means less than 1 mm for typical resins (Figure 15.23). A mesh this fine is unrealistic for a true structure. Most codes contain a local/global strategy whereby an existing coarse (global) FE model has embedded a refined (local) region.

15.12.2 Numerical prediction of foreign object impact damage

High velocity impacts due to bird strike, tyre debris and other foreign object damage are critical safety issues. Computational (FE) methods (e.g. Abacus/Explicit) are required to reduce certification and development times, thereby reducing costs, and to predict SI under impact, etc. (Figure 15.24). The problems involve multiscale and multiphysics modelling for localized impact of bird strike of leading edges. This includes the use of complex constitutive equations at the micromechanics level of delamination and the multiphysics (fluid mechanics) aspects of fluid−structure interactions (gelatin, which represents the 'bird' and ice flow on impact) (Johnson & Holzapfel, 2006).

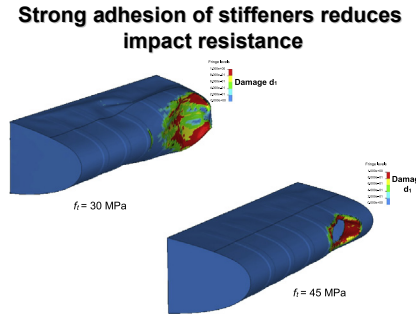

Figure 15.24 Recent developments in multiscale modelling strategies enable virtual mechanical testing of composite structures until failure to be carried out. High velocity impacts due to bird strike, tyre debris and other foreign object damage are critical safety issues (Courtesy of Dr Alastair Johnson) (Johnson & Holzafel, 2006).

In leading edge impact studies, the principal damage mechanisms observed and explicitly taken into account include

1. intralaminar damage using a constitutive equation where elastic constants were degraded progressively as a function of the damage variables;
2. interlaminar damage using interface elements inserted between two adjacent brick elements representing neighbour plies controlled using a simple cohesive crack model.

A critical safety issue for the design of primary aircraft structures using sandwich structures is vulnerability due to foreign object impacts from bird strike, tyre rubber and hard objects (hail, runway debris, metal fragments). Protected from impact damage is by an energy absorbing honeycomb core and an outer cover laminate. Nevertheless, impact damage can occur and is due to the thin composite skins and low strength honeycomb or foam cores.

Impact failure modes in composite/sandwich structures include

- brittle fibre fracture from hard bodies and high energy impacts;
- delamination failure from soft bodies and low energy impacts; and
- skin/core penetration from severe impact loads.

Physical phenomena associated with impact damage and progressive collapse of the honeycomb structure are complex, and predictive models and simulation tools for design and analysis are being investigated. Key issues are the development of constitutive laws for modelling composite in-ply and delamination failures, suitable models for folding and collapse in the composite cores, materials laws for soft body impactors, and the efficient implementation of the materials models into FE codes. These problems involve multiscale modelling techniques. The multiscale aspects arise because impact damage is localized and requires fine-scale modelling of delamination and ply damage at the micromechanics level, whilst the structural length scales are much larger.

In fold-core sandwich structures there are two natural length scales, associated with the core unit cell geometry and the sandwich structure. The approach is to use

mesoscale models based on continuum damage mechanics (CDM) in explicit FE codes, which provide a framework for modelling in-ply and delamination failure. Such models are applied to the sandwich skin laminates, to the core/skin interface and to the folded core elements. Simulation of local damage in larger aircraft sandwich structures requires further development. These are being investigated using homogenization techniques to replace unit cell structures by equivalent solid elements, combined with domain coupling of fine-scale core models in critical regions with homogenized elements. Predictive models to determine core behaviour using parametrized FE models for fold-core unit cells have been developed and applied to the design of fuselage sandwich panels. Impact test programmes include the use of a gas gun to fire projectiles such as steel cubes, ice balls and tyre rubber fragments at impact velocities in the range 50−220 m/s. Failure modes range from rebound from the outer skin, outer skin damage, core penetration, inner skin damage and inner skin penetration. Nondestructive evaluation (NDE) methods such as X-ray, lock-in thermography, ultrasonic C-scans (Figure 15.26) and computer tomography (CT) (Figure 15.25) are used to ascertain the presence and nature of impact damage. CT quantifies internal core damage for fold-core sandwich structures and assesses damage tolerance of damage in 3-D (Figure 15.25). The structure was impacted with an ice cylinder of 15 g, projectile velocity 192 m/s, with 276 J of impact energy. Failure modes include outer skin damage, core penetration, inner skin damage and inner skin penetration.

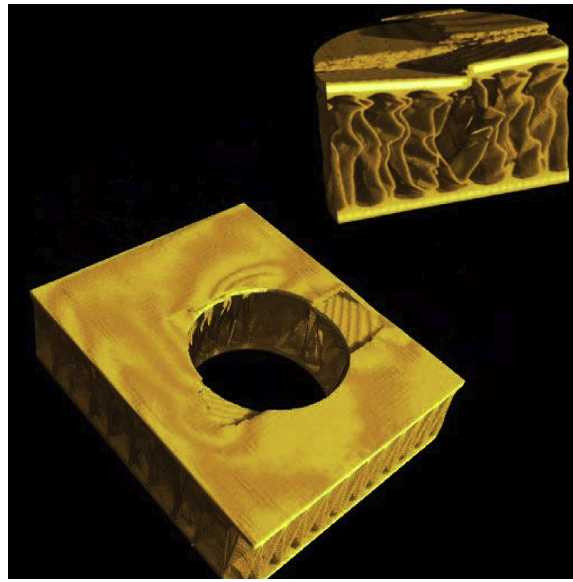

Figure 15.25 Computer tomography (CT) quantifies interior core damage for fold-core sandwich structures and assesses damage tolerance of damage in 3-D. The structure was impacted with an ice cylinder of 15 g, projectile velocity 192 m/s, with 276 J of impact energy. Failure modes include outer skin damage, core penetration, inner skin damage and inner skin penetration (Courtesy of Dr Alastair Johnson).

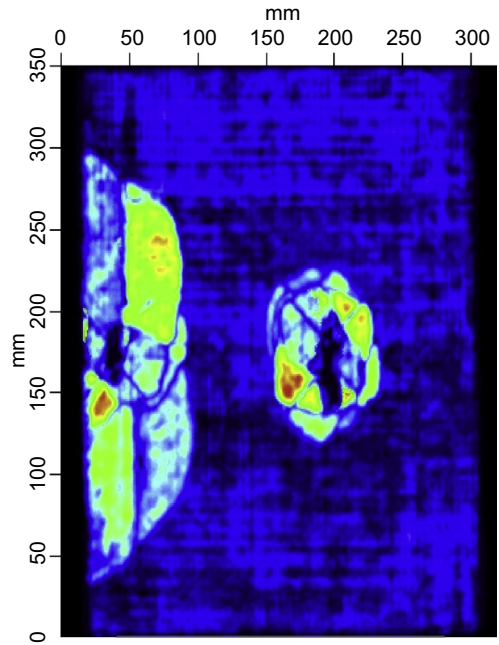

Figure 15.26 C-scan of an 8-mm CFRP composite plate showing areas of delamination for an edge impact (on the left) and a central impact (on the right) (Courtesy of Prof Carlos Gonzales).

15.12.3 Blast impact

The European CAFV programme led by QinetiQ in the United Kingdom is concerned with the application of carbon fibre composites to AFVs. It involves the intelligent selection of the material system, and optimizing the processing and design variables to meet vehicle performance and cost requirements. Advances are made by modelling of mine blast survivability of composite structures using a range of dynamic commercial finite element analysis software (LS-DYNA/AUTODYN). Numerical modelling techniques are used in combination with experimental assessment (Figure 15.26) (Wright & French, 2008).

Due to the nature of the mine blast requirement, and in particular the small stand-off distance between the explosive charge and the target, extreme loading conditions are experienced at the panel surface. Thus, it is extremely difficult to directly measure the blast loading experienced by the panel. At the present time, validation of the blast model is further complicated by the lack of a well-developed material model to describe the response of the candidate composite materials.

By blast loading, the high-pressure shock wave at the front of the target generates a compressive stress wave within the composite, which causes initial crushing in the composite matrix. The stress wave propagates through the material striking the rear face of the target and is reflected as a tensile wave. It is this tensile wave that is responsible for the initial delamination of the composite during blast loading. At longer

timescales, global loading leads to flexure of the panel fibre rupture and widespread delamination along the neutral axis.

In aerospace applications, modelling has focussed mostly on the behaviour of thin sections of composite, and shell element models (plane stress) have developed faster than the equivalent solid element model. For localized blast loading conditions, shell element models have a fundamental disadvantage. Under blast loading conditions, damage due to the propagation of stress waves through the thick target (shock-holing) cannot be explicitly represented by the shell model. While solid element models offer the advantage of being able to represent localized material failure due to shock stress wave effects, shell element models are suited for the prediction of a global structural response.

15.13 Can non-destructive evaluation (NDE) detect defects in laminated structures and bonded structures?

15.13.1 Prediction of structural lifetime by acoustic emission

The types of flaws detectable in laminates and bonded structures using ultrasound, X-ray and acoustic methods include delaminations and fibre fractures, porosity, lack of adhesive bonding, inclusions and foreign materials. Consider damage assessment by acoustic emission testing; for example, the testing of a carbon fibre composite pressure vessel (cf. the A380 or 787 fuselage) by Anthony Bunsell where the source of the emitted sound (energy) is from the breakage of the carbon fibre distributed to begin with more or less randomly throughout the vessel. Progressive fibre fracture is accompanied by an accumulation of acoustic counts and increasing count rate, which can be measured. Once the density of fibre breaks reaches a critical damage state, the reduced strength of the composite equals the applied stress on the vessel. It becomes unstable and instantaneous (catastrophic) failure is unstoppable.

This time dependence (or damage rate) is related to the density of broken fibres in a viscoelastic resin matrix. Initially, individual fibre breaks are isolated, but with increasing load or duration of time, fibre breaks cluster and the stress fields associated with each cluster interact. This leads to an instability and catastrophic fracture of the vessel. A period of steady pressure gives a damage rate and residual strength, which are functions of the instantaneous internal damage state. There is positive feedback. Construction of a FE model leads to the calculation of a master curve, which corresponds to a pressure vessel having exactly the desired service life. A threshold damage level is then determined experimentally. It follows that when the damage accumulation level attains the threshold value in the master curve, the service (design) life of the vessel is realized.

This translates into a test, which involves the monitoring of damage events by acoustic emission over a period of several hours and a comparison made with the number predicted by the master curve. Experimental results obtained on pressure vessels after more than five years in service project that the pressure vessel will survive for more than 20 years in service.

15.13.2 Prediction of the structural adhesive bond lifetime

For the entire second half of the last century, there had been little progress in determining the SI of an adhesive bond. Not only was there no method to detect the dreaded 'kissing bond,' there was no way to guarantee a minimum joint strength although many attempts have been made to measure the bond strength in situ. There are many published claims of success, but follow-up experiments did not yield validate claims. Most studies were based upon two assumptions: (1) that a fundamental relationship exists between strength and stiffness, and (2) that ultrasonic velocity depends on modulus, which is correlated with strength (Crane & Dillingham, 2008).

Those conditions and defects that remain 'invisible' include the 'kissing bond' and intimate contact between adhesive and substrate but with no adhesion, and contamination of the substrate. The latter leads to the lack of adhesion or 'kissing' bond. The inability to discriminate nondestructively between a good bond and a 'kissing' bond has been the key roadblock to the advanced use of bonded structures. As a result, the inability to find these flaws has limited adhesive bonding to secondary (lightly) loaded structures and will continue to do so until NDE is able to ensure that bonded joints remain bonded throughout an aircraft's lifetime. The thought was that if bond strength could not be predicted, then predict quality!

Ideally, an NDE adhesive bond test should be able to guarantee a minimum load-bearing capability; be reliable enough for a material review board evaluation; be usable at the lowest level of assembly; and be inexpensive. The question to be answered was, 'if strength is an intrinsic property, then can a nondestructive test measure it?' And if the ideal cannot be achieved, then just what is possible? Why not simply measure strength directly?

The FAA and DoD require knowledge of joint strength for the certification of a primary structure. Normally, proof testing would be sufficient. However, proof testing is expensive at $1 M for a small aircraft wing. Determining the strength of a part in production requires an entirely new approach. Methods of applying mechanical loads include electron beam pulses, high power ultrasound, electromagnetic pulses and mechanical impact. There are limitations of most proof test methods to measure bond strength. First of all, the load has to be applied to a large area; secondly, all elements must be loaded at same time, and thirdly, a proof test may damage the structure during application. Practical issues include that the impact loads must be applied parallel to surface; the compressional wave velocity is of the order of 2500 m/s; and pulses must be short (200 ns). Lasers produce mega/giga-watt pulses with picosecond durations, and the area probed is small. The use of ultrasonic microscopic inspection of laser shock peened jet engine compressor blades showed that it is easy to apply this technique to bonded composite structures. Preliminary experiments have yielded encouraging results where data showed that it is possible to distinguish between surface treatments, which affect adhesive strength, and to distinguish between adhesive types, which relates to cohesive strength. Furthermore, it is easy to move the site of maximum tensile stress within the sample with optical delay lines.

The last Holy Grail of inspection is to find an NDE method to interrogate a bond and return its approximate strength of an adhesive bond. Are we there yet? No!

Then where are we? A method to detect the dreaded 'kissing bond' is available. Also, NDI can supply strength data to designers for deterministic design. Designers readily accept that introducing small delamination into a joint is equivalent to a small increase in porosity.

Discrete flaws are still detected with traditional methods, but they are expensive; they cannot be easily used on large structures; and they must have a two-sided access. Furthermore, they are used late in the production cycle of components. So where to next? Can NDI detect contamination? We know that all surfaces are contaminated, however, the PABST* programme demonstrated that most contaminates are benign because they (industrial oils, sebum) are soluble in the adhesive. Primary Adhesively Bonded Structural Test was a 1970s USAF programme that attempted to show that adhesive bonding could be used as the primary joining method for a large cargo aircraft. Failure of NDE to find the 'kissing bond' doomed this effort. Some are pernicious – silicone, oils/greases. Understanding the surface chemistry is one approach that may detect this difference.

On April 15, 2004, Dr Bill Baron (AFRL Air Vehicles Directorate) announced: 'With a strength measuring capability based on pulsed laser stress wave induction, I can perform deterministic design with composites. This capability is worth a great deal to me since I can cut the weight of the airframe by as much as 40%'. His claim to have a simple method to detect contamination must be evaluated for a range of polymer matrix systems and contaminants.

The implications for composites structures are great. Designers can be confident that NDE can provide minimum strength estimates. Reliable bonding will enable new designs that utilize the anisotropic capabilities of composites that satisfy the local stress conditions and not the requirement of assembly. There will be a significant impact on structural efficiency, reduced cost of structure, new organic designs will emerge and increased safety becomes possible.

15.14 The future looks bright

Recent innovation in aircraft design includes the use of new energy-absorbing honeycomb sandwich fold-core structures including metal lattices, where the fold-core properties can be tailored by choice of fibre, wall thickness and, particularly, the fold geometry to enhance the absorption of impact energy. Fold-core has an open cell structure, a major advantage for an aircraft fuselage compared with conventional closed-cell honeycomb cores, since the core can be ventilated to prevent moisture uptake. An example of a new structural fold-core concept for fuselage panels is the *Z-crimp core* made from a resin impregnated Aramid or carbon paper, felt or fabrics. Novel composite sandwich structures with energy-absorbing cores protect load-bearing composite structures from impact damage. Key issues include development of models for folding and collapse in the composite cores; development of constitutive laws based on the modelling of the failure mechanisms; and the implementation of the materials models into FE codes. Multiscale modelling arises because impact damage is localized and requires fine-scale modelling of failure processes at the micro level, whilst the

structural length scales are much larger. Solution is to use mesoscale models based on CDM in explicit FE codes providing a framework within which failure processes may be modelled.

There is an increasing amount of work on the cost-effective fabrication of large composite structures. The driver here is the new 'black' large transport aircraft with wings and fuselage in carbon fibre composite. These materials will only be competitive if they can be manufactured into very large shapes through automation production. For example, the one-piece barrel section of Boeing's 787 Dreamliner fuselage includes stringers and requires a computerized lay-down of carbon fibre composite pre-preg tape in its manufacture. The structure is wrapped and cured in one of the largest autoclaves currently available. This composite fuselage section, 7 m long and 6 m wide, offers potential for integrated design concepts.

Current fuselage structures of Boeing's Dreamliner 787 incorporate composites in the fuselage barrel with conventional frame/stringer concept monolithic skins. But the potential is for the application of highly integrated design concepts with complete pressurized fuselages made of carbon fibre composite or hybrid aluminium/composite, where production costs are 40% less and a weight saving of 30%. And projecting forward, the aircraft industry sees twin-walled sandwich structures due to their much higher shell bending stiffness and higher strength/weight ratio. This would allow novel highly efficient fuselage concepts without stringers and larger frame spacing such as would be found in the blended wing aircraft of the future.

The Airbus A380 is the first aircraft with a carbon fibre composite centre wing box made by automatic tape laying (ATL). The wing box is a cantilevered beam that carries the wing to the fuselage and supports leading-edge and trailing-edge devices, control surfaces, engines and landing gear. The test piece represents a portion of the wing section that begins at about the centre of the airplane and stops at approximately one-half of the span of the wing.

It weighs 8.8 tonnes, with 5.3 tonnes of composite, saving over 1.5 tonnes compared to the metallic equivalent. The main challenge here is the wing root joint, with composites up to 45 mm thick, which links to carbon fibre composite keel beams, each one 16 m long and 23 mm thick carrying 450 tonnes. The A380 wing is the largest ever made for a civilian aircraft. It weighs 35 tonnes but is flexible enough to bend 7 m at its tip.

Boeing has completed destructive testing on a full-scale composite wing box of the 787 Dreamliner, the first all-composite wing box ever built for a Boeing commercial airplane. This test is part of the certification process for the all-new jetliner. In addition to determining the strength of the structure, the test helps us verify the analytical methods used to calculate the loads the structure will have to carry. This piece measures approximately 5.5 m at its widest point. The upper and lower surface panels and the spars of the wing are made entirely of the same composite material being used on the fuselage. The wing ribs are monolithic aluminium structures, each machined from a single piece of aluminium plate.

But all is not rosy; a major mishap inside the Global Aeronautica assembly plant in Charleston, South Carolina, caused structural damage to the upper half, or crown

section, of a Dreamliner 787 centre fuselage. This is where the big central fuselage pieces from Italy and Japan come together. A mechanic damaged the structure while attaching fasteners to the crown of the centre fuselage. Apparently, each fastener 'splintered out the hole', causing the carbon-fibre threads in the composite structure to break out from the resin matrix.

Structural testing continues on two full-scale 787 airframes as part of the certification process for the airplane. In particular, at this late time, the composite fuselage is being strengthened on its right side, which delayed the first flight. Those tests will further demonstrate the performance of the structure through multiple lifetimes of normal operational loads and test the structure beyond the points expected to be seen in service.

Future aircraft may have twin-walled sandwich structures (with a higher shell bending stiffness) and far higher strength-to-weight ratios. This would lead to novel fuselage concepts without stringers and much larger frame spacing. A complete sandwich pressurized fuselage in composites or hybrid metal/composite is a big challenge. Critical issues include a requirement of a new sandwich concept with improved impact resistance, and improved design tools for predicting damage tolerance and SI of sandwich structures.

The ultimate in light-weight aircraft is the solar-powered Zephyr High Altitude Long Endurance (HALE) UAV where design is driven by minimum structural mass and a low cost requirement. It is constructed of an ultra-light-weight carbon fibre composite airframe and an 18-m wing span. Components of the airframe are made of slender thin-walled tubular beams weighing 8 kg and a total aircraft mass of 30 kg. It performs in nonlinear (large deflection) behaviour under aerodynamic loading.

Design is optimized by controlling fibre layup for dihedral and cross-jointing where the outer wing is connected to an inner wing, and the fuselage connected to the main wing spar. Maximum operating altitude is above 15,000 m and a persistent platform greater than 3 months. It is designed to carry a 3-kg payment of optical and remote sensing equipment and communication relays.

The damage tolerance aspects of new materials, technologies and the extreme loads on rockets offer exciting challenges. Planning and early design are underway for hardware, propulsion systems and associated technologies for NASA's Ares I crew launch vehicle, a single five-segment solid rocket booster, and Ares V earth departure launch vehicle, a two-stage, vertically stacked launch vehicle. Working together, they form NASA's cost-effective space transportation infrastructure being developed under the Constellation Program to carry human explorers back to the moon and then onward to Mars. For its initial insertion into Earth orbit, the first stage of Ares V relies on two five-and-a-half-segment reusable solid rocket boosters. These are similar to the single booster that serves as the first stage for the cargo vehicle's sister craft, the Ares I crew launch vehicle. Atop the Earth departure stage of Ares V is a composite shroud protecting the Altair lunar lander. This hardware commonality makes operations more cost-effective by using the same manufacturing facilities for both the crew and cargo vehicles. Like the individual fuselage sections of Boeing's 787, these vehicles will also have sections made of carbon fibre composite based on the same fabrication technology. However, at the present time there is no autoclave in the world

that is large enough to take the individual sections. The first test flight of the Ares V is planned for around 2018. The first crewed lunar excursion is scheduled for launch in the 2020 timeframe.

In the area of re-entry vehicles is the C/C-SiC ceramic composite for leading-edge and nose structures, which is structural and capable of withstanding temperatures up to 1800 °C. An example is the demonstrator structures for a crew rescue vehicle.

In Europe, there is considerable interest in OOA materials (out of autoclave), which are cured at temperature, but with vacuum pressure. Here you can make very large structures with an oven or heated tool, still cheaper than an autoclave.

Much work has gone into liquid resin infusion (LRI). In resin transfer moulding the resin is injected along the length of the structure, which limits the size. In LRI the resin diffuses into non-crimp fabrics through the thickness, and vacuum pressure applied on a heated tool. Wing structures up to 15 m are being made in one piece with this technology in research projects. This is also being looked at for wind rotor blades with dimensions up to 30 m.

For wind power, rapid material placement and quick-cure moulding systems combine to reduce layup, infusion and curing time by 50%, producing consistently high-quality parts. The new rapid material placement system (RMPS) brings integrated manufacturing – with automation and repeatable process control – to what has largely been a manual or piecemeal-automated process. RMPS is an automated blade moulding facility unto itself, capable of spraying in-mould coatings, dispensing/layup of glass and carbon fibre materials, and dispensing/application of adhesive. It brings 3 m/sec (10 ft/s) layup speed to placement of materials in blade skin, spar cap, and sheer web moulds, with laser- and vision-based wrinkle detection in cross or longitudinal directions. Depending on the laminate schedule, the system can reduce layup time 85% on a 45-m blade.

15.15 Final remarks

Composite materials are being used increasingly in aerospace applications and designs and analysis methods are based on well-established design practices. 'Black metal design' seems still to be the common word. Material and geometric nonlinearities are not accepted as a common analysis method of composite structures. No-growth damage criteria are still applied, while post-buckling design has not yet been explored in composite wings. Bolted patch repair has become accepted as common practise for military and civil platforms.

And there remains a limitation on operational strains. The dilemma is that conventional analysis methods developed for metallic structures might be too conservative for composite structures.

A major difficulty in designing composite structures is how to predict damage initiation and damage evolution, and safe operating limits to ensure SI. Our comprehension of structural changes in composite materials, which take place continuously and cumulatively, is simply lacking in detail. To predict a result, say lifetime or a stress response by a numerical method, there must be self-evident truth that the mechanism regime in

which the component is operating must have been identified. In other words, the important design issues must all be embedded in the same model of material and component behaviour that also include the dominant mechanism(s) of structural change over orders of magnitude of size and time.

Critical design issues that relate to anisotropy effects should take into account toughness and its manifestation in notch sensitivity. Weaknesses caused by anisotropy should be identified, such as delamination and transverse ply cracking, and de-bonding at interfaces. Mechanisms that govern inelastic strains and redistribute stresses and diminish peak stress magnitudes should be understood.

Damage tolerance certification requires time-consuming, expensive testing. The consequences of changing composite layup and textile architecture are unpredictable and the complete test matrix for materials qualification would have to be repeated at the coupon level. In the design process, a key role has to be played by certain physical length scales in the failure process, which arises from delamination and splitting (shear) cracks, fibre rupture and fibre microbuckling or kink formation, and diffuse microcracking or shear damage. All provide a rationale for making modelling decisions.

With the advent of powerful computers and software that can be purchased at reasonable cost, this means that many of the physical models and computer simulations that would be cumbersome for design engineers to use could be implemented as user-friendly computer applications or integrated within commercial FE design systems. In this respect, mathematical challenges include hierarchical meshing strategies, which must be coarse enough at the largest scales (entire structure), whilst cascading down through finer and finer meshes to atomic scale (if necessary). The real challenge is to formulate design equations that combine continuum (spatially averaged) and discrete damage representations through physical (mechanism) models in a single calculation. And, at the heart of the model lies the mechanism(s) best identified by direct observation.

Successful implementation of physical models or simulations requires knowledge of appropriate phenomena such as impact. Multiscale modelling will arise because impact damage is localized and requires fine-scale modelling of failure processes at the micro level, whilst the structural length scales are much larger. The solution is to use mesoscale models based on CDM in explicit FE codes providing a framework within which failure processes may be modelled. Key issues currently under investigation include the development and implementation of: constitutive laws for modelling failures mechanisms; models for folding and collapse in composite sandwich cores; and materials models into FE codes.

Nevertheless, how much detail of failure mechanisms do we need to know to come up with a successful model for incorporating into a simulated virtual test in order to reproduce the outcome of a real test on an engineering structure? If all else fails, put a patch on it (Figure 15.27)!

Recall the words of Isaac Newton spoken to Robert Hooke at one of The Royal Society soirees in London c.1685: ‘Merely because one says something might be so, it does not follow that it has been proved that it is.’

Figure 15.27 A glass fibre−epoxy patch over a fatigue crack in an aircraft aluminium alloy (Courtesy of Prof Endel Iarve).

'The Curious Life of Robert Hooke: The Man Who Measured London' by Lisa Jardine. Published by HarperCollins Publishers Ltd. First Edition (September 15, 2003). ISBN-10: 0007149441. ISBN-13: 978-0007149445.

Acknowledgements

This chapter raises important issues and topics on structural integrity of composite materials and structures, many that were formally presented and discussed at two research meetings, in Monterey, California (September 2005) and on the Island of Madeira (September 2007), both sponsored by the Engineering and Physical Sciences Research Council (EPSRC), the National Science Foundation (NSF), and the European Office of Aerospace Research and Development (EOARD) London.

Selections of papers presented at those meetings are published in two special issues of the Journal of Materials Science (see Further Reading below).

I have drawn upon material contained in some of those papers and benefited from numerous insightful conversations with the authors over recent years. In particular, I would like to acknowledge Dr Alastair Johnson and Dr Brian Cox, and Professors John Whitcomb, Josef Jančář, Carlos González, Costas Soutis, Tony Bunsell, Scott Case, Glyn Davies and Hideki Sekine for allowing me to adapt some of the figures.

Many conversations over the years with Professor Mike Ashby on solving problems of material behaviour have greatly influenced my group's research at Cambridge.

References

Ashby, M. F. (2005). *Materials selection in mechanical design* (3rd ed.). Oxford, UK: Published by Butterworth-Heinemann.

Beaumont, P. W. R. (2006). Cracking models; broken parts. *Applied Composite Materials, 13*, 265−285.

Cottrell, A. (1963). *Discussion of new materials held at the royal society, 6th and 7th June, 1963, and published in*. Proc. Roy. Soc. Lond. A282, 20th October, 1964.

Cox, B., & Yang, Q. (2006). In quest of virtual test for structural composites. *Science, 314*, 1102−1107.

Crane, R. L., & Dillingham, G. (2008). Composite bond inspection. *Journal of Materials Science, 43*, 6682−6694.

Davies, G. A. O., & Ankersen. (2008). Virtual testing of realistic aerospace composite structures. *Journal of Materials Science, 43*, 6586−6592.

Dimant, R., Shercliff, H., & Beaumont, P. W. R. (2002). Evaluation of a damage-mechanics approach to the modelling of notched strength in KFRP and GRP. *Composites Science and Technology, 62*, 255−263.

Jančář, J. (2008). Review of the role of the inter-phase in the control of composite performance on micro- and nano-length scales. *Journal of Materials Science, 43*, 6747−6757.

Johnson, A. F., & Holzapfel, M. (2006). Numerical prediction of damage in composite structures from soft body impacts. *Journal of Materials Science, 41*, 6622−6630.

Jumahat, A., Soutis, C., & Hodzic, A. (2010). A graphical method predicting the compressive strength of toughened unidirectional composite laminates. *Applied Composite Materials, 18*(1), 65−83.

Kedward, K. T., & Beaumont, P. W. R. (1992). The treatment of fatigue and damage accumulation in composite design. *International Journal of Fatigue, 14*(5), 283−294.

Poursartip, A. P., Ashby, M. F., & Beaumont, P. W. R. (1982). Damage accumulation during fatigue of composites. *Scripta Metallurgica, 16*, 601−606.

Poursartip, A. P., Ashby, M. F., & Beaumont, P. W. R. (1986). Fatigue damage mechanics of a carbon fibre composite laminate: parts 1 and 2. *Composites Science Technology, 25*, 193−218. ibid, 25, 283−299.

Sekine, H., & Beaumont, P. W. R. (1998). A physically based micromechanical theory of macroscopic stress-corrosion cracking in aligned continuous glass fibre- reinforced polymer laminates. *Composites Science Technology, 58*(10), 1659−1665.

Soutis, C. (2009). Modelling the open hole compressive strength of composite laminates tested in hot wet conditions. *Plastics Rubber and Composites, 38*(2/3/4), 55−60.

Spearing, S. M., & Beaumont, P. W. R. (1992). Part 1 fatigue damage mechanics of composite materials. *Composites Science Technology, 44*, 159−168.

Spearing, S. M., & Beaumont, P. W. R. (1998). Towards a predictive design methodology of fibre composite materials. *Applied Composite Materials, 5*(2), 69−94.

Spearing, S. M., Beaumont, P. W. R., & Ashby, M. F. (1992). Part 2 Fatigue damage mechanics of composite materials. *Composites Science and Technology, 44*, 169−177.

Vekinis, G., Ashby, M. F., & Beaumont, P. W. R. (1990). R-Curve behaviour of alumina ceramics. *Acta Metallurgica, 38*(6), 1151−1162.

Vekinis, G., Ashby, M. F., & Beaumont, P. W. R. (1993). The micromechanisms of fracture of alumina and a ceramic-based fibre composite: modelling the failure processes. *Composite Science Technology, 48*, 325.

Vekinis, G., Shercliff, H. R., & Beaumont, P. W. R. (May 1991). Dynamic testing of ceramics and ceramic composites in the SEM. *Metals Materials*, 279−284.

Wright, A., & French, M. (2008). The response of carbon fibre composites to blast loading via the Europa CAFV programme. *Journal of Materials Science, 43*, 6619−6629.

Further reading

Advances in Multiscale Modelling of Composite Material Systems and Components. (October 2006). *Journal of Materials Science, 41*(20). ISSN:0022−2461.

Beaumont, P. W. R. (2005). Cracking models (Chapter 3). In C. Soutis, & P. W. R. Beaumont (Eds.), *Multiscale modelling of composite material systems*. CRC/Woodhead Publishing Limited.

Beaumont, P. W. R. (2004). Physical modelling of damage development in structural composite materials under stress (Chapter 13). In B. Harris (Ed.), *Fatigue in composites*. CRC/Woodhead Publishing Limited.

Stretching the Endurance Boundary of Composite Materials. (October 2008). Pushing the performance limit of composite structures. *Journal of Materials Science, 43*(20). ISSN: 0022−2461.

The control of the residual lifetimes of carbon fibre-reinforced composite pressure vessels

16

A.R. Bunsell[1], A. Thionnet[1,2]
[1]Mines ParisTech, Paris, France; [2]Université de Bourgogne, Dijon, France

16.1 Introduction

The type of carbon fibre that finds its widest use today is made from a polyacrylonitrile (PAN) precursor. Its development at the Royal Aircraft Establishment in the UK during the mid-1960s and first commercial production in 1967, also in the UK, were stimulated by its potential uses in military aircraft and jet engines. Pioneering research in the UK for fibre-reinforced resin matrix composite materials was stimulated and led by the team of Anthony Kelly, who first began studying the processes governing the behaviour of composites under the guidance of Sir Allen Cottrell at the University of Cambridge, before moving to the National Physical Laboratory (NPL) in Teddington, England. The team that he led at the NPL produced many ground-breaking scientific papers on the physical processes that determined the behaviour of filament-reinforced composites, as described in A. Kelly's book *Strong Solids*, first published in 1973 and re-edited several times since 1986. In those early days the potential of carbon fibres for use in a wider range of applications was understood by those involved in the emerging technology of advanced composite materials. However, in the mid-1970s the world production of these carbon fibres was less than 10 t. Today, well into the twenty-first century, the production capacity is over 50,000 tons. The market for these fibres has outstripped that for military planes and even if the latest generation of civil aircraft hits the headlines because of being constructed with more than 50% of carbon fibre composite, this market sector is even trailling non aerospace applications for civil use. The work done by Anthony Kelly and his colleagues continues to inform us and enables new composite applications to be developed and optimised.

In parallel with the growth of new markets, the carbon fibres that have become available have shown incredible improvements in their properties. During the 1970s the two main types of PAN-based carbon fibres were high-strength and high-modulus. The possibility of achieving very high moduli with carbon fibres was a driving force for their initial development, but it was high-strength carbon fibres that found widest use due to their easier handling. High-strength carbon fibres in the 1970s failed with a strain of 1%, whereas today the strain-to-failure thresholds of

Structural Integrity and Durability of Advanced Composites. http://dx.doi.org/10.1016/B978-0-08-100137-0.00016-X

widely used carbon fibres are more than double that; with no decrease in the Young's moduli of those fibres. Carbon fibres of higher strength have also been developed with increased Young's moduli, and this has been associated with a reduction in fibre diameter. Carbon fibres can be made by a number of routes, allowing a wide range of Young's moduli and strengths to be developed, and a large family of carbon fibres is now available (Matsuhisa & Bunsell, 2009). This has allowed a much wider range of applications to be envisaged, benefiting from the high elastic moduli and strengths of the carbon fibres combined with their purely elastic behaviour and light weight. One major application that is rapidly increasing in importance is the use of filament-wound carbon fibre−composite pressure vessels for gas containment at very high pressures. The market for these pressure vessels has been developing since the very beginning of the twenty-first century. Initially, interest was for storing natural gas at pressures usually around 200 atmospheres, or 20 MPa, for use as a fuel in environmentally friendly buses and utility vehicles. Traditional steel pressure vessels made so as to withstand these high pressures would be too heavy for such applications, whereas carbon fibre composites possessed the optimum combination of strength, stiffness and low weight for such uses. These applications foreshadow the use of hydrogen as a fuel that needs to be stored in lightweight containers at pressures of 70 MPa or higher. Such applications require a high measure of safety, as any failure leading to the explosion of the vessel would be very dangerous. The safety of metal pressure vessels, all too often based on accidents, has been an issue for more than 250 years, and a great deal of experience has been acquired and enhanced by the metallurgical studies of failure processes in metals. Today the standards for testing pressure vessels are based on the behaviour of metals, and the use of composites naturally raises the issue of whether these tests are suitable for an entirely different class of material.

The most intuitively obvious technique for testing for the reliability of a pressure vessel is the hydraulic test in which the pressure vessel is briefly subjected to one and one-half times the maximum in-service pressure. The reasoning is, 'if the vessel does not fail at a higher pressure why should it fail at a lower one?' If the vessel survives this test it is deemed safe to continue in service. This is not only intuitive but can be justified by an understanding of the failure processes in metals, which occur by crack propagation. Any incipient crack or defect will provide a site for stress concentration, as shown by Inglis (1913), and if failure does not occur, the plastic deformation created ahead of the crack will impede its development at lower pressures; see Figure 16.1. Composites do not fail in this way, as shown in Figure 16.2. For complete failure of a composite pressure vessel, the fibres must break. The fibres are very fine, usually with diameters of 7 μm, and hundreds of millions of such fibres are in any cross-section of the wall of a pressure vessel. Any population of fibres contains a wide range of strengths that can be described by Weibull statistics, a detailed explanation of which can be found in Bunsell (2009). This range of fibre strengths, coupled with their elastic behaviour, means that the overloading used to test metal pressure vessels, rather than reassuring that the pressure vessel will be reliable at lower pressures, leads to the composite being further damaged whilst offering no assurance of future reliability. This is illustrated schematically in Figure 16.3, which shows how many more fibres are broken during an overload test than were broken at

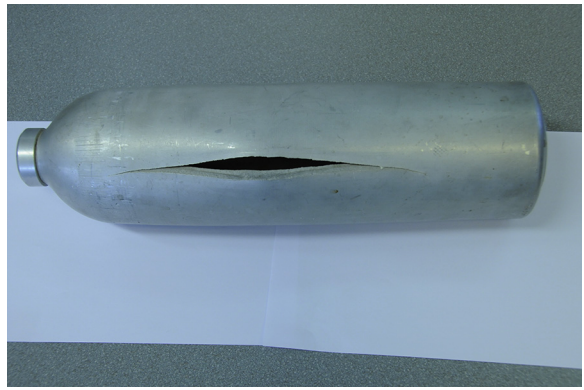

Figure 16.1 Failure of a metallic pressure vessel showing that it was caused by crack propagation. At the tip of the crack the metal is deformed plastically due to stress concentration.

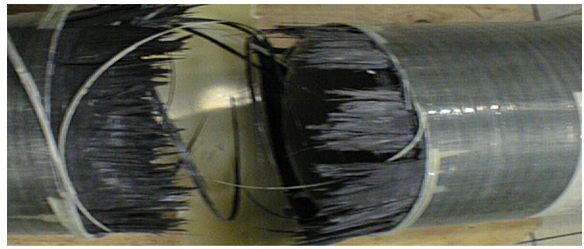

Figure 16.2 Failure of a carbon fibre−reinforced composite pressure vessel.

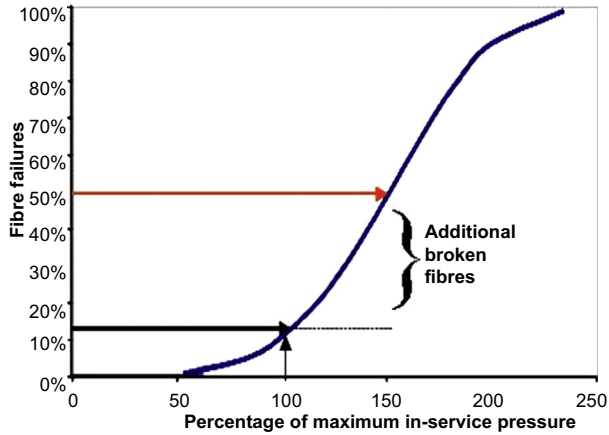

Figure 16.3 An overload inevitably breaks the elastic carbon fibres further, such that the pressure vessel is more damaged after the test than before.

the maximum in-service pressure. This means that the standards for testing metallic pressure vessels are unsuited to composites, so new means of evaluating composite pressure vessels based on their particular processes of damage accumulation are required.

Several composite types can be found in pressure vessels, and use materials such as glass, aramid and carbon fibres. Carbon fibres are the reinforcement of choice for the most demanding structures, as they have very high mechanical properties and do not suffer from time-dependent degradation such as stress corrosion at room temperature. They are elastic and wound, together with the resin, on geodesic paths over a mandrel that later serves as a liner to the pressure vessel. This means that when the composite pressure vessel is under pressure, the fibres experience only tensile loads and support up to 99% of that load. As the behaviour of individual carbon fibres is time independent, it has often been supposed that carbon fibre composites do not suffer from any delayed time-dependent failure in the direction of the reinforcement. It can easily be shown that this is not the case, and delayed failure of carbon fibres in a composite can and does occur. It will be shown below that this process is controlled by the viscoelastic relaxation of the matrix material enveloping the fibres, which leads to some fibres experiencing increased loads that can cause delayed fibre failure.

Failure models have been developed that simulate damage accumulation under sustained loads, and have been validated by experimental tests on plate and filament-wound specimens. This will be explained below, and the understanding of the physical processes involved will be seen as related to many of the ideas developed by A. Kelly and others.

16.2 Delayed fibre failures in carbon fibre composites

Early studies by Fuwa, Bunsell, and Harris (1975) on unidirectional carbon fibre—epoxy specimens as well as filament-wound internally pressurised rings and small pressure vessels, and followed up by Laroche and Bunsell (1980), revealed that under both constant amplitude cyclic loading and steady loading (Figure 16.4), similar ongoing damage could be detected by the acoustic emission technique, and this damage consisted of fibres that were breaking.

On increased loading, it was found that the damage curve as a function of load rejoined the extrapolated earlier damage—load curve, but showed a quiet period at loads just higher than those experienced during the earlier testing, as shown in Figure 16.4. This was subsequently termed the Felicity effect. This observation revealed that the damage that developed under both constant amplitude load cycling and constant load would have occurred in monotonic tests to higher loads than those initially experienced. This damage was then shown to be both due to fibre failure and was irreversible, and thus damage in carbon fibre composites of the most stable form had been shown to be time dependent. These studies evolved into the testing of hydraulically pressurised filament-wound rings and small polar-wound pressure vessels (Fuwa, Bunsell, & Harris, 1976). Later tests would show that no time-dependent failure occurred when single carbon fibres were loaded, either under constant or cyclic loads, to very high

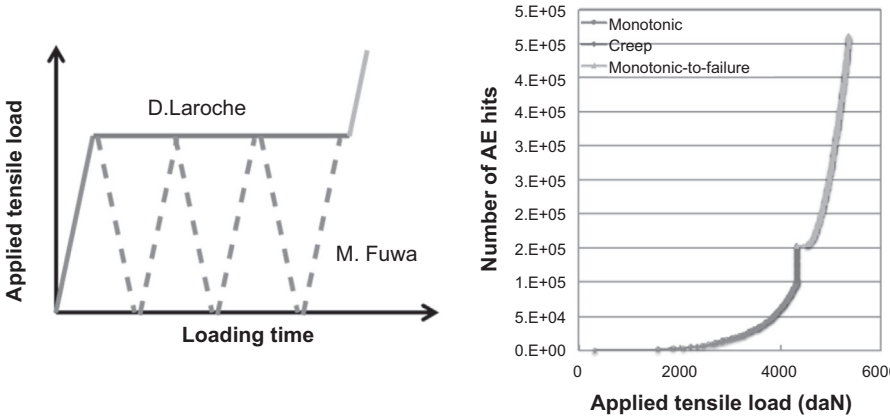

Figure 16.4 Constant amplitude load cycling as conducted by Fuwa et al. and steady loading tests by Laroche and Bunsell (1980) revealed that fibre breaks continued to accumulate. Increasing the applied load after a period of cyclic or steady loading revealed that little damage was immediately detected before the extrapolated original curve was rejoined.

fractions of the their ultimate tensile strength, that is, up to 95% (Somer & Bunsell, 1992). Although the carbon fibres in unidirectional composites under load were supporting around 99% of the applied load, it was clearly the viscoelastic matrix that was the cause of the delayed fibre failures. An understanding of this behaviour was clearly important if the long-term reliability of carbon fibre—composite structures such as pressure vessels was to be achieved, and offered the possibility of proof tests and the lifetime evaluation of these composite structures based on the microstructural failure mechanisms involved. Although additional studies took place and advanced the understanding of the kinetics of fibre failure, it was the progression in computing power, as explained below, that allowed detailed multiscale simulation and better understanding of the kinetics of damage accumulation in these filament-wound structures.

16.3 Development of models of damage accumulation in advanced composites

Developments in computing power have allowed the processes of damage accumulation in composites to be modelled in unprecedented detail. This has resulted in a multiscale model, based on the physical processes involved, that accurately describes damage accumulation in carbon fibre composites, including the effects of relaxation of the matrix over time, and this model has been applied with success to the behaviour of carbon fibre—composite pressure vessels (Thionnet, Chou, & Bunsell, 2015). It takes advantage of increased computing capacity and has developed from a long list of earlier studies, some of which have been used to corroborate its results. It allows the behaviour of the composite material to be understood in greater detail than in previous models. The work examines the limits of the possible use of advanced

composites in which fibre failure controls composite failure, so as to determine the intrinsic limits of the materials. The model is firmly based on physical mechanisms – as such it has its antecedents and directly extends the work of A. Kelly, who recognised the major contribution of Cox (1951) in explaining the basic reinforcing mechanism in composites as being the transfer of loads from the ends of fibres to other fibres through the shearing of the surrounding matrix. As reinforcing fibres in filament-wound structures are wound on geodesic paths, they are subjected primarily to tensile loads when the vessel is under pressure. It is also clear that the fibres have to break for the pressure vessel to fail. An analogy has therefore been made between the behaviour of unidirectional composites and filament-wound structures. The works of Fuwa et al. (1975, 1976), and subsequently others, have justified this analogy.

The first model of damage accumulation based on physical processes was developed by Rosen (1964) and improved by Zweben (1968), by taking into account the effect of stress concentration around fibre breaks. Zweben showed that the failure of a fibre embedded in a matrix resulted in the closest intact fibres neighbouring the break being overloaded, whilst intact fibres, even in the same plane as the break but removed at two or three fibre distances, were unaffected by the breaks. The effect of stress concentrations around fibre breaks was further examined by Hedgepeth (1961) and others (Ochiai, Schulte, & Peters, 1991; Goree & Gross, 1980). A number of authors recognised that the stochastic nature of fibre strength and the effect of individual fibre beaks on intact neighbouring fibres would significantly affect the failure of unidirectional composites (Batdorf, 1982; Berger & Jeulin, 2003; Harlow & Phoenix, 1978, 1981; Kong, 1979; Scop & Argon, 1969). Further studies examined these effects related to the interaction of fibre breaks with the remaining intact unidirectional composite (Nedele and Wisnom, 1994a,b; Wisnom & Green, 1995). Though most of these studies did not take time effects into account, some did, with Lifschitz and Rotem (1970) and others suggesting that the viscoelastic nature of the matrix accounted for the delay of fibre failures (Lagoudas, Hui, & Phoenix, 1989; Landis, Beyerlein, & McMeeking, 2000; Landis & McMeeking, 1999; Phoenix, 1997; Phoenix & Newman, 2009).

The above-mentioned studies reveal the increasingly sophisticated interest in the failure and long-term behaviour of unidirectional composites as well as a deepening understanding of the physical mechanisms involved. These observations are directly relevant to understanding composite behaviour, including the long-term behaviour of filament-wound internally pressurised composite structures. An understanding of the filament-winding process used to make pressure vessels reveals that the fibres determine the ultimate properties, and the role of the matrix is to transfer loads between the fibres. In such a scenario, matrix cracking is of little importance and at this point will be ignored in order to clarify the main processes governing composite behaviour. However, further refinement of the load transfer processes indicates that some additional and largely secondary effects from increased load concentrations may exist, induced by the development of matrix cracks. The layers of an internally pressurised filament-wound structure that support the greatest load are those wound circumferentially. With a typical fibre volume fraction of 60%, the fibres in such layers support

99% of the tensile stress, such that what happens to the fibres is of prime interest. The fibres in the wall of a pressure vessel determine its strength, by supporting the stresses in tension parallel to the wall. As well, the fibres do experience compressive forces normal to the wall surface, so it is conceivable that if these stresses could break the fibres, their ability to support the in-wall tensile stresses could be removed. This possibility has been examined by Joannès and Chou (2013) both theoretically and experimentally, by subjecting the material to 10 times the compressive loads found in the walls of pressure vessels, and was not found to provoke failure of the carbon fibres. This conceivable mechanism for composite degradation has therefore been discarded as unrealistic. The simulation of the behaviour of unidirectional composites subjected to tensile forces must consider the scatter of fibre strengths, which can be obtained experimentally for single fibres removed from fibre bundles used in the manufacture of the composite structure. These results can be quantified using Weibull statistics. This subject has been discussed in detail in many articles to which the reader is referred (e.g. Batdorf, 1982; Berger & Jeulin, 2003; Beyerlein, Zhou, & Schadle, 1998; Bunsell, 2009; Bunsell & Renard, 2005; Curtin, 2000; Curtin & Ibnabdeljalil, 1997; Harlow & Phoenix, 1978, 1981; Kong, 1979; Landis & McMeeking, 1999; Phoenix & Beyerlein, 2000; Phoenix & Newman, 2009; Scop & Argon, 1969; Van den Heuvel, Goutianos, Young, & Prijs, 2004; Van den Heuvel, Wubbolts, Young, & Peijs, 1998).

The objective of the model that has been developed has been for it to reflect closely the physical processes occurring during degradation. As the critical damage governing the failure of unidirectional composites occurs at the level of the fibres, it is necessary to evaluate damage accumulation first at this microscopic scale and then, through a two-stage finite element (FE^2) multiscale modelling process, determine the behaviour of the complete structure. In order to do this, a homogenisation process must be invoked, as it would not be possible to sum the effects on all the millions of individual fibres in the structure. The process requires the identification of representative volume element (RVE), chosen so as to represent all the micro-mechanisms considered to govern damage accumulation. An ideal multiscale approach of the FE^2 type has been used such as illustrated by Feyel (2003), Souza, Allen, and Kim (2008), Thionnet and Renard (1998) and others (Aussedat, Thionnet, & Renard, 1995; Renard & Thionnet, 2007; Thionnet, 2001; Thionnet & Renard, 1999). In order to develop a model that can give a useable result with a reasonable calculation time only the physical mechanisms that are considered the most important in the failure process have been considered. This has been an iterative process that has resulted in a model that represents closely the real behaviour of the composites and their structures but inevitably has involved some simplifications. The result however is a robust model that can be interrogated so as to study processes that would be difficult or impossible to study experimentally.

16.3.1 Description of the microscopic scale

The composite is initially considered unidirectional, loaded in the fibre direction and made with a certain fibre volume fraction. The fibres are carbon fibres having

diameters of the order of 7 μm. They are considered linearly elastic and also, for the sake of simplification, isotropic. It is recognised that this latter characteristic is not true, but later studies have revealed that the simplification has no effect on composite behaviour as seen in pressure vessels, as the failure process for the fibres is in tension along the long fibre axis. The matrix is considered homogeneous and isotropic, whilst recognising that its molecular morphology is greatly modified by the embedded fibres, thus resulting in properties different from those of the unreinforced matrix. In the model, the fibres break in a given section of the RVE when they are loaded to their breaking loads, which show considerable variation within the fibre population. The stress on any intact fibre depends on the applied load and the proximity of the fibre to any neighbouring fibre break. The shear of the matrix around a fibre break means that the load that the fibre had been supporting before failure will be shared by the neighbouring intact fibres within a section of the composite that contains the break. The distance, and therefore the width, of the section over which this increase in load is experienced will also be influenced by debonding of the broken ends of the fibre. These effects will increase over time as the surrounding matrix relaxes and transfers further load to the initially neighbouring intact fibres.

16.3.2 Summary of the modelling of long-fibre composite structure failure induced by fibre breaks

16.3.2.1 The FE^2 type model

The degradation of a composite made up of long or continuous fibres, in which loads are supported primarily by the fibres, is essentially controlled by fibre breakage. A multiscale approach of the type FE^2 allows the mechanisms governing behaviour at the fundamental level of the fibres to be assessed and then summed so as to determine the behaviour of the whole structure. The choice of such an approach was motivated by a desire to capture, as far as possible, the physical mechanisms at the origin of fibre failure. Nevertheless, it was immediately realised that if the objective was to model whole structures, it was not possible simply to sum the effects on all the individual fibres. It was seen that for a finite element mesh containing 200,000 Gauss points, fairly typical of this type of calculation for a simple structure, it would be necessary to carry out finite element calculations for each at, say, one per second on the RVE of the material. Defined at the scale of the constituents, the time to carry out the calculation would become prohibitive. It has therefore been necessary to develop a simplified FE^2 multiscale approach. Below, first, the modelling of fibre failure on the microscopic scale is explained. Secondly, the exploitation of the results obtained is described. Lastly, the construction of a simplified FE^2 multiscale approach is made. It will be shown that this approach allows for both the analysis of the degradation of composites reinforced with continuous fibres and the quantitative analysis of local damage leading up to instability of the composite and the rapid failure of the structure.

16.3.3 Description of the fibre failure model at the microscopic scale

At the microscopic scale, an orthonormal coordinate system is defined such that $R_{loc} = (O, \vec{x}, \vec{y}, \vec{z})$, in which x, y and z are the coordinates at a point M. The vector $\vec{z}$ is aligned parallel to the fibre axis. The studies of Blassiau, Bunsell, and Thionnet (2007) and Baxevanakis (1994) allowed the microstructure of the RVE to be identified. Optical microscopic observations of several cross cross-sections of composite pressure vessels reveal that the fibre distribution in the matrix was relatively regular. Consequently, the description of the RVE could be simply an elementary periodic cell (or more simply, an elementary cell). Observations of these sections reveal regions in which the network of fibres is hexagonal, and other regions where the concentration of fibres is lower and the fibres are arranged in a square network. The arrangement of the reinforcing fibres was therefore taken to be periodic and hexagonal in the plane$(\vec{x}, \vec{y})$. This is a simplification of reality, but will be shown to be acceptable for the simulation of composite behaviour. The size of the RVE for a fibre volume fraction $V_f = 0.64$ (Figure 16.5) has been deduced from the two-dimensional (2-D) work of Baxevanakis (1994), who used multifragmentation tests on a single fibre embedded in a matrix to determine the length of the weakest link of a fibre ($\sim$0.5 mm). By varying the number and length of fibres in a bundle, Baxevanakis (1994) found numerically that if six or more fibres with lengths of $L = 4$ mm were associated in a matrix, the strength of the composite material converged. This allowed the size of the 2-D RVE to be defined. The numerical study showed also that the failure stress reached for a critical state of damage was defined as follows: each fibre fails only once in the 2-D RVE ($L = 4$ mm), and all the fibre breaks were concentrated in the same plane. This implies that although the load transfer length, as defined by Cox (1951), depends on the shear

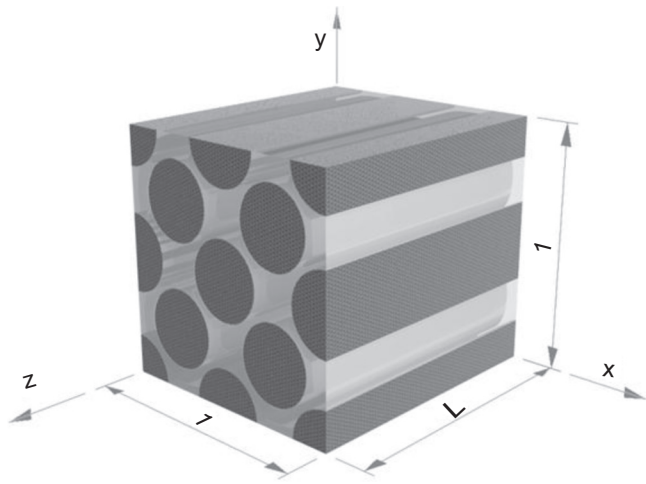

Figure 16.5 One-quarter of the representative volume element (RVE).

modulus of the matrix and the Young's modulus of a single fibre, together with the interfacial bond, the failure of the 2-D RVE containing several fibres is a more complex process leading to a deterministic value of strength not directly related to the behaviour of a single fibre embedded in a block of matrix. This study allowed Blassiau et al. (2007) to extend the 2-D RVE to a 3-D RVE consisting of approximately $6 \times 6 = 36$ fibres. Geometrical constraints determined this number to be 32 fibres arranged regularly in a hexagonal array.

In this case, the RVE of the undamaged material, which is the same as periodic elementary cell CS32, is made up of 32 fibres. The RVE is considered a parallelepiped having its square section in the plane $(\overrightarrow{x}, \overrightarrow{y})$, and consisting of 32 parallel fibres over a length from $z = 0$ to $z = L$, which is identified as 8 mm. The origin O of the coordinates R_{loc} is the geometrical centre contained in the plane $z = 0$. At this scale at point M, the stress tensor is noted as σ and the strain tensor as ε. In this way, Blassiau et al. constructed a model of fibre failure and its consequences, taking into account the following (Blassiau et al., 2007; Blassiau, Thionnet, & Bunsell, 2006, 2008):

- The number of fibre breaks within the RVE for six levels of damage from the undamaged to the fully damaged state, denoted as CS32, C32, C16, C8, C4 and C2, and illustrated in Figure 16.6. The original undamaged CS32 cell has 32 intact fibres, followed by five damaged cells that contain respectively $N = 1$, 2, 4, 8 and 16 broken fibres;
- The load transfer along the axis of intact fibres neighbouring fibre breaks;
- The axial load transfer due to the debonding of the fibre/matrix interface at the point of the fibre break. Ten configurations of debonding have been considered from 3.5 to 35 μm;
- The effects of the viscoelastic characteristics of the matrix, which are taken as linear, on the axial load transfer.

The coefficient of longitudinal load transfer is defined as

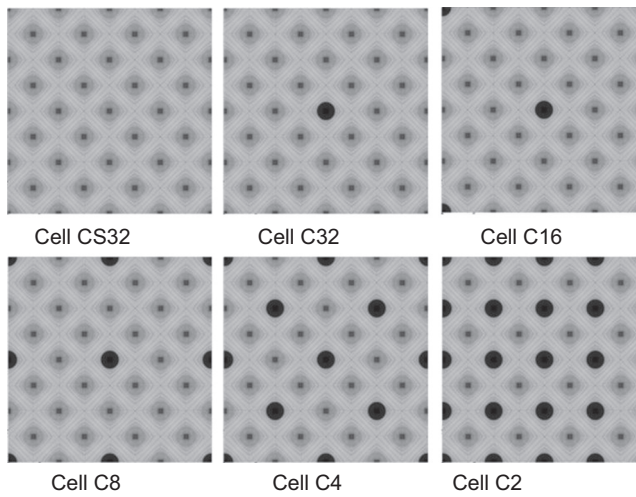

Figure 16.6 Six levels of damage considered at the level of the representative volume element (RVE).

$$k_r(C,d,t,V_f,Z) = \frac{\int_{Z_i}^{Z_{i+1}} \int_{S_F} \sigma_{zz}(C,\ d,\ t,\ V_f,\ x,\ y,\ z)\mathrm{d}x\mathrm{d}y\mathrm{d}z}{\int_{Z_i}^{Z_{i+1}} \int_{S_F} \sigma_{zz}(\mathrm{CS32},\ d\ =\ 0,\ t\ =\ 0,\ V_f,\ x,\ y,\ z)\mathrm{d}x\mathrm{d}y\mathrm{d}z}$$

in which:

C is the cell representing the state of damage considered;
d is the debonded length;
t is the time after fibre failure;
V_f is the fibre volume fraction;
z is the coordinate along the fibre from the plane of failure ($z = 0$);
Z_{i+1} and Z_i are the abscissae of the plane sections between which k_r is calculated;
$Z = \frac{Z_{i+1}+Z_i}{2}$;
S_F indicates the cross-section of the fibre considered;
x, y are the coordinates of the plane section of the cell;
σ_{zz} is the axial stress in the fibre considered; and
σ^0_{zz} is the axial stress in the fibre considered in the undamaged composite.

Regardless of whether debonding occurs at the fibre/matrix interface, or whether the matrix is viscoelastic, the definition for k_r remains valid.

At the microscopic scale, the composite is seen to be composed of fibres, matrix and fibre/matrix interfaces.

Five conditions of fibre failure are considered in the model, from the original CS32 cell containing 32 intact fibres to the C1 cell in which all 32 fibres are broken (to reduce computation time, the C32 cell is omitted − it has been verified that this does not significantly change the simulation results).

The first damage step is from the CS32 to C16 cell, in which two fibres are simultaneously broken. The second is from the C16 to C8 cell; again, two fibres are simultaneously broken. The third step is from the C8 to C4 cell, and four fibres are simultaneously broken. The fourth step is from the C4 to C2 cell, and eight fibres are simultaneously broken. The fifth step is from the C2 to C1 cell, and 16 fibres are simultaneously broken.

Two independent clusters of 32 broken fibres (32-plets) can interact in all directions, thus forming larger clusters (groups of 32-plets).

The different cells defined above introduce the concept of i-plets, such that an i-plet is defined as i fibres broken in the 32 fibres of the RVE. Then, we have the following set of i-plets: 0-plet, 1-plet, 2-plet, 4-plet, 8-plet, 16-plet and 32-plet. The magnitude of an i-plet is given by its 'i' value. A i-plet denotes a zero i-plet, whereas each remaining i-plet, numbered 1−32, denotes a nonzero i-plet. A nonzero i-plet is considered of small order if $i \leq 4$, medium order if $8 \geq i \geq 16$ and high order if $i \geq 32$. All of these are used to describe the damage state and evolution of the composite material.

The microscopic analysis is based on calculations that have been made using the finite element method for a given cell having a given fibre volume fraction and a debonded length of 35 μm (on both sides of the point of break in the fibre), as this results in a maximum value of transferred stress on intact fibres neighbouring a fibre break.

16.3.4 Importing the results at the microscopic scale as a foundation for the FE^2 simplified multiscale model

For calculations of macroscopic structures, the multiscale FE^2 approach has been developed for computational efficiency. This couples a calculation at the microscopic scale (modelling fibres, matrix and their interface explicitly) with a macroscopic calculation (homogenising fibres and matrix in a single orthotropic material). To save computational time, the FE^2 approach has been simplified. In order to do so, the most detrimental configurations have been used, and are defined as the maximum overstressing that occurs along the fibre axis for the closest intact fibre neighbouring the broken fibre, and the maximum stress induced in intact fibres neighbouring a fibre break, which as mentioned above occurs with a debonded length $d = d_{\mathrm{MAX}} = 35$ μm as revealed by the model. In this case, the overstressing coefficient is denoted as k_r^{MAX} and depends on cell C, time t and volume fraction V_f. It must be mentioned that k_r^{MAX} is independent of the debonded length: if the debonded length changes, it can be shown that the maximum overstressing value remains the same but takes place farther along the fibre axis. The multiscale process is then considered simplified, as the finite element analysis is only used for calculation of the macromechanical behaviour of the composite structure.

16.3.5 Description of the macroscopic scale calculations made by FE^2 simplified method

16.3.5.1 General framework and algorithm

Before the calculation starts, a Monte Carlo process (associated with the Weibull distribution of fibre strength) assigns five values of fibre strength at each Gauss point, allowing the damage to evolve from the CS32 to C1 state. The multiscale, simplified FE^2 simulation is iterative. The damage state, quantified as the number of broken fibres at step n, is calculated based on the value obtained at step $n-1$, and is organised in the following manner:

- the increment of time is made with or without the increment of macroscopic loading, depending on whether the structure is being subjected to a varying or steady load;
- the calculation is carried out using finite element analysis at the macroscopic scale so as to deduce the macroscopic stress field;
- a loop is made at the Gauss points for the microscopic scale:
  - the localisation step – using knowledge of the macroscopic stress, damage state of the material, volume fraction and time, the smoothed load transfer function allows the microscopic stress along the axes of the intact fibres to be determined. By comparison with the fibre strength values, this stress then allows the number of broken fibres in the RVE to evolve;
  - the homogenisation step – this allows the macroscopic behaviour of the equivalent homogeneous material to be calculated as a function of the new damage state; and
- a further step in the calculation is then carried out.

16.3.6 Hypotheses used in the macroscopic behaviour model

To reduce the calculation time at the macroscopic scale, it was necessary to make some assumptions concerning the macroscopic behaviour of the unidirectional composite.

These hypotheses are justified by a numerical analysis that observes the fibre failure process at the macroscopic scale and does not significantly modify the robustness of the final result, as against the case with no assumptions. The failure of a unidirectional composite loaded in the fibre direction is assumed to be controlled only by the failure of the fibres. As a consequence, the nonlinear characteristics of off-axis behaviour due to matrix cracking and viscoelasticity of the matrix are not considered. The second hypothesis, based on experimental observations that contrast with what happens on the microscopic scale, is that any nonlinearity due to viscoelastic behaviour parallel to the fibre direction can be ignored, as it is not detectable at the macroscopic scale. Any nonlinearity detected in the equivalent homogeneous material is therefore considered to be exclusively due to the failure of fibres and to reflect the density of their failures. The loss of longitudinal rigidity of the equivalent homogeneous material, as a function of the density of fibre failures, can be calculated by resolving the periodic homogeneous problem. Nevertheless a law of mixtures approximation, which gives an upper bound to the fall in longitudinal modulus, represents closely the exact homogenised behaviour.

Finally, at the macroscopic scale and within the local framework considered, the behaviour of the damaged unidirectional composite can be described at point M by a fourth-order tensor of rigidity, denoted $a(M)$. For the approximation of homogenisation, the longitudinal stiffness component $a_{1111}(M)$ can be described as $a^0_{1111}\left\{1 - \frac{N_R(M)}{N_T}\right\}$, where $a^0(M)$ designates the fourth-order tensor of rigidity for the undamaged material at point M, $N_R(M)$ represents the number of broken fibres and N_T (here equal to 32) represents the number of fibres in the RVE at point M. The behaviour of a unidirectional composite is then nonlinearly elastic.

16.3.7 Data for the analysis

The data necessary for an overall calculation of a structure using the simplified FE^2 process are

- at the macroscopic scale: the characteristics of the undamaged material and the law describing the fall in longitudinal rigidity of the equivalent homogeneous material; and
- at the microscopic scale, for each Gauss point: the random selection of five longitudinal fibre failure stresses according to the Weibull distribution of fibre strength properties, earlier identified experimentally; and the smoothing k_r^{MAX} of the load transfer coefficient (allowing the real axial stress supported by the intact fibres around the broken fibre to be calculated).

16.3.8 The viscoelastic behaviour of the matrix

It is widely accepted that the viscoelastic behaviour of the resin used as the matrix in a composite differs from that of the bulk resin. This is because the resin is constrained by the fibres in the composite. Applying bulk resin behaviour has indeed been shown to give unsatisfactory results, such that the time dependence of k_r^{MAX} has been corrected by a process of reverse engineering so as to make the number of fibre breaks recorded

by acoustic emission monitoring coincide with that obtained by calculation, for the case of a simple tensile test on a unidirectional composite.

16.4 Comparison of results of modelling and observations using high-resolution tomography: validation of the model

The model can be seen to correspond closely to reality when compared with experimentally obtained results, particularly those obtained by high-resolution tomography (Scott et al., 2009, 2011; Scott, Sinclair, Spearing, Hepples, et al, 2010; Scott, Sinclear, Spearing, Mavrogordato, et al, 2010; Scott, Sinclair, Spearing, Thionnet, & Bunsell, 2012; Wright, Fu, Sinclair, & Spearing, 2008; Wright, Moffat, Sinclair, & Spearing, 2010). The high-resolution tomography technique is therefore particularly important in this comparison, as it provides a direct and quantitative observation of the failure process similar to what is possible with the model. High-resolution tomography analyses the failure process with the same finesse as that of the model, which is a major advantage in validating the modelling. In general, the formation of fibre breaks can be considered to take two forms:

- the formation of nonzero *i*-plets from 0-plets;
- the formation of nonzero *i*-plets from nonzero *i*-plets of a lower value. For example, a 32-plet could be produced from a 2-, 4-, 8- or 16-plet.

It was observed on a notched specimen under monotonic tensile loading that the fibre breaks usually occurred randomly from the beginning of loading. Then, as the number of fibre breaks increased with loading, some of the new fibre breaks tended to initiate in the vicinity of existing broken fibres and then coalesce to larger-sized clusters of damaged fibres. This phenomenon is denoted as clustering. The simulation of this test shows that the number of fibre breaks versus loading, and the clustering effect, agree closely with the model (Thionnet et al., 2014):

- initially the fibre breaks are randomly distributed in the composite, which for the model means that the formation of many 1-, 2- and 4-plets occurs directly from 0-plets;
- there follows a coalescence of fibre breaks that produce higher-valued *i*-plets. Clusters of fibre breaks involving high-valued *i*-plets develop just before composite failure. Exactly analogous fibre failure kinetics were observed using high-resolution tomography, and showed clusters of 16 associated fibre breaks occurring just before failure; and
- no modification of the macroscopic properties of the structure was observed, indicating that the nature of the failure was what can be described as a sudden-death failure.

16.5 Consequences of the model

The model is sufficiently robust to allow different scenarios to be examined; for example, the possibility that measurements of residual strength could be an indicator of remaining lifetime, as can be the case for metal structures. The model demonstrates

how the fibres in the RVEs making up the composite structure fail during monotonic or sustained loading. It is observed that damage in the form of fibre failure is largely random during most of the lifetime of the composite, but that failure occurs rapidly after the fibre breaks begin to cluster. The number of broken fibres in an RVE is described using the term *i*-plet, in which *i* represents the number of broken fibres.

16.5.1 Monotonic loading

During a monotonic tensile test, fibres are seen to fail randomly throughout the specimen until clusters of fibre breaks develop, with composite failure occurring almost immediately afterwards as shown in Figure 16.7.

At the point of failure during a monotonic tensile test, it is seen that most (75%) of the RVEs contain no broken fibres and are still in their initial state, as can be seen in Figure 16.7. Just before failure, only approximately 7% of the RVEs contain 32 broken fibres. This explains the lack of warning of imminent failure that is observed with these materials. The model allows a closer examination of the kinetics of fibre failure in the composite whilst it is being loading monotonically to failure.

The simulated tensile test allows a close examination of the kinetics of fibre failure, in this case for a unidirectional composite loaded parallel to the fibres; see Figures 16.7 and 16.8. At the point of nonlinearity, *I*, announcing imminent failure, approximately 5% of all fibres are broken, and only 2% of these are in the form of 32-plet RVEs; however, almost immediately, at *J*, around 7% of the broken fibres are in the form of 32-plets, and an artefact of the calculation shows an instantaneous extension occurring during which fibres in lower-order *i*-plets are broken until point *C* is reached, after which deformation is controlled by the remaining intact matrix prior to complete failure at *D*. It is unrealistic to consider that this rapid final phase could be observed

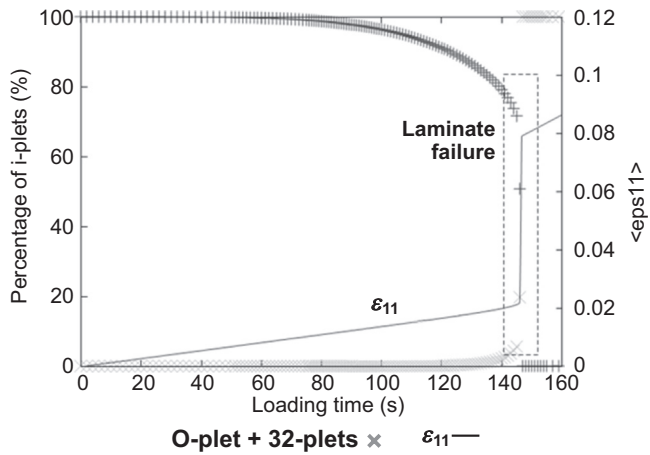

Figure 16.7 An increasing strain imposed on the specimen leading to a monotonic increase in tensile load provokes random failures of fibres and a fall in the number of 0-plets until clusters of breaks develop (32-plets), and failure occurs immediately afterwards.

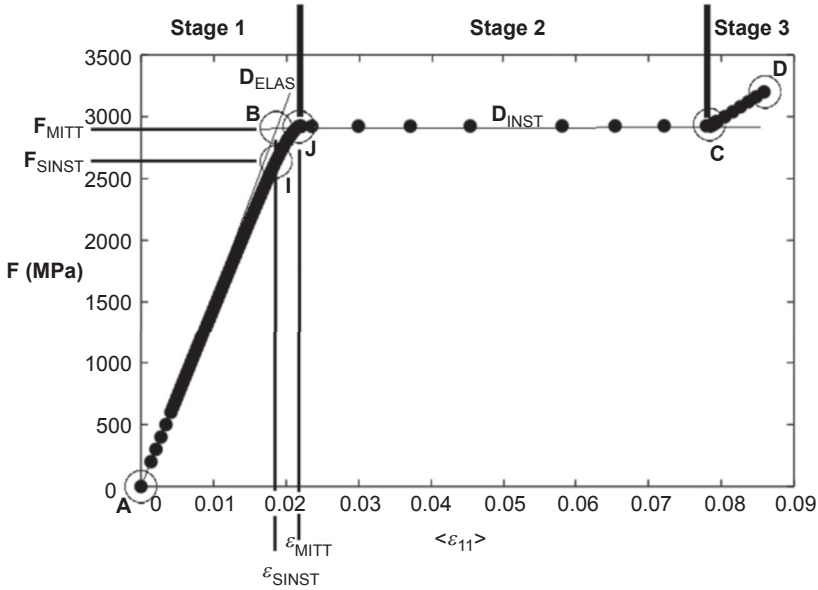

Figure 16.8 The model shows that the stress−strain curve remains linear until point *I*, where the first clusters of 32-plets appear. Almost immediately, at point *J*, the composite becomes unstable and fails.

experimentally. This behaviour has been observed directly by researchers using high-resolution tomography. In these tests, the unidirectional specimens were loaded progressively to higher loads, and the development of local damage consisting of fibres breaks was observed. Clusters of fibre breaks were observed, developing from a small number of breaks until around 16 grouped breaks. The next increase in load produced failure. This is exactly as predicted by the model (Thionnet et al., 2014).

The plateau shown in Figure 16.8 is similar to that predicted by Aveston, Cooper and Kelly (Aveston, Cooper, & Kelly, 1971; Aveston & Kelly, 1973), leading to the final extension shown in the curve due to the remaining matrix extending to failure after the fibres have broken. Experimentally, point *I* should be considered the practical failure point, as beyond that point the kinetics of failure are too fast to be observed, and the curve represents an idealised view of final failure.

It is clear that residual strength tests of composite structures, including pressure vessels, are not suitable for the purposes intended for these materials.

16.5.2 Steady loading

Under constant steady loading conditions, or cyclic loading up to a constant maximum load, damage accumulates in the form of fibre breaks due to relaxation of the matrix within the RVEs. This leads to progressive increases in intact fibres neighbouring fibre breaks, and some eventually fail. As this mechanism continues, some RVEs begin to accumulate several fibre breaks, and clusters of breaks are created. In extreme conditions, this can lead to failure as shown by the experimental results in Figure 16.9.

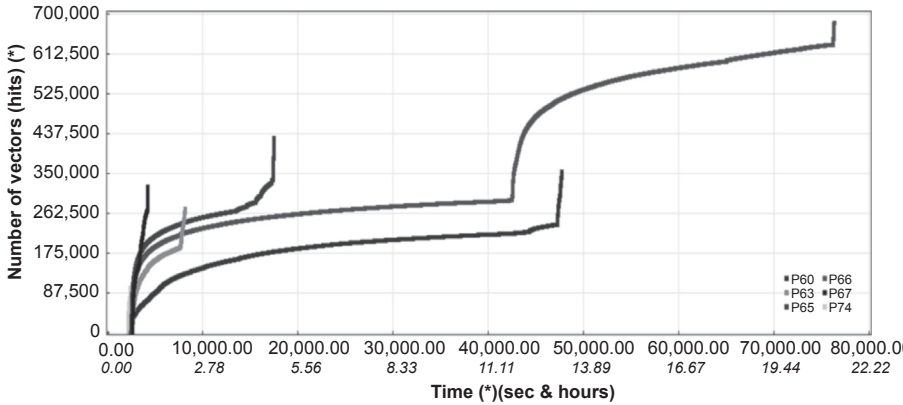

Figure 16.9 Experimental results showing accumulation of fibre breaks recorded from *U*/*D* specimens under steady loads around 96% of mean tensile strength. Failure occurred after varying lengths of time and occurred with no warning.

These results show how several unidirectional composites, loaded in the fibre direction to 96% of mean breaking load, failed after some time under steady loads. The specimens were nominally identical and showed times to failure ranging from less than 2 h to 14 h. Simulations of this type of test reveal that fibre break clusters develop throughout the loading and eventually lead to failure. As the composite is under a load that is less than its ultimate breaking strength in a monotonic test, the material can accumulate more damage during a sustained load than in a simple monotonic tensile test. It could be envisaged that a number of tests are conducted under steady loading at progressively lower loads, so as to determine the possible existence of a threshold load below which failure was very unlikely to occur. The difficulties are that times to failure rapidly become very long as loads are reduced, and also that scatter in lifetimes increases greatly. Simulated tests allow this behaviour to be assessed, as shown in Figures 16.10 and 16.11. It can

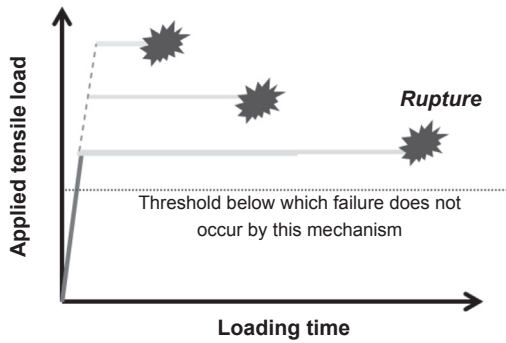

Figure 16.10 Time to failure under steady loads increases greatly as the load is decreased. It is conceivable to conduct such tests so as to identify any threshold below which failure would not occur in any reasonable time, but the time involved in such tests would be prohibitive.

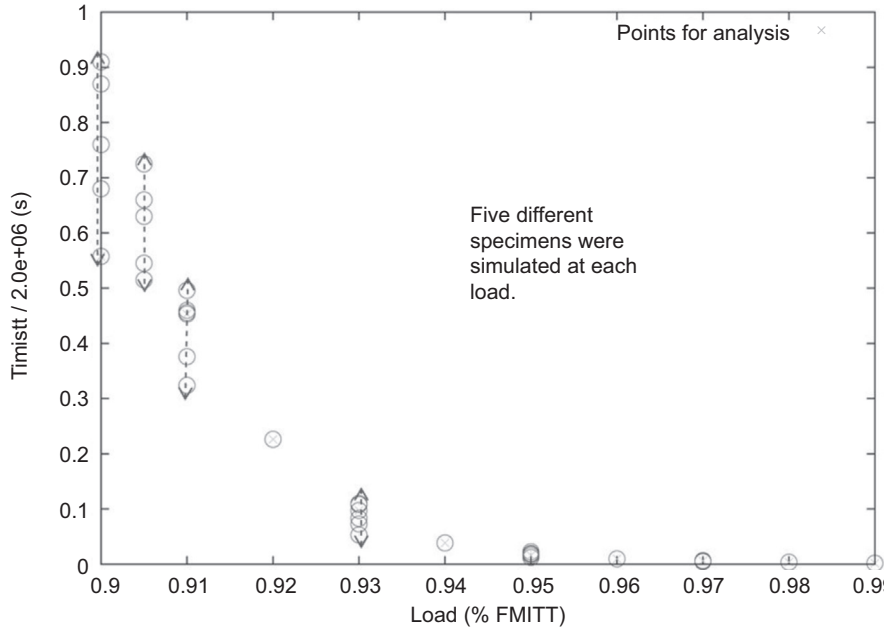

Figure 16.11 Time to failure (in millions of seconds) as the steady load is decreased.

be seen from these figures that times to failure increase rapidly as the load level is reduced. In addition it can be seen that as the load is reduced the scatter of time to failure increases. This is again evidence of the effect of the viscoelastic relaxation of the resin surrounding fibre breaks and resulting in increased loading, locally, on neighbouring intact fibres. The effect becomes more marked as loading times to failure increase. It can be seen that the time to failure increases in such a way as to become asymptotic to a threshold time representing an indefinitely long time to failure.

Figure 16.11 shows the simulated results for specimens held under steady load as the load level is varied. It can be seen that as the load is reduced, the time to failure (Timistt) increases dramatically and the scatter in lifetimes increases greatly.

Sustained loading can lead to a greater level of damage accumulation in the composite than that which provokes failure in a monotonically increasing load test. This is because at a lower load than that which produces a monotonic tensile failure, the remaining intact material is under less overall stress and can support an increased level of damage, as illustrated schematically in Figure 16.12. Under these conditions, the material can support a higher level of clustering, which develops because of the viscoelastic relaxation of the matrix around existing fibre breaks, than in a rapid monotonic loading test. This inevitably leads to an effect on strength based on the loading rate. It is found from the above model, both experimentally and theoretically, that the final failure load reduces as the loading rate is reduced (Bunsell & Thionnet, 2010; Mair, 2013).

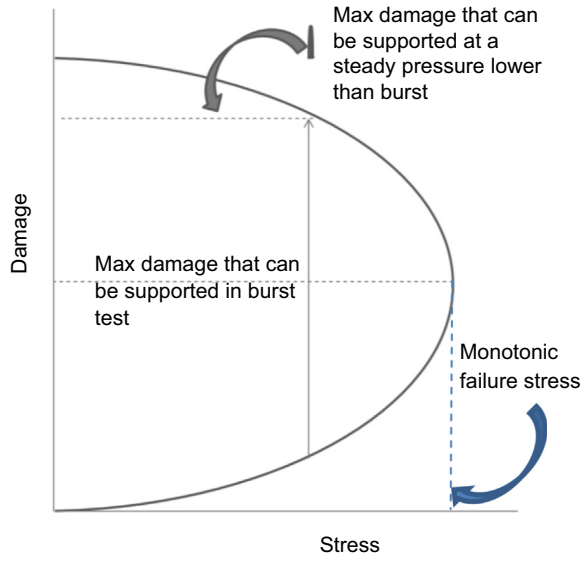

Figure 16.12 Schematic view of damage tolerance as a function of applied stress, showing an increased tolerance at levels lower than the monotonic failure stress.

16.6 Intrinsic limits based on component behaviour

16.6.1 Damage threshold and intrinsic safety factors

Failure has been shown to occur when a threshold of damage is reached, at which point the breaks are seen to be no longer random but grouped in clusters. However, the rate at which this happens and its exact level are functions of the defects and their distribution within the fibre population. Simulations and experimental studies on plate specimens have shown that the time to reach the critical threshold can vary considerably, but can be determined from the nature of the composite constituents. In this way, the probability curve of failure for a given structure subjected to sustained loadings can be drawn, and the time to reach the damage threshold can be calculated (Camara, Bunsell, Thionnet, & Allen, 2011). This has been possible due to the development of simulations of composite behaviour that have been compared favourably to experimental results. Experiments in which plates or pressure vessels would be held under steady loads until they failed could be conceived, but the large scatter in lifetimes would involve a prohibitively high number of costly tests that would last for very long periods. Simulated results, however, allow for this behaviour to be investigated and a threshold level of load or pressure to be determined below which failure will not occur during any reasonable expected in-service lifetime. In this way, a minimum safety factor based on the intrinsic properties of the composite, but not taking into account possible defects due to manufacture or handling, has been calculated (Bunsell & Thionnet, 2010; Bunsell, Thionnet, & Chou, 2014). It is unreasonable, though, to conclude no probability of failure exists however long the pressure vessel is under load. This is inherent in the probabilistic

Table 16.1 Intrinsic lifetimes for carbon fibre structures in which the fibres are primarily loaded in tension determined both theoretically and from experimental results

Study	Lifetime 15 years	Lifetime 150 years
Finite element analysis	78.8% of mean burst pressure (SF = 1.28)	75.5% of mean burst pressure (SF = 1.32)
Experimental study	71.9% of mean burst pressure (SF = 1.39)	71.4% of mean burst pressure (SF = 1.40)

analysis. This means there is no real asymptote of lifetime at which it is considered to be infinite. For this reason, the model has been used to calculate the load level at which the probability of failure is one in a million over a 15-year period, and also over a 150-year period. These results, which compare lifetimes obtained from the model with those determined from experimental data using acoustic emission to determine damage accumulation, are shown in Table 16.1. When these studies are extended to even lower probabilities of failure, it becomes clear that the intrinsic safety factor for these carbon fibre–composite structures lies between 1.4 and 1.6.

Based on the above understanding of damage accumulation in carbon fibre–composite pressure vessels, two means of arriving at these results have been used: one based on acoustic emissions detected during experimental testing of unidirectional specimens, and the other based on the simulation of damage accumulation. The results are similar and show lower risk factors than those previously proposed by other authors. In this way, the minimum safety factor can be quantified rather than being guessed at or based on the behaviour of metal structures. Using values for the probability of one failure in a million over a 150-year period, which must be conservative, a value for the intrinsic safety factor of 1.4 becomes reasonable. However, in order for a realistic safety factor to be assessed, other damaging events should be considered, such as manufacturing difficulties and the risk of accidental or deliberate damage occurring during the in-service life of the pressure vessel. Nevertheless, quantifying the intrinsic safety factor goes a long way towards allowing more realistic factors to be established that should reduce costs whilst not reducing reliability, and together these factors should encourage the industry to grow.

The damage processes discussed above for carbon fibre–reinforced composites will also occur in glass fibre–reinforced composites; however, for the latter material, stress corrosion is likely to dominate in long-term use.

16.7 Long-term failure probability

16.7.1 Determination of reliability

For composite pressure vessels to be widely used with confidence, it must be possible to determine their long-term reliability and assess damage during in-service use. The

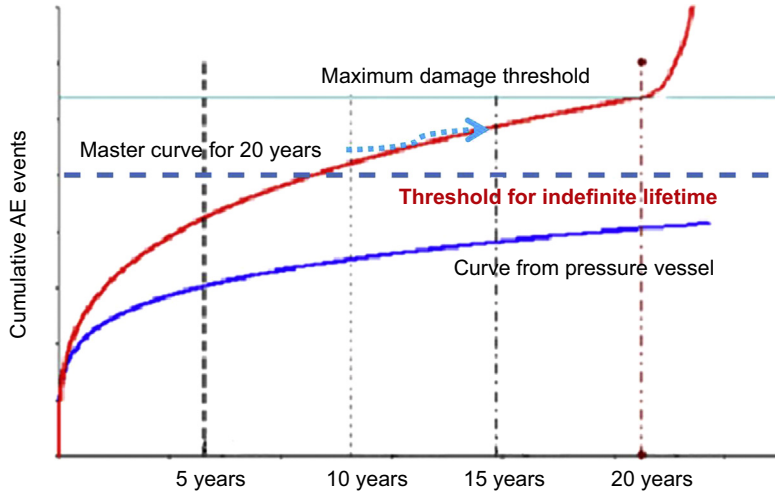

Figure 16.13 Master curve of load accumulation for a vessel destined to be in service for a maximum of 20 years. Possible damage curves are shown as dotted lines, and a vessel could be displaced from a lower curve to a higher one if subjected to unusual conditions. The pressure vessel can remain in service as long as it is on a lower curve than the master curve.

model that has been developed and justified experimentally allows this to be done. A master curve of damage accumulation is drawn for the type of pressure vessel considered, taking into account the intrinsic safety factor described above, as shown in Figure 16.13. Any pressure vessel can then be compared with the master curve throughout its in-service life. It is possible to determine a threshold for a given lifetime, but more useful is the threshold for an indefinite in-service lifetime. Loading that does not take the pressure vessel above this level of damage can be considered acceptable, and this threshold defines the minimum intrinsic safety factor. Unforeseen events such as overheating and other mechanisms could accelerate damage, but if the pressure vessel's damage is seen to fall below the master curve asymptotic to this threshold level, it can be returned to service with confidence.

16.8 Conclusions

Since the development of advanced and particularly carbon fibre—reinforced composites, there has been a continual effort to understand how damage in these materials is accumulated and how it limits the lifetimes of structures made from them. Many authors have contributed to this understanding, but those who contributed to these studies merit special mention. The pioneering work of Kelly (1986) and the even earlier work of Cox (1951) laid the foundations of our present detailed knowledge of damage accumulation in these materials and how it can be applied to structures such as filament pressure vessels that are finding use storing gases at high pressures. These applications require a thorough knowledge of failure processes if their total reliability is to be assured.

Computing power is now such that multiscale modelling has enabled a detailed understanding of damage processes in these materials, and has been verified by experimental techniques such as acoustic emission monitoring of damage, and visualised by high-resolution tomography. It has been seen that the stress concentrations around individual fibre breaks lead to increased stresses in neighbouring intact fibres through the shear of the matrix. Under relatively quick monotonic loading, taking for example just a few minutes, the viscoelastic nature of the matrix has no role to play. In the absence of any stress raisers due to the geometry of the composite, fibres fail in a random manner throughout the composite. These failures are controlled by the stochastic nature of the strengths of the fibres. By chance, neighbouring fibres begin to break in the same plane of the material, and clusters of breaks begin to develop. This very quickly leads locally to instability, and the composite fails with no warning.

Under sustained loading conditions, damage accumulation is controlled by the viscoelastic properties of the matrix that allow some fibres neighbouring fibre breaks to eventually fail. As in monotonic loading, it is the development of clusters of fibre breaks that ultimately causes failure.

Knowledge of these damage processes allows an intrinsic safety factor to be defined. This means a safety factor based on the intrinsic behaviour of the constituent materials, fibres and matrix as well as the fibre/matrix interfacial bond. Clearly, the safety factor for a complete structure should take into account other factors such as variations due to manufacturing techniques.

References

Aussedat, E., Thionnet, A., & Renard, J. (1995). Comportement en compression des composites par une définition du mode de sollicitation en mécanique de l'endommagement. *Comptes-rendus de l'Académie des Sciences de Paris, Séries II, 321*, 533−540.

Aveston, J., Cooper, G., & Kelly, A. (1971). Single and multiple fracture, the properties of fibre composites. In *Proc. Conf. National Physical Laboratories* (pp. 15−24). London: IPC Science and Technology Press Ltd.

Aveston, J., & Kelly, A. (1973). Theory of multiple fracture of fibrous composites. *Journal of Material Science, 8*, 352−362.

Batdorf, S. B. (1982). Tensile strength of unidirectionally reinforced composites − II. *Journal of Reinforced Plastics Composites, 1*, 165−175.

Baxevanakis, C. (December 14, 1994). *Comportement statistique à rupture des composites stratifiés* (Doctoral thesis): Ecole Nationale des Mines de Paris.

Berger, M. H., & Jeulin, D. (2003). Statistical analysis of the failure stresses of ceramic fibres: dependence of the weibull parameters on the gauge length, diameter variation and fluctuation of defect density. *Journal of Materials Science, 38*, 2913−2923.

Beyerlein, I. J., Zhou, C. H., & Schadle, L. S. (1998). Time evolution of stress redistribution around multiple fiber breaks in a composite with viscous and viscoelastic matrices. *International Journal of Solids and Structures, 35*, 3177−3211.

Blassiau, S., Bunsell, A. R., & Thionnet, A. (2007). Damage accumulation processes and life prediction in unidirectional composites. *Proceedings of the Royal Society A, 463*, 1135−1152.

Blassiau, S., Thionnet, A., & Bunsell, A. R. (2006). Micromechanisms of load transfer in a unidirectional carbon fibre reinforced epoxy composite due to fibre failures: Part II. Influence of viscoelastic and plastic matrices on the mechanisms of load transfer. *Composite Structures, 74*, 319−331.

Blassiau, S., Thionnet, A., & Bunsell, A. R. (2008). Micromechanisms of load transfer in a unidirectional carbon fibre reinforced epoxy composite due to fibre failures: Part III. Multiscale reconstruction of composite behaviour. *Composite Structures, 83*, 312−323.

Bunsell, A. R. (2009). *Handbook of tensile properties of textile and technical fibres*. Cambridge: Woodhead Publishing.

Bunsell, A. R., & Renard, J. (2005). *Fundamentals of fibre reinforced composite material*. London: IOP, CRC.

Bunsell, A. R., & Thionnet, A. (2010). Life prediction for carbon fibre filament wound composite structures. *Philosophical Magazine, 90*, 4129−4146.

Bunsell, A. R., Thionnet, A., & Chou, H. Y. (2014). Intrinsic safety factors for glass & carbon fibre composite filament wound structures. *Applied Composites Materials, 21*, 107−121.

Camara, S., Bunsell, A. R., Thionnet, A., & Allen, D. H. (2011). Determination of lifetime probabilities of carbon fibre composite plates and pressure vessels for hydrogen storage. *International Journal of Hydrogen Energy, 36*(10), 6031−6038.

Cox, H. L. (1951). The elasticity and strength of paper and other fibrous materials. *British Journal of Applied Physics, 3*, 72−79.

Curtin, W. A. (2000). Dimensionality and size effects on the strength of fiber-reinforced composites. *Composites Science and Technology, 60*, 543−551.

Curtin, W. A., & Ibnabdeljalil, M. (1997). Strength and reliability of fiber-reinforced composites: localized load sharing and associated size effects. *International Journal of Solids and Structures, 34*, 2649−2668.

Feyel, F. (2003). A multilevel finite element method (Fe^2) to describe the response of highly non-linear structures using generalized continua. *Computer Methods in Applied Mechanics and Engineering, 192*, 3233−3244.

Fuwa, M., Bunsell, A. R., & Harris, B. (1975). Acoustic emission during cyclic loading of carbon fibre reinforced plastics. *Physics D, 8*, 1460−1471.

Fuwa, M., Bunsell, A. R., & Harris, B. (1976). Acoustic emission studies of filament wound carbon fibre reinforced rings and pressure vessels. *Journal of Strain Analysis, 11*, 97−101.

Goree, J. G., & Gross, R. (1980). Stresses in a three-dimensional unidirectional composite containing broken fibers. *Engineering Fracture Mechanics, 13*, 395−405.

Harlow, D. G., & Phoenix, S. L. (1978). The chain-of-Bundles probability model for the strength of fibrous materials I: analysis and Conjectures. *Journal of Composite Materials, 12*, 195−213.

Harlow, D. G., & Phoenix, S. L. (1981). Probability distributions for the strength of composite materials I: a convergence sequence of tight bounds. *International Journal of Fracture, 17*, 601−630.

Hedgepeth, J. M. (1961). *Stress concentrations in filamentary structures*. NASA TND-882. Langley Research Center.

Inglis, C. (1913). Stress in a plate due to the presence of cracks and sharp corners. *Transactions of the Royal Institution of the Naval Architects, 55*, 219−230.

Joannès, S., & Chou, H. Y. (2013). *Private communication*.

Kelly, A. (1986). *Strong solids* (3rd ed.). Oxford: Pergamon/Elsevier.

Kong, P. O. (1979). A monte carlo study of the strength of unidirectional fiber-reinforced composite. *Journal of Composite Materials, 13*, 311−327.

Lagoudas, D. C., Hui, C. Y., & Phoenix, S. L. (1989). Time evolution of overstress profiles near broken fibers in a composite with a viscoelastic matrix. *International Journal of Solids Structures, 25*, 45−66.

Landis, C. M., Beyerlein, I. J., & McMeeking, R. M. (2000). Micromechanical simulation of the failure of fiber reinforced composites. *Journal of the Mechanics and Physics of Solids, 48*, 621−648.

Landis, C. M., & McMeeking, R. M. (1999). Stress concentrations in composites with interface sliding, matrixstiffness and uneven fiber spacing using shear lag theory. *International Journal of Solids and Structures, 36*, 4333−4361.

Laroche, D., & Bunsell, A. R. (1980). Stress and time dependent damage in CFRP. In Bunsell, et al. (Eds.), *Advances in composite materials: Vol. 2. Proceedings of ICCM3, Paris* (pp. 985−997). Oxford: Pergamon Press.

Lifschitz, J. M., & Rotem, A. (1970). Time-dependent longitudinal strength of unidirectional fibrous composites. *Fibre Science and Technology, 3*, 1−20.

Mair, G. (2013). Effect of the loading rate on ultimate strength of composites. Application: pressure vessel slow burst test. *Composite Structures, 104*, 144−153.

Matsuhisa, Y., & Bunsell, A. R. (2009). Tensile failure of carbon fibers. In A. R. Bunsell (Ed.), *Handbook of tensile properties of textile and technical fibres* (pp. 574−602). Oxford: Woodhead Pub./Elsevier.

Nedele, M. R., & Wisnom, M. R. (1994a). Three dimensional finite analysis of the stress concentration at a single fibre break. *Composites Science and Technology, 51*, 517−524.

Nedele, M. R., & Wisnom, M. R. (1994b). Stress concentration factors around a broken fibre in a unidirectional carbon fibre-reinforced epoxy. *Composites, 25*, 549−557.

Ochiai, S., Schulte, K., & Peters, P. W. M. (1991). Strain concentration for fibers and matrix in unidirectional composites. *Composites Science and Technology, 41*, 237−256.

Phoenix, S. L. (1997). Statistical issues in the fracture of brittle matrix fibrous composites: localized load-sharing and associated size effects. *International Journal of Solids and Structures, 34*, 2649−2668.

Phoenix, S. L., & Beyerlein, I. J. (2000). Statistical strength theory for fibrous composite materials. In A. Kelly, & C. Zweben (Eds.), *Comprehensive composite materials* (pp. 559−639). Pergamon-Elsevier Science.

Phoenix, S. L., & Newman, W. I. (2009). Time-dependent fiber bundles with local load sharing. *Physical Review, 80*, 066115.

Renard, J., & Thionnet, A. (2007). Damage in composites: from physical mechanisms to modelling. *Composites Science and Technology*, 642−646.

Rosen, B. W. (1964). Tensile failure of fibrous composites. *AIAA Journal, 2*(11), 1985−1991.

Scop, P. M., & Argon, A. S. (1969). Statistical theory of strength of laminated composites II. *Journal of Composite Materials, 3*, 30−44.

Scott, A. E., Kalantzis, N., Clinch, M., Hepples, W., Sinclair, I., & Spearing, S. M. (2009). Advanced micro-mechanical analysis of highly loaded hybrid composite structures. In *ICCM-17, Edinburgh, and private communications*.

Scott, A. E., Sinclair, I., Spearing, S. M., Hepples, W., Wright, P., & Mavrogordato, M. (2010). Fibre fracture of carbon fibre laminates using ultra high resolution computed tomography. In *14th European conference on composite materials, ECCM 14, paper ID 575-ECCM14, Budapest, Hungary*.

Scott, A. E., Sinclair, I., Spearing, S. M., Mavrogordato, M., Bunsell, A. R., Thionnet, A., et al. (2011). Rupture de fibre: comparison entre un modèle écrit à l'échelle microstructural et une détection du phénomène par tomographie très haute résolution. In *17th Journées Nationales sur les Composites, Poitiers, France*.

Scott, A. E., Sinclair, I., Spearing, S. M., Mavrogordato, M., Bunsell, A. R., & Thionnet, A. (October 2010). Comparison of the accumulation of fibre breaks occurring in a unidirectional carbon/epoxy composite identified in a multi-scale micro-mechanical model with that of experimental observations using high resolution computed tomography. *Matériaux, 2010*, 18−22 (Nantes, France).

Scott, A. E., Sinclair, I., Spearing, S. M., Thionnet, A., & Bunsell, A. R. (2012). Damage accumulation in a carbon/epoxy composite: comparison between a multi-scale model and computed tomography experimental results. *Composites Part A, 43*, 1514−1522.

Somer, A., & Bunsell, A. R. (1992). The tensile and fatigue behaviour of carbon fibres. *Plastics Rubber and Composite Processing and Applications, 18*, 263.

Souza, F., Allen, D., & Kim, Y. (2008). Multiscale model for predicting damage evolution in composites due to impact loading. *Composites Science and Technology, 68*, 2624−2634.

Thionnet, A. (2001). A model for the recovery of thermomechanical properties in strongly anisotropic damaged materials. *Journal of Composite Materials, 35*, 731−750.

Thionnet, A., Chou, H. Y., & Bunsell, A. R. (2015). Fibre break failure processes in unidirectional composites. Part 1: Failure and critical damage state induced by increasing tensile loading. *Applied Composite Materials, 22*(2), 119−140.

Thionnet, A., Chou, H. Y., & Bunsell, A. R. (2015). Fibre break failure processes in unidirectional composites. Part 2: Failure and critical damage state induced by sustained tensile loading. *Applied Composite Materials, 22*(2), 141−155.

Thionnet, A., Chou, H. Y., & Bunsell, A. R. (2015). Fibre break failure processes in unidirectional composites. Part 3: Unidirectional plies included in laminates. *Applied Composite Materials, 22*(2), 157−169.

Thionnet, A., Chou, H-Y., & Bunsell, A. R. (2014). Fibre break processes in unidirectional composites. *Composites part A*, 148−160.

Thionnet, A., & Renard, J. (1999). Modelling unilateral damage effect in strongly anisotropic materials by the introduction of loading mode in damage mechanics. *International Journal of Solids and Structures, 36*, 4269−4287.

Thionnet, A., & Renard, J. (1998). Multi-scale analysis to determine fibre/matrix debonding criteria in SiC/titanium composites with and without consideration of the manufacturing residual stresses. *Composites Science and Technology, 58*, 945−955.

Van den Heuvel, P. W. J., Goutianos, S., Young, R. J., & Peijs, T. (2004). Failure phenomena in fibre-reinforced composites part 6: a finite element study of stress concentrations in unidirectional cfr epoxy composites. *Composites Science and Technology, 64*, 645−656.

Van den Heuvel, P. W. J., Wubbolts, M. K., Young, R. J., & Peijs, T. (1998). Failure phenomena in two-dimensional multi-fibre model composites: 5. A finite element study. *Composites A, 29*, 1121−1135.

Wisnom, M. R., & Green, D. (1995). Tensile failure due to interaction between fibre breaks. *Composites, 26*, 499−508.

Wright, P., Fu, X., Sinclair, I., & Spearing, S. M. (2008). Ultra high resolution computed tomography of damage in notched carbon fibre-epoxy composites. *Journal of Composite Materials, 42*, 1993−2002.

Wright, P., Moffat, A., Sinclair, I., & Spearing, S. M. (2010). High resolution tomographic imaging and modelling of notch tip damage in a laminated composite. *Composites Science and Technology, 70*, 1444−1452.

Zweben, C. (1968). Tensile failure of fiber composites. *AIAA Journal, 6*(12), 2325−2331.

An extension of the point-stress criterion based on a coupled stress and energy fulfilment: application to the prediction of the open-hole tensile strength of a composite plate

17

E. Martin[1], *D. Leguillon*[2], *N. Carrère*[3]
[1]LCTS, CNRS UMR 5801, Univ. Bordeaux, Pessac, France; [2]IJLRA, CNRS UMR 7190, Univ. P. et M. Curie, Paris, France; [3]LBMS, ENSTA Bretagne, Univ. Brest, Brest, France

17.1 Introduction

The presence of stress concentrations reduces the strength of composite materials. Evaluating and predicting the notched strength of composite laminates has been the subject of numerous papers as illustrated by the extensive data collected by Awerbuck and Madhukar (1985). Experimental observations reveal that several damage mechanisms (including matrix cracking and delamination) develop in the vicinity of a notch (Carlsson, Aronsson, & Backlund, 1989; Green, Wisnom, & Hallett, 2007; Wisnom, Hallett, & Soutis, 2010). Modelling the extent of such damage is tractable with the help of nonlinear finite element computations but induces lengthy computational times (Camanho, Maimí, & Dávila, 2007; Laurin, Carrère, & Maire, 2007; Van der Meer, Oliver, & Sluys, 2010). An alternative approach is the use of cohesive zone models inserted along a predefined crack path that link the cohesive traction and crack opening (Needleman, 1987). A crack develops if the dissipated energy reaches the fracture toughness. Convergence problems can still be an issue and faster prediction methods are needed for preliminary design. They rely on the analysis of the elastic stress distribution near the notch or on the use of linear elastic fracture mechanics. The point-stress criterion (PSC) assumes that fracture occurs when the tensile stress σ reaches the unnotched strength σ^c at a characteristic distance d_0 from the notch (Whitney & Nuismer, 1974) with

$$\sigma(d_0) = \sigma^c \tag{17.1}$$

The average stress criterion (Whitney & Nuismer, 1974) considers that failure develops when the average tensile stress over the characteristic distance is equal to σ^c with

Structural Integrity and Durability of Advanced Composites. http://dx.doi.org/10.1016/B978-0-08-100137-0.00017-1

$$\frac{1}{d_0}\int_0^{d_0}\sigma(x)\mathrm{d}x = \sigma^{\mathrm{c}} \tag{17.2}$$

The equivalent flaw model (Waddoups, Eisenmann, & Kaminski, 1971) postulates that fracture happens if the energy release rate for an equivalent critical length a^{c} reaches the material toughness G^{c} with

$$G(a^{\mathrm{c}}) = G^{\mathrm{c}}. \tag{17.3}$$

Thanks to bidimensional elasticity solutions, those fracture criteria can be easily formulated. In each case, a characteristic distance (d_0 or a^{c}) is needed and is assumed a material constant. It is worthy of note that an improved approach combining the average stress criterion and the fracture toughness condition was proposed by Soutis and Fleck (1990) to predict the open-hole compression fracture of composite plates. These methods of analysis belong to the theory of critical distances recently reviewed by Taylor (2008). However, experimental results indicate that this characteristic distance must be related to the notch size and specimen geometry in order to obtain accurate predictions (Kim, Kim, & Takeda, 1995). To estimate the tensile strength of open-hole laminates, Byron Pipes, Gillespie, and Wetherhold (1979) proposed a general relationship between the characteristic distance d_0 and the hole radius R with

$$d_0 = CR^m \tag{17.4}$$

where (C,m) are two constants to be determined experimentally. There is thus a need for a refined model that will avoid this empirical approach.

The aim of this paper is to investigate the use of an improved criterion to analyse crack onset in an open-holed composite plate subjected to tension. The previously mentioned criteria (Eqns (17.1−17.3)) require two parameters either strength σ^{c} or toughness G^{c} and a characteristic distance d_0 or a^{c}. A coupled criterion (CC) has been proposed that combines energy and stress conditions to describe a crack nucleation mechanism in the vicinity of a stress concentrator in brittle materials (Leguillon, 2002). The two needed parameters are σ^{c} and G^{c}, with the characteristic distance no longer considered a material constant. As will be shown in next section, this approach allows the crack length at nucleation to depend on both the material fracture properties and the geometry of the notched specimen. It is a finite fracture mechanics approach: the history of the development of the crack increment that appears in a very short time is not described. This initiation criterion has already been used in various situations including delamination in composite laminates (Martin, Leguillon, & Carrère, 2010), cracking in ceramic laminates (Leguillon & Martin, 2012), failure of bonded joints (Hell, Weißgraeber, Felger, & Becker, 2014; Moradi, Carrère, Leguillon, Martin, & Cognard, 2013), fibre/matrix interfacial cracking (Mantič & García, 2012; Martin, Poitou, Leguillon, & Gatt, 2008) and crack initiation at notches (Leguillon, Quesada, Putot, & Martin, 2007), and was also proposed recently by

Camanho et al. to predict the open-hole strength of composite laminates (Camanho, Erçin, Catalanotti, Mahdi, & Linde, 2012). Our analysis demonstrates that the CC can be considered a 'modified' PSC, for which the characteristic distance can be defined as a function of the material properties, the hole radius and the plate width.

The organisation of the chapter is as follows. Section 17.2 states the general equations required to apply the CC for an open-holed plate submitted to tension. Section 17.3 presents the results obtained for an isotropic plate. Analytical formulations are used, and an infinite plate is first analysed before investigating the influence of finite width. Section 17.4 is devoted to the influence of anisotropy. In this case, finite element computations are required. The last section presents a comparison of CC model predictions with experimental data.

17.2 The coupled criterion

The geometry of the plate is given in Figure 17.1(a). The radius of the central open hole is R. The width and the length of the plate are respectively denoted $2W$ and $2L$. The origin of the coordinate system is located at the centre of the hole, with the y-axis parallel to the longitudinal direction of the plate. The loading σ is applied in direction y. It is assumed that a critical loading σ^* initiates two symmetrical cracks of length a^* emanating from the edges of the hole along direction x (Figure 17.1(b)).

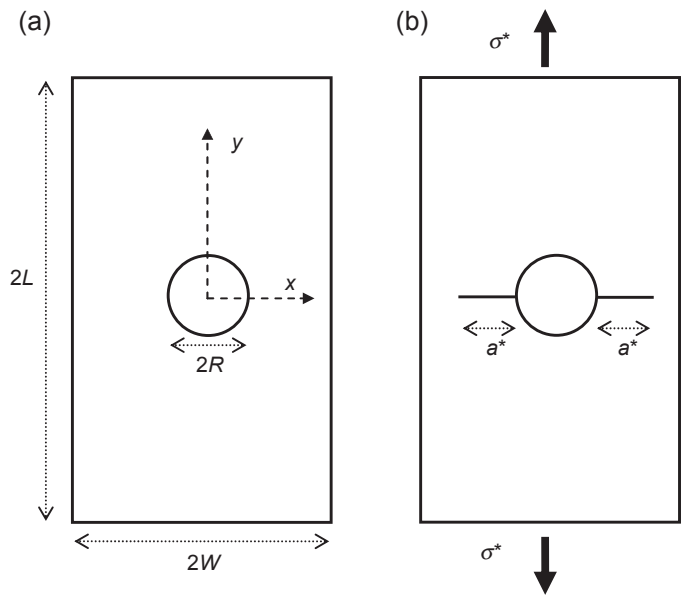

Figure 17.1 (a) The geometry of the open-holed plate; and (b) crack nucleation from the edges of the hole upon a critical tensile loading.

Within the framework of finite facture mechanics, crack initiation in the vicinity of a stress concentration can be described by considering the formation of a crack with a finite area ΔA. The incremental energy release rate (Martin & Leguillon, 2004) is defined by

$$G^{\text{inc}}(a) = -\frac{\Delta P}{\Delta A} \tag{17.5}$$

where P denotes the potential energy stored in the structure. For a bidimensional analysis, the crack area is given by $\Delta A = b\Delta a$, where Δa is the crack length and b is the sample depth. The energy condition is written as

$$G^{\text{inc}}(a) \geq G^{\text{c}} \tag{17.6}$$

where G^{c} is the fracture toughness. Relation (Eqn (17.6)) can be rewritten as

$$G^{\text{inc}}(a) = \frac{A(a)R}{E}\,\sigma^2 \geq G^{\text{c}} \tag{17.7}$$

where E is the Young's modulus of the plate material, $A(a)$ is a dimensionless coefficient and σ is the remote tensile load acting on the plate.

To determine the crack size, an additional condition is needed. Leguillon (2002) proposed using a stress condition that states that the tensile normal stress $\sigma_{yy}(x)$ reaches the tensile strength σ^{c} along the anticipated nucleation length

$$\sigma_{yy}(x, y = 0) \geq \sigma^{\text{c}} \quad \text{for} \quad R \leq x \leq R + a \tag{17.8}$$

which can be written as

$$k_{yy}(x)\sigma \geq \sigma^{\text{c}} \quad \text{for} \quad R \leq x \leq R + a \tag{17.9}$$

Let us assume that $A(a)$ is an increasing function of a and that $k_{yy}(x)$ is a decreasing function of x. As illustrated in Figure 17.2, the energy condition (Eqn (17.6)) provides a lower bound $a^{\min}$ of the crack increment for a given value σ of applied loading. Conversely, the stress condition (Eqn (17.8)) supplies an upper bound $a^{\max}$ of the crack increment. Increasing the loading reduces the lower bound but increases the upper bound. The load at initiation σ^* is the minimum load for which $a^{\min} = a^{\max} = a^*$. Combining the equalities in Eqns (17.7) and (17.9) leads to

$$\frac{A(a^*)}{\left(k_{yy}(a^*)\right)^2} = \frac{L^{\text{c}}}{R} \tag{17.10}$$

where L^{c} is the fracture length of the material $L^{\text{c}} = \frac{EG^{\text{c}}}{(\sigma^{\text{c}})^2}$. Solving Eqn (17.10) is always possible, as its left-hand side is an increasing function of a^* vanishing for

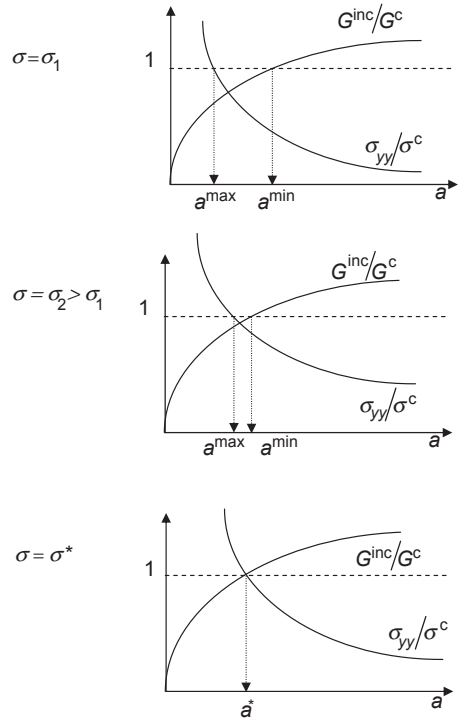

Figure 17.2 Determining the critical load using the coupled criterion (CC). The ratios $\frac{G^{\text{inc}}}{G^{\text{c}}}$ and $\frac{\sigma_{yy}}{\sigma^{\text{c}}}$ are plotted versus the crack length to define the energy and stress conditions. Comparing with the unity value allows for definition of the lower and upper bounds a^{min} and a^{max}. The successive plots are obtained for an increasing load until the initiation load is reached.

$a^* = 0$. This equation indicates that a^* cannot be considered only a characteristic value of the material, but also depends on the hole radius R and the fracture length L^{c}. It must be pointed out that a^* does not represent the final crack length after crack onset. The stress-and-energy analysis demonstrates that crack length is a discontinuous function on the quasi-static timescale, so the crack size at onset cannot be smaller than a^*. However, the nucleated crack is unstable, and a^* is not a crack arrest size but corresponds to the first state after nucleation. The CC can be considered a 'modified' PSC using Eqn (17.1), for which $d_0 = a^*$ is provided by Eqn (17.10). Once the initiation length a^* is determined, the initiation stress σ^* is given by

$$\sigma^* = \frac{\sigma_0}{\sqrt{A(a^*)}} \text{ with } \sigma_0 = \sqrt{\frac{EG^{\text{c}}}{R}} \tag{17.11}$$

or equivalently from

$$\sigma^* = \frac{\sigma^{\text{c}}}{k_{yy}(a^*)} \tag{17.12}$$

The normalised tensile strength $\frac{\sigma^*}{\sigma^c}$ is

$$\frac{\sigma^*}{\sigma^c} = \frac{1}{k_{yy}(a^*)} = \sqrt{\frac{L^c}{R}}\frac{1}{\sqrt{A(a^*)}} \tag{17.13}$$

It should be noted that Camanho et al. (2012) use a slightly different approach, with an average stress condition instead of Eqn (17.8) and an average stress intensity factor condition instead of Eqn (17.6).

17.3 Isotropic plate

The geometry of an infinite and isotropic-holed plate is first examined. In this case, the distribution of the normal stress prior to failure $\sigma_{yy}(x,0)$ only depends on $\frac{x}{R}$ (Timoshenko & Goodier, 1970) with

$$k_{yy}^{\infty}\left(\frac{x}{R}\right) = \frac{1}{2}\left(2+\left(1+\frac{x}{R}\right)^{-2}+3\left(1+\frac{x}{R}\right)^{-4}\right) \tag{17.14}$$

The stress concentration factor at the edge of a hole is independent of the hole radius, but the size of the stress concentration region depends on R. The expression for the stress intensity factor of two symmetrical cracks emanating from a circular hole in an infinite rectangular plate in tension (Tada, Paris, & Irwin, 1985) is

$$K_I^{\infty}(a) = \sigma\sqrt{\pi a}F\left(\frac{a}{R}\right) \text{ with } F\left(\frac{a}{R}\right) = 0.5\left(3-\frac{a}{R}\right)\left(1+1.243\left(1-\frac{a}{R}\right)^3\right) \tag{17.15}$$

Assuming a plane stress state and remembering that the energy release rate is given for a unit thickness by $G(a) = -\frac{dW}{da} = \frac{(K_I^{\infty}(a))^2}{E}$ allows one to estimate the incremental energy release rate $G^{inc}(a) = \frac{1}{a}\int_0^a G(a)da$. Finally, the incremental energy release rate is given by

$$G_{\infty}^{inc}\left(\frac{a}{R}\right) = A_{\infty}\left(\frac{a}{R}\right)\frac{R}{E}\sigma^2 \text{ with } A_{\infty}\left(\frac{a}{R}\right) = \pi\frac{\int_0^{a/R} zF^2(z)dz}{a/R} \tag{17.16}$$

Plotting $k_{yy}^{\infty}\left(\frac{x}{R}\right)$ and $A_{\infty}\left(\frac{a}{R}\right)$ in Figure 17.3 allows one to check that these two functions are respectively decreasing and increasing as postulated in the previous section. Combining Eqns (17.14) and (17.16) allows for estimation of the crack increment at nucleation $\frac{a^*}{R}$ as a function of $\frac{L^c}{R}$ with the help of Eqn (17.10). The corresponding curve is plotted in Figure 17.4 and shows that a^* increases with L^c. Further, it is possible to evaluate the normalised tensile strength $\frac{\sigma^*}{\sigma^c}$ (given by Eqn (17.12)), which

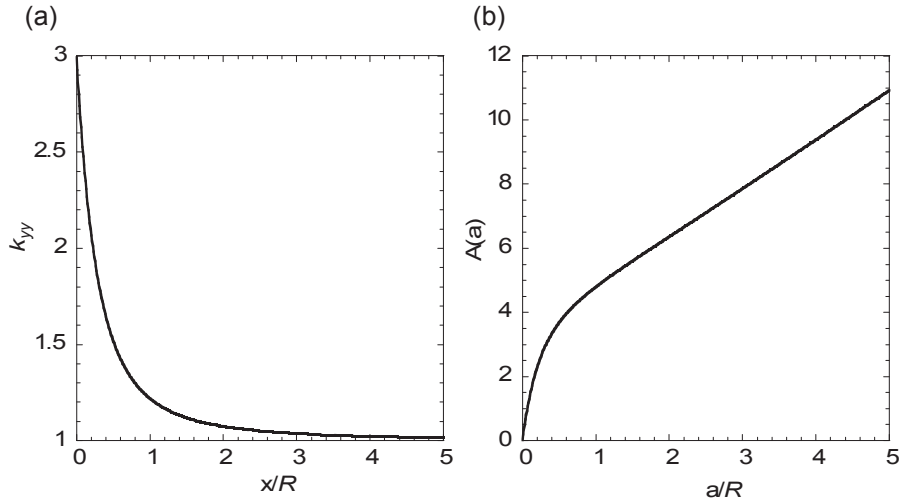

Figure 17.3 The dimensionless coefficients $k_{yy}(x)$ (a) and $A(a)$ (b) for an infinite isotropic open-holed plate.

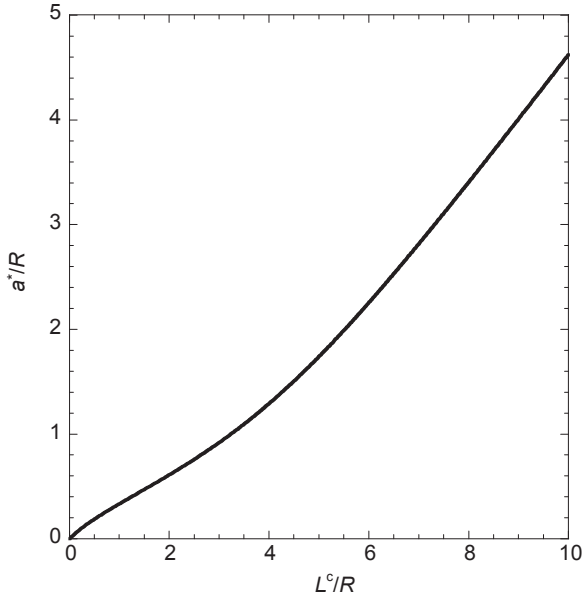

Figure 17.4 The predicted crack increment ratio $\frac{a^*}{R}$ versus the ratio $\frac{L^c}{R}$ for an infinite and isotropic open-holed plate.

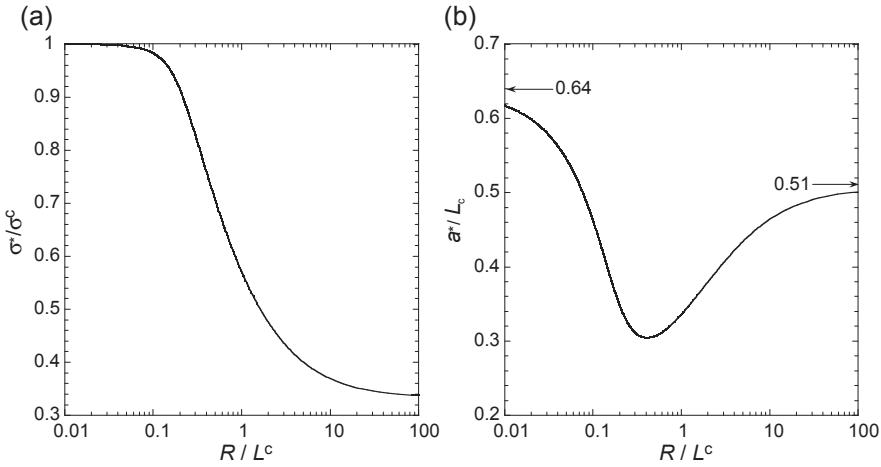

Figure 17.5 (a) Normalised tensile strength versus the ratio $\frac{R}{L^c}$, and (b) crack increment ratio $\frac{a^*}{L^c}$ versus the ratio $\frac{R}{L^c}$, for an isotropic and infinite open-holed plate.

is shown in Figure 17.5(a) as a function of the ratio $\frac{R}{L^c}$. This plot describes the 'hole size effect', whereby strength decreases with increased hole radius. The expected transition is observed between a small hole ($R \ll L^c$), for which $\frac{\sigma^*}{\sigma^c} \to 1$, and a large hole ($R \gg L^c$), for which $\frac{\sigma^*}{\sigma^c} \to \frac{1}{3}$. To emphasise the role of the characteristic length L^c, Figure 17.5(b) represents the ratio $\frac{a^*}{L^c}$ versus $\frac{R}{L^c}$. The influence of the hole can be neglected for a very small radius ($R \ll L^c$). The stress intensity factor is approximated by $K_I^\infty(a) = \sigma\sqrt{\pi a}$, which leads to $G_\infty^{inc}(a) = \frac{\pi}{2} a \frac{\sigma^2}{E}$. The energy condition $G^{inc}(a) = G^c$ with $\sigma^* = \sigma^c$ leads to $a^* = \frac{2}{\pi} L^c = 0.64L^c$. In the case of a large hole ($R \gg L^c$), the condition $a \ll R$ in relation (Eqn (17.15)) leads to $K_I^\infty(a) = 3\sigma 1.122\sqrt{\pi a}$, which gives $G_\infty^{inc}(a) = \frac{9\pi}{2}(1.122)^2 a \frac{\sigma^2}{E}$. The energy condition with $\sigma^* = \frac{\sigma^c}{3}$ provides $a^* = \frac{2}{\pi} \frac{1}{(1.122)^2} L^c = 0.51L^c$. The asymptotic values $0.64L^c$ and $0.51L^c$ are indicated in Figure 17.5(b), which makes clear that the crack length at initiation a^* is not a monotonic function of the hole radius: a^* may be a decreasing function of the hole radius (if $\frac{R}{L^c} < 0.4$), or conversely an increasing function (if $\frac{R}{L^c} > 0.4$), for a fixed value of L^c.

Figure 17.6 plots the evolution of $a^*(R)$ for various values of the fracture length (i.e. various values of a combination of the failure parameters and Young's modulus). This figure shows that the crack increment is proportional to L^c and depends on R. It is thus expected that the PSC (which assumes a constant value $a^*(R) = d_0$ whatever the hole radius) will not provide the same initiation stress, compared with that of the CC. This is confirmed by Figure 17.7, which compares the two criteria for various values of the characteristic distance d_0. A smaller value of d_0 seems to fit the small-hole response while a larger value of d_0 fits the large-hole data. It is interesting to note that Whitney and Nuismer (1974) obtained similar results when comparing data obtained from the PSC with experimental data. Fitting the curve $\frac{a^*}{L^c}$ versus $\frac{R}{L^c}$ allows the determination of

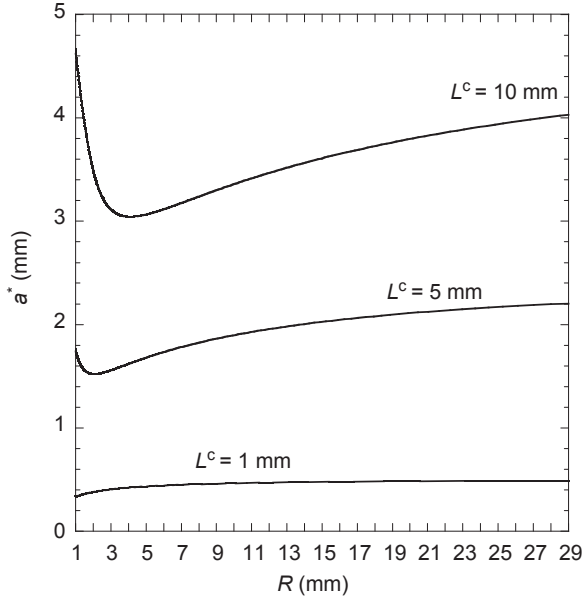

Figure 17.6 The crack increment a^* versus the hole radius R (varying between 1 and 31 mm) for various values of the characteristic length L^c for an infinite plate.

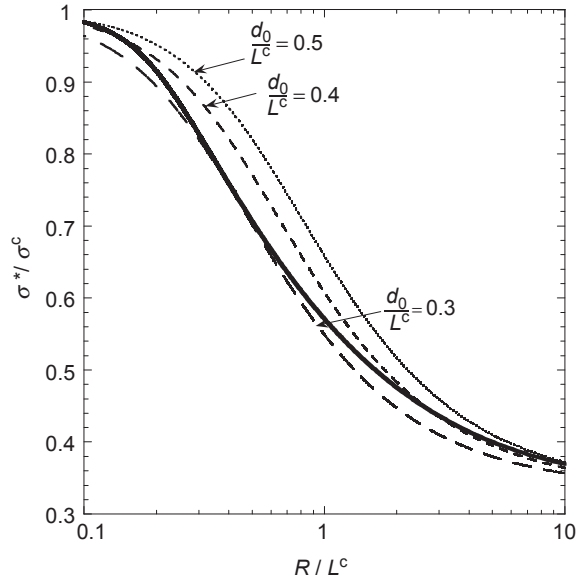

Figure 17.7 Normalised tensile strength versus the ratio $\frac{R}{L^c}$ for an isotropic and infinite open-holed plate, and comparison between the coupled criterion (CC — solid line) and the point-stress criterion (PSC — dotted lines) for various values of the ratio $\frac{d_0}{L^c}$.

$$a^* = \alpha_0 L^c \left(\frac{R}{L^c}\right)^{\beta_0} \text{ with } \alpha_0 = 0.34,\ \beta_0 = 0.15 \text{ for } 0.4 \leq \frac{R}{L^c} \leq 10 \qquad (17.17)$$

Using the PSC (Eqn (17.1)) with $d_0 = a^*$ and a^* provided by Eqn (17.17) allows one to minimise the deviation with the CC (within the interval $0.4 \leq \frac{R}{L^c} \leq 10$). Relation Eqn (17.17) thus establishes the influence of the hole radius on the characteristic distance d_0 for an infinite plate. Such a power law dependence between the characteristic distance and the hole radius has already been proposed to improve the PSC (Byron Pipes et al., 1979). Nevertheless, the exponent determined in the literature to fit experimental data is typically higher ($\approx 0.3-0.5$) than the value $\beta_0 = 0.15$ estimated with Eqn (17.17). It will be shown in the next section that taking into account the finite width of the specimen leads to a higher value of the exponent.

17.3.1 Influence of finite width

For an isotropic open-holed plate with a width $2W$, a finite-width correction factor must be introduced, and the stress distribution of the normal stress $\sigma_{yy}(x,0)$ now depends on $\frac{x}{R}$ and $\frac{R}{W}$ (Tan, 1988) with

$$\begin{aligned} k_{yy}^{w}\left(\frac{x}{R},\frac{R}{W}\right) &= \frac{2+\left(1-\frac{R}{W}\right)^3}{3\left(1-\frac{R}{W}\right)} k_{yy}^{\infty}\left(\frac{x}{R}\right) \\ &= \frac{1}{2}\frac{2+\left(1-\frac{R}{W}\right)^3}{3\left(1-\frac{R}{W}\right)}\left(2+\left(1+\frac{x}{R}\right)^{-2}+3\left(1+\frac{x}{R}\right)^{-4}\right) \end{aligned} \qquad (17.18)$$

The expression for the stress intensity factor of two symmetrical cracks emanating from a circular hole in a finite-width rectangular plate in tension is (Potti, Rao, & Srivastava, 2001)

$$K_I^w(a) = \sigma\sqrt{\pi a}\ \frac{1}{\sqrt{\cos\pi\frac{R}{W}}} H\left(\frac{a}{R},\frac{R}{W}\right) \text{ with}$$

$$\begin{aligned} H\left(\frac{a}{R},\frac{R}{W}\right) = \frac{1}{\sqrt{\cos\pi\frac{R}{W}\left(1+\frac{a}{R}\right)}}\Bigg(1+0.358\left(1+\frac{a}{R}\right)+1.425\left(1+\frac{a}{R}\right)^2 \\ -1.578\left(1+\frac{a}{R}\right)^3+2.156\left(1+\frac{a}{R}\right)^4\Bigg) \end{aligned} \qquad (17.19)$$

Assuming a plane stress state allows the estimation of the incremental energy release rate, which is given by

$$G_{\mathrm{w}}^{\mathrm{inc}}\left(\frac{a}{R},\frac{R}{W}\right) = A_{\mathrm{w}}\left(\frac{a}{R},\frac{R}{W}\right)\frac{R}{E_0}\sigma^2 \text{ with } A_{\mathrm{w}}\left(\frac{a}{R},\frac{R}{W}\right) = \frac{\pi}{\cos\left(\pi\frac{R}{W}\right)}\frac{\displaystyle\int_0^{a/R} zH^2\left(z,\frac{R}{W}\right)\mathrm{d}z}{a/R} \tag{17.20}$$

Relation (Eqn (17.18)) indicates that the finite width increases the stress concentration in the vicinity of the hole and Eqn (17.20) shows that $G_{\mathrm{w}}^{\mathrm{inc}}$ quickly increases as the crack length reaches the free edge of the plate. It can be shown that $G_{\mathrm{w}}^{\mathrm{inc}}$ grows like $\frac{1}{l\mathrm{Ln}^2 l}$ as $l \to 0$, where $l = W - R - a$ is the ligament width (Leguillon, 1990). The finite-width functions $k_{yy}^{\mathrm{w}}\left(\frac{x}{R},\frac{R}{W}\right)$ and $A_{\mathrm{w}}\left(\frac{a}{R},\frac{R}{W}\right)$ are now used to determine a^* by solving Eqn (17.10). As plotted in Figure 17.8, taking into account the finite-width reduces the crack increment (compared with the value obtained for an infinite plate) for higher values of $\frac{L^{\mathrm{c}}}{R}$. As a consequence of the stress concentration increase, the applied stress at crack onset is also smaller than the value obtained for the infinite plate (Figure 17.9(a)). The maximum value of a^* is $W - R$, which is predicted for high values of L^{c} such that $L^{\mathrm{c}} > 10W$. In this case, the asymptotic value of $\frac{a^*}{L^{\mathrm{c}}}$ is 0 (and no longer 0.64) for large

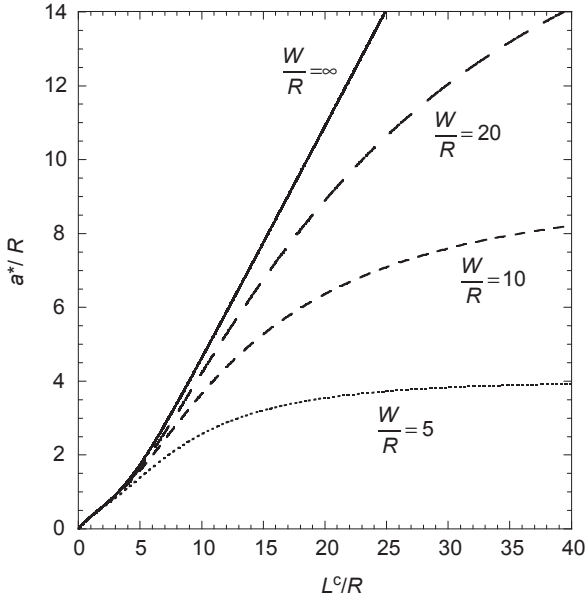

Figure 17.8 The predicted crack increment ratio $\frac{a^*}{R}$ versus the ratio $\frac{L^{\mathrm{c}}}{R}$ for an isotropic open-holed plate with various width ratios $\frac{W}{R}$. The infinite plate corresponds to $\frac{W}{R} = \infty$.

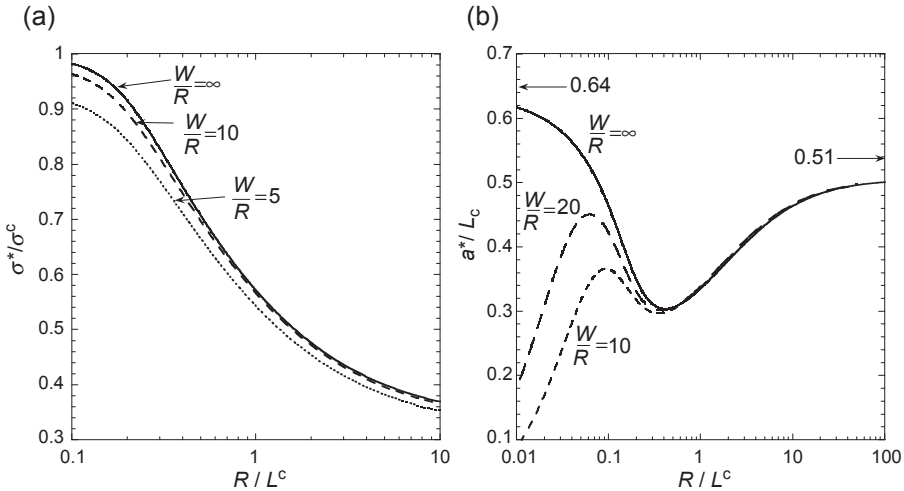

Figure 17.9 (a) The applied stress σ^* at crack onset normalised by the tensile strength σ^c versus the ratio $\frac{R}{L^c}$ for an isotropic open-holed plate with various width ratios $\frac{W}{R}$; and (b) the crack increment ratio $\frac{a^*}{L^c}$ versus the ratio $\frac{R}{L^c}$ for an isotropic open-holed plate with various width ratios $\frac{L^c}{R}$. The infinite plate corresponds to $\frac{W}{R} = \infty$.

values of L^c, as plotted in Figure 17.9(b). This figure also reveals that relation (Eqn (17.17)) is no longer valid for a finite-width plate. Fitting the curve $\frac{a^*}{L^c}$ versus $\left(\frac{R}{L^c}, \frac{R}{W}\right)$ provides

$$a^* = \alpha\left(\frac{R}{W}\right) L^c \left(\frac{R}{L^c}\right)^{\beta\left(\frac{R}{W}\right)} \tag{17.21}$$

$$\text{with } \alpha\left(\frac{R}{W}\right) = \alpha_0 - 0.217\left(\frac{R}{W}\right)^2, \quad \beta\left(\frac{R}{W}\right) = \beta_0 + 0.384\left(\frac{R}{W}\right)^2 \text{ for } 0.4 \leq \frac{R}{L^c} \leq 10$$

Comparing once more with the PSC, this relation defines the influence of the plate width on the characteristic distance d_0 (selected as $d_0 = a^*$), as already suggested by Srivastava and Kumar (2002).

Lastly, Figure 17.10 compares normalised hole strength for various values of the fracture length. Increases in L^c increase the strength. For a sufficiently high L^c, the material can approach the 'notch-insensitive' zone where normalised strength only depends on the geometry, with $\frac{\sigma^*}{\sigma^c} = 1 - \frac{R}{W}$. Conversely, a low L^c implies a 'notch-sensitive' material, as $\frac{\sigma^*}{\sigma^c}$ mainly depends on the stress concentration factor.

17.4 Orthotropic plate

For an infinite orthotropic plate containing a circular hole, a simplified expression of the stress distribution is given by (Konish & Whitney, 1975)

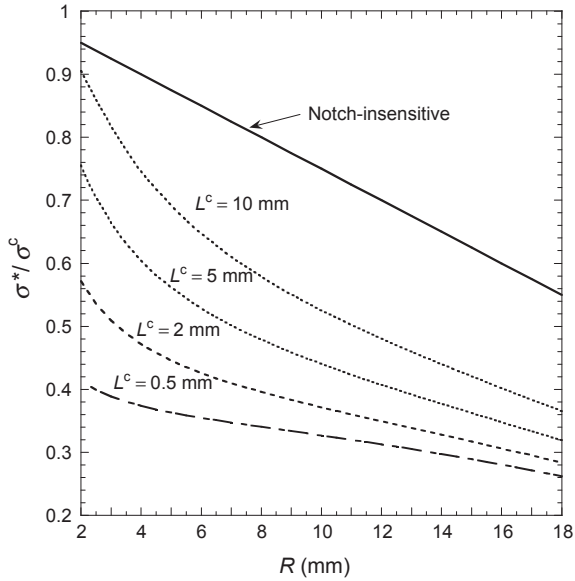

Figure 17.10 Normalised tensile strength versus the hole radius R for an isotropic and finite-width open-holed plate for various values of the characteristic length L^c. The half-width of the plate is $W = 40$ mm.

$$\widehat{k}_{yy}^{\infty}\left(\frac{x}{R}\right) = \frac{1}{2}\left(2 + \left(1+\frac{x}{R}\right)^{-2} + 3\left(1+\frac{x}{R}\right)^{-4} - (K_T - 3)\left(5\left(1+\frac{x}{R}\right)^{-6} - 7\left(1+\frac{x}{R}\right)^{-8}\right)\right) \tag{17.22}$$

with $K_T = 1 + \sqrt{2\left(\sqrt{\frac{E_y}{E_x}} - \nu_{yx}\right) + \frac{E_y}{G_{xy}}}$ and where (E_x, E_y, G_{xy}, ν_{yx}) are the effective engineering elastic constants of the orthotropic material, while K_T is the stress concentration factor, which reduces to $K_T = 3$ for the isotropic case. There is no closed-form solution for the stress intensity factor of cracks emanating from a hole in an anisotropic plate. A finite element analysis is thus used to evaluate the normalised incremental energy release rate $\widehat{A}_{\infty}\left(\frac{a}{R}\right)$. The details of the numerical analysis are provided elsewhere (Martin, Leguillon, & Carrère, 2012). A large value of the ratio $\frac{W}{R}$ is used to simulate an infinite plate. Following the results of Bao, Ho, Suo, and Fan (1992), it was verified numerically that only two parameters (λ,ρ) can be used to determine the influence of in-plane orthotropy on $\widehat{A}_{\infty}\left(\frac{a}{R}\right)$ with

$$\lambda = \frac{E_x}{E_y}, \rho = \frac{\sqrt{E_x E_y}}{2G_{xy}} - \sqrt{\nu_{xy}\nu_{yx}} \tag{17.23}$$

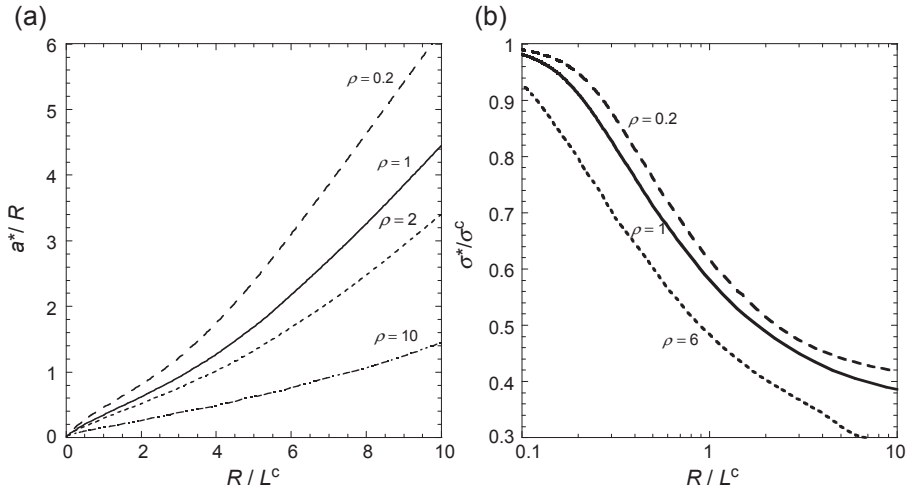

Figure 17.11 (a) Predicted crack increment ratio $\frac{a^*}{R}$ versus the ratio $\frac{L^c}{R}$, and (b) normalised tensile strength versus the ratio $\frac{R}{L^c}$, for an infinite open-holed plate and a quasi-isotropic material ($\lambda = 1$).

An isotropic material coincides with $\lambda = \rho = 1$ and a quasi-isotropic one is specified with $\lambda = 1$. Compared with numerical results, it is found that Eqn (17.22) is not accurate for highly anisotropic materials (i.e. if the values of λ and ρ are very different from unity). In this case, the expression proposed by Russo and Zuccarello (2007) must be preferred. Finite element values of $\widehat{k}_{yy}^{\infty}\left(\frac{x}{R}\right)$ and $\widehat{A}_{\infty}\left(\frac{a}{R}\right)$ are used to solve Eqn (17.10). In this case, it should be noted that the selected value of E is $E = E_y$. Figure 17.11 illustrates the influence of the parameter ρ for a quasi-isotropic material with $\lambda = 1$. For a given ratio $\frac{L^c}{R}$, the crack increment ratio $\frac{a^*}{R}$ at nucleation decreases with an increasing value of ρ (Figure 17.1(a)). The normalised strength thus decreases with an increasing value of ρ (Figure 17.11(b)), following relation (Eqn (17.12)). The same finite element procedure is utilised to evaluate the functions $\widehat{k}_{yy}^{W}\left(\frac{x}{R}, \frac{R}{W}\right)$ and $\widehat{A}_{W}\left(\frac{a}{R}, \frac{R}{W}\right)$, which are necessary to apply the CC for a finite-width orthotropic plate. Figure 17.12 represents the normalised tensile strength versus the hole radius for a finite-width quasi-isotropic plate with $W = 20$ mm. This confirms that increases in ρ reduce the strength.

17.5 Comparison with experimental data

Predictions of the CC are now compared with the experimental data provided by Kim et al. (1995) for woven glass−epoxy specimens. The elastic properties of these composites ($E_x = E_y = 23.6$ GPa, $G_{xy} = 4$ GPa, $\nu_{yx} = 0.11$) correspond to quasi-isotropic materials with $\lambda = 1$ and $\rho = 2.84$. Tensile tests were performed for eight values of radius R_k (between 0.6 and 10 mm) with $W = 20$ mm to determine the strength $\sigma^*_{\text{exp}}(R_k)$ of the open-hole specimens. The experimental scattering is not indicated by the authors, who only provide the average values obtained for three specimens. The unnotched strength is $\sigma^c = 275.3$ MPa. The fracture toughness of the

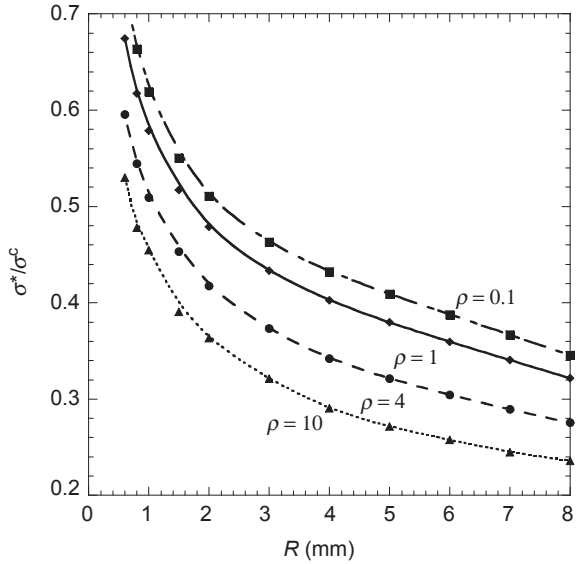

Figure 17.12 Normalised tensile strength versus the hole radius R for a quasi-isotropic open-holed plate for various values of the parameter ρ. The characteristic fracture length is $L^c = 1$ mm and the half width is $W = 20$ mm.

specimens is not known, so an inverse method is used for its identification. More precisely, the fracture energy G^c is estimated by minimising the relative deviation s between the model and experimental results with $s = \sqrt{\frac{1}{8}\sum_{k=1}^{k=8}\left(\frac{\sigma^*_{exp}(R_k)-\sigma^*(R_k)}{\sigma^*_{exp}(R_k)}\right)^2}$. The corresponding data are plotted in Figure 17.13. This plot demonstrates reasonable agreement between predicted and experimental values with $s \leq 6.5\%$. Figure 17.14(a) plots the crack increment length a^* versus the hole radius R as estimated by the CC. It is observed that the CC leads to a nonmonotonic variation of a^*, as shown in a previous section. The length $d_0 = 0.237L^c$, which is selected in order to obtain the best match between PSC predictions and the experimental values, is also plotted and corresponds to an average of $a^*(R)$. The lengths for d_0 that exactly fit the experimental data (using relation (Eqn (17.12)) for each $\frac{R_k}{W}$ are also plotted. Compared with the PSC, it reveals that the CC improves the estimation of d_0 for $\frac{R}{W} \approx 0.1$ but fails for smaller values. Figure 17.14(b) makes clear that a better agreement with experimental data is obtained with a smaller G^c for small holes and a higher G^c for large holes. This must be linked to the observation that notch sensitivity is related to the damage development prior to fracture in the vicinity of the hole (Green et al., 2007; Wisnom et al., 2010). This damage development is ignored by the CC, but experimental results have shown that subcritical damage mechanisms may change with the increase of the hole radius and induce a toughness variation as suggested by Figure 17.14(b).

A second set of experimental data is now analysed using the results provided by Camanho et al. (2007). The specimens are manufactured with IM7-8552 UD plies.

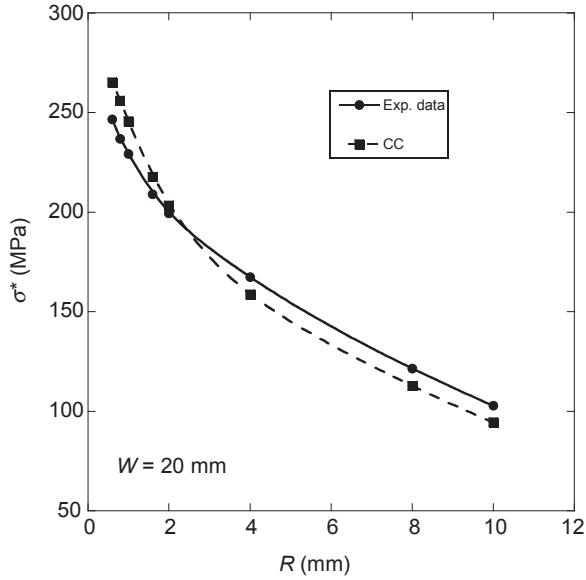

Figure 17.13 Comparison of predicted tensile strengths with the experimental values of Kim et al. (1995) for glass−epoxy specimens.

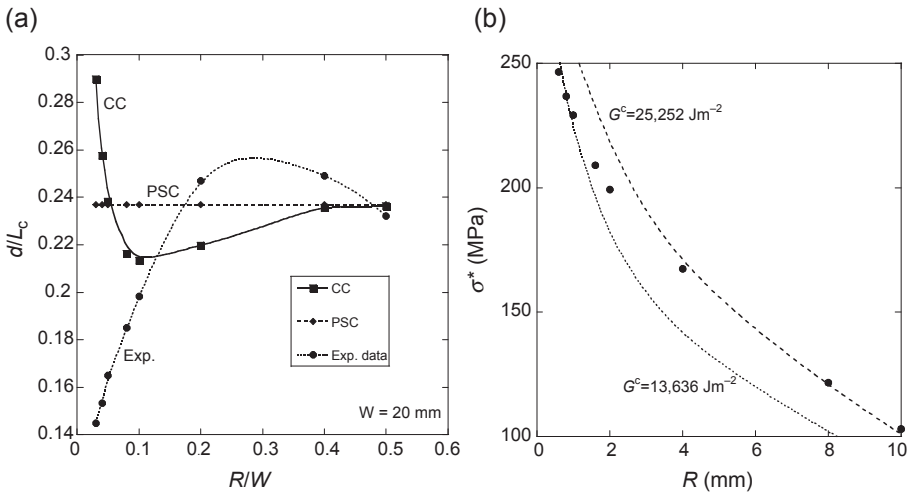

Figure 17.14 (a) Crack increments versus the ratio $\frac{R}{W}$ predicted at fracture onset, for glass−epoxy specimens (Kim et al., 1995). Circles indicate the d^0/L^c values that exactly fit the experimental data using Eqn (17.1), squares represent the a^*/L^c values predicted by the coupled criterion (CC) and diamonds indicate the fixed length $d^0 = 0.237L^c$ selected for the point-stress criterion (PSC); and (b) comparison of predicted tensile strengths with the experimental values for glass−epoxy specimens (Kim et al., 1995). Two different values of the fracture toughness are used to fit the data for small and large holes.

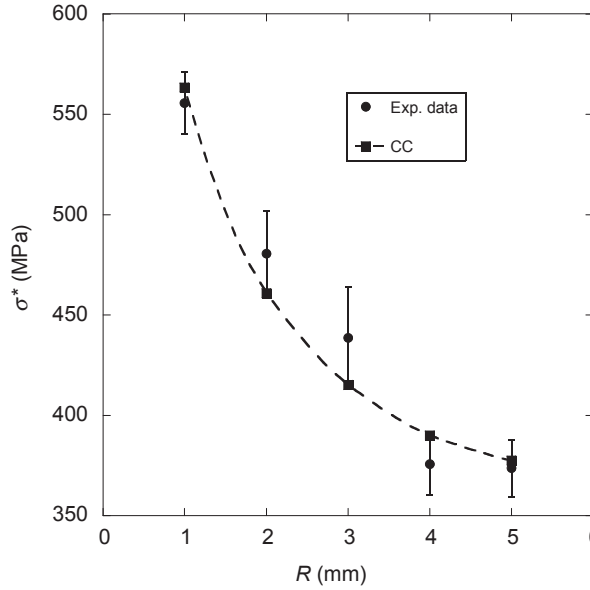

Figure 17.15 Comparison between experimental failure load (Camanho et al., 2007) and numerical prediction as a function of the hole radius.

The stacking sequence is $[90/0/\pm 45]_{3s}$. Different hole radii are investigated ($R_k = 1,2,4,5$ mm) with a constant ratio $\frac{R_k}{W_k} = \frac{1}{12}$. The strength of the unnotched specimen is 845.1 MPa. The toughness of the quasi-isotropic laminate is estimated using the approach proposed by Camanho and Catalanotti (2011), which links the toughness of a multidirectional laminate to the fracture of the 0° ply. This analytical model leads to $G^c = 20\ \text{kJm}^{-2}$. The comparison between the notched strength of the laminate and the prediction of the CC is plotted in Figure 17.15 and shows a good agreement. It is worth mentioning that no test on open-hole specimens has been used to identify the model.

17.6 Conclusions

The present work uses a coupled strength and energy criterion to analyse the fracture onset in the vicinity of a hole within a tensile loaded composite plate. The various configurations of infinite- and finite-width, isotropic and orthotropic plates are investigated with the help of analytical and numerical models. It is shown that this approach (1) describes the hole size effect, whereby the strength decreases when the hole radius is increased, (2) can be considered an improvement of the PSC, for the characteristic distance is now related to fracture characteristics (strength and toughness) and geometry (hole radius and plate width). It is clear that the damage occurring prior to fracture is ignored in the present model. This damage, which may take the form of delamination and axial splitting, modifies the stress concentration and delays the

onset the failure. However, a comparison of model predictions and experimental data is performed for a quasi-isotropic composite plate, and demonstrates an acceptable agreement.

Further work should be directed towards the analysis of filled holes in anisotropic plates submitted to in-plane multiaxial loading. Analytical solutions for the stress distribution around holes (Soutis & Filiou, 1998) or inclusions (Berbinau, Filiou, & Soutis, 2001) in plates submitted to biaxial loading can be used. Experimental data concerning the notched compressive strength of open-hole laminates are also available (Lee & Soutis, 2008). Using a finite element approach coupled with an optimisation procedure (Hebel, Dieringer, & Becker, 2010) is a promising approach.

References

Awerbuck, J., & Madhukar, M. S. (1985). Notched strength of composite laminates: predictions and experiments-a review. *Journal of Reinforced Plastics and Composites, 4*, 3−159.

Bao, G., Ho, S., Suo, Z., & Fan, B. (1992). The role of material orthotropy in fracture specimens for composites. *International Journal of Solids and Structures, 29*, 1105−1116.

Berbinau, P., Filiou, C., & Soutis, C. (2001). Stress and failure analysis of composite laminates with an inclusion under multiaxial compression-tension loading. *Applied Composite Materials, 8*, 307−326.

Byron Pipes, R., Gillespie, J. W., & Wetherhold, R. C. (1979). Superposition of the notched strength of composite laminates. *Polymer Engineering and Science, 19*, 1151−1155.

Camanho, P. P., & Catalanotti, G. (2011). On the relation between the mode I fracture toughness of a composite laminate and that of a the 0° ply: analytical model and experimental validation. *Engineering Fracture Mechanics, 78*, 2535−2546.

Camanho, P. P., Erçin, G. H., Catalanotti, G., Mahdi, S., & Linde, P. (2012). A finite fracture mechanics model for the prediction of the open-hole strength of composite laminates. *Composites Part A: Applied Science and Manufacturing, 43*(8), 1219−1225. http://dx.doi.org/10.1016/j.compositesa.2012.03.004.

Camanho, P. P., Maimí, P., & Dávila, C. G. (2007). Prediction of size effects in notched laminates using continuum damage mechanics. *Composites Science and Technology, 67*(13), 2715−2727. http://dx.doi.org/10.1016/j.compscitech.2007.02.005.

Carlsson, L. A., Aronsson, C. G., & Backlund, J. (1989). Notch sensitivity of thermoset and thermoplastic laminates loaded in tension. *Journal of Materials Science, 24*, 1670−1682.

Green, B. G., Wisnom, M. R., & Hallett, S. R. (2007). An experimental investigation into the tensile strength scaling of notched composites. *Composites Part A: Applied Science and Manufacturing, 38*(3), 867−878. http://dx.doi.org/10.1016/j.compositesa.2006.07.008.

Hebel, J., Dieringer, R., & Becker, W. (2010). Modelling brittle crack formation at geometrical and material discontinuities using a finite fracture mechanics approach. *Engineering Fracture Mechanics, 77*, 3558−3572. http://dx.doi.org/10.1016/j.engfracmech.2010.07.005.

Hell, S., Weißgraeber, P., Felger, J., & Becker, W. (2014). A coupled stress and energy criterion for the assessment of crack initiation in single lap joints: a numerical approach. *Engineering Fracture Mechanics, 117*, 112−126.

Kim, J. K., Kim, D. S., & Takeda, N. (1995). Notched strength and fracture criterion in fabric composite plates containing a circular hole. *Journal of Composite Materials, 29*, 982−998.

Konish, H. J., & Whitney, J. M. (1975). Approximate stresses in an orthotropic plate containing a circular hole. *Journal of Composite Materials, 9*, 157−166.

Laurin, F., Carrère, N., & Maire, J. F. (2007). A multiscale progressive failure approach for composite laminates based on thermodynamical viscoelastic and damage models. *Composites: Part A, 38*, 198−209.

Lee, J., & Soutis, C. (September 2008). Measuring the notched compressive strength of composite laminates: specimen size effects. *Composites Science and Technology, 68*(12), 2359−2366.

Leguillon, D. (1990). Comportement asymptotique du taux de restitution de l'énergie en fin de fracture. *Paris*. t310, série II, pp. 155−160. Comptes rendus de l'Académie des sciences.

Leguillon, D. (2002). Strength or toughness? a criterion for crack onset at a notch. *European Journal of Mechanics A/Solids, 21*, 61−72.

Leguillon, D., & Martin, E. (2012). The strengthening effect caused by an elastic contrast—part I: the bimaterial case. *International Journal of Fracture, 179*(1−2), 157−167. http://dx.doi.org/10.1007/s10704-012-9787-y.

Leguillon, D., Quesada, D., Putot, C., & Martin, E. (2007). Prediction of crack initiation at blunt notches and cavities−size effects. *Engineering Fracture Mechanics, 74*(15), 2420−2436. http://dx.doi.org/10.1016/j.engfracmech.2006.11.008.

Mantič, V., & García, I. G. (2012). Crack onset and growth at the fibre-matrix interface under a remote biaxial transverse load. Application of a coupled stress and energy criterion. *International Journal of Solids and Structures, 49*, 2273−2290.

Martin, E., & Leguillon, D. (2004). Energetic conditions for interfacial failure in the vicinity of a matrix crack in brittle matrix composites. *International Journal of Solids and Structures, 41*(24−25), 6937−6948. http://dx.doi.org/10.1016/j.ijsolstr.2004.05.044.

Martin, E., Leguillon, D., & Carrère, N. (2010). A twofold strength and toughness criterion for the onset of free-edge shear delamination in angle-ply laminates. *International Journal of Solids and Structures, 47*(9), 1297−1305. http://dx.doi.org/10.1016/j.ijsolstr.2010.01.018.

Martin, E., Leguillon, D., & Carrère, N. (2012). A coupled strength and toughness criterion for the prediction of the open hole tensile strength of a composite plate. *International Journal of Solids and Structures, 49*(26), 3915−3922. http://dx.doi.org/10.1016/j.ijsolstr.2012.08.020.

Martin, E., Poitou, B., Leguillon, D., & Gatt, J. M. (2008). Competition between deflection and penetration at an interface in the vicinity of a main crack. *International Journal of Fracture, 151*(2), 247−268. http://dx.doi.org/10.1007/s10704-008-9228-0.

Moradi, A., Carrère, N., Leguillon, D., Martin, E., & Cognard, J.-Y. (2013). Strength prediction of bonded assemblies using a coupled criterion under elastic assumptions: effect of material and geometrical parameters. *International Journal of Adhesion and Adhesives, 47*, 73−82. http://dx.doi.org/10.1016/j.ijadhadh.2013.09.044.

Needleman, A. (1987). A continuum model for void nucleation by inclusion debonding. *Journal of Applied Mechanics, 54*(3), 525−531.

Potti, P. K. G., Rao, B. N., & Srivastava, V. K. (2001). Tensile fracture strength of boron/aluminum laminates with holes and slits. *Materials Science and Engineering: A, 301*, 244−252.

Russo, A., & Zuccarello, B. (2007). An accurate method to predict the stress concentration in composite laminates with a circular hole under tensile loading. *Mechanics of Composite Materials, 43*, 359−376.

Soutis, C., & Filiou, C. (1998). Stress distributions around holes in composite laminates subjected to biaxial loading. *Applied Composite Materials, 5*(6), 365−378.

Soutis, C., & Fleck, N. A. (1990). Static compression failure of carbon fibre T800/924C composite plate with single hole. *Journal of Composite Materials, 24*(5), 536−558.

Srivastava, V. K., & Kumar, D. (2002). Prediction of notched strength of laminated fibre composites under tensile loading conditions. *Journal of Composite Materials, 36*, 1121−1133.

Tada, H., Paris, P., & Irwin, G. (1985). *The stress analysis of cracks handbook*. St Louis, MO: Paris Production Incorporated.

Tan, S. C. (1988). Finite-width correction factors for anisotropic plate containing a central opening. *Journal of Composite Materials, 22*, 1080−1097.

Taylor, D. (2008). The theory of critical distances. *Engineering Fracture Mechanics, 75*(7), 1696−1705.

Timoshenko, S. P., & Goodier, J. N. (1970). *Theory of elasticity*. New York: Mc Graw-Hill.

Van der Meer, F. P., Oliver, C., & Sluys, L. J. (2010). Computational analysis of progressive failure in a notched laminate including shear nonlinearity and fiber failure. *Composites Science and Technology, 70*, 692−700.

Waddoups, M. E., Eisenmann, J. R., & Kaminski, B. E. (1971). Macroscopic fracture mechanics of advanced composite materials. *Journal of Composite Materials, 5*, 446−454.

Whitney, J. M., & Nuismer, R. J. (1974). Stress fracture criteria for laminated composites containing stress concentrations. *Journal of Composite Materials, 8*(3), 253−265. http://dx.doi.org/10.1177/002199837400800303.

Wisnom, M. R., Hallett, S. R., & Soutis, C. (2010). Scaling effects in notched composites. *Journal of Composite Materials, 44*(2), 195−210.

Compressive fracture of layered composites caused by internal instability

18

I.A. Guz[1], M. Menshykova[1], C. Soutis[2]
[1]University of Aberdeen, Aberdeen, UK; [2]University of Manchester, Manchester, UK

18.1 Introduction

18.1.1 Background

Compressive strength is often a design-limiting factor for advanced layered materials: it is generally 30−40% lower than the tensile strength in these materials (Budiansky & Fleck, 1994; Niu & Talreja, 2000; Schultheisz & Waas, 1996; Soutis & Turkmen, 1995). A better understanding of compressive strength and failure mechanisms is therefore fundamental to the development of improved materials.

The work of Dow and Grunfest (1960) was the first to consider the microbuckling of fibres as a form of fracture of a unidirectional composite under compression. Since then, the beginning of fracture process under compression is usually associated with the buckling of the microstructure of the material, in which the critical load is determined by parameters characterising the microstructure of the composite rather than by the dimensions and shape of the specimen or structural member, that is with the internal instability phenomena according to Biot (1965). In this chapter, we adopt the same assumption of linking the onset of fracture to the loss of stability in the internal structure of the material. The task of deriving three-dimensional (3-D) analytical solutions to describe the response of layered materials was always considered as one of great importance (Kouri & Atluri, 1993). Analytical solutions, if obtained, enable us to analyse the behaviour of a structure on the wide range of material properties and loading schemes, without the restrictions imposed by simplified approximate methods.

This chapter revisits the exact 3-D approach to study internal instability in layered media, which is based on the model of a piecewise-homogeneous medium, in which the behaviour of each component of the material is described by the 3-D equations of solid mechanics. The results of this approach can be used as a benchmark for simplified models.

18.1.2 Modelling compressive response of layered materials

Probably the first solutions to the problem of internal instability for a layered material obtained within this approach were reported in works of Guz (1969) and Babich and Guz (1969, 1972), where the problem for linear-elastic layers under uniaxial compression was solved. This solution was included in numerous books and the

Structural Integrity and Durability of Advanced Composites. http://dx.doi.org/10.1016/B978-0-08-100137-0.00018-3

comprehensive review on the topic (Guz, 1992). Later the exact solutions were also derived for more complex problems such as for orthotropic, non-linear-elastic and elastic−plastic types of compressible and incompressible layers, including the case of large (finite) deformations − for example, see Guz (1989a,b, 1998) and Guz and Soutis (2001a) as well as the reviews of Guz (1992) and Guz and Soutis (2001b).

The importance and the complexity of the considered phenomena caused a large number of publications to put forward various approximate methods aimed at tackling the problems with different levels of accuracy: the early papers (Guz, 2005; Guz & Herrmann, 2003; Menshykova, Guz, & Menshykov, 2009) and the numerous subsequent publications reviewed in Budiansky and Fleck (1994), Soutis and Turkmen (1995), Schultheisz and Waas (1996) and Niu and Talreja (2000). It was concluded after detailed analyses (Guz, 1992; Niu & Talreja, 2000; Soutis & Turkmen, 1995) that the approximate methods are not very accurate when compared with experimental measurements and observations.

For instance, one of the earlier models suggested in Guz and Herrmann (2003) involves considerable simplification, such as modelling the reinforcement layers by the thin-beam theory and modelling the matrix as an elastic material using one-dimensional stress analysis, making the results of this method inaccurate even for simple cases. It was shown in Guz (1992), Rosen (1965) and Schuerch (1966) that the approximate model can give results with significant discrepancies in comparison with both the exact approach and experimental data, even for the simplest case of a composite with linear-elastic compressible layers undergoing small precritical deformations and considered within the scope of geometrically linear theory. For small fibre volume fractions, the approximate approach gives physically unrealistic critical strains. It does not describe the phenomenon under consideration even on the qualitative level, since it predicts a different mode of stability loss from that obtained by the 3-D exact analysis. For more complex models, which take into account large deformations and geometric and physical nonlinearity (e.g. those considered in this chapter), the approximate theories are definitely inapplicable, and one could expect even greater variation between the exact and approximate approaches. The exact approach utilised throughout this chapter allows us to take into account large deformations, geometric and physical nonlinearities, and load biaxiality that the simplified methods cannot consider.

Another approach commonly used is based on the investigation of fibre kinking. From the early literature on compressive fracture, it was easy to get the impression that fibre instability (microbuckling) and kinking are competing mechanisms. However, it is now accepted that a kink band is an outcome of the microbuckling failure of actual fibres, as observed experimentally (Guz & Soutis, 2000; Sadovsky, Pu, & Hussain, 1967). Fibre microbuckling occurs first, followed by propagation of this local damage to form a kink band. A comprehensive comparative analysis of the Rosen, Argon−Budiansky (kinking) and Batdorf−Ko models was presented by Soutis and Turkmen (1995). Studies of the kinking phenomenon were also reviewed by Budiansky and Fleck (1994). Soutis and Turkmen (1995) showed that the existing kinking analyses could account for some but not all experimental observations. They correctly predicted that shear strength and fibre imperfections are important

parameters affecting the compressive strength of the composite. However, within this model it is not possible to say exactly how strength varies with fibre content; as well, the value of misalignment is chosen arbitrarily. This model requires knowledge of shear strength properties, the initial fibre misalignment and most importantly the kink band orientation angle, which is a postfailure geometric parameter. The analysis of this approach is outside the scope of the present chapter.

This chapter is concerned with the development of a unified computational procedure for numerical realisation of the 3-D analytical method as applied to various constitutive equations of the layers, different loading schemes (uniaxial or biaxial loading) and different precritical conditions (large or small precritical deformations). It contains many examples of calculation of critical stresses/strains for particular composites as well as analyses of different buckling modes. Some comparisons with available experimental data were discussed earlier (Guynn, Bradley, & Ochoain, 1992; Guz, 1992; Soutis & Guz, 2001).

18.2 A unified computational approach to instability of periodic laminated materials

18.2.1 Formulation of the problem

Let us briefly consider the statement of the problem of internal instability (microbuckling) for layered materials. The detailed formulations for particular types of layers were given, for example, in the works of Guz (1998), Guz and Soutis (2001a,b) and Rosen (1965).

The material consists of alternating layers with thicknesses $2h_r$ and $2h_m$ as shown in Figure 18.1. Two different loading schemes are studied − uniaxial compression and biaxial compression in the plane of the layers. The solution of the problem is sought for four modes of stability loss; for example, see Guz (1998). Using the equations of the 3-D stability theory (Moran, Liu, & Shih, 1995), the following eigenvalue problem must be solved, in which the stability equations for each layer are (Moran et al., 1995)

$$\frac{\partial}{\partial x_i} t_{ij}^r = 0, \quad \frac{\partial}{\partial x_i} t_{ij}^m = 0; \quad i, j = 1, 2, 3 \tag{18.1}$$

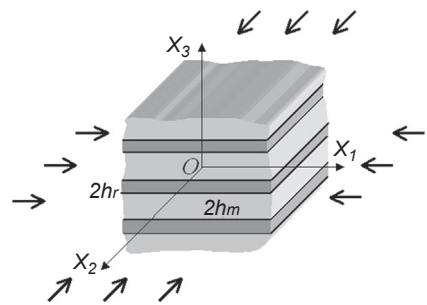

Figure 18.1 Cartesian co-ordinate system and loads for a layered composite system.

where t_{ij} is the nonsymmetrical Piola−Kirchhoff stress tensor (nominal stress tensor).

Tensor t_{ij} has the following form for incompressible solids (Moran et al., 1995):

$$t_{ij} = \kappa_{ij\alpha\beta}\frac{\partial u_\alpha}{\partial x_\beta} + \delta_{ij}\lambda_j^{-1}p \tag{18.2}$$

where

$$\lambda_1\lambda_2\lambda_3 = 1 \tag{18.3}$$

is the incompressibility condition and λ_j is the elongation/shortening factor in the direction of the OX_j axis.

For compressible solids, the form is (Moran et al., 1995)

$$t_{ij} = \omega_{ij\alpha\beta}\frac{\partial u_\alpha}{\partial x_\beta} \tag{18.4}$$

The components of the tensors $\kappa_{ij\alpha\beta}$ and $\omega_{ij\alpha\beta}$ depend on the properties of the layers and the loads. The most general expressions for $\kappa_{ij\alpha\beta}$ and $\omega_{ij\alpha\beta}$ can be found in Moran et al. (1995):

$$\kappa_{ij\alpha\beta} = \lambda_j\lambda_\alpha\left[\delta_{ij}\delta_{\alpha\beta}A_{\beta i} + \left(1-\delta_{ij}\right)\left(\delta_{i\alpha}\delta_{j\beta}\mu_{ij} + \delta_{i\beta}\delta_{j\alpha}\mu_{ji}\right)\right] + \delta_{i\beta}\delta_{j\alpha}S^0_{\beta\beta} \tag{18.5}$$

$$\omega_{ij\alpha\beta} = \lambda_j\lambda_\alpha\left[\delta_{ij}\delta_{\alpha\beta}A'_{\beta i} + \left(1-\delta_{ij}\right)\left(\delta_{i\alpha}\delta_{j\beta}\mu'_{ij} + \delta_{i\beta}\delta_{j\alpha}\mu'_{ji}\right)\right] + \delta_{i\beta}\delta_{j\alpha}S^0_{\beta\beta} \tag{18.6}$$

where $A_{ij}(A'_{ij})$ and $\mu_{ij}(\mu'_{ij})$ are the quantities that characterise the axial and shear stiffnesses. The quantity characterising the precritical state (either the stress component S^0_{11} or the strain component ε^0_{11}) is the parameter for which the eigenvalue problem should be solved.

To complete the problem statement, the boundary conditions should be defined for each interface. The layer interfaces could consist of zones of perfectly connected (bonded) layers and defects such as cracks or delaminations. In this study we consider composites with perfectly bonded layers or 'perfectly lubricated' (sliding without friction) interfaces. For the perfectly bonded layers we have the continuity conditions for the stresses and displacements

$$t^r_{3i} = t^m_{3i}, u^r_i = u^m_i, \quad i = \overline{1,3} \tag{18.7}$$

and for 'the perfectly lubricated layers' (see Berbinau, Soutis, and Guz (1999) and Winiarski and Guz (2008)), only the continuity of the normal components is retained at the surface, with boundary conditions for perturbations of stresses and displacements in the form of

$$t^r_{31} = t^m_{31} = t^r_{32} = t^m_{32} = 0, t^r_{33} = t^m_{33}, u^r_3 = u^m_3 \tag{18.8}$$

Note that in practical cases, the assumption of perfect bonding between neighbouring layers in composites does not correspond to reality due to the various imperfections of interfacial adhesion. Unfortunately when considering a composite with such defects, it is sometimes difficult to identify the set of defects and its influence on the stability of the composite material. Hence, we suggest the following estimation: the critical strain ε_{cr} for a real composite with weakened interfacial adhesion must be larger than the critical strain ε_{cr}^{pl} for the same structure with perfectly lubricated layers, but smaller than the critical strain ε_{cr}^{pb} for the structure with perfectly bonded layers. Thus, we obtain the following bounds for the critical strain:

$$\varepsilon_{cr}^{pl} \leq \varepsilon_{cr} \leq \varepsilon_{cr}^{pb} \tag{18.9}$$

18.2.2 Analytical solution

Solutions of Eqn (18.1) (i.e. perturbations of stresses and displacements) for each of the layers can be expressed through the functions X and Ψ, which are the solutions of the following equations (Moran et al., 1995):

$$\left(\Delta_1 + \xi_1^2 \frac{\partial^2}{\partial x_3^2}\right)\Psi = 0 \tag{18.10}$$

$$\left(\Delta_1 + \xi_2^2 \frac{\partial^2}{\partial x_3^2}\right)\left(\Delta_1 + \xi_3^2 \frac{\partial^2}{\partial x_3^2}\right)X = 0 \tag{18.11}$$

where

$$\Delta_1 = \frac{\partial^2}{\partial x_1^2} + \frac{\partial^2}{\partial x_2^2} \tag{18.12}$$

The parameter ξ_j depends on the components of the tensor $\kappa_{ij\alpha\beta}$ (or $\omega_{ij\alpha\beta}$) and therefore on the properties of the layers and on the loads. It was proved in Guz (1999) and Aboudi (1987) that for elastic compressible and elastic incompressible layers

$$\xi_j^2 > 0, \quad \operatorname{Im}\xi_j^2 = 0 \tag{18.13}$$

and for elastic−plastic incompressible layers

$$\operatorname{Im}\xi_{2,3}^2 \neq 0, \quad \xi_3^2 = \overline{\xi_2^2} \tag{18.14}$$

The characteristic determinants associated with the four modes of stability loss were derived earlier in Guz (1992, 1999), Aboudi (1987) and Librescu and Schmidt (2001) for various constitutive equations of the layers, different loading schemes (uniaxial or biaxial loading) and different precritical conditions (large or small precritical deformations). Similarly, the characteristic equations can be derived for other modes of

stability loss. However, the modes with the larger periods in transverse direction are usually not of practical interest. In this chapter, the characteristic determinants are presented in the unified form in order to facilitate a uniform computational procedure for solving them:

- for perfectly bonded layers

$$\det \begin{Vmatrix} \beta_{11} & \beta_{12} & \beta_{13} & \beta_{14} \\ \beta_{21} & \beta_{22} & \beta_{23} & \beta_{24} \\ \beta_{31} & \beta_{32} & \beta_{33} & \beta_{34} \\ \beta_{41} & \beta_{42} & \beta_{43} & \beta_{44} \end{Vmatrix} = 0 \tag{18.15}$$

- for perfectly lubricated layers

$$\det \begin{Vmatrix} \beta_{11} & \beta_{12} & 0 & 0 \\ \beta_{21} & \beta_{22} & \beta_{23} & \beta_{24} \\ 0 & 0 & \beta_{13} & \beta_{14} \\ \beta_{41} & \beta_{42} & \beta_{43} & \beta_{44} \end{Vmatrix} = 0 \tag{18.16}$$

The expressions for β_{ij} of the determinant for different types of materials and for different loading schemes are given in Guz (1989a,b, 1992, 1998), Rosen (1965), Schuerch (1966) and Soutis and Guz (2006).

18.2.3 Computational procedure

To facilitate the analyses of characteristic determinants, a software package with a graphical user-friendly interface was developed using MATLAB 7.6.0. The software contains a database of material properties for typical layered composites and a library of components of the tensors $\kappa_{ij\alpha\beta}$ and $\omega_{ij\alpha\beta}$ of Eqns (18.5) and (18.6). The fully automated numerical procedure consists of the following steps. First, the characteristic determinants, Eqns (18.15) and (18.16), are computed depending on the user's choice of loading schemes (uniaxial or biaxial loading), initial conditions (large or small precritical deformations) and interfacial properties (perfectly bonded or perfectly lubricated layers). Then the results are analysed, and the critical controlled parameters of the internal instability (including the critical wavelength) are searched for. This analysis is conducted for all four considered modes of stability loss. At the final stage the modes are compared and the critical mode is found.

Some of the results for the cases of perfectly bonded and perfectly lubricated layers are presented in the following subsections of this chapter.

18.2.4 Computing critical loads

18.2.4.1 Hyperelastic incompressible layers

Let the composite consist of alternating nonlinear hyperelastic layers − many new materials fall into this category, for example, see Ling and Atluri (2007). Suppose that the materials of these layers are incompressible, and a simplified version of the Mooney −Rivlin potential, namely the so-called neo-Hookean potential, may be chosen to describe them in the following form:

$$\Phi^r = 2C_{10}^r I_1^r\left(\varepsilon_{ij}^0\right), \quad \Phi^m = 2C_{10}^m I_1^m\left(\varepsilon_{ij}^0\right) \tag{18.17}$$

where Φ is the strain energy density function (elastic potential), C_{10} is a material constant and $I_1(\varepsilon)$ is the first algebraic invariant of the Cauchy−Green strain tensor. This potential is also called the Treloar's potential, after the author who obtained it from an analysis of a model for rubber regarded as a macromolecular network structure made of very long and flexible interlinking chains (Treloar, 1975).

Then the characteristic Eqns (18.15) and (18.16) can be specified for particular modes of stability loss following Guz (1998, 1999). The resulting transcendental equations in terms of λ_1 (shortening factor) and α_r (normalised wavelength) will be different for each of the modes. In the case of biaxial loading (Guz, 1998) for perfectly bonded layers:

- for the first (shear) mode

$$\begin{aligned}
&-\lambda^{-3}\left(1+\lambda_1^6\right)^2\left[1-C_{10}^r\left(C_{10}^m\right)^{-1}\right]^2 \tanh\alpha_r\lambda_1^{-3}\tanh\alpha_m\lambda_1^{-3}\\
&-4\lambda_1^3\left[1-C_{10}^r\left(C_{10}^m\right)^{-1}\right]^2 \tanh\alpha_r\tanh\alpha_m\\
&+\left[2-\left(1+\lambda_1^6\right)C_{10}^r\left(C_{10}^m\right)^{-1}\right]^2 \tanh\alpha_r\lambda_1^{-3}\tanh\alpha_m\\
&+\left[1+\lambda_1^6-2C_{10}^r\left(C_{10}^m\right)^{-1}\right]^2 \tanh\alpha_r\tanh\alpha_m\lambda_1^{-3}\\
&+\left(1-\lambda_1^6\right)^2 C_{10}^r\left(C_{10}^m\right)^{-1}\left(\tanh\alpha_r\tanh\alpha_r\lambda_1^{-3}+\tanh\alpha_m\tanh\alpha_m\lambda_1^{-3}\right)=0
\end{aligned} \tag{18.18}$$

- for the second (extension) mode

$$\begin{aligned}
&-\lambda^{-3}\left(1+\lambda_1^6\right)^2\left[1-C_{10}^r\left(C_{10}^m\right)^{-1}\right]^2 \tanh\alpha_r\lambda_1^{-3}\coth\alpha_m\lambda_1^{-3}\\
&-4\lambda_1^3\left[1-C_{10}^r\left(C_{10}^m\right)^{-1}\right]^2 \tanh\alpha_r\coth\alpha_m\\
&+\left[2-\left(1+\lambda_1^6\right)C_{10}^r\left(C_{10}^m\right)^{-1}\right]^2 \tanh\alpha_r\lambda_1^{-3}\coth\alpha_m\\
&+\left[1+\lambda_1^6-2C_{10}^r\left(C_{10}^m\right)^{-1}\right]^2 \tanh\alpha_r\coth\alpha_m\lambda_1^{-3}+\left(1-\lambda_1^6\right)^2 C_{10}^r\left(C_{10}^m\right)^{-1}\\
&\left(\tanh\alpha_r\tanh\alpha_r\lambda_1^{-3}+\coth\alpha_m\coth\alpha_m\lambda_1^{-3}\right)=0
\end{aligned} \tag{18.19}$$

- for the third mode

$$\begin{aligned}
&-\lambda^{-3}\left(1+\lambda_1^6\right)^2\left[1-C_{10}^r\left(C_{10}^m\right)^{-1}\right]^2 \coth\alpha_r\lambda_1^{-3}\coth\alpha_m\lambda_1^{-3}\\
&-4\lambda_1^3\left[1-C_{10}^r\left(C_{10}^m\right)^{-1}\right]^2 \coth\alpha_r\coth\alpha_m\\
&+\left[2-\left(1+\lambda_1^6\right)C_{10}^r\left(C_{10}^m\right)^{-1}\right]^2 \coth\alpha_r\lambda_1^{-3}\coth\alpha_m\\
&+\left[1+\lambda_1^6-2C_{10}^r\left(C_{10}^m\right)^{-1}\right]^2 \coth\alpha_r\coth\alpha_m\lambda_1^{-3}\\
&+\left(1-\lambda_1^6\right)^2C_{10}^r\left(C_{10}^m\right)^{-1}\left(\coth\alpha_r\coth\alpha_r\lambda_1^{-3}+\coth\alpha_m\coth\alpha_m\lambda_1^{-3}\right)=0
\end{aligned} \tag{18.20}$$

- for the fourth mode

$$\begin{aligned}
&-\lambda^{-3}\left(1+\lambda_1^6\right)^2\left[1-C_{10}^r\left(C_{10}^m\right)^{-1}\right]^2 \coth\alpha_r\lambda_1^{-3}\tanh\alpha_m\lambda_1^{-3}\\
&-4\lambda_1^3\left[1-C_{10}^r\left(C_{10}^m\right)^{-1}\right]^2 \coth\alpha_r\tanh\alpha_m\\
&+\left[2-\left(1+\lambda_1^6\right)C_{10}^r\left(C_{10}^m\right)^{-1}\right]^2 \coth\alpha_r\lambda_1^{-3}\tanh\alpha_m\\
&+\left[1+\lambda_1^6-2C_{10}^r\left(C_{10}^m\right)^{-1}\right]^2 \coth\alpha_r\tanh\alpha_m\lambda_1^{-3}
\end{aligned} \tag{18.21}$$

and for perfectly lubricated layers:

- for the first (shear) mode

$$4\lambda_1^3\left(\frac{C_{10}^r}{C_{10}^m}\tanh\alpha_r+\tanh\alpha_m\right)-\left(1+\lambda_1^6\right)^2\left(\frac{C_{10}^r}{C_{10}^m}\tanh\frac{\alpha_r}{\lambda_1^3}+\tanh\frac{\alpha_m}{\lambda_1^3}\right)=0 \tag{18.22}$$

- for the second (extension) mode

$$4\lambda_1^3\left(\frac{C_{10}^r}{C_{10}^m}\tanh\alpha_r+\coth\alpha_m\right)-\left(1+\lambda_1^6\right)^2\left(\frac{C_{10}^r}{C_{10}^m}\tanh\frac{\alpha_r}{\lambda_1^3}+\coth\frac{\alpha_m}{\lambda_1^3}\right)=0 \tag{18.23}$$

- for the third mode

$$4\lambda_1^3\left(\frac{C_{10}^r}{C_{10}^m}\coth\alpha_r+\coth\alpha_m\right)-\left(1+\lambda_1^6\right)^2\left(\frac{C_{10}^r}{C_{10}^m}\coth\frac{\alpha_r}{\lambda_1^3}+\coth\frac{\alpha_m}{\lambda_1^3}\right)=0 \tag{18.24}$$

- for the fourth mode

$$4\lambda_1^3\left(\frac{C_{10}^r}{C_{10}^m}\coth\alpha_r+\tanh\alpha_m\right)-\left(1+\lambda_1^6\right)^2\left(\frac{C_{10}^r}{C_{10}^m}\coth\frac{\alpha_r}{\lambda_1^3}+\tanh\frac{\alpha_m}{\lambda_1^3}\right)=0 \tag{18.25}$$

The shortening factor λ_1 is related to the value of strain ε_{11}^0 by the following equation

$$u_i^0 = (\lambda_i - 1)x_i, \quad \lambda_i = \text{const}, \quad \varepsilon_{ij}^0 = (\lambda_i - 1)\delta_{ij}, \tag{18.26}$$

where u_i^0 is the axial displacement and ε_{ij}^0 is the strain (in terms of the elongation/shortening factor λ_j in the direction of the OX_j axis). The values of displacement and strain corresponding to the precritical state are marked by the superscript '0' to distinguish them from perturbations of the same values (u_i^0 and u_i, ε_{ij}^0 and ε_{ij}, respectively).

In order to obtain the characteristic equations for the uniaxial loading, λ_1^{-3}, λ_1^3 and λ_1^6 should be replaced respectively by λ_1^{-2}, λ_1^2 and λ_1^4 in Eqns (18.18)–(18.25).

The critical value for the particular mode $\lambda_{\text{cr}}^{(N)}$ (N is the number of the mode) can be found as a maximum of the corresponding curve. The maximum of these values will be the critical shortening factor of the internal instability for the considered layered material

$$\lambda_{\text{cr}}^{\text{pl}} = \max_N \left\{\lambda_{\text{cr}}^{(N)}\right\} = \max_N \left\{\max_{\alpha_r} \lambda_1^{(N)}\right\} \tag{18.27}$$

$$\lambda_{\text{cr}}^{\text{pb}} = \max_N \left\{\lambda_{\text{cr}}^{(N)}\right\} = \max_N \left\{\max_{\alpha_r} \lambda_1^{(N)}\right\} \tag{18.28}$$

Note that maximum shortening factors correspond to minimal strains, and therefore to minimal loads according to Eqn (18.26). The curves corresponding to the third and the fourth modes lie beneath the curves corresponding to the first and the second modes; see Guz (1998). Therefore, the first and second modes appear to be the most common modes of practical interest.

The computed critical values of shortening factors for hyperelastic composites with perfectly bonded layers under biaxial loading are presented in Figures 18.2–18.4. The comparison of the results for the first and second modes of stability loss is presented in Figures 18.2 and 18.3. The shortening factor tends to zero with the decrease of the material constants ratio, and the difference between results for the first and the second modes of stability loss becomes smaller (Figure 18.2). In Figure 18.3 one can see how the ratio of the layer thicknesses influences the value of shortening factor for the first two modes. The shortening factors for the first and second modes coincide, while the reinforcement layer is thin compared with the matrix layer. In the considered case, the difference between the results for the first and second modes becomes noticeable when the ratio of the layer thicknesses reaches a certain value (0.1 for the case of Figure 18.3). It increases with increases in the ratio of the layer thicknesses.

The 3-D plots in Figure 18.4 show the whole picture of the dependences between the shortening factor, the ratio of layer thicknesses and the ratio of material constants for the first and second modes of the stability loss.

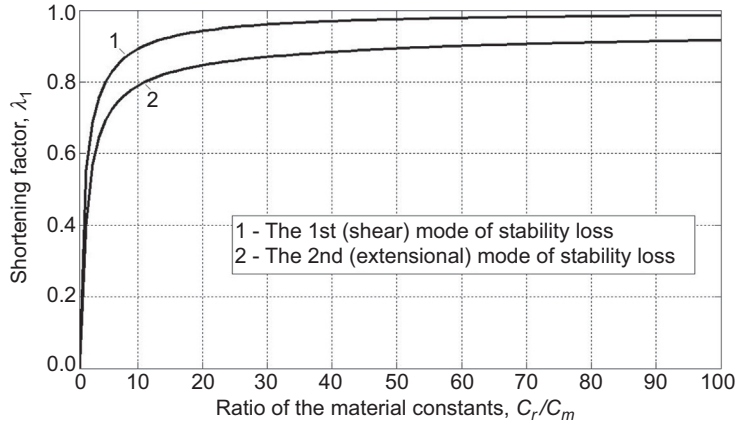

Figure 18.2 Shortening factor against the ratio of material constants; $h_r/h_m = 0.5$.

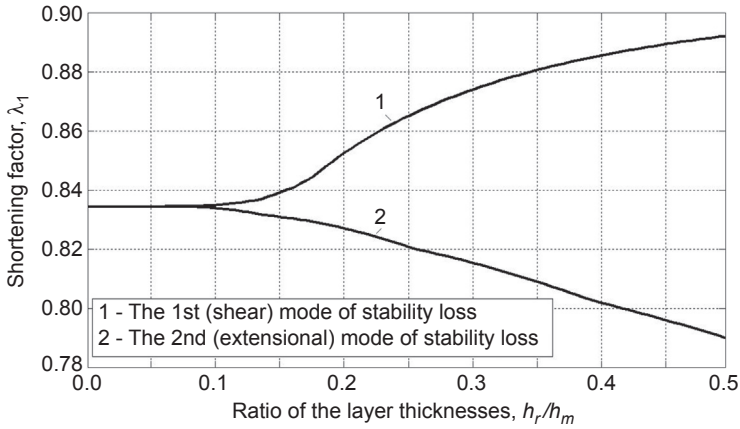

Figure 18.3 Shortening factor against the ratio of the layer thicknesses; $C_r/C_m = 0.2$.

18.2.4.2 Compressible layers

Let us consider a composite consisting of alternating linear-elastic isotropic compressible layers with different elastic properties (the Young's moduli E and the Poisson's ratios ν). Then for the reinforcement layer we have

$$\left(\sigma_{ij}^0\right)^r = \delta_{ij}\frac{E_r\nu_r}{(1+\nu_r)(1-2\nu_r)}\varepsilon_{nn}^0 + \frac{E_r}{1+\nu_r}\varepsilon_{ij}^0 \tag{18.29}$$

and for the matrix

$$\left(\sigma_{ij}^0\right)^m = \delta_{ij}\frac{E_m\nu_m}{(1+\nu_m)(1-2\nu_m)}\varepsilon_{nn}^0 + \frac{E_m}{1+\nu_m}\varepsilon_{ij}^0 \tag{18.30}$$

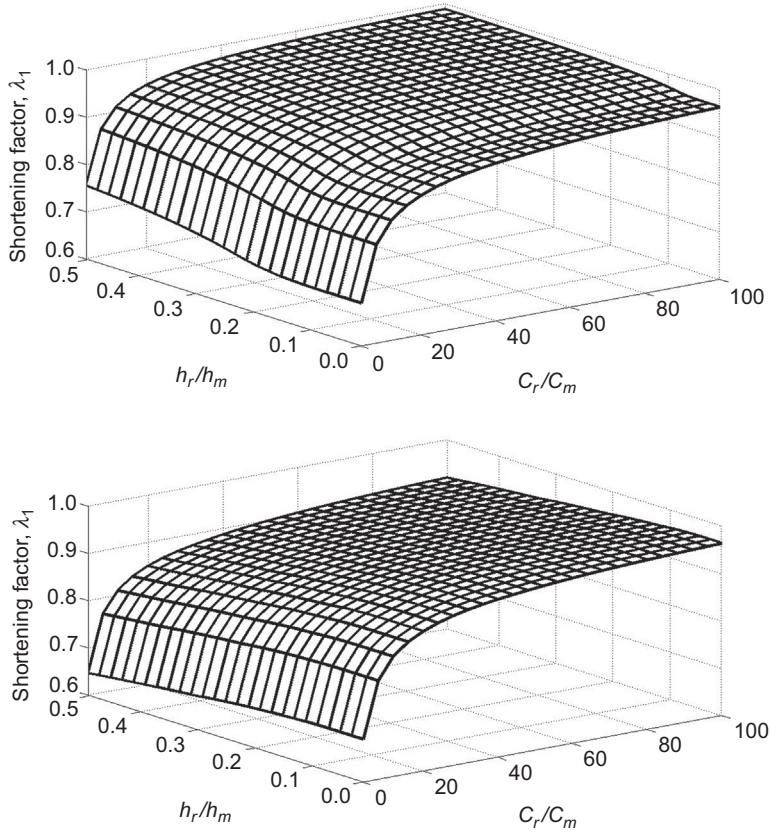

Figure 18.4 The first and the second modes of stability loss.

The components of tensor $\omega_{ij\alpha\beta}$ for such materials are given in Rosen (1965) and Moran et al. (1995) for different types of loading. Following the procedure described in the previous subsection, that is, substituting the expressions for $\omega_{ij\alpha\beta}$ into the characteristic Eqns (18.15) and (18.16), the characteristic equation can be specified for the considered type of composite material; see Guz (1989a, 1992) and Rosen (1965) for more details.

For all modes, we have transcendental equations in terms of two variables, ε_{11}^0 (applied strain) and α_r (normalised half-wavelength). Solving the characteristic equations for different modes of stability loss, the dependences $\varepsilon_{11}^{(N)}(\alpha_r)$ are obtained ($N = 1,2,3,4$ is the number of the mode). The minimum of the corresponding dependence is the critical value for the particular mode $-\varepsilon_{\rm cr}^{(N)}$. The critical strain of internal instability for the considered layered material is the minimum of the four values ($\varepsilon_{\rm cr}^{\rm pl}$ in the case of perfectly lubricated layers, and $\varepsilon_{\rm cr}^{\rm pb}$ in the case of perfectly bonded layers):

$$\varepsilon_{\rm cr}^{\rm pl} = \min_N \varepsilon_{\rm cr}^{(N)} = \min_N \left(\min_{\alpha_r} \varepsilon_{11}^{(N)} \right) \tag{18.31}$$

$$\varepsilon_{\mathrm{cr}}^{\mathrm{pb}} = \min_{N} \varepsilon_{\mathrm{cr}}^{(N)} = \min_{N}\left(\min_{\alpha_r} \varepsilon_{11}^{(N)} \right) \tag{18.32}$$

18.2.4.3 Elastic–plastic layers

Now let us consider the following layered composite: the reinforcement behaves as a linear-elastic isotropic compressible material, Eqn (18.29), and the matrix response is elastic–plastic incompressible, described by the following relationship for equivalent stress (σ_I^0) and strain (ε_I^0):

$$\sigma_I^0 = A_m \left(\varepsilon_I^0\right)^{k_m} \tag{18.33}$$

where k_m and A_m are material constants for an elastic–plastic matrix. The constitutive Eqn (18.33) is typical for metal matrix composites; see Aboudi (1987), Librescu and Schmidt (2001), Honeycombe (1968) and Pinnel and Lawley (1970). Again, using the expressions for $\omega_{ij\alpha\beta}$ and $\kappa_{ij\alpha\beta}$ (Guz, 1998), one can deduce the transcendental equations for each of the considered modes of stability loss; see Aboudi (1987) and Librescu and Schmidt (2001).

The computed values of critical strain for metal matrix elastic–plastic composites under biaxial and uniaxial loading are presented in Figures 18.5–18.8 for different properties of the material. The results show how the bonds between the layers affect the solution for the first two modes of stability loss. Figures 18.5 and 18.6 correspond to the case of perfectly bonded layers, and Figures 18.7 and 18.8 to the case of perfectly lubricated layers.

18.2.5 Bounds for the critical controlled parameters for materials with weakened interfacial adhesion

In this subsection, the critical values of controlled parameters for perfectly bonded and perfectly lubricated layers are compared for hyperelastic and metal matrix composites under different types of loading.

According to Eqn (18.9), these values form the bounds for the critical controlled parameters (i.e. either for critical strains or for critical shortening factors) for practical composites with weakened interfacial adhesion. If for critical strain the bounds have the form of Eqn (18.9), then the critical shortening factors, taking into account Eqn (18.26), are

$$\lambda_{\mathrm{cr}}^{\mathrm{pb}} \le \lambda_{\mathrm{cr}} \le \lambda_{\mathrm{cr}}^{\mathrm{pl}} \tag{18.34}$$

In practice, composites contain not only interlaminar, but also various intralaminar defects. Intralaminar damage effects can be accounted for by considering layers with reduced stiffness properties – for example, see Kashtalyan and Soutis (2001, 2006).

The computed results for four modes of stability loss in hyperelastic incompressible layered material are shown in Figures 18.9 and 18.10. One can see that the bounds for the shortening factor are wider when the ratio of material constants is lower. For the

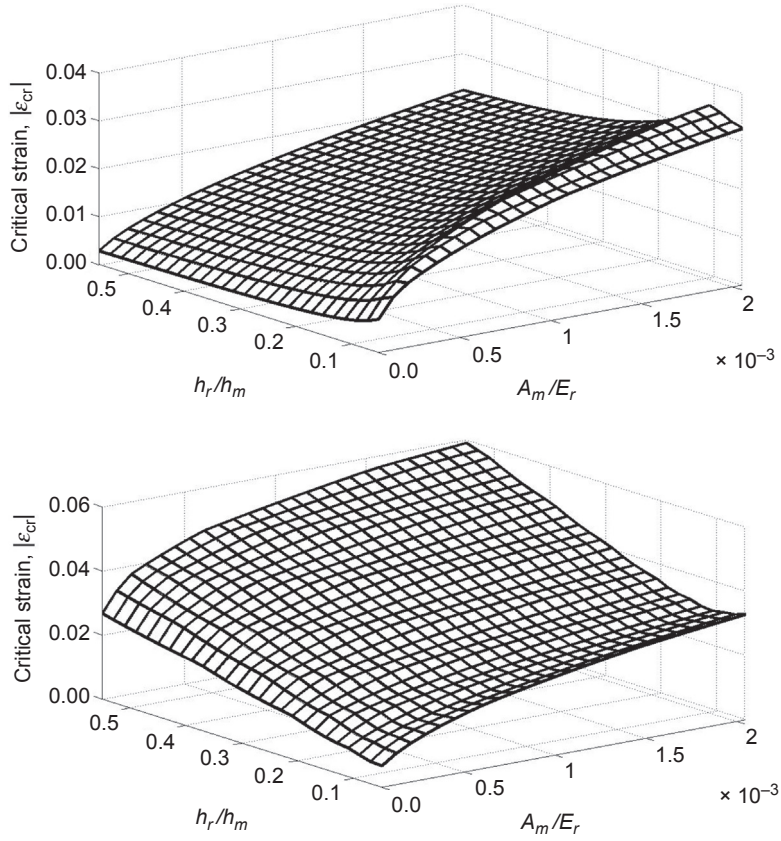

Figure 18.5 The first and the second modes, $k_m = 0.25$, $\nu_r = 0.21$.

second mode, the results for perfectly bonded and perfectly lubricated layers start to coincide when the ratio of material constants reaches a certain value (40 for the case of Figure 18.9).

The results of computation for layered composites with elastic−plastic matrix are shown in Figures 18.11 and 18.12. For the first and second modes of stability loss, the critical strain remains constant, and the difference between the results for perfectly bonded and perfectly lubricated layers does not change while the ratio of the layer thicknesses is lower than a certain value (0.027 for the case of Figure 18.11). Then, with the increase of the difference between layer thicknesses, the bounds for critical strain become narrower. The bounds for critical strain are shown in Figure 18.12 as a function of k_m. With the increase of the coefficient k_m, the distance between the upper and the lower curves significantly decreases for the first mode of stability loss and remains almost the same for the second mode.

The computed bounds are presented for model generic material systems. They appear to give a reasonable estimation for the critical controlled parameters and may be considered as the first approximation on the way to the exact solution of the

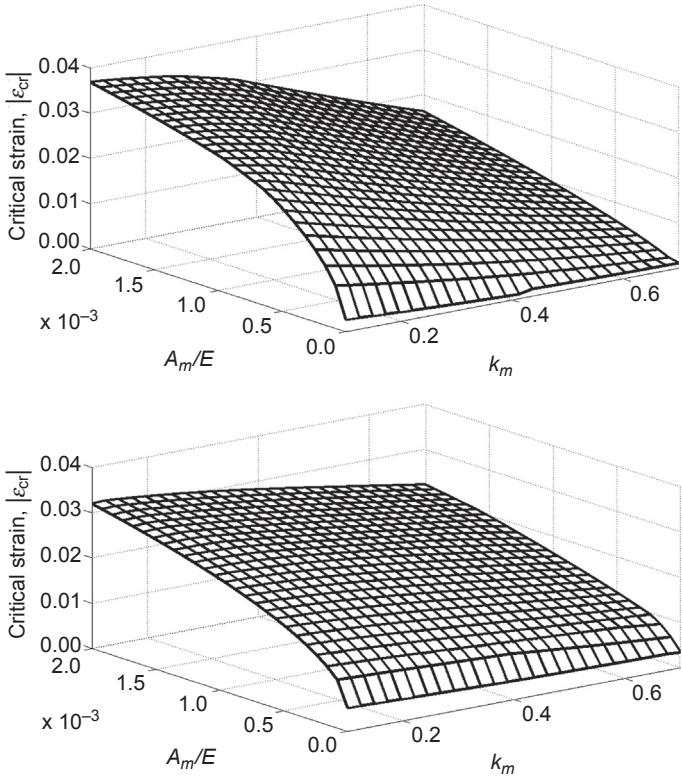

Figure 18.6 The first and the second modes, $\nu_r = 0.21$, $h_r/h_m = 0.1$.

problem of stability in compression along interfacial defects. According to Guz (1989a,b, 1992, 1998, 2005), Guz and Soutis (2001a, b), Guz and Herrmann (2003) and Menshykova et al. (2009), the method works better for layered materials with small to medium volume fraction of stiffer (reinforcing) layers. The applicability of the method to practical materials, for example, composite materials utilised in aerospace, automotive and other industries, or layered rocks, should be discussed separately for each class of materials. Further studies are required to compare the results with experimental observations and measurements.

18.3 Application to the case of a stiffened panel with an open hole

18.3.1 Background

This section gives an example of practical application of the method developed in the previous section.

The investigation of compressive behaviour of stiffened thin-skinned composite panels with stress concentrators is dictated by the demands of the aircraft industry.

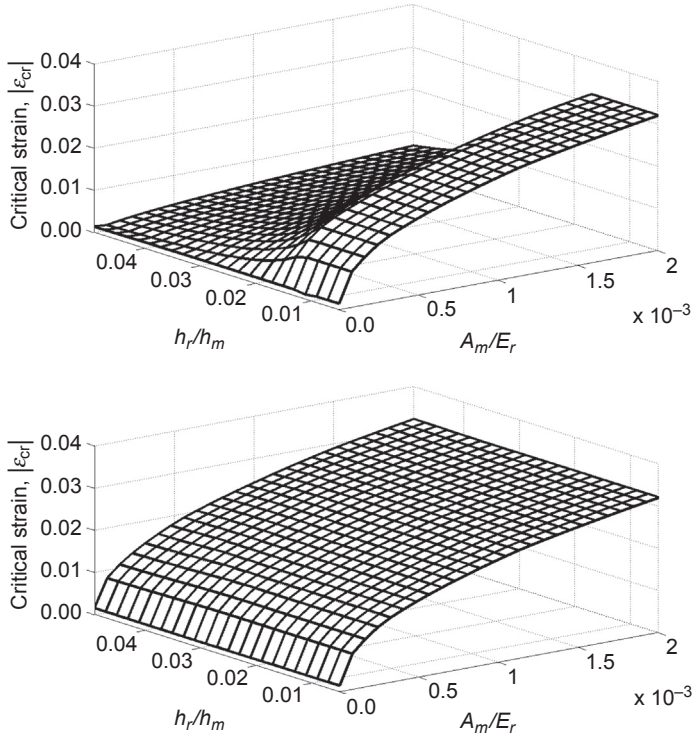

Figure 18.7 The first and the second modes, $k_m = 0.25$, $\nu_r = 0.21$.

A typical aircraft structure such as a fuselage shell or wing surface usually consists of a thin skin reinforced with stiffeners. The need for an open cut-out in a structural component comes from practical concerns. For example, cut-outs in wing spars and cover panels of commercial and military transport wings provide access for hydraulic and electrical lines as well as damage inspection. Also, cut-outs in a fuselage can serve as access panels and lightening holes. However, such cut-outs introduce high local stresses that can initiate damage and lead to premature failures. Low-velocity impact damage caused by dropped tools, runway debris and hailstones can be another source of stress concentration that weakens the structure. During a component's service life, it will experience compressive loads, and therefore its strength is an important design parameter, especially since the compressive strengths of currently used carbon fibre−epoxy composites are only equivalent to 60−70% of their tensile strengths. In some applications, these structural elements are required primarily to resist buckling, whereas in other cases they must carry load well into the postbuckling range in order to yield weight savings. Thus, understanding their buckling and postbuckling behaviour is necessary for their design.

Most of the relevant research has focused on the buckling and postbuckling response of stiffened panels where failure occurs due to large out-of-plane deflections (more than twice the skin thickness) at compressive loads far below the ultimate static

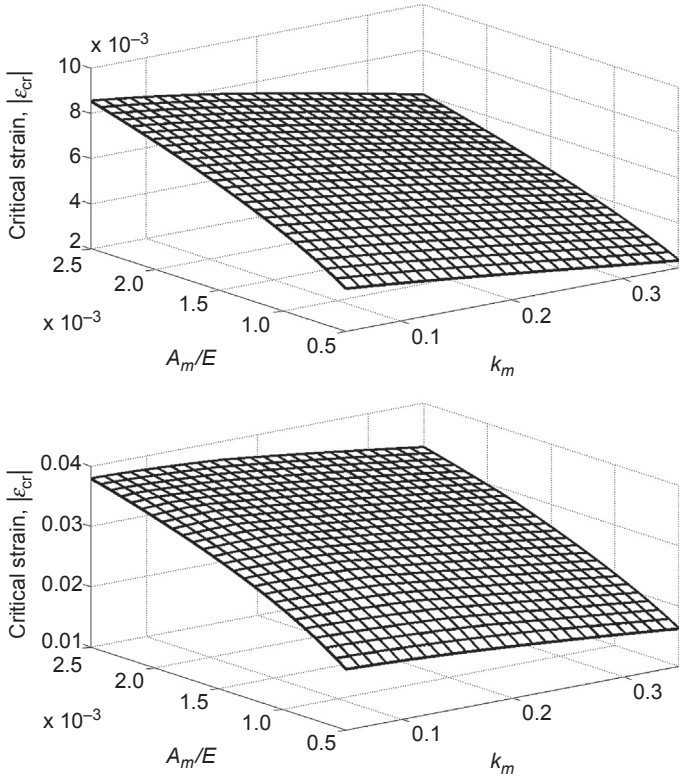

Figure 18.8 The first and the second modes, $\nu_r = 0.21$, $h_r/h_m = 0.05$.

strength of the composite material. A comprehensive review of the early experimental studies of buckling and postbuckling behaviour of laminated composite plates with cut-outs was given in Nemeth (1996). Subsequently, the influence of stiffeners on the behaviours of damaged and undamaged plates was experimentally studied in Greenhalgh et al. (1996), Greenhalgh, Singh, Hughes, and Roberts (1999), Jegley (1992, 1998), Kong, Lee, Kim, and Hong (1998) and Stevens, Ricci, and Davies (1995). The postbuckling compressive strength of undamaged panels with I-stiffeners was reported to be 5−7 times higher than the buckling load for the same plate (Kong et al., 1998). The effect of stiffeners on stress distribution around a hole, as well as on buckling and failure characteristics of lightweight composite panels, is the subject of the survey by Leissa (1987). More recently this subject was addressed in Degenhardt et al. (2007), Diamanti, Soutis, and Hodgkinson (2007), Falzon, Davies, and Greenhalgh (2001), Found, Howard, and Paran (2002), Greenhalgh and Hiley (2003), Greenhalgh and Garcia (2004) and Ishikawa, Matsushima, Hayashi, and Scott (2005) and numerous other publications mentioned in this chapter.

The important point that surfaced in Nemeth (1996) is that understanding the response of stiffened plates with an open hole is very fragmented. There is a definite need for studies that attempt to isolate and articulate each fundamental aspect of the

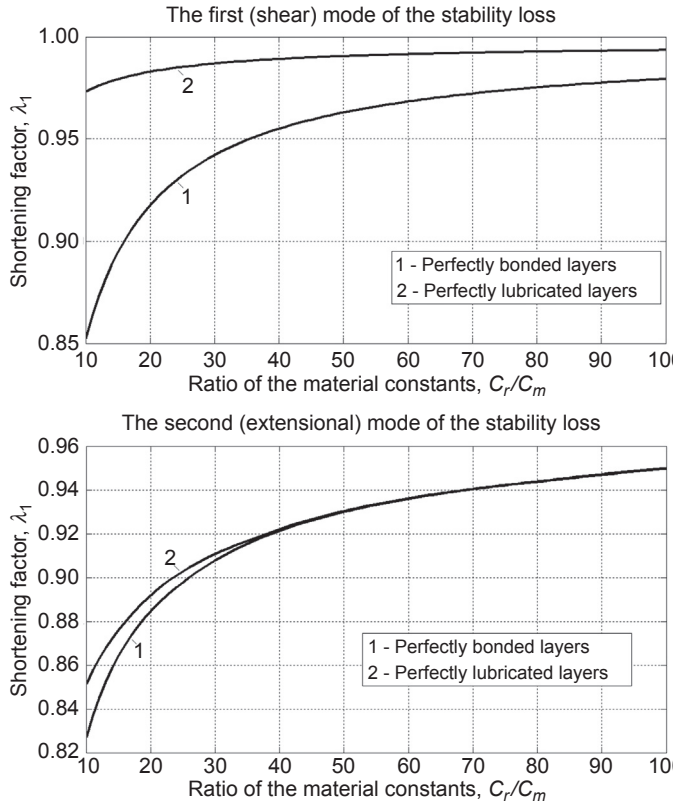

Figure 18.9 The bounds for the first and the second modes for a hyperelastic composite under uniaxial loading; $h_r/h_m = 0.2$.

compressive behaviour in a consistent manner. Based on available experimental data, it was concluded in Nemeth (1996) that careful studying of the behaviour of subcomponents is a necessary fundamental step in any research of composite structures with discontinuities. Knowledge of the basic response of the subcomponent provides a valuable insight into modelling complex structures with general finite element codes. Furthermore, knowledge of the subcomponent response is very useful for identifying erroneous results that may be obtained due to improper finite element modelling. The above observations justify special attention, which is paid within this chapter by the 'step-by-step' analysis of the general problem starting from the simplest fracture mechanisms for subcomponents (i.e. starting from subproblems). In doing so, both special-purpose analytical methods and more general finite element methods with wider domain of applicability have their own distinct advantages. The special-purpose analyses are typically more limited in scope than the finite element methods, but are being used to conduct extensive parametric studies of buckling behaviour. These analyses are valuable because they can easily establish trends in behaviour that are in good qualitative agreement with experimental data Nemeth (1996).

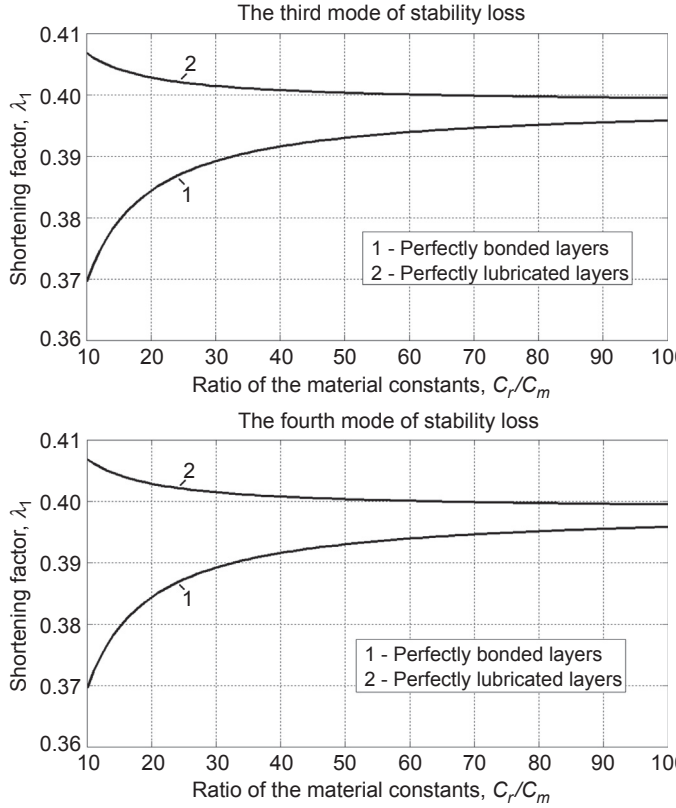

Figure 18.10 The bounds for the third and the fourth modes for a hyperelastic composite under uniaxial loading; $h_r/h_m = 0.2$.

18.3.2 Experimental observations and failure mechanisms

The works of Soutis and Fleck (1990), Soutis, Fleck, and Smith (1991) and Soutis and Curtis (1996) have examined the influence of single and multiple holes on the compressive behaviour of several T800/924C carbon fibre−epoxy laminates without stiffeners. They found that open holes reduce the in-plane compressive strength by more than 40% depending on layup and hole size. Damage is initiated by 0° fibre microbuckling at the edge of the hole at approximately 80% of the failure load, and is accompanied by matrix cracking of the off-axis plies and delamination between the plies. This damage zone continues to grow, first in short discrete increments and then rapidly across the laminate width at a failure load higher than that predicted by the maximum stress criterion. Fibre buckling leads to local delamination when the local strain necessary to accommodate the localised fibre displacement and rotation exceeds the resin ductility. These local delaminations do not propagate to become macroscopic delaminations until final compressive failure occurs. For a 0^o-dominated

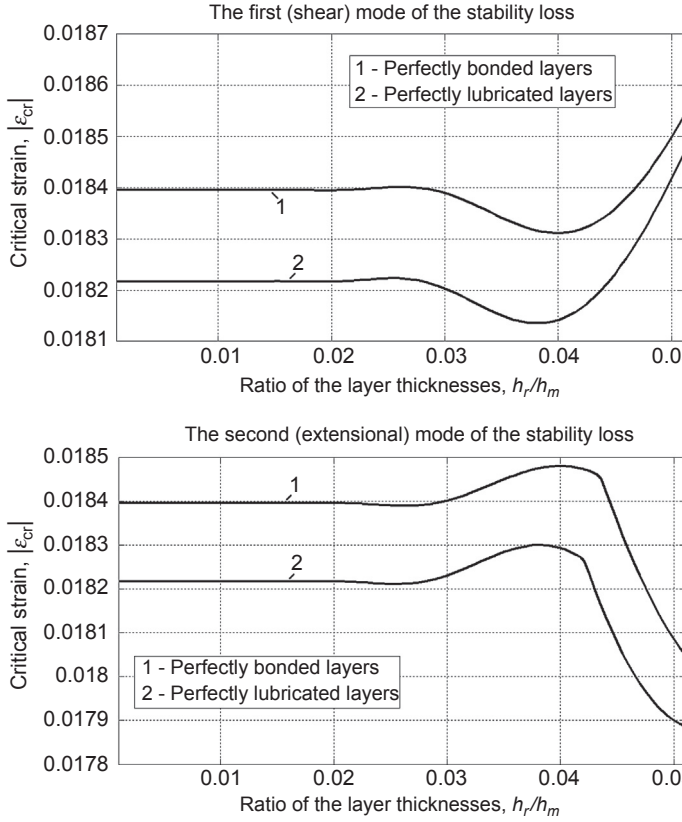

Figure 18.11 The bounds for the first and the second modes for a metal matrix composite under biaxial loading; $A_m/E = 0.0005$, $\nu_r = 0.21$, $k_m = 0.25$.

laminate, the damage zone is more cracklike in nature, its length immediately prior to failure being in the region of 2−3 mm.

A similar damage pattern was observed in plates with impact damage under uniaxial compression (Soutis & Curtis, 1996). The distribution of through-the-thickness damage determined from sectioning studies is roughly cylindrical in shape; ultrasonic C-scan images and X-ray shadow radiographs indicate that the shape of the overall damage is approximately circular (equivalent to an open hole).

Since the analysis of the compressive behaviour of thin-skin stiffened composite panels with stress concentrators is dictated by industrial need, in the present work an effort is made to be as close to the actual geometry, layup and material properties as possible. All these parameters are taken from the experimental investigation funded by the aircraft industry (Greenhalgh et al., 1996, 1999). The general configuration of the panel examined is sketched in Figures 18.13 and 18.14, which are redrawn from Greenhalgh et al. (1999). It is assumed that the hole or equivalent hole that represents impact damage is always located in the middle of the bay, a more critical situation for thin skins according to Jegley (1992).

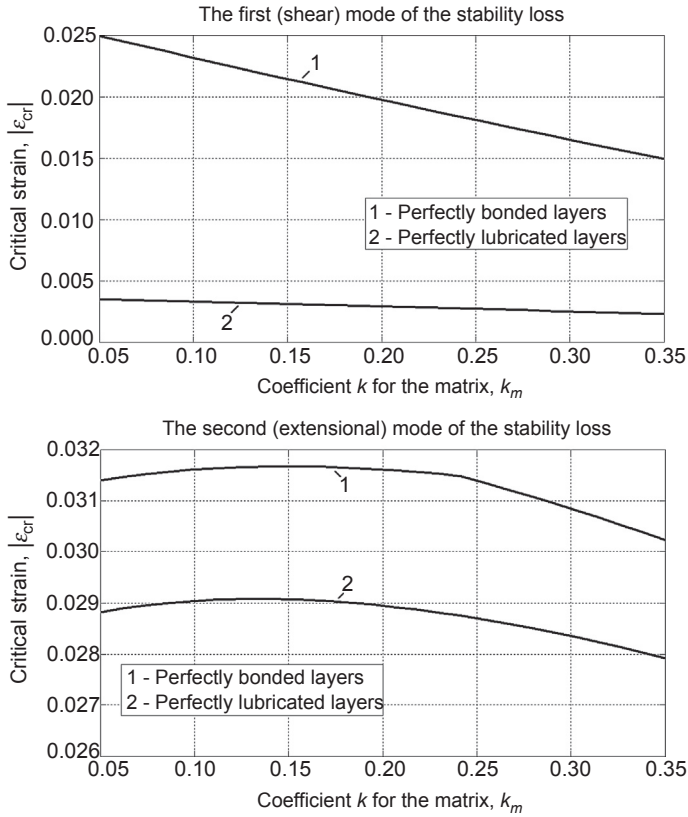

Figure 18.12 The bounds for the first and the second modes for a metal matrix composite under biaxial loading; $A_m/E = 0.001$, $h_r/h_m = 0.25$, $\nu_r = 0.21$.

In this study, three different configurations with an elliptical hole are analysed. The geometric parameters are taken from the literature of Greenhalgh et al. (1999) and are presented in Table 18.1. Each panel is made of a quasi-isotropic skin with a $[45°/-45°/0°/90°]_{4s}$ layup, typical of those used in aircraft construction. Fibredux T800/924 (Toray 800 fibres in Ciba Fibredux 924 epoxy resin) was used as a material for each layer. The I-section stiffener is fabricated from four uncured laminates, consisting of a base, two C-sections placed back-to-back and a spar cap. The base and the C-sections have the same layup $[+45°/-45°/0°]_{2S}$, while that of the spar cap is $[-45°/+45°/0°]_{2S}$ (see Figure 18.13); the material used is also a T800/924 carbon fibre−epoxy system. The properties of the unidirectional composite prepreg used are given in Table 18.2. Each of these panels is subjected to uniaxial compression in the direction of the stiffeners.

An open hole or impact damage introduces high local stresses that may initiate material failures and lead to catastrophic fracture of the structure or component before Euler buckling occurs.

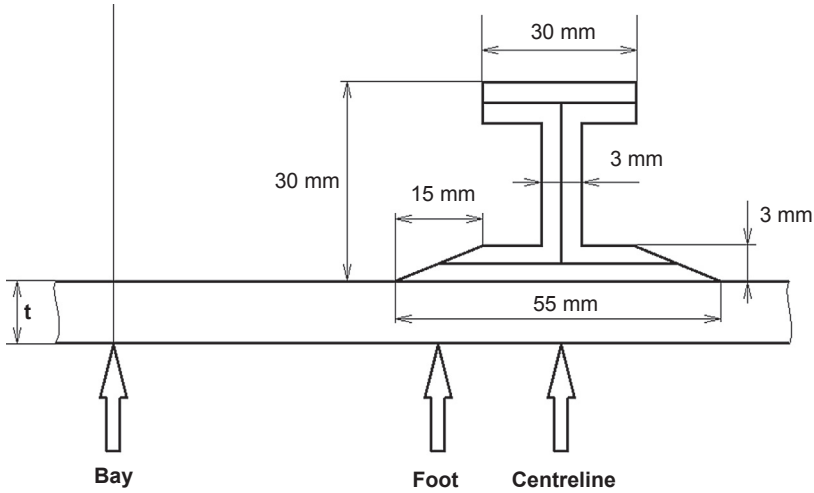

Figure 18.13 Geometry of the stiffened panel.
Redrawn from Greenhalgh et al. (1996).

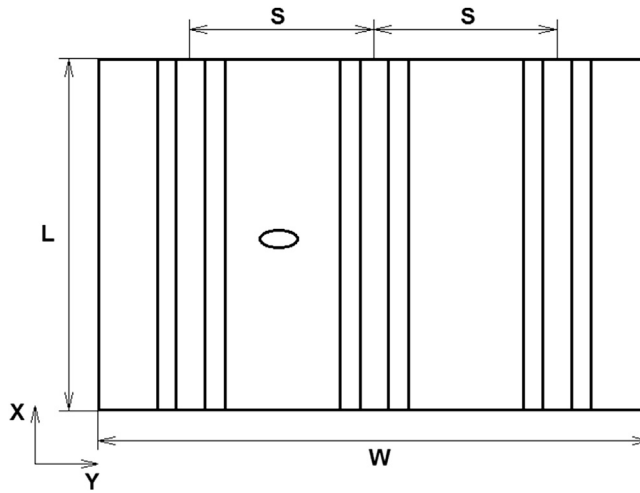

Figure 18.14 Location of the damage site on the stiffened panel.
Redrawn from Greenhalgh et al. (1996).

In the case of compressive loading, near-surface instability or fibre microbuckling in the 0° plies may occur where high stress gradients exist. The critical load can be estimated by using the maximum stress failure criterion, giving a conservative estimate for the failure load; see Zhuk, Soutis, and Guz (2001, 2002). Alternatively, the Soutis–Fleck fracture model (Soutis & Curtis, 1996; Soutis & Fleck, 1990) can be employed, where the microbuckling growing from the edge of the hole is mathematically represented by a through-the-thickness crack, and fracture mechanics concepts are applied – for

Table 18.1 The panel dimensions according to Greenhalgh et al. (1996)

Panel	*t*, mm	*S*, mm	*W*, mm
Type 1	4	120	360
Type 2	4	148	444
Type 3	3	120	360

Table 18.2 The properties of unidirectional fibre−reinforced composite material T800/924 used for manufacturing the three panels

Property	Average (C_v) for T800/924
ρ (kg/m^3)	1630
E_{11} (GPa) − Tension	155.21 (7%)
E_{22} (GPa) − Tension	8.57 (3%)
G_{12} (GPa)	7.40 (5%)
Σ_{11} (MPa) − Tension	1982.90 (2%)
σ_{22} (MPa) − Tension	48.69 (2%)
σ_{11} (MPa) − Compression	−1550
σ_{22} (MPa) − Compression	−250
σ_{12} (MPa)	113.02 (10%)
ε_{11} ($\mu\varepsilon$) − Tension	12776
ε_{22} ($\mu\varepsilon$) − Tension	5681
ε_{11} (MPa) − Compression	−9,986
ε_{22} (MPa) − Compression	−29,171
ε_{12} ($\mu\varepsilon$)	15273
ν_{12}	0.36
G_{IC} (40 mm) (J/m^2)	288 (10%)
G_{IC} (60 mm) (J/m^2)	276 (10%)
G_{IIC} (J/m^2)	575

example, see Zhuk, Soutis, and Guz (2000), Zhuk, Soutis, et al. (2001), Zhuk et al. (2002) and Zhuk, Guz, and Soutis (2001). In both models, a value for the unnotched compressive strength is required, which can be estimated by using a fibre instability model based on a 3-D stability theory of deformable bodies (Guz, 1999).

18.3.3 Fibre/ply level analysis

In the analysis below, the stiffened panel is assumed to be in the prebuckling state. The strategy is to divide the problem into simpler 'subproblems'. In the case of the stiffened panel, the critical load for the unnotched laminated skin is obtained first, then hole or impact damage is introduced, followed by material anisotropy, finite-width effects and finally stiffeners.

In a multidirectional laminate, the location of the 0° layer through the laminate thickness and the orientation of the neighbouring (supporting) ply can have a significant effect on the initiation of damage and final failure. For instance, the failure strain of a laminate with 0° outer layers can be more than 10% lower than that of a similar layup with ±45° outer plies, due to out-of-plane fibre microbuckling (Soutis, 1994). The outer off-axis plies provide better lateral support to the 0° layers, permitting them to fail by in-plane microbuckling, which is a higher-strain failure event.

Using the 3-D stability theory described in Guz (1999) and treating the laminate as a homogeneous anisotropic material, the critical failure stress (σ_{cr}^{s}) for near-surface microbuckling is obtained as

$$\sigma_{\text{cr}}^{s} = G_{12}\left[1 - G_{12}^{2}\,\frac{\tilde{A}_{11}\tilde{A}_{22}}{\left(\tilde{A}_{11}\tilde{A}_{22} - \tilde{A}_{12}^{2}\right)^{2}}\right] = G_{12}\left[1 - \frac{G_{12}^{2}}{E_1 E_2}\right] \tag{18.35}$$

where E_1 and E_2 are the effective Young's moduli in the principal material directions, G_{12} is the effective value of the in-plane shear modulus and $\tilde{A}_{ij}$ are the elastic moduli under generalised Hooke's law. It should be emphasised that Eqn (18.35) describes explicitly the influence of the free surface on the microbuckling phenomenon and implies the loss of material stability near the surface of the anisotropic plate. Indeed, if we do not consider the surface, the critical stress of internal instability (microbuckling away from the surface) is reduced to the Rosen result (Rosen, 1965)

$$\sigma_{\text{cr}}^{\text{int}} = G_{12} \tag{18.36}$$

Equation (18.35) was analytically derived within the scope of the exact approach based on the 3-D stability theory (Guz, 1999). At that, a continuum theory was used to describe the material properties. Of course, describing the behaviour of each constituent (fibre and matrix) at the micro level by 3-D equations of solid mechanics would enable us to investigate the material response in the most accurate way. However, due to its complexity, this approach is restricted to a

very small group of problems. This makes the continuum theory more attractive since it involves significant simplifications: the composite is modelled as a homogeneous anisotropic solid with effective material constants, by means of which physical properties of the original material, shape and volume fractions of the constituents are taken into account. The problems of accuracy and domain of applicability that arise when the continuum theory is used were successfully resolved in Guz and Soutis (2001b), Guz (2005) and Guz and Soutis (1999). It was shown for various composites (including the linear-elastic laminated composites with a polymer matrix that are considered in the present investigation) that the continuum theory of brittle fracture is asymptotically accurate. Estimation of accuracy of the continuum theory for elastic and elastic−plastic models, both linear and nonlinear, was illustrated by numerical results, and the influence of the type of loading (uniaxial or biaxial compression) on the accuracy of continuum theory was determined. At that, it was found that for practical composites (fibre volume fraction higher than 20%), the accuracy of the continuum theory approaches 100% in comparison with the results of the piecewise-homogeneous model, which is the most rigorous approach.

The values of effective constants for the particular layups of the skin are calculated according to the classical laminate theory (Tan, 1994). Equation (18.35), being the result of a 3-D exact solution of the corresponding problem (assuming perfect fibres and interfaces), allows us to identify the affect of material properties on the critical load in a very clear way. However, this does not account for the high-localised-stress field developed near the hole or impact damage. It needs to be modified and applied at the ply level (i.e. ply-by-ply stress analysis).

Considering the plate using effective constants (i.e. as a homogeneous quasi-isotropic), the equation cannot take into account the actual failure initiation, which is always associated with the particular 'critical' layer in the laminated skin. To resolve this issue, the 'first ply failure' concept is adopted. It means that Eqn (18.35) should be applied to the particular 'critical' layer where failure is more likely to initiate, rather than applied to the whole skin using effective (average) elastic constants. In the examined laminated skin, the critical layer is the 0^o ply (0^o fibres parallel to the loading). The critical stress σ_{cr}^{ud} in this layer is given by

$$\sigma_{cr}^{ud} = G'_{12}\left[1 - \frac{G'^2_{12}}{E'_1 E'_2}\right] \tag{18.37}$$

where G'_{12} is the shear modulus of the 0° layer and E'_1, E'_2 are the respective Young's moduli parallel and transverse to the 0° layer.

Fibre waviness within a conventional laminate severely degrades the compressive strength and stiffness of polymeric fibre composites (Berbinau, Soutis, Goutas, & Curtis, 1999). Prepreg tape has an inherent waviness that is compounded during subsequent layering and compaction. Automated tow placement reduces

waviness during placement but does not eliminate it during compaction and cure. Previous works (Berbinau, Soutis, & Guz, 1999; Soutis, 2000) have shown that a misalignment angle between the fibres and the loading axis of only 1° to 2° is sufficient to reduce the compressive strength of the T800/924C carbon fibre−epoxy system by more than 40%. Postfailure examination of the fracture surfaces using a scanning electron microscope revealed that failure is by fibre microbuckling. Equations (18.35) and (18.36) correctly suggest that the critical compressive stress is proportional to the shear modulus of the composite, but they overestimate the value by at least a factor of three. This is because the analysis is elastic and ignores the degree of initial fibre waviness, the nonlinear resin shear constitutive behaviour, fibre interaction and the fibre−matrix interface. Experimental data presented in Soutis and Turkmen (1995) indicate that the compressive strength of a T800/924C unidirectional laminate has a value equivalent to 20−25% of the elastic shear modulus ($G_{12} = 6$ GPa). The microbuckling model developed in Soutis (1994) and Berbinau et al. (1999) or the 3-D stability theory described in Guz (1999) can be used to get a better estimate of the critical buckling stress, but the mathematical expressions involved are more complex to solve.

In the current study, a knockdown factor $F_{k-d} = 0.3$, which is consistent with theoretical findings (Guz, 1992; Berbinau, Sautis, & Guz, 1999; Zhuk, Soutis, et al., 2001; Zhuk et al., 2002), is introduced in Eqn (18.35) or (18.37) to account for the discrepancy caused by the irregular spacing of fibres, matrix plasticity, fibre misalignment and poor fibre−matrix bonding. It helps to maintain the simplicity of the current approach.

18.3.4 Computing the critical load and predicting the strength of stiffened panels

The compressive load carrying capacity of the stiffened panel with an equivalent open hole examined in this study depends mainly on the magnitude of the in-plane direct stress developed at the hole boundary. Assuming that the composite laminate fails in a brittle manner, the maximum stress criterion could be applied to predict the remote failure stress, that is,

$$\sigma_{\mathrm{cr}}^{\mathrm{plate}} = \frac{\sigma_{\mathrm{cr}}^{s}}{K} \tag{18.38}$$

or, if the 'first ply failure' concept is used,

$$\sigma_{\mathrm{cr}}^{\mathrm{plate}} = \frac{E_1 \sigma_{\mathrm{cr}}^{\mathrm{ud}}}{E_1' K} \tag{18.39}$$

where K is the elastic stress concentration factor (SCF) and $\sigma_{\mathrm{cr}}^{\mathrm{ud}}$ is given by Eqn (18.37).

The actual impact damage area observed in the experimental investigation may have a circular or elliptical shape. Hence the shape should be taken into account in

the analytical modelling. For the case of an elliptical cut-out in orthotropic skin, the SCF is (Tan, 1994)

$$K = 1 + \mathrm{Re}\left[\frac{1}{\mu_1 - \mu_2}\left(\frac{-\mu_2\left(1 - i\mu_1\frac{b}{a}\right)}{i\mu_1\frac{b}{a}\left(1 + i\mu_1\frac{b}{a}\right)} + \frac{-\mu_1\left(1 - i\mu_2\frac{b}{a}\right)}{i\mu_2\frac{b}{a}\left(1 + i\mu_2\frac{b}{a}\right)}\right)\right] \tag{18.40}$$

where b and a are the half-axes of the ellipse in the direction of applied loads (i.e. in the direction of stiffeners) and in the perpendicular direction, respectively. Solutions of the characteristic equations for μ_1 and μ_2 are expressed in terms of the elastic constants as (Guz, 1999)

$$\mu_1 = \frac{i}{2}\left(\sqrt{\frac{E_1}{G_{12}} - 2\nu_{12} + 2\sqrt{\frac{E_1}{E_2}}} + \sqrt{\frac{E_1}{G_{12}} - 2\nu_{12} - 2\sqrt{\frac{E_1}{E_2}}}\right)$$

$$\mu_2 = \frac{i}{2}\left(\sqrt{\frac{E_1}{G_{12}} - 2\nu_{12} + 2\sqrt{\frac{E_1}{E_2}}} - \sqrt{\frac{E_1}{G_{12}} - 2\nu_{12} - 2\sqrt{\frac{E_1}{E_2}}}\right) \tag{18.41}$$

For an elliptical cut-out in a quasi-isotropic laminate, the SCF can be found from the simple equation (Timoshenko & Goodier, 1987)

$$K = 1 + 2\frac{a}{b} \tag{18.42}$$

which reduces to the well-known value of $K = 3$ for a circular cut-out in an infinite quasi-isotropic skin. Of course, Eqn (18.42) does not account for the load redistribution that may occur due to local damage near the edge of the hole, resulting in a conservative value for the critical stress predicted by Eqn (18.38) or (18.39). A simple means of incorporating the load redistribution is to apply the point stress or average stress failure criterion, or to reduce the elastic SCF by a constant determined from the best fit to the available experimental data.

All previous considerations assumed an infinite stiffened panel with an open cut-out. Further refinement of the results can be achieved by taking into account the actual dimensions of the panel (i.e. panel size, hole diameter and location of the hole). For this purpose, the finite-width correction (FWC) factor should be introduced.

There are several methods of calculating FWC factors. The FWC factor for an isotropic plate is not a function of material properties, while for a finite-width anisotropic plate, the FWC factor has a more complex form. Moreover, there are several formulae (see Tan, 1994), and each of them has its own domain of applicability depending on the aspect ratio of the cut-out, the distance from the free edge, material

properties and the ratio of anisotropy. Let us denote the FWC factor as C; the critical remote stress in the skin σ_{cr}^{skin} is then

$$\sigma_{cr}^{skin} = C\sigma_{cr}^{plate} \tag{18.43}$$

For a quasi-isotropic panel $a/b < 4$, Tan (1994) suggested the following formula:

$$C = 1 - \frac{a}{w_0}M + \mathrm{Re}\left\{\frac{1}{\mu_1 - \mu_2}\left[\frac{-\mu_2}{1 + i\mu_1\frac{b}{a}}\left(\frac{a}{w_0}M - 1 + i\mu_1\frac{b}{w_0}M + \sqrt{1 - \left(1 + \mu_1^2\frac{b^2}{a^2}\right)\left(\frac{a}{w_0}M\right)^2}\right) + \frac{\mu_1}{1 + i\mu_2\frac{b}{a}}\left(\frac{a}{w_0}M - 1 + i\mu_2\frac{b}{w_0}M + \sqrt{1 - \left(1 + \mu_2^2\frac{b^2}{a^2}\right)\left(\frac{a}{w_0}M\right)^2}\right)\right]\right\} \tag{18.44}$$

with

$$M^2 = \frac{1}{2}\left\{\sqrt{1 - 8\left[3\left(1 - \frac{a}{w_0}\right)\left(2 + \left(1 - \frac{a}{w_0}\right)^3\right)^{-1} - 1\right]} - 1\right\}\left(\frac{a}{w_0}\right)^{-2} \tag{18.45}$$

and w_0 is distance from the plate edge to the centre of the cut-out. In this case, when the cut-out is located in the middle of the bay,

$$w_0 = \frac{1}{2}(W - S) \tag{18.46}$$

where S is the distance between stringers and W is the width of the skin; see Figure 18.14.

For a quasi-isotropic panel, Eqn (18.44) is reduced to

$$C = \left(\frac{b}{a-b}\right)^2 + \frac{a(a-2b)}{(a-b)^2}\sqrt{1 + (b^2 - a^2)\left(\frac{M}{w_0}\right)^2} - \frac{ab^2}{a-b}\left(\frac{M}{w_0}\right)^2\left[1 + (b^2 - a^2)\left(\frac{M}{w_0}\right)^2\right]^{-1/2} \tag{18.47}$$

Once the critical remote stress for the composite laminated skin has been determined, the critical load for the whole stiffened panel can be estimated as

$$P_{\mathrm{cr}} = \sigma_{\mathrm{cr}}^{\mathrm{skin}} \left(W t_{\mathrm{sk}} + N \frac{E_1^{\mathrm{str}}}{E_1} V \right) \tag{18.48}$$

where t_{sk} is the thickness of the skin, V is the cross-section area of the stringer, N is the number of stringers and E_1^{str} is the effective longitudinal Young's modulus for the stringer. The values of the effective constants for the particular layup of the stringer can be calculated using the classical laminate theory (Tan, 1994). The cross-section area of the stringer is given by

$$V = t_{\mathrm{str}}(w_{\mathrm{b}} + w_{\mathrm{c}} + h - 2t_{\mathrm{str}} - w_{\mathrm{t}}) \tag{18.49}$$

where t_{str} is the thickness of the stringer, w_{b} is the width of the base, w_{c} is the width of the cap, h is the height of the stringer and w_{t} is the width of the tapered part of the stringer, Figure 18.13.

Here, the final formula for the critical load P_{cr} of the stiffened panel, accounting for all geometric and material parameters, is derived from the equations of Sections 18.3.3 and 18.3.4. First, for the infinite quasi-isotropic panel with a circular hole, Eqns (18.35), (18.38), (18.48) and (18.49) yield

$$P_{\mathrm{cr}} = \frac{1}{3} G_{12} \left[1 - \frac{G_{12}^2}{E_1 E_2} \right] \left[W t_{\mathrm{sk}} + N \frac{E_1^{\mathrm{str}}}{E_1} t_{\mathrm{str}}(w_{\mathrm{b}} + w_{\mathrm{c}} + h - 2t_{\mathrm{str}} - w_{\mathrm{t}}) \right] \tag{18.50}$$

Taking into account ellipticity of the cut-out, Eqn (18.50) becomes

$$P_{\mathrm{cr}} = G_{12} \left[1 - \frac{G_{12}^2}{E_1 E_2} \right] \left[W t_{\mathrm{sk}} + N \frac{E_1^{\mathrm{str}}}{E_1} t_{\mathrm{str}}(w_{\mathrm{b}} + w_{\mathrm{c}} + h - 2t_{\mathrm{str}} - w_{\mathrm{t}}) \right] \frac{b}{2a + b} \tag{18.51}$$

Introducing through-the-thickness heterogeneity of the skin, results in

$$P_{\mathrm{cr}} = \frac{E_1}{E_1'} G_{12}' \left[1 - \frac{G_{12}'^2}{E_1' E_2'} \right] \left[W t_{\mathrm{sk}} + N \frac{E_1^{\mathrm{str}}}{E_1} t_{\mathrm{str}}(w_{\mathrm{b}} + w_{\mathrm{c}} + h - 2t_{\mathrm{str}} - w_{\mathrm{t}}) \right] \frac{b}{2a + b} \tag{18.52}$$

and incorporating the influence of the FWC factor obtains

$$P_{cr} = \frac{E_1}{E_1'} G_{12}' \left[1 - \frac{G_{12}'^2}{E_1' E_2'}\right] \left[W t_{sk} + N \frac{E_1^{str}}{E_1} t_{str}(w_b + w_c + h - 2t_{str} - w_t)\right] \frac{b}{2a+b}$$

$$\times \left\{ \frac{a(a-2b)}{(a-b)^2} \sqrt{1 + 2\frac{b^2 - a^2}{(W-S)^2} \left[\sqrt{1 - 8\left(3\left(1 - \frac{2a}{W-S}\right)\left(2 + \left(1 - \frac{2a}{W-S}\right)^3\right)^{-1} - 1\right)} - 1 \right]} \right.$$

$$+ \left(\frac{b}{a-b}\right)^2 - \frac{2ab^2}{(a-b)(W-S)^2} \left[\sqrt{1 - 8\left(3\left(1 - \frac{2a}{W-S}\right)\left(2 + \left(1 - \frac{2a}{W-S}\right)^3\right)^{-1} - 1\right)} - 1 \right]$$

$$\left. \times \left[1 + 2\frac{b^2 - a^2}{(W-S)^2} \left(\sqrt{1 - 8\left(3\left(1 - \frac{2a}{W-S}\right)\left(2 + \left(1 - \frac{2a}{W-S}\right)^3\right)^{-1} - 1\right)} - 1 \right) \right]^{-1/2} \right\} \tag{18.53}$$

Finally, considering fibre waviness, fibre interaction and other imperfections, Eqn (18.53) becomes

$$P_{cr} = F_{k-d} \frac{E_1}{E_1'} G_{12}' \left[1 - \frac{G_{12}'^2}{E_1' E_2'}\right] \left[W t_{sk} + N \frac{E_1^{str}}{E_1} t_{str}(w_b + w_c + h - 2t_{str} - w_t)\right] \frac{b}{2a+b}$$

$$\times \left\{ \frac{a(a-2b)}{(a-b)^2} \sqrt{1 + 2\frac{b^2 - a^2}{(W-S)^2} \left[\sqrt{1 - 8\left(3\left(1 - \frac{2a}{W-S}\right)\left(2 + \left(1 - \frac{2a}{W-S}\right)^3\right)^{-1} - 1\right)} - 1 \right]} \right.$$

$$+ \left(\frac{b}{a-b}\right)^2 - \frac{2ab^2}{(a-b)(W-S)^2} \left[\sqrt{1 - 8\left(3\left(1 - \frac{2a}{W-S}\right)\left(2 + \left(1 - \frac{2a}{W-S}\right)^3\right)^{-1} - 1\right)} - 1 \right]$$

$$\left. \times \left[1 + 2\frac{b^2 - a^2}{(W-S)^2} \left(\sqrt{1 - 8\left(3\left(1 - \frac{2a}{W-S}\right)\left(2 + \left(1 - \frac{2a}{W-S}\right)^3\right)^{-1} - 1\right)} - 1 \right) \right]^{-½} \right\} \tag{18.54}$$

Equations (18.54) takes into account all geometric and material variables and provides an easy way of examining the effect of each parameter on the critical failure load of a stiffened composite panel under uniaxial compression, where large out-of-plane deflections do not occur.

Results for the critical load of the type 1 composite panel (Greenhalgh et al., 1999) damaged at the bay (impact energy 15 J, damage width 56.9 mm and damage length 49.5 mm) are presented in Figure 18.15. For computations, the impacted region was replaced by an equivalent open hole (circular or elliptical) determined from C-scan and X-ray images. Geometries of the stiffened plate correspond to Figures 18.13 and 18.14 and Table 18.1. The properties of laminates, which enter Eqns

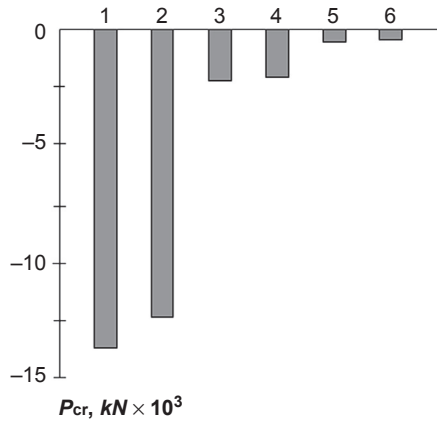

Figure 18.15 Critical loads as predicted by different models: bars one to five are the analytical predictions derived using Eqns (18.50)–(18.54), respectively.
Bar six corresponds to the experimental data of Greenhalgh et al. (1999).

(18.50)–(18.54), were calculated from the classical laminate theory according to the actual layups for the plate and stiffeners (see Section 18.3.4) from the properties of the unidirectional composite given in Table 18.2. Bars one to five in Figure 18.15 are the analytical predictions derived using Eqn (18.50) (circular cut-out), Eqn (18.51) (elliptic cut-out), Eqn (18.52) (effect of the through-the-thickness heterogeneity of the skin), Eqn (18.53) (influence of the skin finite width) and Eqn (18.54) (influence of the fibre waviness and fibre interaction), respectively. Bar six corresponds to the experimental data (Greenhalgh et al., 1999).

In the range of model applicability, critical loads predicted considering the phenomenon at the micro level and taking into account the geometry of plate and stiffeners are close to those of measured data. It should also be said that the scatter in the measurement of material constants could introduce additional errors.

18.4 Concluding remarks

In the first part of the chapter, the investigation of the internal instability for different types of layered materials, namely hyperelastic incompressible, compressible linear-elastic and elastic–plastic layers was held. The analyses of different loading schemes and precritical conditions was carried out using developed software package with fully automated numerical procedure. MATLAB was used to create the software with a graphical user-friendly interface and the database of material properties.

The second part of the chapter dealt with one of the possible applications of the models developed in the first part. Carbon fibre composite materials are sensitive to open holes, defects and low-velocity impact that can cause barely visible damage that can significantly reduce their stiffness and strength properties. To develop structures

that are more damage resistant and tolerant, it is necessary to understand how the damage is caused and how it can affect residual performance. A typical aircraft structure such as a fuselage shell or a wing surface usually consists of a skin reinforced with stiffeners. Most research on open holes and impact damage in carbon-fibre composites are based on testing of small laminates rather than structural elements or full-scale structures. In this chapter, an analytical formula based on 3-D stability theory was presented for calculating the unnotched compressive strength of a multidirectional composite plate. Then the maximum stress failure criterion was employed to estimate the critical load of a stiffened panel with an equivalent open hole loaded in compression; of course other stress based failure criteria could easily be used in the analysis.

In the range of model applicability, critical loads predicted by the model are close to those of measured data. It should also be recognised that the scatter in the measurement of material constants could introduce additional errors. The maximum stress criterion predicts the strength with a reasonable accuracy as long as a reduced-elastic SCF is used. This is to account for stress redistribution due to local damage at the edge of the hole and is determined by fitting the available experimental data and comparing with analytical solution for simpler problems.

Acknowledgements

Financial support of the part of this research by The Royal Society, The Royal Academy of Engineering and The Carnegie Trust for the Universities of Scotland is gratefully acknowledged.

References

Aboudi, J. (1987). Damage in composites − modelling of imperfect bonding. *Composite Science and Technology, 28*(2), 103−128.

Babich, I. Y., & Guz, A. N. (1969). Deformation instability of laminated materials. *Soviet Applied Mechanics, 5*(3), 53−57.

Babich, I. Y., & Guz, A. N. (1972). On the theory of elastic stability of compressible and incompressible composite media. *Polymer Mechanics, 5*.

Berbinau, P., Soutis, C., Goutas, P., & Curtis, P. T. (1999). Effect of off-axis ply orientation on 0°-fibre microbuckling. *Composites Part A, 30*(10), 1197−1207.

Berbinau, P., Soutis, C., & Guz, I. A. (1999). Compressive failure of 0° unidirectional carbon-fibre-reinforced plastic (CFRP) laminates by fibre microbuckling. *Composites Science and Technology, 59*(9), 1451−1455.

Biot, M. A. (1965). *Mechanics of incremental deformations*. New York: Wiley.

Budiansky, B., & Fleck, N. A. (1994). Compressive kinking of fibre composites: a topical review. *Applied Mechanics Reviews, 47*(6), S246−S270.

Degenhardt, R., Kling, A., Klein, H., Hillger, W., Goetting, H. C., Zimmermann, R., et al. (2007). Experiments on buckling and postbuckling of thin-walled CFRP structures using advanced measurement systems. *International Journal of Structural Stability and Dynamics, 7*(2), 337−358.

Diamanti, K., Soutis, C., & Hodgkinson, J. M. (2007). Piezoelectric transducer arrangement for the inspection of large composite structures. *Composites Part A: Applied Science and Manufacturing, 38*(4), 1121−1130.

Dow, N. F., & Grunfest, I. J. (1960). *Determination of most needed potentially possible improvements in materials for ballistic and space vehicles*. General Electric Co., Space Sciences Lab. TISR 60 SD389.

Falzon, B. G., Davies, G. A. O., & Greenhalgh, E. (2001). Failure of thick-skinned stiffener runout sections loaded in uniaxial compression. *Composites Structures, 53*, 223−233.

Found, M. S., Howard, I. C., & Paran, A. P. (2002). Modelling the impact behaviour of thin CERP panels. *Key Engineering Materials, 221−222*, 187−196.

Greenhalgh, E. S., Bishop, S., Bray, D., Hughes, D., Lahiff, S., & Millson, B. (1996). Characterisation of impact damage in skin-stringer composite structures. *Composites Structures, 36*(3−4), 187−207.

Greenhalgh, E., & Garcia, M. H. (2004). Fracture mechanisms and failure processes at stiffener run-outs in polymer matrix composite stiffened elements. *Composites Part A: Applied Science and Manufacturing, 35*, 1447−1458.

Greenhalgh, E., & Hiley, M. (2003). The assessment of novel materials and processes for the impact tolerant design of stiffened composite aerospace structures. *Composites Part A: Applied Science and Manufacturing, 34*, 151−161.

Greenhalgh, E., Singh, S., Hughes, D., & Roberts, D. (1999). Impact damage resistance and tolerance of stringer stiffened composite structures. *Plastics, Rubber and Composites, 28*(5), 228−251.

Guynn, E. G., Bradley, W. L., & Ochoa, O. (1992). A parametric study of variables that affect fibre microbuckling initiation in composite laminates: part 1- analyses, part 2−experiments. *Journal of Composite Materials, 26*(11), 1594−1627.

Guz, A. N. (1969). On setting up a stability theory of unidirectional fibrous materials. *Soviet Applied Mechanics, 5*(2), 156−162.

Guz, I. A. (1989a). Spatial nonaxisymmetric problems of the theory of stability of laminar highly elastic composite materials. *Soviet Applied Mechanics, 25*(11), 1080−1085.

Guz, I. A. (1989b). Three-dimensional nonaxisymmetric problems of the theory of stability of composite materials with a metallic matrix. *Soviet Applied Mechanics, 25*(12), 1196−1201.

Guz, A. N. (Ed.). (1992), *Applied mechanics reviews: Vol. 5. Micromechanics of composite materials: Focus on Ukrainian research* (pp. 15−101).

Guz, I. A. (1998). Composites with interlaminar imperfections: substantiation of the bounds for failure parameters in compression. *Composites Part B, 29*(4), 343−350.

Guz, A. N. (1999). *Fundamentals of the three-dimensional theory of stability of deformable bodies*. Berlin-Heidelberg: Springer-Verlag.

Guz, I. A. (2005). The effect of the multi-axiality of compressive loading on the accuracy of a continuum model for layered materials. *International Journal of Solids and Structures, 42*(2), 439−453.

Guz, I. A., & Herrmann, K. P. (2003). On the lower bounds for critical loads under large deformations in non-linear hyperelastic composites with imperfect interlaminar adhesion. *European Journal of Mechanics, A/Solids, 22*(6), 837−849.

Guz, I. A., & Soutis, C. (1999). Continuum fracture theory for layered materials: Investigation of accuracy. *Zeitschrift für Angewandte Mathematik und Mechanik (ZAMM), 79*(S2), S503−S504.

Guz, I. A., & Soutis, C. (2000). Critical strains in layered composites with interfacial defects loaded in uniaxial or biaxial compression. *Plastics, Rubber and Composits, 29*(9), 489−495.

Guz, I. A., & Soutis, C. (2001a). A 3-D stability theory applied to layered rocks undergoing finite deformations in biaxial compression. *European Journal of Mechanics - A/Solids, 20*(1), 139−153.

Guz, I. A., & Soutis, C. (2001b). Compressive fracture of non-linear composites undergoing large deformations. *International Journal of Solids & Structures, 38*(21), 3759−3770.

Honeycombe, R. W. K. (1968). *The plastic deformation of metals*. London: Edward Arnold.

Ishikawa, T., Matsushima, M., Hayashi, Y., & Scott, M. L. (2005). Experiments and numerical analysis of compression after impact (CAI) behavior of CF/PIXA stiffened panels for HSCT structure. *Advanced Composite Materials: The Official Journal of the Japan Society of Composite Materials, 14*(3), 239−261.

Jegley, D. C. (1992). *Effect of low-speed impact damage and damage location on behavior of composite panels*. NASA Technical Paper 3196.

Jegley, D. C. (1998). Behavior of compression-loaded composite panels with stringer terminations and impact damage. *AIAA*. Paper 98-1785-CP.

Kashtalyan, M., & Soutis, C. (2001). Strain energy release rate for off-axis ply cracking in laminated composites. *International Journal of Fracture, 112*(2), L3−L8.

Kashtalyan, M., & Soutis, C. (2006). Modelling off-axis ply matrix cracking in continuous fibre-reinforced polymer matrix composite laminates. *Journal of Materials Science, 41*(20), 6789−6799.

Kong, C.-W., Lee, I.-C., Kim, C.-G., & Hong, C.-S. (1998). Postbuckling and failure of stiffened composite panels under axial compression. *Composites Structures, 42*(1), 13−21.

Kouri, J. V., & Atluri, S. N. (1993). Analitical modelling of laminated composites. *Composites Science and Technology, 46*(4), 335−344.

Leissa, A. W. (1987). An overview of composite plate buckling. *Composite Structures, 4*(1), 1.1−1.29. Analysis and Design Studies.

Librescu, L., & Schmidt, R. (2001). A general linear theory of laminated composite shells featuring interlaminar bonding imperfections. *International Journal of Solids & Structures, 38*(19), 3355−3375.

Ling, X. W., & Atluri, S. N. (2007). A hyperelastic description of single wall carbon nanotubes at moderate strains and temperatures. *CMES: Computer Modeling in Engineering & Sciences, 21*(1), 81−91.

Menshykova, M. V., Guz, I. A., & Menshykov, O. V. (2009). A unified computational approach to instability of periodic laminated materials. *Computer Modelling in Engineering & Sciences (CMES), 51*(3), 239−259.

Moran, P., Liu, L., & Shih, C. (1995). Kinking band formation and band broadening in fibre composites under compressive loading. *Acta Metallutgica at Materialia, 43*(8), 2943−2958.

Nemeth, M. P. (1996). *Buckling and post buckling behavior of laminated composite plates with a cut-out*. NASA Technical Paper 3587.

Niu, K., & Talreja, R. (2000). Modelling of compressive failure in fiber reinforced composites. *International Journal of Solids & Structures, 37*(17), 2405−2428.

Pinnel, M. R., & Lawley, A. (1970). Correlation of yielding and structure in aluminium-stainless steel composites. *Metallurgical Transactions, 1*(5), 1337−1348.

Rosen, B. W. (1965). Mechanics of composite strengthening. *Fiber Composite Materials, American Society of Metals, Metals Park*, 37−75. ch.3.

Sadovsky, M. A., Pu, S. L., & Hussain, M. A. (1967). Buckling of microfibers. *Journal of Applied Mechanics, 34*(12), 1011−1016.

Schuerch, H. (1966). Prediction of compressive strength in uniaxial boron fibre-metal matrix composite materials. *AIAA Journal, 4*(1), 102−106.

Schultheisz, C., & Waas, A. (1996). Compressive failure of composites, parts I and II. *Progress in Aerospace Science, 32*(1), 1−78.

Soutis, C. (1994). Damage tolerance of open-hole CFRP laminates loaded in compression. *Composite Engineering, 4*(3), 317−327.

Soutis, C. (2000). Compression testing of pultruded carbon fibre-epoxy cylindrical rods. *Journal of Materials Science, 34*(14), 3441−3446.

Soutis, C., & Curtis, P. (1996). Prediction of the post-impact compressive strength of CFRP laminated composites. *Composite Science & Technology, 56*(6), 677−684.

Soutis, C., & Fleck, N. (1990). Static compression failure of carbon fibre T800/924C composite plate with a single hole. *Journal of Composite Materials, 24*(5), 536−558.

Soutis, C., Fleck, N. A., & Smith, P. A. (1991). Failure prediction technique for compression loaded carbon fibre-epoxy laminate with an open hole. *Journal of Composite Materials, 25*(11), 1476−1498.

Soutis, C., & Guz, I. A. (2001). Predicting fracture of layered composites caused by internal instability. *Composites, Part A, 32*(9), 1243−1253.

Soutis, C., & Guz, I. A. (2006). Fracture of layered composites by internal fibre instability: effect of interfacial adhesion. *The Aeronautical Journal, 110*(1105), 185−195.

Soutis, C., & Turkmen, D. (1995). Influence of shear properties and fibre imperfections on the compressive behaviour of CFRP laminates. *Applied Composite Materials, 2*(6), 327−342.

Stevens, K. A., Ricci, R., & Davies, G. A. O. (1995). Buckling and postbuckling of composite structures. *Composites, 26*(2), 189−199.

Tan, S. C. (1994). *Stress concentrations in laminated composites*. Lancaster Basel: Technomic Publishing.

Timoshenko, S. P., & Goodier, J. N. (1987). *Theory of elasticity* (3rd ed.). McGraw-Hill.

Treloar, L. R. G. (1975). *The physics of rubber elasticity*. Oxford University Press.

Winiarski, B., & Guz, I. A. (2008). The effect of fibre volume fraction on the onset of fracture in laminar materials with an array of coplanar interface cracks. *Composites Science and Technology, 68*(12), 2367−2375.

Zhuk, Y., Guz, I. A., & Soutis, C. (2001). Failure analysis of a stiffened composite plate with a hole under compression. *Zeitschrift für Angewandte Mathematik und Mechanik (ZAMM), 81*(S2), S383−S384.

Zhuk, Y., Soutis, C., & Guz, I. A. (2000). Prediction of the compression-after-impact strength of thin-skin stiffened composite panels. *Advanced Composites Letters, 9*(4), 295−301.

Zhuk, Y., Soutis, C., & Guz, I. A. (2001). Behaviour of thin-skin stiffened CFRP panels with a stress concentrator under in-plane compression. *Composites Part B, 32*(8), 697−709.

Zhuk, Y., Soutis, C., & Guz, I. A. (2002). Stiffened composite panels with a stress concentrator under in-plane compression. *International Applied Mechanics, 38*(2), 240−252.

Analysis of delamination in laminates with angle-ply matrix cracks: onset of damage and residual stiffness properties

19

M. Kashtalyan[1], *C. Soutis*[2]
[1]University of Aberdeen, Aberdeen, Scotland, UK; [2]University of Manchester, Manchester, UK

19.1 Introduction

The failure process of fibre-reinforced composite laminates subjected to static or fatigue tensile or thermal loading involves sequential accumulation of intra- and interlaminar damage in the form of matrix cracking and delamination. Intralaminar matrix cracks running parallel to the fibres in off-axis plies of the laminate are the dominant damage mechanism during the initial stages of the failure process. These cracks either are arrested at the interface or cause interfacial failure leading to delamination and/or cracking in the adjacent plies due to high interlaminar stresses at the ply interface. Under quasi-static loading, the strain corresponding to the nucleation of matrix cracking decreases with increasing 90° ply thickness (Parvizi, Garrett, & Bailey, 1978). Under fatigue loading, transverse ply cracking may occur very early in the fatigue life of the specimen, with the cycle number at formation increasing with the decreasing loading amplitude (Daniel & Charewicz, 1986).

Studies of delaminations induced by matrix cracking have been focussing predominantly on delaminations caused by transverse cracks, that is, matrix cracks in the 90° plies of a laminate. Crossman and Wang (1982) made comprehensive observations of transverse cracking and delamination in balanced symmetric $[\pm 25/90_n]_s$, $n = 0.5$, 1, 2, 3, 4, 6, 8 graphite/epoxy laminates. A significant reduction in the delamination onset strain was noted for the laminates with $n \geq 4$. A transition from edge delamination to local delaminations growing from the tip of a matrix crack in the 90° ply occurred between $n = 3$ and $n = 4$. The onset and growth of edge delamination in $[(\pm 30)_2/90/\overline{90}]_s$ graphite/epoxy laminates under static tension and tension−tension fatigue loading was studied by O'Brien (1982). Stiffness loss was monitored simultaneously with delamination growth and found to decrease linearly with delamination size.

Charewicz and Daniel (1986) observed damage accumulation in AS4/3501-6 carbon/epoxy cross-ply laminates under tension−tension fatigue. They observed five different damage mechanisms, namely: transverse cracking in the 90° plies; randomly distributed longitudinal cracking in the 0° plies; profound localised longitudinal cracking; delamination at the 0/90 interface along transverse cracks, particularly

Structural Integrity and Durability of Advanced Composites. http://dx.doi.org/10.1016/B978-0-08-100137-0.00019-5

in $[0/90_4]_s$ and $[90_4/0]_s$ laminates; and small local delamination at the intersection of longitudinal and transverse cracks. Initiation and growth of local delaminations from the tips of transverse cracks in cross-ply $[0/90_n]_s$ $n = 2, 4, 6$ carbon/epoxy laminates under static tension was examined by Takeda and Ogihara (1994) and Takeda, Ogihara, and Kobayashi (1995). Delamination was noted to grow more rapidly and extensively in the laminates with thicker 90° plies.

When a cross-ply laminate is subjected to biaxial tensile or thermal loading, matrix cracking can occur in both the 90° and 0° plies and local delaminations can then initiate and grow from the tips of these cracks. Henaff-Gardin, Lafarie-Frenot, and Gamby (1996b) observed damage development in carbon/epoxy cross-ply $[0_4/90_4]_s$ laminates under thermal cycling in the temperature range from −200 °C to +130 °C. The first damage mode observed consisted of matrix cracks in 0° and 90° plies. These cracks grew in number more or less rapidly and reached a saturation stage. The crack multiplication in the 90° plies was faster than in the 0° plies, which agrees with the observations of Charewicz and Daniel (1986) under mechanical fatigue loading. Most of the matrix cracks spanned the entire width or length of the specimen. In two groups of tests, characterised by heating the specimens to a higher temperature (90 °C or 130 °C), a second damage mode was observed. It consisted of delaminations between 0° and 90° plies along the pre-existing cracks. This kind of damage formed when cracks began to saturate in number. First delaminations nucleated along the 0° ply cracks, followed by delaminations along the 90° ply cracks.

Kobayashi, Terada, Ogihara, and Takeda (2001) observed damage development in carbon/epoxy AS4/PEEK $[0_2/90_2]_s$ cross-ply laminates under thermal cycling in the temperature range from −196 °C to +150 °C or 250 °C. The first damage mode observed consisted of matrix cracks in 0° and 90° plies. Most of the matrix cracks spanned the entire width or length of the specimen. Then delaminations initiated along the matrix cracks in 0° ply.

Delaminations induced by angle-ply matrix cracks in carbon/epoxy $[0_2/\theta_2/-\theta_2]_s$ $\theta = 20°$, 25°, 30° laminates subjected to tension fatigue loading were observed by O'Brien and Hooper (1991) and O'Brien (1991). Matrix cracks formed near the stress-free edge and delaminations, bounded by the free edge and the crack, developed in the $\theta/(-\theta)$ interface. They were termed partial local delaminations.

Figure 19.1 summarises schematically types of crack-induced delaminations in some composite laminates. They include transverse crack tip delaminations in cross-ply and balanced symmetric laminates (Figure 19.1(a)), transverse and longitudinal crack tip delaminations in cross-ply laminates (Figure 19.1(b)), and uniform (Figure 19.1(c)) and partial (Figure 19.1(d)) local delaminations induced by angle-ply matrix cracks and crack-induced edge delaminations (Figure 19.1(e)).

19.2 Residual stiffness of composite laminate with crack-induced delaminations

Stiffness loss due to delaminations has not been as thoroughly investigated as their initiation and growth. O'Brien (1985) was apparently the first who examined the

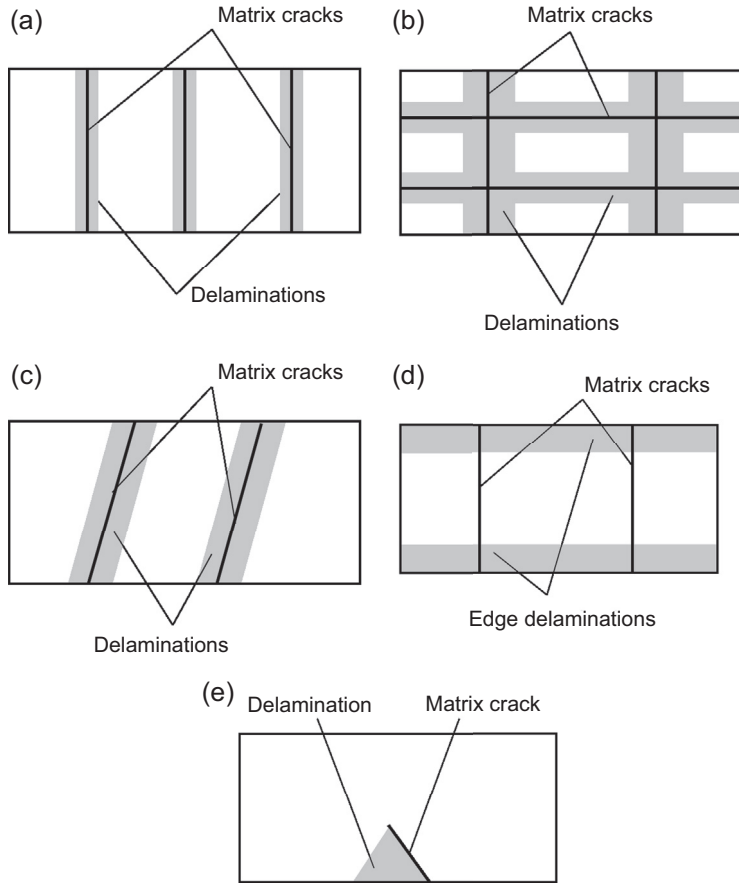

Figure 19.1 Types of matrix crack-induced delaminations in fibre-reinforced composite laminates (front view): (a) transverse crack tip delaminations in cross-ply and balanced symmetric laminates; (b) transverse and longitudinal crack tip delaminations in cross-ply laminates; (c) uniform local delamination induced by angle-ply matrix cracks; (d) edge delamination induced by transverse cracks; (e) partial local delamination induced by angle-ply matrix crack.

influence of matrix crack tip delamination on the laminate stiffness and strength. The linear degradation of the laminate modulus with delamination area, observed for graphite/epoxy laminates (O'Brien, 1985), was predicted also for glass/epoxy laminates using a simple rule of mixture analysis (Caslini, Zanotti, & O'Brien, 1987). A simple 1-D shear lag analysis using the concept of interlaminar shear layer (Fukunaga, Chou, Peters, & Schulte, 1984) was extended by Ogihara and Takeda (1995) to the laminates containing delamination originating from the tips of transverse cracks and used to predict the Young's modulus reduction. Theoretical predictions for the $[0/90_n]_s$ ($n = 2, 4, 6$) carbon fibre-reinforced polymer (CFRP) cross-ply laminates were in good agreement with experimental data. Better agreement of shear lag predictions for the Young's modulus reduction with the experimental data was observed,

however, when the interaction between transverse cracks and delaminations was taken into account (Ogihara & Takeda, 1995).

Zhang, Soutis, and Fan (1994b) extended a modified 2-D shear lag approach (Zhang, Fan, & Soutis, 1992a) to analyse balanced $[\pm\theta_m/90_n]_s$ laminates, damaged by transverse cracking and local delaminations growing from transverse crack tips. Consequently, closed-form expressions were derived for the reduced stiffness properties of the damaged 90° layer, representing them as functions of cracking density and relative delamination area.

Ogihara and Takeda (1995) used a modified shear lag method featuring interlaminar shear layer to predict Young's modulus reduction due to transverse crack tip delaminations in cross-ply $[0/90_n]_s$ laminates.

Transverse ply cracking and transverse crack tip delaminations in the general symmetric laminates with the central 90° ply have been theoretically investigated by Zhang, Fan, and Herrmann (1999). A sub-laminate-wise first-order shear deformation theory was extended to the case of delaminations induced by transverse cracks. The extension stiffness reduction of the constrained 90° ply was calculated as a function of delamination length and transverse cracking spacing. Numerical results have shown that stiffness reduction of the 90° ply strongly depends upon the orientation of the adjacent ply group, with the remote constraining layer having negligible influence.

Zhang and Minnetyan (2006) developed a displacement-based variational model to study the effect of transverse cracking and local delamination in symmetric composite laminates, assuming the crack shape to be a function of crack density and delamination length. Using a variational approach, they examined the effect of delamination on the effective Young's modulus of the laminate and the strain energy release rate.

In all above studies of crack-induced delaminations it was assumed that delamination surfaces, like matrix crack surfaces are stress free. Besides that, delaminations were assumed to behave in a self-similar manner, that is, boundary conditions prescribed at the delaminated surfaces were assumed to be the same for small and large delaminations. More recently, Ashkantala and Talreja (1998) and Berthelot and Le Corre (2000) examined transverse crack tips delaminations in cross-ply laminates with shear friction between the delaminated plies. While Berthelot and Le Corre (2000) assumed the magnitude of the interlaminar shear stress at the delaminated interface to be constant, that is, independent of delamination length, Ashkantala and Talreja (1998) considered both linear and cubic polynomial shear stress distribution at the delamination interface. Selvarathinam and Weitsman (1998, 1999) observed and modelled, by means of finite elements (FE) and shear lag methods, delaminations induced by matrix cracking in cross-ply laminates under environmental fatigue, with delamination surface loaded with hydrostatic pressure.

To estimate degraded stiffness properties of the laminate damaged by cracks and delaminations, stress analysis needs to be carried out first. Figure 19.2 shows a schematic of a symmetric $[(S)/\varphi]_s$ laminate, consisting of the outer sub-laminate (S) and the inner φ-layer damaged by matrix cracks and local delaminations growing from their tips at the $(S)/\varphi$ interface. The outer sub-laminate (S), or layer 1,

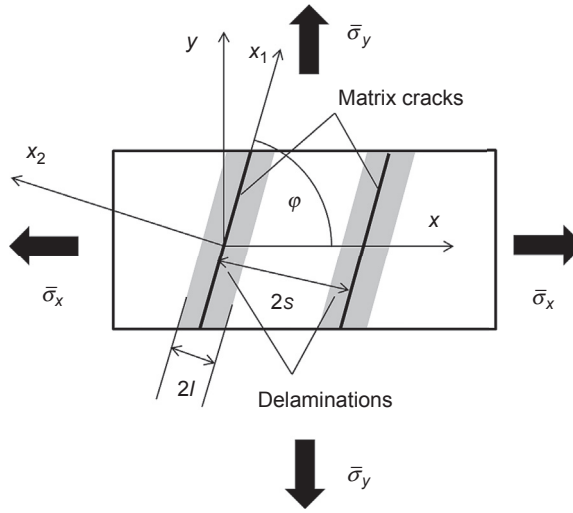

Figure 19.2 Front view of a $[(S)/\varphi]_s$ laminate subjected to biaxial tensile loading and damaged by matrix cracks and uniform local delaminations. Local ($x_1x_2x_3$) and global (xyz) coordinate systems for the damaged φ-layer.

may consist of either a single layer or a group of layers and can also be damaged (in this case it needs to be replaced in the analysis with an equivalent homogeneous layer with reduced stiffness properties). The laminate is referred to the global Cartesian coordinate system xyz and local coordinate system $x_1x_2x_3$, with the axis x_1 directed along the fibres in the damaged φ-layer, or layer 2. The laminate is subjected to in-plane biaxial tension $\overline{\sigma}_x$ and $\overline{\sigma}_y$. Since the laminate is symmetric, no coupling exists between in-plane loading and out-of-plane deformation. Matrix cracks are assumed to be spaced uniformly, with crack spacing $2s$, and span the whole width of the laminate. Local delaminations are assumed to be strip shaped, with strip width 2ℓ, Figure 19.2.

Due to the periodicity of damage, the stress analysis may be carried out over a representative segment containing one matrix crack and two crack tip delaminations. Due to symmetry, it can be further restricted to one quarter of the representative segment, Figure 19.3, referred to the local coordinate system $x_1x_2x_3$.

For cross-ply laminates with transverse and longitudinal crack tip delaminations (Figure 19.1(b)), a representative segment could be defined by intersecting pair of transverse and longitudinal cracks. However, analysis of such segment is rather cumbersome even in the absence of delaminations (Hashin, 1987; Henaff-Gardin et al., 1996; Tsai & Daniel, 1992). Kashtalyan and Soutis (1999a,b, 2000a,b) suggested analysis of cross-ply laminates with damage in both plies using the equivalent constraint model (ECM). Instead of the damaged laminate, two ECM laminates are considered and analysed simultaneously. In the first laminate, 0° layers contain damage explicitly, while 90° plies are replaced with equivalent homogeneous ones with reduced stiffness properties. These reduced stiffness

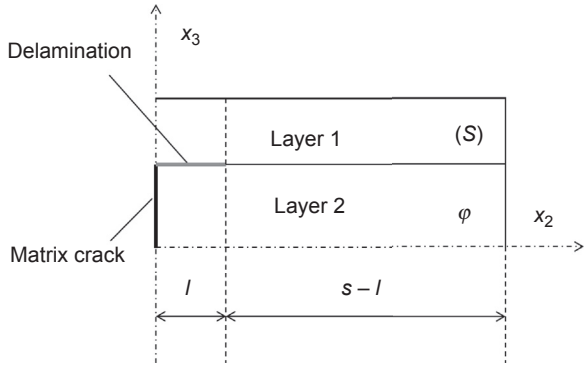

Figure 19.3 A quarter of the representative segment containing matrix crack and delamination.

properties are assumed to be known from the analysis of the second laminate, in which the 90° layer contains damage explicitly, while the damages in 0° plies are replaced with equivalent homogeneous ones with reduced properties, assumed to be known from the analysis of the first laminate. Thus, problems for both laminates are interrelated. Application of the ECM to quasi-isotropic laminates with matrix cracking in all but 0° layers was presented by Zhang and Herrmann (1999) and to angle-ply laminates with matrix cracks by Kashtalyan and Soutis (2000c, 2005).

19.2.1 Stress analysis

Let $\{\tilde{\sigma}^{(1)}\}$ and $\{\tilde{\varepsilon}^{(1)}\}$ denote the in-plane micro-stresses and micro-strains in layer 1, and $\{\tilde{\sigma}^{(2)}\}$ and $\{\tilde{\varepsilon}^{(2)}\}$ denote the in-plane micro-stresses and micro-strains in layer 2 (i.e. stresses and strains averaged across the respective layer thickness). Since it is assumed that there is no frictional contact between the layers in the locally delaminated portion of the representative segment ($0 < |x_2| < \ell$, $|x_3| < h_2$), the in-plane micro-stresses in the delaminated portion are $\tilde{\sigma}_{22}^{(2)} = \tilde{\sigma}_{12}^{(2)} = 0$, that is, this region is stress free. Assumption of stress-free crack tip delamination surfaces, and the resulting implication that the portion of the damaged ply bounded by matrix crack and delamination surfaces is stress-free, has been widely used in the studies of delaminations. Besides that, delaminations are assumed to behave in a self-similar manner, that is, the boundary conditions prescribed at the delaminated surfaces were assumed to be the same for small and large delaminations.

In the perfectly bonded region ($\ell < |x_2| < s$) of the representative segment, the in-plane micro-stresses are determined from the equilibrium equations

$$\frac{\mathrm{d}\tilde{\sigma}_{j2}^{(2)}}{\mathrm{d}x_2} - \frac{\tau_j}{h_2} = 0 \quad j = 1, 2 \tag{19.1}$$

where τ_j are the interface shear stresses and h_2 is the thickness of the φ-layer.

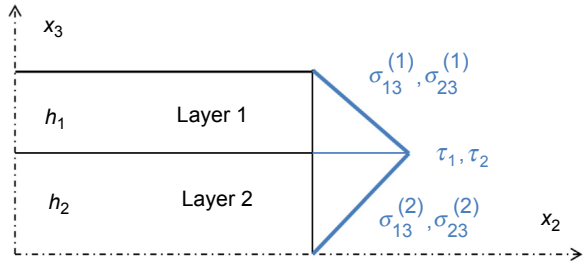

Figure 19.4 Variation of out-of-plane shear stresses through the thickness.

By averaging the out-of-plane constitutive equations for both layers across the layer thickness, the interface shear stresses τ_j can be expressed in terms of the in-plane displacements and shear lag parameters K_{ij} as

$$\tau_j = K_{j1}\left(\tilde{u}_1^{(1)} - \tilde{u}_1^{(2)}\right) + K_{j2}\left(\tilde{u}_2^{(1)} - \tilde{u}_2^{(2)}\right) \tag{19.2}$$

The shear lag parameters K_{11}, K_{22}, $K_{12} \equiv K_{21}$ are determined assuming that the out-of-plane shear stresses $\tilde{\sigma}_{j3}^{(k)}$ vary linearly with x_3 (Figure 19.4); see Appendix A. Substitution of Eqn (19.2) into Eqn (19.1) and subsequent differentiation yields

$$\frac{\mathrm{d}^2\tilde{\sigma}_{j2}^{(2)}}{\mathrm{d}x_2} + K_{j1}\left(\tilde{\gamma}_{12}^{(1)} - \tilde{\gamma}_{12}^{(2)}\right) + K_{j2}\left(\tilde{\varepsilon}_{22}^{(1)} - \tilde{\varepsilon}_{22}^{(2)}\right) = 0, \quad j = 1,2 \tag{19.3}$$

The strain differences $(\tilde{\varepsilon}_{22}^{(1)} - \tilde{\varepsilon}_{22}^{(2)})$ and $(\tilde{\gamma}_{12}^{(1)} - \tilde{\gamma}_{12}^{(2)})$, involved in Eqn (19.3), can be expressed in terms of stresses $\tilde{\sigma}_{12}^{(2)}$, $\tilde{\sigma}_{22}^{(2)}$ using the constitutive equations for both layers, the laminate equilibrium equations below

$$\chi\left\{\tilde{\sigma}^{(1)}\right\} + \left\{\tilde{\sigma}^{(2)}\right\} = (1+\chi)[T]\{\overline{\sigma}\} \tag{19.4a}$$

$$[T] = \begin{bmatrix} \cos^2\varphi & \sin^2\varphi & 2\sin\varphi\cos\varphi \\ \sin^2\varphi & \cos^2\varphi & -2\sin\varphi\cos\varphi \\ -\sin\varphi\cos\varphi & \sin\varphi\cos\varphi & \cos^2\varphi - \sin^2\varphi \end{bmatrix} \tag{19.4b}$$

$$\{\overline{\sigma}\} = \{\sigma_x, \sigma_y, 0\}^T, \quad \chi = h_1/h_2 \tag{19.4c}$$

and the assumption of the generalised plane strain condition

$$\tilde{\varepsilon}_{11}^{(1)} = \tilde{\varepsilon}_{11}^{(2)} \tag{19.5}$$

In the local coordinate system $x_1x_2x_3$, layer 2 is orthotropic,

$$\begin{Bmatrix} \tilde{\varepsilon}_{11}^{(2)} \\ \tilde{\varepsilon}_{22}^{(2)} \\ \tilde{\gamma}_{12}^{(2)} \end{Bmatrix} = \begin{bmatrix} \widehat{S}_{11}^{(2)} & \widehat{S}_{12}^{(2)} & 0 \\ \widehat{S}_{12}^{(2)} & \widehat{S}_{22}^{(2)} & 0 \\ 0 & 0 & \widehat{S}_{66}^{(2)} \end{bmatrix} \begin{Bmatrix} \tilde{\sigma}_{11}^{(2)} \\ \tilde{\sigma}_{22}^{(2)} \\ \tilde{\sigma}_{12}^{(2)} \end{Bmatrix} \tag{19.6a}$$

while layer 1 is anisotropic,

$$\begin{Bmatrix} \tilde{\varepsilon}_{11}^{(1)} \\ \tilde{\varepsilon}_{22}^{(1)} \\ \tilde{\gamma}_{12}^{(1)} \end{Bmatrix} = \begin{bmatrix} \widehat{S}_{11}^{(1)} & \widehat{S}_{12}^{(1)} & \widehat{S}_{16}^{(1)} \\ \widehat{S}_{12}^{(1)} & \widehat{S}_{22}^{(1)} & \widehat{S}_{26}^{(1)} \\ \widehat{S}_{16}^{(1)} & \widehat{S}_{26}^{(1)} & \widehat{S}_{66}^{(1)} \end{bmatrix} \begin{Bmatrix} \tilde{\sigma}_{11}^{(1)} \\ \tilde{\sigma}_{22}^{(1)} \\ \tilde{\sigma}_{12}^{(1)} \end{Bmatrix} \tag{19.6b}$$

where $\left[\widehat{S}^{(k)}\right]$ is the compliance matrix for the kth layer.

Finally, Eqn (19.3) can be reduced to a system of two coupled second-order ordinary differential equations (see Appendix B):

$$\frac{\mathrm{d}^2\tilde{\sigma}_{12}^{(2)}}{\mathrm{d}x_2^2} - N_{11}\tilde{\sigma}_{12}^{(2)} - N_{12}\tilde{\sigma}_{22}^{(2)} - P_{11}\overline{\sigma}_x - P_{12}\overline{\sigma}_y = 0 \tag{19.7a}$$

$$\frac{\mathrm{d}^2\tilde{\sigma}_{22}^{(2)}}{\mathrm{d}x_2^2} - N_{21}\tilde{\sigma}_{12}^{(2)} - N_{22}\tilde{\sigma}_{22}^{(2)} - P_{21}\overline{\sigma}_x - P_{22}\overline{\sigma}_y = 0 \tag{19.7b}$$

Here N_{ij} and P_{ij} are laminate constants depending on the layer compliances $\widehat{S}_{ij}^{(k)}$, layer thickness ratio χ, shear lag parameters K_{11}, K_{22}, K_{12} and angle φ (Appendix B).

Equations (19.7a) and (19.7b) can be uncoupled at the expense of increasing the order of differentiation, resulting in a fourth-order non-homogeneous ordinary differential equation:

$$\begin{aligned} &\frac{\mathrm{d}^4\tilde{\sigma}_{22}^{(2)}}{\mathrm{d}x_2^4} - (N_{11}+N_{22})\frac{\mathrm{d}^2\tilde{\sigma}_{22}^{(2)}}{\mathrm{d}x_2^2} - (N_{21}N_{12} - N_{11}N_{22})\tilde{\sigma}_{22}^{(2)} \\ &\quad + [N_{11}(P_{21}+\alpha P_{22}) - N_{21}(P_{11}+\alpha P_{12})]\overline{\sigma}_x = 0 \end{aligned} \tag{19.8}$$

Here $\alpha = \overline{\sigma}_y/\overline{\sigma}_x$ is the biaxiality ratio. The boundary conditions for Eqn (19.8) are prescribed at the stress-free boundary between locally delaminated and perfectly bonded portions of the representative segment

$$\tilde{\sigma}_{22}^{(2)}\big|_{x_2=\pm\ell} = 0 \quad \tilde{\sigma}_{12}^{(2)}\big|_{x_2=\pm\ell} = 0 \tag{19.9}$$

Finally, the in-plane micro-stresses can be expressed in the following form:

$$\tilde{\sigma}_{11}^{(2)} = a_{22}\tilde{\sigma}_{22}^{(2)} + a_{12}\tilde{\sigma}_{12}^{(2)} + b_x\overline{\sigma}_x + b_y\overline{\sigma}_y \tag{19.10a}$$

$$\tilde{\sigma}_{j2}^{(2)} = \left[A_j \frac{\cosh\lambda_1(x_2 - s)}{\cosh\lambda_1(s - \ell)} + B_j \frac{\cosh\lambda_2(x_2 - s)}{\cosh\lambda_2(s - \ell)} + C_j\right]\overline{\sigma}_x \quad j = 1, 2 \tag{19.10b}$$

where coefficients a_{22}, a_{12}, b_x and b_y are given in Appendix B, λ_j are the roots of the characteristic equation and A_j, B_j and C_j are constants depending on N_{ij} and P_{ij}; see Appendix C.

In cross-ply and balanced laminates the outer sub-laminate (S) is orthotropic, with compliances $\widehat{S}_{16}^{(1)} = \widehat{S}_{26}^{(1)} = 0$ and stiffnesses $\widehat{Q}_{45}^{(1)} = 0$. In this case shear lag coefficients $K_{12} \equiv K_{21} = 0$ vanish, and equilibrium equations are reduced to two uncoupled second-order differential equations. Details of this case are given elsewhere (Kashtalyan & Soutis, 1999a, 2000a; Zhang et al., 1994b).

19.2.2 Stiffness degradation due to crack-induced delaminations

To determine the reduced stiffness properties of the damaged laminate, an 'equivalent' laminate, in which the damaged layer is replaced with an 'equivalent' homogeneous one with degraded stiffness properties, is considered. In the local coordinate system $x_1x_2x_3$, the constitutive equations of the 'equivalent' homogeneous layer are

$$\left\{\overline{\sigma}^{(2)}\right\} = \left[Q^{(2)}\right]\left\{\overline{\varepsilon}^{(2)}\right\} \tag{19.11}$$

In the local coordinates, the modified in-plane stiffness matrix $[Q^{(2)}]$ of the homogeneous layer equivalent to the damaged one is related to the in-plane stiffness matrix $[\widehat{Q}^{(2)}]$ of the undamaged layer as

$$\left[Q^{(2)}\right] = \left[\widehat{Q}^{(2)}\right] - \begin{bmatrix} \left(\widehat{Q}_{12}^{(2)}\right)^2/\widehat{Q}_{22}^{(2)}\Lambda_{22} & \widehat{Q}_{12}^{(2)}\Lambda_{22} & 0 \\ \widehat{Q}_{12}^{(2)}\Lambda_{22} & \widehat{Q}_{22}^{(2)}\Lambda_{22} & 0 \\ 0 & 0 & \widehat{Q}_{66}^{(2)}\Lambda_{66} \end{bmatrix} \tag{19.12}$$

Here $\Lambda_{22}^{(\mu)}$, $\Lambda_{66}^{(\mu)}$ are the in situ damage effective functions (IDEFs) (Zhang, Fan, & Soutis, 1992a). They can be expressed in terms of lamina macro-stresses and macro-strains as

$$\Lambda_{22} = 1 - \frac{\overline{\sigma}_{22}^{(2)}}{\widehat{Q}_{12}^{(2)}\overline{\varepsilon}_{11}^{(2)} + \widehat{Q}_{22}^{(2)}\overline{\varepsilon}_{22}^{(2)}}, \quad \Lambda_{66} = 1 - \frac{\overline{\sigma}_{12}^{(2)}}{\widehat{Q}_{66}^{(2)}\overline{\gamma}_{12}^{(2)}} \tag{19.13}$$

The lamina macro-stresses $\{\overline{\sigma}^{(2)}\}$ and macro-strains $\{\overline{\varepsilon}^{(2)}\}$ are obtained by averaging, respectively, micro-stresses $\{\tilde{\sigma}^{(2)}\}$, Eqn (19.10), and micro-strains $\{\tilde{\varepsilon}^{(2)}\}$, Eqn (19.6a), across the length of the representative segment. The lamina macro-stresses $\overline{\sigma}_{ij}^{(2)}$ are

$$\overline{\sigma}_{11}^{(2)} = a_{22}\overline{\sigma}_{22}^{(2)} + a_{12}\overline{\sigma}_{12}^{(2)} + b_x\overline{\sigma}_x + b_y\overline{\sigma}_y, \quad \lambda_j^* = h_2\lambda_j, \tag{19.14a}$$

$$\overline{\sigma}_{j2}^{(2)} = \left[A_{j2}\frac{D^{mc}}{\lambda_1^*(1-D^{ld})}\tanh\frac{\lambda_1^*(1-D^{ld})}{D^{mc}} + B_{j2}\frac{D^{mc}}{\lambda_2^*(1-D^{ld})}\tanh\frac{\lambda_2^*(1-D^{ld})}{D^{mc}} + C_{j2}\left(1-D^{ld}\right)\right]\overline{\sigma}_x, \quad j = 1,2 \tag{19.14b}$$

where $D^{mc} = h_2/s$ denotes relative crack density and $D^{ld} = \ell/s$ denotes relative delamination area. The macro-strains in the individual homogeneous layers and the laminate are assumed to be equal:

$$\overline{\varepsilon}_{11}^{(1)} = \overline{\varepsilon}_{11}^{(2)} = \overline{\varepsilon}_{11}, \quad \overline{\varepsilon}_{22}^{(1)} = \overline{\varepsilon}_{22}^{(2)} = \overline{\varepsilon}_{22}, \quad \overline{\gamma}_{12}^{(1)} = \overline{\gamma}_{12}^{(2)} = \overline{\gamma}_{12} \tag{19.15}$$

Using the constitutive equations for layer 1, Eqn (19.6b), and equations of the global equilibrium of the laminate, Eqn (19.4), the lamina macro-strains in layer 2 are

$$\left\{\overline{\varepsilon}^{(2)}\right\} = \left[\widehat{S}^{(1)}\right]\chi^{-1}\left((1+\chi)[T]\{\overline{\sigma}\} - \left\{\overline{\sigma}^{(2)}\right\}\right) \tag{19.16}$$

where the transformation matrix $[T]$ is given by Eqn (19.4b). Thus, the lamina macro-stresses, Eqn (19.14), and macro-strains, Eqn (19.16), are determined as explicit functions of the damage parameters D^{mc}, D^{ld}.

Finally, the modified stiffness matrix $[\overline{Q}]_2$ of the 'equivalent' homogeneous layer in the global coordinates xyz can be obtained from the modified stiffness matrix $[Q^{(2)}]$ in the local coordinates, Eqn (19.12), as

$$[\overline{Q}]_2 = [T]^{-1}\left[Q^{(2)}\right][T]^{-T} \tag{19.17}$$

where the transformation matrix $[T]$ is given by Eqn (19.4b). The extension stiffness matrix $[\overline{A}]$ of the 'equivalent' laminate in the global coordinates xyz can then be determined as

$$[\overline{A}] = \sum_k [\overline{Q}]_k h_k \tag{19.18}$$

where $[\overline{Q}]_k$ are the in-plane stiffness matrices of the layers in the global coordinates.

19.2.2 Stiffness properties of cracked angle-ply laminates with delaminations

To validate the developed approach, a case of $[30/90]_s$ laminate with matrix cracks in the 90° ply was considered (Kashtalyan & Soutis, 2006), and the results were compared to predictions made using the generalised plane strain model (McCartney, 1996). The properties of a unidirectional glass/epoxy material system used in the calculations were as follows: ply thickness 0.25 mm, longitudinal Young's modulus $E_A = 45.6$ GPa, transverse Young's modulus $E_T = 16.2$ GPa, in-plane shear modulus $\mu_A = 5.83$ GPa, major Poisson's ratio $\nu_A = 0.278$, minor Poisson's ratio $\nu_T = 0.4$. From the laminated plate theory stiffness properties of the intact $[30/90]_s$ laminate are calculated as follows: axial modulus $\widehat{E}_x = 20.9$ GPa, transverse modulus $\widehat{E}_y = 30.4$ GPa, in-plane shear modulus $\widehat{G}_{xy} = 7.76$ GPa, major Poisson's ratio $\widehat{\nu}_x = 0.2$, axial and transverse shear-extension coupling coefficients $\eta_{xy,x} = -0.53$, $\eta_{xy,y} = -0.014$, respectively. Table 19.1 shows reduction ratio of the laminate's stiffness properties as a function of a crack density in the 90° ply. As one would expect, the present shear lag-based model predicts slightly bigger stiffness reduction than the generalised plane strain approach used in combination with ply refinement technique. For the axial Young's modulus the difference is within 4.1%, for shear modulus within 7.2%, for Poisson's ratio within 3.9%, and for axial and transverse shear-extension coupling coefficients within 5.3% and 3.4%, respectively. It is anticipated that the difference between two approaches would be smaller if lower levels of ply refinement are used in the generalised plane strain model (McCartney, 1996).

Figures 19.5–19.10 show the variation of the laminate residual stiffness properties with the relative delamination area D^{ld} in the unbalanced $[0_2/\theta_2]_s$ laminates for a range of ply orientation angles. Axial modulus E_x (Figure 19.5), transverse modulus E_y (Figure 19.6), shear modulus G_{xy} (Figure 19.7), major Poisson's ratio ν_{xy} (Figure 19.8) and axial and transverse shear-extension coupling coefficients (Figures 19.9 and 19.10) that characterise shearing in the xy plane are normalised by their value for the undamaged laminate.

The material system is AS4/3506-1 graphite/epoxy that was earlier considered by O'Brien and Hooper (1991) and O'Brien (1991). Its lamina properties are as follows: $E_{11} = 135$ GPa, $E_{22} = 11$ GPa, $G_{12} = 5.8$ GPa, $\nu_{12} = 0.301$, single ply thickness $t = 0.124$ mm.

Matrix crack density in the θ-ply is assumed equal to $C = 1$ crack/cm: values at $D^{ld} = 0$ indicate residual stiffness properties of the laminates at this crack density without delaminations. It can be seen that reduction of the laminate moduli and, for the considered lay-up, increase in the Poisson's ratio due to local delaminations are more significant in the unbalanced $[0_2/30_2]_s$ laminate than in the balanced $[0_2/30_2/-30_2]_s$ laminate with the same orientation of the damaged ply (Soutis and Kashtalyan, 2000). Matrix cracking and crack tip delaminations are expected to amplify the shear-extension coupling exhibited in the undamaged unbalanced $[0_2/\theta_2]_s$ laminates. As in balanced $[0_2/\theta_2/-\theta_2]_s$ laminates, crack tip

Table 19.1 Reduction ratios for stiffness properties of a cracked $[30/90]_s$ glass/epoxy laminate

Crack density (crack/cm)	Present model	McCartney's model (1996)	Difference (%)
Axial Young's modulus			
0	1.000	1.000	0.0%
5	0.853	0.863	−1.2%
10	0.750	0.764	−1.8%
15	0.689	0.707	−2.5%
20	0.654	0.676	−3.2%
25	0.633	0.657	−3.7%
30	0.619	0.644	−4.0%
35	0.609	0.635	−4.1%
40	0.603	0.628	−4.0%
Shear modulus			
0	1.000	1.000	0.0%
5	0.877	0.908	−3.4%
10	0.793	0.832	−4.7%
15	0.730	0.775	−5.7%
20	0.685	0.733	−6.6%
25	0.653	0.703	−7.0%
30	0.632	0.681	−7.2%
35	0.616	0.664	−7.2%
40	0.605	0.651	−7.1%
Poisson's ratio			
0	1.000	1.000	0.0%
5	0.881	0.891	−1.1%
10	0.782	0.796	−1.7%
15	0.723	0.741	−2.4%
20	0.688	0.710	−3.1%
25	0.666	0.691	−3.6%
30	0.653	0.678	−3.8%

Table 19.1 Continued

Crack density (crack/cm)	Present model	McCartney's model (1996)	Difference (%)
35	0.643	0.669	−3.9%
40	0.637	0.662	−3.9%
Axial shear-extension coupling coefficient			
0	1.000	1.000	0.0%
5	1.111	1.093	1.7%
10	1.199	1.166	2.8%
15	1.274	1.226	3.9%
20	1.335	1.275	4.7%
25	1.382	1.314	5.2%
30	1.417	1.345	5.3%
35	1.442	1.369	5.3%
40	1.461	1.388	5.2%
Transverse shear-extension coupling coefficient			
0	1.004	1.000	0.4%
5	0.833	0.806	3.4%
10	0.695	0.673	3.1%
15	0.616	0.602	2.4%
20	0.577	0.571	1.0%
25	0.557	0.561	−0.8%
30	0.546	0.551	−1.0%
35	0.539	0.551	−2.2%
40	0.535	0.541	−1.1%

uniform local delaminations in unbalanced laminates result in an increase in the absolute value of the axial shear-extension coupling coefficient for $\theta < 45°$ and of the transverse shear-extension coupling coefficient for $\theta > 45°$. Owing to their unbalanced configuration, $[0_2/\theta_2]_s$ laminates exhibit shear-extension coupling characterised by axial $\eta_{xy,x} = \overline{\gamma}_{xy}/\overline{\varepsilon}_x$ and transverse $\eta_{xy,y} = \overline{\gamma}_{xy}/\overline{\varepsilon}_y$ shear-extension coefficients.

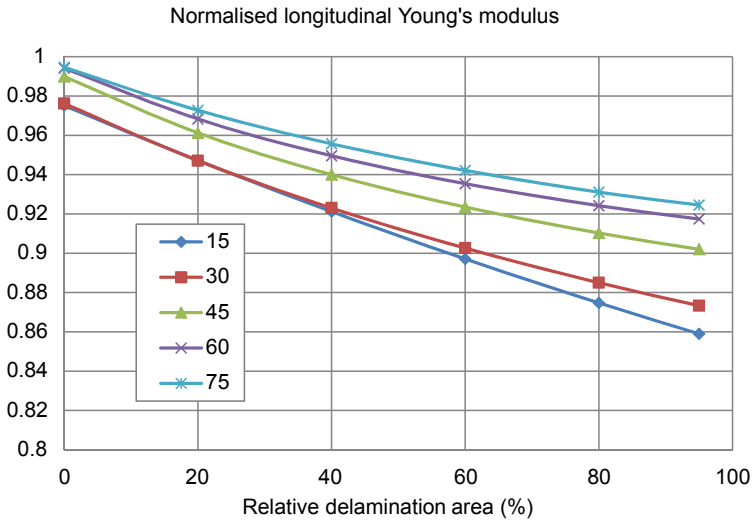

Figure 19.5 Normalised longitudinal Young's modulus of a cracked $[0_2/\theta_2]_s$ AS4/3506-1 laminate as a function of relative delamination area D^{ld} Matrix crack density 1 crack/cm.

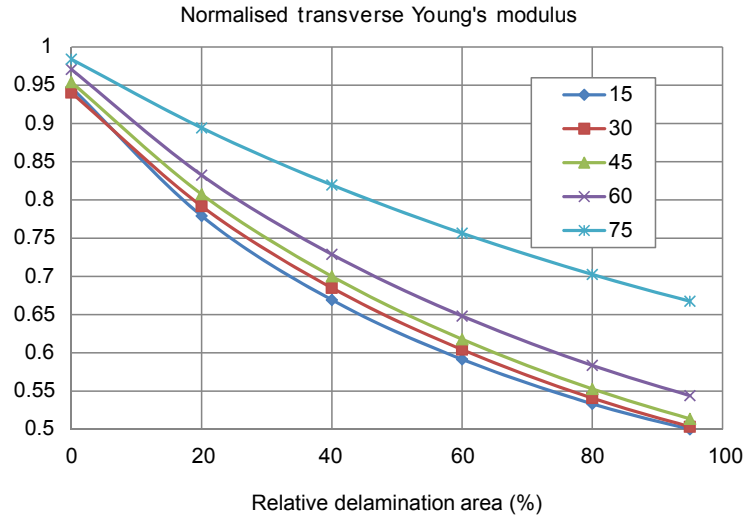

Figure 19.6 Normalised transverse Young's modulus of a cracked $[0_2/\theta_2]_s$ AS4/3506-1 laminate as a function of relative delamination area D^{ld}. Matrix crack density 1 crack/cm.

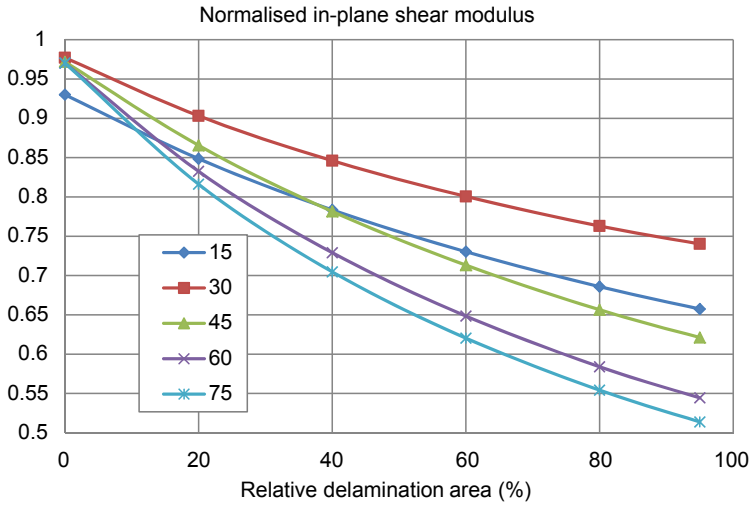

Figure 19.7 Normalised shear modulus of a cracked $[0_2/\theta_2]_s$ AS4/3506-1 laminate as a function of relative delamination area D^{ld}. Matrix crack density 1 crack/cm.

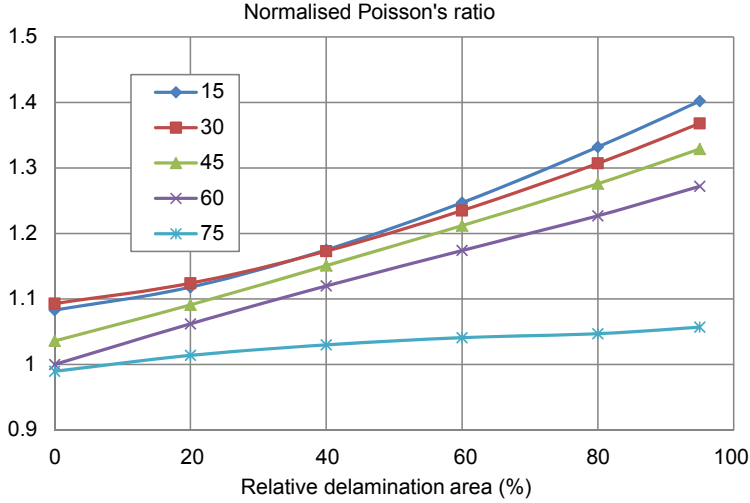

Figure 19.8 Normalised major Poisson's ratio of a cracked $[0_2/\theta_2]_s$ AS4/3506-1 laminate as a function of relative delamination area D^{ld}. Matrix crack density 1 crack/cm.

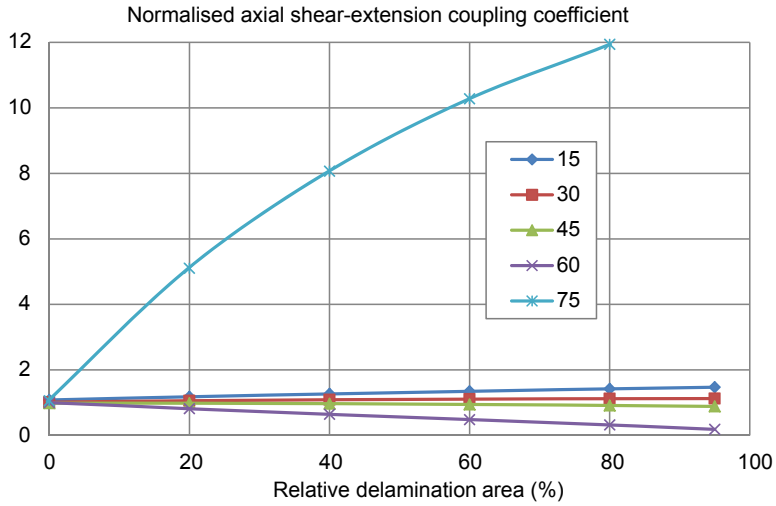

Figure 19.9 Normalised axial shear-extension coupling coefficient of a cracked $[0_2/\theta_2]_s$ AS4/3506-1 laminate as a function of relative delamination area D^{ld}. Matrix crack density 1 crack/cm.

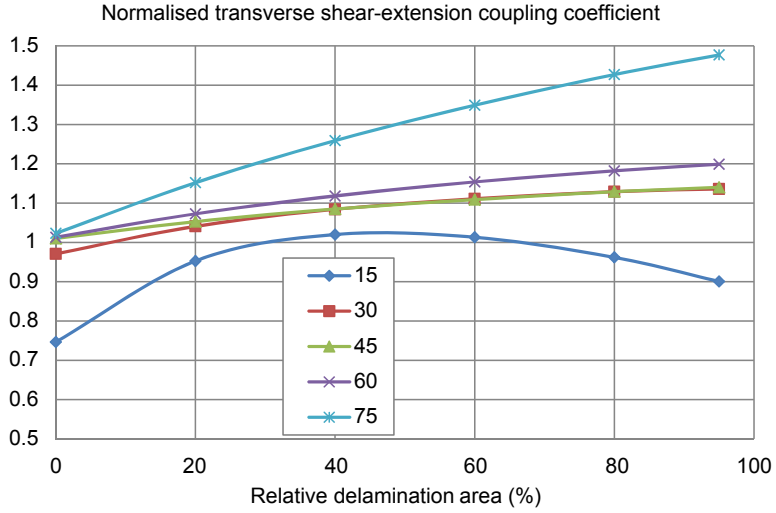

Figure 19.10 Normalised transverse shear-extension coupling coefficient of a cracked $[0_2/\theta_2]_s$ AS4/3506-1 laminate as a function of relative delamination area D^{ld}. Matrix crack density 1 crack/cm.

19.3 Delamination onset and growth prediction

19.3.1 Analytical and finite element modelling of crack tip delaminations

O'Brien (1985) suggested a simple closed-form expression for the strain-energy release rate for local delaminations growing uniformly from transverse crack tips. The expression is based on simple load shearing rules and the classical laminated plate theory. It gives the strain energy release rate that depends only on the laminate lay-up and thickness, the location of the cracked ply and subsequent delaminations, the applied load and the laminate width, and is independent of delamination size and matrix crack density. In the nomenclature of this paper it is given by

$$\frac{G^{ld}}{\bar{\varepsilon}_{xx}^2} = \frac{N\widehat{E}_x^2 h}{2m}\left(\frac{1}{(N-n)\widehat{E}_{ld}} - \frac{1}{N\widehat{E}_x}\right) \tag{19.19a}$$

where h is the laminate thickness, N is the number of plies, n is the number of cracked plies, and $\widehat{E}_x$ and $\widehat{E}_{ld}$ are, respectively, the laminate modulus and the modulus of the locally delaminated sub-laminate as calculated from the laminated plate theory. Parameter m has a value of 2 if the cracked ply is in the interior of the laminate, corresponding to local delamination on either side of matrix crack, and a value of 1 if the cracked ply is a surface ply.

Later, O'Brien (1991) showed that this simple closed-form expression is valid for the total strain energy release rate associated with uniform local delamination growing from an angle-ply matrix crack. For example, strain energy release rate for local delamination in the $(\theta/-\theta)$ interface of a $[0_2/\theta_2/-\theta_2]_s$ laminate with matrix cracks in the $(-\theta)$ ply is

$$\frac{G^{ld}}{\bar{\varepsilon}_{xx}^2} = \frac{3\widehat{E}_x^2 h}{2}\left(\frac{1}{4\widehat{E}_{ld}} - \frac{1}{6\widehat{E}_x}\right) \tag{19.19b}$$

Since the locally delaminated $[0_2/\theta_2]_T$ sub-laminate is asymmetric, the value of $\widehat{E}_{ld}$ in Eqn (19.19b) will depend on whether the presence of bending-extension and shear-extension coupling is reflected in the modulus calculation. For all ply orientation angles θ (i.e. from 5° to 90°), the influence of shear-extension coupling on the value of $\widehat{E}_{ld}$ and therefore the strain energy release rate was found to be significant. The shear constraint resulted in a greater $\widehat{E}_{ld}$ and, hence, correspondingly lower strain energy release rate. However, the effect of bending-extension coupling was proved to be small (O'Brien, 1991). It is worth noticing that the strain energy release rate given by Eqn (19.19) is independent from the delamination size. Also, the effect of matrix cracking is not taken into account when calculating the laminate modulus $\widehat{E}_x$.

Using a quasi-3-D FE analysis, Salpekar and O'Brien (1991) found that the strain energy release rate for uniform local delamination calculated from the expression of O'Brien (1985) matched the value obtained by FE analysis in the laminate interior. FE results for uniform local delaminations initiating from a transverse crack in cross-ply $[0_2/90_4]_s$ and balanced $[\pm 45/90_4]_s$ glass/epoxy laminates indicated that the strain energy release rate was higher near the free edge. It increased with delamination length and reached a constant value at delamination length of about four-ply thicknesses from the transverse crack in the interior as well as near the edges. However, the peak value of strain energy release rate near the free edge has yet to be verified by convergence studies.

Nairn and Hu (1992) used two-dimensional variational mechanics to analyse crack tip delaminations in $[(S)/90_n]_s$ laminates, where (S) denotes a balanced sub-laminate, for example, $(\pm\theta_m)$. They predicted that matrix cracking should reach some critical density before delamination initiates. The critical crack density for delamination initiation is determined by material properties and laminate structure as well as fracture toughnesses for matrix cracking and delamination. It is nearly independent of the properties of the supporting sub-laminate (S). They also showed that O'Brien's expression for strain energy release rate applies only to delaminations induced by isolated matrix cracks, that is, when crack density is very small and the influence of neighbouring cracks is negligible. For crack densities, at which delaminations are observed to initiate, strain energy release rate depends on both delamination size and crack density.

Armanios, Sriram, and Badir (1991) applied a shear deformation theory and sub-laminate approach to analyse local delaminations originating from transverse cracks in CFRP $[\pm 25/90_n]_s$ laminates. Predictions of their model, which also takes into account hygrothermal effects, are in reasonable agreement with delamination onset strain data by Crossman and Wang (1982).

Zhang et al. (1999) studied delaminations induced by transverse cracking at the $(\varphi/90)$ interfaces in $[\ldots/\phi_i/\varphi_m/90_n]_s$ laminates loaded in tension. In particular, they were interested in the constraining effect of the immediate neighbouring plies and remote plies on stiffness reduction and strain energy release rate for delaminations. A sub-laminate-wise first-order shear deformation theory was used to analyse stress and strain fields. It was found that the strain energy release rate for local delamination and stiffness reduction of the constrained transverse plies largely depends on a local lay-up configuration of a damaged laminate. The authors suggested that strain energy release rate for local delamination at the $(\varphi/90)$ interface in a $[\ldots/\phi_i/\varphi_m/90_n]_s$ laminate can be analysed using a $[\varphi_m/90_n]_s$ laminate, where the 90° plies and their next neighbouring plies are subjected to the same laminate strain.

The shear lag method was successfully used by several authors to model onset and growth of transverse crack tip delaminations. Dharani and Tang (1990) used shear lag method to determine the interlaminar shear and normal stresses at the delamination tip. Delamination was assumed to occur when the maximum interlaminar shear stress reached a critical value. Governing equations, formulated in terms of finite differences, were solved numerically using an eigen-value technique.

Zhang, Soutis, and Fan (1994a) and Zhang et al. (1994b) used a 2-D improved shear lag analysis to predict the strain energy release rate for edge and local

delaminations in balanced symmetric $[\pm\theta_m/90_n]_s$ laminates. For edge delamination, they were able to capture a zigzag delamination pattern, that is, edge delamination switching from one (θ/90) interface to another through a matrix crack, and improve O'Brien's formula for strain energy release rate for edge delamination (O'Brien, 1982) incorporating the effect of matrix cracking. For local delaminations, they obtained the strain energy release rate as a function of crack density and delamination area. Their predictions for delamination onset strain agree well with experimental data of Crossman and Wang (1982) and capture the transition from edge to local delamination quite accurately.

Ogihara and Takeda (1995) used a modified shear lag method featuring interlaminar shear layer to predict the strain energy release rate for transverse crack tip delaminations in cross-ply $[0/90_n]_s$ laminates and to model interaction between transverse cracking and delamination. However, the effect of cracking/delamination interaction was found to be negligible in prediction of delamination growth.

Selvarathinam and Weitsman (1998, 1999) observed and modelled, by means of FE and shear lag methods, delaminations induced by matrix cracking in cross-ply laminates under environmental fatigue. By comparing strain energy release rates associated with matrix cracking and delamination, they were able to explain the extensive delaminations and reduced crack densities that arise under immersed fatigue conditions, as compared with fatigue in air.

Kashtalyan and Soutis (1999a, 2000a) examined the effect of crack tip delaminations on stiffness reduction using an improved 2-D shear lag method (Zhang et al., 1992a) and the ECM of the damaged ply (Fan & Zhang, 1993; Kashtalyan & Soutis, 1999b, 2000b). For cross-ply $[0_m/90_n]_s$ laminates, local delaminations along transverse as well as longitudinal cracks were considered. It was established that reduction in the laminate shear modulus and Poisson's ratio is much more significant than in the axial modulus. For balanced symmetric $[\pm\theta_m/90_n]_s$, the effect of constraining ply orientation angle θ on reduction of the laminate in-plane stiffness properties was also examined.

Rebiere and Gamby (2004, 2008) proposed an energy criterion based on the computation of the partial strain energy release rates associated with transverse cracking, longitudinal cracking and crack-induced delamination and used it to predict initiation of these damage modes in symmetric cross-ply laminates subjected to uniaxial loading.

Lim and Li (2005) evaluated the energy release rate associated with matrix cracking and crack-induced delamination and used them to critically evaluate damage mode transition from transverse cracking to delamination.

Blazques, Mantic, Paris, and McCartney (2008) used the boundary element method to carry out a numerical study of the stress state in the neighbourhood of matrix crack-induced delamination in a cross-ply laminate, in order to clarify the mechanisms of damage interaction between transverse cracking and delamination.

Farrokhabadi, Hosseini-Toudeshky, and Mohammadi (2011) proposed a micromechanical approach to analysis of transverse crack-induced delaminations in angle-ply and quasi-isotropic laminates under general in-plane loading.

Maimi, Camanho, Mayugo, and Turon (2011a,b) carried out a comprehensive study of matrix cracking and crack-induced delaminatons and proposed a plastic damage model to simulate the stress−strain state of the damaged ply and used it to analyse evolution of matrix cracking and crack-induced delamination.

Zubillaga et al. (2014) proposed a new failure criterion for predicting delamination induced by matrix cracking. The criterion, based on comparison of the energy release rate available for delamination extension near a matrix crack and the fracture toughness of the interface, predicts failure loads that agree well with experimental data available in the literature.

While transverse crack tip delaminations have been the subject of numerous studies in the literature, delaminations growing from the tips of angle-ply cracks have received considerably less attention.

O'Brien and Hooper (1991) and O'Brien (1991) observed matrix crack-induced delaminations in symmetric angle-ply $[0_2/\theta_2/-\theta_2]_s$ carbon/epoxy laminates under quasi-static and fatigue tensile loading ($\theta = 15°, 20°, 25°, 30°$). Delaminations occurred in the $(\theta/-\theta)$ interface, bounded by the cracks in the $(-\theta)$ ply and the stress-free edge. The laminated plate theory and a quasi-3-D FE analysis were used to examine stresses in the $(-\theta)$ ply. For the considered range of ply orientations, stresses normal to the fibres were found to be compressive and shear stresses along the fibres to be high in the laminate interior, while near the free edge high-tensile stresses normal to the fibres were present.

O'Brien and Hooper (1991) and O'Brien (1991) observed matrix crack-induced delaminations in symmetric angle-ply $[0_2/\theta_2/-\theta_2]_s$ carbon/epoxy laminates under quasi-static and fatigue tensile loading ($\theta = 15°, 20°, 25°, 30°$). Two closed-form expressions for strain energy release rate were derived on the basis of simple load shearing rules: one for a local delamination growing from an angle-ply matrix crack with a uniform delamination front across the laminate width (Figure 19.1(c)), and one for a partial local delamination growing from an angle-ply matrix crack and bounded by the free edge (Figure 19.1(e)). As for the transverse crack tip delamination (O'Brien, 1985), strain energy release rate for uniform local delamination was independent of delamination size and matrix crack density, while for partial local delamination it depended on delamination length. However, when the matrix crack length and the corresponding delamination length along the free edge was small, the difference between the uniform and partial delamination solutions was found to be insignificant.

Salpekar and O'Brien (1993) used a 3-D FE analysis to study matrix crack-induced delaminations in $(0/\theta/-\theta)_s$ graphite/epoxy laminates ($\theta = 15°, 45°$) loaded in tension. For $(0/45/-45)_s$ laminate, the strain energy release rate for local delamination growing uniformly in the $(45/-45)$ interface from the matrix crack in the $(-45°)$ ply was found to be higher near the laminate edge than in the interior of the laminate.

Later, Salpekar, O'Brien, and Shivakumar (1996) computed strain energy release rates associated with local delamination originating from matrix cracks and bounded by the free edge in $(0/\theta/-\theta)_s$ and $(\theta/-\theta/0)_s$ graphite/epoxy laminates using a 3-D FE method. The total strain energy release rate was calculated using three different techniques: the virtual crack closure technique, the equivalent domain integral

technique, and a global energy balance technique. For both lay-ups analysed, the fraction of the total strain energy release rate associated with mode I was greatest near the matrix crack and decreased near the free edge. It also decreased with increasing delamination length and was influenced by matrix crack length. However, no comparison with O'Brien's (1991) closed-form expressions for uniform and partial local delaminations was made.

19.3.2 Calculation of strain energy release rate using the equivalent constraint model

The total strain energy release rate G^{ld} associated with local delaminations growing from the tips of matrix cracks is equal to the first partial derivative of the total strain energy U stored in the damaged laminate with respect to the total delamination area A^{ld}, provided the applied strains $\{\bar{\varepsilon}\}$ are fixed and the matrix crack density $C = (2s)^{-1}$ remains unchanged:

$$G^{ld} = -\left.\frac{\partial U}{\partial A^{ld}}\right|_{\{\bar{\varepsilon}\},C} \tag{19.20}$$

The strain energy release rate can be effectively calculated using the 'equivalent' laminate introduced in the previous section. In the global coordinates, the total strain energy stored in the laminate element with a finite gauge length L and width w is

$$U = \frac{wL}{2}\sum_k (z_k - z_{k-1})\left(\{\bar{\varepsilon}\} + \left\{\bar{\varepsilon}_k^{\text{thermal}}\right\} + \left\{\bar{\varepsilon}_k^{\text{hygro}}\right\}\right)^T [\overline{Q}]_k \left(\{\bar{\varepsilon}\} + \left\{\bar{\varepsilon}_k^{\text{thermal}}\right\} + \left\{\bar{\varepsilon}_k^{\text{hygro}}\right\}\right) \tag{19.21}$$

where $\{\bar{\varepsilon}_k^{\text{thermal}}\}$ and $\{\bar{\varepsilon}_k^{\text{hygro}}\}$ are, respectively, residual thermal and residual hygroscopic strains in the laminate due to the temperature and moisture difference between the stress-free and actual state, and $[\overline{Q}]_k$ is the in-plane reduced stiffness matrix of layer k in the global coordinates.

Noting that the area of a single crack tip delamination is $a^{ld} = 2\ell w/|\sin\varphi|$, Figure 19.2, the total delamination area is equal to

$$A^{ld} = 2a^{ld}CL = 2LwD^{ld}/|\sin\varphi| \tag{19.22}$$

If hygrothermal effects are neglected, the strain energy release rate, calculated from Eqns (19.20)–(19.22), is

$$G^{ld}\left(\bar{\varepsilon}, D^{mc}, D^{ld}\right) = -\frac{h_2}{2}\{\bar{\varepsilon}\}^T \frac{\partial [\overline{Q}]_2}{\partial D^{ld}}\{\bar{\varepsilon}\}|\sin\varphi| \tag{19.23}$$

Under uniaxial strain, Eqn (19.23) simplifies to

$$G^{ld}\left(\overline{\varepsilon}_{xx}, D^{mc}, D^{ld}\right) = -\frac{h_2}{2}\,\overline{\varepsilon}_{xx}^2 \frac{\partial \overline{Q}_{xx,2}}{\partial D^{ld}} |\sin\varphi| \tag{19.24}$$

Calculation of the residual in-plane axial stiffness $\overline{Q}_{xx,2}$ using Eqn (19.12) and the transformation formulae given by Eqn (19.17) yields the strain energy release rate associated with local delamination in terms of the IDEFs Λ_{22}, Λ_{66} and stiffness properties of the undamaged material $\widehat{Q}_{ij}^{(2)}$ as (Kashtalyan & Soutis, 2002)

$$G^{ld}\left(\overline{\varepsilon}_{xx}, D^{mc}, D^{ld}\right) = \frac{h_2}{2}\,\overline{\varepsilon}_{xx}^2 \left[\left(\frac{\widehat{Q}_{12}^{(2)2}}{\widehat{Q}_{22}^{(2)}}\cos^4\varphi + 2\widehat{Q}_{12}^{(2)}\sin^2\varphi\cos^2\varphi + \widehat{Q}_{22}^{(2)}\sin^4\varphi\right)\frac{\partial \Lambda_{22}}{\partial D^{ld}} + 4\widehat{Q}_{66}^{(2)}\sin^2\varphi\cos^2\varphi\frac{\partial \Lambda_{66}}{\partial D^{ld}}\right]|\sin\varphi| \tag{19.25}$$

The first partial derivatives of IDEFs that appear in Eqn (19.25) are explicit functions of the damage parameters D^{mc}, D^{ld} and can be calculated analytically.

Comparison of normalised strain energy release rates $G^{ld}/\overline{\varepsilon}_{xx}^2$ calculated on the basis of Eqns (19.19a) and (19.25) is given in Table 19.2. Crack density is taken as 1 crack/cm, which is equivalent to crack spacing of approximately 80 ply thicknesses.

Figure 19.11 shows predictions of the normalised strain energy release rate $G^{ld}/\overline{\varepsilon}_{xx}^2$ associated with uniform local delamination in unbalanced $[0_2/\theta_2]_s$ laminates calculated from Eqn (19.25).

Results are plotted as a function of the relative delamination area D^{ld} and are given for the range of ply orientation angles θ from 15° to 90°. Matrix crack density in the inner θ ply of the laminate is assumed equal to 1 crack/cm. It can be observed that the strain energy release rate decreases as the delamination area increases, with the dependence of the normalised strain energy release rate on the relative delamination area being nonlinear for all ply orientation angles.

Table 19.2 Normalised strain energy release rate $G^{ld}/\overline{\varepsilon}_{xx}^2$ (MJ/m^2) in $[0_2/\theta_2]_s$ laminates (crack density $C^{mc} = 1$ crack/cm)

Angle θ (Degrees)	O'Brien formula, Eqn (19.19a)	Present approach, Eqn (19.25) with $D^{ld} = 0$	Difference (%)
45°	2.331	1.633	42.7%
75°	1.664	2.363	−29.5%
60°	1.567	2.278	−31.2%
90°	1.589	1.479	7.47%

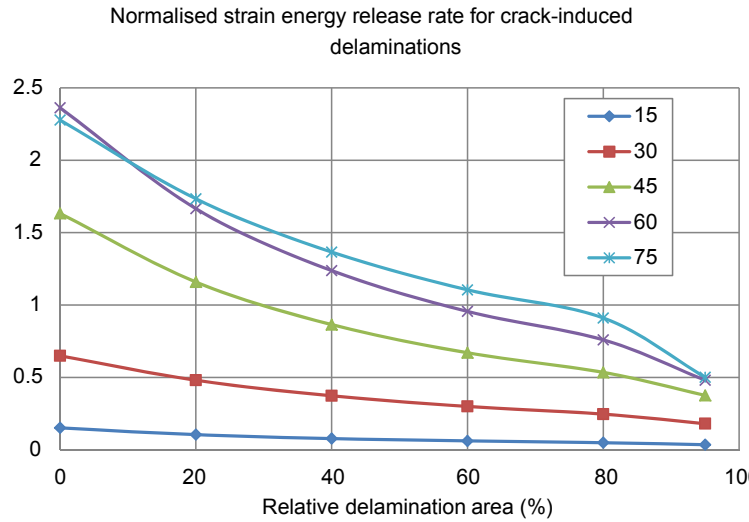

Figure 19.11 Normalised strain energy release rate $G^{ld}/\bar{\varepsilon}_{xx}^2$ for uniform local delamination in a cracked $[0_2/\theta_2]_s$ AS4/3506-1 laminate as a function of relative delamination area D^{ld}. Crack density 1 crack/cm.

Figure 19.12 shows predictions of the normalised strain energy release rate $G^{ld}/\bar{\varepsilon}_{xx}^2$ at the onset of local delamination ($D^{ld} = 0$) as a function of the crack density in the θ ply of AS4/3506-1 unbalanced $[0_2/\theta_2]_s$ laminates. For all ply orientation angles θ, strain energy release rate at the delamination onset depends linearly on matrix

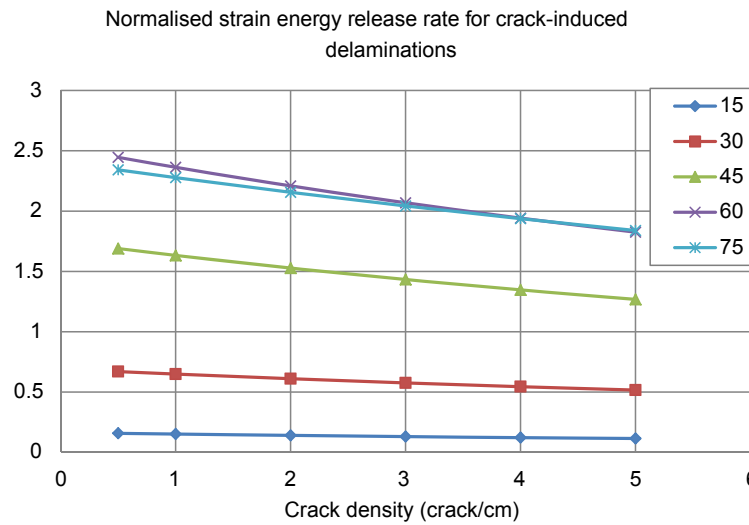

Figure 19.12 Normalised strain energy release rate $G^{ld}/\bar{\varepsilon}_{xx}^2$ for uniform local delamination in a cracked $[0_2/\theta_2]_s$ AS4/3506-1 laminate as a function of crack density. Relative delamination area $D^{ld} = 0$ (onset of delamination).

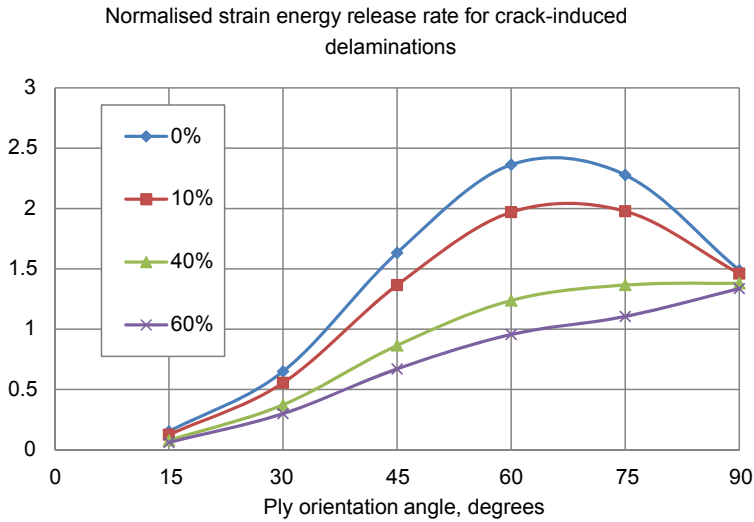

Figure 19.13 Normalised strain energy release rate $G^{ld}/\bar{\varepsilon}_{xx}^2$ for uniform local delamination in a cracked $[0_2/\theta_2]_s$ AS4/3506-1 laminate as a function of ply orientation angle. Crack density 1 crack/cm.

crack density, slightly decreasing as the crack density increases. This will translate into an increase in the delamination onset strain in laminates with higher matrix crack density.

Dependence of strain energy release rate on ply orientation angle is illustrated in Figure 19.13 for a range of relative delamination areas. Crack density is taken as 1 crack/cm. It can be observed that for the same delamination area, the normalised strain energy release rate associated with local delamination is not necessarily higher for greater values of θ. For example, for delaminations with $D^{ld} = 10\%$ the value strain energy release rate for the $[0/60]_s$ laminate is greater than for the cross-ply $[0/90]_s$ laminate, while for $D^{ld} = 60\%$ the opposite is true.

The issue of transition from angle-ply matrix cracking to delamination is not addressed here and is a subject of ongoing research. For transverse cracking in the 90° ply, energy considerations governing transition to local delamination have been examined by Nairn and Hu (1992) and Selvarathinam and Weitsman (1998, 1999).

19.3.3 Mode separation (mode I and II)

Even under the uniaxial loading, damage development in the off-axis plies of general symmetric laminates always occurs under mixed-mode conditions due to shear-extension coupling. It is therefore important in the calculation of the total strain energy release rate to be able to separate mode I and mode II contributions. For a $[(S)/\varphi]_s$ laminate with damaged φ-layer modelled by an 'equivalent' laminate, the total strain energy release rate for crack tip uniform local delaminations is equal to the first partial

derivative of the portion of the total strain energy stored in the 'equivalent' homogeneous layer with respect to damage area

$$G^{ld} = -\left.\frac{\partial U^{(2)}}{\partial A^{ld}}\right|_{\{\overline{\varepsilon}\},C} \tag{19.26}$$

In the local coordinates (Figure 19.2), this portion of the total strain energy can be separated into extensional and shear parts:

$$U^{(2)} = U_{\mathrm{I}}^{(2)} + U_{\mathrm{II}}^{(2)} = Lwh_2\left(\overline{\sigma}_{11}^{(2)}\overline{\varepsilon}_{11}^{(2)} + \overline{\sigma}_{22}^{(2)}\overline{\varepsilon}_{22}^{(2)}\right) + Lwh_2\overline{\sigma}_{12}^{(2)}\overline{\gamma}_{12}^{(2)} \tag{19.27}$$

Under uniaxial strain $\overline{\varepsilon}_{xx}$, strains and stresses in the 'equivalent' homogeneous layer are

$$\begin{aligned}\left\{\overline{\varepsilon}^{(2)}\right\} &= \left\{\cos^2\varphi, \sin^2\varphi, 2\cos\varphi\sin\varphi\right\}^T\overline{\varepsilon}_{xx}\\ \left\{\overline{\sigma}^{(2)}\right\} &= \left[Q^{(2)}\right]\left\{\cos^2\varphi, \sin^2\varphi, 2\cos\varphi\sin\varphi\right\}^T\overline{\varepsilon}_{xx}\end{aligned} \tag{19.28}$$

where the modified stiffness matrix $[Q^{(2)}]$ of the 'equivalent' homogeneous layer in the local coordinates is given by Eqn (19.12). Substitution of Eqns (19.22), (19.27) and (19.28) into Eqn (19.26) gives mode I and mode II contributions into the total strain energy release rate as follows:

$$G_{\mathrm{I}}^{ld} = -\frac{\partial U_{\mathrm{I}}^{(2)}}{\partial A^{ld}} = \overline{\varepsilon}_{xx}^2 f_1\left(D^{ld}\right) \tag{19.29a}$$

$$f_1\left(D^{ld}\right) = \frac{h_2}{2}\left(\frac{\widehat{Q}_{12}^{(2)2}}{\widehat{Q}_{22}^{(2)}}\cos^4\varphi + 2\widehat{Q}_{12}^{(2)}\sin^2\varphi\cos^2\varphi + \widehat{Q}_{22}^{(2)}\sin^4\varphi\right)\frac{\partial\Lambda_{22}^{(2)}}{\partial D^{ld}}|\sin\varphi| \tag{19.29b}$$

$$G_{\mathrm{II}}^{ld} = -\frac{\partial U_{\mathrm{II}}^{(2)}}{\partial A^{ld}} = \overline{\varepsilon}_{xx}^2 f_2(D^{ld}) \tag{19.30a}$$

$$f_2\left(D^{ld}\right) = 2h_2\widehat{Q}_{66}^{(2)}\frac{\partial\Lambda_{66}^{(2)}}{\partial D^{ld}}\cos^2\varphi|\sin^3\varphi| \tag{19.30b}$$

These expressions can be used with appropriate fracture criteria to estimate the onset of local delamination in an already cracked laminate. The resulting total strain energy release rate $G^{ld} = G_{\mathrm{I}}^{ld} + G_{\mathrm{II}}^{ld}$ coincides with Eqn (19.25). Figures 19.14 and 19.15 show contributions of mode I and mode II into the total strain energy release rate $G^{ld}/\overline{\varepsilon}_{xx}^2$ at the onset of local delamination ($D^{ld} = 0$) in unbalanced $[0_2/\theta_2]_s$ laminates as a function of the relative delamination area and crack density, respectively.

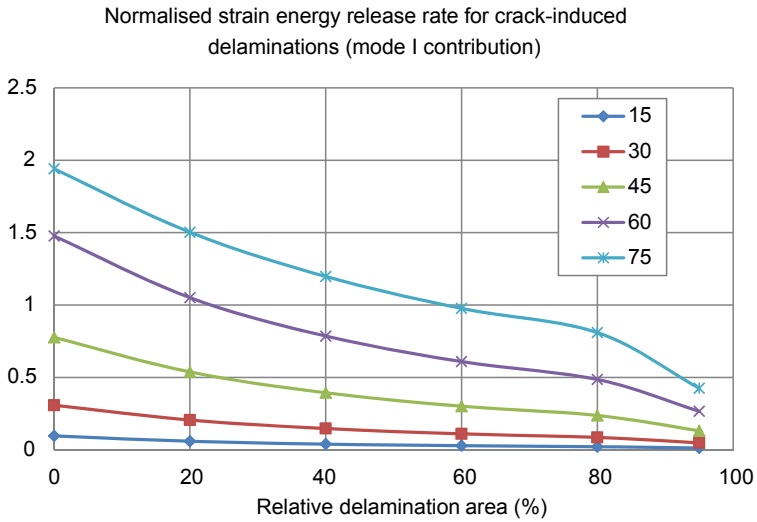

Figure 19.14 Mode I contribution into the strain energy release rate $G^{ld}/\bar{\varepsilon}_{xx}^2$ for uniform local delamination in a cracked $[0_2/\theta_2]_s$ AS4/3506-1 laminate as a function of relative delamination area D^{ld}. Crack density 1 crack/cm.

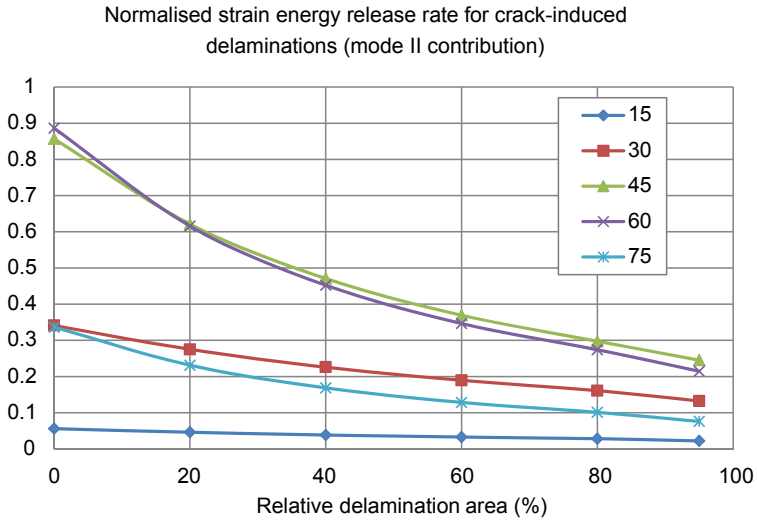

Figure 19.15 Mode II contribution into the strain energy release rate $G^{ld}/\bar{\varepsilon}_{xx}^2$ for uniform local delamination in a cracked $[0_2/\theta_2]_s$ AS4/3506-1 laminate as a function of relative delamination area D^{ld}. Crack density 1 crack/cm.

To predict the onset of delamination in an already cracked $[(S)/\varphi]_s$ laminate under static loading, a mixed-mode fracture criterion can be used

$$\left(\frac{G_{\mathrm{I}}}{G_{\mathrm{IC}}}\right)^{M} + \left(\frac{G_{\mathrm{II}}}{G_{\mathrm{IIC}}}\right)^{N} = 1 \tag{19.31}$$

where G_{IC} and G_{IIC} are, respectively, mode I and mode II interlaminar fracture toughnesses, and M and N are exponents dependent on the material system. For example, for a glass/epoxy system, following Rikards et al. (1998), the exponents M and N can be taken as $M = 1$, $N = 2$. Then, to predict cracking onset strains, G_{I}^{ld} and G_{II}^{ld} values are calculated from Eqns (19.29) and (19.30), and the delamination onset strain $\overline{\varepsilon}_{xx}$ can be found as a root of the following equation:

$$\overline{\varepsilon}_{xx}^{4}\left(\frac{f_2\left(D^{ld}\right)}{G_{\mathrm{IIC}}}\right)^{2} + \overline{\varepsilon}_{xx}^{2}\left(\frac{f_1\left(D^{ld}\right)}{G_{\mathrm{IC}}}\right) = 1 \quad \text{when } D^{ld} = 0 \tag{19.32}$$

Further work is required to validate theoretical predictions. For the lay-ups, damage modes and loading conditions examined in this study, the experimental data are currently not available.

19.4 Conclusions

The failure process of composite laminate under quasi-static or fatigue loading involves sequential accumulation of intra- and interlaminar cracking. Matrix cracks parallel to the fibres in the off-axis plies is the first intralaminar damage mode observed in laminated composites subjected to static or fatigue in-plane tensile loading. They reduce laminate stiffness and strength and trigger development of other damage modes, such as delaminations. This chapter is concerned with theoretical modelling of continuous fibre-reinforced polymer matrix composite laminates with delaminations induced by off-axis ply cracks. Predictions of stiffness reduction due to crack-induced delaminations show that the laminate axial and transverse moduli of unbalanced angle-ply laminates are reduced more significantly than respective stiffness properties of cross-ply laminates, while for the shear modulus, the opposite is true. Matrix cracking and delamination in the off-axis plies can also result in an increase in the Poisson's ratio of the laminate.

Closed-form analytical expressions are derived for mode I and mode II and the total strain energy release rates associated with crack-induced delaminations, representing them as linear functions of the first partial derivatives of the effective elastic properties of the damaged layer with respect to appropriate damage parameters. These expressions can be used with appropriate fracture criteria to estimate the onset and growth of damage in off-axis plies. Comparison with results obtained by O'Brien (1991) shows that O'Brien's closed-form expression for uniform local delamination significantly overestimates the value of the total strain energy release

rate, leading to lower theoretical strains for the initiation of local delamination and therefore over-conservative designs. Also, it gives the total strain energy release rate as independent of delamination area and does not take into account the cumulative effect of damage.

Acknowledgements

Financial support of this research by the Engineering and Physical Sciences Research Council (EPSRC/GR/L51348) and the British Ministry of Defence is gratefully acknowledged.

References

Armanios, E. A., Sriram, P., & Badir, A. M. (1991). Fracture analysis of transverse crack-tip and free-edge delamination in laminated composites. In T. K. O'Brien (Ed.), *Composite materials: Fatigue and fracture, ASTM STP 1110*. Philadelphia, PA: ASTM.

Ashkantala, N., & Talreja, R. (1998). A mechanistic model for fatigue damage evolution for composite laminates. *Mechanics of Materials, 29*(2), 123−140.

Berthelot, J. M., & Le Corre, J. F. (2000). A model for transverse cracking and delamination in cross-ply laminates. *Composites Science and Technology, 60*(7), 1055−1066.

Blazques, A., Mantic, V., Paris, F., & McCartney, L. N. (2008). Stress state characterisation of delamination cracks in [0/90] symmetric laminates by BEM. *International Journal of Solids and Structures, 45*(6), 1632−1662.

Caslini, M., Zanotti, C., & O'Brien, T. K. (1987). Study of matrix cracking and delamination in glass/epoxy laminates. *Journal of Composites Technology and Research, 9*(4), 121−130.

Charewicz, A., & Daniel, I. M. (1986). Damage mechanisms and accumulation in graphite/epoxy laminates. In H. T. Hahn (Ed.), *Composite materials: Fatigue and fracture, ASTM STP 907* (pp. 274−297). Philadelphia, PA: ASTM.

Crossman, F. W., & Wang, A. S. D. (1982). The dependence of transverse cracking and delamination on ply thickness in graphite epoxy laminates. In K. L. Riefsnider (Ed.), *Damage in composite materials, ASTM STP 775* (pp. 118−139). Philadelphia, PA: ASTM.

Daniel, I. M., & Charewicz, A. (1986). Fatigue damage mechanisms and residual properties of graphite/epoxy laminates. *Engineering Fracture Mechanics, 25*(5−6), 793−808.

Dharani, L. R., & Tang, H. (1990). Micromechanics characterization of sublaminate damage. *International Journal of Fracture, 46*(2), 123−140.

Fan, J., & Zhang, J. (1993). In-situ damage evolution and micro/macro transition for laminated composites. *Composites Science and Technology, 47*(2), 107−118.

Farrokhabadi, A., Hosseini-Toudeshky, H., & Mohammadi, B. (2011). A generalised micromechanical approach for the analysis of transverse crack and induced delamination in composite laminates. *Composite Structures, 93*(2), 443−455.

Fukunaga, H., Chou, T. W., Peters, P. W. M., & Schulte, K. (1984). Probabilistic failure strength analysis of graphite/epoxy cross-ply laminates. *Journal of Composite Materials, 18*(4), 339−356.

Hashin, Z. (1987). Analysis of orthogonally cracked laminates under tension. *Transactions ASME Journal of Applied Mechanics, 25*(5−6), 771−778.

Henaff-Gardin, C., Lafarie-Frenot, M. C., & Gamby, D. (1996a). Doubly periodic matrix cracking in composite laminates Part 1: General in-plane loading. *Composite Structures*, *36*(1−2), 113−130.

Henaff-Gardin, C., Lafarie-Frenot, M. C., & Gamby, D. (1996b). Doubly periodic matrix cracking in composite laminates Part 2: Thermal biaxial loading. *Composite Structures*, *36*(1−2), 131−140.

Kashtalyan, M., & Soutis, C. (1999a). A study of matrix crack tip delaminations and their influence on composite laminate stiffness. *Advanced Composites Letters, 8*(4), 149−156.

Kashtalyan, M., & Soutis, C. (1999b). Application of the equivalent constraint model to investigate stiffness properties of transversally cracked and split FRP laminates. *Advanced Composite Letters, 8*(5), 205−211.

Kashtalyan, M., & Soutis, C. (2000a). The effect of delaminations induced by transverse cracking and splitting on stiffness properties of composite laminates. *Composites Part A: Applied Science and Manufacturing, 31*(2), 107−119.

Kashtalyan, M., & Soutis, C. (2000b). Stiffness degradation in cross-ply laminates damaged by transverse cracking and splitting. *Composites Part A: Applied Science and Manufacturing, 31*(4), 335−351.

Kashtalyan, M., & Soutis, C. (2000c). Modelling stiffness degradation due to matrix cracking in angle-ply composite laminates. Plastics. *Rubber and Composites, 29*(9), 482−488.

Kashtalyan, M., & Soutis, C. (2002). Analysis of local delamination in composite laminates with angle ply matrix cracks. *International Journal of Solids and Structures, 39*(6), 1515−1537.

Kashtalyan, M., & Soutis, C. (2005). Analysis of composite laminates with intra- and inter-laminar damage. *Progress in Aerospace Sciences, 41*(2), 152−173.

Kashtalyan, M., & Soutis, C. (2006). Modelling off-axis ply cracking in continuous fibre-reinforced polymer matrix composite laminates. *Journal of Materials Science, 41*(20), 6780−6799.

Kobayashi, S., Terada, K., Ogihara, S., & Takeda, N. (2001). Damage mechanics analysis of matrix cracking in cross-ply CFRP laminates under thermal fatigue. *Composites Science and Technology, 61*(12), 1735−1742.

Lim, S.-H., & Li, S. (2005). Energy release rate for transverse cracking and delamination induced by transverse cracks in laminated composites. *Composites Part A: Applied Science and Manufacturing, 36*(11), 1467−1476.

Maimi, P., Camanho, P. P., Mayugo, J. A., & Turon, A. (2011a). Matrix cracking and delamination in laminated composites. Part I: ply constitutive law, first ply failure and onset of delamination. *Mechanics of Materials, 43*(4), 169−185.

Maimi, P., Camanho, P. P., Mayugo, J. A., & Turon, A. (2011b). Matrix cracking and delamination in laminated composites. Part II: evolution of crack density and delamination. *Mechanics of Materials, 43*(4), 194−211.

McCartney, L. N. (1996). *Stress transfer mechanics for ply cracks in general symmetric laminates* (Vol. 50). NPL Report CMMT(A).

Nairn, J. A., & Hu, S. (1992). The initiation and growth of delaminations induced by matrix microcracks in laminated composites. *International Journal of Fracture, 57*(1), 1−24.

O'Brien, T. K. (1982). Characterization of delamination onset and growth in a composite laminate. In K. L. Reifsnider (Ed.), *Damage in composite materials, ASTM STP 775*. Philadelphia PA: ASTM.

O'Brien, T. K. (1985). Analysis of local delamination and their influence on composite laminate behavior. In W. S. Johnson (Ed.), *Delamination and debonding of materials, ASTM STP 876*. Philadephia PA: ASTM.

O'Brien, T. K. (1991). *Local delamination in laminates with angle ply matrix cracks: Part II Delamination fracture analysis and fatigue characterization*. NASA Technical Memorandum 104076/AVSCOM Technical Report 91-B-011.

O'Brien, T. K., & Hooper, S. J. (1991). *Local delamination in laminates with angle ply matrix cracks: Part I Tension tests and stress analysis*. NASA Technical Memorandum 104055/ AVSCOM Technical Report 91-B-010.

Ogihara, S., & Takeda, N. (1995). Interaction between transverse cracks and delamination during damage progress in CFRP cross-ply laminates. *Composites Science and Technology, 54*(4), 395−404.

Parvizi, A., Garrett, K. W., & Bailey, J. E. (1978). Constrained cracking in glass fibre-reinforced epoxy cross-ply laminate. *Journal of Materials Science, 13*(1), 195−201.

Rebiere, J.-L., & Gamby, D. (2004). A criterion for modelling initiation and propagation of matrix cracking and delamination in cross-ply laminates. *Composites Science and Technology Structures, 64*(13−14), 2239−2250.

Rebiere, J.-L., & Gamby, D. (2008). A decomposition of the strain energy release rate associated with the initiation of transverse cracking, longitudinal cracking and delamination in cross-ply laminates. *Composite Structures, 84*(2), 186−197.

Rikards, R., Buchholz, F.-G., Wang, H., Bledzki, A. K., Korjakin, A., & Richard, H.-A. (1998). Investigation of mixed mode I/II interlaminar fracture toughness of laminated composites by using a CTS type specimen. *Engineering Fracture Mechanics, 61*(3−4), 325−342.

Salpekar, S. A., & O'Brien, T. K. (1991). Combined effect of matrix cracking and free edge on delamination. In T. K. O'Brien (Ed.), *Composite materials: Fatigue and fracture, ASTM STP 1110*. Philadelphia PA: ASTM.

Salpekar, S. A., & O'Brien, T. K. (1993). Analysis of matrix cracking and local delamination in $(0/\text{theta}/-\text{theta})_s$ graphite epoxy laminates under tensile load. *ASTM Journal of Composites Technology and Research, 15*(2), 95−100.

Salpekar, S. A., O'Brien, T. K., & Shivakumar, K. N. (1996). Analysis of local delaminations caused by angle-ply matrix cracks. *Journal of Composite Materials, 30*(4), 418−440.

Selvarathinam, A. S., & Weitsman, Y. J. (1998). Transverse cracking and delamination in cross-ply gr/ep composites under dry, saturated and immersed fatigue. *International Journal of Fracture, 91*(2), 103−116.

Selvarathinam, A. S., & Weitsman, Y. J. (1999). A shear-lag analysis of transverse cracking and delamination in cross-ply carbon-fibre/epoxy composites under dry, saturated and immersed fatigue conditions. *Composites Science and Technology, 59*(14), 2115−2123.

Soutis, C., & Kashtalyan, M. (September 25−27, 2000). Delamination growth and residual properties of cracked orthotropic laminates under tensile loading. In O. O. Ochoa, T. K. O'Brien, D. Lagoudas, & H. J. Sue (Eds.), *Proceedings of the 15th Annual Technical Conference of ASC/ASTM* (pp. 1153−1160). Texas, USA: Texas A&M University.

Takeda, N., & Ogihara, S. (1994). Initiation and growth of delamination from the tip of transverse cracks in CFRP cross-ply laminates. *Composites Science and Technology, 52*(3), 309−318.

Takeda, N., Ogihara, S., & Kobayashi, A. (1995). Microscopic fatigue damage progress in CFRP cross-ply laminates. *Composites, 26*(12), 859−867.

Tsai, C. L., & Daniel, I. M. (1992). Behavior of cracked cross-ply composite laminates under shear loading. *International Journal of Solids and Structures, 29*(4), 3251−3267.

Zhang, J., Fan, J., & Herrmann, K. P. (1999). Delaminations induced by constrained transverse cracking in symmetric composite laminates. *International Journal of Solids and Structures, 36*(6), 813−846.

Zhang, J., Fan, J., & Soutis, C. (1992a). Analysis of multiple matrix cracking in $[\pm\theta_m/90_n]_s$ composite laminates. Part 1: in-plane stiffness properties. *Composites, 23*(5), 291−298.

Zhang, J., Fan, J., & Soutis, C. (1992b). Analysis of multiple matrix cracking in $[\pm\theta_m/90_n]_s$ composite laminates. Part 2: development of transverse ply cracks. *Composites, 23*(5), 299−304.

Zhang, J., & Herrmann, K. P. (1999). Stiffness degradation induced by multilayer matrix cracking in composite laminate. *Composites Part A, 30*(5), 683−706.

Zhang, H., & Minnetyan, L. (2006). Variational analysis of transverse cracking and local delaminations in $[\theta_m/90_n]_s$ laminates. *International Journal of Solids and Structures, 43*(22−23), 7061−7081.

Zhang, J., Soutis, C., & Fan, J. (1994a). Effects of matrix cracking and hygrothermal stresses on the strain energy release rate for edge delamination in composite laminates. *Composites, 25*(1), 27−35.

Zhang, J., Soutis, C., & Fan, J. (1994b). Strain energy release rate associated with local delamination in cracked composite laminates. *Composites, 25*(9), 851−862.

Zubillaga, L., Turon, A., Maimi, P., Costa, J., Mahdi, S., & Linde, P. (2014). An energy based failure criterion for matrix crack induced delamination in laminated composite structures. *Composite Structures, 112*(1), 339−344.

Appendix A: out-of-plane shear stresses

Variation of the out-of-plane shear stresses has the form

$$\sigma_{j3}^{(2)} = \frac{\tau_j}{h_2} x_3, \quad 0 \le |x_3| \le h_2, \quad j = 1,2$$

$$\sigma_{j3}^{(1)} = \frac{\tau_j}{h_1}(h - x_3), \quad h_2 \le |x_3| \le h \tag{A1}$$

Constitutive equations for the out-of-plane shear stresses:

$$\begin{Bmatrix} \sigma_{13}^{(k)} \\ \sigma_{23}^{(k)} \end{Bmatrix} \approx \begin{bmatrix} Q_{55}^{(k)} & Q_{45}^{(k)} \\ Q_{45}^{(k)} & Q_{44}^{(k)} \end{bmatrix} \frac{\partial}{\partial x_3} \begin{Bmatrix} u_1^{(k)} \\ u_2^{(k)} \end{Bmatrix}, \quad i = 1,2 \tag{A2}$$

After substituting Eqn (A2) into Eqn (A1), multiplying them by x_3 and by $h - x_3$, respectively, and integrating with respect to x_3, we get

$$\frac{h_1}{3} \begin{Bmatrix} \tau_1 \\ \tau_2 \end{Bmatrix} = \begin{bmatrix} \widehat{Q}_{55}^{(1)} & \widehat{Q}_{45}^{(1)} \\ \widehat{Q}_{45}^{(1)} & \widehat{Q}_{44}^{(1)} \end{bmatrix} \left(\begin{Bmatrix} \tilde{u}_1^{(1)} \\ \tilde{u}_2^{(1)} \end{Bmatrix} - \begin{Bmatrix} V_1 \\ V_2 \end{Bmatrix} \right),$$

$$\frac{h_2}{3} \begin{Bmatrix} \tau_1 \\ \tau_2 \end{Bmatrix} = \begin{bmatrix} \widehat{Q}_{55}^{(2)} & 0 \\ 0 & \widehat{Q}_{44}^{(2)} \end{bmatrix} \left(\begin{Bmatrix} V_1 \\ V_2 \end{Bmatrix} - \begin{Bmatrix} \tilde{u}_1^{(2)} \\ \tilde{u}_2^{(2)} \end{Bmatrix} \right) \tag{A3}$$

Here $\{V\} = \{u^{(1)}\}\Big|_{x_3=h_2} = \{u^{(2)}\}\Big|_{x_3=h_2}$ are the in-plane displacements at the interface. After rearranging Eqn (A3) becomes

$$\begin{Bmatrix} \tilde{u}_1^{(1)} \\ \tilde{u}_2^{(1)} \end{Bmatrix} - \begin{Bmatrix} \tilde{u}_1^{(2)} \\ \tilde{u}_2^{(2)} \end{Bmatrix} = \left(\frac{h_1}{3} \begin{bmatrix} \widehat{Q}_{55}^{(1)} & \widehat{Q}_{45}^{(1)} \\ \widehat{Q}_{45}^{(1)} & \widehat{Q}_{44}^{(1)} \end{bmatrix}^{-1} + \frac{h_2}{3} \begin{bmatrix} \widehat{Q}_{55}^{(2)} & 0 \\ 0 & \widehat{Q}_{44}^{(2)} \end{bmatrix}^{-1} \right) \begin{Bmatrix} \tau_1 \\ \tau_2 \end{Bmatrix} \tag{A4}$$

Inversion of Eqn (A4) leads to

$$\begin{Bmatrix} \tau_1 \\ \tau_2 \end{Bmatrix} = \begin{bmatrix} K_{11} & K_{12} \\ K_{21} & K_{22} \end{bmatrix} \left(\begin{Bmatrix} \tilde{u}_1^{(1)} \\ \tilde{u}_2^{(1)} \end{Bmatrix} - \begin{Bmatrix} \tilde{u}_1^{(2)} \\ \tilde{u}_2^{(2)} \end{Bmatrix} \right), \tag{A5}$$

with

$$[K] = \left(\frac{h_1}{3} \begin{bmatrix} \widehat{Q}_{55}^{(1)} & \widehat{Q}_{45}^{(1)} \\ \widehat{Q}_{45}^{(1)} & \widehat{Q}_{44}^{(1)} \end{bmatrix}^{-1} + \frac{h_2}{3} \begin{bmatrix} \widehat{Q}_{55}^{(2)} & 0 \\ 0 & \widehat{Q}_{44}^{(2)} \end{bmatrix}^{-1} \right)^{-1} \tag{A6}$$

Appendix B: shear lag parameters

On referring to the constitutive equations, Eqn (19.6), the generalised plane strain condition, Eqn (19.5), becomes

$$\widehat{S}_{11}^{(1)} \tilde{\sigma}_{11}^{(1)} + \widehat{S}_{12}^{(1)} \tilde{\sigma}_{22}^{(1)} + \widehat{S}_{16}^{(1)} \tilde{\sigma}_{12}^{(1)} = \widehat{S}_{11}^{(2)} \tilde{\sigma}_{11}^{(2)} + \widehat{S}_{12}^{(2)} \tilde{\sigma}_{22}^{(2)} \tag{B1}$$

Using the laminate equilibrium equations, Eqn (19.4), stresses in the constraining layer (layer 1) can be excluded, so that the micro-stress component $\tilde{\sigma}_{11}^{(2)}$ is given by

$$\tilde{\sigma}_{11}^{(2)} = a_{22} \tilde{\sigma}_{22}^{(2)} + a_{12} \tilde{\sigma}_{12}^{(2)} + b_x \overline{\sigma}_x + b_y \overline{\sigma}_y \tag{B2}$$

$$a_{22} = -\frac{\widehat{S}_{12}^{(1)} + \chi \widehat{S}_{12}^{(2)}}{\widehat{S}_{11}^{(1)} + \chi \widehat{S}_{11}^{(2)}}, \quad a_{12} = -\frac{\widehat{S}_{16}^{(1)}}{\widehat{S}_{11}^{(1)} + \chi \widehat{S}_{11}^{(2)}}$$

$$b_x = \frac{(1+\chi)\left(\widehat{S}_{11}^{(1)}\cos^2\varphi + \widehat{S}_{12}^{(1)}\sin^2\varphi - \widehat{S}_{16}^{(1)}\sin\varphi\cos\varphi\right)}{\widehat{S}_{11}^{(1)} + \chi\widehat{S}_{11}^{(2)}}$$

$$b_y = \frac{(1+\chi)\left(\widehat{S}_{11}^{(1)}\sin^2\varphi + \widehat{S}_{12}^{(1)}\cos^2\varphi + \widehat{S}_{16}^{(1)}\sin\varphi\cos\varphi\right)}{\widehat{S}_{11}^{(1)} + \chi\widehat{S}_{11}^{(2)}}$$

Strain differences are expressed in terms of stresses as

$$\begin{Bmatrix} \tilde{\gamma}_{12}^{(1)} - \tilde{\gamma}_{12}^{(2)} \\ \tilde{\varepsilon}_{22}^{(1)} - \tilde{\varepsilon}_{22}^{(2)} \end{Bmatrix} = -\frac{1}{\chi}\begin{bmatrix} L_{11} & L_{12} \\ L_{21} & L_{22} \end{bmatrix}\begin{Bmatrix} \tilde{\sigma}_{12}^{(2)} \\ \tilde{\sigma}_{22}^{(2)} \end{Bmatrix} + \frac{1}{\chi}\begin{bmatrix} M_{11} & M_{12} \\ M_{21} & M_{22} \end{bmatrix}\begin{Bmatrix} \overline{\sigma}_x \\ \overline{\sigma}_y \end{Bmatrix} \tag{B3}$$

Here

$$L_{11} = \widehat{S}_{66}^{(1)} + a_{12}\widehat{S}_{16}^{(1)} + \chi\widehat{S}_{66}^{(2)}, \quad L_{12} = \widehat{S}_{26}^{(1)} + a_{22}\widehat{S}_{16}^{(1)}$$

$$L_{21} = \widehat{S}_{26}^{(1)} + a_{12}\widehat{S}_{12}^{(1)} + \chi a_{12}\widehat{S}_{12}^{(2)} \quad L_{22} = \widehat{S}_{22}^{(1)} + a_{22}\widehat{S}_{12}^{(1)} + \chi\left(\widehat{S}_{22}^{(2)} + a_{22}\widehat{S}_{12}^{(2)}\right) \tag{B4a}$$

$$\begin{aligned} M_{11} &= (1+\chi)\Big[\left(\widehat{S}_{16}^{(1)} + a_{12}\widehat{S}_{11}^{(2)}\right)\cos^2\varphi + \left(\widehat{S}_{26}^{(1)} + a_{12}\widehat{S}_{12}^{(1)}\right)\sin^2\varphi \\ &\quad -\left(\widehat{S}_{66}^{(1)} + a_{12}\widehat{S}_{16}^{(1)}\right)\sin\varphi\cos\varphi\Big] \\ M_{21} &= (1+\chi)\Big[\left(\widehat{S}_{12}^{(1)} + a_{22}\widehat{S}_{11}^{(1)}\right)\cos^2\varphi + \left(\widehat{S}_{22}^{(1)} + a_{22}\widehat{S}_{12}^{(1)}\right)\sin^2\varphi \\ &\quad -\left(\widehat{S}_{26}^{(1)} + a_{22}\widehat{S}_{16}^{(1)}\right)\sin\varphi\cos\varphi\Big] \\ M_{12} &= (1+\chi)\Big[\left(\widehat{S}_{16}^{(1)} + a_{12}\widehat{S}_{11}^{(2)}\right)\sin^2\varphi + \left(\widehat{S}_{26}^{(1)} + a_{12}\widehat{S}_{12}^{(1)}\right)\cos^2\varphi \\ &\quad +\left(\widehat{S}_{66}^{(1)} + a_{12}\widehat{S}_{16}^{(1)}\right)\sin\varphi\cos\varphi\Big] \\ M_{22} &= (1+\chi)\Big[\left(\widehat{S}_{12}^{(1)} + a_{22}\widehat{S}_{11}^{(1)}\right)\sin^2\varphi + \left(\widehat{S}_{22}^{(1)} + a_{22}\widehat{S}_{12}^{(1)}\right)\cos^2\varphi \\ &\quad +\left(\widehat{S}_{26}^{(1)} + a_{22}\widehat{S}_{16}^{(1)}\right)\sin\varphi\cos\varphi\Big] \end{aligned} \tag{B4b}$$

Substitution into the equilibrium equations, Eqn (19.3), yields the following coupled second-order differential equations:

$$\frac{\mathrm{d}^2}{\mathrm{d}x_2}\begin{Bmatrix}\tilde{\sigma}_{12}^{(2)}\\ \tilde{\sigma}_{22}^{(2)}\end{Bmatrix} - \frac{1}{h_1}\begin{bmatrix}K_{11} & K_{12}\\ K_{21} & K_{22}\end{bmatrix}\left(\begin{bmatrix}L_{11} & L_{12}\\ L_{21} & L_{22}\end{bmatrix}\begin{Bmatrix}\tilde{\sigma}_{12}^{(2)}\\ \tilde{\sigma}_{22}^{(2)}\end{Bmatrix} + \begin{bmatrix}M_{11} & M_{12}\\ M_{21} & M_{22}\end{bmatrix}\begin{Bmatrix}\overline{\sigma}_x\\ \overline{\sigma}_y\end{Bmatrix}\right) = 0 \quad \text{(B5)}$$

or

$$\frac{\mathrm{d}^2}{\mathrm{d}x_2}\begin{Bmatrix}\tilde{\sigma}_{12}^{(2)}\\ \tilde{\sigma}_{22}^{(2)}\end{Bmatrix} - \begin{bmatrix}N_{11} & N_{12}\\ N_{21} & N_{22}\end{bmatrix}\begin{Bmatrix}\tilde{\sigma}_{12}^{(2)}\\ \tilde{\sigma}_{22}^{(2)}\end{Bmatrix} + \begin{bmatrix}P_{11} & P_{12}\\ P_{21} & P_{22}\end{bmatrix}\begin{Bmatrix}\overline{\sigma}_x\\ \overline{\sigma}_y\end{Bmatrix} = 0 \quad \text{(B6)}$$

where $[N] = h_1^{-1}[K][L]$ and $[P] = h_1^{-1}[K][M]$, with matrices $[K]$, $[L]$ and $[M]$ defined by Eqns (A6), (B4a) and (B4b), respectively.

Appendix C: material constants A_j, B_j and C_j

$$A_1 = \frac{\lambda_1^2 - N_{22}}{N_{21}}A_2, \quad B_1 = \frac{\lambda_2^2 - N_{22}}{N_{21}}B_2, \quad C_1 = -\frac{C_2N_{22} + P_{21} + \alpha P_{22}}{N_{21}} \quad \text{(C1)}$$

$$A_2 = -\frac{(P_{21} + \alpha P_{22})(N_{21}N_{12} - N_{11}N_{22}) + R\lambda_2^2}{(\lambda_2^2 - \lambda_1^2)(N_{21}N_{12} - N_{11}N_{22})}, \quad \text{(C2)}$$

$$B_2 = \frac{(P_{21} + \alpha P_{22})(N_{21}N_{12} - N_{11}N_{22}) + R\lambda_1^2}{(\lambda_2^2 - \lambda_1^2)(N_{21}N_{12} - N_{11}N_{22})} \quad \text{(C3)}$$

$$C_2 = \frac{R}{N_{21}N_{12} - N_{11}N_{22}}, \quad R = N_{11}(P_{21} + \alpha P_{22}) - N_{21}(P_{11} + \alpha P_{12}) \quad \text{(C4)}$$

Blast resistance of polymeric composite sandwich structures

20

M. Kelly, H. Arora, J.P. Dear
Imperial College London, London, UK

20.1 Introduction

Owing to their low density, adaptable mechanical properties and low radar signatures, polymeric sandwich composites are of increasing interest in naval applications. With the threat of explosive attacks likely in military applications, this research project considers the blast resistance of typical styrene acrylonitrile (SAN) foam−glass fibre-reinforced polymer (GFRP) face-sheet sandwich panels when subject to different explosive blast threats and establishes appropriate test and instrumentation techniques. In addition, a novel graded core is also evaluated using the techniques developed. Three studies have been performed in this research focussing on the role of the core on blast wave mitigation. The first study considers the testing of sandwich panels that undergo inelastic deformation in the form of core cracking and front face-sheet failure. This is captured using high-speed cameras, and the resulting digital image correlation (DIC) allows the locations of the damage to be established. The second study allows the difference in elastic response of a 40- and 30-mm-thick core to be established in order to evaluate how the reduced flexural stiffness due to a lower second moment of area affects the dynamic blast response of the sandwich panel. The third study compares two different constructions of sandwich panel, with similar areal densities, one with a stepwise graded-density core and another with a single-density core. In this research, the effect of increasing the density of the foam core in a stepwise fashion away from the front (blast) face was explored. This chapter will outline the test setup and instrumentation of these tests, whilst presenting and explaining the results of the experiments. Best practice for tracking the strain and displacement of the sandwich panels is discussed, and an explanation of how to interpret the DIC data to establish damage and response type is provided. The literature review will consider analytical and numerical research in predicting the blast response of sandwich panels, as well as summarise research performed using shock tubes to simulate blast loading on scaled sandwich structures.

20.2 Literature review

The high cost of blast testing means that a significant amount of research is performed using simulations. However, it is important to validate these findings with well-defined

Structural Integrity and Durability of Advanced Composites. http://dx.doi.org/10.1016/B978-0-08-100137-0.00020-1

full-scale blast experiments. It is also important to appreciate the potential modes in which the sandwich panel could fail, as well as to possess some understanding of the dynamic response properties of the sandwich structure. Andrews and Moussa (2009) developed failure mode maps for sandwich structures with isotropic unidirectional GFRP face-sheets, and PVC and balsawood cores of varying densities. The failure modes considered were compressive front face-sheet (blast side) failure, shear core failure and back face-sheet tensile failure, and the response of the sandwich panel is represented by a single-degree-of-freedom mass-spring system. In this analysis the failure type is determined with static loading by considering face-sheet thickness and core density, with the applied pressure being the peak pressure from the blast wave, and then using the panel compliance and the natural frequency of the panel response, the dynamic failure index is predicted for blast loading. Analytical solutions of sandwich panels to blast loading were also developed by Hoo Fatt and Palla (2009), in which the response to blast loading was split into three phases: an initial core-crushing phase, in which a local indentation of the foam core is determined; the second bending phase, where the panel deflection is determined; and finally the vibration phase, where the transverse shear wave reflects back and forth from the clamped boundary to the centre of the blast panel. This method of analysis allowed the amount of foam indentation to be determined, and then Hashin's damage criteria was incorporated into the solution for the face-sheets and core to determine the critical impulse to cause cracking in the face-sheet and core. These predictions were then compared to finite element analysis results and showed good correlation in damage predictions. Damage predictions for an example case of a 25-mm-diameter clamped plate, with 2-mm-thick E-glass face-sheets and a 25-mm-thick core, predicted failure of the distal face-sheet in cases with 100, 200 and 300 kg/m^3 for the respective critical impulse. Similar analytical solutions were developed by Qiu, Deshpande, and Fleck (2004) for metallic foam sandwich composites, with the addition of a fluid–structure interaction phase before the core-crushing phase, to determine how much momentum is carried into the sandwich panel from the surrounding air or water in an air or underwater blast test, respectively. Librescu, Oh, and Hohe (2004) produced constitutive equations for the response of sandwich panels to blast loading based on an Airy stress function. The solution assumes a simply supported rectangular panel and solves the dynamic problem using the extended Galerkin method, and studies are performed with varying charge size, stand-off distance and panel composition. Furthermore, a comparison of the response of an identical panel subjected to air and underwater blast is performed. Hause and Librescu (2005) further developed these explosive response solutions to consider anisotropy in the face-sheets, to account for the directional response in the sandwich panel face-sheets (Hause & Librescu, 2005), which was developed even further to consider underwater blast loading (Librescu, Oh, & Hohe, 2006). The problem of core compressibility and face-sheet wrinkling was incorporated into the solution by Hohe, Librescu, and Oh (2006), in order to establish the effects on panel response, and this was also developed for curved sandwich panels. Core compressibility during blast was also investigated by Li, Kardomateas, and Simitses (2008), again implementing the extended Galerkin method, and a Kirchoff–Love relationship assumed for the face-sheets. The core

compressibility took the form of a fourth-order polynomial with terms for the displacement of each of the two face-sheets and the mid-plane of the core. This study allowed core cavitation to be accounted for during blast response simulations, and predicted that compressive damage in the blast incident face-sheet is the most likely mode of failure. Core compressibility is more prominent in underwater explosion due to a greater peak pressure on the sandwich panel. Panciroli and Abrate (2012) incorporated core compressibility into a solution for underwater blast problems, and this solution is valid for flat and curved beams and plates.

In order to predict blast response, shock tubes are also utilised for dynamic testing of composite sandwich panels. Jackson and Shukla (2011) used a shock tube setup to test 60-mm-thick SAN foam GFRP sandwich beams with peak shock pressures of around 9 MPa. During blast loading the damage observed was core cracking and debonding of the join in the centre of the sandwich panel. A comparison was also made with sandwich beams subjected to low- and high-velocity impacts prior to blast loading, to determine the extent of strength reduction with varying amounts of damage present in the construction. The shock tube was further implemented by Wang and Shukla (2011) to test sandwich beams with in-plane compressive loading during blast, to better imitate the conditions expected in use. The sandwich panels had loads of 15 and 25 kN applied in-plane, and were subjected to blast loads with a peak pressure of 1 MPa. In this study it was again found that core cracking dominates for the case of no load, but when in-plane compressive loading was present the sandwich panel buckled before undergoing core cracking. In an effort to increase the blast resistance of composite structures, through-thickness stitching was developed to prevent debonding and delamination during deformation. Mouritz (2001) performed underwater explosive impacts on through-thickness-stitched GFRP sandwich panels with 0.03 or 0.05 kg charges at a stand-off distance of 1 m. The post-blast flexural strength of the composite panels was then determined using four-point-bending tests to understand the increase in blast resistance of increasing the amount of stitching. LeBlanc, Shukla, Rousseau, and Bogdanovich (2007) conducted a similar study on three-dimensional (3D) woven carbon fibre composite panels subjected to a 2.5 MPa peak shock pressure. Post-blast damage was assessed via an edge-wise compression test in order to discover the effects on blast resistance of various fibre architectures, thicknesses and areal densities. Further research was performed on 3D stitched foam core sandwich panels, subjected to 5.5 MPa shock loads. The damage observed was much lower for the stitched foam cores than for the non-stitched case (Tekalur, Bogdanovich, & Shukla, 2009).

The face-sheets of foam core sandwich panels tend to be either GFRP or carbon fibre-reinforced polymer (CFRP), and a comparison of these two materials for blast resistance has been made by Arora et al. (2012). Sandwich panels with 25-mm-thick SAN foam cores were subjected to 100 kg nitromethane charges in air, at a stand-off distance of 14 m. It was found that the deflection of the CFRP panel was significantly less, and also demonstrated much less face-sheet and core cracking, than the GFRP face-sheet counterpart. Arora et al. (2014) performed further post-blast testing on GFRP and CFRP face-sheet sandwich panels, by loading sectioned blast panels in edgewise compression to determine their residual strength after blast. It was found that the CFRP panel was much stronger in edgewise compression with small amounts

of damage, due to stiffer face-sheets, but as core damage increased and so decoupling of the two face-sheets occurred, the GFRP and CFRP sandwich panels had similar residual strengths. Blast testing was performed by Tekalur, Shivakumar, and Shukla (2008), in which woven GFRP and CFRP panels were subjected to 1.8 MPa peak pressure shock waves for comparison. In line with the direction of altering face-sheets for improved blast resistance, Tekalur, Shukla, and Shivakumar (2008) performed shock tube testing on sandwich composite materials incorporating a polyurea (PU) layer between two E-Glass GFRP layers, and in front of GFRP layers. It was found that by locating the PU layer at the front of the panel, the blast wave is mitigated, thus reducing blast damage. Damage is also reduced by sandwiching the PU layer between GFRP layers, but by a lesser amount than placing it at the front of the panel. Simulations of the implementation of a PU layer were performed by Bahei-El-Din, Dvorak, and Fredricksen (2006), where a conventional polymeric foam sandwich panel was compared to the same design but with a thin PU layer between the foam and back face-sheet during blast loading. It was found that the blast wave caused compression of the PU layer, allowing structural reinforcement of the back face-sheet, thus reducing the amount of deflection observed. Another alteration to the conventional sandwich panel design is to use multiple polymeric foam layers in the sandwich panel core, of varying densities. Wang, Gardner, and Shukla (2009) performed tests implementing three to five layers of foam in the sandwich panel. It was found that the acoustic impedance of the shock wave caused by the changing density reduces the strength of the shock wave, reducing damage observed in the sandwich panel. The response is improved by adding more layers of foam, with different densities. The use of graded cores with PU layers was investigated by Gardner, Wang, Kumar, and Shukla (2011) in which three layers of gradation were implemented, with a PU layer between the foam and front face-sheet, or between the foam and back face-sheet. Better blast resistance was observed when the PU layer was located in front of the back face-sheet due to the compression of the lower-density foam layers lowering the intensity of the blast wave before reaching the back face-sheet of the sandwich panel.

This literature review provides a comprehensive list of some of the more recent research performed into the blast resistance of polymeric foam composites, an area upon which the research presented in the following sections of this chapter aims to build.

20.3 Materials

The sandwich panels tested in the research presented in this chapter contained polymeric SAN foam cores with symmetric 2-mm-thick GFRP face-sheets on either side. The GFRP face-sheets were comprised of two layers of QE1200 infused with one of three different resin systems: Ampreg22; ST 94; or SR 8500. All of these resin systems provide very similar properties. All foam cores were SAN polymer of either 30 or 40 mm thick, depending on the study. Four different SAN foams were used for the testing of eight sandwich panels subjected to various charge sizes at various

stand-off distances. The SAN foam sheets were supplied by Gurit UK, and were P800; M100; M130; and M200. Table 20.1 shows the various sandwich panels tested, alongside the charge size and stand-off distance used in the test. The core type for the 30 mm core subject to a 100 kg charge shown in Table 20.1 has three foams listed, which is due to this sandwich panel containing a graded-density core. Each core layer was 10 mm thick, orientated such that the lowest-density (M100) layer was on the blast side of the panel, the medium-density (M130) layer was in the centre and the high-density (M200) layer was on the back face. The mechanical properties for all of the constitutive materials in the sandwich panels tested are shown in Table 20.2 and Figure 20.1 provides a schematic of the construction of the various sandwich panels. The fibre orientations of the sandwich panels were [BLAST SIDE]/0/90/+45/−45/−45/+45/90/0/[FOAM]/0/90/+45/−45/−45/+45/90/0.

The eight blast tests performed were part of four different comparative studies. The first of these studies (Study A) was to demonstrate the difference between the elastic and inelastic response of sandwich panels to blast loading. These tests were both 40 mm P800 foam cores, subjected to 30 kg C4 charges at 16 and 8 m stand-off distances, the former showing no damage, and the latter showing significant core cracking and front face-sheet damage. A third test was performed in this study, which shows the response of a sandwich panel subjected to a 100 kg nitromethane charge at 14 m stand-off; in this case the core was 25 mm M130. The second study performed (Study B) was to consider the effect of core thickness on blast response.

Table 20.1 List of blast tests performed on the various sandwich panel constructions

Test number	Skin configuration	Core type	Core thickness	Charge size (kg TNT-equivalent)	Stand-off distance (m)
1	QE1200/ Ampreg22	P800	40	38.4	8
2	QE1200/ Ampreg22	P800	40	38.4	16
3	QE1200/ Ampreg22	P800	30	38.4	14
4	QE1200/ Ampreg22	P800	40	38.4	14
5	QE1200/ Ampreg22	M130	25	100.0	14
6	ST94 (GFRP)	M100/M130/ M200	30	100.0	15
7	QE1200/SR 8500	M100	40	100.0	15

Table 20.2 Mechanical properties of constitutive materials

Material property	QE1200	P800	M100	M130	M200
Density (kg/m^3)	1750	155	107.5	140	200
Tensile modulus (GPa)	17	0.14	0.11	0.18	0.33
Compressive modulus (GPa)	–	0.13	0.11	0.17	0.32
Tensile strength (MPa)	260	2.85	2.11	2.85	4.29
Compressive strength (MPa)	200	2.8	1.55	2.31	3.8
Shear strength (MPa)	6500	61	1.45	59	2.95
Tensile failure strain (%)	1.5	2.2	–	1.6	–
Shear failure strain (%)	–	58	52	43	20

S.P. Gurit.

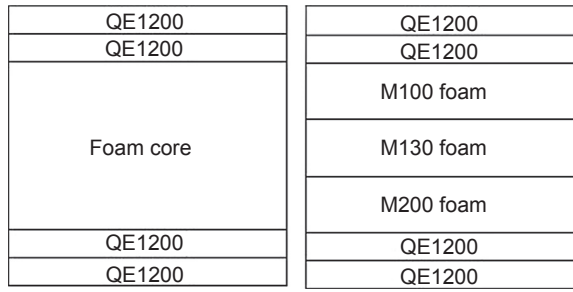

Figure 20.1 Schematic showing the constructions of the single-core (left) and graded-core (right) sandwich panels.

The two tests representing this study are both 30 kg C4 charges at 14 m stand-off distances, with 30 and 40 mm P800 cores. A 100 kg nitromethane test (Study C) compared a 30-mm-thick graded-density core with a 40-mm-thick constant-density core. In these two tests the charge size and stand-off distance were kept consistent, as were the areal densities of the sandwich panels, and the results of Study B on core thickness effects were considered in comparing the 30- and 40-mm-thick cores of Study C.

20.4 Experimental

All air blast testing was performed at GL Noble Denton, RAF Spadeadam, UK. The two different charge sizes used were a 30 kg C4 plastic explosive, which has a trinitrotoluene (TNT) equivalence of 38.4 kg, and a 100 kg nitromethane charge, with a TNT equivalence of 100 kg. The test pad layout for blast testing is shown in Figure 20.2, showing the test cubicle and charge location. For the 30 kg C4 charge

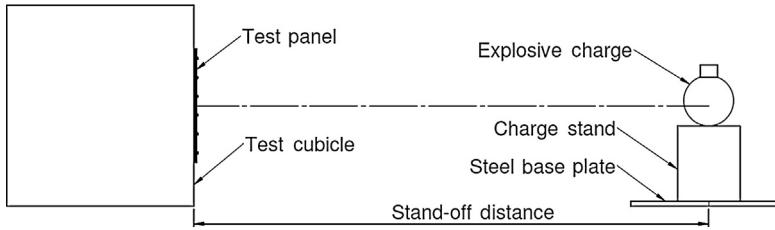

Figure 20.2 Test pad layout.

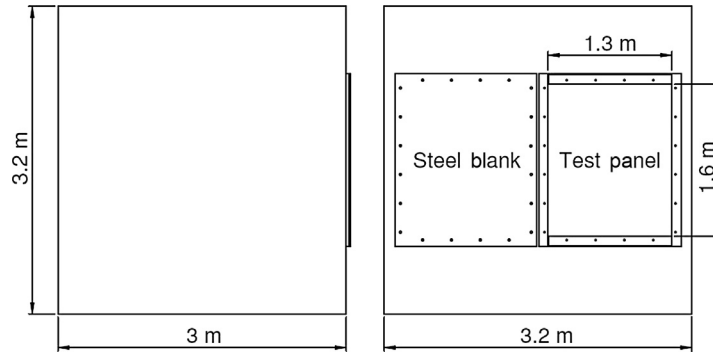

Figure 20.3 Steel test cubicle.

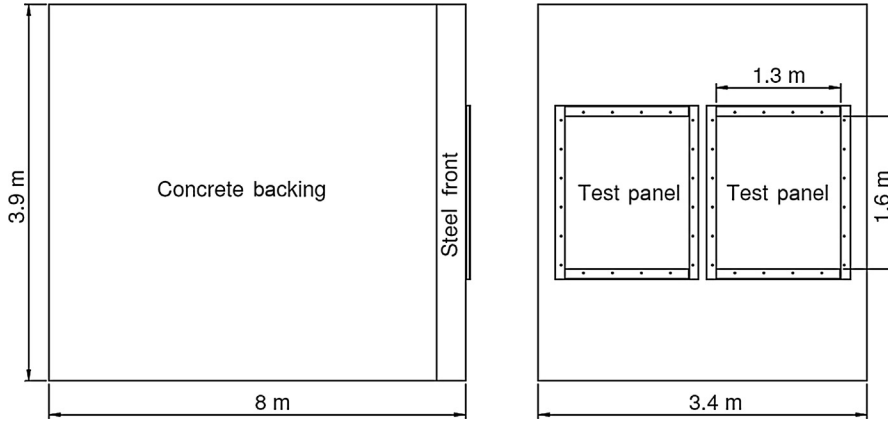

Figure 20.4 Concrete test cubicle.

sizes a steel cubicle was used with one sandwich panel bolted into the cubicle window and the second window blanked off. A diagram of this test cubicle is shown in Figure 20.3. Due to the high energy of the 100 kg charges, the steel cubicle was replaced with a concrete-backed cubicle, which had a steel front similar to that of the steel cubicle. In these tests two sandwich panels were situated in the cubicle during one test; and a diagram of this cubicle is shown in Figure 20.4. In order to produce quasi-built-in boundary conditions, 5 × 100 mm mild steel plates were adhered to

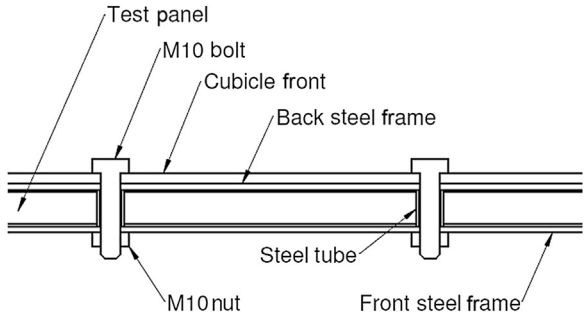

Figure 20.5 Test panel clamping arrangement.

the edges of both sides of the panel using Sikaflex 291i marine sealant. The sandwich panel was then held onto the cubicle front using 20 × M10 bolts, with the bolts passing through the steel plates and the panel itself. Steel tubes were inserted into the holes in the sandwich panel before the steel plates were attached in order to prevent core crushing when tightening the sandwich panel onto the cubicle front. A schematic of the clamping arrangement of the sandwich panel is shown in Figure 20.5.

20.5 Instrumentation

The deflection and back face-sheet strain of the sandwich panels was measured using DIC. For this a random speckle pattern was applied to the back face of the sandwich panel such that the coverage of the panel in speckles was about 50%. Pairs of high-speed cameras were then used to track the displacement of the panel during loading, as well as the strain on the surface of the back face-sheet. The size of the speckles was determined by the resolution of the high-speed camera used, such that one speckle was around five pixels in diameter. The pairs of cameras used were Photron SA3s, Photron SA5.1s and Photron SA7s. Table 20.3 outlines the cameras used for each test, the resolution and frame rate used to record the panel response, the type of cubicle used for the test and the comparative study performed. The cameras were positioned such that they were at a 25° viewing angle to each other, and such that their bisector was perpendicular to the back face of the panel, and their plane was in the vertical centre of the panel. This setup implied a distance of about 1.5 m between the cameras and 3.5 m from the panel, although this required fine adjustment during the actual test to ensure that everything was in shot. Figure 20.6 illustrates the high-speed camera layout. For the 30 kg C4 tests, a laser gauge was also positioned inside the cubicle to measure the central deflection of the sandwich panel, alongside the DIC data.

20.6 Results

This section provides the results of the three studies performed, and highlights key parts of the DIC results presented.

Table 20.3 Cameras and cubicles used in each blast test

Test number	Cameras used	Resolution (pixels)	Frame rate (frames/s)	Cubicle type	Blast number	Study
1	Photron SA3	1×10^6	2000	Steel	1	A
2	Photron SA3	1×10^6	2000	Steel	2	A
3	Photron SA3	1×10^6	2000	Concrete	3	A
4	Photron SA3	1×10^6	2000	Steel	4	B
5	Photron SA3	1×10^6	2000	Steel	5	B
6	Photron SA7	1×10^6	7000	Concrete	6	C
7	Photron SA5.1	1×10^6	5400	Concrete	7	C

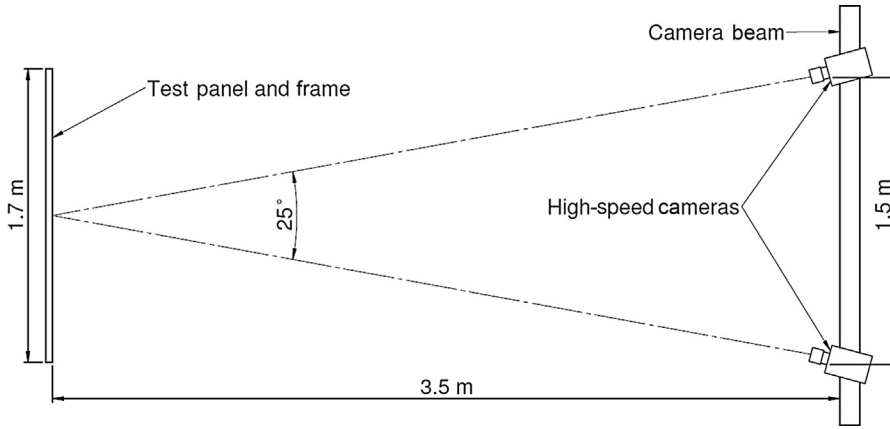

Figure 20.6 High-speed camera setup.

20.6.1 Study A – response type

This study was performed to investigate the different responses of sandwich panels to varying charge sizes and stand-off distances, showing both elastic and inelastic loading. The study objective was to quantify the suitability of DIC for identifying the location and extent of damage during blast loading. The central response of the sandwich panel was determined via DIC, and the reflected loading pressure on the panel was also measured using a gauge block at the same stand-off distance from the charge. The response of the 30 kg C4 loading on the 40 mm P800 panel at 8 m is shown in Figure 20.7. Figure 20.7(a) shows the two-dimensional contour plots of out-of-plane displacement and maximum principal strain (ε_{max}) at 0.5 ms intervals. Figure 20.7(b) shows the central displacement with time of the 40-mm-thick P800

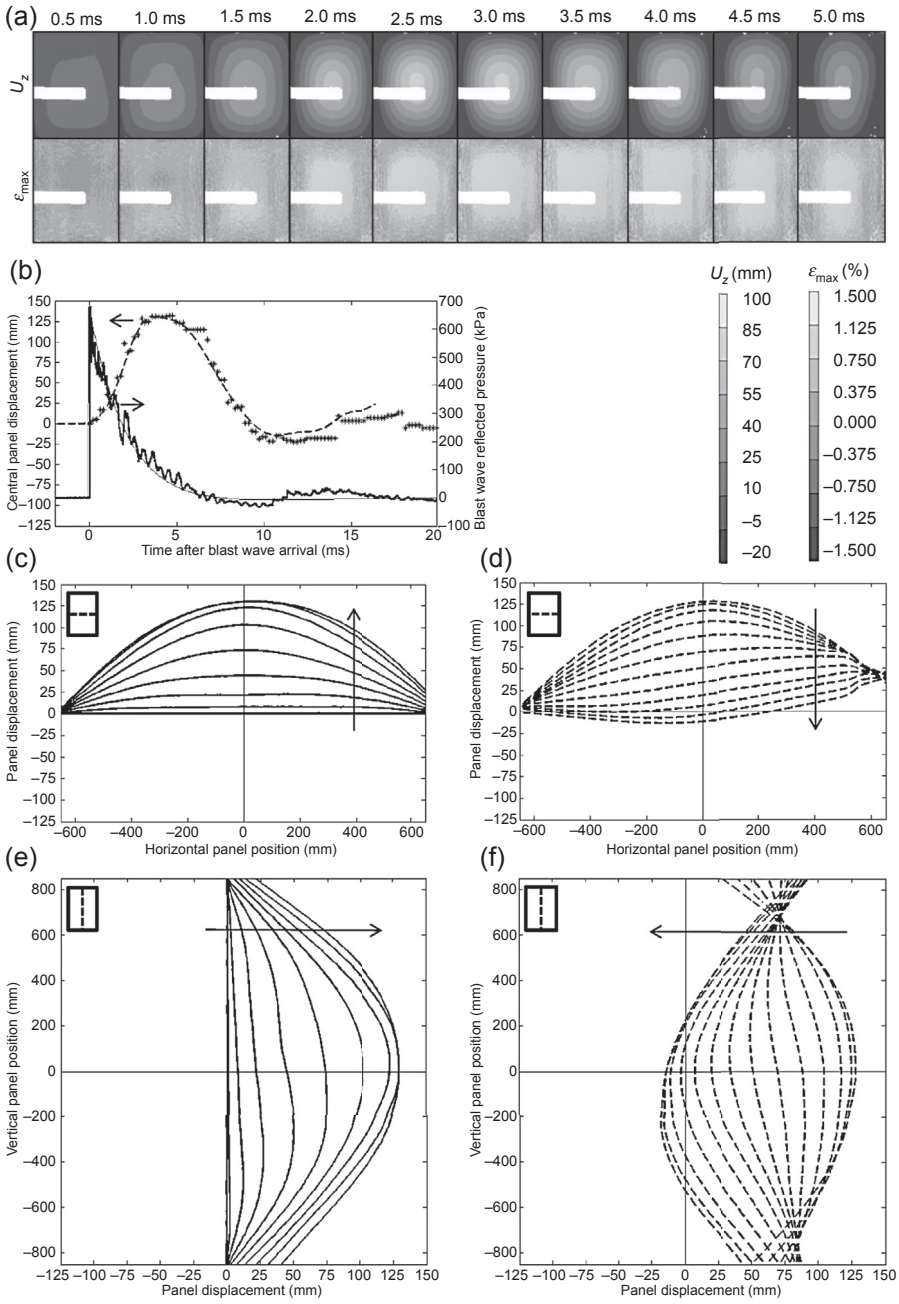

Figure 20.7 Results for the 40 mm P800 sandwich panel at 8 m stand-off from a 30 kg C4 charge. (a) DIC contour plots of out-of-plane displacement (U_z) and maximum principal strain (ε_{max}), with missing data due to laser gauge arm. (b) Measured and predicted reflected pressure during the test (solid), central panel deflection using DIC (dashed) and central panel deflection using a laser gauge (starred). (c) Horizontal centre positive phase. (d) Horizontal centre negative phase. (e) Vertical centre positive phase. (f) Vertical centre negative phase.

sandwich panel at 8 m stand-off, measured using DIC and a laser gauge situated behind the sandwich panel, where strong agreement is visible between the laser gauge data and DIC. The pressure profile shows a peak reflected pressure of 900 kPa and the peak displacement measured during the test was 134 mm. The pressure data shown is both experimental and predicted, showing good correlation to the predicted loading curve. Figure 20.7(c–f) shows the profiles of the deflection across the horizontal centre line and the vertical centre line of the sandwich panel during blast loading, for the initial positive phase deflection (on the left) and then the negative phase (on the right), respectively. In Figure 20.7(c–f) sharp changes in gradient are visible along the right-hand edge, which indicates core cracking under the surface, reducing the panel stiffness in this area. Furthermore, high strain concentrations are visible along the right-hand edges of the ε_{max} contour plots presented in Figure 20.7(a), implying subsurface damage has taken place. The missing data across the centre of the contour plots (from the left-hand edge to the centre) is due to the presence of the laser gauge during the test and the shift in the curves of Figure 20.7(c–f) are due to movement of the test cubicle during blast loading.

The response of the 30 kg C4 loading of the 40 mm P800 panel at 16 m is shown in Figure 20.8, with contour plots of out-of-plane displacement and ε_{max} shown in Figure 20.8(a), where no areas of high strain are visible, indicating no subsurface damage. Figure 20.8(b) shows a peak displacement of 52 mm and a peak predicted reflected pressure of 112 kPa (the pressure data acquisition system failed in this test, hence the pressure shown here is predicted (Smith & Hetherington, 1994)). The centre-line profiles during loading are shown in Figure 20.8(c–f), which depicts no sharp changes in gradient, indicating no damage to the panel. No damage was observed at 16 m stand-off when inspected after blast loading. This is markedly different from the situation presented in Figure 20.7 when the same charge of 30 kg was used at a stand-off of 8 m, which exhibited severe skin and core cracking.

Figure 20.9 shows the response of the 25 mm M130 sandwich panel subjected to 100 kg at 14 m and the contour plots presented in Figure 20.9(b) indicate subsurface damage due to high strain concentrations on the vertical sides of the sandwich panel. Front face-sheet cracking was also observed on the front face-sheet of the panel after testing, in the same location on the right-hand side. Figure 20.9(b) provides a trace of the central deflection with time for the sandwich panel, alongside the measured overpressure during the test. The peak measured overpressure was 250 kPa, translating to a peak expected reflected pressure of 354 kPa (Smith & Hetherington, 1994), and the peak central deflection was 140 mm. Figure 20.9(c–d) shows the horizontal profile plots of the panel during blast loading, in which a clear change in gradient is present on the right-hand side during rebound on the horizontal plane. The vertical centre displacement profile is shown in Figure 20.9(e–f), which does not show any changes in gradient, highlighting the fact that damage is taking place across the short dimension of the sandwich panel, as expected.

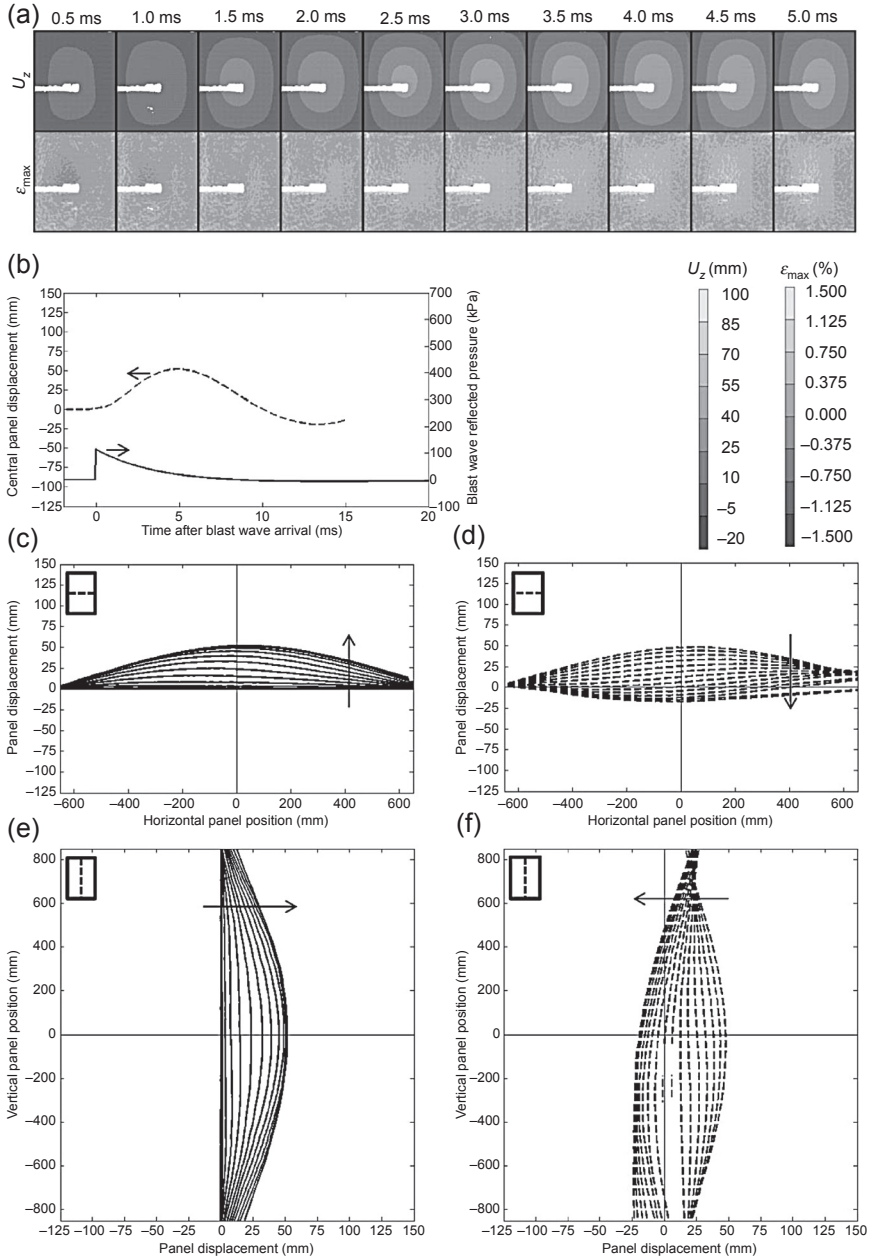

Figure 20.8 Results for the 40 mm P800 sandwich panel at 16 m stand-off from a 30 kg C4 charge. (a) DIC contour plots of out-of-plane displacement (U_z) and maximum principal strain (ε_{max}), with missing data due to laser gauge arm. (b) Predicted reflected pressure during the test (solid) and central panel deflection using DIC (dashed). (c) Horizontal centre positive phase. (d) Horizontal centre negative phase. (e) Vertical centre positive phase. (f) Vertical centre negative phase.

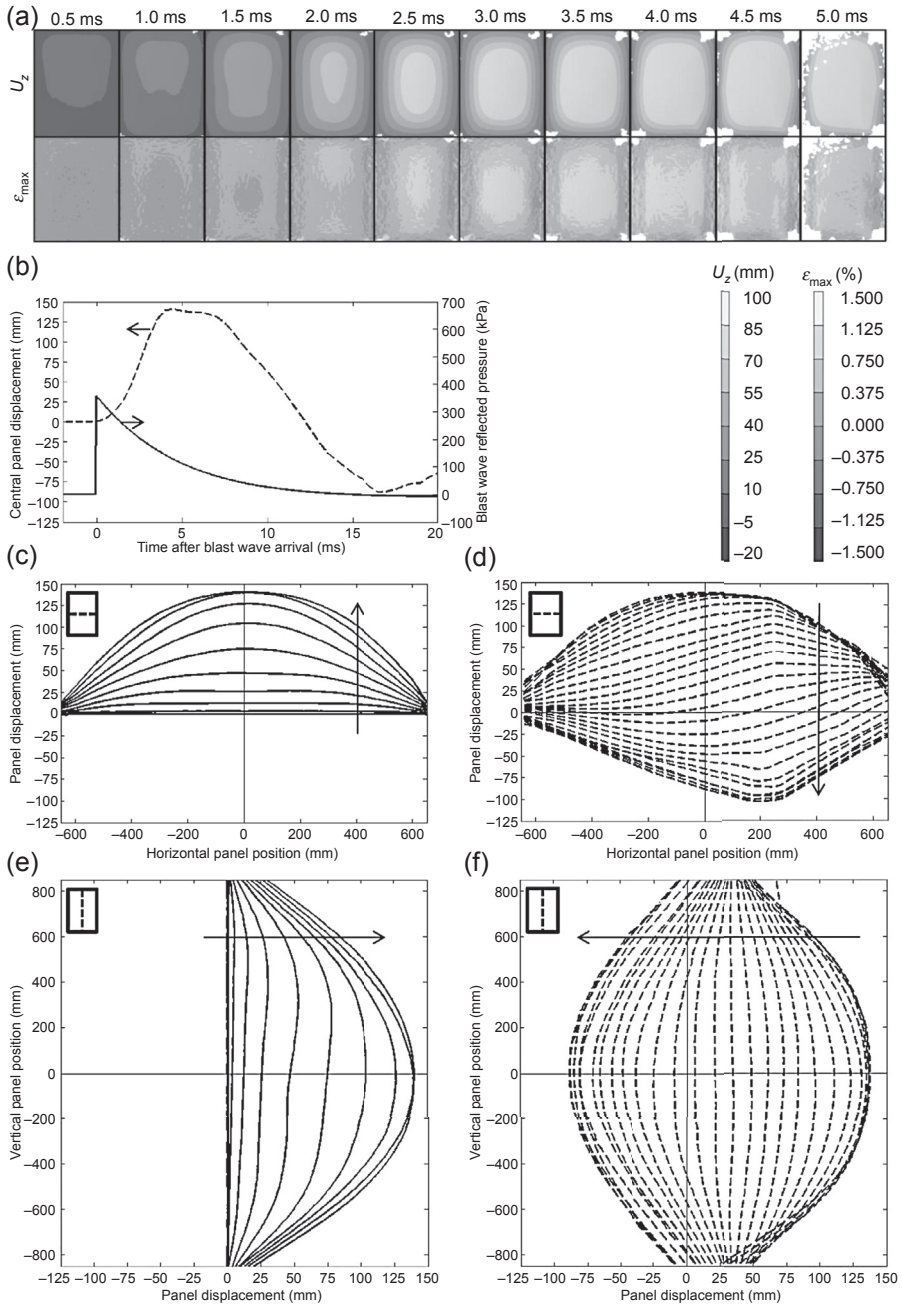

Figure 20.9 Results for the 25 mm M130 sandwich panel at 14 m stand-off from a 100 kg C4 charge. DIC contour plots of out-of-plane displacement (U_z) and maximum principal strain (ε_{max}). (b) Predicted reflected pressure during the test (solid) and central panel deflection using DIC (dashed). (c) Horizontal centre positive phase. (d) Horizontal centre negative phase. (e) Vertical centre positive phase. (f) Vertical centre negative phase.

20.6.2 Study B – core thickness

By reducing the thickness of the sandwich panel, the second moment of area is reduced, which results in a lower bending stiffness. This study explored the effect of this reduction by comparing a panel with a 30 mm core to a panel with a 40 mm core subjected to 30 kg C4 charges at 14 m. Both of these tests were performed at 14 m stand-off distances to allow elastic responses, so that a direct comparison could be drawn. Figure 20.10 shows the response of the 30 mm core sandwich panel and Figure 20.11 shows that of the 40 mm sandwich panel, and the DIC contour plots are provided in Figures 20.10(a) and 20.11(a), respectively. Figure 20.10(b) shows the central response of the 30 mm core sandwich panel with time using DIC and a laser gauge, and also shows the reflected pressure profile measured during the test. Figure 20.10(c–f) illustrates the profiles of the deflection of the centre lines. From Figure 20.10(b) a peak deflection of 78 mm is visible, and a peak reflected pressure of 180 kPa. This compares to a peak deflection of 61 mm for the 40-mm-thick core comparison, the central deflection and pressure profile of which is shown in Figure 20.11(b); Figure 20.11(c–f) shows the centre line profiles. In these two tests the horizontal profiles all show continuous gradients, indicating no core cracking. The reduction in core thickness from 40 to 30 mm caused the peak central deflection of the sandwich panel to increase from 61 to 78 mm, which is a 28% increase.

20.6.3 Study C – effect of using a graded-density core

In order to improve blast resistance it was hypothesised that introducing stepwise grading into the foam core of the sandwich panel would reduce the amount of damage observed during blast loading, and the results from this study are presented in this section. The graded-density panel is compared directly to a sandwich panel with a single-density core. The foams were chosen to provide equivalent areal densities of the sandwich panels, and resulted in the single-density panel having an aerial core density of 4.0 kg/m^2 and the graded-core panel having an aerial core density of 4.3 kg/m^2. The response of the graded-density core to the 100 kg charge at 15 m is shown in Figure 20.12, and Figure 20.12(a) shows the DIC contour plots of out-of-plane displacement (U_z) and maximum principal strain (ε_{max}). The central displacement and overpressure trace of the graded sandwich panel is shown in Figure 20.12(b), indicating a maximum central displacement of 110 mm and a peak reflected pressure of 300 kPa. The horizontal and vertical section plots are shown in Figure 20.12(c–f), and some minor core cracking is implied by discontinuities in gradient on the negative phase of displacement. In the cases of the graded and single-density cores, the sandwich panels were sectioned into 16 pieces after blast loading, to visually inspect damage patterns. Figure 20.13(a) and (b) shows edge photographs of the sectioned graded panel along the short and long edges, respectively. Foam cracking and debonding of the foam layers from each

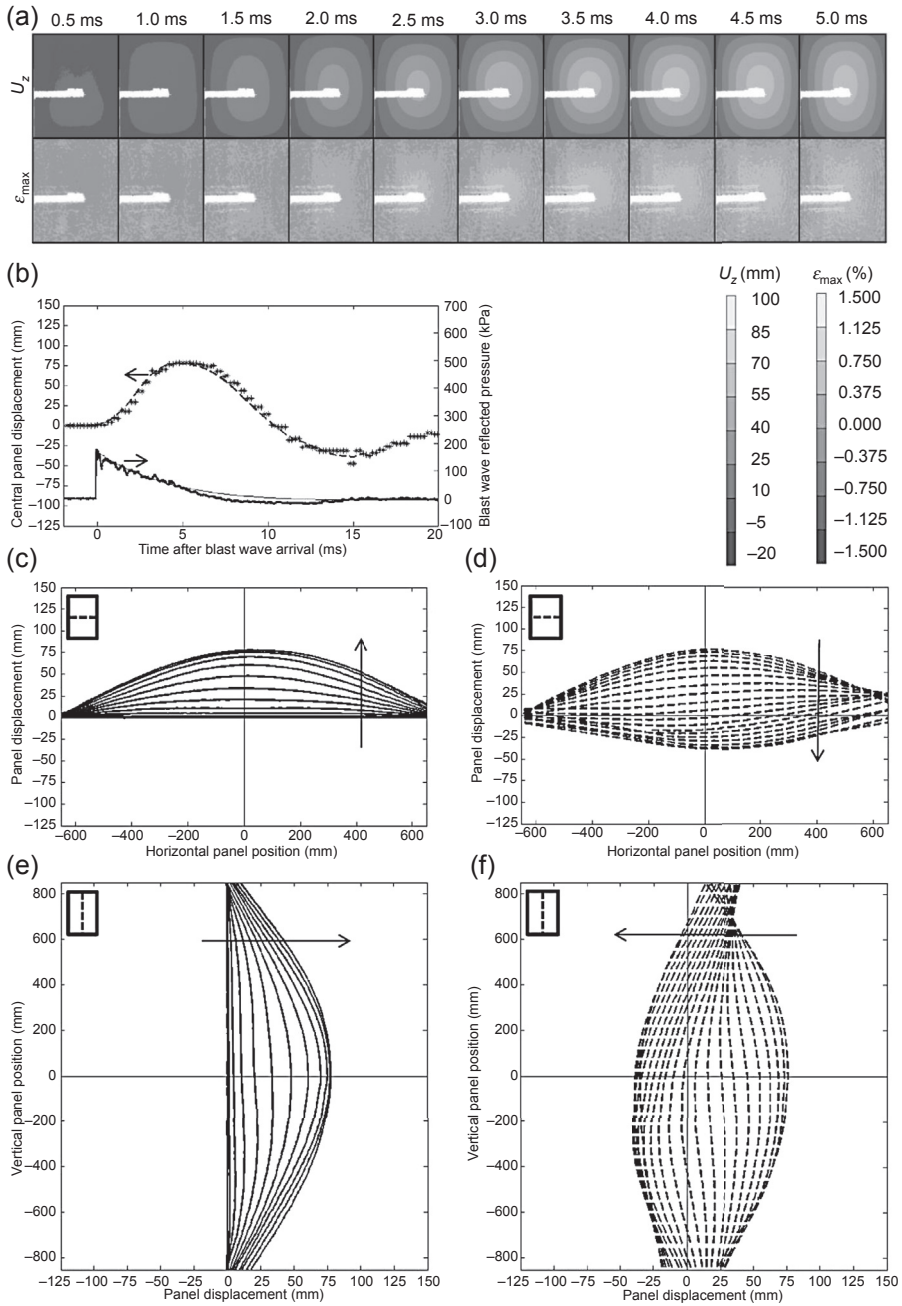

Figure 20.10 Results for the 30 mm P800 sandwich panel at 14 m stand-off from a 30 kg C4 charge. (a) DIC contour plots of out-of-plane displacement (U_z) and maximum principal strain (ε_{max}), with missing data due to laser gauge arm. (b) Measured and predicted reflected pressure during the test (solid), central panel deflection using DIC (dashed) and central panel deflection using a laser gauge (starred). (c) Horizontal centre positive phase. (d) Horizontal centre negative phase. (e) Vertical centre positive phase. (f) Vertical centre negative phase.

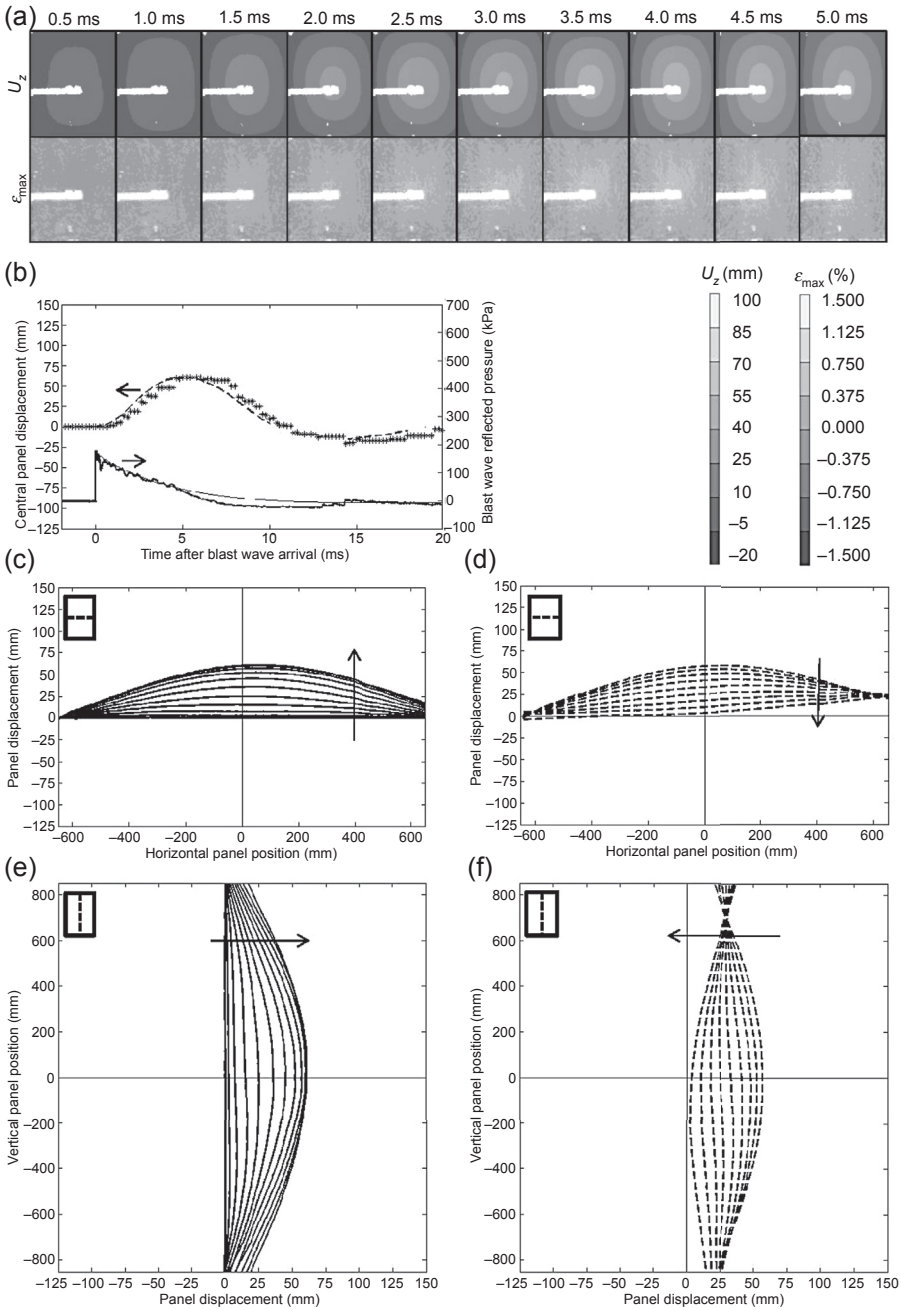

Figure 20.11 Results for the 40 mm P800 sandwich panel at 14 m stand-off from a 30 kg C4 charge. (a) DIC contour plots of out-of-plane displacement (U_z) and maximum principal strain (ε_{max}), with missing data due to laser gauge arm. (b) Measured and predicted reflected pressure during the test (solid), central panel deflection using DIC (dashed) and central panel deflection using a laser gauge (starred). (c) Horizontal centre positive phase. (d) Horizontal centre negative phase. (e) Vertical centre positive phase. (f) Vertical centre negative phase.

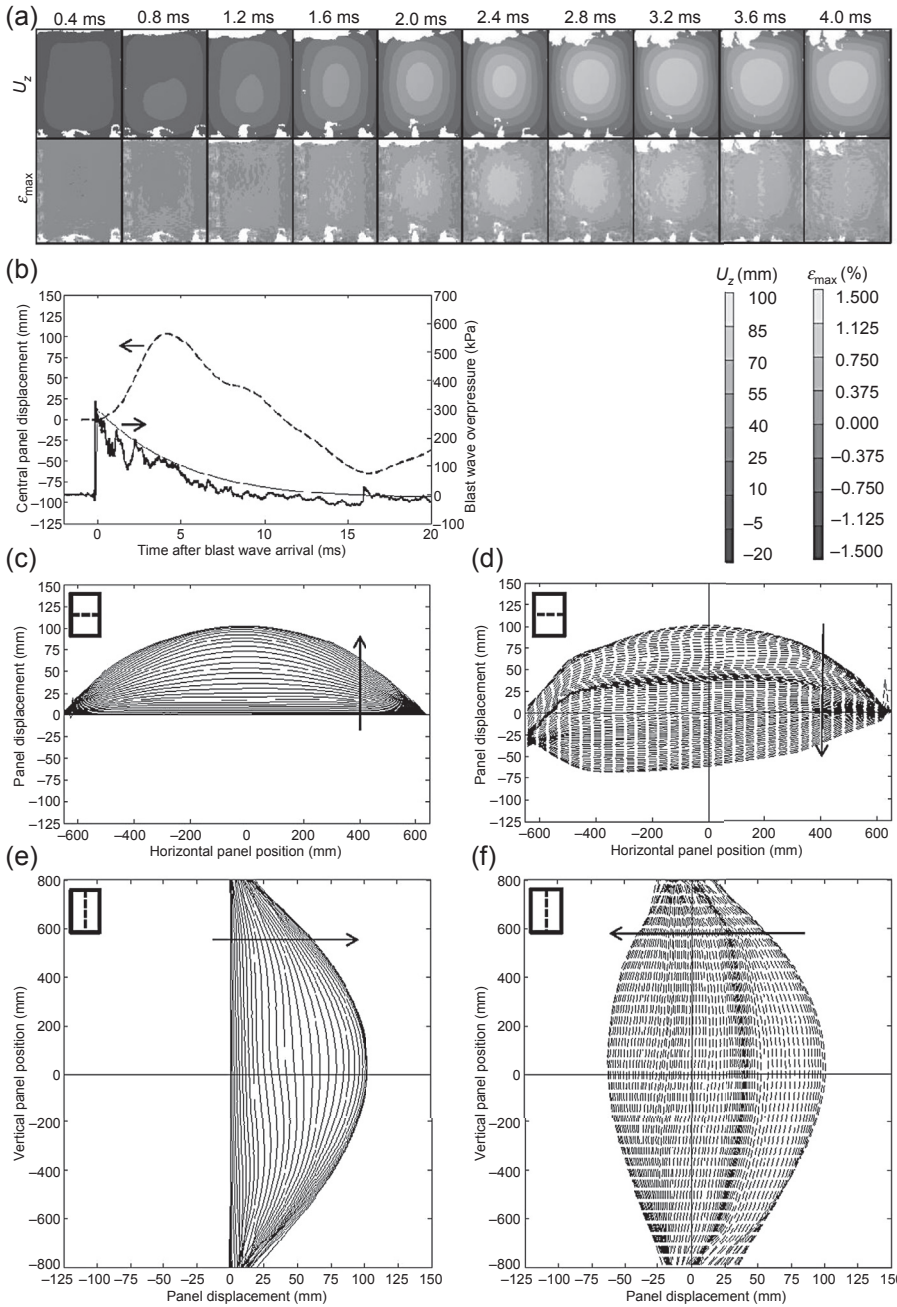

Figure 20.12 Results for the 30 mm graded sandwich panel at 15 m stand-off from a 100 kg C4 charge (a) DIC contour plots of out-of-plane displacement (U_z) and maximum principal strain (ε_{max}). (b) Measured and predicted reflected pressure during the test (solid), central panel deflection using DIC (dashed) and central panel deflection using a laser gauge (starred). (c) Horizontal centre positive phase. (d) Horizontal centre negative phase. (e) Vertical centre positive phase. (f) Vertical centre negative phase.

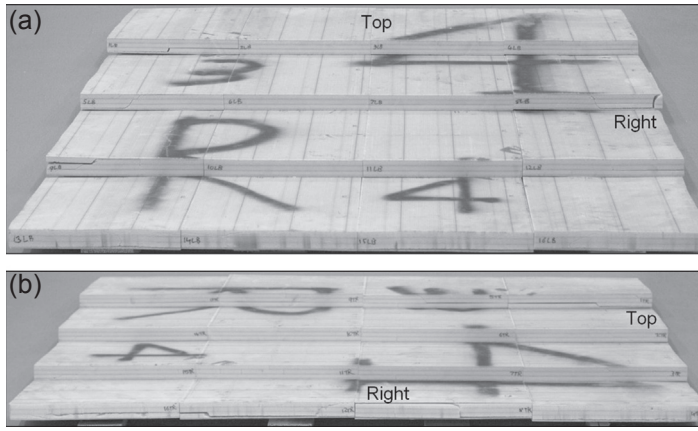

Figure 20.13 (a) Short edge photograph and (b) long edge photograph of the graded-density sandwich panel.

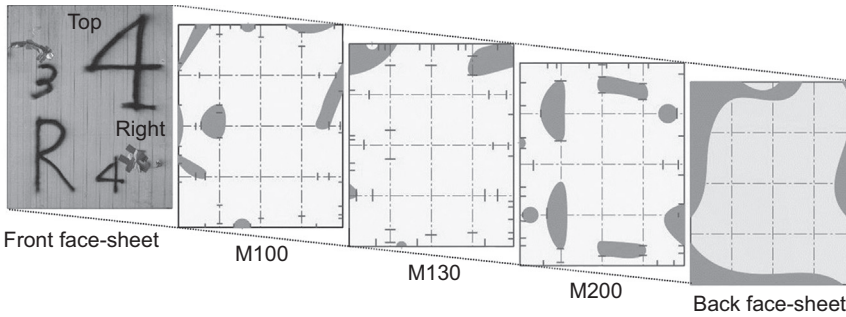

Figure 20.14 Damage map of each layer in the graded-density sandwich panel, showing debonds (shaded areas) and cracks (dashes).

other and from the face-sheet is clearly visible, and Figure 20.14 provides a map of the crack and debond locations throughout the panel thickness. Figure 20.15 shows the response of the 40 mm single-density M100 core, and contour plots are provided in Figure 20.15(a). The central displacement and pressure trace for the single-density core test is shown in Figure 20.15(b), indicating a maximum central deflection of 100 mm and a peak reflected pressure of 300 kPa. Based on Study B, a change in core thickness from 40 to 30 mm, if all test parameters are kept constant, would predict a maximum central displacement of 128 mm for a 30-mm-thick composite sandwich panel. This is 18 mm more displacement than actually observed. Figure 20.15(c–f) illustrates the deflection shape of the centre lines of the sandwich panel, which show significant amounts of core cracking, and on post-blast inspection front-face damage was observed. Photographed edges, as shown in Figures 20.16 and 20.17 provide maps of debonding and core cracking.

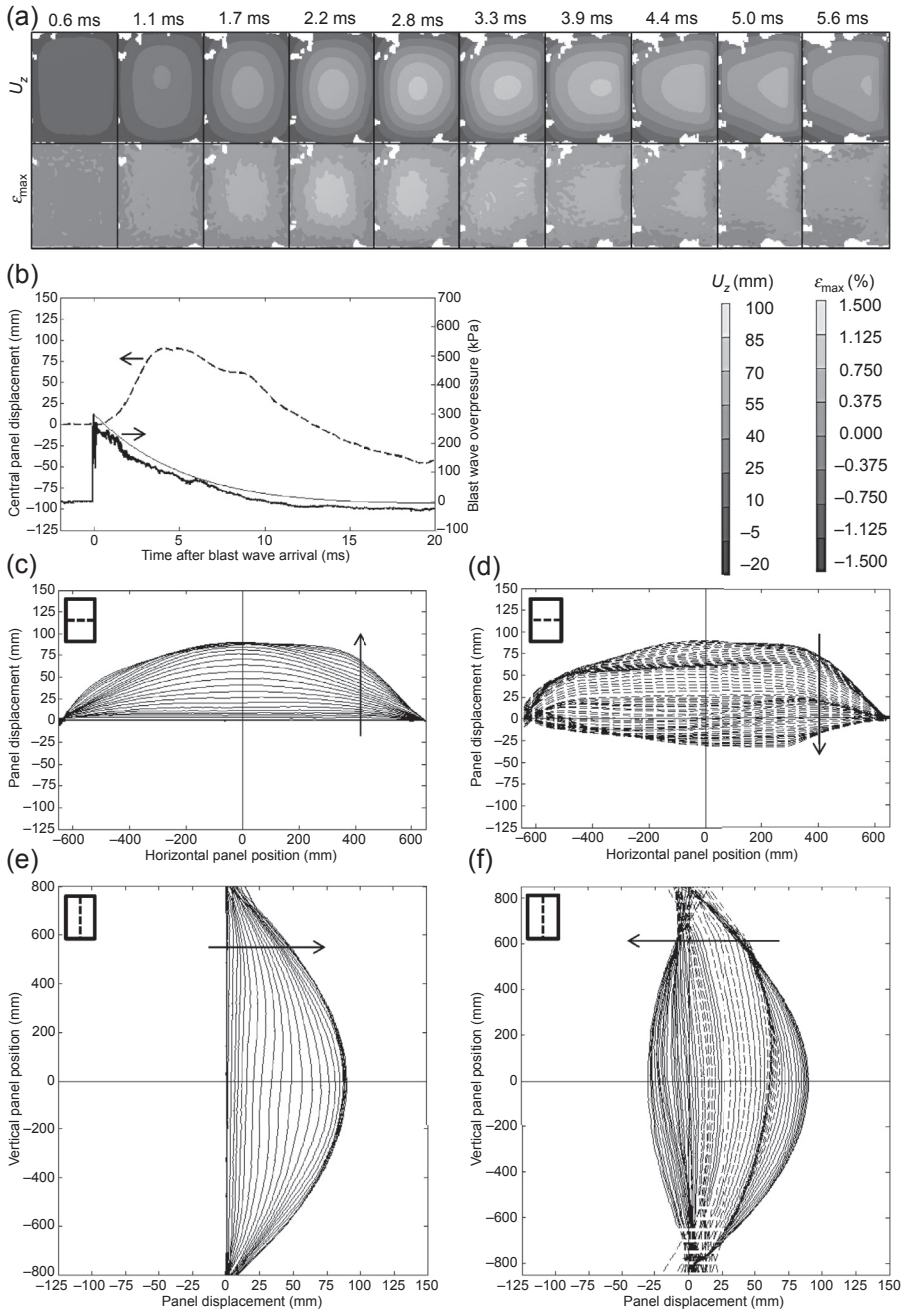

Figure 20.15 Results for the 40 mm M100 sandwich panel at 15 m stand-off from a 100 kg C4 charge (a) DIC contour plots of out-of-plane displacement (U_z) and maximum principal strain (ε_{max}). (b) Measured and predicted reflected pressure during the test (solid), central panel deflection using DIC (dashed) and central panel deflection using a laser gauge (starred). (c) Horizontal centre positive phase. (d) Horizontal centre negative phase. (e) Vertical centre positive phase. (f) Vertical centre negative phase.

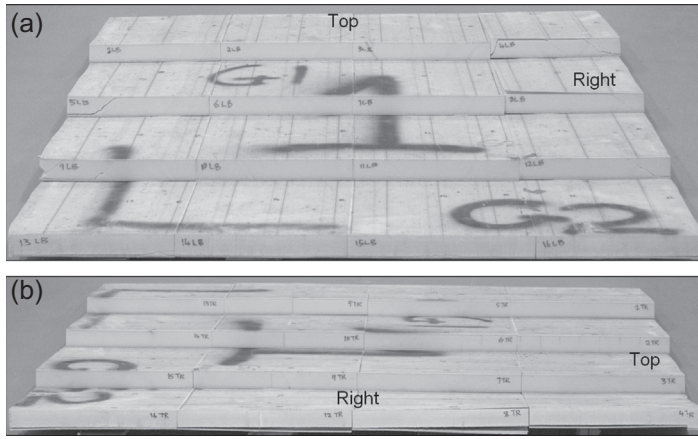

Figure 20.16 (a) Short edge photograph and (b) long edge photograph of the 40 mm M100 sandwich panel.

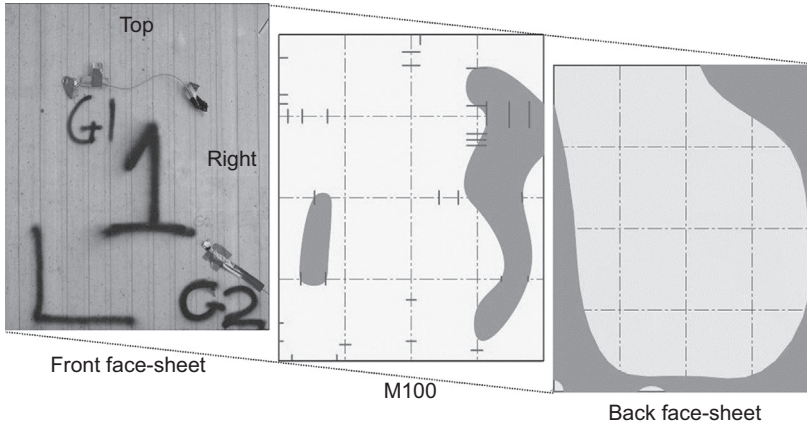

Figure 20.17 Damage map of each layer in the 40 mm M100 sandwich panel, showing debonds (shaded areas) and cracks (dashes).

20.7 Discussion

The results of Study A aimed to demonstrate the effect on sandwich panel response from stand-off distance and charge size. It was shown that core cracking can be observed from a change in gradient of the out-of-plane displacement across the sandwich panel and from high strain concentrations on the back face-sheet during blast loading. Damage was mostly observed through gradient changes horizontally across the panel, due to constraint on the rectangular panel. The use of DIC for measuring deflection has been validated via a comparison with a laser displacement gauge, situated behind the sandwich panels in the 30 kg C4 blast tests. The results of the

40-mm-thick P800 foam core test at 8 m with a 30 kg C4 charge and the 25-mm-thick M130 foam core test at 14 m with a 100 kg nitromethane charge indicate that the first failure type observed during blast loading of SAN−GFRP sandwich composites is shear cracking in the core, followed by compressive cracking of the front face in extreme cases, and this coincides well with the predictions made by Andrews and Moussa (2009) on predicting the failure types in polyvinyl chloride (PVC)−GFRP sandwich composites. These failure mode maps imply core shear failure to be the dominant failure type in the same configuration but with a PVC core, which provides a fair prediction that the failure type will be similar in an SAN core. If equal strain is to be expected on the front face-sheet as on the back face-sheet, front face-sheet failure is expected during these two tests, as the contour plots shown in Figures 20.7(a) and 20.9(a) show strain in excess of 1.5% (the tensile failure strain of QE1200 as per Table 20.2). The GFRP face-sheets are weaker in compression than in tension, as compressive failure is often initiated by failure of the fibre−matrix interface (Cooper & Kelly, 1969), so this strain aligns well with the front face-sheet cracking observed in the two tests. The use of DIC on the back face can also be used to highlight areas of core cracking in the sandwich panel, due to localised changes in strain in the area of the cracks. This is observed in the 100 kg nitromethane M130 foam core test, the DIC contour plot for which is shown in Figure 20.9(a). In the ε_{max} plots changes in strain are observed along the vertical edges of the panel, where core cracking took place, and sharp gradient changes are also observed in Figure 20.9(d). Sharp changes in strain are also observed in Figure 20.7(a) for the 40 mm P800 sandwich panel at 8 m stand-off to a 30 kg C4 blast.

A core thickness study was performed in Study B, considering the responses of two sandwich panels with all parameters kept constant except for the thickness of the core. The sandwich panels were the 30 and 40 mm P800 cores, tested at 14 m stand-off to a 30 kg C4 charge. Both of these tests provided an elastic response, and gave an indication of how the flexural stiffness as a result of increased second moment of area reduces the deflection of the sandwich panel during blast loading. The elastic response is shown in Figures 20.10 and 20.11 for the 30 and 40 mm core respectively, where sharp changes in gradient are not present and the deflection curves are smooth, indicating no damage. It was found that the maximum central deflection reduced by 28% by increasing the core thickness by 10 mm, which enabled a comparative study to be performed in Study C, where areal density but not thickness was kept constant. In this case a single-density core was compared to a sandwich panel with graded-density core layers, in order to understand the effects of providing step increases in density as the blast wave travels through the panel, as well as the effects of the step changes in density on the bending response. It was discovered that the extent of debonding and core cracking was similar in the two panels, but that in the graded-density core the cracks were hindered by the foam layer boundaries. Furthermore, the debonding of the back face in the single-density core was much greater than in the graded-density core. Another aspect in determining the suitability of the single and graded cores is the deflection during blast loading. The maximum deflection of the graded-core panel was 110 mm, and that of the single-core panel was 100 mm, but due to the difference

in thickness, and thus second moment of area, it was expected that the graded-density core would deflect significantly more. Using the comparison of the 40 and 30 mm cores from Study B, it is expected that the increase in deflection from reducing the core thickness from 40 to 30 mm is 28%, implying an expected deflection of the graded core of 128 mm, 18 mm more than actually observed. The beneficial results observed in the graded-density blast test agree well with the study performed by Wang, Gardner and Shukla (2012). It was found that the lower-density foam layers on the blast side reduced the intensity of the blast wave due to compression. However, in this study the blast intensity is not great enough to cause compression of even the lowest-density foam, which has a compressive strength of 1.55 MPa, as shown in Table 20.2, whereas the peak pressure during blast was measured to be 300 kPa, as shown in Figure 20.12(b). Nonetheless, the blast wave is reduced due to the change in densities throughout the sandwich panel, and damage is reduced due to the impedance of cracks travelling through the panel thickness. Damage is further reduced as a result of more bonded surface areas, meaning that debonding due to the panel bending requires more energy. By using much faster high-speed cameras in the graded-density and M100 sandwich panel tests, it was possible to observe much more clearly the development of the deflection curves. From Figure 20.12(c–f) the smoothness of the deflection is much greater than that in Figure 20.15(c–f). This is due to the graded foam layers inhibiting crack propagation through the panel thickness, thus retaining more local stiffness in the vicinity of damage than in the M100 sandwich panel. The DIC contour plots in Figures 20.12(a) and 20.15(a) do not show any sharp changes in strain, due to the lower severity of damage observed in these tests than in those of Study A. Another feature of the deflection was also highlighted with the use of faster high-speed cameras, observed during the rebound of both sandwich panels in Study C. Figure 20.12(d) and (f) and Figure 20.15(d) and (f) show a deceleration in rebound (visible in the higher density of lines on the positive axis of the plots). This deceleration is due to the unloading wave of the sandwich panel reaching the damaged areas at the sides of the sandwich panel where stiffness is lower due to cracking, reducing the rebound speed of the panel momentarily. This deceleration is also visible in the central displacement traces in Figures 20.12(b) and 20.15(b) at about 7.5 ms after the blast wave arrival.

20.8 Conclusion

The three studies performed have demonstrated the varying response types of SAN–GFRP sandwich panels to blast loading. The difference between elastic and inelastic loading to the same charge size has been demonstrated with a 40-mm-thick P800 foam core at 8 and 16 m stand-off, showing that the location of subsurface core damage can be determined using the maximum principal strain measured on the back face-sheet by DIC. Core cracking is also highlighted by sharp changes in gradient of deflection profiles during blast loading, as high bending is observed in the vicinity of a core crack. This method of observing

subsurface damage is further verified using the 25-mm-thick M130 foam core subject to a 100 kg nitromethane charge at 14 m, and the 40-mm-thick M100 foam core and 30-mm-thick graded foam core subject to 100 kg nitromethane charges at 15 m; however, the latter two cases did not exhibit sufficient core cracking to be highlighted in maximum principal strains. The use of DIC for displacement tracking was also verified with the positioning of a laser gauge behind the sandwich panel in three of the 30 kg C4 tests, which showed close agreement. The effect of core thickness has been considered using P800 foam cores subjected to 30 kg C4 charges at 14 m stand-off distances, with a 30-mm-thick and a 40-mm-thick core. The stand-off distance was chosen to ensure that the response type was elastic, to investigate the effect of the decreased flexural stiffness due to reduced thickness. It was found that by reducing the thickness of the core by 10 mm from 40 mm, the maximum central deflection increased from 61 to 78 mm, or a 28% increase. This result allowed a prediction on the expected deflection of the 30-mm-thick graded-density foam core, based on the 40-mm-thick single-density M100 foam core, to be 128 mm, instead of the 110 mm actually observed. This reduced deflection, alongside much lower damage observed upon post-blast inspection, indicates an improvement in blast resistance of the graded-density core to a single-density core of the same areal density. A further result from the blast tests performed is that when a camera with a higher frame rate is used, the development of the deflection profile reveals the time after blast that damage occurs within the sandwich panel. Furthermore, the greater number of frames captured during the test illustrates a deceleration in the rebound of the sandwich panel, caused by a lower flexural stiffness of the panel owing to core cracking at the edges. The three studies described here provide insight into testing methods for polymeric foam sandwich composite panels, and illustrate the various damage types expected.

The main findings from the research presented in this chapter can be summarised in the following points:

- The use of DIC reveals the location and severity of subsurface core cracking in foam core sandwich panels during blast loading. This is due to high strain concentrations on the back face-sheet and sharp changes in gradient of the out-of-plane deflection profile in the vicinity of core cracking.
- Damage in foam sandwich panels is dominated by core shear cracking initially, which leads to increased localised bending, resulting in front face-sheet cracking, most marked in GFRP, as it is weaker in compression than in tension.
- The effect of reducing the core thickness from 40 to 30 mm increases the central deflection of the panel by 28%, when the loading response is elastic. This is for large composite sandwich panels of 1.3 $\times$ 1.6 m rigidly supported along their edges.
- By using a graded-density foam core in the sandwich panel, the out-of-plane deflection is reduced, and core cracks are prevented from propagating across the whole core thickness. This also prevents localised bending and cracking on the front face-sheet.
- The use of faster high-speed cameras provides new information on the development of the out-of-plane deflection profile during blast loading, as well as highlights a deceleration in rebound of the sandwich panel due to reduced stiffness caused by core cracking.

Acknowledgements

We very much thank Dr Yapa Rajapakse of the Office of Naval Research (N00014-12-1-0403 and N00014-08-1-1151) for supporting Mark Kelly and Dr Hari Arora for their PhDs. Much appreciated is help and support from GOM UK, LaVision, Slowmo Camera Hire, CPNI, Gurit and DNV GL.

References

Andrews, E. W., & Moussa, N. A. (2009). Failure mode maps for composite sandwich panels subjected to air blast loading. *International Journal of Impact Engineering, 36*(3), 418−425. http://dx.doi.org/10.1016/j.ijimpeng.2008.08.005.

Arora, H., Hooper, P. A., Del Linz, P., Yang, H., Chen, S., & Dear, J. P. (2012). Modelling the behaviour of composite sandwich structures when subject to air-blast loading. *The International Journal of Multiphysics, 6*(3), 199−218. http://dx.doi.org/10.1260/1750-9548.6.3.199.

Arora, H., Kelly, M., Worley, A., Del Linz, P., Fergusson, A., Hooper, P. A., et al. (2014). Compressive strength after blast of sandwich composite materials. *Proceedings of the Philosophical Transactions of Royal Society, 372*, 20130212. http://dx.doi.org/10.1098/rsta.2013.0212.

Bahei-El-Din, Y. A., Dvorak, G. J., & Fredricksen, O. J. (2006). A blast-tolerant sandwich plate design with a polyurea interlayer. *International Journal of Solids and Structures, 43*(25−26), 7644−7658. http://dx.doi.org/10.1016/j.ijsolstr.2006.03.021.

Cooper, G., & Kelly, A. (1969). Role of the interface in the fracture of fiber-composite materials. *Interfaces in composites* (pp. 90−106). Pennsylvania: American Society for Testing and Materials.

Gardner, N., Wang, E., Kumar, P., & Shukla, A. (2011). Blast mitigation in a sandwich composite using graded core and polyurea interlayer. *Experimental Mechanics, 52*(2), 119−133. http://dx.doi.org/10.1007/s11340-011-9517-9.

Gurit, S.P. *Material data sheets*. www.gurit.com. Accessed May 2015.

Hause, T., & Librescu, L. (2005). Dynamic response of anisotropic sandwich flat panels to explosive pressure pulses. *International Journal of Impact Engineering, 31*(5), 607−628. http://dx.doi.org/10.1016/j.ijimpeng.2004.01.002.

Hohe, J., Librescu, L., & Yong Oh, S. (2006). Dynamic buckling of flat and curved sandwich panels with transversely compressible core. *Composite Structures, 74*(1), 10−24. http://dx.doi.org/10.1016/j.compstruct.2005.03.003.

Hoo Fatt, M. S., & Palla, L. (2009). Analytical modeling of composite sandwich panels under blast loads. *Journal of Sandwich Structures and Materials, 11*(4), 357−380. http://dx.doi.org/10.1177/1099636209104515.

Jackson, M., & Shukla, A. (2011). Performance of sandwich composites subjected to sequential impact and air blast loading. *Composites Part B: Engineering, 42*(2), 155−166. http://dx.doi.org/10.1016/j.compositesb.2010.09.005.

LeBlanc, J., Shukla, A., Rousseau, C., & Bogdanovich, A. (2007). Shock loading of three-dimensional woven composite materials. *Composite Structures, 79*(3), 344−355. http://dx.doi.org/10.1016/j.compstruct.2006.01.014.

Librescu, L., Oh, S.-Y., & Hohe, J. (2004). Linear and non-linear dynamic response of sandwich panels to blast loading. *Composites Part B: Engineering, 35*(6−8), 673−683. http://dx.doi.org/10.1016/j.compositesb.2003.07.003.

Librescu, L., Oh, S.-Y., & Hohe, J. (2006). Dynamic response of anisotropic sandwich flat panels to underwater and in-air explosions. *International Journal of Solids and Structures, 43*(13), 3794−3816. http://dx.doi.org/10.1016/j.ijsolstr.2005.03.052.

Li, R., Kardomateas, G. A., & Simitses, G. J. (2008). Nonlinear response of a shallow sandwich shell with compressible core to blast loading. *Journal of Applied Mechanics, 75*(6), 061023. http://dx.doi.org/10.1115/1.2937154.

Mouritz, A. P. (2001). Ballistic impact and explosive blast resistance of stitched composites. *Composites Part B: Engineering, 32*(5), 431−439. http://dx.doi.org/10.1016/S1359-8368(01)00015-4.

Panciroli, R., & Abrate, S. (2012). Dynamic response of sandwich shells to underwater blasts. *Central European Journal of Engineering, 2*(4), 509−522. http://dx.doi.org/10.2478/s13531-012-0024-2.

Qiu, X., Deshpande, V. S., & Fleck, N. A. (2004). Dynamic response of a clamped circular sandwich plate subject to shock loading. *Journal of Applied Mechanics, 71*(5), 637. http://dx.doi.org/10.1115/1.1778416.

Smith, P., & Hetherington, J. G. (1994). *Blast and ballistic loading of structures* (1st ed.). Oxford: Butterworth-Heinemann Ltd.

Tekalur, S. A., Bogdanovich, A. E., & Shukla, A. (2009). Shock loading response of sandwich panels with 3-D woven E-glass composite skins and stitched foam core. *Composites Science and Technology, 69*(6), 736−753. http://dx.doi.org/10.1016/j.compscitech.2008.03.017.

Tekalur, S. A., Shivakumar, K., & Shukla, A. (2008). Mechanical behavior and damage evolution in E-glass vinyl ester and carbon composites subjected to static and blast loads. *Composites Part B: Engineering, 39*(1), 57−65. http://dx.doi.org/10.1016/j.compositesb.2007.02.020.

Tekalur, S. A., Shukla, A., & Shivakumar, K. (2008). Blast resistance of polyurea based layered composite materials. *Composite Structures, 84*(3), 271−281. http://dx.doi.org/10.1016/j.compstruct.2007.08.008.

Wang, E., Gardner, N., & Shukla, A. (2009). The blast resistance of sandwich composites with stepwise graded cores. *International Journal of Solids and Structures, 46*(18−19), 3492−3502. http://dx.doi.org/10.1016/j.ijsolstr.2009.06.004.

Wang, E., & Shukla, A. (2011). Blast performance of sandwich composites with in-plane compressive loading. *Experimental Mechanics, 52*(1), 49−58. http://dx.doi.org/10.1007/s11340-011-9500-5.

Maintenance and monitoring of composite helicopter structures and materials

21

M. Martinez[1], *M. Yanishevsky*[2], *B. Rocha*[2], *R.M. Groves*[1], *N. Bellinger*[2]
[1]Delft University of Technology, Delft, The Netherlands; [2]National Research Council of Canada, Ottawa, ON, Canada

21.1 Introduction

The maintenance and monitoring strategies used for primary aerospace structures depend on the philosophy to which the structures were designed and the intended operations. For the benefit of the reader, a discussion of helicopter structural design philosophies, maintenance approaches and trends, and future structural integrity methodologies and processes is presented.

21.1.1 Discussion of helicopter structural design philosophies

Historically, helicopter structural design had to meet safe-life requirements, demonstrating durability for a given period under typical expected production and service conditions. Inspection was not considered in the design or testing process, typically being an afterthought, conducted at times of opportunity to deal with accidental/unexpected damage. To guarantee safety, the US Federal Aviation Administration (FAA) has recently established certification guidelines requiring the demonstration of damage tolerance for helicopter structures made of composite materials (Federal Aviation Regulation, 2012). Helicopter principal structural elements (PSE) in composite material must now be designed to account for discrete and inherent manufacturing induced and/or service induced damages, such as those originating from fatigue, environmental effects, intrinsic and discrete flaws, impact, or other accidental damages at critical locations. Consideration is also given to account for damage detectability of inspection techniques to determine inspection intervals and establish a scheduled maintenance plan, as well as the variability of material properties and manufacturing process/fabrication.

Some helicopter structures cannot be designed to meet damage tolerance requirements in a practical way, because they are either noninspectable and/or have constraints in geometry or weight. Some of these structures are also subjected to high frequency dynamic loads, typically accumulating hundreds of thousands of cycles per hour, in which significant damage growth above a detectable size can occur in a short period, on the order of tens of operating hours or less. Original equipment manufacturers (OEMs) are now adopting the flaw tolerant safe life route, also accounted for

Structural Integrity and Durability of Advanced Composites. http://dx.doi.org/10.1016/B978-0-08-100137-0.00021-3

in FAR 29.573 (Federal Aviation Regulation, 2012), demonstrating the survivability of the structure considering the existence of maximum acceptable manufacturing flaws and in-service damage—providing evidence that these will not grow to a size affecting residual strength between inspections, with the parts being retired at an established service life.

21.1.2 Maintenance approaches and trends

At this time, there is also a requirement by the different helicopter operators, whether civilian or military, to reduce cost and maintenance, while increasing the availability without compromising structural integrity. For nondynamic components, a planned maintenance approach requires the aircraft to be removed from service while a complete inspection of the structure is performed. For the case of dynamic components, not only is there a planned maintenance approach, but these are replaced once they have achieved their expected allowable service lives. As the complexity of the structures increases, the maintenance requirements and expense to maintain the health of the structure tend to also increase. Inspection and maintenance intervals are usually modified throughout the life of the aircraft based on service experience, with structural components being subjected to regular inspections, although the number of times these inspections take place can vary dramatically. With helicopter platform age and with the opportunity for unexpected service damage increasing, the inspection frequency and need for repair will also increase, causing a significant rise in maintenance costs.

In an attempt to reduce this economic burden, research is being carried out internationally to develop new maintenance approaches and techniques (Bellinger & Martinez, 2009; Jardine, Lin, & Banjevic, 2006; Liao, 2010; Ofsthun, 2002; Scanff et al., 2007). These approaches have a common objective: to reduce the maintenance cost of an asset by more accurately determining the remaining useful life of a component while maintaining safety.

21.1.2.1 Condition based maintenance

One approach that attempts to reduce the maintenance burden is known as condition based maintenance (CBM). In the CBM approach, specific data are collected, processed, and analysed with the sole purpose of making a maintenance decision, such as can the aircraft continue to fly safely, or are there enough indications that the structure needs to be repaired or replaced before flight operations continue or within a subsequent determined period of operation. The collection of data can be handled either manually or by an automated system, and in most cases, a combination of both is considered. The type of data collected varies, as described by Jardine et al. (2006), and may be divided into event data and condition monitoring data. The first describes all breakdowns, overhauls, and the findings of what caused these damages. The second will depend on the conditions being monitored, for example:

- The quality of the oil in an engine gearbox is monitored to identify metallic particles that can result from wear (fretting) damage or cracked gears (Howe & Muir, 1998);

- Vibration is monitored using a variety of accelerometers strategically located around the structure to determine the potential for damage (Zhang, Schulz, Naser, Ferguson, & Pai, 1999);
- Temperature is monitored in key areas using a variety of sensors to detect overheating conditions; and,
- Ultrasonic sensors, fibre Bragg grating (FBG) sensors (Betz, Thursby, Culshaw, & Staszewski, 2003), and/or acoustic emission sensors (Gagar, Irving, Foote, & McFeat, 2012) are used to detect specific types of damage in critical areas.

All of these various sensors provide data in different forms; however, they have all been shown to provide information that may lead to the identification and, in some cases, the quantification of a possible upcoming failure scenario (Miller & Kitaljevich, 2000).

The data acquisition process for CBM, however, may be filled with errors introduced during the manual logging of event data after the flight (e.g. missed logging of an extraordinary flight condition such as an unusually sharp turn) or through faulty sensors. In the initial stages of processing, the data are cleaned (through elimination of noise and erroneous measurements or through data reduction processes) for use in a variety of models and mathematical algorithms pertaining to specific failure mechanisms. The results of these mathematical algorithms aid in the decision-making process through diagnostics and prognostics.

Diagnostics provide the operator with the current physical state of the aircraft, while prognostics attempt to provide a look into the future by predicting failure before it actually occurs. The primary objective of prognostics is to aid in determining the remaining life of aerospace components based on the physical state (health) of the structure and its subcomponents and presumed future usage. In this approach, fault isolation and damage forecasting in real-time are necessary elements informing operators of upcoming failure scenarios. It is foreseeable that in extreme cases, the pilot or maintainers would be informed of eminent danger in this approach (Hess & Fila, 2002); however, this is highly unlikely until the reliability of the systems providing this information can be confirmed. Still, this additional real-time information on the health of critical structures can provide operators with new capabilities to prepare for upcoming repairs and, if necessary, modify flight operations, thus potentially creating a proactive scenario for structural inspection and maintenance, and for the efficient management of resources—repair teams and spare part supply chains (Hess & Fila, 2002).

Note that in some cases in the open literature prognostics is referred to as either prognostic health management or prognostic health monitoring (PHM). The latter terminology is used to distinguish the engineering tasks associated with “PHM” from the business management and cost−benefit tasks of its implementation (Leão, Fitzgibbon, Puttini, & de Melo, 2007).

It is not uncommon for many of the terminologies used to describe CBM and PHM to be applied interchangeably by the community. However, and even if these three processes and approaches are deeply interlinked and complementary, they do not rely on the same fundamental process or approach, or have the exact same objectives.

21.1.2.2 Inspection of helicopter structures and structural health monitoring

Currently, several non-destructive inspection (NDI) techniques are used to inspect in-service aircraft, such as ultrasonic (Hillger et al., 2012); acoustic emission (AE) (Miller Hill, & Moore, 2005); electromagnetic (Udpa & Moore, 2004); leaky ultrasonic (Jackson, Sherlock, & Moore, 1997); liquid penetrant (Tracy & Moore, 1999); magnetic particle (Moore & Moore, 2008); radiography (Bossi, Iddings, Wheeler, & Moore, 2002); thermal infrared (Maldague & Moore, 2001); and visual (Allgaier, Cameron, & Moore, 2010). NDI systems interrogate a structure for material discontinuities that pre-exist within a material or have developed during service. However, these types of inspections currently require a high level of human interaction and are intended for local or focused inspections, requiring in most cases access to the area of interest, with the consequent grounding of the aircraft and long and expensive disassembly and assembly operations, as described in Roach and Neidigk (2012). To address these drawbacks, in the last three decades the concept of structural health monitoring (SHM) has been examined for the identification and quantification of structural damage. SHM may be defined as the continuous, autonomous in-service monitoring of the physical condition of a structure by means of embedded or attached sensors with minimum manual intervention. The data obtained from an SHM system can then be used for the CBM approach.

Currently, there are no unique standard guidelines for certifying SHM for use on helicopters, and thus operators must address regulatory concerns on a case-by-case basis. Different committees are presently writing guidelines to have SHM approved by the different airworthiness authorities (Aerospace Standards Newsletter, 2010). To assess the performance and capabilities of SHM equipment, the National Research Council of Canada (NRC) has developed a series of full-scale fatigue test facilities that range in complexity from a simple cantilever beam to a full-scale test of an aircraft wing (http://www.globalspec.com/NRCIARSMPL/Ref/STR-04.pdf, last accessed September 2012; http://www.nrc-cnrc.gc.ca/eng/solutions/advisory/materials_testing.html, last accessed September 2012) and helicopter structures. These facilities enable SHM equipment manufacturers, academia, and aircraft operators, maintainers, and related OEMs to determine the capability of SHM systems to detect and monitor damage under constant and standardized variable loading spectra, such as fighter aircraft loading standard for fatigue (FALSTAFF) (Schijve, 2009). These facilities also allow SHM systems to be tested under simulated conditions for use on new and legacy aircraft and to allow developers to operate these systems alongside approved NDI techniques to determine their accuracy and reliability. One of the goals for these test facilities is to assist regulatory agencies and operators to build confidence in SHM systems, to ultimately reduce, if not completely replace, the need for scheduled NDIs. However, this goal is recognized to be a long-term objective of SHM. Currently, these systems are only being implemented at specific hot spots to monitor the formation of known damage, being operated in parallel with scheduled NDIs. An immediate requirement for SHM systems is to be capable of detecting damage to structural composite or metallic-bonded repairs carried out on military aircraft to maintain structural integrity and safety of flight (Baker, McKenzie, & Jones, 2004).

SHM and NDIs are comparable fields of engineering science. It is important to note that in the aerospace industry SHM has yet to be fully accepted by airworthiness authorities, such as the FAA, the European Aviation Safety Agency, and Transport Canada, although one of the ultimate goals of these systems is to contribute to the replacement of scheduled maintenance and for helicopter operators to obtain maintenance credits. This may also have a potential future effect on OEMs adopting newer design approaches considering SHM from the outset such that they are able to design lighter, more efficient aircraft with enhanced mission performance capability. Another important factor is the lack of a clear understanding of the cost benefit (Hess & Fila, 2002) associated with using SHM instead of approved scheduled NDIs.

21.1.3 Future structural integrity methodologies and processes

Many involved in these research fields believe that several of the methodologies and processes mentioned above are not sufficient and that an in depth understanding of the reasons why structural damage occurs is required. To meet this, NRC and the scientific community have been working on a physics-based approach to structural integrity known as the holistic structural integrity process (HOLSIP). The goal of HOLSIP is to more accurately assess the reliability and structural integrity of aerospace structures (Hoeppner, 2011; http://www.holsip.com/, last accessed September 2012; Liao & Renaud, 2010) by understanding the service loads, the initial and current material and structural conditions, and environmental effects on the structural performance. All these conditions and properties can interact, and thus a multiphysics-based model is required, which is a fundamental part of HOLSIP, to assess the remaining useful component life of an aerospace structure, as shown in Figure 21.1.

The usage monitoring flow chart, shown in Figure 21.1, uses two distinct approaches to estimate/measure the loads within a helicopter. The first approach, flight conditioning monitoring, uses transfer function-based methods, such as machine learning algorithms using neural networks (Liu, Cheung, & Martinez, 2011) with the incorporation of fuzzy logic (Yen & Bui, 1997) to estimate the loads on the structure based on the flight state and control parameters, that is altitude, attitude and other manoeuvre-related parameters, such as velocity and acceleration, and aircraft weight. The second approach, known as flight load monitoring, combines the use of sensors to directly measure structural health, through SHM techniques, and usage, by analysing the direct measurements of loads acting on the structure. The obtained load spectra and the assessed condition of the structure can then be used either directly to determine the remaining life of a critical structure or indirectly to develop appropriate load spectra for other critical locations through the use of transition algorithms.

The implementation of SHM, PHM and CBM can have the biggest impact in situations in which there are significant changes in missions, operations, and environment, which affect the ageing process of civilian and military fleets. It is not uncommon to find military helicopters that were originally acquired by their governments for search and rescue (SAR) operations in a maritime environment to be performing military duties in a desert. The differences in environment and manoeuvres have an effect on the life of a structural component. This has a direct effect on the operational

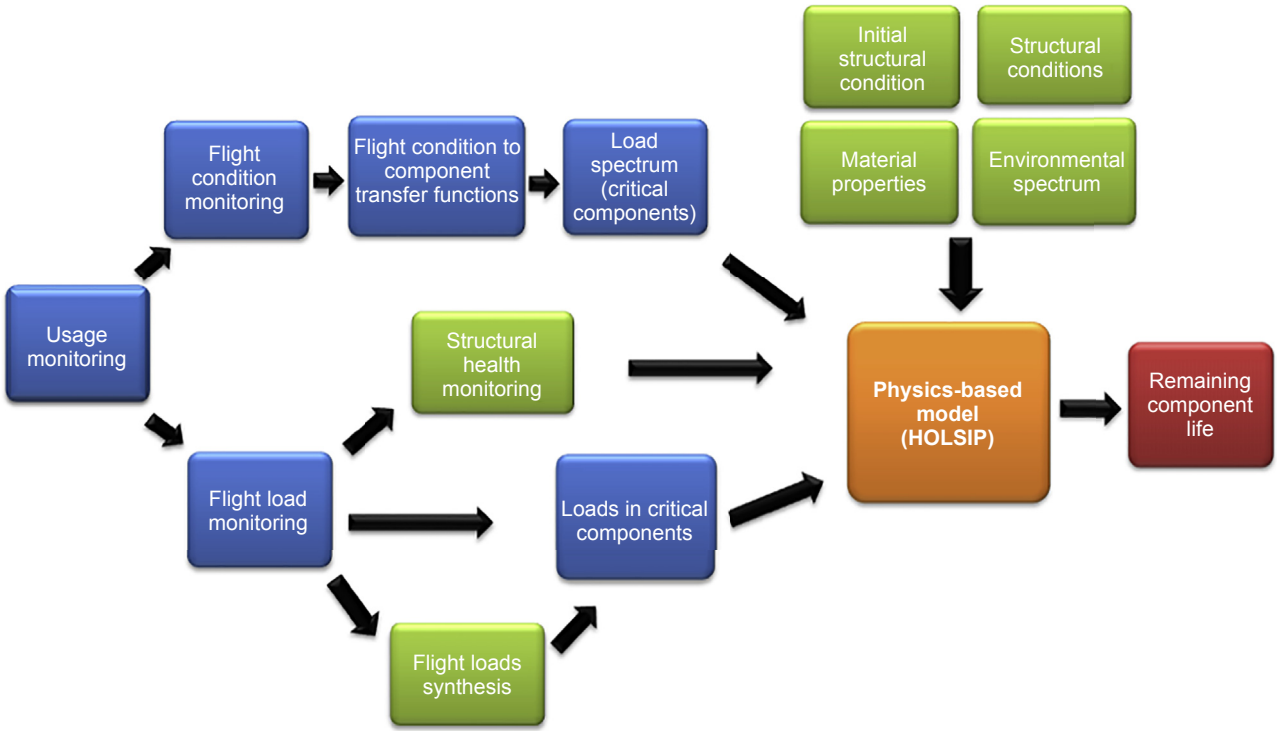

Figure 21.1 HOLSIP—usage monitoring flow chart.
Martinez, M., Rocha, B., Li, M., Shi, G., Rutledge, R., & Yanishevsky, M. Load monitoring of aerospace structures using micro-electro-mechanical systems (MEMS). In *Proceedings of the ASME 2012 conference on smart materials, adaptive structures and intelligent systems SMASIS 2012*, 19−21 September 2012, Stone Mountain, Georgia, USA.

and particularly on the maintenance costs of a helicopter. As shown by Sen and Everett (2000), the second largest cost in the maintenance of medium and heavy helicopters is incurred by dynamic components. The structural maintenance costs of an airframe represent approximately 1% of the total life cycle cost of the aircraft, while just the labour component of the maintenance costs associated with dynamic components and drivetrain represents approximately 10%.

In summary, many of the above-mentioned multidisciplinary fields are working toward reducing the maintenance burden and costs in helicopter and fixed-wing aircraft due to ageing or structural degradation in diverse operational service environments. The next section describes briefly some of the damages found in aerospace structures as they relate to composite structures/materials.

21.2 Explanation of damage degradation modes

The introduction of composites into the aerospace industry has been a real benefit in the development of more efficient aircraft, due to properties such as their high specific strength. However, these types of materials are considered 'brittle' in that there is little warning (yielding) that takes place prior to failure, a behaviour which is normally exhibited by metallic materials. This lack of warning is one reason why aircraft manufacturers are looking at implementing SHM systems for composite components. One of the primary challenges of these types of structures, when compared to their metallic counterparts, is the variability in mechanical properties resulting from their manufacturing processes. In metallic structures, when an alloy has been developed it is usually characterized by properties such as static strength, Young's Modulus, fracture toughness, etc. However, with composite materials, two different structures can be produced with the same fibre and resin system and exhibit different mechanical properties and structural behaviour. This variation is governed by the manufacturing process that is used to produce the structures, which in turn creates an extra level of complexity in the development of a unified database of composite material parameters. In addition, composite structures fail in different ways than previously experienced by their metallic material counterparts.

Composite structures are affected by disbonds, inclusions, resin-rich and resin-starved areas, fibre breakage, core crushing (honeycomb material), impact damage, and environmental degradation effects. The next few pages describe in more detail some of the typical damages that have been found in aerospace composite structures.

21.2.1 Disbonds

Harsh environments and severe operational service loading conditions may lead to the formation of many types of damage in aerospace structures. One of these types is known as a disbond, which is defined as the separation at the adhesive bond line of a bonded joint. In the aerospace industry, it is common to find composite-to-composite, composite-to-metal, and metal-to-metal joints. Figure 21.2 shows a typical test that is performed for analysing disbonds of a composite sandwich structure.

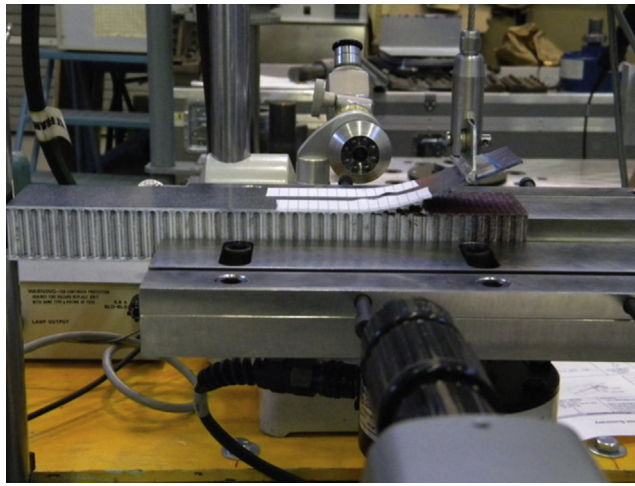

Figure 21.2 Disbond test of composite sandwich structure.

Regardless of the type of materials used, a poor bond may lead to catastrophic failure. The study of bonded joints has acquired a lot of interest in recent years due to the development of the Airbus A380 and Boeing Dreamliner, which use large amounts of composite materials. Disbonds have also been identified as the source of structural failures, such as in the case of the Airbus A310-308 rudder loss during Air Transat flight TSC961from Varadero, Cuba, to Québec City, Canada, on March 6, 2005, with 262 passengers and nine crew members on board (Aviation Investigation Report, 2005; Southward, Horrigan, Mallinson, & Jayraman, 2007). The cause of this accident was the presence of a pre-existing disbond, that is an in-plane core fracture damage on the rudder that was not detectable from the outside. The OEM recommended inspection program for this structure was not adequate for the detection of this type of discontinuity, and also the design of the structure did not include any means of stopping disbond growth before the damage reached a critical size (Aviation Investigation Report, 2005). As a consequence, industry and many research organizations have been examining this type of failure mechanism and are investigating several NDI and SHM techniques for disbond identification and quantification (Genest, Martinez, Mrad, & Renaud, 2008; Habib, Martinez, Artemev, & Brothers, 2013; Yanishevsky et al., 2010).

However, bonded joints are not only of interest as part of the original design and manufacturing process, but also as bonded patches for repair or fatigue enhancements to locations where full-scale tests have demonstrated that given enough fatigue cycles, damage will form. Such adhesively bonded fatigue enhancement patches have been tested by the Royal Canadian Air Force to evaluate life extension of critical primary structures during full scale testing, such as the CF188 fighter aircraft centre barrel (Landry, 1999).

Many researchers within the scientific community have been studying the development of a ‘smart patch’ concept to guarantee that a bonded joint or bonded repair

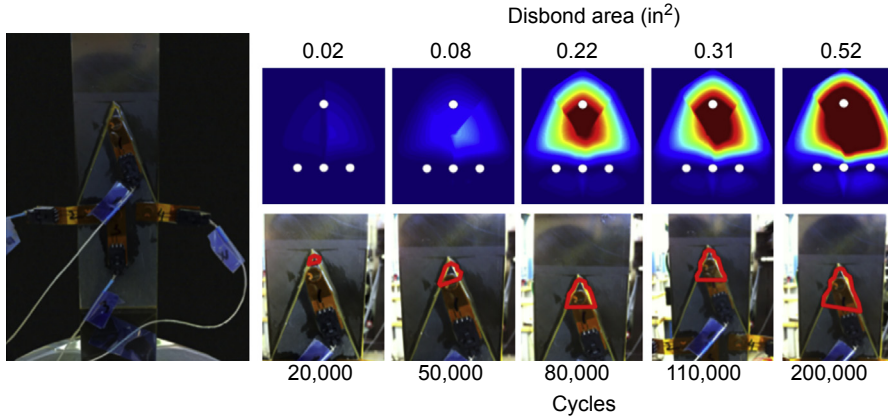

Figure 21.3 Smart patch bonded repair concept of a composite-to-composite joint.
Habib. F. (2012). Structural health monitoring of adhesively bonded composite joints (M.A.Sc. thesis). Ottawa, Canada: Department of Mechanical and Aerospace Engineering, Carleton University.

containing a disbond would continue to carry the loads. One of these studies is described in Davis, Baker, Moss, Galea, and Jones (2002). In this study, piezoelectric transducers (actuators and sensors), for the application of Lamb waves, were used to monitor the physical state of a repair patch adhesively bonded to a coupon undergoing cyclic loading, as depicted in Figure 21.3. The primary objective of the smart patch concept is to monitor the integrity of the adhesive bond line and thus provide reliable information that will allow maintenance personnel to assess whether the repair is intact and carrying the load, or that it has disbonded/failed. In some cases, bonded patches have been used on in-service aircraft as fatigue enhancements, in areas where service experience has demonstrated that the area is prone to cracking (Galea et al., 2001; Russell, 1988). In the case of the Royal Australian Air Force (RAAF) F-111C, patching over an existing crack was required to allow the aircraft to remain in-service (Davis et al., 2002). In this case, there is a requirement for the smart patch repairs to monitor the formation or growing of potential damage in and under the repair. Similarly, the rotary wing aircraft industry is also considering the use of bonded repairs as a means for extending the useful lives of their fleets.

In the development of these bonded repair scenarios, several NDI and experimental mechanic techniques have been identified as technologies that can be used to evaluate the capabilities of SHM systems to identify disbonds, as shown in Figure 21.4. One such technique is known as thermoelastic stress analysis (TSA). This technique has been shown in Backman, Martinez, Renaud, Genest, and Chisholm (2007) to be able to monitor the disbond growth process in both composite-to-composite and composite-to-metallic bonded joints in real-time. In practical applications, a smart patch concept needs to be able to reliably identify when a disbond has developed. This would direct further NDIs of the repair and potentially other necessary actions to maintain the structural integrity of the aircraft.

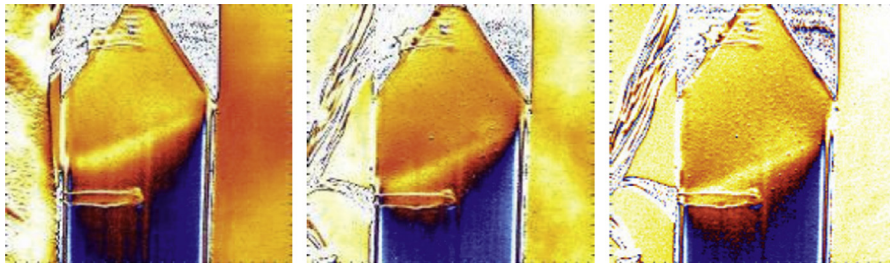

Figure 21.4 Thermoelastic stress analysis of a composite patch disbonding from a metallic substrate.
Martinez, M., Renaud, G., Backman, D., Genest, M., & Delannoy, M. (2007). Demonstration of an instrumented patch. *Presented in the proceedings of SPIE:* Vol. 6530, ISBN: 9780819466518.

21.2.2 Delamination

Delamination may be considered to be analogous to cracks in metallic structures and may be defined as the separation of plies or laminas within a composite, as shown in Figure 21.5. Several reasons have been identified as the cause for delaminations: poor manufacturing, thermal residual stresses, chemical shrinkage (Bolotin, 1996), impact damage, excessive loading in the orthogonal direction to fibre alignment, and buckling loads during operational service of the structure to name a few. Whatever the reasons, a delamination in a structure is a major concern, particularly if it continues to grow, and when this is identified in rotary aircraft structures, it is sufficient to ground the aircraft until its cause and requisite plan of action can be determined. Often this entails a good understanding of the operational loads and the undertaking of complex analyses (F.A.A. Advisory Circular, 2009).

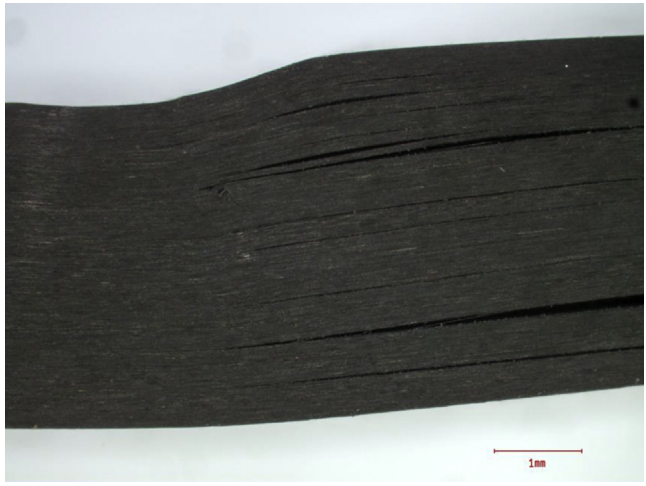

Figure 21.5 Delamination in an epoxy carbon short beam shear test.

Delaminations may occur internally in the structure, in multiple locations, as shown in Figure 21.5. However, they are not only found in bulk composite materials, but also in sandwich structures, where their high strength and stiffness makes them ideal candidates for rotary wing applications. In sandwich structures, there are potential failure modes at the skin and at the core of the structure. In the past 10 years, much work has been performed by the research community in the development of failure theories for composite structures. However, these theories do not always have the same level of sophistication and maturity as their metallic counterparts. Thus, the implementation of composite structures is usually preceded by the conduct of a large experimental program that identifies the shortfalls of these materials and structures and a clear understanding of the load carrying capabilities of these structures.

21.2.3 Voids

During the manufacturing process of composite materials, there is the risk that voids may form internally within the material, as shown in Figure 21.6. The formation of these types of internal discontinuities is due to a variety of manufacturing issues such as entrapment of air during the resin flow and/or entrapment of volatile substances during the curing cycle (Aviation Investigation Report, 2005). Thus the American Society for Testing and Materials (ASTM) has developed a standard (ASTM D2734-94d) to characterize the void ratio in reinforced plastics. Unfortunately, it has been shown that the size and shape of the voids have an impact on the interlaminar shear strength and an increase in the ultrasonic attenuation of laminated composites (Jeong, 1997). In addition, a larger void content makes the material more susceptible to water ingress, which can lead to premature failure of the structure. It has been shown that the presence of voids in the composite matrix will produce a large scatter and thus produce ultrasonic attenuation, which can then be used to determine the level of porosity in

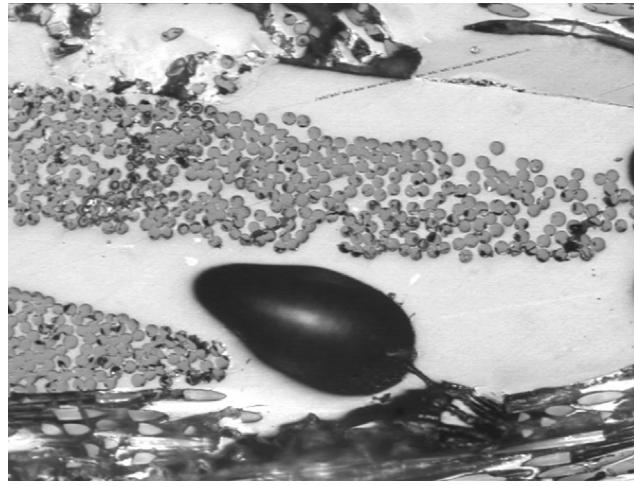

Figure 21.6 Voids in a composite polyether ether ketone (PEEK) glass fibre structure.

the material (Jeong, 1997). These phenomena, by means of which NDI techniques are able to measure and characterize the void content, can aid in determining the structural integrity of composite materials. SHM techniques based on analogous technology have a similar potential.

21.3 Maintenance of materials

This section focuses on the structural maintenance of helicopter floorboards as an example of the operational service scenarios that composite structures can be subjected to. This section provides an overview of the type of testing that is required for introducing new protection schemes while maintaining what could be considered a resistant structure, such as is the case of a helicopter floorboard.

Floorboards are lightweight highly stiffened panels often made out of composite facesheet and aluminium honeycomb sandwich material, as shown in Figures 21.7 and 21.8. These structures are vulnerable to:

- Impact
- Disbond (separation of the facesheet from the aluminium honeycomb core when the adhesive bond is broken)
- Dents (core crushing with or without disbond)
- Scores
- Punctures (with core crushing).

The acceptable damage limits that will not affect the helicopter structural integrity are often dimensionally small, requiring thorough and costly inspections, repairs, and component replacement. Even small levels of damage require repairing or replacing complete components and/or subcomponents. Unfortunately, it has been found that during military battle operations, transport of military personnel, and SAR operations, inadvertent impacts can transfer small amounts of kinetic energy to the floorboards, which can create impact damage requiring costly repairs.

These impact damages may create a variety of structural failure conditions in the floorboard panels. One of these types of damages is a disbond, as depicted in Figure 21.9. This type of damage, when undetected, has been shown to cause component failure (Southward et al., 2007). Excessive loading conditions, improper bonding of the facesheet to the core, or barely visible impact damage cause this type of failure mechanism.

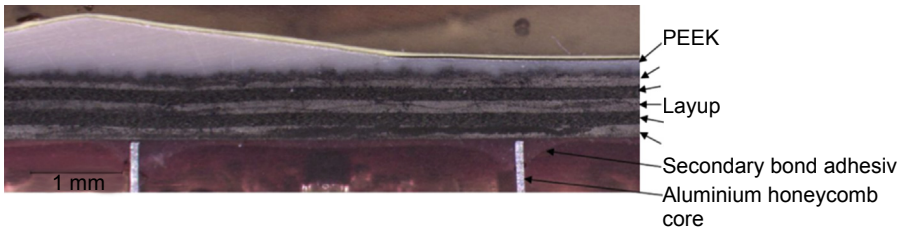

Figure 21.7 Example of a composite sandwich construction used in helicopter floorboards. PEEK, polyether ether ketone.

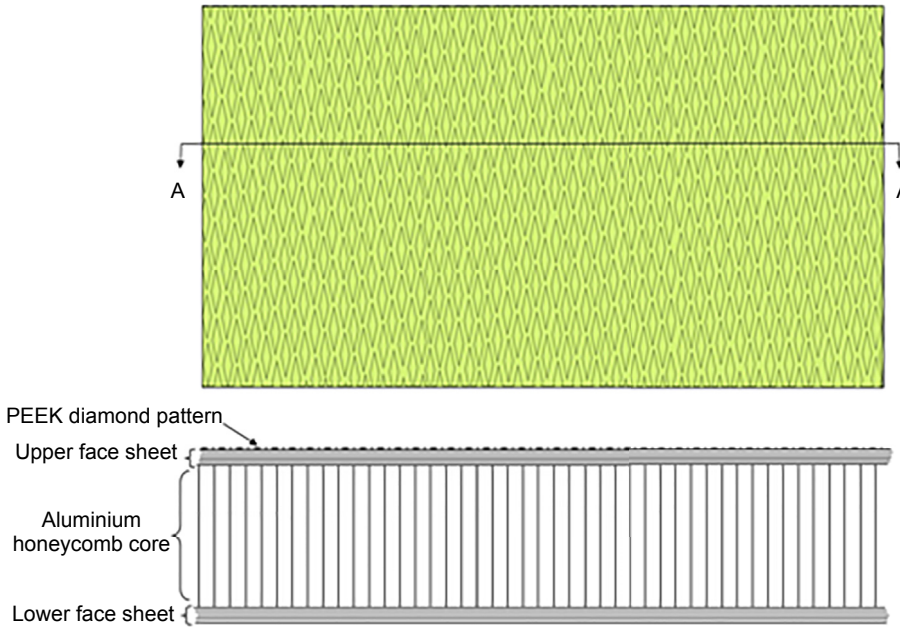

Figure 21.8 Undamaged main cabin floor panel.

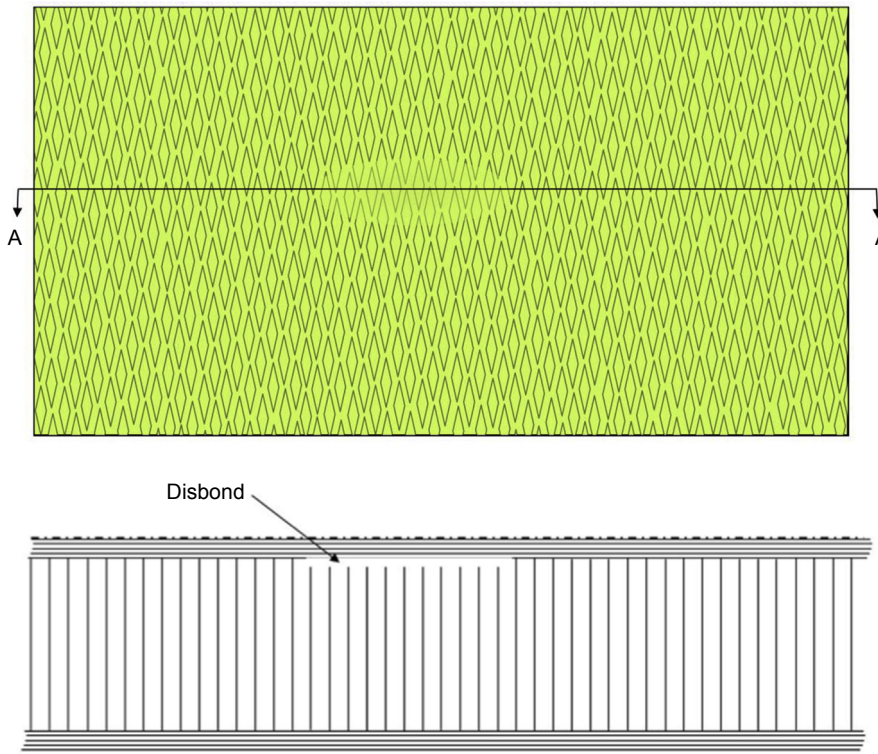

Figure 21.9 Facesheet to core disbond in a main cabin floor panel.

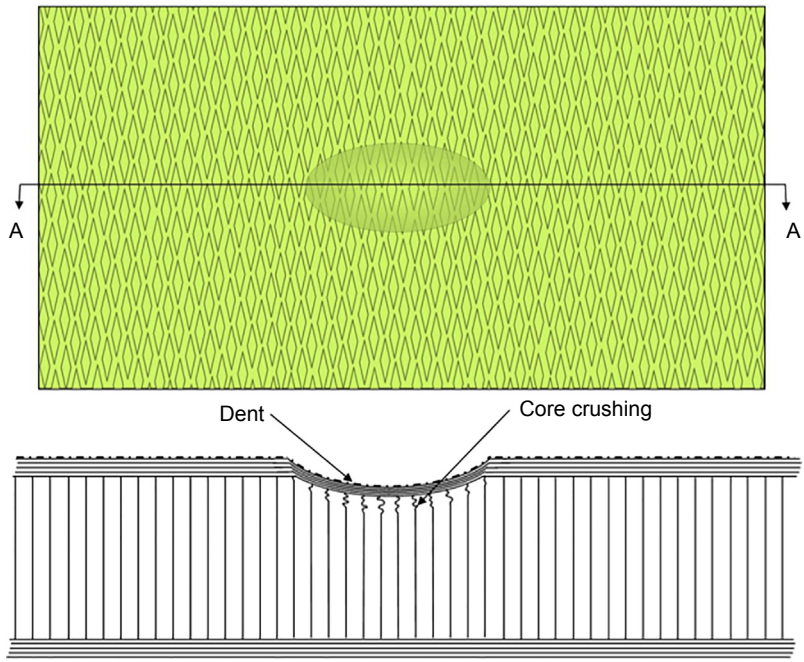

Figure 21.10 Facesheet dent with core crush.

It is not uncommon for impact damage to occur in helicopter floorboards from thrown/dropped backpacks, weapons, and safety and rescue equipment (including scuba tanks and rescue frames), as shown in Figure 21.10. Helicopter floorboards are considered primary structure, and their integrity is essential in ensuring cabin crashworthiness. The replacement of this type of structure is a costly and time-consuming effort, with this structure being identified as a critical area requiring inspection and preventive maintenance. Therefore, military operators have been searching for floorboard protection schemes that have a high level of impact resistance and yet are fire resistant, lightweight, and have low water/chemical absorption properties. These protection schemes would be attempting to prevent internal core crushing that would affect the structural integrity of the panel, as shown in Figure 21.10.

Because not all dents are required to be repaired, military operators tend to spend significant effort assessing the damage itself. However, when the dent has sharp transitions or sharp crimps and creases or there exist abrupt changes in the direction of the dent as depicted in Figure 21.11, these are indications that the floor panel needs to be repaired or replaced.

In some cases, dropped tools, movement of equipment, and personnel ingress/egress of the vehicles with sharp stones trapped in the footwear might perforate the panel, puncturing the facesheet and damaging the core, as shown in Figure 21.12. During operations, one of the concerns resulting from these types of events is water ingress in the structure, promoting corrosion of their metallic constituents, with the possible loss of residual strength capability of the structure in the future and an additional weight gain.

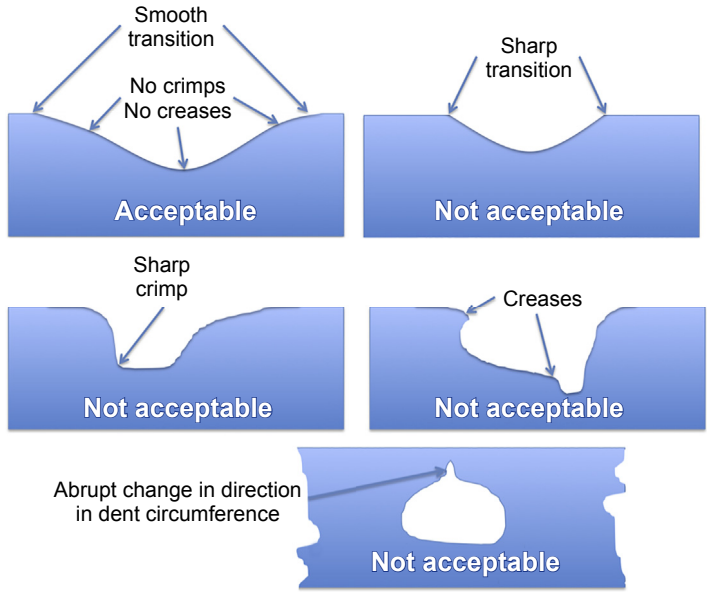

Figure 21.11 Dent examples for composite surfaces.

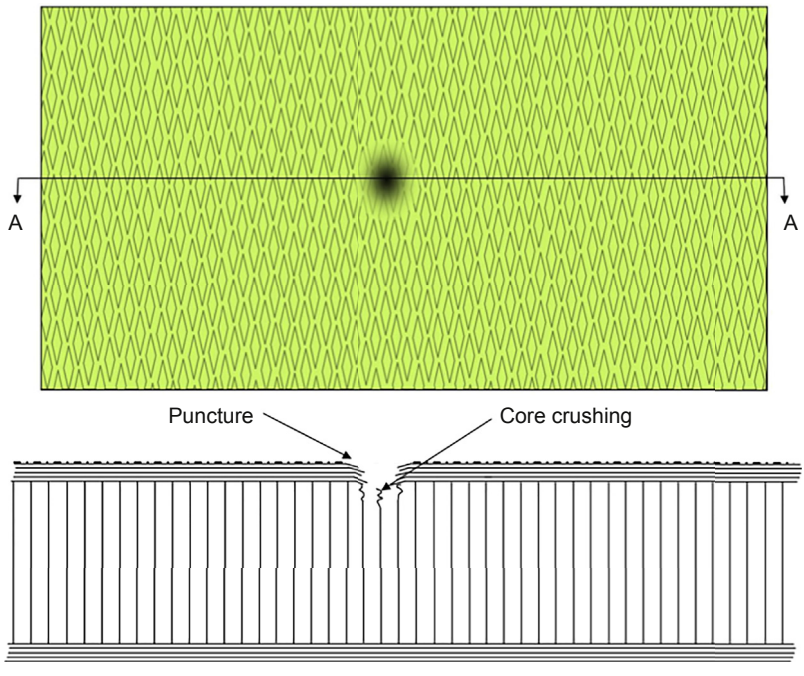

Figure 21.12 Facesheet puncture with core crush.

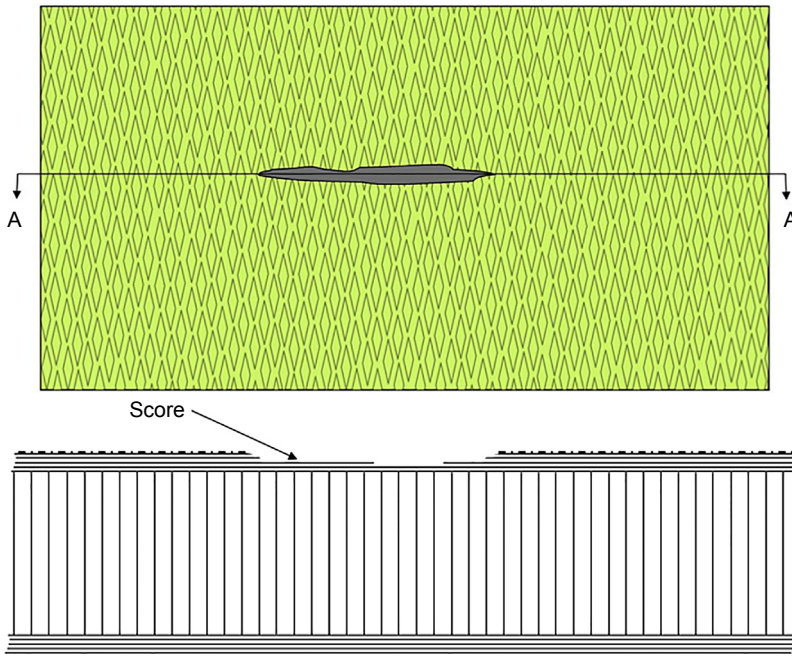

Figure 21.13 Facesheet scores/gouges.

In other circumstances, scores/gouges are created during service, as shown in Figure 21.13. This type of surface damage results from the sliding of a hard object over the facesheet causing fibre breakage. A gouge or score in some cases may produce a deep enough penetration to expose the internals of the panel, thus allowing water and perhaps salt to ingress into the composite structure, which can lead to other environmental issues affecting the structural integrity of the panel.

To this end, the NRC investigated a diverse range of floorboard protection schemes, from aircraft-approved vinyl carpet to marine plywood. A complete list of all the materials tested by NRC as floorboard panel protection schemes and their associated weight penalties can be found in Table 21.1.

As part of the evaluation, impact testing, as shown in Figure 21.14, was carried out at two energy levels, 4.5 and 45 J. To put the energy levels in context, an impact of 4.5 J would be similar to the impact of a 500 g tool dropped from approximately 1 m, while the 45 J impact would be similar to the impact energy of a partially filled aluminium scuba tank being dropped approximately 0.3 m and falling on a rounded edge.

Materials used in helicopter cabin interiors must pass testing for fire resistance (Federal Aviation Administration, 1964; Federal Aviation Administration) based on criteria found in FAR 29.853 and Appendix F of FAR 25 (Federal Aviation Administration, 1964; Federal Aviation Administration). In a typical vertical burn test, materials are cut with exposed edges, because it is the most conservative test protocol. A flame is applied to the bottom edge of a vertically oriented test sample

Table 21.1 Floorboard panel protection schemes

Letter	Floorboard protection scheme	Aerial density (g/cm^2)	Total weight (17 m^2 coverage assumed) (kg)
A	No protection—direct impact onto 1.6 mm thick aluminium 2024-T3 clad sheet	–	–
B	Vinyl carpet (aircraft approved)—(single layer) [2 mm thick base/2.5 mm thick at raised features]	0.217	36.90
F	13 mm thick construction-grade plywood	0.610	103.63
G	19 mm thick construction-grade plywood.	0.904	153.64
H	3.4 mm thick polycarbonate sheet (aircraft approved)	0.384	65.20
I	1.2 mm thick four-ply carbon-polyphenylene sulphides (PPS)	0.185	31.38
K	1.6 mm thick neoprene rubber (firm) Shore A 65	0.428	72.82
L	3.2 mm thick neoprene rubber (firm) Shore A 65	0.855	145.37
V	3.4 mm thick polycarbonate sheet (aircraft approved) + 3.2 mm thick neoprene rubber [H + L]	1.239	210.57
X	Four-ply PPS + 3.2 mm thick neoprene rubber [I + L]	1.040	176.75
Y	Vinyl carpet (aircraft approved) + four-ply PPS + 3.2 mm thick neoprene rubber [B + X + L]	1.257	213.65
AC	1.6 mm thick neoprene rubber + four-ply PPS [K + I]	0.613	104.20
AB	20 mm polypropylene with embedded glass fibre facesheets with polypropylene core	0.431	73.30
AD	14 mm polypropylene with embedded glass fibre facesheets with polypropylene core	0.468	79.63

Continued

Table 21.1 Continued

Letter	Floorboard protection scheme	Aerial density (g/cm^2)	Total weight (17 m^2 coverage assumed) (kg)
AE	15 mm thick Nomex core composite sandwich (2.3 mm top face, 0.5 mm bottom face)	0.580	98.65
AF	13 mm thick marine plywood with anti-skid coating	0.905	153.89

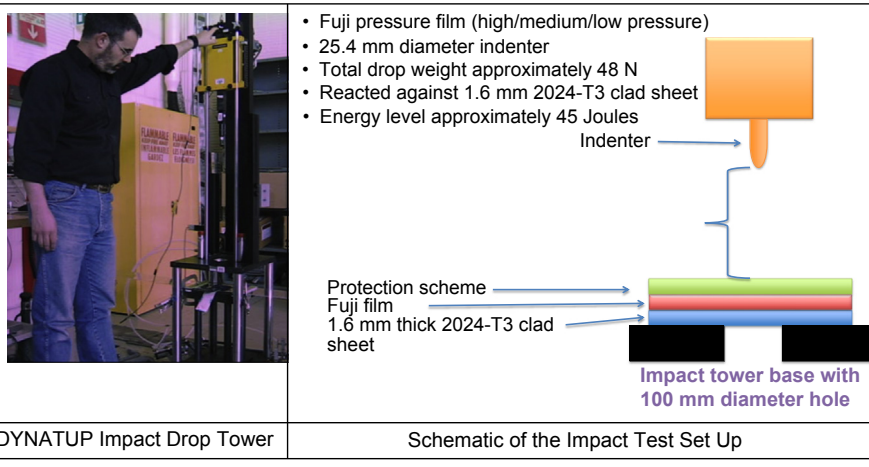

Figure 21.14 DYNATUP impact test setup.

with exposed edges for 12 s, after which the flame is removed. According to the FAR 29.853 specification, the material must be self-extinguishing and there must be no flame left after 15 s. Also, the average burn length must not exceed 203 mm, and any dripping must not continue flaming past an average of 5 s. Protection schemes that consist of multiple layers are tested for fire resistance in individual layers. In other words, a two-layer protection scheme would have each individual layer undergo a burn test. If one component failed the test, the multilayer protection scheme would be considered to have also failed the test. Table 21.2 shows the results of the pass/fail criteria for burn tests for the protection schemes presented in Table 21.1, with observations of the results for different combination of protection schemes.

21.3.1 Water absorption

Helicopters undertaking SAR operations will inevitably be in contact with water. It is essential that large amounts of water are not absorbed by the floorboard protection

Table 21.2 Floorboard burn test results

Protection scheme	Pass/fail	Comments
B	Pass	Self-extinguished immediately, strong odour present afterwards
F	Fail	Extinguished with water after 30 s
G	Pass	Self-extinguished immediately
H	Pass	Some melting of material, self-extinguished within limits
I	Pass	Self-extinguished almost immediately, slight odour afterwards
K	Fail	Large flame and strong odour, did not self-extinguish
L	Fail	Extinguished with water after 30 s
V	Fail	Consisted of H (pass) and L (fail)
X	Fail	Consisted of I (pass) and L (fail)
Y	Fail	Consisted of B (pass), I (pass), and L (fail)
AC	Fail	Consisted of K (fail) and I (pass)
AB	Fail	Extinguished with water after 30 s, drippings self-extinguished within limits
AD	Fail	Extinguished with water after 30 s, did not drip; glass fibres from facesheet were loosened (visible in image) when extinguished with water
AE	Pass	Self-extinguished immediately, sooty smoke present afterwards
AF	Pass	Both painted and unpainted edges self-extinguished immediately

scheme, thereby damaging the protection scheme and increasing the weight of the aircraft. To select and maintain the floorboard panels, the protection schemes are usually tested for their water absorption property. These tests are usually fairly simple. Initially the test coupons, cut to size (75−100 mm square), are dried in an oven for 4 h at 27 °C before being weighed on a scale, with this weight being considered to be the dry weight of each floorboard protection scheme. Specimens are then submerged in water at room temperature for 24 h, patted dry with a lint-free cloth, and then weighed again. The percent of water absorption can then be calculated taking the difference between the wet and dry weight and dividing this difference by the dry weight. In some cases, protection schemes are then resubmerged for a second 24 h soak to give another data point to rank relative water absorption. This gives each protection scheme both 24 and 48 h percent water absorption values. Additional tests are also

required to qualify cabin materials for helicopter and aircraft use, which are not mentioned in this chapter.

21.3.2 Summary of findings on floorboard protection schemes

Any protection scheme that may be used in helicopters would have to consider a method of attachment. The protection schemes should have machined attachment holes corresponding to existing fastener points to minimize the cost of installation. Some materials, such as composites, would have significantly higher cost due to their specialized construction, and they would be more difficult to machine and install due to the equipment needed to cut or shape the material. Also, considerations must be made to allow access to fuel tanks and other access panels below the floorboards themselves. These areas should remain accessible at all times.

Two schemes were recommended for floorboard protection from impact damage (refer to Table 21.1): [scheme AE], the 15 mm Nomex core composite was recommended for its overall performance, and [scheme G], the 19 mm construction-grade plywood was recommended for its ease of installation and inexpensive material cost. Both protection schemes would provide adequate impact protection to protect the floorboards from minor impact damage, having demonstrated capabilities to fulfil the described requirements in terms of burn and water ingress properties.

Other top performing protection schemes provided adequate impact protection; however, the burn characteristics did not meet the FAR 29.853 requirements. Manufacturers interested in further developing their protection schemes need to make changes to these materials to improve their burn characteristics.

21.4 SHM and NDI techniques

NDI, also known as non-destructive testing (NDT), is the current acceptable means of interrogating aircraft for damage. Certified technicians are trained on specific NDI techniques and regularly recertified to remain qualified to perform inspections on aerospace structures. Because as of yet there are no certified SHM technologies, it is expected that SHM systems will initially be applied in parallel with and be complementary to traditional NDI techniques. SHM will most likely be required to be validated and certified using NDI. As confidence is gained in their reliability, regulators may allow operators to rely solely on SHM systems to determine the condition of a component. Having this level of acceptance would be a true leap forward in achieving the implementation of CBM. Furthermore, there is a longer term possibility that as the reliability of the sensing systems increase, it may become possible for OEMs to start reducing their conservative safety factors based on the ability of SHM systems to provide early damage detection. This long-term vision will only be possible with the aid of those who have developed the present NDI technologies. SHM will not be able to achieve its wide acceptance in industry without support from this community working in close collaboration with structural, electrical, and communication engineers

and statisticians aiding in the development of reliable solutions to the challenge of damage and load identification and quantification for complex aerospace structures.

NDIs comprise a range of monitoring techniques and procedures for the assessment of structures during all stages of the lifetime of the aircraft, from the manufacturing of components and subassemblies in the factory to the final maintenance check before decommissioning. During manufacturing, NDI techniques are part of the quality assurance (QA) procedures to monitor and improve the production process and quality control (QC) procedures to accept or reject parts. When an aircraft enters service, NDI techniques are used during scheduled maintenance to assess the state of critical components.

Ibrahim and Scala (2008) reviewed the state of the art of smart sensing for aerospace applications. Their approach was to consider a wide range of sensors and measurement parameters that could provide direct or indirect information about the structure and its future condition, including environmental parameters related to corrosion processes and related technologies, such as energy harvesting, micropower electronics, and wireless communication. Abdel-Latif provided an overview of NDI/NDT in engineering design and how NDI techniques relate to the damage tolerance procedures (Abdel-Latif, 2010). Liew et al. assessed NDT methods for typical helicopter parts, including carbon-fibre reinforced plastic (CFRP), Nomex honeycomb core sandwich panels, and CFRP frame-skin joint panels (Liew et al., 2011). Ghoshal et al. assessed multisensor fusion from heterogeneous sensors and commercial off-the-shelf technologies (Ghoshal, Ayers, Haile, Shia, & Le, 2012). Oster discussed NDI applications for helicopter rotor blades and the NH90 fuselage at Eurocopter (Oster, 2012). The following sections describe some of the NDI and SHM techniques used and considered in the helicopter industry.

21.4.1 Radiography

Radiography is an NDI technique based on the ability of X-rays or gamma rays to pass through materials under examination. An X-ray generator or radioactive isotope is used as the radiation source. Transmitted rays produce photographic records when they reach the film (target) positioned in the opposite side of the part to be inspected, with respect to the radiation source. Discrepancies, such as damages or discontinuities in the component being inspected, are determined by visual observation of the film, which may be at times aided by magnification. The absorption of X-rays depends on, among other properties, the density; thickness and atomic configuration of the material under inspection and therefore X-rays and gamma rays can be used to show discontinuities and inclusions within a component (Ting, Jensen, & Gray, 1993). The sensitivity of this method is also a function of the sharpness and contrast of the radiographic film. This is affected by many factors, such as the rays' source size; film focus distance; distance between film and material and rays' source; film type; screen type; energy of radiation; and film development.

One drawback with this technique is the safety requirements associated with the use of gamma and X-rays and their harmful effects on the human body. Ideally, components should be removed and positioned in specifically designed protected chambers,

where the inspection will take place in isolation, thus reducing the risk of exposure for the inspector and the general population in the inspection vicinity.

Radiography has been broadly applied for damage detection in helicopter structural components, particularly for composite material structural components. Several studies have been presented using radiography (X-rays and neutron beam) by Balasko, Svab, Molnar, and Veres (2005). The study, which was used to extend the life of the helicopter structure (Balasko, Endroczi, Veres, Molnar, & Korosi, 2001), demonstrated the capability of this technique to detect representative operational damage including water ingress and manufacturing discrepancies (Balasko, Veres, Molnar, Balasko, & Svab, 2004). Computational tomography has also been used to enhance the application of X-ray-based inspections, as described in Oster (1999). Oster (2012) showed that it could also be used to identify porosity, and Abdel-Latif (2010) showed how this technique could provide information for a damage tolerance assessment.

21.4.2 Infrared thermography

Infrared thermography is not currently a certified NDI technique for use on aircraft, but it has demonstrated great promise in detecting damage within composite structures. It represents an alternative approach to standard NDI techniques, being based on material and physical properties that traditional NDI methods do not sense, that is the effects of temperature and heat transfer.

Infrared thermography is a noncontact inspection technique capable of detecting, locating, and characterizing subsurface discontinuities, through the analysis of radiated energy from the inspected material. It can be applied to a wide range of materials, from CFRP to concrete and metals, as long as the materials being inspected present good thermal conductivity.

This technique consists of monitoring surface temperature variation, during transient heating or cooling of the structural component under inspection. The area under inspection is heated by an external source (i.e. heat lamps), and its thermal energy, or wave, propagates by diffusion through the material. Simultaneously, an infrared camera monitors the temperature variation over the surface of the component, recording the resulting thermal transient. Existence of a material discontinuity, such as a crack, ply delamination, or foreign material inclusion, disturbs the perfect inner material contact, hence affecting local heat transfer properties perpendicular to the damage. Such disruptions lead to detectable shifts in the heat flow path, producing variations in the surface temperature field (Avdelidis et al., 2004).

The principal disadvantage of this inspection technique is its maximum achievable penetration depth. For thin flat structural components, it has been proven to be a useful tool. However, its application to more complex geometries raises some challenges. Inner damage in thick components causes smaller disturbances in the heat flow, which does not have a large effect on the surface temperature field. It is generally assumed that the loss of thermal contrast in the surface temperature field is proportional to the cube of the discontinuity depth. Also, damage dimensions play an important role; for reliable detection, damage diameter should be approximately one to two times the distance of the damage location below the material surface.

Furthermore, achieving an initial imposed uniform thermal load distribution over an area of a component can be difficult, as well as trying to minimize thermal losses, either convective or irradiative. Finally, equipment cost can still be prohibitive for certain applications.

Within this method there are three developed and slightly different techniques. They are categorized and named in accordance with the external source used to stimulate the component under inspection: pulse thermography; step heating; and lock-in thermography. The three different methods were the focus of several research efforts and applications to helicopter composite structures (Anastasi, Zalameda, & Madaras, 2004; Callinan, Wang, & White, 2010; Dragan, Kornas, Latoszek, & Salacinski, 2010; Heida & Platenkamp, 2012; Liew et al., 2011; Rajic, Rowlands, & Tsoi, 2010; Servais & Gerlach, 2005; Tsoi & Rajic, 2011).

21.4.2.1 Pulse thermography

In pulse thermography, the component to be inspected is briefly exposed to an externally applied pulsed heat source, as shown in Figure 21.15. Afterwards, the surface temperature decay is monitored, while the thermal front propagates through the material by diffusion. The existence of a subsurface discontinuity reduces the local heat transfer diffusion rate, causing the accumulation of heat and thereby leading to higher surface temperatures, with time, around the projected discontinuity position to the surface (Sakagami & Kubo, 2002).

During the inspection process, the observation of thermal contrast can be performed in either transmission or reflection modes. In transmission mode, the heating source and infrared camera are positioned on opposite sides of the structural component being inspected, whereas in reflection mode, both the thermal source and detector are located on the same side of the component. The reflection mode is better suited to identify discontinuities located close to the heated surface, while the transmission approach should be selected for sub-surface discontinuities closer to the nonheated side.

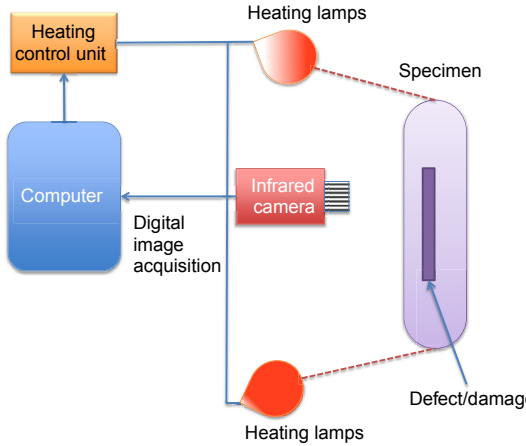

Figure 21.15 Pulse heating infrared thermography.
Rocha, B., & Suleman, A. (December 2009). Notes on NDT&E. In Advanced course on structural health monitoring, Barcelona, Spain.

When there is only access to one side, the only alternative is to perform the inspection applying the reflection mode. An important aspect is that the depth at which the discontinuities exist cannot be accurately estimated, particularly in transmission mode, because the transit time of the thermal front propagating through the total material thickness does not change with varying discontinuity depth.

21.4.2.2 Step heating

In step heating, the increase in surface temperature is monitored, while the component material under inspection is heated continuously, at low power.

21.4.2.3 Lock-in thermography

In lock-in thermography, a continuous harmonic modulated (sinusoidal) heat source and consequent heat wave is applied into the structure under inspection. The heat wave is partially reflected when it encounters surfaces, as for instance in an anomaly in the structure. Either a spotlight or a laser might be used as a heat source, while an infrared camera detects the change in the wave pattern at the surface of the component being inspected. The regions on the surface around sub-surface discontinuities exhibit a different phase in the heat wave pattern with relation to areas with no subsurface discontinuities. Fourier analysis of surface temperature modulation can be performed to obtain a phase and magnitude image (Meola, Carlomagno, Squillace, & Vitiello, 2006).

This method is capable of detecting damages at a depth of 3 mm in plastics, 6 mm in fibre-reinforced plastics, and 12 mm in metals. The properties of the material (heat conductivity, heat capacity, and density) are of the utmost importance when the attenuation of the heat wave is considered.

21.4.3 Shearography

Shearography is an optics-based technique, closely related to holography, which measures surface displacement gradients of a loaded structure (Francis, Tatam, & Groves, 2010). Its main application in aerospace is as an NDI technique, particularly for disbonds. Krupka, Walz, and Ettemeyer (2004) reported on the well-known application of automatic shearography inspection of helicopter rotor blades at Eurocoptor. This system comprises a vacuum chamber to apply the loading and is used to assess composite rotor blades with foam or honeycomb core and CFRP skin. Findeis, Gryzagoridis, and Musonda (2008) assessed damage detection in composite rotor blades from the Atlas Oryx helicopter using shearography with thermal loading. They were able to identify damage at different depths over the range of 2−64 mm. The same research group also assessed impact damage on honeycomb using shearography with thermal loading (Gryzagoridis & Findeis, 2010) and vibration excitation methods (Findeis, Gryzagoridis, & Gerona, 2010) for the rotor section, achieving good detectability of damages. Hofmann, Pandarese, Revel, Tomasini, and Pezzoni (2008) studied the optimization of excitation procedures in shearography using a contrast-to-noise ratio approach, applied to the detection of discontinuities in honeycomb Nomex core and

CFRP skin samples prepared by AgustaWestland. Heida and Platenkamp (2011) assessed the Steibichler ISISmobile 3100 shearography instrument for a range of damages and identified that the best performance was in assessing impact damage. Oster (2012) identified that shearography was able to detect delamination and undulation damage in monolithic fibre composite materials, but was not able to detect porosity and fibre cracking in the prepared samples. Kadlee and Růžek (2012) determined that low energy impact damage in the range of 10–40 J could be detected by shearography, with 5 J impact damages being partially detected. Ochôa et al. assessed the limit of detection in shearography for a CFRP composite laminate and determined that damages resulting from 5 J impacts could be reliably detected, while damages from 3 J impacts were undetectable (Ochôa, Infante, Silva, & Groves, 2012).

21.4.4 Low frequency vibration-based damage detection methods

By assessing changes in the vibration pattern behaviour, such as natural frequencies, mode shapes, vibration energy, or, more specifically, the response to high frequency excitations (waves), changes to the deformation and/or strain field can be assessed and related with structural condition, which has become an area of study for SHM systems. Most of these systems are based on comparisons made between an actual response and a baseline reference response. Some techniques, however, are using the direct structural response, without the requirement of any external, dedicated actuation systems. Such methods can sense deformation and strain changes to infer structural health, at different wave frequency ranges (from quasistatic to high frequencies), as a response to naturally applied flight loads, to the free vibration of the structure, or to the bulk energy emitted by existing damage, in the form, for instance, of mechanical strain waves, AEs.

The inspection area of the different methods is generally inversely related to the frequency range on which the methodology is based, and the minimum detectable damage size usually grows proportionally with the inspection area for the same number of applied transducers (sensors and actuators). Therefore, in an attempt to enhance detection capabilities, sensor system accuracy will be highly dependent on the selected technique and transducer itself, the acquisition hardware system, and data post-processing analysis schemes.

As an advantage, low frequency or vibration-based SHM systems can, theoretically, assess the structure condition more globally, with the density of the transducer network being dependent on the target minimum damage detectable size. These techniques do not require complex state-of-the-art data acquisition systems with high sampling rates and sensors having to work at high frequencies. However, they do require highly accurate and precise measurement systems and well-defined data acquisition requirements. A wide range of transducer types has been considered within these systems, including widely applied and commonly available strain gauges, piezoceramic transducers (PZTs), and fibre optic sensors (FOS), such as FBGs. The disadvantage of low frequency methods is that, with a simple and direct approach for data analysis, a dense transducer network has to be used, so that the

distance between a potential existing damage to a sensor in the network is small. An alternative approach is to increase sensor sensitivity to damage or discontinuities present in the structure, where these must have considerable dimensions to be reliably detected, that is their influence in terms of mass and/or rigidity change must be substantial. Simultaneously, there are, possibly, particular locations in the structure (depending on the structure's geometry, material, etc.), where certain changes in mass accompanied by certain changes in rigidity will not result in significant changes in the structure's natural frequencies or natural modes of vibration (Rocha, Silva, & Suleman, 2006). Low frequency (vibration)-based damage detection techniques for structural global monitoring are ideal for structures designed to be capable of sustaining relatively large damages before collapse and where damage growth monitoring is not required with a high fidelity.

To improve damage detection capabilities of low-frequency methods, their precision, and reliability, significant research has been performed in the development of data post-processing techniques, data mining, and data fusion from several sources, which are also relevant to high frequency methods. These techniques include statistical methods, neural networks, application of fuzzy logic principles, signal filtering and signal wavelet reconstruction, genetic algorithms for damage search, etc. (Fritzen, 2005; Montalvão, Maia, & Ribeiro, 2006).

Vibration-based SHM techniques applied to damage detection in helicopter composite structures have been the focus of several recent research studies. Cuc (2002) and Giurgiutiu, Cuc, and Goodman (2001) researched the application of several vibration-based data post-processing techniques with the objective to detect damage in helicopter structures by integrating them into a health and usage monitoring system architecture. Wavelet and short-time Fourier transforms and Wigner-Ville distributions were explored, based on the review performed by Giurgiutiu et al. (2001), which also included an initial exploration into the use of neural networks. Zwink, Prewett, Adams, and Koester (2008) used frequency response functions and modal response to identify impact loads in a 5 m composite helicopter blade. Pre- and post-impact frequency characterization was used to estimate force and to locate and quantify impacts, with frequency coherence. Optimum sensor network morphology and the sensitivity of each method to environmental conditions were also assessed. A finite element (FE) model was also developed to assist in the study. This study was performed for the US Marine Corps, to enable subsequent CBM of their helicopter assets through the use of load monitoring and foreign object impact damage detection. Subsequently, Zwink, Adams, Evans, and Koester (2009) presented results on the exploration of a simplistic analytical model and on the experimentation using carbon fibre laminate composite panels with aramid honeycomb core, for characterization of natural frequency shifts (applying frequency response functions) due to impact induced damage.

More specifically, Ganguli (2001) presented the first research effort on fuzzy logic systems applied to SHM of helicopter rotors using modal characteristics. Yam, Yan, and Jiang (2003) presented their results on the application of neural networks and wavelet transforms for vibration-based damage detection in composite structures, while in a complementary effort, Roy and Ganguli (2005) dedicated their research

to develop a simplified FE model of a composite blade element of a Eurocopter Bo105 helicopter. The objective of these research efforts was to verify changes to the natural frequencies and different modes of vibration (mainly on flap−out-of-plane bending; lag−in-plane bending and torsion) caused by several types of damage typically found in helicopter components manufactured with composite materials (i.e. delamination and fibre matrix disbonding). Damage was simulated at the 30% and 60% spans of the blade by changes in stiffness in the FE model. In an attempt to better prepare a future vibration-based SHM system for the noise effects observed in realistic experimental sensor signals, data filters based on recursive median filters, using more complex radial basis function, neural networks and wavelets were studied and compared to a moving average filter. A weight recursive median filter based on a genetic algorithm presented similar results to the more complex and computational resource and time-consuming neural networks and exhibited better performance than the wavelet-based method. Reddy and Ganguli (Pawar & Ganguli, 2003) had previously shown the use of a radial basis function in neural networks for damage detection applications in a helicopter rotor blade. In this study, they also briefly discussed the complexity behind obtaining and using a model for fatigue damage growth, and its influence on vibration characteristics, for the different damage types in composite materials. (Pawar and Ganguli, 2005a,b,c, 2006, 2007a,b,c) and Reddy and Ganguli (2003) continued the work initially developed by Roy and Ganguli (2005) by applying genetic fuzzy systems and neural networks. Furthermore, Pawar and Jung (2008) subsequently developed a support vector machine-based method for damage type and severity classification.

21.4.5 High frequency damage detection methods

Higher frequency methods are based on acoustic wave propagation in the structure of interest and the analysis on the influence that damage has on the propagation pattern. High frequency damage detection can be divided into three main groups.

21.4.5.1 Impedance methods

Impedance-based methods include the application of burst actuations to the structure, usually involving more intermediate frequencies (as an evolution of sonic inspections) and, in general, without any regard for the types of excitation waves/waveforms. These particular techniques assess the structural condition and perform damage detection based on impedance changes in the material due to the presence of damage (Park, Sohn, Farrar, & Inman, 2003). In this method, damage detection is ensured by the use of sensors directly bonded or acoustically coupled to the structure, based on electromechanical impedance effects. The more common applied sensors are piezoelectric. The damage-generated wave reflections, their amplitudes, wave velocity and phase changes, and mode conversion, among other characteristics of the propagating waves, are monitored. As an example, the time of flight (ToF) of detected waves being reflected by a known end boundary condition can be measured, that is the time between the burst actuation and sensing the reflected wave. Knowing the ToF and

the distance travelled by the original generated wave and boundary reflection, the reference wave velocity can be determined. In the presence of damage, it is expected that a damage reflection will be sensed before the end boundary reflection, based on the measured baseline/reference ToF data. Because this damage-reflected wave will have the same propagation velocity as the original generated wave, the new ToF data enable the determination of the distance travelled by the original and damage reflected waves, thus allowing for the identification of the damage position (Peairs, Park, & Inman, 2004). In practice, impedance assessment techniques still suffer from considerable minimum detectable damage dimensions, in the order of several centimetres. In general, actuation is not tuned to generate a particular type of wave or wave frequency. Due to this, sensors cannot be tuned a priori. To overcome these deficiencies, relatively powerful actuations, which can be applied due to the characteristic burst excitation signal, are necessary to guarantee that propagating waves (generated, boundary and potential damage reflections) have sufficient amplitude/energy to be reliably detected. This technique is being widely researched for its application to beams (Spanos, Failla, Santini, & Pappatico, 2006). Because these piezoelectric transducers are not usually tuned for a particular wave/frequency, they are more prone to detect any type of wave/frequency being emitted. The requirements for the actuation and data acquisition systems are also not as stringent, with lower frequencies and sampling rates. However, significant filtering of sensor signals is usually required.

21.4.5.2 Acoustic emissions

AEs have also been researched for several decades (Gorman, 1991; Miller & McIntire, 1987; Pollock, 1989; Ziola & Gorman, 1991) and continue to be explored for their application to SHM systems (Hock, McInerney, Morefield, Majumdar, & Carlyle, 2005; Luo et al., 2005; Pullin, Holford, & Baxter, 2005). Their principle of operation hinges on the fact that when a crack grows in a component, sound waves are emitted in the crack tip region, due to material deformation and the creation of new crack surfaces during growth. When such events occur, bursts of waves of different modes and frequencies are generated, propagating through the material and structure with different and undetermined velocities and wavelengths. The generated waves also present different amplitudes/energy and propagation amplitude damping characteristics, depending on the host material, wave mode, and frequency. Higher amplitudes are more likely to be detected, which depend largely on the type of discontinuity, dimension, orientation (also relative to sensors), and growth characteristics. However, AEs usually present small amplitudes and low SNR. Both the undetermined wavelengths and low SNR present difficulties for the selection of the sensor types (dimensions and positions), required to detect these waves reliably, and consequently the existence of damage and its growth. The development of appropriate data acquisition systems and the implementation of data post-processing schemes is also a complex task, even more so if the method is intended to capture a specific frequency. Previous work has been conducted on achieving optimum sensor selection, data acquisition, and signal processing for different, specific types of damage (Luo et al., 2005). Regulations for AE testing have been developed

(ASME Boiler & Pressure Vessel code, 1995a,b,c) based on the results of benchmark experiments executed in certain materials. AE systems can be effortlessly embedded into the structure to be monitored, enabling continuous real-time structural condition assessment by these passive systems. In the case of piezoelectric sensors, no energy is consumed to power the sensors (power is only needed for data acquisition and signal processing). This is an important factor when longer endurance systems are being considered with continuous SHM, while having limited energy resources. FBG and strain gauge sensors can also be applied for the detection of AEs.

In AE systems, damage detection is related to the assessment of sensor signals and the detection of the corresponding crack development/growth generated sound waves. The determination of damage location involves the application of multiple sensors in different positions on the component and the implementation of triangulation schemes (Luo et al., 2005), which require the knowledge of wave propagation velocities, being dependant of wave frequency for specific wave modes. In some cases, sensor type and dimensions are previously selected to tune the system to a specific frequency, that is optimizing the system for detection of specific wave frequencies, enabling the application of triangulation schemes for damage localization, through the knowledge of these waves' propagation velocities. These tuned systems are, however, not optimized to detect all types of discontinuities. When the system is not designed to be tuned to a certain frequency, using broadband sensors, filters, and/or wavelet signal reconstruction can be applied to search for AEs at different frequencies. After finding AE signals and knowing their corresponding frequencies and propagation velocities, again triangulation algorithms can be implemented.

21.4.5.3 Ultrasonics

High frequency-based SHM systems may be considered an evolution of ultrasonic inspections and involve the direct activation and propagation of sound waves in solids. Ultrasonic inspection comprises a range of techniques based on acoustic wave propagation higher than 20 kHz frequencies. In comparison studies, Ochôa et al. and Heida and Platenkamp used C-scan through the thickness ultrasound as the reference for assessing other NDI techniques (Heida & Platenkamp, 2011; Ochôa et al., 2012). Oster assessed through-transmission and pulse-echo ultrasound as having a good performance at Eurocopter Deutschland for assessing delamination and porosity (Oster, 2012) of composite materials. Liew et al. (2011) also concluded that these systems performed well, having detected low energy impact damage in helicopter airframes. One other interesting study was focused on portable A-scan and C-scan systems using an ultrasonic camera, in a project with Bell Helicopter and Boeing, as described by Lasser, Lasser, Kula, Rich, and Westernik (2010). Ibrahim and Scala (2008) identified phasedarray ultrasonic inspection as being able to greatly increase the scanning capabilities of ultrasonic NDI. In particular, a study by Rideout and Taylor (2009) and Rideout, Dussault, and Taylor (2011) was dedicated to develop and assess techniques for the detection of subsurface damage in helicopter components, such as in a UH-60 Black Hawk tail rotor with damaged areas and composite samples from a CH-47

Chinook root blade end. In this research, a deep focus acoustic microscope is described, which is able to focus the inspection effort to a particular region, namely for the detection of subsurface damage. Ultrasonic techniques can also be based on the application of guided waves, as described by Qi, Rose, and Smith (2010) for assessing the skin and Nomex honeycomb structure of the trailing edge of a rotor blade. In plate composite structures, ultrasonic Lamb waves may also be used for damage detection and damage localization (Luo et al., 2005; Wandowski, Kudela, Malinowski, & Ostachowicz, 2011).

The application of sound waves for damage detection is based on their propagation characteristics and particularly on the fact that they are reflected by any discontinuity in the host material. Similarly to the previously referred high frequency SHM systems, different wave types can be considered: body waves, specifically longitudinal and/or shear/transverse; creep; Stoneley; Love; Rayleigh waves; or Lamb waves (Frederick & Worlton, 1962; Lamb, 1917; Mindlin, 1960; Rayleigh, 1885; Rose, 1999; Viktorov, 1967; Worlton, 1961). The main consideration for their application is the geometry of the component being inspected.

Considering their application in SHM systems, some of the important aspects are related to:

- The detection capability of discontinuities/damages with smaller dimensions, requiring the application of waves with smaller wavelength and higher frequencies. At the same time, the frequency of the waves to be applied should be maintained as low as possible so as to not have stringent requirements in terms of the actuation and data acquisition systems;
- Permit transducer embedment, for wave excitation and sensing; and
- The intended capability for monitoring larger areas of the structure with a single and simpler system. To achieve the latter, sound waves to be applied must be able to propagate farther with little amplitude attenuation (small propagation damping).

Besides their highly scattering behaviour, body wave amplitudes are highly damped along their propagation, which is the reason for their localized application in conventional NDI sonic-ultrasonic methods. Lamb waves, on the other hand, are able to propagate over longer distances without showing significant amplitude damping, which is ideal for SHM systems. Their small propagation amplitude damping is related to the fact that Lamb waves propagate in plate-like (or low curvature shell) structures with limited thickness, that is with two parallel and close-by free boundaries (conditions) imposing small damping. Most structural components can in fact be decomposed into plate-like sections. For this reason, Lamb waves are prime candidates to be applied in SHM (Dalton, Cawley, & Lowe, 2001; Giurgiutiu & Bao, 2002; Raghavan & Cesnik, 2007; Rose, 2001; Ye & Su, 2009).

21.4.6 Fibre optic systems

FOSs for SHM applications have been reviewed by Takeda in Takeda (2008). The main sensor types are FBGs and fibre Fabry−Pèrot (F−P). In both cases, reflected signal characteristics can be related to strain. An example of the application of FBG sensors was provided by Mizutani and Groves, which used these sensors to

simultaneously detect axial and bending strains in composite plates (Mizutani & Groves, 2010). Another application of FOS is the monitoring of corrosion related parameters using fluorescence based chemical sensors, an example of which is given in a study by Ibrahim and Scala (2008). Relating to specific helicopter applications, Pitropakis et al. described how FBG sensors written in single-mode and polarization-maintaining optical fibres can be used to detect impact in a Eurocopter EC 135 composite tail boom (Pitropakis, Pfeiffer, & Wevers, 2010). The best SNR was achieved using the single-mode fibre, while at the same time the characteristic ringing associated with the use of typical PZT sensors was attenuated. In addition, to the FOS mentioned above, optical backscattering techniques for strain measurements are being considered for structural and load monitoring applications (Sang, Froggatt, Gifford, Kreger, & Dickerson, 2008). The use of backscattering allows for strain measurements to be acquired along the entire length of a fibre, forming a distributed sensing system without the need of creating gratings along the fibre. This type of system has been demonstrated to provide strain measurements every 5 mm in a 10 m long fibre at a frequency of 10 Hz (Martinez, Beltempo, Yanishevsky, Rutledge, & Rocha, 2012).

21.5 Future trends

For SHM systems to be widely accepted in the aerospace industry, there is a need to validate system accuracy, performance, and reliability. Several research organizations around the world are slowly moving toward ultimate certification of these technologies. However, at present, different players following different methodologies are pursuing this certification process. Research organizations, the academic community and OEMs, in collaboration with usually small and medium enterprise SHM system developers, are working together to establish a set of unified guidelines that will provide a clear vision on how the implementation of SHM technology might serve the aerospace industry. The guidelines presently being developed provide the opportunity to evaluate SHM technologies in parallel with current NDI techniques. It is envisioned that once SHM systems have attained the necessary confidence levels and demonstrated reliability, OEMs and operators will be able to make decisions on maintenance and scheduling based on SHM data alone.

The miniaturization of sensors that are reliable, self-powered, and with wireless communication capabilities will be characteristics of new SHM sensor systems in the future for monitoring aerospace structures, and in particular to helicopters, regarding the need to monitor rotating components. Wireless communication has already seen applications in commercial airliners for entertainment purposes. Thus, it is not unforeseen that similar wireless technology will be used for the acquisition of sensor data in PHM systems. Wireless technology has become faster, enabling higher data transmission rates, and more reliable, thus promoting the deployment of sensor networks that can reliably collect, process, and transmit information over relatively large distances, and creating immediate weight savings through the elimination of wiring. The miniaturization of these sensors and the wider acceptance of composite

materials will create opportunities for mixing the sensing and materials, for the development of smart material structures that are lighter and environment friendly.

The use of optical systems has received substantial attention in past years, meeting electromagnetic interference and compatibility requirements. These optical technologies will eventually gain acceptance within the community, thanks to the development of systems such as the ones based on distributed sensing, with the analysis of the optical signal backscatter from all positions along the fibre, thus providing the possibility to measure strain along its entire length. This presents an interesting opportunity for its use in full-scale tests, followed by its ultimate implementation in fixed and rotary wing structures.

As SHM systems become more reliable and cost-effective, it is foreseeable that these technologies will contribute to a change in the present lifing methodologies and maintenance schedules, thus providing an individual assessment of a specific structure versus a conservative estimate for a general condition. This will impact design, operation, and maintenance philosophies that will require taking into account the inputs provided by SHM and load monitoring systems, which may also lead to less conservative safety factors. The future of the aerospace industry looks very promising, providing a great opportunity for development of safer, reliable and cost-effective SHM technologies.

21.6 Conclusions

There is a clear need for the SHM community to collaborate with the NDI community to develop and establish probability of detection methods for SHM that airworthiness authorities will be able to adopt. It is foreseeable that until the required confidence level on SHM sensing systems is established, NDI/NDT applied at specific intervals will continue to be used to validate the findings of SHM systems. Current NDT methodologies require advanced instrumentation to support traditional visual inspection and manual inspection procedures. Instrumentation from a number of fields of physics is being applied in NDT to solve the challenging problems of the complexity of structures, materials, and measurement environments. The NDT instruments typically send an acoustic, thermal, or electromagnetic wave into the structure and monitor changes in the response from discontinuities. Alternatively the structure may also be statically, or vibratory mechanically loaded to induce the structural response from the damage. Many authors have published case studies of NDI measurement applications, including comparisons of techniques.

Environmental and operational damage in composite structures can be minimized, but not fully eliminated. Thus, there is a need for SHM and load monitoring systems that will provide the necessary inputs for a holistic approach to structural integrity. The SHM community needs to rethink their approach to the techniques currently found in the literature. Although SHM algorithms currently tend to be complex in nature, it is important to keep in mind who the final end user of the technologies will be. The current SHM techniques presented in the open literature present, in their majority, a low technology readiness level or require the use of highly qualified

personnel with specialized knowledge of the algorithms used for damage detection and quantification. This level of sophistication, currently inherent to SHM equipment, makes it a barrier to achieving acceptance by aircraft operators in the short term. For SHM technology to obtain wide acceptance by the aerospace industry, these technologies will have to become more reliable and simple to operate, providing valuable decision-making capabilities for users, such that the benefits outweigh SHM system costs.

Acknowledgements

The authors would like to thank Dr Chun Li and Dr Behnam Ashrafi from the National Research Council of Canada for their contribution of several of the images presented in this manuscript.

References

Abdel-Latif, A. M. (2010). An overview of the applications of NDI/NDT in engineering design for structural integrity and damage tolerance in aircraft structures. *Damage and Fracture Mechanics: Failure Analysis of Engineering Materials and Structures*, 93−100.

Aerospace standards newsletter (Vol. II)(1) (June 2010). http://www.sae.org/standardsdev/news/P101683.pdf. Last Accessed June 2012.

Allgaier, M. W., & Cameron, R. E. (Technical Eds.), Moore, P. O. (Ed.) (2010). *Nondestructive testing handbook* (3rd ed.). *Vol. 9. Visual testing*. American Society for Nondestructive Testing. ISBN: 978-1-57117-186-3.

Anastasi, R., Zalameda, J., & Madaras, E. (2004). Damage detection in rotorcraft composite structures using thermography and laser-based ultrasound. In *SEM X international congress & exposition on experimental and applied mechanics*. Costa Mesa, CA, June.

ASME Boiler & Pressure Vessel Code. (1995a). Section V, non-destructive examination. In *Acoustic emission examination for metallic vessels during pressure testing, Article 12* (pp. 233−250).

ASME Boiler & Pressure Vessel Code. (1995b). Section V, non-destructive examination. In *Continuous acoustic emission monitoring, Article 13* (pp. 251−271).

ASME Boiler & Pressure Vessel Code. (1995c). Section V, non-destructive examination. In *Acoustic emission examination for fiber-reinforced plastic vessels, Article 11* (pp. 207−232).

Avdelidis, N. P., Almond, D. P., Dobbinson, A., Hawtin, B. C., Ibarra-Castanedo, C., & Maldague, X. (2004). Aircraft composites assessment by means of transient thermal NDT. *Progress in Aerospace Sciences, 40*, 143−162.

Aviation Investigation Report A05F0047. (06 March, 2005). *Loss of rudder in flight air transat, airbus A310−308 C-GPAT, Miami, FL, 90 nm S*. Transportation Safety Board of Canada.

Backman, D., Martinez, M., Renaud, G., Genest, M., & Chisholm, K. (2007). Thermoelastic stress analysis to detect disbonding in a composite patch. In *Proceedings of the society of experimental mechanics*.

Baker, W., McKenzie, I., & Jones, R. (2004). Development of life extension strategies for Australian military aircrafts, using structural health monitoring of composite repairs and joints. *Composite Structures, 66*, 133−143.

Balasko, M., Endroczi, G., Veres, I., Molnar, Gy., & Korosi, F. (8–11 October 2001). Research of extension of the life cycle of helicopter rotor blade in Hungary. In *RTO AVT specialists' Meeting on "Life management techniques for ageing air vehicles"*. Manchester, UK: RTO-MP-079(II).

Balasko, M., Svab, E., Molnar, Gy., & Veres, I. (2005). Classification of defects in honeycomb composite structure of helicopter rotor blades. *Nuclear Instruments and Methods in Physics Research, 542A*, 45–51.

Balasko, M., Veres, I., Molnar, Gy., Balasko, Zs., & Svab, E. (2004). Composite structure of helicopter rotor blades studied by neutron and X-ray radiography. *Physica B: Condensed Matter, 350*(1–3), 107–109.

Bellinger, N. C., & Martinez, M. (September 2009). Environmental monitoring of aircraft. In C. Boller, F. Chang, & Y. Fujino (Eds.), *Encyclopedia of structural health monitoring* (pp. 1523–1530). Chichester, UK: John Wiley & Sons Ltd. http://dx.doi.org/10.1002/9780470061626.shm191.

Betz, D. C., Thursby, G., Culshaw, B., & Staszewski, W. J. (2003). Acousto-ultrasonic sensing using fiber Bragg gratings. *Smart Materials and Structures, 12*, 122–128. Online at stacks.iop.org/SMS/12/122.

Bolotin, V. V. (1996). Delaminations in composite structures: its origin, buckling, growth and stability. *Composites: Part B, 27B*, 129–145.

Bossi, R. H., Iddings, F. A., & Wheeler, G. C. (Technical Eds.), Moore, P. O. (Ed.) (2002). *Nondestructive testing handbook* (3rd ed.). *Vol. 4. Radiographic testing*. American Society for Nondestructive Testing. ISBN: 1-57117-045-6.

Callinan, R., Wang, J., & White, C. (2010). Residual strength of a helicopter composite structure subjected to small arms fire. *Materials Science Forum, 654–656*, 2596–2599.

Cuc. A. (2002). *Vibration-based techniques for damage detection and health monitoring of mechanical systems* (M.A.Sc. thesis). University of South Carolina.

Dalton, R., Cawley, P., & Lowe, M. (2001). The potential of guided waves for monitoring large areas of metallic aircraft fuselage structures. *Journal of Non-Destructive Evaluation, 20*(1).

Davis, C., Baker, W., Moss, S., Galea, S., & Jones, R. (2002). In situ health monitoring of bonded composite repairs using a novel fibre Bragg grating sensing arrangement. *Proceedings of SPIE - The International Society for Optical Engineering, 4934*, 140–149.

Dragan, K., Kornas, L., Latoszek, A., & Salacinski, M. (2010). Diagnostics of composite aircraft structures using non-destructive tests with thermographic, ultrasound and acoustic methods. *Fatigue of Aircraft Structures, 1*(2), 19–22.

F.A.A. Advisory Circular AC 20-107B. (08 September 2009). *Composite aircraft structure*. http://www.faa.gov/documentLibrary/media/Advisory_Circular/AC20-107B.pdf. Last Accessed 23.10.12.

Federal Aviation Administration. (December 1964). *FAR 29*. Section 853.

Federal Aviation Administration. FAR 25, airworthiness standards: Transport category airplanes, Appendix F.

Federal Aviation Regulation (FAR) 29.573. (2012). Damage tolerance and fatigue evaluation of composite rotorcraft structures (with an effective date of 30 January 2012).

Findeis, D., Gryzagoridis, J., & Gerona, L. M. (2010). Vibration excitation methods applied to digital shearography and ESPI. In *Conference Proc. SEM: Vol. 4. Application of imaging techniques to mechanics of materials and structures* (pp. 259–266).

Findeis, D., Gryzagoridis, J., & Musonda, V. (2008). NDT detection and quantification of induced defects on composite helicopter rotor blades and UAV wing sections. In *Proc. SPIE* (Vol. 7155, p. 71551N).

Francis, D., Tatam, R. P., & Groves, R. M. (2010). Recent developments in shearography (invited paper) *Measurement Science and Technology, 21*, 102001.

Frederick, C., & Worlton, D. (1962). Ultrasonic thickness measurements with lamb waves. *Journal of Non-Destructive Testing, 20*, 51−55.

Fritzen, C. (2005). Vibration-based structural health monitoring − concepts and applications. In *Proceedings of VI DAMAS - Damage assessment of structures*.

Gagar, D., Irving, P., Foote, P., & McFeat, J. (2012). Investigation of AE generation from fatigue cracks for structural health monitoring in 2014 aluminum alloy. In *Conference proceedings of the 6th european workshop on structural health monitoring & 1st european conference on the prognostic and health management (PHM) society, Dresden, Germany, July 3−6, 2012*.

Galea, S. C., Powlesland, I. G., Moss, S. D., Konak, M., Velden van der, S., Stade, B., et al. (2001). Development of structural health monitoring systesm for composite bonded repairs on aircraft structures. *Proceedings of SPIE - The International Society for Optical Engineering, 4327*, 246−257.

Ganguli, R. (2001). A fuzzy logic system for ground based structural health monitoring of a helicopter rotor using modal data. *Journal of Intelligent Material Systems and Structures, 12*, 397−407.

Genest, M., Martinez, M., Mrad, N., & Renaud, G. (February 2008). Pulsed thermography for non-destructive evaluation and damage growth monitoring of bonded repairs. JA-SMPL-2007-0088, *Journal of Composites Structures, 88*, 112−120.

Ghoshal, A., Ayers, J. T., Haile, M., Shia, M., & Le, D. D. (2012). Sensor applications for structural diagnostics and prognosis in aerospace systems. In *Proc. SPIE: Vol. 8345. Sensors and smart structures technologies for civil, mechanical and aerospace systems* (p. 83452E).

Giurgiutiu, V., & Bao, J. (2002). *Embedded ultrasonic structural radar with piezoelectric wafer active sensors for the NDE of thin-wall structures*. New Orleans, US: ASME International Mechanical Engineering Congress.

Giurgiutiu, V., Cuc, A., & Goodman, P. (2001). Review of vibration-based helicopters health and usage monitoring methods, new frontiers in integrated diagnostics and prognostics. In *proceedings of the 55th meeting of the society for machinery failure prevention technology, Virginia Beach, Virginia, 2−5 April*.

Gorman, M. (1991). Plate wave acoustic emission. *Journal of the Acoustic Society of America, 90*(1), 358−364.

Gryzagoridis, J., & Findeis, D. (2010). Impact damage detection on composites using optical NDT techniques. *Proc. BINDT2009, 52*(5), 248−251.

Habib. F. (2012). *Structural health monitoring of adhesively bonded composite joints* (M.A.Sc. thesis). Ottawa, Canada: Department of Mechanical and Aerospace Engineering, Carleton University.

Habib, F., Martinez, M., Artemev, A., & Brothers, M. (2013). Structural health monitoring of bonded composite repairs - a critical comparison between ultrasonic lamb wave approach and surface mounted crack sensor approach. *Composites Part B: Engineering*. ISSN: 1359-8368. http://dx.doi.org/10.1016/j.compositesb.2012.11.002. Available online 20 November 2012.

Heida, J. H., & Platenkamp, D. J. (2011). *Evaluation of non-destructive inspection methods for composite aerospace structures*. International Workshop of NDT Experts.

Heida, J., & Platenkamp, D. (2012). In-service inspection guidelines for composite aerospace structures. In *18th world conference on nondestructive testing, Durban, South Africa, 16−20 April*.

Hess, A., & Fila, L. (2002). *The joint strike fighter (JSF) PHM concept: potential impact on aging aircraft problems*. IEEEAC paper No. 403.

Hillger, W., Szewieczek, A., Schmidt, D., Sinapius, M., Aldave, I. J., Venegas Bosom, P., et al. (2012). Advanced NDT techniques for damage detection in a honeycomb composite

helicopter tailboom. In V. Paipetis, et al. (Eds.), *Emerging technologies in non-destructive testing*. London: Taylor and Francis Group, ISBN: 978-0-415-62131-1.

Hock, V., McInerney, M., Morefield, S., Majumdar, A., & Carlyle, J. (2005). Investigating fundamental mechanics of microcracks in concrete using acoustic signature modelling. In *Proceedings of VI DAMAS − Damage assessment of structures*.

Hoeppner, D. W. (2011). Fretting fatigue considerations in holistic structural integrity based design processes (HOLSIP) − a continuing evolution. *Tribology International, 44*, 1364−1370.

Hofmann, D., Pandarese, G., Revel, G. M., Tomasini, E. P., & Pezzoni, R. (2008). Optimization of the excitation and measurement procedures in non-destructive testing using shearography. *Review of Scientific Instruments, 79*, 115105.

Howe, B., & Muir, D. (1998). *In-line oil Debris monitor (ODM) for helicopter gearbox condition assessment*. DTIC, Information for the Defense Community. URL ADA347503 http://oai.dtic.mil/oai/oai?verb=getRecord&metadataPrefix=html&identifier=ADA347503. Last accessed November 2012.

Ibrahim, M. E., & Scala, C. M. (2008). Innovations in smart materials and integrated structural health monitoring in the Australian Defence Force. *Advances in Science and Technology, 56*, 545−550.

Jackson, C. N., & Sherlock, C. N. (Technical Eds.), Moore, P. (Ed.). (1997). *Nondestructive testing handbook* (3rd ed.). *Vol. 1. Leak testing*. American Society for Nondestructive Testing. ISBN: 1-57117-071-5.

Jardine, A. K. S., Lin, D., & Banjevic, D. (October 2006). A review on machinery diagnostics and prognostics implementing condition-based maintenance. *Mechanical Systems and Signal Processing*. ISSN: 0888-3270, *20*(7), 1483−1510. http://dx.doi.org/10.1016/j.ymssp.2005.09.012.

Jeong, H. (1997). Effects of voids on the mechanical strength and ultrasonic attenuation of laminated composites. *Journal of Composite Materials, 31*(3).

Kadlee, M., & Růžek, R. (2012). A comparison of laser shearography and c-scan for assessing a glass/epoxy laminate impact damage. *Applied Composite Materials 19*, 393−407.

Krupka, R., Walz, T., & Ettemeyer, A. (2004). Advanced inspection of helicopter composite structures using shearography. In *Proceedings of 16th WCNDT 2004-world conference on NDT*.

Lamb, H. (1917). On waves in an elastic plate. In *Proceedings of the royal society, mathematical, physical and engineering sciences* (Vol. 93, pp. 114−128).

Landry, N. (1999). The Canadian air force experience selecting aircraft life extension as the most economical solution, Defense Technical information Center Compilation Part Notice ADP010316, *Paper presented at the RTO SCI symposium on "Aircraft Update programmes. The economical alternative"*, held in Ankara, Turkey, 26−28 April 1999 and published in RTO MP-44.

Lasser, R., Lasser, M., Kula, J., Rich, D., & Westernik, R. (2010). Remote, simple nondestructive testing of composite defects with an ultrasound camera: a Boeing study. In *Proceedings of Composites*.

Leão, B. P., Fitzgibbon, K. T., Puttini, L. C., & de Melo, G. P. B. (2007). *Cost-benefit analysis methodology for PHM applied to legacy commercial aircrafts*. IEEEAC Paper No. 1562, Version 4.

Liao, M. (January 2010). Dislocation theory based short crack model and its application for aircraft aluminum alloys. *Engineering Fracture Mechanics*. ISSN: 0013-7944, *77*(1), 22−36. http://dx.doi.org/10.1016/j.engfracmech.2009.07.022.

Liao, M., & Renaud, G. (2010). Fatigue analysis for CF-18 component: wing fold shear-tie lug. *Procedia Engineering*. ISSN: 1877-7058, *2*(1), 1673−1682. http://dx.doi.org/10.1016/j.proeng.2010.03.180.

Liew, C. K., Veidt, M., Rajic, N., Tsoi, K., Rowlands, D., & Morton, H. (2011). Inspections of helicopter composite airframe structures using conventional and emerging nondestructive testing methods. *Journal of Testing and Evaluation, 39*(6), 1−11.

Liu, A., Cheung, C., & Martinez, M. (March 2011). Use of artificial neural networks for helicopter load monitoring. In *Proc. 7th DSTO international conference on health and usage monitoring*, Melbourne, Australia.

Luo, Y., Zhao, G., Gu, J., Zhu, J., Gong, R., & Liu, Z. (2005). New method of planar location of acoustic emission source and its application. *Structural Health Monitoring*, 953−960.

Maldague, X. P. V. (Technical Ed.), Moore, P.O. (Ed.). (2001). *Nondestructive testing handbook* (3rd ed.). *Vol. 3. Infrared and thermal testing*. American Society for Nondestructive Testing. ISBN: 1-57117-044-8.

Martinez, M., Beltempo, A., Yanishevsky, M., Rutledge, R., & Rocha, B. (March 2012). *Load monitoring on SHM platform 1A using Luna technologies distributed sensing fibre optic system*. NRC Publication. No. LTR-SMPL-2012-0047.

Martinez, M., Renaud, G., Backman, D., Genest, M., & Delannoy, M. (2007). Demonstration of an instrumented patch. In *Proceedings of SPIE* (Vol. 6530), ISBN: 9780819466518.

Martinez, M., Rocha, B., Li, M., Shi, G., Rutledge, R., & Yanishevsky, M. (2012). Load monitoring of aerospace structures using Micro-electro-mechanical systems (MEMS). In *Proceedings of the ASME 2012 conference on smart materials, adaptive structures and intelligent systems SMASIS 2012, September 19−21 2012, Stone Mountain, Georgia, USA*.

Meola, C., Carlomagno, G. M., Squillace, A., & Vitiello, A. (2006). Non-destructive evaluation of aerospace materials with lock-in thermography. *Engineering Failure Analysis, 13*, 380−388.

Miller, R. K., & Hill, E. v. K. (Technical Eds.), Moore, P.O. (Ed.). (2005). *Nondestructive testing handbook* (3rd ed.). *Vol. 6*. Acoustic emission testing. American Society for Nondestructive Testing. ISBN: 1-57117-106-1.

Miller, J. L., & Kitaljevich, D. (2000). *In-line oil debris monitor for aircraft engine condition assessment*. IEEE 0-7803 5846-5/00.

Miller, R., & McIntire, P. (1987). Non-destructive testing handbook. In *Acoustic emission testing* (Vol. 5). Columbus, OH, USA: American Society for Non-Destructive Testing.

Mindlin, R. (1960). Waves and vibrations in isotropic, elastic plates. *Structural Mechanics*, 199−232.

Mizutani, Y., & Groves, R. M. (2010). Multi-functional measurement using a single FBG sensor, Determination of strain, bending moment and vibration frequency from a single fibre Bragg grating. *Experimental Mechanics, 51*, 1489−1498. http://dx.doi.org/10.1007/s11340-011-9467.

Moore, D. G. (Technical Ed.), Moore, P.O. (Ed.). (2008). *Nondestructive testing handbook* (3rd ed.). *Vol. 8. Magnetic testing*. American Society for Nondestructive Testing. ISBN: 978-1-57117-184-9.

Montalvão, D., Maia, N., & Ribeiro, A. (2006). A review of vibration-based structural health monitoring with special emphasis on composite materials. *The Shock and Vibration Digest, 38*(4), 295−324.

Ochôa, P., Infante, V., Silva, J. M., & Groves, R. M. (2012). Multiple low-energy impact damage detection in composite plates using ultrasonic Lamb wave techniques. In *Proc. XIII Portugese conference on fracture*.

Ofsthun, S. (September 2002). Integrated vehicle health management for aerospace platforms. *Instrumentation & Measurement Magazine, IEEE, 5*(3), 21−24. http://dx.doi.org/10.1109/MIM.2002.1028368.

Oster, R. (1999). Computed tomography as a non-destructive test method for fiber main rotor blades in development, series and maintenance. In *Proceedings of the international symposium on computerized tomography for industrial applications and image processing in radiology, 15−17 March, Berlin, Germany* (Vol. 4(7)). Available in NDT.net.

Oster, R. (2012). Non-destructive testing methodologies on helicopter fiber composite components: challenges today and in the future. In *Proc. 18th world conference on nondestructive testing 2012*.

Park, G., Sohn, H., Farrar, C., & Inman, D. (2003). Overview of piezoelectric impedance-based health monitoring and path forward. *The Shock and Vibration Digest, 35*(6), 451−463.

Pawar, P., & Ganguli, R. (2003). Genetic fuzzy system for damage detection in beams and helicopter rotor blades. *Computer Methods in Applied Mechanics and Engineering, 192*(16−18), 2031−2057.

Pawar, P., & Ganguli, R. (2005). On the effect of matrix cracks in composite helicopter rotor blade. *Composites Science and Technology, 65*(3−4), 581−594.

Pawar, P., & Ganguli, R. (2005). Matrix cracking detection in thin-walled composite beam using genetic fuzzy system. *Journal of Intelligent Material Systems and Structures, 16*(5), 381−468.

Pawar, P., & Ganguli, R. (2005). Modeling multi-layer matrix cracking in thin-walled composite rotor blade. *Journal of the American Helicopter Society, 50*(4), 354−366.

Pawar, P., & Ganguli, R. (2006). Modeling progressive damage accumulation in thin walled composite beams for rotor blade applications. *Composites Science and Technology, 66*(13), 2337−2349.

Pawar, P., & Ganguli, R. (2007a). On the effect of progressive damage on composite helicopter rotor system behaviour. *Composite Structures, 78*(3), 410−423.

Pawar, P., & Ganguli, R. (2007b). Genetic fuzzy system for matrix cracks and debonding/delamination detection in composite helicopter rotor blades. *Mechanical Systems and Signal Processing, 21*(5), 2212−2236.

Pawar, P., & Ganguli, R. (2007c). Fuzzy-logic-based health monitoring and residual-life. *Journal of Aircraft, 44*(3), 981−995.

Pawar, P., & Jung, S. (2008). Support vector machine based online composite helicopter rotor blade damage detection system. *Journal of Intelligent Material Systems and Structures, 19*, 1217−1228.

Peairs, D., Park, G., & Inman, D. (2004). Improving accessibility of the impedance-based structural health monitoring method. *Journal of Intelligent Material Systems and Structures, 15*(2), 129−140.

Pitropakis, I., Pfeiffer, H., & Wevers, M. (2010). Impact damage detection in composite materials of aircrafts by optical fibre sensors. In *10th European conference and exhibition on nondestructive testing (10th ECNDT)*.

Pollock, A. (1989). *Acoustic emission inspection, metals handbook* (Vol. 17). ASM International, 278−294.

Pullin, R., Holford, K., & Baxter, M. (2005). Modal analysis of acoustic emission signals from artificial and fatigue crack sources in aerospace grade steel. In *Proceedings of VI DAMAS − Damage assessment of structures*.

Qi, X., Rose, J. L., & Smith, E. (2010). Guided wave subsurface damage detection for a composite on a halfspace structure. *AIP Conf. Proc., 1211*, 1135.

Raghavan, A., & Cesnik, C. (2007). Review of guided-wave structural health monitoring. *The Shock and Vibration Digest, 39*(2), 91−114.

Rajic, N., Rowlands, D., & Tsoi, K. (2010). An australian Perspective on the application of infrared thermography to the inspection of military aircraft. In *Second international symposium on NDT in aerospace, Hamburg, Germany, November*.

Rayleigh, J. (1885). On waves propagated along the plane surfaces of an elastic solid. In *Proceedings of the London mathematical society, London, UK*.

Reddy, R., & Ganguli, R. (2003). Structural damage detection in a helicopter rotor blade using radial basis function neural networks. *Smart Materials and Structures, 12*, 232−241.

Rideout, C. A., Dussault, P. L., & Taylor, S. C. (2011). *Field inspection of localized damage on composite rotorcraft components*. IEEEAC paper #1187.

Rideout, C. A., & Taylor, S. C. (2009). *Advanced deep focus acoustic microscope for nondestructive inspection of metals and composite materials*. IEEEAC paper #1187.

Roach, D., & Neidigk, S. (June 2012). *Industry survey of structural health monitoring technology and usage*. Combined report of the FAA Airworthiness Assurance Center and Sandia Laboratories, Org. 6620 Transportation Safeguards and Surety.

Rocha, B., Silva, C., & Suleman, A. (2006). Vibration-based health monitoring of aircraft structures. In *Third European workshop on structural health monitoring*, Granada, Spain.

Rocha, B., & Suleman, A. (Dec. 2009). *Notes on NDT&E*. Advanced Course on Structural Health Monitoring, Barcelona, Spain.

Rose, J. (1999). *Ultrasonic waves in solid media*. New York, US: Cambridge University Press.

Rose, J. (2001). A vision of ultrasonic guided wave inspection potential. In *Proceedings of the seventh ASME NDE topical conference* (Vol. 20, pp. 1−5). NDE.

Roy, N., & Ganguli, R. (2005). Helicopter rotor blade frequency evolution with damage growth and signal processing. *Journal of Sound and Vibration, 283*(3), 821−851.

Russell, A. J. (December 1988). *A damage tolerance assessment of bonded repairs to CF- 18 composite components. Part I: Adhesive properties*. Defence Research Establishment Pacific. AD-A210 253.

Sakagami, T., & Kubo, S. (2002). Applications of pulse heating thermography and lock-in thermography to quantitative nondestructive evaluations. *Infrared Physics & Technology, 43*, 211−218.

Sang, A. K., Froggatt, M. E., Gifford, D. K., Kreger, S. T., & Dickerson, B. D. (2008). One centimeter spatial resolution temperature measurements in a nuclear reactor using Rayleigh scatter in optical fiber. *Sensors Journal, IEEE, 8*(7), 1375−1380. http://dx.doi.org/10.1109/JSEN.2008.927247.

Scanff, E., Feldman, K. L., Ghelam, S., Sandborn, P., Glade, M., & Foucher, B. (December 2007). Life cycle cost impact of using prognostic health management (PHM) for helicopter avionics. *Microelectronics Reliability*. ISSN: 0026-2714, *47*(12), 1857−1864. http://dx.doi.org/10.1016/j.microrel.2007.02.014.

Schijve, J. (2009). *Fatigue of structures and materials, 2nd edition with CD-ROM*. Springer. ISBN:13: 978-1-4020-6807-2.

Sen, J. K., & Everett, R. A. (2000). Structural integrity and aging related issues for helicopters. *Paper presented at RTO AVT lecture series on "Aging engines, Avionics, Subsystems and helicopters", Atlantic city, USA, 23−24 October 2000; Madrid, Spain 26−27 October 2000*. RTO EN-14.

Servais, P., & Gerlach, N. (2005). Development of a NDT method using thermography for composite material inspection on aircraft using military thermal imager. In *Proceedings of the Fifth international workshop on advances in signal processing for non destructive evaluation of materials, Québec City, Canada, 2−4 August*.

Southward, T., Horrigan, D. P. W., Mallinson, G. D., & Jayraman, K. (2007). Failure of sandwich composite structure containing face-sheet/core disbonds − an experimental study. In *Proceedings of the Fifth Australasian Congress on applied mechanics*. ACAM.

Spanos, P., Failla, G., Santini, A., & Pappatico, M. (2006). Damage detection in Euler-Bernoulli beams via spatial wavelet analysis. *Structural Control & Health Monitoring, 13*(1), 472−487.

Takeda, N. (2008). Fiber optic sensor-based SHM technologies for aerospace applications in Japan. *Proc. SPIE, 6933*, 693302.

Ting, J., Jensen, T., & Gray, J. (1993). Using energy dispersive X-ray measurements for quantitative determination of material loss due to corrosion. In D. O. Thompson, & D. E. Chimenti (Eds.), *Review of progress in quantitative nondestructive evaluation* (Vol. 12, pp. 1963−1969). New York, USA: Plenum Press.

Tracy, N., & Moore, P. O. (1999). *Nondestructive testing handbook* (3rd ed.). In *Liquid penetrant testing Vol. 2*. (3rd ed.). American Society for Nondestructive Testing, ISBN: 1-57117-028-6

Tsoi, K., & Rajic, N. (2011). *Non-destructive evaluation of aircraft structural components and composite materials at DSTO using sonic thermography*. DSTO−TN−0986.

Udpa, S. S. (Technical Ed.), Moore, P. O. (Ed.). (2004). *Nondestructive testing handbook* (3rd ed.). *Vol. 5. Electromagnetic testing*. American Society for Nondestructive Testing. ISBN: 1-57117-046-4.

Viktorov, I. (1967). *Rayleigh and Lamb waves: Physical theory and applications*. New York, US: Plenum Press.

Wandowski, T., Kudela, P., Malinowski, P., & Ostachowicz, W. (2011). Lamb waves for damage localisation in panels. *Strain, 47*, 449−457.

Worlton, D. (1961). Experimental confirmation of Lamb waves at megacycle frequencies. *Journal of Applied Physics, 32*, 967−971.

Yam, L., Yan, Y., & Jiang, J. (2003). Vibration-based damage detection for composite structures using wavelet transform and neural network identification. *Composite Structures, 60*(4), 403−412.

Yanishevsky, M., Martinez, M., Mandache, C., Khan, M., Fahr, A., & Backman, D. (December 2010). Artificial seeding of fatigue cracks in NDI reference coupons. *Insight, 52*(12), 664−671.

Yen, G., & Bui, T. (1−8 Feb 1997). Health monitoring of vibration signatures in rotorcraft wings. In *Proceedings., IEEE: Vol. 1. Aerospace conference, 1997* (pp. 279−288). http://dx.doi.org/10.1109/AERO.1997.574419.

Ye, L., & Su, Z. (2009). Identification of damage using Lamb waves. *Lecture Notes in Applied and Computational Mechanics, 48*, 4−5. Springer Ed.

Zhang, H., Schulz, M. J., Naser, A., Ferguson, F., & Pai, P. F. (September 1999). Structural health monitoring using transmittance functions. *Mechanical Systems and Signal Processing*. ISSN: 0888-3270, *13*(5), 765−787. http://dx.doi.org/10.1006/mssp.1999.1228.

Ziola, S., & Gorman, M. (1991). Source location in thin plates using cross correlation. *Journal of the Acoustic Society of America, 90*(5), 2551−2556.

Zwink, B., Adams, D., Evans, R., & Koester, D. (2009). Wide-area damage detection in military composite helicopter structures using vibration based reciprocity measurements. In *Proceedings of the IMAC XXVII − SEM − Society for experimental mechanics, Orlando, FL, 9−12 February*.

Zwink, B., Prewett, E., Adams, D., & Koester, D. (2008). Load estimation and damage detection in helicopter rotor blades. In *Proceedings of the IMAC XXVI − SEM − Conference & exposition on structural dynamics, Orlando, FL, 2−7 February*.

Dynamic fractures of adhesively bonded carbon fibre-reinforced polymeric joints

22

J.P. Casas-Rodriguez[1], *I.A. Ashcroft*[2], *V.V. Silberschmidt*[3]
[1]Universidad de los Andes, Bogota, Colombia; [2]University of Nottingham, Nottingham, UK; [3]Loughborough University, Loughborough, UK

22.1 Introduction

The use of advanced materials in the aeronautic industry is continuously increasing. In the last decades, advanced composites, such as carbon fibre-reinforced polymers (CFRPs) have become one of the most important structural materials in this industry due to their excellent stiffness and low strength-to-weight ratio. As reported by the manufacturer, in the Airbus A380 airplane 16% of the structural weight are composites, with a typical example being the centre wingbox with 60 wt% of 45-mm-thick CFRP laminates (Ekh, 2006). In Boeing 787 Dreamliner and Airbus 350XWB, the use of composites exceeds 50%.

The adhesive joining technology in aeronautic industry is mainly used to attach stringers to fuselage and wing skins to stiffen the structure against buckling. In addition, it is also used to manufacture lightweight structures of metal honeycomb for flight control components such as elevators, ailerons, spoilers, etc. (Higgins, 2000). Like most engineering materials, structural adhesives are susceptible to fatigue. Hence, this phenomenon should be analysed in detail to compare performance of adhesive joints in fatigue with that of other types of joints. This should be an important parameter for a designer to consider when selecting a structural adhesive along with factors such as joint shape, type of surface, pretreatment, etc.

Fatigue is a common phenomenon linked to cyclic loading, which occurs in service operation of structural components and can result in premature failure of the material compared to quasistatic conditions. In addition, complex patterns of real in-service loads have an effect on the progress of failure in composites or adhesives compared to results obtained under fatigue with constant load amplitude. Failure by fatigue in laminate composites is manifested by various types of damage: fibre breaking, transverse matrix cracking, debonding between fibres and matrix, and debonding of adjacent plies of the laminate commonly referred as delamination. In adhesives, failure by fatigue is identified as cohesive cracks in the adhesive, as cracks at the interface of the joint between adhesive and adherent or crack in the adherend in the case of adhesively bonded CFRP joints. With respect to fatigue, the term damage usually

Structural Integrity and Durability of Advanced Composites. http://dx.doi.org/10.1016/B978-0-08-100137-0.00022-5

refers to microcracks or macrocracks—discontinuities in the material changing the initially continuous medium.

Though adhesive joints have a good fatigue performance, there is still a concern that cyclic low-velocity impact loading experienced by mechanical structures, for example, in aeronautic systems, can lead to deterioration of their integrity and produce failure of bonded joints in cases when a long service life is expected. In operation, as was described in Cantwell, Curtis, and Morton (1984) and Owen (1972), aeronautic as well as maritime, automotive, and other components and structures can be exposed to cyclic or singular low-velocity impacts, resulting in delamination damage of parts with fibre-reinforced polymeric composite (FRPC) as adherends. Obviously, from the mechanical point of view, impact results in stress waves that propagate through the structure affecting all their interacting components. Hence, if adhesive joints are used in such structures, they are also exposed to such loading conditions.

Prediction of performance of various structures and components under real-life loads are usually based on models of fundamental material behaviour. These models are validated by experimental studies performed on specimens using relevant types of mechanical loads; an isothermal case is considered here. Such loads are a generalisation of ones experienced in service and normally limited to quasistatic, cyclic, dynamic, creep and relaxation tests. A need for these various types of tests is linked to different responses of the same materials to various loading conditions, and there is a general understanding that results, obtained in experiments of one type can hardly be sufficient to predict outcomes for other experiments. One of the examples is a dynamic overshoot factor, nearly doubling the maximum magnitude of the nominal load due to the weight if it is suddenly applied to a component. Still, one loading regime has yet not obtained the attention, which it undoubtedly deserves. This is a repetition of low-velocity impacts, with each impact being insufficient to cause the total failure of a structure or component. This type of loading is known as impact fatigue (IF) and is at the centre of this chapter.

22.2 Fatigue in adhesively bonded joints

22.2.1 General consideration

During operation, structures are exposed to a variety of loads with the varying frequency, amplitude and direction entirely depending on the location and moment at which those features are analysed. For example, maritime structures suffer load fluctuation as a result of variation with time of the sea waves, resulting in a cyclic load during the time that the structure is in use (Davies and ChoqueseHarris, 2000). However, in laboratory simulations, these load conditions usually are represented as a sinusoidal load wave. Other load shapes can be used—square, trapezium, sawtooth and spikes—that can have a constant amplitude (CA) or a variable-load block pattern. The presence of such load patterns results in introduction of different approaches in fatigue studies, differentiating CA fatigue and variable-amplitude (VA) fatigue. However, to simulate real load-time events, expensive and time-consuming experiments need to be performed.

For this reason, VA fatigue is frequently simulated using blocks of CA fatigue loads. This simplification helps to analyse VA fatigue with the same techniques used for CA tests. However, the necessity to include also effects that are produced only by the change of the monotony on the load conditions were also emphasised. For instance, it was found in Van Paepegem and Degrieck (2002a,b) working with FRPCs that a transition from a low mean stress to a high one was more harmful than the reverse, with the tendency being strongly dependent on the number of transitions.

CA fatigue, commonly using a sinusoidal waveform, is normally characterised by its loading or displacement pattern and also by a number of parameters such as the maximum (σ_{max}) and minimum (σ_{min}) stresses, frequency, and load or displacement control. These parameters are used to identify the following parameters: mean stress (σ_m), stress amplitude (σ_a) and load ratio R (minimum to maximum load or stress). In this chapter, this kind of load conditions is referred to as standard fatigue (SF).

22.2.2 Fatigue models

Extensive research on fatigue modelling of adhesively bonded joints has been done during the last decades. The main proposed models could be divided into three groups: (1) phenomenological, (2) based on a crack growth rate and (3) continuum damage mechanics (CDM). To have a spectrum of fatigue models, some models specifically for adherends, that is, CFRP, are reviewed here. For a more detailed study of the first two types of models, especially for FRPCs, the readers are referred to Degrieck and Van Paepegem (2001). In addition, a deeply reviewed work on the area of fatigue in adhesively bonded joints can be found in Abdel Wahab (2012). For a deep understanding of CDM, the authors can recommend Lemaitre, Sermage, and Desmorat (1999), Chaboche (1987) and Lemaitre (1984).

22.2.3 Phenomenological models

Phenomenological models are based on changes in the macroscopic mechanical characteristics of the sample after fatigue damage; these schemes commonly use such characteristics as fatigue life, residual stiffness and strength. In the fatigue life approach, experimental fatigue results are commonly presented as $S-N_F$ curves or Wöhler plots. In these plots, a loading parameter such as stress, strain, load or displacement is related to the number of cycles N_F, needed to generate failure in a specimen under a specific type of load (i.e. for constant R and constant frequency). Although researchers pointed out limitations of this model, basically it can be stated that $S-N_F$ graphs are still useful to analyse fatigue. However, such graphs do not give information on crack initiation and propagation; this technique is not suitable to analyse fatigue in such cases. Some effects of loading condition on $S-N_F$ graphs for adhesive joints have been described by researchers. In Crocombe and Richardson (1999), the effect of the load ratio was analysed, and it was observed that, for a given fatigue life, a lower load range was expected to produce failure when R increases. It was suggested that the fatigue process is more controlled by the maximum load rather than by the load range.

A series of cumulative models was proposed by researchers to use the data obtained with $S-N_F$ graphs to predict the fatigue life of specimens under varying cyclic conditions. Most models presented below are related to those used to analyse fatigue in adhesively bonded joints; however, some of them are more commonly used to analyse fatigue in FRPC.

The most common method to analyse fatigue life is the Palmgren−Miner model. This method was initially proposed by Palmgren (Gledhill, Shaw, & Tod, 1990) and then developed by Miner (da Silva & Öchsner, 2008). This method is based on the assumption that a constant work is absorbed in each cycle. For a CA load, the Miner's rule is defined as

$$C = \frac{n}{N_F} \tag{22.1}$$

in which n is the number of cycles at a given stress amplitude σ_a ($\sigma_a = (\sigma_{max}-\sigma_{min})/2$); N_F is the number of cycles to failure at σ_a; and C is called the Miner's sum and is theoretically equal to one at the point of complete rupture.

Approximations for cumulative damage in VA fatigue can be developed using the Miner's rule. Such methods are based on the determination of damage accumulation (D) as a linear combination of damage for each load block:

$$D = \sum_{i=1}^{j} \left(\frac{n}{N_F}\right)_i \tag{22.2}$$

in which j is the number of CA blocks. Rupture is expected when $D = 1$. It was shown that this kind of model can give satisfactory results in many cases. However, it was proved in Erpolat, Ashcroft, Crocombe, and Abdel-Wahab (2004a,b) that when it was used to predict the fatigue life in adhesively bonded joints under VA fatigue, it produced nonconservative fatigue-life predictions as a result of crack growth acceleration due to load interaction.

Other types of D are defined as was proposed in the Marco−Starkey model, in which a nonlinear damage accumulation law was defined as (da Silva et al., 2009)

$$D = \left(\frac{n}{N_F}\right)^{\propto} \tag{22.3}$$

in which α is an independent constant. In the same way, the model proposed by Howe and Oven (Miner, 1945), based on experimental work demonstrated nonlinear cumulative damage in glass-reinforced composites:

$$D = \sum_{i=1}^{j} \left[A\left(\frac{n_i}{N_i}\right) + B\left(\frac{n_i}{N_i}\right)^2 \right] \tag{22.4}$$

in which A and B are the material's parameters.

Authors like Adams and Harris (Gathercole, Reiter, Adam, & Harris, 1994) proposed other type of damage models called constant-life analysis, based on experiments with CFRP under conditions of CA fatigue. The authors showed that using positive and negative R-ratios but with similar $\sigma_{\max}$, comparable levels of life were obtained, suggesting that

$$\frac{\sigma_a}{\sigma_t} = f \times \left(1 - \frac{\sigma_m}{\sigma_t}\right)^u \left(\frac{\sigma_c}{\sigma_t} + \frac{\sigma_m}{\sigma_t}\right)^v \tag{22.5}$$

in which $\sigma_m = (\sigma_{\max} + \sigma_{\min})/2$, and σ_t and σ_c are tensile and compressive strength, respectively. Additionally, u and v are material parameters having a linear relation with log (N_F), and f is the fatigue parameter defined by the following relation:

$$f = \frac{\sigma_a/\sigma_t}{\left(1 - \sigma_m/\sigma_t\right)\left(\sigma_c/\sigma_t - \sigma_m/\sigma_t\right)} \tag{22.6}$$

A further work (Adam, Gathercole, Reiter, & Harris, 1994) defined a model for VA fatigue based on experimental studies of CFRP. As a simplification, this model was first defined for two load blocks and then extrapolated to i blocks supposing that a specimen has initial damage D_0. After the first block of load, the damage level increases to D_1 defined by Marco−Starkey's model (Marco, 1954):

$$D_1 = \left(D_0 + \left(\frac{n}{N_F}\right)_1\right)^{\alpha_1}. \tag{22.7}$$

The effect of block−load transition is included into this model using an equivalent fractional life model $(n/N_F)_{2,1}$; the latter is defined for the first block in terms of α for the second load block (α_2) and for the first load block (α_1).

$$\left(\frac{n}{N_F}\right)_{2,1} = (D_1)^{\alpha_1/\alpha_2} \tag{22.8}$$

Finally, damage before the second block is defined assuming $D_0 = 0$:

$$D_2 = \left[\left[0 + \left[\frac{n}{N_F}\right]_1\right]^{\alpha_1/\alpha_2} + \left[\frac{n}{N_F}\right]_2\right]^{\alpha_2} \tag{22.9}$$

Generalising the damage model in Eqn (22.9), damage for i blocks is defined:

$$D = \left[\left[\left[\ldots\left[0 + \left[\frac{n}{N_F}\right]_1\right]^{\alpha_1/\alpha_2} + \left[\frac{n}{N_F}\right]_2\right]^{\alpha_2/\alpha_3} + \left[\frac{n}{N_F}\right]_3\right]^{\alpha_3/\alpha_4} + \ldots + \left[\frac{n}{N_F}\right]_i\right]^{\alpha_i} \tag{22.10}$$

in which exponent α_i is the constant of Marco−Starkey's model for the i-th block.

Other types of models were proposed based on extended static unidirectional models to include cyclic loading, like in Jen-Ming and Lee (1998). Their model is defined in terms of the stress supported by a plate with fibres oriented at an angle θ to the load axis. They showed that for multidirectional laminates, subjected to plane-stress multiaxial fatigue loading with positive R, the following equation applies:

$$\left(\frac{\sigma_{11}}{L}\right)^2 + \left(\frac{\sigma_{22}}{t}\right)^2 - \left(\frac{\sigma_{11}\sigma_{22}}{L^2}\right) + \left(\frac{\sigma_{12}}{\tau}\right)^2 = 1 \tag{22.11}$$

in which directions one and two are parallel and perpendicular to the fibre, respectively, $L = L(n, R_{11})$; $t = t(n, R_{22})$; $\tau = \tau\ (n, R_{12})$; and $R_{ii} = (\sigma_{ii})_{\min}/(\sigma_{ii})_{\max}$ and N are the cycles under stress ratio R_{ii}.

On the other hand, stiffness-based models deal with changes in material or structural components under fatigue. Such changes are caused by a combination of all damage mechanisms, making it difficult to differentiate between the effects of each of these mechanisms. Hence, they are analysed with phenomenological models that, as mentioned in Zhang, Vassilopoulos, and Keller (2008), have the advantage compared with the strength models. This is due to the fact that the residual stiffness data have lower scatter than the strength data, highly sensitive to damage progression. In addition, this method can be used as a nondestructive measure that can be used during service. In Van Paepegem and Degrieck (2002a,b), it is stated that a typical experimental result on stiffness degradation in composites in fatigue can be presented as a three-stage graph, schematically shown in Figure 22.1. The character of stiffness deterioration in composites is characterised by an initial stage with an observed reduction of 2−5% caused by

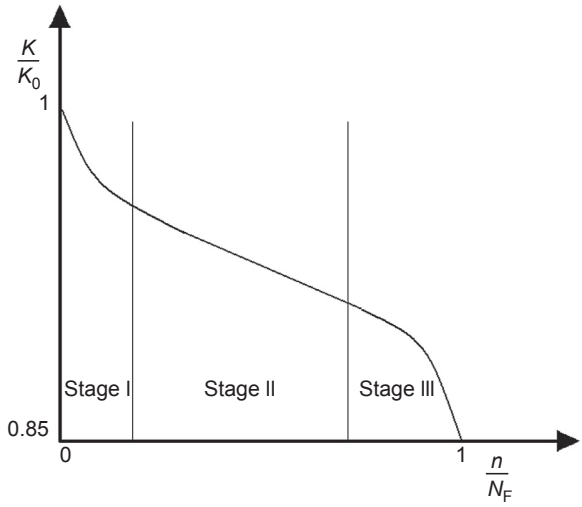

Figure 22.1 Typical stiffness degradation curves in composite materials.

transversal cracks, the second stage with an additional decrease between 1% and 5% with damage dominated by the edge delamination and longitudinal cracks, and the final stage when an abrupt failure happens.

22.2.3.1 Residual strength models

One of the types of models is the Yao–Himmel approach. This model considers that experimental data have a sinusoidal character (similar at the three stages presented in Figure 22.1) when the residual strength σ_R is plotted against the normalised fatigue life and is defined in the following form:

$$\sigma_R = \sigma^{\text{static}} - \left(\sigma^{\text{static}} - \sigma_{\max}\right) \frac{\sin\left(\beta\left(n/N_{\text{F}}\right)\right)\cos\left(\beta-\alpha\right)}{\cos\left(\beta\left(n/N_{\text{F}}\right)-\alpha\right)\sin\beta} \tag{22.12}$$

in which β and α are empirically defined parameters (Yao & Himmel, 2000).

The Yao–Himmel's model was extended in Hosoi, Kawada, and Yoshino (2006) to VA fatigue defining a cumulative damage rule for each load block i with respect to residual strength σ_{Ri} for the block i, as follows:

$$D_i = \frac{\sigma^{\text{static}} - \sigma_{Ri}}{\sigma^{\text{static}} - \sigma_{\max}} \tag{22.13}$$

Assuming that no interaction exists and that the specimen ruptures when the residual strength is equal to the maximum loading level, it follows that

$$D_i = \frac{\sin\left(\beta\left(n/N_{\text{F}}\right)\right)\cos\left(\beta-\alpha\right)}{\cos\left(\beta\left(n/N_{\text{F}}\right)-\alpha\right)\sin\beta} \tag{22.14}$$

Another residual strength methodology to analyse the evolution of damage in composites was defined in Schaff and Davidson (1997). That model was based on the residual strength $\sigma_R(n)$ of a specimen during fatigue. This model assumes that the initial residual strength is equal to σ^{static} (static strength), and it decreases as the number of cycles increases. Failure occurs after N_{F} cycles when $\sigma_R(n)$ reaches the same value that has the maximum stress from the sinusoidal load spectrum ($\sigma_R(N_{\text{F}}) = \sigma_{\max}$). It is considered that in cycle n, $\sigma_R(n)$ has the following magnitude:

$$\sigma_R(n) = \sigma^{\text{static}} - \left(\sigma^{\text{static}} - \sigma_{\max}\right)\left(\frac{n}{N_{\text{F}}}\right)^{v} \tag{22.15}$$

in which v is a degradation parameter. In VA fatigue, introduction of a second block into the model makes it necessary to introduce an equivalent number of cycles n_{eff}

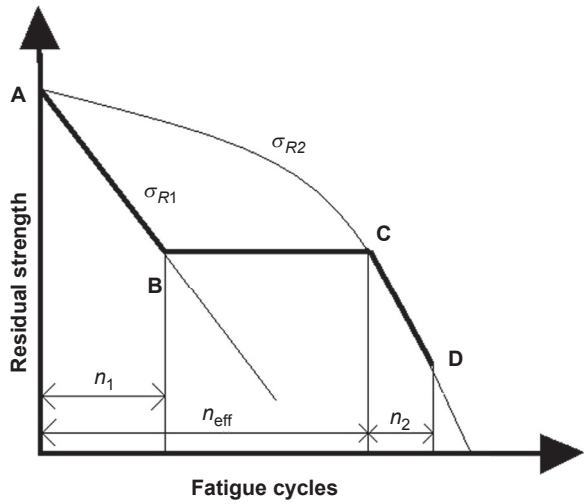

Figure 22.2 Schaff and Davidson's method. Schaff and Davidson (1997).

that are shown in Figure 22.2. Here, curve ABCD represents the residual strength after completing two load blocks. In this case, by definition, $\sigma_{R1} > \sigma_{R2}$, and σ_{R1} has a linear strength degradation ($v_1 = 1$). This model assumes that the specimen will be at point B when it is loaded at $\sigma_{1\max}$ by n_1 cycles, and the strength will be defined by Eqn (22.15). However, when the second load block is introduced, the system will follow along ACD, and point C represents an equivalent strength that a specimen has before being loaded at $\sigma_{2\max}$.

To correlate B and C, an effective number of cycles should be determined, assuming that the specimen has the same strength between these points:

$$n_{\text{eff}} = \left[\frac{\sigma^{\text{static}} - \sigma_{R1}(n)}{\sigma^{\text{static}} - \sigma_{2\max}}\right]^{1/v_2} n_2 \tag{22.16}$$

Finally, strength at point D is defined in terms of the effective number of cycles at C plus n_2 as

$$\sigma_R(n_1 + n_2) = \sigma^{\text{static}} - \left(\sigma^{\text{static}} - \sigma_{2\max}\right)\left(\frac{n_{\text{eff}} + n_2}{N_2}\right)^{v_2} \tag{22.17}$$

Additionally, the authors developed an important model to evaluate loading sequences with small cycle blocks. To include changes in the magnitude of the mean stress from one segment to the next, it was proposed to include the cycle mix (CM) factor, correcting the residual strength:

$$(\sigma_R(n))_{\text{eqv}} = \sigma_R(n) - \text{CM} \tag{22.18}$$

in which CM is the mix factor defined as

$$\mathrm{CM} = C_m \sigma^{\mathrm{static}} \left[\frac{\Delta\sigma_{mn}}{\sigma_R(n)} \right]^{\left(\Delta\sigma_p / \Delta\sigma_{mn}\right)^2} \tag{22.19}$$

in which $\Delta\sigma_p$ is the change in the peak stress magnitude and $\Delta\sigma_{mn}$ is the change in the mean stress magnitude. In Erpolat et al. (2004a,b), a modification of the CM factor was presented to predict complex load patterns such as block-load changes in CA and inclusion of overloads. This term was included in a linear residual degradation expression for $\sigma_R(n)$, making it capable to predict N_F for a complex load pattern with high accuracy.

22.2.4 Fatigue crack-growth-rate curve approach

The fatigue crack-growth-rate curve (FCGR-curve) approach is a common technique used to characterise the FCGR ($\mathrm{d}a/\mathrm{d}n$) at which the crack grows, as a function of the number of cycles with respect to some fracture-mechanics parameter. A typical way to show these results is by plotting log ($\mathrm{d}a/\mathrm{d}n$) versus log (ΔK), in which ΔK is the amplitude stress intensity factor ($K_{\max} - K_{\min}$) determined for the maximum and minimum load values. Three different regions can be identified in this graph. Region I is characterised by a threshold value, below which no fatigue failure is present. In region II, there is a quasilinear relation between log (ΔK) and log ($\mathrm{d}a/\mathrm{d}n$). Finally, in region III, the crack has a fast-growth tendency, having an asymptotic value ΔK_c.

Usually for adhesives and composites, G is used as the fracture-mechanics parameter in preference to K. In addition, it is common to use $G_{\max}$ rather than ΔG (i.e. $G_{\max} - G_{\min}$), because the cracked surface can be affected by friction in the unloading process. This factor increases the real value of $G_{\min}$ (Ashcroft, 2005). The critical region between region II and III, it is defined by G_c, which is the energy release rate for failure in quasistatic conditions, as seen in Figure 22.3.

An empirical relation between $\mathrm{d}a/\mathrm{d}n$ and K was defined in Paris and Erdogan (1963) and commonly referred to as Paris law. His studies concluded that for region II the FCG has the following tendency:

$$\frac{\mathrm{d}a}{\mathrm{d}n} = C\Delta K^m \tag{22.20}$$

in which C and m are material constants. Some studies replace the parameter ΔK with ΔG.

In Shivakumar, Chen, Abali, Le, and Davis (2006) a total-life model for composite samples subjected to mode I fatigue loading was developed. That model was based on the interlaminar fracture toughness resistance (G_{IR}), defined as instantaneous material resistance, that is a function of the crack size and critical energy release rate (G_{Ic}). Experimentally, it was observed that $G_{IR} = G_{Ic}$ when

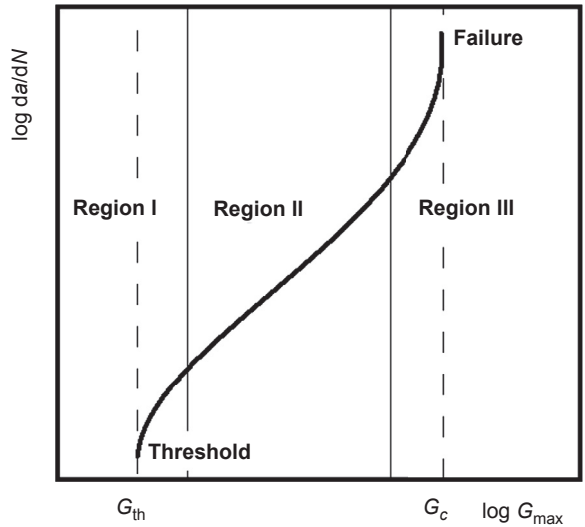

Figure 22.3 Typical fatigue crack growth curve.

delamination began to grow; however, as the crack size increased, G_{IR} started exceeding G_{Ic}. This phenomenon was explained as a reason for matrix cracking and fibre bridging in the case of unidirectional composites. It was also supposed that (da/dn) was proportional to the cyclic force G_{Imax}, but inversely proportional to resistance G_{IR}. Finally, (da/dn) was limited by the threshold energy release rate G_{IR} (da/d$n = 0$) and G_R (da/d$n = \infty$):

$$\frac{\mathrm{d}a}{\mathrm{d}n} = C\left(\frac{G_{\max}}{G_{IR}}\right)^{m}\left[\frac{1-\left(G_{\mathrm{th}}/G_{\mathrm{Imax}}\right)^{m1}}{1-\left(G_{\max}/G_{IR}\right)^{m2}}\right] \tag{22.21}$$

in which C, m, $m1$ and $m2$ are material constants.

22.2.5 Geometry effects

DCB specimens have been traditionally used to analyse the FCGR-curve, because this kind of specimen is tested in mode I of failure. However, there are other types of joints, such as a lap strap joint (LSJ) (Figure 22.4), known under different names: cracked lap shear specimen (Johnson, 1987; Papini, Fernlund, & Spelt, 1994), in which cracks usually grow in the middle of adhesive, and strap lap joint (Ashcroft, Hughes, & Shaw, 2001). These joints are tested in tension or three-point bending. The LSJ is a representative joint for many aeronautic structures such as stiffened panels and shells, selective plate reinforcement, bonded edge doubler for flush mechanical attachments, etc. This kind of joint is useful to researchers

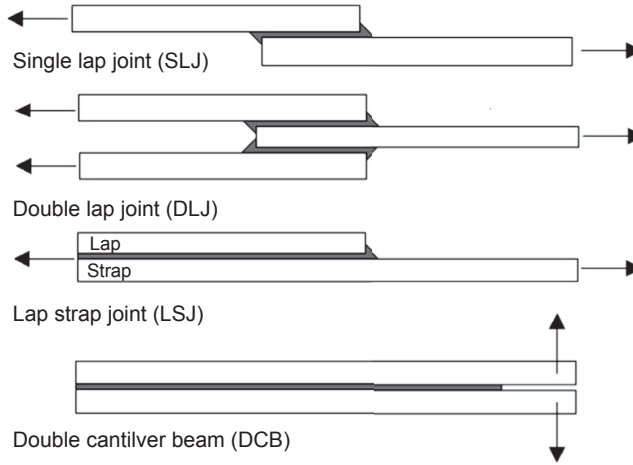

Figure 22.4 Typical adhesive joints.

when the fracture behaviour of bonded joints needs to be analysed under mixed-mode loading at one overlap end. The LSJ has been used to study metal joints, composite joints, joints between composites and metals, and interlaminar fracture. In Johnson (1987), a typical relation of G_I/G_{II} for LSJ between 0.2 and 0.3 was determined using a nonlinear geometric finite-element analysis. During experimentation, analytical solutions for G are required not only to verify the obtained results, but also to determine the fracture energy of the adhesive joint. In Tong and Luo (2008), the research conducted on this kind of joint is summarised.

22.2.5.1 Load effects in fatigue crack growth

Researchers have analysed the effect of loading conditions on the FCG to identify crack acceleration phenomena and their effect on the normal behaviour of the FCGR-curve. A review of the effect produced by variation of each of the test parameters follows.

Effect of frequency

It was found that adhesive joints were sensitive to the frequency of applied loading. The effect of different frequencies on the FCG behaviour on DCB steel-bonded joints was studied in Xu, Crocombe, and Smith (1996), in which two types of adhesives were used, tested at three frequencies of 0.02, 0.2 and 2 Hz. No significant effect on the FCG was detected for one adhesive. However, in another adhesive, it was found that a decrease in frequency caused a reduction in the threshold value and acceleration of the crack growth. Such behaviour is justified by an increase in the load application time in experiments performed at positive load ratios and low frequency, making creep behaviour more likely to occur. These conclusions can also be used to analyse the results presented in Al-Ghamdi, Ashcroft, Crocombe, and Abdel-Wahab (2003). In these tests, three frequency levels were applied to

adhesively bonded CRFP and mild steel specimens; it was also observed that the FCG increased and the fatigue threshold decreased as the frequency decreased.

Effect of R-ratio

In Erpolat et al. (2004a,b), changes of the FCG caused by the load ratio were investigated using a DCB specimen based on a CFRP-epoxy adhesive system. It was observed that the fatigue threshold decreased with the decreasing load ratio. For instance, FCGR curves showed similar tendencies when they were plotted as a function of ΔG; however, when curves were plotted as a function of G_{max}, it was observed that as R decreased, a high crack growth occurred. Similar changes of graphs were also reported in Mall, Ramamurthy, and Rezaizdeh (1987). In Pirondi and Nicoletto (2004), the influence of R and the frequency on the FCGR-curve were analysed, concluding that the effect of the frequency is much lower than that of R; it was explained that such behaviour was due to viscoelastic properties of the adhesive.

Effect of bonding thickness

Thickness of the adhesive layer was shown to affect the fracture energy measured for adhesive specimens, basically, due to a relation between thickness and the size of a plastic region. However, some researchers mentioned that the relation could affect the FCG only for particular specimen configurations (Schon & StarikovHarris, 2003). In Abou-Hamda, Megahed, and Hammouda (1998), working with a DCB specimen and a specific range of adhesive thickness, it was observed that the greater the thickness, the lower is the FCGR. This effect is explained as results of increases in the stress distribution near the crack tip at lower adhesive thickness and, consequently, an increase in the FCGR. However, there exists a limit thickness, for which no changes in the FCG can be perceived (Mall & Ramamurthy, 1989).

Effect of mode mix

As analysed by various researchers, fracture toughness under mode I in quasistatic conditions is lower than in mode II (Choupani, 2008); this suggests that under fatigue, lower FCG resistance can be expected in mode I than in mode II. This type of trend was observed in Xu, Crocombe, and Smith (1995) for an LSJ in three-point bending in which a lower FCG was found under a mixed mode of loading than in a pure mode I. On the other hand, comparison of the G_{th} value at various temperatures was presented in Ashcroft and Shaw (2002), dealing with different joint configurations: DCB, LSJ and DLJ. It was observed that for all temperatures measured (−50 °C, 22 °C and 90 °C), the variation of G_{th} followed the relation $(G_{th})_{DLJ} < (G_{th})_{DCB} < (G_{th})_{LSJ,}$ being almost constant for the temperature range used except for low temperatures in DLJ. However, differences in the definition of thresholds in specimens can affect these trends; in the case of DCB, it was defined as a level at which the crack suffered an arrest, but in LSJ and DLJ it was defined as the load that could support 10^6 cycles in the specimen without formation of a macrocrack. In a recent work (Pirondi & Nicoletto, 2006), the FCG of an

aluminium alloy adhesively bonded under pure mode I, mode II and controlled mixed modes was analysed using a compact tension shear specimen. An increase in the FCG resistance in the mixed mode and mode II was found compared to mode I, confirming similar results found earlier. However, those results did not support the difference found for quasistatic values. It was proposed in Pirondi and Nicoletto (2006) that for some adhesives the viscoelastic behaviour could produce such changes in addition to heating at the crack tip due to hysteresis, in which a softened material can exist during fatigue. It would result in a stress redistribution that differs from that for the quasistatic behaviour. In conclusion, the effect of the FCG under pure mode I, mode II and the mixed mode is not always obvious and depends, in particular, on the type of adhesive used.

Effect of environment

Analyses of FCG in CFRP composites, adhesively bonded as DCB, were carried out at different temperatures in Ashcroft and Shaw (2002). It was found that when the temperature increased, G_{th} increased, and the ratio G_{th}/G_c decreased; the failure occurred in the composite adherends at low temperature and in the adhesive layer, cohesively, at higher temperature. A similar behaviour was presented in Pirondi and Nicoletto (2004), with changes in the slope of FCGR curve being caused by changes of the temperature; the environmental factor was studied using LSJs under four-point bending. It was observed for specimens tested at room temperature that as the temperature increased, the FCG resistance increased. However, when specimens were tested at higher temperatures (90 °C), the behaviour changed, decreasing considerably the FCG resistance; no explanation to that behaviour was given. An additional conclusion that was obtained in that work is that at constant temperature, a change in environment condition from air to a salt water environment decreases FCG resistance in all the cases.

Effects on G_{th} at different temperatures and humidity levels were studied in Ashcroft, Wahab, Crocombe, Hughes, and Shaw (2001), in which similar values of G_{th} in dry conditions were found for LSJ tested at different temperatures. In addition, it was found that specimens tested at high temperatures or high moisture content did not demonstrate significant changes in G_{th}; however, when LSJs were tested at both conditions, a drastic decrease in G_{th} was found. The authors explained that behaviour indicating that G_{th} decreased when test conditions were near to the glass transition temperature T_g), and T_g was reduced by the moisture level observed in LSJs tested at high temperatures. Finally, it was suggested that fatigue crack initiation, damage patterns and failure modes were influenced by environmental conditions.

22.2.5.2 Damage-shift model

A model to analyse VA fatigue in adhesive joints based on the fatigue crack growth approach is presented in Ashcroft (2004). It was supposed that under CA block a, fatigue could be analysed using the FCG approach and represented by G_{th}, G_c and two Paris constants C and m (Eqn (22.22)). For instance, it was determined that when a CA load block referenced as a was applied (with Paris' law constants C_a

and m_a), it produced ΔG_a, which resulted in a growth rate $(da/dn)_a$. However, when an overload was superimposed on the load pattern a, the damage level in the process zone could increase and, therefore, decrease the resistance to crack propagation. It was proposed that such increases of damage would shift the FCGR-curve by ψ_E; as the crack grew in the damage zone, an equilibrium position of the FGG was reached, and the parameter ψ_E could be calculated as

$$\Psi_E = f(N_R, R_{ol}), \tag{22.22}$$

in which N_R is the number of overloads, and R_{ol} is the ratio between ΔG_a and ΔG_{ol} (the latter is ΔG at the overload). Special attention should be taken, as emphasised by the author, when ΔG_a increases as the crack grows, because it is possible that it reaches the critical value $(\Delta G_a)_C$ for the shifted FCGR-curve (Figure 22.5). It was suggested that, in that case, an unstable or quasistatic crack appeared, producing a catastrophic failure of the specimen. However, in the case when the ΔG_a decreased as the crack grew, it was possible that eventually the crack would stop, but with an arrest strain-energy release ΔG_{arr} lower than the value that was without overload.

That model was proposed to explain the acceleration phenomenon observed experimentally when an intermittent overload was introduced into a CA load pattern. In the case of a failure growth inside the FRPC adherend, X-ray analyses of adhesively bonded structures showed the existence of a damage region ahead of the crack tip where small debonding or fibre debonding could exist, generating a decrease in the energy necessary for a crack growth (Ashcroft, 2004). In the case when the overload was imposed, an increase of the damage zone could be detected, confirming a faster crack growth (Erpolat et al., 2004a,b).

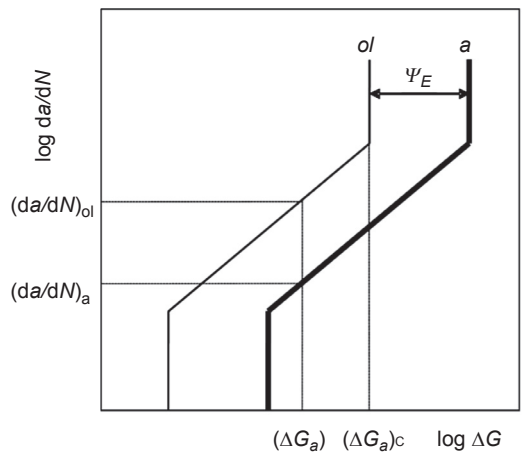

Figure 22.5 Damage-shift model.
Ashcroft (2004).

22.3 Impact and impact fatigue

It is a well-established fact (Johnson, 2004) that research into IF started effectively at the same time as the one into SF, that is, in the middle of the nineteenth century (Hodgkinson, 1849). More than a century ago a 'shock-fatigue' test, defined as a one 'involving a large number of relatively small blows' was used to study a response of steels to this type of loading in comparison with a static test and a 'single-blow' test (Stanton & Bairstow, 1908). Those tests were performed with specially designed testing machines for impacts in bending, tension and compression. The tests in bending were implemented for loading histories of up to 10^6 cycles, while those for tensile impacts, 'owing to the relatively slow speed of the direct-impact tester,' were limited to 50,000 impacts (Stanton & Bairstow, 1908). A difference between effects due to IF and both single-impact loading and SF was apparent at that time as well as the absence of a durability limit (named 'limiting resistance').

Still, more than a 100 years after those conclusions, the area of IF is considerably less studied than that of SF. There are several reasons for such a situation. One of them is ambiguity in the choice of the loading parameter. For an SF, an obvious parameter is the stress amplitude that comes back to the notion of Wöhler's $S{-}N_F$ diagrams in stress-controlled fatigue. In IF, a maximum stress magnitude can be hardly used as a sole parameter because, depending on the loading conditions, especially the impact velocity, the same level of this parameter can correspond to different levels of the applied energy. As a result, different authors have been using various loading parameters in their studies.

Another reason is the specificity of IF realisation in different types of materials. Already in 1908, Stanton and Bairstow (Stanton & Bairstow, 1908) noticed 'remarkable endurance for lighter blows' in brittle specimens. Some authors even mention a higher resistance of specimens exposed to IF conditions as compared to SF. This can be explained by a link between the levels of impact energy, contact duration and damping properties resulting in a specific type of spatial localisation of the stresses and their decay with propagation from the contact area. This linkage can differ with kinematics of impact-induced deformation and the specimen geometry and type of fixture. One extreme example is shot peening, which is a process of repetitive impacting with tiny particles, resulting in improved fatigue performance due to strengthening of a near-surface layer (Hertzberg, 1996). Another example is repetitive impacting of laminated composites in drop-weight test systems (see e.g. Jang, Kowbel, & Jang, 1992; Schrauwen & Peijs, 2002), in which the most affected zone is situated below the contact area, resulting in delamination initiation in this part of laminate and its subsequent spreading to other parts of tested specimens.

Impact events that arise in aerospace structures and components due to gusts, storms and landing can be masked in load history diagrams, presenting thousands of loading cycles with various amplitudes. The existing methods to treat such diagrams, for example a so-called 'rainflow technique' (Khosrovaneh & Dowling, 1990), are considered with a proper way of counting events, making no distinction

between impacts and relatively slow cycles that can be treated as non-IF events. This can be very dangerous, because impacts with lower amplitude can be more damaging than nonimpact cycles with higher amplitudes.

22.3.1 Impact tests

Research into impact loading of materials is mostly limited to analysis of the material's response to a single impact, studying its dependency on the impact velocity, impact force and impact direction (transversal, in-plane impacts or oblique impacts). Three main types of tests are used to analyse the effect of impacts: (1) experiments with pendulum impact testers with impact rates less than 5 m/s; (2) drop-weight tests, with rates up to 10 m/s; and (3) a split Hopkinson pressure bar (SHPB) testing technique for rates up to 100 m/s (Bezemer, Guyt, & Vlot, 1998). Specifically, in the area of adhesives, two standard tests were proposed to evaluate the impact strength in adhesives: ASTM D950-03 Standard Test Method for Impact Strength of Adhesive Bonds (ASTM-D950, 2003) and (ISO-11343, 2003) Adhesives—Determination of dynamic resistance to cleavage of high-strength adhesive bonds under impact conditions, the wedge impact method (ISO-11343, 2003). The first of these standard methods uses two bonded-together blocks, as seen in Figure 22.6; the bottom block is rigidly secured in the test rig, and a pendulum hammer strikes the top block, generating a shear load in the adhesive layer. In Adams and Harris (1996), the block impact test was analysed, and it was concluded that the stress condition was uncertain due to complex dynamic effects generated by uncertainties in the contact interface between the block and hammer. The second method was originally proposed in Adams and Harris (1996); this test method uses a wedge inserted into the specimen, as seen in Figure 22.7; as the wedge is moved under impact, the adherends start to deform producing a peeling loading in the adhesive. Disadvantages of this method were also discussed by the authors, describing that the local stress in the adhesive depended strongly on deformation of the adherend and on the angle of the wedge; in addition, friction between the wedge and the broken adhesive could not be measured. Another disadvantage is that high levels of energy are consumed by plastic deformation of the adherend, which increases as the thickness grows. In Blackman, Kinloch, Taylor, and Wang (2000), this technique was used experimentally and modelled by FEM to analyse a variety of rubber-toughened epoxy adhesives. In that work, it was found that the shape affected test measurements, and the obtained FEM results depended on

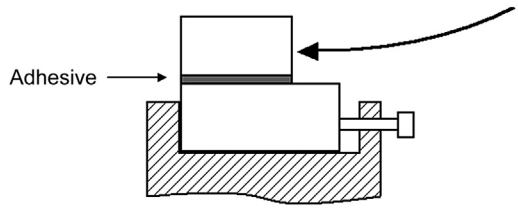

Figure 22.6 Schematic of impact block test.

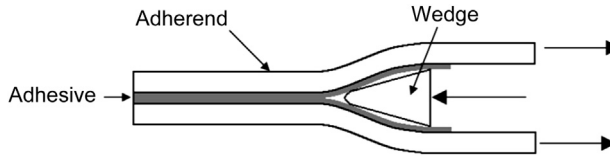

Figure 22.7 Schematic of wedge impact specimen.

the friction coefficient μ between the wedge and the fracture surface and, obviously, on the G_c value of the adhesive. However, as expected, the results depended mainly on G_c rather than on μ, but the latter also caused differences in the results.

Other setups were proposed by various researchers to analyse impact in adhesive joints. The single-lap impact test in Ekh (2006) was proposed as an alternative; and it was reported in Blackman et al. (2000) that the deformation of the adherend was affected by the plastic deformation of the adhesive. However, this is a more similar technique than those normally used to analyse SF or quasistatic fracture behaviour.

22.3.2 Impact in composites

High-performance FRPCs are now well established in many applications such as military aircraft, high-speed marine vessels and sports equipment. Increasing usage is also being found in civil aircraft, automotive and building applications. The original reason to use these materials was their high specific (i.e. per unit mass/density) strength and stiffness; however, other potential advantages include reparability, insulating properties, corrosion resistance, possible use in stealth applications and fatigue resistance. In fact, good resistance of FRPCs to fatigue led to an early design philosophy based on quasistatic strength alone. However, with further research and increased studies of components after extended periods in service, it is now recognised that fatigue is potentially damaging to composites and, hence, is worthy of serious study. Furthermore, fatigue is also linked with two of the main drawbacks of these materials: (1) the initial damage is subsurface, and hence difficult to detect, and (2) the transfer from a stable to unstable crack growth can occur at short crack lengths. Together, these two features can mean that the first visible sign of fatigue damage can be complete failure of the structure. This led to research into fatigue of composites, including the fatigue-related propagation of subsurface cracks caused by low-energy impact, such as a classic scenario of a dropped tool during a maintenance work (Cantwell et al., 1984; Clark & Saunders, 1991; Ramkumar, 1983). Most of this research work has been conducted using SF or, in some cases, simplified versions of load spectra taken from experimental measurements using techniques such as the rainflow method. However, the in-service load spectra for structural applications can, in some cases, contain repetitive low-energy impacts, that is, IF. This type of loading has received little attention to date, but has been shown to be damaging to composite materials. The next subsections detail some of the research performed on the analysis of impact and IF in FRPC both experimentally and in modelling.

22.3.2.1 FRPC under impact

In the case of impacts, materials are exposed to different loading conditions compared with those at static loading, because they involve dynamic factors of loads such as inertia; besides, materials respond differently to these loading conditions. These were the reasons for researchers to use different ways to analyse experimentally the behaviour of composites exposed to impacts. A description of the principal experimental studies conducted by various researchers for impacts is presented below.

A preliminary step to study FRPCs at impacts is to analyse the load rate sensitivity of materials. In general, it is well known (Hiley, Dong, & Harding, 1997; Hosur et al., 2005, Hosur, Waliul, Vaidya, Dutta, & Jeelani, 2004; Lifshitz & Leber, 1998) that the inter-laminar shear strength (ILSS) of carbon fibre/epoxy composites increases with strain rate. In Hosur et al. (2005), working with an SHPB setup, it was suggested that such behaviour could be attributed to the time-dependent deformation of the material, which is a result of the viscoelastic behaviour of the composite matrix. In addition, it was found that even in specimens that do not exhibit failure, the stress−strain behaviour in the unloading part is principally different from that in impacting loading. This was attributed to the heat generated by high strains affecting the structure of the matrix material. A further study (Hosur et al., 2004) showed that the maximum stress supported by the material in a single impact decreased considerably with an increase in the temperature. However, it was concluded in Hiley et al. (1997), working with a CFRP composite, that increases in the ILSS in specimens tested at impact were not accompanied by any significant differences in fracture surfaces compared to samples that failed under quasistatic loads. For instance, in Hosur, Abraham, Jeelani, and Vaidya (2001), a relation between the ILSS and the level of the impacting energy was found; the residual ILSS after an impact decreased as the impact energy increased because of the damage size growth.

To understand the effect of an impact, a common method was to define the residual strength of a material that had been previously impacted with a lower energy. In Wyrick and Adams (1988), a tensile and compressive strength degradation of CFRP was observed when it was exposed to impacts, influenced mainly by their level and number; however, that degradation was limited to the region near the impact point. Another way to analyse the effect of impacts in CFRP was to apply a transversal impact over a plate clamped with a special device. The transversal impact caused visible damage and delamination in the plate (Cantwell et al., 1984), affecting significantly its mechanical properties and being the reason for a high reduction of compression strength (Ding, Yan, & McIlhagger, 1995; Harris, 2000). However, such reduction can be decreased by the manufacturing process when woven laminate (Sanchez-Saez, Barbero, Zaera, & Navarro, 2005), stitched woven CFRP (Hosur et al., 2003) and pretensioned high-strength fibres (Potter, Schweickhardt, & Wisnom, 2000) were used.

A decrease in the mechanical properties of FRPCs can also be analysed, measuring the impact fracture energy necessary to break a pre-impacted specimen. In Bora, Çoban, Sinmazçelik, Cürgül, and Günay (2009) and Sınmazçelik, Arıcı,

and Günay (2006), such specimens were tested with a critical impact energy using a commercial CFRP and an instrumented Izod machine to cause complete failure. The results showed that the energy necessary to break specimens could be divided into three ranges in terms of the pre-impacted energy level: the first range when insufficient damage was produced by the pre-impact to enlarge microcracks and debonding; the second range, characterised by a transition zone where micro-cracks produced in the matrix as a result of previous impacts merged, generating a debonding zone that decreased considerably the fracture energy; and, finally, a third range when specimens that did not completely fail in the pre-impact had an extremely low, nearly constant fracture energy. For instance, the division into the regions for the IF was also detected in curves of local damage versus the number of impacts (Çoban, Bora, Sinmazçelik, Cürgül, & Günay, 2009). An additional study also showed that an impact could affect the fatigue behaviour of FRPC; in Ding et al. (1995), the fatigue life of CFRP laminates was investigated with sinusoidal in-plane loads combined with a single transversal impact. It was found that fatigue strength of CFRP was affected by the sequence, with the effect being more pronounced in the case in which the sinusoidal load followed the impact than in the inverse sequence. Similar experiments were performed with a glass fibre-reinforced composite (GFRP) (Yuanjian & Isaac, 2007), in which it was found that a single transversal impact had a significant effect on the fatigue life and that behaviour was strongly related to the post-impact residual strength.

22.3.2.2 FRPC under impact and fatigue

Analysis of IF in FRPCs was principally aimed at characterisation of the fatigue life reduction with the increasing load. In Ding et al. (1995) and Yuan, Friedrich, and Karger-Kocsis (1995), the $S-N_F$ diagram was used to describe the fatigue life reduction. It was found that an increasing amount of impact damage followed by the cyclic tensile impacts reduced the fatigue performance of the material having, in general, a linear trend in semi-logarithmic coordinates.

However, a more common way to analyse the fatigue life reduction during IF was to use the curves presenting a link between the level of energy and the number of cycles to failure ($E-N_F$) plotted in most cases in semi-logarithmic coordinates (Jang et al., 1992; Khan, Rao, & Venkataraman, 1995; Ming-Hsiung, Hwang, Doong, & Fung, 1999; Ray, Sarkar, & Bose, 2002; Roy, Sarkar, Rana, & Bose, 2001; Sınmazçelik et al., 2006). In Ray et al. (2002), a jute/vinyl-ester composite in a cyclic Charpy test showed an increase in the material's endurance as the impact energy decreased. Such graphs are divided by some researchers into several regions (Roy et al., 2001), and in some cases, it was possible to identify a threshold energy, below which no visible delamination was observed (Khan et al., 1995; Sınmazçelik et al., 2006). However, it was mentioned in Harris (2000) that in FRPCs, low-energy transversal impacts, which were insufficient to leave any visible damage under the surface, could produce internal damage capable to grow under the influence of subsequent cyclic loading. This suggests that not enough experimental work is available to clarify the existence of an endurance limit in FRPCs.

Some research was aimed at analysis of the dependency of IF on the orientation of fibres in CFRP. In this way in Yuan et al. (1995), using a Charpy test and different adhesive interlayers and lay-ups, it was found that quasi-isotropic laminates had a better fatigue life than cross-ply ones when tested with transversal impacts. However, other variables can increase resistance to transversal impacts, for example, composition of the matrix. In Schrauwen and Peijs (2002), for GFRP tested with a drop-weight machine, it was observed that a damage area after one transversal impact was highly dependent on the fibrous architecture (woven or multi-axial stitched) and resin (brittle or ductile) used. The most critical factor was the matrix composition, and it was found that the lowest damage area was observed for a ductile toughened resin. However, when similar materials were analysed in IF, no difference for different fibres and matrices was found in the $E-N_F$ graph, especially when the energy was normalised in terms of the penetration energy defined as the energy necessary for a falling weight to penetrate the laminate.

Another variable analysed in transversal IF is an interval time defined as a time between subsequent impacts. It was found that increases in the interval time resulted in a lower number of cycles to crack initiation and failure, especially when the applied impact load was small. In addition, they found that those results contrasted with the test data for standard tensile fatigue. Such behaviour was explained by the fact that at the higher interval time there was enough time to recover deformation, confining the damage zone to a small area. However, in the case of low-interval impacts, the damage zone is delocalised because the area of contact with the striker increased without the deformation recovering process, increasing the portion of the specimen that can absorb energy in the impact, thus resulting in a greater number of impacts to failure.

Researchers also tried to develop models to describe IF in FRPCs. In Azouaoui et al. (2001), an investigation of a model for damage and failure of GFRP plates under low-velocity IF was carried out. In these experiments, a crank mechanism introduced transversal cyclic impacts. It was shown that IF caused a reduction in bending stiffness. And even low-energy impacts produced internal delamination causing a decrease in the laminate's strength, although there was no observable damage. A local damage parameter defined in terms of bending stiffness was suggested; in addition, it was observed that three regions described the damage evolution in the material under IF when damage was plotted against the number of impacts. The first region is linked with initiation and growth of delamination zones under the surface; the second zone is characterised by saturation of delamination, when propagation of existing delamination zones and development of new ones are stopped. Finally, the third region is related to ply cracking with fibre breaking, when damage accelerates until final failure. However, no corroboration of that model with experimental work was presented.

22.3.2.3 Modelling impacts in FRPC

In this section, a description of the major work conducted on modelling impact in FRPCs is carried out. The main strategies used are mentioned; however, the authors recommend (Hampson & Moatamedi, 2007) for an in-depth review of this area.

Criteria of failure for laminate composite structures used in impact conditions were proposed in Hou, Petrinic, and Ruiz (2001), Hou, Petrinic, Ruiz, and Hallett (2000). Those criteria are described, in general, as a stress-based relation accounting for a delaying effect of compressive stress on delamination initiation. They were verified for simulation of a single low-velocity transversal impact. The criteria involved different damage modes: matrix cracking, matrix crushing and delamination. An interaction between those damage mechanisms was compared with experimental studies and was reported to be in a good agreement. Other authors Changliang, Mingfa, Wei, and Haoran (2006) also used Chang−Chang's damage criterion, proposed originally for tensile loading (Chang & Chang, 1987), to analyse low-velocity transversal impacts in a vessel with and without full internal pressure using their own finite-element code. Special attention was taken to define the Hertzian contact law to calculate the contact force between the impact body and the impacted cylindrical vessel. In Hyung Yun and Chang (1992), an extension to Chang−Chang's damage criterion was proposed to predict damage initiation under transversal impacts in CFRP composite. That failure criterion for estimation of delamination was defined in terms of three stress components: plane stress, inter-laminar shear stress of the immediately lower ply of the concerned interface and inter-laminar shear stress of the upper one. Some empirical constants were included into the model that should be evaluated with experimental studies. The author concluded that the model-based predictions were in agreement with the test data.

A review of the strategies used by researchers to model delamination with previous transversal impacts was presented in Maranon (2005). The strategies were classified into four main groups according to the type of interface between the delaminated and base regions: (1) hybrid elements, (2) a de-equivalence crack, (3) a degraded inter-laminar layer and (4) a substructure. In strategies based on hybrid elements, the upper plies and lower plies divided by delamination are connected by beams, springs or some type of contact. In the second group, an artificial delamination area is included without connection between these groups of plies. The models with degraded interlaminar layers have a thin layer placed between plies, and delamination is simulated as a reduction in the elastic properties of the isotropic element. Finally, delamination is treated as a substructure when only the delaminated region is modelled, assuming that its thickness is small compared with that of the adjacent plies.

Many works in the area used cohesive elements and CDM to analyse damage evolution under low-velocity transversal impacts. In Aymerich, Dore, and Priolo (2008), a two-parameter bilinear cohesive law was used to describe the interfacial behaviour under mode I and mode II, calibrated with experimental results. It was concluded that cohesive elements were suitable to simulate the sequence and location of damage areas under transversal impacts predicting them well in terms of shape, orientation and sizes for a range of impact energies. For instance, in Guinard, Allix, Guedra-Degeorges, and Vinet (2002), a study of damage in CFRP using CDM was conducted, with two damage variables used to represent fibre−matrix debonding and transverse cracks effects. It was mentioned that the use of CDM eliminated critical problems with mesh refinement or necessity to know the crack path to generate a mesh using classical fracture mechanics.

22.3.3 Impact in polymers

Considerable research in the area of impact and dynamic testing of polymers has been conducted in an attempt to model the most severe conditions that such material can withstand. In general, impact in polymers is tested using the Charpy and Izod methods, and it was concluded that, in general, the presence of a notch or stress concentrator and high load rates made those materials predisposed to brittle failure. In Williams (1984), that phenomenon was explained by the increase in the yield stress as a consequence of increases in the constraint and the material rate-dependency. Despite all the work conducted to understand behaviour of polymers in single-impact conditions, little research has been performed in the area of IF to develop theories of failure under such loading conditions. For instance, most research until recently was concentrated on experimental analysis of the phenomenon, and in some cases it was concluded that it was a critical-load scenario that should be taken into account in design because it could affect the material (Du Pont, 1988). Below, a short experimental review in the area of IF in polymers is given.

One of the oldest work on IF in polymers with debatable conclusions was reported in Adams (1987). There, the results obtained in a single impact were compared with those found in IF for a precracked Charpy specimen and using various polymers in a drop-weight machine. It was found that in a single impact of a brittle polymer, failure occurred catastrophically once the maximum load was reached; in contrast, in a ductile polymer, about 60% of the absorbed energy was consumed in propagation. The analysis on IF of those materials demonstrated that for a brittle polymer the force—displacement relation did not change with the growing number of impacts. However, for the ductile polymer, that relation changed as the number of impacts increased, decreasing the maximum force reached at the impact and increasing the displacement as the crack grew due to the effect of fatigue.

Experimental results also showed that crystalline polymers and toughened modified ones generally required higher impact energies to have a failure for the same number of impacts than noncrystalline and nontoughened modified materials. A parameter called retained energy for each impact was used and defined as the difference between the impact energy and the energy returned to the impact block. That parameter was used to analyse the fracture energy during IF and a single impact. It was found that for both cases that parameter had a constant value that was higher in the case of IF for similar materials. The author explained the difference found between those fracture-energy levels by an additional energy dissipation process in IF, suggesting that could be heat generation. Analysing those results with the theory of fatigue, especially with fatigue crack growth, it was found that a constant value for the fracture-energy release rate during entire crack propagation resulted in the extremely unstable crack growth caused fatigue resulting in a nearly vertical portion of the fatigue crack growth graph in IF.

Expectedly, the fatigue life and fatigue-crack-growth analyses were used to study fatigue under impact conditions. In Gomaa, Hamdy, and Moet (1992), studies with PMMA demonstrated that the Paris law could be used to analyse IF in polymers.

For instance, performance of such materials in SF and IF was compared by testing samples in four-point bending in an SHPB system. They found that both IF and SF demonstrated the convectional S-shaped character of the fatigue crack-growth graph; however, it was obvious that the material was more resistant to crack propagation under IF than under SF. In addition, it was observed that those S-shaped graphs depended also on the level of load imposed during IF; as the load decreased, the material was more resistant to crack propagation. That conclusion was also supported by the dependency of K_{Ic} on loading conditions: for impact loads, K_{Ic} was several times the value predicted for SF, decreasing for both cases as the imposed force increased. More work to obtain K_{Ic} for PMMA was conducted in Maekawa and Shibata (1995); K_{Ic} for PMMA also reduced when the impact velocity was increased.

The fatigue-life studies were also used to analyse IF. In Ming-Hsiung et al. (1999), working with polycarbonate/acrylanitrile-butadiene-styrene material and a drop-weight impact tester, it was observed that the impact life increased as the impact energy decreased and the data points seemed to follow an exponential curve. In addition, an energy-accumulation term was used to compare the energy necessary to produce failure in specimens with a single impact. It was found that the higher the impact life, the higher the energy accumulation: 35−45 times higher than for a single impact.

A comparison of the results found under IF and under SF was conducted in Yamamoto, Higashihara, and Kobayashi (2003) for an epoxy resin with and without silica particles. Various ways to analyse the behaviour of those materials were used. Using $S-N$ diagrams, it was observed that specimens tested under SF had a higher fatigue life that those tested in IF. For instance, analysing the fatigue crack growth in those materials, it was found that higher crack growth rates were observed in IF. The results also showed that tendencies of the fatigue behaviour for each composition for specific loading condition could not be used to predict the behaviour for other loading conditions, concluding that different fracture mechanisms existed for each shape and structure of the silica used. Results that corroborated previous work with those materials demonstrated also that the volume fraction of silica affected IF (Ninomi, Uway, Kobayashi, & Okahara, 1991).

22.3.4 Impact in adhesives

In this section, a description of the experimental and modelling works conducted with adhesives is given, defining some mechanism of failure presented in those materials, especially due to impact. Some works in the area of IF for adhesives and adhesive joints are reviewed; however, in general, this area is characterised by a lack of research work.

22.3.4.1 Adhesives under an impact

Research into impact loading of adhesive joints is mostly limited to studies of their response to a single impact showing, except for some cases, that tensile strength

increases as the load rate increases. Some researchers reported similar results for impact and quasistatic conditions, for example, for a single-lap joint tested in a pendulum impact machine in Harris and Adams (1985). In Beevers and Ellis (1984), higher strength was measured in impact loading; it was supposed that the result was due to the strain-rate sensitivity of the adherends. An analysis of the shear response of a joint with thick adherends, subjected to various stress waves generated by impact, showed that their type of fracture was associated with the level of the incident stress wave (Kihara, Isono, Yamabe, & Sugibayashi, 2003).

Investigations in the area of single impacts in adhesive joints using the SHPB test (Yokoyama, 2003; Yokoyama & Shimizu, 1998) demonstrated a considerable increase in the magnitude of tensile strength with the loading rate; that also depended on the type of adherends. In that study, an optimum adhesive thickness was identified when the effect of the type of adherends vanished. Similar results were observed in Crocombe (1995) for a commercial epoxy in a DCB specimen: as the test speed increased, joint strength also increased. However, in Bezemer et al. (1998) it was found that increases in the energy absorption (area under the force−displacement graph) at higher strain rates were observed only for some adhesives.

To analyse the effect of impacts on adhesive joints, researchers studied interaction between the specimen's geometry, loading rate and fracture toughness-crack velocity relationship. It is well known that most of the adhesives are viscoelastic materials and, consequently, are load-rate-sensitive. In Goglio, Peroni, and Rossetto (2007), in tests with a commercial epoxy bicomponent adhesive using SHPB, it was found that as the load rate increased, the compressive and tensile elastic modulus did not demonstrate high variations; however, a large increase in the yield stress was detected for both cases. It was also concluded that the influence of the load rate in tensile conditions was higher than in compression. Researchers also proposed viscoelastic models to model adhesives at high loading rates, using the Voigt model with five elements; a good agreement between experimental and predicted results for SHPB tests of an epoxy adhesive was observed (Sato & Ikegami, 2000). On the other hand, in analysis of dynamic conditions, a stress wave can undergo reflection and amplification increasing its level for a short time, thus increasing stresses, especially in regions with stress concentrators. The response of adhesive joints for specimens with similar overlap length was analysed in Sato and Ikegami (2000), which concluded that the dynamic stress concentrators were higher in single-lap joints than in tapered lap joints and scarf joints. It was suggested that the most effective geometry to reduce the stress concentration for the geometries analysed in dynamic and static conditions was the scarf joint.

A third factor that also affects the dynamic crack growth is the relationship between toughness and crack velocity. According to the theory of fracture mechanics, cracks can grow under quasistatic conditions when there exists an energy balance between the applied energy and the energy dissipated in crack growth and plastic deformations of the adherends. It was mentioned in Sun, Thouless, Waas, Schroeder, and Zavattieri (2008) that in rate-dependent materials a quasistatic crack growth could also exist, and there should be an equilibrium between the driving force for crack propagation and energy dissipated. When the energy available for

the crack growth exceeds the energy necessary to generate a new surface and deform plastically the adherends, the system becomes unstable, and the crack propagates dynamically. However, the way that the crack would propagate depends on the relation between fracture toughness and the load rate. It is summarised in Bandyopadhyay (1990) and Maugis (1985) that for toughened modified epoxy adhesives under quasistatic conditions, G_c usually decreases with increase in the load rate, having a slip-stick behaviour at lower load rates and a continuous crack propagation at higher rates.

Researchers suggested two general types of crack propagation: continuous (stable) and intermittent stick-slip type (unstable) (Kinloch & Williams, 1980) and differentiated each mainly by the fracture surface and the force−displacement graph when specimens were tested in displacement control under quasistatic conditions. It is defined that for stick-slip crack propagation, there exists a noncontinuous force growth tendency that is described as a succession of periods of rapid growth and arrests. In contrast, under stable crack-growth conditions, the force has a more continuous behaviour in the force−displacement graph (Ashcroft, Hughes, et al., 2001).

The stick-slip response of the epoxy adhesive is attributed mainly to the combination of two mechanisms: crack blunting and viscoelastic adhesive behaviour. The blunting mechanism (Kinloch & Williams, 1980) describes that in cases when a blunt crack is formed, it generates a lower stress concentrator than a sharp tip; consequently, a higher applied stress is required to reach a critical stress intensity factor for the material at a specific distance. For instance, the yield behaviour in the vicinity of the crack tip controls the plastic deformation that occurs locally, and as the yield stress decreases due to the application of lower load rates, the crack blunting mechanism becomes more severe. Finally, dynamics of stick-slip mechanism is explained as follows: after a crack arrest, a plastic zone is formed near the crack tip that is highly blunted so that crack can grow again until the highest value of G known as strain-energy release rate initiation G_i is reached; after that, a crack is observed propagating fast through the virgin material, and it is arrested at the value of G_{arr}.

22.3.4.2 Adhesives under impact fatigue

In contrast to considerable research into the single-impact loading of adhesive joints, IF has so far received little attention. In many cases, the analysis of repetitive impacting was limited to relatively short series of impacts. A representative study in the area of IF has been dedicated to analysis of modified adhesively bonded impact blocks bonded with an epoxy adhesive and tested using a drop-weight method; various contact times were applied in the tests (Usui & Sakata, 1984). It was demonstrated that the joint's IF strength depended on the stress magnitude and the loading time applied. For instance, the longer the contact time, the shorter the maximum force necessary to generate failure under a constant number of impacts and the larger the absorbed energy per impact (the difference between the impactor kinetic energy before and after an impact). Some researchers (Bandyopadhyay, 1990) tried to analyse IF

in an adhesive using a Charpy specimen made of a toughened epoxy adhesive. It was reported that no evidence for a threshold value of the applied energy was found; in addition, the fatigue crack growth was found to be a suitable technique to analyse the damage accumulation process in IF.

A comparison of responses of single-lap joints in IF and SF was conducted in Imanaka, Kishimoto, Okita, Nakayama, and Shirato (1985) using fatigue life diagrams. It was observed that IF presented a more rapid decrease in the number of cycles to failure than SF. Additionally, the IF behaviour depended on the overlap length identifying that the increasing overlap length resulted in the increased number of cycles to failure at the same load.

22.3.4.3 Modelling impacts in adhesives

An initial description of modelling of adhesive joints was presented in Section 22.3.1. Most of the publications on impact in adhesive joints deal with crack propagation or stress propagation under a single impact. In Sun et al. (2008), it was found that cohesive zone elements (CZEs) could be suitable to reproduce a crack in an adhesively bonded wedge specimen with a load rate-dependent adhesive. The obtained experimental results demonstrated that cracks could have both stable and unstable behaviours; hence, two types of CZEs were defined to reproduce them. The first type of CZEs had a trapezoidal traction-separation law that was used to model a quasistatic crack growth; these elements were defined mainly by two essential fracture parameters, namely toughness and cohesive strength (obtained experimentally). The shape of the law was necessary to reproduce properly the elastic−plastic deformation of the adhesive. The second type of CZEs had a triangular-shaped traction-separation law that was used to reproduce brittle behaviour observed experimentally. The latter elements were defined with the similar cohesive strength and slopes (initial and final) as the trapezoidal CZEs, but avoiding the plateau region. The experimental study concluded that a crack changed from the stable to unstable behaviour by a stochastic mechanism, and such changes could be more frequent at higher load rates. Obviously, a nonphysical mechanism was used to include these elements into the models. Implementation of both types of CZEs was only carried out to reproduce the distribution of different crack behaviours observed experimentally. The FEM results allowed a conclusion that the proposed CZEs were rate-independent and the fracture toughness of the brittle mode was about four times lower than that for a quasistatic crack growth. In addition, it was established that most of the energy available in the system was consumed by the friction between the wedge and the adhesive.

Another way to analyse impact in adhesive joints was based on the study of the effect of a transversal impact on an SLJ using CFRP as an adherend (Vaidya, Gautam, Hosur, & Dutta, 2006). The adhesive was modelled as an elastic−plastic material with kinematic hardening exposed to a transversal impact over the adhesive region as seen in Figure 22.8. It was found with the use of a dynamic FEM that such conditions produced a mixed-mode load but as the crack propagated through the adhesive, mode II became the main loading mode.

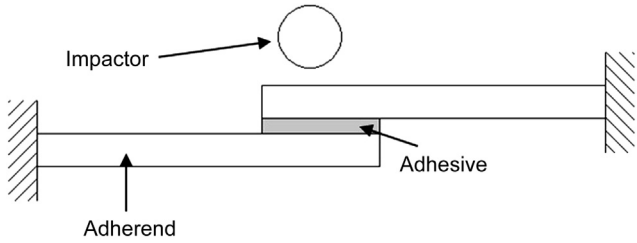

Figure 22.8 Schematic of impact of SLJ in Ekh (2006). Vaidya et al. (2006).

22.3.4.4 Phenomenological models of impact fatigue

Researchers, working mainly with steels, proposed various models to study the IF behaviour. A review of these models is presented below.

Fatigue life

In Johnson and Storey (2007), a phenomenological model was proposed to analyse the IF behaviour in special under plain carbon steel. (The results obtained in that study are not relevant for this research; however, it is important to emphasise the methodology used for analysis of results). The model is based on the fact that the effect of IF conditions on a material can be presented in an $E{-}N_{\mathrm{F}}$ graph. Two types of models were proposed—one for high-cycle IF and another for low-cycle IF. In the case of high-cycle fatigue, it was shown that the phenomenon could be described by the equation

$$E_i = E_0 + E_k N_{\mathrm{F}}^{-p} \tag{22.23}$$

in which E_0 is the fatigue limit proposed as a material constant, E_k and p are the IF parameter and IF exponent; for steels, p has a value of 0.6. In the case of low-cycle fatigue E_i and E_0 are related by the equation

$$E_i = E_0 + mN_{\mathrm{F}}^{-q} \tag{22.24}$$

in which E_0, m and q are material parameters that can differ for various steels. An empirical relation between q and m was proposed:

$$q = \log_e m + D \tag{22.25}$$

in which D is a constant. Finally, it was suggested that a material under IF can be modelled with the following relation:

$$E_i = E_0 + \exp\left(\frac{q-D}{C}\right) N_{\mathrm{F}}^{-q} \tag{22.26}$$

Accumulated load-time model

Researchers identified that under cyclic impacts, the IF strength depended on the impact stress and the loading time and proposed empirical relations to characterise IF. The most popular approach is to relate the cumulative time $N_F T$ to the maximum stress amplitude in the impact σ_{max} (Ninomi et al., 1991; Tanaka, Kinoshita, & Nakayama, 1992; Yamamoto et al., 2003; Yu, Peter, & Huang, 1999):

$$\sigma_{max}(N_F T)^m = C \tag{22.27}$$

in which N_F is the number of cycles to failure, T is the loading time, and C and m are empirical IF parameters. In this work, the relation described by Eqn (22.26) will be referred to as the accumulated load-time model.

22.4 Fatigue crack growth in lap strap joint specimens

In Ashcroft, Casas-Rodriguez, and Silberschmidt (2008) and Casas-Rodriguez, Ashcroft, and Silberschmidt (2008), working with LSJs, the fatigue crack growth in adhesively bonded joints was analysed. The LSJs were manufactured by adhesively bonding cured T800/5245C (CFRP) panels, which is known as secondary bonding and is distinguished from co-bonding, in which the adhesive and CFRP are cured together. The advantage of secondary bonding is that different (optimum) curing cycles can be used for the adhesive and CFRP and that distortion of the CFRP in the joint area during curing can be avoided. The assembled joints of EA 9628 adhesive and CFRP panels were cured in an autoclave at 600 kPa for 60 min at 120 °C.

22.4.1 Standard fatigue

A comparison of the FCG measurements of two specimens (SF1 and SF2) tested under SF is presented in Figure 22.9; the length of the crack in all the tests was measured on both edges of the studied specimen. It is seen that in the initial period both specimens have similar FCG behaviour. However, this similarity is interrupted when SF2 experiences crack growth acceleration at a crack length of approximately 20 mm. The comparison of crack growth rates for the two samples shown in Figure 22.10 corroborates this observation. It is found that the crack propagation rate in the initial stages is around 3×10^{-4} mm/cycle for both specimens, with a slight decelerating trend. The crack growth continues to decelerate throughout the fatigue life in SF1, when there is an abrupt change in FCGR in SF2 at 20 mm.

A study of the fracture surfaces of LSJ specimens loaded in SF indicated their two different types. The first type (SF1) exhibited cohesive failure in the adhesive layer, subsequently termed simply cohesive failures, over the entire fracture surface. Figure 22.11 shows a typical fracture surface, exhibiting ductile tearing,

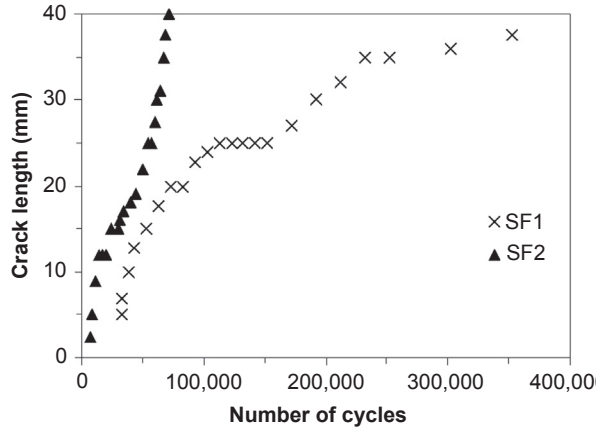

Figure 22.9 Crack growth in LSJ specimens in SF.
Silberschmidt, Casas-Rodriguez and Ashcroft (2008).

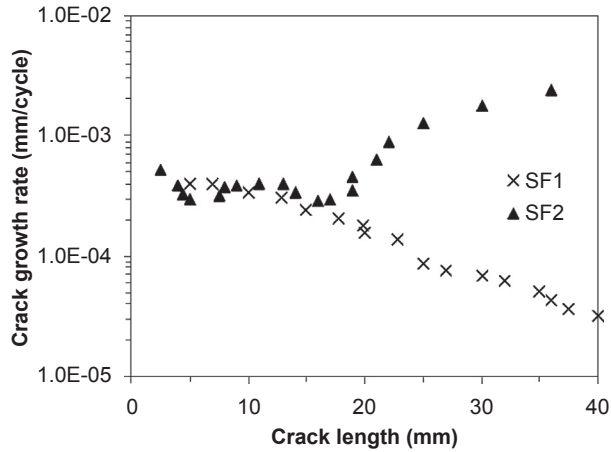

Figure 22.10 Crack growth rate in LSJ specimens in SF.
Silberschmidt et al. (2008).

voids and cavitation of rubber particles (Isik, Yilmazer, & Bayram, 2003; Kinloch, 1997). The 'wavy' fracture surface indicates a mixed-mode fracture process.

The second type of fracture, as seen in specimen SF2, was more complex. Two different regions were found here, as shown in Figure 22.12. The first region (region I in Figure 22.12) corresponds to cohesive failure in the adhesive layer. The second region (region II) is a transition region, in which a mixture of failure in the adhesive and in the 0° plies of the CFRP, adjacent to the adhesive, can be seen. In Figure 22.12, it is apparent that region I is similar to SF1 type failure. In region II, failure in the CFRP is located predominantly in the 0° ply adjacent

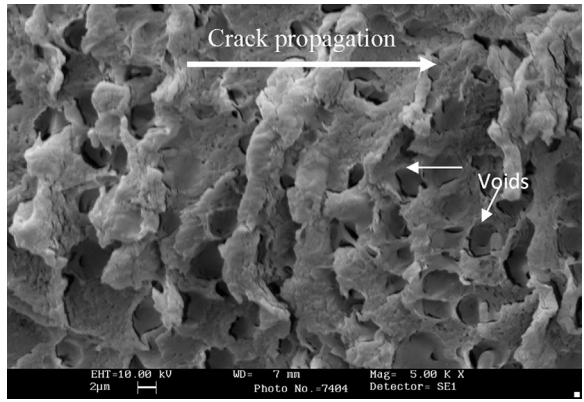

Figure 22.11 Detail of cohesive failure in SF1 LSJ specimen tested in SF. Casas-Rodriguez et al. (2008).

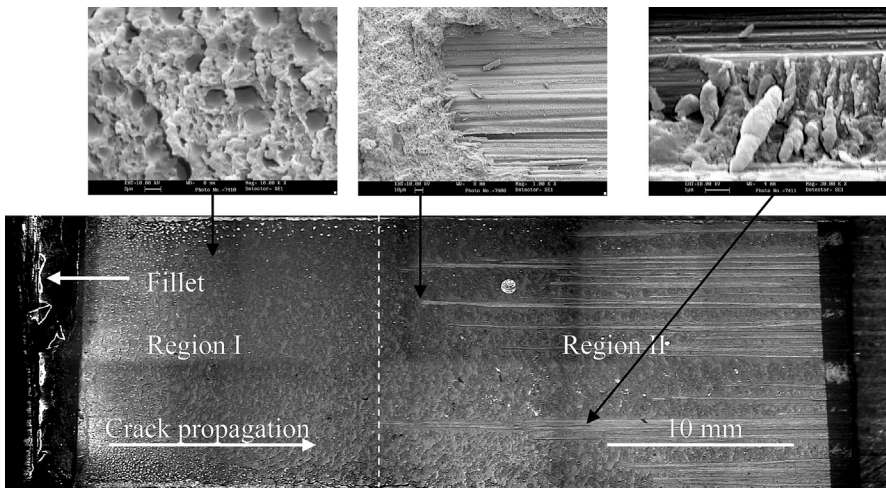

Figure 22.12 Type SF2 crack propagation in LSJ in standard fatigue. Silberschmidt et al. (2008).

to the adhesive. It can be seen that fracture is a mix of failure in the matrix and fibre debonding. Rollers and plastically deformed shear cusps are present in the areas of matrix failure. Incipient shear cusps are generally related with fracture in static conditions. However, in fatigue, these are more prominent showing a high plastic deformation. In addition, it is observed that when mode-II loading is present in fatigue, these cusps are transformed to matrix rollers due to the effect of the continuous fretting of the surface. Some fibre breakage is also seen in the fracture surface; however, the main crack front does not break through the fibres and, hence, remains in the plane parallel to the ply adjacent to the adhesive.

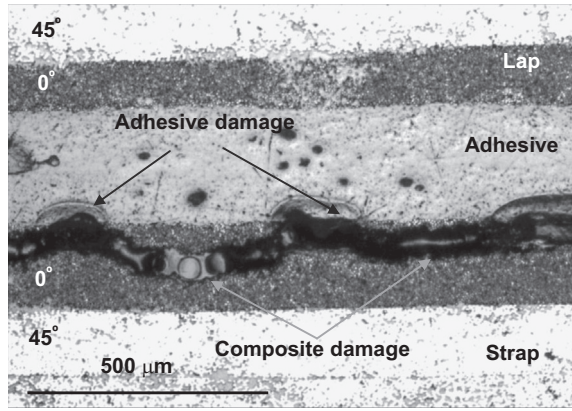

Figure 22.13 Transverse cross-section through region II of fracture surface in LSJ.

A polished transverse cross section through region II of the SF2 fracture surface is presented in Figure 22.13. It is seen that the crack propagates in some regions in the adhesive and in others in the composite.

22.4.2 Impact fatigue

The FCG of LSJ specimens in IF was obtained using optical measurements and is plotted in terms of the number of cycles in Figure 22.14. In this figure, the results can be divided into two main groups. A rapid FCG was found in two specimens (IF6 and IF7), and the other five specimens demonstrate a mixed FCG behaviour. Crack initiation varied, but in most specimens it was observed to occur at around 2×10^2 cycles.

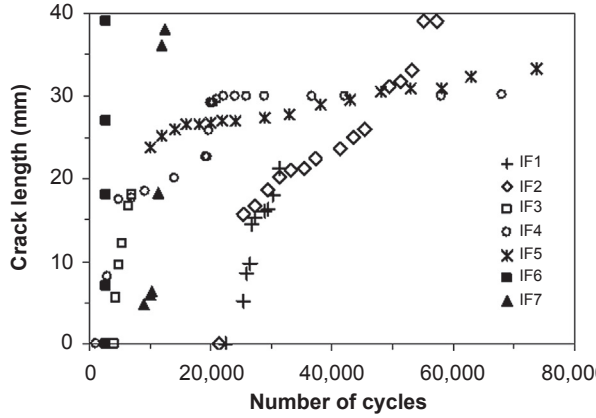

Figure 22.14 Crack growth in LSJ specimens in IF.
Casas-Rodriguez et al. (2008).

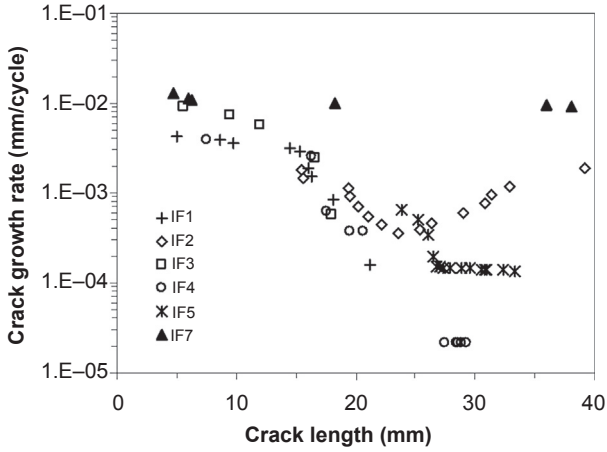

Figure 22.15 Crack growth rate in LSJ specimens in IF. Casas-Rodriguez et al. (2008).

Plots of FCGR as a function of crack length in IF are seen in Figure 22.15. A general trend in these specimens is an initial crack speed of approximately 10^{-2} mm/cycle, similar to that seen on the specimens with fast FCG (IF6 and IF7). A reliable crack growth rate for IF6 could not be obtained because of the low number of impacts to produce complete failure; however, a crack growth rate of approximately 10^{-2} mm/cycle was calculated over the entire fatigue life of IF7, as shown in Figure 22.15. Once a crack length of around 10 mm was reached, a decrease in the crack growth rate started. The decreasing trend changed when the crack reached a length of approximately 27 mm, when a constant-rate plateau was observed for some samples. Some variation of this FCGR behaviour was observed, especially with IF2, when acceleration in the FCGR is noticeable when the crack reached a length of approximately 27 mm. Analysis of the fracture surface in the next section gives the reason for this acceleration behaviour.

A macroscopic examination of specimens tested under IF conditions shows patterns of failure similar to those observed for LSJ specimens in SF, as seen in Figure 22.16. The first region, denoted A in Figure 22.16, was predominantly cohesive failure of the adhesive. This was followed by a transition region (region B), with a mixture of failure in the adhesive and CFRP. In region C, crack growth was predominantly in the 0° composite ply adjacent to the adhesive. However, a deviation from the general behaviour was found in specimen IF2, with the failure in region C combined with delamination between 0° and 45° plies at the specimen edges and failure in the 0° layer adjacent to the adhesive in the middle of the sample. This explains the acceleration in FCG in region C of IF2, as seen in Figure 22.15.

Additional analysis of the fracture surfaces was carried out using SEM. Figure 22.17 shows a micrograph of region A for the specimen with fast FCG. The fracture surface is characterised by a lack of cavitating rubber particles. In a previous study

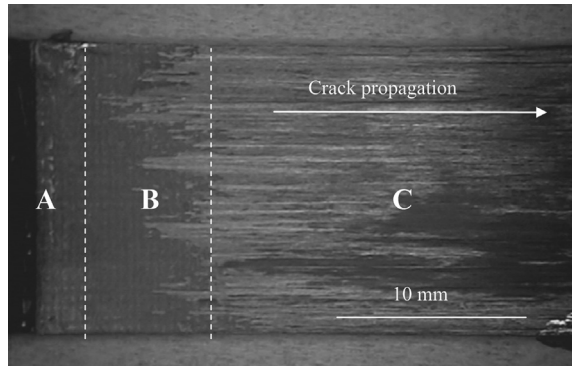

Figure 22.16 Failure surface of LSJ tested in impact fatigue.
Casas-Rodriguez et al. (2008).

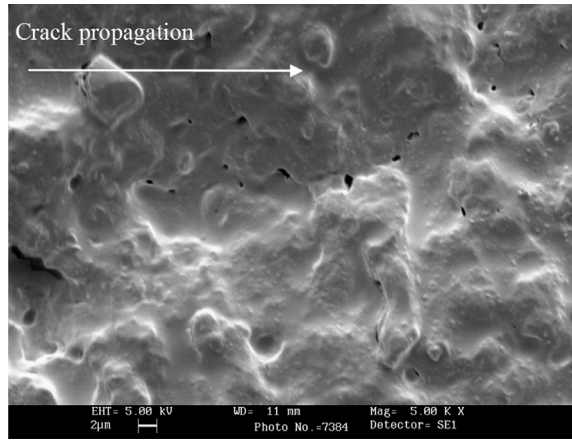

Figure 22.17 Fracture in region A in specimen with fast crack growth tested in impact-fatigue conditions IF7.
Casas-Rodriguez et al. (2008).

(Takeshi, 1999), it was found that rubber particles could remain intact in the fast-FCG region, resulting in an indistinct difference between the epoxy matrix and the rubber in micrographs. It was shown in Li et al. (1994) that under certain load conditions the cavitation process could be suppressed. No differences were found in the fracture toughness of rubber-modified and nonmodified epoxies when this was the case. This behaviour was explained as a consequence of the decrease in the shear-banding effect due to insufficient levels of plastic deformation caused by the rubber particles. In this work, it is seen that the cavitation process in the rubber-modified epoxy adhesive can be suppressed when specimens are tested under IF.

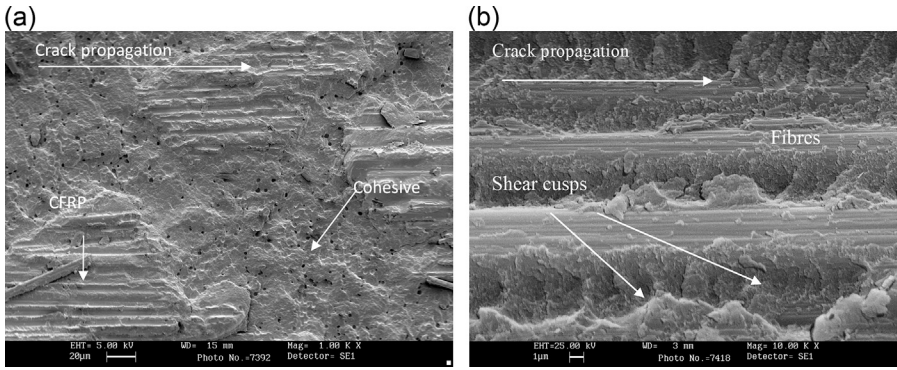

Figure 22.18 Failure in IF specimen IF7 with fast FCG behaviour: (a) details of failure in region B of the lap; (b) details of failure in region C.
Casas-Rodriguez et al. (2008).

Analysis of region B in IF7 shows that this area exhibits a non-uniform fracture behaviour, as illustrated in Figure 22.18(a). This is characterised by the presence of 'islands', that is, changes in the fracture path, when a crack propagation mechanism suddenly changes from cohesive failure to damage in the composite and later returns to cohesive failure of the adhesive. This behaviour can be explained by the nucleation of microcracks in front of the main crack front, generating a local pattern of failure that in time merges with the main crack. Previous studies (Ashcroft, 2004), based on X-ray radiography for similar type of specimens, showed small regions of secondary debonding ahead of the main crack that can cause this behaviour. In region C, damage occurs predominantly in the composite-matrix layer adjacent to the adhesive, as shown in Figure 22.18(b). Fracture in the matrix demonstrates a brittle character, with none of the rollers found in SF.

A decelerating FCGR in IF was seen in two specimens (IF4 and IF5 in) when the crack reached a length between 15 and 25 mm. This behaviour can be explained by a change of the FCG mechanisms. Figure 22.19(a) shows a fracture surface in region A of IF5, and although some voiding is present, there are no signs of rubber cavitation. The fracture surface in region B is presented in Figure 22.19(b), where signs of multiple damage initiation and termination sites can be seen. In some areas, there are imprints of fibres on the fracture surface indicating that damage is close to, or in, the composite, but then returns to the adhesive layer. Micrographs from region C of the IF fracture surface are given in Figure 22.19(c) and (d). Obviously, the fracture of fibres is a common mechanism; this is explained by the level of bending produced during IF in the free end of the specimen, increasing considerably tensile stress until fibre failure. Fracture in the composite matrix can be observed more clearly in Figure 22.19(c). In contrast to the fast FCG in IF, shear cusps can be seen randomly distributed over the matrix. However, the matrix demonstrates a general brittle behaviour, as seen in Figure 22.19(d).

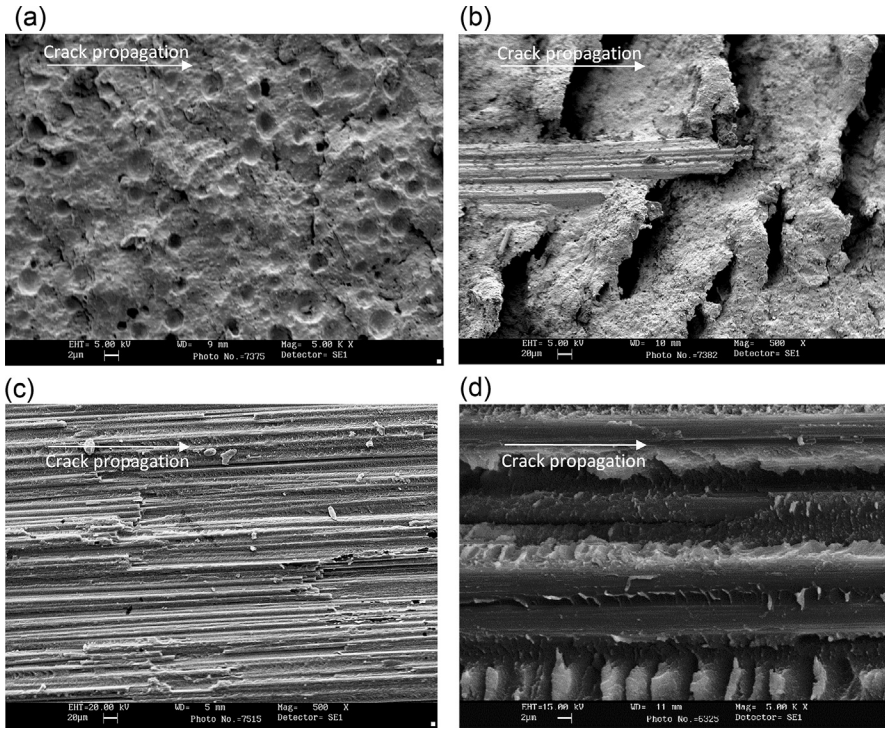

Figure 22.19 SEM of fracture surfaces in sample IF5 tested in IF with a slow FCG behaviour. (a) Region A, (b) region B of the lap, (c) and (d) region C.
Casas-Rodriguez et al. (2008).

Additional analysis of fracture in the vicinity of the crack front was performed by cutting and polishing fractured specimens. It was found that cracks in region C can combine matrix composite failure in the 0° ply of the strap with delamination between the 0° and 45° plies (see Figure 22.20).

22.4.3 Combined impact and standard fatigue

A study of combined impact and standard fatigue (CISF) was implemented by means of testing two specimens under combination of IF and SF regimes. The load spectrum consisted of IF blocks with 100 tensile impacts, followed by SF blocks of 5000 sinusoidal cycles. The IF tests had an initial energy of 1.07 J. The SF cycles had a maximum load of 7.8 kN, load ratio of 0.1 and frequency of 5 Hz.

The FCG of both specimens tested during CISF is presented in Figure 22.21. Two main trends of FCG were observed: fast crack growth in specimen CISF 1 and slower crack growth in specimen CISF 2. Apparently, in both cases, a stable crack growth behaviour prevailed until the crack reached a length of 10 mm; after

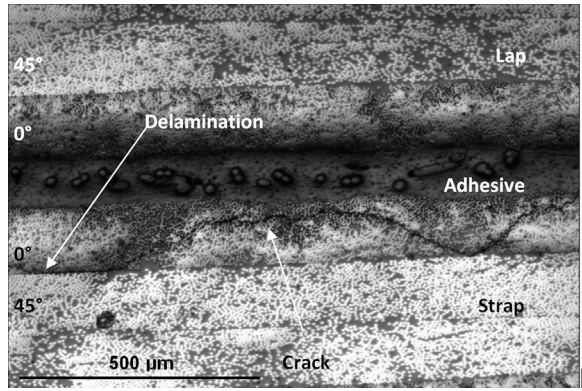

Figure 22.20 Damage across the strap width near to the crack tip under IF.

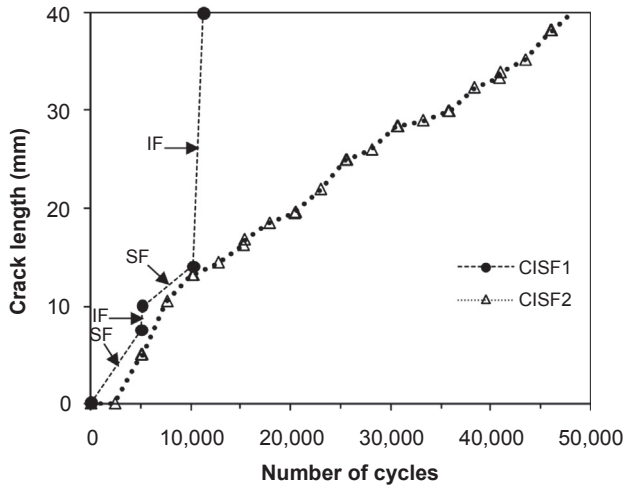

Figure 22.21 Crack growth in combined impact and standard fatigue.

that the FCG in CISF 1 becomes unstable. A reliable crack growth rate for CISF 1 after 10 mm could not be obtained because of this unstable behaviour; however, the FCGR in the early stages of this specimen is similar to that found in CISF 2. The FCGR in the CISF tests is presented in Figure 22.22. It was found that the FCGR tended to decrease until a crack size of around 15 mm was reached. Then, a transition occurred to a practically constant average value of crack growth rate of approximately 8×10^{-3} mm/cycle until eventual failure.

Macroscopic analysis of the fracture surfaces revealed two main mechanisms of failure. In the case of fast-FCG failure, an intermittent adhesive-CFRP mechanism was seen (specimen CISF1). The specimen with the slow FCG (CISF 2) exhibited cohesive failure. Results of SEM performed for the fast-FCG specimen tested in CISF conditions are presented in Figure 22.23. The analysis of region A, as seen in

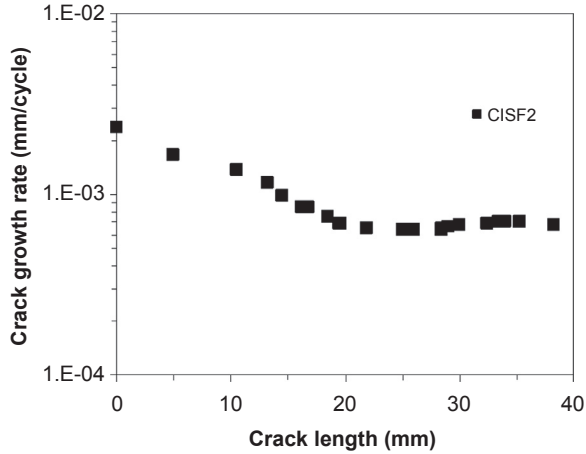

Figure 22.22 Crack growth rate in combined impact and standard fatigue.

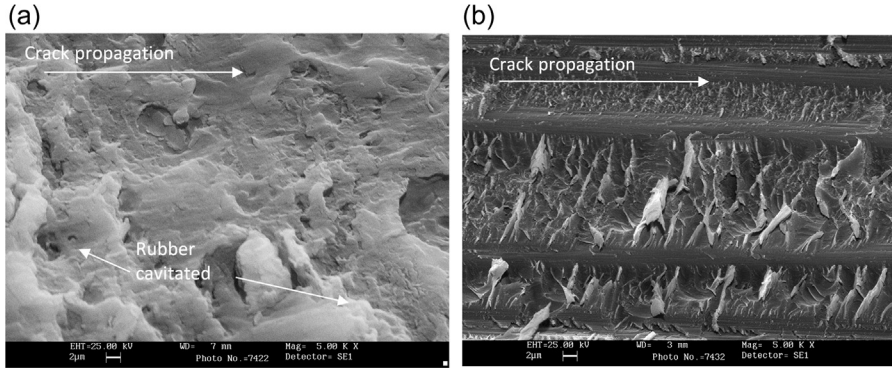

Figure 22.23 SEM of fracture surfaces in samples with fast FCG behaviour tested in CISF: (a) region A, (b) region C.
Casas-Rodriguez et al. (2008).

Figure 22.23(a), shows some number of cavitating rubber particles, demonstrating that the toughening effect is active before the onset of the unstable crack growth in some regions. In addition, a significant number of broken fibres are observed that are more common near the boundary between regions B and C. Matrix damage in the ply adjacent to the adhesive is shown in Figure 22.23(b). This is characterised by the presence of small and poorly developed shear cusps.

SEM analysis of the cohesive fractured surfaces revealed that IF affects the uniformity of the fracture (Figure 22.24(b)). Changes in the failure mechanism are localised in specific areas and characterised by the presence of small valleys where smooth fractured surfaces of the adhesive are present. Additional studies showed that the toughening mechanism due to cavitation was active during the SF block of the test, but resulted in irregular hole sizes. A comparison of the

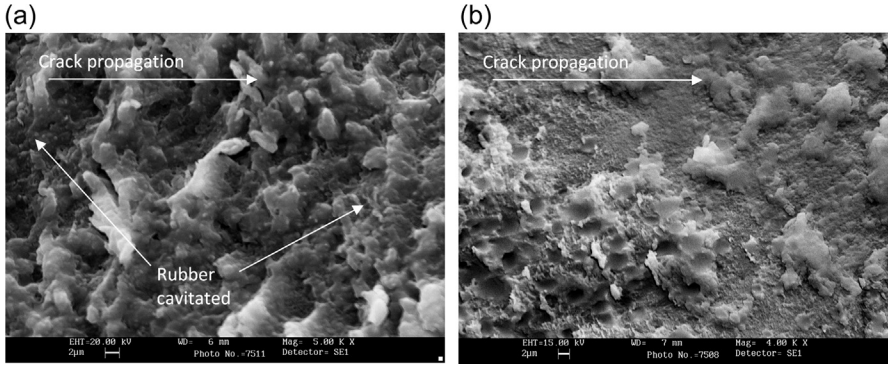

Figure 22.24 SEM of fracture surfaces in specimens with cohesive failure tested in CISF: (a) SF region, (b) IF region.

hole size for IF and SF load blocks (Figure 22.24(a) and (b)) shows that as failure changes from IF to SF, there is a gradual increase in cavitation of rubber particles, until at some point holes reach the maximum size producing the strongest toughening effect. In general, the fracture mechanism exhibits a fracture pattern close to that in specimens tested in SF. This mechanism of failure can be explained by the fact that the crack growth depends on the loading history, being affected by the damage zone ahead of the crack front, where micro-damage can be initiated.

Analysis of the FCG and fracture surfaces revealed the presence of two main mechanisms of failure: the fast FCG associated with an intermittent adhesive−CFRP failure mechanism and the slow FCG with predominantly cohesive failure.

A comparison on the FCGR for LSJ under SF and CISF that presented similar patterns of failure (only cohesive) is conducted in Figure 22.25. In this case, the

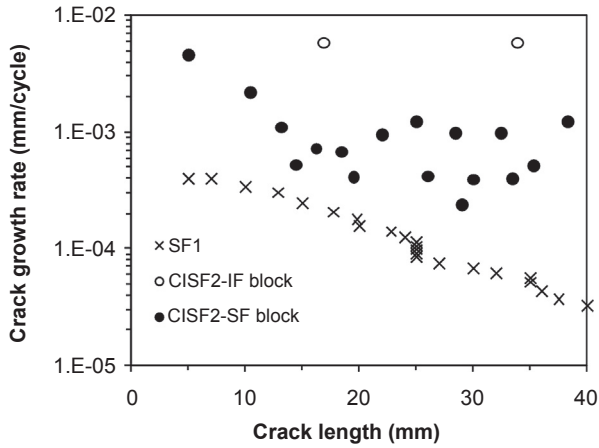

Figure 22.25 Comparison of crack growth rate in CISF and SF. Casas-Rodriguez et al. (2008).

modified method was used to obtain the FCGR. In the case of CISF 2, the FCGR was obtained as the local FCGR and defined based on the crack length measurements at two consecutive opportunities. The advantage of this method in comparison with the one used before that used a function to approximate the crack growth, is that local changes produced only by IF in the CISF load pattern can be observed.

As follows from Figure 22.22, in general, the FCGR under CISF is always higher than that in SF. It was found that the FCGR under CISF was approximately one order of magnitude higher than that measured under SF. In addition, it is obvious that in the cases in which the FCGR was possible to measure only for the IF load block, those values were extremely higher. In general, as experiments demonstrated, the inclusion of a small number of impacts into an SF load regime affects considerably the normal FCGR.

22.5 Modelling fatigue crack growth in bonded carbon fibre-reinforced polymeric lap strap joints

22.5.1 Fracture-mechanics analysis of lap strap joints

In Ashcroft et al. (2008), a method to calculate fracture parameters for LSJ specimens was presented using finite-element models. The strain-energy release rate was determined from a geometric nonlinear models using the virtual-crack-closure technique (Sethuraman & Maiti, 1988); it was termed G_{gnl}. The effect of crack location on G_{gnl} was investigated. Three crack-growth scenarios (cohesive, interface and strap) were studied; the obtained results are presented in Figure 22.26. It can

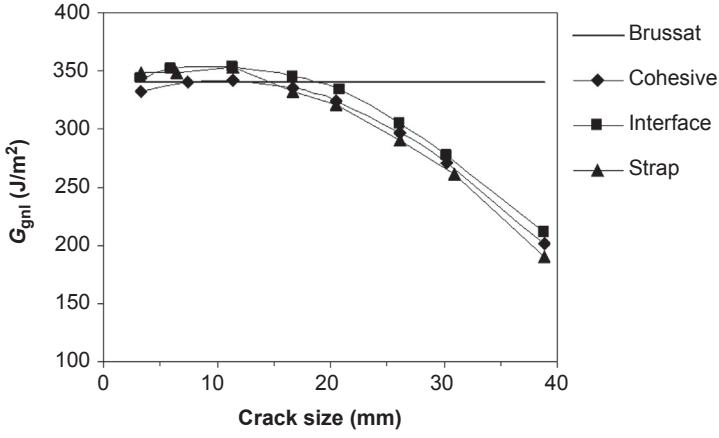

Figure 22.26 Comparison of G_{gnl} for different fracture paths. Ashcroft et al. (2008).

be seen that the crack location seems to have only a minor effect on the value of G_{gnl}. However, Figure 22.27 shows that the same cannot be said for mode-mixity, although it should be noted that the determination of the individual components of G may be more susceptible to the influence of singularities at the bimaterial interface than for G_T. The Brussat's model (Takeshi, 1999) is also presented as a reference (it is an analytical model for this kind of joint geometry).

Under dynamic loading conditions, the reaction force and the strain at a specific point are highly time dependent. Hence, G is also a time-dependent parameter. To analyse the dynamic strain-energy release rate G_{dyn} at low-velocity impacts, two methods were used: (1) a geometric nonlinear model with elastic material properties (G_{dyn}) and (2) a geometric nonlinear model with elastic−plastic material properties (J_{dyn}).

The first analysis conducted studied the variation of G_{dyn} during a single impact in a precracked specimen. A FEM model with a cohesive crack size of 11 mm was used; the calculated variation in G_{dyn} with time is presented in Figure 22.28. It can be seen that there is an increasing tendency interrupted for a short period before reaching a maximum and starting to decrease. A similar pattern was seen in all the models with cohesive failure; however, in some cases a more pronounced interrupted period was found. Investigating the reason for interruption in the increasing tendency of G_{dyn}, it was observed that this is the result of a change in the contact point between the hammer and the impact block. At some time, the contact point changed providing an opportunity for an increased crack opening and, consequently, increased G_{dyn}.

The second study was performed to analyse the effect of crack location on G_{dyn}. In this case, it was assumed that crack propagation can be related to the maximum dynamic strain-energy release rate G_{dyn}^{max} reached during an impact. Similar to the study in SF, three cases of crack propagation were analysed (cohesive, interfacial or a

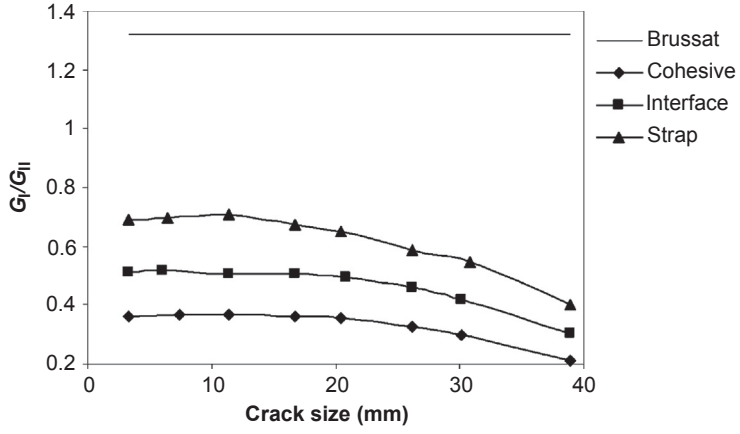

Figure 22.27 Comparison of G_{gnl} mode ratio (G_I/G_{II}) for different fracture paths in LSJ. Ashcroft et al. (2008).

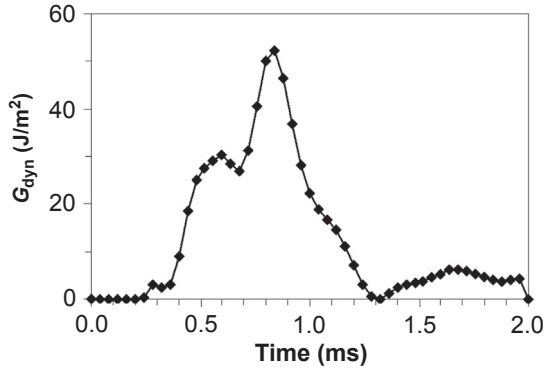

Figure 22.28 Changes in dynamic strain-energy release rate for cohesive-crack size of 11 mm in LSJ.

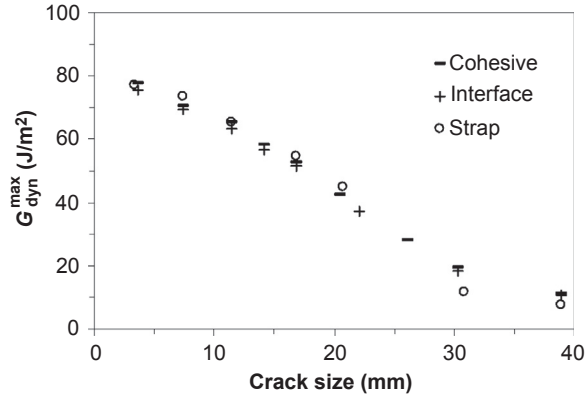

Figure 22.29 Comparison of G_{gnl} for different fracture paths in LSJ.

composite strap), and the results are presented in Figure 22.29. Apparently, in all three cases G^{max}_{dyn} has similar values and a decreasing tendency as the crack increases.

The third analysis was focused on comparison of the maximum dynamic strain-energy release rate when the crack is modelled as a cohesive crack and the adhesive material as either an elastic (G^{max}_{dyn}) or elastic−plastic material (J^{max}_{dyn}). Figure 22.30 shows this comparison, and it is noticeable that in this case there is no difference in the fracture-mechanics parameters for two material formulations for the adhesive. This is explained by a low stress level at the crack tip, with the material below the yield stress.

22.5.1.1 Fatigue crack-growth-rate curve in SF

Experimental data for crack growth rate and numerical simulations of G with respect to crack size were presented in previous sections. Those results are used

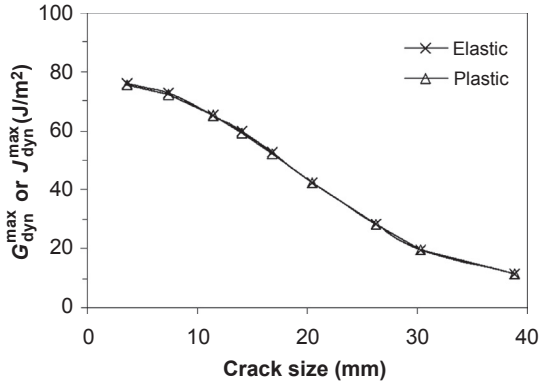

Figure 22.30 Comparison of G_{dyn} and J_{dyn} with linear-elastic or elastic−plastic adhesive material in LSJ.

to determine the fatigue crack growth as function of G in LSJ specimens. In addition, two main mechanism of failure observed for LSJs in SF were described. The first is cohesive failure in the adhesive, which shows a steadily decreasing crack growth rate as crack length increases. The second is a mixed-failure path, with a cohesive failure at a first stage; however, once the crack starts to propagate predominantly in the composite there is a sharp increase in the crack growth rate, although this levels as the crack length increases further.

Figure 22.31 shows the FCGR curve for the LSJ specimens tested under SF. The sample with the cohesive failure shows the classic three-zone fatigue crack growth

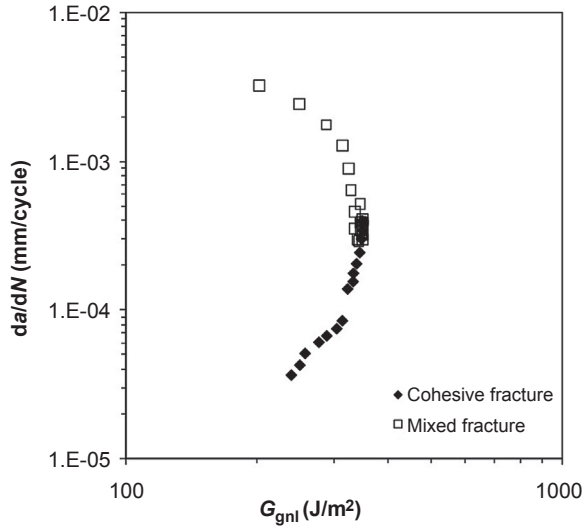

Figure 22.31 Fatigue crack growth during standard fatigue.
Ashcroft et al. (2008).

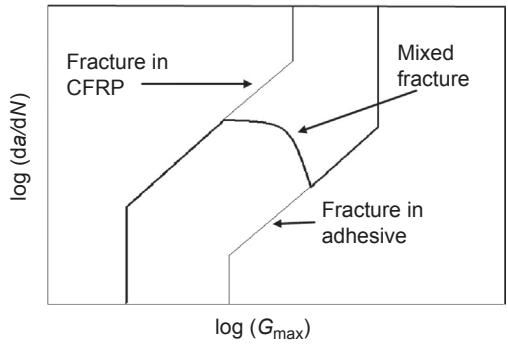

Figure 22.32 Mixed-mode fracture model.
Ashcroft et al. (2008).

behaviour, with a threshold region at approximately 140 J/m^2 and a fast-growth region at approximately 350 J/m^2. Between these two regions there is an area in which log (da/dn) is proportional to log G_{gnl}, as proposed by the Paris law. The fatigue-crack-growth plot for the mixed-mode failure is coincident with the cohesive failure plot at high levels of G_{gnl}, in which failure for both samples is cohesive. However, as G_{gnl} decreases with the crack length, there is an increase in the rate of crack growth. For a homogeneous type of fracture, this would seem a nonsensible result; however, it is perfectly explainable in the mixed-failure case. It was shown that, for this system, the fatigue resistance of the CFRP matrix was less than that for the adhesive at room temperature (Ashcroft & Shaw, 2002), thus the crack growth rate in the CFRP would be expected to be higher than that for the adhesive for a given value of G_{gnl}. This would result in different fatigue−crack-growth plots for failure in the adhesive and CFRP, as shown schematically in Figure 22.32. It is easy to see from this figure how an increasing crack growth rate with decreasing G is obtained as the fracture path moves from the adhesive to the CFRP.

22.5.1.2 Fatigue-crack-growth-rate curve in IF

Similar to SF, the experimental data and numerical models were used to generate plots of the crack growth rate in terms of G during IF. In this case, G_{dyn}^{max} results were used in the analysis. It was not possible to measure the fracture in the adhesive because of the extremely fast crack propagation rate. However, the crack propagation rate associated with matrix cracking could be measured.

Figure 22.33 shows the FCGR curve for an IF specimen with a slow FCG in LSJ exhibiting matrix cracking as the main fracture mode. A linear relationship suggests that Paris' type law can be used to characterise FCG under IF. Values of G_c and G_{th} for the matrix-cracking failure are approximately 75 J/m^2 and 26 J/m^2, respectively, with $m = 3.58$.

In some specimens, a delamination zone between the adhesive 0° ply and the 45° ply over the strap was observed. This change in failure mode can also be seen in the

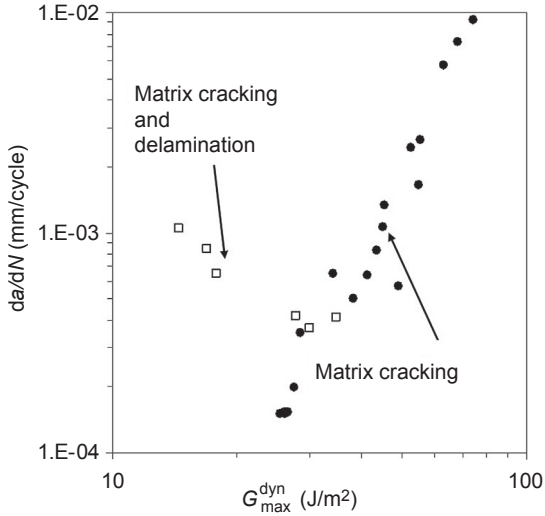

Figure 22.33 Fatigue crack growth during impact fatigue.

FCG graph (Figure 22.33). From analysis of the FCG in IF, it is obvious that the delamination process works as an accelerator for crack growth, and a change from one failure mechanism to another, similar to that found in SF, is noticeable.

22.5.2 Mixed-mechanism fracture model

Analysing the results obtained with the SF specimens, it is observed that there is a difference in the fatigue crack behaviour in the case when the crack growth is in the adhesive and the case when the failure is a combination of fracture in the adhesive and adherend. It was described previously that the mixed-mode failure began as a cohesive fracture and then progressively changed to a combination of cohesive and matrix failure in the ply adjacent to the adhesive. This means that two completely different mechanisms are present simultaneously, with competing crack growth behaviours. Combining these two behaviours, it is supposed that, in general, the FCG for a specimen with a mixed-mode fracture needs to have a first region following the same FCG pattern as that in a fully cohesive failure followed by a progressive change to a matrix-failure-based FCG behaviour. In this work, it is assumed that the net FCGR in mixed-mode failure is a fraction of the rates for cohesive and matrix failure in the specimen.

Image analysis was carried out on the fracture surfaces with the aim of distinguishing between cohesive and matrix damage. It is possible to observe the regions of each failure mode, where white represents matrix cracking and black adhesive failure. To determine the fraction of each mechanism at a specific crack size, small areas (region with grey colour in Figure 22.34) were analysed with a subroutine in Matlab. This allowed assessment of fraction of each mechanism. It is supposed

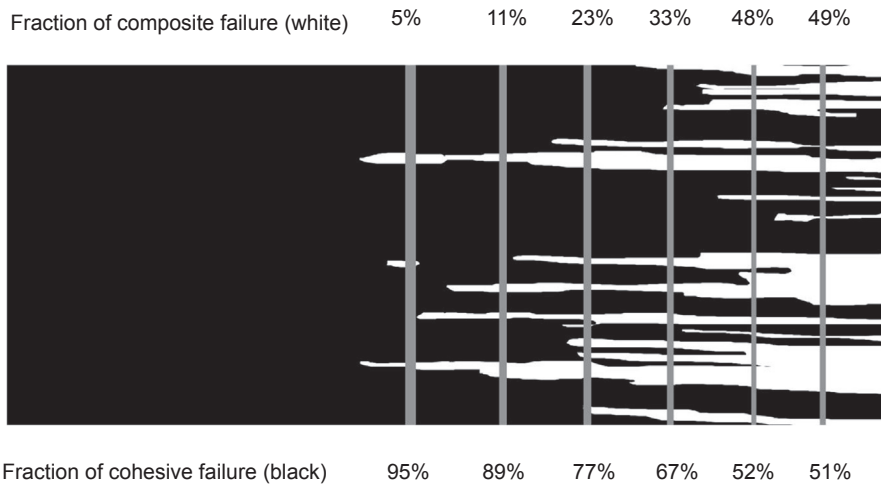

Figure 22.34 Failure in mixed fracture model under SF.

that the area is small enough to be approximated as a line. Some of the measurements are presented in Figure 22.34.

The crack-growth rate at a specific crack size when both fracture mechanism are observed can be analysed as a weighted sum of the crack growth rates for each failure mechanism. Linear or nonlinear relations can be proposed to have a general rule of mixtures; however, this relation needs to be obtained by an optimisation of the values. The following expression is proposed and referred to as the mixed-mechanism fracture model (MMFM):

$$\mathrm{Log}\left(\frac{\mathrm{d}a}{\mathrm{d}N}(a)\right)_T = A^{n1} \times \mathrm{Log}\left(\frac{\mathrm{d}a}{\mathrm{d}N}(a)\right)_{\mathrm{MC}} + B \times \mathrm{Log}\left(\frac{\mathrm{d}a}{\mathrm{d}N}(a)\right)_{\mathrm{Coh}} \tag{22.28}$$

in which the subscripts T, Coh and MC refer to the mechanism of failure: total, cohesive and matrix cracking; A and B are the fractions of cohesive failure and matrix cracking, respectively; and $n1$ is an exponent calibrated with the experimental data.

FCG for a fully cohesive failure is presented in Figure 22.31; however, to obtain the FCG curve for matrix cracking, the previous work should be reviewed. In Ashcroft and Shaw (2002), a DCB specimen with similar adhesive/adherend system to that used in this research was used to define the FCG. It was found that at room temperatures failure occurred in the adhesive or composite and $G_{\mathrm{Ic}} = 200 \pm 50\ \mathrm{J/m^2}$ for failure in the composite. However, information on G_{Ith} and m (parameter of Paris' law) was not provided. It was also mentioned that in a specimen tested at low temperature, only composite failure was observed, and the parameters for crack growth were: $G_{\mathrm{Ic}}\ 250 \pm 50\ \mathrm{J/m^2}$, $G_{\mathrm{Ith}} = 80 \pm 50\ \mathrm{J/m^2}$, $m = 8.8 \pm 0.9$. These data are used in this research to define FCG with the mechanism of matrix cracking.

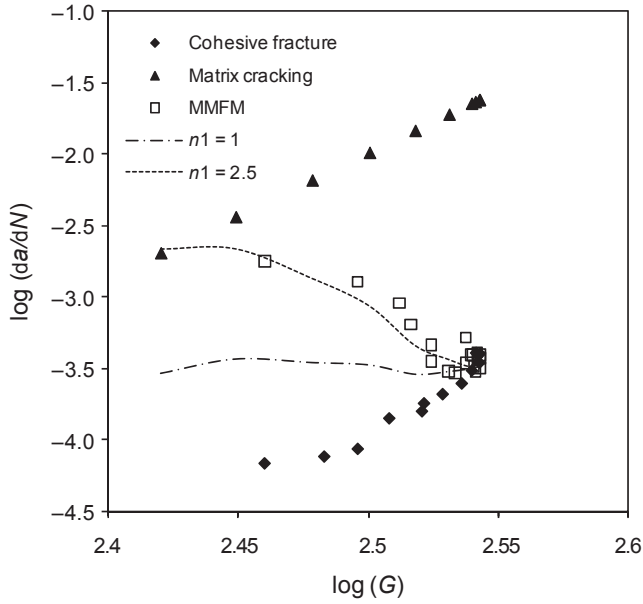

Figure 22.35 Optimisation of $n1$ in mixed-mechanism fracture model.

An optimisation analysis was conducted for the constant n in Eqn (22.28); Figure 22.35 shows its application with three values for this constant. It is observed that as n_1 increases, the change from cohesive to matrix cracking is faster. From this analysis it is concluded that $n1 = 2.5$ gives a good approximation to the experimental data.

22.5.3 Numerical crack growth integration

Numerical crack growth integration (NCGI) is an established technique to predict crack growth in VA fatigue based on the results of constant-amplitude fatigue (Erpolat, 2004). In this work, this technique was implemented to analyse CISF based on the results obtained from IF and SF.

22.5.3.1 Cohesive failure during SF

NCGI was used to predict crack growth in SF to validate the technique and also to corroborate the FCGR curves shown in Section 22.5.1.1 for LSJs with a cohesive failure. A comparison between the experimental data and the NGCI prediction of cohesive failure in LSJ during SF is presented in Figure 22.36. It is seen that the NCGI gives a good prediction of the experimental data.

22.5.3.2 CISF

An extension of the use of the NCGI technique is to analyse the FCG in CISF specimens. The experimental data demonstrated that, in some cases, a cohesive

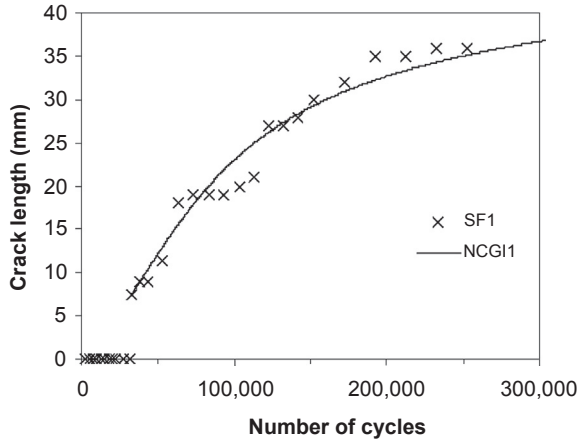

Figure 22.36 NCGI prediction of cohesive failure in LSJ under SF.

failure is found when specimens were tested under CISF. A first case was to use NCGI with the $(FCGR)_{SF}$ curve to predict failure in CISF. Figure 22.37 shows a comparison of the FCG in a cohesive failure under CISF and the NCGI-predicted failure using the $(FCGR)_{SF}$ curve for a cohesive failure. As expected, the NCGI method underpredicts crack growth as the enhanced crack growth in the IF region is increased. However, the plot usefully shows the significant effect of a relatively small number of low-energy impacts included into an SF spectrum.

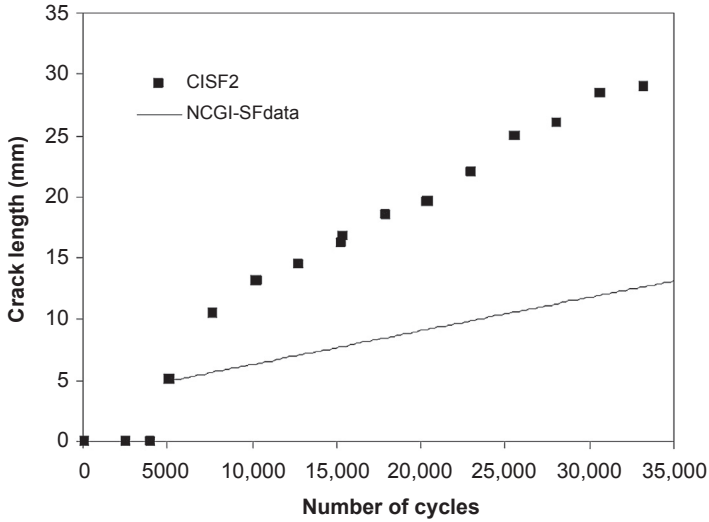

Figure 22.37 NCGI of cohesive failure LSJs under CISF.

The next step was to modify the method to incorporate load-interaction effects. As described before the FCGR for a cohesive failure in IF could not be measured because of the high FCGR and the small area with this type of failure. However, to include the effect of IF in the NCGI method, it was assumed that the $(FCGR)_{IF}$ curve could be obtained using a 'damage-shift' model (DSM), as explained before. The empirical DSM was originally proposed to account for the inclusion of interaction effects in VA SF. This model suggests the existence of a function ψ_E, which is associated with a lateral displacement of the FCGR curve. In this work, it is assumed that the FCGR-curve should be moved to the left, in order to predict the FCGR during CISF for a similar G to that obtained during SF, shows schematically this FCGR shift. In implementation of the DSM for CISF, it is supposed that during the transition for SF to the FCGR, $(da/dn)_i$ changes suddenly from the SF FCG curve to the IF one, as described by region 1 During the 100 impacts, described as region 2 the FCG follows the $(FCGR)_{IF}$ curve. After IF, a more gradual change to the $(FCGR)_{SF}$ curve is introduced to account for interaction effects, as represented by region 3 in Figure 22.38. Various scenarios for a change from IF to SF were investigated. The first was of the abrupt change in the FCGR from SF to IF, as in Figure 22.39 (DSM_{abr}), then continuing to follow the $(FCGR)_{SF}$ curve for the subsequent 5000 SF cycles (region 4 in). Additionally, other scenarios were investigated, in which damage ahead of the crack tip produced by the IF caused the higher FCGR in region 3 than that predicted by DMS_{abr}. A second scenario is of a gradual decrease in the FCGR over all 5000 SF cycles, in which case region 4 disappears. This scenario is shown in Figure 22.39 and denoted as $DSM_{lin.}$. A variation of this scenario is when the damage ahead of the crack tip only affects a part of 5000 SF cycles as presented in Figure 22.39 (denoted DSM_{frac}).

Following the scenarios of FCGR deterioration described above, each of these cases was used to predict crack growth in CISF. The first case was the use of

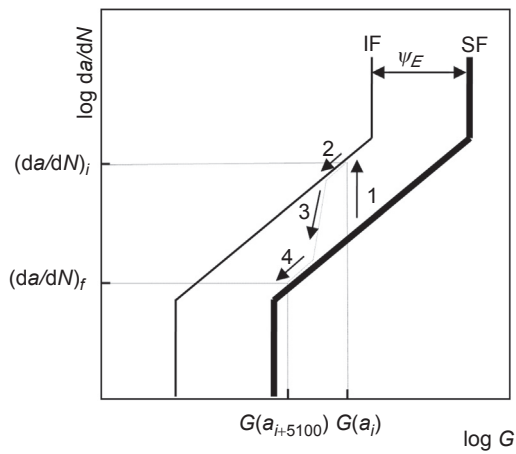

Figure 22.38 Schematic of CISF in damage-shift model.

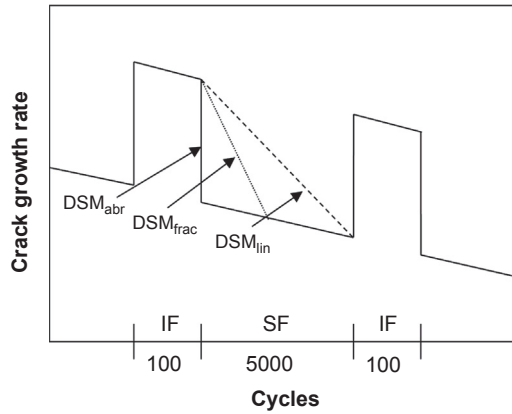

Figure 22.39 Schematic of FCGR changes from IF to SF in CISF.

$(FCGR)_{SF}$ curve and DSM_{abr} to predict the FCG behaviour of CISF with a cohesive failure. The value of ψ_E was obtained by changing the empirical constant C used in the Paris law (Eqn (22.20)) and keeping m (i.e. slope of the FCGR-curve) constant to try to minimise the error between the predicted and experimental data. A comparison of the NCGI and the experimental data is presented in Figure 22.40. The FCG behaviour is described as a step-increasing tendency, which is a product of the sudden changes from SF to IF.

The FCGR-curve of CISF is presented in Figure 22.41, in which the $(FCGR)_{SF}$ curve and the constructed $(FCGR)_{IF}$ curve are included. As expected, a drastic change from SF to IF is apparent. The ψ_E necessary to obtain the $(FCGR)_{IF}$ curve in log-scale was 0.26 J/m^2.

The second crack-growth scenario investigated was the use of the $(FCGR)_{SF}$ curve together with DSM_{lin}. In Figure 22.42 a comparison between CISF data

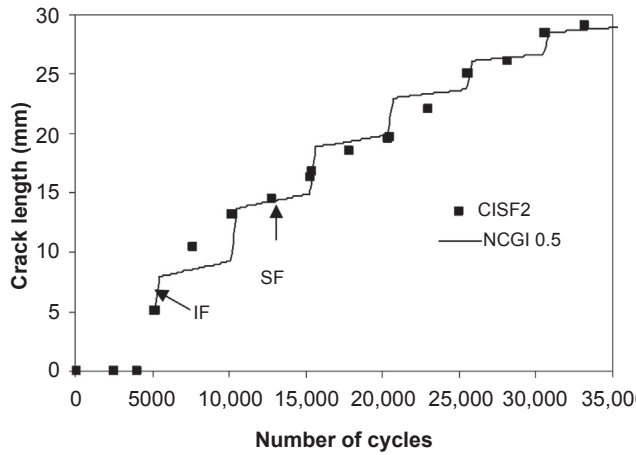

Figure 22.40 NCGI curve using DSM_{abr}.

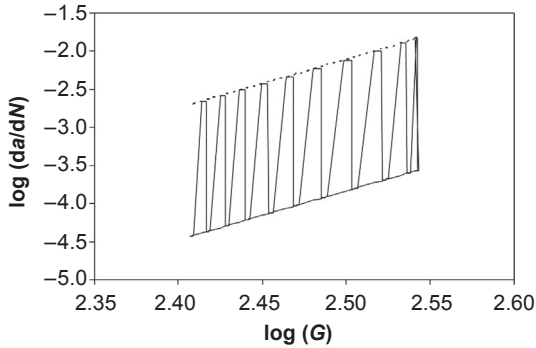

Figure 22.41 FCGR curve for CISF assuming DSM_{abr}.

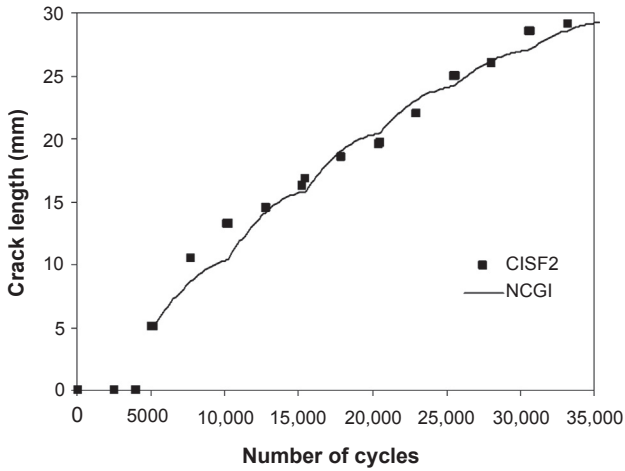

Figure 22.42 NCGI curve using DSM_{lin}.

and the NCGI-predicted crack growth is demonstrated. A good correspondence between the predicted and experimental data can be seen. Comparing Figures 22.40 and 22.42, the softening effect of including the more gradual change in FCGR from IF to SF is obvious.

The FCGR-curve for the CISF and DSM_{lin} scheme is presented in Figure 22.43. As expected, the FCGR shows a gradual change varying between IF and SF. The value of ψ_E was 0.13 J/m^2.

The third crack-growth scenario assumed that IF damage affected only a fraction of the SF load block. In this case it was supposed that only 20% of the SF block was affected by this damage. A comparison between the experimental and the corrected NCGI using the DSM_{frac} scenario is presented in Figure 22.44. In this case, step increases in FCG are seen; however, they are less abrupt than those obtained with the DSM_{abr} assumption. This is also seen in Figure 22.45. In this case ψ_E was 0.21 J/m^2.

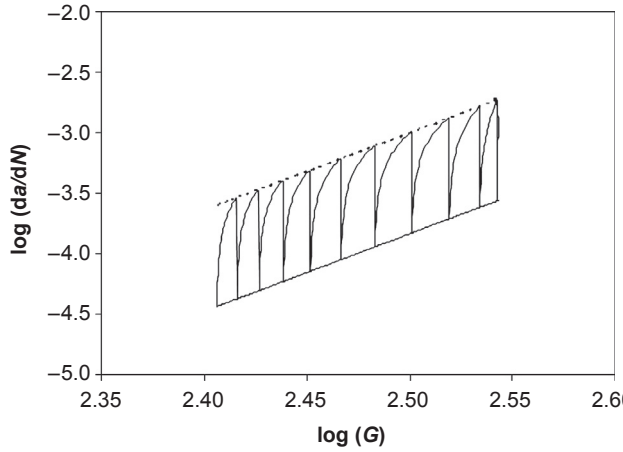

Figure 22.43 FCGR-curve for CISF assuming DSM_{lin}.

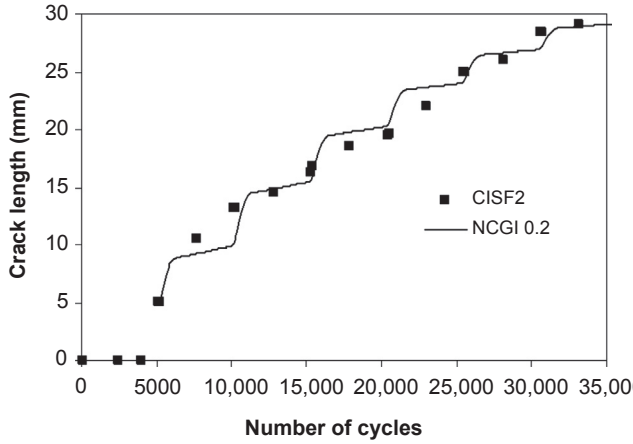

Figure 22.44 NCGI curve using DSM_{frac}.

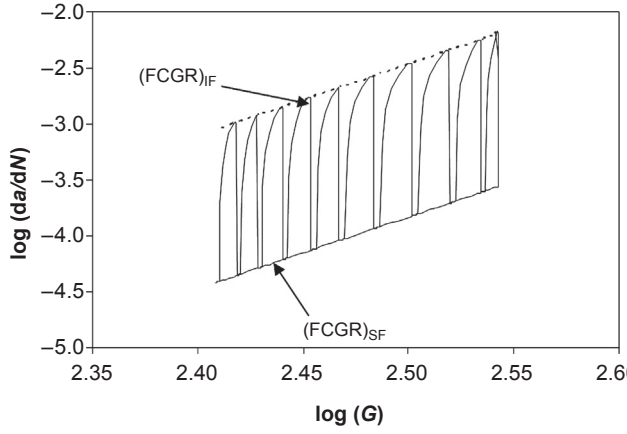

Figure 22.45 FCGR-curve for CISF assuming DSM_{fra}.

22.6 Conclusions

A methodology to construct FCG diagrams under SF and IF was proposed. Values of the strain-energy release rate obtained numerically were compared with the experimental results for the crack growth rate in LSJs. The results were also compared with the previous work conducted in the area and found to be within the range reported previously. The FCG graphs for similar load conditions and the realisation of a single failure mechanism show a tendency similar at those proposed by the Paris' law, where a threshold and stable and unstable regions are presented. The changes in the mechanism of failure (at similar loading conditions) manifest themselves with anomalous crack growth behaviour that could be explained by a transition from between the FCG plots of respective mechanisms. To account for this behaviour, a model was proposed presenting the FCG of the system as a function of the fractions of failure and the crack growth rates for single failure mechanisms. This model depends on the contributions to damage by each mechanism and the expected single-mechanism crack growth rate. Changes from cohesive to matrix-cracking fracture were studied and the proposed mixed-failure crack-growth model was used to predict the FCG under a combination of fracture modes in a specimen. This model is a combination of fractions of each FCG, with a penalty term n for the matrix cracking that has the highest FCGR. The model was found to predict the mixed crack growth behaviour well if the correct value of $n1$ was selected.

Experimental work shows that the inclusion of a small number of impacts changed the FCG drastically, and this was confirmed by this approximation. The use of the damage-shift model helped to modify the prediction of the NCGI. In this study, three scenarios of the FCGR change from IF to SF were studied, and in all of them the $(FCGR)_{IF}$ curve was obtained using the damage-shift model. Apparently, the effect of IF on damage in the adhesive can be represented in the model by controlling the rate of change of crack growth in the transition from IF to SF. An abrupt change in the crack-growth rates represents no interaction effects, whereas a gradual change results in the accelerated crack growth in SF thanks to IF-generated damage ahead of the crack tip. This has a direct effect on the predicted crack growth behaviour.

22.7 Future trends

The importance of IF for future applications will continue to increase; one trend for this is a broadening use of composites and related adhesively bonded joints in automotive and wind-energy industries. Due to a complex nature of damage evolution in composites in IF, the failure criteria for this regime require further investigation. Fracture mechanisms should be studied extensively, initially with homogeneous materials, for example, PMMA. This will help to decrease the extent of complexity of spatio-temporal evolution of fracture scenarios and enable analysis of the problem in a more fundamental way.

A useful extension to the work in this chapter could be to analyse IF using the strength-degradation data obtained in IF and SF in conjunction with a cohesive-zone-element (CZE) theory. An apparent limitation of the CZE is identified as the lack of experimentally based relations between the reaction force and the displacement in an element before and after its deterioration due to failure. The study of strength degradation can provide experimental data to underpin respective laws that can be included into the CZE theory and in this way improve analysis of fatigue. In addition, after identification of these laws (in this specific case, for both IF and SF), it will be possible to establish and quantify differences in fatigue processes. This could be used to predict impact damage and fatigue deterioration of bonded joints subjected to IF and SF.

References

Abdel Wahab, M. M. (2012). Fatigue in adhesively bonded joints: a review. *ISRN Materials Science, 2012*, 25.

Abou-Hamda, M. M., Megahed, M. M., & Hammouda, M. M. I. (1998). Fatigue crack growth in double cantilever beam specimen with an adhesive layer. *Engineering Fracture Mechanics, 60*, 605−614.

Adam, T., Gathercole, N., Reiter, H., & Harris, B. (1994). Life prediction for fatigue of T800/5245 carbon-fibre composites. II. Variable-amplitude loading. *International Journal of Fatigue, 16*, 533−547.

Adams, G. C. (1987). Impact fatigue of polymers using an instrumented drop Tower device. In S. L. Kessler, G. C. Adams, S. B. Driscoll, & D. R. Ireland (Eds.), *Instrumented impact testing of plastics and composite Materials, ASTM ST* (pp. 281−301). Philadelphia: ASTM.

Adams, R. D., & Harris, J. A. (1996). A critical assessment of the block impact test for measuring the impact strength of adhesive bonds. *International Journal of Adhesion and Adhesives, 16*, 61−71.

Al-Ghamdi, A., Ashcroft, I. A., Crocombe, A. D., & Abdel-Wahab, M. M. (2003). Crack growth in adhesively bonded joints subjected to variable frequency fatigue loading. *Journal of Adhesion, 73*, 1161−1182.

Ashcroft, I. A. (2004). A simple model to predict crack growth in bonded joints and laminates under variable-amplitude fatigue. *Journal of Strain Analysis for Engineering Design, 39*, 707−716.

Ashcroft, I. A. (2005). Fatigue. In R. D. Adams (Ed.), *Adhesive bonding science, technology and applications*. Woodhead Publishing Limited.

Ashcroft, I., Casas-Rodriguez, J., & Silberschmidt, V. (2008). Mixed-mode crack growth in bonded composite joints under standard and impact-fatigue loading. *Journal of Materials Science, 43*, 6704−6713.

Ashcroft, I. A., Hughes, D. J., & Shaw, S. J. (2001). Mode I fracture of epoxy bonded composite joints: 1. Quasi-static loading. *International Journal of Adhesion and Adhesives, 21*, 87−99.

Ashcroft, I. A., & Shaw, S. J. (2002). Mode I fracture of epoxy bonded composite joints 2. Fatigue loading. *International Journal of Adhesion and Adhesives, 22*, 151−167.

Ashcroft, I. A., Wahab, M. M. A., Crocombe, A. D., Hughes, D. J., & Shaw, S. J. (2001). The effect of environment on the fatigue of bonded composite joints. Part 1: testing and fractography. *Composites Part A: Applied Science and Manufacturing, 32*, 45−58.

ASTM-D950. (2003). *Standard test method for impact strength of adhesive bonds*. ASTM International, West Conshohocken, PA, USA.

Aymerich, F., Dore, F., & Priolo, P. (2008). Prediction of impact-induced delamination in cross-ply composite laminates using cohesive interface elements. *Composites Science and Technology, 68*, 2383−2390.

Azouaoui, K., Rechak, S., Azari, Z., Benmedakhene, S., Laksimi, A., & Pluvinage, G. (2001). Modelling of damage and failure of glass/epoxy composite plates subject to impact fatigue. *International Journal of Fatigue, 23*, 877−885.

Bandyopadhyay, S. (1990). Review of the microscopic and macroscopic aspects of fracture of unmodified and modified epoxy resins. *Materials Science and Engineering A, 125*, 157−184.

Beevers, A., & Ellis, M. D. (1984). Impact behavior of bonded mild steel lap joints. *International Journal of Adhesion and Adhesives, 4*, 13−16.

Bezemer, A. A., Guyt, C. B., & Vlot, A. (1998). New impact specimen for adhesives: optimization of high-speed-loaded adhesive joints. *International Journal of Adhesion and Adhesives, 18*, 255−260.

Blackman, B., Kinloch, A. J., Taylor, A. C., & Wang, Y. (2000). The impact wedge-peel performance of structural adhesives. *Journal of Materials Science, 35*, 1867−1884.

Bora, M. Ö., Çoban, O., Sinmazçelik, T., Cürgül, I., & Günay, V. (2009). On the life time prediction of repeatedly impacted thermoplastic matrix composites. *Materials & Design*. *30*, 145−153.

Cantwell, W. J., Curtis, P. T., & Morton, J. (1984). Impact and subsequent fatigue damage growth in carbon fibre laminates. *International Journal of Fatigue, 6*, 113−118.

Casas-Rodriguez, J. P., Ashcroft, I. A., & Silberschmidt, V. V. (2008). Delamination in adhesively bonded CFRP joints: standard fatigue, impact-fatigue and intermittent impact. *Composites Science and Technology, 68*, 2401−2409.

Chaboche, J. L. (1987). Continuum damage mechanics: present state and future trends. *Nuclear Engineering and Design, 105*, 19−23.

Chang, F. K., & Chang, K. Y. (January 1, 1987). A progressive damage model for laminated composites containing stress concentrations. *Journal of Composite Materials, 21*, 834−855.

Changliang, Z., Mingfa, R., Wei, Z., & Haoran, C. (2006). Delamination prediction of composite filament wound vessel with metal liner under low velocity impact. *Composite Structures, 75*, 387−392.

Choupani, N. (2008). Mixed-mode cohesive fracture of adhesive joints: experimental and numerical studies. *Engineering Fracture Mechanics, 75*, 4363−4382.

Clark, G., & Saunders, D. S. (1991). Morphology of impact damage growth by fatigue in carbon fibre composite laminates. *Materials Forum, 15*, 333−342.

Çoban, O., Bora, M. Ö., Sinmazçelik, T., Cürgül, I., & Günay, V. (2009). Fracture morphology and deformation characteristics of repeatedly impacted thermoplastic matrix composites. *Materials & Design*, *30*, 628−634.

Crocombe, A. D. (1995). Modelling and predicting the effects of test speed on the strength of joints made with FM73 adhesive. *International Journal of Adhesion and Adhesives, 15*, 21−27.

Crocombe, A. D., & Richardson, G. (1999). Assessing stress state and mean load effects on the fatigue response of adhesively bonded joints. *International Journal of Adhesion and Adhesives, 19*, 19−27.

Davies, P., & Choquese, D. (2000). Fatigue and durability of marine composites. In B. Harris (Ed.), *Fatigue in composites* (pp. 709−729). Woodhead Publishing Limited.

Degrieck, J., & Van Paepegem, W. (2001). Fatigue damage modeling of fibre-reinforced composite materials: Review. *Applied Mechanics Reviews, 54*, 279.

Ding, Y. Q., Yan, Y., & McIlhagger, R. (1995). Effect of impact and fatigue loads on the strength of plain weave carbon-epoxy composites. *Journal of Materials Processing Technology, 55*, 58−62.

Du Pont. (1988). Impact fatigue the long term toughness parameter. *Materials & Design, 9*, 229−230.

Ekh, J. (2006). *Multi-fastener single lap joints in composite structures* (Ph.D. thesis). Stockholm: Royal Institute of technology.

Erpolat, S. (2004). *Variable amplitude fatigue loading of adhesively bonded joints* (Ph.D. thesis). Loughboorugh: Loughboorugh University.

Erpolat, S., Ashcroft, I. A., Crocombe, A. D., & Abdel-Wahab, M. M. (2004a). A study of adhesively bonded joints subjected to constant and variable amplitude fatigue. *International Journal of Fatigue, 26*, 1189−1196.

Erpolat, S., Ashcroft, I. A., Crocombe, A. D., & Abdel-Wahab, M. M. (2004b). Fatigue crack growth acceleration due to intermittent overstressing in adhesively bonded CFRP joints. *Composites Part A: Applied Science and Manufacturing, 35*, 1175−1183.

Gathercole, N., Reiter, H., Adam, T., & Harris, B. (1994). Life prediction for fatigue of T800/5245 carbon-fibre composites: I. Constant-amplitude loading. *International Journal of Fatigue, 16*, 523−532.

Gledhill, R. A., Shaw, S. J., & Tod, D. A. (1990). Durability of adhesive-bonded joints employing organosilane coupling agents. *International Journal of Adhesion and Adhesives, 10*, 192−198.

Goglio, L., Peroni, M., & Rossetto, M. (2007). Effect of the strain rate on the mechanical behaviour of epoxy adhesives. *Key Engineering Materials, 347*, 671−676.

Gomaa, A., Hamdy, A., & Moet, A. (1992). Subcritical crack propagation under cyclic stress impulse. *International Journal of Fracture, 53*, 187−199.

Guinard, S., Allix, O., Guedra-Degeorges, D., & Vinet, A. (2002). A 3D damage analysis of low-velocity impacts on laminated composites. *Composites Science and Technology, 62*, 585−589.

Hampson, P. R., & Moatamedi, M. (2007). A review of composite structures subjected to dynamic loading. *International Journal of Crashworthiness, 12*, 411−428.

Harris, B. (2000). A historical review of the fatigue behaviour of fibre-reinforced plastics. In B. Harris (Ed.), *Fatigue in composites*. Woodhead Publishing Limited.

Harris, J., & Adams, R. D. (1985). An assessment of the impact performance of bonded joints for use in high energy absorbing structures. *Proceedings of the Institution of Mechanical Engineers, Part C: Journal of Mechanical Engineering Science, 199*, 121−131.

Hertzberg, R. W. (1996). *Deformation and fracture mechanics of engineering materials* (4th ed.). New York: Wiley & Sons.

Higgins, A. (2000). Adhesive bonding of aircraft structures. *International Journal of Adhesion and Adhesives, 20*, 367−376.

Hiley, M. J., Dong, L., & Harding, J. (1997). Effect of strain rate on the fracture process in interlaminar shear specimens of carbon fibre-reinforced laminates. *Composites Part A: Applied Science and Manufacturing, 28*, 171−180.

Hodgkinson, E. (1849). *Report of the commission appointed to enquire into the application of iron to railway structures*. London.

Hosoi, A., Kawada, H., & Yoshino, H. (2006). Fatigue characteristics of quasi-isotropic CFRP laminates subjected to variable amplitude cyclic two-stage loading. *International Journal of Fatigue, 28*, 1284−1289.

Hosur, M. V., Adya, M., Alexander, J., Jeelani, S., Vaidya, U., & Mayer, A. (July 1, 2003). Studies on impact damage resistance of affordable stitched woven carbon/epoxy composite laminate. *Journal of Reinforced Plastics and Composites, 22*, 927−952.

Hosur, M. V., Abraham, A., Jeelani, S., & Vaidya, U. K. (2001). Studies on the influence of through-the-thickness reinforcement on low-velocity and high strain rate response of woven S2-glass/vinyl ester composites. *Journal of Composite Materials, 35*, 1111−1133.

Hosur, M. V., Waliul-Islam, S. M., Vaidya, U. K., Kumar, A., Dutta, P. K., & Jeelani, S. (2005). Dynamic punch shear characterization of plain weave graphite/epoxy composites at room and elevated temperatures. *Composite Structures, 70*, 295−307.

Hosur, M. V., Waliul, I. S. M., Vaidya, U. K., Dutta, P. K., & Jeelani, S. (2004). Experimental studies on the punch shear characterization of satin weave graphite/epoxy composites at room and elevated temperatures. *Materials Science and Engineering A, 368*, 269−279.

Hou, J. P., Petrinic, N., & Ruiz, C. (2001). A delamination criterion for laminated composites under low-velocity impact. *Composites Science and Technology, 61*, 2069−2074.

Hou, J. P., Petrinic, N., Ruiz, C., & Hallett, S. R. (2000). Prediction of impact damage in composite plates. *Composites Science and Technology, 60*, 273−281.

Hyung Yun, C., & Chang, F.-K. (January 1, 1992). A model for predicting damage in graphite/epoxy laminated composites resulting from low-velocity point impact. *Journal of Composite Materials, 26*, 2134−2169.

Imanaka, M., Kishimoto, W., Okita, K., Nakayama, H., & Shirato, M. (1985). On the impact fatigue strength of adhesive-bonded lap joint. *Journal Society of Material Science Japan, 34*, 1296−1300.

Isik, I., Yilmazer, U., & Bayram, G. (2003). Impact modified epoxy/montmorillonite nanocomposites: synthesis and characterization. *Polymer, 44*, 6371−6377.

ISO-11343. (2003). *Adhesives. Determination of dynamic resistance to cleavage of high-strength adhesive bonds under impact conditions, wedge impact method.*

Jang, B. P., Kowbel, W., & Jang, B. Z. (1992). Impact behavior and impact-fatigue testing of polymer composites. *Composites Science and Technology, 44*, 107−118.

Jen-Ming, H. R., & Lee, C. H. (1998). Strength and life in thermoplastic composite laminates under static and fatigue loads. Part II. *International Journal of Fatigue, 20*, 617−629.

Johnson, W. S. (1987). Stress analysis of the cracked-lap-shear specimen - an ASTM round-robin. *Journal of Testing and Evaluation, 15*, 303−324.

Johnson, A. A. (2004). Impact fatigue - an emerging field of study. *Engineering Integrity, 15*, 14−20.

Johnson, A. A., & Storey, R. (2007). The impact fatigue properties of iron and steel. *Journal of Sound and Vibration, 308*, 458−466.

Khan, B., Rao, R., & Venkataraman, N. (1995). Low velocity impact fatigue studies on glass epoxy composite laminates with varied material and test parameters-effect of incident Energy and fibre volume fraction. *Journal of Reinforced Plastics and Composites, 14*, 1150−1159.

Khosrovaneh, A. K., & Dowling, N. E. (1990). Fatigue loading history reconstruction based on the rainflow technique. *International Journal of Fatigue, 12*, 99−106.

Kihara, K., Isono, H., Yamabe, H., & Sugibayashi, T. (2003). A study and evaluation of the shear strength of adhesive layers subjected to impact loads. *International Journal of Adhesion and Adhesives, 23*, 253−259.

Kinloch, A. J. (1997). Adhesives in engineering. *Proceedings of the I Mechanical Engineers, Part G: Journal of Aerospace Engineering, 211*, 307−335.

Kinloch, A. J., & Williams, J. G. (1980). Crack blunting mechanisms in polymers. *Journal of Materials Science, 15*, 987−996.

Lemaitre, J. (1984). How to use damage mechanics. *Nuclear Engineering and Design, 80*, 133−245.

Lemaitre, J., Sermage, J. P., & Desmorat, R. (1999). A two scale damage concept applied to fatigue. *International Journal of Fracture, 97*, 67−81.

Li, D., Yee, A. F., Chen, I.-W., Chang, S.-C., & Takahashi, K. (1994). Fracture behaviour of unmodified and rubber-modified epoxies under hydrostatic pressure. *Journal of Materials Science, 29*, 2205−2215.

Lifshitz, J. M., & Leber, H. (1998). Response of fiber-reinforced polymers to high strain-rate loading in interlaminar tension and combined tension/shear. *Composites Science and Technology, 58*, 987−996.

Maekawa, I., & Shibata, H. (1995). Characteristic property of impact fracture toughness. *JSME International Journal Series A, 38*, 80−83.

Mall, S., & Ramamurthy, G. (1989). Effect of bond thickness on fracture and fatigue strength of adhesively bonded composite joints. *International Journal of Adhesion and Adhesives, 9*, 33−37.

Mall, S., Ramamurthy, G., & Rezaizdeh, M. A. (1987). Stress ratio effect on cyclic debonding in adhesively bonded composite joints. *Composite Structures, 8*, 31−45.

Maranon, A. (2005). *Characterising delamination in composite materials* (Ph.D. thesis). Loughborough: Loughborough University.

Marco, W. L. S. S. M. (1954). A concept of fatigue damage. *Transactions of the American Society of Mechanical Engineers, 76*, 626−662.

Maugis, D. (1985). Subcritical crack growth, surface energy, fracture toughness, stick-slip and embrittlement. *Journal of Materials Science, 20*, 3041−3073.

Miner, M. (1945). Cumulative damage in fatigue. *Journal of Applied Mechanics, 12*, 159−164.

Ming-Hsiung, H., Hwang, J. R., Doong, J. L., & Fung, G. P. (1999). Impact fatigue of a polycarbonate/acrylonitrile-butadiene-styrene blend. *Polymer Engineering & Science, 39*, 708−720.

Ninomi, M., Uway, K., Kobayashi, K., & Okahara, A. (1991). Impact fatigue properties of epoxy resin filled with SiO_2 particles. *Engineering Fracture Mechanics, 38*, 439−449.

Owen, R. J. H. M. J. (1972). The accumulation of damage in a glass-reinforced plastic under tensile and fatigue loading. *Journal of Physics D: Applied Physics, 5*, 1637−1649.

Papini, M., Fernlund, G., & Spelt, J. K. (1994). The effect of geometry on the fracture of adhesive joints. *International Journal of Adhesion and Adhesives, 14*, 5−13.

Paris, P. C., & Erdogan, F. (1963). A critical analysis of crack propagation laws. *Transactions of the ASME Series D, 85*, 528−535.

Pirondi, A., & Nicoletto, G. (2004). Fatigue crack growth in bonded DCB specimens. *Engineering Fracture Mechanics, 71*, 859−871.

Pirondi, A., & Nicoletto, G. (2006). Mixed mode I/II fatigue crack growth in adhesive joints. *Engineering Fracture Mechanics, 73*, 2557−2568.

Potter, K. D., Schweickhardt, F., & Wisnom, M. R. (2000). Impact response of unidirectional carbon fibre rod elements with and without an impact protection layer. *Journal of Composite Materials, 34*, 1437−1455.

Ramkumar, R. L. (1983). Effect of low-velocity impact damage on the fatigue behaviour of graphite/epoxy laminates. In T.. K. O'Brien (Ed.), *Long term behaviour of composites', ASTM STP 813* (pp. 116−135). Philadelphia: ASTM.

Ray, D., Sarkar, B. K., & Bose, N. R. (2002). Impact fatigue behaviour of vinylester resin matrix composites reinforced with alkali treated jute fibres. *Composites Part A: Applied Science and Manufacturing, 33*, 233−241.

Roy, R., Sarkar, B. K., Rana, A. K., & Bose, N. R. (2001). Impact fatigue behaviour of carbon fibre-reinforced vinylester resin composites. *Bulletin of Materials Science, 24*, 79−86.

Sanchez-Saez, S., Barbero, E., Zaera, R., & Navarro, C. (2005). Compression after impact of thin composite laminates. *Composites Science and Technology, 65*, 1911−1919.

Sato, C., & Ikegami, K. (2000). Dynamic deformation of lap joints and scarf joints under impact loads. *International Journal of Adhesion and Adhesives, 20*, 17−25.

Schaff, J. R., & Davidson, B. D. (1997). Life prediction methodology for composite structures. Part I−Constant amplitude and two-stress level fatigue. *Journal of Composite Materials, 31*, 128−157.

Schon, J., & Starikov, R. (2003). Fatigue of joints in composite structures. In B. Harris (Ed.), *Fatigue in composites* (pp. 621−643). Woodhead Publishing Limited.

Schrauwen, B., & Peijs, T. (2002). Influence of matrix ductility and fibre architecture on the repeated impact response of glass-fibre-reinforced laminated composites. *Applied Composite Materials, 9*, 331−352.

Sethuraman, R., & Maiti, S. K. (1988). Finite element based computation of strain energy release rate by modified crack closure integral. *Engineering Fracture Mechanics, 30*, 227−231.

Shivakumar, K., Chen, H., Abali, F., Le, D., & Davis, C. (2006). A total fatigue life model for mode I delaminated composite laminates. *International Journal of Fatigue, 28*, 33−42.

Silberschmidt, V. V., Casas-Rodriguez, J. P., & Ashcroft, I. A. (2008). Impact fatigue in adhesive joints. *Proceedings of the Institution of Mechanical Engineers, Part C: Journal of Mechanical Engineering Science, 222*(10), 1981−1994.

da Silva, L. F. M., Carbas, R. J. C., Critchlow, G. W., Figueiredo, M. A. V., & Brown, K. (2009). Effect of material, geometry, surface treatment and environment on the shear strength of single lap joints. *International Journal of Adhesion and Adhesives, 29*, 621−632.

da Silva, L., & Öchsner, A. (2008). *Modeling of adhesively bonded joints*. Springer, Hildeberg.

Sınmazçelik, T., Arıcı, A. A., & Günay, V. (2006). Impact−fatigue behaviour of unidirectional carbon fibre reinforced polyetherimide (PEI) composites. *Journal of Materials Science, 41*, 6237−6244.

Stanton, T. E., & Bairstow, L. (1908). The resistance of materials to impact. In *Proceedings of the institute of mechanical engineers* (pp. 889−919).

Sun, C., Thouless, M. D., Waas, A. M., Schroeder, J. A., & Zavattieri, P. D. (2008). Ductile-brittle transitions in the fracture of plastically deforming, adhesively bonded structures. Part II: numerical studies. *International Journal of Solids and Structures, 45*, 4725−4738.

Takeshi, O. (1999). *The fatigue of toughened epoxy polymers* (Ph.D. thesis). London: Imperial College of Science.

Tanaka, T., Kinoshita, K. I., & Nakayama, H. (1992). Effect of loading time on high-cycle range impact fatigue strength and impact fatigue crack growth rate. *JSME International Journal. Series A, Solid Mechanics and Material Engineering, 35*, 108−116.

Tong, L., & Luo, Q. (2008). Analysis of cracked lap shear joints. In L. F. Martins-da Silva, & A. Ochsner (Eds.), *Modeling of adhesively bonded joints*. Springer.

Usui, Y., & Sakata, O. (1984). Impact fatigue strength of adhesive joints. *Bulletin of the Japan Society of Precision Engineering, 18*, 213−218.

Vaidya, U. K., Gautam, A. R. S., Hosur, M., & Dutta, P. (2006). Experimental-numerical studies of transverse impact response of adhesively bonded lap joints in composite structures. *International Journal of Adhesion and Adhesives, 26*, 184−198.

Van Paepegem, W., & Degrieck, J. (2002a). Effects of load sequence and block loading on the fatigue response of fiber-reinforced composites. *Mechanics of Advanced Materials and Structures, 9*, 19−35.

Van Paepegem, W., & Degrieck, J. (2002b). A new coupled approach of residual stiffness and strength for fatigue of fibre-reinforced composites. *International Journal of Fatigue, 24*, 747−762.

Williams, J. G. (1984). *Fracture mechanics of polymers*. E. Horwood.

Wyrick, D. A., & Adams, D. F. (January 1, 1988). Residual strength of a carbon/epoxy composite material subjected to repeated impact. *Journal of Composite Materials, 22*, 749−765.

Xu, X. X., Crocombe, A. D., & Smith, P. A. (1995). Mixed-mode fatigue and fracture behaviour of joints bonded with either filled or filled and toughened adhesive. *International Journal of Fatigue, 17*, 279−286.

Xu, X. X., Crocombe, A. D., & Smith, P. A. (1996). Fatigue crack growth rates in adhesive joints tested at different frequencies. *Journal of Adhesion, 58*, 191−204.

Yamamoto, I., Higashihara, T., & Kobayashi, T. (2003). Effect of silica-particle characteristics on impact/usual fatigue properties and evaluation of mechanical characteristics of silica-particle epoxy resins. *JSME International Journal. Series A: Solid Mechanics and Material Engineering, 46*, 145−153.

Yao, W. X., & Himmel, N. (2000). A new cumulative fatigue damage model for fibre-reinforced plastics. *Composites Science and Technology, 60*, 59−64.

Yokoyama, T. (2003). Experimental determination of impact tensile properties of adhesive butt joints with the split Hopkinson bar. *Journal of Strain Analysis for Engineering Design, 38*, 233−245.

Yokoyama, T., & Shimizu, H. (1998). Evaluation of impact shear strength of adhesive joints with the split Hopkinson bar. *JSME International Journal Series A: Solid Mechanics and Material Engineering, 41*, 503−509.

Yuan, Q., Friedrich, K., & Karger-Kocsis, J. (1995). Low-energy Charpy impact of interleaved CF/EP laminates. *Applied Composite Materials, 2*, 19−133.

Yuanjian, T., & Isaac, D. H. (2007). Combined impact and fatigue of glass fiber reinforced composites. *Composites Part B, 39*, 505−512.

Yu, J., Peter, K., & Huang, M. (1999). The impact-fatigue fracture of metallic materials. *JOM Journal of the Minerals, Metals and Materials Society, 51*, 1543−1851.

Zhang, Y., Vassilopoulos, A. P., & Keller, T. (2008). Stiffness degradation and fatigue life prediction of adhesively-bonded joints for fiber-reinforced polymer composites. *International Journal of Fatigue, 30*, 1813−1820.

Damage tolerance and survivability of composite aircraft structures

23

B. Rasuo
University of Belgrade, Belgrade, Serbia

23.1 Introduction

The analysis of the dynamic behaviour of damaged constructions can provide knowledge about the acceptable level of damages and likely chances for aircraft survival. The aircraft's ability to survive even after exposure to severe damage to the vital and load-carrying parts of the aircraft construction is imperative not only for combat aircraft but also for civil aircraft (Ball, 2003; Raymer, 1999; Richards, Hastings, Rhodes, Ross, & Weigel, 2009; Schwarz & Drake, 2001).

Vulnerability, as an element of survivability, is one of the most important exploitable characteristics of contemporary aircraft. With respect to survivability, composite laminated materials demonstrate the best behaviour and results compared to other materials that are currently used in aviation (Rasuo, 1995). Requirements and guidelines for the general programme are contained in the standards MIL-STD-2069, FAR/JAR 25.571, and, for bird strike requirements, FAR/JAR 25.631 (Eschenfelder, 2005; Petit, Bouvet, Bergerot, & Barrau, 2007; Rasuo, 2004).

Predicting damage in laminated composite aircraft components due to impact events such as runway debris, hail, and birds is an area of ongoing research (see Figures 23.1−23.3). To reduce certification and development costs, computational methods are required by the aircraft industry to be able to predict structural integrity of composite structures under high-velocity impacts from hard objects, such as metal fragments and stone debris, and from soft or deformable bodies such as birds, hailstones, and tyre rubber. Key issues are the development of suitable constitutive laws for modelling composites in ply, determination of composite parameters from dynamic materials tests, materials laws for deformable impactors, and the efficient implementation of the materials models into finite element codes (Soutis, 2005; Soutis & Beaumont, 2005).

Impact damages in aircraft structures made from laminated composites are very complex; the most common are matrix cracking, fibre failure, and delamination (Gerlach, Siviour, Wiegand, & Petrinic, 2012). The ability to predict the initiation and growth of damage is crucial for predicting performance and developing reliable and safe designs of composites (Sultan, Worden, Staszewski, & Hodzic, 2012). By use of simulation in modelling the impact damage, the test costs of aircraft structures made from composite laminates will be reduced (Kreculj & Rasuo, 2009).

Structural Integrity and Durability of Advanced Composites. http://dx.doi.org/10.1016/B978-0-08-100137-0.00023-7

Figure 23.1 Impact-induced mechanical damage of inlet cone of a MiG-21bis fighter aircraft. Courtesy Moma Stanojlovic Company.

Figure 23.2 Hail strike-induced mechanical damage on nose cone of a Cessna 650 aeroplane. Courtesy Prince Aviation Company.

Due to the wide-scale use of composite materials in different aircraft structures, it is necessary to introduce new approaches for impact damage modelling. Efficient methodologies are modelling composite structures by applying specialized finite element methods that take into account macromechanical structural properties, as well as by using numerical methods with complicated analysis codes. In order to validate those methodologies for further use in the structures' strength design, numerical model verification has to be done. A comparison of the obtained experimental and numerical results is further made to determine if the proposed models are accurate and valid (Kreculj & Rasuo, 2013).

Figure 23.3 Impact-induced mechanical damage of the thrust reverser door on a Boeing 737-700.
Courtesy JAT Tehnika Company.

Composite damages exist at the micro-scale level, while impact loads are applied at the structural level. Hence, it is necessary to consider a multi-scale approach for that kind of problem (Soutis & Beaumont, 2005).

The development of suitable constitutive laws for modelling composite laminate failures and material models with finite element codes under impact provides significant assistance in the design and exploitation phases of specified structures. The most well-known failure criteria (two- and three-dimensional) for composite materials are Tsai-Wu, Chang−Chang, and Hashin. They are used to predict the level or degree of damage, fracture, and failure of composite structures (Soutis & Beaumont, 2005).

Development of computational models and simulations is necessary in studying the onset and growth of impact damages. In numerical simulation of impacts on composite structures, two- or three-dimensional models exist. For impact damage analysis of composite laminates, commercial software ABAQUS and LS-DYNA are most frequently used. Pro/ENGINEER, ANSYS, and some noncommercial software is also suitable for the same purpose. By using it in some circumstances (geometry, boundary conditions, mesh, load, etc.), the distribution of damage, stress, strain, and deformations can be analysed and presented (Kreculj & Rasuo, 2013).

Essentially, when considering impact damage modelling in laminated composites of aeronautical structures, the dynamic response of composite laminates under impact is investigated and damage initiation/growth in such structures is predicted (Guyett & Cardrick, 1980; Poon, 1990). For such analysis, numerical modelling and simulations provide important and valuable results. Due to the anisotropy of composite laminates and nonuniform distribution of stress under dynamic loading, the failure process of laminates is very complex. The dynamic response of composite structures subjected to transient dynamic loading has been studied for years in terms of analytical, numerical, and experimental works (Bayandor, Thomson, Scott, Nguyen, & Elder, 2003).

23.2 Experimental methodology for evaluation of damage tolerance and survivability

Taking into account the quantum of considered problems of damage tolerance or survivability of composite aircraft structures in this chapter, the focus is on experimental investigation and methodology for evaluation of damage tolerance or survivability and results for a particularly interesting group of aircraft with vertical take-off and landing, that is helicopters (Vignjevic & Meo, 2002).

Helicopters are given special attention in this analysis as they are rather specific, highly vulnerable, and greatly exposed to threats due to their vertical take-off and landing, low speed, flight altitudes, etc. (Kelly, 2011).

This chapter presents the analysis of the dynamic behaviour of a heavy transport multipurpose helicopter tail rotor blade (Figures 23.4 and 23.5) before and after ballistic damages caused by 7.9-mm-calibre shoulder weapons that may occur as a consequence of combat as well as terrorist actions (see Figure 23.6). First, non-damaged tail rotor blade behaviour was analysed by exposing the blade to static and dynamic loads in extreme flight conditions; after that, the blade was exposed to long-lasting dynamic loads to define fatigue characteristics; and finally, the blade behaviour after suffering penetrating damage was analysed on its most vital load-carrying part (that is, at the root of the spar), following the same testing program (Figures 23.7 and 23.8). For each of these tests, identical special blades made in the same two-part metal die were used (Carlsson, Adams, & Pipes, 2002; Rasuo, 1995).

In the tail rotor blade, the conventional composite materials with epoxy resin matrix, fibreglass filament spar, 18-section laminated fabric skin of fibreglass filament, some carbon filament embedded along the trailing edge, a foam core, leading-edge protection strips, polyurethane, etc., were used (Rasuo, 1997, 2001, 2007).

23.2.1 Vibratory testing

The aim of the tail rotor blade vibratory testing was to determine the basic aeroelastic properties of the blade. The vibratory test program included experimental determination

Figure 23.4 Heavy transport multipurpose helicopter – Mi-8.
Courtesy Moma Stanojlovic Company.

Figure 23.5 Heavy transport multipurpose helicopter: the tail rotor blades. Courtesy Moma Stanojlovic Company.

Figure 23.6 Ballistic damage to helicopter's windshield. Courtesy Moma Stanojlovic Company.

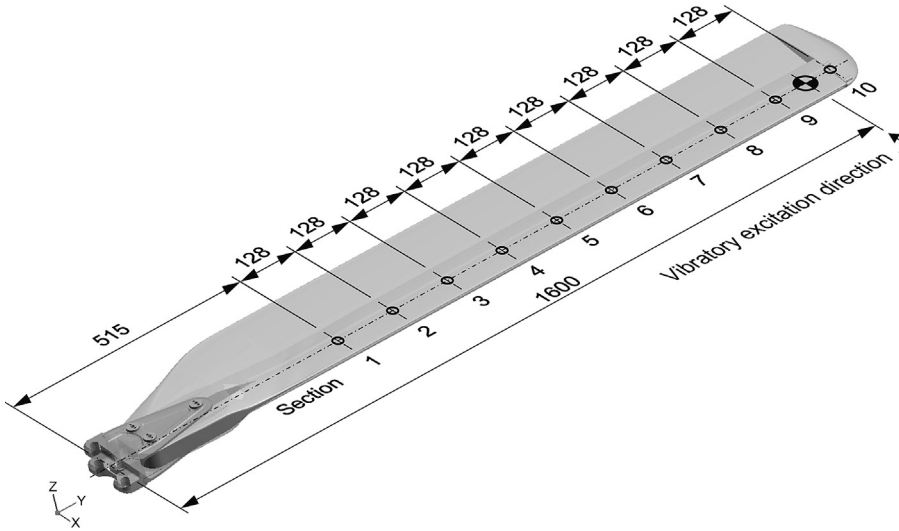

Figure 23.7 Measurement points in vibratory testing.

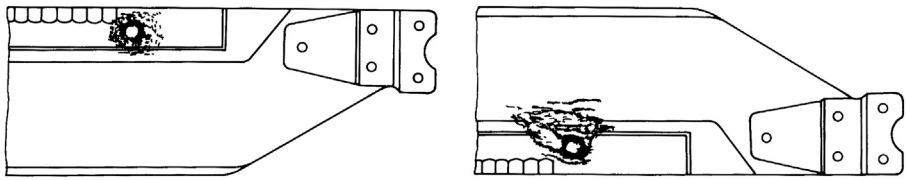

Figure 23.8 Helicopter tail rotor blade made of composite laminated materials after ballistic damage made by the bullet of 7.9-mm-calibre shoulder weapons, in-going (left) and out-going (right) penetration.

of the natural oscillation modes and the tail blade natural frequency as well as its structural damping (Ferreira & Fasshauer, 2007; Herman, Orifici, & Mouritz, 2013).

All the tests on the helicopter tail rotor blade were performed at Belgrade University, Faculty of Mechanical Engineering and Aeronautical Department Laboratory (Rasuo, 2010a,b, 2011a).

The main objective of the testing to be done on non-damaged and damaged helicopter tail rotor blades was to verify experimentally the level of the blade survivability, which is defined as the degradation degree of its vital mechanical characteristics after ballistic damage. On this occasion, only one particular case was analysed: damage on the most vital load-carrying part of the blade; that is, at the root of the spar (Figure 23.8).

The resulting damage, together with its in-going and out-going penetration, presents as vital structural damage on the load-carrying part in the area commonly exposed to the heaviest loads. The investigations carried out on both tail rotor blades follow a standard practice used by the majority of scientific and research aeronautical institutions (Carlsson et al., 2002).

A very robust facility frame made of steel U- and L-profiles tied together with screws was used in the course of the tail rotor blade attachment vibratory testing programme. All the elements used in this testing are shown in Rasuo (2010a,b, 2011a). It can be clearly seen that all the elements were divided into two functional sections: The first one was composed of excitation apparatus, while the second one was made of response-detection equipment (see Figure 23.9). Measuring points were placed along the elastic axes of the blade in the same order, as shown in Figure 23.7.

The excitation apparatus consisted of a pulse generator, signal amplifier, digital timer and frequency counter, vibration exciter (shaker), and an aerofoil clamp, while the response-detection group was made of piezoelectric accelerometers, oscilloscope with voltmeters, and a multichannel *X-t* recorder (see Figure 23.9). The link between the vibration exciter and the rotor blade was formed of a rigidly tied aluminium alloy pipe with adjustable length and by use of a panel aerofoil clamp that was shaped so as to fit the rotor blade cross-section at the location of the application of excitation (see Figure 23.10).

For displacement measurement in these investigations, piezoelectric accelerometers were used; they measured displacements at selected points on the blade, as shown in Figure 23.7. A special kind of cement was used to provide a close link between the pick-up and the blade in the course of measurement (Figure 23.10).

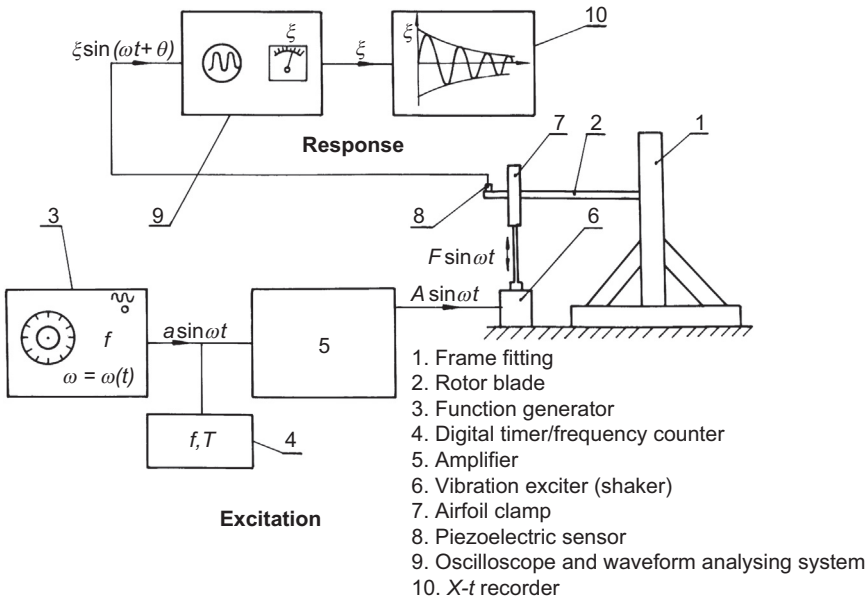

Figure 23.9 Equipment used in vibratory testing.
Rasuo (2010a).

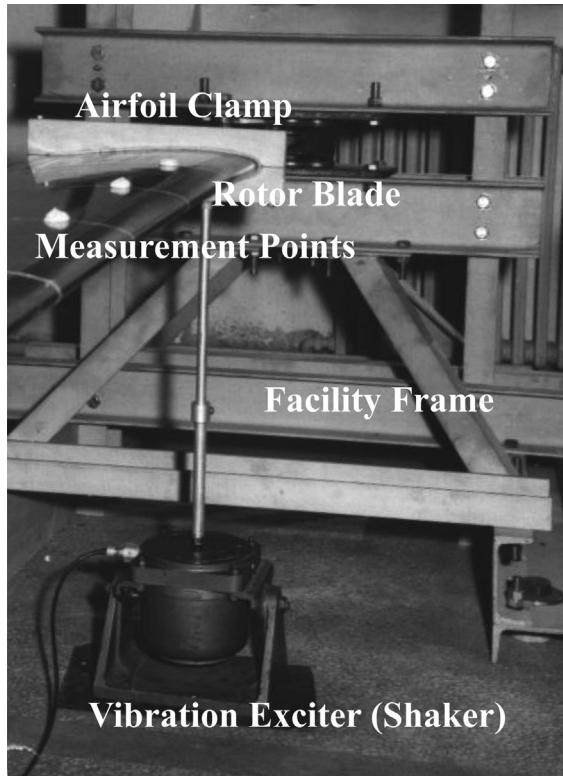

Figure 23.10 Rotor blade in vibratory testing.

23.2.2 Fatigue testing

The fatigue test program included interlaminar separation (delamination) testing and geometric deformation of the blade cross-sections following the fatigue test program during which real tail rotor blade loads were simulated – the same loads to which the blade is exposed under extreme flight conditions, before and after ballistic damage to the blade (Rasuo, 2000, 2011b).

Fatigue testing of the root part of the blade spar is one of the most important investigations of the helicopter blades made of composite laminated materials, with respect to their load-carrying ability and survivability check-ups. These tests are carried out to define likely delamination of the composite laminated structure, changes of shape of the root part of the blade, and the loss of its load-carrying ability after exposure to a certain cycle of alternating variable loads, which, on their part, are a consequence of the in-flight, combined load influence. The applied test loads include simulated steady centrifugal, vibratory chordwise bending, vibratory flapwise bending, and vibratory torsional pitch motion (Rasuo, 2011b).

The simulated forces' values were as follows: the centrifugal force was 11,350 daN, while resulting excitation alternating variable load that was vertical to the rotation

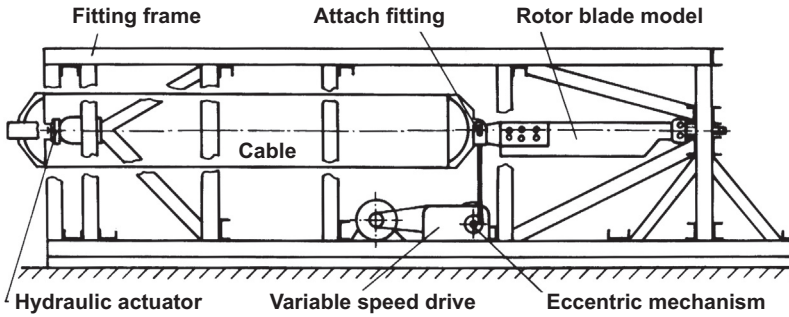

Figure 23.11 Helicopter tail rotor blade fatigue test facility.

plane and originated from vibratory chordwise bending, vibratory flapwise bending, and vibratory torsional pitch motion had a value of 500 daN at the 6.5 Hz (390 rpm) frequency and at the angle of attack of 18°. A special facility frame (Figure 23.11) was constructed to simulate these combined and heavy loads. The facility test frame used in the helicopter tail rotor blade fatigue testing was constructed as a very robust three-dimensional frame made of steel U- and L-profiles and was composed of several basic modules: the facility to which the tail rotor blade was attached and fixed, the excitation group, and modules for centrifugal force simulations (Figures 23.11 and 23.12).

The excitation group consisted of an electric motor with a rating of 2.2 kW and a rotation speed of 1420 rpm, a belt drive with a transmission ratio of 1:3, a variable-speed drive (variable reduction gear) with a transmission ratio of 1−3.25, an eccentric

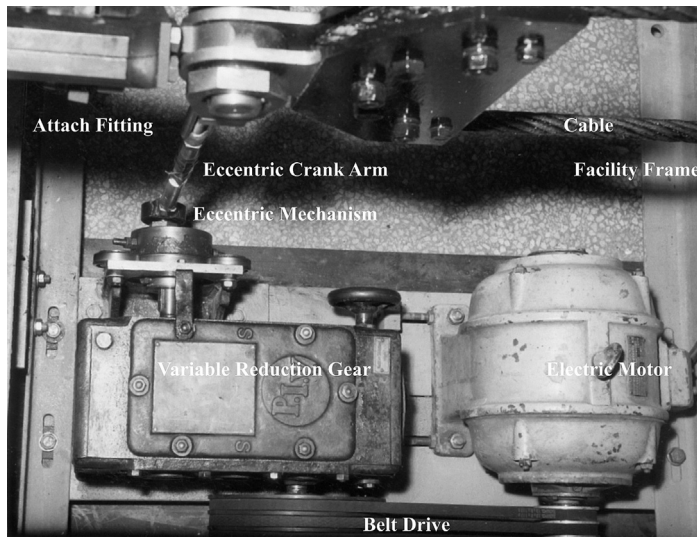

Figure 23.12 The excitation group.

mechanism with an adjustable eccentricity of 0−25 mm, and an eccentric crank arm with bonded strain gages for excitation for selection (Figure 23.12). The variable transmission ratio enabled the desired excitation force frequency to be adjusted. A stroboscope was used for an accurate detection of excitation force frequency, whereas the changeable eccentricity of the eccentric arm allowed adjustment of the excitation force intensity (Rasuo, 2011b).

The module for the centrifugal force simulation included a section for the static load generation, that is the centrifugal force, the section that transmitted the force to the blade root section, and the blade root attachment fitting, at which centrifugal force was applied at one end and, at the same time, excitation force was applied at the other end.

A hydraulic servo-controlled actuator composed of a hydraulic cylinder, distribution system with oil lines and a pump with a servomotor, and control manometer was used as the centrifugal force generator. Its maximum force was 40,000 daN. Thanks to this system, the basic functioning of the facility frame became automatic (Rasuo, 2011b).

The fatigue testing program of the root part of the tail rotor blade, aimed at the assessment of its load-carrying ability and survivability, included (in accordance with the standards) time fatigue tests together with the simulated centrifugal force−relaxing loading program for both damaged and non-damaged blades (Guyett & Cardrick, 1980; Rasuo, 2000, 2011b). The blades were tested for time fatigue by applying the excitation force at a frequency of 6.5 Hz with simultaneous application of full-magnitude centrifugal force in duration corresponding to 1.5×10^6 cycles. After every 3×10^5 cycles, the blade root relaxation was performed by gradually increasing and decreasing the intensity of the centrifugal force in a 0−11350−0 daN range (Figure 23.13).

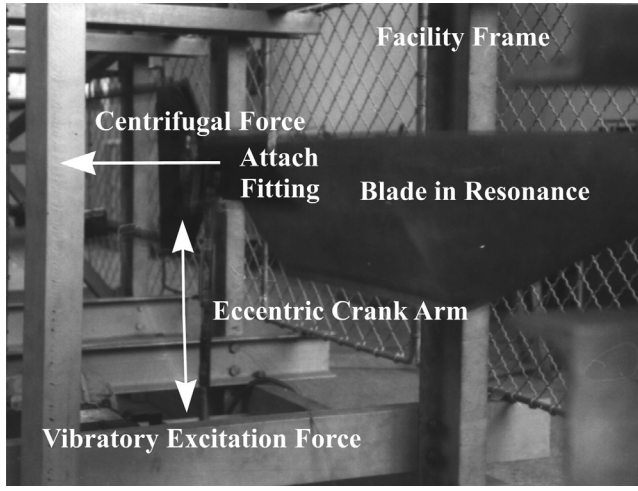

Figure 23.13 Rotor blade in fatigue testing.

23.3 Results: a case study

As a first step within the vibratory investigations, a harmonic analysis for both tail rotor blade types was performed. After the frequencies for the first four harmonics' natural (resonant) modes of oscillations were determined, displacement vectors for the first four basic oscillation modes were measured. Some measurement results are shown in Figures 23.14 and 23.15. Figure 23.14 shows the harmonic analysis results of the first four oscillation harmonics for the non-damaged tail rotor blade, while Figure 23.15 gives a comparative presentation of the second oscillation mode for both a non-damaged and a damaged tail rotor blade.

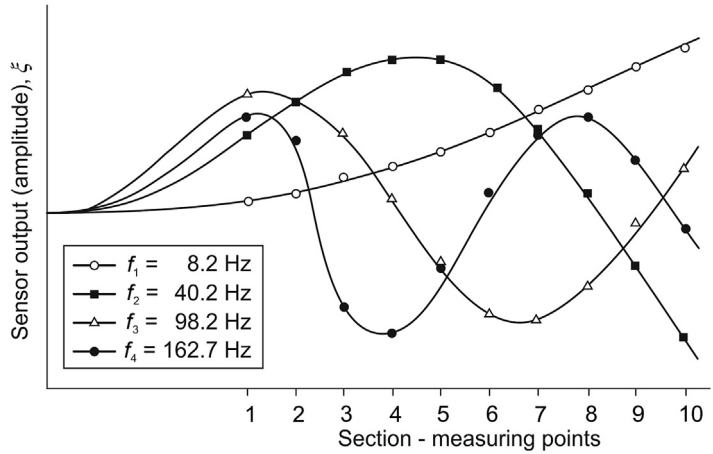

Figure 23.14 Natural modes of oscillation for the non-damaged tail rotor blade.

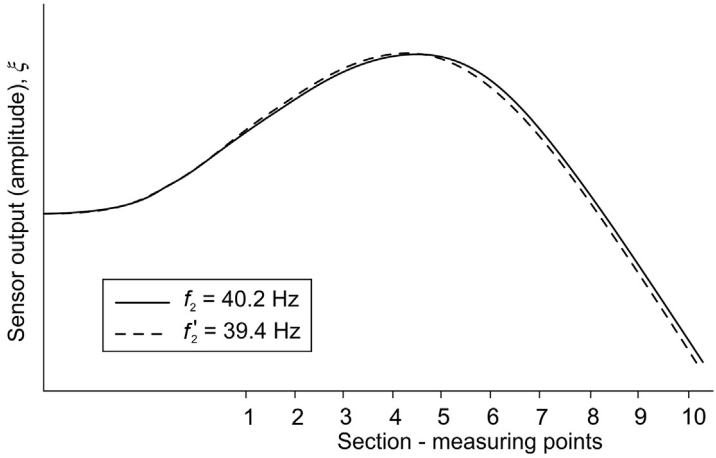

Figure 23.15 The second oscillation mode for both non-damaged ($f_2 = 40.2$ Hz) and damaged ($f_2' = 39.4$ Hz) tail rotor blade.

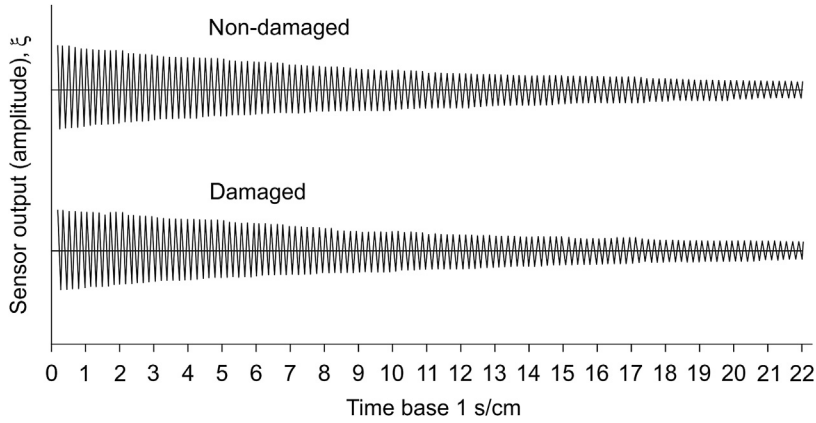

Figure 23.16 Structural damping for both non-damaged and damaged tail rotor blade.

The tail rotor blades' structural damping was determined from amplitude reduction of free vibrations. Initially, the blades were excited to vibrate with the first basic (resonant) oscillation mode, with gradually decreasing amplitude due to the damping effects of the structure.

The original records obtained from these tests for non-damaged and damaged tail rotor blades at the measured cross-section 10 with time base 1 s/cm are shown in Figure 23.16.

The logarithmic decrement of the free vibrations was utilized to characterize the structural damping diagram (Figure 23.17). Its value is determined as follows:

$$\delta = \frac{1}{n} \ln \frac{x_k}{x_{k+n}} \tag{23.1}$$

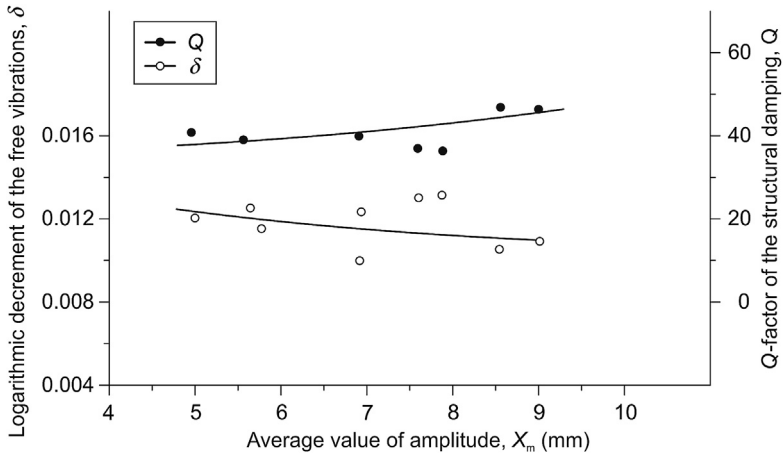

Figure 23.17 Logarithmic decrement and Q-factor of non-damaged tail rotor blade.

where $n = 10$ is the number of observed oscillations and x_k is observed initial amplitude in the time interval, whereas the corresponding average value of amplitude is

$$x_m = \frac{1}{2}(x_k + x_{k+n}) \tag{23.2}$$

The Q-factor is also commonly used to define the structural damping; it gives relative energy (E) reduction in successive oscillations. The Q-factor is defined as

$$Q = \frac{E_1}{E_1 - E_2} \approx \frac{1}{2\delta} \tag{23.3}$$

where $E_1 - E_2$ is the relative energy reduction in successive oscillations (the energy dissipation in successive oscillations).

The structural damping results for the non-damaged tail rotor blade expressed by the logarithmic decrement and Q-factor are given in Figure 23.17.

In the course of fatigue investigations the behaviour of the blade, particularly of the damaged parts, was closely followed. No further damages or delamination of the structures (i.e. no further changes) were observed at the damaged areas in the course of the testing itself (Heida & Platenkamp, 2012; Rasuo, 2011b).

When the fatigue testing program was completed on both non-damaged and damaged blades, further detailed check-ups on the deformation and degradation of the geometrical shape of the blades and delaminations were carried out. No changes were observed on either type of blade. Also, no delamination was observed and the damaged areas of the blades were not expanded in any way (Mikulik & Haase, 2012; Rasuo, 2011b).

23.4 Result analysis and discussion

The vibratory testing results were, surprisingly, the same for non-damaged and damaged heavy transport helicopter tail rotor blades. The obtained differences in frequencies and displacement vectors for some basic types of oscillation were within the 2−5% range. The structural damping results coincided to an even higher degree and the differences in the logarithmic decrement and Q-factor were less than 2% (Figure 23.17). These minor differences in basic dynamic characteristics of non-damaged and damaged helicopter tail rotor blades made of composite laminated materials cannot significantly change or endanger the helicopter flight security.

The results of the damaged tail rotor blade fatigue testing have proved that such a severely damaged blade is capable of performing all its vital functions on the helicopter, even after 65 working hours in extremely difficult flight conditions (Ball, 2003; Rasuo, 2004).

A very interesting and extremely important result is that the damaged blade survived the entire testing program with all and full loads relevant to the non-damaged blade. This result certainly proves the superiority of composite laminated materials for the production of aircraft vital and load-carrying parts.

The degradation level of the vital mechanical characteristics after penetrating/ballistic damage (Figure 23.8) is within such limits that the mission of this heavy transport helicopter (Figure 23.4) can safely be continued and extended much longer than the minimum 30-min flight prescribed by standards to reach the emergency landing site (Ball, 2003; Rasuo, 2004). Considering the results achieved in vibratory testing as well as in fatigue investigations on non-damaged and damaged tail rotor blades made of composite laminated materials, the obtained level of blade survivability is of such a nature that the aircraft could and would survive even considerably worse damages in both the root and other parts of the blade (Figures 23.15–23.17).

23.5 Conclusions

The stochastic nature of the impact that ballistic damages produce on the helicopter tail rotor blade prevents us from going into more precise and detailed quantitative analysis of the survivability level, and thus we are left only with the possibility to estimate it. The very low levels of differences in the results obtained through the investigation of vibratory characteristics, structural damping, and fatigue characteristics (less than 5%) all point to a low-level vulnerability of composite laminated materials to damages.

Well-designed composite laminated structures can provide a high degree of damage tolerance, and in practice, it is still very difficult to utilize the full fibre strength potential of composite structures. That is why those materials yield constructions with exceptionally high levels of survivability – levels that are so important in both military and civil aviation.

23.6 Sources of further information and advice

- ASNT – The American Society for Nondestructive Testing: https://www.asnt.org
- ASTM – American Society for Testing and Materials: http://www.astm.org
- CEN – European Committee for Standardization: https://www.cen.eu
- CODAMEIN – Composite Damage Metrics and Inspection, EASA: http://easa.europa.eu/
- Composite Structures Damage Tolerance Analysis Methodologies: http://ntrs.nasa.gov/archive/nasa/casi.ntrs.nasa.gov
- Crashworthiness of Composite Aircraft Structures: http://www.dtic.mil/dtic/
- Damage tolerance of composite structures in aircraft industry: http://www.carbon-composites.eu/
- ISO – International Organization for Standardization: www.iso.org
- Journal of Testing and Evaluation (JOTE): www.astm.org/DIGITAL_LIBRARY/JOURNALS/TESTEVAL
- Probabilistic Design of Damage Tolerant Composite Aircraft Structures: http://www.faa.gov/about/office_org/headquarters_offices/ang/offices/tc/http://arc.aiaa.org
- Rotorcraft Structures and Survivability: http://vtol.org/events/rotorcraft-structures-and-survivability

- Structural Composites Armour Works − Expert In Survivability: http://www.armourworks.co.uk/products/exterior-platform-protection/composites/structural-composites/
- Survivability/Vulnerability Information Analysis Center: http://www.bahdayton.com/SURVIAC/index.htm
- The Aircraft Combat Survivability Education Website: http://www.aircraft-survivability.com

Acknowledgements

The author is grateful for the funding provided by the Ministry of Education, Science and Technological Development of Republic of Serbia through Grant no. TR35006. Also, the author is grateful to the following companies: Prince Aviation, JAT Tehnika, and Moma Stanojlovic, for granted pictures.

References

Ball, R. E. (2003). *The fundamentals of aircraft combat survivability analysis and design* (2nd ed.). New York: AIAA Inc. AIAA Education Series.

Bayandor, J., Thomson, R. S., Scott, M. L., Nguyen, M. Q., & Elder, D. J. (2003). Investigation of impact and damage tolerance in advanced aerospace composite structures. *International Journal of Crashworthiness, 8*(3), 297−306.

Carlsson, L. A., Adams, D. F., & Pipes, R. B. (2002). *Experimental characterization of advanced composite materials*. Cambridge, England: Woodhead Publishing Limited.

Eschenfelder, P. (2005). High speed flight at low altitude: hazard to commercial aviation? In *2005 bird strike Committee-USA/Canada seventh annual meeting, Vancouver, BC, bird strike committee proceedings, 7-15-2005*. University of Nebraska − Lincoln.

Ferreira, A. J. M., & Fasshauer, G. E. (July 2007). Analysis of natural frequencies of composite plates by an RBF-pseudospectral method. *Composite Structures, 79*(2), 202−210.

Gerlach, R., Siviour, C. R., Wiegand, J., & Petrinic, N. (07 February 2012). In-plane and through-thickness properties, failure modes, damage and delamination in 3D woven carbon fibre composites subjected to impact loading. *Composites Science and Technology, 72*(3), 397−411.

Guyett, P. R., & Cardrick, A. W. (July 1980). The certification of composite airframe structures', symposium on large-scale composite structures. *Aeronautical Journal, 84*(830/3), 188−203.

Heida, J. H., & Platenkamp, D. J. (2012). In-service inspection guidelines for composite aerospace structures. In *18th world conference on nondestructive testing, 16−20 April 2012, Durban, South Africa* (pp. 1−14).

Herman, A. P., Orifici, A. C., & Mouritz, A. P. (October 2013). Vibration modal analysis of defects in composite T-stiffened panels. *Composite Structures, 104*, 34−42.

Kelly, A. (2011). A materials scientist on: Composites, energy technology, climate change-sustainable development. In *Celebrating 20 years of DFC, a joint Sheffield-Cambridge conference, deformation and fracture of composites (DFC-11) & structural integrity and multi-scale modelling (SI-5), conference chairs: Costas Soutis, Alma Hodzic and Peter Beaumont, Plenary Lecture, 12−15 April 2011*. Cambridge, UK: The Queenś College, The University of Cambridge.

Kreculj, D., & Rasuo, B. (2009). *The problem of impact on aircraft constructions from composite laminates, Tehnika* (Vol. LXIV). No. 6, Belgrade (in Serbian), M1−M8.

Kreculj, D., & Rasuo, B. (June 2013). Review of impact damages modelling in laminated composite aircraft structures. *Technical Gazette, 20*(3), 485−495.

Mikulik, Z., & Haase, P. (2012). *Composite damage metrics and inspection, EASA.2010.C13 final report*. Hamburg: Bishop GmbH − Aeronautical Engineers.

Petit, S., Bouvet, C., Bergerot, A., & Barrau, J.-J. (2007). Impact and compression after impact experimental study of a composite laminate with a cork thermal shield. *Composites Science and Technology, 67*, 3286−3299.

Poon, C. (1990). *A review of crashworthiness of composite aircraft structures*. Ottawa: National Aeronautical Establishment. Aeronautical Note, NAE-AN-63, NRC NO. 31276.

Rasuo, B. (1995). *Aircraft production technology*. Faculty of Mechanical Engineering, University of Belgrade (in Serbian).

Rasuo, B. (1997). Testing of the helicopter tail rotor blade made of composite laminated materials after ballistic damages. In M. L. Scott (Ed.), *11th international conference on composite materials, ICCM-11, Gold Coast, Queensland, Australia, proceedings volume. 2 (Impact), 485−495, Cambridge, England, Woodhead Publishing Limited, July 1997*.

Rasuo, B. (2000). Full-scale fatigue testing of helicopter blades from composite laminated materials. In *The European conference on composite materials, ECCM-9, 4−7 June 2000, Brighton, UK, IOM Communication Ltd. (CD-ROM)*.

Rasuo, B. (2001). Design, fabrication and testing of the helicopter tail rotor blade from composite laminated materials. In *13th international conference on composite materials, ICCM-13, Beijing, China (CD-Rom), June 2001*.

Rasuo, B. (2004). *Aeronautical safeguarding*. Belgrade: Military Academy (in Serbian).

Rasuo, B. (2007). An experimental methodology for evaluating survivability of an aeronautical constructions from composite materials: an overview. *International Journal of Crashworthiness, 12*(1), 9−15. Woodhead Publishing Limited, Abington Hall, Abington, Cambridge (Taylor & Francis, London).

Rasuo, B. (2010a). Experimental study of the structural damping of composite helicopter blades with different cores. *Plastics Rubber and Composites, 39*(1), 1−5. Maney Publishing, Institute of Materials, Minerals and Mining, London.

Rasuo, B. (2010b). Design, fabrication and testing of the helicopter tail rotor blade from composite materials: an experience, the Royal aeronautical society. In *2010 RAeS structures & materials conference − 2nd aircraft structural design conference, 26−28 October 2010, London, UK (CD-Rom)*.

Rasuo, B. (2011a). An experimental methodology for evaluating survivability or damage tolerance of an aeronautical construction from composite materials. In *Celebrating 20 years of DFC, a joint Sheffield-Cambridge conference, deformation and fracture of composites (DFC-11) & structural integrity and multi-scale modelling (SI-5), conference chairs: Costas Soutis, Alma Hodzic and Peter Beaumont, 12−15 April 2011*. Cambridge, UK: The Queenś College, The University of Cambridge.

Rasuo, B. (March 2011b). Experimental techniques for evaluation of fatigue characteristics of laminated constructions from composite materials: full-scale testing of the helicopter rotor blades. *Journal of Testing and Evaluation (JTE), 39*(2), 237−242. ASTM International, USA.

Raymer, D. P. (1999). *Aircraft design: A conceptual approach* (3rd ed.). Washington: AIAA Inc. AIAA Education Series.

Richards, M. G., Hastings, D. E., Rhodes, D. H., Ross, A. M., & Weigel, A. L. (2009). Design for survivability: concept generation and evaluation in dynamic trade space exploration. In *Second international symposium on engineering systems, MIT, Cambridge, MA, 15−17 June 2009*.

Schwarz, C. R., & Drake, H. (May 2001). Survivability engineering. In *Aerospace systems survivability handbook series, joint technical coordinating group on aircraft survivability (JTCG/AS)* (Vol. 4). JTCG/AS-01-D-005, Arlington, VA.

Soutis, C. (2005). Fibre reinforced composites in aircraft construction. *Progress in Aerospace Sciences, 41*(1), 43−51.

Soutis, C., & Beaumont, P. W. R. (Eds.). (2005). *Multi-scale modelling of composite material systems*. Cambridge, England: Woodhead Publishing Limited.

Sultan, M. T. H., Worden, K., Staszewski, W. J., & Hodzic, A. (08 June 2012). Impact damage characterisation of composite laminates using a statistical approach. *Composites Science and Technology, 72*(10), 1108−1120.

Vignjevic, R., & Meo, M. (2002). A new concept of a helicopter sub-floor structure crashworthy in impacts on water and rigid surfaces. *International Journal of Crashworthiness, 7*(3), 321−331.

Computational and experimental study of composite scarf bonded joints

24

Y.W. Kwon
Naval Postgraduate School, Monterey, CA, USA

24.1 Introduction

There are many ways to fabricate polymer composite structures. One of the fabrication techniques for polymer composite structures is the vacuum-assisted resin transfer molding (VARTM) technique. This technique can be applied to virtually any size of polymer composite structure because the fabrication procedure does not require special equipment, like an oven, to contain the composite structure to be constructed. The layered composites are wrapped with a plastic material and the resin is drawn inside the wrapped composites to fill in the gaps among composite layers. Figure 24.1 illustrates the resin flow filling the composite layers using the VARTM technique at a laboratory.

When the composite structures are not too big, they can be constructed using the VARTM technique as a single piece. However, some structures need to be constructed by joining multiple parts because they are too large or they have complex parts. In that case, multiple parts must be connected together. There are various ways to fasten two composite pieces together. One of them is using mechanical joints. Another way is the application of the adhesive bonding technique, such as the single and double lap joints.

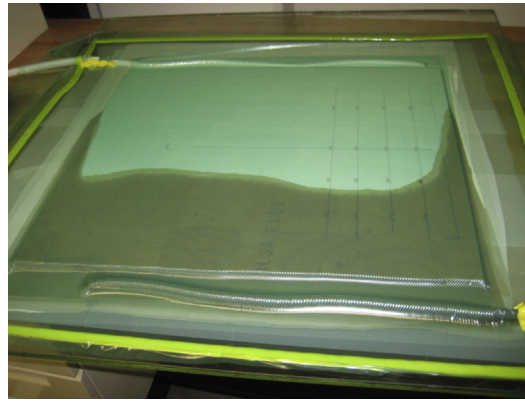

Figure 24.1 Resin running through a sample using the vacuum-assisted resin transfer molding technique.

Structural Integrity and Durability of Advanced Composites. http://dx.doi.org/10.1016/B978-0-08-100137-0.00024-9

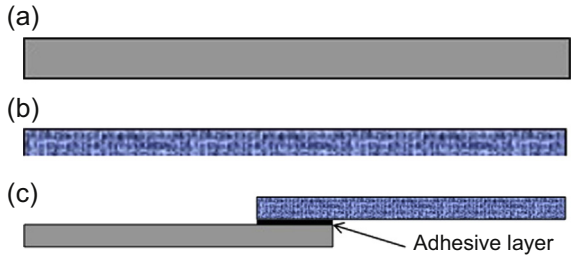

Figure 24.2 Procedure for adhesive bonding technique: (a) construct the first part, (b) construct the second part, (c) apply adhesive to bond two parts.

The scarf joint (Hart-Smith, 1973; Lubkin, 1957) is another joining method. Each binding technique has its own advantages and disadvantages. One of the major differences between the adhesive bonding and scarf joints is the joining process. The adhesive bonding joint is undertaken by applying an adhesive material to the joining interface of the two already fabricated parts, as sketched in Figure 24.2. On the other hand, the scarf joint technique fabricates the second part with partial overlapping with the first part, which was already constructed previously. Therefore, it does not require a separate adhesive material. Figure 24.3 illustrates the scarf joint technique. The same resin/epoxy used to construct the composites can be used for the joining technique. Both parts can also be constructed together using the scarf joining technique. The scarf joint process can be applied to not only a new construction but also a repair of a damaged section.

One of the features of the scarf joint is that the joint section has the same thickness as the other part of the structure. Figure 24.4 shows three different configurations of the scarf joint. The standard scarf joint is the step-butted scarf joint, as sketched in Figure 24.4(a). The second scarf joint is the bevel-stepped scarf joint, as shown in Figure 24.4(b). In this case, the edge of the scarf joint section of the first part is grinded to be smooth. Then, the layers of the second part are stacked at the smooth joint section. This configuration is common for repairs because a damaged section cannot easily be cut out like a stepped shape. The third configuration is called the step-overlapped scarf joint, as seen in Figure 24.4(c). This is similar to the step-butted scarf

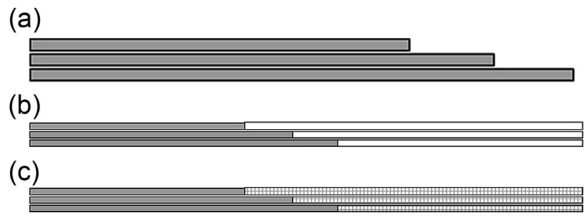

Figure 24.3 Procedure for scarf joint technique: (a) construct the first part using the vacuum-assisted resin transfer molding (VARTM) technique; (b) stack woven layers made of fibers with partial overlap with the first part; (c) apply the VARTM process to construct the second part, which was overlapped with the first part.

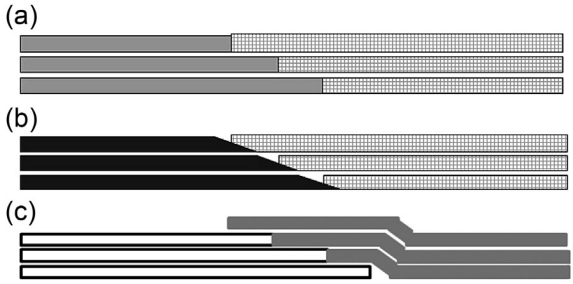

Figure 24.4 Various scarf joint configurations: (a) step-butted scarf joint, (b) bevel-stepped scarf joint, (c) step-overlapped scarf joint.

joint except that each newly applied layer goes over the counterpart layer of the first part. For example, the bottom layer of the second part is on top of the bottom layer of the first part at the scarf joint section. This overlapped joint does not maintain the same thickness at the joint section. However, if there are many layers at the scarf joint section, the thickness of the overlapped section would be very close to the nominal thickness without the overlapping. The overlapped joint has the largest interface area between the two parts, which results in an increase of the joint strength. As a result, the overlapped joint is the most commonly used technique. This chapter will mostly talk about the overlapped joint.

The scarf joint section does not have continuous fibers from one part to the other. As a result, the joint becomes the weakest link of the composite structure, in general. That means failure occurs at the joint section. This chapter discusses the strength of the scarf joint. Both numerical and experimental studies on the scarf joint strength are presented. Because the scarf joint consists of multiple interfaces, the general interface strength is discussed first and the scarf joint strength is discussed later. The interfaces between the layers made of the same materials or different materials are also considered. The computational study is focused on how to model the interface so as to predict the interface strength accurately and reliably. Additionally, a technique to strengthen the interface using nanoparticles, especially carbon nanotubes (CNT), is also presented. Usage of proper nanoparticles may prevent failure at the scarf joint interface, and may change the failure mode and location and, eventually, the failure strength of the whole composite structure. The nanoparticles can be also used as a crack growth sensor. That means the nanoparticles are introduced at the interface with multifunctional purposes.

24.2 Computational modeling of joint interface

24.2.1 Interface modeling

Interface failure is one of the common failure modes in composite structures. The interface can be at different length scales. At the micro-length scale, there is an interface between the particle/fiber and matrix materials. On the other hand, an interlayer between two neighboring layers is an interface at the macro-length scale. The interface of the scarf joint is the macro-length scale. However, the scarf joint interface consists

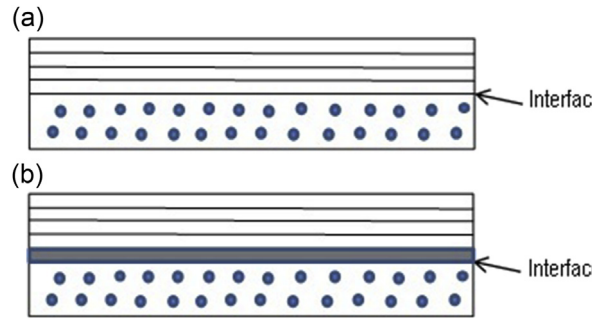

Figure 24.5 Comparison between infinitely thin and finite-thickness interface layers: (a) infinitely thin interface layer, (b) finite-thickness interface layer.

of multiple piecewise interlaminar interfaces constructed at different layer locations, as shown in Figure 24.3.

Modeling an interface can be conducted in two different ways. The first way is to neglect the thin resin layer between the two composite layers, called an infinitely thin interface layer. The second technique is to include the thin resin layer, called a finite-thickness interface layer, as sketched in Figure 24.5. Previous studies suggested that it is necessary to determine the stress at the interface layer in order to predict the interface failure reliably (Kwon & Craugh, 2001; Kwon & Marron, 2009). In other words, the interface layer must be included explicitly in the analysis, as shown in Figure 24.5(b).

The interface layer is generally much thinner than the thickness of the composite structure, even compared to an individual layer of the composite. Therefore, finite element modeling of the interface layer is computationally cumbersome or expensive. One way to alleviate such a problem is using a solid-like shell element. The geometry of the plate/shell element is like a three-dimensional (3-D) brick element with six sides and eight corners. At each node, the plate/shell element has three displacement degrees of freedom but no rotational degree of freedom. One difference is that the plate/shell element is very thin along the thickness direction, such that the aspect ratio of the side length to the thickness becomes very high. Such a large aspect ratio is not permitted in a typical 3-D solid element model because such a large ratio would affect the accuracy of the solution. Therefore, the solid-like plate/shell element can model the interface layer very effectively.

24.2.2 Solid-like plate/shell finite element

The detailed formulation of the solid-like plate/shell finite element was given at Kwon (2013), Craugh and Kwon (2013) and is briefly presented here. The plate/shell element, sketched in Figure 24.6, has eight nodes like a 3-D brick element. The development of high-order plate/shell elements is straightforward from this element so that the eight-node element is discussed here. Since the element has nodal displacements at both top and bottom surfaces, the elements can be stacked together to represent a laminated composite. Additionally, very thin interface layers can be also modeled with ease using this element.

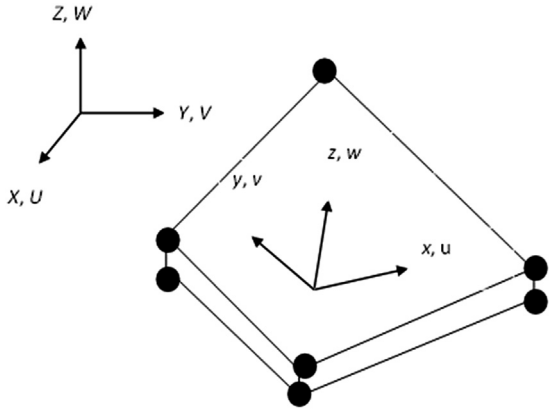

Figure 24.6 Eight-node plate/shell element. The lowercase letters indicate the local coordinate system while the uppercase letters denote the global coordinate system.

The finite element formulation uses a high-order bending theory such that the total strain energy includes the bending strains, transverse shear strains, and transverse normal strain. As a result, the plate/shell element stiffness matrix in terms of its local axes, that is, the lowercase letter system in Figure 24.6, is expressed as

$$[K_{\text{local}}] = \int_{\Omega^e} [B_b]^T [D_b][B_d] \mathrm{d}\Omega + \int_{\Omega^e} [B_s]^T [D_s][B_s] \mathrm{d}\Omega + \int_{\Omega^e} [B_z]^T D_z [B_z] \mathrm{d}\Omega \tag{24.1}$$

where the matrix related to the bending strains is

$$[B_b] = [B_{b1} \quad B_{b2}] \tag{24.2}$$

$$[B_{bi}] = \begin{bmatrix} H_i \frac{\partial N_1}{\partial x} & 0 & 0 & H_i \frac{\partial N_2}{\partial x} & 0 & 0 & H_i \frac{\partial N_3}{\partial x} & 0 & 0 & H_i \frac{\partial N_4}{\partial x} & 0 & 0 \\ 0 & H_i \frac{\partial N_1}{\partial y} & 0 & 0 & H_i \frac{\partial N_2}{\partial y} & 0 & 0 & H_i \frac{\partial N_3}{\partial y} & 0 & 0 & H_i \frac{\partial N_4}{\partial y} & 0 \\ H_i \frac{\partial N_1}{\partial y} & H_i \frac{\partial N_1}{\partial x} & 0 & H_i \frac{\partial N_2}{\partial y} & H_i \frac{\partial N_2}{\partial x} & 0 & H_i \frac{\partial N_3}{\partial y} & H_i \frac{\partial N_3}{\partial x} & 0 & H_i \frac{\partial N_4}{\partial y} & H_i \frac{\partial N_4}{\partial x} & 0 \end{bmatrix} \tag{24.3}$$

the matrix associated with the transverse shear strains is

$$[B_s] = [B_{s1} \quad B_{s2}] \tag{24.4}$$

$$[B_{si}] = \begin{bmatrix} N_1 \frac{\partial H_i}{\partial z} & 0 & H_i \frac{\partial N_1}{\partial x} & N_2 \frac{\partial H_i}{\partial z} & 0 & H_i \frac{\partial N_2}{\partial x} & N_3 \frac{\partial H_i}{\partial z} & 0 & H_i \frac{\partial N_3}{\partial x} & N_4 \frac{\partial H_i}{\partial z} & 0 & H_i \frac{\partial N_4}{\partial x} \\ 0 & N_1 \frac{\partial H_i}{\partial z} & H_i \frac{\partial N_1}{\partial y} & 0 & N_2 \frac{\partial H_i}{\partial z} & H_i \frac{\partial N_2}{\partial y} & 0 & N_3 \frac{\partial H_i}{\partial z} & H_i \frac{\partial N_3}{\partial y} & 0 & N_4 \frac{\partial H_i}{\partial z} & H_i \frac{\partial N_4}{\partial y} \end{bmatrix} \tag{24.5}$$

$$[B_z] = [B_{z1} \quad B_{z2}] \tag{24.6}$$

and the matrix for the transverse normal strain is

$$[B_{zi}] = \left[0 \quad 0 \quad N_1 \frac{\partial H_i}{\partial z} \quad 0 \quad 0 \quad N_2 \frac{\partial H_i}{\partial z} \quad 0 \quad 0 \quad N_3 \frac{\partial H_i}{\partial z} \quad 0 \quad 0 \quad N_4 \frac{\partial H_i}{\partial z}\right] \tag{24.7}$$

Additionally, $N_i(\xi, \eta)$ $(i = 1, 2, 3, 4)$ is the 2-D isoparametric shape function for the displacement interpolation on the in-plane while H_j (ζ) $(j = 1, 2)$ is the 1-D isoparametric shape function for the displacement interpolation along the thickness direction. Thus, the 3-D shape function is obtained from the product of the 2-D and 1-D shape functions. Furthermore, $[D_b]$ and $[D_s]$ are the composite material property matrices for the bending and transverse shear terms. If the elastic modulus $[D_z]$ is selected as an arbitrary large number, the third term in Eqn (24.1) is equivalent to applying the penalty method for the transverse displacements. In order to prevent transverse shear locking, the second term is integrated using a reduced integration technique. The corresponding nodal displacement vector is given as

$$\{d_{\text{local}}\}^T = \{d_1 \quad d_2 \quad d_3 \quad d_4 \quad d_5 \quad d_6 \quad d_7 \quad d_8\} \tag{24.8}$$

$$\{d_i\} = \{u_i \quad v_i \quad w_i\} \tag{24.9}$$

For an analysis of a curved-shell composite structure, the coordinate transformation is conducted from the local coordinate system to the global coordinate system. Let (l_1, m_1, n_1) be the direction cosines between x- and X-axis, (l_2, m_2, n_2) be the direction cosines between y- and Y-axis, and (l_3, m_3, n_3) be the direction cosines between z- and Z-axis. The compatibility of displacements between the two coordinate systems results in

$$\begin{Bmatrix} u^i \\ v^i \\ w^i \\ u^{i+4} \\ v^{i+4} \\ w^{i+4} \end{Bmatrix} = \frac{1}{2} \begin{bmatrix} l_1 + 1 & m_1 & n_1 & l_1 - 1 & m_1 & n_1 \\ l_2 & m_2 + 1 & n_2 & l_2 & m_2 - 1 & n_2 \\ l_3 & m_3 & n_3 + 1 & l_3 & m_3 & n_3 - 1 \\ l_1 - 1 & m_1 & n_1 & l_1 + 1 & m_1 & n_1 \\ l_2 & m_2 - 1 & n_2 & l_2 & m_2 + 1 & n_2 \\ l_3 & m_3 & n_3 - 1 & l_3 & m_3 & n_3 + 1 \end{bmatrix} \begin{Bmatrix} U^i \\ V^i \\ W^i \\ U^{i+4} \\ V^{i+4} \\ W^{i+4} \end{Bmatrix} \tag{24.10}$$

where the superscript "i" changes from 1 to 4, representing the four nodes at the bottom surface of the plate/shell element. As the transformation matrix in Eqn (24.10) is

denoted by matrix [T], the nodal displacement vector and the element stiffness matrix in terms of the global coordinate system are expressed as

$$\{d_{\text{local}}\} = [T]\{d_{\text{global}}\} \tag{24.11}$$

$$\left[K_{\text{global}}\right] = [T]^T[K_{\text{local}}][T] \tag{24.12}$$

24.2.3 Numerical example of interface layer model

In order to compare the two different interface models as sketched in Figure 24.5, a cross-ply composite plate is studied. The composite plate is clamped along the boundary with a uniform pressure loading on the top surface and has the layer-up configuration of [0°/90°/90°/0°]. Each composite layer has the material properties as given below: $E_{\text{L}} = 145$ GPa $(21 \times 10^6$ psi), $E_{\text{T}} = 9.7$ GPa $(1.4 \times 10^6$ psi), $G_{\text{LT}} = 4.1$ GPa $(0.6 \times 10^6$ psi), $G_{\text{TT}} = 3.4$ GPa $(0.5 \times 10^6$ psi), $\nu_{\text{LT}} = 0.3$; $\nu_{\text{TT}} = 0.4$, where subscripts "L" and "T" denote the longitudinal and transverse directions, respectively. When the thin interface layers are modeled explicitly, each layer is assumed to be one tenth of the single layer. The interface layer is considered as an isotropic material, usually the resin material used for the composite. In this study, the elastic modulus is 6.9 GPa $(1 \times 10^6$ psi) and the Poisson's ratio is 0.25.

Figures 24.7 and 24.8 compare the contour plots of the shear stresses at the interface location between the 0° layer and 90° layer. The finite element model without the explicit interface layers also has plate/shell elements at the interface locations even

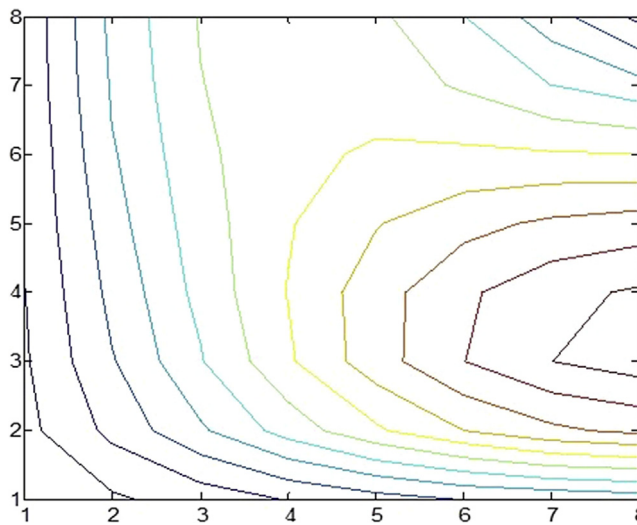

Figure 24.7 Shear stress contour at the interface location without modeling the interface explicitly.

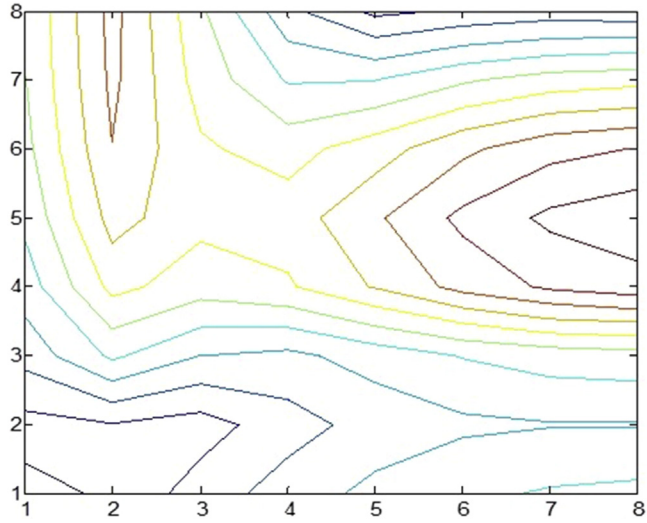

Figure 24.8 Shear stress contour at the interface location with modeling the interface explicitly.

though those elements use the composite material property rather than the resin material property. By doing so, an apples-to-apples comparison of the shear stresses can be made at the same location of the composite plate. As expected, the magnitudes of the shear stresses are very different between the two models with and without explicit interface layers. Even more interesting, the contour plots show a major difference between the two models. The results again suggest that modeling the interface layer explicitly is important to predict failure at the interface.

24.2.4 Scarf joint modeling

The finite element analysis models are developed to predict the strength of the scarf joints. As discussed previously, modeling the interface layer at the critical location of the scarf joint is important to predict the joint strength reliably. Modeling all interface layers discretely at the scarf joint section is time-consuming and computationally expensive. However, if the critical location is not known a priori, a finite element analysis can be performed for the joined structure without incorporation of the discrete interface layers in order to determine the critical location where the failure is expected. For example, global finite element analysis is conducted for a scarf joined structure as shown in Figure 24.9(a) subjected to an axial loading. Examination of the stress distribution around the joined section reveals that the area of the lower ply termination of the overlapped scarf joint has the highest level of stress, as shown in Figure 24.9(b). Then, the local section is isolated for the next-level analysis, which includes the interface layer explicitly. Therefore, this is called the global−local analysis. The displacement boundary condition of the local model is obtained from the solution of the global analysis. One thing to be

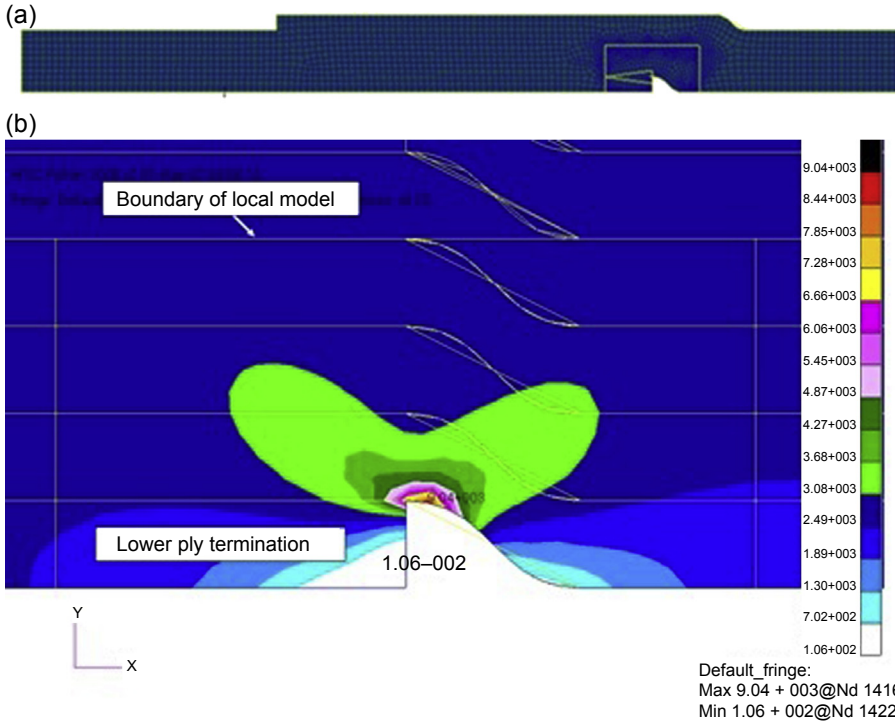

Figure 24.9 (a) Finite element mesh for the whole structure without explicit interface layers. (b) Finite element solution of a section of the global model surrounding the lower ply termination.

noted is that the size of the local model should be large enough such that the effect of the boundary condition would be minimal on the location of the failure zone. Figure 24.10 shows the local model with a discrete interface layer; the local model is denoted by white lines inside the global model as shown in Figure 24.9(a). The discrete interface layer is modeled as a triangular shape because of the boundary condition to be applied from the analysis of the global model. Because the global model does not have the discrete interface layer, the interface layer ends at the boundary of the local model.

In order to predict the strength of the scarf joint, a small-size crack is introduced at the interface layer and fracture mechanics is applied to determine the critical load. There are different ways in which a crack is located inside the interface resin layer. One way is to put the crack parallel to the interface layer, which is called stepped, as sketched in Figure 24.10. Additionally, the crack can be at the interface between the bottom composite layer and the resin layer, inside the resin layer as shown in Figure 24.10, or at the interface between the resin layer and the upper composite layer. The other way is to model the crack in an inclined orientation, as shown in Figure 24.10; this is called tapered. For the inclined crack, the angle must be determined. The joint strength will be different depending on the crack orientation. In order

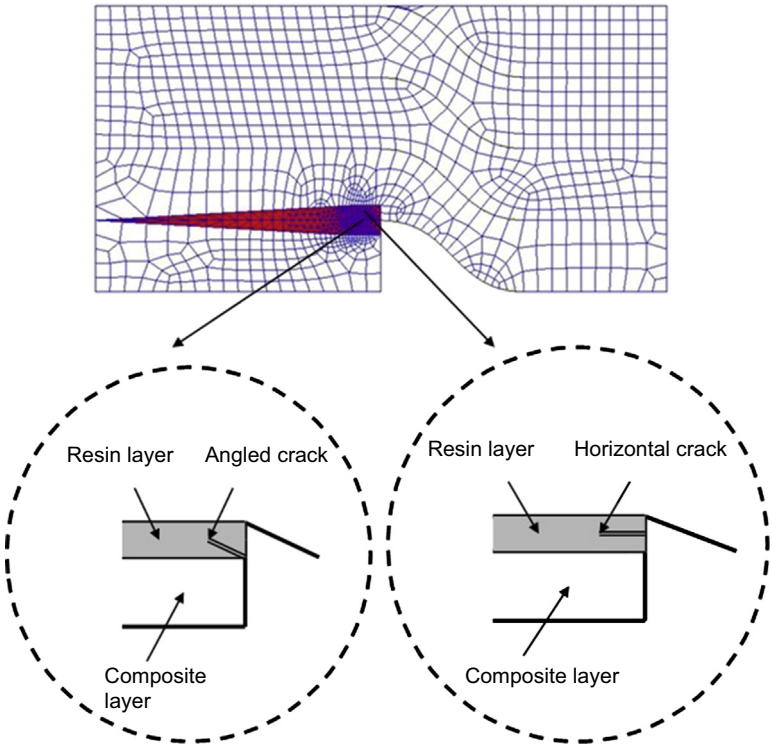

Figure 24.10 Interface layer explicitly included in the local model.

to determine the crack angle uniquely, the angle is selected to be the same as the angle of the taper ratio of the scarf joint section, in other words, the ratio of the scarf joint thickness to the joint length.

Once the crack is assumed at the interface layer, the maximum applicable load is computed such that the stress field at the crack tip reaches the critical value. For example, when the energy release rate at the crack tip becomes the critical energy release rate, the applied stress becomes the joint strength. Because the crack tip has mixed fracture modes, mostly mode I and mode II under in-plane loading, it is necessary to determine a reliable mixed-mode criterion. Reference work (Reeder, 1992) compared multiple mixed-mode fracture criteria.

Some of the common mixed-mode criteria are listed below in terms of mode I and mode II.The simplest and independent criterion is given in terms of the strain energy release rate (SERR), as below:

$$\frac{G_{\mathrm{I}}}{G_{\mathrm{Ic}}} = 1 \text{ or } \frac{G_{\mathrm{II}}}{G_{\mathrm{IIc}}} = 1 \tag{24.13}$$

where subscripts I and II denote mode I and mode II, respectively, and Ic and IIc indicate the critical value of each mode. The mixed linear and quadratic criteria are, respectively

$$\frac{G_{\mathrm{I}}}{G_{\mathrm{Ic}}}+\frac{G_{\mathrm{II}}}{G_{\mathrm{IIc}}}=1 \tag{24.14}$$

$$\left(\frac{G_{\mathrm{I}}}{G_{\mathrm{Ic}}}\right)^2+\left(\frac{G_{\mathrm{II}}}{G_{\mathrm{IIc}}}\right)^2=1 \tag{24.15}$$

The interactive biquadratic criterion (Kwon & Marron, 2009) is expressed as

$$\left(\frac{G_{\mathrm{I}}}{G_{\mathrm{Ic}}}\right)^2+m\left(\frac{G_{\mathrm{I}}}{G_{\mathrm{Ic}}}\right)\left(\frac{G_{\mathrm{II}}}{G_{\mathrm{IIc}}}\right)+\left(\frac{G_{\mathrm{II}}}{G_{\mathrm{IIc}}}\right)^2=1 \tag{24.16}$$

in which m is the interactive constant between mode I and mode II, and it is determined from mixed-mode test data. If the interactive constant becomes zero, the interactive criterion is equal to the mixed quadratic criterion (Eqn (24.15)). If the interactive constant is positive, the mixed modes result in a reduction in the critical applied load when compared to that for the single-mode failure.

In order to evaluate different modeling schemes discussed above, multiple scarf joint specimens are modeled and the predicted strengths are compared to the experimental data. There are four variations in the scarf joint geometry that are used for modeling. The first variation is the thickness. One set of joints has 16 plies of 24-oz glass, giving a total specimen thickness of 0.968 cm. The other set has 24 plies, with a total thickness of 1.463 cm. For each thickness, the second variation is in the scarf taper ratio (length to thickness). The two taper ratios studied are 4:1 and 8:1, one for each thickness, yielding a total of four different geometries to be modeled, as listed in Table 24.1. The two initial crack modeling techniques (stepped and tapered) are considered along with different mixed-mode fracture criteria.

The first crack model is the stepped crack parallel to the bottom layer. Then, three different mixed-mode criteria are used to predict the joint strength of the E-glass composite, which has elastic modulus 17.2 GPa and Poisson's ratio 0.24. The resin

Table 24.1 Scarf configuration matrix

Configuration	Thickness (t) (cm)	Taper ratio (L/t)
Scarf joint 1	0.968	4:1
Scarf joint 2	1.463	4:1
Scarf joint 3	0.968	8:1
Scarf joint 4	1.463	8:1

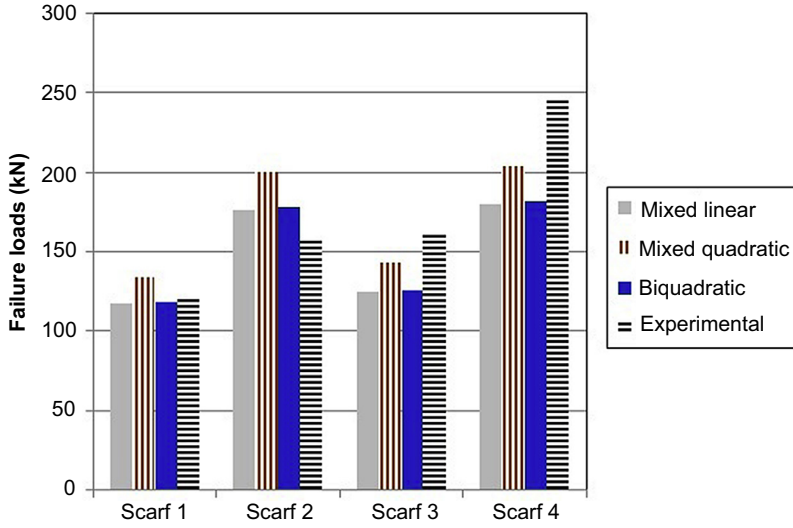

Figure 24.11 Scarf tensile load predictions with stepped crack.

interface layer has elastic modulus 8.34 GPa and Poisson's ratio 0.28. Figure 24.11 compares the four different mixed-mode criteria against the experimental data for the tensile loading. In this study, the mixed linear criterion has an average magnitude of error of 16% compared to experimental data. The mixed quadratic criterion has an error of 17%. The interactive biquadratic criterion, with the "m" variable tuned to −1.8, produces an error of 15%.

The second crack model is the tapered crack. The same three criteria are compared. The mixed linear criterion has an average magnitude of error of 41%. The mixed quadratic criterion has an error of 31%, and the interactive biquadratic criterion has an error of 10%. These results are compared in Figure 24.12. The results suggest

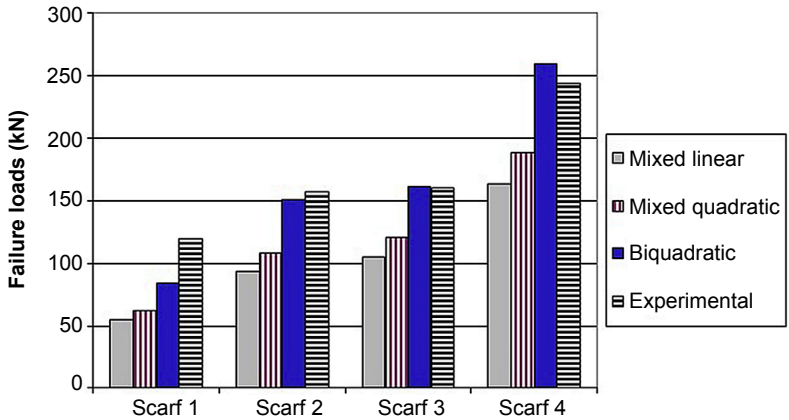

Figure 24.12 Scarf tensile load predictions with tapered crack.

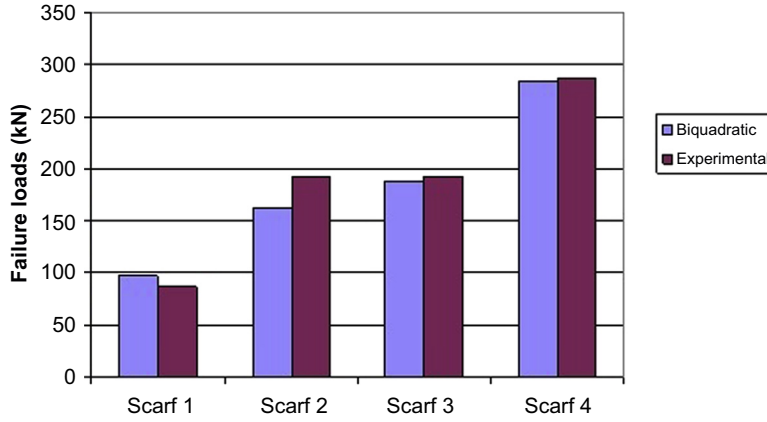

Figure 24.13 Scarf compression load predictions using tapered crack model.

that the best model to predict the scarf joint strength is the tapered crack model inside the interface layer using the mixed biquadratic criterion.

In order to further asses this model, compressive loading is applied to the scarf joined structures that were used in the tensile tests. The predicted compressive strength is compared to the experimental result, as shown in Figure 24.13. The average magnitude of error was 8% for the interactive biquadratic criterion.

24.3 Experimental study of joint interface

24.3.1 Interface strength tests of specimens

In order to measure the critical SERR for mode I and mode II, respectively, the double cantilever beam and three-point bending specimens are tested for an interface crack. The test specimens are sketched in Figure 24.14 and Figure 24.15, respectively. The critical SERRs are computed using the following equations. For the mode I case (ASTM, 2002), the critical SERR is computed from

$$G_{\mathrm{I}} = \frac{3P_{\mathrm{c}}\delta}{2b(a+|\Delta|)} \tag{24.17}$$

where P_{c} is the load when the crack propagates, δ is the displacement at the load point, b is the sample width, a is the initial crack length, and Δ is the horizontal axis intercept from a versus the one-third power of the compliance of the test data. For the mode II case (Todo, Nakamura, & Takahashi, 2000), the critical SERR is determined from

$$G_{\mathrm{II}} = \frac{9a^2P_{\mathrm{c}}^2C}{2b(2L^3+3a^3)} \tag{24.18}$$

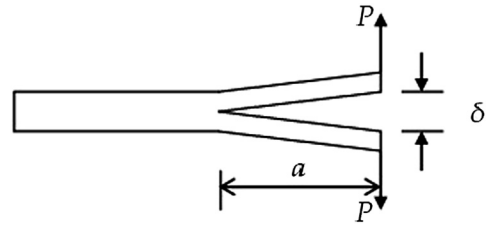

Figure 24.14 Double cantilever beam specimen for mode I testing of interface.

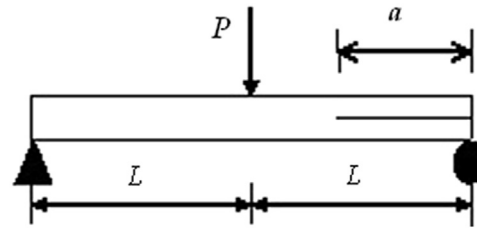

Figure 24.15 Three-point bending specimen for mode II testing of interface.

in which P_c is the critical load when the crack propagates, C is the compliance, a is the initial crack length, b is the sample width, and L is half of the span length.

Test samples with initial cracks were fabricated using the VARTM technique using the Teflon film, which was inserted in the crack location as shown in Figure 24.16 because the Teflon film does not adhere to the resin during the fabrication process. The resin flow during the VARTM process is shown in Figure 24.17. Then, specimens were tested as shown in Figures 24.14 and 24.15.

Figure 24.18 shows the critical SERR for mode I for woven fabric carbon composite samples. The average critical SERR is 264.0 N/m and the standard deviation is 24.4 N/m. Using the digital image correlation (DIC) technique, an image just before the crack propagation is shown in Figure 24.19 for the transverse normal strain component perpendicular to the crack orientation.

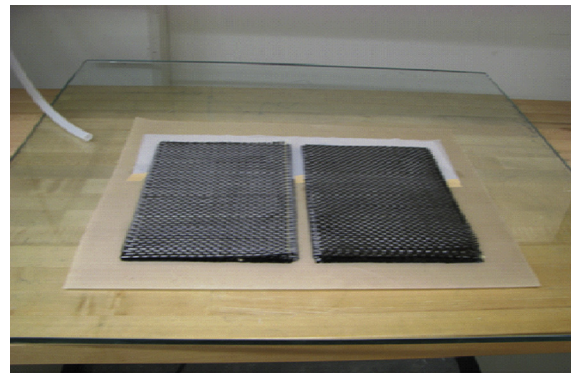

Figure 24.16 Layers of carbon fiber fabric stacked on peel ply.

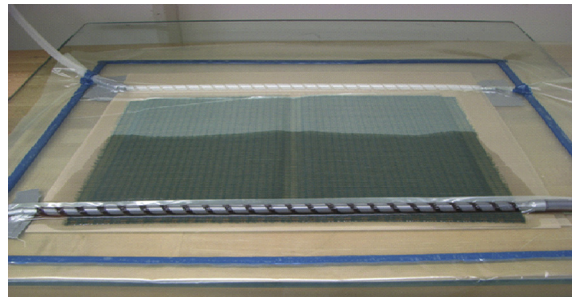

Figure 24.17 Resin flow through carbon fiber layers.

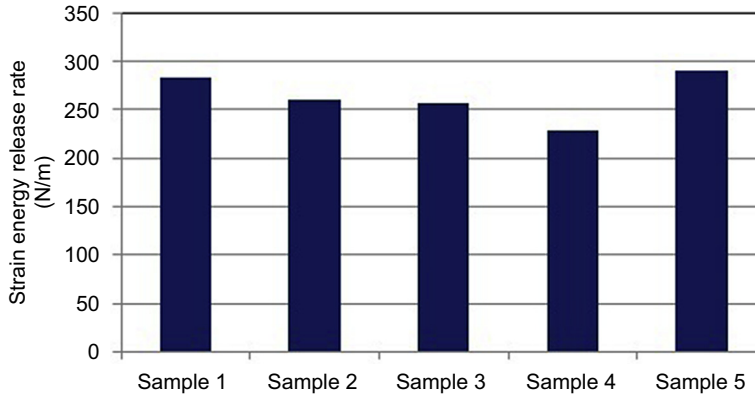

Figure 24.18 Critical strain energy release rate for mode I of woven fabric carbon composites.

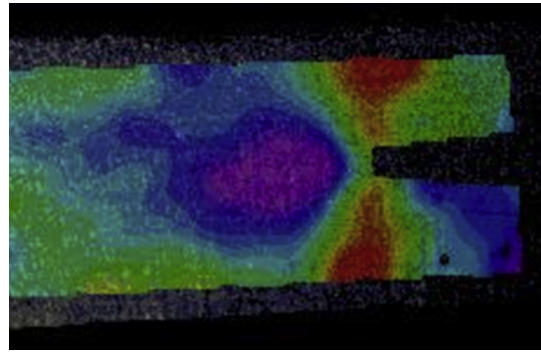

Figure 24.19 Image of transverse normal strain just prior to mode I crack propagation.

Figure 24.20 compares the critical SERR for mode II for woven fabric carbon composite samples. The average critical SERR is 1558.0 N/m and the standard deviation is 111.9 N/m. As expected, the critical SERR is several times greater for mode II when compared to mode I. The ratio of the standard deviation to the average value for the critical SERR is smaller for mode II as compared to mode I.

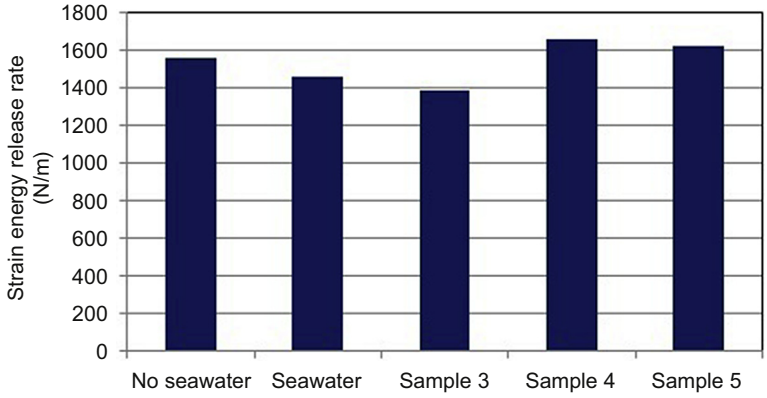

Figure 24.20 Critical strain energy release rate for mode II of woven fabric carbon composites.

24.3.2 Effect of seawater absorption on interface strength

In order to test the effects of seawater absorption on interface strength, samples were soaked in seawater until saturation and then tested in mode II. Seawater was prepared using substrate conforming to ASTM Standard D1141-98 and samples were soaked at room temperature, nominally 70−80 °F (ASTM, 2008). Dimensions and the weight of each sample were recorded prior to soaking. Seawater absorption was tracked by weighing each sample periodically during soaking. When weight no longer changed significantly, the samples were determined to be saturated and mode II testing was conducted as described previously.

The change in weight was negligible after approximately 50 days of soaking, and the percentage of the weight change was 1.4% after 90 days. Samples were removed from the seawater, patted dry, and tested. The test results are compared to those without seawater soaking in Figure 24.21. The seawater reduced the critical SERR by 6%.

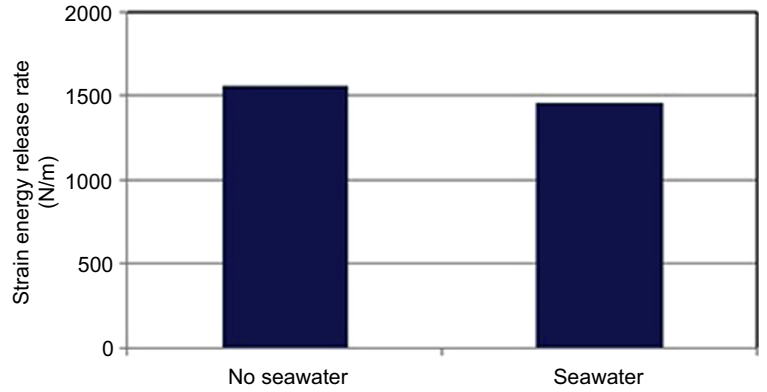

Figure 24.21 Comparison of critical strain energy release rate for mode II of woven fabric carbon composites with and without seawater soak.

Figure 24.22 First half of the scarf joint with four steps.

24.3.3 Scarf joint tests

Scarf joints were constructed using 300 g/m^2 woven Toray T700 carbon fiber fabric as the reinforcement material along with Derakane 510A as the base matrix resin. Each sample consisted of 16 plies of Toray T700 carbon fiber fabrics that combine to form a four-step interface. Each step consisted of four plies of carbon fiber fabric. The total thickness of each test joint was approximately 0.9 cm. The length of each step was approximately 1.3 cm. This generated an overall joint interface of 3.8 cm with an overlap of approximately 1.3 cm. The resulting aspect ratio, interface length divided by overall thickness, was approximately equal to 4.0. Figure 24.22 shows the first half of the scarf joint with four steps, and Figure 24.23 shows a final sample constructed with scarf joint.

The constructed samples were tested for compressive loading. The compressive failure stresses of the scarf joint specimens are shown in Figure 24.24. The failure stress was computed from the applied load at failure divided by the nominal cross-section of the specimen where the load is applied. The average failure stress is 159.5 MPa and the standard deviation is 8.4 MPa. The sample of failed scarf joint is shown in Figure 24.25. As expected, the scarf joint failed at the interface of the joint. For the most of the scarf joint samples, the crack initiates at the bottom end of the joint interface, as illustrated in Figure 24.9.

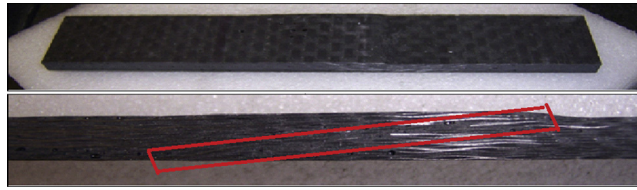

Figure 24.23 Specimen constructed with scarf joint.

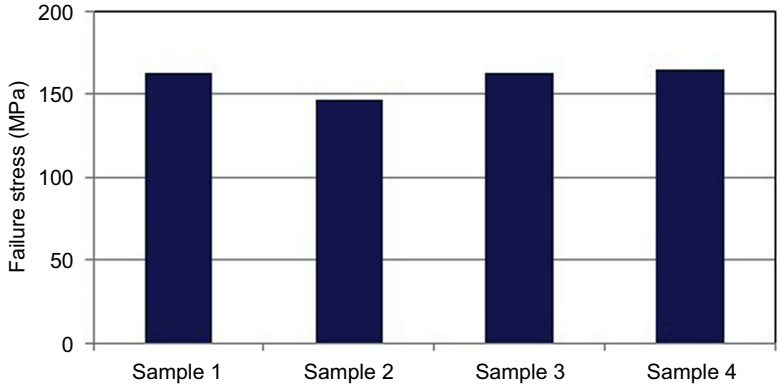

Figure 24.24 Failure stress of scarf joints made of carbon fiber woven fabric composites.

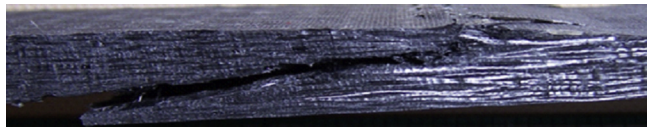

Figure 24.25 Failed scarf joint.

24.3.4 Scarf joint made of different composite materials

The scarf joint specimens were constructed using glass and carbon woven fabric composites (Kwon & Marron, 2009). Because of the difference in thickness between carbon and glass fibers, carbon composites have 16 layers and glass composites have 12 layers to balance the difference in thickness of both materials. Three different samples were created for this experiment. The first of the samples consisted of glass as the base and carbon as the patch, as shown in Figure 24.26. For this study a combination of carbon (as the base) and glass (as the patch) will be referred to as carbon/glass and vice-versa.

The carbon composite side of the joint was first created and cured for 72 h before sanding down the joint in preparation for creating the second half of the joint with glass fiber composites. After both sides were joined and allowed to cure for another 72 h period, the samples were cut to a size of 22.86 × 3.81 cm. The same method was applied for the scarf joint consisting of glass composite as the base and carbon composite as the patch. However, a third joint was created consisting of carbon as the base and glass as the patch, but instead of creating each separately, both were created as a single set for comparison.

The specimens were placed under a compressive load until failure. Figure 24.27 compares the experimental failure loads among the three sets of samples. Key observations are summarized from the test results as follows. For the glass/carbon joint, one

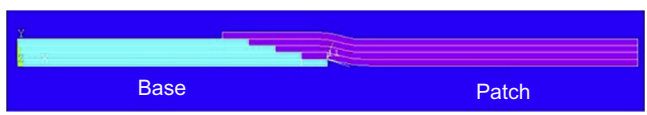

Figure 24.26 Geometry showing base and patch sides.

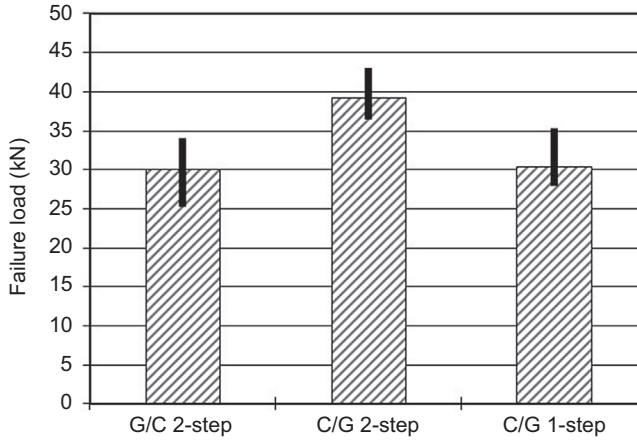

Figure 24.27 Experimental compressive results for all three experiments.

of six samples failed through the joint interface, as shown in Figure 24.25, producing the highest failure load. The other six samples failed through the carbon section near the bottom layer tip of the glass fiber, as shown in Figure 24.28. In the carbon/glass tests, two samples failed through the joint interface and two failed through the carbon section. The carbon/glass joints have greater failure loads than the glass/carbon joints. This suggests that when we have straight carbon layers, there is an increase in the failure strength under compression. In the one-step curing process for the carbon/glass, three samples failed through the joint interface, which produced less strength than the other two samples that failed on the carbon side.

The two-step carbon/glass combination has an average 39 kN failure load compared to a 30 kN load for the one-step process. This is a 30% increase in the failure load. One of the main reasons why the two-step fabrication yields a stronger interface is that the sanding and cleaning process associated with the two-step fabrication seems to provide a stronger interface bonding. Comparing the joints made of hybrid materials to those constructed of the same materials, the carbon/carbon joints are the strongest, as expected. Their joint strength is 170 kN. Glass/glass joints are still multiple times stronger than the carbon/glass or glass/carbon joints (Kwon & Marron, 2009). Finally, the scarf joints for the carbon/glass and glass/carbon joint composites were predicted using the computer model discussed in the previous section. Figure 24.29 shows the von Mises stress plot of a hybrid composite joint. The computed results are compared to the experimental data in Figure 24.30. The computer model overestimates the failure load by 14%.

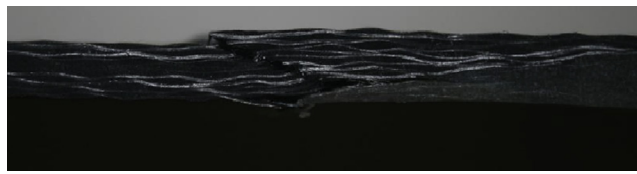

Figure 24.28 Compressive test of glass/carbon composite with carbon side failure.

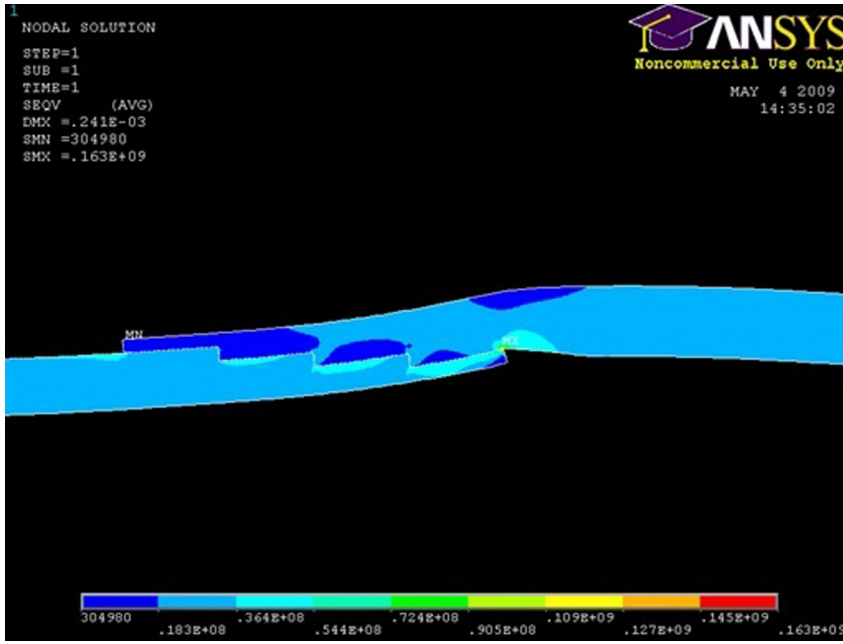

Figure 24.29 von Mises stress plot of a hybrid composite joint.

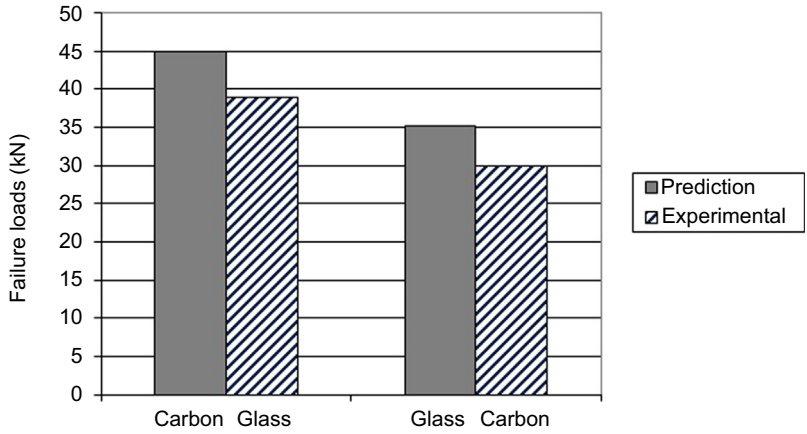

Figure 24.30 Experimental versus finite element method prediction under compression.

24.4 Improvement of interface strength

24.4.1 Interface strength with carbon nanotube inclusion

Because the interface is usually the weakest spot for failure initiation, it is necessary to improve the strength at the interface in order to enhance the overall integrity of the composite structure. To achieve this goal, nanoparticles were introduced at the

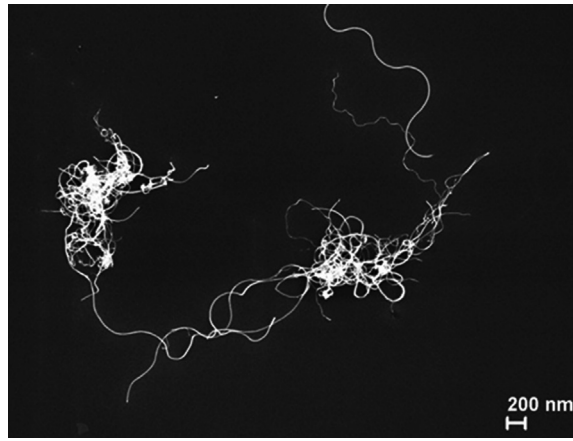

Figure 24.31 Carbon nanotubes viewed using scanning electron microscope.

interface. In particular, CNT was introduced to the interface to increase its resistance to failure (Bily, Kwon, & Pollak, 2010; Burkholder, Kwon, & Pollak, 2011; Faulkner, Kwon, Bartlett, & Rasmussen, 2009). Figure 24.31 illustrates CNT clustered together viewed using a scanning electron microscope.

Figure 24.32 shows a sample with an interface crack at the middle, which is represented by a thick solid line. The CNT was applied at the same interface layer ahead of the crack tip. The thick broken line in Figure 24.32 is the location where CNT was applied. Because CNT was introduced to the interface surface, the amount of CNT was varied in terms of the CNT mass per unit surface area of the interface. Using this measure, three different concentration rates were used for the woven fabric carbon composite samples in order to measure the SERR for the second mode. The rates were 5 g/m^2, 7.5 g/m^2, and 10 g/m^2. The test results are summarized in Figure 24.33 for carbon fiber woven fabric composites. The SERR is largest with the CNT concentration rate of 7.5 g/m^2, and the concentration rate of 10 g/m^2 has an SERR value very close to the former case. The SERR was increased by 20% compared with that without CNT, as shown in Figure 24.33. However, the low concentration rate of 5 g/m^2 yielded a lower SERR value than that without CNT. The test results suggest that a too-small concentration rate of CNT is not effective to improve the interface strength and there is an optimal concentration rate for the interface strength.

Because 7.5 g/m^2 performed the best among the three choices, it is used for the rest of the study. Using this concentration rate, the first mode fracture tests were conducted,

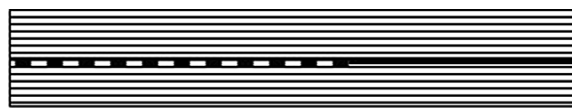

Figure 24.32 Side view of the tested sample with carbon nanotubes (CNT) introduced at the interface.

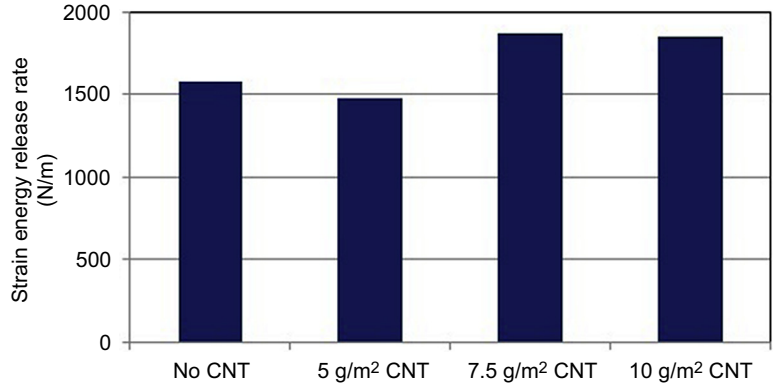

Figure 24.33 Comparison of strain energy release rates of the second mode for interface cracks in carbon fiber woven fabric composites with and without carbon nanotubes applied to the interface.

and the data are compared to that without CNT, as seen in Figure 24.34. The CNT at the interface increased the SERR value by approximately 15%. Both mode I and mode II fracture tests showed that the inclusion of CNT at the interface delays the crack growth at the same interface. The DIC technique was used to view the crack growth at the interface. If there is no CNT at the interface, the initial crack grows at the crack tip as expected.

On the other hand, the CNT resists the crack growth at the tip of the initial crack. This is believed to result from mechanical interlocking of the nanotubes with the resin material at the interface rather than any chemical bonding between the two materials. Some locations at the interface have weaker strength than others, since the distribution of CNT is not uniform. As a result, cracks form at the locations of weak interfaces.

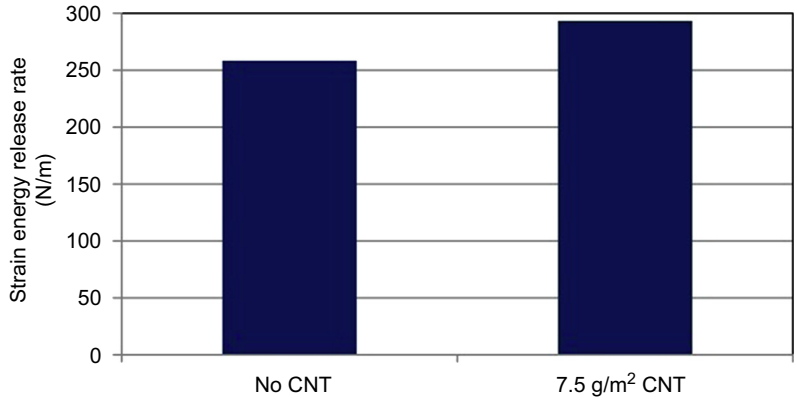

Figure 24.34 Comparison of strain energy release rates of the first mode for interface cracks in carbon fiber woven fabric composites with and without carbon nanotubes applied to the interface.

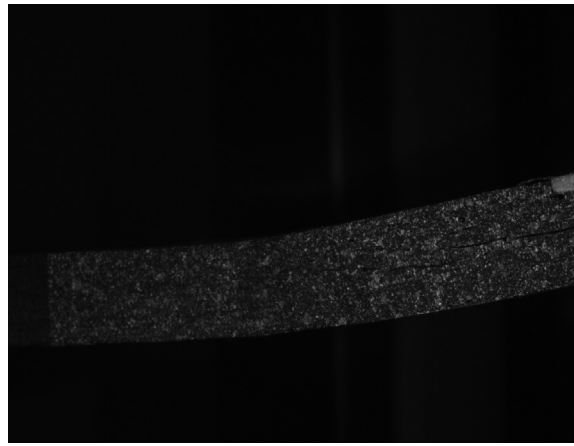

Figure 24.35 Growth of initial crack at the interface containing carbon nanotubes.

Then, the cracks grow and eventually join neighboring cracks. Figure 24.35 shows the cracks at the interface containing CNT. As seen in the figure, there is a gap between the initial crack on the right and a new crack on the left. Furthermore, the fractured interface surfaces were examined for specimens with and without CNT, respectively. The fractured surface without CNT was relatively smooth, while that with CNT was much rougher on both sides. A close examination showed that some continuous fibers were broken and a small chunk was chipped from one side and attached to the other side. This indicates that a crack was forced to propagate through the fibers due to the CNT located in the interface, which resists cracking.

The effect of CNT at the interface was more significant for the E-glass woven fabric composites. Figures 24.36 and 24.37 plot the load versus displacement of the three-point bending tests for mode II without and with CNT at the interface of the E-glass composites, respectively. The SERR values obtained from the plots are compared in

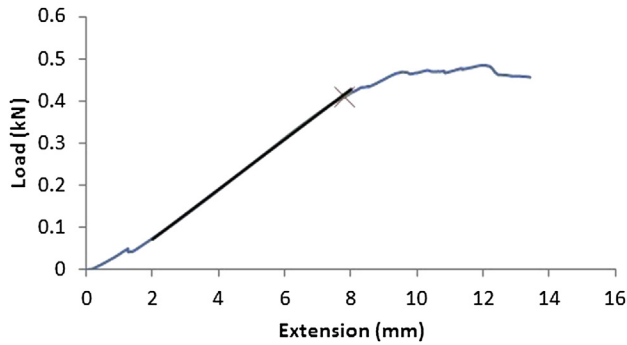

Figure 24.36 Plot of load−displacement curve of the three-point bending specimens for mode II without carbon nanotubes (CNT) at the interface.

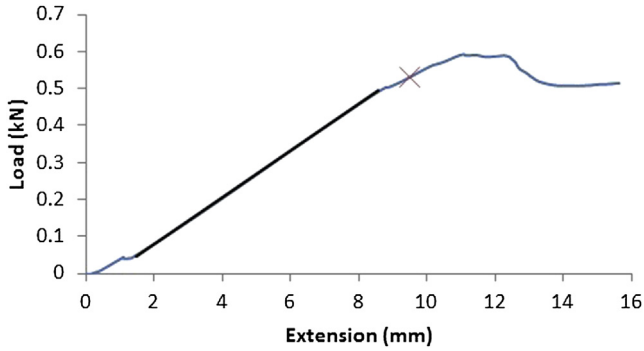

Figure 24.37 Plot of load–displacement curve of the three-point bending specimens for mode II with carbon nanotubes (CNT) at the interface.

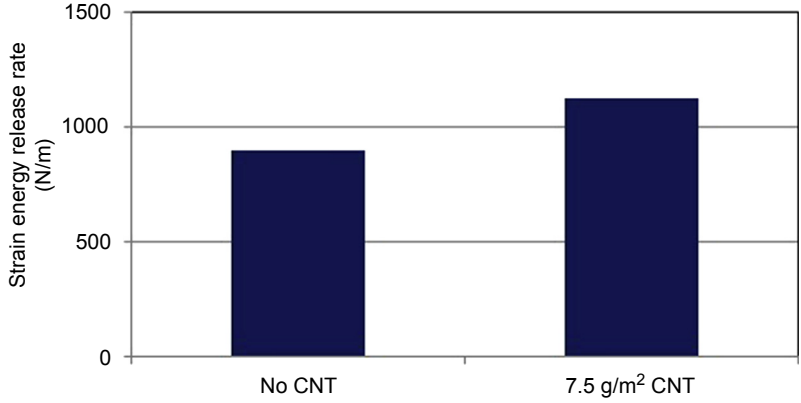

Figure 24.38 Comparison of strain energy release rates of the first mode for interface cracks in E-glass fiber woven fabric composites with and without carbon nanotubes applied to the interface.

Figure 24.38. The increase in SERR is 30% with CNT at the interface. More interestingly, the initial interface crack did not go through the interface containing CNT and deflected into the next layer of the composite, as illustrated schematically in Figure 24.39. Additionally, Figure 24.40 shows the fractured surface of E-glass fiber composites. The picture shows the two parts of a fractured specimen side by side. As seen in the figure, CNT is located below a thin fiber/resin layer on one part.

24.4.2 Interface strength with cyclic loading

The MTS 858 Mechanical Testing System was used for the cyclic testing. The samples were loaded in a three-point bending setup at 2 and 10 Hz cyclic frequencies. Samples were loaded at 2 Hz frequency initially. Later, the frequency was increased to 10 Hz to reduce the loading time for 150,000 cycles. No noticeable difference was observed between the test results at these two frequencies.

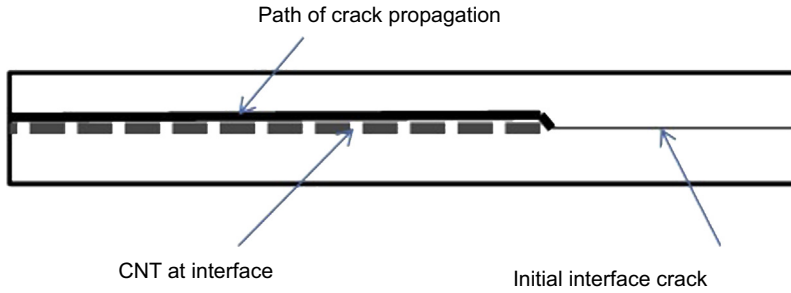

Figure 24.39 Schematic drawing for crack propagation with carbon nanotubes (CNT) at the interface for E-glass woven fabric composites.

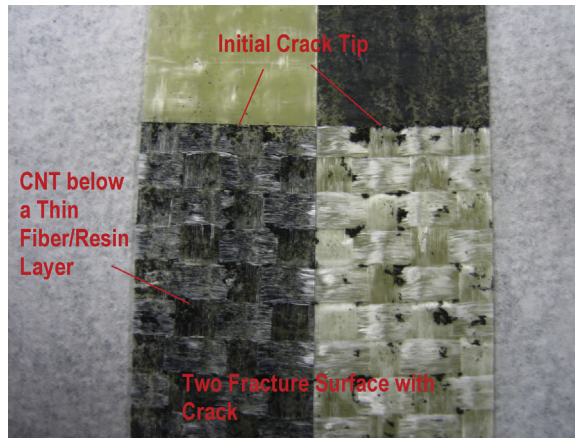

Figure 24.40 Fractured surface of E-glass woven fabric composite with carbon nanotubes (CNT).

Extra precautions were needed to minimize the slippage of the specimen during the cyclic loading. The samples were first subjected to a monotonically increasing loading on the MTS machine (at 1 mm/s displacement rate) to determine the test specifications for the cyclic loading. Due to the difference in stiffness (from the results of the monotonic loading), all the samples were loaded to different displacements in order to have a comparable applied force. The non-reinforced samples were loaded to a 5 mm average displacement with 4 mm cyclic amplitude. Reinforced samples were loaded to a 4 mm average displacement with 3 mm cyclic amplitude.

Each sample was loaded to 150,000 cycles at either 2 or 10 Hz frequencies. Each loading cycle produced a cyclic load such that the maximum and minimum applied forces were as close as possible among differently reinforced samples. Since the two different frequency tests did not result in any major noticeable difference in their results, 10 Hz was used for the rest of the testing so as to reduce testing time. Every non-reinforced or reinforced cyclic testing was conducted for four test coupons, respectively.

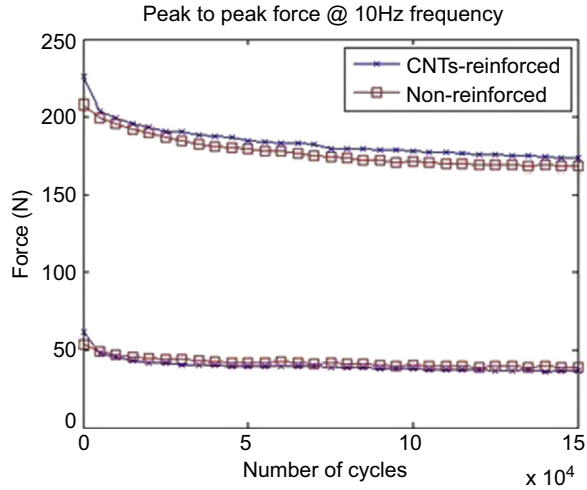

Figure 24.41 Maximum and minimum force plots as a function of load cycles for carbon nanotubes (CNT)-reinforced and non-reinforced samples.

The peak-to-peak (F_{max} and F_{min}) curves showed gradual decreases in the maximum and minimum forces with increasing cycles, as seen in Figure 24.41. This could be due to the accumulating micro-level damage resulting in reduction of the stiffness of the samples. The initial steep change in the forces could be due to the sudden movement of the crosshead of the testing machine. The peak-to-peak curves did not vary much between CNT-reinforced, carbon nanofiber (CNF)-reinforced, and non-reinforced samples. No clear-cut deduction can be derived from these data, though the reinforced samples clearly had higher forces at the same applied displacement.

The crack propagation pattern was observed under a microscope with 10× magnification. There were significant differences between reinforced (both CNT and CNF) and non-reinforced samples. The microscope image showed a crack propagated straight through the resin matrix with little resistance inside the non-reinforced samples.

Very different crack propagation paths were observed in both the CNT-reinforced and CNF-reinforced samples. Perpendicular and 45° crack propagations to the interface layers were widely observed in those samples. The CNT and CNF reinforcement provided strong resistance to the crack propagation, making it more difficult for crack growth. This resulted in the crack propagation seeking alternative paths with lower resistance, which were regions with lower or little concentration of nanoparticle reinforcement due to uneven dispersion of CNT and CNF. The stronger CNT and CNF bonded with the resin matrix increased the fracture toughness of the joint interface. There was also evidence of crack nucleation away from the plane/path of the crack propagation, but still along the joint interface.

The crack lengths of the samples after 150,000 loading cycles were measured by tracing the crack path under a microscope. The crack lengths were averaged across all the samples, as the different frequency loadings did not result in any significant difference in the crack length. The averaged crack length on the non-reinforced

Table 24.2 Averaged crack length after 150,000 cycles

Type	Averaged crack length (mm)
Non-reinforced	11.79
CNT-reinforced	6.21
CNF-reinforced	7.01

samples was approximately twice that of the CNT- and CNF-reinforced samples. The shorter crack length observed on reinforced samples was mainly due to the higher resistance to crack propagation. The CNT and CNF bonded in the resin blocked the crack propagation such that the reinforced samples would require higher loading cycles to achieve the same crack length as the non-reinforced samples. The results in Table 24.2 and microscopy images show that the CNT and CNF reinforcement delays crack growth and further increases structure integrity and service life.

One of the CNT-reinforced samples had a crack length that was relatively longer than the rest. This was due to a crack nucleated in the adjacent resin matrix away from the reinforced joint interface. This region was not reinforced, allowing the crack to propagate through the resin matrix. Therefore, it is important to keep in consideration that any defect in the structure might cause crack nucleation away from the reinforcement region, reducing the overall fracture toughness. However, depending on the application, crack nucleation away from the joint interface might have a less catastrophic effect than failure at the joint interface.

24.4.3 Interface strength under impact loading

Impact testing was conducted using a specially designed drop-weight testing system, described in Kwon, Owens, Kwon, and Didoszak (2010). The carbon fiber composite samples were sandwiched in between two aluminum plates at each end and clamped to the test frame, as shown in Figure 24.42. This setup represented clamped−clamped boundary conditions during impact. A weight of 2 kg was dropped from between 0.45 and 1.05 m height, at a 0.15 m interval, to produce different impact energies. Trial

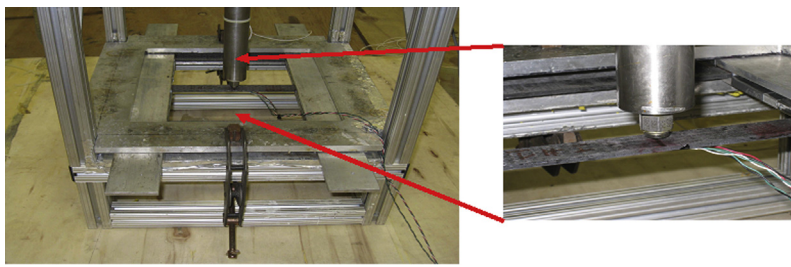

Figure 24.42 Test sample placed on impact test machine.

tests were first conducted to determine the region where damage and crack propagation would occur.

The transient response of the samples upon impact was measured in terms of forces and strains. The force response was measured via an ICP® force sensor manufactured by PCB Piezotronics, Inc. Each sample had a strain gage bonded at the mid-span on the underside for longitudinal strain measurement.

The impact force and strain data from the impact machine for the test samples were compared and analyzed. As an average, five test coupons were tested for each reinforced case even though there was a slight variation from case to case. The force and strain graphs of the CNT-reinforced samples were observed to be smoother, while those for the non-reinforced samples had a more distinct "jerking" shape on the recovery side, as shown in Figures 24.43 and 24.44. This indicates that the non-reinforced samples suffered more damages at the respective impact height.

The plot in Figure 24.43 shows that the impact force for the CNT-reinforced samples is greater than that of the non-reinforced samples. This was expected due to the increased stiffness through the CNT reinforcement at the joint interface. The strain at the center of the beam was also observed to be higher for the CNT-reinforced samples. The higher impact forces experienced by the CNT-reinforced samples therefore translated to higher strain.

The crack lengths for the samples were measured visually at the drop heights of 0.75 and 0.90 m and tabulated in Table 24.3. For the purpose of discussion in this study, failure of the sample was defined as having a crack propagated to the mid-span of the beam. All the samples had comparable crack lengths at drop height of 0.75 m. CNF-reinforced samples had the shortest crack length, averaging 3 mm. However, the differences among the samples were not significant enough to draw a clear-cut conclusion.

Two thirds of the non-reinforced samples failed at a subsequent drop height of 0.90 m, with the other third failing at a drop height of 1.05 m. None of the CNT-reinforced samples failed at 0.90 m drop height. The CNT-reinforced samples failed at drop heights of 1.05 m and above. The CNT reinforcement at the joint interface significantly increased the impact strength and fracture toughness of those samples. Performance of CNF-reinforced samples was comparable to non-reinforced samples in the impact test. Two thirds of CNF-reinforced samples failed at the drop height of 0.90 m.

The samples were viewed under a microscope with 2.5× magnification. The crack patterns for the non-reinforced samples under impact loading were observed to be straight-through, as shown for the cyclic loading. On the CNT-reinforced samples, multiple cracks or "shattered" patterns were widely observed. This indicated that the CNT bonded to the resin provided strong resistance to crack propagation. A higher-impact force was thus required for the crack to propagate through. The crack patterns on the CNF-reinforced samples did not differ much from those of non-reinforced samples. The observations are consistent with the previous discussion on the failure drop height experienced by the respective samples.

After the testing and measurement, the samples were manually pulled apart to inspect the crack surfaces. It was observed that the crack had broken through the resin

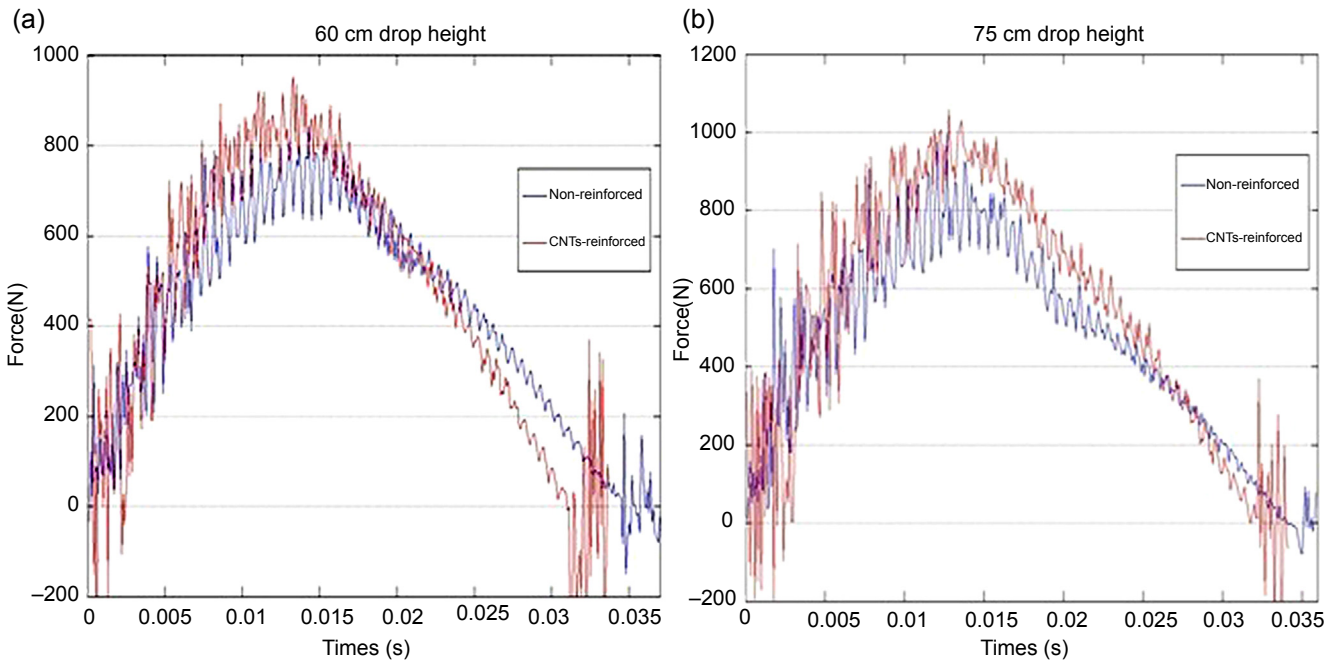

Figure 24.43 Impact force between non-reinforced and carbon nanotubes (CNT)-reinforced samples: (a) samples at 60 cm drop height, (b) samples at 75 cm drop height.

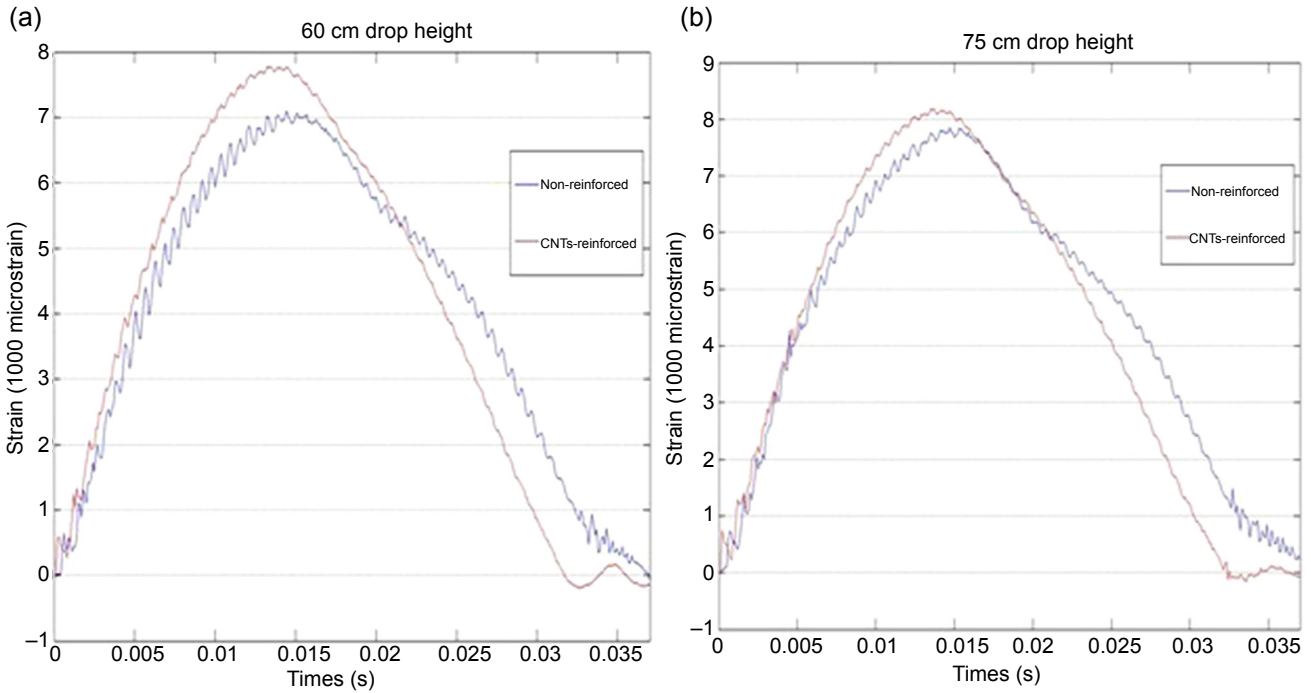

Figure 24.44 Strain between non-reinforced and carbon nanotubes (CNT)-reinforced samples: (a) samples at 60 cm drop height, (b) samples at 75 cm drop height.

Table 24.3 Averaged crack length at drop height of 75 and 90 cm

	0.75 m height	0.90 m height
CNT-reinforced	4.5 mm	9.5 mm (no failure at this impact height)
CNF-reinforced	4 mm	66% failure, 10 mm for nonfailure samples
Non-reinforced	3 mm	66% failure, 12 mm for nonfailure samples

on the non-reinforced samples. There were pieces of broken resin on the crack surface. Traces of the broken resin ceased at the end of the crack growth, indicating that the broken resin was due to the crack propagation during impact test.

The CNT-reinforced samples failed much differently from the non-reinforced samples. There were no obvious broken pieces of resin on the crack surface. Instead, it was observed that the carbon fiber layers were broken through. This showed that the CNT bonded to the resin at the joint interface blocked the crack propagation through the resin. The crack had to break through relatively weaker layers of carbon fiber away from the resin at the joint interface. This resulted in the higher-impact force required for the failure of CNT-reinforced samples. The breakage of the carbon fiber layers resulted in a relatively flatter crack surface, whereas the non-reinforced sample surface maintained the contours of intact carbon fiber fabric weave.

24.4.4 Study of scarf joint strength with carbon nanotube inclusion

Figure 24.45 illustrates how to apply the CNT at the scarf joint interface during the construction of composite samples. Two different CNT concentration rates were

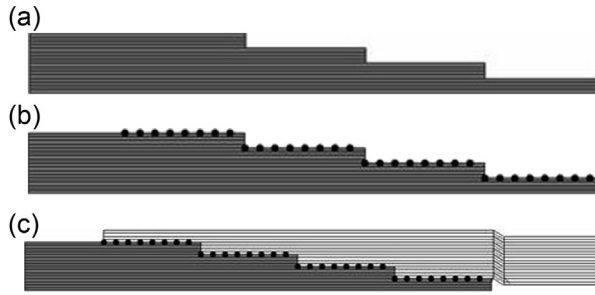

Figure 24.45 Construction of scarf joint with carbon nanotubes (CNT) applied at the interface: (a) fabrication of the bottom layer, (b) application of CNT to the bottom layer, (c) fabrication of the top layer on top of the bottom layer, including CNT at the interface.

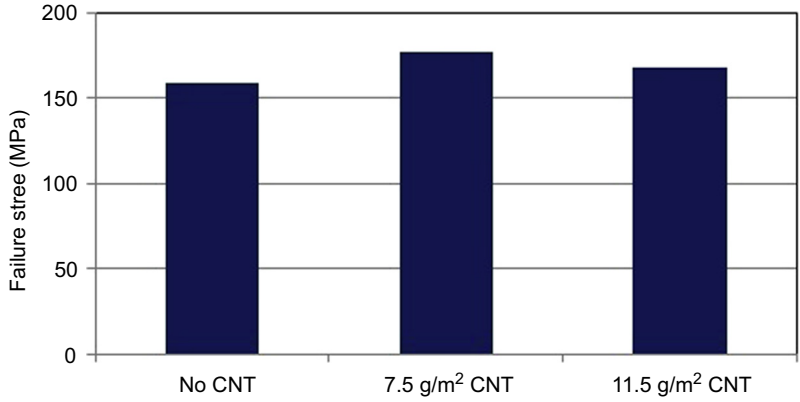

Figure 24.46 Failure stress of the carbon fiber scarf joints with and without carbon nanotubes (CNT) reinforcement at the joint interface.

used: 7.5 g/m^2 and 11.5 g/m^2. Additionally, specimens without CNT reinforcement were also constructed. Several specimens were tested for each case: no CNT, 7.5 g/m^2 CNT, and 11.5 g/m^2 CNT. Figure 24.46 shows the test results. The reinforcement of CNT at the joint interface increases the failure stress. Additionally, as before, the CNT level of 7.5 g/m^2 results in a larger increase in the failure stress, confirming that there is an optimum CNT concentration level. Even though the test data were scattered for multiple specimens, as expected, the lowest maximum stress in the 7.5 g/m^2 data set is greater than the maximum stress of the non-reinforced data set.

Figure 24.47 compares the failure stresses of the scarf joints reinforced with different kinds of CNT at the joint interface. Table 24.4 lists the CNT used in the study. The figure shows that all CNT improved the joint stress. Especially,

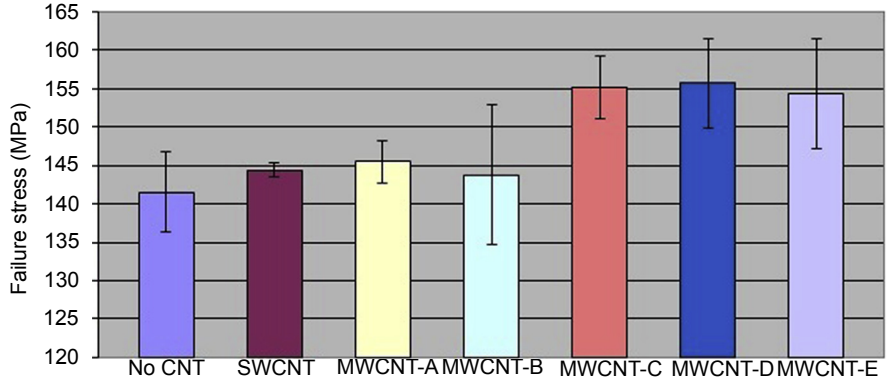

Figure 24.47 Comparison of failure stresses with different kinds of carbon nanotubes (CNT) applied to the interfaces of scarf joints.

Table 24.4 Description of different carbon nanotubes (CNT) samples

A	Multiwall carbon nanotubes, outer diameter 30 ± 15 nm, length 1−5 μm, purity >95%
B	Multiwall carbon nanotubes, outer diameter 25 ± 5 nm, length 10−30 μm, purity >95%
C	Multiwall carbon nanotubes, outer diameter 30 ± 15 nm, length 5−20 μm, purity >95%
D	Bamboo-structure multiwall carbon nanotubes, outer diameter 30 ± 15 nm, length 1−5 μm, purity >95%
E	Bamboo-structure multiwall carbon nanotubes, outer diameter 30 ± 15 nm, length 5−20 μm, purity >95%

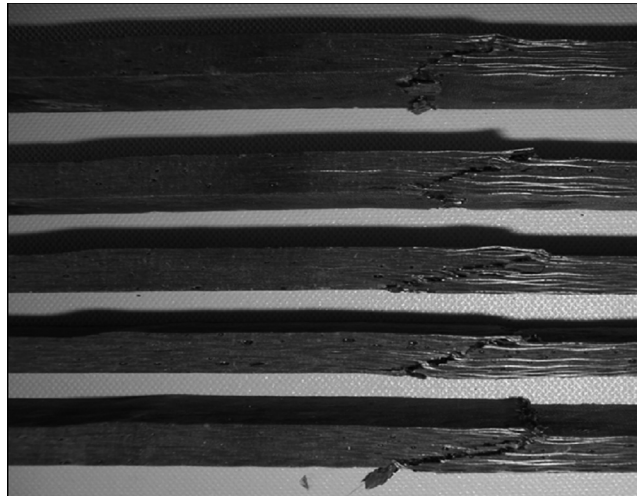

Figure 24.48 Fractured scarf joint samples reinforced with MWCNT-E.

MWCNT-C, D, and E resulted in the largest increase in the failure stress. One thing to be noted is that those CNT yielded failure not at the interface but through the section of the undulation, as shown in Figure 24.48. This suggests that the joint interface is not the weakest link. If the undulated section is modified, this would increase the failure stress even further. Figure 24.49 shows the stress−strain graphs of the scarf joint samples. The CNT at the interface increases not only the failure stress but also the stiffness of the scarf joint. The maximum increase in stiffness among the different CNT is MWCNT-A, which yielded more than 25% increase.

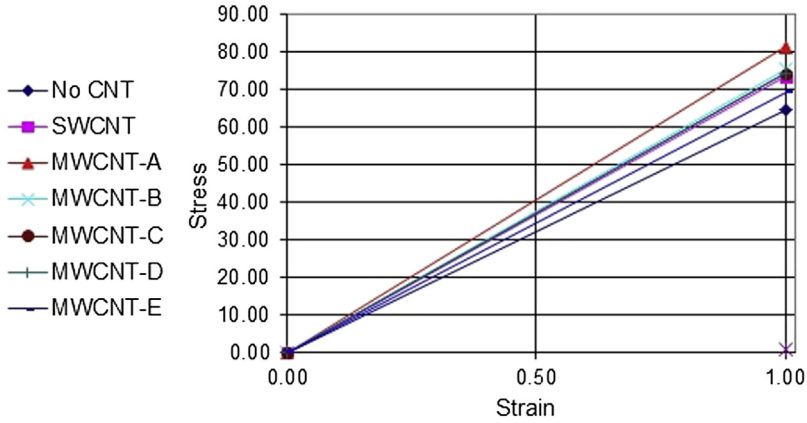

Figure 24.49 Stress−strain graphs of scarf joined samples with carbon nanotubes (CNT) reinforcement.

24.5 Conclusion

The results of the study suggest the following considerations to be included in numerical modeling. One is to model the interface layer using a discrete layer made of a proper material, such as a resin material. Another is to assume an initial crack in the same orientation as the taper ratio of the scarf joint. One more note is that the mixed quadratic failure criterion works well for mixed-mode fractures.

The experimental study showed that nanoparticle reinforcement at the joint interfaces enhances the fracture strength of the composite specimens when they are subjected to static, dynamic, and cyclic loads. Additionally, such an addition of CNT even altered the fracture location of the scarf joints. The scarf joint interface was no longer the weakest part with proper interface reinforcement with CNT. There is an optimal concentration level to maximize the effect of the CNT reinforcement.

References

ASTM Standard D 1141-98. (August 2008). *Standard practice for the preparation of substitute ocean water*.

ASTM Standard D 5528-01. (March 2002). *Mode I interlaminar fracture toughness of unidirectional fiber-reinforced polymer matrix composites*.

Bily, M. A., Kwon, Y. W., & Pollak, R. D. (2010). Study of composite interface fracture and crack growth monitoring using carbon nanotubes. *Applied Composite Materials, 17*(4), 347−362.

Burkholder, G. L., Kwon, Y. W., & Pollak, R. D. (2011). Effect of carbon nanotube reinforcement on fracture strength of composite adhesive joints of naval interest. *Journal of Materials Sciences, 46*(10), 3370−3377.

Craugh, L. E., & Kwon, Y. W. (2013). Coupled finite element and cellular automata methods for analysis of composite structures with fluid-structure interaction. *Composite Structures, 102*, 124−137.

Faulkner, S. D., Kwon, Y. W., Bartlett, S., & Rasmussen, E. A. (2009). Study of composite joint strength with carbon nanotube reinforcement. *Journal of Materials Science, 44*(11), 2858−2864.

Hart-Smith, L. J. (1973). *Adhesively-bonded scarf and stepped-lap joints*. NASA Technical Report CR 112237.

Kwon, Y. W. (2013). Analysis of laminated and sandwich composite structures using solid-like shell elements. *Applied Composite Materials, 20*(4), 355−373.

Kwon, Y. W., & Craugh, L. E. (2001). Progressive failure modeling in notched cross-ply fibrous composites. *Applied Composite Materials, 8*(1), 63−74.

Kwon, Y. W., & Marron, A. (2009). Scarf joint of composite materials: testing and analysis. *Applied Composite Materials, 16*, 365−378.

Kwon, Y. W., Owens, A. C., Kwon, A. S., & Didoszak, J. M. (2010). Experimental study of impact on composite plates with fluid-structure interaction. *The International Journal of Multiphysics, 4*(3), 259−271.

Lubkin, J. L. (1957). A theory of adhesive scarf joints. *Journal of Applied Mechanics, 24*, 255−260.

Reeder, J. R. (February 1992). *An evaluation of mixed-mode delamination failure criteria*. NASA Technical Memorandum 104210.

Todo, M., Nakamura, T., & Takahashi, K. (2000). Effects of moisture absorption on the dynamic interlaminar fracture toughness of carbon/epoxy composites. *Journal of Composite Materials, 34*, 630−648.

Composite bond inspection

25

R.G. Dillingham
Brighton Technologies Group, Inc., Cincinnati, OH, USA

25.1 What are the drivers for creating adhesively bonded aircraft structures?

Aircraft design has always outrun the available materials technologies; an early example would be Leonardo DaVinci's brilliant fifteenth-century concept for a helicopter (Figure 25.1), rather difficult to implement with linen, wood, rope, and cast iron. The most advanced twenty-first-century ideas for the next-generation composite aircraft are no different. These designs depend on adhesive bonding to permit organic, bird-inspired shapes while reducing weight and avoiding stress concentrations. However, these designs cannot be realized until adhesive bonding technology matures to the point where it is as reliable a joining method as mechanical fasteners. Due to the technical challenges and expenses inherent in tooling and autoclaving of complex composite structures, structures composed of simpler components that are secondarily bonded allow utilization of significantly cheaper manufacturing processes than do monolithic or co-cured structures (Hart-Smith, 2002).

When properly executed, the adhesive/adherend interface in a well-designed composite–composite adhesive joint is stronger than either the substrate or the adhesive, and loading to failure results in crack propagation either through the adhesive or

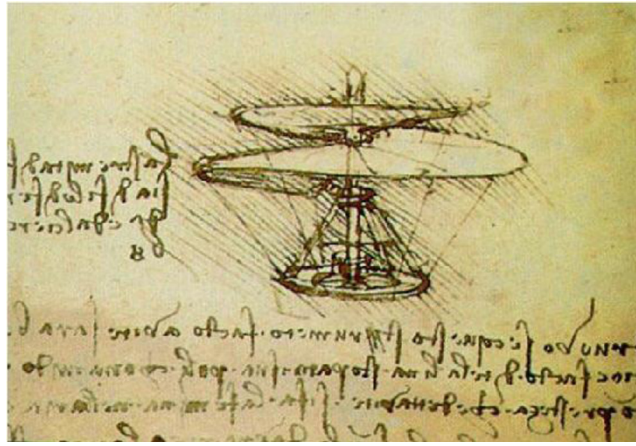

Figure 25.1 DaVinci's helicopter design. A lack of appropriate materials prevented construction and testing.

Structural Integrity and Durability of Advanced Composites. http://dx.doi.org/10.1016/B978-0-08-100137-0.00025-0

between composite lamina close to the bond line. The issue is *proper execution* of the bonding process, and it is the possibility of improper execution that puts such importance on both process control and nondestructive evaluation to create quantifiable confidence in the bonded structure.

There are two approaches to ensuring the quality of adhesive bonds: process control during manufacture and nondestructive testing (NDT) of bonds after manufacture. This chapter discusses promising new technologies for bond process control as well as nondestructive inspection of bonded assemblies. Recent research developments for both approaches will be discussed, advances highlighted, and future opportunities presented. These techniques will allow for a true paradigm shift in aircraft design, and reliable and durable bonded composite structures will become much more commonplace.

25.2 Brief description of an adhesive bond and how it works: bulk properties, interphases, and interfaces

An adhesive bond is created by bringing a liquid adhesive into contact with two adherends, establishing equilibrium contact between the liquid and solid, then inducing a liquid–solid phase change in the liquid. Adhesion results from molecular-scale interactions between the liquid molecules and the solid surface. These are generally secondary molecular interactions: nonspecific Van der Waals and hydrogen bonds. In some adhesive–adherend systems, primary (covalent) chemical bonds are formed, but these are the exception rather than the rule. The phase change converts this liquid–solid interface into a solid–solid interface that is capable of transmitting stress from one substrate to the other through the intermolecular interactions occurring across the interface.

When a bonded structure is loaded, the strain energy is partitioned between each of these components. If loaded to failure, failure occurs in the component having the lowest fracture toughness. The analogy of a chain that fails in its weakest link is very appropriate (Figure 25.2). In a properly executed adhesively bonded structure, the interfacial toughness is generally not in question, and failure is usually limited to cohesive failure within the adhesive or within the laminate (Hart-Smith, 2002). While incomplete adhesive cure due to poor temperature control, poor adhesive mixing, or improper stoichiometry is possible, the most common reason for failure of

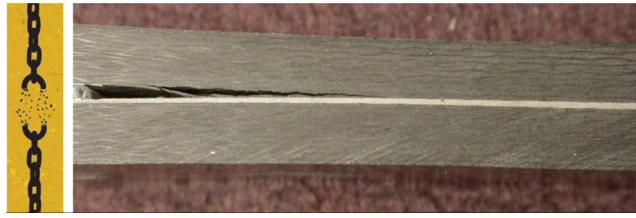

Figure 25.2 Bonded graphite/epoxy composite loaded to failure in mode I. Crack propagation is in the composite, the phase with the lowest fracture toughness in this structure.

bonded repairs is believed to be due to deficiencies in the surface preparation of the area to be bonded (Composite materials handbook-17). For reasons discussed below, surface preparation is very sensitive to seemingly subtle process variables, and the prepared surface prior to application of the adhesive is fragile and subject to damage. Effective, reproducible surface preparation can be challenging even under controlled laboratory conditions.

The properties of the final bonded structure (including static strength, fatigue resistance, and durability) are determined by the bulk properties of the substrate and adhesive, as well as by the interface between them. The bulk substrate properties are established during manufacture of the substrate. The bulk properties of the cured adhesive are determined both by the properties of the incoming material (established by the material supplier) and by processing during the adhesive bonding process.

The properties of the interface between the adhesive and substrate are determined by the composition and structure of a zone extending usually no more than a few molecular layers to either side of the interface (sometimes referred to as the interphase). This component of a bonded structure is created during the bonding process by the interaction of the treated surface and the adhesive. Seemingly small inconsistencies in the surface treatment process can result in adhesive/substrate interfaces with widely varying properties. Because of the modulus mismatch between the substrate and the adhesive, it is the most highly stressed zone in a bonded structure. The combination of difficult-to-control properties along with high stresses makes the interface the most critical component of a bonded structure.

25.3 History of bonded aircraft construction

World War II saw success in all-bonded wood aircraft, such as the de Havilland Mosquito, followed by bonded metallic structures such as the Havilland Dove commuter aircraft, the Fokker F-27 Friendship turbo-prop, and the de Havilland Comet jetliner (Hart-Smith, 2002). The first large-scale bonded composite aircraft were sailplanes manufactured in Germany in the 1950s. From there, composite bonding technology spread to small powered aircraft, general aviation, and then military and transport aircraft. More recently, composite bonding technology is appearing extensively in large commercial aircraft such as the Boeing 787 and the Airbus A350 XWB.

25.4 Composite versus metallic bonded structures

Adhesive bonding of composite structures and metal structures presents distinct challenges. Clean, well-prepared metal surfaces have very high surface energies and interact with adhesives to create strong adhesive bonds. However, the same properties that create strong bonds with adhesives (high chemical reactivity) result in susceptibility to oxidation when exposed to typical service environments. Advances in metal bonding technology have focused on developing pretreatments that create surfaces

that are stable to these environments. Two successful approaches have been chemical passivation through anodization, and barrier coatings such as sol−gel-applied ceramics. Structural metal bonding in aircraft is widely accepted in both manufacture and repair.

Bonding of composite structures is hampered by the relatively low surface energy (low reactivity) of typical prepared composite surfaces. Surface treatments are frequently focused on increasing surface energy though abrasion and fracture (sanding or grit blasting, peel ply removal) or sometimes plasma treatment. Unlike bonded metal structures, bonded composite structures have either no interface (for co-cured structures) or an interface of low reactivity. This low reactivity means that once a good bond is established, the susceptibility to attack by harsh environments is low and bond durability is good.

25.5 Composite bonding processes in aircraft manufacture

Aircraft manufacturing is inherently low volume and is characterized by a large amount of skilled handwork. A typical bonding process involves surface preparation, application of film or paste adhesive, vacuum bagging of the joint, and curing.

Three types of adhesive bonding are commonly employed for manufacture of composite structures (Composite materials handbook-17): secondary bonding, co-curing, and co-bonding. Secondary bonding is the adhesive joining of two precured parts; surface treatment of both surfaces (usually peel ply removal) is required. Co-curing is the simultaneous cure of two parts in contact with an included adhesive film. Co-bonding is the process where a cured structure is laid up against an uncured or partially cured (green) laminate with an adhesive at the interface. The laminate and adhesive are co-cured during a vacuum bag or autoclave cycle.

Co-cured adhesive joints have no discernable interface in the cured structure due to interdiffusion of the adhesive and laminate during cure. They are not sensitive to surface treatment and failures in these structures are uncommon. Secondary bonded and co-bonded joints have at least one interface, however, and failures in these structures are usually interfacial, due either to contaminants such as silicones, prebond moisture (Composite materials handbook-17; Comyn, 1983; Gledhill & Kinloch, 1974; Hart-Smith, 2002; Kinloch, 1987, p. 441), or condensation on a film adhesive due to improper handling after removal from refrigerated storage (Composite materials handbook-17).

25.6 Bonding processes in composite aircraft repair

Adhesive bonding processes are required for many composite aircraft repair procedures. Bonded repairs allow complex shaped patches to be blended into critical aerodynamic surfaces without loss of performance. They also avoid the necessity of

Figure 25.3 Bonded boron/epoxy composite doubler for repair of aluminum aircraft (Hart-Smith, 1999).

introducing the stress concentrations that accompany the holes necessary for mechanical fasteners. Figure 25.3 shows an example of a repair that involved bonding a composite patch onto an aluminum aircraft skin.

A major concern with any bonded repair are disbonds that can occur at installation of the doubler or at any time during the service life of the aircraft (Baker, McKenzie, & Jones, 2004; Gieske, Roach, & Walkington, 1998; Hart-Smith, 1999). Bonded repairs are secondary bonding processes; discrete interfaces are created during the bonding process. Successful bonded repair of aircraft structures involves creating a small area of carefully controlled surface composition on metallic or polymeric surfaces. This area to be bonded is located within a larger area of material that has been in service and is contaminated with a variety of soils picked up during normal aircraft operation: organic and inorganic soils, fuel, hydraulic fluids, etc. Because of the reactivity of freshly prepared surfaces and the proximity and mobility of contaminants in the surrounding area, cleaning of these surfaces sufficiently to obtain reliable adhesive bonds can be particularly difficult in field situations. Furthermore, because the difference between a well-cleaned surface and a contaminated one may only be a few molecular layers, it can be difficult for the technician to establish when the surface has been properly prepared.

25.7 Control of bond quality

The two general types of surface pretreatments used to prepare composite materials for adhesive bonded repairs are *chemical* and *mechanical*. Chemical treatments are generally limited to plasma treatment of the laminate surface. This process is capable of removing small amounts of contaminant along with partially oxidizing the surface,

thereby increasing the surface energy and improving adhesion (Encinas et al., 2014). More recently, laser ablation is being investigated as a composite surface preparation technique (Palmieri, Belcher, Wohl, Blohowiak, & Connell, 2013). These approaches for chemical cleaning and surface oxidation can create excellent bonds but are seeing only limited commercial application due to the expense and unwieldy nature of the process equipment.

Mechanical treatments, including peel ply removal, hand sanding, and grit blasting, are the most commonly used pretreatments for adhesive bonding of aerospace materials, and can produce excellent results. They remove contaminants and weak oxides while roughening the surface. This cleaning and roughening provides for improved wetting (Chin & Wightman, 1996) and allows for mechanical interlocking between the adhesive and substrate (Boerio, Roby, Dillingham, Bossi, & Crane, 2005; Chin & Wightman, 1996; Pocius & Wenz, 1985). Furthermore, abrasion can create reactive sites through fracture of the composite, which increases surface energy and may provide for covalent bond formation in some systems.

The variables associated with mechanical pretreatments are not well understood. Although common (and attractive) due to its simplicity, peel ply produces a notoriously unreliable bonding surface (Hart-Smith, 2002). Hand sanding is better, but process uniformity depends strongly on the skill of the individual mechanic performing the operation. As a manufacturing process, this can be very difficult to control, and results in variable adhesive joint performance. This is an unacceptable outcome for adhesive bonding of critical structures. It is especially a problem for bonds made using room-temperature-curing paste adhesives, but less of a problem when using high-temperature-curing adhesives.

Uniform coverage and reproducible results are more readily obtained using a grit blasting process, particularly when robotic control of the blasting process is used, and it has been vigorously promoted as the ideal surface pretreatment for adhesive bonding of composites (Hart-Smith, 2002). Grit blasting has been successfully employed for years for preparation of metal surfaces. However, unlike metals, composites are very susceptible to damage from overly aggressive abrasive blasting. This can lead to weakening of surface plies and decreased G_{Ic} values for the adhesive joint. Damage may be induced below the surface of the laminate by the blasting process, and has been strongly implicated in weakening of the laminate (Dillingham, Conyne-Rapin, Boerio, Bossi, & Crane, 2003). Furthermore, containment of grit can be a difficult issue. As a result, most repair procedures rely on hand or mechanical sanding followed with solvent wiping.

The difficulty in ensuring precise control of manual surface treatment and bonding processes in manufacturing and repair environments places a premium on development and use of inspection tools, both for process control during bonding operations and for inspection of bonded assemblies. These inspections are not straightforward. The quality of a surface preparation process is defined by the structure and composition of a zone of the laminate that is perhaps 2−3 nm thick: this corresponds to two to three molecular layers. When the bonded structure has been completed, the interface zone that determines the quality of the adhesive joint is now buried beneath many millimeters of laminate and adhesive. The buried interfacial region makes up only about

one millionth of the volume of the bonded assembly. Obtaining useful information about the quality of this buried interface is a challenging task.

25.8 Defects in adhesive joints

Adhesive joint defects can be divided into three categories (Brotherhood, Drinkwater, & Dixon, 2003): gross defects, cohesive defects, and adhesive defects. Gross defects consist of cracks, disbonds, porosity, and voids. These are detectable using conventional NDT techniques such as ultrasonic C-scan. Cohesive defects (defects in cohesive properties) result from errors in materials processing, such as component ratios or poor temperature control during curing, or perhaps environmental attack during service. The degradation in modulus that results from these defects can frequently be identified through other NDT evaluations such as ultrasonic velocity measurements (Jiao & Rose, 1991). Adhesive defects (poor adhesion) result from an adhesive–adherend interface of reduced strength (Jeenjitkaew, Luklinska, & Guild, 2010). Because there is usually no discontinuity or void associated with such defects, they are difficult or impossible to detect using conventional NDT.

25.9 Bond inspection tools

Bond inspection tools can be divided into two classes, those useful for monitoring quality during the bonding process and those useful for inspection of the complete bonded structure. In-process inspection is preferable from an economic standpoint, as quality issues are detected before completion of the structure, when correction becomes extremely expensive. However, certification typically requires some sort of inspection of the completed structure. Unfortunately, there are few inspection techniques available that provide useful information about bonded structure quality.

Tools for in-process inspection include those that monitor quality and consistency of surface preparation and those that provide information regarding the chemical structure of the adhesive and substrate.

Quality and consistency of surface preparation can be monitored through wetting measurements. Adhesive bonding is a wetting phenomenon, that is, it fundamentally rests on the interaction between a liquid adhesive and a solid surface. Wetting is a strong function of surface chemical composition. One way of assuring the quality and consistency of a surface prepared for adhesive bonding is through assuring that the surface has the desired wetting properties (Dillingham & Oakley, 2006). A common approach is through the water break test (ASTM F22-13, 2013), where the surface is flooded with water and uniform flow of the water over the surface is an indicator of the absence of hydrophobic contaminants. This test is not quantitative and is typically restricted to applications where a go/no go evaluation of cleanliness will suffice.

A quantitative and sensitive method for monitoring surface properties is through measurement of contact angle established between a probe liquid and the laminate

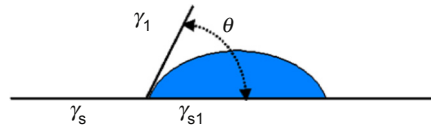

Figure 25.4 Definition of contact angle θ between a liquid and solid surface. γ_s, γ_l, and γ_{sl} refers to the liquid surface tension, the solid surface energy, and the interfacial energy, respectively.

surface. The contact angle is the angle formed by a tangent to a liquid drop and the plane of the laminate surface at the point of contact (Figure 25.4). Conceptually, when a liquid is brought into contact with a solid surface, the liquid molecules partition between continued interaction with other liquid molecules or establishing interaction with molecules in the surface. If interaction with the surface is energetically favored, the interfacial area is maximized and the liquid spreads, establishing a low contact angle. The contact angle established is defined by the Young–Dupré equation:

$$\theta = \cos^{-1}\left(\frac{\gamma_s - \gamma_{sl}}{\gamma_l}\right)$$

which shows that high surface energies (γ_l) correspond to low contact angles.

One method for utilizing contact angles as a means of evaluating the suitability of a surface for bonding involves construction of wettability envelopes from contact angles obtained using multiple liquids of different surface tensions γ_l (Boerio, Roby, Dillingham, Bossi, & Crane, 2006; Smith & Kaelble, 1981). However, it is experimentally unwieldy to perform these measurements in manufacturing and repair environments. It has been demonstrated to be generally sufficient to measure the contact angle of a single liquid as a surrogate for the liquid adhesive; this approach has shown excellent predictive ability (Dillingham, Oakley, et al., 2012). A convenient way to obtain these wetting measurements in a challenging manufacturing or repair environment is through ballistic deposition of a water drop followed by determination of an average contact angle established by the drop perimeter with the surface (Dillingham, Oseas, Gilpin, & Ganance, 2012; Tracey & Flinn, 2012). This approach has shown excellent sensitivity to consistency of surface treatment of both metal and polymeric surfaces and is beginning to see significant acceptance as an in-process quality inspection method.

Surface and bulk chemical analysis. Fourier transform infrared spectroscopy has been in use for many decades as a sensitive technique for quantitative detection of functional groups in polymers. The recent advent of handheld instrumentation coupled with either attenuated total reflectance or diffuse reflectance techniques permits these measurements to be performed on composite structures; several investigators have been demonstrating the use of these techniques to identify the presence of undesirable peel ply residues, contaminants, and thermally degraded laminate surfaces (Tracey & Flinn, 2012).

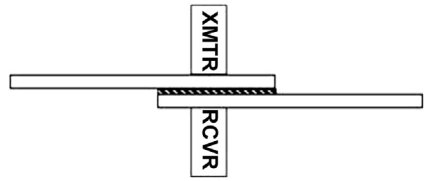

Figure 25.5 Ultrasonic inspection of a lap joint. XMTR = transmitting transducer, RCVR = receiving transducer.

Inspection of bonded composite structures consists of detection of voids or cracks and disbonds, or local proof testing of the interface.

Voids and cracks. The most popular ultrasonic methods use through transmission (Crane & Dillingham, 2008) or reflected (Forsyth, Yolken, & Matzkanin, 2006) ultrasound (typically 20−400 kHz). While the specifics of each of the ultrasonic techniques differ slightly, the basic configuration remains very similar to that shown in Figure 25.5. In the through transmission technique, transducers are coupled to the specimen surface, either through direct contact or through water as a coupling medium. The transducers are then scanned over the specimen. Physical discontinuities in the path of the sound waves represent discontinuities in the acoustic impedance of the part. These discontinuities are detected either by attenuation of the signal amplitude or reflection of the signal, which causes a change in the duration between excitation and reception. The signals are processed to create a map of the acoustic impedance of the interior of the structure.

The presence of disbonds or other void-type defects is not very important unless they are close to the edge of a joint where the stresses are significant (Crane & Dillingham, 2008). In fact, it is possible to completely eliminate the central region of this joint without affecting the structural performance of the joint (Forsyth et al., 2006; Schonhorn, Ryan, & Wang, 1971; Wang, Ryan, & Schonhorn, 1972). However, this is the region of the joint that is the most difficult to inspect with ultrasound due to diffraction of the relatively long-wavelength acoustic waves. So while bond quality as defined by absence of voids can be measured by ultrasonic techniques, these measurements are of limited usefulness in predicting bond strength.

Thermal imaging is another method for interrogating bonded structures that is sensitive to the discontinuities in thermal conductivity that correspond to voids or disbonds, but is not as confounded by the proximity of edges. These methods are characterized by the use of thermal measurements of a test object as it undergoes a response to a stimulus (Shepard, 2007). In pulsed thermography, the surface of a sample is heated with a brief (a few milliseconds) pulse of light from a xenon flash lamp array. An infrared camera monitors the time-dependent response of the sample surface temperature. Where the sample surface is close to a thermal discontinuity (such as a defect), the heat flow from the surface into the sample is obstructed. This causes a local temperature increase at the surface. The time required for these temperature deviations to occur is a function of the depth of the discontinuity, so it is possible to measure the depth below the surface of the defect.

25.10 Proof testing

The major impediments to composite bond inspection have been alluded to. The defects that are readily detectable by NDI techniques are only peripherally related to the quality of the interface, which is the primary determinant of adhesive bond performance. A recent approach to establishing the strength of bonded joints is a localized proof test based on laser shock peening technology (Bossi, Housen, Shepherd, & Voss, 2001; Bossi, Housen, & Shepherd, 2004; Bossi, Housen, & Shepherd, 2002; Bossi, Housen, & Walters, 2005). In this approach, a brief laser pulse applied to the surface creates a high-amplitude compression wave in the specimen. This wave traverses the specimen and reflects off the opposite free surface as a tensile wave. When this tensile wave passes across the bonded interface, it subjects the interface to a normal stress of controllable magnitude. Substandard bonds will be broken by the proof load, which can be detected with standard ultrasonic scanning methods or by noting the deflection of the surface produced by the traversing pulses. If the area of the proof loading is small, then even if the bond is fractured the structure will still meet acceptance standards. Furthermore, this interrogation method may be conducted in areas that carried little load (e.g., far from the joint edge) and thus would not be detrimental to joint integrity. This technique is difficult to apply over large bonded areas due to the cost and time involved in its application. Therefore, traditional inspection techniques must still be utilized to detect and quantify physical flaws, such as delaminations, excess porosity, inclusions, missing adhesive, etc. These flaw types must be detected in high-stress areas of the structure where their presence is significant to bond reliability. Because it is applied late in the manufacturing cycle, that is, after assembly and cure, an integrated inspection regime needs to include strict process control and inspection to avoid the expense associated with rework of substandard assemblies.

25.11 Conclusions

Because adhesive bond performance is so dependent on surface preparation quality and consistency, surface preparation of aircraft structures for bonded assembly represents a particular challenge. Reliable surface preparation for bonding requires sensitive tools for confirming surface condition. Traditional NDI techniques are less than satisfactory for revealing substandard bonded assemblies. Recent advances in proof testing methods can detect weak, substandard assemblies, but their complexity and expense currently limits their more widespread application.

References

ASTM F22-13. (2013). *Standard test method for hydrophobic surface films by the water-break test*. West Conshohocken, PA: ASTM International.

Baker, W., McKenzie, I., & Jones, R. (2004). Development of life extension strategies for Australian military aircraft, using structural health monitoring of composite repairs and joints. *Composite Structures, 66*, 133−143.

Boerio, F. J., Roby, B., Dillingham, R. G., Bossi, R. H., & Crane, R. L. (2005). In *Proc. 37th Natl. SAMPE Symp.* (Vol. 37).

Boerio, F. J., Roby, B., Dillingham, R. G., Bossi, R. H., & Crane, R. L. (2006). Effect of grit-blasting on the surface energy of graphite/epoxy composites. *The Journal of Adhesion, 82*, 19−37.

Bossi, R. H., Housen, K. R., & Shepherd, W. B. (2002). Using shock loads to measure bonded joint strength. *Materials Evaluation, 60*(11), 1333−1338.

Bossi, R. H., Housen, K. R., & Shepherd, W. B. (2004). Application of stress waves to bond inspection. In *SAMPE conference: M&P technology-60 years of SAMPE progress, Long Beach, CA*.

Bossi, R. H., Housen, K. R., Shepherd, W. B., & Voss, M. E. (2001). *Bond strength measurement system using shock loads*. Application No. 20030079552, Assigned to Boeing.

Bossi, R. H., Housen, K., & Walters, C. (June 2005). Laser bond inspection device for composites: has the Holy Grail been found? *NTIAC (Nondestructive Testing Information Analysis Center) Newsletter, 30*(2).

Brotherhood, C. J., Drinkwater, B. W., & Dixon, S. (2003). *Ultrasonics, 41*(7), 521−529.

Chin, J. W., & Wightman, J. P. (1996). *Composites, 27A*, 419.

Composite materials handbook-17 (CMH-17) V3. SAE International. ISBN:978-0-7680-7823-7.

Comyn, J. (1983). In A. J. Kinloch (Ed.), *Durability of structural adhesives* (pp. 85−129). London, New York: Applied Science Publishers. Ch. 3.

Crane, R. L., & Dillingham, G. (2008). Composite bond inspection. *Journal of Materials Science, 43*(20), 6682−6694.

Dillingham, R. G., Conyne-Rapin, S., Boerio, F. J., Bossi, R., & Crane, R. (2003). In *Proc 26th Ann Meeting of the Adhesion Society* (Vol. 26, p. 285).

Dillingham, R. G., & Oakley, B. R. (2006). Surface Energy and adhesion in composite-composite adhesive bonds. *The Journal of Adhesion, 82*(4), 407−426.

Dillingham, R. G., Oakley, B. R., Van Voast, P. J., Shelley, P. H., Blakley, R. L., & Smith, C. B. (2012). Quantitative detection of peel ply derived contaminants via wettability measurements. *Journal of Adhesion Science and Technology, 26*, 1563−1571.

Dillingham, R. G., Oseas, E. S., Gilpin, A. D.,Ganance, F. C. (2012). *Device and method to measure wetting characteristics*. U.S. Pat. 8,272,254.

Encinas, N., Oakley, B. R., Belcher, M. A., Blohowiak, K. Y., Dillingham, R. G., Abenojar, J., et al. (2014). Surface modification of aircraft used composites for adhesive bonding. *International Journal of Adhesion and Adhesives, 50*, 157−163.

Forsyth, D. S., Yolken, H. T., & Matzkanin, G. A. (2006). A brief introduction to nondestructive testing. *The AMMTIAC Quarterly, 1*(2).

Gieske, J. H., Roach, D. P., & Walkington, P. D. (1998). Ultrasonic inspection technique for composite doubler/aluminum skin bond integrity for aircraft. In S. R. Doctor, C. A. Nove, & G. Y. Baaklini (Eds.), *SPIE Proceedings:* (Vol. 3396). *Nondestructive evaluation of materials and composites II* (pp. 148−447).

Gledhill, R. A., & Kinloch, A. J. (1974). *Journal of Adhesion, 6*, 315−330.

Hart-Smith, L. J. (1999). *International Journal of Adhesion and Adhesives, 19*, 181−191.

Hart-Smith, L. J. (July 2002). Adhesive bonding of composite structures-progress to date and some remaining challenges. *Journal of Composites, Technology and Research, 24*(3), 133−153.

Jeenjitkaew, C., Luklinska, Z., & Guild, F. (2010). Morphology and surface chemistry of kissing bonds in adhesive joints produced by surface contamination. *International Journal of Adhesion and Adhesives, 30*, 643−653.

Jiao, D., & Rose, J. L. (1991). *Journal of Adhesion Science and Technology, 5*(8), 631−646.

Kinloch, A. J. (1987). *Adhesion & adhesives: Science & technology*. London & New York: Chapman Hall. p. 441.

Palmieri, F. L., Belcher, M. A., Wohl, C. J., Blohowiak, K. Y., & Connell, J. W. (2013). Laser ablation surface preparation of carbon fiber reinforced epoxy composites for adhesive bonding. *International SAMPE Technical Conference*, 554.

Pocius, A. V., & Wenz, R. P. (1985). In *Proc. 30th Natl. SAMPE Symp.* (Vol. 30, p. 1073).

Schonhorn, H., Ryan, F. W., & Wang, T. T. (1971). Effects of symmetrical bonding defects on tensile shear strength of lap joints having ductile adhesives. *Journal of Applied Polymer Science, 15*(5), 1069−1078.

Shepard, S. M. (2007). Flash thermography of aerospace composites. In *Proc. IV Pan American conference in NDE, [CD-ROM], Buenos Aires, Argentina October 22−27*. Available online http://www.ndt.net/article/panndt2007/papers/132.pdf.

Smith, T., & Kaelble, D. H. (1981). In R. L. Patrick, & M. Dekker (Eds.), *Treatise on adhesives and adhesion* (Vol. 5, pp. 139−292). New York: Marcel Dekker.

Tracey, A. C., & Flinn, B. D. (2012). Infrared spectroscopy: a potential in process quality assurance method for composite bonding surface preparation. International SAMPE Technical Conference. In *SAMPE Tech 2012 conference and exhibition: Navigating the global landscape for the new composites*.

Wang, T. T., Ryan, F. W., & Schonhorn, H. (1972). Effects of bonding defects on shear strength in tension of lap shear joints having brittle adhesives. *Journal of Applied Polymer Science, 16*(8), 1901−1909.

Tensile failure of composite scarf repair

26

E.V. Iarve[1], T. Breitzman[2], E.R. Ripberger[2]
[1]University of Dayton Research Institute, Dayton, OH, USA; [2]Air Force Research Laboratory, Dayton, OH, USA

26.1 Introduction

Growing fleets of composite aircraft make structural composite repairs unavoidable, including the repair of primary load-bearing components. In the present chapter, we will consider bonded composite repair, specifically scarf repair, as one of the most important types of composite repair, capable of restoring the original mechanical characteristics of the structure and maintaining its aerodynamic characteristics, while only minimally altering the aircraft's outer mold line (OML). On military aircraft, such repair has been reported in Grimsley and Michaels (1994). A large 76.2 by 177.8 cm^2 skin was scarfed out and replaced without altering the OML, while adding additional composite load channels on the inner mold line (IML) for load distribution. The scarf repair was chosen over four other repair options as feasible while minimally affecting load redistribution. However, by virtue of its bonded character, the certification of scarf repair is subject to restrictions concerned with the difficulty of assessing adhesive bond line integrity over the life of the structure. Therefore, to assure the safety and integrity of the structure, a fail-safe approach was used for the repair design. This requirement essentially means that even with complete failure of the bond line, the structure repair will be able to carry the design limit load for a specified period of unrepaired usage. To satisfy this requirement, a number of fasteners were installed through the repair patch in the IML channels (Grimsley & Michaels, 1994). Such stringent certification requirements are justified by aircraft safety concerns, and are unlikely to be relaxed without increased understanding and improved reliability of bonded repairs. Even though the importance of the chemical and physical aspects of surface preparation and repair procedures cannot be overestimated, the design of the repair is of significant interest from the standpoint of load redistribution and repair durability. In the present chapter, we will concentrate on mechanical aspects of composite scarf repair, namely on designs to reduce stress in the adhesive layer. Lowering stress concentrations in adhesives is also important for improving the durability of the repair. As pointed out in a review by Rousseau and Iarve (2012) devoted to the durability of bonded and bolted joining, the long-term behavior and failure modes of bonded joints can be different from those in a static regime. In the case of bonded joining, the joint and the adhesive materials are designed to prevent adhesive failure entirely, so failure should occur in the adherends. Unfortunately,

Structural Integrity and Durability of Advanced Composites. http://dx.doi.org/10.1016/B978-0-08-100137-0.00026-2

after a lifetime of fatigue and creep, the joint may experience adhesive failure as a result of degradation in the adhesive. From a mechanical standpoint it is therefore important to consider possibilities to minimize stress concentrations in the adhesive bond line.

The foundation of the mechanics of adhesive scarf joints has been established for more than half a century, with Lubkin (1957) showing the uniformity of stress distribution in the adhesive layer, joining uniform and similar adherends in the framework of plane stress (strain) formulation. Two critical aspects that must be considered in extending this philosophy to composite scarf repair are the through-the-thickness heterogeneity of laminated composite parent material and the three-dimensionality of the load path. The two-dimensional (2-D) scarf configuration has been used extensively for evaluating the scarf angle effects in joint strength.

Experimental investigation of unidirectional (UD) 2-D carbon fiber—reinforced composite scarf joints under tensile and compressive loading was performed in Kumar, Sridhar, Sivashanker, Osiyemi, and Bag (2005, 2006), respectively. In both cases, the scarf angle was varied from 0.5° to 5°. In the case of tensile loading, the adherend failure typical of UD composites in the form of fiber failure and splitting occurred for scarf angles of less than 1°, whereas adhesive failure occurred for joints with higher scarf angles. For compression-loaded joints, adherend failure typical of UD composites in the form of kink-band formation was observed for scarf angles less than 3°, whereas adhesive failure again occurred at higher scarf angles. The key observation was that for both tension and compression, failure stress was dependent on scarf angle, even for small angles, for which the failure occurred in the adherends and the failure stress was significantly lower than that of pristine composites.

The through-the-thickness heterogeneity of composites within the 2-D stress analysis framework was at the root of design guidelines for composite scarf repair (Hart-Smith, 1973; USAF, 1973), allowing for the calculation of shear stress in the adhesive layer as a function of the scarf angle and thickness coordinate (USAF, 1973). The maximum shear stress was more than 20% higher than the uniform shear stress in the joint, for adherends having equivalent homogenized properties obtained by classical lamination theory. This effect was studied using the finite element analysis of Harman and Wang (2006, 2007) and Baker (1999). It was established that high shear stress concentrations occur near 0° ply locations; moreover, their amplitude appears to decrease with increasing thickness of the adherends. Moiré interferometry was used in a recent study by Fredricson, Schoeppner, Mollenhauer, and Palazotto (2007) that investigated stress distribution in the adhesive layer of a 2-D scarf joint between two quasi-isotropic adherends. A significant nonuniformity of shear and normal stress distribution in the adherends was observed and correlated with stress analysis predictions.

The effects of tip blunting in the 2-D scarf joints were considered in Adkins and Pipes (1985). It was shown that the stress concentration factors arising due to the tip blunting are higher for small scarf angles. A significant body of recent work, the review of which is beyond the scope of the present paper, is devoted to the impact response of 2-D scarf joints; for example, Hoshi, Nakano, and Iwahori (2007), Gamma, Mahdi, Cichanowski, Yarlagadda, and Gillespie (2005) and Harman and Wang (2007).

Actual scarf repair has a three-dimensional (3-D) nature and provides a load path around the affected area, possibly affecting the scarf angle considerations arrived at in 2-D models and experiments. This was investigated under compressive loading performed in the works of Soutis and Hu (1998, 2003). The adherends were assumed to be orthotropic but homogeneous. It was pointed out that not all of the load in scarf repair is carried through the adhesive, such that the application of 2-D design methodology may lead to overly conservative predictions. It was indeed found that the 3-D design predicted a significantly larger optimal scarf angle due to lower peak stress in the adherends.

Finally, the effects of three-dimensionality of the load path and heterogeneity of the laminated adherends on stress concentration were studied in Wang and Gunnion (2006). Both 3-D and 2-D analyses of stress distribution in the adherends were performed. It was shown that similar to the 2-D model, shear stress in the adhesive in the 3-D model exhibits a sharp stress concentration at the location of the 0° plies in the adherend and patch. Moreover, examination of the failure criteria in the adhesive and adherends has led authors to conclude that scarf joint strength predictions based on 2-D models are surprisingly consistent with those from 3-D models. In other words, the heterogeneity of the adherends has a dominating effect on stress distribution, compared with the effect of load path dimensionality.

In most previous work, the composition was considered the same for both the patch and the repair panel. This is a natural concept transpiring from the basic mechanics of scarf joints (Lubkin, 1957), which result in uniform shear stress distribution in the adhesive between similar adherends. Another consideration is stiffness restoration, which effectively requires the patch composition to be identical to that of the panel under repair. It is worth pointing out, however, that these considerations are not entirely intuitive when applied to the repair of laminated composite panels. Indeed, in the case of scarf joints and/or repairs in identical but nonunidirectional laminates, shear stress distribution in the adhesive is highly nonuniform, and has been well established both by analysis and by experiment as indicated in Wang and Gunnion (2008) and Fredricson et al. (2007).

Moreover, in the case of uniaxial loading the stress concentration occurs at the juncture of stiff (0°) plies with respect to loading direction, and suggests the possibility of reducing the stress concentration by changing the ply orientations in the patch. The second argument for the ply-by-ply replacement methodology of the repair, namely stiffness restoration, is also not straightforward. In contrast to repair and modeling of scarf joints manufactured in the laboratory, field repair typically is characterized by only one-sided access to the scarf area. As discussed in the specimen preparation section that follows, this restriction yields to possible staggering of the ply stacking sequence in the scarf patch and host panel. Thus the restoration of stiffness and elimination of bending-tension coupling in repaired panels obtain relative meaning and must be tolerated within range. Because of this, the patch layup design may be considered an optimization problem aimed at lowering the stress concentration in the adhesive while still maintaining the stress transfer required to avoid stress concentration in the adherends. Such a problem was posed for the first time in Breitzman et al. (2009) and will be considered in detail below.

Prior to addressing the patch design issue, we will briefly discuss the issue of residual stress and the related issue of dimensional change in scarf joints due to cure. These are important aspects in evaluating repair feasibility with mismatched stacking sequences in the repair patch and adherends or parent laminates. Indeed, an analysis of shape change (i.e., warping) is required for each proposed mismatching repair layout. The amount of work that has been devoted to the measurement and modeling of adhesive joints and scarf repair in particular is very limited. Experimental measurement and simplified computation of the processing of residual strain due to thermal expansion in bonded composites was performed by Schoeppner, Mollenhauer, and Iarve (2004). In this work, two quasi-isotropic $[0_2/45_2/-45_2/902]_s$ and symmetric IM6/3501−6 laminated plates were bonded with AF-191-U adhesive and cured at 177 °C, approximately equal to the cure temperature of the composite. Next, a Moiré interferometry grating was introduced on a machined edge of the bonded specimen and a saw cut introduced through the thickness perpendicular to the longitudinal edge. The deformation caused by releasing the residual stress near the cut was measured using Moiré interferometry and compared with predictions from the B-spline approximation analysis method. The analysis performed was purely elastic, with distortion caused by thermal expansion of the composite plies and adhesive by assuming the temperature difference was −150 °C. Good agreement between prediction and analysis was observed for transverse shear strain. Larger disagreements were seen for transverse normal strain, which was partially explained by Mollenhauer, Fredrickson, Schoeppner, Iarve, and Palzotto (2008) as the influence of grating stiffness. Thus it was shown that a simplistic elastic estimate of the residual processing stress based on thermal mismatch evaluation could be used with reasonable accuracy. Nonlinear cure simulation of composite repair, by taking into account chemical changes such as cure shrinkage, is of significant interest and a direction of future work. The recent paper by Bestley, Brown, and Alston (2011) is devoted to cure kinetics−based modeling of scarf repair and lays important groundwork in this direction.

Subsequently, the chapter describes the methodology of repair sample preparation with the aim of achieving highly repeatable specimens and testing. We then discuss patch composition design optimization, and conclude by reviewing selected results and outlining further work and recommendations.

26.2 Experimentation

Laboratory fabrication and testing of scarf repair requires high repeatability of the repair as well as the ability to deal with large specimen sizes and loading capacities. This section will cover specimen design to accommodate these requirements as well as repair procedures and test methods.

26.2.1 Specimen design

Initially a series of six $[45/0/-45/90]_S$ quasi-isotropic panels measuring 30 × 61 cm were manufactured using IM6/3501−6 graphite/epoxy UD prepreg. The panels

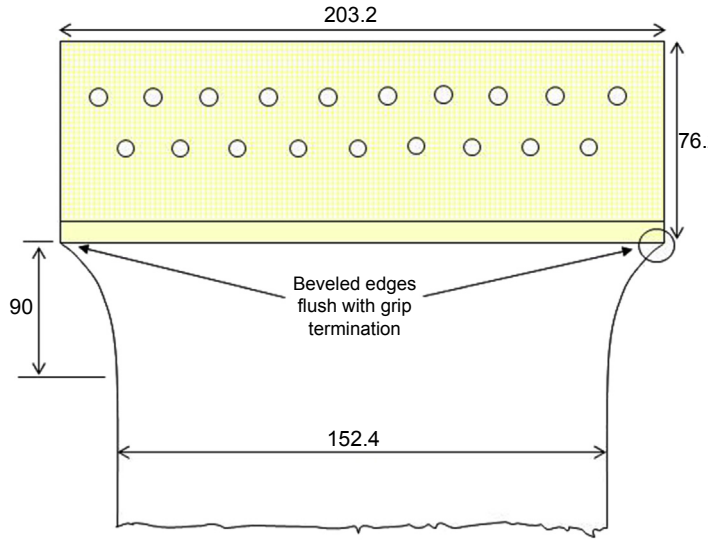

Figure 26.1 Grip section of the dogbone scarf repair specimens.
Brietzman, T.D., Iarve, E.V., Cook, B.M., Schoeppner, G.A., & Lipton, R.P. Optimization of a composite scarf repair patch under tensile loading. *Composites Part A: Applied Science and Manufacturing*, *40*(12), 1921−1930.

were cured using the manufacturer's recommended cure cycle and then ultrasonically scanned to ensure that the panels were free of defects. The panels had a nominal thickness of 1.13 mm. Five panels were subsequently trimmed and cut in half to yield 10 13.31 × 57.15 cm test panels with the 0° fibers parallel to the 57.15 cm sides. Glass-reinforced epoxy tabs measuring 5.08 × 13.31 cm were bonded to the front and back face of each specimen end with EPON 828 epoxy, a room temperature cure-bonding system with EPI-CURE 3140 as the hardener. Due to the large loads to be introduced into the specimen (particularly the virgin specimens), bolted end fixtures were used to help transfer the load into the specimen without having to rely solely on tab adhesive shear strength. A special fixture was designed and fabricated to precisely drill holes through the tabs and specimens to align with holes in the loading fixture and ensure uniform specimen loading. The specimen was attached to each load frame grip using 13 0.635-cm-diameter finely threaded (11 threads/cm) standard bolts torqued to 16.95 Nm, which represents the recommended maximum torque for the grade of bolts used in the testing. Sandpaper was placed between the specimen and the grips (grit side toward specimen) to increase the load transfer from the grips to the specimen. Three of the 10 specimens were set aside for testing to determine large-panel base strength. However, determining the virgin panel strength proved difficult with the described panel design due to grip failures. This finding was indicative of the problems with testing of repairs with high strength retention data, which we were hopeful to achieve with optimization of the patch design. To address this issue, a dogbone specimen design was utilized with the grip geometry shown in Figure 26.1.

In addition to the large-panel tests, a series of standard tensile coupons was manufactured for obtaining the basic tensile properties of the laminates to be used in the analysis section. The 25.4 × 2.54 cm strength coupons were tested in accordance with ASTM D-3039M, and all dimensions adhered to the specimen size tolerances of ASTM D-3039M except that the laminate thickness selected was the same as that of the layup used in the large-panel test program. The tensile tests were performed using displacement control at a crosshead speed of 0.127 cm/min.

26.2.2 Scarf repair

The laboratory repair procedure was set up to provide high repeatability of repair. A key component of such a setup is an automated scarfing procedure, which was accomplished and precisely controlled with the scarfing machine shown in Figure 26.2. The machine consists of a pneumatic grinder with a diamond bit attached to an arm that can be both rotated and translated to cut circular scarfs at specified scarf angles in flat panels. Using a scarfing machine, repeatable scarf cuts were made on all seven panels with minor variability. A 2.54 cm hole was cut into the center of each of the seven specimens using a scarf angle of 20:1, as illustrated in Figure 26.3. High repeatability of the scarfed panel geometry was confirmed by evaluating the variation in the diameter of the scarfed area, as measured by laser interferometry for each specimen at select locations. The scarf angle of 174° was recovered with coefficient of variation of 0.2%. Three scarfed specimens were set aside for testing to determine the notched (scarfed) strength to be used as a baseline in determining the restoration of strength due to patching of the specimens.

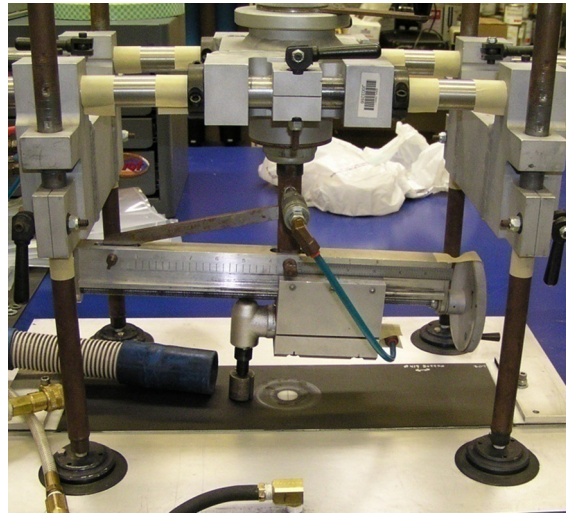

Figure 26.2 Scarfomatic with scarfed panel held by vacuum.
Brietzman, T.D., Iarve, E.V., Cook, B.M., Schoeppner, G.A., & Lipton, R.P. Optimization of a composite scarf repair patch under tensile loading. *Composites Part A: Applied Science and Manufacturing*, *40*(12), 1921−1930.

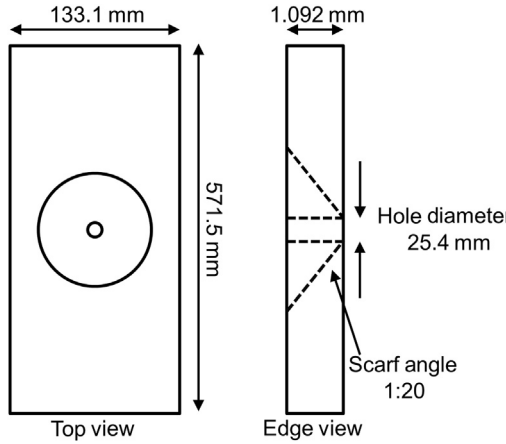

Figure 26.3 Scarf panel dimensions and layout.
Brietzman, T.D., Iarve, E.V., Cook, B.M., Schoeppner, G.A., & Lipton, R.P. Optimization of a composite scarf repair patch under tensile loading. *Composites Part A: Applied Science and Manufacturing*, *40*(12), 1921−1930.

Both standard ply-by-ply and optimized-design (described in the next section) scarf repairs were fabricated. The only difference between the two is the stacking of the plies in the patch. Therefore, only the procedure for a standard one-sided repair will be described. Starting with the bottom 45° ply of the laminate, a 2.54-cm-patch filler ply is used to fill the 2.54-cm hole. It is a common assumption that the orientation of the filler ply (0° in this case) is of little consequence because it is not expected to carry any load within the patch. This is assumed because the filler ply does not overlap any parent panel plies through which shear load could be transferred. Instead, it is assumed that load can only be transferred to the filler ply through an adhesive butt joint with the bottom 45° ply. Since butt joints are inherently weak, it is assumed that the filler ply carries no load. The standard practice continues with matching of the orientation of the second patch ply (45°) to the orientation of the first bottom ply of the parent panel. Assuming a 20:1 scarf ratio and a ply thickness of 0.14 mm (0.0055 inches), the diameter of the second patch ply will equal approximately 3.10 cm and overlap the bottom parent ply by 0.56 cm, through which shear load can be transferred. The overlap, through which most load is assumed to be transferred to the ply, occurs for each patch ply. Therefore, the orientation of the patch plies (with the exception of the filler ply) is offset by one-ply thickness from the orientation of the parent laminate plies. Using this practice, it is recognized that the scarf patch has one more ply than the parent panel. The orientation of the final patch ply (sometimes referred to as the overply) typically matches that of the top ply of the parent panel.

The repair procedure included laying up or stacking the patch repair plies, cutting a piece of Cytec FM 300M adhesive film to match the outer radius of the top ply or overply, and cutting a center hole in the adhesive film to match the outer radius of the filler ply of the patch. This gave the film adhesive a doughnutlike appearance. The adhesive

was selected in part for its 177 °C cure temperature that is equal to the maximum cure temperature of the IM6/3501-6 patch material. After assembly, the patch and film adhesive were cocured to the scarfed panel in an autoclave using standard vacuum bagging procedures and then ultrasonically scanned to detect patch and bond line defects, and were found to be free of ultrasonically detectable defects.

26.2.3 Testing methodology

All specimens were instrumented with uniaxial and rosette strain gages to monitor strains in far-field surfaces, on the patch overply, and adjacent to the patch on the parent specimen, during tensile loading of the repaired specimens (see Figure 26.4). At various plane view locations on the specimen, back-to-back (front and back of the specimen) gages were mounted to measure localized bending strains caused by eccentricity of the specimen response. For each test panel, grips were bolted to each end of the specimen, and the assembly was loaded into the hydraulic grips, at which time

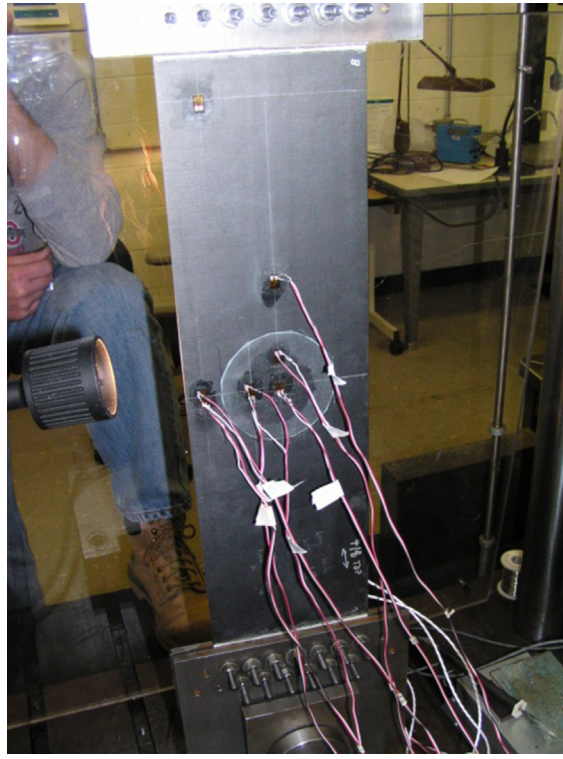

Figure 26.4 Test setup of large tensile specimens to include soldered strain gages. Brietzman, T.D., Iarve, E.V., Cook, B.M., Schoeppner, G.A., & Lipton, R.P. Optimization of a composite scarf repair patch under tensile loading. *Composites Part A: Applied Science and Manufacturing*, *40*(12), 1921−1930.

the strain gage leads were connected to the data acquisition equipment. The tests were conducted at the prescribed constant crosshead displacement rate of 0.127 cm/min up to specimen failure.

In addition to large panels, a set of standard coupons cut out of additional panels was tested for characterization of tensile strength properties required for the analysis described below.

As mentioned before, the testing of the 13.31 × 57.15 cm virgin test panels was problematic due to stress concentrations in the grip region that led to premature failure of the specimens. Despite attempts to provide an effective load transfer from the grips into the specimens by maximizing the torque on the grip bolts, the typical failure mode was net section failure through a line of bolt holes within the tab region. Therefore, the strength of 416 MPa with 15% coefficient of variation reported for the virgin panels is not representative of the expected strength of the panels, if failure had occurred in the gage section away from stress concentrations. In response, the dogbone specimens shown in Figure 26.1 were manufactured and used for testing in order to mitigate this problem. Considering the cost of such specimens, however, only one copy was used for virgin panel strength testing, yielding 668 MPa. In the present work, the ASTM D-3039M coupon tensile strength of 704 MPa with a coefficient of variation of 6.4% was used as a reference value to characterize the repaired specimen strength restoration.

26.2.4 Adhesive property determination

The Poisson's ratio and thermal expansion properties of FM 300M film adhesive were determined by testing a neat adhesive plaque fabricated by stacking several layers of adhesive film having an areal density of 244 g/m^2. Approximately 30 layers of film, each slightly greater than 10 × 10 cm, were stacked together, consolidated, and cured using the manufacturer's recommended cycle. The FM 300M film contains a low-volume-fraction random-fiber-mat carrier to aid in handling and bond line thickness control. After curing, the plaque was ultrasonically scanned and found to have no significant flaws or porosity internal to the plaque, but a slight warp was present. The nominal thickness of the plaque was 0.58 cm. The plaque was trimmed to approximately 10 × 10 cm, from which two 10 × 1.9 cm specimens used for tensile testing and two 5 × 5 cm specimens used to determine coefficient of thermal expansion (CTE) were cut. Each CTE specimen was instrumented with two strain gages bonded at a 90° angle to each other at the specimen center. The specimens were placed into a temperature-controlled oven and the temperature was then varied from −23 to 88 °C, during which strain measurements were taken after 15 min temperature equilibrium hold times at discrete temperatures. After temperature compensation of the strain measurements, the temperature-dependent expansion and contraction was used to determine the CTE of the neat adhesive. The CTE was found to be constant over the temperature range tested and was determined to be $\alpha = 0.7 \times 10^{-6}$/C°.

The tensile specimens were instrumented with 0°−90° rosette strain gages to determine the tensile modulus and Poisson's ratio. Figure 26.5(a) shows the axial and transverse stress−strain curves for the neat adhesive FM 300M tensile test specimens. It can

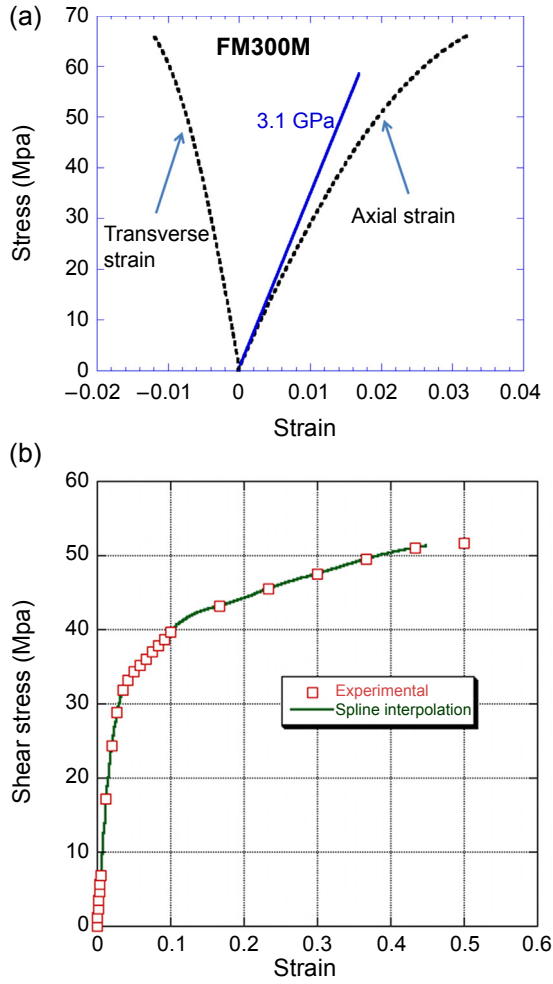

Figure 26.5 FM 300M tensile (a) and shear (b) response.
Brietzman, T.D., Iarve, E.V., Cook, B.M., Schoeppner, G.A., & Lipton, R.P. Optimization of a composite scarf repair patch under tensile loading. *Composites Part A: Applied Science and Manufacturing*, *40*(12), 1921−1930.

be seen that the response is nonlinear with an initial elastic modulus of 3.1 GPa and the Poisson's ratio was determined to be $v = 0.38$ and appeared practically constant. The initial tensile modulus and Poisson's ratio are consistent with the initial shear modulus in Figure 26.5(b). The shear response was obtained from manufacturer-supplied KGR-1 test curves (FM 300, 2005). The nonlinear elastic constitutive equations for the adhesive material considered only variation of the Young's moduli and assumed a constant Poisson's ratio in accordance with experimental observations. The shear modulus G was expressed as

$$G = \min\left[\frac{E_1(J_1)}{2(1+\nu)},\ G_2(J_2)\right] \tag{26.1}$$

where the elastic modulus E_1 is a monotonic function of strain calibrated using cubic spline interpolation from the tensile testing results (see Figure 26.5(a)) and is expressed through the dilatational strain invariant J_1. Similarly, G_2 is the shear modulus calibrated using the KGR-1 test results (Figure 26.5(b)) and is expressed though the distortional strain invariant J_2, where

$$\begin{aligned} J_1 &= \varepsilon_1 + \varepsilon_2 + \varepsilon_3 \\ J_2^2 &= (\varepsilon_1 - \varepsilon_2)^2 + (\varepsilon_3 - \varepsilon_2)^2 + (\varepsilon_1 - \varepsilon_3)^2 \end{aligned} \tag{26.2}$$

and ε_i are the principle components of the strain tensor.

26.3 Modeling methodology

The goal of the analysis was to predict the ultimate strength of the scarfed and scarfed/repaired specimens, taking into account the nonlinear material behavior of the adhesive as well as the geometrically nonlinear behavior of both the adhesive and composite materials. The model consisted of a 571.5 × 133.096 × 1.0922-mm rectangular panel with a 25.4-mm-diameter hole (see Figure 26.6). The scarf ratio was 20:1. For repaired models, the adhesive layer between the adherend and the repair patch was explicitly modeled and was 0.127 mm thick. When an overply was used, its diameter was 76.2 mm. The layers within the laminate and the repair were modeled explicitly. The elastic properties of the IM7/3501-6 UD composite and the initial elastic properties of the FM 300M adhesive used in the models are summarized in Table 26.1. The layup for the laminate was [+45/0/−45/90]s.

Three types of ply layups for the repair are discussed. The first is ply-by-ply replacement, consisting of matching the fiber orientation in the repair ply to that of its corresponding ply in the original layup. Thus, the [+45/0/−45/90]s laminate would have a [+45/0/−45/90]s repair patch orientation. The second layup examined was an offset ply layup. As mentioned in the experimental section, this repair methodology assumes that for a long-term repair, the bottom repair ply is a filler ply and does not contribute to the repair strength because it acts as a butt joint. For a [+45/0/−45/90]s laminate, this repair layup would be [+45/+45/0/−45/90/90/−45/0] for a flush repair, and if used an overply would have 45° fiber orientation (matching the top ply of the laminate). In the experimental section, the repairs used a 0° filler ply (bottom repair ply) instead of a 45° filler ply. The third stacking sequence of the repair patch will be obtained through analysis as described in the optimization section.

26.3.1 Strength prediction

The strength of the scarfed panels with and without repair was determined based on the fiber failure criterion in the parent panel. In the case of the repaired panels, a nonlinear

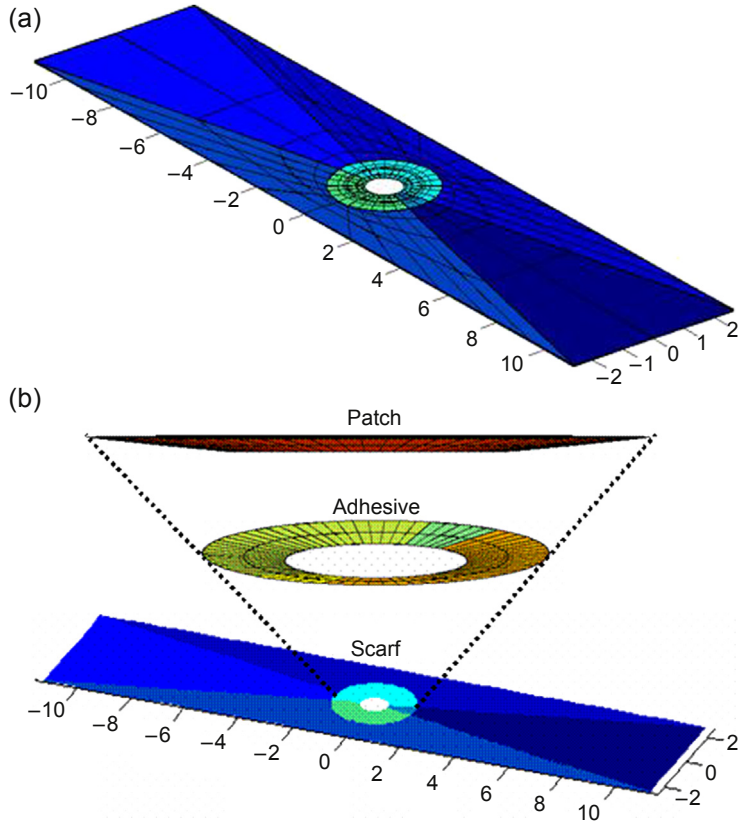

Figure 26.6 Scarf panel geometry with repair. (a) Scarfed panel and (b) repair. Brietzman, T.D., Iarve, E.V., Cook, B.M., Schoeppner, G.A., & Lipton, R.P. Optimization of a composite scarf repair patch under tensile loading. *Composites Part A: Applied Science and Manufacturing*, *40*(12), 1921−1930.

Table 26.1 Elastic properties of IM7/3501-6 and FM 300

	IM7/3501-6	**FM 300M**
E_a	175 GPa	3.12 GPa
E_t	9.79 GPa	
G_a	5.52 GPa	1.13 GPa
G_t	3.68 GPa	
ν_a	0.33	0.38
ν_t	0.449	

Brietzman, T.D., Iarve, E.V., Cook, B.M., Schoeppner, G.A., & Lipton, R.P. Optimization of a composite scarf repair patch under tensile loading. *Composites Part A: Applied Science and Manufacturing*, *40*(12), 1921−1930.

analysis was performed and both geometric and adhesive nonlinearity (Eqn (26.1)) were taken into account. By increasing the load, the adhesive progressively softened, resulting in increased load transfer through the parent laminate, creating a subsequent stress concentration in the adherend that eventually led to failure. The fiber failure load in the presence of a stress concentration was predicted using the critical failure volume (CFV) method (Iarve, Mollenhauer, Whitney, & Kim, 2006a,b). In the present work, no details of matrix damage initiation and propagation and/or their effect on fiber-direction stress redistribution were taken into account. Such simplification of analysis is justified by low delamination propensity in the vicinity of large holes (Iarve, Mollenhauer, & Kim, 2004), and thereby the relatively mild effects of other matrix damage on the stress distribution in the fiber direction. The statistical nature of CFV requires the scatter of fiber-direction strength, which was determined in Wisnom, Khan, Green, Jiang, and Hallet (2005) and found to be well approximated by Weibull distribution with $\alpha = 40$. The average tensile strength of a UD ply was calculated from ASTM standard coupon strength data described above at $X_t = 704$ MPa with control volume $V_0 = 1335$ mm^3. The control volume equals the volume of the 0° ply in the laminates. Note that the coefficient of variation of the experimental data for tensile coupons was not utilized in the statistical analysis. Schematics of the repair strength prediction algorithm are shown in Figure 26.7. The typical relationship between the applied load and predicted fiber failure

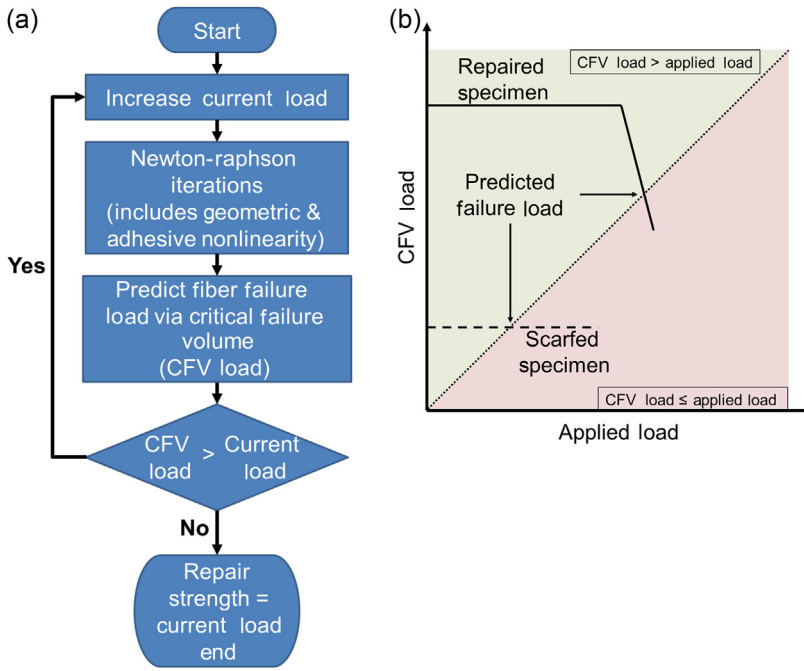

Figure 26.7 (a) Repair strength prediction algorithm, (b) typical loading diagram.
Brietzman, T.D., Iarve, E.V., Cook, B.M., Schoeppner, G.A., & Lipton, R.P. Optimization of a composite scarf repair patch under tensile loading. *Composites Part A: Applied Science and Manufacturing*, *40*(12), 1921−1930.

load in the process of incremental analysis is shown in Figure 26.7(b). The failure of the repair is sudden in nature. The adhesive transfers load almost to its failure point, keeping the stress concentration low and the fiber failure load in the panel high and constant. The adhesive then breaks suddenly, transferring all of the load to the adherends and causing them to fail. Figure 26.7(b) illustrates the relative level of failure loads of the scarfed unrepaired panels, which is approximately half that of the repaired panels. The strength prediction of the unrepaired scarfed panels was also performed via CFV.

26.3.2 Optimization of the repair patch stacking sequence

This section discusses improving the strength of the repair under uniaxial tension load by optimizing the orientation of the fibers within each repair ply. Based on the analysis performed above, the repair strength was determined by the load at which the adhesive failure occurred. Hence, the optimization algorithm attempted to increase the strength of the repair by reducing the von Mises stress in the adhesive. Note that the nonlinear algorithm in Figure 26.7 was not directly used for optimization. Instead, the adhesive stress state was calculated using initial elastic properties. After the optimal stacking sequence was obtained, a nonlinear analysis for this particular patch composition was performed as described above and the repair failure load reported. To reduce the von Mises stress in the adhesive domain, the optimization algorithm adjusted the fiber orientations in the repair plies. Within one repair layer, the fiber orientation was uniform, but the orientation of each layer in the repair could change independently of the other repair layers. The downhill simplex global optimization method (Press, Flannary, Teukolsky, and Vetterling, 1989) was used to minimize the L^p norm of the von Mises stress in the adhesive domain, where

$$L^p = \sqrt[p]{\frac{1}{V}\iiint_V (\sigma_M)^p \mathrm{d}V} \tag{26.3}$$

Use of the L^p norm instead of the von Mises stress enabled the algorithm to concentrate on reducing actual volumes of large stresses, rather than focusing on near-zero-volume points in the adhesive domain arising in the linear elastic analysis as a result of singularities near the ply interfaces and the adhesive interface. The value of p was chosen as $p = 12$ based on prior work by Iarve, Mollenhauer, and Kim (2005). It is important, however, that this parameter does not enter the actual strength prediction and is merely used to facilitate a better optimization framework based on elastic stress fields.

26.4 Results and discussion

26.4.1 Patch optimization

26.4.1.1 Flush repair

The optimal stacking sequence for the flush repair was determined to be [+50/+47/−31/+68/+106/−72/−36/36] (see Table 26.2). It was clear that altering the fiber

Table 26.2 Results of optimizations

Adherend	Optimized flush repair	Optimized OP2	Optimized OP1
N/A	N/A	5.26	−54.7
+45	36	11.75	43.81
0	−36	−45.28	−37.44
−45	−72	0.11	−121.78
90	106	91.27	67.23
90	68	−12.12	15.00
−45	−31	−25.16	−54.14
0	47	48.47	44.78
+45	50	50.42	57.46

Brietzman, T.D., Iarve, E.V., Cook, B.M., Schoeppner, G.A., & Lipton, R.P. Optimization of a composite scarf repair patch under tensile loading. *Composites Part A: Applied Science and Manufacturing*, *40*(12), 1921−1930.

orientations in the repair would change the stiffness and thus produce bending. Figure 26.8 illustrates the out-of-plane displacements along the top of the specimen for the ply-by-ply, offset, and optimized repair layups. The materials are all linear elastic with an applied tension load of 68.9 MPa. The points plotted are taken along the full length, on the centerline (with respect to width), and on the top of the model (see Figure 26.8).

As expected, ply-by-ply repair produces the least out-of-plane displacement because of its perfect matching of ply stiffness from adherend to repair. The optimized

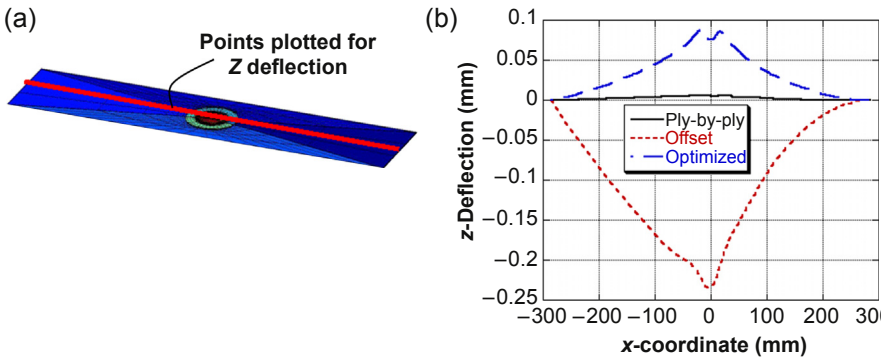

Figure 26.8 Out-of-plane deflection for flush repairs. (a) Schematics, (b) profile. Brietzman, T.D., Iarve, E.V., Cook, B.M., Schoeppner, G.A., & Lipton, R.P. Optimization of a composite scarf repair patch under tensile loading. *Composites Part A: Applied Science and Manufacturing*, *40*(12), 1921−1930.

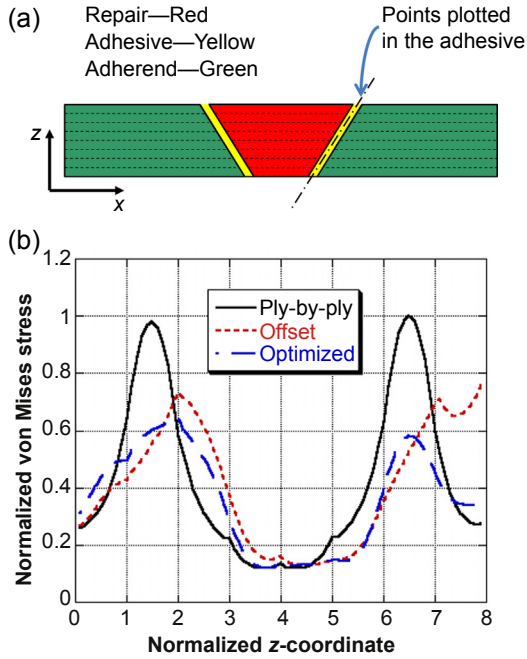

Figure 26.9 Normalized von Mises stress in the adhesive in the flush repair. (a) Schematics, (b) through-the-thickness distribution.
Brietzman, T.D., Iarve, E.V., Cook, B.M., Schoeppner, G.A., & Lipton, R.P. Optimization of a composite scarf repair patch under tensile loading. *Composites Part A: Applied Science and Manufacturing*, *40*(12), 1921−1930.

repair, however, has less than half the displacement of the offset repair. Therefore, the optimal design results in less bending-tension coupling than does the offset method and is thus plausible for practical repair.

The stress distribution in the adhesive for different repair patch configurations is displayed in Figure 26.9. The line plots of the von Mises stress in the adhesive from the bottom of the model ($z = 0$) to the top of the model ($z = 8$) are displayed. The points were chosen along the midline of the adhesive layer between the adherend and repair patch on the $y = 0$ axis. The areas of high von Mises stress are the areas attaching the 0° plies of the adherend to the repair patch or attaching the adherend to the 0° plies of the repair patch. The optimal design results in the lowest stress concentration in the adhesive, at least in the elastic regime. This is achieved by favoring a softer patch to avoid excessive stress transfer through the adhesive, especially near the 0° plies in the adherend.

26.4.1.2 Repair with overply

The introduction of an overply increased the complexity of the model geometry. Schematics of the two models that were studied are shown in Figure 26.10. The

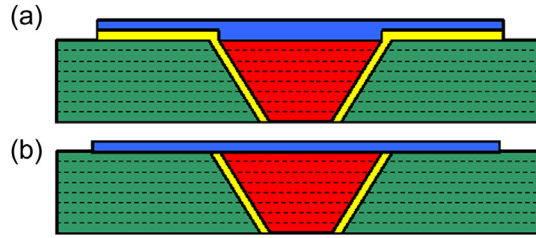

Figure 26.10 2-D schematic of repair model geometries with an overply ((a) OP1 and (b) OP2). Brietzman, T.D., Iarve, E.V., Cook, B.M., Schoeppner, G.A., & Lipton, R.P. Optimization of a composite scarf repair patch under tensile loading. *Composites Part A: Applied Science and Manufacturing*, *40*(12), 1921−1930.

increased complexity resided in the adhesive layer (yellow) between the adherend (green) and the overply (blue). For repairs in the field, adhesive is used to bond the overply to the adherend, but no adhesive is present between the overply and the repair patch (red), since the overply and patch are cocured. Since the adhesive layer thickness is 0.0762−0.127 mm, inclusion of the adhesive between the overply and the adherend required a slightly thicker overply to fill the space (see model OP1 in Figure 26.10). In reality, the excess volume created by requiring strict lamination is taken up by the slight thickness nonuniformity of the adhesive. Another idealized geometric model, named OP2 (see Figure 26.10(b)), was considered to better represent the mechanical effect of the overply, and contained no adhesive between the overply and the adherend. In this idealized model, no delamination of the overply was allowed. This model was used to evaluate the effect of the overply on stress relief in the adhesive as well as to understand the driving factors for the overply angle definition.

Model OP2 was used to understand the effect of the overply on von Mises stress in the adhesive. The adherend was the same eight-ply [+45/0/−45/90]s quasi-isotropic laminate as in the ply-by-ply repair. Two overply angles were considered: 45° coinciding with the top ply angle, and 0° coinciding with the loading direction. The von Mises stress in the adhesive is compared for the case of zero-, one-, two-, four-, and eight-ply thickness overplies. The resulting von Mises stress distributions were normalized by the maximum von Mises stress occurring in the ply-by-ply replacement without the overply, and are given in Figure 26.11. Both overply orientations reduced the stress in the adhesive near the top 0° ply in the adherend (normalized z-coordinate between 6 and 7). Thicker overplies resulted in larger reductions of the stress. Regardless of overply thickness, both overply fiber orientations failed to affect the high-stressed volume near the bottom 0° ply (normalized z-coordinate between 1 and 2).

Next, the effect of the overply angle on the maximum von Mises stress occurring in the adhesive domain was observed. The repair layups compared are ply-by-ply, offset, and optimal design (optimized with no overply). The overply was then added to the model. The maximum von Mises stress was computed for overply fiber orientations between −90° and 90° and was normalized by the von Mises failure stress of the adhesive. Plots of the results for the two overply models are given in Figure 26.12.

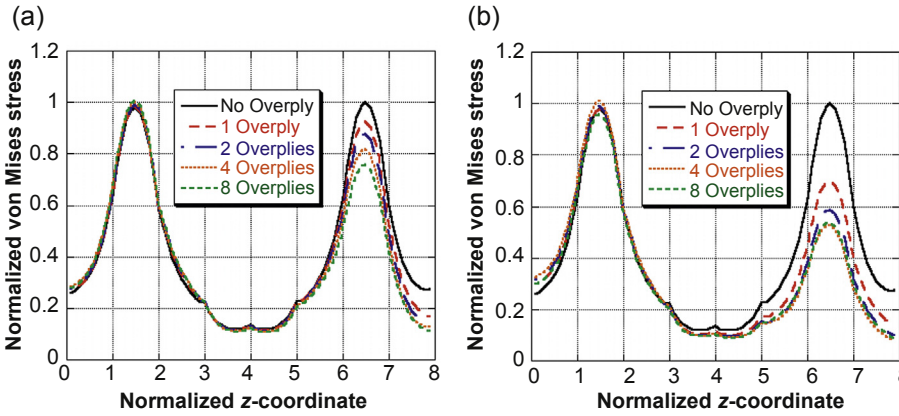

Figure 26.11 Effect of (a) 45° overply and (b) 0° overply thickness on the von Mises stress in the adhesive.
Brietzman, T.D., Iarve, E.V., Cook, B.M., Schoeppner, G.A., & Lipton, R.P. Optimization of a composite scarf repair patch under tensile loading. *Composites Part A: Applied Science and Manufacturing*, *40*(12), 1921−1930.

Without adhesive (in model OP2, Figure 26.12(a)), the preference is clearly toward a near-0° overply. Indeed, it provides the most load translation through the overply, and respectively the most stress relief in the adhesive around the repair. In the more realistic case of OP1 (Figure 26.12(b)), where the adhesive is used to connect the overply

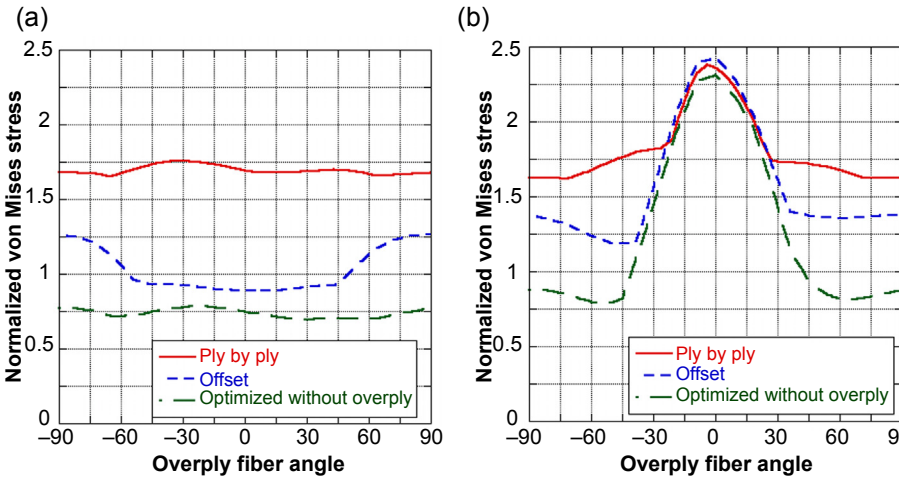

Figure 26.12 Effect of overply fiber orientation on adhesive in models (a) OP2 and (b) OP1.
Brietzman, T.D., Iarve, E.V., Cook, B.M., Schoeppner, G.A., & Lipton, R.P. Optimization of a composite scarf repair patch under tensile loading. *Composites Part A: Applied Science and Manufacturing*, *40*(12), 1921−1930.

to the adherend, large peel stresses occur near the outer edge of the adhesive when a near-0° overply is used. Hence, the preference is 54° or −54° for the overply fiber orientation in order to minimize the stress in the adhesive.

The optimal repair patch stacking sequence was determined for both overply models as well. The results of all optimizations are shown in Table 26.2. The flush repair (optimized flush repair) patch optimization was described in the previous section. The other columns show the OP1 and OP2 overply repair optimization results. In both cases, the fiber orientation in the overply was treated as an optimization variable independent of the other repair layers. The column Optimized OP2 used the OP2 overply model, while the column Optimized OP1 used the OP1 overply model.

The differences seen between the optimization results using models OP1 and OP2 reflect the trend discussed above. In the idealized case of the attached overply (OP2), its optimal orientation is calculated at 5.26° and the repair patch contains several near-0° layers. This phenomenon is due to the ability to directly transfer load from the adherend to the overply without loading the adhesive. Thus, the overply carries large loads and wants to be in near-0° orientation. This tendency, however, is different than the trend exhibited in both the flush (no overply) repair and the repair using adhesive to connect the overply to the adherend (OP1). Both of these optimal designs avoided the use of 0° plies in the repair plies, including the overply.

Finally, the strength of the laminates with an optimized repair patch was calculated. The algorithm shown in Figure 26.7 was utilized along with adhesive constitutive Eqn (26.1).

26.4.2 Repair strength retention

Five specimen types were tested for tensile strength, consisting of ASTM tensile coupons, large virgin panels, large panels having an unrepaired scarfed hole, and two types of panels with scarf repair (standard ply-by-ply replacement with overply and optimized patch layup without overply). For large virgin panels, the test results only include dogbone panels, since all rectangular panels had inadmissible grip failures. For the scarfed and not repaired, as well as the repaired specimens, rectangular and dogbone geometries are reported as a single group.

All three scarfed (unrepaired) panels failed through the center of the scarf cutout as shown in Figure 26.13. The average failure for the three specimens occurred at 207 MPa with a coefficient of variation of 2.3%. Recorded strain responses were similar for gages at identical locations on the three specimens. Benchmark comparisons for strength of the small coupon, virgin, and scarfed unrepaired panels are shown in Figure 26.14. Two predicted values of tensile strength are also shown for the large virgin panels and scarfed unrepaired panes. The predicted strength of the virgin panels was obtained by Weibull scaling the strength of ASTM coupons with modulus $\alpha = 40$. The basis for scaling was the volume of the 0° plies in the two specimens. The strength of the scarfed unrepaired panels was predicted using CFV as described in the strength prediction methodology section above. Good agreement between the prediction and

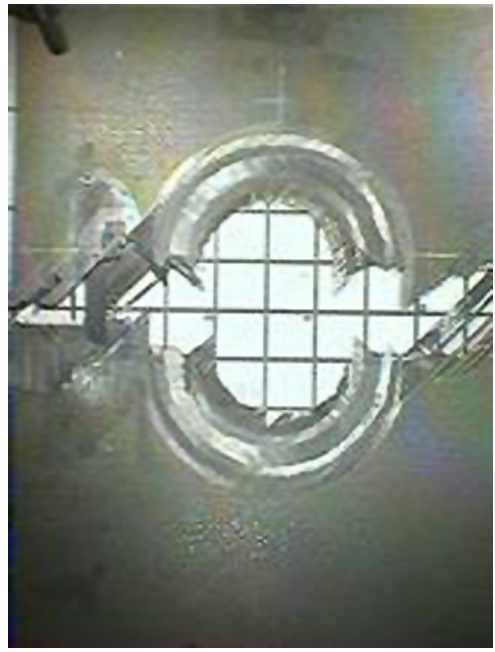

Figure 26.13 The front of scarfed panel 419T after failure.
Brietzman, T.D., Iarve, E.V., Cook, B.M., Schoeppner, G.A., & Lipton, R.P. Optimization of a composite scarf repair patch under tensile loading. *Composites Part A: Applied Science and Manufacturing*, *40*(12), 1921−1930.

experiment provides confidence in the fiber failure prediction methodology, which is used in combination with the nonlinear adhesive modeling to predict strength of the repaired specimens. All strength data are normalized by the average strength of 704 MPa for ASTM coupon specimens.

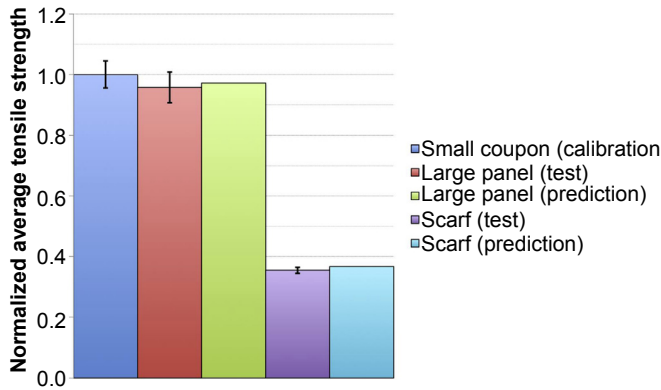

Figure 26.14 Normalized strength of virgin and scarfed laminates.

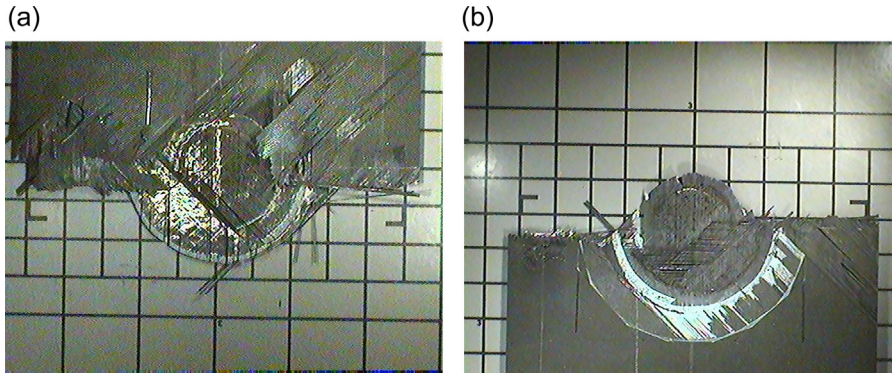

Figure 26.15 Front view of the (a) top and (b) bottom half of panel 418T after failure. Brietzman, T.D., Iarve, E.V., Cook, B.M., Schoeppner, G.A., & Lipton, R.P. Optimization of a composite scarf repair patch under tensile loading. *Composites Part A: Applied Science and Manufacturing*, *40*(12), 1921−1930.

Four of the repaired panels failed through the repaired region of the panels. In the case of the specimen shown in Figure 26.15, the patch was split in half, with the remaining sections attached to both halves of the panel. The lighter-colored material on the laminate is the adhesive used to bond the patch to the laminate. Slight variations in strain gage response were observed when comparing specimens, but all specimen strain responses followed the same trends. The repaired panels with the dogbone configuration were slightly stronger, and several specimens exhibited failures not traversing the patch, especially in the case of the optimized repair, which was only performed on the dogbone specimens.

Normalized experimental and predicted values of tensile strength of the repaired panels are shown in Figure 26.16. The experimental values were obtained for standard ply-by-ply repair with overply and optimized patch repair without overply, and thus the latter repair contained one ply less. Predictions were made for the ply-by-ply repair with and without overply as well as the optimized patch repair with and without overply, as well as with the overply ideally attached to the top of the laminate without adhesive (hypothetical case). As expected, the overply has a positive effect on the strength retention of repair for all patch compositions. The optimal design−predicted strength for the repair without the overply is 33% larger than the ply-by-ply strength. The optimal design configuration using model OP1 pushed the repair strength up to 90% of the virgin material strength. The idealized design using model OP2 predicted a repaired strength of 103% of the virgin laminate strength. The predicted strength values of the standard repair with the overply and the optimized flush repair are quite close to the experimental data, even though the strength of the standard repair is underpredicted and the strength of the optimized repair is overpredicted. It is experimentally observed, however, that the optimized flush repair is stronger than the standard repair with the overply, despite the extra ply carrying load in the latter case.

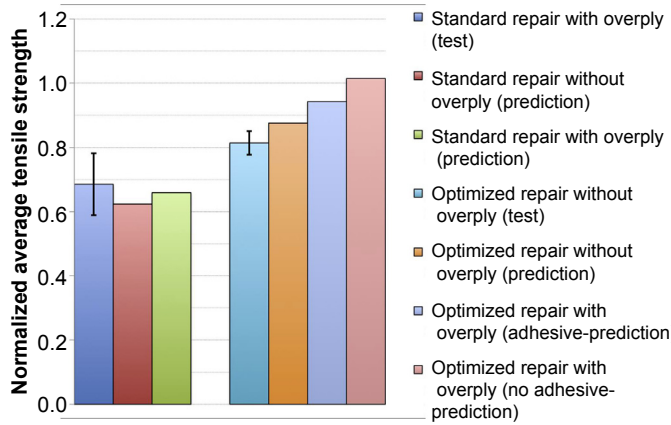

Figure 26.16 Predicted strength comparison for repaired laminates.

The fiber failure load predicted via CFV for the repaired laminates is shown as a function of the applied load in Figure 26.17. As previously described, CFV predicts the applied load at which the fibers in the 0° ply will fail macroscopically, causing a catastrophic failure of the laminate. Thus, failure is predicted to occur when the CFV-predicted fiber failure load is less than or equal to the applied load. For all repair cases in Figure 26.17, the CFV fiber failure load is constant at low loads. This corresponds to loads at which the adhesive is perfectly intact. At approximately 450 MPa of applied load for standard repair, the adhesive fails cohesively, suddenly overloading the 0° fibers and causing a steep descent in the CFV load that indicates laminate failure. It is interesting that the optimized repair with no overply and the optimized repair with overply in the OP1 configuration do not display similar behavior; that is, the adhesive does not fail before the fibers. The lower initial CFV load in these repairs indicates that the fibers in the adherend are carrying more load, which is consistent

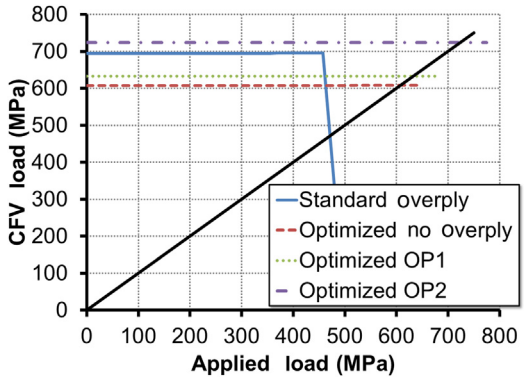

Figure 26.17 Predicted fiber failure loads for repaired laminates.

with optimized repairs being more compliant due to the minimization of high stress in the adhesive. However, due to the reduction in stress in the adhesive, both optimized repairs maintain the integrity of the adhesive right up to fiber failure in the laminate. The optimized repair with overply in the OP2 configuration clearly shows the advantage of having a repair load path that does not pass through any adhesive. The stiff overply reduces the load in the laminate, increasing the CFV load. The optimized patch also minimizes the stress in the adhesive, producing a repair that is stronger than the ASTM coupon specimens.

26.5 Conclusions

The mechanics of composite repair were examined under tensile loading with and without overlay plies for nontraditional patch ply orientations. Three-dimensional nonlinear analysis was performed for the prediction of repair failure occurring as a result of adhesive failure. Only cohesive failure inside the adhesive was taken into account, with tensile strength properties measured on bulk adhesive and KGR-1 shear response. The failure of the adherend was predicted by a statistical criterion applied to the tensile fiber failure mode only. Good baseline comparisons for open-hole scarfed panels and panels repaired by standard ply-by-ply replacement patch composition were achieved.

Von Mises stress distributions in the adhesive were examined as a function of thickness and orientation of the overply for standard repair patch composition. Similar to the flush repair case, the adhesive stress peaked at the junction of the 0° plies, which coincided with the loading direction. It was shown that the overply only reduced the stress concentration at the 0° ply joint nearest to itself. Increasing the overply thickness had only a small effect on the stress concentration at the juncture of the 0° plies on the opposite side of the plate.

Multidimensional optimization was performed to calculate the repair patch ply orientations that reduce von Mises stress in the adhesive. These optimal stacking sequences achieved significant reduction of stress levels and resulted in predictions of up to 85% and 90% strength restoration, respectively, for flush and single-ply thickness overply repair. Experimental results agree with the predicted trends and show higher strength retention in the flush optimized repair than in the standard repair with the overply, despite the latter having an extra ply to carry the load.

Practical realization of optimized composite repair requires further study of the sensitivity of strength retention to the orientation of the patch plies. Field conditions often result in repair ply orientation accuracy error within $\pm 5^\circ$.

26.6 Future trends and recommendations

Composite repair is an integral and critical aspect of the service and maintenance of growing fleets in the aerospace, automotive, and marine composite−vehicle industries. The aim of today's stringent certification requirements for the aerospace primary

structure is to assure that the structure can be operated safely for the certified service life of the vehicle. The US Air Force has developed and uses a damage-tolerance methodology for primary structure certification that requires the utilization of either a slow-damage-growth or a fail-safe approach to structure design. In the absence of validated slow-damage-growth analysis tools for composites, the aerospace industry has resorted to a no-damage-growth criterion to satisfy damage-tolerance requirements. As damage-growth-analysis tools for composites are developed, matured, and validated, the perceived conservative designs required to meet the no-damage-growth criterion may eventually lead to less conservative designs with lower margins of safety. These lower-margin-of-safety structures are likely to result in greater instances of fatigue, wear, and damage that will correspond with a greater number of needed repairs. The development of validated composite repair optimization analysis tools and analysis tools that can predict the service life of bonded repairs, including the effects of the service environment (hygrothermal aging) and bond line defects, are critical to meeting the future sustainment needs of composite aircraft structures. Additionally, the reliance on bonded repairs will require development and/or maturation of nondestructive evaluation tool to provide a high confidence level in the initial repair quality as well as the integrity of the repair throughout the life of the structure. Repair, and composite repair in particular, is frequently addressed by special symposia organized by the committees of professional societies (e.g., ASTM Committee D30 on Composite Materials and ASTM Committee F16 on Fasteners).

Acknowledgments

The authors acknowledge the support of the analytical portion of the work by the Air Force Office of Scientific Research under contract FA9550-07-1-0028 to the University of Dayton Research Institute. Numerous and frequent discussions with Dr. Gregory Schoeppner, Dr. David Mollenhauer, James Mazza, and Dr. Brett Bolan of the AFRL Materials and Manufacturing Directorate in the course of the work and manuscript preparation are greatly appreciated. Authors are especially thankful to Ms. Carrie Roemer for editing and formatting the manuscript.

References

Adkins, D. W., & Pipes, R. B. (1985). End effects in scarf joints. *Composites Science and Technology, 22*, 209−221.

Baker, A. A. (1999). Scarf repairs to highly strained graphite/epoxy structure. *International Journal of Adhesion and Adhesives, 19*(1), 161−171.

Bestley, C. C. N., Brown, S. G. R., & Alston, S. M. (2011). Experimental validation of a thermal model of adhesively bonded scarf repairs for CFRP composite materials incorporating cure kinetics. In *Proceedings fifth international conference on computational methods and experiments in materials characterisation,13−15 June, 2011, Kos, Greece*.

Brietzman, T. D., Iarve, E. V., Cook, B. M., Schoeppner, G. A., & Lipton, R. P. (2009). Optimization of a composite scarf repair patch under tensile loading. *Composites Part A: Applied Science and Manufacturing, 40*(12), 1921−1930.

FM300 (2005). *High shear strength modified epoxy film adhesive, cytec engineering materials*.

Fredricson, B. M., Schoeppner, G. A., Mollenhauer, D. H., & Palazotto, A. N. (2007). Application of three-dimensional spline variational analysis for composite repair. *Composite Structures, 83*(2), 119−130. http://dx.doi.org/10.1016/j.compstruct.2007.04.017.

Gamma, B. A., Mahdi, S., Cichanowski, Yarlagadda, S., & Gillespie, J. W. (2005). Static and strength of scarf-repaired thick-section composite. In K. T. Kedward, & H. Kim (Eds.), *Joining and repair of composite structures, ASTM STP 1455*. West Conshohocken, PA: ASTM International, 2004.

Grimsley, F. M., & Michaels, C. E. (1994). *Structural repair of burned composite skin*. AIAA-94-1432-(CP).

Harman, A. B., & Wang, C. H. (2006). Improved design methods for scarf repairs to highly strained composite aircraft structures. *Composite Structures, 75*, 132−144.

Harman, A. B., & Wang, C. H. (2007). Damage tolerance and impact resistance of composite scarf repair. In *Proceedings 16th international conference on composite materials, Kyoto, July, 8−13, 2007* (pp. 2−7).

Hart-Smith, L. J. (1973). *Adhesive-bonded scarf and stepped-lap joints*. NASA CR-112237.

Hoshi, H., Nakano, K., & Iwahori, Y. (2007). Study on repair of CFRP laminates for aircraft structures. In *Proceedings 16th international conference on composite materials, Kyoto, July, 8−13, 2007* (pp. 2−7).

Iarve, E. V., Mollenhauer, D. H., & Kim, R. (2004). Mesh-independent modeling and Moiré interferometry studies of damage accumulation. *Mechanics of Composite Materials, 40*(5), 419−426.

Iarve, E. V., Mollenhauer, D., & Kim, R. (2005). Delamination onset prediction in joints by using critical weibull failure volume method. In *Proceedings of ICCM-15, Durban, SA*.

Iarve, E. V., Mollenhauer, D. H., Whitney, T., & Kim, R. (2006). Three dimensional stress analysis and Weibull statistics based strength prediction in open hole composites. *Composites Part A: Applied Science and Manufacturing, 38*(1), 282−294.

Iarve, E. V., Mollenhauer, D. H., Whitney, T., & Kim, R. (2006). Strength prediction in composites with stress concentrations: classical Weibull and critical failure volume methods with micromechanical considerations. *Journal of Material Science, 41*(20), 6610−6622.

Kumar, S. B., Sivashanker, S. I., Osiyemi, S. O., Bag, A., & Sridhar, I. (2005). Failure of aerospace composite scarf-joints subjected to uniaxial compression. *Materials Science and Engineering A, 412*, 117−122.

Kumar, S. B., Sridhar, I., Sivashanker, S. I., Osiyemi, S. O., & Bag, A. (2006). Tensile failure of adhesively bonded CFRP composite scarf joints. *Materials Science and Engineering B, 132*, 113−120.

Lubkin, J. L. (1957). A theory of adhesive scarf joints. *Journal of Applied Mechanics, 24*, 255.

Mollenhauer, D. H., Fredrickson, B. M., Schoeppner, G. A., Iarve, E. V., & Palzotto. (2008). Moiré interferometry measurements of composite laminate repair behavior: influence of grating thickness on interlaminar response. *Composites: Part A, 39*, 1322−1330.

Press, W., Flannary, B. P., Teukolsky, & Vetterling, W. T. (1989). *Numerical recipes*. Cambridge. pp. 690.

Rousseau, C. Q., & Iarve, E. V. (2012). Durability of structural joints. In K. V. Pochiraju, G. P. Tandon, & G. A. Schoeppner (Eds.), *Long-term durability of polymeric matrix composite* (p. 483), Springer.

Schoeppner, G. A., Mollenhauer, D. H., & Iarve, E. V. (2004). Prediction and measurement of residual strains for a composite bonded joint. *Mechanics of Composite Materials, 40*(2), 119−134.

Soutis, C., & Hu, F. Z. (1998). *A 3-d failure analysis of scarf patch repaired CFRP plates*. AIAA-98−1943.

Soutis, C., & Hu, F. Z. (2003). Strength analysis of adhesively bonded repairs. In L. Tong, & C. Soutis (Eds.), *Recent advances in structural joints and repairs for composite materials* (pp. 141−170). London: Kluwer Academic Publishers.

United States Air Force (1973). Advanced composite design guide. In *AFML Wright- Patterson air force base* (Vol. II). United States Air Force (Analysis).

Wang, C. H., & Gunnion, A. (2006). *Design methodology for scarf repairs to composite structures*. DSTO-RR-0317.

Wang, C. H., & Gunnion, A. J. (2008). On the methodology of scarf repairs to composite laminates. *Composite Science and Technology, 68*, 35−46.

Wisnom, M. R., Khan, B., Green, B., Jiang, W., & Hallet, S. R. (2005). Specimen size effects on tensile strength and failure mechanisms of carbon/epoxy composites. In *JNC14 Conference, Compiegne, March 2005*.

Carbon and titanium dioxide nanotube polymer composite manufacturing – characterization and interphase modeling

27

G.C. Papanicolaou, D.V. Portan
University of Patras, Patras, Greece

27.1 Introduction

The nano-sized world has opened the gate to a "fantastic hidden corner" of our universe. This world was long ago intuited by our ancestors—those original scientists and philosophers who did not have the means to prove, but simply knew. For centuries, when coming face to face with proof, an explosion of enthusiasm would fill a scientist's heart. Despite that, understanding things at a nano level did not seem to be an easy task, proved by the continued intense investigation of well-known pioneering subjects of nanoresearch in several scientific fields. Such an example in the area of nanocomposite materials is the use of carbon nanotubes (CNTs) in the reinforcement of polymers.

CNT-reinforced polymers are considered the most popular nanocomposites. Moniruzzaman and Winey (2006) published a diagram indicating the number of publications and patents related to CNTs and CNT-reinforced polymers. As can be seen in Figure 27.1, immediately after their discovery in 1991, interest in these nanostructures and composites increased exponentially, while the number of published studies grew tremendously.

One may ask "why CNTs, and why CNT-reinforced polymers?" Considering that between 2000 and 2010 research has been directed toward, or better said resumed in, these applicable innovations, it must be acknowledged that the first motivation to reinforce polymers with CNTs was to take advantage of the potential efficiency of this combination. Owing to their unique mechanical properties (high tensile strength and modulus), CNTs were considered ideal candidates for polymer reinforcement (Coleman, Khan, & Gun'ko, 2006); further on, they were also chosen for their electrical and physical properties in addition to the aforementioned mechanical ones.

For those who still wanted to study CNT-reinforced polymers from a purely scientific viewpoint, these composites became extremely challenging. The load transfer efficiency from the surrounding matrix to CNTs in CNT-reinforced polymers has been a primary issue and the subject of several investigations (Hwang, Shieh, & Hwang, 2004; Jia-Lin & Ting-Chu, 2009; Xiao & Zhang, 2004). After all, "the bridge"

Structural Integrity and Durability of Advanced Composites. http://dx.doi.org/10.1016/B978-0-08-100137-0.00027-4

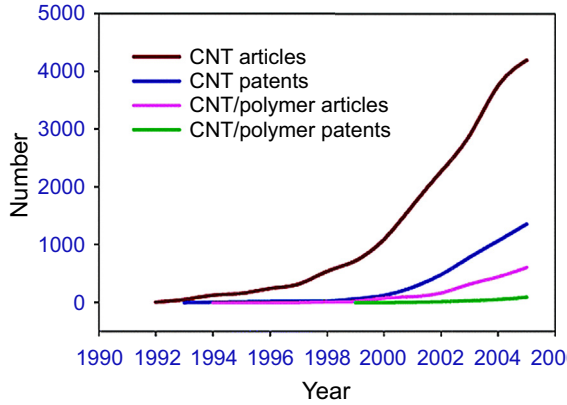

Figure 27.1 Number of publications and patents on CNTs or CNT-reinforced polymers to 2006. Reprinted with permission of Moniruzzaman M. & Winey K. I. (2006). *Journal of Macromolecules*. Copyright 2006 American Chemical Society.

between the reinforcing phase and the matrix in micro- and nano-composites is assumed to be the main responsible factor influencing composite performance, while the load transfer is directly connected to and dependent on it (Grande, Mandell, & Hong, 1988; Pulickel, Jonghwan, & Nikhil, 2006). This bridge was initially called the *interface*, denoting a line separating two phases in a material that were different with respect to their chemical or physical properties. The *interface* was not a realistic concept and was used mostly in mathematical or computerized modeling; in time it was proved that it did not fit very well with practical experimentation, thus limiting advanced predictions of composite behavior. In reality, a rather complex situation develops around an inclusion embedded in a matrix, consisting of areas of imperfect bonding, mechanical stresses due to shrinkage, high stress gradients, or even stress singularities due to the geometry of the inclusion, voids, microcracks, etc. Moreover, the interaction of the filler surface with the matrix material is usually something much more complicated than a simple mechanical effect, as it results in a quite inhomogeneous region. This complex region has been termed the *interphase* and is described as a third phase created between the matrix and a filler with properties different from those of the two initial phases, where a number of phenomena of various natures occur (Papanicolaou, Paipetis, & Theocaris, 1978). Although it was affirmed long ago that the interphase plays a crucial role in composite structure (Kinloch, Littlea, & Watts, 2000; Swain, Reifsnider, Jayaraman, & El-Zein, 1990), it is also certain that in the minuscule nanoworld, each property of the composing phases is highly important. To focus on the interphase, one must be aware of all advantageous and disadvantageous properties introduced by the constituent phases. In this case, the need to control the structures and properties of the parts that make up a composite material is immediate.

CNTs can hardly be organized in a layer or other well-defined structure. The need for self-organization in interphase investigation at the nanoscale level brought the

titanium dioxide (TiO_2) nanotube (also known as a titania nanotube or by the acronym TNT) to the attention of researchers. The electrochemical anodizing method is often applied for the synthesis of TNT layers, a type of self-organized substrate (Portan, Kroustalli, Deligianni, & Papanicolaou, 2012; Portan, Papaefthymiou, Arvanita, Jiga, & Papanicolaou, 2012; Yan-Tao et al., 2003). TNTs are extremely convenient when manufacturing multilayered hybrid nanocomposites because they allow the interaction of two nanostructured substrates, resulting in the creation of an interphase between them; titania hybrid nanocomposites permit the study of nanostructured interphases from a purely scientific viewpoint, and are promising for use in advanced applications.

Finally, using different composite architectures such as CNT or TNT nanocomposites, one may approach the interphase concept and obtain experimental results that represent the basis for achieving the predictive modeling of nanocomposites. The present chapter describes the most important aspects related to the synthesis methods and characterization of CNT and TNT composites. The manuscript includes the state of the art as well as the results from other authors on these topics. Further on, the viscoelastic hybrid interphase model (VHIM) is applied for the prediction of the mechanical behavior of manufactured nanocomposites. Both experimental and theoretical investigations are analyzed and compared in summary in specific sections.

27.2 Carbon nanotubes

27.2.1 Background and short history

During the last few decades, major breakthroughs in carbon science and technology have delivered new carbon materials such as carbon fibers, fullerenes, and CNTs, and some envisage the carbon age replacing the silica era (Endo, Tsuruoka, & Ichihara, 2008). When found in sp^2 hybridization form, occurring between one s-orbital and two p-orbitals, carbon can form a variety of amazing structures. Apart from the well-known graphite, carbon can build closed and open cages with a honeycomb atomic arrangement. The first such structure to be discovered was the C_{60} molecule, and CNTs came subsequent to that discovery. Since their observation more than a decade ago (Boehm, 1997; Iijima, 1991), CNTs have been the focus of considerable research, and numerous investigators have since reported remarkable physical and mechanical properties for this new form of carbon. From unique electrical properties and thermal conductivity higher than that of diamonds, to mechanical properties where the stiffness, strength, and resilience exceed those of any other currently known materials, CNTs offer tremendous opportunities for development of fundamentally new material systems. In particular, the exceptional mechanical properties of CNTs combined with their low density offer scope for the development of nanotube-reinforced composite materials. The potential for nanocomposites reinforced with carbon tubes having extraordinary specific stiffness and strength represents a tremendous opportunity for the application of such materials during the twenty-first century (Thostenson, Ren, & Chou, 2001).

Most reports in the literature attribute the discovery of hollow, nanometric-sized tubes composed of graphitic carbon to the work of Iijima, published in 1991 (Iijima, 1991), whereas the single-walled carbon nanotube (SWCNT) concept was firstly reported in 1993 in two independent papers published by *Nature*, one by Iijima and the other by Bethune et al. (1993). Iijima's (1991) paper evidenced the possibility of growing CNTs without the need of a catalyst, and boosted research on multiwalled CNTs (MWCNTs), although the possibility of growing carbon filaments from the thermal decomposition of gaseous hydrocarbon was first reported much earlier, in 1889 (Hughes & Chambers, 1889). Even though controversy existed on the CNT synthesis subject, the papers of Schützenberger and Schützenberger (1890) and Pélabon and Pélabon (1903) can be considered the earliest evidence of the growth of CNTs, and this is due to advanced technology that permitted a high-quality investigation. It is good to recall that a much older paper published by Oberlin, Endo, and Koyama (1976) presents a figure illustrating a nanotube, perhaps a SWCNT; the authors did not state that it was a nanotube structure, and due to magnification issues the number of walls could not be determined. Until now, there has been no clear evidence of a CNT discoverer, but the work is still worthy of our appreciation to all the ones mentioned above for their great contributions. Although they do not have a long history, CNTs have been widely studied both separate and combined (composite) formulas. Due to length limitations, only a few of the investigations on CNTs and CNT composites are presented in this chapter.

The year 2014 has just started and new research on CNTs has been already performed. Thus, we find out that incorporating pentagons and heptagons into the hexagonal networks of pristine CNTs may form various CNT-based nanostructures (Liu, Liu, & Zhao, 2014). Subsequent to that work, CNT nanocomposites were present in the manufacturing of cation exchange resin nanocomposites based on MWCNTs exhibiting increased stability and environmental safety (Fathy, Abdel Moghny, Awad Allah, & Alblehy, 2014), while a CNT circuit integration with sub-20 nm channel length has been synthesized and reported by Shulaker et al. (2014). As far as can be seen, intensive research continues on this subject, bringing new extraordinary ideas to the original science. Further on, aspects related to the manufacturing, structure, and health issues of CNTs are presented.

27.2.2 Carbon nanotube synthesis, structure, and health issues

As the fields of nanotechnology and nanoscience push their investigations forward to produce CNTs with suitable parameters for diverse applications, it is evident that new approaches to CNT synthesis need to be developed and optimized. CNT preparation methods include arc discharge, laser ablation, and chemical vapor deposition. In between, the rarely used CNT manufacturing method also mentioned in literature is the arc discharge deposition involving arc discharge in liquid solutions, which is contrary to the standard of using deposition in a gas atmosphere. In addition, a uniform vertically aligned CNT synthesis using lithographic techniques for catalyst deposition, as well as a method utilizing a nanoporous anodized aluminum oxide as a pattern for selective CNTs growth, is another method used to synthesize

CNTs. A schematic representation of CNT preparation methods is given in Figure 27.2 (Prasek et al., 2011).

The CNT structure is a hollow cylinder of carbon atoms with the appearance of rolled tubes of graphite, such that their walls are hexagonal carbon rings often formed in large bundles. The ends of CNTs are domed structures of six-membered rings capped by a five-membered ring. There are two basic types of nanotubes, single-walled nanotubes (SWNTs) and multiwalled nanotubes (MWNTs), which differ in the arrangement of their graphene cylinders. SWNTs have only one single layer of graphene cylinders, while MWNTs have many layers (approximately 50). Depending on their structure, the three types of nanotubes are (1) armchair, (2) zigzag, and (3) chiral. CNTs can be either metal or semiconductor in nature; they differ symmetrically and can vary in function due to the way they "roll up." The diameter of a CNT can be 50,000 times thinner than a human hair, yet a nanotube is stronger than steel per unit weight (Dresselhaus, Dresselhaus, & Avouris, 2001; Ganesh, 2013).

Despite their popularity, CNTs are not the best choice to work with due to some important health issues. The field of nanotechnology has burgeoned in recent years, and today the market includes more than 1000 nanoproducts. The technology involves modifying material at virtually the atomic level. Concerning CNTs, their extremely small particles may constitute a health risk, including, among others, the risk that CNTs may lead to cancer in the worst case, or to various forms of allergies after direct contact with even an extremely small amount of CNT powder

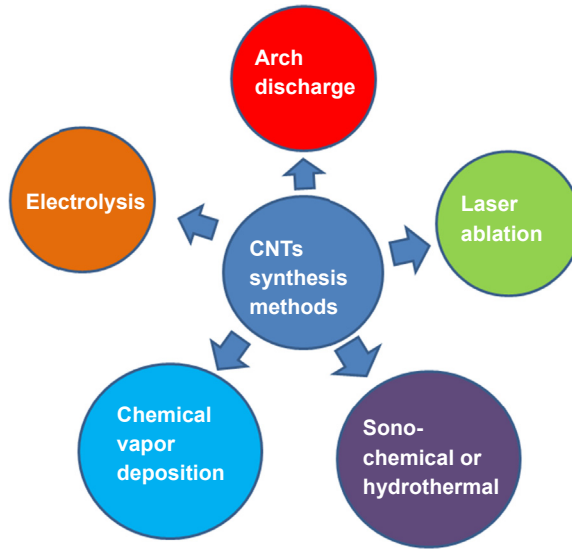

Figure 27.2 Main CNTs synthesis methods.
Reproduced with permission of Jan Prasek et al. (2011). *Journal of Materials Chemistry*. Copyright 2011 Royal Society of Chemistry.

(Lam, 2006; Ryman-Rasmussen et al., 2009). The advice of specialists is that secure measures should be taken when working with carbon nanostructures.

27.2.3 Mechanical properties of carbon nanotubes

SWCNTs can hardly be obtained as isolated tubes, whereas bundles (ropes) are formed from single-walled tubes bonded through weak van der Waals forces. Changes in synthesis parameters lead to the production of MWCNTs. In the "early days" the high elastic modulus of CNTs was taken as a given. The first experiments were performed using tubes obtained by arch discharge or laser ablation methods, primarily chemical carbon vapor deposition (CCVD). Multiwalled CCVD can produce CNTs with deceivingly low Young's moduli—below 100 GPa. Until now, only double-walled CCVD-grown tubes have reached 1 TPa, opening the way for mass applications that use their extraordinary mechanical properties: high flexibility, high moduli, and high strength combined with low density (Kulik, Kis, Lukic, Lee, & Forró, 2007, p. 583).

CNTs are expected to have high stiffness and axial strength as a result of carbon−carbon sp^2 bonding, and efforts have been applied to the experimental and theoretical investigation of these properties. Theoretically, the tensile strength and Young's moduli of CNTs have been found to be upwards of ~140 GPa and ~1 TPa, respectively, but experimentally no nanotube of any kind has been found to have a practical strength even close to its theoretical value. This is caused predominantly by material defects that can lower tensile strength values by as much as 85%. It is commonly known that a chain is only as strong as its weakest link, and this phenomena also applies to CNTs, as they also are only as strong as their weakest segment. Mechanically, it is also important to know that CNTs have very low densities, around 1.3−1.4 g/cm^3 depending on their type. This means that they are also of very light weight, another desirable property in almost all situations. Because these tubes are hollow, they have astonishing energy-absorption properties, where the tubes bend elastically and convert kinetic energy into potential energy before they bend back to their original position. In addition, multiwalled CNTs exhibit a striking telescoping property, where an interior nanotube may slide linearly or rotationally with almost zero friction (Coleman et al., 2003; Coleman, Khan, Werner, & Gun'ko, 2006; Tran, Humphries, Smith, Huynh, & Lucas, 2009; Yu et al., 2000).

A major application of CNTs is in the reinforcement of polymers in processing composite materials, as it has been experimentally found that CNTs possess splendid mechanical properties in such formulas. Various experimental studies have been conducted in order to understand the mechanical properties of a variety of CNT and CNT-based composite materials. The systematized data of past research results of CNT and their nanocomposites are extremely useful to improve processing and design criteria for new nanocomposites in further studies. In this context, the next section deals with the manufacturing and characterization of epoxy resin/MWCNT composites.

27.3 Manufacturing and characterization of epoxy resin/carbon nanotube composites

Many investigators have endeavored to fabricate advanced CNT composite materials that exhibit improved mechanical or electrical properties when compared with other forms of carbon-reinforced matrices. For example, CNTs are quite effective compared with traditional carbon black microparticles, primarily due to their large aspect ratios. In between the three main categories of CNTs (single-, double-, and multi-walled), MWCNTs are preferred due mainly to their accessible price and ease in manufacturing. In this section, the manufacturing method of epoxy resin/MWCNT composite is described.

27.3.1 Epoxy resin/carbon nanotube composite preparation and processing

Polymer nanocomposites play emergent roles in materials innovations that make possible stiffer, lighter-weight, and higher-performance products. Unlike other plastics, a polymer nanocomposite is fabricated by introducing a small amount of solid nanoscale fillers (normally less than 5 wt%) such as nano-clay, CNTs, or nanofibers into a plastic resin to dramatically enhance its stiffness, strength, and thermal properties (Gangopadhyay & De, 2000; Han & Fina, 2011). The difference between nanocomposites and conventional fiber composites is that the added fillers are extremely small, about one-millionth of a millimeter thick, and provide a much larger interface area per unit volume, thus greatly improving the interfacial bonding effect between nanofillers and the polymer matrix (Ma, Mo, Tang, & Kim, 2010; Zeng, Yu, & Lu, 2008). As was reported by Eitan, Fisher, Andrews, Brinson, and Schadler (2006), the large nanotube surface area in a nanotube−polymer composite results in a significantly thicker interphase region of immobilized polymer that contributes as a supplementary reinforcement mechanism for the composite. Previous investigations show that the lengths of nanofibers/nanotubes play an important role in the toughening mechanism of nanocomposites (Wan, Delale, & Shen, 2005; Zhang, Picu, & Koratkar, 2008). Excepting that, the manufacturing method of polymer/CNT composites, and especially the step consisting of the dispersion of the reinforcement in the matrix, is crucial for a good final composite product.

Some of the various processing methods used in polymer/CNT composite preparation are solution mixing, in situ polymerization, electrospinning, and melt blending. Among the polymer matrices, epoxy resins are more often used in CNT/thermoset composite manufacturing. Epoxy resins have shown extremely low percolation threshold when CNTs are added. This is an interesting issue in terms of industrial applications, because it facilitates processing and contributes to lower final prices (Chapartegui et al., 2011).

Due to the high surface energy of nanotubes, they have a tendency to aggregate together owing to the strong attractive forces between CNTs themselves. The attractive van der Waals interactions, owing to the high aspect ratios of MWCNTs, lead to

agglomeration of CNTs in epoxy resins. The aggregated CNTs are in the form of bundles or ropes, usually with highly entangled network structures that are very difficult to disperse. The homogeneous dispersion of nanofillers within the polymer matrix is a prerequisite of any composite and is a problem to be solved for nanotube-reinforced epoxies. In the last few decades, the ultrasonication method used for CNT dispersion in the matrix material became one of the most popular mixing methods, especially in laboratory research. The literature on ultrasonic dispersion of nanoparticles in epoxy resin showed differing information about optimum processing parameters. These parameters include sonication power and amplitude, sonicator probe diameter, sonicator probe immersion depth, sonication mode (pulsing or continuous) and pulsing mode intervals, sonication temperature, sonication energy and energy densities, and container materials and dimensions (Alnefaie, Aldousari, & Khashaba, 2013). A final conclusion has not been given regarding the most efficient method for CNT/epoxy resin manufacturing, but many investigations are ongoing on this subject.

27.3.2 Nanotube dispersion methods and quality

The dispersion of CNTs in the matrix system is a main problem to be solved for nanotube-reinforced polymers (Chen, Liu, He, Huang, & Hwang, 2010). Nanoscale particles exhibit enormous surface areas (1000 m^2/g and more) that are several orders of magnitude larger than those of conventional fillers. This surface area acts as the interface for stress transfer, but is also responsible for the strong tendency of CNTs to form agglomerates. Extended research activities related to CNT-reinforced polymer composites and other possible CNT applications are being carried out in an effort to exploit their unique behaviors. To a large extent, this can be achieved by improving the dispersion conditions of the nanofillers in the resin, which leads to better wetting of the nanotubes and increases in the size of surface contact areas between constituent phases (Ci & Bai, 2006; Li, Zaiser, & Koutsos, 2004; Luo & Daniel, 2003; Miyagawa & Drzal, 2004; Schlabach, Ochs, Hanemann, & Szabó, 2011).

The dispersion of nanotubes in the matrix can be enhanced through physical−mechanical or chemical processes. Physical methods involve breaking up the agglomerates through impact (ball milling), shear (high-speed shearing), and high-frequency oscillation (ultrasonication) or a combination of them. Concerning the chemical methods, the purification procedure involves removal of the metallic catalyst residues that arise from CNT synthesis, and creation of functional groups on the surface or caps of CNTs. These functional groups are the reactive sites of the CNT surfaces during further chemical modifications. They can also improve polymer−CNT interfacial interactions. However, functionalization is not recommended in all cases, especially in some cases where results from thermogravimetric analysis indicated a compromise between the functionalization parameters (sonication, concentration of acid treatment, etc.) and damage of the graphitic structure of CNTs (Aviles, Cauich-Rodriguez, Moo-Tah, May-Pat, & Vargas−Coronado, 2009).

In the next section, a case study on the type of mixing method applied for manufacturing MWCNT-reinforced epoxy resins as well as their mechanical response depending on the manufacturing protocol are presented.

27.3.3 Case study on multiwalled carbon nanotube–reinforced epoxy resins

With the purpose to achieve the predictive modeling of composites behavior, Papanicolaou et al. manufactured and investigated different microtube- and nanotube-reinforced composites (Papanicolaou, Lagas, Papadimitropoulos, & Ioannou, 2010; Papanicolaou, Xepapadaki, & Angelakopoulos, 2012). In this context, CNT-reinforced epoxy resins were prepared and characterized, and their mechanical behavior has been predicted through analytical modeling in a number of studies; in the present chapter, two case studies are presented. The investigation of the interphase viscoelastic behavior of CNT-reinforced nanocomposites, and their modeling by means of the VHIM is described in Section 6.2 of this chapter.

An investigation on specimens of MWCNT–epoxy nanocomposites prepared by two different dispersion methods, respectively the ultrasonication and high-speed shear mixing methods, was performed (Papanicolaou, Papaefthymiou, Koutsomitopoulou, Portan, & Zaoutsos, 2012). The dispersion degree between MWCNT and polymer resin was optically analyzed using scanning electron microscopy technology. Further on, the effect of nanotube dispersion on the properties of the nanocomposite was studied through static three-point bending tests and dynamic mechanical thermal analysis. Interesting results concerning the dispersion effect of MWCNTs added in the polymer matrix, on storage and loss moduli as well as on tanδ and T_g values, were derived. Representative SEM micrographs are observed in Figures 27.3 and 27.4, while a comparison between the dynamic mechanical properties of nanocomposites manufactured by the sonication method and those manufactured by the shearing method is shown in Table 27.1.

The final conclusions were that nanocomposites produced by the shearing method were characterized by a limited aggregation, while those manufactured by the sonication method showed individual nanotubes scattered in the matrix and no aggregation was observed. The evaluation of the dispersion quality made using the photomicrographs was confirmed by the reinforcing efficiency of the nanotubes. A general result that can be derived is that except for the glass transition temperature, all static and dynamic properties of nanocomposites manufactured by the sonication method are superior when compared with respective properties of nanocomposites manufactured by the shearing method.

27.4 Titanium dioxide nanotubes

27.4.1 Titanium dioxide nanotube background and short history

Titanium dioxide (also known as titania) is a widely used inorganic material that occurs in various structural types and can be engineered into many different forms such as nanoparticles, sol–gels, nanofibers, and nanotubes. Titania also shows good biocompatibility and stability. In 1999, first reports showed the feasibility of growing

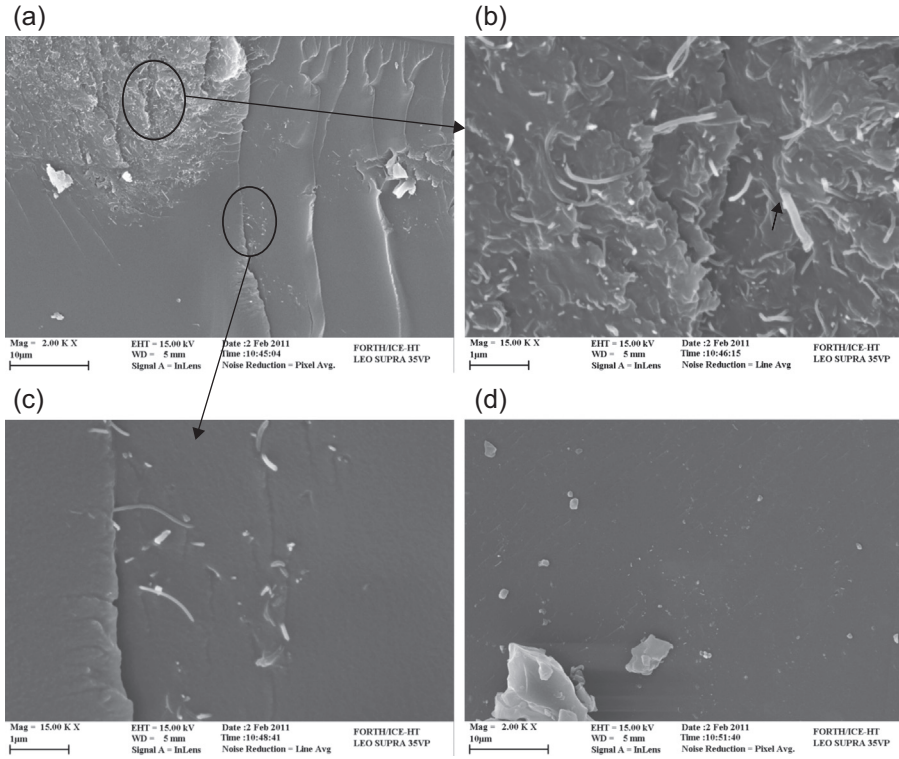

Figure 27.3 SEM images for 0.1 wt% MWCNT−epoxy nanocomposite manufactured by means of the high speed shearing method: (a) low-magnification−high-detail image illustrating regions of agglomerated and exfoliated CNTs coexisting and (b) high-magnification image of a CNT bundle. The arrow indicates "sword-in-sheath" rupture of CNTs: (c) high-magnification image of a dispersed pulled out CNT and (d) low-magnification−high-detail image illustrating a region where no agglomeration of CNTs is observed.
Papanicolaou et al. (2012).

highly ordered arrays of TNTs by a simple but optimized electrochemical anodization of titanium metal sheet (Figure 27.5). This finding stimulated intense research activities that focused on growth, modification, properties, and applications of these one-dimensional nanostructures (Norani Muti, Dzilal, & Dennis, 2008; Prida et al., 2007; Yin, Liu, & Shen, 2010).

TNTs became the research hot spot due to their superior performance and extensive application to various research and industrial fields. One-dimensional TNTs, owing to their large length−diameter ratio, have physical, electrical, and chemical properties that are different from those of other forms. Recent studies have shown that the structures of TNTs are diverse; the different synthesis parameters, such as temperature, pH, and TiO_2 concentration may result in TNTs with different diameters, degrees of porosity, and crystalline structures. Different crystalline structures of the nanotube walls have been suggested, for example, shell structure models based on anatase

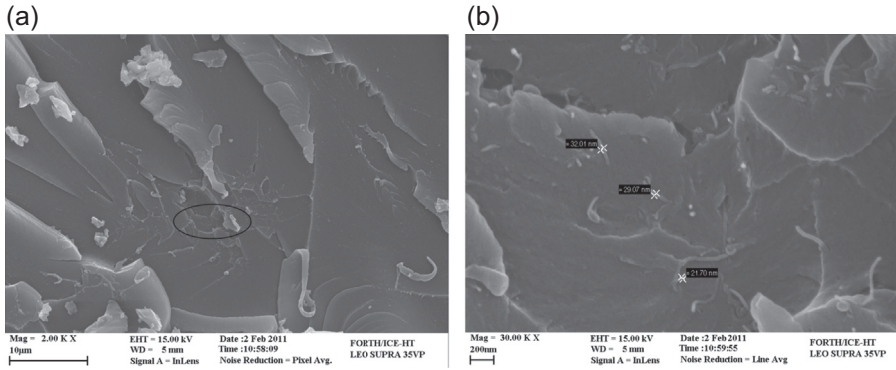

Figure 27.4 SEM images of the 0.1 wt% MWCNT−epoxy nanocomposite manufactured by means of the sonication method at (a) low magnification−high detail and (b) high magnification−high detail (no agglomeration of CNTs is observed).
Papanicolaou et al. (2012).

Table 27.1 Comparison between the dynamic mechanical properties of nanocomposites manufactured by the sonication method and those manufactured by the shearing method

E'_{so}/E'_{sh} at 25 °C	E''_{so}/E''_{sh} at 25 °C	$\tan\delta_{so}/\tan\delta_{sh}$ at 25 °C	$(E'_{so}/E'_{sh})_{max}$ at 25 °C	$(E''_{so}/E''_{sh})_{max}$ at 70 °C	$(\tan\delta_{so}/\tan\delta_{sh})_{max}$ at 80 °C
1.2	2.3	2.0	1.2	6.0	22.0

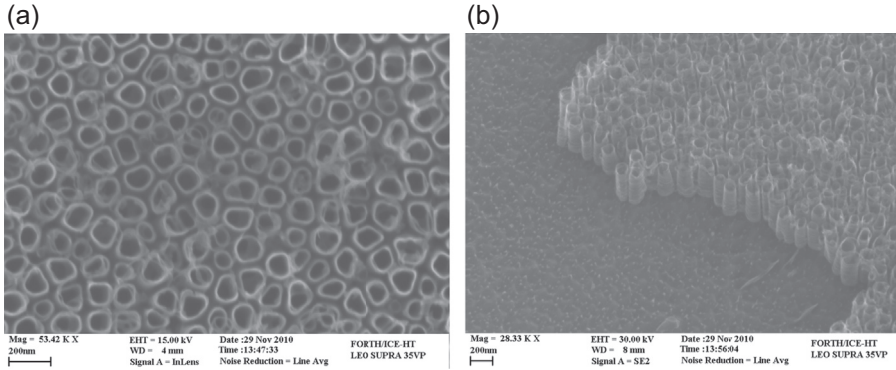

Figure 27.5 SEM images of titanium dioxide nanotubes: (a) panoramic view and (b) lateral view.
Papanicolaou et al. (2012).

and protonic titanates. Due to the unusual nanotubular structure and the interesting physicochemical properties, TNTs are used in many applications such as gas sensors, dye-sensitized solar cells (DSSCs), battery materials, and optical biosensors.

27.4.2 TNT fabrication methods and generations

Generally, there are three strategies used in the fabrication of TNTs: template synthesis, hydrothermal methods, and electrochemical synthesis (anodization of a titanium sheet). A few aspects related to these three methods are presented below.

27.4.2.1 Template synthesis

An advantage of template synthesis, electrodeposition, and chemical vapor deposition are the ease and speed with which they can be changed and applied to new research areas. In the scheme of template synthesis it is possible to identify three different steps: (1) the creation of the building blocks, (2) the assembly of the building blocks, and (3) the fabrication and control of the contact to the macroscopic world. Highly ordered TNTs and nano-fibrils can be synthesized by the sol−gel template method within the pores of anodic alumina template membrane. If the experiment is well organized and carefully handled, the synthesized nanotubes have uniform lengths and diameters, and form a highly ordered array. This method can be employed for obtaining a large surface area of TNTs for use in photocatalysis as well as for electrodes in solar cells (Maiyalagan, Viswanathan, & Varadaraju, 2006).

27.4.2.2 Hydrothermal method

The *hydrothermal method* is a simple way to prepare individual nanotubes, but only randomly aligned tubes can be obtained. In addition, this approach only produces protonated titanate nanotubes ($H_{2m}TiO_{2n+m}$) rather than TiO_2. These disadvantages limit further electrical application in nanodevices. The hydrothermal synthesis implicates the anatase conversion by hydrothermal synthesis to delaminated anatase inorganic nanotubes and titanate nanoribbons that are of potential interest as catalytic supports and photocatalysts. In the synthesis, the steps are (1) anatase is mixed with 10 M sodium hydroxide and heated at 130 °C for 72 h, and (2) the reaction product is washed with dilute hydrochloric acid and heated at 400 °C for another 15 h. The yield of nanotubes is quantitative, and the tubes have an outer diameter of 10−20 nm, an inner diameter of 5−8 nm, and a length of 1 μm.

27.4.2.3 Electrochemical anodizing

The anodic transformation of the titanium surface to produce nanotubes can be performed with a standard two-electrode electrochemical cell. A typical anodizing procedure involves the following steps:

1. The titanium foil and platinum/graphite plate are ultrasonically cleaned with acetone, isopropanol, ethanol, and deionized water.
2. After electrodes are dried, they are clipped onto the electrodes of a power supply and positioned in parallel with an interspacing of ∼2 cm.

3. A Teflon container is filled with 50 ml electrolyte solution, and the electrodes are submerged in the solution without stirring.
4. The power supply is turned on, and the anodization is carried out at room temperature (~22 °C).
5. Anodizing continues for several hours (usually during the anodizing process, the titanium foil surface turns colorful and dark with time).
6. At the end of the anodizing process, the titanium foil surface is rinsed several times with deionized water.
7. The unwanted surface deposits or leftover particles are removed by ultrasonication in deionized water for about 1 min, and then the samples are dried in air. For SEM imaging, a small region of the anodized titanium foil is analyzed.

So far, there have been three main generations of anodic titanium oxide nanotubes. In the first generation, TNTs were fabricated in HF-based aqueous solutions. Some other inorganic acids and fluoride compounds such as H_3PO_4/NaF, $NH_4F/(NH_4)_2SO_4$, and Na_2SO_4/NaF were used as substitutes for poisonous HF. Due to the rapid chemical dissolution rate, the length of the obtained nanotube was limited to 500 nm. These low-aspect-ratio tubes could not satisfy the requirements for applications in DSSCs or filter membranes. Through adjusting of the electrolyte pH, second-generation TNTs were fabricated and tube length was increased to a few micrometers. In the third generation, using an almost water-free polar solution, especially in viscous glycerol or ethylene glycol electrolytes, tens and even hundreds of micron-length TNTs were easily prepared.

27.4.3 Parameters affecting the morphological and structural characteristics of TNTs

Various TNT manufacturing methods have been proposed in the literature. Among them, electrochemical anodizing is a low-cost process, yet it also allows for superior control of nanotube dimensions compared with other methods. It is now well established that the properties of nanotube arrays are dependent upon their specific architectures, including length, wall thickness, wall roughness, pore diameter, and tube-to-tube spacing. The geometrical features of nanotube arrays are controlled by a variety of parameters including anodizing potential, electrolyte composition, and properties thereof (conductivity, viscosity, etc.), as well as anodizing time and temperature (Mohamed Ael, Kasemphaibulsuk, Rohani, & Barghi, 2010). Electrolyte pH plays a determinant role in increasing the length of nanotube arrays. The utilization of nonaqueous electrolytes renders better shaped and ordered tubes without sidewall heterogeneities (Won, Chan, & Hyuk, 2008). Another parameter that affects nanotube length and diameter is the etching rate. When the anodizing duration exceeds a certain limit, nanotubes have been observed to shorten, presumably due to dissolution-induced cleaving (Paulose et al., 2006). Further on, another crucial factor that influences nanotube diameter growth is the electric voltage applied. It is generally accepted that after a threshold value is exceeded and an ionic current is produced, nanotube diameter increases proportionally with voltage (Neupane et al., 2011). On the other hand, the rate of pore size increase is strongly dependent on the type of electrolyte utilized, and each research group chose it depending on its efficiency, toxicity, and the type of application for

which the nanotubes were created. A tremendous number of studies are dedicated to the investigation of parameters affecting the morphological and structural characteristics of TNTs, and a good number of synthesis receipts are given.

27.4.4 Titanium dioxide nanotube applications

Owing to their uncommon nanotubular structure that renders outstanding properties, TNTs are used in diverse applications; for example, photocatalysis, gas sensors, photoelectrochemistry, DSSCs, biomedical devices, electrochromic materials, and basis layers in advanced composite materials, as well as utilization as electrode materials in lithium ion batteries with high power/energy densities.

The Boeing Company (Chicago, IL) has developed a method to create self-cleaning superhydrophobic surfaces made up of titanium dioxide nanotubes for their aircrafts. The titanium oxide nanocoating increases the safety of the aircraft by preventing the buildup of ice and other contaminants. The titanium dioxide nanotubes also reduce maintenance costs by catalytically harnessing sunlight to help keep functional surfaces such as wings and rotors clean. Boeing earned US Patent 7695767 for its process to create self-cleaning superhydrophobic surfaces, which includes applying a coating of hydrofluoric acid over a titanium substrate. Many other future advanced applications of TNTs have come to the attention of researchers.

27.5 Experimental investigation of titania nanotubes (TNTs)

27.5.1 Case studies: titanium dioxide nanotubes—manufacturing and investigation

TNTs have been synthesized by Papanicolaou et al. on pure titanium sheets, using the electrochemical anodizing method (Portan, Kroustalli, Deligianni, & Papanicolaou, 2012; Portan, Papaefthymiou, Arvanita, Jiga & Papanicolaou, 2012). The main synthesis methods were presented in Section 27.4.2.3 of this chapter. The influence of three main parameters (anodizing time, anodizing voltage, and electrolyte type) on the geometry of nanotubes was studied. Figure 27.6 shows the histogram illustrating TNT diameter for various anodizing conditions. Statistical results confirm the influence of anodizing parameters on the electrochemical and energetic processes that occur in the electrochemical cell during the anodizing procedure. As can be observed in the 3-D diagram of Figure 27.6, anodizing parameters enabled the formation of nanotubes with mean outer diameter ranging from 26 to 127 nm. The nanotube array synthesized in organic electrolytes, for example, glycerol, shows a more uniform and regular shape than for those synthesized in aqueous electrolyte.

Usually TNTs grow in monolayers; however, when multilayered nanotubes form an organized nanoarchitecture, they actually form superimposed layers of nanotubes in which the upper level is on top of the base one. A double- or multi-layered nanoarchitecture is an interesting target with respect to the application of the nanotube layer in

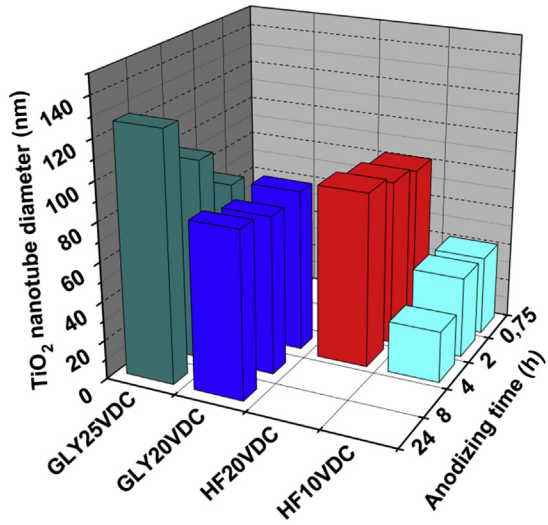

Figure 27.6 Histogram illustrating the diameter of titanium dioxide nanotubes for various anodizing conditions.
Papanicolaou et al. (2012).

photovoltaic cells and bioengineering areas. Such multilayered TNTs were previously synthesized (Portan, Papanicolaou, Jiga, & Caposi, 2012); their manufacturing process represented a big challenge for the electrochemistry community. Figure 27.7(a) shows an SEM image of superimposed TNT layers. The multilayered structure appeared after simultaneously anodizing two titanium plates in contact, both clipped to an anodic wire and mounted in parallel with a graphite cathode (Figure 27.7(b)). Factors such as the released cations, ion transfer, and concentration gradient, as well as forces acting on sample surfaces, create the proper electrochemical environment for the formation of multilayered TNTs. The partial separation of the bottom and surface layers of nanotubes can be achieved through ultrasonication and enables the observation of the stratified nanoarchitecture.

Except for these types of complex TNT layers, an even higher target was that the synthesizing of multilayered hybrid nanocomposites could permit the investigation of different nanostructured substrates coming into contact, and subsequently their interphases. Such a study is presented in the section below.

27.5.2 Manufacturing and characterization of hybrid nanocomposites

Nanocomposites manufactured by combining two nanostructured phases are quite rare. While industry is seeking materials to meet difficult challenges with unique properties, there is no "rule of mixtures" to identify how to mix multiple nanomaterials in a composite structure and make available all required properties. Nanomaterials often have unique properties that could enable composite materials with multiple

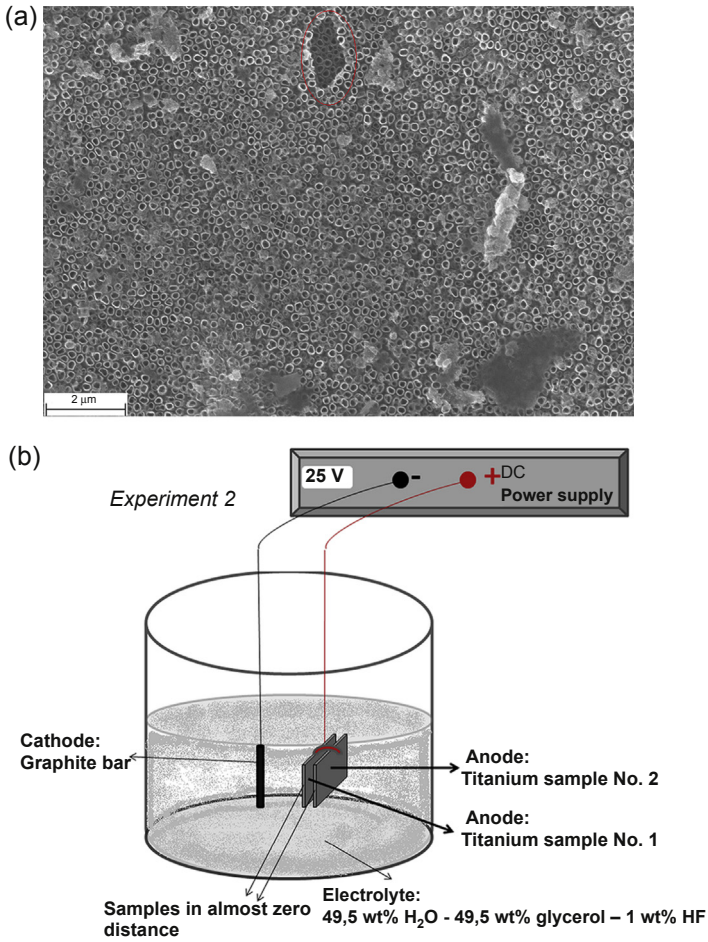

Figure 27.7 (a) SEM image—superimposed titanium dioxide nanotube layers and (b) schematic representation of the electrochemical installation used for double-layered TNT synthesis. Papanicolaou et al. (2012).

unique properties simultaneously; however, it is often challenging to achieve these properties in large-scale nanocomposite materials. Furthermore, it is important for nanomaterials to have desirable properties that cannot be achieved through use of conventional chemicals and materials. This remains a provocation for future studies in nanoscience.

A study of multilayered nanocomposites was recently conducted (Papanicolaou, Charitidis, Portan, Perivoliotis, & Koklioti, 2014). More precisely, the following four different types of multilayered hybrid nanocomposites were manufactured and tested: pure titanium—CNTs—epoxy; pure titanium—epoxy—CNTs; TNTs—CNTs—epoxy, and TNTs—epoxy—CNTs. The basic TNT layer was synthesized through the previously described electrochemical anodizing method. A CNT solution was prepared through

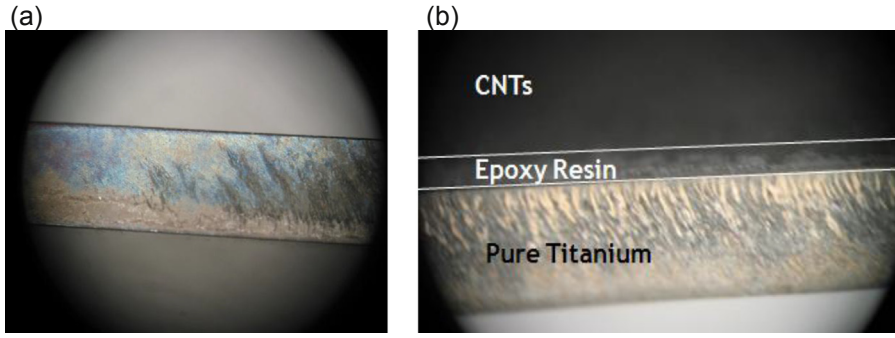

Figure 27.8 Stereoscopic lateral view of (a) anodized titanium substrate and (b) three-layer nanocomposite.
Papanicolaou et al. (2014).

ultrasonication and injected onto the TNT plates. The epoxy layer was applied on titanium, TNT, or CNT substrate through spraying. Samples are shown in Figure 27.8. The nanomechanical properties of the above-mentioned nanocomposites were investigated using nanoindentation technique. Young's modulus comparative results are given in the diagram in Figure 27.9.

Young's moduli and hardness attained much higher values where the CNT layer was externally placed, and this is clearly due to the great difference in the nature of this material and epoxy resin. Further on, a significant difference in nanomechanical

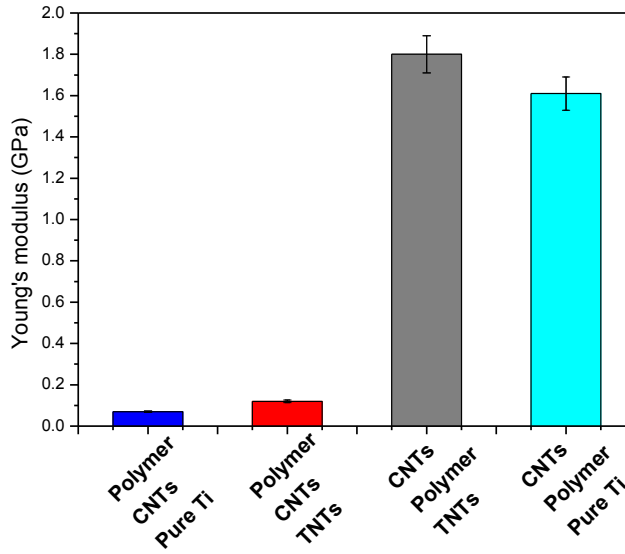

Figure 27.9 Young's modulus of hybrid nanocomposites at 2000-nm-indentation depth.
Papanicolaou et al. (2014).

properties could be observed when the epoxy intermediate layer connects TNTs and CNTs; thus the TNT (primer layer)−epoxy−CNT (external layer) nanocomposite represents improved mechanical properties in comparison with all other combinations, and can be considered the most efficient structure of the four. In this context, the importance of a proper interphase is proved. Epoxy resin acts as an adhesive, creating a smooth and homogeneous environment between TNTs and CNTs for stress transfer as well as other events that could decrease the mechanical performance of the composite. As shown in a number of previous studies, the interphase has a main role in the mechanical behavior of the whole composite, independently of the working scale. In the following section, applications of the predictive modeling of nanocomposite behavior through the concept of the viscoelastic interphase are presented.

27.6 Interphase modeling

27.6.1 The viscoelastic hybrid interphase model

Since the material properties of polymeric matrix composites are strongly rate-dependent, the elastic approach cannot accurately predict the residual-stress-and-strain fields at the interphase. Therefore, appropriate stress analysis is required to predict composite behavior through the interfacial zone. The time-dependent material properties of the interphase might significantly affect the structural performance of fiber-reinforced composites under elevated environmental conditions. The VHIM developed by Papanicolaou et al. is a semiempirical model that predicts the variation of mechanical properties within the interphase region as a function of position and time. The concept of the hybrid interphase is based on two assumptions. The first accepts a nonhomogeneous interphase whose material properties depend on the respective properties of a homogeneous fiber and matrix, and whose thickness depends on volumetric composition of composite; the second assumption introduces imperfect adhesion between fiber and matrix materials by proper definition of material properties. Thus, as shown in the literature (Papanicolaou et al., 2011; Papanicolaou, Demetrescu, Portan, & Papaefthymiou, 2011), the degradation of the elastic properties within the hybrid viscoelastic interphase region is given by

$$E_{\mathrm{i}}(r,t) = E_{\mathrm{m}}(t) + (k_E E_{\mathrm{f}} - E_{\mathrm{m}}(t))\exp\left\{-\frac{k_{\mathrm{E}}}{1-k_{\mathrm{E}}}\,\frac{E_{\mathrm{l}}}{E_{\mathrm{t}}}\,\frac{r-r_{\mathrm{f}}}{r_{\mathrm{f}}}\right\}$$

$$\text{with } r_{\mathrm{f}} \le r \le r_{\mathrm{iE}}$$

where

E_{f} is the fiber's (nanotube) modulus;
E_{i} is the interphase modulus;
$E_{\mathrm{m}}(t)$ is the matrix time depended modulus;

E_l & E_t are the macroscopic elasticity moduli of the composite along the longitudinal and the transverse direction, respectively; and $k_E = \frac{E_i(r=r_f^+)}{E_f}$ is the nanotube–matrix adhesion efficiency coefficient.

27.6.2 Application of the viscoelastic hybrid interphase model to carbon nanotube/polymer interphases

The effect of CNT content as well as of the tensile stress level applied upon the linear viscoelastic creep response of CNT–polymer nanocomposites was investigated. Experimental findings were modeled by means of the newly developed HVIM. According to this model, the viscoelastic interphase thickness does not have a constant value, but is dependent upon the property considered at the time as well as on the creep time. In addition, the parameter of imperfect bonding is introduced through the degree of adhesion. Experimental findings combined with analytical results gave a better understanding of the viscoelastic response of epoxy resin CNT nanocomposites (Papanicolaou et al., 2011; Papanicolaou, Demetrescu et al., 2011).

In Figure 27.10(a) and (b), the prediction of the VHIM as a function of the distance from a CNT is shown, while in Figure 27.11, the thickness prediction of the VHIM in MWCNT–epoxy nanocomposite as a function of creep time can be observed.

27.6.3 Application of the viscoelastic hybrid interphase model to titanium dioxide nanotube/polymer interphases

The modeling of TNT–polymer interphase behavior is of high interest in biomedical applications (Papanicolaou, Demetrescu, et al., 2011). The variation of the interphase modulus within TNT–polymer interphase in the radial direction is shown in Figure 27.12. In the case of biomaterials, a high interphase modulus is absolutely necessary to assure flexibility and a good integration of the implant into the host body. The study of the Young's modulus through modeling has proved to be a very important factor in biomedical applications. Therefore, it is known that the interphase modulus should not present an abrupt change of values within the interphase areas; in Figure 27.12 we can observe that the softest value change happens for only 30% assumed adhesion between phases (TNT and polymer). This is a very significant observation, as a well-known rule in biomedical materials research is that two materials coming into contact will be compatible if great differences in their properties do not exist, or if one of the two materials can adapt to the other.

The variation of interphase thickness with the coefficient of adhesion is shown in Figure 27.13. As one can observe, interphase thickness is linearly reduced as the adhesion coefficient is increased. Depending on the degree of adhesion, different curves are obtained showing the extent of the interphase area within the polymer matrix.

Mechanical modeling and material biocompatibility are two fields which have proved to be extremely valid, and they fit together well in biomedical materials research.

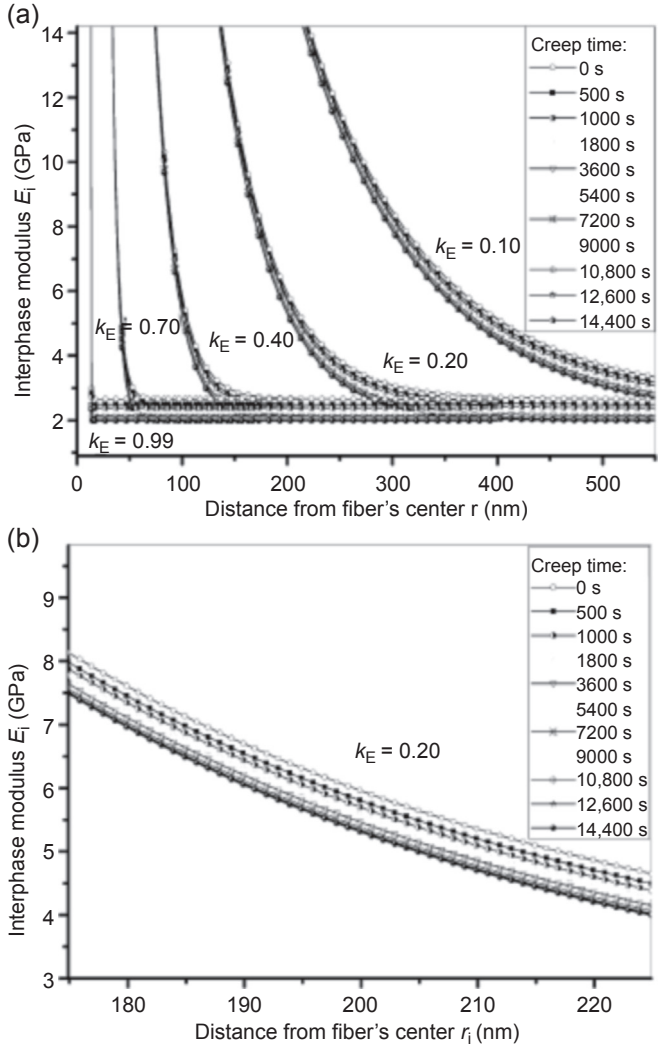

Figure 27.10 Prediction of viscoelastic hybrid interphase modulus as a function of the distance from the nanotube, for (a) various values of adhesion efficiency coefficient (k_E) and (b) adhesion efficiency coefficient k_E of 20% in MWCNT−epoxy nanocomposite. The dots represent theoretical values, while the continuous line is the best fitting curve.

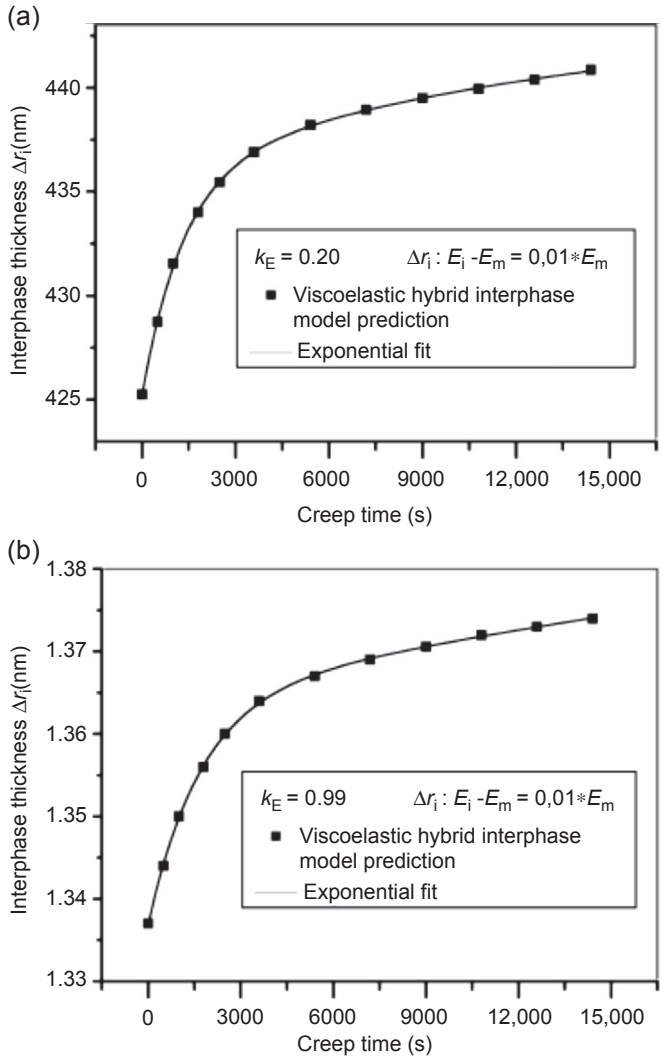

Figure 27.11 Prediction of the thickness of the viscoelastic hybrid interphase in MWCNT−epoxy nanocomposite as a function of creep time (a) for poor quality of adhesion (k_E of 20%) and (b) assuming perfect adhesion (k_E of 99%). The dots represent the theoretical values, while the continuous line is the best fitting curve.

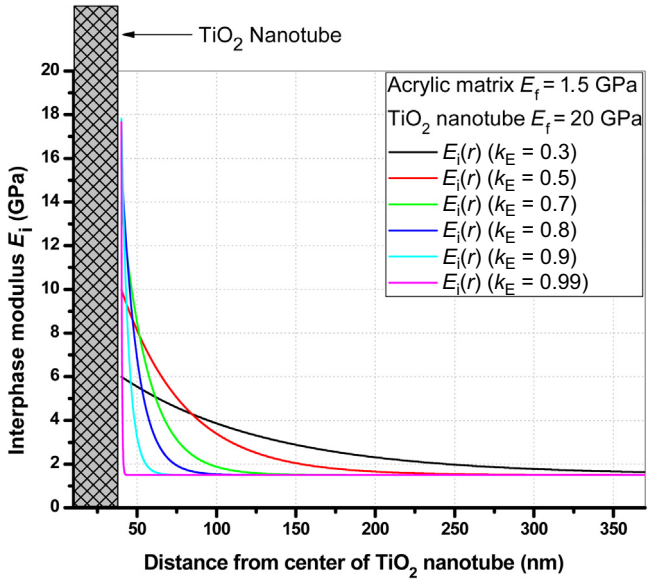

Figure 27.12 Interphase modulus variation as a function of radial distance from titanium dioxide nanotube (TNT) fiber in a resin−TNT system.

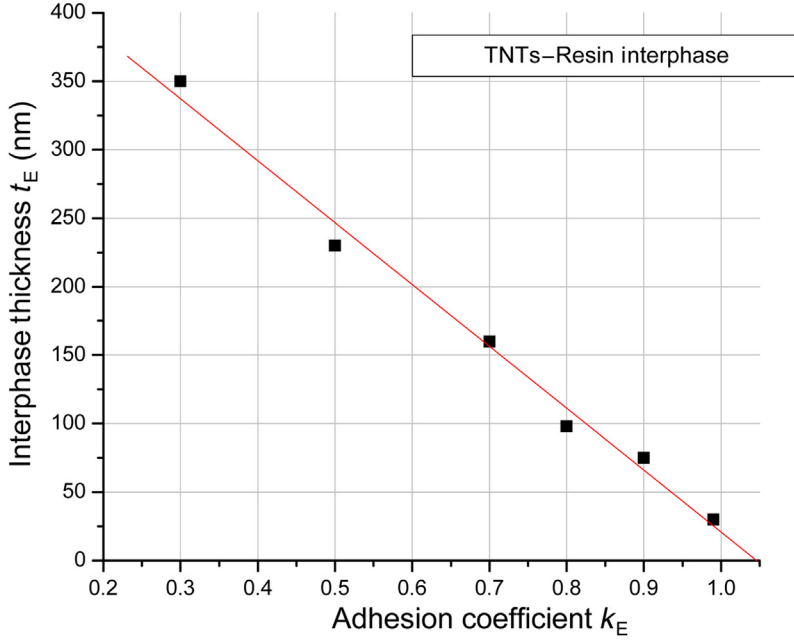

Figure 27.13 Interphase thickness variations as a function of the adhesion coefficient in a resin−titanium dioxide nanotube system.

27.7 Conclusions

In the present chapter, the manufacturing, investigation, and modeling of two types of composites involving at least one nanoscaled phase are described. State-of-the-art CNT and TNT nanocomposites are presented, with emphasis on phenomena taking place at their interphases. Thus, issues such as nanotube dispersion in the matrix material, adhesion efficiency between phases, and the role of nanocomposites for both basic and applicative research are discussed. Further on, a description of the VHIM and its application in predicting the mechanical properties of nanocomposites is achieved.

CNT nanocomposites were widely studied in the past; despite this, research still must be done to understand CNT behavior in both free form and as a reinforcement in nanocomposites. The interphase created between CNTs and polymers is a key factor for the interpretation and predictive modeling of nanocomposites. However, in nanocomposites CNTs can agglomerate and produce secondary effects, while they are not a highly organized material. On the opposite end, TNTs are well organized on titanium substrate and create an ideal environment for nanoindentation research and other investigations that are decisive for a better understanding of nanocomposites and their behavior with respect to their interphase side. Further studies are needed to manage the modeling of hybrid nanocomposites; it is expected that a deep understanding of micro- and nano-composite behavior is crucial for the advanced application of nanomaterials.

Dedicated to Tony Kelly

Most of us have likely come to accept, on an everyday basis, that the aspirations of the new generation are totally different from the ones we had at their age; in fact, that is not a problem but rather a form of progress. In any event, it is worth awakening and opening our consciousness to observe that there is continuity in nearly everything. In the past, as much as now, those to whom we ultimately give our deepest love, respect, and appreciation are those who have through passion for science, discipline, perseverance, and lack of material interest participated to a great extent in enlarging the limited human database of knowledge. One such personality is Tony Kelly, and we wish to express our sincere gratitude to him for surpassing all expectations in bringing inestimable contributions, reflected in a great number of written documents, to those who are just now starting to explore the world of composite materials.

References

Alnefaie, K. A., Aldousari, S. M., & Khashaba, U. A. (2013). New development of self-damping MWCNT composites. *Composites: Part A, 52*, 1−11. http://dx.doi.org/10.1016/j.compositesa.2013.04.011 (Online).

Aviles, F., Cauich-Rodriguez, J. V., Moo-Tah, L., May-Pat, A., & Vargas − Coronado, R. (2009). Evaluation of mild acid oxidation treatments for MWCNT functionalization. *Carbon, 47*(13), 2970−2975. http://dx.doi.org/10.1016/j.carbon.2009.06.044 (Online).

Bethune, D. S., Kiang, C. H., Devries, M. S., Gorman, G., Savoy, R., Vazquez, J., et al. (1993). Cobalt-catalysed growth of carbon nanotubes with single-atomic-layer walls. *Nature, 363*, 605−607. http://dx.doi.org/10.1038/363605a0 (Online).

Boehm, H. P. (1997). The first observation of carbon nanotubes. *Carbon, 35*, 581−584.

Chapartegui, M., Markaide, N., Florez, S., Elizetxea, C., Fernandez, M., & Santamaria, A. (2011). Curing of epoxy/carbon nanotubes physical networks. *Polymer Engineering & Science, 52*(3), 662−670. http://dx.doi.org/10.1002/pen.22131 (Online).

Chen, Y., Liu, B., He, X., Huang, Y., & Hwang, K. (2010). Failure analysis and the optimal toughness design of carbon nanotube-reinforced composites. *Composites Science and Technology, 70*(9), 1360−1367. http://dx.doi.org/10.1016/j.compscitech.2010.04.015 (Online).

Ci, L., & Bai, J. B. (2006). The reinforcement role of carbon nanotubes in epoxy composites with different matrix stiffness. *Composites Science and Technology, 66*(3−4), 599−603. http://dx.doi.org/10.1016/j.compscitech.2005.05.020 (Online).

Coleman, J. N., Blau, W. J., Dalton, A. B., Muñoz, E., Collins, S., Kim, B. G., et al. (2003). Improving the mechanical properties of single-walled carbon nanotube sheets by intercalation of polymeric adhesives. *Applied Physics Letters, 82*(11), 1682−1684 (Online) http://dx.doi.org/10.1063/1.1559421.

Coleman, J. N., Khan, U., Werner, J. B., & Gun'ko, Y. K. (2006). Small but strong: a review of the mechanical properties of carbon nanotube−polymer composites. *Carbon, 44*(9), 1624−1652. http://dx.doi.org/10.1016/j.carbon.2006.02.038 (Online).

Coleman, J. N., Khan, U., & Gun'ko, Y. K. (2006). Mechanical reinforcement of polymers using carbon nanotubes. *Advanced Materials, 18*, 689−706. http://dx.doi.org/10.1002/adma.200501851 (Online).

Dresselhaus, M. S., Dresselhaus, G., & Avouris, P. (Eds.). (2001). *Carbon nanotubes: Synthesis, structure, properties, and applications*. Springer, 447 page(s).

Eitan, A., Fisher, F., Andrews, R., Brinson, L., & Schadler, L. (2006). Reinforcement mechanisms in MWCNT-filled polycarbonate. *Composites Science and Technology, 66*(9), 1162−1173. http://dx.doi.org/10.1016/j.compscitech.2005.10.004 (Online).

Endo, M., Tsuruoka, S., & Ichihara, G. (2008). Carbon nanotubes in historical and future perspective summary of an extended session at carbon in Nagano. *Particle and Fibre Toxicology, 5*, 21. http://dx.doi.org/10.1186/1743-8977-5-21 (Online).

Fathy, M., Abdel Moghny, T., Awad Allah, A. E., & Alblehy, A. E. (2014). Cation exchange resin nanocomposites based on multi-walled carbon nanotubes. *Applied Nanoscience, 4*(1), 103−112. http://dx.doi.org/10.1007/s13204-012-0178-5 (Online).

Ganesh, E. N. (2013). Single walled and multi walled carbon nanotube, structure, synthesis and applications. *International Journal of Innovative Technology and Exploring Engineering (IJITEE), 2*(4), 311−320.

Gangopadhyay, R., & De, A. (2000). Conducting polymer nanocomposites: a brief overview. *Chemistry of Material, 12*(3), 608−622. http://dx.doi.org/10.1021/cm990537f (Online).

Grande, D. H., Mandell, J. F., & Hong, K. C. C. (1988). Fibre-matrix bond strength studies of glass, ceramic, and metal matrix composites. *Materials Science, 23*(1), 311−328. http://dx.doi.org/10.1007/BF01174071 (Online).

Han, Z., & Fina, A. (2011). Thermal conductivity of carbon nanotubes and their polymer nanocomposites: a review. *Progress in Polymer Science, 36*(7), 914−944. http://dx.doi.org/10.1016/j.progpolymsci.2010.11.004 (Online).

Hughes, T. V. & Chambers, C. R. (1889). *Manufacture of 0 N Filaments*. US Patent, Publication number: 405480 A.

Hwang, G. L., Shieh, Y.-T., & Hwang, K. C. (2004). Efficient load transfer to polymer-grafted multiwalled carbon nanotubes in polymer composites. *Advanced Functional Materials, 14*, 487–491. http://dx.doi.org/10.1002/adfm.200305382 (Online).

Iijima, S. (1991). Helical microtubules of graphitic carbon. *Nature, 354*, 56–58. http://dx.doi.org/10.1038/354056a0 (Online).

Jia-Lin, T., & Ting-Chu, L. (2009). Investigating the load transfer efficiency in carbon nanotubes reinforced nanocomposites. *Composite Structures, 90*(2), 172–179.

Kinloch, A. J., Littlea, M. S. J., & Watts, J. F. (2000). The role of the interphase in the environmental failure of adhesive joints. *Acta Materialia, 48*(18–19), 4543–4553. http://dx.doi.org/10.1016/S1359-6454(00)00240-8 (Online).

Kulik, A. J., Kis, A., Lukic, B., Lee, K., & Forró, L. (Eds.). (2007). *Fundamentals of friction and wear, chapter: Mechanical properties of carbon nanotubes*. Springer. http://dx.doi.org/10.1007/978-3-540-36807-6_26. pp. 583–600 (Online).

Lam, Chiu-wing (2006). A review of carbon nanotube toxicity and assessment of potential occupational and environmental health risks. *Critical Reviews in Toxicology, 36*(3), 189–217. http://dx.doi.org/10.1080/10408440600570233 (Online).

Liu, L., Liu, F., & Zhao, J. (2014). Curved carbon nanotubes: from unique geometries to novel properties and peculiar applications. *Review Article, Nano Research, 7*(5), 626–657. http://dx.doi.org/10.1007/s12274-014-0431-1 (Online).

Li, Q., Zaiser, M., & Koutsos, V. (2004). Carbon nanotube/epoxy resin composites using a block copolymer as a dispersing agent. *Physica Status Solidi, 201*(13), R89–R91. http://dx.doi.org/10.1002/pssa.200409065 (Online).

Luo, J. J., & Daniel, I. M. (2003). Characterization and modeling of mechanical behavior of polymer/clay nanocomposites. *Composites Science and Technology, 63*(11), 1607–1616. http://dx.doi.org/10.1016/S0266-3538(03)00060-5 (Online).

Maiyalagan, T., Viswanathan, B., & Varadaraju, U. V. (2006). Fabrication and characterization of TiO_2 nanotube arrays by sol–gel template method. *Bulletin of Materials Science, 29*(7), 705–708.

Ma, P., Mo, S., Tang, B., & Kim, J. (2010). Dispersion, interfacial interaction and re-agglomeration of functionalized carbon nanotubes in epoxy composites. *Carbon, 48*(6), 1824–1834. http://dx.doi.org/10.1016/j.carbon.2010.01.028 (Online).

Miyagawa, H., & Drzal, L. T. (2004). Thermo-physical and impact properties of epoxy nanocomposites reinforced by single-wall carbon nanotubes. *Polymer, 45*(15), 5163–5170. http://dx.doi.org/10.1016/j.polymer.2004.05.036 (Online).

Mohamed Ael, R., Kasemphaibulsuk, N., Rohani, S., & Barghi, S. (2010). Fabrication of titania nanotube arrays in viscous electrolytes. *Journal of Nanoscience and Nanotechnology, 10*(3), 1998–2008.

Moniruzzaman, M., & Winey, K. I. (2006). Polymer nanocomposites containing carbon nanotubes. *Macromolecules, 39*(16), 5194–5205. http://dx.doi.org/10.1021/ma060733p (Online).

Neupane, M. P., Park, C., Bae, T. S., Yi, H. K., Watari, F., & Lee, M. H. (2011). Synthesis and morphology of TiO_2 nanotubes by anodic oxidation using surfactant based fluorinated electrolyte. *Journal of the Electrochemical Society, 158*(8), C242–C245. http://dx.doi.org/10.1149/1.3598164 (Online).

Norani Muti, M., Dzilal, A. A., & Dennis, J. O. (2008). Effect of synthesis parameters on the structure of titania nanotubes. *Journal of Engineering Science and Technology, 3*(2), 163–171.

Oberlin, A., Endo, M., & Koyama, T. J. (1976). Filamentous growth of carbon through benzene decomposition. *Journal of Crystal Growth, 32*, 335–349. http://dx.doi.org/10.1016/0022-0248(76)90115-9 (Online).

Papanicolaou, G. C., Demetrescu, I., Portan, D. V., & Papaefthymiou, K. P. (2011). Interphase modelling of human osteoblasts spread on pure titanium surface covered with TiO_2 nanotubes. *Composite Interfaces, 18*, 23−35.

Papanicolaou, G. C., et al. (2011). Interphasial viscoelastic behavior of CNT reinforced nanocomposites studied by means of the concept of the hybrid viscoelastic interphase. *Journal of Applied Polymer Science, 124*(2), 1578−1588. http://dx.doi.org/10.1002/app.35202 (Online).

Papanicolaou, G.C., Papaefthymiou K.P., Koutsomitopoulou, A.F., Portan, D.V., & Zaoutsos, S.P. (2012). Effect of dispersion of MWCNTs on the static and dynamic mechanical behavior of epoxy matrix nanocomposites. *Journal of Material Science*, *47*(1), 350−359. (Online) DOI: 10.1007/s10853-011-5804-1.

Papanicolaou, G. C., Charitidis, C. A., Portan, D. V., Perivoliotis, D. K., & Koklioti, M. A. (2014). Investigation of nanomechanical properties of multilayered hybrid nanocomposites. *Meccanica*. http://dx.doi.org/10.1007/s11012-013-9871-z (Online).

Papanicolaou, G. C., Lagas, G., Papadimitropoulos, K., & Ioannou, A. (2010). Manufacturing and mechanical behavior of hybrid building materials. *Journal of Applied Polymer Science, 124*, 1081−1095. http://dx.doi.org/10.1002/app.35093 (Online).

Papanicolaou, G. C., Paipetis, S. A., & Theocaris, P. S. (1978). The concept of boundary interphase in composite mechanics. *Colloid & Polymer Science, 256*(7), 625−630. http://dx.doi.org/10.1007/BF01784402 (Online).

Papanicolaou, G. C., Xepapadaki, A. G., & Angelakopoulos, G. A. (2012). Modeling the mechanical properties of notched aluminum—epoxy particulate composites. *Journal of Applied Polymer Science, 126*, 559−568. http://dx.doi.org/10.1002/app (Online).

Paulose, M., Shankar, K., Yoriya, S., Prakasam, H. E., Varghese, O. K., Mor, G. K., et al. (2006). Anodic growth of highly ordered TiO_2 nanotube arrays to 134 μm in length. *Journal of Physical Chemistry B, 110*(33), 16179−16184. http://dx.doi.org/10.1021/jp064020k (Online).

Pélabon, C., & Pélabon, H. C. R. (1903). Sur une variété de carbone filamenteux. *Academy of Sciences, Paris, 137*, 706−708.

Portan, D. V., Kroustalli, A. A., Deligianni, D. D., & Papanicolaou, G. C. (2012). On the biocompatibility between TiO_2 nanotubes layer and human osteoblasts. *Biomedical Materials Research Part A, 100A*(10), 2546−2553. http://dx.doi.org/10.1002/jbm.a.34188 (Online).

Portan, D. V., Papaefthymiou, K., Arvanita, E., Jiga, G., & Papanicolaou, G. C. (2012). A combined statistical and microscopic analysis of TiO_2 nanotubes synthesized under different electrochemical anodizing conditions. *Materials Science, 47*, 4696−4705. http://dx.doi.org/10.1007/s10853-012-6338-x (Online).

Portan, D. V., Papanicolaou, G. C., Jiga, G., & Caposi, M. (2012). A novel experimental method for obtaining multi-layered TiO_2 nanotubes through electrochemical anodizing. *Journal of Applied Electrochemistry, 42*, 1013−1024. http://dx.doi.org/10.1007/s10800-012-0468-3 (Online).

Prasek, J., Drbohlavova, J., Chomoucka, J., Hubalek, J., Jasek, O., Adamc, V., et al. (2011). Methods for carbon nanotubes synthesis—review. *Journal of Materials Chemistry, 21*, 15872−15884. http://dx.doi.org/10.1039/C1JM12254A (Online).

Prida, V. M., Manova, E., Vega, V., Hernandez-Velez, M., Aranda, P., Pirota, K. R., et al. (2007). Temperature influence on the anodic growth of self-aligned titanium dioxide nanotube arrays. *Journal of Magnetism and Magnetic Materials, 316*(2), 110−113. http://dx.doi.org/10.1016/j.jmmm.2007.02.021 (Online).

Pulickel, M. A., Jonghwan, S., & Nikhil, K. (2006). Utilizing interfaces in carbon nanotube reinforced polymer composites for structural damping. *Materials Science, 41*(23), 7824−7829. http://dx.doi.org/10.1007/s10853-006-0693-4 (Online).

Ryman-Rasmussen, J. P., Cesta, M. F., Brody, A. R., Shipley-Phillips, J. K., Everitt, J. I., Tewksbury, E. W., et al. (2009). Inhaled carbon nanotubes reach the subpleural tissue in mice. *Nature Nanotechnology, 4*, 747–751. http://dx.doi.org/10.1038/nnano.2009.305 (Online).

Schlabach, S., Ochs, R., Hanemann, T., & Szabó, D. V. (2011). Nanoparticles in polymer-matrix composites. *Microsystem Technologies, 17*(2), 183–193. http://dx.doi.org/10.1007/s00542-010-1176-8 (Online).

Schützenberger, P., & Schützenberger, L. C. R. (1890). Sur quelques faits relatifs à l'histoire du carbone. *Acad. Sci. Paris, 111*, 774–778.

Shulaker, M. M., Van Rethy, J., Wu, T. F., Liyanage, L. S., Wei, H., Li, Z., et al. (2014). Carbon nanotube circuit integration up to sub-20 nm channel lengths. *ACS Nano, 8*(4), 3434–3443. http://dx.doi.org/10.1021/nn406301r (Online).

Swain, R. E., Reifsnider, K. L., Jayaraman, K., & El-Zein, M. (1990). Interface/Interphase concepts in composite material systems. *Thermoplastic Composite Materials, 3*(1), 13–23. http://dx.doi.org/10.1177/089270579000300102 (Online).

Thostenson, E. T., Ren, Zhifeng, & Chou, Tsu-Wei (2001). Advances in the science and technology of carbon nanotubes and their composites: a review. *Composites Science and Technology, 61*(13), 1899–1912. http://dx.doi.org/10.1016/S0266-3538(01)00094-X (Online).

Tran, C. D., Humphries, W., Smith, S. M., Huynh, C., & Lucas, S. (2009). Improving the tensile strength of carbon nanotube spun yarns using a modified spinning process. *Carbon, 47*(11), 2662–2670. http://dx.doi.org/10.1016/j.carbon.2009.05.020 (Online).

Wan, H., Delale, F., & Shen, L. (2005). Effect of CNT length and CNT-matrix interphase in carbon nanotube (CNT) reinforced composites. *Mechanics Research Communications, 32*(5), 481–489. http://dx.doi.org/10.1016/j.mechrescom.2004.10.011 (Online).

Won, H. R., Chan, J. P., & Hyuk, S. K. (2008). Synthesis of highly ordered TiO_2 nanotube in malonic acid solution by anodization. *Journal of Nanoscience and Nanotechnology, 8*(10), 5467–5470. http://dx.doi.org/10.1166/jnn.2008.1141 (Online).

Xiao, K. Q., & Zhang, L. C. (2004). The stress transfer efficiency of a single-walled carbon nanotube in epoxy matrix. *Materials Science, 39*(14), 4481–4486. http://dx.doi.org/10.1023/B: JMSC.0000034141.48785.d2 (Online).

Yan-Tao, P., Pang, Y. T., Meng, G. W., Zhang, L. D., Shan, W. J., et al. (2003). Synthesis of ordered Al nanowire arrays. *Solid State Science, 5*(7), 1063–1067. http://dx.doi.org/10.1016/S1293-2558(03)00088-8 (Online).

Yin, H., Liu, H., & Shen, W. Z. (2010). The large diameter and fast growth of self-organized TiO_2 nanotube arrays achieved via electrochemical anodizing. *Nanotechnology, 21*, 1–7. http://dx.doi.org/10.1088/0957-4484/21/3/035601 (Online).

Yu, M. F., Lourie, O., Dyer, M. J., Moloni, K., Kelly, T. F., & Ruoff, R. S. (28 January 2000). Strength and breaking mechanism of multiwalled carbon nanotubes under tensile load. *Science, 287*(5453), 637–640. http://dx.doi.org/10.1126/science.287.5453.637 (Online).

Zeng, Q. H., Yu, A. B., & Lu, G. Q. (2008). Multiscale modeling and simulation of polymer nanocomposites. *Progress in Polymer Science, 33*(2), 191–269. http://dx.doi.org/10.1016/j.progpolymsci.2007.09.002 (Online).

Zhang, W., Picu, R. C., & Koratkar, N. (2008). The effect of carbon nanotube dimensions and dispersion on the fatigue behavior of epoxy nanocomposites. *Nanotechnology, 19*(28), 285709. http://dx.doi.org/10.1088/0957-4484/19/28/285709 (Online).

Recycling of reinforced plastics

28

R.D. Adams[1,2], A. Collins[1], D. Cooper[1], M.W. Digby[1], A.W. Farmer[1], A. Laurence[1], K. Patel[1], M. Stevens[1], R. Watkins[1]
[1]University of Bristol, Bristol, UK; [2]University of Oxford, Oxford, UK

28.1 Introduction

Today, we are being strongly encouraged to recycle or reuse almost everything, but there is much nonsense spoken by people who have no idea of the processes or consequences of recycling. But is all recycling good? For instance, while a paper bag might seem a good alternative to a plastic shopping bag, its carbon footprint is three times larger, and it is quite useless if you encounter rain on the way home. In the consequent landfill disposal, the paper bag degrades and produces methane, which is a harmful greenhouse gas. Recycling is being forced on us by legislation. While in some ways this makes sense, it can have consequences that might contradict the good intentions. Various forms of life cycle analysis have been proposed to try and assess the true impact of a product from 'cradle to grave', but these can give uncertain results, to say the least. Even so, they will generally encourage recycling because this retains some of the original chemical feedstock.

But here we are considering advanced composites in the form of high strength and stiffness fibres in a thermosetting polymer matrix, usually an epoxy or a polyester resin. Designers are increasingly changing to use composite materials for solving problems, improving performance and productivity, and innovating new products. This is not surprising considering the many benefits associated with composite materials, such as:

- high strength and stiffness that can be orientated to meet specific design requirements;
- low weight;
- design flexibility – can be formed into virtually any shape;
- dimensional stability – yield point is the breaking point
- high dielectric strength – good electrical insulating properties;
- corrosion resistance – resin systems can provide long-term resistance to degradation;
- parts consolidation – mouldings can often replace assemblies;
- finishing – colour can be moulded in for long-lasting appearance;
- low tooling costs – can be lower than tooling and finishing costs for materials such as steel.

Fibre-reinforced composites have become an important structural component in many industrial sectors, especially in transport, but this inevitably has led to a growing rate of waste accumulation. Most of this waste is disposed to landfill sites because there is no economic means of reclaiming the material for reuse. Unlike materials such as steel and aluminium that have high scrap values, companies see no economic return from recycling composites.

Structural Integrity and Durability of Advanced Composites. http://dx.doi.org/10.1016/B978-0-08-100137-0.00028-6

However, under pressure from governments and consumers, new legislation regarding extended producer responsibility (EPR) has been developed, and this forms the main driver behind the need for effective composite recycling. EPR is the extension of responsibility of producers for the environmental impacts of their products through the entire product life cycle, in particular the recycling or disposal of end of life products. EPR programs can be either mandatory of voluntary. Mandatory programs are those that result from laws and regulations, while voluntary initiatives are generally only implemented when a company can make a profit or gain some market advantage by recycling end of life products.

An example of mandatory EPR is the end of life vehicle (ELV) directive recently approved by the European Union (EU) commission, which aims to minimise the impact of ELVs on the environment by ensuring that a high proportion of passenger cars are recycled. Currently, ELVs are among the most highly recycled products in the world, with about 75% of their weight being made up of recyclable metals such as steel and aluminium. The EU directive is targeting the remaining 25% waste that consists of plastics, composites, glass, textiles, fluid, and paint, stating that 85% by weight of ELVs must be recycled by the year 2006 and that 95% must be recycled by 2015. But there is no similar EU directive for fibre-reinforced plastic (FRP) boats, and this is building into a considerable problem. One desperate contributor to YouTube was recently looking for a home for 500 FRP boats.

For motor vehicles, lightness usually means that less energy is used, especially for vehicles in a city environment with many stops and starts. But if the vehicle is travelling at a steady speed, lightness is largely irrelevant. However, for an aircraft, a reduction in structural weight is good because drag is directly associated with lift. The Boeing 787 airliner contains some 30 tonnes of carbon fibre-reinforced plastic (CFRP), which is about half its dry weight (although when fuel and passengers are added, the proportion of composite is much less). Our extreme transport examples are aerospace and motor sport, in which the drive is to use advanced composites to replace metals as much as possible. So why has there has not been a substantial move to replace steel and aluminium in cars by composites (except inexpensive so-called supercars). This unfortunate situation can be laid at the feet of recycling legislation and the European End of Life Directive. While it is relatively easy to recycle steel and aluminium by melting, the question that remains is how to recycle composites.

But let us look at the existing possibilities for recycling of composites.

28.1.1 Grinding or crushing

Grinding or crushing is currently the main recycling process for composites (Telfeyan, 2002). It can be applied to any components made from thermosetting FRP from cheap glass-reinforced plastic (GRP) products to expensive CFRP, such as in aircraft. The bulk parts are broken into 50−200 mm pieces, which are crushed or ground into different grades using a hammer mill or similar device. The finest powder grades are used as fillers (Henshaw, Han, & Owens, 1996). The larger grades can be used

as fillers with some minor reinforcement benefits in bulk moulded compound or sheet moulded compound.

When reground GRP is used as a filler or reinforcement in a resin matrix, the stiffness is increased, but the strength is much lower than that of the virgin material. A regrind content of 30% in the recycled material produces a 40% reduction in flexural strength (Bledzki & Goracy, 1993). This is caused by poor resin bonding to the recyclate, stress concentrations, and the lower effective fibre content of the new material (Telfeyan, 2002).

28.1.2 Pyrolysis

In pyrolysis, the organic resin matrix is decomposed in an inert atmosphere (Meyer, Schulte, & Grove-Nielsen, 2009; Telfeyan, 2002). The reaction products can be used as fuels or ingredients for other petrochemical-based materials. The presence of fibres in the resin means that substantial postprocessing is needed to reclaim any useful material. Pyrolysis is much less cost-effective than grinding or crushing.

A fluidised bed process, operating at temperatures between 450 and 650 °C, has been developed for separating the fibres from the resin (Kennerley, Kelly, Fenwick, Pickering, & Rudd, 1998). The strength of the recovered fibres was reduced by 50%. Also, the process leaves the fibres randomly orientated, which diminishes their usefulness. Feraboli et al. (2012) used boiling sulphuric acid to separate carbon fibres from an epoxy matrix; the fibres were recovered as a tangled mat from the original woven format. Also, they could only achieve a 33% volume fraction compared with 62% in the original composite.

28.1.3 Hydrolysis

Hydrolysis involves depolymerisation of the resin matrix using water and an acid or base catalyst (Allred, Gosau, & Shoemaker, 2001). The products can be used as ingredients in other processes. This process can only be used to decompose polyethylene, polyester, and polyamides. Polyester is the only commonly used matrix with FRPs. The main problems with this process are that the scrap material has to be separated into matrix polymer types before recycling and postprocessing is needed to recover the fibres. The fibres themselves are likely to be degraded by the action of the water and acid.

28.1.4 Energy recovery

Composites have a high thermal energy content, despite the existence of inorganic reinforcements. It was estimated that the energy equivalent of the 1990 composite production of the United States was 30−35 million litres of crude oil (Henshaw et al., 1996). Typically, the material is burnt at temperatures around 1000 °C. As well as recovering the heat, scrubbers need to be used to remove the harmful contaminants from the flue gases before they are released. Environmental damage is caused

by the flue gases, and the residue has few uses and has to be buried in landfill sites. However, at least the chemical feedstock is converted into heat rather than being buried in the ground.

28.1.5 Cautionary note

Finally, it is important to remember that it is not necessarily a sound policy to recycle all products. Compromises are always present when considering the recyclability of a product and often a complex analysis is necessary. The fundamental way of discriminating between a product that should or should not be recycled is to discover whether performing recycling results in a greater environmental impact than not performing recycling. In particular, an aspect that many people overlook is the environmental impact of transportation involved in recycling materials. For example, Germany's packaging take-back system initially discouraged local processing by banning local incineration for energy production. This led to large shipments of plastic around the country, using fuel and causing pollution.

The environmental benefits of recycling processes must be subject to scrutiny. If the energy used in implementing and maintaining a recycling process results in greater environmental damage than not recycling the product, then it is preferable from both environmental and economic standpoints not to recycle. In this case, further development of recycling processes is required to make them more efficient and hence to facilitate implementation. Deciding not to recycle a product seems inherently wrong, but analysis may show that it will sometimes be the best solution until a more environmentally favourable and/or economically viable recycling process can be developed. So, we adopt as our motto Altiora etiam petamus, which means, 'Let us seek even higher'.

28.2 Objective

Existing techniques for recycling composites are not very effective or are very expensive, while burning is a last resort. Our aim, therefore, was to investigate and develop methods for recycling glass and carbon composite materials while retaining as much as possible of the beneficial and desirable properties of the original composite. By thinking 'outside of the box', we wanted to develop novel recycling methods and to investigate their feasibility by converting them into practice and measuring the resulting properties. We prefer to use the term 'remanufacture' instead of 'recycle', as this better conveys the philosophy behind the work. Our objective was therefore to convert end of life components into some form that could be used to make some alternative component, while retaining the chemical feedstock and as much as possible of the mechanical properties, such as the tensile strength, modulus, and interlaminar shear strength (ILSS).

Within the finite facilities at our disposal, we wanted to make some objects to show that it was indeed possible to remanufacture.

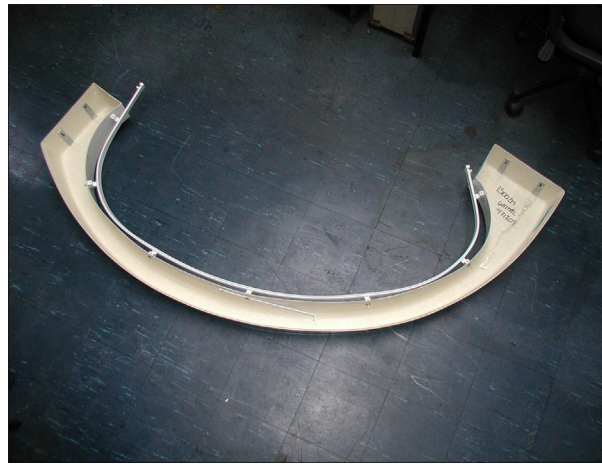

Figure 28.1 GRP bathroom shower curtain rail cowl.

28.3 Materials and components used

Our laboratory was well-equipped for manufacturing test pieces from carbon and glass fibres, using wet lay-up, vacuum bag, hot pressing, and so on. In addition, we obtained some end of life components in GRP. One of these was a doubly curved GRP shower curtain rail (Figure 28.1), but our most prolific source was an old GRP motor boat (about 10 m long), from which we were allowed to cut large sections (Figure 28.2). These were used because they were commercially produced components and at the same stage as a typical end of life structure we wanted to remanufacture. For a comparison, we also made some composite parts from virgin fibres and resins, the properties of which are given in Tables 28.1 and 28.2.

Figure 28.2 Boat hull after stripping the decking prior to cutting into sections.

Table 28.1 Manufacturer's resin data

Manufacturer	Resin	Type	Gel time at 20 °C	Curing schedule
SP systems	Ampreg 20	Epoxy	4 h 25 min	24 h at 20 °C and 5 h at 80 °C
Scott bader	Resin A	Polyester	12−15 min	24 h at 20 °C and 3 h at 80 °C

Table 28.2 Composite materials used throughout the project

Composite	Fibre type	Resin	Lay-up
Random mat GFRP bathroom component & boat hull	Random mat	Unknown	Recycled sections glued to form various structures
Directional GFRP	[0,90] plain weave 200 gsm	Ampreg 20	$[0,90/0,90/0,90/0,90/0,90]_s$
Carbon fibre pre-preg	Unidirectional	SE-84 LV	$[0/90/0]_s$
Directional CFRP	Twill weave	Ampreg 20	$[0,90/0,90/0,90]_s$

GFRP, glass fibre-reinforced plastic.

28.4 Preparation of composite for remanufacturing

Before we could remanufacture, it was necessary to devise methods of creating feedstock from the end of life material (ELM) and to devise some methods of forming this into a new object. The basic techniques were crippling (controlled crushing), splitting, and hot forming. Combinations of these actions, sometimes with the application of heat at temperatures above glass transition temperature (T_g), were used to remanufacture various components. The outcome was a recyclable composite material, which has been abbreviated to Remat. Note that not all the methods are suitable for all ELMs.

28.4.1 Splitting or delaminating

In preparing the waste material for remanufacture, it was necessary to split the composite into thinner sheets. Furniture veneers have been made like this for hundreds, if not thousands, of years (there is evidence that the ancient Egyptians used glued veneers). Most composites have low transverse tensile strength, so they can easily

be delaminated into sheets or strips with reasonably constant thickness. A crack can be initiated by a saw cut and the composite split by forcing a wedge (such as a screwdriver or chisel) into the laminate. Because this is a weak mode of failure, relatively little force is needed. The splitting process causes little damage to the fibres, which makes this an efficient method of breaking down a thick laminate into easily processed Remat layers.

The recycled GRP boat was not a simple structure to recycle because it had ribs and other stiffeners and fittings. First, the ribs and stiffeners were split from the hull. There was also a rather thick gel coat, used to protect the GRP hull from scrapes, scratches, and water ingress, but which contains few if any fibres. This was removed using the same splitting technique described above. Commercial gel coat removers, which grind the protective coating into powder, could have been used, but these create a lot of dust. The layers of composite resulting from the splitting process, such as those obtained from the GRP boat, are not flat, so any curved pieces were flattened by pressing them at a temperature at or above T_g to provide a suitable Remat. The thickness of the Remat will be chosen from experience. Thinner laminae will need more operations to produce, and it is therefore best, for cost reasons, to have as thick a lamina as possible.

28.4.2 Crushing or crippling at room temperature (C)

In this technique, a strip of FRP could be crushed while keeping the fibres largely intact and only fracturing the resin in parts. In the first method used, two spur gears were mounted on a bracket so that they were free to rotate. The spacing between the gears was such that they only partially meshed and the material was crushed by feeding it through the rotating gear teeth. Because the gear teeth cause the laminate to be bent through large angles, the composite is fractured in a way analogous to the classical three-point bend ILSS test. In effect, the strip was reduced mechanically to a continuous floppy form that could be flattened or bent as needed. The new form can then be impregnated with resin to consolidate into the final product.

Preliminary work showed that such a method could be used to crush the composite while leaving the fibres, and most of the resin matrix, largely intact so that the Remat strip could now be formed into some other shape. The ‘damage’ to the composite could be controlled by using gear tooth profiles that had less severe tip radii than the involute profile that is normally used. The method has many opportunities for further development by optimising the tooth profiles and the spacing between the teeth.

28.4.3 Crushing at room temperature using a roller rig (C)

A development of the toothed gear rig was to replace the teeth with rollers. However, in-plane tensions were built up because of the large transverse displacements and friction. These tensile stresses were large enough to fracture the composite. The advantage of this rig was that it could accommodate much wider sheets and the crushing parameters could be adjusted via the roller spacing and diameter.

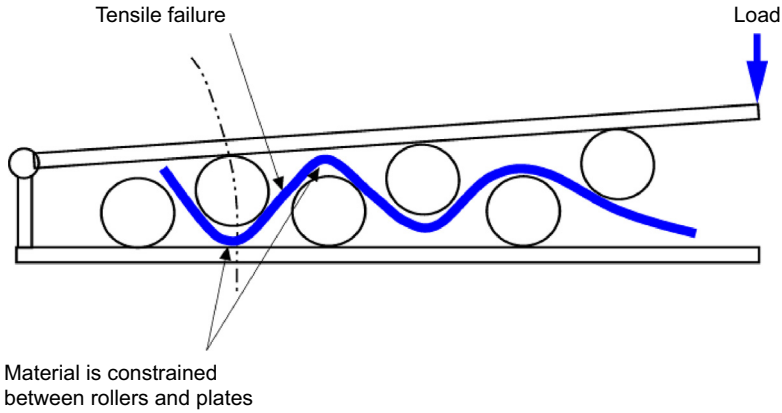

Figure 28.3 A diagram showing the position of tensile failures that occur during cold crushing using a hinged lever rig.

To overcome the tensile fracture problem, a modified roller rig was made using a lever principle. The specimen was crushed progressively from the hinged end, leaving the material at the open end unconstrained and allowing the composite to be drawn toward the rollers, thus reducing the risk of tensile failures occurring in the laminate. The spacing and diameter of the rollers need to be chosen according to the thickness of the laminate. The laminate can be crushed sufficiently so it can be reformed easily afterward to some new shape before reimpregnation. Figure 28.3 shows that delamination occurs where there is the greatest curvature, while tensile failure can occur in bending or between the rollers.

The effectiveness of the lever rig depends on the diameter and spacing of the rollers and the thickness of the material it is crushing. Layers 1 and 4 (Figure 28.4) do not show the pronounced corrugated pattern of shear failures that are visible in the thicker layers because they are too thin for the configuration of rollers used. The extensive

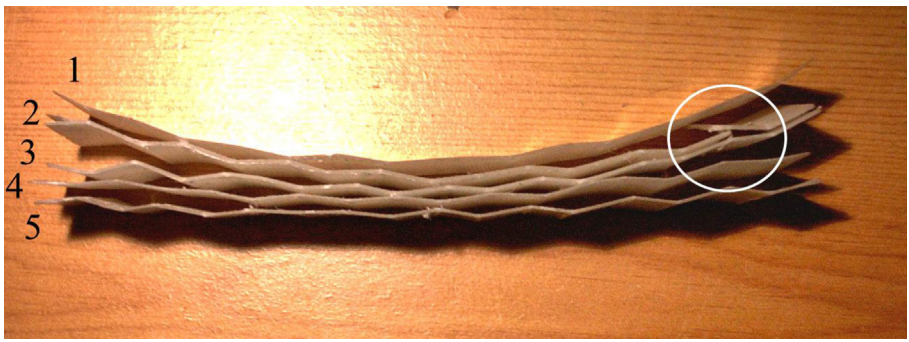

Figure 28.4 Edge view of the cold crushed layers with a tensile failure in layer 2 (ringed). Reprinted from Adams et al. (2014), with kind permission from Springer Science and Business Media.

shear failures and high flexibility of the crushed material imply that layer 5 is the optimum thickness for 10 mm diameter roller configuration used here. The thickest layer, layer 2, has a complete failure at one end because it has a higher stiffness that makes it harder for the material to conform to the profile of the rollers causing increased local forces and friction. The optimum configuration for the rollers is a function of the composite feedstock and its thickness.

28.4.4 Crushing at high temperature using the lever-roller rig (H + C)

If the composite is heated to above the glass transition temperature, T_g, the specimen in the lever rig has a much reduced shear strength and stiffness and is more ductile, allowing it to bend around the profile of the rollers, generating almost continuous interlaminar shear failures. Figure 28.5 shows an edge view of a plate crushed in the hinged roller rig at 140 °C. After hot crushing in the roller rig, the specimen was extremely flexible, even at room temperature. This makes it the most practical method for remoulding.

28.4.5 Cold and hot forming (F, F + H)

In some remanufacturing processes, the Remat can be used in the form of flat sheets. These can be produced by flattening in a press, either hot (usually higher than T_g) or cold, depending on the nature of the original composite.

28.4.6 Use of hot water to soften the reinforced plastic components (F + HW)

Exposing composites in a hot wet environment for an extended period results in water absorption, a large reduction in T_g, and an increase in ductility. This process was investigated with the aim of producing a higher degree of flexibility in the recycled material,

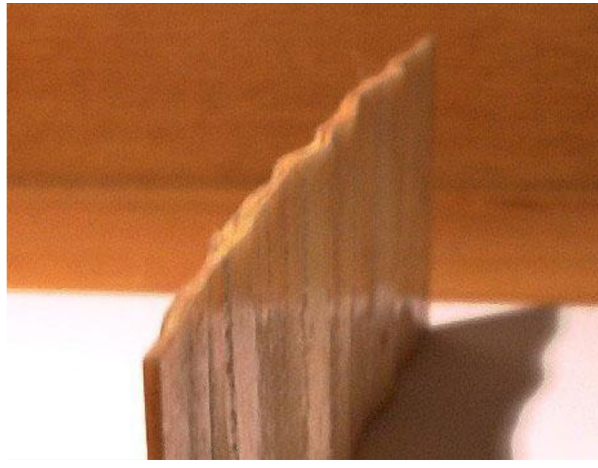

Figure 28.5 Edge view of a 10-ply plate after crushing in the lever rig at 140 °C.

particularly for very stiff carbon fibre laminae. This method is energy intensive and no better than hot pressing.

28.5 Manufacture of virgin specimens

Virgin specimens were made from carbon and glass fibre, impregnated with a laminating resin, Ampreg 20, so as to obtain a baseline comparison for the mechanical properties. Some specimens were flat, while others were made curved as shown in Figure 28.6. The curved composites were then recycled into a flat format so that the effect of processing could be assessed. Consolidation was by using a vacuum bag in an oven at 30 °C, followed by a post cure at 80 °C. The dry fibres were in the form of woven mats.

In addition preimpregnated (pre-preg) carbon fibre was used. Pre-preg carbon fibre consists of directional fibres embedded in a partially cured resin matrix. To avoid further curing of the resin, the pre-preg is stored at low temperature before manufacturing. Production is by laying the required number and direction of laminates while ensuring good adhesion with no disbonds between layers. The pre-preg was cured at 120 °C either in a hot press or in a vacuum bag.

28.6 Mechanical testing

Various mechanical and thermal tests were carried out so that comparisons could be made before and after each recycling process. Sometimes, it was not easy to comply fully with the standard tests, but these were kept to as closely as possible.

28.6.1 Tensile strength

As far as possible, the tensile tests were carried out according to ASTM D 3039-76. Alignment tabs were used to ensure that there was no bending or shear present during the test, but problems due to the inconsistent surface finish of the random glass material

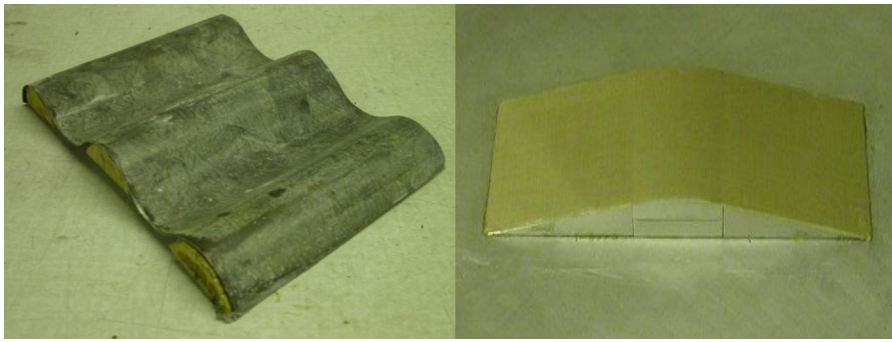

Figure 28.6 Moulded specimens.

from the boat hull and thickness variations prevented this from being achieved. Bending was therefore used for the random mat specimens rather than tension (see below).

28.6.2 Flexural strength

Four-point bending was used to measure the flexural strength of the glass random mat sections from the boat hull. The maximum fibre stress, S, was calculated from Eqn (28.1a) or (28.1b), depending on the maximum displacement at the centre of the beam, δ_{max}.

$$\text{If } \delta_{max} \leq 0.1 \cdot \frac{L}{3}: \quad S = \frac{P \cdot L}{b \cdot d^2} \tag{28.1a}$$

$$\text{If } \delta_{max} > 0.1 \cdot \frac{L}{3} \quad S = \left(\frac{P \cdot L}{b \cdot d^2}\right) \cdot \left[1 + \frac{4.70 \cdot \delta_{max}^2}{L^2} - \frac{7.04 \cdot \delta_{max} \cdot d}{L^2}\right] \tag{28.1b}$$

in which L is the support span (m); P is the failure load (N); b is the width (m); and d is the thickness (m).

The tests were carried out to the ASTM D 790-71 standard with a 16:1 span to depth ratio.

28.6.3 Young's (E) modulus

A vibration method was used to obtain the Young's modulus as this is more accurate than trying to measure the slope of a stress−strain curve. A rectangular beam was supported at the nodes for its first flexural natural frequency. The elastic modulus, E, was found by using Eqn (28.2):

$$E = \frac{f^2 \cdot \rho \cdot l^4}{1.027^2 \cdot t^2} \tag{28.2}$$

in which f is the fundamental natural frequency (Hz); ρ is the specimen density (kg/m^3); t is the beam thickness (m); and l is the length (m).

28.6.4 Interlaminar shear strength

The short beam ILSS (ASTM D 2344-76) with a 4:1 span-to-depth ratio was used to determine the strength and quality of the bond between the fibres and the matrix of the virgin and recycled material, except for the randomly orientated fibres in the specimen from the boat because the results are uncertain or meaningless.

28.6.5 Thermal tests

The T_g is the region of temperature at which a polymer changes from a hard material to one that is softer or more rubbery. When heating a polymer through T_g, we observe

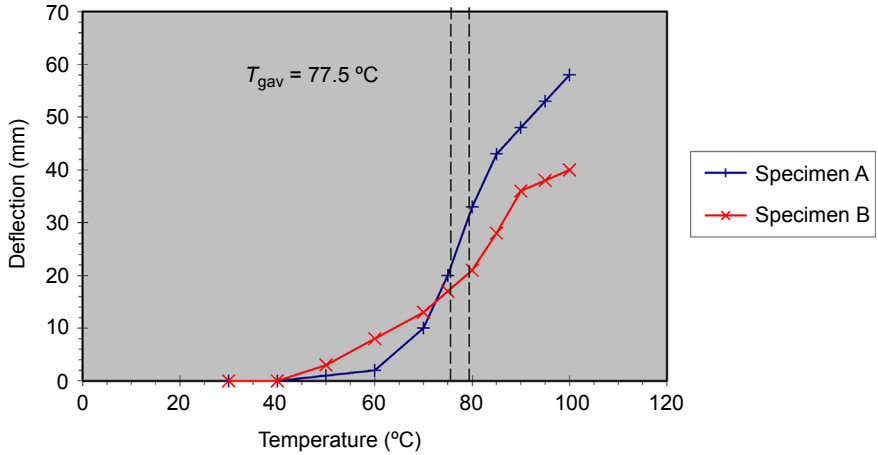

Figure 28.7 Droop test for the glass random mat boat material.

an increase in damping, a decrease in modulus, and an increase in the coefficient of thermal expansion. The first two parameters are usually obtained by using a dynamic mechanical analyser (DMA). Other techniques, such as differential scanning calorimetry, can also be used. An in-house DMA test and a simple droop test were used to determine T_g. The droop test is the cheapest and requires nothing other than an oven for determining the temperature at which the adhesive softens. A typical test on two specimens taken from different parts of the GRP boat is shown in Figure 28.7.

28.7 Effect on mechanical properties of recycling of virgin material and GRP boat specimens

The next major objective was to subject the virgin material that had been made into non-flat shapes to the splitting and crushing processes described above and then to compare the mechanical properties of this material with those of the original, virgin material that had been kept flat. It was also possible to make nonrecycled specimens from the GRP boat by choosing a suitable flat area.

28.7.1 Woven carbon and glass specimens

28.7.1.1 Tensile strength

The tensile strength retention of the carbon and glass fibre woven composites is shown in Figure 28.8. The H + C and F + HW processes are more effective for the carbon specimens because the carbon fibres are tougher and sustain less damage during

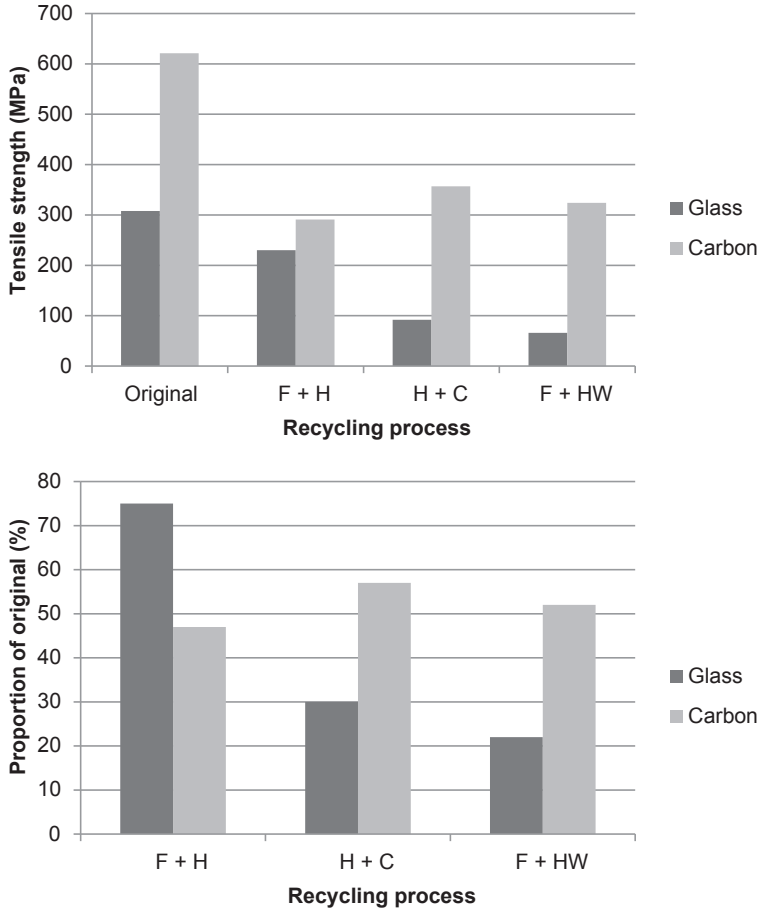

Figure 28.8 Tensile strength retention of recycled woven carbon and glass laminates impregnated with Ampreg 20 and percentage of original strength.

recycling than the glass fibres. In addition, the loss of resin strength through thermal or hydrothermal degradation has less of an impact on the strength of the composite due to the high fibre strength. Also, some of the glass tensile specimens were not fully flattened by the H + C or F + HW processes, leading to bending during the tensile test resulting in lower apparent strengths.

For the glass fibre composites, the F + H process is more effective in terms of strength retention, possibly because of the difference in ILSS strength between the carbon and glass. Because the glass has a relatively low ILSS strength of 39 MPa, there will be more delaminations in the glass specimen after processing. Because Ampreg 20 does not have a low viscosity, it will more readily penetrate large delaminations. The lack of full reimpregnation in the carbon specimen will lead to voids, creating weaknesses and acting as stress raisers.

28.7.1.2 E *modulus*

Figure 28.9 shows the retention of Young's modulus after various recycling processes. The carbon composites perform slightly worse than the glass for the H + C and F + HW processes, the F + H process being the most effective for the modulus retention of the carbon fibre.

The F + H process produced higher modulus retention than the H + C, which proves that moderate global damage reduces the modulus more than severe local damage.

The effect of each process on the elastic modulus is similar for each material because each process damages the materials globally in the same way. A consistently high elastic modulus can be retained, and this is far more predictable than the tensile strength retention.

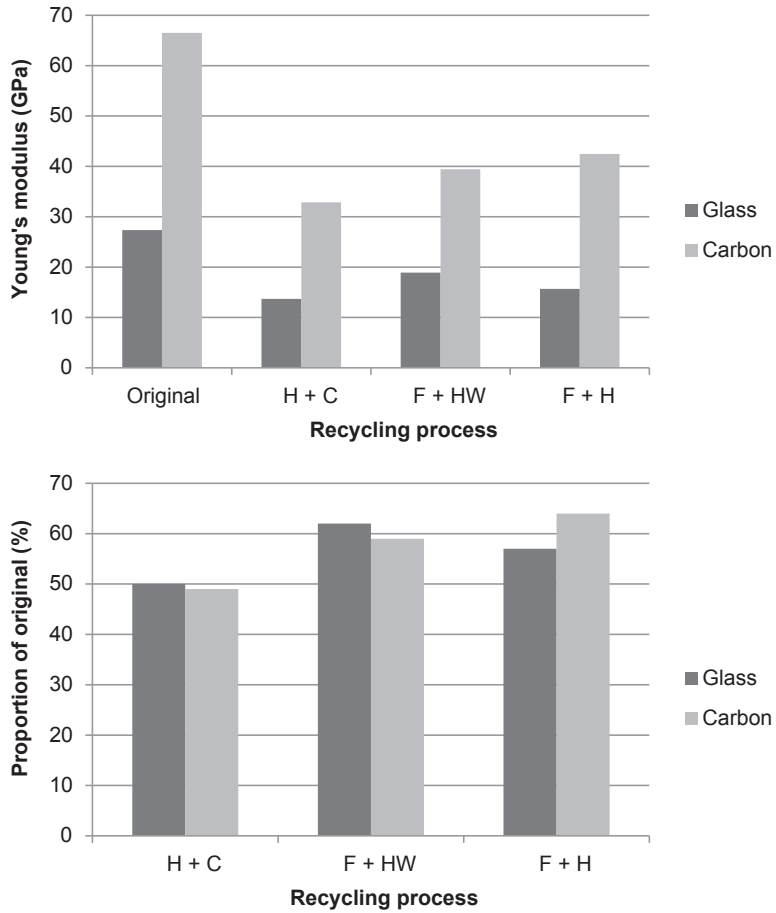

Figure 28.9 Young's modulus retention of recycled woven carbon and glass laminates impregnated with Ampreg 20 and percentage of original modulus.

28.7.1.3 Interlaminar shear strength

The ILSS values for the carbon pre-preg and the virgin woven composites are shown in Figure 28.10; these are typical for such materials. Figure 28.11 shows that the F + HW process has the best ILSS retention for both directional materials, which is surprising given the apparent effects of moisture on the strength of the Ampreg 20 resin. The F + HW glass specimens have ILSSs that are consistently higher than the virgin materials. While this may be helped by postcuring, the steam appears to have no adverse effects on the bond strength between the fibre and resin. It is possible that for the short exposure used, the water may have only penetrated the outer layers of the specimens leaving most of the resin unaltered. Note that the ILSS specimens fracture in the midplane, i.e. well away from the surface.

Following the F + H and F + HW processes, the remanufactured carbon specimens are the weakest. This implies that the reimpregnation of the carbon was less effective than the glass. Although the delaminations caused by the rollers are relatively large, it is impossible to ensure that the resin reaches all of the voids. Dry areas were clearly visible on the glass specimens, but it was impossible to determine by eye whether the carbon specimens were fully reimpregnated. The 58% ILSS strength retention and the extensive delaminations present for H + C after processing imply that reimpregnation was more effective for the carbon specimen.

28.7.1.4 GRP boat specimens

By selecting some flat parts of the boat hull, it was possible to measure the virgin strength of this material. Three processes were used, flattening cold in a press (F), and flattening with the application of heat and/or hot water (F + H, F + HW). The roller press was too severe, although 'softer' settings could have been developed given more time.

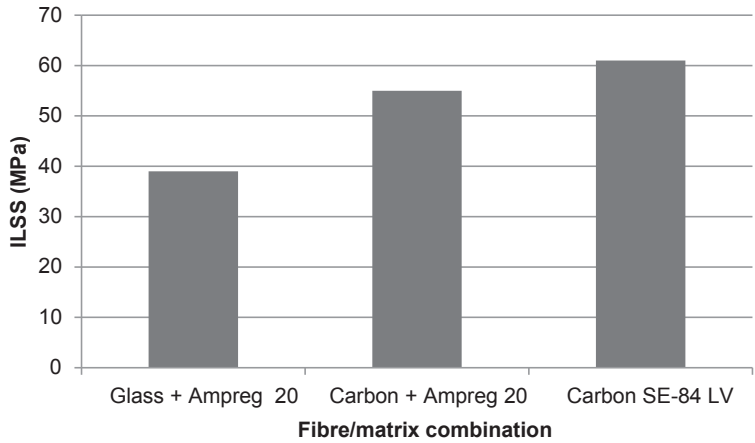

Figure 28.10 Interlaminar shear strength (ILSS) strengths of the virgin hand lay-ups of woven glass and carbon fibre in Ampreg 20 resin and the carbon fibre pre-preg (SE-84 LV).

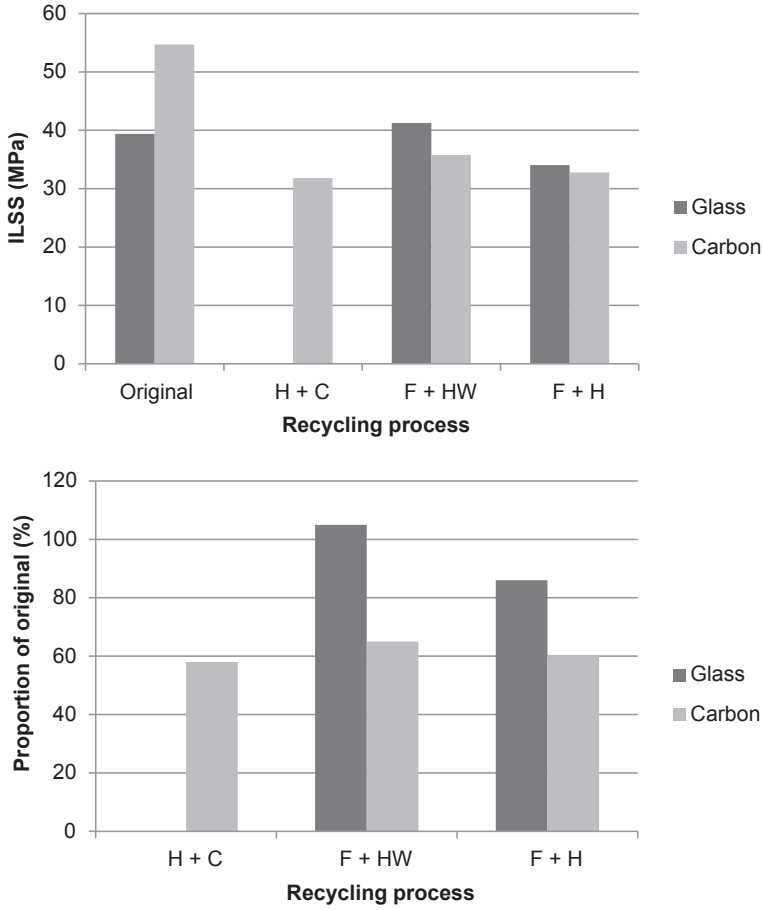

Figure 28.11 Interlaminar shear strength (ILSS) retention of recycled woven carbon and glass laminates impregnated with Ampreg 20 and percentage of original ILSS.

Figure 28.12 shows that the 'F' cold press process retained the most flexural strength, as expected because there was little curvature on the original panel and no heat was used. The strength reduction is due to fibre and resin damage sustained during flattening without heat. The fibres on the concave surfaces tend to fail in tension, and it is likely that shear failure occurs in the middle (thickness) of the panel. Only the areas between each layer were reimpregnated so the shear damage would remain.

The F + H process retains the most strength, which is consistent with the directional materials and supports the inference that the difference in strength retention is due to moisture damage to the resin in the F + HW process.

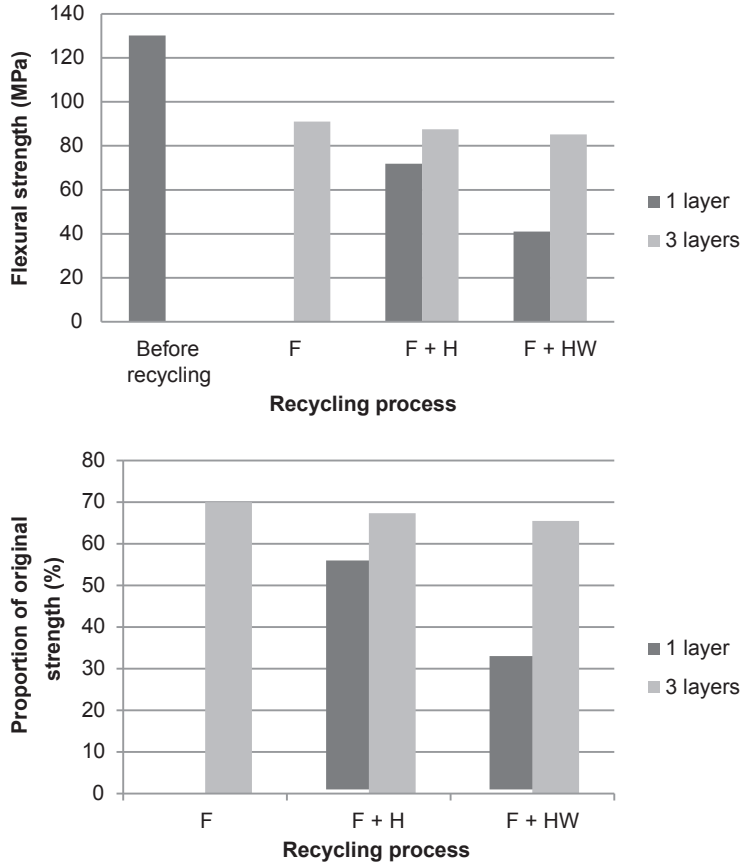

Figure 28.12 Flexural strength retention of the single and multilayered recycled plates of glass random mat from the boat and percentage of the original.

For single-layer specimens, the effect of the F + H and F + HW processes is large. There is a severe loss of strength for the F + HW specimen that can be attributed to the action of moisture, while the single layer F + H specimen has retained only 55% of its original strength. The three-layer specimens have strength retentions that are comparable to those of the cold-formed 'F' specimen. The structure of the Remat therefore must dominate its recycled properties, and this can be used to counter the damaging effects of heat and moisture. The layered structure supports the weak points and joins within the material and provides an effective system by which a continuous plate can be manufactured.

The stiffness retention for the random mat is higher than for the woven composites. The retention for CFRP was 64%, whereas the lowest retention for the random mat is 73%, as shown in Figure 28.9. The modulus reduction is directly affected by the magnitude of global fibre damage. The random mat has a low volume fraction of

short, randomly oriented fibres, so the damage will have less of an effect on its overall stiffness.

The F specimen has the lowest elastic modulus retention, which is unexpected because it has not been exposed to heat or moisture. Voids within the material and damage caused during recycling will reduce the local stiffness.

As with the flexural strength, the multilayered specimens provide the highest modulus retention (Figure 28.13). The combination effect of the layered structure results in no overall loss of modulus for the F + HW process and only a 3% loss for the F + H process.

The single-layer F + HW specimen retains less stiffness than does the single-layer F + H specimen, probably due to the effect of moisture on the resin.

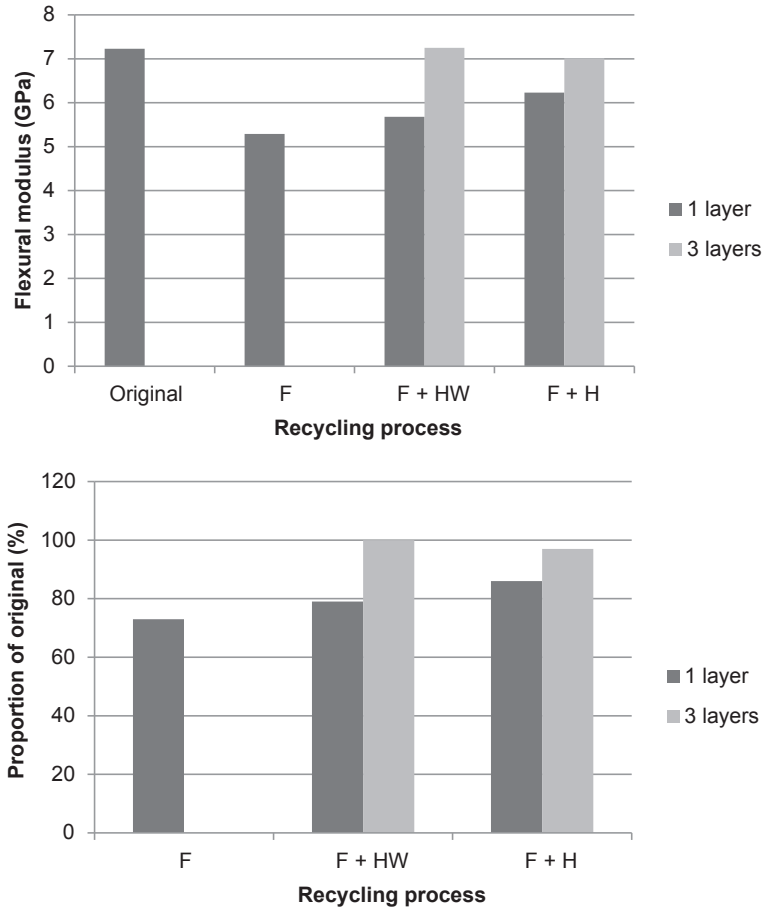

Figure 28.13 Elastic moduli retention of the glass random mat from the boat and proportion of the original.

28.7.1.5 Recycling of CFRP pre-preg

The most challenging material to recycle was the unidirectional CFRP composite made using the SE-84 LV pre-preg. The specimens were made using the corrugated and single curvature moulds shown in Figure 28.6.

When the specimens were heated in the F + H process, a large force was needed to flatten them, and many fibre failures were heard. The carbon specimens were by no means flat after removal from the hot press, as shown in Figure 28.14, although they could easily be flattened by hand because they were extensively delaminated. There were tensile failures visible on the peaks and troughs of the corrugated section where the fibres had been unable to accommodate the large strains applied during hot pressing.

Because processing using the F + HW process produces no discernible differences to using F + H, there is little advantage in using the F + HW process on pressure-consolidated high-performance carbon pre-preg. In early experiments using the hot crushing technique (H + C), the material at each end fractured completely, while the high stiffness of the composite prevented the central area containing the largest curvature from being delaminated fully. To improve the process, the roller pitch was reduced so that load span was reduced and interlaminar shear failures occur before tensile failures. Figure 28.15 shows a specimen that had been crushed using H + C. Some tensile failures have only occurred at the surface, but the specimen remains intact along its length, apart from almost continuous shear failure along the length of the specimen, resulting in a large degree of flexibility.

Because of the high elastic modulus in the direction of the fibres, it is difficult to use thermal forming to flatten a curved plate. Unidirectional CFRP, such as that produced from pre-preg, should therefore receive the crushing treatment to produce a flexible Remat laminate that can be used for remanufacturing.

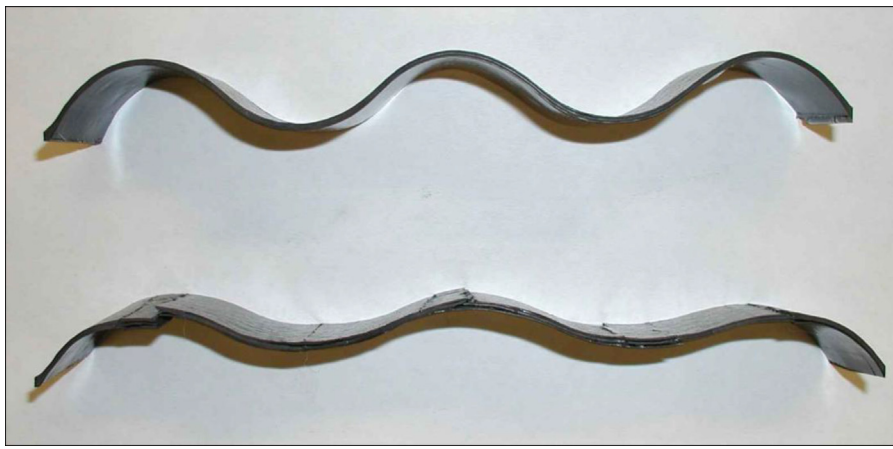

Figure 28.14 SE-84 LV corrugated plate (top) before recycling and (bottom) after forming at high temperature (F + H).
Reprinted from Adams et al. (2014), with kind permission from Springer Science and Business Media.

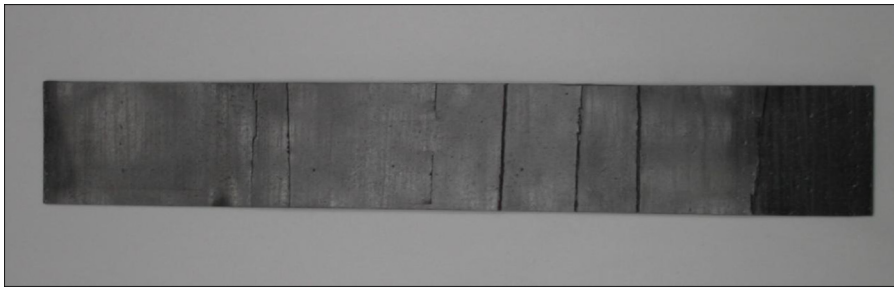

Figure 28.15 SE-84 LV single curvature specimen after crushing at high temperature with a roller pitch of 20 mm.

28.8 Remanufacturing

It has been shown above that it is possible to convert end of life components into a product that can be used to make specimens to test to see how much of the original properties remain after the material has been reimpregnated with a laminating resin. It was also shown that a high proportion, at least 50% in most cases, of the original mechanical properties was retained. The question now remains as to whether the product can be made into some other shapes that are more challenging. The Remat should be flexible, with long fibre retention, and be readily impregnated with a polyester or epoxy laminating resin. Different methods of creating a suitable Remat should be used depending on the input material and the form to be created.

28.8.1 Remanufacturing of the bathroom component

The bathroom component was curved in two directions, was of variable thickness, and was made of low-grade material. After cutting into sections, it was converted to flat sheets in a hot press, which were cut into flat rectangular plates.

To maintain as many of the beneficial properties of the composites as possible, it is extremely important, if bonding a number of sections together, to align component parts so that joints are flush and do not run continuously throughout the recycled product. This method was used to create the flat plates and is shown in Figure 28.16, while

Figure 28.16 Possible arrangements for spreading joints throughout recycled material.

Figure 28.17 A multilayered plate manufactured from the bathroom component.

Figure 28.17 shows the finished product (15 × 70 × 15 mm). Because the original material was of variable thickness and less than 2 mm thick on average, it was impossible to create uniform thickness sheets of Remat.

28.8.2 Remanufacturing from the GRP boat

A similar procedure was used as for the bathroom component, except that the boat GRP was much thicker (about 10 mm) and less curved. The gel coat, about 5 mm thick, needed to be split from the GRP. Removal was achieved by splitting the gel coat away from the rest of the composite at the point where the gel coat and the fibre-rich area of the composite meet. One problem was that the gel coat on the boat varied in thickness, resulting in either incomplete removal of the gel coat or removal of some of the fibre-rich area.

28.8.2.1 Plates

The GRP Remat was pressed flat either with heat F + H or cold F. Some of these pieces were then split into sheets 1−4-mm thick. The thicker sheets were made into flat plates by reimpregnation and then cured in a press. A corner view of a three-layer plate is shown in Figure 28.18. As can be seen from Figures 28.12 and 28.13, the three-layer (thinner Remat) plates were consistently stronger and stiffer than the one-layer plate that had been flattened in the hot press. The flat plates had a flexural strength of about 150 MPa compared with 300 MPa for the woven glass and an E modulus of 3.5−4.8 GPa compared with 27 GPa for the woven glass. Some ground recyclate from another project was used as a filler in the same epoxy resin used for making the recycled plates, with a resin-to-filler ratio of about 4:1. This high resin/filler ratio was needed to wet out the recyclate. While the flexural E modulus was similar to that of the recycled GRP, the flexural strength was only about 45 MPa.

Figure 28.18 A multilayered plate manufactured from the boat hull.

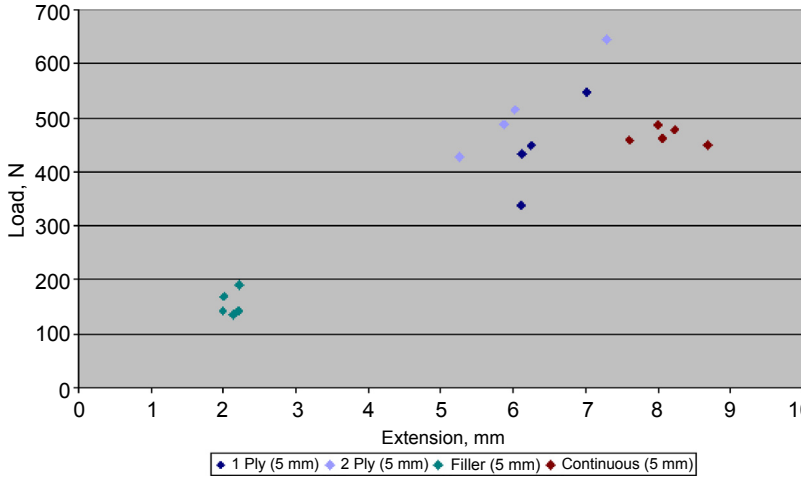

Figure 28.19 Maximum load versus maximum displacement for 5-mm beam specimens in three-point bending.

Figure 28.19 shows the load versus deflection for a series of 5-mm-thick beams tested in three-point bending. The beams cut from plates made from the recycled boat showed good strength and deflection and were close in performance to beams made from virgin woven glass fibre-reinforced plastic (GFRP). But note that beams made from the ground filler were both weak and had little deformation to failure.

28.8.2.2 Tubes

Tubes were made from some of the Remat with an internal diameter of 60 mm, a length of 390 mm, and a wall thickness of 4—7 mm. The tubes were tested in three-point bending to compare their strength with that of a similar tube made from woven glass fibre in a polyester resin matrix.

Several methods of making tubes were tried. In method A, hot, thin strips of GRP were wrapped circumferentially around a hot mandrel. Some problems arose in aligning the join where the ends of the laminate meet. With thin laminates, it was possible to overlap the join, but care needed to be taken to avoid gaps or bulges. This procedure produces a tube with a smooth and cylindrical inner surface, although the finish of the outer surface is not so easily controlled (Figure 28.20), and making long tubes was not easy because the hot GRP sheet was rather difficult to handle, although a suitable machine could be devised to solve this problem.

In method B, a longer tube was made by helically winding 25 mm strips around a steel mandrel. The strips were heated at 140 °C to make them malleable. They were then wound around the mandrel at an angle of 30°. Two layers were wound, one on top of the other. Because this technique was difficult to control, the method was abandoned, but a machine could surely be constructed to achieve success given more time and money.

Figure 28.20 Finished A range tube.

A further series of tubes (C, D, E) was manufactured that were designed to exploit and retain the longitudinal strength of the GRP Remat while using the minimum necessary quantity of virgin cloth. Strips of the Remat were cut, first at 8 mm wide (C-Range) and then at 16 mm wide (D-range). The strips, about 3−5 mm thick, were laid on woven glass cloth that had been impregnated with the Ampreg resin. The assembly was then wrapped around a 60-mm-diameter mandrel, and a further layer of impregnated glass cloth wound round the outside to hold the strips in position. Cure then took place in a vacuum bag, with post-cure as required. The lay-up used is shown in Figure 28.21, and a finished tube is shown in Figure 28.22.

To use more Remat, in the *E* range tubes the outer layer of virgin cloth was replaced by a hot-formed laminate wrapped around the outside of the strips. Other

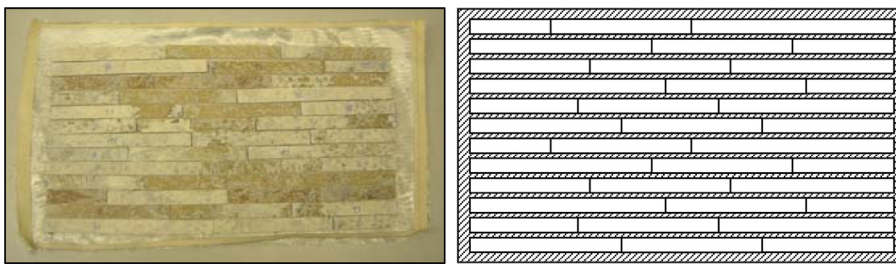

Figure 28.21 Lay-up of strips for C, D and E range tubes.

Figure 28.22 Finished D range tube.
Reprinted from Adams et al. (2014), with kind permission from Springer Science and Business Media.

than this, the manufacturing procedure for this component exactly replicates those illustrated for the C and D tubes. The pressure applied via the vacuum bag pressed the two layers together, and an excess of resin was supplied to fill any voids between the two layers; this method was only partially successful, and it was difficult to eliminate voids.

The tubes were tested in three-point bending, as shown in Figure 28.23, using steel loading rollers of 50-mm diameter to avoid crushing the specimen locally. Table 28.3 shows how the stiffness and strength of the remanufactured tubes compared with those of the virgin woven GFRP tubes. Note that while the remanufactured tubes were only about half as strong and stiff as the virgin GFRP tubes, the virgin tubes were made from woven glass cloth, which would have been stronger and stiffer.

Figure 28.23 Three-point bending of the tubes.

Table 28.3 Stiffness and strength of the remanufactured tubes compared with virgin woven glass

Tube range	Percentage of stiffness of virgin GRP	Percentage of strength of virgin GRP
C	66.1	52.5
D	68.1	52.6
E	56.1	56.1

28.9 Hot forming (F + H)

By heating the Remat to a temperature higher than T_g, the resin becomes highly flexible, thus making forming easy, reducing the likelihood of fibre damage during the recycling process, and minimising the need to delaminate before attempting to reshape. After bending to shape, the material can be cooled to retain its shape, and any disbonds are reimpregnated. Figure 28.24 shows a strip of woven GFRP being bent by hand at 140 °C. A detail, shown in Figure 28.25, shows delaminations due to buckling on the compressive faces. These are generated as each specimen is forced around the rollers. The reduction in modulus of the resin forces the fibres to take the compressive load, but without the support of the resin, the fibres buckle. This also means that little force is needed to bend the hot specimen. As the fibres carrying the compressive load are aligned longitudinally so the buckling occurs in bands across the width of the plate.

At room temperature, the 'H' specimen retains stiffness when force is applied to open the bends. This means that the compressive strength of the fibres on the convex

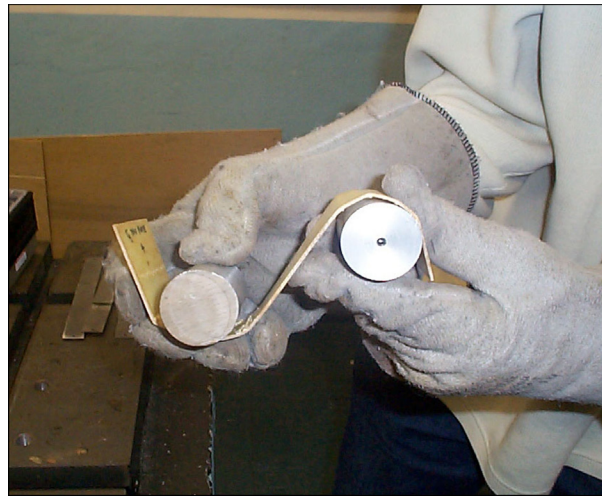

Figure 28.24 Forming the F + H specimen between two steel bars at 140 °C.

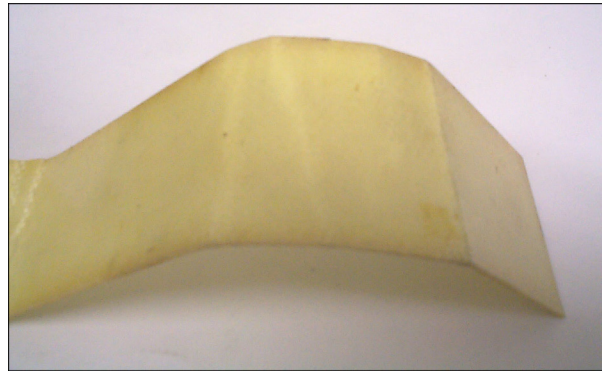

Figure 28.25 Detail of the tensile surface of the 'F + H' specimen.

surface and the tensile stiffness of the buckled fibres on the concave surface have been retained. The loss of compressive stiffness on the concave faces means that closing the bends requires less force. This could be restored by reimpregnation of this zone.

The F + H process looks attractive, but there can be complications. If the formed part is kept cool (well below its T_g) it should retain its shape for a long time. But if the part is reheated to above T_g, it will flatten almost completely as the residual stresses in the resin and fibres are allowed to relax. The effect of resin relaxation on a thermally formed recyclate means that such materials may be unsuitable for applications where they will reach a temperature at which they will begin to return to their original shape. A radial relaxation method was devised to determine the effect of resin relaxation on two of the recycling processes used, and the effect of fibre reinforcement on the rate and magnitude of relaxation was investigated.

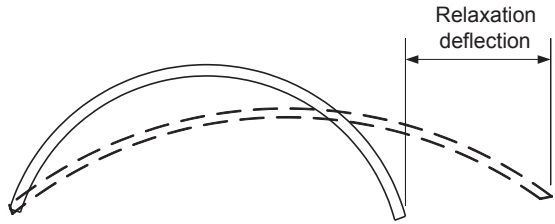

Figure 28.26 Deflection observed as the resin in the composite relaxes to its original position.

Table 28.4 Relaxation of hot formed (±45) GFRP

Time (min)	Deflection (mm)		
	F + H	H + C	H + C reinforced
0	0	0	0
2	67.5	13	3.5
4	67.5	16	3.5

Three identical specimens of $(-45/+45)_s$ glass fibre impregnated with Ampreg 20 resin were heated to 140 °C and bent into an arc and then cooled. One was crushed at 140 °C by the H + C process. Two others were formed into a radius (F + H) while at 140 °C and left to cool. One of these was then reinforced on the concave face by a single ply of (±45) glass fibre impregnated with Ampreg 20.

The specimens were placed in an oven preheated to 120 °C so that they would relax. At 2-min intervals, the deflection of each specimen was measured against a scale as it 'opened', as shown in Figure 28.26. The results are given in Table 28.4 and show that the F + H specimen without reinforcement relaxed quickly to almost its original shape in 2 min, as shown in Figure 28.27. However, the other two specimens (H + C process) retained much of their original shape, particularly the reinforced specimen (Figure 28.28).

These experiments show that while hot forming is possible, there needs to be some additional process such as crushing/reimpregnation or reinforcement to promote stability.

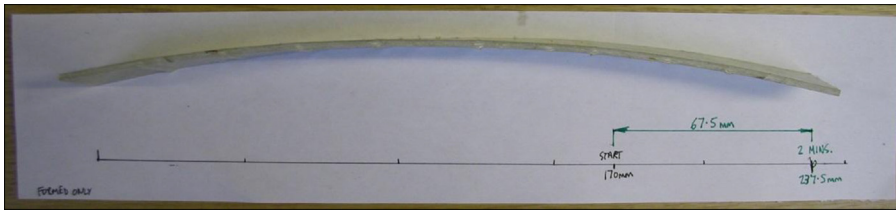

Figure 28.27 The F + H specimen after heating showing almost complete relaxation.

Figure 28.28 A reinforced F + H specimen after relaxation showing very little deflection.

28.10 Conclusions

The recyclability of fibre-reinforced composite materials has been investigated. Novel recycling methods have been tested on a variety of composite materials, ranging from glass fibre random mat in a polyester resin to high-grade carbon fibre composite.

It was shown that GFRP random mat is the most recyclable material. Not only does the material have consistently high property retentions for the F + H and F + HW processes, but also this material is relatively easy to flatten and split into thinner layers. These layers can be moulded and bonded to each other to fabricate products such as pipes and plates. The F + HW recycling process enhances the formability of the F + H process, but reduces the flexural strength by 5−10%. There is little effect on the elastic modulus.

For directional composites, the F + HW and F + H processes consistently produce retentions of tensile strength and elastic modulus of more than 50% after recycling. However, there are several factors that inhibit recycling. When trying to heat and form quasi-isotropic directional composites, anticlastic curvature is observed perpendicular to the forming direction. In addition, relaxation strains have been discovered that result in moulded components returning to their original shape at temperatures approaching T_g. Possible solutions to this problem include the addition of a reinforcement to prevent relaxation or reimpregnation with a resin with a higher T_g.

The high-grade carbon fibre pre-preg was found to be the most difficult to recycle. None of the recycling methods applied could successfully reform the material apart from hot crushing (H + C) with a reduced roller pitch in the lever crushing rig.

What this work has shown is that it is possible to recycle continuous and short fibre-reinforced thermosetting resins while keeping almost the whole of the original material, both fibres and matrix, within the recyclate. By splitting, crushing hot or cold, and hot forming, it is possible to create a Remat that can then be used to remanufacture other shapes, examples of plates and tubes being demonstrated. Not only can remanufacturing be done, but it has been shown that more than 50% of the original mechanical properties can be retained.

References

Adams, R. D., Collins, A., Cooper, D., Digby, M. W., Farmer, A. W., et al. (2014). Recycling of reinforced plastics. *Applied Composite Materials, 21*(1), 263−284.

Allred, R. E., Gosau, J. M., & Shoemaker, J. M. (2001). In *46th International SAMPE Symposium* (pp. 179−192).

Bledzki, A. K., & Goracy, K. (1993). The use of recycled fibre composites as reinforcement for thermosets. *Mechanics of Composite Materials, 29*, 352−356.

Feraboli, P., Kawakami, H., Wade, B., Gasco, F., DeOto, L., & Masini, A. (2012). Recyclability and reutilization of carbon fiber fabric/epoxy composites. *Journal of Composite Materials, 46*, 1459−1473.

Henshaw, J. M., Han, W., & Owens, A. D. (1996). An overview of recycling issues for composite materials. *Journal of Thermoplastic Composite Materials, 9*(1), 4−20.

Kennerley, J. R., Kelly, R. M., Fenwick, N. J., Pickering, S. J., & Rudd, C. D. (1998). The characterisation and reuse of glass fibres recycled from scrap composites by the action of a fluidised bed process. *Composites Part A, 29A*, 839−845.

Meyer, L. O., Schulte, K., & Grove-Nielsen, E. (2009). CFRP-recycling following a pyrolysis route: process optimization and potentials. *Journal of Composite Materials, 43*, 1121−1132.

Telfeyan, E. (2002). *Recycling of glass fibre composites*. NYS College of Ceramics. ceer.alfred.edu/research/derosaposter.ppt.

Design and performance of novel aircraft structures with folded composite cores

29

A. Johnson[1], S. Kilchert[2], S. Fischer[3], N. Toso-Pentecôte[4]
[1]Stuttgart, Germany (formerly of German Aerospace Center (DLR), Stuttgart, Germany); [2]Fraunhofer Ernst Mach Institute, Germany (formerly of German Aerospace Center (DLR), Stuttgart, Germany); [3]Institute of Aircraft Design, University Stuttgart, Stuttgart, Germany; [4]German Aerospace Center (DLR), Stuttgart, Germany

29.1 Introduction

Weight reduction by structural optimisation is a driving principle in aircraft design. In aircraft fuselages, a sandwich design concept could yield significant weight savings compared to an aluminium reference fuselage, through increasing frame spacing and elimination of stringers. Aircraft sandwich structures are traditionally composed of thin carbon fibre/epoxy skins, and the main core materials are polymer foams such as Polymethacrylimide (PMI) and honeycomb cores made from aluminium or impregnated aramid paper. Sandwich panels from these materials have excellent stiffness and strength-to-weight ratios and are established in small general aviation aircraft such as the Beechcraft Premier I and in transport aircraft as secondary structures such as flaps, radomes and nacelles. Major drawbacks of sandwich structures are, among others, the problem of humidity accumulation in closed-cell cores, which causes core degradation or skin/core debonding, and their vulnerability to impact loads. Impact resistance is a critical aspect of the design of primary aircraft structures due to a wide range of foreign object impact threats from bird strike, burst tyre rubber, runway debris, metal fragments and hail.

This chapter focuses on novel sandwich structures with open cellular composite cores manufactured by folding thin sheet base materials into a three-dimensional structure, as shown schematically in Figure 29.1. Typical core materials are aluminium foil and thermoplastic or resin-impregnated sheets reinforced by synthetic or natural fibres. By varying core materials and geometry, structural cores with a wide range of properties may be produced. Folded composite cores or 'foldcore' manufactured from resin-impregnated aramid paper have similar densities and mechanical properties to Nomex honeycomb. Furthermore, they allow ventilation to prevent moisture build-up due to their open cell design and can be manufactured cost-efficiently in a continuous process. Thus they are of interest for aircraft structures in which sandwich panel impact performance may be improved by using base materials with high energy absorption and by suitable design of the foldcore cell geometry.

The plan of this chapter is as follows. The foldcore concept is described in Section 29.2, with typical base sheet materials, core geometries and fabrication

Structural Integrity and Durability of Advanced Composites. http://dx.doi.org/10.1016/B978-0-08-100137-0.00029-8

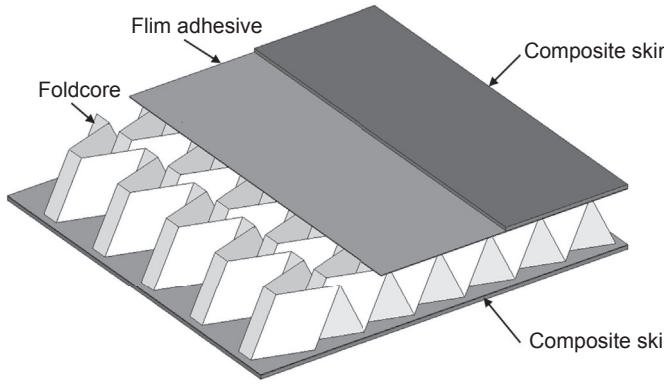

Figure 29.1 Sandwich plate concept structure with folded structural core.

technology suitable for continuous manufacturing processes. Folded core properties and design are discussed in Section 29.3, with test methods used for measuring thin base sheet properties and determining core through-thickness compression and shear failure modes and strength properties. Core design is based on micromechanics cell models used in FE methods for simulating progressive damage and collapse mechanisms to provide core properties for use in sandwich structural analysis and design of sandwich structures. Section 29.4 is concerned with impact behaviour of foldcore sandwich structures. The damage tolerance of sandwich panels with carbon fibre/epoxy skins and aramid fibre/phenolic folded core is discussed, based on experimental investigations by drop tower and gas gun impact tests. Observed failure modes depend on impactor type and impact energy, ranging from impactor rebound, outer skin damage, core microbuckling, core penetration, and inner skin damage or penetration. FE methods are then presented for prediction of local impact damage and skin/core penetration in foldcore sandwich structures by adding composite skins to the foldcore micromodels. Comparison between observed and computed failure behaviour for a range of impact load cases shows good agreement, indicating that the FE methods could provide the basis for design and certification of these advanced aircraft sandwich structures. Concluding remarks and future outlook in Section 29.5 are followed by sources of further information and references.

29.2 Folded core materials, cell geometry and manufacture

Foldcore is an origami-like sandwich core that is manufactured by folding a flat base material. Because the focus is on technical applications, foldcore is sometimes referred to as technical origami. Early concepts and manufacturing studies of foldcore with regard to technical application were presented by Miura (1972). He introduced a

so-called 'Zeta-Core' as novel sandwich core. The Zeta-Core can be seen as the basis for the zigzag unit cell. In the past 10 years, foldcore developments in design and manufacture for aircraft structures have been carried out at the Institute of Aircraft Design (IFB), University Stuttgart, as described in Klett (2013), which will be presented in some detail in this chapter. Further foldcore developments for aircraft sandwich structures were studied in collaboration with Airbus in the German national project EMIR (2003) and the European Union Project CELPACT (2009), which investigated a range of advanced core materials with improved impact characteristics. Another centre for foldcore developments is Kazan State Technical University, Kazan, Russia (KSTU), which has developed foldcore structures for the Russian aircraft industry and the oil and gas distribution industries (see Zakirov, Nikitin, Akishev, Rückert, and Mudra (2005), Zakirov, Nikitin, Alexeev, and Mudra (2006) for more information).

29.2.1 Cell geometry

Foldcore is manufactured by folding a flat sheet, and a nomenclature HAP (German: Hauptachsenpaar) is used for the number of axes around which the sheet is folded. A wide range of base materials are suitable for fabrication into foldcore structures, as discussed in the next subsection. Following the nomenclature, a corrugated board has a 1-HAP unit cell. The Zeta-Core form is developed into the zigzag foldcore (also called 2-HAP), as discussed by Kehrle and Kolax (2006), while other unit cells are important, such as the 3-HAP unit cell that has better mechanical properties in compression than zigzag foldcore. The basic cell geometry for 3-HAP foldcore is defined in Figure 29.2. This unit cell has five independent geometric parameters: L, S, H, V and S_{CW}. Varying these parameters leads to an infinite number of specific cell geometries. It is clear that foldcore can be adapted to different applications by adjusting base material, base material thickness, core height H, and varying remaining geometry parameters to change the cell shape and hence core density. Note that the general unit-cell turns into a zigzag-type unit cell by setting S_{CW} to zero.

Foldcore has an open-cellular structure in the W-direction, which makes ventilation possible; see Figure 29.3 for definition of directions L and W. This is a major advantage over closed-cell sandwich cores such as honeycomb, which in aircraft structures cause humidity accumulation with degradation of core mechanical properties under flight temperature and humidity cycles. Geometry data for cores used in this chapter are listed in Table 29.1, with core density values based on an aramid fibre/phenolic resin

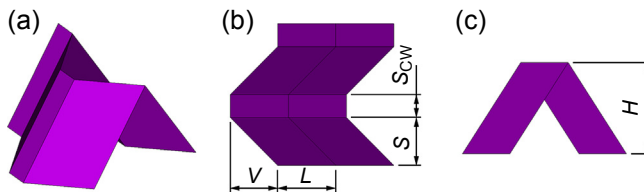

Figure 29.2 Unit-cell geometry of 3-HAP foldcore: a) isometric view, b) top view, c) side view.

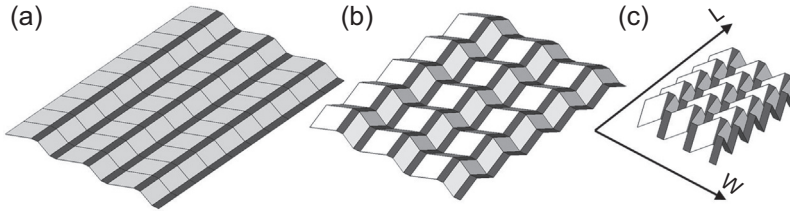

Figure 29.3 Principle of folding a flat base material: (a) first fold, (b) intermediate step, (c) final configuration.

Table 29.1 Geometry parameters of foldcores investigated

Geometry	H [mm]	V [mm]	L [mm]	S [mm]	S_{CW} [mm]	ρ [kg/m^3]
Celpact 21	20	10.77	5.03	6.34	5	75
Celpact 30	20	10.77	2.70	6.34	5	138
Celpact 31	20	10.77	3.31	6.34	5	113
IFB 165	20	7.87	7.87	7.87	0	45

paper sheet with thickness of approximately 0.3 mm. For improved sandwich impact performance, foldcore geometries with high compression and shear strengths are required. These geometries have 3-HAP unit cells with core densities between 75 kg/m^3 and 138 kg/m^3. In the CELPACT project, static tests were performed on all types, with impact tests carried out on high-density foldcore type 30.

29.2.2 Folded core materials

A range of materials are suitable as base materials for foldcore. Typical base materials for structural applications are metal foils, plastic foils, or paper-like materials made out of synthetic or natural fibres. Also, low-cost materials such as paper or cardboard are applicable in less critical applications requiring reduced mechanical properties. Metal foils, due to their high elastic modulus, are an excellent base material for creating foldcore with high stiffness. In particular, aluminium has proven suitable for the folding process. Regarding transverse shear, mechanical properties of aluminium foldcore are comparable to those of aluminium honeycomb, as shown by Fischer and Drechsler (2008, 2011). The elastic−plastic behaviour of aluminium makes it suitable for aluminium foldcore in energy-absorbing structures. High core deformations at relative high stress levels are possible before global core failure, as found in aluminium foldcore tests in compression, compaction and impact.

Another class of promising base materials are thermoplastics. Especially high-performance plastics such as Polyether ether ketone (PEEK) provide good mechanical

performance in foldcore. Thermoplastics are available as foils in different thicknesses and can also be reinforced using particles or fibres, as discussed in Grzeschik et al. (2000). PEEK has a high fracture strain, making large plastic deformations of the core without rupture possible. When reinforced with fibres, high stiffness and high strength can be achieved. For aircraft applications, a base material is needed, which is flame resistant and has good mechanical properties. Therefore, aramid paper is chosen as base material for further investigation here on aircraft structures requiring good impact performance. This base material is a paper-like material that consists of randomly orientated aramid fibres impregnated with phenolic resin. The material is similar to Nomex® paper, which is a standard material used for honeycomb cores in aerospace sandwich structures (Bitzer, 1997).

29.2.3 Manufacture

Manufacturing of foldcore from aramid paper at the University Stuttgart is mainly a two-step process. The first step is the folding, which can be performed in a continuous process due to the repeated assembly of unit cells (Kehrle & Drechsler, 2004). In this step, the aramid paper is in a pre-cured state. The second step is then curing. The principle of the folding step is shown in Figure 29.3. A pattern is embossed into the base material, which gives the edges of the cell geometry. The base material is then folded around these edges, giving the final cell geometry. This can be done in a continuous or a discontinuous process. The material between the folding edges stays unaffected by the manufacturing process. Aramid paper is well suited for manufacture because, being preimpregnated, it can be easily folded while in a pre-cured state. After the folded sheet has reached its final geometry, it is cured. This is usually done in a standard circulating air oven, giving the foldcore its final shape and stability. Two routes are followed in foldcore production: a discontinuous process for rapid prototyping and a continuous process for larger scale production. The rapid prototyping process uses automated embossing followed by a manual folding process. The advantage of this method is that different unit cell geometries can be produced without retooling the machine used for embossing. The continuous process was proven to work and is currently under further development (see Kehrle and Kolax (2006)). Here, each unit cell type is produced with a specific set of tools, but in an automated, and therefore fast, continuous process.

29.3 Folded core properties and design

This section discusses material properties and design methods for the IFB University Stuttgart foldcore materials listed in Table 29.1. This includes determination of the aramid/phenolic base material properties, typical foldcore compression and shear properties, and development of micromechanics cell models for use in FE simulation of foldcore progressive damage and collapse required for design of foldcore sandwich structures.

29.3.1 Cell-wall materials properties

The standard base material for foldcore production is an 'aramid paper,' consisting of random orientated short aramid fibres impregnated by phenolic resin, with a mean thickness of 0.3 mm and a mass per unit area of 0.24 kg/m^2. Figure 29.4 shows a micrograph of the paper cross-section, which is irregular through the thickness. The aramid fibres are concentrated at the paper midplane, with a thickness of approximately 0.2 mm, and nonuniform layers of phenolic resin are at the outer surfaces. The aramid paper in-plane properties have some slight orthotropy due to increased fibre alignment in the paper milling direction. Aramid fibres are elastic in tension, but exhibit some plasticity in axial compression. It follows that in-plane paper tension and compression properties and paper flexural properties will be different. These properties are required to understand foldcore behaviour and for use in core modelling studies.

Test programmes to determine the aramid paper properties are discussed in Fischer, Drechsler, et al. (2009), Fischer, Heimbs, et al. (2009). Tension tests were performed in the mill and cross-mill directions using waisted specimens with gauge lengths 180 × 15 mm and strains measured optically, because bonded strain gauges could stiffen the paper specimens. Specimens exhibited some nonlinearity with brittle failures at strains of 1.4−2.0%. Due to the extremely thin paper sheet, determination of compression and bending properties is challenging. To measure in-planar compression properties, it is important to avoid premature buckling failures. This was achieved in a thick cylinder axial crush test (Kilchert, 2013) made by winding aramid paper to give

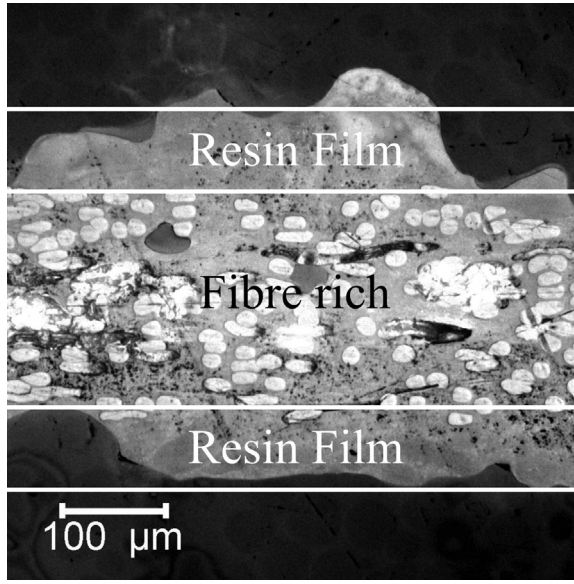

Figure 29.4 Micrograph of aramid paper cross-section, with schematic of fibre-rich ply and outer resin films.

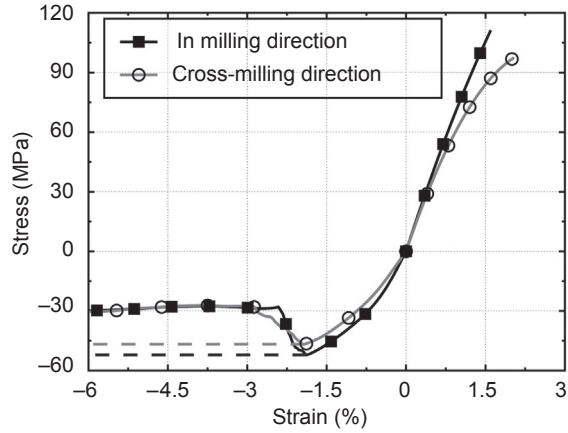

Figure 29.5 In-plane stress−strain behaviour of aramid paper measured from coupon tension and cylinder crush tests.

cylindrical tube specimens 30 mm long and 4 mm thick. These exhibited nonlinear elastic behaviour followed by plastic yielding at about 2% compression strain. Figure 29.5 shows compilation stress−strain curves for aramid paper in-plane tension and compression properties for the mill and transverse mill directions. Additional properties measured were in-plane shear behaviour from thick wall beam shear tests on beams 80 × 20 × 6.3 mm, composed of 24 sheets of aramid paper, which showed nonlinear elastic−plastic properties similar to the compression curves in Figure 29.4. Finally, flexural moduli of the aramid paper were determined from free vibration cantilever bending tests, as described further in Baranger et al. (2008). Table 29.2 lists the main elastic moduli and strength properties of the aramid paper as measured in these test programmes.

29.3.2 Core compression and shear behaviour

The main requirements of sandwich cores are low weight combined with good through-thickness compression and transverse shear stiffness and strength properties. The standard tests to characterise sandwich core materials are flatwise compression tests to ASTM C365/C365M-11 (2011) and transverse shear tests to ASTM C273/C273M-11A (2011). These tests are also suitable for foldcore, in which the transverse shear test has to be performed in both principal directions of the core, called *L*- and *W*-directions (see Figure 29.3). This is necessary due to the orthotropic material behaviour of foldcore arising from the unit-cell geometry. In the tests, the foldcore is bonded to composite face sheets to form a sandwich plate, which is then loaded between large platens attached to a universal test machine. Test method details and some foldcore through-thickness stress-strain curves in compression are shown in Heimbs, Middendorf, Kilchert, Johnson, and Maier (2007) and under shear loads in Fischer et al. (2009).

Table 29.2 Moduli and strength of aramid paper measured under different loading conditions

Test type	Coupon test			Cylinder crush test		Flexure vibration test	Thick beam shear test
Property	Tension modulus [GPa]	Tension strength [MPa]	Poisson's ratio −	Compression modulus [GPa]	Compression strength [MPa]	Flexure modulus [GPa]	Shear modulus [GPa]
In milling direction	7.7	111	0.3	5.0	53	4.7	2.3
Cross-milling direction	7.1	98	0.4	4.6	47	4.7	2.3

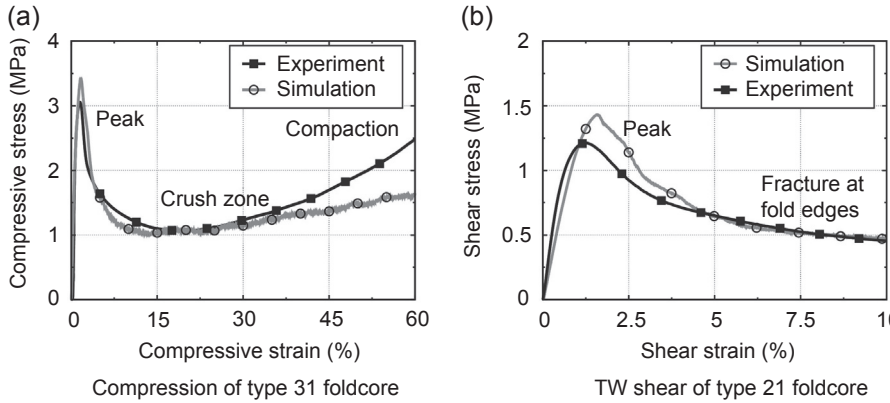

Figure 29.6 Comparison of foldcore stress−strain curves from test and simulation with baseline FE model: (a) flatwise compression, (b) transverse shear (*W*-direction).

Typical stress−strain curves under compression and transverse shear are shown in Figure 29.6, including a comparison with FE simulation results discussed in Section 29.3.3. The qualitative characteristics of the stress−strain curves are similar to those of other core materials such as Nomex® honeycomb. The first part until peak stress is fairly linear, from which an initial elastic modulus is determined. After that, the curve may show some degradation before reaching a sharp peak stress. This value is taken as the compression or shear strength of the foldcore. The abrupt failure is initiated by local buckling in the cell walls, which causes a rapid decrease in stress until a plateau stress is reached. This plateau stress stays more or less constant for a large strain increment. In compression tests, foldcore compaction then takes place, causing a further increase in stress at compression strains higher than 30%. The shear stress−strain curve follows a similar path to the compression curve, but exhibits local fracture in the cell walls, causing failure without any stress increase due to compaction. In compression, the initial elastic range is shorter with lower peak failure strains and higher moduli than in shear. In shear, compaction occurs only for unit cell geometries with a sufficiently high core density, otherwise rupture occurs before compaction.

Table 29.3 summarises through-thickness stiffness and strength properties of several foldcore types from a detailed test series at IFB, University Stuttgart, and in the CELPACT project as reported by Baranger et al. (2008). Mean values are provided for each material from six through-thickness compression tests with transverse shear tests performed in both *L*- and *W*-directions. The compression and shear moduli are initial values from the test curves, while the strength values are defined as the peak stresses at onset of foldcore buckling. These data are important core properties for the design of sandwich structures, and the table shows the wide range of properties available as the foldcore unit cell geometry is varied. Comparing IFB 165 with Celpact 30 shows that closer packing of the unit cells provides higher core density, which leads directly to considerably improved core properties.

Table 29.3 Measured moduli and strengths of foldcore types in compression and transverse shear

	Density	Compression		Transverse shear			
Foldcore type	ρ [kg/m^3]	E_C [MPa]	σ_C [MPa]	G_L [MPa]	τ_L [MPa]	G_W [MPa]	τ_W [MPa]
IFB 165	45	74	0.86	58	0.52	72	0.65
Celpact 21	75	280	1.9	98	1.1	95	1.1
Celpact 30	138	480	3.0	175	2.0	180	1.6

29.3.3 FE micromodels for core design

The foldcore flatwise compression and transverse shear tests discussed above have shown that core failures are initiated by microbuckling in the core cell walls, followed at higher loads by foldcore folding, tearing and fracture at cell wall edges, before compaction at higher strains. Failure modes and peak stresses were also seen to be highly dependent on small changes in unit cell geometry and base material properties. It follows that fine-scale FE micromodels are required to analyse foldcore behaviour, which take account of the detailed cell wall geometry and the observed properties of the aramid paper. Two modelling methods are discussed here: a basic model with fixed unit-cell geometry and a refined model that contains additional geometry features such as bond lines and cell wall irregularities. Both approaches require a suitable model for the cell walls of aramid paper to correctly describe folding and failure properties.

29.3.3.1 Cell wall modelling

Aramid paper properties were presented in Section 29.3.1, which showed that the material is orthotropic in-plane, elastic in tension, elastic/plastic in compression, and inhomogeneous through the thickness with aramid fibres in the midplane and resin rich outer regions. In the foldcore FE models, the aramid paper is modelled by shell elements in which a four-layered shell is proposed with two central fibre mat plies and two outer resin plies with different constitutive properties, as seen schematically in the overlay in Figure 29.4. The phenolic resin is isotropic elastic/plastic, and the fibre mat is orthotropic elastic/brittle in tension and elastic/plastic in compression. The initial elastic properties of the fibre mat and resin are derived by an inverse analysis of the experimentally measured aramid paper properties in tension, compression and bending from Table 29.2. A damage model with a single modulus damage function was used for both ply materials, which modelled degradation in elastic properties prior to yield. Details of the model development and validation are given in Kilchert (2013), Kilchert, Johnson, and Voggenreiter (2008, 2014). Validation studies of the aramid paper-layered shell model were carried out using FE models in PAM-CRASH^{TM} of the aramid paper tension tests and a set of thin wall aramid paper cylinders that failed in compression buckling with local folding.

29.3.3.2 Baseline foldcore micromodel

A foldcore structure may be generated from a parametric mathematical description of the unit-cell geometry, as described in Hachenberg, Mudra, and Nguyen (2003). A 3-HAP foldcore unit cell shown in Figure 29.2 is made up of plane rectangles or parallelograms and may be described by the five independent geometrical parameters marked in the figure, with values listed in Table 29.1 for several IFB foldcore geometries used in this chapter. The parametric model is used in a mesh generation code, which allows each plane rectangle to be meshed by four-node shell elements of a specified size. The FE model for the foldcore structures as used in the compression tests discussed above were based on generating a 3×6 cell type 31 foldcore model. This is smaller than the full size of the tested plates, but large enough for free edge

effects to be insignificant. Fine-scale meshes with element lengths of approximately 1 mm were used, which have been shown to be suitable for modelling buckling, folding and compaction in foldcore structures.

As foldcore test data have shown, failure is initiated by cell wall microbuckling, which for thin wall structures is critically dependent on geometrical imperfections. Micrographs of foldcore indicate that the paper has nonconstant thickness, and foldcore structures have geometrical defects due to manufacture. Numerical methods for geometrical imperfections introduce 'randomness' into the model by applying a stochastic distribution of a certain type of irregularities such as random shifts in node position or geometry, curvature of faces, variance in material properties, and cell wall thicknesses. They offer the advantage of simple numerical implementation, but are not usually based on measured properties. Such effects should be considered in the analysis. For the baseline foldcore model, the irregular nature of the real geometry was considered by an implementation of node shaking to each unit cell (Heimbs et al., 2007). Node shaking refers to initial random displacements of the nodes parallel and/or perpendicular to the foldcore faces. These random displacements are small, and in the model here, the in-plane displacements of 0.05 mm were larger than the out-of-plane displacements of 0.0025 mm. The foldcore FE mesh is attached at the upper and lower faces to plane rigid surfaces by tied contacts in PAM-CRASH™, which prevent skin–core debonding. The foldcore model uses self-contact with an assumed friction coefficient of 0.2. For the compression test, the rigid faces move toward each other with a relative velocity of 0.2 m/s.

Figure 29.6(a) depicts the stress–strain behaviour from test and numerical modelling in flatwise compression. Good agreement is observed for the initial elastic behaviour, the collapse by microbuckling in the crush zone, but the simulation overestimates the peak stress considerably with 3.4 MPa predicted and 3.0 MPa in the test. There is also significant deviance in the compaction region, where the model considerably underestimates the measured stress at high strains. This is to be expected using shell elements to model compaction that are eliminated on failure, because in the test at high strains it is the volume of compressed aramid paper with edge tearing and frictional forces that absorbs the crush energy. Figure 29.7 compares foldcore deformations between test and simulation for compression strains of 1%, 5% and 10%. At these lower strains, there is excellent agreement in the failure mode due to buckling, folding and kinking. It is also apparent that the fine 1-mm mesh sizes are necessary to capture the local folding behaviour.

A similar foldcore FE model was developed for type 21 foldcore and applied to simulate the stress–strain behaviour of the transverse shear test in the *W*-direction, with test curve and simulation results shown in Figure 29.6(b); see Kilchert (2013) for more details, including deformation plots. The figure shows that the initial buckling and global shear stress–strain behaviour is well captured, except at failure initiation, when peak stresses are overestimated by about 20%. It is considered that this is due to the inherent simplifications in the foldcore model, which include: idealised cell geometry with node shaking, not real cell geometry with defects; neglect of the skin–core bond where the additional resin adhesive supports the cell walls at the skin interface and modifies buckling and skin/core debonding; and the weakening

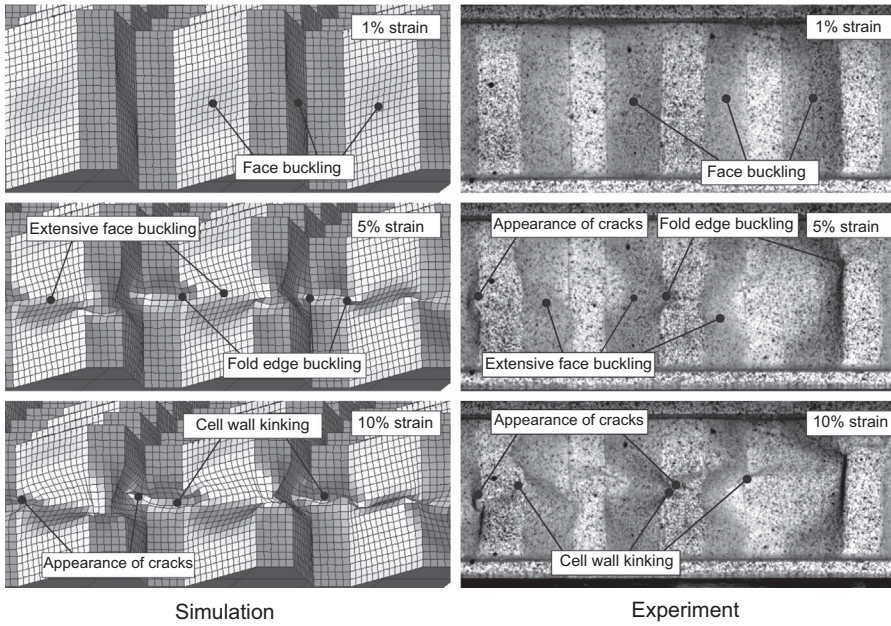

Figure 29.7 Comparison of computed and measured deformation plots of type 31 foldcore in flatwise compression at strains of 1%, 5%, and 10%.

effect of the scored fold lines during manufacturer, which will cause premature foldcore failure at corners. However, the baseline foldcore model has advantages for FE analysis of larger foldcore structures because the geometry is fixed in each unit cell, and it gives good predictions of damage modes and energy absorbed at moderate strains. It is used in Section 29.4.3 as basis of the sandwich impact models.

29.3.3.3 Refined foldcore micromodel with bondlines

Model improvements are now considered in the refined foldcore model for better understanding of failure initiation to improve fold core strength and stiffness analysis, which is vital for basic design of new structures. Detailed knowledge of foldcore irregularities is required to replace the simplified node-shaking method in the baseline model. A better physically based approach is to use geometry for FE mesh generation based on an optical or computed tomography (CT) scanning of manufactured foldcore structures, or to develop a numerical modelling of the complete folding process starting with the aramid paper sheet. Use of an optical scan of a foldcore cell or structure to generate an exact geometry for basis for meshing is discussed here, with further details in Fischer (2012). The advantage is a good capture of geometrical imperfections, with the disadvantage that at least one sample cell or structure has to be manufactured. The scanning system used here is ATOS by GOM. The fabricated unit cell is scanned without contact. Scanning of larger structures is possible, because the system is able

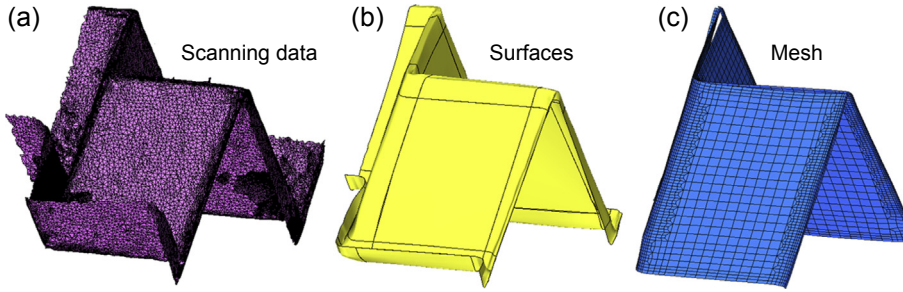

Figure 29.8 Re-engineering scanned cell geometry data of type 165 foldcore into an FE shell model: a) raw scanning data, b) re-engineered CAD data, c) FE model.

to integrate together data from more than one scan. Scanned data are then exported in the stl-data format. The CAD geometry surfaces are re-engineered from stl-data and used as input into a mesh generation program. Afterward, the scanned surface mesh is displaced by a half wall-thickness from the outside surface, to provide a mid-plane surface suitable for meshing with shell elements, as seen in Figure 29.8.

Another imperfection in foldcore is the local weakening of the cell wall at the folded edges due to the scoring prior to the folding step. Depending on the manufacturing process, the degradation of edge properties can have a considerable influence on foldcore failure stress and collapse behaviour, because the folded edges play an important part in the stiffening of the foldcore structure, as discussed by Fischer (2012). Micrographs show that the fold edges of the aramid paper presented are considerably degraded, with loss of the outer resin layer. The embossing of the folding edges and the folding process itself stress the edges of the foldcore, which means they may be prestressed. Because the stress-concentrations during compression and shear are also inside the edges, their stress-state should be determined with high accuracy. Aramid paper is folded while it is pre-cured and cured after folding, so there are no residual stresses to be considered. However, the embossing process before folding damages the outer resin-rich layer. In the refined foldcore FE model, this layer is omitted in the aramid paper ply model at the folded edges.

The sandwich skin-foldcore bond determines the structural integrity of the sandwich structure and also has an influence on stiffness and strength of the core. First the bonding is not perfectly rigid, but has some compliancy. Thus use of a tied interface in the FE model overestimates the stiffness. Second, the bonding introduces resin beads that support the sides of the joint with a fillet seam at the fold, as seen in Figure 29.9(a). This stabilises the foldcore and makes it less sensitive to buckling. Because foldcore strength is influenced by buckling of the cell walls, the strength is increased by the fillet seam. Modelling of the bondline can either be done with solid-elements Figure 29.9(b) or with added composite shell elements to represent the thicker layers at the bondline Figure 29.9(c), where the thicker shells represent the foldcore sheet plus adhesive.

This refined model that includes scanning-based geometry, the weakened fold edges, and the added bondlines is now used in an FE model to compute the stiffness

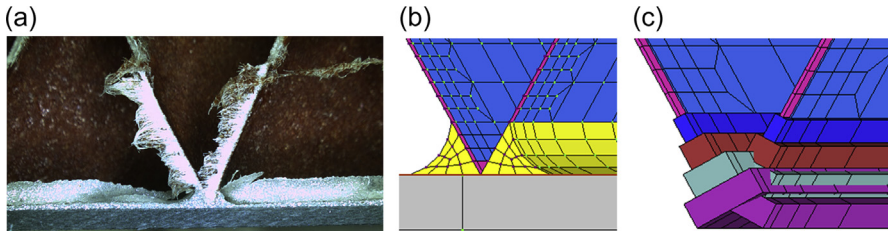

Figure 29.9 (a) Bondline at skin interface, (b) FE model with solid elements, (c) FE shell model.

and strength of foldcore in compression and shear. Figure 29.10 shows the setup of the FE model for the compression test. The unit cell is a type 165, which gives a zigzag foldcore structure. To have the same boundary conditions as in tests, the complete core with 36 unit cells is modelled. Load introduction is performed via bonded face sheets with a coupled rigid plate for contact conditions. The aramid paper is modelled as a layered shell, as discussed above for the baseline foldcore model.

In this case, the FE models were performed with ABAQUS/Explicit using reduced integration S4R shell elements and the layered shell aramid paper model in the form of a user-defined subroutine to define material behaviour (VUMAT) (Fischer, 2012). Figure 29.11 shows von Mises' equivalent stress contours for a section of the model after initial buckling has been initiated, close to peak compression stress, when the cell walls buckle but rupture has not occurred. The computed stress−strain curves from compression and shear tests and simulations are displayed in Figure 29.12 up to the point of peak stresses and failure initiation. Simulations show good agreement with the mean curves from six tests carried out for each load case. Computed modulus and strength values are displayed in Table 29.4 and compared with test data. There is excellent agreement with mean values from the tests, which confirms the refined foldcore model is better able to predict core strengths and stiffness than the simpler baseline model. However, this is at the expense of increased complexity and the need for more detailed geometry data by scanning manufactured foldcore unit cells.

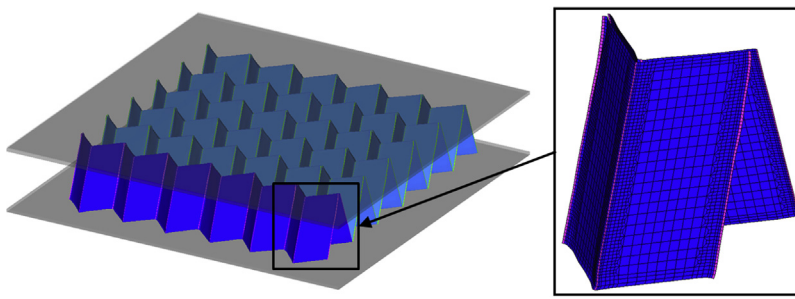

Figure 29.10 Refined FE model of compression test with bondlines, modified edge folds, and optically scanned cell geometry.

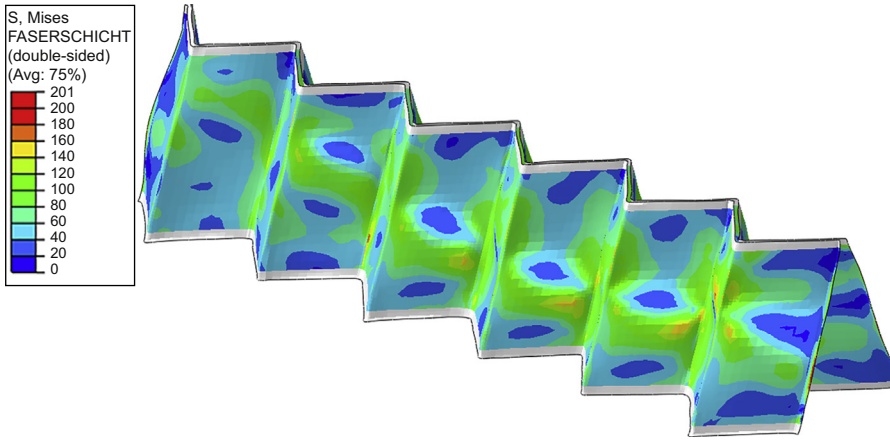

Figure 29.11 Refined FE model of type 165 foldcore during flatwise compression.

29.4 Impact performance of foldcore composite sandwich panels

A critical safety issue for the design of primary aircraft structures is vulnerability and damage tolerance due to foreign object impacts from bird strike, hail, tyre rubber and metal fragments. Standard aircraft sandwich structures are particularly vulnerable to impact damage, due to the thin, brittle carbon fibre/epoxy resin skins and low strength cores of polymer foam or Nomex® honeycomb, as discussed in Bitzer (1997) and Abrate et al. (2013). Thus, for foldcore composite sandwich structures to be considered for primary aircraft structures in fuselage and wing panels, particular attention has to be given to impact behaviour and damage tolerance under a range of impact threats. Section 29.4.1 summarises impact damage and failure modes seen in low- and high-velocity impact tests on foldcore sandwich panels carried out in the CELPACT project, with further detailed information presented in Kilchert et al. (2014) and Heimbs, Middendorf, Hampf, Hähnel, and Wolf (2009), Heimbs, Cichosz, Klaus, Kilchert, and Johnson (2010). The test data support the development of FE models for prediction of impact damage in 29.4.2 and their validation in 29.4.3.

29.4.1 Impact damage observed in low- and high-velocity tests

The experimental work presented here focuses on two distinct impact scenarios that need to be evaluated for aircraft sandwich structures. These are low-velocity, high-energy blunt impacts that represent ground impact, for example by contact with a vehicle during baggage handling or tool drop on sandwich panels during maintenance. The second scenario is foreign object damage (FOD) from high-velocity impact (HVI) by low-mass projectiles that could represent runway debris, damaged engine fragments, or burst tyre and wheel rim pieces.

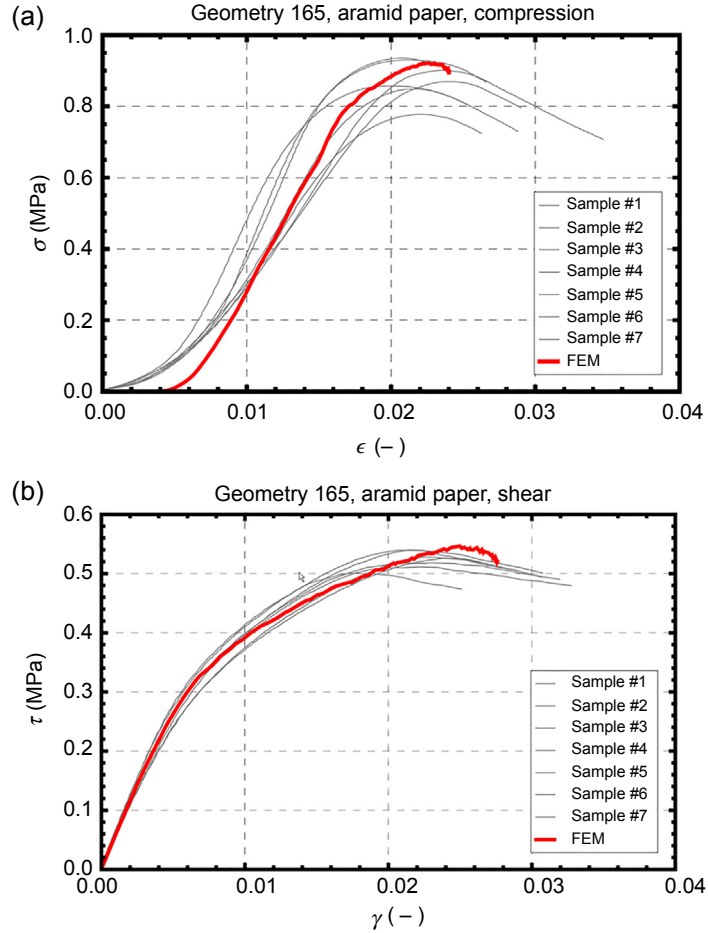

Figure 29.12 Comparison of type 165 foldcore stress−strain curves from test and simulation with refined FE model for determination of peak stresses. (a) Flatwise compression, (b) transverse shear (*W*-direction).

29.4.1.1 High-energy blunt impact tests

A drop tower impact test programme was carried out at the DLR on foldcore sandwich panels aramid/phenolic foldcore type 30 with a core thickness of 20 mm, core density of 138 kg/m^3, and carbon fibre-reinforced polymer (CFRP) skins. The CFRP skins consisted of 16 unidirectional (UD) epoxy plies of Cytech 977-2-35-12kHTS-134-300 with a quasi-isotropic layup $[45°/90°/-45°/0°/+45°/90°/-45°/0°]_s$ and laminate thickness of 1.8 mm. The sandwich plates with dimensions 300 × 300 × 24 mm were supported by corner clamps on a steel box section frame, giving test plate dimensions of 250 × 250 mm. Impact was at the centre of the plate upper face by a 23.6 kg impactor making contact through a 50-mm-diameter spherical indenter. One plate

Table 29.4 Stiffness and strength properties of Foldcore 165: Test data and refined FE model results

	Test			
	Minimum	**Maximum**	**Mean**	**FE model**
E_C [MPa]	42	99	74	76
σ_C [MPa]	0.78	0.93	0.86	0.91
G_L [MPa]	55	64	58	58
τ_L [MPa]	0.50	0.54	0.52	0.55
G_W [MPa]	60	103	72	65
τ_W [MPa]	0.62	0.69	0.65	0.71

was first tested up to ultimate penetration and failure by applying quasistatic constant velocity loads at 100 mm/min to the central indenter, from which it was possible to estimate energy levels for outer skin damage, core damage and complete penetration. These measured energy levels were then used to select impact velocities for the low-velocity (LV) impact tests to provide impact kinetic energies similar to the critical energies measured in the constant velocity test. In the drop tower tests, three impact velocities were selected in the range 2.21−5.77 m/s, with kinetic energy levels from 57.7 to 393.4 J, which provided information on different failure modes, ranging from rebound of the impactor at the upper skin to penetration of the core with high core energy absorption.

Contact force−time data were measured at the load cell attached to the indenter, and displacement−time of the cross-head was measured by an electromagnetic device in the drop tower frame. The impact process was recorded by a high-speed camera system. Internal structural damage in the sandwich cores was quantified by post-test CT scans. Full details of the impact test setup and results are reported in Kilchert et al. (2014). Table 29.5 summarises the quasistatic and impact test conditions, with observed damage from the CT scans in Figure 29.13. Measured load−deflection curves at the indenter are presented in Figure 29.14. The quasi-static (Q/S) loading test LV1 shows that the indenter fractures the outer CFRP skin, then crushes through the foldcore and penetrates the inner skin. The CT images show the failure zone is localised to a circle of about 80 mm diameter, with foldcore cells undamaged if they are about 10−15 mm away from the indenter position. Both inner and outer CFRP skins show significant delamination in the damage regions. The failure sequence is shown in the load−deflection curve for LV1 in Figure 29.14, with elastic penetration until outer skin fracture at about 9 mm deformation and 17 kN load, then extensive core crushing at a constant load of about 10 kN, followed by loading of the inner skin at about 20 mm deformation then increasing loads up to inner skin penetration at about 33 mm and 26 kN load. The absorbed energy data, Kilchert et al. (2014), indicate outer skin penetration at about 80 J and inner skin penetration at about 450 J.

Table 29.5 Overview of LV tests on type 30 foldcore sandwich plates

Shot number	Impactor	Mass [kg]	Velocity [m/s]	Impact energy [J]	Comments
FC-LV1	Steel indenter diam. 50 mm		100 mm/min	Max. 550 J	Quasistatic loading by indenter at 100 mm/min up to complete penetration at 50 mm and 550 J absorbed energy
FC-LV4	Steel ball diam. 50 mm	23.63	2.21	57.7	Impactor bounced off plate; some small damage on outer skin
FC-LV2	Steel ball diam. 50 mm	23.63	3.42	138.2	Indentation of outer surface; impactor rebounded; no core penetration, but some damage
FC-LV3	Steel ball diam. 50 mm	23.63	5.77	393.4	Indentation of outer surface and skin fracture; core penetration and damage; impactor stopped by inner skin

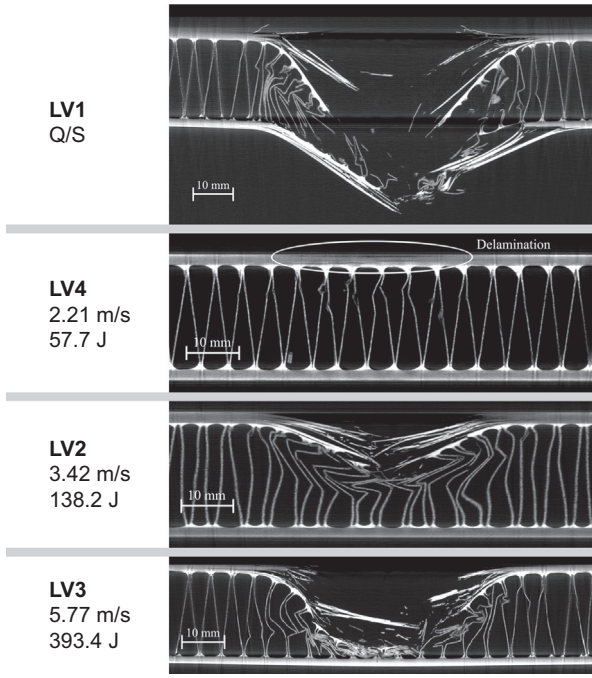

Figure 29.13 CT images of contact damage by the indenter in Q/S and LV impact tests on type 30 foldcore sandwich plates.

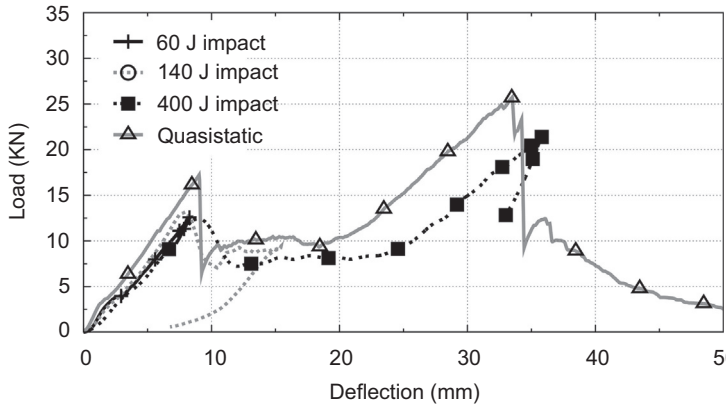

Figure 29.14 Load−deflection curves measured at the indenter in Q/S and LV impact tests on type 30 foldcore sandwich plates.

It is apparent that the failure modes of Q/S test are reproduced in the impact tests, dependent on the impact energies. In test LV4 with lowest impact velocity of 2.21 m/s and impact energy of 57.7 J, the impactor rebounds at about 9 mm displacement, causing some delamination damage to the outer skin and slight foldcore buckling, with no outer skin fracture. At impact velocity in LV2, 3.42 m/s, and 138.2 J, the outer skin is penetrated with some core crushing, followed by impactor rebound at about 15 mm displacement. In the higher velocity test LV3, 5.77 m/s, and 393.4 J, after outer skin penetration the core is crushed down completely under the impactor, which then loads the inner skin and is stopped by this at about 35 mm displacement, but the skin is not fractured, and the impactor slowly rebounds. These LV high-impact energy tests show that the type 30 foldcore provides excellent impact resistance in CFRP sandwich panels due to good core compression and shear stiffness, which provide a compact support for the skins, plus the excellent core crush characteristics. Because the failure sequence in the LV impact tests followed closely that observed in a simpler Q/S penetration test, it may be used in design of foldcore sandwich structures for estimating critical energy levels for skin damage and penetration.

29.4.1.2 High-velocity impact damage in foldcore sandwich panels

Foldcore sandwich panels were evaluated under HVI loads by a test series with the DLR gas gun. The cases reported here represent FOD from steel cubes, steel bars, and tyre rubber bars, at impact velocities in the range 40−125 m/s, which are representative of impacts occurring during takeoff and landing. The foldcore sandwich panels had the same foldcore type and CFRP skins as those used for the LV tests. In this case, the panel dimensions were 500 × 500 mm, with sandwich thickness of 24 mm. For HVI tests with these relatively small projectiles, the impact damage was localised to the impact position, allowing four or five impact tests per panel. An overview of the impact conditions and observed damage in the HVI tests is given in Table 29.6. No direct force−time pulses on the projectile were measured during the HVI experiments, because the projectile is in flight. Such measurements are usually only possible in the case of LV impacts where the indenter is instrumented with a load cell. For a qualitative comparison of experiment and simulation, the high-velocity video sequences of the impact event and after-impact CT scans are usually compared to simulation results.

The 12-mm steel cubes had a mass of 13.5 g with impact velocities normal to the panel in the range 55.6−109 m/s and kinetic energies of 20.9−79.0 J. Different failure modes were observed, dependent on impact velocity and projectile kinetic energy. Results for steel cubes in Table 29.6, with DLR data from other sharp-edged projectiles, indicated that up to 20-J impacts the projectile rebounds from the outer skin, with minor surface scratches. Skin perforation is in the range of 20−40 J, then at 45−80 J the projectile is stopped by the foldcore, which absorbs the impact energy by folding and fracture. Figure 29.15 shows in test HV1-1 that the steel cube with 45.2-J energy penetrated about halfway through the 20-mm-thick core, whereas in the lower velocity test, HV1-2 with 20.9 J, it rebounded from the outer skin, which

Table 29.6 Overview of HVI tests on type 30 foldcore sandwich plates

Shot number	Projectile shot angle	Mass [10^{-3} kg]	Velocity [m/s]	Impact energy [J]	Comments
FC-HV1-1	Steel cube 90°	13.5	81.8	45.2	Penetration of outer skin; impactor was stopped by foldcore; cube was stuck in core
FC-HV1-2	Steel cube 90°	13.5	55.6	20.9	Impactor rebounded from sandwich; outer skin damaged
FC-HV1-3	Steel cube 90°	13.3	99.5	66.8	Penetration of outer skin; cube was stuck in core; minor damage visible at inner skin
FC-HV1-5	Steel cube 90°	13.3	109.0	79.0	Penetration of outer skin; cube was stuck in core; visible crack at inner skin
FC-HV2-1	Steel bar 60°	101.7	86.3	372.0	Bar penetrated the sandwich plate
FC-HV2-2	Steel bar 60°	101.7	67.9	234.7	Bar penetrated the sandwich plate
FC-HV2-3	Steel bar 60°	101.7	39.3	78.7	Outer skin was penetrated; bar was stuck in core and rotated during penetration; no visible damage on inner skin
FC-HV3-1	Rubber bar 90°	103	105.0	568.1	No visible damage; surface deformed and yielded to pressure in a region 5 cm in diameter and 2 mm deep
FC-HV3-2	Rubber bar 90°	103	82.9	353.9	No visible damage; surface slightly deformed and yielded to pressure ($\sim$0.5 mm in depth)
FC-HV3-3	Rubber bar 90°	103	125.7	814.2	No visible damage; surface deformed and yielded to pressure in a region 6–7 cm in diameter and 3 mm deep

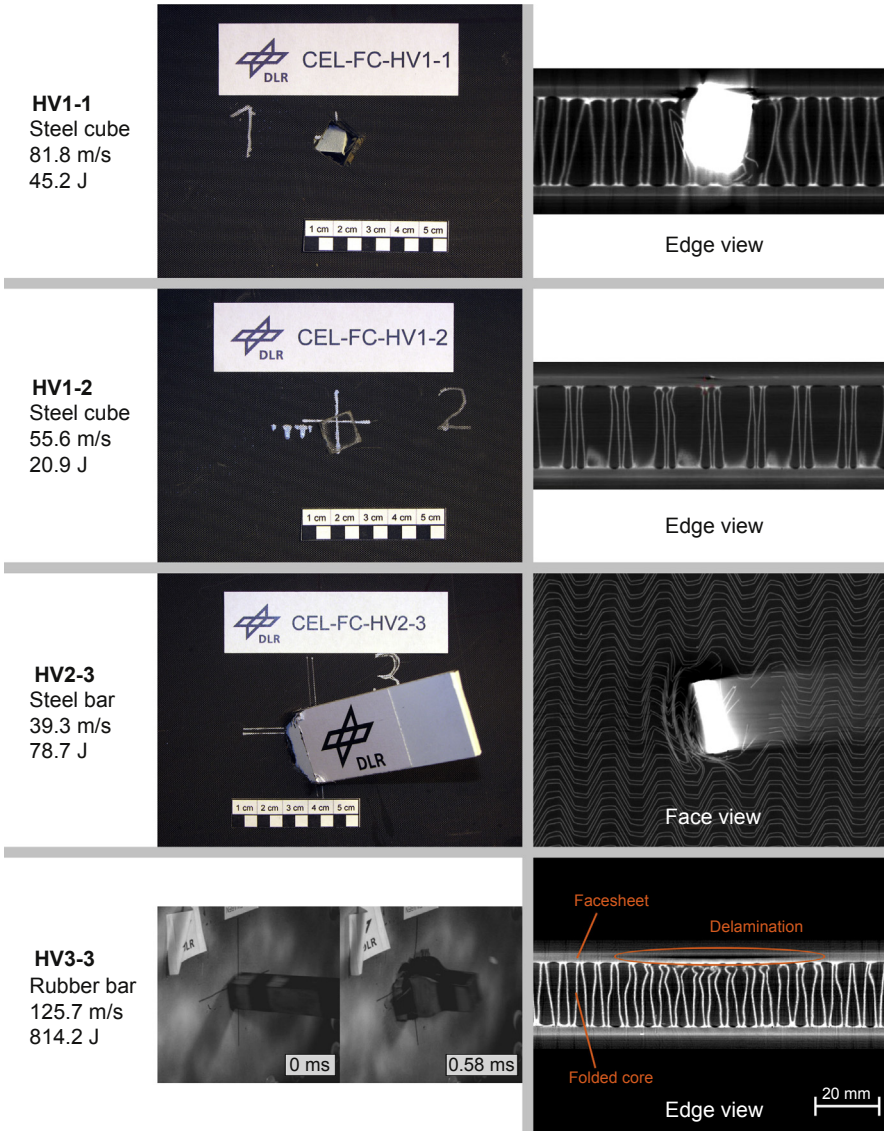

Figure 29.15 CT images of contact damage after HVI impact tests on type 30 foldcore sandwich plates.

had local delamination damage. For the foldcore sandwich studied here, hard body impacts above 80 J (>109 m/s for the 12-mm steel cube) would be required for complete penetration of the inner skin.

The steel bars were 109 × 30 × 4 mm in size, with a mass of 102 g, and impact tests were performed with a contact angle 60° to the plate surface. Table 29.6 indicates

that for test HV2-3 at the lowest impact velocity of 39.3 m/s (78.7 J), there was outer skin and core penetration, with the bar stopped by the inner skin, as seen in Figure 29.15. At higher impact velocities in test HV2-2 at 67.9 m/s, 234.7 J, and test HV2-1 at 86.3 m/s, 372 J, there was complete penetration of the sandwich specimen. It is interesting to note that in both the steel cube and steel beam tests the foldcore sandwich panel stopped the projectiles with energies up to 79 J, while higher energy impacts caused penetration.

The third test series HV3 used rubber beam projectiles with dimensions $132 \times 30 \times 25$ mm and mass of 103 g. They were shot end-on to the sandwich panel with a 90° impact angle. Impact velocities were in the range of 82.9−125.7 m/s, with high impact energies of 568.1−814.2 J. The response to the three tests was similar. High speed (HS) film showed that the rubber beam is deformed in axial compression on contact, followed by bending before it straightens up and rebounds at high velocity from the panel. Considering the high impact energy, there was little damage to the foldcore sandwich, with no visible damage to the composite skins. An imprint was visible in the contact region, and this contact area yields to finger pressure in a region of approximately 2 mm in depth and 5 cm in diameter, indicating a debonded skin/core interface. The CT scan of HV3-3 showed delamination of the outer skin at the contact position, with buckling damage to the foldcore structure.

Failure mechanisms in foldcore sandwich panels are similar to those reported on foam core and Nomex core sandwich panels, as discussed in the review articles of Abrate (1997, 1998). For the blunt impactors used here the foldcore provided considerable resistance to penetration, such that an LV steel indenter with 394.2 J energy was stopped by the sandwich plate. For the HVI gas gun impact tests failure modes are critically dependent on the projectile type, geometry, impact velocity and critical impact energies, as discussed in Christopherson, Mahinfalah, Nakhaie Jazar, and Rastgaar Aagaah (2005). In the tests here steel cubes and beams caused outer skin fracture with foldcore penetration: at lower energies projectiles could be stopped in the core, but above a critical energy there was complete penetration of the sandwich panels. An impact energy threshold of 80 J was measured at which 12-mm steel cubes were stopped in the core. Soft body impacts, in this case from rubber beams rebounded from the sandwich panels at high impact energies up to 814.2 J, causing outer skin delamination damage but no skin penetration. The foldcore sandwich panels showed good impact resistance for a range of different impact scenarios. An important feature of foldcore was demonstrated that core geometry and hence core impact resistance could be tailored to different impact threats: to provide high compression stiffness to support composite skins for blunt and soft body impacts, or with a denser core packing to prevent core penetration from small hard body projectiles.

29.4.2 FE models for sandwich impact behaviour

Design of aircraft sandwich panels with glass or carbon/epoxy skins and lightweight cores of polymer foam or Nomex® honeycomb are based on FE models composed typically of orthotropic composite shell elements bonded to solid elements with homogeneous core properties measured from core compression tests; see for example

Aktay, Johnson, and Holzapfel (2005), Buitrago, Santiuste, Sánchez-Sáez, Barbero, and Navarro (2010). This procedure is appropriate for design of sandwich panels under static loads, but is inadequate when core failure occurs under impact loads because homogenised core properties take no account of localisation effects in core failure. This is seen in impact test failure modes shown in Figures 29.13 and 29.15, in which core failure is initiated by foldcore buckling and folding away from the impact point. To correctly model core failures under impact, it is necessary to use detailed core micromodels, which include failure initialisation and progression. FE models for impact behaviour of foldcore sandwich structures discussed here use the baseline core micromodels developed and validated in Section 29.3, with composite skins modelled by shell elements attached to the core model through an adhesive interface.

Due to the observed skin damage, sandwich impact analysis requires FE models for the skin laminates that include damage, fracture and delamination failures. A mesoscale composite model is used in the work presented here, in which a composite laminate is modelled by layered shell elements. The shells are composed of composite plies assumed to be homogeneous orthotropic elastic or elastic−plastic damaging materials, the properties of which are degraded by microcracking prior to ultimate brittle failure. The ply properties assigned were based on a composite ply damage model for unidirectional (UD) composites with shear plasticity, Ladevèze and Le Dantec (1992), which was extended to fabric plies by Johnson, Pickett, and Rozycki (2001). The ply model introduces three scalar damage parameters, d_1, d_2 and d_{12}, which have values $0 \leq d_i \leq 1$ and represent modulus reductions under different loading conditions due to microdamage in the material. For UD plies, d_1 and d_2 are associated with damage or failure along and transverse to the fibres, and d_{12} is associated with in-plane shear damage. The ply model is completed by assuming damage evolution equations that have a specific form requiring additional parameters to be determined from specimen tests, as discussed further in Johnson (2005). For in-plane shear, ply deformations are controlled by matrix behaviour that may be inelastic, or irreversible, due to the presence of extensive matrix cracking or resin plasticity. On unloading, this can lead to permanent deformations in the ply. A plasticity model is included for the shear plasticity with an elastic domain function and hardening law, which requires additional cyclic shear tests for the plies to determine a power law plastic hardening function. Failure in the ply is controlled by fibre failure strains in tension or compression or by reaching ply shear failure as determined by the shear damage energy at failure.

Sandwich composite skin failures observed in impact tests show delamination in the carbon/epoxy skins in the LV impact tests, Figure 29.14, and as skin damage in the HVI tests with soft body rubber projectiles, Figure 29.15. The meso-scale FE models were extended in Johnson et al. (2001) and Greve and Pickett (2006) to include stacked shell elements for the composite laminate connected through cohesive interfaces to model delamination failure. This can be described as a 2.5D FE model, in which the stacked shell technique allows a composite laminate to split into plies or sublaminates when the cohesive interface fails and delamination occurs. The cohesive interface is controlled by an interface traction-displacement law such that interface contact is broken when the interface energy dissipated

reaches the mixed mode delamination energy criteria. The proposed delamination model is applied to model interface fracture between composite plies, in which measured fracture energies G_{IC} and G_{IIC} from through-thickness tension and shear tests on composite laminates with an interface crack are the main materials parameters required. The ply damage and failure models have been implemented in the commercial explicit crash and impact code PAM-CRASH^{TM} in collaboration with the software company Engineering Systems International. They have been tested and validated extensively for modelling impact damage in composite plate and stringer stiffened panel structures; see Johnson (2005), Johnson and Toso-Pentecôte (2008).

29.4.3 Validation of FE models for sandwich impact performance

The modelling procedures have recently been applied to foldcore sandwich panels with detailed validation studies on the high-energy LV impact test data reported in Section 29.4.1; see Kilchert (2013), Kilchert et al. (2014), Johnson, Toso-Pentecôte, and Kilchert (2013). These studies confirmed the suitability of the FE modelling techniques for LV impact on foldcore sandwich panels, showing good agreement with observed failure modes and measured energy absorption for a range of impact velocities. They will now be applied here to two HVI test cases from Table 29.6, with impact penetration by a steel bar impact (HV2-3) and high-energy impact from a rubber bar, causing rebound (HV3-3).

Figure 29.16 shows the FE model for steel beam impact on a foldcore sandwich panel, which represents test HV2-3. It shows the detailed foldcore model, CFRP skins, and the steel beam just before impact, which is modelled as a rigid body. A representative panel size was used based on 9 × 36 unit cells of type 30 foldcore elements. The foldcore and surface skins were modelled in PAM-CRASH by four-node Belytschko-Tsai shell elements with a four-ply layered shell model with damage and plasticity for the aramid paper. The CFRP composite skins of the sandwich were composed of 16 UD mesoscale plies with a quasi-isotropic layup, modelled here by four stacked shells of sublaminates with three cohesive interfaces to allow for possible delamination

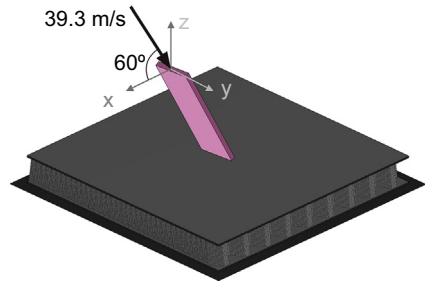

Figure 29.16 FE model of steel bar impact on type 30 foldcore sandwich panel.

failure. Materials tests at the DLR determined the UD carbon/epoxy ply properties required for the mesoscale damage and failure models; see Kilchert (2013), Kilchert et al. (2014). The foldcore and skins are connected by a contact interface using tied nodes with a linear penalty algorithm to prevent interpenetration. No damage and failure conditions are defined for the core−skin bond, because skin−core debonding was not seen to be significant in the tests. The number of shell elements in the complete model is about $4 \cdot 10^5$, with an average element length of 1.5 mm.

The numerical predictions obtained with the commercial code PAM-CRASH™ are now compared with experimental observations from the HV tests summarised in Section 29.4.1. The evaluation of the numerical model is based on a comparison of impact sequences with characteristic damage and failure modes, as no dynamic load or deformation response was measured during these HVI tests. As seen in Figure 29.15, the damage observed for hard body impacts from steel cubes and beams is localised and governed by facesheet failure, foldcore compaction and fracture. The extent of delamination predicted in the outer skin by the FE analysis was found to be small for this hard body impactor. These failure mechanisms are well represented in the detailed FE model, as seen in Figure 29.17 for the case of a steel bar impact (HV2-3) with impact velocity of 39.3 m/s and impact energy of 78.7 J.

Impact behaviour from experiment and simulation is in good agreement. In both cases, the steel beam projectile penetrated through the outer skin, crushed the foldcore, and was stopped by the inner skin on reaching the maximum penetration depth after about 2 ms. The numerical model captured the relevant damage characteristics with localised in-ply fracture in the facesheet. The foldcore was correctly predicted to densify and tear at the impactor, with moderate damage and permanent foldcore deformation in the surrounding region. Delamination was for both experiment and simulation negligible. The correct prediction of penetration is important, because different failure modes−undamaged sandwich, penetration of outer facesheet, core penetration, damage or penetration of inner facesheet−can be associated with specific magnitudes of projectile kinetic energy and energy absorption, which may then be related to structural safety requirements.

Rubber projectiles are highly deformable and require detailed modelling in impact simulations, as shown by Karagiozova and Mines (2007) and Toso-Pentecôte, Schwinn, and Johnson (2010). The rubber beam here was modelled by eight-node solid elements using a hyperelastic Mooney-Rivlin material model available in PAM-CRASH™. Suitable parameters for the rubber model are given in Kilchert (2013) based on tests on tyre rubber at the DLR. As shown here, delamination damage to the composite skins may occur under soft body impact. The sandwich plate model was generated with CFRP skins represented by four stacked shells of sublaminates with three cohesive interfaces to represent the delamination failure. In contrast to hard body impact, rubber projectiles spread out over the structure on impact. The damage observed for these soft body impacts is typically over a wide area and governed by face sheet delamination and foldcore buckling/collapse, with little or no skin penetration. The image sequence of a rubber beam impact HV3-3 with initial kinetic energy 814.2 J is presented in Figure 29.18 and compared with the numerical simulations. There is good agreement between measured and simulated deformation of the rubber

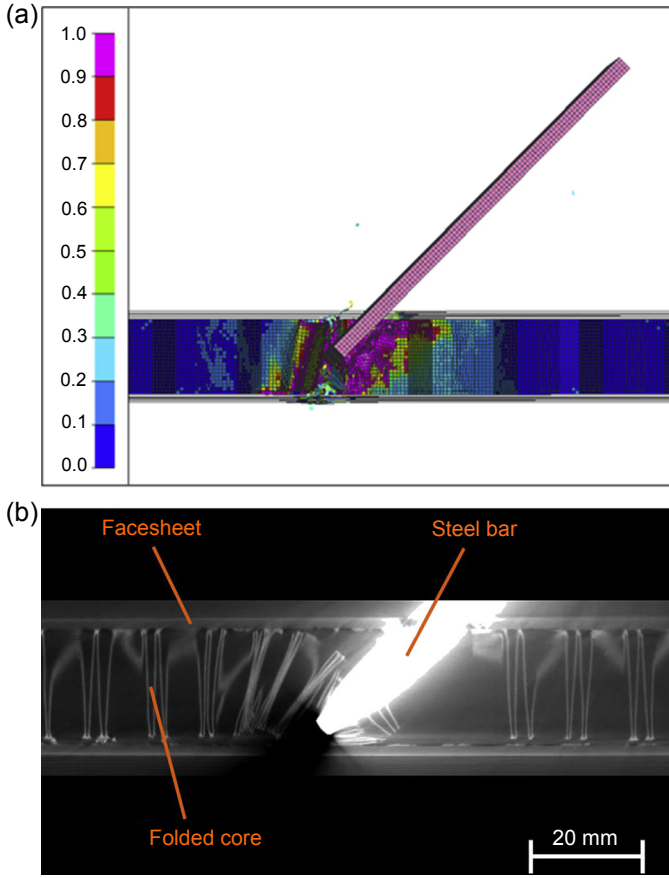

Figure 29.17 Comparison of damage in test and simulation for steel beam impact in test HV2-3 (78.7 J). (a) FE simulation of core damage, (b) CT scan of post-test damage.

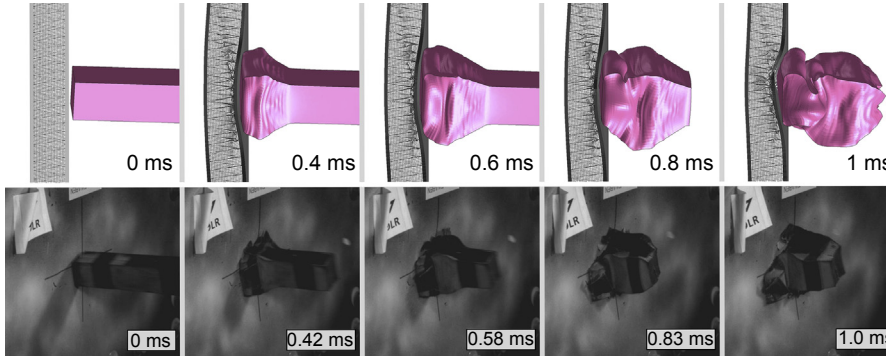

Figure 29.18 Comparison of impact sequence from numerical model (above) and HS film (below) for rubber impact in test HV3-3 (814.2 J).

beam and sandwich skin indentation. Both indicate significant axial compression of the rubber beam, which starts to rebound after about 0.8 ms. In both cases, the outer facesheet is deformed locally under the projectile, but is not penetrated. Figure 29.19(a) shows details of the numerical simulation at 0.8 ms, with local buckling and damage to the foldcore, which was able to resist the high-contact forces from the impact and supported the composite skin without collapsing. Figure 29.19(b) shows the delamination damage parameter contours in the upper skin laminate, with the predicted delamination area being of similar size to the delamination zone observed in the test.

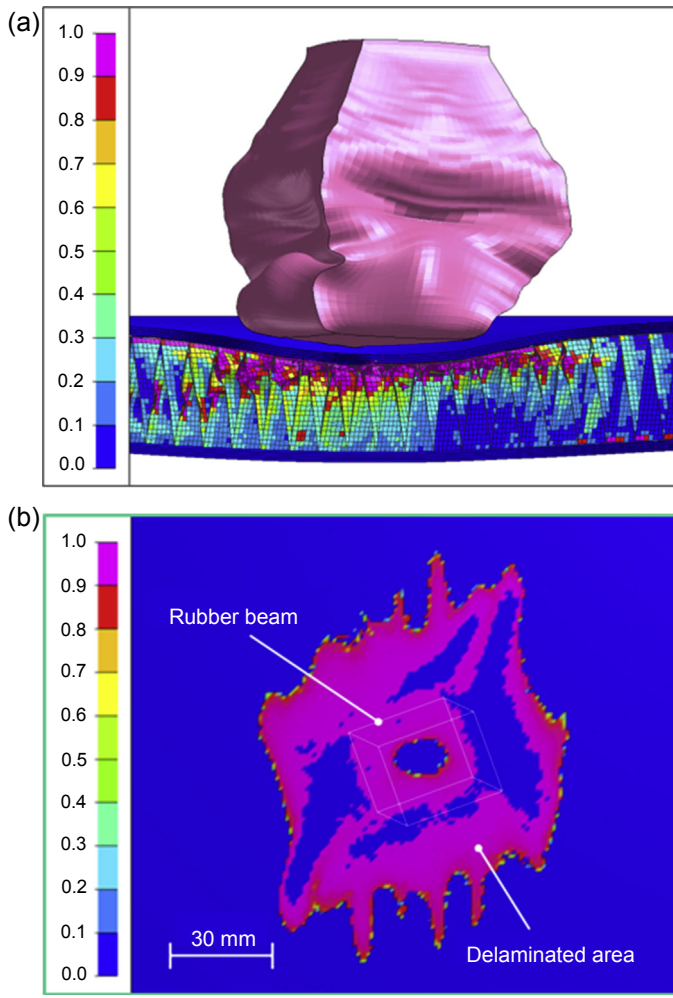

Figure 29.19 FE simulation of damage after rubber beam impact in test HV3-3 (814.2 J). (a) Damage parameter in foldcore, (b) delamination zone in composite face skin.

In conclusion, the detailed studies of LV impact and HVI damage from steel cubes, beams and spherical indenters in a range of foldcore sandwich panels showed good agreement between impact penetration sequence and resulting postimpact damage, when compared to HS films from the test and CT images of the damaged sandwich plates. Impact modelling was based on the simpler fine scale core micromodels discussed in Section 29.3, with a fixed unit cell geometry and defects modelled by node shaking. The core model was attached through a contact interface to layered shell composite skins or stacked shells with cohesive interfaces when delamination was significant. These models tended to overestimate impact damage, showing that the models are conservative for design of sandwich structures. In addition to the influence of delamination damage, it should be noted that in tests frictional forces during foldcore compaction and in composite debris are very important in slowing down and stopping impactors. As reported in Kilchert et al. (2014), an energy balance analysis derived from the simulation of the LV rebound test LV-2 showed that at rebound when the impactor was stopped, energy absorbed by friction in the model was about 25%, with a further 40% absorbed by deformation and failure in the foldcore. Friction parameters required in the models for self-contact between foldcore shell elements and contact between steel projectiles and composite facesheets or aramid paper were determined by Coulomb friction tests. However, the shell models used cannot accurately describe foldcore compaction and damaged skin material after impact, which slow the impactor down and would explain why predicted damage was greater than that observed in tests. Further improvements to the impact model could use the refined foldcore models of Section 29.3 for the adhesive bonds and the influence of the folded edge defects, which would allow more accurate simulation of initial impactor penetration, at the expense of increased complexity in the FE model and its input data requirements.

29.5 Conclusions and outlook

29.5.1 Modelling and simulation methods

This chapter has focused on novel sandwich structures with composite cores from foldcore, a cellular core made from phenolic resin impregnated aramid paper manufactured at IFB Univerity Stuttgart using origami folding principals. Focus was on microscale modelling for the foldcore structures and applying these to develop FE methods for the analysis and design of advanced sandwich structures under impact loads. This was supported by quasistatic and both LV impact and HVI tests on foldcore sandwich panels to assess performance and to validate the analysis methods. The numerical simulation methods developed for prediction of impact damage in foldcore sandwich composite panels were based on fine-scale core micromodels attached to layered shell composite skins through contact interfaces. A baseline unit cell model was used to generate a complete fold core FE mesh, with imperfections included by a node perturbation procedure. New models were developed for the aramid paper based on a three-ply structure of central fibre mat with phenolic surface layers. Refinements to the

baseline impact modelling procedures were examined for CFRP skin laminates by the use of ply damage models in a stacked shell laminate model with cohesive interfaces to model delamination in the skins, which was observed in tests. The baseline impact model was validated by careful comparison with test results on damage, failure and energy absorbed. An important conclusion was the role of composite skins in impact where correct skin material modelling should include in-ply damage and delamination failure. If no interlaminar failure is included in the model, more energy is absorbed by intralaminar failure, which leads to a higher number of eliminated elements and to a deeper penetration of the impactor and more core damage. If the skin behaviour is not correctly represented, then the sandwich structure failure is different to that in the simulation.

Refinements to the foldcore model were considered that used actual foldcore geometry with defects, considered the influence of the folded seam damage arising from manufacture, and developed methods to model the influence of adhesive bondlines at the foldcore/skin interface. These were successfully applied to improve the accuracy of foldcore flatwise compression and transverse shear strength calculations, important for design of sandwich structures. In the future, these refinements could be integrated into the baseline impact models; however, this will lead to unacceptably large FE models for a sandwich structure and require more detailed materials information, such as the exact geometrical deviations in cell geometry and size of the adhesive bond lines. An alternative could be stochastic analyses in which core deviations in geometry, thickness, and variability in aramid paper and composite ply properties are introduced into the models through distribution functions rather than exact measurements of defects.

The current baseline FE model for impact uses elements typically 1 mm in size, because core microbuckling is initiated at these length scales. It follows that impact simulations of large aircraft sandwich structures are currently not feasible with such detailed micromodels. Current analysis methods for sandwich structures use large homogenised solid elements in the core for structural analysis, but these are unsuitable for predicting impact damage in which failure initiation is nonlocal. In future developments, multimodel coupling techniques are urgently required that couple microscale core models at impact damage locations with homogeneous solid core elements away from damage. In this way, it is possible to use refined models in critical regions for damage initiation, with large-scale elastic models in the remainder of the structure.

29.5.1.1 Structural concepts

It has been demonstrated here and in the CELPACT project that foldcore sandwich structures with aramid paper cores are highly suited for use in aircraft applications in which impact loads are critical. However, the additional complexity of manufacture, advanced analysis methods and cost factors make it difficult to compete directly with established core materials such as Nomex® in aircraft sandwich structures. Future developments with alternative foldcore sandwich concepts with low-cost thermoplastic cores and skins could be promising for automotive structures. Besides being a replacement for established foam and honeycomb core materials, foldcore offers

additional multifunctional properties for cores in other technology fields. Multifunctional structural aspects for sandwich structures that include filtration, fluid transport, heat exchange, sound deadening and structural stability are all feasible.

An example in which a demonstrator structure has been successfully manufactured and tested is the concept of variable geometry foldcore for control of failure modes in sandwich structures, by triggering failure initiation. The concept is to change the core density inside a sandwich material by a change of unit cell geometry inside the panel. This is achieved, for example, by a change in the geometry parameter L or S_{CW} in the unit cell. The foldcore structure is still produced in one continuous process. As shown in Table 29.1, core density is closely linked to stiffness and strength of the core, so that local core reinforcement or weakening is possible. This has been used as a trigger-mechanism to control the failure of a sandwich structure in an aircraft fuselage side wall under crash conditions, as shown in Sturm, Klett, Kindervater, and Voggenreiter (2014). In this case, a middle region of the side panel had a lower density foldcore, which initiated bending failures under vertical fuselage crash loads and provided an energy-absorbing structural hinge. In this case study, foldcore is seen as a promising future sandwich core structure not just a replacement for existing core materials.

29.6 Further reading

The chapter has focused on design, analysis and impact behaviour of sandwich structures with carbon epoxy skins and foldcore, a novel core manufactured by folding aramid mat/phenolic paper into lightweight open cellular structures. Space did not allow the review of alternative sandwich materials with comparative properties or other approaches to modelling structural behaviour and determining impact resistance, which is left for further reading. For detailed information on impact behaviour of composites and particularly sandwich structures, the reader is referred to the work of Abrate (1997, 1998) and Abrate et al. (2013). The latter book has an excellent chapter by Heimbs (2013) that gives a detailed review of sandwich materials, focusing particularly on folded cores from KSTU made from aramid and carbon fabric-reinforced plastics. Further information on the manufacture and properties of these materials is given in Zakirov et al. (2005, 2006). For aircraft sandwich structures, the established core is Nomex® honeycomb, which is included in the reviews by Abrate. Further information on LV impact and HVI performance of honeycomb cores can be found in Anderson and Madenci (2000) and Dear, Lee, and Brown (2005).

Acknowledgements

The work was carried out and part funded in the European Union CELPACT Project within the EC Sixth Framework Programme (contract AST5-CT-2006-031038, 2006−2009). The authors gratefully acknowledge the EC funding of the research activities and scientific contributions from the CELPACT partners.

Two of the authors (A.F. Johnson, S. Kilchert) carried out much of the work presented here while at the German Aerospace Center (DLR), Institute of Structures and Design, Stuttgart. They wish to acknowledge the support of the DLR and in particular give sincere thanks to their colleagues H. Kraft, A. Reiter and H. Abu El-Hija for assistance with mechanical testing and R. Jemmali for the CT images. S. Fischer would like to thank his colleagues at IFB, University Stuttgart, in particular Y. Klett for his help in design and production of samples and M. Grzeschik for his assistance in mechanical testing. Sincere thanks also go to R. Kehrle and K. Drechsler for valuable discussions about the research.

References

Abrate, S. (1997). Localized impact on sandwich structures with laminated facings. *Applied Mechanics Reviews, 50*(2), 69−82.

Abrate, S. (1998). *Impact on composite structures*. Cambridge University Press.

Abrate, S., Castanié, B., & Rahapakse, Y. D. S. (Eds.). (2013). *Dynamic failure of composite and sandwich structures*. Springer.

Aktay, L., Johnson, A. F., & Holzapfel, M. (2005). Prediction of impact damage on sandwich composite panels. *Computational Materials Science, 32*, 252−260.

Anderson, T., & Madenci, E. (2000). Experimental investigation of low-velocity impact characteristics of sandwich composites. *Composite Structures, 50*(3), 239−247.

ASTM C273/C273M-11A. (2011). *Standard test method for shear properties of sandwich core materials*. West Conshohocken, PA: ASTM International. www.astm.org.

ASTM C365/C365M-11. (2011). *Standard test method for flatwise compressive properties of sandwich cores*. West Conshohocken, PA: ASTM International. www.astm.org.

Baranger, E., Cluzel, C., Winterberger, D., Klaus, M., Fischer, S., Kilchert, S., et al. (2008). CELPACT D31−2: baseline composite and CHC core properties. In *Cellular structures for impact performance (CELPACT), contract no.: FP6-031038. Sixth framework programme FP6-2005-Aero-1, 2008*.

Bitzer, T. (1997). *Honeycomb technology, materials, design, manufacturing, applications and testing*. Chapman & Hall.

Buitrago, B. L., Santiuste, C., Sánchez-Sáez, S., Barbero, E., & Navarro, C. (2010). Modelling of composite sandwich structures with honeycomb core subjected to high-velocity impact. *Composite Structures, 92*(9), 2090−2096.

CELPACT. (2009). Cellular structures for impact performance. In *EU Research Project, FP6−031038, 2006−2009*.

Christopherson, J., Mahinfalah, M., Nakhaie Jazar, G., & Rastgaar Aagaah, M. (2005). An investigation on the effect of a small mass impact on sandwich composite plates. *Composite Structures, 67*(3), 299−306.

Dear, J. P., Lee, H., & Brown, S. A. (2005). Impact damage processes in composite sheet and sandwich honeycomb materials. *International Journal of Impact Engineering, 32*, 130−154.

EMIR. (2003). Engineering mehrfunktionaler Integralstrukturen CfK-Rumpf. In *LuFo III (German National Aeronautics Research Project), BMBF, 2003−2007*.

Fischer. S. (2012). *Numerische Simulation der mechanischen Eigenschaften von Faltkern-Sandwichstrukturen* (Ph.D. thesis). Institute of Aircraft Design, University of Stuttgart, ISBN 978344012583.

Fischer, S., & Drechsler, K. (2008). Aluminium foldcores for sandwich structure application. In *CELLMET, Dresden, Germany*.

Fischer, S., & Drechsler, K. (2011). Aluminium Faltkerne für den Einsatz in Sandwichstrukturen. In *Landshuter Leichtbau-Colloquium, Landshut, Germany*.

Fischer, S., Drechsler, K., Kilchert, S., & Johnson, A. F. (2009). Mechanical tests for foldcore base material properties. *Composites Part A: Applied Science and Manufacturing, 40*(12), 1941−1952.

Fischer, S., Heimbs, S., Kilchert, S., Klaus, M., & Cluzel, C. (2009). Sandwich structures with folded core: manufacturing and mechanical behaviour. In *SAMPE Europe 30th Int Techn Conf, Paris*.

Greve, L., & Pickett, A. K. (2006). Delamination testing and modelling for composite crash simulation. *Composites Science and Technology, 66*, 816−826.

Grzeschik, M., Fach, M., Fischer, S., Klett, Y., Kehrle, R., & Drechsler, K. (2000). Isometrically folded high performance core materials. Paper 76. In *Proc and fabr of advanced materials (PFAM)XIX, Auckland, New Zealand*.

Hachenberg, D., Mudra, C., & Nguyen, M. (2003). Folded structures—an alternative sandwich core material for future aircraft concepts. In *Deutscher Luft- und Raumfahrt Kongress, München*.

Heimbs, S. (2013). Foldcore sandwich structures and their impact behaviour: an overview. In S. Abrate, B. Castanié, & Y. D. S. Rahapakse (Eds.), *Dynamic failure of composite and sandwich structures*. Springer.

Heimbs, S., Cichosz, J., Klaus, M., Kilchert, S., & Johnson, A. F. (2010). Sandwich structures with textile-reinforced composite foldcores under impact loads. *Composite Structures, 92*, 1485−1497.

Heimbs, S., Middendorf, P., Hampf, C., Hähnel, F., & Wolf, K. (2009). Aircraft sandwich structures with folded core under impact load. *Composite Solutions Aero & Space, 3*, 7−13.

Heimbs, S., Middendorf, P., Kilchert, S., Johnson, A. F., & Maier, M. (2007). Experimental and numerical analysis of composite folded sandwich core structures under compression. *Applied Composite Materials, 14*, 363−377.

Johnson, A. F. (2005). Modelling impact damage in composite structural elements. In P. Beaumont, & C. Soutis (Eds.), *Multiscale modelling of composite materials and systems*. Cambridge: Woodhead.

Johnson, A. F., Pickett, A. K., & Rozycki, P. (2001). Computational methods for predicting impact damage in composite structures. *Composites Science and Technology, 61*, 2183−2192.

Johnson, A. F., & Toso-Pentecôte, N. (2008). Determination of delamination damage in composites under impact loads. In S. Sridharan (Ed.), *Delamination behaviour of composites*. Cambridge: Woodhead.

Johnson, A. F., Toso-Pentecôte, N., & Kilchert, S. (2013). Validation of damage modeling in composite fuselage structures under high velocity impact. *CEAS Aeronautical Journal, 4*(3), 253−264.

Karagiozova, D., & Mines, R. A. W. (2007). Impact of aircraft rubber tyre fragments on aluminium alloy plates: II−numerical simulation using LS-DYNA. *International Journal of Impact Engineering, 34*(4), 647−667.

Kehrle, R., & Drechsler, K. (2004). Manufacturing of folded core-structures for technical applications. In *Proc of the 25th Int SAMPE Europe Conference, Paris* (pp. 508−513).

Kehrle, R., & Kolax, M. (2006). Sandwich structures for advanced next generation fuselage concepts. In *SAMPE Europe Technical Conference, Toulouse, September 2006*.

Kilchert. S. (2013). *Nonlinear FE modeling of degradation and failure in folded core composite sandwich structures* (Ph.D. thesis). Institute of Aircraft Design, University of Stuttgart, ISRN DLR-FB−; 2013−22.

Kilchert, S., Johnson, A. F., & Voggenreiter, H. (2008). Finite element modelling of phenolic resin impregnated aramid paper adopted in foldcore sandwich structures. In *Proc of the 9th Int Conf on Computational Structures Technology, Athens* (p. 316).

Kilchert, S., Johnson, A. F., & Voggenreiter, H. (2014). Modelling the impact behavior of sandwich structures with folded composite cores. *Composites Part A, 57*, 16−26.

Klett. Y. (2013). *Auslegung multifunktionaler isometrischer Faltstrukturen für den technischen Einsatz* (Ph.D. thesis). University of Stuttgart, ISBN 978−3843910255.

Ladevèze, P., & Le Dantec, E. (1992). Damage modelling of the elementary ply for laminated composites. *Composites Science and Technology, 43*, 257−267.

Miura, K. (1972). *Zeta core sandwich—its concept and realization*. Report 480. Inst of Space and Aeronautical Science, University of Tokyo, 137−164.

PAM-CRASH™ FE Code, Engineering systems International, F-94513 Rungis Cedex, France.

Sturm, R., Klett, Y., Kindervater, C., & Voggenreiter, H. (2014). Failure of CFRP airframe sandwich panels under crash-relevant loading conditions. *Composite Structures, 112*, 11−21.

Toso-Pentecôte, N., Schwinn, D., & Johnson, A. F. (2010). Modelling and simulation of tyre impacts on stiffened composite panels. In *SAMPE Europe 31st Int. Tech. Conf., SEICO 10, Paris*.

Zakirov, I. M., Nikitin, A., Akishev, N., Rückert, C., & Mudra, C. (2005). Technology research and equipment development for fabrication of folded structure sandwich core from new material. In *SAMPE Europe Int Conf, Paris* (pp. 429−434).

Zakirov, I. M., Nikitin, A., Alexeev, K., & Mudra, C. (2006). Folded structures: performance, technology and production. In *SAMPE Europe Int Conf, Paris* (pp. 234−239).

Index

Note: Page numbers followed by “b”, “f” and “t” indicate boxes, figures and tables respectively.